

# Handbook of Heterogeneous Catalysis

**Volume 3**

Edited by

G. Ertl, H. Knözinger, J. Weitkamp

# Contents

<b>1</b>	<b>Introduction</b>	<b>1</b>			
1.1	Principles of Heterogeneous Catalysis	1			
1.1.1	Introduction	1			
1.1.2	Catalytic Cycle	1			
1.1.3	Kinetic Steady State	2			
1.1.4	Microscopic Reversibility	2			
1.1.5	Principle of Sabatier	3			
1.1.6	Active Sites and Catalyst Modifiers	5			
1.1.6.1	Ideal Surfaces	5			
1.1.6.2	Real Surfaces	5			
1.1.6.3	Catalyst Modifiers	6			
1.1.7	Catalyst Life Cycle	7			
1.1.7.1	Preparation	7			
1.1.7.2	Activation	8			
1.1.7.3	Reconstruction	8			
1.1.7.4	Deactivation	8			
1.1.7.5	Regeneration	9			
1.1.7.6	Decommission	9			
1.1.8	Tradeoffs	9			
1.1.8.1	Activity and Selectivity	10			
1.1.8.2	Accessibility	10			
1.1.8.3	Activity, Selectivity, Stability, and Accessibility	11			
1.1.9	Principles of Assisted Catalyst Design	11			
1.2	Development of the Science of Catalysis	13			
1.2.1	Early Concepts: Berzelius, Liebig, Faraday	13			
1.2.2	Wilhelm Ostwald	17			
1.2.3	The Concepts of Kinetics and Intermediate Compounds	18			
1.2.4	Negative Catalysis – Autocatalysis	22			
1.2.5	Adsorption	22			
1.2.6	Active Site – Geometric or Electronic?	24			
1.2.7	Selected Systems	27			
1.2.7.1	Ammonia Synthesis	27			
1.2.7.2	Acid Catalysis	28			
1.2.7.3	Zeolites	29			
1.2.7.4	Ions in Catalysis	29			
1.2.7.5	Hydrogenation	30			
1.2.7.6	Oxidation	32			
1.2.8	Summary	33			
1.3	Development of Industrial Catalysis	35			
1.3.1	Introduction	35			
1.3.2	The Period from 1910 to 1938	36			
1.3.3	The Period from 1938 to 1965	37			
1.3.3.1	Catalytic Cracking	38			
1.3.3.2	Catalytic Alkylation	40			
1.3.3.3	Catalytic Dehydrogenation and Catalytic Reforming	40			
1.3.3.4	Hydrogenation and Hydrodesulfurization	41			
1.3.3.5	Hydrocracking	41			
1.3.3.6	Dehydrogenation	41			
1.3.3.7	Isomerization	42			
1.3.3.8	Oxidation	42			
1.3.3.9	Polymerization	43			
1.3.3.10	Zeolites	43			
1.3.4	The Period from 1965 to 1990	44			
1.3.4.1	Shape Selectivity	44			
1.3.4.2	Environmental Catalysis	44			
1.3.4.3	Other Industrial Applications of Catalysis	47			
<b>2</b>	<b>Preparation of Solid Catalysts</b>	<b>49</b>			
2.0	Developing Industrial Catalysts	49			
2.0.1	Properties and Characteristics of Industrial Catalysts	49			
2.0.1.1	Activity	49			
2.0.1.2	Selectivity	49			
2.0.1.3	Stability	49			
2.0.1.4	Morphology	50			
2.0.1.5	Mechanical Strength	50			
2.0.1.6	Thermal Characteristics	50			
2.0.1.7	Regenerability	50			
2.0.1.8	Reproducibility	50			
2.0.1.9	Originality	51			
2.0.1.10	Cost	51			
2.0.2	The Ideal Catalyst and the Optimum Catalyst	51			
2.0.3	Catalyst Development	51			
2.0.3.1	Devising the First Catalytic Formulas	52			
2.0.3.2	Optimization of a Typical Catalytic Formula	53			
2.1	Bulk Catalysts and Supports	54			
2.1.1	Fused Catalysts	54			
2.1.1.1	Introduction	54			
2.1.1.2	Concept of Fused Catalysts	54			
2.1.1.3	Thermodynamic and Kinetic Considerations	57			
2.1.1.4	Sulfuric Acid Catalyst	59			
2.1.1.5	Metallic Glasses	60			
2.1.1.6	Mesostructure of Fused Catalyst Materials	63			
2.1.2	Skeletal Metal Catalysts	64			
2.1.2.1	Introduction	64			
2.1.2.2	General Aspects	64			
2.1.2.3	Skeletal Nickel Catalysts	66			
2.1.2.4	Promoted Skeletal Nickel Catalysts	67			

2.1.2.5	Skeletal Cobalt Catalysts	67	2.1.9.9	Carbon on Noble-Metal Catalysts	152
2.1.2.6	Skeletal Copper Catalysts	67	2.1.9.10	Carbon Formation in Zeolites	153
2.1.2.7	Promoted Skeletal Copper Catalysts	69	2.1.9.11	Graphitization of Carbons	155
2.1.2.8	Skeletal Copper-Zinc Catalysts	69	2.1.9.12	Reaction of Oxygen with Carbon	156
2.1.3	Precipitation and Coprecipitation	72	2.1.9.13	Surface Chemistry of Carbon	161
2.1.3.1	Introduction	72	2.1.9.14	Non-Oxygen Heteroelements on Carbon Surfaces	163
2.1.3.2	General Principles Governing Precipitation from Solutions	73	2.1.9.15	Surface Oxygen Groups	165
2.1.3.3	Influencing the Properties of the Final Product	77	2.1.9.16	Carbon as Catalyst Support	177
2.1.3.4	Prototypical Examples of Precipitated Catalysts and Supports	80	2.1.9.17	Carbon as Catalyst	181
2.1.4	Sol-Gel Process	86	2.1.9.18	Case Studies of Catalytic Applications	182
2.1.4.1	Introduction	86	2.1.9.19	Catalytic Removal of NO by Carbon	183
2.1.4.2	Important Parameters in Sol-Gel Preparation	86	2.1.9.20	Removal of Carbon Deposits From Catalyst Materials	184
2.1.4.3	Advantages of Sol-Gel Preparation	89	2.1.9.21	Activation of Oxygen on Carbon Surfaces	185
2.1.4.4	Catalytic Membranes	93	2.1.9.22	Conclusions	188
2.1.4.5	Other Sol-Gel Materials	93	2.2	Supported Catalysts	191
2.1.4.6	Summary	93	2.2.1	Deposition of Active Component	191
2.1.5	Flame Hydrolysis	94	2.2.1.1	Impregnation and Ion Exchange	191
2.1.5.1	Manufacture	94	2.2.1.2	Anchoring and Grafting of Coordination Metal Complexes onto Oxide Surfaces	207
2.1.5.2	Physicochemical Properties of Fumed Oxides	95	2.2.1.3	Spreading and Wetting	216
2.1.5.3	Preparation of Formed Supports	98	2.2.1.4	Heterogenization of Complexes and Enzymes	231
2.1.5.4	Applications	99	2.2.1.5	Preparation of Supported Catalysts by Deposition-Precipitation	240
2.1.6	Solid-State Reactions	100	2.2.1.6	Redox Methods for Preparation of Bimetallic Catalysts	257
2.1.6.1	Why Solid-State Reactions?	100	2.2.2	Formation of Final Catalysts	264
2.1.6.2	Description of Preparative Methods	105	2.2.2.0	Introduction and Background	264
2.1.6.3	Conclusions and Prospects	117	2.2.2.1	Activation of Supported Catalysts by Calcination	271
2.1.7	Heteropoly Compounds	118	2.2.2.2	Activation of Supported Catalysts by Reduction	273
2.1.7.1	Structure and Catalytic Properties	118	2.2.2.3	Reduction-Sulfidation	278
2.1.7.2	Heteropolyacids - Acid Forms in Solid State and in Solution	119	2.2.2.4	Other Methods of Activation	282
2.1.7.3	Salts of Heteropolyacids - Cation-Exchanged Forms	123	2.2.2.5	Conclusions	283
2.1.7.4	Mixed-Coordinated Heteropoly Compounds	125	2.3	Zeolites and Related Molecular Sieves	286
2.1.7.5	Metal-Coordinated Heteropolyanions	126	2.3.1	A Synoptic Guide to the Structures of Zeolitic and Related Solid Catalysts	286
2.1.7.6	Heteropolyanions Intercalated in Layered Double Hydroxides	128	2.3.1.1	Introduction	286
2.1.7.7	Supported Heteropoly Compounds	128	2.3.1.2	Framework Density, Nomenclature and Secondary Building Units	287
2.1.8	High-Surface Transition Metal Carbides and Nitrides	132	2.3.1.3	Microporous Solids as Catalysts	290
2.1.8.1	General Properties of Transition Metal Carbides and Nitrides	132	2.3.1.4	Survey of Zeolitic and Related Catalysts	290
2.1.8.2	Thermodynamic Considerations in the Preparation of Carbides and Nitrides	132	2.3.1.5	Mesoporous Solids as Catalysts	308
2.1.8.3	Survey of Preparative Methods	134	2.3.2	Hydrothermal Zeolite Synthesis	311
2.1.9	Carbons	138	2.3.2.1	Introduction	311
2.1.9.1	Introduction	138	2.3.2.2	Zeolitization in General	311
2.1.9.2	Structural Chemistry of Carbon	138	2.3.2.3	Synthesis of Industrial Zeolites	321
2.1.9.3	Overview	139	2.3.3	Acidity and Basicity in Zeolites	324
2.1.9.4	Basic Structures	140	2.3.3.1	Introduction	324
2.1.9.5	Loosely Defined Structures	142	2.3.3.2	Experimental Methods for Identification and Quantification of Acid and Base Sites in Zeolites	324
2.1.9.6	Formation of Carbon Materials, General Pathways	148	2.3.3.3	Acid Properties of Aluminosilicate-Type Zeolites	329
2.1.9.7	Formation of Carbon Materials, Mechanistic Aspects	149	2.3.3.4	Acid Properties of Metallosilicates	340
2.1.9.8	Catalytic Formation of Carbon from Molecules	151	2.3.3.5	Acid Properties of Phosphate-Based Zeolites	343

2.3.3.6	Basicity of Zeolites	354	2.4.1.1	Preparative Methods	404
2.3.4	Metal Clusters in Zeolites	365	2.4.1.2	Morphology and Surface Properties	405
2.3.4.1	Introduction	365	2.4.1.3	Structure of Superacid Sites	407
2.3.4.2	Metal Clusters Versus Macroscopic Metals	365	2.4.1.4	Catalytic Properties	408
2.3.4.3	Preparation of Mono- or Bimetallic Clusters in Zeolites	366	2.4.2	Other Solid Superacids	410
2.3.4.4	Interaction of Metal Clusters and Zeolite Protons	367	2.5	Catalyst Forming	412
2.3.4.5	Effects of Zeolite Geometry on Catalysis	371	2.5.1	Forming Microgranules	412
2.3.5	Zeolite-Entrapped Metal Complexes	374	2.5.2	Forming Granules	414
2.3.5.1	Synthesis of Zeolite-Entrapped Metal Complexes	374	2.5.2.1	Pelletizing	414
2.3.5.2	Characterization	378	2.5.2.2	Extrusion	416
2.3.5.3	Catalysis by Zeolite-Entrapped Transition Metal Complexes	382	2.5.2.3	Pan Granulation	416
2.3.6	Pillared Clays	387	2.5.2.4	Miscellaneous Forming Operations	417
2.3.6.1	Introduction	387	2.5.3	Organizing a Catalyst-Manufacturing Process	417
2.3.6.2	Pillars	390	2.6	Computer-Aided Catalyst Design	419
2.3.6.3	Pillared Clays	393	2.6.1	Introduction	419
2.3.6.4	Catalytic Properties	400	2.6.2	Heuristics in Catalyst Design	420
2.3.6.5	Conclusions	402	2.6.2.1	Knowledge-Based Systems	421
2.4	Solid Superacids	404	2.6.2.2	Neural Networks	423
2.4.1	Sulfate-Treated Metal Oxides, Mixed Oxides, and Those Modified with Platinum	404	2.6.3	Deterministic Methods in Catalyst Design	424
			2.6.4	Chemical Reaction Engineering Aspects	
			2.6.5	Conclusions	425

# Contents

<b>5</b>	<b>Elementary Steps and Mechanisms</b>	<b>911</b>			
5.1	Chemisorption	911	5.2.4.3	Transition Metal Surface Chemistry	994
5.1.1	Principles of Chemisorption	911	5.2.4.4	Transition Metal Sulfide Catalyzed Desulfurization	1000
5.1.1.1	Introduction	911	5.2.4.5	Reactivity of Oxidic Surfaces	1001
5.1.1.2	Thermodynamics and Energetics	912	5.2.4.6	Conclusions	1004
5.1.1.3	Sticking	921	5.2.5	Isotopic Labeling and Kinetic Isotope Effects	1005
5.1.1.4	Surface Diffusion	926	5.2.5.1	Introduction	1005
5.1.1.5	Structure Sensitivity	927	5.2.5.2	Isotope Labeling in Heterogeneous Catalytic Reactions	1006
5.1.2	Chemisorption Theory	942	5.2.5.3	Kinetic Isotope Effect	1010
5.1.2.1	Introduction	942	5.2.6	Transient Catalytic Studies	1012
5.1.2.2	Formal Chemisorption Theory	943	5.2.6.1	Importance of In Situ Transient Studies	1012
5.1.2.3	Concepts in Chemisorption	952	5.2.6.2	Experimental Method	1014
5.1.2.4	The Surface Chemical Bond: A Summary	956	5.2.6.3	Kinetics of Adsorption and Desorption	1015
5.2	Microkinetics	958	5.2.6.4	Catalysis	1017
5.2.1	Rates of Catalytic Reactions	958	5.2.6.5	Summary	1022
5.2.1.1	Introduction	958	5.2.7	Positron Emitters in Catalysis Research	1023
5.2.1.2	Turnover Rate or Turnover Frequency: Generalities	959	5.2.7.1	Introduction	1023
5.2.1.3	Examples of Turnover Rate Measurements	960	5.2.7.2	Characteristics of $\beta$ -Emitters	1024
5.2.1.4	Comparison of Rate Data	961	5.2.7.3	Production of Labeled Compounds	1025
5.2.1.5	Relationships between Thermodynamics and Kinetics	963	5.2.7.4	Detection of $\beta^-$ and Annihilation Radiation	1026
5.2.1.6	Most Abundant Reactive Intermediates and Kinetically Significant Steps	964	5.2.7.5	Application to Heterogeneous Catalysis	1027
5.2.1.7	Kinetic Coupling in Catalytic Cycles: Effect on Rate	966	5.2.7.6	Conclusions	1031
5.2.1.8	Kinetic Coupling between Catalytic Cycles: Effect on Selectivity	969	5.2.8	Nonlinear Dynamics: Oscillatory Kinetics and Spatio-Temporal Pattern Formation	1032
5.2.1.9	Conclusions	970	5.2.8.1	Introduction	1032
5.2.2	Dynamics of Surface Reactions	972	5.2.8.2	Overview of the Theoretical Background	1034
5.2.2.1	Introduction	972	5.2.8.3	CO Oxidation on Pt(110): A Case Study of a Uniform Isothermal System	1035
5.2.2.2	Direct Versus Trapping-Mediated Surface Reactions	972	5.2.8.4	Oxidation of Carbon Monoxide on Other Surfaces	1040
5.2.2.3	Transition State Theory of Surface Reaction Rates	974	5.2.8.5	Other Isothermal Systems with Oscillatory Kinetics	1042
5.2.2.4	Trapping-Mediated Surface Reactions	979	5.2.8.6	Thermokinetic Phenomena	1044
5.2.2.5	Synopsis	983	5.2.8.7	Some Consequences and Future Prospects	1045
5.2.3	Theoretical Modeling of Catalytic Reactions	984	5.3	Factors Influencing Catalytic Action	1051
5.2.3.1	Introduction	984	5.3.1	Substituent Effects	1051
5.2.3.2	Different Approaches to Simulations of Surface Reaction Kinetics	985	5.3.1.1	Substituent, Reaction Center, and Surface Reaction Complex	1051
5.2.3.3	Simplest Mean-Field Approach	987	5.3.1.2	Mass and Specific Effects of Substituents	1052
5.2.3.4	Selected Examples	990	5.3.1.3	Quantitative Treatment of Substituent Effects	1054
5.2.4	Theory of Surface-Chemical Reactivity	991			
5.2.4.1	Introduction	991			
5.2.4.2	Outline	993			

5.3.1.4	Catalyst Characterization by the Slopes of LFER	1057	5.4.2.6	Carbocations and Conversions of Long Alkanes on Bifunctional Zeolites	1143
5.3.1.5	Substituent Effects as a Tool for Elucidation of Mechanisms	1059	5.4.2.7	Mechanistic Concepts on Protonation of Hydrocarbons in Acid Zeolites	1144
5.3.1.6	Prospects	1062	5.4.2.8	Transition States of Acid-Catalyzed Alkane Transformations on Zeolites	1145
5.3.2	Spillover Effects	1064	5.4.2.9	Transition States of Acid-Catalyzed Transformations of Alkenes on Zeolites	1146
5.3.2.1	Definitions	1064	5.4.2.10	Conclusions	1148
5.3.2.2	Direct Experimental Observations of Spillover	1064	5.5	Computer Simulations	1149
5.3.2.3	Interpretation of Spillover and Factors Affecting Spillover	1068	5.5.1	Computer Simulation of Structures	1149
5.3.2.4	Chemical Nature of Spillover Species	1071	5.5.1.1	Introduction	1149
5.3.2.5	Applications of Spillover in Heterogeneous Catalysis	1072	5.5.1.2	Methods	1149
5.3.2.6	Conclusions	1076	5.5.1.3	Applications	1153
5.3.3	Ensemble and Ligand Effects in Metal Catalysis	1077	5.5.1.4	Summary and Conclusion	1164
5.3.3.1	Introduction: Adsorption Sites on Metal Surfaces	1077	5.5.2	Molecular Simulation of Adsorption and Diffusion in Zeolites	1165
5.3.3.2	Dissociative Chemisorption, Ensemble Requirements	1078	5.5.2.1	Introduction	1165
5.3.3.3	"Electronic" Ligand Effect	1081	5.5.2.2	Constructing a Molecular Model	1169
5.3.3.4	Pure and "Mixed" Ensembles on Binary Alloys	1081	5.5.2.3	Molecular Simulation Techniques	1171
5.3.4	Promoters and Poisons	1084	5.5.2.4	Example Calculations and Comparison with Experiment	1174
5.3.4.1	Introduction	1084	5.5.2.5	Conclusions	1185
5.4.3.2	Brief History and Present Directions of Research	1085	<b>6</b>	<b>Kinetics and Transport Processes</b>	<b>1189</b>
5.4.3.3	Case Studies of Modifiers in Selected Reactions Studied by a Combination of Techniques	1087	6.1	Rate Procurement and Kinetic Modeling	1189
5.4.3.4	Modifiers for Important Reactions that Require More Detailed Studies	1098	6.1.1	Introduction	1189
5.3.5	Heterogeneous Catalysis and High Electric Fields	1104	6.1.2	Rate Procurement – Laboratory Reactors	1189
5.3.5.1	Introduction	1104	6.1.2.1	Laboratory Reactors	1190
5.3.5.2	Electric Fields	1104	6.1.3	Kinetic Modeling	1195
5.3.5.3	Applications of Electric Fields	1107	6.1.3.1	Rate Expression	1195
5.3.5.4	Field-Induced Surface Phenomena	1118	6.1.3.2	Deactivation Kinetics	1197
5.3.5.5	Field-Induced Phenomena on Extended Surface Planes	1120	6.1.4	Parameter Estimation – Model Discrimination	1198
5.3.5.6	Summary	1120	6.1.4.1	Data Regression	1198
5.4	Organic Reaction Mechanisms	1123	6.1.4.2	Kinetic Data Handling	1201
5.4.1	Hydrocarbon Reaction Mechanisms	1123	6.1.4.3	Model Testing	1201
5.4.1.1	Introduction	1123	6.1.4.4	Discrimination Between Rival Models	1203
5.4.1.2	Acid-Base Catalysis	1123	6.1.4.5	Sequential Experimental Design	1204
5.4.1.3	Carbocations and Their Reactions	1124	6.1.4.6	Multiresponse Models	1206
5.4.1.4	Catalytic Reactions Involving Carbocation Intermediates	1129	6.1.5	Concluding Remarks	1207
5.4.1.5	Metal Surface Catalysis	1134	6.1.6	Symbols	1207
5.4.2	Reaction Mechanisms of Acid-Catalyzed Hydrocarbon Conversions in Zeolites	1137	6.2	Simultaneous Heat and Mass Transfer and Chemical Reaction	1209
5.4.2.1	Introduction	1137	6.2.1	Introduction	1209
5.4.2.2	Alkylcarbenium and Alkylcarbonium Ions	1138	6.2.2	Mathematical Description	1212
5.4.2.3	Reactions of Aliphatic Alkylcarbenium Ions in Liquid Superacids	1139	6.2.3	Single Reactions (Conversion Problem)	1214
5.4.2.4	Carbocations in Acid Zeolites	1141	6.2.3.1	Pore Diffusion in an Isothermal Pellet	1216
5.4.2.5	Carbocations and Conversions of Short Alkanes on Bifunctional Zeolites	1142	6.2.3.2	Film and Pore Diffusion in an Isothermal Pellet	1219
			6.2.3.3	Film and Pore Diffusion Together with Interphase Heat Transfer	1219
			6.2.3.4	Film and Pore Diffusion Together with Interphase and Intraparticle Heat Transfer	1222
			6.2.3.5	External Heat and Mass Transfer	1225
			6.2.3.6	Use of Complex Rate Expressions	1226

6.2.4	Temperature Dependence and Reaction Order of Transport-Limited Reactions	1229	7.8.2	Metal Recovery	1279
6.2.4.1	Intraparticle Diffusion	1230	7.8.3	Encapsulation/Stabilization	1280
6.2.4.2	Interphase Mass Transfer	1231			
6.2.5	Diagnostic Criteria and Experimental Methods for Estimating the Influence of Heat and Mass Transfer on the Effective Reaction Rate	1231	<b>8</b>	<b>Special Catalytic Systems</b>	<b>1283</b>
6.2.5.1	Experimental Criteria	1232	8.1	Chemical Sensors Based on Catalytic Reactions	1283
6.2.5.2	Theoretical Criteria	1233	8.1.1	Introduction	1283
6.2.5.3	Experimental Methods for Estimating the Influence of Heat and Mass Transfer Effects	1233	8.1.1.1	Definitions and Classifications	1283
6.2.6	Multiple Reactions (Selectivity Problem)	1235	8.1.1.2	Typical Examples	1283
6.2.6.1	Type I Selectivity	1236	8.1.1.3	Chemical Sensors and Heterogeneous Catalysts: Similarities and Differences	1289
6.2.6.2	Type II Selectivity	1237	8.1.2	Electronic Conductance Sensors	1290
6.2.6.3	Type III Selectivity	1240	8.1.2.1	Basic Concepts	1291
6.2.7	Control of Selectivity in Zeolite Catalyzed Reactions by Utilizing Diffusion Effects	1242	8.1.2.2	Electronic Conductance Sensors Based on SnO <sub>2</sub>	1295
6.2.7.1	Shape-Selective Catalysis	1242	8.1.2.3	Schottky-Diode-Type Conductance Sensors Based on TiO <sub>2</sub>	1303
6.2.7.2	Modeling of Shape-Selectivity Effects	1244	8.1.2.4	Bulk Defect Sensors Based on BaTiO <sub>3</sub> and Related Oxides	1304
6.2.7.3	Controlled Modification of the Pore Structure	1250	8.1.3	Calorimetric Sensors	1305
6.3	Determination of Diffusion Coefficients in Porous Media	1252	8.1.4	Solid Electrolyte Sensors	1306
6.3.1	Definitions	1252	8.1.5	Conclusions	1308
6.3.2	Measurement of Transport Diffusion	1254	8.2	Electrochemical Modification of Catalytic Activity	1310
6.3.2.1	Steady State Measurements	1254	8.2.1	Introduction	1310
6.3.2.2	Time Lag Measurements	1254	8.2.2	Solid Electrolyte Cells and their Relevance to Catalysis	1310
6.3.2.3	Sorption Rate Measurements	1254	8.2.2.1	Solid Electrolytes	1310
6.3.2.4	Frequency Response Measurements	1255	8.2.2.2	Solid Electrolyte Potentiometry (SEP)	1311
6.3.2.5	Chromatographic and Flow Methods	1256	8.2.2.3	Potential-Programmed Reduction	1312
6.3.3	Measurement of Self-Diffusion	1257	8.2.2.4	Electrocatalytic Operation of Solid Electrolyte Cells	1313
6.3.3.1	Elementary Steps of Diffusion	1257	8.2.3	The Active Use of Solid Electrolytes in Catalysis	1314
6.3.3.2	Quasielastic Neutron Scattering	1257	8.2.3.1	Electrochemical Promotion or In Situ Controlled Promotion: The NEMCA Effect	1314
6.3.3.3	Pulsed Field Gradient NMR	1258	8.2.3.2	Transient and Steady-State Electrochemical Promotion Experiments	1315
6.3.3.4	Tracer Techniques	1258	8.2.3.3	Definitions and Some Key Aspects of Electrochemical Promotion	1316
6.3.4	Diffusion in Multicomponent Systems	1259	8.2.3.4	Spectroscopic Studies	1317
6.3.5	Correlation Between the Different Diffusivities	1259	8.2.4	Purely Catalytic Aspects of In Situ Controlled Promotion	1319
<b>7</b>	<b>Deactivation and Regeneration</b>	<b>1263</b>	8.2.4.1	Rate Enhancement Ratio $\rho$	1319
7.1	Introduction	1263	8.2.4.2	Promotion Index $P_i$	1319
7.2.1	Catalyst Poisoning	1264	8.2.4.3	Electrophobic and Electrophilic Reactions	1320
7.2.2	Catalyst Fouling	1265	8.2.4.4	The Work Function of Catalyst Films Interfaced with Solid Electrolytes	1320
7.2.3	Thermal Degradation	1266	8.2.4.5	Dependence of Catalytic Rates and Activation Energies on Catalyst Work Function $e\Phi$	1321
7.3	Catalyst Deactivation by Poisoning	1266	8.2.4.6	Selectivity Modification	1322
7.4	Fouling	1267	8.2.4.7	Promotional Effects on Chemisorption	1322
7.4.1	Coke formed in Gas Phase Processes	1267	8.2.4.8	In Situ Controlled Promotion Using Aqueous Electrolytes	1323
7.4.1.1	Non-catalytic Gas-Phase Coke	1268			
7.4.1.2	Coking in Gas-Solid Catalytic Reactions	1269			
7.5	Coke Formed in Liquid-Phase Catalytic Processes	1273			
7.6	Catalyst Regeneration: Coking	1275			
7.7	Thermal Deactivation	1276			
7.8	Treatment of Spent Catalyst	1278			
7.8.1	Catalyst Rejuvenation	1279			

8.2.5	Potential Applications	1324	8.6.2.5	Polymerization Catalysts	1356
8.2.6	Conclusions	1324	8.6.3	Concluding Remarks	1356
8.3	Electrocatalysis	1325	<b>9</b>	<b>Laboratory Reactors</b>	<b>1359</b>
8.3.1	Definition and Relationship to Heterogeneous Catalysis	1325	9.1	Laboratory Catalytic Reactors: Aspects of Catalyst Testing	1359
8.3.2	Some Fundamentals of Redox Reactions at Electrodes	1326	9.1.1	Introduction	1359
8.3.2.1	Galvani Potential, Overvoltage and Current/Voltage Curves	1326	9.1.2	Reactor Systems	1361
8.3.2.2	Theoretical Model on the Basis of the Franck-Condon Principle	1326	9.1.2.1	Classification	1361
8.3.2.3	Redox Reactions Occurring in Several Steps	1327	9.1.2.2	Balance Equations	1362
8.3.3	Catalysis of One-Electron Transfer Reactions	1328	9.1.2.3	Continuous-Flow Stirred-Tank Reactor (CSTR)	1362
8.3.4	Hydrogen Electrode Reaction	1328	9.1.2.4	Plug-Flow Reactor (PFR)	1363
8.3.5	Oxygen Electrode Reaction	1331	9.1.2.5	Laboratory Systems	1365
8.3.5.1	Energetics	1332	9.1.3	Mass and Heat Transfer	1365
8.3.5.2	Bridge Bonding of Oxygen Molecules and Reduction Pathway	1333	9.1.3.1	Extraparticle Gradients	1365
8.3.5.3	Comments on Catalysis of the Oxygen Electrode	1333	9.1.3.2	Intraparticle Gradients	1366
8.3.6	Trends in the Application of Electrocatalysis	1333	9.1.3.3	Catalyst Bed Gradients	1369
8.3.6.1	Fuel Cells	1333	9.1.4	Comparison Criteria	1370
8.3.6.2	Production of Chemicals	1334	9.1.4.1	Mass Transport	1371
8.3.6.3	Electrochemical Sensors	1335	9.1.4.2	Heat Transport	1371
8.3.6.4	Non-Faradaic Electrochemical Modification of Catalytic Activity: NEMCA	1337	9.1.5	Effect of Particle Transport Limitations on the Observed Behavior	1371
8.4	Catalysis in Supercritical Media	1339	9.1.6	Diagnostic Experimental Tests	1372
8.4.1	Properties of Supercritical Fluids	1339	9.1.6.1	Extraparticle Concentration Gradients	1372
8.4.2	Thermodynamics and Kinetics of Reactions in Supercritical Fluids	1340	9.1.6.2	Intraparticle Concentration Gradients	1372
8.4.2.1	Clustering	1340	9.1.6.3	Temperature Gradients	1373
8.4.2.2	Pressure Effects	1341	9.1.7	Proper Catalyst Testing and Kinetic Studies	1373
8.4.2.3	Phase Behavior	1342	9.1.8	Notation	1374
8.4.3	Motivation for Catalysis in Supercritical Media	1342	9.2	Ancillary Techniques in Laboratory Units for Catalyst Testing	1376
8.4.4	Case Studies of Heterogeneous Catalysis in SCFs	1344	9.2.1	Introduction	1376
8.4.5	Other Applications of SCFs and Catalysis	1346	9.2.2	Overall Equipment	1377
8.4.6	Concluding Remarks	1346	9.2.3	Generation of Feed Streams	1378
8.5	Microwave Heating in Catalysis	1347	9.2.4	Devices for Product Sampling	1380
8.5.1	Microwave Energy and Microwave Heating	1347	9.2.5	Elemental Analysis of Carbonaceous Deposits on Catalysts	1383
8.5.2	Dielectric Polarization	1348	9.2.6	Concluding Remarks	1386
8.5.3	Interfacial Polarization	1348	9.2.7	Acknowledgements	1386
8.5.4	Ionic Conduction	1348	9.3	Catalytic Membrane Reactors	1387
8.5.5	Microwave Heating	1348	9.3.1	Introduction	1387
8.5.6	Current Research	1349	9.3.2	Features of Catalytic Membrane Reactors	1387
8.6	Sonocatalysis	1350	9.3.2.1	Development of CMRs	1387
8.6.1	Introduction and the Origins of Sonochemistry	1350	9.3.2.2	Membranes for CMR Applications	1387
8.6.2	Effects of Ultrasound on Heterogeneous Catalysts	1352	9.3.2.3	Characterization of Porous Membranes	1389
8.6.2.1	Metal Powders	1352	9.3.2.4	Gas Transport and Separation in Porous Membranes	1390
8.6.2.2	Metal Oxides as Oxidation Catalysts	1354	9.3.2.5	Catalyst-Membrane Combinations	1391
8.6.2.3	Silica, Alumina, and Zeolites	1354	9.3.3	Applications of CMRs	1392
8.6.2.4	Supported Metal Catalysts	1355	9.3.3.1	Equilibrium-Restricted Reactions	1392
			9.3.3.2	Controlled Addition of Reactants	1393
			9.3.3.3	Active Contactor	1394
			9.3.4	Conclusions	1395
			9.3.5	Glossary	1396



<b>10</b>	<b>Reaction Engineering 1399</b>		
10.1	Catalytic Fixed-Bed Reactors 1399	10.3.3	Types of Slurry Reactors 1445
10.1.1	Introduction 1399	10.3.4	Hydrodynamics of Slurry Reactors 1446
10.1.2	Catalyst Shapes for Fixed-Bed Reactors 1401	10.3.4.1	Minimum Suspension Criteria 1446
10.1.2.1	Random Packings 1401	10.3.4.2	Gas Holdup 1449
10.1.2.2	Monoliths 1402	10.3.4.3	Axial Mixing in Slurry Reactors 1450
10.1.2.3	Gas Flow and Pressure Drop in Fixed Beds 1404	10.3.5	Mass Transfer with Chemical Reaction 1452
10.1.2.4	Heat Transfer in Catalyst-Filled Tubes 1405	10.3.5.1	The Volumetric Liquid-Side Mass Transfer Coefficient at the Gas-Liquid Interface 1453
10.1.2.5	Comparison of Different Catalyst Shapes 1406	10.3.5.2	The True Gas-Liquid Specific Contact Area ( $a$ ) and the Liquid-Side Mass Transfer Coefficient ( $k_L$ ) 1456
10.1.3	Types of Fixed-Bed Reactors 1406	10.3.5.3	The Volumetric Gas-Side Mass Transfer Coefficient ( $k_G a$ ) 1456
10.1.3.1	Adiabatic Reactors 1406	10.3.5.4	The Mass Transfer Coefficient at the Liquid-Solid Interface $k_S$ 1456
10.1.3.2	Multistage Reactors 1408	10.3.6	Enhancement of Gas-Liquid Mass Transfer 1458
10.1.3.3	Fixed-Bed Reactors which are Cooled or Heated Through the Wall 1410	10.3.6.1	Enhancement by Physical Adsorption 1458
10.1.3.4	Autothermal Reactors 1415	10.3.6.2	Particles Catalyze a Chemical Reaction Involving the Absorbed Gas Phase Component 1459
10.1.3.5	Multifunctional Reactors 1420	10.3.7	Towards High-Intensity Slurry Reactors 1460
10.1.4	Parametric Sensitivity, Runaway and Safety of Fixed-Bed Reactors 1422	10.3.8	Symbols 1460
10.1.4.1	Runaway 1422	10.4	Unsteady-State Reactor Operation 1464
10.1.4.2	Safety Aspects 1423	10.4.1	Introduction 1464
10.1.5	Conclusions 1423	10.4.2	Dynamic Kinetic Model 1465
10.1.6	List of Symbols 1424	10.4.3	General Approaches to Reactor Modeling 1467
10.1.7	References 1424	10.4.4	Analysis and Optimization of Cyclic Processes 1470
10.2	Fluidized-Bed Reactors 1426	10.4.4.1	General Optimal Periodic Control Problem 1470
10.2.1	Introduction 1426	10.4.5	Reaction Performance Improvement 1471
10.2.1.1	The Fluidization Principle 1426	10.4.6	Dynamic Phenomena in a Fixed-Bed Reactor 1472
10.2.1.2	Forms of Fluidized Beds 1426	10.4.7	Reverse-Flow Operation in Fixed-Bed Reactors 1474
10.2.1.3	Advantages and Disadvantages of the Fluidized-Bed Reactor 1427	10.4.8	Reaction-Separation Processes 1476
10.2.2	Fluid-Mechanical Principles 1427	10.4.8.1	Continuous Countercurrent Moving-Bed Chromatographic Reactor 1476
10.2.2.1	Minimum Fluidization Velocity 1427	10.4.8.2	Reaction Pressure Swing Adsorption 1476
10.2.2.2	Fluidization Properties of Typical Bed Solids 1429	10.4.9	Partial Oxidation in Fluidized-Bed and Riser Reactors 1477
10.2.2.3	Gas Distribution 1429	10.4.9.1	Internal Circulation of a Catalyst in Fluidized Beds 1477
10.2.2.4	Gas Jets in Fluidized Beds 1430	10.4.10	Miscellaneous Examples 1477
10.2.2.5	Bubble Development 1430	10.4.10.1	Fluctuations of the Inlet Temperature in Fixed-Bed Catalytic Reactors 1477
10.2.2.6	Elutriation 1431	10.4.10.2	Stabilization of Unstable Steady State 1477
10.2.2.7	Circulating Fluidized Beds 1432	10.4.10.3	Liquid-Gas-Solid Reactor Systems 1478
10.2.2.8	Attrition of Solids 1433	10.5	Reactive Distillation 1479
10.2.3	Gas Mixing in Fluidized-Bed Reactors 1435	10.5.1	Introduction 1479
10.2.3.1	Gas Mixing in Bubbling Fluidized Beds 1435	10.5.2	Conceptual Approach to Reactive Distillation 1480
10.2.3.2	Gas Mixing in Circulating Fluidized Beds 1435	10.5.3	Computational Procedures 1480
10.2.4	Industrial Applications 1436	10.5.3.1	Problem Definition 1480
10.2.4.1	Heterogeneous Catalytic Gas-Phase Reactions 1436	10.5.3.2	Evolution of Algorithms 1480
10.2.4.2	Polymerization of Alkenes 1438	10.5.3.3	Relaxation Techniques 1481
10.2.5	Modeling of Fluidized-Bed Reactors 1438		
10.2.5.1	Bubbling Fluidized-Bed Reactors 1438		
10.2.5.2	Circulating Fluidized-Bed Reactors 1439		
10.2.6	Scale-Up 1441		
10.3	Slurry Reactors 1444		
10.3.1	Introduction 1444		
10.3.2	Properties of Slurry Reactors 1444		

- 10.5.3.4 Tearing and Partitioning 1481
- 10.5.3.5 Global Approaches 1481
- 10.5.4 Practical Realization of Reactive Distillation 1482
  - 10.5.4.1 Packed Towers 1483
  - 10.5.4.2 Tray Towers 1483
- 10.5.5 Selected Processes 1484
- 10.5.6 Conclusions 1485
  
- 11 Annexes 1489**
  - 11.1 Standard Catalysts 1489
    - 11.1.1 Introduction 1489
    - 11.1.2 EUROCAT Metal Catalysts 1490
      - 11.1.2.1 EUROPT-1 1490
      - 11.1.2.2 EUROPT-3 and EUROPT-4 1495
      - 11.1.2.3 EURONI-1 1496
    - 11.1.3 Other EUROCAT Catalysts 1497
      - 11.1.3.1 Vanadia-Titania EUROCAT Oxides 1497
      - 11.1.3.2 EUROTTS-1 Zeolite 1499
      - 11.1.3.3 EUROCOMO Catalyst 1500
    - 11.1.4 Other Programmes 1500
      - 11.1.4.1 Japanese Programme 1500
      - 11.1.4.2 Russian Programme 1501
      - 11.1.4.3 Northwestern University Programme 1502
      - 11.1.4.4 American Society for Testing Materials (ASTM) 1502
      - 11.1.4.5 British Standards Institute (BSI) 1502
      - 11.1.4.6 IUPAC/SCI/NPL Programme 1502
  - 11.1.4.7 Measurements of Surface Area and Porosity 1502
  - 11.1.5 Summary and Conclusions 1502
  - 11.2 IUPAC Recommendations 1503
    - 11.2.1 Reporting Physisorption Data for Gas/Solid Systems 1503
      - 11.2.1.1 Introduction 1503
      - 11.2.1.2 General Definitions and Terminology 1504
      - 11.2.1.3 Methodology 1505
      - 11.2.1.4 Experimental Procedures 1507
      - 11.2.1.5 Evaluation of Adsorption Data 1508
      - 11.2.1.6 Determination of Surface Area 1510
      - 11.2.1.7 Assessment of Mesoporosity 1512
      - 11.2.1.8 Assessment of Microporosity 1513
      - 11.2.1.9 General Conclusions and Recommendations 1514
    - 11.2.2 Catalyst Characterization 1516
      - 11.2.2.1 Introduction 1516
      - 11.2.2.2 Catalyst Formulation and Methods of Its Preparation 1516
      - 11.2.2.3 Physical Properties 1520
      - 11.2.2.4 Fine Structure 1522
      - 11.2.2.5 Catalytic Properties 1524
    - 11.2.3 Methods and Procedures for Catalyst Characterization 1529
      - 11.2.3.1 Introduction 1529
      - 11.2.3.2 Catalyst Preparation 1529
      - 11.2.3.3 Characterization of Surface Properties by Adsorption Methods 1536
      - 11.2.3.4 Fine Structure of Catalysts [20] 1540
      - 11.2.3.5 Catalytic Properties 1546

---

## 2 Preparation of Solid Catalysts

---

### 2.0 Developing Industrial Catalysts

#### 2.1 Bulk Catalysts and Supports

#### 2.2 Supported Catalysts

#### 2.3 Zeolites and Related Molecular Sieves

#### 2.4 Solid Superacids

#### 2.5 Shaping of Catalysts and Supports

#### 2.6 Computer-aided Catalyst Design

---

### 2.0 Developing Industrial Catalysts<sup>x)</sup>

J. F. LEPAGE

Once an active species and perhaps its support have been selected, the task is to construct from precursors of these active species a catalytic structure whose properties and characteristics will meet the demands of an industrial user. One must avoid creating a structure that is only a laboratory curiosity which for technical or economic reasons can not be manufactured on industrial scale.

#### 2.0.1 Properties and Characteristics of Industrial Catalysts

In addition to the fundamental properties that come from the very definition of a catalyst, i.e., activity, selectivity, and stability, industrial applications require that a catalyst be regenerable, reproducible, mechanically and thermally stable, original, economical, and possess suitable morphological characteristics.

---

<sup>x)</sup> Reprinted with permission from J. F. Le Page, *Applied Heterogeneous Catalysis - Design, Manufacture, Use of Solid Catalysts*, Editions Technip, Paris, 1987.

#### 2.0.1.1 Activity

A high activity will be reflected either in high productivity from relatively small reactors and catalyst volumes or in mild operating conditions, particularly temperature, that enhance selectivity and stability if the thermodynamics is more favorable.

#### 2.0.1.2 Selectivity

High selectivity produces high yields of a desired product while suppressing undesirable competitive and consecutive reactions. This means that the texture of the catalyst (in particular pore volume and pore distribution) should be improved toward reducing limitations by internal diffusion, which in the case of consecutive reactions rapidly reduces selectivity.

#### 2.0.1.3 Stability

A catalyst with good stability will change only very slowly over the course of time under conditions of use and regeneration. Indeed, it is only in theory that a catalyst remains unaltered during reaction. Actual practice is far from this ideal. Some of the things that lead to a progressive loss of activity or selectivity or mechanical strength are as follows:

- (a) Coke forms on some catalysts through the intervention of parasitic reactions of hydrogenolysis, polymerization, cyclization, and hydrogen transfer.
- (b) Reactants, products or poisons may attack active agents or the support.
- (c) Volatile agents, such as chlorine, may be lost during reactions such as reforming.
- (d) The crystals of a deposited metal may become enlarged or regrouped. A change in the crystalline structure of the support can cause a loss of mechanical strength.
- (e) Progressive adsorption of trace poisons in the feed or products may reduce activity. It has been pointed out that industrial feedstocks are rarely pure products, but mixtures containing portions of impurities that must sometimes be eliminated beforehand so that the catalyst can be used.

### 2.0.1.4 Morphology

The external morphological characteristics of a catalyst, i.e. its form and grain size, must be suited to the corresponding process. For moving or boiling bed reactors the spherical form is recommended for reducing problems of attrition and abrasion. In a fluid bed, a spherical powder is preferred for limiting attrition, and its grains should have well determined size distributions for obtaining good fluidization. In a fixed bed, beads, rings, pellets, extrudates, or flakes can be used; but their form and dimensions will have an influence on the pressure drop through the bed. Thus for a given equivalent diameter, catalysts can be classified according to the relative pressure drops they cause, as follows:

Rings < beads < pellets < extrudates < crushed

This pressure drop must be high enough to ensure an even distribution of the reaction fluid across the catalytic bed, but it must not be so high as to cause an increase in the cost of compressing and recycling any gases.

Let us point out again that the grain density and especially the filling density are properties that greatly preoccupy the user; and these depend on the morphology in terms of pore volume. The catalyst is bought by weight with the purpose of filling a given reactor, and the cost of the catalyst charge will depend on its filling density. Finally, with respect to morphology, we point out that catalysts in the form of beads lend themselves better to handling, filling and emptying reactors, as well as any sieving that may appear necessary for eliminating fines after a number of regenerations.

### 2.0.1.5 Mechanical Strength

The mechanical strength of a catalyst is demonstrated by its resistance to crushing, which enables the catalyst to pass undamaged through all the strains, both foreseen and accidental, that occur within the catalyst bed. Mechanical strength is also demonstrated by the resistance of the grains to attrition through rubbing, which produces fines and can cause an increase in the pressure drop in a catalytic bed. In the case of powdered catalysts destined for fluid or boiling beds, a resistance to abrasion on the walls or to erosion by the fluids is also required.

### 2.0.1.6 Thermal Characteristics

For certain catalysts thermal conductivity and specific heat require consideration. High thermal conductivity

of the catalytic mass leads to reduced temperature gradients within the grain, as well as in the catalytic bed, for endothermic or exothermic reactions, by improving heat transfer. For other catalysts, the specific heat assumes more importance; a high specific heat permits a catalytic cracking catalyst to carry a large thermal load from the combustion of coke back to the endothermic cracking reaction, where it is usefully consumed. By contrast, catalysts in catalytic mufflers are more efficient when they are quickly carried to a high temperature by the combustion gases, and a low specific heat can be advantageous.

### 2.0.1.7 Regenerability

As we have pointed out in relation to stability, it is only in theory that the catalyst is found intact at the end of the reaction. All catalysts age; and when their activities or their selectivities have become insufficient, they must be regenerated through a treatment that will return part or all of their catalytic properties. The most common treatment is burning off of carbon, but scrubbing with suitable gases is also frequently done to desorb certain reversible poisons; hydrogenolysis of hydrocarbon compounds may be done when the catalyst permits it, as well as an injection of chemical compounds. When the treatment does not include burning off carbon deposits, it is often called rejuvenation.

The shorter the cycle of operating time between two regenerations, the more important the regeneration. It becomes apparent that it is not enough for the catalyst to recover its activity and selectivity, it must also preserve its mechanical strength during successive regenerations or rejuvenations.

### 2.0.1.8 Reproducibility

Reproducibility characterizes the preparation of a catalyst as much as the catalyst itself; it is of concern to industrial users who want to be assured of the quality of successive charges of catalyst; and it also preoccupies the various engineers responsible for developing the catalyst from the laboratory on to industrial manufacture. Indeed, the preparation of a catalyst generally takes place in several rather complex stages dependent on a large number of variables difficult to control simultaneously. The result is that it is indispensable to rapidly verify that the reproducibility of the preparation is feasible, as well as to keep in mind that the formula developed in the laboratory should be capable of extrapolation to pilot scale and to industrial scale under acceptable economic conditions.

### 2.0.1.9 Originality

It is also important that the catalyst and the process in which it will be used can be exploited legally through licenses. This is only possible either if the catalyst is original, which is rare, or if it belongs to the public domain, which is more frequent. In the first case, it can be protected by fundamental patents; in the second case, the possible patents can apply only to improvements. The greater the originality, the higher the potential royalties associated with the catalyst or with the process for which it is the controlling part.

### 2.0.1.10 Cost

Even when a catalyst possesses all the properties and characteristics just enumerated, there remains one last requirement: it must withstand comparison with competitive catalysts or processes with equivalent functions from the point of view of cost; or at least its cost should not place too heavy a burden on the economics of the process for which it will be used.

## 2.0.2 The Ideal Catalyst and the Optimum Catalyst

All of the above properties and characteristics are not independent; when one among them is changed with a view to improvement, the others are also modified, and not necessarily in the direction of an overall improvement. As a result, industrial catalysts are never ideal. Fortunately, however, the ideal is not altogether indispensable. Certain properties, such as activity and reproducibility, are always necessary, but selectivity, for example, has hardly any meaning in reactions like ammonia synthesis; and the same holds true for thermal conductivity in an isothermal reaction. Stability is always of interest but becomes less important in processes that include continuous catalyst regeneration, when it is regenerability that must be optimized. Furthermore, originality can be of secondary importance for certain manufacturing situations such as those relevant to national defense.

The goal, therefore, is not an ideal catalyst but the optimum, which may be defined by economic feasibility studies concerning not only the catalyst but also the rest of the process. And when the catalytic process is established and the catalyst in question must compete as a replacement, the replacement catalyst's cost and method of manufacture predominate in arriving at the optimum formula.

Depending on the use and the economic competition, therefore, the optimization studies establish an hierarchy among the properties and characteristics of a catalyst; and knowledge of this hierarchy helps to better orient the efforts of the research team responsible for creating and developing the catalyst and its process. Even when the hierarchy is not fixed at the start, it can evolve in the course of developing the catalyst, sometimes even after industrialization.

## 2.0.3 Catalyst Development

A real-life solid catalyst is something entirely different to its user, its manufacturer, or its creator.

The user considers the catalyst within the framework of its function of promoting a chemical reaction, and its properties.

The engineer responsible for manufacturing the catalyst considers it from a different point of view, although still recognizing the needs of the user. For this engineer, the catalyst is primarily a chemical product characterized by its composition and its method of preparation, from the nature of its precursor salts of the active agents, through the conditions of various unit operations used for constructing the catalytic solid. All these operations, precipitation, ripening, filtration, washing, forming, drying, impregnation, calcination and activation, need to be meticulously controlled so that at the end of the manufacturing process the catalyst fits the range of specifications guaranteed to the user.

Finally, although the physical chemist who designs a solid catalyst will be interested in the two preceding points of view, he or she will concentrate on defining it in intrinsic physicochemical terms, such as its texture (pore distribution, specific surface of the overall solid, surface of the deposited active agents, structural density and grain density), its crystallographic characteristics (X-ray or electron diffraction examination to precisely determine the presence of a definite compound, a solid solution, or an alloy), its electronic properties (energy levels of the electrons, valence state of certain elements, or the *d* character for other elements or metallic alloys), and especially its surface properties either isolated or preferably in its reaction atmosphere (the thermodynamic characteristics of chemisorption, the chemical and electronic modifications of the catalytic surface, state of surface oxidation or reduction, acidity or basicity, and nature of the bonds in the adsorbed phase).

These various aspects of the catalyst are related through cause and effect. The properties sought in the industrial catalyst by the user flow from its intrinsic physico-chemical characteristics; and both industrial

properties and physicochemical properties closely depend on the method of preparation. Therefore, it is essential that the research team and the engineers in charge of developing a catalyst and its corresponding process be trained for and given the tools for following the development of the catalyst through all its various aspects, economic and legal ones included. Considering this complexity, the approach to an optimum catalyst can only be an experimental procedure advancing step-by-step through trial and error.

### 2.0.3.1 Devising the First Catalytic Formulas

An initial hierarchy of required qualities arises out of the detailed analysis of the chemical transformation plus the data from exploratory tests to select the catalytic species. This hierarchy depends on general laws of kinetics and chemical engineering, as well as observations of industrial operations that are more or less analogous. The steps of its articulation are as follows:

- Starting with the selected active species in the laboratory, one prepares a family of catalysts that are related through variations in the manufacturing process, such as sequence of the unit operations, of which certain ones are considered *a priori* critical by reason of their influence on the catalyst properties. The catalysts of this initial family are not chosen at random, but on the basis of general knowledge of inorganic chemistry and chemistry of the solid, plus the know-how acquired from analogous catalysts that seem closest to the fixed objective.
- Subsequently one prepares a list of physicochemical characteristics to be determined for the various catalysts of the family. These characteristics will be those most likely to produce meaningful results from correlations with mechanical and catalytic properties or with the conditions of preparation.

The catalysts of this initial family are then submitted to experiments whose results should permit:

- (a) A good estimation of the predicted performances, the preferred conditions of preparation, and the physicochemical characteristics.
- (b) An identification of critical properties for the catalyst (i.e., those properties most difficult to obtain), as well as the key unit operations (i.e., those essential to the performance of the catalyst), and the physicochemical characteristics on which the performance of the catalyst depends.

Next, a second series of tests is carried out for the purpose of clarifying points shown to be most important at the end of the first series of tests, both in the

preparation of the catalysts and in determination of the performance and physicochemical characteristics.

At the end of this second series, and possibly a third, the results should be good enough for the following three partial objectives:

- (a) To establish some correlations between the properties of the catalyst, the intrinsic characteristics of the solid, and the conditions of preparation, as illustrated in Fig. 1. These correlations will provide a basis for perfecting the catalyst, and they can be ultimately used for defining the control tests during industrial manufacture.
- (b) To make an initial selection of some acceptable catalysts to be studied more thoroughly.
- (c) To start using one of the acceptable catalysts for a practical study of the problems of the chemical reaction process. It would be indeed illogical to delay studying the problems of the overall process for formulation of the optimum catalyst, since according to the economic criteria the idea of an optimum catalyst has meaning only within the framework of the total problems posed by the unit. Thus it is necessary to begin the study of these problems on a catalyst that is judged acceptable, in order to deduce those elements that will orient optimization of the industrial catalyst.

At this stage it is time for a few practical remarks:

- (a) Although the study of catalytic properties can sometimes be made on model molecules for the initial preparation, it is generally preferable to operate with industrially representative feedstocks, and under industrially representative conditions, as early as possible.
- (b) For the initial catalysts, one sometimes omits the study of stability, a property that essentially demands a great deal of time for evaluation. Generally, stability is studied only with formulas that are already acceptable and often after having developed a test for accelerated aging.
- (c) For a catalyst to be regarded as acceptable, a study of its manufacturing process should have been started and advanced to the pilot scale for judging its production feasibility. Indeed, from this point on, experimenting becomes costly, and it is necessary to make sure that the catalyst is not just a laboratory curiosity.
- (d) As soon as the first results from the study of the process are obtained with the initial acceptable formula, an economic analysis and possibly a legal review should be undertaken for judging more accurately the industrial viability of the proposed process. If the results that one can expect from these reviews deviate too far from commercial requirements, the research project should be aban-

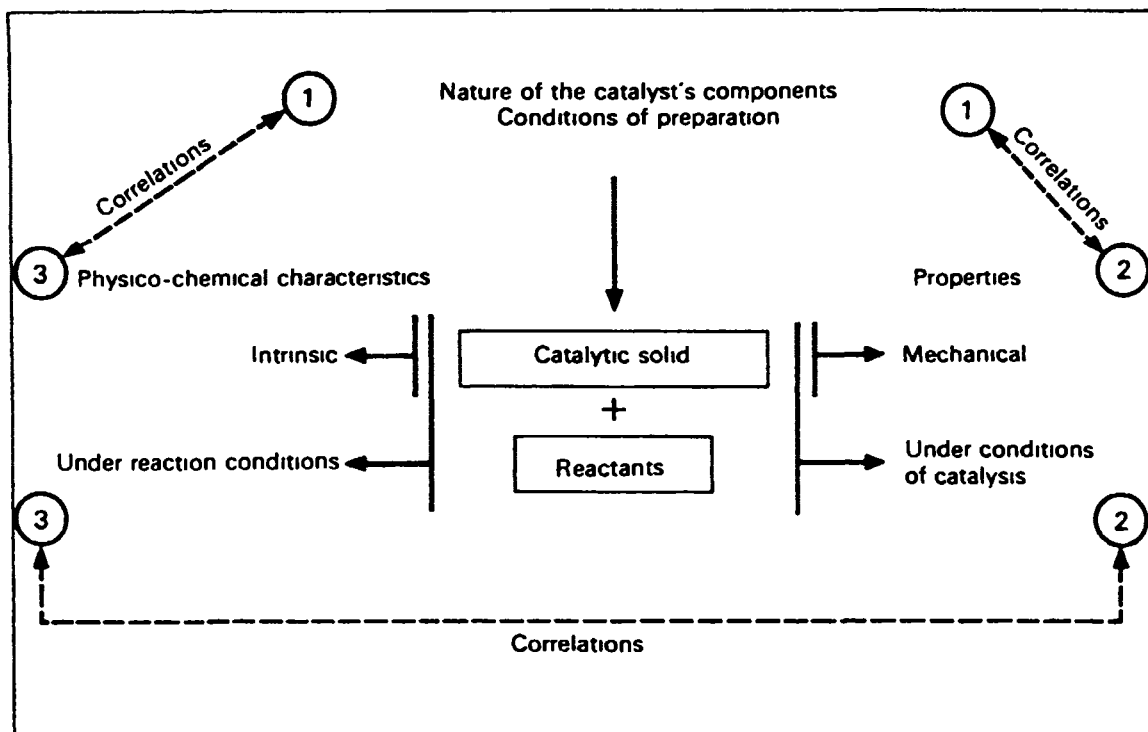


Figure 1. The different aspects of catalysis and their interrelations (adopted from ref [1])

done. If the proposed process is shown to be economically viable, one continues on to the optimization of the catalyst, taking into account the problems to be encountered in the course of its use in the proposed process.

### 2.0.3.2 Optimization of a Typical Catalytic Formula

This optimization is achieved by exploiting to the utmost the correlations established during definition of the initial catalytic formulas. It should not only take into account the problems raised by the study of use but also the need for a simple and economical preparation that can be expanded to industrial scale. Therefore, the problems of extrapolating to industrial scale the various unit operations perfected in the laboratory have to be resolved in the pilot plant. This study consists of

- Pilot preparation of a certain number of samples whose performances must be tested. Examination of the results makes it possible to specify the operating conditions for each stage of the future industrial operation.
- Forecasting a price for the industrial catalyst.
- Establishing a manufacturing process using existing equipment as far as possible.

- Production of enough catalyst by the manufacturing process for the catalyst to be representative of industrial production.

One must remember that a catalyst optimized in this way represents only a transitory optimum, experience has shown that hardly is any catalyst industrialized before it is subject to improvements, either for correcting deficiencies revealed through the industrial experience or for improving a competitive position. Sometimes it happens that a change occurs in the very nature of the catalytic agent, and at that point it is a veritable matter of catalyst renovation, involving a procedure identical to that which has just been described for the genesis of the initial formula.

Perfecting an industrial catalyst is thus the culmination of a long and complicated process that requires a knowledge as broad as possible of the methods relative to the preparation of catalysts, to the study of catalytic and mechanical properties, and to the determination of the physicochemical characteristics.

### References

- R. MONTARNAL, and J. F. LE PAGE, *La catalyse au laboratoire et dans l'industrie* 1967 Masson 1967, 231-287.

## 2.1 Bulk Catalysts and Supports

### 2.1.1 Fused Catalysts

R. SCHLÖGL

#### 2.1.1.1 Introduction

A small number of heterogeneous catalysts is prepared by fusion of various precursors. The obvious group of compounds are metal alloy catalysts which are applied in unsupported form like noble metal gauze for the ammonia oxidation to nitric oxide. Melting of the elements in the appropriate composition is the only way to produce bulk amounts of a chemical mixture of the constituent atoms. The process is well-described by thermodynamics and a large database of phase diagrams and detailed structural studies is available. Metallurgy provides the technologies for preparation and characterization of the products [1]. This enables the synthesis of a large number of bulk alloys with well-defined properties. An interesting development in the use of such bulk-phase metallic alloy catalysts is the application of bulk metallic glasses in the form of ribbons with macroscopic dimensions [2–5]. In this class of materials the atomic dispersion in the liquid alloy is preserved in the solid state as a single phase, although the material may be metastable in its composition. This allows the preparation of unique alloy compositions which are inaccessible by equilibrium synthesis. The solidification process by rapid cooling (cooling rates above  $10^4 \text{ K s}^{-1}$ ) creates “glassy” materials with well-defined short range order but without long range order. The difference in free energy between compositional equilibration and crystallization, stored in the metallic glass, can be used to transform the material in an initial activation step from a glassy state into a nanocrystalline agglomerate with a large internal surface interface between crystallites. This still metastable state is the active phase in catalysis and the final transformation into the stable solid phase mix with equilibrium composition terminates the life of such a catalyst. Application of metallic glasses as model systems is also treated in Section A.4.4.

In oxide materials [2] which are fused for catalytic applications, two additional factors contribute to the unique features of this preparation route. Many oxides in their liquid states are thermodynamically unstable with respect to the oxygen partial pressure present in ambient air, i.e. they decompose into lower-valent oxides and release molecular oxygen into the gas phase. This process can be fast on the time-scale of the fusion process, such as with vanadium pentoxide or man-

ganese oxides, or may be slow, as with iron oxides. The existence of such decomposition reactions and the control of their kinetics [6] can create a unique quenched solid which is thermodynamically metastable at ambient conditions with respect to its oxygen content. In addition, by controlling the phase nucleation, a local anisotropy of phases, i.e. a mixture of particles of different oxide forms interdispersed with each other, can be obtained. Such oxides exhibit a complex and reactive internal interface structure which may be useful either for direct catalytic application in oxidation reactions or in predetermining the micromorphology of resulting catalytic material when the fused oxide is used as precursor.

The application of the fusion process can lead to a control over structure-sensitive reactions for unsupported catalysts. The prototype example for such a catalyst is the multiply-promoted iron oxide precursor used for ammonia synthesis. In Section B.2.1.1 a detailed description is given of the necessity for oxide fusion and the consequences of the metastable oxide mixture for the catalytic action of the final metal catalyst.

Another feature of fused catalytic compounds can be the generation of a melt during catalytic action. Such supported liquid phase (SLP) catalysts consist of an inert solid support on which a mixture of oxides is precipitated which transform into a homogeneous melt at reaction conditions. These systems provide, in contrast to the case described before, a chemically and structurally homogeneous reaction environment. The standard example for this type of catalyst is the vanadium oxide contact used for oxidation of  $\text{SO}_2$  to  $\text{SO}_3$ .

#### 2.1.1.2 Concept of Fused Catalysts

The preparation of non-supported catalysts by fusion is an expensive and very energy-consuming high-temperature process. It has to compete with the concept of wet chemical preparation by the mixing-precipitating-calcining process which can be used in oxidative and reductive modes to obtain oxides and metals. Sol-gel preparation or flame hydrolysis are derivatives of the general approach. Another unconventional alternative to this important route of catalyst preparation is offered by tribochemical procedures; however, these are still in an early stage of research.

This enumeration shows that the term “fused catalyst” is not synonymous with “unsupported catalyst”, but designates a small subgroup of unsupported catalytic materials. Fused catalysts have passed through the molten state at least once during their preparation. In this respect fused catalyst are fundamentally different from other catalysts prepared at high temperatures, such as carbons which are produced by gas-solid re-



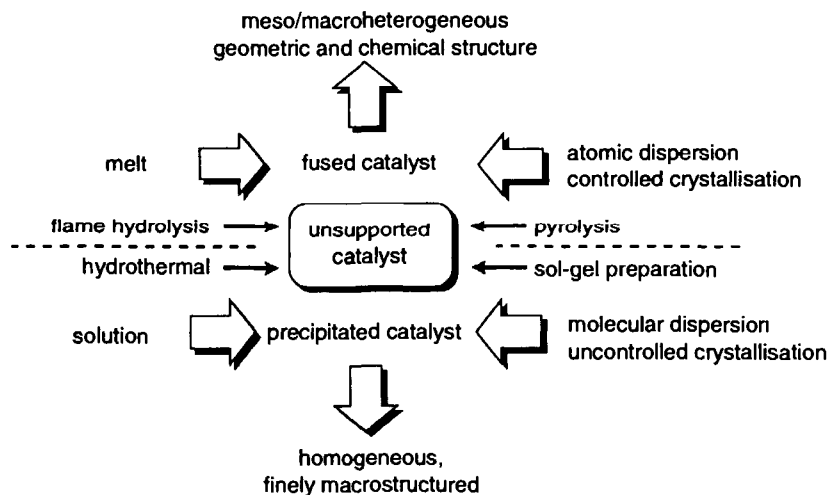


**Figure 1.** Principal pathways to generate unsupported catalytic materials. The methods indicated in the centre of the scheme are discussed in other sections of this book. The methods of fusion and precipitation will be discussed more in detail to illustrate the consequences of the different reaction environments on the structural properties of the final products. The dashed line separates solution methods (bottom) from high-temperature reactions (top).

**Table 1.** Main reaction steps in precipitation and fusion of catalytic solids.

Step	Wet chemical	Fusion
Mixing of atoms Preformation of compounds	in solution frequently, with solvent ligands	in melt possible for alloys (E-L-TM), always for compounds (oxides)
Compositional modification	frequently, by ligand exchange and incorporation of solvent	possible with volatiles, frequently with compounds by thermochemical reduction
Solidification	precipitation, difficult to control, very fine particles with molecular homogeneity	cooling, very important to control, affects chemical structure (exsolution) and long- range ordering
Calcination	required for ligand removal, complex reaction, difficult to control	not required
Formulation	pressing, extrusion precipitation onto supports	crushing, sieving, production of wires and gauze

action processes with substantially kinetic differences compared to melt-solidification reactions.

Figure 1 summarizes the main differences and objectives between the major preparation strategies. A collection of the major individual reaction steps for the synthesis of unsupported catalysts can be found in Table 1. One fundamental insight from this rather schematic comparison is that differences in the reaction kinetics of the synthesis of a given material will lead to different mesoscopic and macroscopic structures which considerably affect the catalytic performance. It is necessary to control these analytically difficult-to-describe parameters with much the same precision as the atomic arrangement or the local electronic structure. Whereas these latter parameters influence the nature of the active site, it is the meso/macrostructure which controls the distribution and abundance of active sites on a given material. It is necessary in certain cases to apply the costly method of fusion as there is no other way to

obtain the desired (and in most cases unknown) optimal meso/macrostructure of the final catalyst.

Details of the chemistry in the precipitation process can be found in other sections of this handbook. This section focuses on fused catalysts. The reader may contrast the following discussion with the contents of Table 1.

Fused catalysts allow the combination of compounds and elements in atomic dispersions which do not mix either in solution (e.g. oxides) or in the solid state. Melting provides the necessary means to generate an intimate, eventually atomically disperse distribution; a carefully controlled solidification can preserve the metastable situation in the melt down to operation temperature. In the melt the preformation of “molecules” such as oxo complexes or alloy clusters can occur. The final short-range order of the catalyst is predetermined. Examples are alloys of noble metals with elements located in the main group sections or in

the early transition metal groups of the periodic table (E-L TM alloys). In the case of oxides the partial pressure of oxygen has the chance to equilibrate between the gas phase environment of the melting furnace and the liquid oxide. With compounds in high formal oxidation states this can lead to thermochemical reduction, as for iron oxide (reduction of hematite to magnetite and wustite), or for silver oxide which reduces to the metal. Compounds in low oxidation states, such as  $\text{MnO}$ ,  $\text{Sb}_2\text{O}_3$  or  $\text{VO}_2$ , will oxidize to higher oxidation states and thus also change the chemical structure.

The kinetics to reach the equilibrium situation can be quite slow, so that the holding time and mechanical mixing of the melt will crucially affect the extent of the chemical conversion. Early termination of the holding time will lead to metastable situations for the melt with local heterogeneity in the chemical composition of the final product. This can be desirable, as in the case of the iron oxide precursor for ammonia synthesis, or it can be unwanted as in most intermetallic compounds. Also, the dissolution of, for example, one oxide into another, can be a prolonged process and early cooling will lead to a complex situation of disperse binary compounds coexisting with ternary phases. Examples are alumina and calcium oxide promoters in iron oxide melts where ternary spinel compounds can be formed, provided that sufficient trivalent iron is present. This requires the addition of activated forms of the binary oxides in order to dissolve some of the ions before the thermochemical reduction has removed the trivalent iron in excess of that required for the formation of the matrix spinel of magnetite. These examples illustrate that both the starting compounds, their purity and physical form, and the heating program will severely affect the composition and heterogeneity of the resulting material. Scaling-up of such fusion processes is a major problem as heat and ion transport determine, to a significant extent, the properties of the material. Also the gas phase over the melt and its control are of high importance as its chemical potential will determine the phase inventory of the resulting compound.

Besides the complex cases of mixed oxides, there exist more simple problems of oxide and scale formation in alloy production. The detrimental effect of oxide shells around metal particles preventing intermixing is well known. The compositional changes resulting from preferential oxidation of one component have also to be taken into account. Instability of the product and/or drastic changes in the thermochemical properties of the material after shell formation (such as massive increases in the required fusion temperature in noble metal eutectic mixtures) are common, in particular in small-scale preparations. These effects still set limits to the availability of catalytically desired alloys for practical purposes (e.g. for compounds with Zr, Si, alkali, Mg).

In addition to these more practical problems of catalyst preparation, there are also severe theoretical problems associated with the prediction of the chemistry in the fluid state of a compound. The motion of all structural elements (atoms, ions, molecules) is controlled by a statistical contribution from Brownian motion, by gradients of the respective chemical potentials (those of the structural elements and those of all species such as oxygen or water in the gas phase which can react with the structural elements and thus modify the local concentration), and by external mechanical forces such as stirring and gas evolution. In electric fields (as in an arc melting furnace), field effects will further contribute to nonisotropic motion and thus to the creation of concentration gradients. An exhaustive treatment of these problems can be found in a textbook [6] and in the references therein.

The second step in the process is the cooling of the melt. Slow cooling will result in equilibration of the mix according to the thermodynamic situation. Only in simple cases will this yield the desired compound. In most cases the mixture of structural elements stable in the melt will be metastable at ambient conditions. Techniques of supercooling are applied to maintain the desired composition [7]. Rapid solidification with temperature gradients up to about  $100 \text{ K s}^{-1}$  are required to generate metastable crystalline solids. Local heterogeneity (such as concentration gradients or undissolved particles) will disturb the equilibrium formation [8] of crystals and lead to unusual geometries of the grain structure. The crystallite size is also affected by the cooling rate, in particular at temperatures near the solidus point where the abundance of (homogeneous) nuclei is determined. Rapid cooling limits the growth of large crystals as the activation energies for diffusion and dissolution of smaller crystallites is only available for a short time. Annealing of the solid after initial solidification can be used to modify the crystallite size, provided that no unwanted phase transition occurs in the phase diagram at or below the annealing temperature. Knowledge of the complete phase diagram for the possible multicomponent reaction mixture is mandatory for the design of a temperature-time profile for a catalyst fusion experiment. In many cases these phase diagrams are not available or not known with sufficient accuracy, so that a series of experiments is required to adjust this most critical step in the whole process. Frequently, empirical relationships between characteristic temperatures in the phase diagram and the critical temperatures for stable-to-metastable phase transformations (e.g. the ratio between an eutectic temperature and the crystallization temperature of a binary system) are used to predict compositions of stable amorphous compounds of metals and metalloids [8, 9].

Cooling rates between  $100$  and  $10\,000 \text{ K s}^{-1}$  can lead to a modification of the long-range order of the mate-

rial. Under such rapid solidification conditions the time at which the activation energy for motion of structural elements is overcome is so short that the mean free pathlength reaches the dimension of the structural unit. Then the random orientation of the units in the melt is preserved and the glassy state is obtained. Such solids are X-ray amorphous and contain no grain boundary network and exhibit no exsolution phenomena. They are chemically and structurally isotropic [6]. These solids preserve, however, the energy of crystallization as potential energy in the solid state. It is possible to transform these glasses into cascades of crystalline states, some of which may be also metastable at the crystallization condition as the activation energy, for falling into the state of equilibrium, is not high enough. Glassy materials are thus interesting precursors for the formation of metastable compositions and/or metastable grain boundary structures which are inaccessible by precipitation and calcination. The critical glass-forming temperatures vary widely for different materials, with alkali silicates requiring low cooling rates of several  $100 \text{ K s}^{-1}$  and transition metal oxides and E-L TM alloys rates above  $1000 \text{ K s}^{-1}$ . Pure elements cannot be transformed into the glassy state. By utilizing these differences, composite materials with a glassy phase coexisting with a crystalline phase can be obtained. Examples are amorphous oxide promoter species dispersed between the iron oxides of the ammonia synthesis catalyst precursor.

The third step in the catalyst preparation process is the thermal treatment known as calcination, which is essential in all wet chemical processes. It leads to solvent-free materials and causes chemical reactions between components with the oxidation states of all elements reaching their desired values. All this is already accomplished during preparation of the fluid phase and during precipitation of the fused catalyst, and hence such a step is rarely required for these catalysts. This feature significantly reduces the difference in energy input to the final catalyst, between fusion and precipitation. The fact that the conditioning of the catalytic material occurs in the fluid state for a fused catalyst and in the solid state for the precipitated catalyst has two important consequences. First, the temperature levels of conditioning are different and so is the composition of the resulting material in particular with respect to volatile components. Secondly, the calcination reaction occurs as solid-solid state reaction with diffusion limitations and eventual topochemical reaction control, both giving rise to spatial heterogeneity in large dimensions relative to the particle size. In fused systems the fluid state allows very intimate mixing and hence isotropic chemical reactivity, provided that the composition is either stable during cooling or quenched so rapidly that no demixing occurs. Chemical heterogeneity at any dimensional level can be created or oc-

curs unintentionally with no gradients between particle boundaries if the cooling process is suitably adjusted to allow partial equilibration of the system.

The last step of catalyst preparation is the activation which is required for both types of materials. In this step, which often occurs in the initial stages of catalytic operation, (in situ conditioning) the catalyst is transformed into the working state which is frequently chemically and/or structurally different from the as-synthesized state. It is desirable to store free energy in the catalyst precursor which can be used to overcome the activation barriers into the active state in order to initiate the solid state transformations required for a rapid and facile activation. These barriers can be quite high for solid-solid reactions and can thus inhibit the activation of a catalyst.

A special case is catalysts which are metastable in their active state with respect to the catalytic reaction conditions. In this case a suitable lifetime is only reached if the active phase is regenerated by solid state reaction occurring in parallel to the substrate-to-product conversion. In this case it is of special relevance to store free energy in the catalyst precursor as insufficient solid state reaction rates will interfere with the substrate-to-product reaction cycle. A class of catalyst in which this effect is of relevance are oxide materials used for selective oxidation reactions.

### 2.1.1.3 Thermodynamic and Kinetic Considerations

The following general considerations are intended to illustrate the potential and complications when a fused catalyst material is prepared. The necessary precondition is that the starting state is a homogeneous phase (the fluid).

Figure 2 shows a general free energy versus composition diagram [10] for a fused catalyst system. The composition coordinate may be a projection [11] through a multinary phase diagram. The melt will solidify in the phase (1) with little compositional variation, if the melt is cooled slowly. This path leads to a stable solid with little problems in its preparation and identification. If the melt is cooled suitably to follow the solidus curve further down in free energy it reaches the eutectic point (2) and can then be rapidly quenched without any compositional variation. This creates a metastable solid with a large amount of free energy stored in the solid state. The resulting material is a characteristic fused catalyst (or precursor). If the cooling is slowed down, the composition will split in a primary crystallization [11] of the supersaturated solution. The melt is then enriched in one component according to the tangent line (2) and the solid is depleted until it reaches the composition of the metastable solid (3). The enriched melt can either crystallize in (1) or react

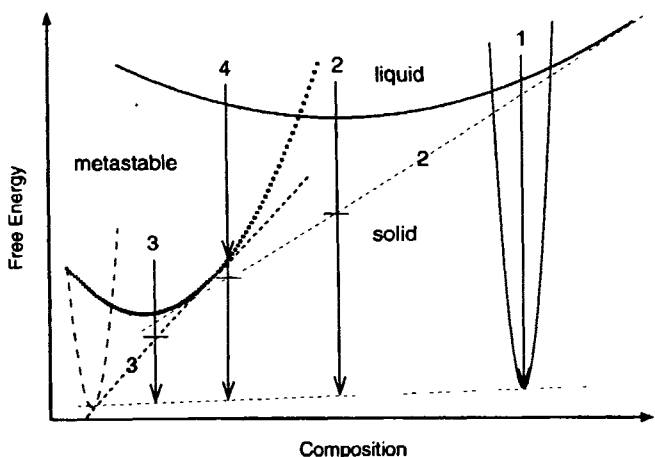


**Figure 2.** The thermodynamic situation upon solidification of a multinary system. The vertical lines designate principal reaction pathways, the dashed tangent lines illustrate the compositional changes arising from an equilibrium solidification at the respective pathways (interrupt lines on the vertical arrows). The narrow areas of existence designate stable phases with a finite phase width, the area designated metastable indicates the existence of a single phase solid which is unstable at ambient conditions.

along pathway 3 provided that enough energy of crystallization is released and the cooling conditions [12] are still adequate. The metastable solid (3) may either be quenched and form a further metastable component of the phase mix or it can undergo equilibration in the same way as system (2) along the tangent line (3). The cooling conditions and eventual annealing intervals will decide over the branching ratio. A further possibility is the formation (4) of a supersaturated solid solution (the metastable solid in Figure 2) directly from the melt followed by either quench cooling to ambient temperature leading to another metastable phase in the mix or by equilibration according pathway (3).

The solidification kinetics and compositional fluctuations in the melt will decide over the crystallization pathway which can be followed by all of the melt. If local gradients in temperature or composition exist in the system the crystallization pathway can be locally inhomogeneous and create different metastable solids at different locations in the macroscopic solidified blocks.

This simple consideration shows that a wide variety of stable and metastable solids can be produced from a homogeneous melt if the solidification conditions are suitably chosen. In this way a complex solid phase mix can be obtained which is inaccessible by the wet chemical preparation route. The metastable phase mix may either contain an active phase or may be used to generate it by a suitable activation procedure at relatively low temperatures. A stable phase which is catalytically useful should be accessible by other less complex and costly ways and is thus not be considered here.

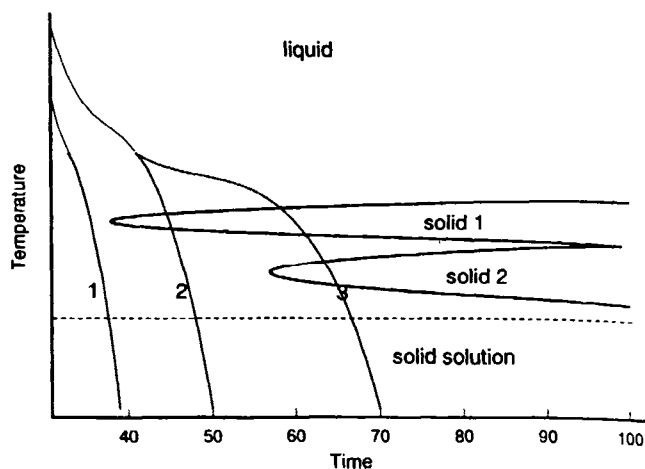


**Figure 3.** Kinetics of solidification illustrating how various cooling programmes (pathways 1 to 3) can affect the final inventory of phases which differ in their respective crystallization kinetics. The characteristic times are in the microsecond regime for metallic alloys but extend into the time-scales of days for compounds such as oxides.

The kinetic situation is generalized in Figure 3. For a fused catalyst system a liquid phase is assumed to coexist with a metastable solid solution. Additional solid phases crystallize with retarded kinetics and form lenses in the time-temperature diagram of Figure 3. Three characteristic cooling profiles are sketched. Rapid quenching (1) leads to only the solid solution without compositional changes and without mesoscopic heterogeneity. Intermediate quenching (2) passes through the solid 1 area and leads to a branching of the solid products between solid 1 and the solid solution with a modified composition (primary crystallization, path 2 in Figure 2). Cooling with a holding sequence (3) allows preformation of structural units in the melt and leads to the formation of three solids with different compositions. Moving the holding temperature further down into the ranges occupied by the solid phases provides control over the branching of the solid products. It can be seen that rapid cooling of the fused melt leads to a clear situation with respect to the solid as all free energy is transferred into the solid phase and liberated only in solid-solid reactions. If the cooling rate is intermediate or if the cooling rate is not isokinetic in the whole melt, then we obtain complex situations with wide variations in chemical and local compositions of the final solids.

The reduced fused iron oxide for ammonia synthesis is a perfect example illustrating in its textural and structural complexity the merit of this preparation strategy which allows to create a metastable porous form of the element iron. The necessary kinetic stabilization of the metastable solid is achieved by the exclusion of irreducible oxide phases of structural promoters. Some of them precipitate during solidification,

whereas others are liberated from the matrix during activation. A pre-requisite for the very important secondary ex-solution species is the intimate phase mixture of ternary iron earth alkali oxides, which cannot be achieved by wet chemical precipitation techniques due to the extremely different coordination chemistry of the various cations in solvent media.

#### 2.1.1.4 Sulfuric Acid Catalyst

The reaction of gaseous  $\text{SO}_2$  with molecular oxygen in the contact process seems to proceed over two independent mechanisms [13] one of which is the direct oxidation of a vanadium pentoxide-sulfur dioxide adduct by oxygen and the other proceedings via a redox cycle involving  $\text{V}^{4+}$  and  $\text{V}^{3+}$  intermediate species [13–15].

The technical catalyst is a supported liquid phase system of vanadium pentoxide in potassium pyrosulfate [16, 17]. Other alkali ions influence the activity [18] at the low-temperature end of the operation range, with Cs exhibiting a particular beneficial effect [13].

It is necessary to work at the lowest possible temperature in order to achieve complete conversion. Only at temperatures below 573 K is the equilibrium conversion of  $\text{SO}_2$  practically complete, with about 99.5% conversion. The binary phase diagram vanadium-oxygen shows the lowest eutectic for a mixture of pentoxide and the phase  $\text{V}_3\text{O}_7$  at 910 K. All binary oxides are stable phases from their crystallization down to ambient temperature. The pyrosulfate promoter is thus an essential ingredient rather than a beneficial additive to the system. Compositions of 33% alkali (equals to 16.5% pyrosulfate) solidify at around 590 K. This temperature is still too high as at around 595 K the activation energy increases sharply, even although the system is still liquid. The liquid state is thought to be essential for the facile diffusion [13, 19] of oxygen to the active sites [13].

The small mismatch between required and achieved minimum operation temperature has the severe consequence that a special preabsorption stage has to be included in the reactor set-up in order to achieve the essential complete conversion. In this manner the partial pressure of the  $\text{SO}_3$  product is lowered before the last stage of conversion, rendering acceptable incomplete conversion of the overheated catalyst. If the reason why the catalyst does not operate efficiently down to its solidification point could be eliminated one may circumvent the intermediate absorption stage and thus facilitate the reactor design considerably.

Catalyst fusion is essential to bring and keep the pyrosulfate–vanadium oxide system into a homogeneous state which is the basis for operating the system at the eutectic in the ternary phase diagram. The reaction mechanism and the fact that the operation point of the

catalyst is at the absolute minimum in the  $\text{V}^{5+}\text{--O}_2$  section of the phase diagram point to the existence of a supersaturated solution of partly reduced vanadium oxides in the melt. The point at which the activation energy for  $\text{SO}_2$  oxidation changes over to a lower (transport-controlled) value marks thus the stage at which crystallization of the supersaturated solution begins under catalytic conditions. This hypothesis could be verified in pioneering studies by Fehrmann and co-workers using electric conductivity measurements and preparative isolation techniques [16, 17]. They isolated crystals of a variety of  $\text{V}^{4+}$  and  $\text{V}^{3+}$  ternary alkali sulfates. These precipitates can be redissolved in a regeneration procedure of the catalyst involving a heat treatment to 800 K under oxidizing conditions [17]. In a rather elegant in situ electron paramagnetic resonance (EPR) study the deactivation mechanism was experimentally confirmed on an industrial supported catalyst in which the phase  $\text{K}_4(\text{VO})_3(\text{SO}_4)_5$  was identified as  $\text{V}^{4+}$  deactivating species which could also be redissolved by a high temperature treatment. [20]

The accurate analysis of the problem is complicated as, under reaction conditions (presence of oxygen), all redox equilibria between  $\text{V}^{5+}$  and the lower oxidation states are shifted towards the pentavalent state. The generation of realistic model systems in which, for example, conductivity experiments can be performed, thus requires the exact control of the gas phase in contact with the melt.

The real pseudobinary phase diagram [16] of  $\text{V}_2\text{O}_5/\text{S}_2\text{O}_7\text{M}_2$  with  $\text{M} = \text{K}$  or  $\text{Na}$  is rather complex in the interesting range around the eutectic which is displayed in Figure 4. The formation of a complex salt with the composition  $3\text{M}_2\text{S}_2\text{O}_7 \cdot x\text{V}_2\text{O}_5$  interferes with the eutectic and gives rise to two eutectic points with fusion temperatures of 587 K and of 599 K. It is interesting to note that the chemistry of vanadium pentoxide in molten alkali sulfates is different from the present case with pyrosulfates where no vanadium oxo oligomers are formed. This is an indication of a complex formation between pyrosulfate and vanadium oxide in the sense of preformed molecules in the fused melt. The dashed lines in Figure 4 indicate the estimated continuation of the phase boundaries which are inaccessible experimentally as in this regime glassy oxides with unknown compositions are formed.

These observations on the sulfuric acid catalyst are full in line with the general thermodynamic behaviour of fused catalyst systems. The metastable solid in Figure 2 has to be replaced in this case by a cascade of the partly reduced vanadium ternary sulfates. The processes sketched above occur under thermodynamic control in a quaternary phase diagram, vanadium-oxygen-sulfur-alkali, as illustrated by the reversibility of the exsolution of the partly reduced vanadium compounds under suitable partial pressures of oxygen

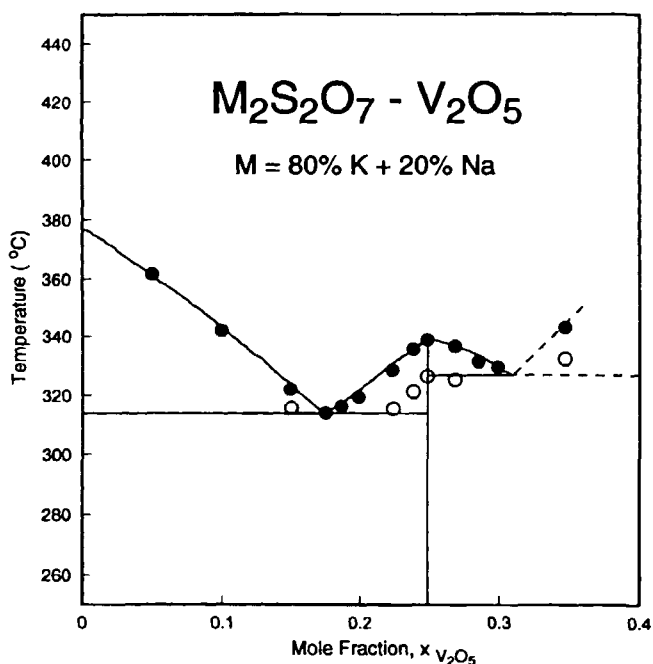


**Figure 4.** Section of the pseudobinary phase diagram of the sulfuric acid SLP catalytic material. The data were taken from Ref. 16. The data points were derived from anomalies of the conductivity versus temperature curves of the respective mixtures. At the high compositional resolution and in the range of the global eutectic, the formation of a vanadate-sulfato complex causes the local maximum in the solidus curve. It is noted that extreme precision in the experimental procedures was necessary to derive this result illustrating the characteristic of fused systems that compound formation can well occur in the molten state.

within the melt. This partial pressure is adjusted by the operating temperature. The desired low operation temperature increases the viscosity of the melt and hence increases the diffusion barrier of the gas in the liquid. This in turn facilitates the exsolution of reduced vanadium sulfates which further inhibit the oxygen diffusion.

### 2.1.1.5 Metallic Glasses

Amorphous metals can be prepared in a wide variety of stable and metastable compositions with all catalytically relevant elements. This synthetic flexibility and the isotropic nature of the amorphous state with no defined surface orientations and no defect structure (as no long-range ordering exists) provoked the search for their application in catalysis [21]. The drastic effect of an average statistical mixture of a second metal component to a catalytically active base metal was illustrated in a model experiment of CO chemisorption on polycrystalline Ni which was alloyed by Zr as a crystalline phase and in the amorphous state. As CO

chemisorbs as a molecule on Ni and dissociates on Zr, it was observed that on the crystalline alloy a combination of molecular and dissociative chemisorption in the ratio of the surface abundance occurred. This additive behavior was replaced by a synergistic effect of the Zr in the amorphous state where molecular adsorption with a modified electronic structure of the adsorbate was observed [22]. This experiment led to the conclusion that with amorphous metals a novel class of catalytic materials with tuneable electronic properties might be at our disposal.

First attempts to check this hypothesis [23] revealed a superior catalytic activity of iron in amorphous iron-zirconium alloys in ammonia synthesis compared to the same iron surface exposed in crystalline conventional catalysts. A detailed analysis of the effect subsequently revealed that the alloy, under catalytic conditions, was not amorphous but crystallized into platelets of metastable epsilon-iron supported on Zr-oxide [24, 25].

This was the first proven example of the operation of the principle that free energy stored in the metastable amorphous alloy can be used to create a catalytically active species which is still metastable against phase separation and recrystallization, but which is low enough in residual free energy to maintain the catalytically active state for useful lifetimes.

In Pd-Zr alloys a different principle of usage for the excess free energy can be found. Amorphous alloys of the composition PdZr<sub>2</sub> were activated in several procedures and compared to a Pd on ZrO<sub>2</sub>-supported catalyst for the activity in CO oxidation applications [26, 27]. In situ activation of the amorphous alloy caused crystallization into small nanocrystalline Pd + O solid solution particles and larger pure Pd particles, which are both embedded into a high interface area of zirconia being present as poorly crystalline phase mix of monoclinic and tetragonal polymorphs. This phase mix is still metastable against formation of large particles of pure Pd and well crystallized large particles of zirconia with little common interface area as it is obtained from conventional impregnation techniques. A detailed analysis of the surface chemistry of the in situ activated amorphous alloy, which is metastable against segregation of a thick layer of zirconia in air, revealed that only under crystallization in the reaction mixture is the intimate phase mix between zirconia and Pd present at the outer surface of the material. It was concluded from kinetic data [26] that the intimate contact between zirconia and Pd should facilitate the spillover of oxygen from the oxide to the metal.

Figure 5 illustrates schematically the advantages of the metastable structure of the active surface. It remains speculative as to whether the beneficial effect is really spillover of oxygen from the oxide through the

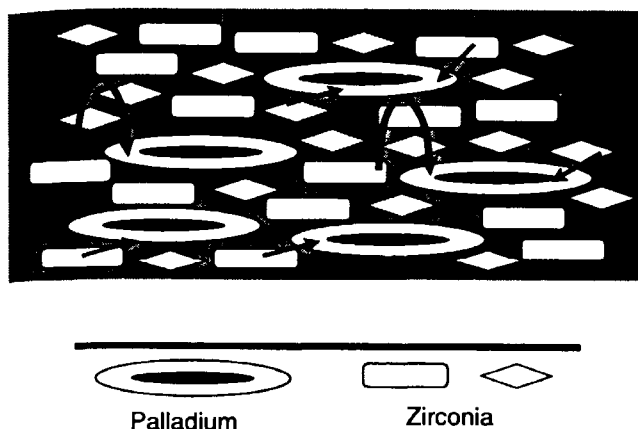


**Figure 5.** Schematic arrangement of the surface of a partly crystallized E-L TM amorphous alloy such as Pd-Zr. A matrix of zirconia consisting of the two polymorphs holds particles of the L transition metal (Pd) which are structured in a skin of solid solution with oxygen (white) and a nucleus of pure metal (black). The arrows indicate transport pathways for activated oxygen either through bulk diffusion or via the top surface. An intimate contact with a large metal-to-oxide interface volume with ill-defined defective crystal structures (shaded area) is essential for the good catalytic performance. The figure is compiled from the experimental data in the literature [26, 27].

surface and/or bulk diffusion [26], or whether the structural stabilization of the known [27] oxygen storage phase in the Pd (the solid solution) by the defective zirconia matrix is the reason for the superior catalytic performance.

Most relevant for the oxygen transport should be the defective crystal structure of both catalyst components. The defective structure and the intimate contact of crystallites of the various phases are direct consequences of the fusion of the catalyst precursor and are features which are inaccessible by conventional wet chemical methods of preparation. Possible alternative strategies for the controlled synthesis of such designed interfaces may be provided by modern chemical vapor deposition (CVD) methods with, however, considerably more chemical control than is required for the fusion of an amorphous alloy.

The metastable character of amorphous alloys under catalytic conditions is illustrated in Figure 6. Thermogravimetric and differential thermal analysis (TG/DTA) responses are shown for the treatment of a Pd-Zr alloy in reducing and oxidizing atmospheres. In pure hydrogen the formation of hydride intercalation compounds are revealed by the small reversible weight changes in the temperature range between 300 K and 600 K. It is interesting to note that the low-temperature intercalation is an endothermal process (formation of a palladium hydride), whereas the high-temperature intercalation causes no thermal response (formation of a zirconium-hydrogen solid solution). All this does not

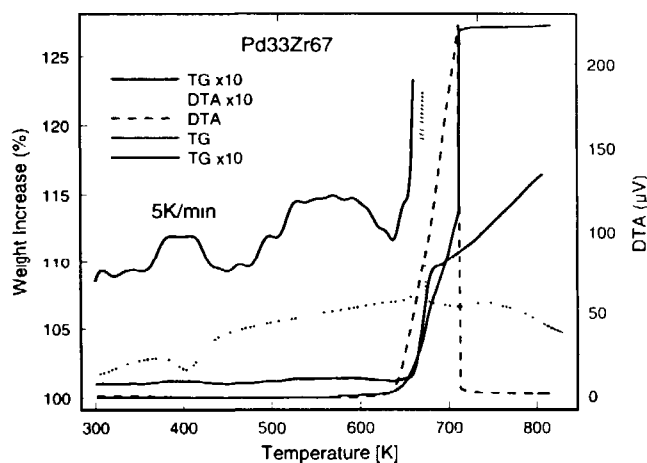


**Figure 6.** Compilation of TG/DTA responses for the crystallization of the amorphous alloy Pd<sub>33</sub>Zr<sub>67</sub> which was prepared by the melt-spinning technique. The red data were obtained in hydrogen, the blue data in oxygen. The responses in hydrogen are enlarged by a factor of 10, the enlarged weight curve by a factor of 100 relative to the ordinate scales. A SEIKO instrument was used and gas flows of 100 ml min<sup>-1</sup> were adjusted for sample masses of ca. 4 mg.

affect the amorphous character of the alloy which crystallizes in a single exothermic step at 663 K. The concomitant weight gain indicates the extreme reactivity of the fresh zirconium metal surface formed by the segregation and crystal growth leading to a gettering effect of impurities present in the hydrogen gas stream. Their transportation into the bulk of the alloy is reflected by the increasing weight above 680 K. In oxygen the crystallization temperature is the same as in hydrogen, indicating the absence of drastic chemically induced segregation phenomena as cause for the bulk crystallization. The oxidation of Zr metal is a highly exothermic process occurring after the alloy has transformed into a crystalline phase mix. This stepwise conversion with surface and bulk reactivity is reflected in the stepped weight increase. The thermal signal is overloaded by the heat evolution caused by the Zr oxidation so that little structure is seen in the DTA signals. The data show that the amorphous alloy is passivated at room temperature and can be used in oxygen up to the crystallization temperature which breaks the passivation layer due to formation of a new mesostructure causing mechanical stress and strain on the protective coating. However, hydrogen, can penetrate the passivation layer and form hydrides in the amorphous metallic subsurface regions. The shape of the TG signals indicates transport limitations arising from the nonisothermal experiment. The interaction of the hydrogen with the alloy was not strong enough to overcome the activation barrier for crystallization. Such a diluted palladium catalyst may thus be used up

to temperatures of 623 K. The lifetime of the system is not derived by this type of experiment which is too insensitive to detect surface crystallization which would induce slow bulk reactions at lower temperatures than seen in the TG/DTA experiments.

In a study of the application of Pd-Si amorphous alloys as selective hydrogenation catalysts [3] it was found that in situ activation provides a route to active and selective catalysts, whereas ex situ activation caused the crystallization of the system into the thermodynamically stable Pd + SiO<sub>2</sub> system, which is indistinguishable in its activity and poor selectivity from conventional catalysts of the same composition. In this study it was possible to show conclusively that all amorphous alloys are not amorphous on their surfaces as they undergo, in reaction gas atmospheres, chemically-induced phase segregation which starts the crystallization process according to Figure 2 (pathway 2).

The function of the fused amorphous alloys is thus to serve as a precursor material for the formation of a metastable active phase characterized by an intimate mixture of phases with different functions. This mixture is preformed during preparation of the metallic melt and preserved by rapid solidification. The micromorphology consists of quenched droplets allowing subsequent segregation into platelets. In situ activation is the method to prevent crystallization in the structure with the global free energy minimum. This activation allows the transformation of the supersaturated solution from the fusion process to only crystallize until the metastable state of the tangent line (2) in Figure 2 is reached. At this stage of transformation the catalytically active state is present. This principle of application of amorphous alloys is also highlighted in review articles [3–5] on the subject which describe a variety of other catalytic applications of this class of fused materials.

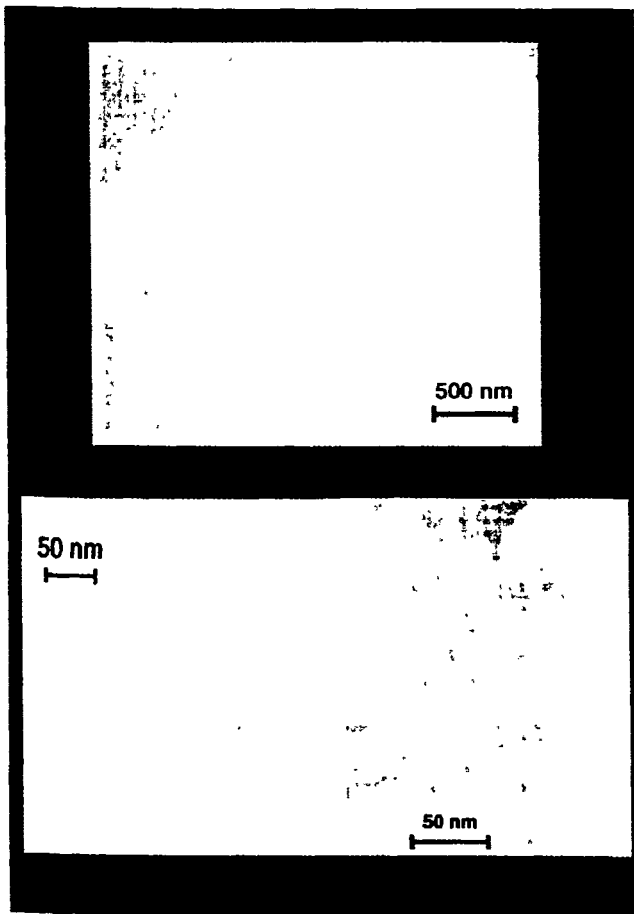


**Figure 7.** High-resolution SEM images of the activated fused iron catalyst for ammonia synthesis. The anisotropic mesostructure and the high internal surface area are visible. The small probe size of a 200 keV electron beam in a JEOL CX 200 instrument was used for backscattering detection of the scanning image from very thin objects.

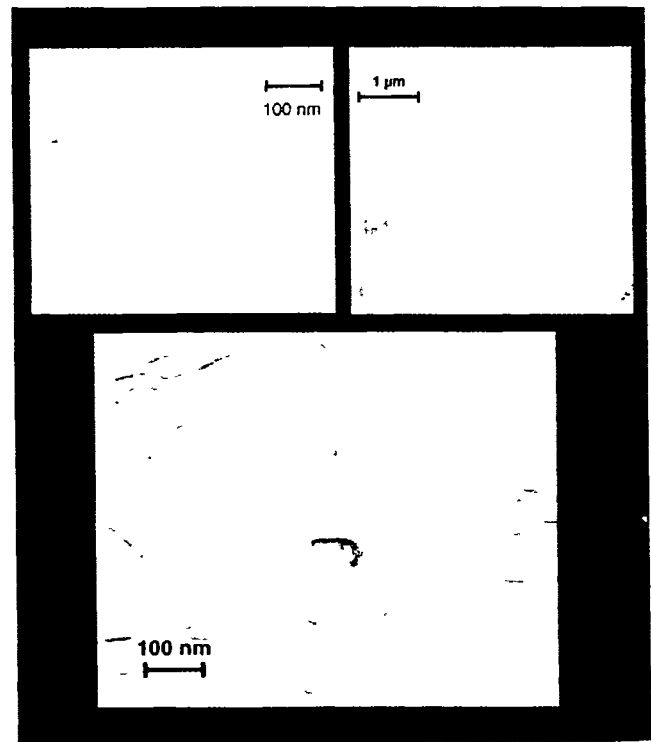


**Figure 8.** SEM surface images of partly crystallized sections of an activated Fe<sub>91</sub>Zr<sub>9</sub> alloy used for ammonia synthesis [23, 24]. The main image reveals the formation of a stepped iron metal structure with a porous zirconium oxide spacer structure. An almost ideal transport system for gases into the interior of the catalyst is created with a large metal-oxide interface which provides high thermal and chemical stability of this structure. The edge contrast in the 200 keV backscattered raw data image arises from the large difference in emissivity between metal and oxide. It is evident that only fusion and segregation-crystallization can create such an interface structure.



### 2.1.1.6 Mesostructure of Fused Catalyst Materials

The aim of fusion and controlled solidification of a catalytic material is the generation of a metastable catalytic material. The thermodynamic instability can be caused by a nonequilibrium composition, by a nonequilibrium morphology, or by a combination of both. In the case of the SLP catalysts the desired effect is to avoid the formation of solidification in order to maintain a structureless state of the active material.

The detection of metastable phases by spectroscopic and local structure-sensitive methods has been described in case studies [3, 28–31]. The detection of nonequilibrium mesostructures is rather difficult and less frequently carried out due to the fact that the relevant size range is between local atomic microstructural motives and macroscopic crystal morphologies. For this reason conventional scanning electron microscopy as well as transmission electron microscopy (which reveals only two-dimensional projections) are not ideally suited to the study of such mesostructures. High-resolution scanning electron microscopy (SEM) with high-voltage probes and field emission instruments or scanning probe microscopies [25] are suitable techniques to retrieve the information about the metastable mesostructure. This information is of significant catalytic relevance as many reactions are structure-sensitive and thus exhibit different kinetics on different surface orientations. The generation of nonisotropic particles with the consequence of preferred abundancies of selected orientations (i.e. basal planes of platelets) or with large interfaces between different phases in the catalysts are key issues in the process of improving or even tailoring catalytic performance.

Fused materials provide a viable route to bulk amounts of nonisotropic particles prepared in a controlled yet complex procedure. This is illustrated in the micrographs of Figures 7 and 8 which show metallic iron in nonequilibrium mesostructures generated by fusion processes. Figure 7 shows sections of the activated technical ammonia synthesis catalyst. In the top image the perimeter of an isotropic iron crystallite (a cube) can be seen. The high resolution image reveals, however, that the iron cube is of a spongy structure. The close-up images reveal stacks of platelets with a quite irregular basal plane shape. This irregular shape provides the opportunity to form stacks with irregular edges forming a pore system with a size range of about 10 nm. This pore system is suitable to bring gaseous reactants in the interior of the iron crystal. Only the fusion process of the oxide precursor is responsible for this clearly nonequilibrium mesostructure of a bcc metallic element (see also Section B 2.1.1).

In Figure 8 typical perspectives of an activated iron-zirconium metallic glass ( $\text{Fe}_{91}\text{Zr}_9$ ) also used for am-

monia synthesis [24, 32] can be seen. The top view in the large image shows the formation of a large-area interface between the metallic iron islands and the meandering system of exsolved zirconium oxide. The shape of the pattern is reminiscent of a spilled liquid and is the consequence of the supercooled liquid state of the amorphous precursor. The side views of the two components reveals clearly the different organization of the crystallites in the metallic part, with regular steps of prism faces from platelets for the iron metal, and the spongy porous structure of the zirconia, imaged here in a location with a large oxide patch allowing suitable orientation of the specimen. A similar organization was also shown to be characteristic of the Pd-Zr system used for CO oxidation [27]. The images of Figure 8 illustrate one view of the schematic structure given in Figure 5 for partly crystallized amorphous metals.

## References

- 1 A Cottrell, *An Introduction to Metallurgy*, Jesus College, 1975
- 2 *Amorphous Metallic Alloys*, (Ed F E Luborsky), Butterworths, London, 1983
- 3 K Noack, C Rehren, H Zbinden, R Schlogl, *Langmuir* 1995, 11, 2018–2030
- 4 A Baker, *Faraday Discuss Chem Soc* 1989, 87, 239–251
- 5 A Molnar, G V Smith, M Bartok, *Adv Catal* 1989, 36, (36), 329–383
- 6 *Chemical Kinetics of Solids*, (Ed H Schmalzried), VCH, Weinheim 1995
- 7 D R Uhlmann, *J Non-cryst Solids* 1972, 7, 337
- 8 H A Davies, B G Lewis, *Scripta Met* 1975, 9, 1107–1112
- 9 D Turnbull, *Contemp Phys* 1969, 10, 473–488
- 10 U Koster, P Weiss, *J Non-cryst Solids* 1975, 17, 359
- 11 M von Heimendahl, H Oppolzer, *Scripta Met* 1978, 12, 1087–1090
- 12 P G Boswell, *Scripta Met* 1977, 11, 701–707
- 13 F J Doering, D A Berkel, *J Catal* 1987, 103, 126–139
- 14 G K Borekov, G M Polyakova, A A Ivanov, V M Mastikhin, *Dokl Akad Nauk* 1973, 210, 626
- 15 G K Borekov, A A Ivanov, B S Balzhinimaev, L M Karnatovskaya, *React Kinet Catal Lett* 1980, 14, 25–29
- 16 D A Karydis, S Boghosian, R Fehrmann, *J Catal* 1994, 145, 312–317
- 17 S Boghosian, R Fehrmann, N J Bjerrum, G N Papatheodorou, *J Catal* 134, 119, 121–134
- 18 L G Simonova, B S Balzhinimaev, O B Lapina, Y O Bulgakova, T F Soshkina, *Kin Katal* 1991, 32, 678–682
- 19 F P Holroyd, C N Kenney, *Chem Eng Sci* 1971, 26, 1971
- 20 K M Eriksen, R Fehrmann, N J Bjerrum, *J Catal* 1991, 132, 263–265
- 21 R Schlogl, *Rapidly Quenched Metals*, 1985, 1723–1727
- 22 R Hauert, P Oelhafen, R Schogl, H-J Guntherodt, *Rapidly Quenched Metals* 1985, 1493–1496
- 23 E Armbruster, A Baker, H Baris, H-J Guntherodt, R Schlogl, B Walz, *J Chem Soc, Chem Comm* 1986, 299–301
- 24 A Baker, R Schlogl, E Armbruster, H-J Guntherodt, *J Catal* 1987, 107, 221–231

25. R. Schlögl, R. Wiesendanger, A. Baiker, *J. Catal.* **1987**, *108*, 452–466.
26. A. Baiker, D. Gasser, J. Lenzner, A. Reller, R. Schlögl, *J. Catal.* **1990**, *126*, 555–571.
27. R. Schlögl, G. Loose, M. Wesemann, A. Baiker, *J. Catal.* **1992**, *137*, 139–157.
28. H. Yamashita, M. Yoshikawa, T. Funabiki, S. Yoshida, *J. Catal.* **1986**, *99*, 375–382.
29. H. Yamashita, M. Yoshikawa, T. Funabiki, S. Yoshida, *J. Chem. Soc., Faraday Trans. I* **1987**, *83*, 2883–2893.
30. B. Schleich, D. Schmeisser, W. Göpel, *Surf. Sci.* **1987**, *191*, 367–384.
31. P. Oelhafen, M. Liard, H.-J. Güntherodt, K. Berresheim, H. D. Polaschegg, *Solid State Comm.* **1979**, *30*, 641–644.
32. A. Baiker, H. Baris, R. Schlögl, *J. Catal.* **1987**, *108*, 467–480.

## 2.1.2 Skeletal Metal Catalysts

M. S. WAINWRIGHT

“It is in the preparation of catalysts that the Chemist is most likely to revert to type and to employ alchemical methods. From all evidence, it seems the work should be approached with humility and supplication, and the production of a good catalyst received with rejoicing and thanksgiving” [1].

### 2.1.2.1 Introduction

Murray Raney graduated as a Mechanical Engineer from the University of Kentucky in 1909 and in 1915 he joined the Lookout Oil and Refining Company in Tennessee with responsibility for installation of electrolytic cells for the production of hydrogen which was used in the hydrogenation of vegetable oils. At the time the industry used a nickel catalyst that was prepared by hydrogen reduction of supported nickel oxide. Raney believed that better catalysts could be produced and in 1921 he formed his own research company. In 1924 he produced a 50% nickel–silicon alloy which he treated with aqueous sodium hydroxide to produce a greyish metallic solid which was tested by hydrogenation of cottonseed oil. He found the activity of his catalyst to be five times greater than the best catalyst then in use and he therefore applied for a patent which was issued on December 1, 1925 [2].

Subsequently Raney produced a nickel catalyst by leaching a 50 wt% Ni–Al alloy in aqueous sodium hydroxide and that catalyst was even more active and a patent application was filed in 1926 [3]. This class of

materials is generically called “skeletal” or “sponge” metal catalysts. The choice of an alloy containing 50 wt% Ni and 50 wt% Al was fortuitous and without scientific basis, and is part of the alchemy referred to above. However, it is of interest to note that it is the preferred alloy composition for production of skeletal nickel catalysts currently in use. In 1963 Murray Raney sold his business to the W. R. Grace and Company whose Davison Division produces and markets a wide range of these catalysts. Because Raney® catalysts are protected by registered trademark, only those products produced by Grace Davison are properly called “Raney Ni”, “Raney Cu” etc. Alternatively the more generic “skeletal” is used to refer to catalysts in the following. In addition, “Ni–Al” or “Cu–Al” etc. rather than “Raney alloy” is used to refer generically to the precursor to the catalyst.

Following the development of sponge-metal nickel catalysts by alkali leaching of Ni–Al alloys by Raney, other alloy systems were considered. These include iron [4], cobalt [5], copper [6], platinum [7], ruthenium [8], and palladium [9]. Small amounts of a third metal such as chromium [10], molybdenum [11], or zinc [12] have been added to the binary alloy to promote catalyst activity. The two most common skeletal metal catalysts currently in use are nickel and copper in unpromoted or promoted forms. Skeletal copper is less active and more selective than skeletal nickel in hydrogenation reactions. It also finds use in the selective hydrolysis of nitriles [13]. This chapter is therefore mainly concerned with the preparation, properties and applications of promoted and unpromoted skeletal nickel and skeletal copper catalysts which are produced by the selective leaching of aluminum from binary or ternary alloys.

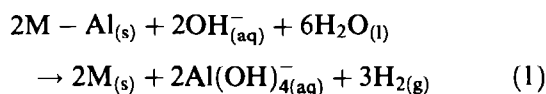
### 2.1.2.2 General Aspects

#### A Alloy Preparation

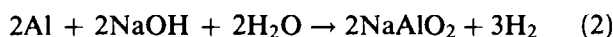
Alloys are prepared commercially and in the laboratory by melting the active metal and aluminum in a crucible and quenching the resultant melt which is then crushed and screened to the particle size range required for a particular application. The alloy composition is very important as different phases leach quite differently leading to markedly different porosities and crystallite sizes of the active metal. Mondolfo [14] provides an excellent compilation of the binary and ternary phase diagrams for aluminum alloys including those used for the preparation of skeletal metal catalysts. Alloys of a number of compositions are available commercially for activation in the laboratory or plant. They include alloys of aluminum with nickel, copper, cobalt, chromium–nickel, molybdenum–nickel, cobalt–nickel, and iron–nickel.

### B Activation Using Alkali Leaching

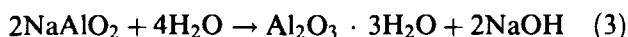
Skeletal catalysts are generally prepared by the selective removal of aluminum from alloy particles using aqueous sodium hydroxide. The leaching reaction is given by



The dissolution of aluminum in aqueous sodium hydroxide may be represented more simply by



The formation of sodium aluminate ( $NaAlO_2$ ) requires that high concentrations (20–40 wt%) of excess sodium hydroxide are used in order to avoid the formation of aluminum hydroxide which precipitates as bayerite:



and causes blocking of pores and surface site coverage in the sponge metals formed during leaching. The bayerite deposition leads to loss of surface area and hence catalyst activity. Care must be taken during activation of the alloys to vent the large quantities of hydrogen that are produced by reaction in order to prevent explosions and fires.

The temperature used to leach the alloy has a marked effect on the pore structure and surface area of the catalyst. The surface areas of skeletal catalysts decrease with increasing temperature of leaching due to structural rearrangements leading to increases in crystallite size analogous to sintering [15]. Leaching of aluminum from certain alloys can be extremely slow at low temperatures and hence a compromise in the temperature of leaching must be reached in order to produce a catalyst with an appropriate surface area in a reasonable period of time.

A convenient method to produce powdered skeletal catalysts is to use the procedure described by Freil and co-workers [16] for Raney nickel. The same relative proportions of alloy and leachant can be used to maintain the leach reaction relatively isothermal when larger quantities of catalyst are desired. In their method an aqueous solution containing 40 wt% NaOH is added stepwise to 30 g of alloy powder and 150 ml of distilled water in a vessel at 313 K. Alkali additions are made at approximately 2-min intervals. For the first 20-min period the volume of alkali added is 2 ml, and 5-ml additions are made thereafter. A reaction time of around 3 h is sufficient to fully leach 500- $\mu$ m particles of aluminium-nickel or aluminium-copper alloys at 313 K. After extraction the catalysts are washed with distilled water at ambient temperature, first by decantation and then by water flow in a vessel until the pH is lowered to around 9. The samples can then be stored in

a closed vessel under deaerated distilled water to prevent oxidation prior to use.

Activated skeletal catalysts including nickel, copper, cobalt and molybdenum or chromium-promoted nickel are available commercially.

### C Storage and Handling

Skeletal metal catalysts are extremely pyrophoric due to the small sizes of the metal crystallites that form during the leaching process. If the catalysts are allowed to dry in air the metal particles rapidly oxidize generating large amounts of heat such that the particles glow red. The heat may cause ignition of combustible materials in the vicinity. It is therefore important that after preparation, the catalysts be properly stored in a liquid. In general, water is used as the storage medium. However, there is the possibility that hydrolysis of any residual sodium aluminate will occur according to Equation 3 leading to the formation of hydrated alumina resulting in catalyst deactivation by surface and pore blocking. For this reason storage under slightly alkaline conditions (pH 9 to 11) is preferred. Studies of storage of catalysts using aliphatic alcohols suggest that isopropanol is a better storage medium than water. However, this does not have significant practical importance.

### D Advantages of Skeletal Metal Catalysts

The principal advantage of skeletal catalysts is that they can be stored in the form of the active metal and therefore require no prereluction prior to use as do conventional catalysts which are in the form of the oxide of the active metal supported on a carrier. These catalysts can also be prepared on demand by a simple caustic leaching procedure. They have very high activity since the BET surface area (typically up to 100 m<sup>2</sup> g<sup>-1</sup> for skeletal nickel and 30 m<sup>2</sup> g<sup>-1</sup> for skeletal copper) is essentially the metal surface area. Skeletal catalysts are low in initial cost per unit mass of metal and therefore provide the lowest ultimate cost per unit mass of active catalyst. The high metal content provides good resistance to catalytic poisoning.

Because alloy composition and leaching conditions can be carefully controlled, skeletal catalysts exhibit excellent batch to batch uniformity. The particle size of the catalyst can be easily controlled through crushing and screening. Thus ultrafine powders can be produced for use in slurry-phase reactors whilst large granules can be produced for use in fixed-bed applications. The relatively high densities of skeletal catalysts (particularly nickel) provide excellent settling characteristics compared with supported catalysts when used in slurry-phase reactors. The high thermal conductivity of the all-metal skeletal catalyst is a further advantage.

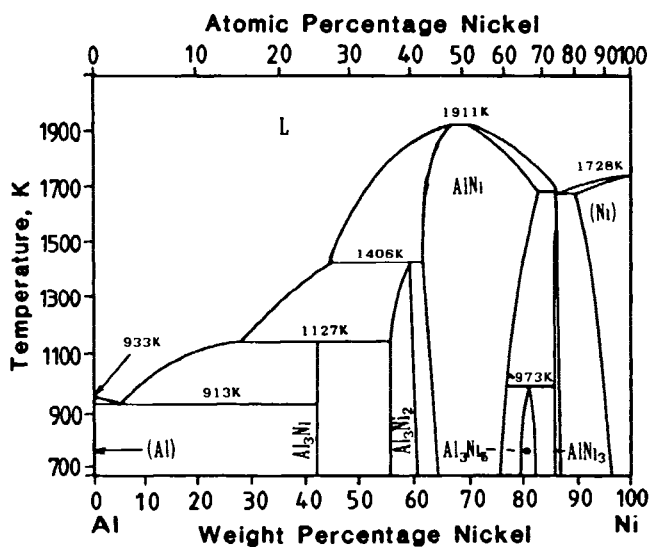


Figure 1. Al-Ni phase diagram.

### 2.1.2.3 Skeletal Nickel Catalysts

#### A Skeletal Nickel Catalysts – Alloy Preparation

Skeletal nickel catalysts used industrially are produced from alloys that typically contain 40–50 wt% nickel, with the 50% composition being most commonly used. The alloys are produced by adding molten aluminum to nickel which dissolves by a highly exothermic reaction. For laboratory preparations the use of an induction furnace and graphite crucibles provides a very convenient method of preparation. The melt is rapidly quenched in water leading to alloys with quenched structures consisting of the intermetallics  $\text{Ni}_2\text{Al}_3$ ,  $\text{NiAl}_3$ , and some frozen eutectic. It has been found [17] that the eutectic material leaches more rapidly than  $\text{NiAl}_3$  which leaches much more rapidly than  $\text{Ni}_2\text{Al}_3$ .

The phase diagram for the Al-Ni system is shown in Figure 1. An alloy of composition 42 wt% nickel corresponds to  $\text{NiAl}_3$  whilst  $\text{Ni}_2\text{Al}_3$  contains approximately 60 wt% nickel. A study of the selective leaching of essentially pure  $\text{NiAl}_3$  and  $\text{Ni}_2\text{Al}_3$  intermetallics [17] showed that  $\text{NiAl}_3$  readily leached in 20 wt% aqueous NaOH at temperatures from 274 to 323 K producing porous nickel which was friable and readily disintegrated. On the other hand, at those temperatures  $\text{Ni}_2\text{Al}_3$  was unreactive, requiring temperatures from 343 to 380 K to produce significant extents of leaching. The reaction between  $\text{Ni}_2\text{Al}_3$  and the NaOH solution proceeded in two steps. At first a two-phase mixture of  $\text{Ni}_2\text{Al}_3$  plus Ni was produced and at longer times, nickel alone. It is apparent that the 50 wt% Ni alloy that is commonly used industrially represents a composition that is a compromise between the readily leached  $\text{NiAl}_3$  which produces mechanically weak cat-

alysts and  $\text{Ni}_2\text{Al}_3$  which is more difficult to leach but which forms a strong residual material.

It is not only composition of the melt but also the rate of cooling that determines the metallography of the resulting alloy. In order to produce essentially pure phases it is necessary to undertake very controlled annealing procedures [17]. Freil *et al.* [16] used metallographic techniques to determine the phase compositions of two commercial aluminium-nickel alloys containing 50 wt% Ni and 42 wt% Ni, respectively. They found that the 50 wt% Ni alloy contained 58 vol%  $\text{Ni}_2\text{Al}_3$ , 40 vol%  $\text{NiAl}_3$ , and 2% eutectic, whereas the 42 wt% Ni alloy contained 30 vol%  $\text{Ni}_2\text{Al}_3$ , 45 vol%  $\text{Ni}_2\text{Al}_3$  and 25 vol% eutectic.

#### B Skeletal Nickel Catalysts – Properties

Skeletal nickel catalysts have BET surface areas typically in the range 50 to 100  $\text{m}^2\text{g}^{-1}$ . The theoretical pore volumes for fully leached  $\text{NiAl}_3$  and  $\text{Ni}_2\text{Al}_3$  are 0.48  $\text{cm}^3\text{g}^{-1}$  and 0.17  $\text{cm}^3\text{g}^{-1}$ , respectively. The large pore volume for the material prepared from  $\text{NiAl}_3$  accounts for its low mechanical strength. Table 1 presents typical characteristics of Raney nickel catalysts produced by leaching a 50 wt% Ni alloy using an NaOH:Al molar ratio of approximately 1.8:1. The results in Table 1 show that increased temperature of leaching leads to increased pore diameter, increased crystallite size, and lower total surface area.

A remarkable property of skeletal nickel is its ability to store hydrogen that is produced during the leaching process. It has been shown that the amount of hydrogen present in a freshly prepared sample of skeletal nickel can exceed by an order of magnitude the amount of hydrogen that could be chemisorbed on the surface nickel atoms. There have been a large number of explanations for this phenomenon. Suffice to say, the ability to store hydrogen accounts for the high activity of Raney nickel in a wide range of hydrogenation reactions.

#### C Skeletal Nickel Catalysts – Uses

Raney nickel catalysts are used in a wide range of organic synthesis reactions including:

- hydrogenation of nitro compounds
- hydrogenation of alkenes
- hydrogenation of carbonyl compounds
- hydrogenation of nitriles
- ammonolysis of alcohols
- hydrogenation of alkynes
- hydrogenation of aromatic compounds
- reductive alkylation
- methanation.

Table 2 lists some typical industrial applications.

**Table 1.** Surface properties of skeletal nickel catalysts produced by leaching a 50 wt% Ni alloy in aqueous sodium hydroxide solution (compiled from refs. 16, 18 and 19).

Activation temp. (K)	BET surface area (m <sup>2</sup> g <sup>-1</sup> )	Pore volume (cm <sup>3</sup> g <sup>-1</sup> )	Average pore Diameter (nm)	Crystallite size (nm)	Surface as Ni (%)
323	100	0.064	2.6	3.6	59
380	86	0.125	5.8	5.7	75

**Table 2.** Industrial applications of skeletal nickel catalysts.

Reaction	Reactant	Product
Hydrogenation of nitro compounds	2,4-dinitrotoluene 2-nitropropane	2,4-toluenediamine isopropylamine
Hydrogenation of alkenes	sulfolene	sulfolane
Hydrogenation of carbonyl compounds	dextrose	sorbitol
Hydrogenation of nitriles	2-ethylhexanal stearonitrile	2-ethylhexanol stearylamine
Ammonolysis of alcohols	adiponitrile	hexamethylenediamine
Hydrogenation of alkynes	1,6-hexanediol	hexamethylenediamine
Hydrogenation of aromatics	1,4-butyne diol benzene	1,4-butanediol cyclohexane
Reductive alkylation	phenol	cyclohexanol
Methanation	dodecylamine + formaldehyde synthesis gas (CO/CO <sub>2</sub> /H <sub>2</sub> )	<i>N,N</i> -dimethyldodecylamine methane

#### 2.1.2.4 Promoted Skeletal Nickel Catalysts

The addition of a second component in metal catalysts is widely used in order to enhance activity and/or selectivity. In the case of skeletal nickel catalysts it is a simple procedure to add small amounts of a second metal during the alloy preparation stage. Although other metals have been used in laboratory studies, the most common metals used to promote skeletal nickel catalysts employed industrially are Co, Cr, Cu, Fe, and Mo.

Montgomery [11] has made a detailed study of the functional group activity of promoted Raney nickel catalysts. He prepared catalysts by leaching alloy powders of the type Al (58 wt%)/Ni (37–42 wt%)/M (0–5 wt%), where M = Co, Cr, Cu, Fe, and Mo, in aqueous sodium hydroxide (NaOH/Al (molar) = 1.80) at 323 K. The activities of the catalysts were measured by the rates of hydrogenation of various organic compounds including an alkene, a carbonyl compound, a nitro compound and a nitrile compound. Of the metals tested molybdenum was found to be the most effective promoter. All the metals tested were found to increase the activity of Raney nickel in the hydrogenation of a nitrile compound. It was found that the optimum level of promoter present in the precursor alloy was Cr = 1.5 wt%, Mo = 2.2 wt%, Co = 2.5–6.0 wt%, Cu = 4.0 wt%, and Fe = 6.5 wt%. The effect of promoters was most apparent for the hydrogenation of a nitrile compound. Table 3 summarizes the results of

Montgomery [11] showing the catalysts with optimum activity.

#### 2.1.2.5 Skeletal Cobalt Catalysts

Cobalt catalysts have activities in hydrogenation reactions between those of nickel and copper. For example, nickel catalyzes methanation, cobalt catalyzes higher alcohol and low molecular weight hydrocarbon synthesis, whilst copper catalyzes methanol synthesis. Skeletal Co has less activity but greater selectivity than skeletal Ni and is effective in converting nitriles to primary amines in the absence of ammonia. Skeletal cobalt can be readily prepared from a nominal 50 wt% Co alloy. For example, when particles of a 48.8 wt% Co, 51.3 wt% Al alloy were leached in a 40% aqueous sodium hydroxide solution, 97.5% of the Al was leached resulting in porous cobalt with a BET surface area of 26.7 m<sup>2</sup> g<sup>-1</sup> and a bimodal pore size distribution with pore diameter maxima of 4.8 nm and 20 nm [20]. The crystallite size of the extracted catalyst was 4.7 nm. There appears to be scope for considerably more studies of and practical applications for skeletal cobalt catalysts.

#### 2.1.2.6 Skeletal Copper Catalysts

##### A Skeletal Copper Catalysts – Alloy Preparation

The earliest study of copper catalysts prepared by the skeletal method was that of Fauconnau [6] who used

**Table 3.** Effect of metallic promoters in the hydrogenation of organic compounds using Raney® nickel (compiled from Ref. 11).

Promotor (M)	Alloy composition $\frac{M \times 100}{Ni + M + Al}$	Organic compound	Relative activity <sup>(a)</sup> $\frac{r(M + Ni)}{r(Ni)}$
Mo	2.2	butyronitrile	6.5
Cr	1.5	"	3.8
Fe	6.5	"	3.3
Cu	4.0	"	2.9
Co	6.0	"	2.0
Mo	2.2	acetone	2.9
Cu	4.0	"	1.7
Co	2.5	"	1.6
Cr	1.5	"	1.5
Fe	6.5	"	1.3
Fe	6.5	sodium <i>p</i> -nitrophenolate	2.1
Mo	1.5	"	1.7
Cr	1.5	"	1.6
Cu	4.0	"	1.3
Mo	2.2	sodium itaconate	1.2

(a) Ratio of reaction rate for promoted catalyst to reaction rate over unpromoted Raney® nickel

Devarda's alloy (45 wt% Cu, 50 wt% Al, and 5 wt% Zn) and aluminum bronze (90 wt% Cu and 10 wt% Al). A later study by Stanfield and Robins [21] investigated the influence of the composition of the precursor Cu–Al alloy along with leaching conditions. They found that a catalyst prepared from a 40 wt% Cu, 60 wt% Al alloy was the most active in hydrogenation reactions. The most commonly used alloy has a nominal composition of 50 wt% Cu and 50 wt% Al which corresponds to an almost pure  $CuAl_2$  phase with a small amount of Al– $CuAl_2$  eutectic.

### B Skeletal Copper Catalysts – Properties

The temperature and time of leaching has a marked effect on the surface area of skeletal copper catalysts. The surface area decreases with increasing temperature of leaching whilst prolonged contact with caustic solutions leads to structural rearrangements causing significant reductions in surface area [15]. Skeletal copper consists of rods as shown in Figure 2. Leaching of Al takes place at the alloy interface and rods of copper form through the transformation of the parent phase into a highly ordered structure as shown. The products of the leaching process are the copper rods and the sodium aluminate which fills the newly created pores. The spacing  $S$  is the sum of the diameter of the copper rod and the intervening pore.

Table 4 shows the surface properties of skeletal copper catalysts produced by leaching a 50 wt% Cu alloy in aqueous sodium hydroxide solution at 293 K. It shows that the surface area decreases with increasing particle size of the alloy. Table 5 shows the effect of temperature of extraction on the surface area and pore structures of completely leached 1000–1180  $\mu m$  particles of the 50 wt% Cu alloy. The results show

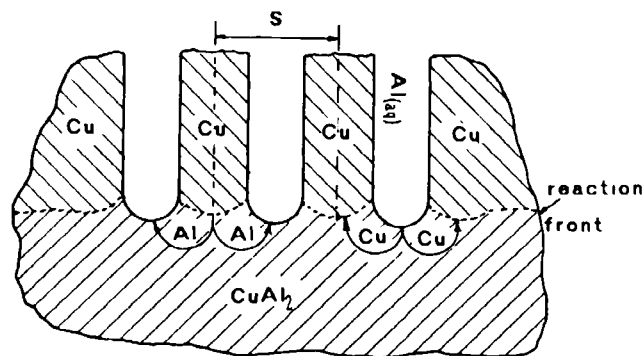


**Figure 2.** Schematic representation of a  $CuAl_2$ –Cu grain and the alloy-reaction product interface.

that increased temperature of leaching from 275 to 363 K leads to a steady decrease in surface area from  $25.4 m^2 g^{-1}$  to  $12.7 m^2 g^{-1}$ .

### C Skeletal Copper Catalysts – Uses

Skeletal copper catalysts are used in a range of selective hydrogenation and dehydrogenation reactions. For example, they are highly specific for the hydrogenation of the 4-nitro group in 2,4-dinitro-1-alkyl-benzene to the corresponding 4-amino derivative. They are used for hydrogenation of aldehydes to the corresponding alcohols, dehydrogenation of alcohols to aldehydes or ketones, hydrogenation of esters to alcohols, dehydrogenation of methanol to produce methyl formate, and steam reforming of methanol. Thus skeletal copper catalysts can be used in a wide range of gas-phase and liquid-phase hydrogenation and dehydrogenation processes.

A major industrial process that uses skeletal copper catalysts is the liquid-phase hydrolysis of nitriles to

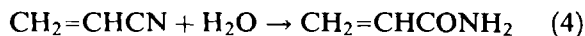
**Table 4.** Surface and pore structure data for particles of CuAl<sub>2</sub> alloy that are fully leached at 293 K (Ref. 22).

Particle size (μm)	S <sub>BET</sub> (m <sup>2</sup> g <sup>-1</sup> )	Pore diameter 2r <sub>p</sub> (nm)	Pore volume (cm <sup>3</sup> g <sup>-1</sup> )	Crystallite size (nm)	Copper rod diameter (nm)
105–180	31.4	23.6	0.214	8.7	20.6
353–420	25.3	31.6	0.203	8.2	28.5
710–850	23.5	34.2	0.197	8.7	31.5
1000–1180	24.0	33.8	0.197	8.5	31.1
1400–1676	23.9	34.2	0.197	8.5	31.5
2000–2360	21.4	38.2	0.195	8.2	35.4

**Table 5.** The effect of the temperature of extraction on the surface area and pore structure of completely leached 100–1180 μm particles of CuAl<sub>2</sub> alloy (Ref. 22).

Extraction temperature (K)	S <sub>BET</sub> (m <sup>2</sup> g <sup>-1</sup> )	Pore diameter 2r <sub>p</sub> (nm)	Crystallite size (nm)	Copper rod diameter (nm)
275	25.4	30.2	7.5	27.5
293	24.0	33.8	8.5	30.8
308	22.6	55.0	11.2	50.1
323	18.5	61.0	12.0	55.6
343	16.9	75.0	13.7	68.3
363	12.7	107.6	14.6	98.0

produce the corresponding amides. The most important of these reactions is the hydrolysis of acrylonitrile to produce acrylamide [13] according to:



This process is conducted in the liquid phase using fixed beds of skeletal copper catalysts and temperatures from 300 to 400 K. Higher temperatures lead to catalyst fouling by polymerization of the product acrylamide. This deactivation can be reversed by washing the catalyst with caustic soda solution. This regeneration is a positive advantage of skeletal copper over other forms of copper catalysts used in this industrial process.

### 2.1.2.7 Promoted Skeletal Copper Catalysts

The addition of other metals to promote skeletal catalysts has been the subject of a number of investigations including the use of V, Cr, Mn, and Cd for hydrogenation of nitro compounds [23], Cd in the hydrogenation of unsaturated esters to unsaturated alcohols [24], and Ni and Zn for the dehydrogenation of cyclohexanol to cyclohexanone. The use of Cr as a promoter is particularly attractive as copper chromite catalysts are used in a wide range of industrial applications. Laine and co-workers [25] have made a detailed study of the structure of chromium promoted skeletal copper catalysts.

### 2.1.2.8 Skeletal Copper–Zinc Catalysts

**A Skeletal Copper–Zinc Catalysts – Alloy Preparation**  
Skeletal Cu–Zn catalysts show great potential as alternatives to coprecipitated CuO–ZnO–Al<sub>2</sub>O<sub>3</sub> catalysts used commercially for low temperature methanol synthesis and water gas shift (WGS) reactions. They can also be used for other reactions such as steam reforming of methanol, methyl formate production by dehydrogenation of methanol, and hydrogenolysis of alkyl formates to produce alcohols. In all these reactions zinc oxide-promoted skeletal copper catalysts have been found to have high activity and selectivity.

Fauconnau [6] was the first to use a skeletal copper catalyst containing zinc. He prepared his catalysts from Devarda's alloy which contained 45 wt% Cu, 50 wt% Al, and 5 wt% Zn. Marsden and co-workers [12] were the first to use skeletal catalysts prepared from Cu–Zn–Al alloys for methanol synthesis. Alloys containing 50 wt% Al and 0–50 wt% Cu with the balance Zn were employed. Optimum activity for low temperature methanol synthesis was found for catalysts prepared by leaching alloys containing 50 wt% Al, 33–43 wt% Cu and 7–17 wt% Zn. Friedrich *et al.* [26] showed that catalysts prepared from alloys containing approximately 50 wt% Al, 30–36 wt% Cu and 14–20 wt% Zn had greatest activity for methanol synthesis. Bridgewater and co-workers [27] made a systematic study to optimize alloy composition and catalyst preparation. The catalysts prepared from alloys containing approximately 38 wt% Cu, 48 wt% Al, and 14 wt% Zn (alloy

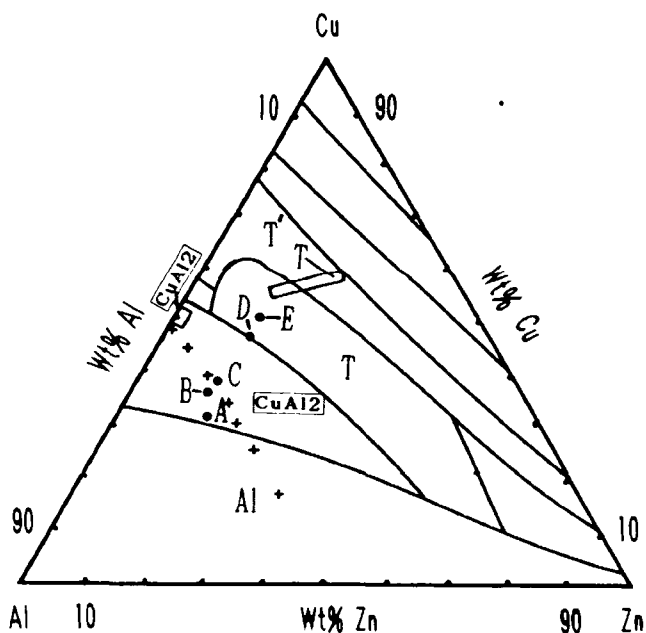


Figure 3. Al-Cu-Zn phase diagram, liquidus projection (Ref. 14): (+) alloys investigated by Friedrich *et al.* [26]; (•) alloys investigated by Bridgewater *et al.* [27].

D in Figure 3) and 47 wt% Cu, 39 wt% Al, and 14 wt% Zn (alloy E in Figure 3) had the highest activities of those tested.

Recently Andreev and co-workers [28] and Mellor [29] have made extensive studies of skeletal Cu-Zn catalysts for the water gas shift reaction. Andreev *et al.* used an alloy of composition 42.2 wt% Cu, 43.5 wt% Al, and 14.3 wt% Zn, whilst Mellor used alloys containing 10–50 wt% Cu, 50 wt% Al, and 0–40 wt% Zn, and 43 wt% Cu, 39 wt% Al, and 18 wt% Zn.

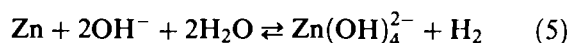
Figure 3 shows the composition of the Cu-Zn-Al alloys used by a number of investigators plotted on the liquidus projection of the Al-Cu-Zn phase diagram [14]. The alloys used by Friedrich *et al.* [26] are shown by the + symbols in this figure. The primary precipitate for alloys containing 0–17 wt% Zn is  $\text{Cu}(\text{Zn})\text{Al}_2$  which is  $\text{CuAl}_2$  containing dissolved Zn. As the Zn content of the melt is increased the Zn content of the  $\text{Cu}(\text{Zn})\text{Al}_2$  phase increases. For melts containing more than 17 wt% Zn the primary precipitate is an aluminum-based solution. Bridgewater *et al.* [27] showed that alloys containing greater than 39 wt% Cu (compositions D and E in Figure 3) were in the ternary phase region of the liquidus projection and large amounts of this difficult to leach phase were detected in the quenched alloy.

Alloys of Cu-Zn-Al are readily prepared in carbon crucibles heated in an induction furnace as described by Marsden *et al.* [12]. Copper, having the highest melting point, is melted and then aluminum is added. After vigorous stirring with a carbon rod the melt is cooled to below the boiling point of zinc before zinc is

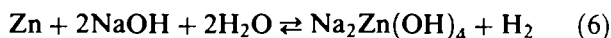
added to the melt with stirring. The melt is then rapidly quenched by pouring into cold water or onto a chilled plate. The resulting alloy is then crushed and screened. It has been shown that quenched structures are more readily leached and produce higher surface area catalysts with resultant higher activities.

### B Skeletal Copper-Zinc Catalysts – Leaching Studies

The incorporation of the Zn in Cu-Al alloys complicates the leaching process since the Zn is readily leached by aqueous caustic solutions according to Reaction 5.



If NaOH is the alkali used in the leaching step the dissolution of zinc is given by



When the concentration of NaOH is low the sodium zincate ( $\text{Na}_2\text{Zn}(\text{OH})_4$ ) precipitates as zinc hydroxide according to



It is the reprecipitation of  $\text{Zn}(\text{OH})_2$  in the porous skeletal copper which provides promotion in methanol synthesis, water gas shift, and other reactions. The highly dispersed reprecipitated  $\text{Zn}(\text{OH})_2$  decomposes at around 400 K to form ZnO which is an active promoter of copper catalysts.

When leaching aluminum alloys it is generally desirable to use high concentrations of sodium hydroxide in order to remove the Al as  $\text{NaAlO}_2$  and avoid reprecipitation of Al as bayerite ( $\text{Al}_2\text{O}_3 \cdot 3\text{H}_2\text{O}$ ). In the case of leaching of Cu-Zn-Al alloys this is particularly important since bayerite decomposes at around 600 K to form  $\gamma\text{-Al}_2\text{O}_3$  which catalyzes methanol dehydration to form dimethyl ether as a byproduct in methanol synthesis. For this reason a large excess of 40 wt% aqueous NaOH is generally used. Under these conditions much of the Al is washed from the resultant catalyst but sufficient  $\text{Zn}(\text{OH})_2$  remains precipitated on the surface of the porous copper.

More recently Curry-Hyde *et al.* [30] have improved the activity of skeletal Cu-Zn catalysts for methanol synthesis by adding sodium zincate to the sodium hydroxide leach liquor in order to achieve reprecipitation of greater amounts of  $\text{Zn}(\text{OH})_2$  on the surface of the copper. Alloys containing 53 wt% Cu and 47 wt% Al, and 43.2 wt% Cu, 17.7 wt% Zn and 39 wt% Al were leached in 6.1 M aqueous NaOH containing 0.62 M sodium zincate at 274 K and 303 K. They found that the addition of sodium zincate slows the rate of leaching of both alloys leading to increased surface areas. Electron microprobe analysis of the catalysts produced from the Cu-Zn-Al alloy leached in pure 6.1 M NaOH and a solution containing 0.62 M sodium zincate revealed that the ZnO concentration profile was



**Table 6.** Properties of skeletal copper–zinc catalysts produced by leaching Cu–Al–Zn alloys in aqueous sodium hydroxide solution at 323 K (Ref. 26).

Sample	Alloy composition (wt%) <sup>(a)</sup>			Catalyst composition (wt%) <sup>(a)</sup>			$S_{\text{BET}}$ ( $\text{m}^2 \text{g}^{-1}$ )	Pore volume ( $\text{cm}^3 \text{g}^{-1}$ )	Pore diameter $2r_p$ (nm)	Copper crystallite diameter (nm)
	Cu	Zn	Al	Cu	Zn	Al				
1	50.6	0	50.2	98.7	0	1.6	17.0	0.385	45.8	11.2
2	44.6	5.3	50.7	98.0	0.8	1.1	18.6	0.242	35.4	11.2
3	39.3	9.8	50.3	97.5	1.4	1.3	21.9	0.241	33.8	10.4
4	36.2	13.6	51.2	96.9	2.1	1.5	24.5	0.239	32.0	—
5	33.5	17.1	49.7	97.1	2.8	1.6	26.8	0.238	28.4	10.4
6	30.5	20.6	50.2	94.5	4.4	2.1	29.4	0.233	27.2	—
7	24.6	26.0	49.8	90.0	8.7	2.0	30.6	0.238	23.0	7.0

<sup>(a)</sup> Compositions of alloys and catalysts were determined by chemical analysis of acid-digested samples. The values in the table have not been normalized.

far superior when sodium zincate was added to the leach liquor. Furthermore, when sodium zincate was present in the leachant for the Cu–Al alloy containing no Zn, significant amounts of ZnO were present in the leached catalyst. Mellor [29] has successfully used sodium zincate in the sodium hydroxide leach solution when preparing catalysts from Cu–Zn–Al alloys for the water gas shift reaction.

### C Skeletal Copper–Zinc Catalysts – Properties

The properties of skeletal Cu–Zn catalysts depend on the composition of the precursor alloy, the composition of the leach solution, and the temperature and time of leaching. Table 6 shows the properties of catalysts used by Friedrich *et al.* [26]. The leaching conditions used to prepare the catalysts were 323 K, 40 wt % NaOH, and sufficient time for complete reaction of the Zn and Al with the NaOH. Thus, the catalysts were fully leached. Table 6 shows that by replacing copper by zinc in the precursor alloy catalysts with increased BET surface areas, decreased pore volumes, decreased pore diameters, and decreased copper crystallite sizes are produced. It also shows the effect of the precursor alloy composition on the surface and pore properties of the catalysts.

As stated earlier, lower leaching temperatures result in increased surface areas of skeletal catalysts. Furthermore, slowing the leaching process by the addition of sodium zincate to the leach solution leads to higher surface areas. Thus leaching of  $\text{CuAl}_2$  in 6.1 M NaOH containing 0.62 M sodium zincate at 274 K leads to a catalyst of surface area of  $58.1 \text{ m}^2 \text{g}^{-1}$  compared with a surface area of  $28.0 \text{ m}^2 \text{g}^{-1}$  when no sodium zincate is present.

### D Skeletal Copper–Zinc Catalysts – Methanol Synthesis

Skeletal Cu–Zn catalysts have activities and selectivities comparable to the best commercially available coprecipitated  $\text{CuO-ZnO-Al}_2\text{O}_3$  catalysts. Table 7 shows the comparative performance of skeletal Cu–Zn

**Table 7.** Methanol yields at 493 K and 4.5 MPa for skeletal catalysts (produced using different leaching conditions) compared to coprecipitated catalysts tested under the same conditions (Ref. 30).

Catalyst (a)	Space velocity ( $\text{h}^{-1}$ )	Methanol yield ( $\text{kg/l/h}$ )
I	36 000	1.12
I	15 000	0.80
IIa	36 000	0.64
IIb	36 000	0.61
III	12 000	0.60
IV	36 000	0.60
IV	15 000	0.44
V	15 000	0.45

(a) I: Cu–Al–Zn leached in 6.1 M NaOH/0.62 M Na zincate, at 303 K. II: Cu– $\text{Al}_2$  leached in 6.1 M NaOH/0.62 M Na zincate, (a) 274 K (b) 303 K. III: Cu–Al–Zn leaching 6.1 M NaOH, at 274 K. IV and V: Commercial coprecipitated catalysts.

and commercial catalysts. The skeletal catalysts clearly have great potential for use as methanol synthesis catalysts. One particular application is in liquid-phase methanol synthesis in which very finely divided powder catalysts are used. This is analogous to the use of finely divided skeletal nickel and skeletal copper in liquid-phase organic syntheses.

### E Skeletal Copper–Zinc Catalysts – Water Gas Shift Reaction

Andreev and co-workers [28] and Mellor [29] have prepared catalysts by leaching Cu–Zn–Al in aqueous sodium hydroxide solutions. Their studies have shown that skeletal Cu–Zn catalysts have significantly greater activities than commercial WGS catalysts when operated at temperatures below 573 K.

### Acknowledgments

The author wishes to acknowledge the strong support of the following people and organisations. Professor

R B (Bob) Anderson who introduced him to the fascinating world of skeletal catalysts in 1977. Dr. S. R. (Stewart) Montgomery who researched skeletal catalysts for Davison Chemical Division of W. R. Grace and Co has provided him with great insight into the life of Murray Raney along with considerable advice over many years. The many postgraduate students and research fellows who have worked with him on various skeletal catalyst systems and have made outstanding contributions. The financial support of the research into skeletal catalysts over an extended period by the Australian Research Council is gratefully acknowledged.

## References

- 1 M Raney, *Ind Eng Chem* **1940**, *32*, 1199
- 2 M Raney, *US Patent*, 1563587, **1925**
- 3 M Raney, *US Patent* 162810-, **1927**
- 4 M Raney, *US Patent*, 1915473, **1933**
- 5 B V Aller, *J Appl Chem* **1957**, *7*, 130
- 6 L Fauconnau, *Bull Soc Chim* **1937**, *4(5)*, 58
- 7 A A Vendenyapın, N D Zubareva, V M Akimov E I Klabunovskii, N G Giorgadze, N F Barannikova, *Izv Akad Nauk SSSR Ser Khim* **1976**, *10*, 2340
- 8 K Urabe, T Yoshioka, A Ozaki, *J Catal* **1978**, *54*, 52
- 9 T M Grishina, L I Lazareva, *Zh Fiz Khim* **1982**, *56*, 2614
- 10 R Paul, *Bull Soc Chim Fr* **1946**, *13*, 208
- 11 S R Montgomery in *Catalysis of Organic Reactions* (Ed W R Moser), Dekker, New York, USA, **1981**, p 383
- 12 W F Marsden, M S Wainwright, J B Friedrich, *Ind Eng Chem Prod Res Dev* **1980**, *19*, 551
- 13 N I Onuoha, M S Wainwright, *Chem Eng Commun* **1984**, *29*, 1
- 14 L F Mondolfo, *Aluminum Alloys Structure and Properties*, Butterworths, London, UK, **1976**
- 15 A D Tomsett, D J Young, M R Stambach, M S Wainwright, *J Mat Sci* **1990**, *25*, 4106
- 16 J Freil, W J M Pieters, R B Anderson, *J Catal* **1969**, *14*, 247
- 17 M L Bakker, D J Young, M S Wainwright, *J Mat Sci* **1988**, *23*, 3921
- 18 J Freil, S D Robertson, R B Anderson, *J Catal* **1970**, *18*, 243
- 19 S D Robertson, R B Anderson, *J Catal* **1971**, *23*, 286
- 20 J P Orchard, A D Tomsett, M S Wainwright, D J Young, *J Catal* **1983**, *84*, 189
- 21 J A Stanfield, P E Robbins, *Actes Congr Intern Catal (2nd) Paris*, **1960**, *2*, 579
- 22 A D Tomsett, *Pore Development in skeletal Copper Catalysts*, PhD Thesis, University of New South Wales, Sydney, Australia, **1987**
- 23 K Wimmer, O Suchnoth, *Ger Offen* 875519, **1953**
- 24 Kyowa Hakko Kogyo Co Ltd, *UK Patent* 1029502, **1966**
- 25 J Laine, Z Ferrer, M Labady, V Chang P Frias, *Appl Catal* **1988**, *44*, 11
- 26 J B Friedrich, M S Wainwright, D J Young, *J Catal* **1983**, *80*, 1
- 27 A J Bridgewater, M S Wainwright, D J Young, J P Orchard, *Appl Catal* **1983**, *7*, 369
- 28 A Andreev, V Kafedjuskı, T Halachev, B Kuner, M Kaltchev, *Appl Catal* **1991**, *78*, 199
- 29 J R Mellor, *The Water Gas Shift Reaction Deactivation Studies*, PhD Thesis, University of Witwatersrand Johannesburg, South Africa, **1993**
- 30 H E Curry-Hyde, M S Wainwright, D J Young, in *Methane Conversion - Studies in Surface Science and Catalysis Volume 36* (Eds D Bibby, C C Chang), Elsevier Amsterdam, The Netherlands, **1988**, p 239

## 2.1.3 Precipitation and Coprecipitation

F. SCHUTH AND K. UNGER

### 2.1.3.1 Introduction

The preparation of catalysts and supports by precipitation or coprecipitation is technically very important [1]. However, precipitation is usually more demanding than several other preparation techniques, due to the necessity of product separation after precipitation and the large volumes of salt-containing solutions generated in precipitation processes. Techniques for catalyst manufacture thus have to produce catalysts with better performance in order to compensate for the higher cost of production in comparison, for instance, to solid-state reactions for catalyst preparation.

Nevertheless, for several catalytically relevant materials, especially for support materials, precipitation is the most frequently applied method of preparation. These materials include mainly aluminum and silicon oxides. In other systems precipitation techniques are also used, for instance in the production of iron oxides, titanium oxides or zirconias. The main advantages of precipitation for the preparation of such materials is the possibility of creating very pure materials and the flexibility of the process with respect to final product quality.

Other catalysts, based on more than one component, can be prepared by coprecipitation. According to IUPAC nomenclature [2], coprecipitation is the simultaneous precipitation of a normally soluble component with a macrocomponent from the same solution by formation of mixed crystals, by adsorption, occlusion or mechanical entrapment. However, in catalyst preparation technology, the term is usually used in a more general sense in that the requirement of one species being soluble is dropped. In many cases, both components to be precipitated are essentially insoluble under precipitation conditions, although their solubility products might differ substantially. We will therefore use the term coprecipitation for the simultaneous precipitation of more than one component. Such systems prepared by coprecipitation include Ni/Al<sub>2</sub>O<sub>3</sub>, Cu/Al<sub>2</sub>O<sub>3</sub>, Cu/ZnO, and Sn-Sb oxides.

**Table 1.** Some industrially relevant catalysts and supports obtained by precipitation or coprecipitation techniques.

Material	Use	Important examples
Al <sub>2</sub> O <sub>3</sub> (mostly $\gamma$ , in special cases $\alpha$ or $\eta$ )	support, catalyst	Claus process, dehydration of alcohols to alkenes and ethers, support of hydrotreating catalysts, support for three-way catalyst
SiO <sub>2</sub>	support	noble metal/SiO <sub>2</sub> for hydrogenation reactions, Ni/SiO <sub>2</sub> for hydrogenation reactions, V <sub>2</sub> O <sub>5</sub> /SiO <sub>2</sub> for sulfuric acid production
Al <sub>2</sub> O <sub>3</sub> /SiO <sub>2</sub>	catalyst	acid-catalyzed reactions such as isomerizations
Fe <sub>2</sub> O <sub>3</sub>	catalyst, catalyst component	Fischer-Tropsch reactions, major component of catalyst for ethylbenzene reaction to styrene
TiO <sub>2</sub>	support, catalyst, catalyst component	major component of DeNO <sub>x</sub> catalyst
ZrO <sub>2</sub>	catalyst	acid catalyst after sulfate modification
Cu/ZnO	catalyst	methanol synthesis
(VO) <sub>2</sub> P <sub>2</sub> O <sub>7</sub>	catalyst	selective oxidation – for instance butane to maleic anhydride
Cu–Cr oxides	catalyst	combustion reactions, hydrogenations
AlPO <sub>4</sub>	support, catalyst	polymerization, acid-catalyzed reactions
Sn–Sb oxide	catalyst	selective oxidation – for instance isobutene to methacrolein
Bi molybdates	catalyst	selective oxidation – for instance propene to acrolein (mostly supported)

Coprecipitation is very suitable for the generation of a homogeneous distribution of catalyst components or for the creation of precursors with a definite stoichiometry, which can be easily converted to the active catalyst. If the precursor for the final catalyst is a stoichiometrically defined compound of the later constituents of the catalyst, a calcination and/or reduction step to generate the final catalyst usually creates very small and intimately mixed crystallites of the components. This has been shown for several catalytic systems and is discussed in more detail later in this article. Such a good dispersion of catalyst components is difficult to achieve by other means of preparation, and thus coprecipitation will remain an important technique in the manufacture of heterogeneous catalysts in spite of the disadvantages associated with such processes. These disadvantages are the higher technological demands, the difficulties in following the quality of the precipitated product during the precipitation, and the problems in maintaining a constant product quality throughout the whole precipitation process, if the precipitation is carried out discontinuously.

To stress the technical relevance of precipitated catalysts, Table 1 gives an overview of industrially used precipitated catalysts and supports. Since the catalyst compositions, and even less the catalysts preparation procedures for many industrial processes are not disclosed by the companies, this list is by no means comprehensive.

### 2.1.3.2 General Principles Governing Precipitation from Solutions

Precipitation processes are not only relevant for catalysis, but also for other industries, as for instance the production of pigments. However, in spite of the tre-

mendous importance of precipitation from solution, many basic questions in this field are still unsolved and the production of a precipitate with properties that can be adjusted at will is still rather more an art than a science. This is primarily due to the fact that the key step, nucleation of the solid from a homogeneous solution, is a very elusive one, and is difficult to study using the analytical tools currently available. Spectroscopies using local probes are not sensitive enough to study larger arrangements of atoms on the one hand. Diffraction methods, on the other hand, are not suitable for analysis either, since a nucleus is not large enough to produce a distinctive diffraction pattern. Thus, investigations of crystallization and precipitation processes from solution often have to rely on indirect and theoretical methods. Figure 1 depicts a general flow scheme for the preparation of a precipitated catalyst.

#### A Physico-Chemical Considerations

In order for a solid to precipitate from homogenous solution, first a nucleus has to form. The formation of a particle is governed by the free energy of agglomerates of the constituents of the solution. The total free energy change due to agglomeration,  $\Delta G$ , is determined by

$$\Delta G = \Delta G_{\text{bulk}} + \Delta G_{\text{interface}} + \Delta G_{\text{others}}$$

where  $\Delta G_{\text{bulk}}$  is the difference of the free energy between solution species and solid species,  $\Delta G_{\text{interface}}$  is the free energy change related to the formation of the interface, and  $\Delta G_{\text{others}}$  summarizes all other contributions, as for instance strain or impurities, which can be neglected here. The agglomeration will be energetically favored if  $\Delta G$  is negative. At supersaturation conditions  $\Delta G_{\text{bulk}}$  is always negative but, to create an interface, energy is needed;  $\Delta G_{\text{interface}}$  is thus positive. For very small particles the total free energy change is positive. If spherical particles are formed,  $\Delta G_{\text{bulk}}$  in-

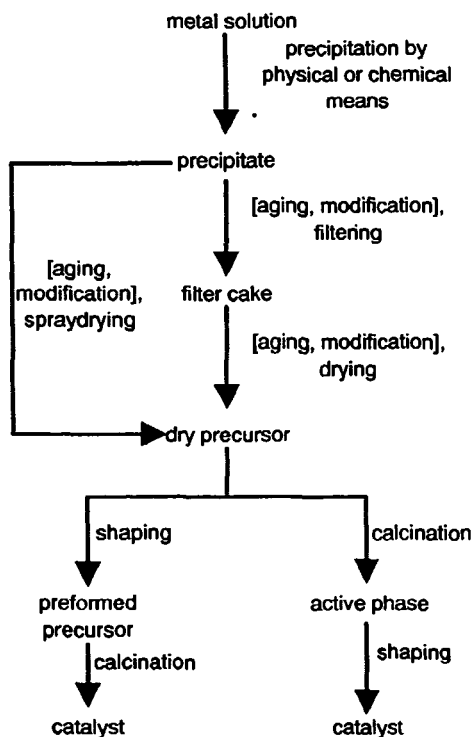


Figure 1. Preparation scheme for precipitated catalysts. Optional preparation steps are indicated by square brackets.

creases with  $4\pi r^3/3$ , while the interfacial energy only increases with  $4\pi r^2$ . There is thus a critical size  $r$  of the agglomerate, from which on  $\Delta G_{\text{bulk}}$  predominates the total free energy change and the total free energy decreases with the particle size. This critical size is the size of the nucleus.

The general process of the formation of a solid from a solution can be described in a simplified form as indicated in Fig. 2. The most important curve is the nucleation curve which describes the development of the precursor concentration with time. Such a precursor could, for instance, be the hydrolysis product of the metal ions in solution. Only if the precursor concentration exceeds a critical threshold concentration will a nucleus form, and the precipitation begins. The nucleus is defined as the "smallest solid-phase aggregate of atoms, molecules or ions which is formed during a precipitation and which is capable of spontaneous growth" [2]. As long as the concentration of precursor species stays above the nucleation threshold, new particles are formed. As soon as the concentration falls below the critical concentration due to consumption of precursors by nucleation or by the growth process, only particle growth of existing particles prevails. Thus, in the framework of this simple concept which was introduced mainly by the work of LaMer in the early 1950s [3] and later used extensively by Matijevic [4] who produced a large number of different monodispersed oxides or hydroxides, particles with a narrow

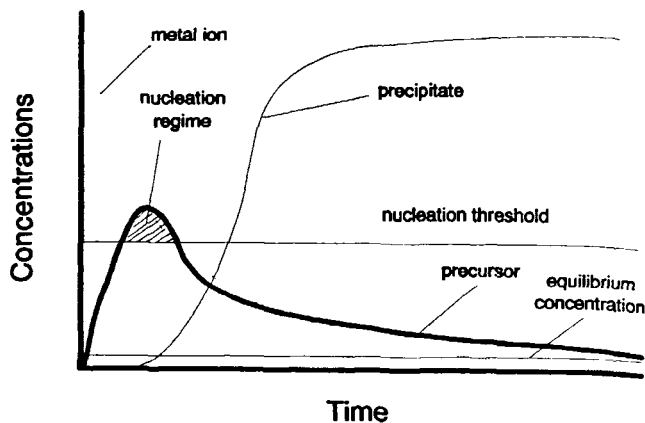


Figure 2. Simplified scheme for the formation of a solid product from solution. From the metal ions a precursor species is formed, for instance by hydrolysis or raising the pH. When the concentration of the precursor species exceeds the nucleation threshold, precipitation of the product begins, consuming precursor by nucleation and growth. New nuclei are only formed in the shaded area.

particle size distribution will result from a short nucleation burst, and a wide particle size distribution will result from nucleation over a longer period of time. The size of the particles finally resulting from a precipitation process will be dependent on the area of the shaded section between the nucleation curve and the nucleation threshold. The larger the area, the more particles nucleate and the smaller the resulting particles will be. The nucleation process is strongly temperature dependent, since the rate constant for homogenous nucleation usually does not follow an Arrhenius-type law, but is, for instance, better described by [5]

$$dN/dt = \beta \exp(-A/\ln^2 s)$$

where  $\beta$  is a preexponential term,  $A$  the interfacial energy parameter  $16\pi\sigma^3\Gamma^2/3(kT)^3$ ,  $\sigma$  the solid-fluid interfacial energy,  $\Gamma$  the solid molecular volume,  $s$  the supersaturation. However, this is only one possible expression for the nucleation rate. Several others have been proposed.

Nucleation and growth processes can be described mathematically by sets of differential equations balancing the concentrations of the various species in the system. The most well known approach to this problem is the so-called population balance formalism introduced in the early 1960s [6]. Although such models can give valuable insight into the basic ideas of particle formation from solution, it is an extremely simplified concept. The models are usually only formulated for the formation of a single phase. If more than one phase is possible, the model does not provide information on the nature of the phase eventually formed. According to the Ostwald rule of successive phase transformation, initially the thermodynamically most unstable phases

are formed which then transform to more stable phases. Another factor, which is relatively difficult to implement, is the lack of information on the decisive solution species for many systems. Usually species responsible for nucleation are also considered to be the species contributing to the particle growth. However, the nucleation might involve relatively complex species, while growth – at least of the primary particles – in many cases is assumed to proceed via monomer addition. The model also completely neglects the role of aggregation and agglomeration processes which further contribute to growth and can result in the formation of fewer, but larger particles than predicted for the simple nucleation burst model. Such processes can be of great importance in the formation of technically relevant hydroxides and oxides [7]. However, even if aggregation and agglomeration occurs, narrow particle size distributions, which are often desired, can be obtained. The uniformity in the final particle size distribution can be reached by size dependent aggregation rates [8]. In addition, mechanical agitation or other processes can lead to fragmentation of growing crystals, thus forming secondary nuclei which can alter the particle size distribution.

Another way to induce precipitation without needing a homogeneous nucleation step is the seeding of the solution. Best results are usually obtained if seeding is done with the desired phase. If the solution is seeded, usually no nucleation takes place, since the precursor concentration never exceeds a critical threshold. The precipitation rates in seeded systems normally follow Arrhenius-type rate laws. Precipitation of  $\text{Al}(\text{OH})_3$  in the Bayer process is described by [7]

$$-dc/dt = k \exp(-E/RT)A(c - c_{\text{eq}})^2$$

where  $c$  is the  $\text{Al}_2\text{O}_3$  concentration,  $k$  the rate constant,  $E$  the activation energy (about  $59 \text{ kJ mol}^{-1}$ ),  $R$  the gas constant,  $T$  the temperature,  $A$  the seed surface area and  $c_{\text{eq}}$  the equilibrium concentration. However, here as well, temperature dependencies can be complicated, since the equilibrium concentration might vary strongly with temperature.

From the facts considered above, it is clear that supersaturation of the solution from which precipitation occurs is one of the key factors of the precipitation process. Supersaturation can be reached either by physical means, which is usually cooling down the reaction mixture, or evaporation of the solvent, or by chemical means, i.e. addition of a precipitating agent. The precipitating agent either changes the pH, thus leading to condensation of precursors to form the hydroxides or the oxides, or introduces additional ions into the system by which the solubility product for a certain precipitate is exceeded. The influence of such precipitating agents is discussed in the next section.

If catalysts are prepared by coprecipitation, the relative solubilities of the precipitates and the possibility for the formation of defined mixed phases are essential. If one of the components is much more soluble than the other, there is a possibility that sequential precipitation occurs. This leads to concentration gradients in the product and less intimate mixing of the components. If this effect is not compensated by adsorption or occlusion of the more soluble component, the precipitation should be carried out at high supersaturation in order to exceed the solubility product for both components simultaneously. Precipitation of the less soluble product will proceed slightly faster, and the initially formed particles can act as nucleation sites for the more soluble precipitate which forms by heterogeneous precipitation. The problem is less crucial if both components form a defined, insoluble species. This is for instance the case for the coprecipitation of nickel and aluminum which can form defined compounds of the hydroxalite type (see the extensive review by Cavani et al. [9] and the summary by Andrew [10]).

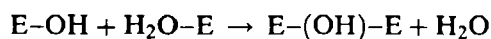
## B Chemical Considerations

It is generally desirable to precipitate the desired material in such a form, that the counterions of the precursor salts and the precipitation agent, which can be occluded in the precipitate during the precipitation, can easily be removed by a calcination step. If precipitation is induced by physical means, i.e. cooling or evaporation of solvent to reach supersaturation of the solution, only the counterion of the metal salt is relevant. If precipitation is induced by addition of a precipitating agent, ions introduced into the system via this route also have to be considered. Favorable ions are nitrates, carbonates, or ammonium, which decompose to volatile products during the calcination. For catalytic applications usually hydroxides, oxohydrates, oxides (in the following the term “hydroxides” is used in a rather general sense, comprising hydroxides and oxides with different degrees of hydration) are precipitated; in some cases carbonates, which are subsequently converted to the oxides or other species in a calcination step, are formed. Also the precipitation of oxalates as precursors for spinel-type catalysts have occasionally been reported to give good results [11]. If the ions do not decompose to volatile products, careful washing of the precipitate is advisable.

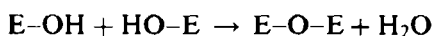
In many cases it has been found advantageous to work at low and relatively constant supersaturation which is achieved homogeneously in the whole solution (precipitation from homogeneous solution, PFHS). This can also be employed for deposition–precipitation processes, see Section A.2.2.1.5. This can be reached by using a precipitating agent which slowly decomposes to form the species active in the precipitation. The most commonly employed precursor for the liberation of

ammonia is urea, which has been used in many precipitation processes [12]. The ammonia is liberated homogeneously over the whole precipitation vessel, thus avoiding higher concentrations at the inlet point which can occur if aqueous ammonia is used. In addition, the carbon dioxide released during the urea hydrolysis can keep the solution essentially oxygen free. These differences can lead to markedly different products [13]. For the preparation of sulfides thioacetamide might be used.

The precipitation of the hydroxides can be performed either starting from an alkaline solution which is acidified, or from acidic solutions by raising the pH. In the first case, the formation of the solid product proceeds via polyanionic species. These polyanionic species undergo condensation reactions, either via olation reactions



or via oxolation reactions



A prototypic example for such precipitation reactions from alkaline solutions is  $\text{SiO}_2$ , which is prepared from silicates, as for instance sodium water glass by acidification. However, most hydroxides for technical applications are precipitated from acidic solutions by the addition of a precipitating agent. Usually ammonia or sodium carbonate are used as the precipitating agent. If other ions do not adversely influence the catalytic performance,  $\text{Ca(OH)}_2$  or  $\text{NaOH}$  can be used. Depending on the metal ion and the precipitating agent, either the hydroxides, carbonates or hydroxycarbonates precipitate. Precipitation from acidic solutions mostly proceeds via polycations and – as in the basic case – by olation or oxolation reactions. However, intermediate states are not as well known as for the polyanionic species. Only a few defined polycations are known in most cases.

### C Process Considerations

There are several ways to carry out the precipitation process (Fig. 3) [14]. The simplest implementation of the precipitation reaction is the batch operation where the solution from which the salt is to be precipitated is usually present in the precipitation vessel and the precipitating agent is added. The advantage of this mode of operation is the simple way in which the product can be obtained; the most severe disadvantage is the variation of batch composition during the precipitation process. This can lead to differences between the product formed during the initial stages of the precipitation and the precipitate formed at the end of the process. If a coprecipitation is carried out this way, it is important to decide which compounds are present in the vessel and which compounds are to be added. If the pre-

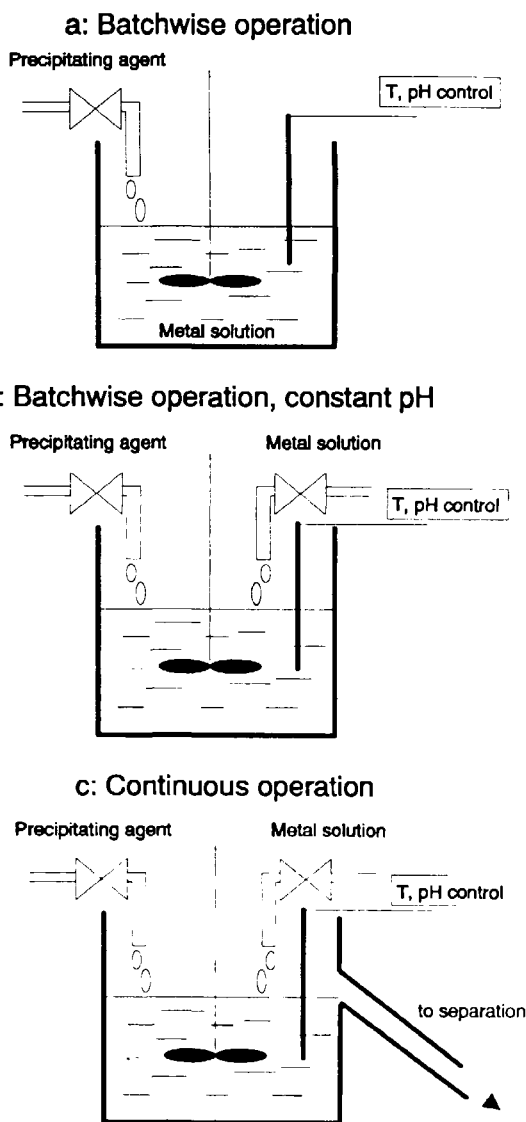


**Figure 3.** Possible implementations of precipitation processes (after [14]). In the batchwise process (a) the pH and all other parameters except for the temperature change continuously during the precipitation due to consumption of the metal species. Coprecipitation should be carried out in the reversed arrangement by addition of the metal species to the precipitating agent to avoid sequential precipitation. In process (b) the pH is kept constant, but the batch composition and the residence time of the precipitate change continuously. In process (c) all parameters are kept constant.

cipitating agent is present in the precipitator and the mixed metal solutions are added, the product tends to be homogeneous, since the precipitation agent is always present in large excess. If, on the other hand, the precipitating agent is added to a mixed metal solution, the precipitate with the lower solubility tends to precipitate first, thus resulting in the formation of an inhomogeneous product.

A slightly more complex process is the simultaneous addition of both reagents under strict control of the pH

and the reagent ratios. If the precipitation is carried out following this procedure, the ratio of the metal salt and precipitating agent remains constant; all other concentrations, however, change during the process. Homogeneity of the product is usually better than in the first process described, but might still vary between the first precipitate and the precipitate formed last. This is due to the different concentrations of the other ions which are not precipitated and might be occluded in the precipitate to a larger extent during the final stages of the procedure. Moreover, the precipitates first formed are aged for a longer time in the solution. Thus, phase transitions might have already occurred, while fresh precipitates are still formed.

These problems are avoided if a continuous process is employed for the precipitation; however, this makes higher demands on the process control. In a continuous process all parameters as temperature, concentrations, pH, and residence times of the precipitate can be kept constant or altered at will. Continuous operation is, for instance, used for the precipitation of aluminum hydroxide in the Bayer process. Bayer aluminum hydroxide is the main source for the production of catalytically active aluminas. The precipitation step of the Bayer process is carried out continuously. An aluminum solution supersaturated with respect to  $\text{Al}(\text{OH})_3$ , but not supersaturated enough for homogeneous nucleation, enters the precipitation vessel which already contains precipitate so that heterogeneous precipitation is possible. The nucleation rate has to be controlled very carefully to maintain constant conditions. This is usually done by controlling the temperature of the system to within 2–3 degrees [7].

The continuous process usually allows precipitation at low supersaturation conditions, since seeds are already present in the precipitation vessel. Thus, no homogeneous precipitation, which needs high levels of supersaturation, is necessary, and nucleation occurs heterogeneously with the associated lower supersaturation levels.

### 2.1.3.3 Influencing the Properties of the Final Product

Basically all process parameters, some of which are fixed and some of which are variable, influence the quality of the final product of the precipitation. Usually precipitates with specific properties are desired. These properties could be the nature of the phase formed, chemical composition, purity, particle size, surface area, pore sizes, pore volumes, separability from the mother liquor, and many more, including the demands which are imposed by the requirements of downstream processes, like drying, pelletizing, or calcination. It is therefore necessary to optimize the parameters in order

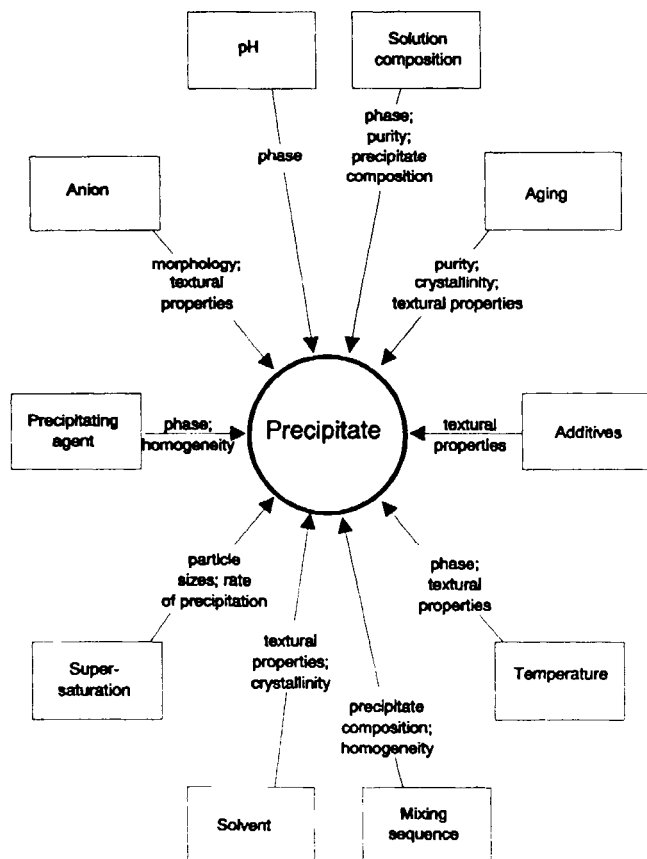


Figure 4. Parameters affecting the properties of the precipitate and main properties influenced.

to produce the desired material. Figure 4 summarizes the parameters which can be adjusted in precipitation processes and the properties which are mainly influenced by these parameters. The following discussion attempts to give some general guidelines concerning the influence of certain process parameters on the properties of the resulting precipitate. It should, however, be stressed, that the stated tendencies are only trends which might vary in special cases. The exact choice of precipitation parameters is usually the result of a long, empirically driven optimization procedure and a well-guarded secret of catalyst manufacturers or the producers of precursors for catalysts.

#### A Influence of Raw Materials

As stated above, precursors are usually chosen with counterions that can easily be decomposed to volatile products. These are preferably the nitrates of metal precursors and ammonia or sodium carbonate as the precipitating agent. Also, oxalates have occasionally been employed. If the precipitation is carried out in the presence of ions which can be occluded, repeated washing steps are necessary, if the ions adversely affect the catalytic performance of the later catalyst. Ions as chlorides or sulfates act as poisons in many catalytic

reactions. Such ions should therefore be avoided in the precipitation. The problem is reduced if supersaturation is reached by physical means. However, higher degrees of supersaturation, and thus more rapid precipitation and smaller particle sizes, are better achieved by changing the pH.

The nature of the ions present in the precipitation solution can strongly influence the properties of the final product. This was demonstrated effectively by the work of Matijevic who investigated the precipitation of many different metals, primarily as hydroxides [15]. The anions present do not only influence particle morphologies and particle sizes, but can even result in the formation of different phases. One striking example is given by Matijevic [15]: a solution of 0.0315 M  $\text{FeCl}_3$  and 0.005 M  $\text{HCl}$  results in the formation of Hematite,  $\alpha\text{-Fe}_2\text{O}_3$ ; at higher concentrations (0.27 M  $\text{FeCl}_3$  and 0.01 M  $\text{HCl}$ )  $\beta\text{-FeOOH}$  is formed; in the presence of nitrate (0.18 M  $\text{Fe}(\text{NO}_3)_3$ ) and sulfate (0.32 M  $\text{Na}_2\text{SO}_4$ ) ferric basic sulfate ( $\text{Fe}_3(\text{OH})_5(\text{SO}_4)_2 \cdot 2\text{H}_2\text{O}$ ) precipitates; finally, with phosphate (0.0038 M  $\text{FeCl}_3$  and 0.24 M  $\text{H}_3\text{PO}_4$ )  $\text{FePO}_4$  is formed.

The precipitates differ both in the phase formed and also in their morphologies. Depending on the conditions, rather spherical on the one hand, or needle-like crystals on the other hand, can be formed.

Other examples of the influence of the starting materials are the precipitation of  $\text{MoO}_3$  [16] or the preparation of  $\text{AlPO}_4$  [17]. For  $\text{MoO}_3$  small particles with relatively high surface area are formed with  $\text{Na}_2\text{MoO}_4$  as the precursor salt, whereas larger particles with lower surface area precipitate from solutions containing  $(\text{NH}_4)_6\text{Mo}_7\text{O}_{24}$ . In the  $\text{AlPO}_4$  system the type of anion has a strong influence on the recrystallization behavior. Recrystallization to the  $\alpha$ -crystalite form occurs at 1073 K for  $\text{AlPO}_4$  precipitated from aluminum nitrate. If the sulfate is used, even at calcination temperatures of 773 K, recrystallization to tridymite takes place. The chloride only begins to recrystallize at 773 K; however, at these temperatures large fractions of amorphous material are present. The phases formed are tridymite and, at temperatures above 1200 K,  $\alpha$ -crystalite. As in the case of the iron oxides, textural properties can vary drastically.

### B Influence of Concentration and Composition

In most cases it is desirable to precipitate at high concentration levels of the metal ions. This increases the space-time yields by decreasing the vessel volume for the same mass of precipitate. Moreover, the higher degrees of supersaturation lead to faster precipitation. Thus, plant investment is reduced. With respect to the quality of the product obtained, smaller particle sizes and higher surface areas are usually achieved at higher concentration levels due to increased nucleation rates at higher supersaturation if homogeneous nucleation

takes place. If for some reason the precipitation is carried out at low concentration levels, for instance to produce larger primary particles, the precipitation has to be performed either in continuous systems where seeds are present in the stationary state, or seeds have to be added to the solution.

If catalysts are prepared by coprecipitation, the composition of the solutions determine the composition of the final product. Often the composition of the precipitate will reflect the solution concentrations, as was shown for  $\text{CuO}/\text{ZnO}$  catalysts for methanol synthesis [18], but this is not necessarily the case. For aluminum phosphates it was found that at low P:Al ratios the precipitate composition is identical to the solution composition, but if the P:Al ratio in the solution comes close to and exceeds unity, the precipitate composition asymptotically approaches a P:Al ratio of 1 [19]. Deviations from solution composition in coprecipitation processes will generally occur if solubilities of the different compounds differ strongly and precipitation is not complete or, if in addition to stoichiometric compounds, only one component forms an insoluble precipitate; this the case for the aluminum phosphate.

### C Solvent Effects

For economic reasons water is almost exclusively used as the solvent for precipitation processes, at least for bulk catalysts and supports; organic solvents are much more expensive than water. This economic disadvantage is even more severe than would be expected from the price difference, because solubilities for most metal salts are much lower in organic solvents. Thus, to reach the same space-time yield, larger systems usually have to be employed. Moreover, increased environmental problems are associated with the use of organic solvents. However, there are some reports in the literature that organic solvents can be advantageous for the precipitation of certain materials. The low solubilities of the precursor materials may, for instance, result in very low supersaturations, which means slow crystallization. Therefore, particle size distributions can be altered, or phases closer to the equilibrium phases can be formed. The disadvantages of the use of the organic solvents in precipitation processes have to be compensated by superior product qualities which cannot be achieved by other means.

One of the most important systems which can be prepared advantageously from organic solvents is the  $(\text{VO})\text{HPO}_4 \cdot 0.5\text{H}_2\text{O}$  precursor for vanadium-phosphorus mixed oxides. This is the best known catalyst for the selective conversion of *n*-butane to maleic anhydride. This system will be discussed in more detail below.

The possibility of obtaining higher surface-area precipitates from organic solvents is described by Desmond et al. [20]; polar compounds such as alcohols,



aldehydes, esters, glycols, etc. are used. Due to low solubilities of the precipitating agent (preferably  $\text{Na}_2\text{CO}_3$  or  $\text{K}_2\text{CO}_3$ ) in the organic solvent ( $10^{-1}$ – $10^{-6}$  mol L $^{-1}$ ), Group VIIIA, IB and IIB metal oxides can be prepared with higher surface area than from aqueous solutions. This is believed to be due to a constant, low concentration of the precipitating agent which is dissolved as the metal oxide precipitates. The patent claims that different structures can be formed as compared to precipitation from aqueous solutions. Iron oxide, for instance, precipitates as magnetite ( $\text{Fe}_3\text{O}_4$ ) while in water usually hematite ( $\alpha\text{-Fe}_2\text{O}_3$ ) or maghemite ( $\gamma\text{-Fe}_2\text{O}_3$ ) are formed. One of the problems associated with this technique are the long precipitation times of several days. The materials are reported to exhibit surface areas about twice as high as for comparative catalysts prepared from water; the yield in Fischer–Tropsch reactions was about 50% higher than over conventionally prepared catalysts.

In two cases, however, precipitation from organic solvents is used to obtain the catalyst, due to the very nature of the system. This is the hydrolysis of organic precursors and the formation of polymerization catalysts in nonpolar media. In the hydrolysis of organic precursors, alkyls or alkoxides, especially of silicon or aluminum, are hydrolyzed by the action of aqueous bases or water. This process can be carried out in water as the solvent. The reversed system, with the organometallic compound itself as the solvent or an additional solvent have also been described. This process has the advantage that catalyst particles with predetermined shapes, usually spheres, can be formed directly [21]. Moreover, materials resulting from hydrolysis processes are very pure due to the high purity of the starting materials. The aluminum oxide obtained from the hydrolysis of aluminum alcoholates were initially only a byproduct of detergent production but, due to the high quality of the resulting aluminas (for instance PURAL<sup>®</sup>-type aluminas) became the main product of the process. Catalyst production processes based on the hydrolysis of organic precursors are discussed in more detail in a later chapter.

If polymerization catalysts, for instance for alkene polymerization (Ziegler–Natta-type catalysts), are prepared by precipitation methods, they can be formed by precipitation from organic solvents, as claimed in several patents [22]. In these patents the precipitation of titanium–magnesium compounds in THF with hexane as precipitating agent is used for the formation of the catalyst. Many important Ziegler–Natta initiators are solids, and heterogeneous initiator systems seem to be necessary for the production of isotactic polyalkenes [23]. However, not much information on the details of catalyst preparation is available in the open literature.

Summarizing this section, the use of organic solvents for the precipitation of catalysts seems to be of only

minor importance. Only in special cases are the higher costs and problems involved in such processes justified by the superior properties of the final catalyst.

### D Influence on Precipitation of Temperature

As outlined above, nucleation rates are extremely sensitive to temperature changes. Therefore, precipitation temperature is a decisive factor in controlling precipitate properties such as primary crystallite sizes, surface areas, and even the phases formed. However, it is very difficult to state how the precipitation temperature has to be adjusted to achieve a product with specific properties. The optimum precipitation temperature usually is a parameter which has to be determined experimentally.

In general, most precipitation processes are carried out above room temperature, often close to 373 K. One obvious reason for this is that precipitation is more rapid, provided that high levels of supersaturation are maintained.

Depending on the kinetics of the different elementary processes involved in the formation of the precipitate, a temperature increase might lead to an increase in crystallite size, as was observed for the crystallization of pseudoboehmite [24] or iron molybdates [25]. However, in other cases no influence of the precipitation temperature on the crystallite size of the final catalyst was reported [26], or a decrease was reported, as for the ZnO system [27].

For some systems, however, the influence of the temperature on the phase composition can be predicted based on chemical considerations. For instance, the composition of bismuth molybdate catalysts is believed to be determined by the nature of the molybdate anion present in solution [28] which is dependent on the solution temperature. For Ni/SiO $_2$  catalysts the differences between catalysts prepared at high or low temperatures are explained by the formation of nickel hydrosilicate at high temperatures, while at low temperature the main precipitate is nickel hydroxide [29].

### E Influence of pH

Since the pH directly controls the degree of supersaturation, at least if hydroxides are precipitated, this should be one of the crucial factors in precipitation processes. As for many other parameters, the influence of pH is not a simple one and it has to be investigated experimentally for a specific system. Even in a relatively well-known system such as iron oxide [30] the effect which the precipitation pH has on the properties of the final product is not yet clear. There is no clear relationship between the precipitation pH and the textural and catalytic properties of the precipitate. It is relatively well known what phases are formed under specific conditions, due to the importance of iron

oxides as pigments, but the influence of pH with respect to catalytic properties is not well studied.

In the aluminum oxide system the precipitation pH is one of the variables which controls the nature of the phase eventually obtained. However, aging conditions of the initially formed amorphous precipitate are at least equally important. In general, it can be stated that precipitation above  $\text{pH} = 8$  leads to the formation of bayerite, while precipitation under more acidic conditions favors the subsequent formation of boehmite. Hydrargillite is formed as the product of the Bayer process by seeding a supersaturated alkali containing aluminum solution. The formation of bayerite is strongly facilitated by the presence of alkali cations which stabilize the structure.

#### F Influence of Additives

The properties of precipitates can be strongly influenced by additives. Additives are substances which are not a necessary ingredient of a precipitation reaction. Thus, although anions of precipitation agents might strongly influence product properties, they are not considered as additives, because they are unavoidable in the precipitation reaction.

The most widely used additives are organic molecules which are added to the precipitate in order to control the pore structure [31]. Such organic molecules can later be removed from the precipitate in a calcination step. A very promising route to the preparation of high surface area oxides (M41S) is the use of surfactants as additives which was introduced in 1992 by scientists of Mobil [32]. The surfactants are able to form liquid crystal-like structures in cooperation with the silicates present in solution [33]. Removing the surfactant by a calcination step leaves a silica negative of the organic liquid crystal with a relatively perfect hexagonal arrangement of pores, the diameters of which can be adjusted between about 2 and 10 nm (Fig. 5). The pore size distribution is very sharp, as can be seen by sorption analysis [34]. In subsequent publications it was shown that the concepts can be generalized to the preparation of other oxides [35]. BET surface areas can be as high as  $1200 \text{ m}^2 \text{ g}^{-1}$  for the silicate. A special case is the formation of oxides with anionic surfactants such as alkylsulfates or alkylsulfonates. Decomposition of zirconias or titanias precipitated with such surfactants leads directly to the formation of sulfated zirconias or titanias which exhibit remarkable stabilities and excellent performance in acid-catalyzed reactions [36].

Since the use of additives to control the precipitation of catalysts is a wide field, and is usually treated as trade secrets, this topic cannot be discussed in more detail in the context of this chapter.

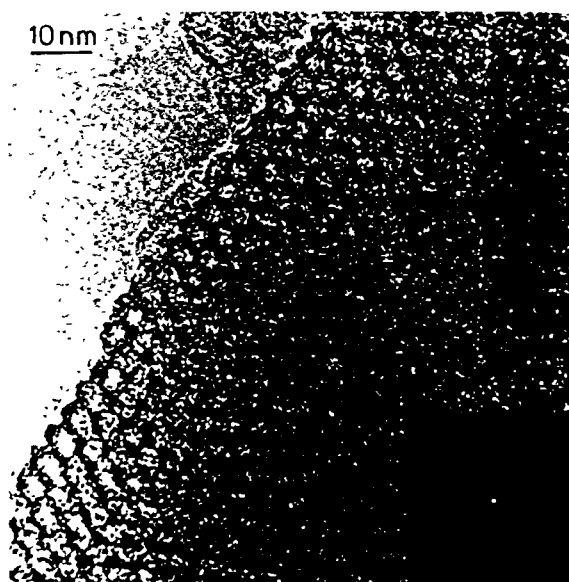


**Figure 5.** Transmission electron micrograph of a mesoporous M41S-type silicate with pore sizes of 4 nm. The regular hexagonal arrangement of the pores can be seen in the micrograph and in the diffraction pattern shown in the inset.

#### 2.1.3.4 Prototypical Examples of Precipitated Catalysts and Supports

This section shows, for four examples of increasing complexity, how precipitates are formed and how the properties of the precipitates are controlled to produce a material suitable for catalytic applications. The first two examples comprise silica, which is primarily used as support material and is usually formed as an amorphous solid, and alumina, which is also used as a catalytically active material, and which can be formed in various modifications with widely varying properties as pure precipitated compounds. The other examples are the results of coprecipitation processes, namely  $\text{Ni}/\text{Al}_2\text{O}_3$  which can be prepared by several pathways and for which the precipitation of a certain phase determines the reduction behavior and the later catalytic properties, and the precipitation of  $(\text{VO})\text{HPO}_4 \cdot 0.5\text{H}_2\text{O}$  which is the precursor of the V/P/O catalyst for butane oxidation to maleic anhydride, where even the formation of a specific crystallographic face with high catalytic activity has to be controlled.

##### A Silica as Support Material

Silica applied as a support for catalysts is an X-ray-amorphous form of silicon dioxide [37]. It is manufactured in two steps. First, a silica hydrogel is formed by means of a sol-gel process [38] (Section A.2.1.4). Secondly, the silica hydrogel is subjected to aftertreatment followed by dehydration to remove water. The product

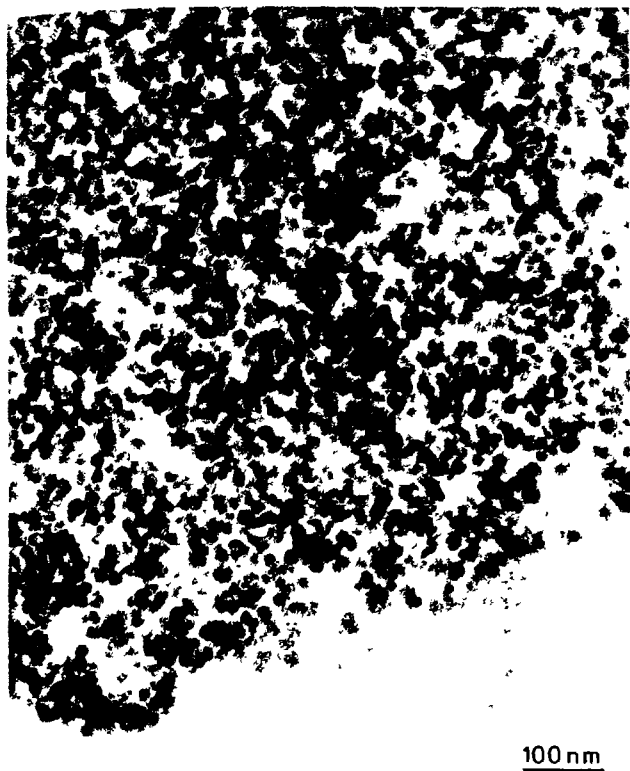


Figure 6. Globular structure of a silica xerogel; magnification  $\times 240\,000$ .

is a silica xerogel composed of hard porous granules. The granules can be milled to a powder and sized to the desired particle size. Silica beads are obtained in the course of the sol-gel process by dispersing sol droplets into a water-immiscible liquid whereby gelling of the droplets into hydrogel beads occurs [39].

In the sol-gel process sodium silicate (water glass) solution is acidified with sulfuric acid. By decreasing the pH of the water glass solution silicic acids are formed which immediately undergo polycondensation and further growth to colloidal silica particles. Depending on the final pH, the silica concentration, the type and concentration of the electrolyte, the temperature, and other parameters, the dispersion of the colloid particles can be stabilized as a silica sol, or agglomeration of the colloidal particles occurs to silica hydrogel. The silica hydrogel represents a coherent system composed of a three-dimensional network of agglomerated spheres with sodium sulfate solution as dispersing liquid. The pores are preformed by the interstices between the agglomerated nonporous silica globules. The pore structure is thus determined by the size of the globules and their coordination in the agglomerate. Figure 6 visualizes the globular structure of a silica xerogel. The silica hydrogel ages, i.e. it shrinks by expelling water whereby its mechanical strength

increases. This process is called syneresis. To convert the hydrogel to the silica xerogel it is washed to remove the salt solution and subjected to drying at about 423–473 K. The drying conditions also affect the specific surface area and the pore structure parameters of the xerogel. When the dried xerogel is exposed to air it adsorbs water to about 5–10 wt% depending on its specific surface area. In the course of aging, washing and drying the hydrogel, a number of procedures can be applied to systematically vary the pore structure, comprised under the term modification. These procedures could be washing with acids or bases, hydrothermal treatment, etc. As a result the pores are enlarged and the specific surface area decreases. This step is important for the preparation of catalyst supports in which transport limitations are minimized.

Large-pore granules of silica xerogel are not suitable as catalyst supports due to the lack of large macropores which are necessary for a good mass transfer and due to low stability when packed in a fixed-bed reactor. It is advisable to subject the powdered xerogel to pelletization on a rotary plate or to extrusion. In both cases a binder has to be applied to control the porosity and size of macropores and to obtain sufficient mechanical stability (crushing strength and attrition resistance).

Silica beads 2–3 mm in size can be formed in the course of the sol-gel process. The sol passes an orifice where liquid droplets are formed which then settle in a water-immiscible liquid. During settling the liquid droplets solidify to silica hydrogel beads.

The xerogel contains inorganic impurities which depend on the purity of the water glass and which might affect catalytic performance. Most common are sodium, aluminum, and titanium at concentrations exceeding 1000 ppm. These impurities affect the thermal stability of the xerogel and the catalytic properties of the final catalyst. The silica surface is covered by hydroxyl groups and adsorbed water. At full hydroxylation the concentration of hydroxyl groups amounts to about  $8\ \mu\text{mol m}^{-2}$ . There are different types of Brønsted sites, namely isolated (or free), geminal, and vicinal. They can be monitored by  $^{29}\text{Si}$  CP MAS NMR (Cross Polarization Magic Angle Spinning Nuclear Magnetic Resonance) spectroscopy [40], IR spectroscopy [41] and other techniques. The Brønsted sites on the silica surface are weakly acidic ( $\text{p}K_{\text{a}} \approx 7$ ). Dispersed in electrolyte solution, silica xerogel thus acts as a weak cation exchanger which makes it possible to impregnate silicas by equilibration with the ion to be loaded. It is worth noting that silica xerogel is soluble in solutions of  $\text{pH} > 9$ .

One major advantage of silica xerogel over other support materials is the ease of adjustment and control of mean pore diameter, specific surface area and the specific pore volume. Supports for catalytic applica-

tions require a sufficiently high specific surface area which is generated by mesopores with mean pore diameters between 5 and 50 nm and a sufficient amount of macropores of a mean pore diameter >50 nm to ascertain a rapid mass transfer. Also important is a high degree of pore connectivity which requires a high porosity. Enhancing the porosity, however, reduces the mechanical strength of the support particles. Thus, a compromise has to be found. Silica xerogels usually have a specific pore volume between 0.5 and 1.0 cm<sup>3</sup> g<sup>-1</sup> which corresponds to a porosity of about 50–70%. Silica xerogels are typical mesoporous adsorbents with a mean pore diameter between 5 and 50 nm and corresponding specific surface areas of between 50 and 600 m<sup>2</sup> g<sup>-1</sup>. Macropores of a mean pore diameter of >50 nm are generated in the course of the formulation and the shaping process.

Silicas are used as supports in a variety of catalytic processes. Typical applications are Ni-, Pd-, or Pt-supported catalysts for hydrogenation reactions and V<sub>2</sub>O<sub>5</sub>-supported catalysts in the oxidation of SO<sub>2</sub> in gases from roasting sulfides or sulfur to yield SO<sub>3</sub>.

### B Active Aluminas

Active aluminas are much more widely used in catalytic applications than silicas, since they are not only excellent support materials, but also very active as catalysts in their own right for several applications. However, the chemistry of aluminas is much more complicated than that of silica, since many crystallographic modifications exist, only few of which are useful as catalysts.

Porous aluminas are manufactured by a controlled dehydration from aluminum hydroxide (Al(OH)<sub>3</sub> = Al<sub>2</sub>O<sub>3</sub> · 3H<sub>2</sub>O) or aluminum oxide hydrates (AlOOH = Al<sub>2</sub>O<sub>3</sub> · H<sub>2</sub>O). Aluminum hydroxide exists in various crystalline forms as gibbsite (= hydrargillite), bayerite, and nordstrandite [42]. These hydroxides are nonporous. Thermal treatment of gibbsite formed in the Bayer process at about 423 K gives microcrystalline boehmite with a specific surface area of about 200–400 m<sup>2</sup> g<sup>-1</sup>. The best Bayer precursor for the preparation of catalysts is the fine crystalline material deposited as a hard crust on the precipitator wall which is removed periodically from the precipitators. Further treatment between 673 K and 1273 K yields a series of porous crystalline transition aluminas assigned by Greek letters as chi (χ), kappa (κ), gamma (γ), eta (η), theta (θ) and delta (δ). The most important transition oxides for catalytic applications are γ-alumina and the η-alumina. Calcination above 1273 K yields α-alumina as a crystalline nonporous product. This material is sometimes used as a low surface area support material.

Figure 7 shows the pathways for the formation of different aluminas between Al(OH)<sub>3</sub> and Al<sub>2</sub>O<sub>3</sub>. γ-

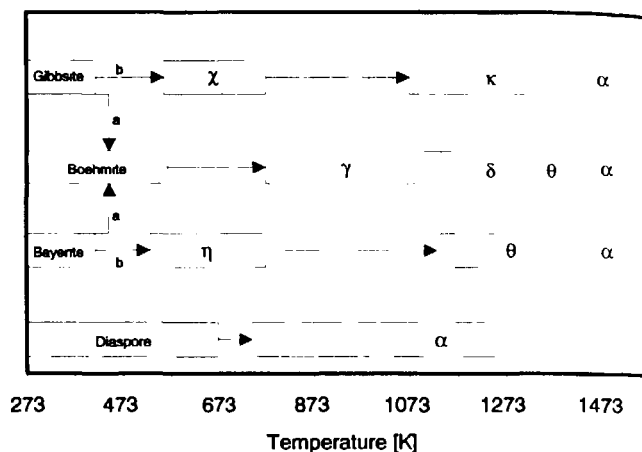
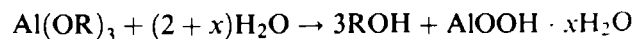


**Figure 7.** Sequence of phases formed after thermal treatment of aluminum hydroxides and aluminum oxide hydroxides. Pathway (a) is favored by pressures exceeding 1 bar, moist air, heating rates higher than 1 K min<sup>-1</sup> and particle sizes higher than 100 μm. Pathway (b) is favored by pressures of 1 bar, dry air, heating rates below 1 K min<sup>-1</sup> and particle sizes below 10 μm.

Alumina and η-alumina are also called active aluminas. These materials are seldom phase pure and contain other transition aluminas as impurities. Their properties strongly depend on the type of starting materials, the procedure chosen for thermal treatment, and the operation parameters such as temperature and pressure. Highly active γ-alumina has been prepared by shock calcination followed by rehydration [43].

In addition to gibbsite there are other routes to manufacture Al(OH)<sub>3</sub> and the consecutive transition oxides. One is the precipitation of Al(OH)<sub>3</sub> from aluminum salts by adjusting the pH between 7 and 12 by adding bases. Precipitation at elevated temperatures and high pH leads to formation of bayerite, whereas at lower pH pseudoboehmite and subsequently boehmite are formed. By heating, these materials can be converted to the active transition aluminas.

A third, very important source of aluminum oxide hydroxides is the hydrolysis of aluminum alcoholates. Due to the high purity of the alcoholate, almost no impurities, except for carbon residues at low concentrations, are present in the product:



where R can vary.

Using such procedures, high purity pseudoboehmite is produced (PURAL<sup>®</sup>, Condea Chemie, Brunsbüttel). With this type of microcrystalline pseudoboehmite spheres of γ-alumina can be manufactured. PURAL can also be extruded to pellets with binders and then subjected to calcination to prepare γ-alumina. The extrusion of various aluminum hydroxides and oxide hydroxides with binders to pellets is covered in Ref. [44]. The properties of the different aluminum hydrox-

**Table 2.** Properties of different precursors used for active alumina preparation.

Property	Bayer hydroxide	Precipitated hydroxides	Ziegler hydroxides
Raw material	bauxite	aluminum salt solutions	aluminum alcoholates
Process	digestion in NaOH and crystallization	neutralization with bases at pH 7–12	hydrolysis
Phase	gibbsite	pseudoboehmite, bayerite, nordstrandite, gibbsite	pseudoboehmite
Size of primary particles (nm)	500–15 000	10–1000	4–10
Main impurity	Na <sub>2</sub> O	chloride, sulfate, nitrate	carbon (very low concentrations)
Weight loss on calcination (wt%)	35	18–40	22–28
Maximum of pore radius distribution (nm)	1.2–2.2	1.2–2.2	3.0–7.5
BET surface area (m <sup>2</sup> g <sup>-1</sup> )	0.5–10	200–400	160–600

ide and oxide hydroxide precursors for the preparation of active aluminas are summarized in Table 2.

The structure of  $\gamma$ -alumina resembles that of the spinel-type MgAl<sub>2</sub>O<sub>4</sub>;  $\eta$ -alumina has a very similar structure. The difference lies in the concentration of stacking faults which is caused by the difference in the structures of the precursors boehmite and bayerite [45]. The concentration of stacking faults is higher in the  $\eta$ -alumina.

$\gamma$ -Alumina exhibits Brønsted acidity, Lewis acidity, and Lewis basicity [46]. Towards electrolytes it acts as a cation and anion exchanger, depending on the pH [47].  $\gamma$ -alumina develops mesoporosity with specific surface areas between 50 and 300 m<sup>2</sup> g<sup>-1</sup> and specific pore volumes up to 0.6 cm<sup>3</sup> g<sup>-1</sup>. Following special procedures, highly porous  $\gamma$ -alumina can be prepared with a specific pore volume up to 0.9 cm<sup>3</sup> g<sup>-1</sup> (Kali Chemie, Hannover, FRG).  $\alpha$ -Alumina (corundum) is nonporous and has a low specific surface area. It is also marketed as a ceramic support with a specific surface area of around 3–5 m<sup>2</sup> g<sup>-1</sup>, a porosity of 50%, and a pellet size of 2–4 mm (Rosenthal Technik AG, Selb, FRG).

Aluminas are used in various catalytic applications.  $\alpha$ -,  $\gamma$ -, and  $\eta$ -aluminas are all used as support materials, the first one in applications where low surface areas are desired, as in partial oxidation reactions. The latter two, and especially  $\gamma$ -alumina, in applications where high surface areas and high thermal and mechanical stability are required. One of the most prominent applications of  $\gamma$ -alumina as support is the catalytic converter for pollution control, where an alumina washcoat covers a monolithic support. The washcoat is impregnated with the catalytically active noble metals. Another major application area of high-surface aluminas as support is in the petrochemical industry in hydrotreating plants. Alumina-supported catalysts with Co, Ni, and/or Mo are used for this purpose. Also, all noble metals are available as supported catalysts based on aluminas. Such catalysts are used for hydrogenation reactions or sometimes oxidation reactions. If high

mechanical stability and low surface area of the catalyst support is desired,  $\alpha$ -alumina instead of  $\gamma$ -alumina might be used. This is the case, for instance, for ammonia catalysts which often contain alumina as support material.

$\gamma$ -Alumina is not only used as a support material but also as a catalyst in its native form, for instance in alcohol dehydration reaction (Section B.4.11), due to the acidic nature of its surface and, most prominently, as the catalyst in the Claus process (Section B.2.3). Due to the severe conditions of the Claus process, high-stability aluminas have to be employed here.

### C Ni/Al<sub>2</sub>O<sub>3</sub> Catalysts by Coprecipitation

Alumina-supported nickel catalysts are an excellent example for the advantages of and the problems associated with coprecipitation processes for the manufacture of catalysts. Such catalysts are accessible via several pathways, as impregnation, deposition/precipitation, coprecipitation from alumina gels, and more conventional coprecipitation routes. Also, for coprecipitation, different routes are possible, the first examples originating from the 1920s [48]. Starting from the nitrate solutions of nickel and aluminum, there are at least three different routes:

- (i) The most frequently applied route is the precipitation of a hydrotalcite (HTlc)-like compound with the general formula  $[M_{1-x}^{II}M_x^{III}(\text{OH})]^{x+}(\text{A}^{n-})_{x/n} \cdot n\text{H}_2\text{O}$  where  $M^{II} = \text{Mg, Ni, Zn, } \dots, M^{III} = \text{Al, Fe, Cr, } \dots$ , and  $\text{A}^{n-} = \text{CO}_3^{2-}, \text{SO}_4^{2-}, \text{NO}_3^- \dots$ , using Na<sub>2</sub>CO<sub>3</sub> as the precipitating agent.

The composition of the nickel–alumina hydroxycarbonate (NiAlCO<sub>3</sub>–HTlc) may thus vary, but an idealized composition is that of the mineral takovite Ni<sub>6</sub>Al<sub>2</sub>(OH)<sub>16</sub>CO<sub>3</sub> · 4 H<sub>2</sub>O. Hydrotalcites as catalytic precursors, amongst them NiAlCO<sub>3</sub>–HTlc, are discussed in an excellent recent review [49].

- (ii) Nickel aluminum coprecipitates can be prepared in the complete absence of carbonate ions, for in-

stance by precipitation with NaOH in carbonate-free solutions [50]. In this case no mixture of hydroxides is obtained, but nitrates are incorporated and a mixed hydroxynitrate precipitates.

- (iii) The same holds for ammonia solutions, from which the precipitation can be carried out by evaporating the ammonia. If the ammonia is removed without excluding the carbonates, the normal hydroxycarbonate forms. If carbonate is excluded, the hydroxynitrate precipitates [50].

An alternative approach is precipitation by combining an alkaline  $\text{NaAlO}_2$  solution with an acidic nickel nitrate solution [51]. In this case as well, hydrotalcite-like species are probably formed first although, due to the very high nickel contents reported, some nickel hydroxide forms as well. Pure hydrotalcite-like structure are reported to form for Ni:Al atomic ratios between 2 and 3 [52] or 4 [53]; outside this range the hydroxides of the excess species form as additional phases. Rapid precipitation tends to form pure  $\text{Al}(\text{OH})_3$  due to the lower solubility. Aging can lead to recrystallization of some of the pure hydroxides to the hydrotalcite structure as well.

The formation of the hydrotalcite highlights one of the key advantages of coprecipitation techniques. It can provide intimate mixing of the catalyst constituents on an atomic scale at very high loadings. This intimate mixing leads to a very different behavior on calcination and reduction as compared to impregnated catalysts [54]. Whereas impregnated or mechanically mixed catalysts form surface-mixed oxides of the spinel structure at best, which segregate again on reduction to result in the formation of a separate nickel phase on a  $\gamma$ -alumina support, the coprecipitation technique leads to formation of a high surface-area mixed-oxide with varying composition between NiO and the spinel-type  $\text{NiAl}_2\text{O}_4$ , depending on the composition of the precursor. On reduction of this oxide, nickel crystallites are formed which exhibit a high degree of "paracrystallinity", i.e. highly defective nickel crystallites with aluminate groups as the defects [55]. The impregnated catalysts are easier to reduce than the coprecipitated materials, as could be expected from the structure of the precursors [56].

The thermal treatment is one of the factors which controls the properties of the final catalyst [56]. The total surface area (in the range between 100 and  $300\text{ m}^2\text{ g}^{-1}$ ) decreases with increasing reduction temperature; however, the nickel surface area (typically  $20\text{--}50\text{ m}^2\text{ g}^{-1}$ ) increases which is probably due to a higher degree of reduction. The best precursor with respect to a high surface area is the hydroxycarbonate. The surface areas of catalysts prepared from hydroxychlorides and nitrates are smaller by about a factor of two. Nickel particle sizes are in the order of 5 nm for such catalysts.

$\text{Ni}/\text{Al}_2\text{O}_3$  catalysts prepared by coprecipitation exhibit excellent sintering stability and can be used in many catalytic reactions. The most important ones are certainly steam reforming (Section B.3.3) and methanation (Section B.3.6) reactions.

The preparation of mixed oxide catalysts from hydroxycarbonates is not restricted to  $\text{Ni}/\text{Al}_2\text{O}_3$ , but also possible for several other systems. One example is the technically very important methanol catalyst based on  $\text{CuO}/\text{ZnO}$ . It can be prepared from a hydrotalcite-like precursor as well [57], but mostly a hydrozincite or aurichalcite precursor is used [58]. On reduction of aurichalcite precursors, epitaxial relationships between the copper and the ZnO were observed. Such preferential formation of certain orientations is also the decisive factor in the last example discussed here.

### D V/P/O Catalysts for Butane Oxidation to Maleic Anhydride

The V/P/O ( $(\text{VO})_2\text{P}_2\text{O}_7$ ) catalyst is a very specialized material which has a unique activity for the oxidation of *n*-butane to maleic anhydride. Its activity is related to the presence of (100) planes in the catalyst, in which the arrangement of surface atoms ideally matches the geometry of the reacting molecules [59]. Since the cited reviews exist and a very recent review has been given by Cavani and Trifirò [60], only the important findings concerning the preparation of the precursor are reported here, since this example highlights the problems involved in creating high fractions of certain crystallographic faces. In the case of the V/P/O catalyst there exists a pseudomorphic relationship between the precursor  $(\text{VO})\text{HPO}_4 \cdot 0.5\text{ H}_2\text{O}$  and the final catalyst. The equilibrium shape of  $(\text{VO})_2\text{P}_2\text{O}_7$  exhibits only about 32% of the optimum (100) faces. The hemihydrate precursor now is special in that it can be precipitated in a morphology that leads to formation of a much higher (100) fraction, since the (001) of the precursor is structurally related to the (100) of the pyrophosphate.

There are several pathways described for the preparation of the precursor [60]. Usually,  $\text{V}_2\text{O}_5$  is reductively dissolved in water or an organic solvent such as alcohols to yield  $\text{V}^{\text{IV}}$  species. To this solution phosphoric acid is added and the solid precursor precipitates. Precipitation is often carried out under reflux. There is general agreement that preferentially (001) planes should be exposed in the precursor and that a precursor with a high concentration of stacking faults is superior to more ordered materials. This can best be achieved by precipitation in organic solvents as can be seen by comparison of the X-ray patterns of samples produced either from organic or aqueous media [61].

In a recent study on the precipitation conditions for the hemihydrate [62] the influence of several parameters on the morphology of the precipitate formed was studied. The surface area of the precursors formed was

mainly related to the thickness of the crystals. The thicker the crystals (meaning exposure of undesired faces) the lower the surface area. High surface areas could be achieved with a high-boiling alcohol. The conditions favoring the formation of thin, high surface area (VO)HPO<sub>4</sub> · 0.5 H<sub>2</sub>O platelets (H<sub>3</sub>PO<sub>4</sub> 85%, P:V = 1.1–1.2, isobutanol/benzylalcohol, addition of tetraethylorthosilicate) are identical to conditions defined earlier for obtaining the best performing catalyst [63]. The example of the V/P/O catalyst convincingly shows how control of the precipitation conditions, based on a knowledge of the catalytic process, can eventually result in the formation of a highly active catalyst.

## References

- 1 C L Thomas, *Catalytic Processes and Proven Catalysts*, Academic Press, New York, 1970, Chapters 11 and 14, A B Stiles, *Catalyst Manufacture – Laboratory and Commercial Preparations*, Marcel Dekker, New York, 1983
- 2 Recommendations on Nomenclature for Contamination Phenomena in Precipitation from Aqueous Solution, *Pure Appl Chem* 1975, 37, 463–468
- 3 V K LaMer, R H Dinegar, *J Am Chem Soc* 1950, 72, 4847
- 4 For instance E Matijevic, *Acc Chem Res* 1981, 14, 22
- 5 C J J den Ouden, R W Thompson, *J Colloid Interface Sci* 1991, 143, 77
- 6 A D Randolph, M A Larson, *AIChE J* 1962, 8, 639, the concepts are described in more detail in A D Randolph, M A Larson, *Theory of Particulate Processes*, 2nd ed., Academic Press, San Diego, 1988
- 7 For instance L K Hudson, C Misra, K Wefers, *Ullmann's Encycl Ind Chem 5th ed* 1985 Vol A1, p 575
- 8 G H Bogusch, C F Zukoski IV, *J Colloid Interface Sci* 1991, 142, 19
- 9 F Cavani, F Trifiro, A Vaccari, *Catal Today* 1991, 11, 173
- 10 S P S Andrew in *Preparation of Catalysts I* (Eds B Delmon, P A Jacobs, G Poncelet), Elsevier, Amsterdam, 1976, p 429
- 11 P Peshev, A Toshev, G Gyurov, *Mater Res Bull* 1989, 24, 33
- 12 For instance G Pass, A B Littlewood, R L Burwell Jr, *J Amer Chem Soc* 1960, 82, 6281, M P McDaniel, R L Burwell Jr, *J Catal* 1975, 36, 384, C Sivaraj, P Kantaro, *Appl Catal* 1988, 45, 103, C Sivaraj, B R Reddy, B R Rao, P K Rao, *App Catal* 1986, 24, 25
- 13 K Tanabe, M Itoh, K Morishige, H Hattori in *Preparation of Catalysts I* (Eds B Delmon, P A Jacobs, G Poncelet), Elsevier, Amsterdam, 1976, p 65
- 14 P Courty, C Marcilly, *Stud Surf Sci Catal* 1983, 16, 485
- 15 E Matijevic, *Pure Appl Chem* 1978, 50, 1193, identical to E Matijevic, *Stud Surf Sci Catal* 1979, 3, 555
- 16 A Dalas, C Kordulis, P G Koutsoukos, A Lycourghiotis, *J Chem Soc, Faraday Trans* 1993, 89, 3645
- 17 J M Campelo, A Garcia, D Luna, J M Marina, *J Catal* 1988, 111, 106
- 18 P Porta, S de Rossi, G Ferraris, M Lo Jacono, G Minelli, G Moretti, *J Catal* 1988, 109, 367, G C Shen, S I Fujita, N Takezawa, *J Catal* 1992, 138, 754
- 19 T T P Cheung, K W Wilcox, M P McDaniel, M M Johnson, *J Catal* 1986, 102, 10
- 20 M J Desmond, M A Pepera, US Patent 4686203, 1987 (Standard Oil Company)
- 21 T Kawaguchi, K Kouhei, *J Non-Cryst Solids* 1990, 121, 383
- 22 M Matsura, T Fujita, Jpn Patent 62257906 A2 871110 Showa (CA 108 76086), M Kioka, N Norio, EU Patent 279 586 A2 880 824 (CA 110 8810), K Yamaguchi, N Kanoh, T Tanaka, E Toru, N Enokido, A Murakami, S Yoshida, Ger Patent 2 515 211 751 016 (CA 84:74876)
- 23 A E Hamielec, H Tobita, *Ullmann's Encycl Ind Chem 5th ed* 1992 Vol A21, p 305
- 24 D Damyanov, I Ivanov, L Vlaev, *Zh Prikl Khim* 1989, 62, 486
- 25 F Traina, N Pernicone, *Chim Ind (Milan)* 1970, 52, 1
- 26 A S Ivanova, E M Moroz, G S Litvak, *Kinet Katal* 1992, 33, 1208
- 27 A Vian, J Tijero, E Guardiola, *Actas Sump Iberoam Catal*, 9th Volume 2, Soc Iberoam Catal, Lisbon, 1984, p 1601
- 28 F Trifiro, H Hoser, R D Scarle, *J Catal* 1972, 25, 12, F Trifiro, P Forzatti, P L Villa in *Preparation of Catalysts I* (Eds B Delmon, P A Jacobs, G Poncelet), Elsevier, Amsterdam, 1976, p 147
- 29 Y Nitta, T Imanaka, S Teranishi, *J Catal* 1985, 96, 429 and references therein
- 30 R A Diefenbach, D J Fauth, *J Catal* 1986, 100, 466
- 31 D Basmadjian, G N Fulford, B I Parsons, D S Montgomery, *J Catal* 1962, 1, 547
- 32 C T Kresge, M E Leonowicz, W J Roth, J C Vartuli, J S Beck, *Nature* 1992, 359, 710
- 33 A Monnier, F Schuth, Q Huo, D Kumar, D Margolese, R S Maxwell, G D Stucky, M Krishnamurty, P Petroff, A Frouzi, M Janicke, B Chmelka, *Science* 1993, 261, 1299
- 34 O Franke, G Schulz Ekloff, J Rathousky, J Starek, A Zukal, *J Chem Soc, Chem Commun* 1993, 724, P J Branton, P G Hall, K S W Sing, *J Chem Soc, Chem Commun* 1993, 1257, P L Llewellyn, H Reichert, Y Grillet, F Schuth, K K Unger, *Micropor Mater* 1994, 3, 345, P J Branton, P G Hall, K S W Sing, H Reichert, F Schuth, K Unger, *J Chem Soc Faraday Trans* 1994, 90, 2965
- 35 Q Huo, D Margolese, U Ciesla, P Feng, T Gier, P Sieger, R Leon, P M Petroff, U Ciesla, F Schuth, G Stucky, *Nature* 1994, 368, 317, U Ciesla, D Demuth, R Leon, P Petroff, G Stucky, K Unger, F Schuth, *J Chem Soc, Chem Commun* 1994, 1387
- 36 U Ciesla, T Suharto, W Jacobs, F Schuth, *unpublished results*
- 37 R K Iler, *The Chemistry of Silica and Silicates*, Wiley, New York, 1979, D Barby in *Characterization of Powder Surfaces* (Eds G D Parfitt, K S W Sing), Academic Press, London, 1976, p 353, K K Unger, *Porous Silica*, J Chromatogr Libr Vol 16, Elsevier, Amsterdam, 1979, H Ferch, A Kreher, *Chemische Technologie (Winnacker-Kuchler) 4 Aufl* 1983 Bd 3, Anorgan Technologie 2, p 75
- 38 J F Brinker, G W Scherer, *Sol-Gel Science The Physics and Chemistry of Sol-Gel Processing*, Academic Press, Boston, 1990
- 39 C W Higginson, *Chem Eng* 1974, 98
- 40 G Engelhardt, D Michel, *High Resolution Solid State NMR of Silicates and Zeolites*, Wiley, Chichester, 1987
- 41 B A Morrow, *Stud Surf Sci Catal* 1990, 57A, 161
- 42 K Wefers, G M Bell, *Oxides and Hydroxides of Aluminum* Alcoa Research Laboratories Technical Paper No 19, 1972, K Bielefeldt, G Winkhaus, *Chemische Technologie (Winnacker-Kuchler) 4 Aufl* 1983 Bd 3 Anorgan Technologie 2, p 2, L K Hudson, C Misra, K Wefers, *Ullmann's Encycl Ind Chem 5th ed* 1985 Vol A2, p 575
- 43 U Bollmann, *Habilitationschrift*, Bergakademie Freiberg, FRG, 1992

44. A. Danner, K. K. Unger, *Stud. Surf. Sci. Catal.* **1987**, *31*, 343; W. Stoepler, K. K. Unger, *Stud. Surf. Sci. Catal.* **1983**, *16*, 643.
45. B. C. Lippens, J. H. de Boer, *Acta Crystallogr.* **1964**, *17*, 1312; H. Sallfeld, B. B. Mehrotra, *Naturwissenschaften* **1966**, *53*, 128.
46. H. Knözinger, P. Ratnasamy, *Catal. Rev.-Sci. Eng.* **1978**, *17*, 31.
47. C. Laurent, H. A. H. Billet, L. de Galaan, *Chromatographia* **1983**, *17*, 253.
48. N. Zelinsky, W. Kommarewsky, *Chem. Ber.* **1924**, *57*, 667.
49. F. Cavani, F. Trifirò, A. Vaccari, *Catal. Today* **1991**, *11*, 173.
50. E. C. Kruissink, L. L. van Reijen, J. R. H. Ross, *J. Chem. Soc., Faraday Trans. I* **1981**, *77*, 649.
51. J. Zielinski, *Appl. Catal.* **1993**, *A94*, 107; J. Zielinski, *J. Mol. Catal.* **1993**, *83*, 197; R. Lamber, G. Schulz-Ekloff, *J. Catal.* **1994**, *146*, 601.
52. E. C. Kruissink, L. E. Alzamora, S. Orr, E. B. M. Doesburg, L. L. van Reijven, J. R. H. Ross, G. van Veen, *Stud. Surf. Sci. Catal.* **1979**, *3*, 143.
53. J. Rathousky, G. Schulz-Ekloff, J. Starek, A. Zukal, *Chem. Eng. Technol.* **1994**, *17*, 41.
54. D. C. Puxley, I. J. Kitchener, C. Komodromos, N. D. Parkyn, *Stud. Surf. Sci. Catal.* **1983**, *16*, 237.
55. C. J. Wright, C. G. Windsor, D. C. Puxley, *J. Catal.* **1982**, *78*, 257.
56. L. E. Alzamora, J. R. H. Ross, E. C. Kruissink, L. L. van Reijen, *J. Chem. Soc., Faraday Trans. I*, **1981**, *77*, 665.
57. J. G. Nunan, P. B. Himmelfarb, R. G. Herman, K. Klier, C. E. Bogdan, G. W. Simmons, *Inorg. Chem.* **1989**, *28*, 3868.
58. P. Porta, S. De Rossi, G. Ferraris, M. Lo Jacono, G. Minelli, G. Moretti, *J. Catal.* **1988**, *109*, 367.
59. J. C. Burnett, R. A. Keppel, W. D. Robinson, *Catal. Today* **1987**, *1*, 537; R. M. Contractor, A. W. Sleight, *Catal. Today* **1987**, *1*, 587; G. Centi, *Catal. Today* **1993**, *16*, 5; G. Centi, *NATO ASI Ser. Ser. C* **1993**, *398*, 93.
60. F. Cavani, F. Trifirò, *Stud. Surf. Sci. Catal.* **1995**, *91*, 1.
61. L. M. Cornaglia, C. A. Sanchez, E. A. Lombardo, *Appl. Catal. A* **1993**, *95*, 117.
62. E. Kesteman, M. Merzouki, B. Taouk, E. Bordes, R. Contractor, *Stud. Surf. Sci. Catal.* **1995**, *91*, 707.
63. H. S. Horowitz, C. M. Blackstone, A. W. Sleight, G. Teufer, *Appl. Catal.* **1988**, *38*, 193.

gel, which is a diphasic material with a solid encapsulating a solvent. Alternatively, a gel can be produced by destabilizing a solution of preformed sols. In either case the materials are referred to aquasol (or aquagel) when water is used as a solvent, and alcosol (or alcogel) when alcohol is used. The encapsulated liquid can be removed from a gel by either evaporative drying or drying with supercritical extraction (supercritical drying for short). The resulting solid products are known as a xerogel and an aerogel, respectively.

The single most important characteristic of the sol-gel preparation of catalytic materials is its *ease of control* that translates into the following advantages:

- (i) the ability to maintain high purity (because of purity of starting materials);
- (ii) the ability to change physical characteristics such as pore size distribution and pore volume;
- (iii) the ability to vary compositional homogeneity at a molecular level;
- (iv) the ability to prepare samples at low temperatures;
- (v) the ability to introduce several components in a single step;
- (vi) the ability to produce samples in different physical forms.

The purpose of this article is to teach catalytic researchers how to realize some of these advantages in their work. To this end we start by identifying the various steps in a sol-gel process and the key parameters in each step that have been shown to impact on the physical and/or chemical properties of the products. We then give selected examples of recent literature results.

#### 2.1.4.2 Important Parameters in Sol-Gel Preparation

Figure 1 shows the four key steps in taking a precursor to a particular product form via sol-gel preparation: formation of a gel, aging of a gel, removal of solvent, and heat treatment. The versatility of this preparative approach lies in the number of parameters that can be manipulated in each of these steps.

##### A Solution Chemistry

The precursor in a sol-gel preparation can either be a metal salt/alkoxide dissolved in an appropriate solvent or a stable colloidal suspension of preformed sols. Metal alkoxides have been the most extensively used because they are commercially available in high purity and their solution chemistry has been documented [1-3]. At its simplest level, sol-gel chemistry

## 2.1.4 Sol-Gel Process

E. I. Ko

### 2.1.4.1 Introduction

The sol-gel process involves first the formation of a sol followed by that of a gel. A sol, which is a liquid suspension of solid particles ranging in size from 1 nm to 1 micron, can be obtained by the hydrolysis and partial condensation of a precursor such as an inorganic salt or a metal alkoxide. The further condensation of sol particles into a three-dimensional network produces a



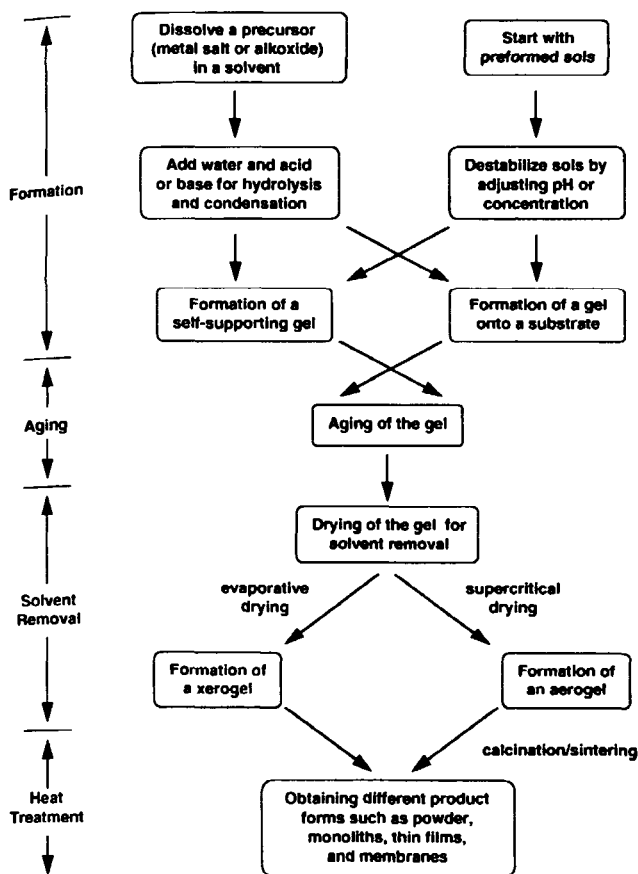
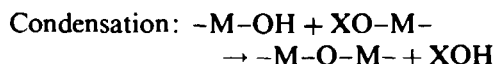
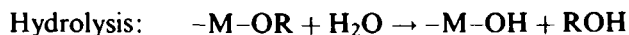


Figure 1. Schematic diagram showing the various steps of a sol-gel process.

with metal alkoxides can be described in terms of two classes of reactions:



where X can either be H or R (an alkyl group).

Such a description oversimplifies the overall process because it does not correctly represent the molecular formulas of the intermediates and end products, nor does it depict the simultaneous occurrence of the two reactions. However, this oversimplification captures the key phenomenological idea that a three-dimensional gel network comes from the condensation of partially hydrolyzed species. Any parameters that affect either or both of these reactions are thus likely to impact on the properties of the product. In fact, Livage et al. [4] pointed out that the important variables are the *relative* rates of hydrolysis and condensation.

Figure 2 shows the rates of hydrolysis and condensation of tetraethylorthosilicate (TEOS), which is the most widely studied precursor, vary as a function of pH [5]. Under acidic conditions hydrolysis occurs at

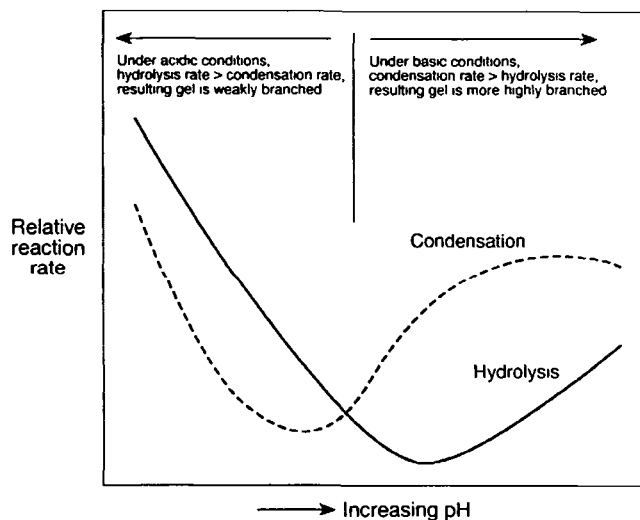


Figure 2. Schematic diagram showing the variation of hydrolysis and condensation rates of tetraethylorthosilicate with pH, and the effect of relative rate on gel structure.

a faster rate than condensation and the resulting gel is weakly branched. Under basic conditions the reverse is true and the resulting gel is highly branched and contains colloidal aggregates. Subsequently dried and heat-treated samples have different surface functionalities [6] and pore structures [7].

Because hydrolysis and condensation are both nucleophilic displacement reactions, the reactivity of metal alkoxides is dependent on the positive partial charge of the metal atom and its coordination number [8]. For example, TEOS, with a small positive partial charge on silicon, is the least reactive among the common alkoxides [4]. In general, the longer and bulkier the alkoxide group attached to a particular metal atom, the less reactive that precursor is in hydrolysis and condensation [9]. Changing the type of precursor and/or its concentration are thus effective means of controlling the reaction rates.

The amount of water used in sol-gel preparation and the rate by which it is added also influence gel characteristics. The former is usually expressed in terms of the hydrolysis ratio  $h$ , defined as the moles of water per mole of metal alkoxide,  $\text{M}(\text{OR})_m$ . There are three specific regions of interest [4]:

- (i)  $h < 1$ : An infinite network seldom forms due to the low functionality of the precursor towards condensation. Because there are few M-OH groups for cross-linking, gelation or precipitation cannot occur when there is no local excess of water.
- (ii)  $1 < h < m$ : Polymeric gels can form.
- (iii)  $h > m$ : Cross-linked polymers, particulate gels, or precipitates can form when an excess of water is added to the alkoxides.

For a given amount of water, another level of control comes from the rate of addition. Common approaches in adding water slowly are using a micropipette, absorbing moisture from a controlled humidity environment, and generating water in the solution with another chemical reaction.

Two other important sol-gel parameters are temperature and solvent. Both hot and cold plates are commercially available and can be used to increase and decrease the reaction rates, respectively. Varying the temperature is most effective when it can alter the *relative* rates of competing reactions. Solvent can change the nature of an alkoxide through solvent exchange or affect the condensation reaction directly. It is also possible to prepare a gel without a solvent as long as another means, such as ultrasound irradiation [10] (see Section A.8.6), is used to homogenize an otherwise immiscible alkoxide/water mixture.

Using preformed sols instead of metal alkoxides as precursors is an attractive alternative in sol-gel preparation because recent advances in inorganic colloidal dispersions allow some control over the characteristics of the starting sols [11]. Often a colloidal suspension of sol particles is stabilized (i.e. prevented from flocculation) by pH adjustment. Thus, pH of the solution, which can be changed by the addition of either acid or base, is the single most important parameter in obtaining a gel from preformed sols. Other parameters that can impact on gel quality are the size and concentration of the starting sol particles.

For any of the sol-gel parameters discussed so far, its effect on gel properties can often be followed by an experimental observable known as *gel time*. Gel time is defined as the time it takes for a solution to undergo a rapid rise in viscosity that corresponds to the transition from a viscous fluid to an elastic gel [9]. At the *gel point* there is a continuous solid phase containing a structure that reflects the formation and branching of particles under specific growth conditions. This particular phase is important because it is the genesis of structural evolution that takes place in all subsequent processing steps [9, 12].

## B Aging

Aging represents the time between the formation of a gel and the removal of solvent. As long as the pore liquid remains in the matrix, a gel is not static and can undergo many transformations [9, 12]. For alkoxide-derived gels, condensation between surface functional groups continue to occur after the gel point. This process can actually be desirable because it leads to a more cross-linked network that is mechanically stronger and easier to handle. However, extensive condensation causes the gel to shrink to the point that solvent is actually expelled, in a phenomenon called *syneresis*. Coarsening, or ripening, is a physical process driven by

differences in solubility associated with surfaces that have different radii of curvature. Coarsening basically involves the dissolution and reprecipitation of particles, resulting in an increase in the average pore size of the gel and a decrease in its specific surface area.

Parameters that affect these aging processes include temperature, time, and pH of the pore liquid. Common approaches in manipulating these parameters are immersing the gel in or washing it with another liquid, exposing the gel to a different humidity, heating the gel, and using hydrothermal conditions. Even though all these approaches have been demonstrated to change the gel characteristics, an understanding of the cause and effect is at best qualitative at present. For this reason aging is often an overlooked step in the sol-gel preparation of catalytic materials. The recent work of Smith et al. [13], who developed an *in situ* NMR technique for following the aging process, may open up new opportunities in this area.

## C Drying

As the pore liquid is evaporated from a gel network, the capillary pressure associated with the liquid-vapor interface within a pore can become very large for small pores. For example, the capillary pressure with water evaporating from a pore with a radius of 1 nm is on the order of  $1.5 \times 10^8$  pa. With a distribution of pore sizes in a gel, as is commonly the case, the differential pressure across pores of different sizes leads to a collapse in the pore structure. Thus, strategies that are effective in maintaining the integrity of a gel network aim at minimizing either the differential pressure or the capillary pressure itself.

One approach to minimize capillary pressure is to prepare gels containing uniform-sized pores or at least a narrow pore size distribution. This can be done by adding organics such as formamide and glycerol, which are called drying control chemical additives (DCCA), to control the rates of hydrolysis and condensation and in turn the pore size distribution. There are many examples showing that glasses and ceramics prepared with DCCA can better withstand drying due to a more uniform pressure distribution across the gel network [14]. The use of DCCA in preparing catalytic materials has not been common, partly because there are alternatives that do not introduce potential impurities into the system.

The easiest way to understand approaches that are effective in minimizing the capillary pressure directly is to examine the equation

$$P = 2\sigma \cos(\alpha)/r$$

where  $P$  is capillary pressure,  $\sigma$  is surface tension,  $\alpha$  is the contact angle between liquid and solid, and  $r$  is the pore radius. For a given pore size, then, the capillary

pressure can be reduced by (i) using a solvent with a lower surface tension or with a contact angle close to  $90^\circ$  and (ii) eliminating the liquid–vapor interface altogether with either supercritical or freeze drying.

Smith and co-workers have aged silica gels in either ethanol or water and subsequently washed them in various aprotic solvents that cover a range of surface tensions [15, 16]. Their results clearly demonstrated the effect of surface tension on microstructure because the resulting xerogels have a wide range of surface area and pore volume. Furthermore, the effect is dependent on the initial network rigidity as acid-catalyzed and base-catalyzed gels respond to the treatment differently. The fact that some of these xerogels have comparable physical properties to aerogels obtained by supercritical drying suggests an attractive alternative in preparing high-surface-area, low-density materials at ambient pressure.

*Supercritical drying* is a high-pressure approach aimed at eliminating the liquid–vapor interface and the accompanying capillary pressure. Since the pioneering work of Kistler [17], the technology of supercritical drying has evolved from a tedious, multistep process to a simpler and safer semicontinuous process [18]. One major advance came from the group of Teichner who used alcoholic solutions of metal alkoxides in preparing gels with a minimal amount of water. In prior preparations that used a large amount of water, tedious washing and solvent exchange steps were necessary because water would dissolve the gel structure at high temperatures [19]. There are now numerous examples showing that aerogels can be prepared to give high porosities, high specific surface areas, low apparent densities, and good textural stability [20]. These advantages can be realized because, in addition to eliminating the liquid–vapor interface, supercritical drying is done at moderate temperatures. In fact, one often overlooked advantage in supercritical drying is its ability to preserve the amorphous structure of an aerogel. For example, it has been reported that a niobia aerogel is slower to crystallize than a xerogel upon further heat treatment and hence better able to retain its high acid strength along with acid site density [21].

Similar to aging, a gel is not static during drying and, for that reason, drying can be viewed as part of the overall aging process. The properties of a product are thus dependent on the drying method and even with a single method, the drying conditions. Most supercritical drying experiments have been done with alcohol because of its use as a solvent in the sol–gel step. But ever since supercritical carbon dioxide was shown to be an effective agent for displacing alcohol [18], many researchers have reported on the effect of drying agent on the properties of aerogels such as silica [14, 15], titania [22], and titania–silica [23]. Because different substances have different critical temperatures, these

results can be understood in terms of the accelerated aging of a gel at a higher drying temperature. For example, recently Brodsky and Ko showed that varying the temperature while using a single drying agent, carbon dioxide, can also change the textural and structural properties of calcined titania aerogels [24]. Besides temperature, other parameters that are important in supercritical drying include the path to the critical point, depressurization, and composition of the drying medium [20, 25]. In particular, reduction is prone to occur when an autoclave is filled with hydrogen during drying [20].

One other approach in bypassing a liquid–vapor interface is freeze drying, in which the pore liquid is frozen into a solid that subsequently sublimates to give a product called a cryogel. Data on the characteristics of cryogels are limited because freeze drying has not been used as extensively as supercritical drying in preparing catalytic materials.

### D Calcination/Sintering

After the removal of pore liquid, further heat treatment is necessary to convert a xerogel or aerogel into a catalytically useful form. Often, heating is done in the presence of a reactive gas (e.g. flowing air, oxygen, or hydrogen) in order to burn off any residual organics or to oxidize (or reduce) the sample. Exposing the sample to a high temperature over an extended period of time leads to sintering and consequently a decrease in surface area. The process can also cause the material to crystallize into different structural forms. Thus, the physical characteristics of a product depend on parameters such as temperature, heating rate, time, and gaseous environment. It is common practice to subject a sample to a more severe heat treatment than it is likely to encounter in a reactor to ensure at least the stability of its textural and structural properties during reaction.

### E Summary

Table 1 provides a quick reference to the four key steps in a sol–gel process, the purpose of each step, and the associated experimental parameters that can be varied. Since each of these parameters can potentially affect the properties of a product, literature results on sol–gel preparation should be reported or examined in a similar format to allow a meaningful comparison among different studies. As an example, Table 2 shows the parameters used in the preparation of titania [22] and zirconia [26] aerogels.

#### 2.1.4.3 Advantages of Sol–Gel Preparation

Table 3 is a representative and by no means exhaustive list of reactions that have been catalyzed by sol–gel

Table 1. Important parameters in the various steps of a sol-gel process.

Step	Purpose	Important parameters
Solution chemistry	to form a gel	type of precursor; type of solvent; pH (acid/base content); water content; precursor concentration; temperature
Aging	to allow a gel to undergo changes in properties	time; temperature; composition of the pore liquid (e.g. pH); aging environment (e.g. humidity)
Drying	to remove solvent from a gel	drying method (e.g. evaporative vs. supercritical vs. freeze drying); temperature and heating rate; pressure and pressurization rate; time
Calcination/sintering	to change the physical/chemical properties of the solid, often resulting in crystallization and densification	temperature and heating rate; time; gaseous environment (e.g. inert vs. reactive gases)

Table 2. Examples of sol-gel parameters in the preparation of titania and zirconia aerogels.

Step	Parameter	Final oxide	
		TiO <sub>2</sub> <sup>a</sup>	ZrO <sub>2</sub> <sup>b</sup>
Solution chemistry	precursor	Titanium <i>n</i> -butoxide (Ti(C <sub>4</sub> H <sub>9</sub> O) <sub>4</sub> )	Zirconium <i>n</i> -propoxide (Zr(C <sub>3</sub> H <sub>7</sub> O) <sub>4</sub> )
	solvent	methanol	<i>n</i> -propanol
	nitric acid content	0.125 mol/mol of precursor	0.83 mol/mol of precursor
	water content	4 mol/mol of precursor	2 mol/mol of precursor
	precursor concentration	0.625 mmol/mL of methanol	1.0 mmol/mL of <i>n</i> -propanol
	temperature	room temperature	room temperature
Aging	time	2 h	2 h
	temperature	room temperature	room temperature
	environment	covered beaker	covered beaker
Drying	method	Semicontinuous supercritical	Semicontinuous supercritical
	drying agent	carbon dioxide (CO <sub>2</sub> )	carbon dioxide (CO <sub>2</sub> )
	temperature	343 K	343 K
	pressure	2.1 × 10 <sup>7</sup> Pa	2.1 × 10 <sup>7</sup> Pa
	time	2 h	2 h
	CO <sub>2</sub> flow rate	85 L h <sup>-1</sup> downstream	85 L h <sup>-1</sup> downstream
Calcination/sintering	first step	383 K in a vacuum oven for 3 h	383 K in a vacuum oven for 3 h
	second step	523–573 K in a vacuum oven for 3 h	773 K in flowing oxygen for 2 h
	third step	773 K in flowing oxygen (24 L h <sup>-1</sup> ) or 2 h (with a heating rate of 10 K min <sup>-1</sup> from room temperature to 773 K)	

<sup>a</sup> From Ref. 22.<sup>b</sup> From Ref. 26.

materials including both xerogels and aerogels. Its purpose is to demonstrate the potential range of applications and, more importantly, the wide variety of catalytic materials that can be obtained by this preparative approach. Catalysts in this table include supported metals, mixed oxides, promoted oxides, and several three-component systems. This section high-

lights the advantages sol-gel preparation brings to these different classes of materials.

### A Varying the Pore Structure

The classic example of using a sol-gel parameter to vary the pore structure (surface area, pore volume, and pore size distribution) of products is the effect of pH

**Table 3.** Examples of reactions that have been catalyzed by sol-gel materials.

Reaction	Catalyst	Reference
Hydrogenation of phenylacetylene	Pd/SiO <sub>2</sub>	27
Oxidation of CO	Pt/TiO <sub>2</sub>	28
Oxidative dehydrogenation of ethane	Li <sup>+</sup> /MgO promoted by Cl <sup>-</sup>	29
Nitroxidation of alkenes	PbO-ZrO <sub>2</sub> , PbO-Al <sub>2</sub> O <sub>3</sub>	30
Hydrotreating of gas oil	Ni-Mo/TiO <sub>2</sub> -ZrO <sub>2</sub>	31
Selective catalytic reduction of NO by NH <sub>3</sub>	V <sub>2</sub> O <sub>5</sub> , V <sub>2</sub> O <sub>5</sub> -TiO <sub>2</sub> , V <sub>2</sub> O <sub>5</sub> -TiO <sub>2</sub> -SiO <sub>2</sub>	32
Isomerization of 1-butene	Nb <sub>2</sub> O <sub>5</sub> -SiO <sub>2</sub>	33
Fluorination of C <sub>2</sub> Cl <sub>3</sub> F <sub>3</sub> with HF	Cr <sub>2</sub> O <sub>3</sub>	34
Dehydrocyclization of <i>n</i> -heptane	Pt-Sn/Al <sub>2</sub> O <sub>3</sub>	35
Polymerization and co-polymerization of $\alpha$ -alkenes	Transition metal/Al <sub>2</sub> O <sub>3</sub>	36

on the properties of silica. As discussed in Section 2.1.4.2.A (see also Fig. 2), acid- and base-catalyzed silica gels give rise to products that contain micropores and mesopores, respectively, because of the different extent of branching in the gel. Brinker et al. [37] recently pointed out that other sol-gel parameters, including those in the aging and drying steps, can also significantly change the pore structure of dried gels or films that are made of silicate, multicomponent silicate, and aluminosilicate. In the case of aluminosilicate, changing the alumina content can lead to products having either no porosity, microporosity, or macroporosity. These authors further noted that similar results and concepts should be applicable to non-silicate systems.

Using preformed sols instead of metal alkoxides as precursors is another effective way to change the pore structure, as recently demonstrated for the sol-gel preparation of zirconia [38]. The two key parameters in this approach are the starting sol size and the intrinsic porosity of the sol particles.

Zou and Gonzalez [39] have varied the pore size distributions of a series of Pt/SiO<sub>2</sub> catalysts by changing the amount of water used in the sol-gel step. The average pore size decreases from 7.5 to 3.5 nm as the hydrolysis ratio, defined as H<sub>2</sub>O:TEOS, increases from 10 to 60. This variation of average pore size is significant because the catalysts are more resistant to sintering in oxygen (up to 948 K for Pt loadings of 0.2–0.3 wt%) when the average pore diameter matches the particle size of Pt.

### B Controlling Homogeneity in Mixed Oxides

Mixed oxides, which contain two or more components, are of catalytic interest because they can be used as supports, catalysts, or precursors to other materials. One particularly interesting property that arises by mixing oxides is the generation of strong acidic sites associated with the interface or linkage between the two components [40]. In order to maximize the number

of these sites, it is desirable to prepare samples that are homogeneously mixed at a molecular level.

Sol-gel preparation offers excellent control of mixing because of its ability to alter relative precursor reactivity. Qualitatively, we expect good mixing when the two precursors have similar reactivities and poor mixing when they do not. As pointed out in Section 2.1.4.2.A, both hydrolysis and condensation are nucleophilic displacement reactions. Effective strategies in matching precursor reactivity thus include:

- (i) using a precursor containing a different alkoxy group;
- (ii) giving a less reactive precursor a head-start by “prereacting” it with water, in a process known as prehydrolysis;
- (iii) slowing down a more reactive precursor by replacing some of its alkoxy groups with different ligands, in an approach known as chemical modification;
- (iv) performing the preparation in a different temperature.

The application of all four strategies to the preparation of zirconia-silica aerogels has recently been reported [41]. On the evidence of 1-butene isomerization activity, Miller et al. concluded that the first three strategies lead to well-mixed samples. Specifically, their results show that in the cogelling of two alkoxides, the reactivities of the two alkoxides must be fairly well matched to achieve homogeneous distribution. If this is not accomplished, then the more reactive component tends to form a “core” onto which the less reactive component attaches. The latter situation is not necessarily bad because the notion of controlling mixing means that one can prepare an inhomogeneous sample if that is what the application calls for. For example, Handy et al. [42] prepared two titania-silica samples as supports for vanadia, one with prehydrolysis to promote mixing and one without prehydrolysis. They

found that the former sample is actually less active for the selective catalytic reduction of NO with  $\text{NH}_3$ . Apparently the titania crystallites that are present in the less well-mixed sample are necessary to stabilize the active vanadia phase.

The work of Toba et al. [43] is another example showing that better mixing can be accomplished with sol-gel than other preparation methods. These authors prepared alumina-titania samples by complexing-agent-assisted sol-gel (with an ethanol/hexylene glycol solution), coprecipitation, and hydrogel kneading. They concluded that the two oxides are the best mixed (or most homogeneous) in the sol-gel sample because titania resists crystallization the most upon heating and the number of acidic sites, associated with Ti-O-Al bonds, is the highest.

### C Changing Dispersion and Stability of Supported Metals

In the sol-gel preparation of supported metals, a metal precursor is usually added directly to the solution prior to gelling. Regardless of whether the metal precursor participates in hydrolysis and/or condensation, it will become part of the network as the gel forms. Thus, any parameters that are important in solution chemistry (Table 1) could affect the properties of the metal upon activation. An example is the work of Zou and Gonzalez [39] cited in Section 2.1.4.3.A. When these authors used water content as a variable to change the pore size distribution of a series of Pt/SiO<sub>2</sub> catalysts, they found that the particle size distribution of reduced Pt (in the form of crystallites) is also dependent on the hydrolysis ratio. The average Pt particle size nearly doubles (from about 1.7 to 3 nm) as the hydrolysis ratio increases from 10 to 60. As noted earlier, the stability of these catalysts, in terms of the resistance of Pt particles towards sintering, is a function of how well the pore diameter and particle size match.

Lopez et al. [27] prepared Pd/SiO<sub>2</sub> catalysts under both acidic (pH = 3) and basic (pH = 9) conditions in the sol-gel step and reported that an acid medium promotes the formation of small metal crystallites. This finding is consistent with the formation of a microporous silica gel network at a low pH. By comparing samples prepared by the sol-gel method and impregnation, these authors found in the former a stronger metal-support interaction which they ascribed to the square planar palladium complex used as a precursor. Finally, their results showed that the method of preparation as well as the conditions used in each method impact on how these catalysts deactivate in the hydrogenation of phenylacetylene.

In general, the activation and deactivation of metal particles in a sol-gel sample is dependent on how much of the metal is actually occluded (or incorporated) in the support network. In the two examples above, the

extent of occlusion is minimal for Pt/SiO<sub>2</sub> and larger for Pd/SiO<sub>2</sub>. A telltale sign of occlusion is when the metal particle sizes determined by chemisorption and transmission electron microscopy (or X-ray diffraction) do not agree and there is no reason to believe that such a difference is caused by electronic effects.

Some occlusion of the metal particles is not necessarily bad. In fact, unlike other methods such as impregnation and ion exchange, sol-gel preparation actually allows a certain amount of control over what fraction of a metal particle is accessible at the support surface. As long as there are exposed metal atoms available for catalysis, a partially buried metal particle may better resist deactivation due to sintering. For example, Lopez et al. [44] found that a Ru/SiO<sub>2</sub> sample prepared by sol-gel is more stable than one prepared by ion exchange. The sol-gel sample, which contains partially occluded Ru particles, does not sinter or volatilize under oxygen treatment at 723 K, whereas the ion-exchange sample does.

### D Preparing Samples in a Single Step

One advantage of preparing supported samples by the sol-gel method is that the supported phase, be it a metal or an oxide, can be introduced *during* instead of *after* the formation of the support. Other than the convenience of saving a step, this feature may introduce unique metal-oxide or oxide-oxide interactions that are inaccessible with other preparation methods. The tradeoff is the activation of the supported phase is likely to be more difficult if it is incorporated within the support structure.

The ability to introduce several components into solution during the sol-gel step makes this approach especially attractive for the preparation of multicomponent oxides and bimetallic catalysts. Of course, the solution chemistry becomes more complex with additional components. But many of the concepts that we have discussed, such as matching relative precursor reactivity and changing the microstructure of the gel network, remain valid in principle. Furthermore, a promoter or an active species can be introduced the same way. There have been recent reports on the one-step preparation of zirconia-sulfate aerogels [45] and Li/MgO catalysts [46]. These samples are active in the isomerization of *n*-butane and the oxidative coupling of methane, respectively.

Finally, by using preformed sols instead of metal alkoxides as precursors, it is possible to use the sol particles as building blocks and form a gel around them, again in a single step. As discussed in Section 2.1.4.3.A, this approach offers control over the pore structure and the distribution of active components. For example, the use of a nonporous sol particle effectively prevents incorporation of other species within the particle itself.

#### 2.1.4.4 Catalytic Membranes

Zaspalis and Burggraaf [47] have summarized typical membrane reactor configurations, different membrane/catalyst combinations, and a large number of membrane reactor studies. Their article clearly shows that inorganic membranes prepared by the sol-gel method, with their dual ability in catalysis and separation, have many unique advantages over other product forms. At the same time, it is important to realize that the parameters which affect a membrane's characteristics and the advantages which the sol-gel process offers are similar to what has been presented thus far.

Self-supporting inorganic membranes can be formed with or without a substrate. In either case the precursor sol, consisting of either a colloidal suspension or a polymeric solution, must be formed. To produce a membrane supported on a substrate (i.e. a supported membrane), a preformed porous support is dipped in the precursor sol and a gel forms at the surface of the support typically by the slipcasting method [48]. Another approach is spin coating, in which an excess amount of liquid is deposited onto a substrate and then thinned uniformly by centrifugal force [12]. To produce a non-supported membrane, the liquid is simply poured into a mold of appropriate shape and allowed to dry. All these processes need to be done before the gel point which is accompanied by a large increase in viscosity.

The microstructure of a sol, in terms of the nature and concentration of sol particles, significantly affect a membrane's properties such as average pore diameter and pore size distribution. Other critical parameters are the temperature and rate of evaporation used in the drying and calcination steps. Even though it is economical to obtain the final product form quickly, too rapid a drying rate forms cracks in the membrane. Crack formation is also dependent on thickness of the membrane. The work of Cini et al. [49], who prepared supported microporous  $\gamma$ - $\text{Al}_2\text{O}_3$  membranes as catalyst supports, illustrates many of these effects.

As with other product forms, sol-gel preparation offers excellent control of the chemical composition of catalytic membranes. Again, a second or even a third component can be introduced directly in the solution. Such an approach was used by Xu and Anderson [50], who mixed titanium and zirconium precursors in order to improve the thermal stability of microporous titania and zirconia membranes. Alternatively a second component can be introduced to a preformed membrane. By using the so-called reservoir method, Zaspalis et al. [51] filled the pores of a  $\gamma$ - $\text{Al}_2\text{O}_3$  membrane with a solution of silver nitrate, thereby achieving a high loading of silver in the top layer of the membrane. These and numerous other examples have demonstrated the feasibility of preparing multicomponent membranes. However, many of the strategies men-

tioned in Section 2.1.4.3 (e.g. controlling homogeneity) have yet to be fully explored. Thus, tremendous opportunities exist for researches to exploit the sol-gel process to fine-tune the physical and chemical properties of inorganic membranes.

#### 2.1.4.5 Other Sol-Gel Materials

Due to space limitation, this article has focused primarily on inorganic materials because of their important catalytic applications. But it must be pointed out that some exciting and rapidly developing areas of sol-gel chemistry involve inorganic-organic hybrids [52], gel-entrapped enzymes and proteins [53], and organic gels [54]. The basic principles covered above should enable the readers to learn about these variations of the sol-gel technique and, in turn, to explore the potential applications of a still wider range of materials.

#### 2.1.4.6 Summary

With its versatility and excellent control over a product's characteristics, sol-gel processing has played an important role in catalyst preparation and no doubt will continue to do so. Advances in this area are likely to come from two related fronts. First, it is important to have a better understanding of the chemistry underlying all the processing steps, from gelation to aging to drying. Second, this understanding should be made as quantitative as possible to allow the development of predictive models. As many researchers are actively working towards these goals, it is almost certain that in the next few years we will see many new syntheses, exciting properties, and creative applications of catalytic materials prepared by the sol-gel method and, along with these findings, a better understanding of catalysis itself.

#### References

- 1 D C Bradley, R C Mehrota, P D Gaur, *Metal Alkoxides*, Academic, New York, 1978
- 2 D C Bradley, *Chem Rev* 1989, 89, 1317-1322
- 3 R C Mehrota, *J Non-Cryst Solids* 1992, 145, 1-10
- 4 J Livage, M Henry, C Sanchez, *Prog Solid St Chem* 1988, 18, 259-341
- 5 H D. Gesser, P C Goswami, *Chem Rev* 1989, 89, 765-788
- 6 J Y Ying, J B Benziger, *J Am Ceram Soc* 1993, 76, 2571-2582
- 7 B Handy, K L Walther, A Wokaun, A Baiker in *Preparation of Catalysts V* (Eds P. A Jacobs, P Grange, B Delmon), Elsevier, Netherlands, 1991, pp 239-246
- 8 J Livage, C Sanchez, *J Non-Cryst Solids* 1992, 145, 11-19
- 9 L L Hench, J K West, *Chem Rev* 1990, 90, 33-72
- 10 J Zarzycki in *Ultrastructure Processing of Advanced Materials* (Eds D R Uhlmann, D. R Ulrich), Wiley, New York, 1992, pp 135-148

- 11 E Matijevic, *Langmuir* **1994**, *10*, 8–16
- 12 C J Brinker, G W Scherer in *Sol-gel Science The Physics and Chemistry of Sol-gel Processing*, Academic, New York, **1990**
- 13 D M Smith, R Desphande, C J Brinker, W L Earl, B Ewing, P J Davis, *Catal Today* **1992**, *14*, 293–303
- 14 D R Ulrich, *J Non-Cryst Solids* **1988**, *100*, 174–193
- 15 D M Smith, R Desphande, C J Brinker in *Better Ceramics through Chemistry V* (Eds M J Hampden-Smith, W G Klemperer, C J Brinker), Materials Research Society, Pittsburgh, **1992**, 271, pp 567–572
- 16 R Desphande, D M Smith, C J Brinker, *ibid*, pp 553–558
- 17 S S Kistler, *Nature* **1931**, *127*, 741
- 18 R J Ayen, P A Iacobucci, *Rev Chem Eng* **1988**, *5*, 157–198
- 19 S J Teichner, *CHEMTECH* **1991**, *21*, 372–377
- 20 G M Pajonk, *Appl Catal* **1991**, *72*, 217–266
- 21 S M Maurer, E I Ko, *J Catal* **1992**, *135*, 125–134
- 22 L K Campbell, B K Na, E I Ko, *Chem Mater* **1992**, *4*, 1329–1333
- 23 M Beghi, P Chiurlo, L Costa, M Palladino, M F Pivini, *J Non-Cryst Solids* **1992**, *145*, 175–179
- 24 C J Brodsky, E I Ko, *J Mater Chem* **1994**, *4*(4), 651–652
- 25 G W Scherer, in *Drying* (Ed A S Mujumdar), Elsevier, Netherlands, **1992**, pp 92–113
- 26 D A Ward, E I Ko, *Chem Mater* **1993**, *5*, 956–969
- 27 T Lopez, P Bosch, J Navarrete, M Asomoza, R Gomez, *J Sol-Gel Sci & Tech* **1994**, *1*, 193–203
- 28 R Gomez, T Lopez, S Castillo, R G Gonzalez, *J Sol-Gel Sci & Tech* **1994**, *1*, 205–211
- 29 S J Conway, L H Lunsford, *J Catal* **1992**, *131*, 513–522
- 30 R Tleimat-Manzalji, T Manzalji, G M Pajonk *J Non-Cryst Solids* **1992**, *147/148*, 744–747
- 31 J G Weissman, E I Ko, S Kaytal, *Appl Catal A* **1993**, *94*, 45–59
- 32 B E Handy, M Maciejewski, A Baiker, *J Catal* **1992** *134* 75–86
- 33 S M Maurer, E I Ko, *Catal Lett* **1992**, *12*, 231–238
- 34 E Carlson, J N Armor, W J Cunningham, A M Smith, US Patent 4 828 818 **1989**
- 35 R Gomez, V Bertin, M A Ramirez, T Zamudio, P Bosch, I Schifter, T Lopez, *J Non-Cryst Solids* **1992**, *147/148*, 748–752
- 36 A J Fanelli, A K Price, US Patent 3 378 987 **1984**
- 37 C J Brinker, D M Smith, R Deshpande P M Davis S Hietala, G C Frye, C S Ashley, R A Assink, *Catal Today* **1992**, *14*, 155–163
- 38 D A Ward, E I Ko, *Langmuir* **1995**, *11*, 369–372
- 39 W Zou, R D Gonzalez, *Appl Catal A* **1993**, *102*, 181–200
- 40 K Tanabe in *Catalysis Science and Technology* (Eds J R Anderson, M Boudart), Springer-Verlag, Berlin, **1981**, Vol 2, pp 231–273
- 41 J B Miller, S E Rankin, E I Ko, *J Catal* **1994**, *148*, 673–682
- 42 B E Handy, A Baiker, M Schraml Marth, A Wokaun, *J Catal* **1992** *133*, 1–20
- 43 M Toba, F Mizukami, S Niwa, Y Kiyozumi, K Maeda, A Annala V Komppa, *J Mater Chem* **1994**, *4*(4), 585–589
- 44 T Lopez, L Herrera, R Gomez, W Zou, K Robinson, R D Gonzalez, *J Catal* **1992**, *136*, 621–625
- 45 D A Ward, E I Ko, *J Catal* **1994**, *150*, 18–33
- 46 T Lopez, R Gomez, A Ramirez-Solis, E Poulain, O No varo, *J Mol Catal* **1994**, *88*, 71–84
- 47 V T Zaspalis, A J Burggraaf in *Inorganic Membranes Synthesis Characteristics, and Applications*, Van Nostrand Reinhold, New York, **1991**, pp 177–207
- 48 A J Burggraaf, K Keizer, *ibid*, pp 10–63
- 49 P Cini, S R Blaha, M P Harold, K Venkataraman, *J Membrane Sci* **1991**, *55*, 199–225

- 50 Q Xu, M A Anderson, *J Am Ceram Soc* **1993**, *76*(8), 2093–2097
- 51 V T Zaspalis, W van Praag, K Keizer, J G van Ommen, J R H Ross, A J Burggraaf, *Appl Catal* **1991**, *74*, 235–248
- 52 U Schubert, N Husing, A Lorenz, *Chem Mater* **1995**, *7*, 2010–2027
- 53 D Avnir, S Braun, O Lev, M Ottolenghi, *Chem Mater* **1994**, *6*, 1605–1614
- 54 G C Ruben, R W Pekala, *J Non-Cryst Solids* **1995** *186* 219–231

## 2.1.5 Flame Hydrolysis

H JACOBSEN AND P. KLEINSCHMIT

### 2.1.5.1 Manufacture

The term flame hydrolysis describes a process in which a gaseous mixture of a precursor (a metal chloride in many cases), hydrogen and air or oxygen is brought to reaction in a torch installed in a continuously operated flame reactor. The precursor compound is hydrolyzed by the water vapor produced by the oxyhydrogen reaction. Different to this method is the so-called flame oxidation in which the precursor compound is not hydrolyzed but oxidized. The so-called chloride process uses the reaction of  $\text{TiCl}_4$  with oxygen to produce coarser pigment grade  $\text{TiO}_2$  [1]. The reaction is only weakly exothermic and requires a high reaction temperature.  $\text{TiCl}_4$  and oxygen are therefore heated up to  $1000^\circ\text{C}$  before reaction. A related process that has also been the subject of many investigations is spray pyrolysis. Whereas the first two processes describe gas-to-particle processes, spray pyrolysis is an example of a droplet-to-particle process. In many cases spray pyrolysis is used for the manufacture of modern ceramics and high-temperature superconductors. It is common in the literature to use the generic term 'aerosol processes' for gas-to-particle and droplet-to-particle processes. An overall view of aerosol processing of materials in general can be found in Ref. 2.

Of all these processes only flame hydrolysis is used to produce oxides with high surface areas on a large industrial scale. Therefore, the emphasis of this article lies on this subject. In general, this process is suitable for any volatile compound that can be decomposed at a high temperature to form an oxide. Possible precursor compounds that can be used are metal chlorides, carbonyls such as  $\text{Ni}(\text{CO})_4$  or  $\text{Fe}(\text{CO})_5$ , and volatile alcoholates. Reactions that have been studied are, for example, the manufacture of  $\text{Al}_2\text{O}_3$  from  $\text{AlCl}_3$  [3].



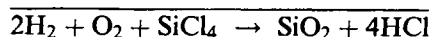
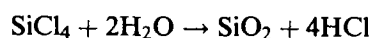
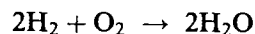
**Table 1.** Oxides produced by flame hydrolysis.

Product	Starting material
Al <sub>2</sub> O <sub>3</sub>	AlCl <sub>3</sub>
AlPO <sub>4</sub>	AlCl <sub>3</sub> /PCl <sub>3</sub>
AlBO <sub>3</sub>	AlCl <sub>3</sub> /BCl <sub>3</sub>
Al <sub>2</sub> O <sub>3</sub> /SiO <sub>2</sub> (mixed oxide)	AlCl <sub>3</sub> /SiCl <sub>4</sub>
Bi <sub>2</sub> O <sub>3</sub>	BiCl <sub>3</sub>
Cr <sub>2</sub> O <sub>3</sub>	CrO <sub>2</sub> Cl <sub>2</sub>
Fe <sub>2</sub> O <sub>3</sub>	Fe(CO) <sub>5</sub> , FeCl <sub>3</sub>
GeO <sub>2</sub>	GeCl <sub>4</sub>
NiO	Ni(CO) <sub>4</sub>
MoO <sub>3</sub>	MoCl <sub>5</sub> , MoO <sub>2</sub> Cl <sub>2</sub>
SiO <sub>2</sub>	SiCl <sub>4</sub>
SnO <sub>2</sub>	SnCl <sub>4</sub> , Sn(CH <sub>3</sub> ) <sub>4</sub>
TiO <sub>2</sub>	TiCl <sub>4</sub>
V <sub>2</sub> O <sub>5</sub>	VOCl <sub>3</sub>
WO <sub>3</sub>	WCl <sub>6</sub> , WOCl <sub>4</sub>
ZrO <sub>2</sub>	ZrCl <sub>4</sub>

TiO<sub>2</sub> from TiCl<sub>4</sub> [4], Fe<sub>2</sub>O<sub>3</sub> from FeCl<sub>3</sub> [5], MoO<sub>3</sub> from MoO<sub>2</sub>Cl<sub>2</sub> [6], and SiO<sub>2</sub> from SiCl<sub>4</sub> [7]. Alcoholate precursors that have been found to be suitable are titanium propylate and butylate, as well as secondary aluminum butylate [8, 9]. In this case, no flame-generated H<sub>2</sub>O is needed for the reaction, and the alcoholates can be decomposed in a hot wall reactor. Certain alkylhalidosilanes such as methyltrichlorosilane are other industrially used sources of silicon, because they are easily accessible byproducts of the silicone industry.

Since the invention of the flame hydrolysis process for the production of SiO<sub>2</sub> by Degussa [10] many different oxides have been manufactured via this route. Table 1 summarizes the oxides that have been prepared so far [11]. In principle, any mixed oxide that is a combination of the oxides SiO<sub>2</sub>, Al<sub>2</sub>O<sub>3</sub>, TiO<sub>2</sub> and ZrO<sub>2</sub> can be produced as well [12]. On a commercial scale SiO<sub>2</sub>, Al<sub>2</sub>O<sub>3</sub>, Al<sub>2</sub>O<sub>3</sub>/SiO<sub>2</sub> mixed oxides, TiO<sub>2</sub>, and ZrO<sub>2</sub> are available. Of these, fumed silica is by far the most widely produced oxide [13]. Although fumed silica was originally developed as a reinforcement filler for rubber (white carbon), it has found its way into numerous branches of industry of which catalysis is a comparably new one. The worldwide production capacity for fumed silica was estimated to be approximately 100 000 tons per annum in 1991. Main producers are Degussa (Aerosil<sup>®</sup>), Wacker (HDK<sup>®</sup>), Cabot (Cabosil<sup>®</sup>) and Tokuyama Soda (Reolosil<sup>®</sup>). The manufacturing process is briefly described below; further details are given in Ref. 14 and the patents and papers cited therein.

SiCl<sub>4</sub> is vaporized, mixed with dry air and hydrogen and then fed into a flame reactor. The SiCl<sub>4</sub> hydrolyzes to SiO<sub>2</sub> and HCl under the influence of the oxyhydrogen reaction, which includes the formation and reaction of radicals.



The silica so produced can be described as an aerosol of nanometer sized particles. The primary particles coagulate to form aggregates by intergrowth in the flame and further agglomerates by cohesion forces during and after cooling. The formation of this structure is essential for the resulting properties of the product. Filters or cyclones separate the silica from the hydrochloric acid containing off-gas. Residual hydrochloric acid adsorbed on the large surface of the silica can be removed by a steam/air treatment in a fluidized bed reactor. A simplified flow sheet of the flame hydrolysis process is shown in Fig. 1. The size of primary particles and aggregates can be influenced by the flame temperature, the hydrogen to oxygen ratio, the SiCl<sub>4</sub> loading, and the residence time in the flame. Basic research on the flame hydrolysis process itself and on factors influencing the particle formation in flames were published in Refs 15–17.

### 2.1.5.2 Physicochemical Properties of Fumed Oxides

The physicochemical data of fumed oxides are published in a series of documents [18]. The surface area of the fumed oxide is mainly determined by the size of the primary particles. Surface areas range from 25 to 400 m<sup>2</sup> g<sup>-1</sup>. In the case of fumed silica products with specific surface areas less than 300 m<sup>2</sup> g<sup>-1</sup> the primary particles are dense and have no inner surface. Products with a specific surface area above 300 m<sup>2</sup> g<sup>-1</sup> show a certain amount of microporosity instead of further reduced primary particle size. The average particle diameter in the 300 m<sup>2</sup> g<sup>-1</sup> product is 7 nm. For comparison, a product with 50 m<sup>2</sup> g<sup>-1</sup> has primary particles with diameters of 40 nm. This relationship is shown in Figs 2 and 3. TiO<sub>2</sub> and ZrO<sub>2</sub> have a lower specific surface area when compared with SiO<sub>2</sub> of the same particle size because of their higher density. The structures of two Aerosil types with different particle sizes are shown in the TEM diffraction photographs in Figs 4 and 5. In the TEM photograph of the product with 300 m<sup>2</sup> g<sup>-1</sup> it can be seen that a certain number of primary particles of 5–10 nm are aggregated in irregularly shaped arrangements. The 50 m<sup>2</sup> g<sup>-1</sup> product consists mainly of isolated primary particles and only a very small number of aggregates. When freshly produced, Aerosil has a bulk density of about 15 g L<sup>-1</sup>. Because this is hard to handle, the product is compacted to 50–100 g L<sup>-1</sup> depending on the application. Al<sub>2</sub>O<sub>3</sub> (aluminum oxide C with 100 m<sup>2</sup> g<sup>-1</sup>, Degussa) is available with an apparent density of 80 g L<sup>-1</sup>.

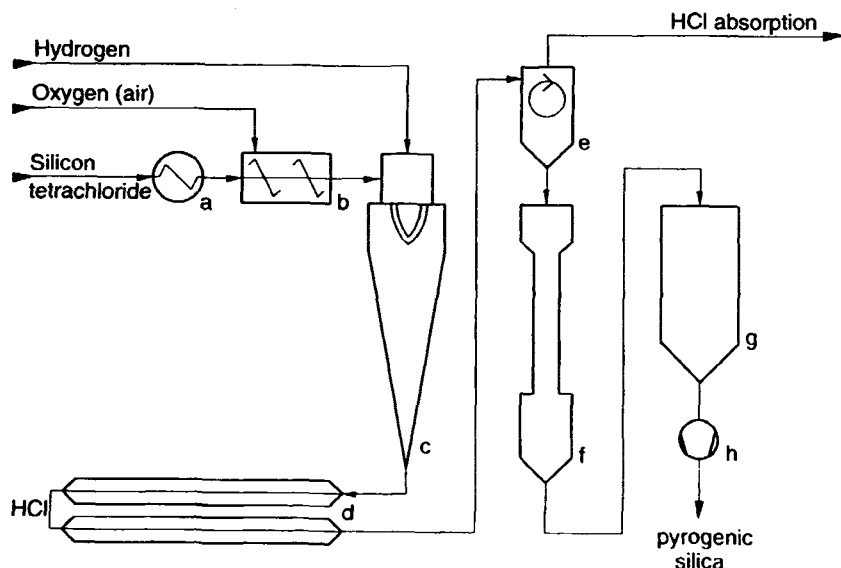


**Figure 1.** Flow sheet of a fumed silica plant: (a) vaporizer, (b) mixing chamber, (c) burner, (d) cooling section, (e) separation, (e) separation, (f) deacidification, (g) hopper, (h) compactor.

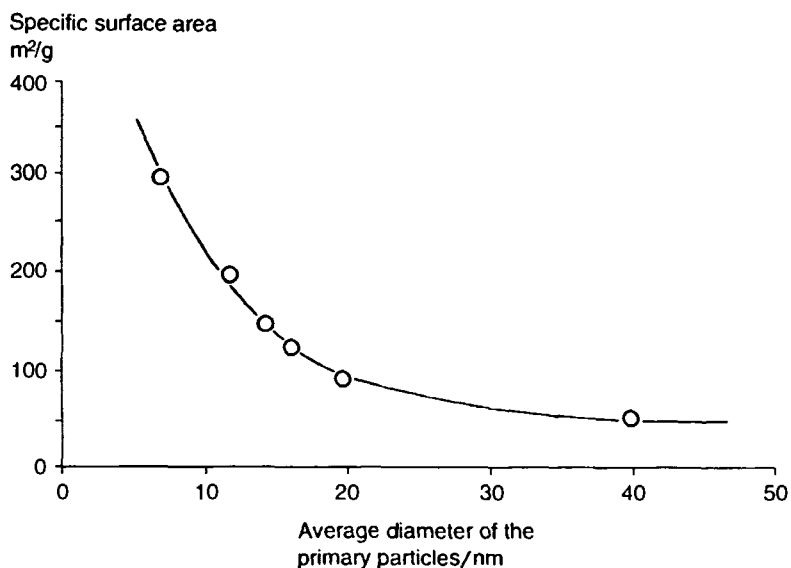


**Figure 2.** Relationship between primary particle size and specific surface area.

Fumed silica is always found to be amorphous, and therefore does not cause silicosis. The respective  $\text{Al}_2\text{O}_3$  is crystalline and consists of the thermodynamically metastable  $\delta$  form instead of the stable  $\alpha$  form. It can be transformed to the  $\alpha$ - $\text{Al}_2\text{O}_3$  phase by heating to  $1200^\circ\text{C}$ . This conversion is associated with a loss of surface area and an increase of hardness and abrasiveness. In the commercial  $\text{TiO}_2$  obtained by flame hydrolysis, the thermodynamically metastable modification anatase is the main phase, with about 30% rutile. The lattice transformation towards higher amounts of rutile becomes notable at temperatures above  $700^\circ\text{C}$ . It is also associated with a decrease of

specific surface area. The preference of a high temperature phase is also found in pyrogenic  $\text{ZrO}_2$ , that is obtained in the metastable tetragonal modification instead of the monoclinic room temperature phase. If the freshly produced  $\text{ZrO}_2$  is treated with hot moist air at about  $800^\circ\text{C}$ , in order to reduce the amount of adsorbed hydrochloric acid, a conversion towards higher amounts of the monoclinic phase takes place [19].

Another point concerning the suitability of fumed oxides for catalytic applications, that has to be taken into consideration, is their surface chemistry. Siloxane (Si-O-Si) and silanol groups (Si-OH) occur at the surface of the silica particles. The former are hydro-

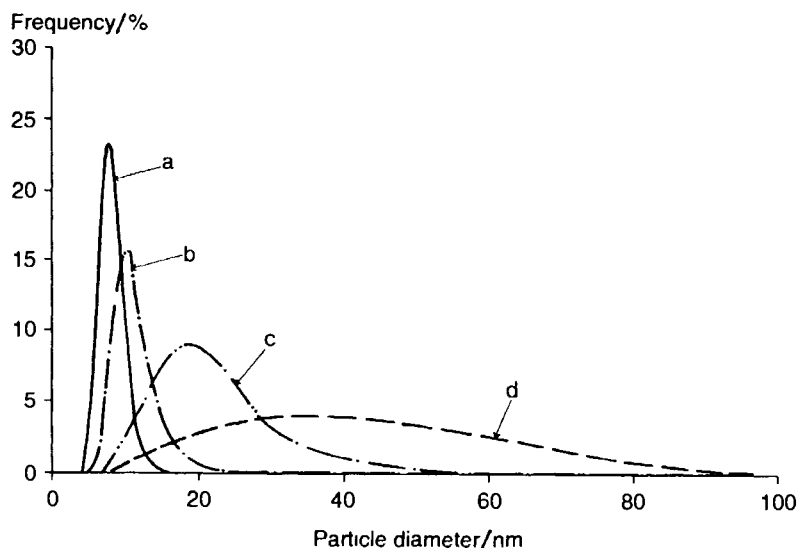


Figure 3. Particle size distribution in fumed silicas with different specific surface areas: (a)  $300 \text{ m}^2 \text{ g}^{-1}$ , (b)  $200 \text{ m}^2 \text{ g}^{-1}$ , (c)  $90 \text{ m}^2 \text{ g}^{-1}$ , (d)  $50 \text{ m}^2 \text{ g}^{-1}$ .

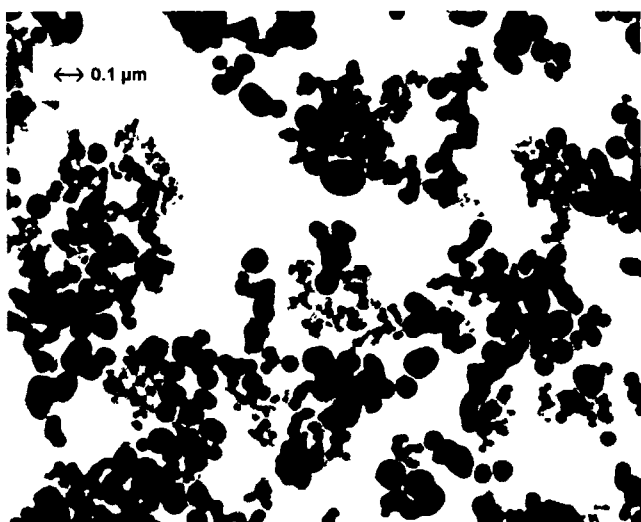


Figure 4. TEM photograph of a pyrogenic silica with an average particle size of  $\approx 40 \text{ nm}$  and a specific surface area of  $\approx 50 \text{ m}^2 \text{ g}^{-1}$ .

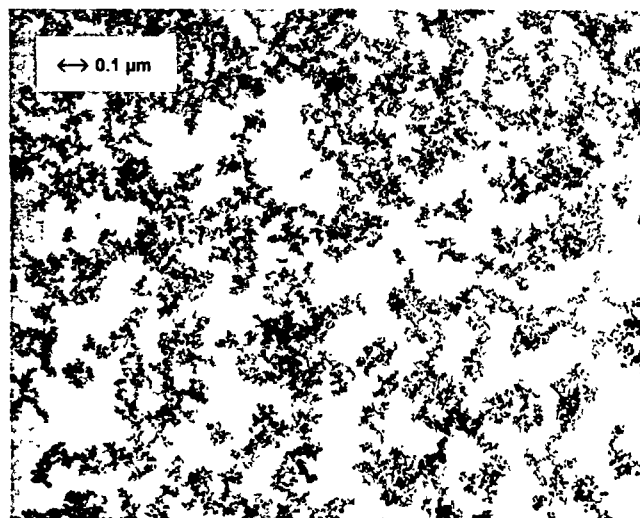


Figure 5. TEM photograph of a pyrogenic silica with an average particle size of  $\approx 7 \text{ nm}$  and a specific surface area  $\approx 300 \text{ m}^2 \text{ g}^{-1}$ .

phobic while the latter are hydrophilic and make the pyrogenic silica wettable. The density of silanol groups determined, for example, by reaction with lithium aluminum hydride, is between 2.0 and  $2.5 \text{ Si-OH nm}^{-2}$ . This is significantly lower than the values typically found for precipitated silica. The silanol groups are acidic, which corresponds to an isoelectric point at a pH value of 2. Immediately after production, pyrogenic silica shows mainly isolated silanol groups. In the course of time, adsorbed water reacts with strained siloxane groups and builds further silanol groups. By heating the silica to  $400^\circ\text{C}$  the reaction can be reversed. This can easily be followed by IR spectroscopy [13]. Pyrogenic  $\text{Al}_2\text{O}_3$  has basic hydroxy groups at its

surface which correspond to an isoelectric point at a pH value of 9. On complete removal of water, aluminum ions are located at the surface which are coordinated by only five oxygen atoms and therefore represent Lewis acid centers. They can add pyridine or again form hydroxy groups through the adsorption of water. The hydroxy groups at the surface of titania are basic or acidic, depending on the surrounding. An isoelectric point at a pH value of 6.5 has been reported [20]. The acidic sites accumulate ammonia and can be esterified with diazomethane. The basic sites can be detected by exchange reactions with certain anions [21].  $\text{ZrO}_2$  has acidic and basic sites at its surface as well, but is more basic than  $\text{TiO}_2$ . This corresponds to an iso-

electric point at pH 8.2. Compared with the pure oxides,  $\text{Al}_2\text{O}_3$ - $\text{SiO}_2$  mixed oxides are strong solid acids. Even stronger acids or superacids are sulphated  $\text{TiO}_2$  or  $\text{ZrO}_2$  (see Section A.3.2.3). Due to the above outlined manufacturing process that differs significantly from precipitation or sol-gel processes, the oxides so produced have very special properties, the most important of which have been discussed in this section. The outstanding properties that make pyrogenic oxides so interesting for catalysis are:

- high chemical purity;
- well defined, spherical primary particles;
- practically no internal surface;
- very low drying and ignition loss.

### 2.1.5.3 Preparation of Formed Supports

Formed supports are much more convenient for commercial-scale processes than powders, especially particles with diameters within the millimeter range are preferred. Unfortunately, fumed oxides are not easy to shape because of their extreme fineness. Several routes to prepare formed supports from pyrogenic powders have been developed. A very simple approach is the use of silica sol and alcohols as binders.  $\text{SiO}_2$ ,  $\text{Al}_2\text{O}_3$  and  $\text{TiO}_2$  have been treated in this way. The pyrogenic oxide is mixed with water, silica sol and glycerol, extruded, dried and calcined at  $550^\circ\text{C}$ . The resulting support has not lost much of its original surface area and has a pore volume of 60% which, in the case of silica, corresponds to  $0.3\text{ cm}^3\text{ g}^{-1}$  [22]. The high amount of silica introduced by the use of the silica sol can be a drawback in oxide systems other than silica. This can be avoided by using small amounts of decomposable organic or inorganic acids instead of silica sol as binding agents and small amounts of graphite as a formulation aid. The graphite and the acid can be removed by firing the support. The purity of the support is therefore only determined by the used pyrogenic oxide itself. For example, from pyrogenic  $\text{TiO}_2$  with a specific surface area of  $48\text{ m}^2\text{ g}^{-1}$ , supports with  $44\text{ m}^2\text{ g}^{-1}$  and  $0.3\text{ cm}^3\text{ g}^{-1}$  pore volume were produced [23]. If higher pore volumes and crushing strengths are required, the following process can be applied to the above-mentioned pure oxides as well as mixed oxides.

The oxides are mixed with kaolin, graphite, urea and additional water, until a well homogenized paste is obtained. The paste is dried at  $100^\circ\text{C}$ , optionally ground, and then formed by tableting or extruding. The produced pellets or extrudates are then calcined at  $800$ – $900^\circ\text{C}$  [24]. When fumed silica with  $200\text{ m}^2\text{ g}^{-1}$  is used, the resulting supports have a pore volume of  $1.2\text{ cm}^3\text{ g}^{-1}$  and a specific surface area of  $195\text{ m}^2\text{ g}^{-1}$ . If the support itself is used as a catalytically active component as in the case of  $\text{TiO}_2$ , the described route is not favorable,

**Table 2.** Typical physicochemical data of a  $\text{TiO}_2$  support.

BET surface area (raw oxide)	$55\text{ m}^2\text{ g}^{-1}$
Composition	99.5% $\text{TiO}_2$ (75% anatase, 25% rutile)
Diameter	4 mm
BET surface area	$48\text{ m}^2\text{ g}^{-1}$
Pore volume	$0.34\text{ cm}^3\text{ g}^{-1}$
Pore distribution	no pores below 2 nm, 90% between 2 and 30 nm
Hardness	44 N

because the binder remains on the support and affects the catalytic activity. For  $\text{TiO}_2$  it is therefore proposed to use cellulose derivatives (e.g. tylose) as binders and lactic acid as a plasticizer instead of kaolin and graphite. The amount of additives has to be carefully controlled; best results were achieved with 0.3% lactic acid and 1% tylose. Furthermore, a certain amount of water and a well adjusted pH are necessary [25]. Typical properties of so produced supports are listed in Table 2. Some large-scale processes use fixed-bed reactors several cubic meters in volume. In these applications a very high breaking strength is an important requirement for the used supports. Fumed silica pellets with the required increased breaking strength can be produced by using magnesium or aluminum stearate in addition to urea and methyl cellulose. Small amounts of stearate are sufficient for optimal results, therefore again a high purity of the supports is obtained [26]. The physicochemical data of support types made from fumed silica with different surface areas are listed in Table 3. Depending on the surface area and primary particle size of the fumed oxide used, it is possible to manufacture tablets with corresponding pore size distributions, as shown for various fumed silicas in Fig. 6. Oxides with high surface areas result in supports with small pore sizes and vice versa.

In general, it can be said that supports on the basis of fumed oxides are in many respects superior to those prepared from other oxides: the high chemical purity is a result of the flame hydrolysis process, in which volatile raw materials purified by rectification are used. Together with the unique particle structure, the high purity leads also to a well defined surface chemistry. The good mechanical properties and the high resistance against sintering have been described [25].

A different approach to make fumed oxides more useful as supports for active compounds is spray granulation. In this process a suspension of fumed oxide in water is fed to a spray drying device. The oxide content of the suspension controls, among other parameters, the size of the resulting particles. A grain size distribution in the submillimeter range is obtainable with this method. The pore size and the pore size distribution can be adjusted by selecting oxides with different particle size distribution and specific surface area, respec-

Property	BET surface area of raw oxide ( $\text{m}^2 \text{g}^{-1}$ )			
	50	130	200	300
Composition (% $\text{SiO}_2$ )	>99	>99	>99	>99
Diameter (mm)	5	6	6	6
BET surface area ( $\text{m}^2 \text{g}^{-1}$ )	45	110	160	230
Pore volume ( $\text{cm}^3 \text{g}^{-1}$ )	0.6	0.8	0.75	0.8
Pore distribution (nm)	no pores < 8, 90% 10–40	no pores < 7, 90% 10–40	no pores < 6, 90% 10–30	no pores < 4, 90% 7–25
Hardness (N)	125	60	60	80

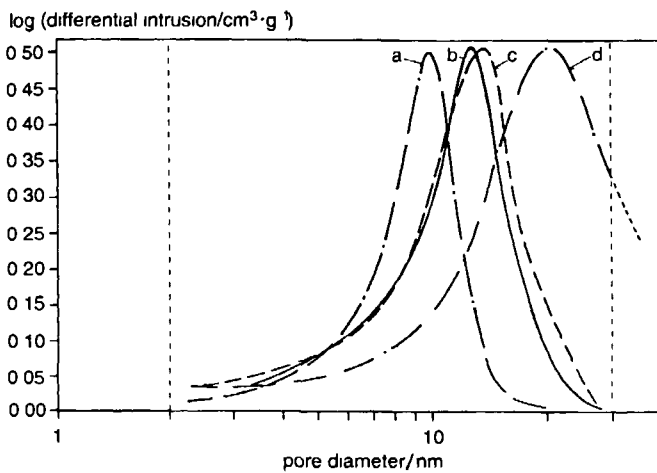


**Figure 6.** Influence of the surface area of fumed silica on the final pore size distribution after the forming process: (a)  $380 \text{ m}^2 \text{ g}^{-1}$ , (b)  $300 \text{ m}^2 \text{ g}^{-1}$ , (c)  $200 \text{ m}^2 \text{ g}^{-1}$ , (d)  $90 \text{ m}^2 \text{ g}^{-1}$ .

tively. Spray granulated supports are mainly needed for catalytic processes using fluidized bed reactors [27].

#### 2.1.5.4 Applications

Because of the unique physicochemical properties of fumed oxides they are attractive for catalytic investigations from several points of view. Pure fumed oxide powders have served as model substances in basic catalysis research. For a review with about a hundred references see Ref. 28. Pyrogenic  $\text{Al}_2\text{O}_3$  has been the subject of an entire series of studies. It serves as a support for catalytically active metals; among the investigated reactions are hydrogenations and polymerizations. The activity of the unloaded oxide has also been tested. The special surface characteristics of pyrogenic  $\text{SiO}_2$  are also of interest to numerous research groups. Emphasis has been laid on  $\text{Ni}/\text{SiO}_2$ ,  $\text{Ag}/\text{SiO}_2$  and  $\text{Pt}/\text{SiO}_2$  with many examples for applications. The oxide as such was also studied, especially with regard to adsorption problems. Interest in titanium oxide has been expanding during recent years, however, it has not yet found many commercial applications in catal-

ysis. A very promising research field is photocatalysis [29, 30].  $\text{TiO}_2$  has been shown to be able to oxidize various organic compounds, when irradiated with sunlight or UV radiation [31, 32]. The activity of pyrogenic  $\text{TiO}_2$  is found to be much higher than pigment grade  $\text{TiO}_2$ . The high photocatalytic activity is used in some environmental processes, for example in the cleaning of waste water from various hazardous chemicals. Other studies on  $\text{TiO}_2$  and especially pyrogenic  $\text{TiO}_2$  report the usefulness in the synthesis of phenol from benzene, nitrate from nitrite, or aldehydes from alcohols [33, 34]. The photoconducting effect of  $\text{TiO}_2$  has been studied in detail in conjunction with the photolysis of water [35–37]. The reaction takes place in a dispersion or colloidal solution of  $\text{TiO}_2$ , to which colloidal ruthenium and colloidal platinum oxide are added. The current generated by UV light in the  $\text{TiO}_2$  is conducted to a platinum layer in which water is split into hydrogen and hydroxy ions. The hydroxy ions are decomposed into oxygen and water at the ruthenium oxide sites. Another catalytic reaction of potential industrial and academic interest is the methanation of carbon dioxide.  $\text{Ru}/\text{RuO}_x$  supported on  $\text{TiO}_2$  catalyzes this reaction even at room temperature and ambient pressure [38]. In several patents, catalysts for the Fischer–Tropsch process using various metals on  $\text{TiO}_2$  are described [39]. Furthermore, the use of  $\text{TiO}_2$  in the ammoxidation of aromatics has been reported [40].

For commercial processes, formed supports are more useful. Compared with other supports, fumed oxide supports showed new catalytic effects [41]. Some intensively investigated applications for these supports are abstracted in the following.  $\text{SiO}_2$  pellets have been successfully introduced in a new generation of precious metal supports in vinylacetate monomer production [42]. This resulted in better selectivities and an up to 50% higher space–time yield compared with supports based on natural aluminosilicates. In alkene hydration fumed silica pellets serve as a support for phosphoric acid. In this case, an increased catalyst lifetime and a higher space–time yield were observed [43]. Pyrogenic  $\text{TiO}_2$  powder can be used as a starting material for the manufacture of monolithic catalysts [44] for the selective reduction of  $\text{NO}_x$  with ammonia.

## References

- 1 P Woditsch, A Westerhaus, *Ullmann's Encycl Ind Chem 5th ed* 1993, Vol A20, p 281
- 2 A Gurav, T Kodas, T Pluym, Y Xiong, *Aerosol Sci Technol* 1993, 19, 411–452
- 3 R Caillat, J P Cuer, J Elston, F Juillet, R Pointud, M Prettre, S Teichner, *Bull Soc Chim France* 1959, 152–156
- 4 F Juillet, F Lecomte, H Mozzanega, S J Teichner, A Thevenet, P Vergnon, *Farad Symp Chem Soc* 1973, 7, 57–62
- 5 P G Vergnon, H B Landoust, *Ind Eng Prod Res Dev* 1980, 19, 147–151
- 6 D Bianchi, J L Bernard, M Camelot, R Benali-Chaoui, S J Teichner, *Bull Soc Chim France* 1980, 7–8, 275–280
- 7 N S Subramanian, Ph D Thesis, University of New Hampshire, 1975
- 8 J L Gass, S J Teichner, *Bull Soc Chim France* 1972, 6, 2209–2213
- 9 J L Gass, F Juillet, S J Teichner, *Bull Soc Chim France* 1973, 2, 429–435
- 10 H Klopfer German Patent 762 723 1942 (Degussa)
- 11 A T Liu, P Kleinschmit, *British Ceramic Proc* 1986, 38, 1–10
- 12 A T Liu, P Kleinschmit German Patent 3 611 449 1986 (Degussa)
- 13 M Ettlinger *Ullmann's Encycl Ind Chem 5th ed* 1993, Vol A23, pp 635–642
- 14 H Ferch, H Fratzscher, *Kautschuk Gummi, Kunststoffe* 1967, 20, 578, Degussa AG, Frankfurt am Main, *Technical Bulletin Pigments*, 5th ed, 1993, p 11
- 15 J D Landgrebe, S E Pratsinis, *J Colloid Interface Sci* 1990, 139, 63–86
- 16 S E Pratsinis, *J Colloid Interface Sci* 1988, 2, 416–427
- 17 G D Ulrich, *Chem Eng News* 1984, 62, 22–29
- 18 Degussa AG, Frankfurt am Main, *Technical Bulletin Pigments*, 6th ed, 1993, p 56
- 19 W Hartmann, A T Liu, D Peukert, P Kleinschmit, *Mater Sci Eng* 1989, A109, 243–246
- 20 J Lyklema, *Chem Ind* 1987, 21, 741
- 21 H-P Boehm, *Chem-Ing Techn* 1974, 46, 716
- 22 M Ettlinger, H Ferch, D Koth, E Simon German Patent 3 132 674 1983 (Degussa)
- 23 M Ettlinger, H Ferch, D Koth, E Simon German Patent 3 217 751 1983 (Degussa)
- 24 B Despeyroux, K Deller, H Krause, *Chemische Industrie* 1993, 10, 48–49, K Deller, R Klingel, H Krause German Patent 3 803 894 1988 (Degussa), K Deller, R Klingel H Krause German Patent 3 803 895 1988 (Degussa), K Deller, R Klingel, H Krause German Patent 3 803 897 1988 (Degussa), K Deller, M Ettlinger, R Klingel, H Krause German Patent 3 803 898 1988 (Degussa), K Deller R Klingel, H Krause, K-P Bauer German Patent 3 803 899 1988 (Degussa)
- 25 M Bankmann, R Brand, B H Engler, J Ohmer, *Catal Today* 1992, 14, 225–242, R Brand, B Engler, M Foerster, W Hartmann, P Kleinschmit, E Koberstein, J Ohmer, R Schwarz German Patent 4 012 479 1991 (Degussa)
- 26 K Deller, M Foerster, H Krause German Patent 3 912 504 1989 (Degussa)
- 27 H Biegler, G Kallrath German Patent 1 209 108 1966 (Degussa)
- 28 D Koth, H Ferch, *Chem Ing Techn* 1980, 52, 628, Degussa AG, Frankfurt am Main, *Technical Bulletin Pigments*, 2nd ed 1991, p 72
- 29 M Formenti, F Juillet, P Meraudeau, S J Teichner, P Vergnon in *Aerosols and Atmospheric Chemistry* (Ed G M Hidy) Academic Press, New York, 1972, p 45
- 30 M Formenti, S J Teichner, *Catalysis* 1978, 87–108
- 31 Z Wang, C Kutal, *Chemosphere* 1995, 30, 1125–36
- 32 J Papp, S Soled, K Dwight, A Wold, *Chem Mater* 1994, 6, 496–500
- 33 H P Boehm, *Angew Chem* 1966, 78, 617
- 34 M A Malati, N J Seager, *J Oil Chem Assoc* 1981, 64, 231
- 35 M Graetzel, *Acc Chem Res* 1981, 14, 376
- 36 V H Houlding, M Graetzel, *J Am Chem Soc* 1983, 105, 5695–5696
- 37 M Graetzel, *Dechema-Monographien*, 1987, 106, 189–204
- 38 K R Thampi, J Kiwi, M Graetzel, *Nature* 1987, 327, 506–508
- 39 R A Fiato, S Misco US Patent 4 749 677 1988 (Exxon Res & Eng Co), C C Chersich, R A Fiato, I E Wachs US Patent 4 559 365 1985 (Exxon Res & Eng Co) German Patent 2 712 909 1977, US Patent 4 042 614 1977
- 40 H Beschke, H Friedrich, J Helios German Patent 3 107 755 1982 (Degussa)
- 41 M Bankmann, B Despreyroux, H Krause, J Ohmer R Brand, *Stud Surf Sci Catal* 1993, 75, 1781–1784
- 42 F Wunder, G Roscher, K Eichler German Patent 3 803 900 1989 (Hoechst) R Abel K-F Worner European Patent 634 214 1995 (Hoechst)
- 43 G J Haining P Lusman A D Melville European Patent 578 441 1994 (BP Chemicals)
- 44 H Hellebrand, N Landgraf H Schmelz German Patent 3 938 155 1990 (Siemens), R Brand, H B Engler, W Honnen, P Kleine-Moellhoff, E Koberstein German Patent 3 740 289 1989 (Degussa)

## 2.1.6 Solid-State Reactions

P G MENON AND B DELMON

## 2.1.6.1 Why Solid-State Reactions?

The methods most commonly used for preparing catalysts are precipitation (Section A 2 1 3) and impregnation (Section A 2 2 1 1). In both of them, the catalytically active material is transferred from a liquid phase, usually an aqueous solution, to a solid. By contrast, other catalysts are obtained from solid precursors. Solid state reactions, namely solid-to-solid reactions in which both the starting material (the catalyst precursor) and the catalyst are solids, offer convenient methods to prepare several industrial catalysts, especially those containing two or more metallic elements or their oxides. The reason of the conspicuous efficiency of these methods to prepare phases containing two or several metallic elements is due to special features of solid-state reactions, compared to liquid-to-solid or gas-to-solid reactions. This section briefly outlines these peculiarities and presents the most frequent types of solid-state processes used in preparing catalysts.

**Table 1.** Some important mixed-oxide catalysts used in industry.

Catalyst	Active phases	Industrial processes
Copper chromite	CuCr <sub>2</sub> O <sub>4</sub> , CuO	CO conversion (low temp.), oxidations, hydrogenation, hydrogenation–hydrogenolysis
Zinc chromite	ZnCr <sub>2</sub> O <sub>4</sub> , ZnO	methanol synthesis (high pressure)
Copper/zinc chromite	Cu <sub>x</sub> Zn <sub>1-x</sub> Cr <sub>2</sub> O <sub>4</sub> , CuO	methanol synthesis (low pressure)
Iron molybdate	Fe(MoO <sub>4</sub> ) <sub>3</sub> , MoO <sub>3</sub>	methanol to formaldehyde
Iron oxide/potassium oxide	KFeO <sub>2</sub> , K <sub>2</sub> Fe <sub>22</sub> O <sub>34</sub>	ethylbenzene to styrene
Bismuth molybdate + promoter oxides	mixed molybdates	propene to acrolein propene to acrylonitrile oxidative dehydrogenation
Zinc ferrite	ZnFe <sub>2</sub> O <sub>4</sub>	Benzene/butene to maleic anhydride
Vanadia–molybdena	V <sub>2</sub> O <sub>5</sub> –MoO <sub>3</sub> solid solution	Dehydrogenation of light alkanes
Chromia alumina	Cr <sub>x</sub> Al <sub>2-x</sub> O <sub>3</sub>	catalytic combustion
Mixed oxides	perovskite type	catalytic combustion (support)
Barium hexaaluminate	BaAl <sub>12</sub> O <sub>19</sub>	

The necessity to have more than one component in a catalyst arises from many needs: those linked to the polyfunctionality often required for the different steps in a reaction, the need to enhance the rate of some reaction steps, inhibition of unwanted side reactions, provision of adequate thermal stability, to take advantage of observed synergetic effects. From a fundamental point of view, the presence of several metal elements in a common structure permits the adjustment of the local electronic properties, imposes well defined coordinations, limits the extent of oxidation–reduction phenomena, and may stabilize the whole catalyst by retarding sintering. Mixed oxide catalysts are used as such, or as precursors of active catalysts, for a whole range of important industrial processes, a representative selection of which is given in Table 1.

Preparation of atomically homogeneous multicomponent catalysts by conventional methods, however, is often difficult due to three main reasons:

- (i) deposition of active precursors either as a precipitate or onto a support often gives separate moieties, instead of a single phase of uniform chemical composition;
- (ii) segregation of the active components can occur during the thermal treatment of the catalyst precursor;
- (iii) the support can selectively interact with one of the active components at one or the other stage of the formation of the mixed oxide.

A good example of the latter case is the reaction of iron with silica in silica-supported iron molybdate, a fact which made impossible the use of silica as a support in the case of catalysts used for the oxidation of methanol to formaldehyde. Some of the methods to overcome these difficulties in catalyst preparation are the subject of this section.

This section deals with a small group of solid-to-solid reactions which are relevant to the preparation of certain mixed-oxide catalysts.

In principle, liquids are ideal precursors when atomically homogeneous mixtures are desired. The reason is that the ordinary liquid state has no long-range structure, and hence permits a statistical repartition of its contents at a molecular scale. However, segregation almost invariably occurs when liquids are reacted to give solids (e.g. by precipitation, when one element usually precipitates before the other component or components). In the use of solid-state reactions, the guiding principle is that, unlike in a liquid, the diffusion of atoms or ions in a solid is very difficult and it is practically frozen at relatively low temperatures. Whenever a solid of complex composition cannot be obtained by a direct reaction, an indirect method can be tried. This is possible if a solid can be obtained of a composition which differs from the desired solid (e.g. a hydroxide, salts of organic acids, etc.), but which contains the metallic elements in the proportion required by the catalyst. The key reaction is then the solid-state transformation of this hydroxide or salt to the desired oxide. Keeping the material in the solid state throughout the transformation permits powerful control (Fig. 1) which prevents all unwanted atomic restructuring in the bulk during catalyst preparation. In practice, two goals can be achieved here:

- (i) As mentioned above, when specific compositions can be prepared with homogeneity at the molecular level, but in a thermally unstable state (as salts, hydroxides, complexes, or vitreous compounds), these can be decomposed into the ultimately desired mixed-oxide catalyst;
- (ii) Solid-state chemistry offers an additional advantage in that specific structures and even textures (as for the layers of phyllosilicate in pillared clays (Section A.2.3.6), can be preserved intact throughout these solid-state transformations.

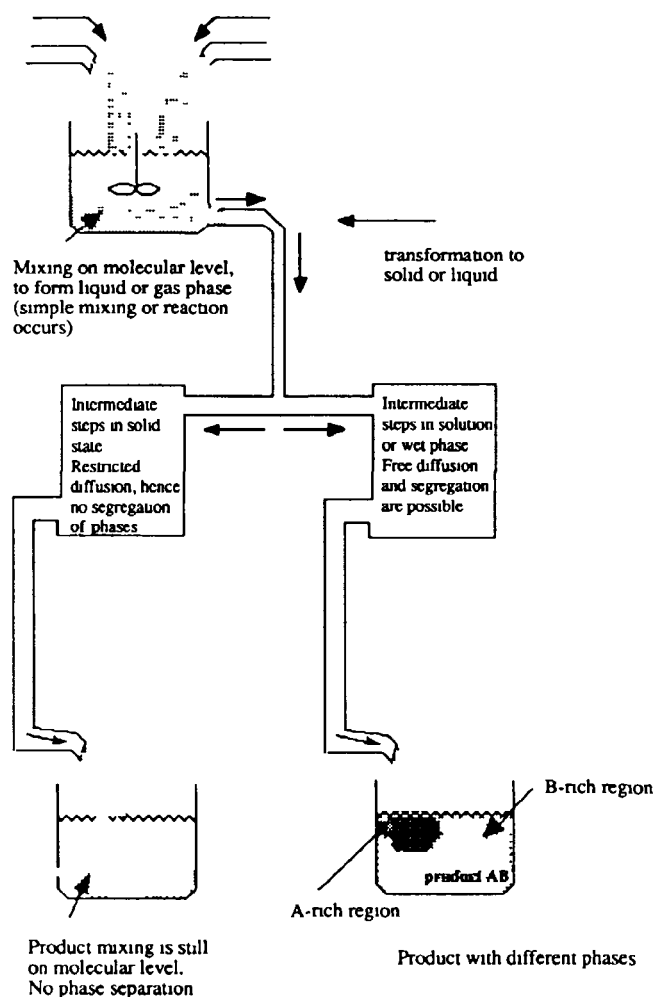


**Figure 1.** Schematic representation of the vital role of solid-state reactions in preparing single-phase catalysts.

Even more important, for the catalysts considered here, control of the transformation conditions of the precursor to the final catalyst allows, to a certain extent, the preparation of highly dispersed oxides with well defined porosity. This is the main theme of this section. The preparative methods described here are typical cases, selected to highlight how goals (i) and (ii) are achieved in practice in various procedures.

### A Some General Concepts and Parameters in Solid-State Reactions

When multicomponent solid systems are used to prepare a catalyst, homogenization of the precursors (mixing at the molecular level) is extremely important. The activity of the finished catalyst should not differ in the different parts of a catalyst charge, or from batch to batch of it. Two fundamental aspects of solid-state reactions involved in the preparation of catalysts are nucleation and the growth from solution of the nuclei or elementary particles into distinct solid phases in the

surrounding liquid medium. Both of these are involved in the preparation of many catalysts and supports as well as in the deposition or dispersion of an active catalyst component on the support surface. The problem is that nucleation is, by essence, a process which favors segregation, thus it goes against the goal of preserving homogeneity at a molecular or atomic scale. Supersaturation of the medium essentially controls both nucleation and growth processes, thus determining ultimately the size, structure, and phases of elementary catalyst particles. The only important fact to remember is that the relative contribution of surface energy in the whole energy context is considerable in small particles of any phase in contact with vacuum or any other phase (gas, liquid, solid) in comparison to that of large particles or flat surfaces (this is expressed by the Gibbs–Thomson law). Nevertheless, nucleation can take place because of statistical fluctuations, whose efficiency in triggering nucleation increases dramatically in a narrow range of supersaturation. The kinetics of nucleation are extremely important when the synthesis of highly dispersed materials is considered. A detailed discussion of these aspects and the relevant literature are given in the reviews by Marcilly [1] and Marcilly and Franck [2]. The importance of nucleation and growth phenomena in solid-state reactions in catalyst preparation will be discussed briefly in the next section. Their vital role and the different ways to control them during the preparation of supported catalysts is discussed in Sections A.2.2.1.5 and A.2.2.1.6. General surveys of solid-state reactions involved in catalyst preparation or production can be seen in Courty et al. [3], Courty and Marcilly [4, 5], and Delmon and de Keyser [6]. Several aspects of this subject are also covered and updated in the International Symposia on Scientific Bases for the Preparation of Heterogeneous Catalysts, held in 1975, 1978, and then every 4 years at Louvain-la-Neuve, Belgium [7–12].

The thermodynamics of formation and transformation of a solid phase into another are characterized by two aspects, both of them explaining the difficulty to produce solids of homogeneous composition. The more important of these is nucleation. The other is the tendency of certain components of the solid to diffuse to, or away from, surfaces. These aspects, however, cannot be considered in isolation. Chemical reactions involve the breaking of bonds and formation of new ones. This involves kinetically limited processes. In many cases, diffusion brings about additional kinetic limitations. The final result is the combination of the effects of all these processes.

Nucleation in solid-state reactions essentially obeys laws similar to those ruling the formation of solids from liquid or gases. The only difference is the enhanced role of diffusion limitations. The simpler case of nucleation from liquids will be sufficient for explaining the prob-



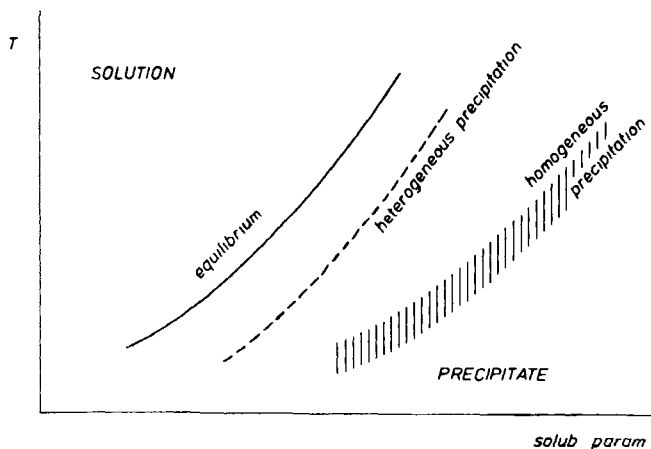


Figure 2. Schematic representation of the precipitation conditions for a given compound.

lems encountered in the formation of homogeneous solids in all cases.

Figure 2 is a kind of phase diagram with two intensive parameters: here they are the temperature  $T$  and any parameter (indicated as *solub. param.*) on which the solubility or dissociation constant depends. For example this could be the pH or the concentration of a reactant or a precipitating agent. It is also possible to use as coordinates two of these *solub. param.* parameters, holding the temperature constant. This diagram indicates the limits of concentration of a given compound or of a third component (or temperature) for which either a liquid solution or a solution containing a precipitated solid is observed. The line label equilibrium corresponds to the exact equilibrium curve separating the monophasic domain (upper left) from the biphasic domain (lower right). The special kinetics of nucleation ensure that, as explained above, the new phase is not formed for a small supersaturation unless a patch of surface of that phase is already formed; in that case, deposition can take place. In the absence of any solid surface, precipitation will only occur in supersaturation conditions represented by the curve "homogeneous precipitation". In truth this is not a curve, but a band, as actual deposition will depend on the rate at which the *solub. param.* changes. The upper left hand border of this band corresponds to so-called critical nucleation conditions, namely those below which no nucleation occurs. The dotted curve represents the conditions where precipitation can occur when a foreign surface is present, i.e. heterogeneous precipitation. The fact that this curve lies at an intermediary position is explained by the fact that the surface energy necessary for forming the precipitate is diminished in comparison to homogeneous precipitation, but not zero as in the presence of a flat surface of the precipitating compound, i.e. at equilibrium.

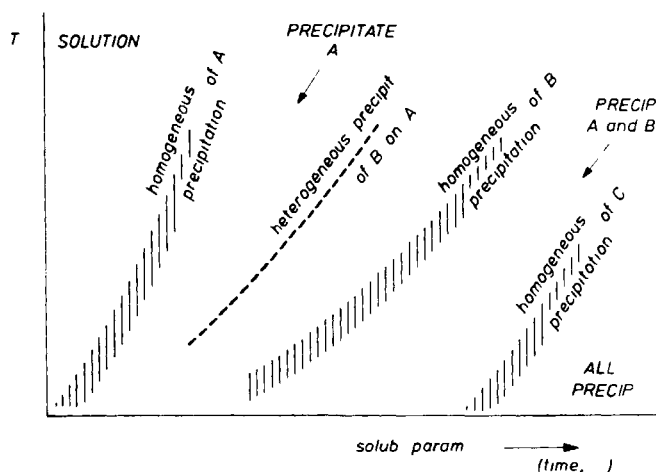
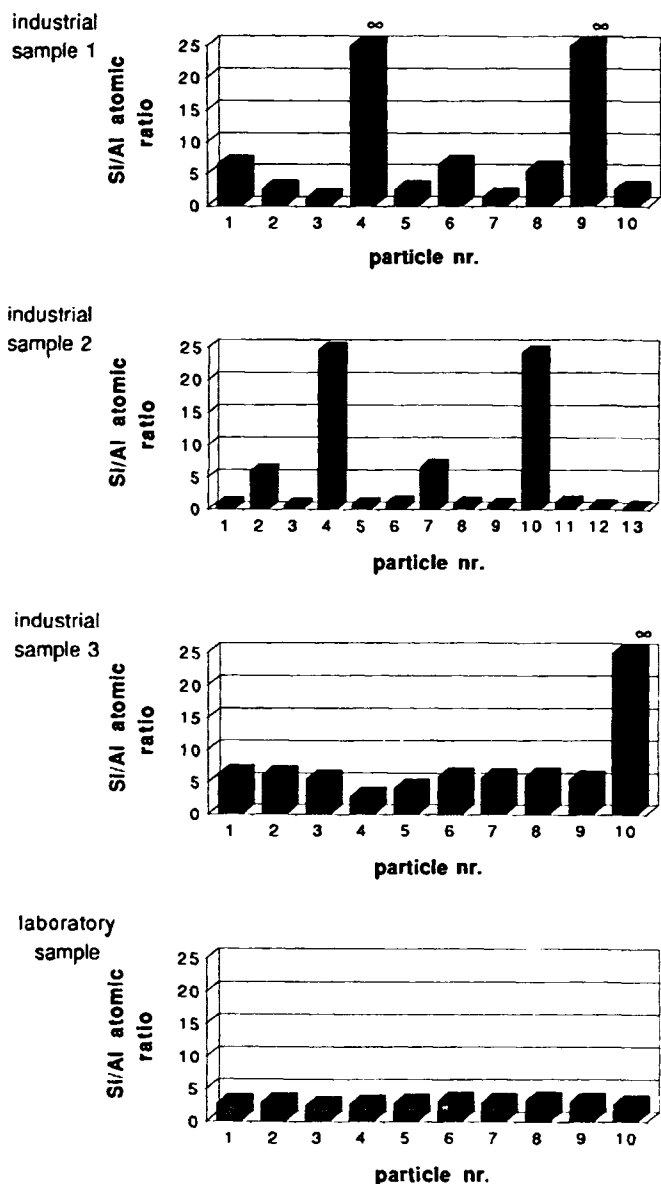


Figure 3. Schematic representation of precipitation from a solution containing the compounds A, B, and C.

Let us now consider a solution containing more than one compound. There will be as many curves of equilibrium, heterogeneous precipitation, and homogeneous precipitation as there are compounds. Figure 3 represents homogeneous precipitation for components A, B and C – a similar figure would represent the situation for the other curves of Fig. 2. The consequence is that the various compounds in a solution precipitate sequentially, namely bring about a segregation and create a solid of heterogeneous composition when the *solub. param.* changes (e.g. with time, in the direction of the arrow in Fig. 3). This can be very easily seen in coprecipitated silica–alumina, where pure silica is very frequently observed and considerable fluctuations of the Si:Al ratio by factors of 2 to  $\infty$  are measured over a distance of several tens of nanometers for the best, and several micrometers for most samples [13,14]. Such measurements can be made by analytical microscopy, for example (Fig. 4). This shows that most available silica–aluminas are by no means homogeneous at the atomic scale.

It is possible to increase the homogeneity by taking advantage of the difference in the form of the kinetic laws corresponding to nucleation, on the one hand, and growth of precipitated crystallites, on the other hand. The basis for such attempts is represented schematically in Fig. 5 [15], corresponding to one given compound. On the right of the figure, the rate of nucleation will be very high in comparison to growth, and very tiny particles will be obtained. The situation represented on the left corresponds to large particles and even, below the critical limit for nucleation, to Ostwald ripening. At very high supersaturations of all compounds present in a solution, finely interdispersed particles will be formed. But this will not produce atomically homogeneous solids. Extremely rapid mix-



**Figure 4.** Inhomogeneity of silica-aluminas prepared by various methods. A series of 17 commercial samples of silica-aluminas from seven different producers was submitted to microanalysis. All of them showed considerable fluctuations of composition at the scale of several tens of nanometers to several micrometers. These samples were prepared by coprecipitation or by the sol-gel method. It is not known whether some of these samples were prepared from alkoxides. Smaller but significant fluctuations at the micrometer scale were also observed for two laboratory samples prepared from alkoxides. The samples were dispersed in water with an ultrasonic vibrator. A drop of the resulting suspension was deposited on a thin carbon film supported on a standard copper grid. After drying, the samples were observed and analyzed by transmission electron microscopy (TEM) on a JEOL-JEM 100C TEMSCAN equipped with a KEVEX energy dispersive spectrometer for electron probe microanalysis (EPMA). The accelerating potential used was 100 kV.

First observed was the general aspect of the sample, looking at the whole grid. Then, different points were analyzed (2-3) of various particles (from 10 to 25). The diameter of the static spot was  $0.2 \mu\text{m}$ . The duration of each microanalysis (accumulation) varied between 60 and 240 s [13].

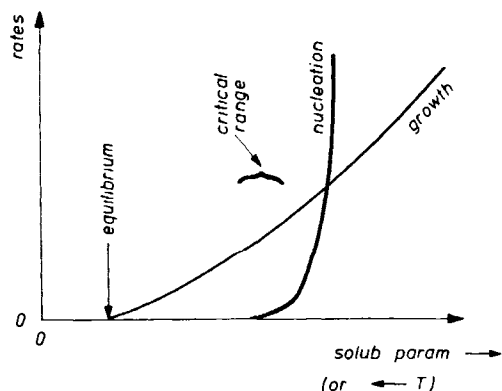


**Figure 5.** Qualitative comparison of the dependency of the rates of nucleation and growth of precipitate particle as a function of the solubility parameter (increasing from left to right) or  $T$  (opposite direction).

ing can produce such finely interdispersed phases. Rapid cooling is generally unsuccessful, because diffusion in the liquid phase will considerably perturb the processes leading to nucleation.

When such strategies are used to produce approximately homogeneous solids, the other phenomenon mentioned above can occur, namely *heterogeneous precipitation* of one compound on the surface of the already formed precipitate of another phase. This is shown in Fig. 3, for the precipitation of compound B after A has already precipitated. This has given rise to severe misinterpretations of physico-chemical characterization of precipitated solids, especially when surface-sensitive techniques such as X-ray photoelectron spectroscopy (XPS) were used.

As indicated above, elementary thermodynamic considerations show that the creation of a surface is accompanied by a positive free-energy change. This leads to another phenomenon, one which takes place inside an already formed mixed oxide. In order to minimize the positive free-energy change, the solid component with the lowest free energy tends to migrate from the bulk to the surface [16, 17]. Since the migration of a constituent of a solid from its interior to its surface usually involves an activation energy barrier to be overcome, such a process necessarily requires a higher temperature. As a rule of thumb, the Tammann temperature (ca. half the melting temperature) is generally believed to be sufficient to make the atoms or ions in the bulk sufficiently mobile for bulk-to-surface migrations, while the Hüttig temperature (ca. one-third the melting temperature) is enough to make the species, which are already on the surface, sufficiently mobile to undergo agglomeration or sintering. Since working temperatures in catalytic processes often exceed the Hüttig temperatures of metals or oxides used as catalysts, one objective of catalyst preparation is to anchor the active species on to the catalyst/support and thus retard/prevent their free motion or migration under the

process conditions. This is why homogeneous compound oxides may be useful for stabilizing the coordination of an oxide element and maintaining dispersion.

### B Section Objective

The previous part of this section makes clear that, unless a method is found to directly prepare a catalytic phase (usually an oxide) containing all the wanted metallic elements, and in the required proportions, some more indirect method should be selected. In general, however, direct preparation from the gas or liquid phase will be impossible for the reasons given above. It becomes necessary to resort to a two-step or multiple-step approach using at least one solid precursor.

Several cases need to be distinguished when an atomically homogeneous multielement catalyst is required:

- (i) Direct preparation by various sorts of reactions (e.g. precipitation). There are very few examples. In practice, this is only possible if an anion, e.g. a molybdate, reacts with a cation to produce the precipitate. The stoichiometry is dictated by the chemistry of the reaction and has little flexibility.
- (ii) A two-step process, through preparation of another type of homogeneous solid of exactly the same composition (e.g. carbonate, hydroxide, oxalate or other precursors, for making finally, in a second step, an oxide) and solid-state reaction of this precursor.
- (iii) Preparation of a solid approximately homogeneous followed by solid-state transformation, hoping that a higher homogeneity will be achieved during this second step.

The first category is the subject of Section A.2.1.4. Here, attention is given to the two other categories. Category (ii) corresponds to two different cases, those where the precursor is crystalline, and those where it is amorphous. However, the following discussion is organised according to the technique used, without distinguishing between (ii) and (iii) or whether it is crystalline or not. In each case comments are made on the potential of the technique to produce atomically homogeneous solid precursors.

The details concerning the transformation of the precursors to the final catalysts are mentioned in each case. However, a general comment has to be made here which is that the strategy consisting of starting from a homogeneous solid precursor and transforming it to the desired catalyst is only successful if diffusions in the solid state potentially leading to segregation are made difficult. This requires that only precursors decomposing to the final solid at low temperature, below the Tammann temperatures, be used. On the other hand, for reasons which cannot be presented here in detail, it

is advantageous that the solid precursor decomposes with production of large quantities of gases. A coupling between the solid-state transformation and the formation of pores is necessary and the formation of pores is obviously promoted by the evolution of gases. Coupling effects in catalyst preparation are discussed in several articles [18, 19].

In practice, hydroxides, carbonates, hydroxycarbonates, nitrates, and salts of organic acids (oxalates, formates, citrates, etc.) satisfy both requirements. But there are potentially many other possible compounds; some examples are given.

### 2.1.6.2 Description of Preparative Methods

In very rare cases catalysts can be prepared by dry methods, namely reactions in the solid state. However, the most commonly used methods for preparation of mixed oxide catalysts start from a liquid (Fig. 6). Since complete mixing at the molecular level is possible in solution, a solution of all the concerned salts is often taken as the common starting material. One can essentially distinguish two steps in the procedure: the preparation of a homogeneous solid precursor and the careful decomposition of this precursor to the oxide. For the first step, it is crucial to avoid the segregation of the oxide species into separate solid phases. This is usually achieved by:

- (i) physical methods such as evaporation to dryness, drying by vaporization, freeze drying, and crystallization – for the reasons explained above, the operation should be extremely rapid;
- (ii) a physico-chemical method like some gelation methods;
- (iii) chemical methods such as precipitation, coprecipitation, oil-drop, oil-up, and complexation. Oil-drop and oil-up involve processes pertaining to categories (ii) and (iii) above.

### A Dry Methods

One common method to prepare mixed-oxide catalysts is to grind or ball-mill them together, either dry or in a wet slurry; this is followed by calcination to temperatures of 900–1300 K. The operation may be repeated several times. Catalysts for the styrene process are generally prepared in this way from KOH and oxides of Fe and Cr and other (proprietary) promoter components. The solid–solid reaction during calcination can be accelerated by priming or catalyzing by a little of the product premixed with the reactant oxides. Ammonia synthesis catalysts which are prepared by mixing the components in the molten state does not pertain to this section, strictly speaking. A fluid energy mill, operated with steam injection at 670–970 K and 5–

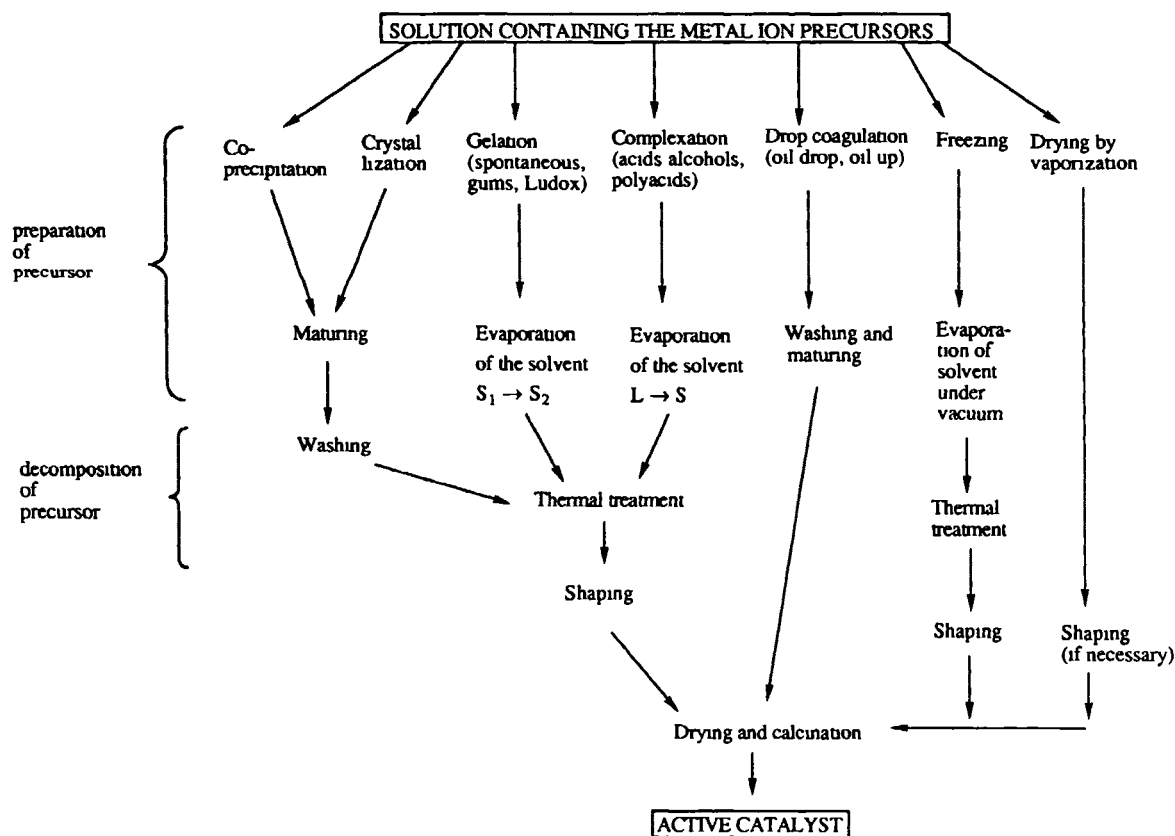


Figure 6. General scheme of various methods for the preparation of unsupported catalysts (from Ref 6)

15 bar steam pressure, is applied in some cases. Some other techniques, used only rarely, are dry chemical oxidation of alloys, and electrolytic deposition.

The calcination step can sometimes have a more subtle importance than is generally realized. For instance, at a calcination temperature of 870 K, a promoter such as Li can be mixed to modify a catalyst such as  $\text{TiO}_2$ , whereas at 1200–1300 K it can be incorporated into the lattice structure of  $\text{TiO}_2$ . For the former, optimum performance in the oxidative coupling of methane (OCM) is shown at 17 wt%  $\text{Li}_2\text{O}$  loading and its catalytic activity for OCM dropped by a factor of five after 2 days on stream [20, 21]. For the catalyst calcined at 1200–1300 K, the optimal  $\text{Li}_2\text{O}$  loading was only 1–2 wt%, it is active for OCM at higher temperatures and its stability over several days was much better [22].

In general, the methods described in this subsection give solids with a low surface area.

## B Wet Methods

### a Coprecipitation

The most common method for mixed-oxide catalyst preparation is crystallization or precipitation or coprecipitation in solution of a precursor form (hydroxide,

oxide, insoluble salt) of the catalyst. Other specific steps, for example either addition of an extra component or its removal by partial extraction, may sometimes be necessary to adjust the final catalyst composition and ensure homogeneity.

One of the most studied cases, and also the most successful, was that of hydroxycarbonate for preparing catalysts containing copper and zinc or chromium with additional elements (e.g. Co or Al). The reason for these studies was the practical importance of catalysts used for making synthesis gas and methanol. Table 2 [5], which gives the composition of various precursors with their structure, suggests the mixed oxides which could be formed by decomposition. Additional data can be found elsewhere [5, 23–26].

As discussed earlier, precipitation (or simple crystallization) involves two main steps, nucleation and growth. At the nucleation stage, the first minute crystals of the solid phase are formed, these have a high specific surface area and high surface energy, and hence are unstable. Below a certain critical nuclei size, the free energy of formation of the solid phase is less than its surface energy and the new phase is thermodynamically unstable. Above this critical size, the solid particles can grow. According to the conditions, this growth step is mainly controlled by interface or

**Table 2.** Hydroxycarbonate precursors for Cu/Zn/Cr catalysts.

Phase	Formula
Hydrotalcite-type phase	$M_6^{2+}M_2^{3+}(\text{OH})_6\text{CO}_3 \cdot 4\text{H}_2\text{O}$ $M^{2+} = \text{Cu}^{2+}, \text{Co}^{2+}, \text{Zn}^{2+}, \text{Mg}^{2+}$ $M^{3+} = \text{Al}^{3+}, \text{Cr}^{3+}, \text{Fe}^{3+}$
Malachite-type phase (rosasite)	$\text{Cu}_{2-x}^{2+}\text{Zn}_x^{2+}(\text{OH})_2\text{CO}_3$
Copper-zinc hydroxycarbonate (aurichalcite)	$\text{Cu}_{5-x}^{2+}\text{Zn}_x^{2+}(\text{OH})_6(\text{CO}_3)_2$

diffusion phenomena. The first case generally corresponds to the formation of complicated solid structures. The second is more common in the precipitation processes used in catalyst preparation. An overview is given in references given previously [1, 2, 15]. An excellent detailed treatment of nucleation and growth phenomena can be cited [27]. Only more general statements or rules of thumb can be given here.

For nucleation:

- (i) the higher the supersaturation, the higher will be the nucleation rate;
- (ii) any interface may play the role of a heterogeneous nucleus by lowering the surface free-energy of the new phase, and thus increase the rate of nucleation;
- (iii) in general, higher temperatures lower the nucleation rate by increasing the critical size of the nuclei – the upper left boundary of the homogeneous nucleation band reflects this trend.

All this has been represented schematically in Fig. 2.

For growth:

- (i) the higher the supersaturation the higher will be the growth rate, but it is rapidly limited by diffusion processes;
- (ii) since an increase of temperature enhances the diffusion rates, the higher the temperature, the higher will be the growth rate of the new phase.

Combining the above guidelines, and considering Fig. 5, some general rules for obtaining a fine precipitate can be formulated:

- (i) A vigorous stirring of the solution while adding the precipitant is beneficial in two ways: first, each elementary volume of solution reaches rapidly the highest degree of supersaturation; second, it comes into contact several times with the agitator and the walls of the vessel, thereby promoting heterogeneous nucleation also.
- (ii) A rapid addition of the precipitating agent ensures a rapid reaching of the highest degree of supersaturation in the whole volume of the solution,

hence a maximum nucleation rate is obtained. For the same reason, the best precipitating agent is the one giving the precipitate with the lowest solubility product.

- (iii) Although the situation may be very different from case to case, precipitation is often advantageously made at the lowest practical temperature, as this often favors nucleation over growth.

In the coprecipitation process, the multi-element product can be of 3 types:

- (i) Metals combined in an insoluble single compound, for instance  $\text{BaTiO}_3$ , can be obtained by precipitation of a hydrated oxalate and subsequent thermal decomposition of this oxalate ( $\text{BaTiO}(\text{C}_2\text{O}_4)_2 \cdot 4\text{H}_2\text{O}$ ). Other instances are precipitations as chromates, molybdates, and tungstates.
- (ii) Some metals precipitate into a single-phase solid solution or a single-phase mixed structure, e.g. precipitation by sodium carbonate of aluminates or hydroxyprecursors of aluminates of Cu, Fe, Ni, Zn, and Mg. Divalent metal oxalates can also be precipitated in this way [28].
- (iii) Some metals precipitate more or less simultaneously, but in separate phases, e.g. metal hydroxides precipitated by NaOH, KOH, and  $\text{NH}_4\text{OH}$ . Normally,  $\text{NH}_4\text{OH}$  is preferable for precipitation, especially when washing off all alkali from the catalyst is a prerequisite for the preparation of the final catalyst. An exception to this is when  $\text{NH}_4\text{OH}$  can form ammino complexes as with transition metals (Ni, Co, Cu, Zn).

Tables 3 to 7 constitute partial lists of mixed salts which have been claimed to be obtained by coprecipitation: dashes join the symbols of elements which can be associated.

#### *b Spray Drying, Spray Calcination*

Spray drying is a versatile method which can produce mixtures of phases with a high degree of interdispersion and a relatively high degree of homogeneity, although there is, in principle, no atomic level homogeneity. This is essentially an improved evaporation method.

Very often, slow evaporation of a homogeneous solution of two precursor salts, e.g.  $\text{MgSO}_4$  and  $\text{Al}_2(\text{SO}_4)_3$ , leads to segregations of the two salts in the solid phase. To prevent this, it is advantageous to eliminate rapidly the solvent, either by spray drying or hot petroleum drying. Spray drying can also be used with the active phase, for removing water. In certain cases, the temperature in the equipment can be raised enough to permit the reaction between the salts to produce an oxide combining two metallic elements. This has been done from solutions of  $\text{MgSO}_4$  and  $\text{Al}_2(\text{SO}_4)_3$  to make

**Table 3.** Precursors associating elements of identical valency inorganic compounds (adapted from Ref 6)

Valency	Hydroxides	Carbonates	Nitrates	Sulphates		
				Simple	Schoenites	Alums
I		Li-Na, Li-K, Na-K, K-Ag	Na-Ag, K-Ag, Ag-Rb, Ag-Tl	Li-Na, Li-K		
II	Mg-Mn-Fe-Co-Ni, Zn-Cd-Sn	Mg-Mn, Mn-Co, Mn-Zn, Mg-Fe-Ni-Zn-Cd, Sn-Pb		Mg-Mn-Fe-Co-Ni-Cu-Zn-Cd	Mg-Mn-Fe-Co-Ni-Cu	
III	Cr-Fe, Al-Cr-Fe-Tl-Re	rare earth	Al-Fe, Al-Cr, Cr-Fe	rare earth metals, Ce-Th		Al-Ti-V-Cr-Mn, Fe-Co-Ga
IV	Ti-Zr-Sn-Ce-Ta-Th			Zr-Ce-Th		
V	Nb-Ta					
VI	Mo-W					

**Table 4.** Precursors associating elements of identical valency organic compounds (adapted from Ref 6)

Valency	Formates	Acetates	Oxalates	Oxalato complexes	Malonates	Succinates	Maleates	Tartrates	Citrates
I	Li-Na-K	Li-Na-K, Cu-Ag				Li-Na-Ag, Na-K	K-Ag	Na-Rb, Li-K-Rb-Cs, Na-K	Li-Na, Li-K, Na-K
II	Cu-Sr, Cu-Ba, Zn-Ba, Cd-Ba, Mg-Mn-Fe-Co-Ni-Zn-Cd	Cu-Ca, Be-Mg, Ca-Ba, Mn-Ni, Zn-Cd-Hg, Sn-Pb-Bi	Mg-Ni		Co-Ba, Mg-Co, Zn-Ba	Cu-Zn-Sr-Ba-Cd-Pb, Mn-Ni	Ca-Sr-Ba, Ni-Cu, Zn-Cd	Cu-Ba, Ca-Sr	Ca-Cu, Co-Ni, Sr-Ba, Sr-Pb, etc
III	Al-V-Cr-rare earths	Al-Cr-Fe-Co-rare earths	rare earths	Al-V-Cr, Al-Cr-Fe, Ti-Mn-Co-Ga	Cr-Fe-Rh rare earths	rare earths	rare earths	rare earths	rare earths, As-Sb
IV		Sn-Pb	Th-U						
V									
VI				Mo-W				Mo-W	

**Table 5.** Precursors associating elements of different valencies: inorganic precursors (adapted from Ref. 6).

Valency	II	III	IV	V	VI
I	carbonates Co-Na, Co-K, Ni-Na, Ni-K nitrates Zn-alkali metals sulphates (schoenites) Mg-Na	carbonates Al-K, Ce-Na nitrates rare earth-alkali metals sulphates (alums) Me <sup>III</sup> -alkali metals	carbonates Ce-alkali metals nitrates Ce-alkali metals sulphates U-alkali metals	alkali metals vanadates	alkali metal chromates, Ag chromate, alkali metal molybdates and tungstates
II		hydroxides Al-Ni nitrates rare earth-Mg, Bi-Mg sulphates Cr-Mg, Cr-Mn, Cr-Fe, Cr-Zn	nitrates Ce-Mg, Ce-Zn	Cu vanadate	alkaline earth chromates, molybdates, and tungstates
III			hydroxides Zr-Nd	Cr vanadate	Fe chromate, rare earth chromates and molybdates, Bi molybdate
IV				uranyl vanadate	Zr chromate, Th chromate, Th molybdate

References see page 117

**Table 6.** Precursors associating elements of different valencies: organic precursors (adapted from Ref. 6).

Valency	II	III	IV	V	VI
I	formates Sn-alkali metals oxal. compl. (Be, Mg)-alkali metals malonates Be-Na, Be-K, Co-K succinates Mg-K, Co-K, Ni-K, Zn-K, Pb-K maleates Cu-K tartrate Fe-Na, Co-Na, Ni-Na, Cu- Na, Zn-Na, Pb-Na crystallized citrates	formates Cr-Na, Cr-Ag oxal. compl. M <sup>III</sup> -alkali metals; M <sup>III</sup> = Al, Ti, V, Cr, Fe, Co, Ga malonates Cr-Na, Cr-K, Mn-Li, Mn- Na, Mn-K, Fe-K, Fe-Rb, Fe-Tl, Co-K, Rh-K tartrates Al-K-Na, Cr-K, Mn-Li, Mn-Na, Mn-K, Fe-Na, Sb-Ag, Ce-Na, Bi-Na, Bi-K crystallized citrates	formates (Sn or Th)-alkali metals oxal. compl. M <sup>IV</sup> -alkali metals; M <sup>IV</sup> = Zr, Hf, Th or U maleates Zr-K crystallized citrates	malonates VO-alkali metals and Ag tartrates VO-Na, VO-K crystallized citrates	formates Mo-Na, Mo-K malonates U-Na tartrates Mo-Na, Mo-K, W-Na crystallized citrates
II		acetates Cr-Fe, Ca-Au, Pb-Au oxal. compl. Al-Mg, Cr-Mg, Fe-Ba malonates Cr-Ba tartrates Al-Ca, Sb-Co, Sb-Ba, Sb- Pb	formates Th-Sr, Th-Ba	malonates VO-Ca, VO-Sr, VO-Ba, VO-Tl, VO-Pb	formates Cr <sup>VI</sup> -Ca acetates U-Fe, U-Ni, U-Zn oxal. compl. Mo-Ba tartrates Mo-Mg crystallized citrates
III			crystallized citrates		acetates Cr <sup>VI</sup> -Ce



Table 7. Crystallized mixed citrates (C. Marcilly, unpublished results).

Valency	I	II	III
I	Li <sub>2</sub> Na(C <sub>6</sub> H <sub>5</sub> O <sub>7</sub> ) Li <sub>2</sub> K(C <sub>6</sub> H <sub>5</sub> O <sub>7</sub> ) Na <sub>3</sub> K <sub>3</sub> (C <sub>6</sub> H <sub>5</sub> O <sub>7</sub> ) <sub>2</sub> · 6.5H <sub>2</sub> O		
II	CaAg <sub>2</sub> (C <sub>6</sub> H <sub>4</sub> O <sub>7</sub> ) · 0.5H <sub>2</sub> O FeNa(C <sub>6</sub> H <sub>5</sub> O <sub>7</sub> ) CoK(C <sub>6</sub> H <sub>5</sub> O <sub>7</sub> ) · 4H <sub>2</sub> O CoK <sub>4</sub> (C <sub>6</sub> H <sub>5</sub> O <sub>7</sub> ) <sub>2</sub> CuK <sub>10</sub> (C <sub>6</sub> H <sub>4</sub> O <sub>7</sub> ) <sub>3</sub> · 12H <sub>2</sub> O ZnNa <sub>2</sub> (C <sub>6</sub> H <sub>4</sub> O <sub>7</sub> ) ZnNa <sub>6</sub> (C <sub>6</sub> H <sub>4</sub> O <sub>7</sub> ) <sub>2</sub>	Ca <sub>2</sub> Cu(C <sub>6</sub> H <sub>5</sub> O <sub>7</sub> ) <sub>2</sub> · 9H <sub>2</sub> O	
III	2HBO <sub>2</sub> + K <sub>2</sub> C <sub>6</sub> H <sub>7</sub> O <sub>7</sub> + C <sub>6</sub> H <sub>8</sub> O <sub>7</sub> 2HBO <sub>2</sub> + K <sub>2</sub> C <sub>6</sub> H <sub>7</sub> O <sub>7</sub> 3HBO <sub>2</sub> + K <sub>3</sub> C <sub>6</sub> H <sub>5</sub> O <sub>7</sub> Na <sub>3</sub> H <sub>3</sub> [Fe <sub>2</sub> (C <sub>6</sub> H <sub>4</sub> O <sub>7</sub> ) <sub>3</sub> ] FeK <sub>6</sub> (C <sub>6</sub> H <sub>5</sub> O <sub>7</sub> ) <sub>3</sub> Fe <sub>2</sub> K <sub>6</sub> (C <sub>6</sub> H <sub>4</sub> O <sub>7</sub> ) <sub>3</sub> K <sub>3</sub> [La(C <sub>6</sub> H <sub>5</sub> O <sub>7</sub> ) <sub>2</sub> ] Na <sub>3</sub> [Nd(C <sub>6</sub> H <sub>5</sub> O <sub>7</sub> ) <sub>2</sub> ] K <sub>3</sub> [Nd(C <sub>6</sub> H <sub>5</sub> O <sub>7</sub> ) <sub>2</sub> ] (AsO)Na <sub>3</sub> (C <sub>6</sub> H <sub>5</sub> O <sub>7</sub> ) <sub>2</sub> · 3.5H <sub>2</sub> O (AsO)K <sub>3</sub> (C <sub>6</sub> H <sub>5</sub> O <sub>7</sub> ) <sub>2</sub> · 4.5H <sub>2</sub> O (SbO)Na <sub>3</sub> (C <sub>6</sub> H <sub>5</sub> O <sub>7</sub> ) <sub>2</sub> · H <sub>2</sub> O (SbO)K <sub>3</sub> (C <sub>6</sub> H <sub>5</sub> O <sub>7</sub> ) <sub>2</sub> · 2H <sub>2</sub> O NaBi(OH) C <sub>6</sub> H <sub>5</sub> O <sub>7</sub> · 3H <sub>2</sub> O KBi(OH) C <sub>6</sub> H <sub>5</sub> O <sub>7</sub> · 3H <sub>2</sub> O Na(BiO) <sub>2</sub> C <sub>6</sub> H <sub>5</sub> O <sub>7</sub> Bi C <sub>6</sub> H <sub>5</sub> O <sub>7</sub> + 6Na <sub>3</sub> (C <sub>6</sub> H <sub>5</sub> O <sub>7</sub> ) Na(BiO) <sub>2</sub> (C <sub>6</sub> H <sub>5</sub> O <sub>7</sub> ) amorphous	2HBO <sub>2</sub> + Mg (C <sub>6</sub> H <sub>7</sub> O <sub>7</sub> ) <sub>2</sub> HBO <sub>2</sub> + Mg(C <sub>6</sub> H <sub>7</sub> O <sub>7</sub> ) 6HBO <sub>2</sub> + Mg <sub>3</sub> (C <sub>6</sub> H <sub>5</sub> O <sub>7</sub> ) <sub>2</sub> Ca <sub>3</sub> [La(C <sub>6</sub> H <sub>5</sub> O <sub>7</sub> ) <sub>2</sub> ] <sub>2</sub> Ca <sub>3</sub> [Nd(C <sub>6</sub> H <sub>5</sub> O <sub>7</sub> ) <sub>2</sub> ] <sub>2</sub>	Ce[Nd(C <sub>6</sub> H <sub>5</sub> O <sub>7</sub> ) <sub>2</sub> ] · 3H <sub>2</sub> O
IV	(NaTiO <sub>2</sub> ) <sub>3</sub> C <sub>6</sub> H <sub>5</sub> O <sub>7</sub> (TiO)K <sub>2</sub> (C <sub>6</sub> H <sub>6</sub> O <sub>7</sub> ) <sub>2</sub> · H <sub>2</sub> O ZrK <sub>3</sub> H (C <sub>6</sub> H <sub>4</sub> O <sub>7</sub> ) <sub>2</sub> · 9.5H <sub>2</sub> O		[Cr <sub>3</sub> (C <sub>6</sub> H <sub>5</sub> O <sub>7</sub> ) <sub>2</sub> (OH) <sub>2</sub> ] <sub>2</sub> PtCl <sub>6</sub> · 10H <sub>2</sub> O [Fe <sub>3</sub> (C <sub>6</sub> H <sub>5</sub> O <sub>7</sub> ) <sub>2</sub> (OH) <sub>2</sub> ] <sub>2</sub> PtCl <sub>6</sub> · 10H <sub>2</sub> O
V	(VO <sub>2</sub> )Ag <sub>3</sub> C <sub>6</sub> H <sub>4</sub> O <sub>7</sub> (VO) <sub>2</sub> Na <sub>4</sub> (C <sub>6</sub> H <sub>5</sub> O <sub>7</sub> ) <sub>2</sub> O · 12H <sub>2</sub> O (VO) <sub>2</sub> K <sub>4</sub> (C <sub>6</sub> H <sub>5</sub> O <sub>7</sub> ) <sub>2</sub> O · 12H <sub>2</sub> O  [MSb(C <sub>6</sub> H <sub>5</sub> O <sub>7</sub> ) <sub>2</sub> (H <sub>2</sub> O)] [M <sub>3</sub> Sb(C <sub>6</sub> H <sub>5</sub> O <sub>7</sub> ) <sub>2</sub> (H <sub>2</sub> O)]  M = Na or K		
VI	(MoO <sub>2</sub> )Na <sub>2</sub> (C <sub>6</sub> H <sub>6</sub> O <sub>7</sub> ) <sub>2</sub> (MoO <sub>2</sub> )K <sub>2</sub> (C <sub>6</sub> H <sub>6</sub> O <sub>7</sub> ) <sub>2</sub> (WO <sub>2</sub> )Na <sub>3</sub> H(C <sub>6</sub> H <sub>6</sub> O <sub>7</sub> ) <sub>3</sub> · 0.5H <sub>2</sub> O (WO <sub>2</sub> )K <sub>3</sub> H(C <sub>6</sub> H <sub>6</sub> O <sub>7</sub> ) <sub>3</sub> · 0.5H <sub>2</sub> O	(MoO <sub>2</sub> )Ba(C <sub>6</sub> H <sub>6</sub> O <sub>7</sub> ) <sub>2</sub> · 5H <sub>2</sub> O (WO <sub>2</sub> ) <sub>2</sub> Ba <sub>3</sub> H <sub>2</sub> (C <sub>6</sub> H <sub>6</sub> O <sub>7</sub> ) <sub>6</sub> · 10H <sub>2</sub> O	

highly dispersed MgAl<sub>2</sub>O<sub>4</sub>. The success of the method, in this case, is the very small size of the crystallites obtained by rapid drying and their excellent interdispersion, this promoting solid-state reactions at the higher temperature.

This technique is used industrially to produce powders for the fabrication of ceramics [29]. Mainly single-metal oxides are made in this way, but it is claimed that MnFe<sub>2</sub>O<sub>4</sub>, NiFe<sub>2</sub>O<sub>4</sub>, NiAl<sub>2</sub>O<sub>4</sub>, dopant-stabilized zirconium oxide and titanates can be obtained. Powders of surface area up to 20 m<sup>2</sup> g<sup>-1</sup> can be produced. The powder is usually in the form of aggregates of 0.2–

0.4 μm in the best cases, but often of over 100 μm in diameter [29].

By use of this technique, it is possible to prepare fine spherical catalyst particles in the 10–100 μm diameter range, as are required for typical fluidized-bed catalytic processes. In this technique used for large-scale catalyst manufacture, the feed is generally dilute hydrogel or sol that is sprayed from the top of a tower while hot air is blown in a cocurrent or countercurrent direction to dry the droplets before they reach the bottom of the tower. The fine droplets are produced or atomized by pumping the hydrogel or sol under pressure either

through nozzles or onto wheels or discs rotating at a high speed. The method is also convenient to embed crystalline particles of micron or submicron size in an amorphous matrix of 10–100  $\mu\text{m}$  diameter. The best known examples are to embed multicomponent bismuth molybdates in 50% silica matrix for amoxidation of propylene to acrylonitrile, and to incorporate  $<1\text{--}3\ \mu\text{m}$  zeolite crystallites in amorphous silica-alumina/clay matrix for fluid catalytic cracking (FCC) catalysts. The use of spray drying for making atomically homogeneous mixed oxide does not seem to have gone beyond the development stage.

#### *c Hot-Petroleum Drying*

Hot-petroleum drying constitutes an alternative to spray drying. It was developed by Reynen and Bastius [30], initially for small-scale preparations. However, the development of what industry improperly calls the sol-gel method, namely integrated conventional precipitation and gelling, makes it now a large scale preparation method. The principle consists in dropping a fluid material containing the active elements in kerosene. This fluid material may be a gel, a solution in the course of gelling, a stabilized emulsion of a salt solution and kerosene, or an aqueous solution of salts. The temperature of the kerosene bath is maintained at about 440 K. The kerosene bath may be vigorously agitated if necessary. The water evaporates and the powder or, according to processes, the small solid spheres obtained are easily filtered and dried at around 520 K. The product is a free-flowing powder consisting of a homogeneous mixture of salts. The hot-petroleum drying method, contrary to the spray-drying variant (called spray calcination) does not permit the solid-state reactions needed to form the oxides, but the highly dispersed and intermixed salts can be thermally decomposed without phase segregations. Just as spray drying, this method is also dependent on the evaporation of water being faster than the segregation phenomena. The controlling factors are thus the temperature of the hot kerosene and the rate of water evaporation from the droplets. The advantages of this method are the simple setup, the kerosene can be recycled, and the energy consumption is lower than that for spray drying.

#### *d Freeze Drying*

Freeze drying corresponds to the same purpose as both above-mentioned methods, but the strategy is different. In order to limit segregation, it is the diffusion process that is slowed down. This can be achieved either by rapid cooling (freeze drying) or by increasing the viscosity of the solution (by some of the methods described below, addition of hydroxycellulose or gums, for example; this increase of viscosity also

plays a role in the more elaborate amorphous citrate process described in the next subsection).

Undercooling is the driving force in freeze drying. An aqueous salt solution is introduced dropwise into an immiscible liquid (hexane or a petroleum fraction such as kerosene) cooled below 243 K. The individual droplets are frozen instantaneously and the solid particles are decanted or filtered. The frozen particles are then sublimed in a vacuum to obtain a homogeneous powder of fairly uniform particle size. Important parameters in freeze drying are the final temperature of the salt solution and the cooling rate. These can be controlled to some extent, but only on a small scale. Hence the method is not very suited for large-scale manufacture of catalysts.

### **C Chemical Complexation Methods**

#### *a Crystalline Complex Salts*

Oxalates [31], tartates [32], and citrates [33] (Tables 4 and 6) of various metals can form well-crystallized complex salts, e.g.  $\text{Mg}(\text{NH}_4)_4(\text{Al}_x\text{Cr}_{1-x}(\text{C}_2\text{O}_4)_3)_2 \cdot n\text{H}_2\text{O}$ , which on thermal decomposition at moderate temperatures can yield mixed oxides. Although these complex salts permit substitution in large ranges, or even in all proportion in some cases of elements of the same volumes, their stoichiometry is still rather rigid and this imposes a serious limitation on any wide applicability of this method. This limitation is conspicuous when comparing the chemical formulas of crystallized citrates (Table 7) [29] with the very flexible composition of the compounds which will be described in the next subsection. The same remark holds when oxalate complexes are considered:  $\text{M}^{\text{I}}(\text{NH}_4)_4[\text{M}^{\text{III}}(\text{C}_2\text{O}_4)_3]_2 \cdot n\text{H}_2\text{O}$ , where  $\text{M}^{\text{I}}$  and  $\text{M}^{\text{III}}$  both represent a single metal or a mixture of metals or ions (e.g. VO) of the corresponding valency. The problem is further complicated due to the possibility of non-homogenization or phase separation during the chain of downstream unit operations involved in catalyst production. The amorphous complex method, described next, provides an escape from most of these difficulties.

#### *b Amorphous Precursor "Citrate" Method: General*

The principle of this method consists of preparing a stable amorphous or glassy precursor which, thanks to this amorphous structure, tolerates an enormously wide range of composition. The starting solution is a mixture of metallic salts and a hydroxy acid such as citric, malic, tartaric, lactic, or glycolic acid [3, 34–36]. The metals are preferably in the form of nitrates or ammonium salts, which will not leave any residues on thermal decomposition at a later stage and the decomposition of the nitrate and ammonium ions promotes surface area and porosity, due to the large amount of

gas the decomposition evolves. Typical concentrations are 1 g equivalent organic acid per equivalent of total metal content. The solution is concentrated by rapid evaporation under vacuum, for instance in a Rotavapor, until its viscosity exceeds 500 cP at ambient temperature. A very stable syrup is obtained in this way. It can be dehydrated under vacuum at about 350 K to a rigid-foam (meringue) precursor, which is amorphous to X-rays, hygroscopic, and exhibits the color of the metallic ions present. The amorphous precursor appears to be some sort of a three-dimensional polymer in which the multifunctional organic acids are linked to two or more cations. The thermal decomposition of the amorphous mass may proceed more or less continuously or in two distinct steps at 350–370 K and 520–670 K. Because of the danger of violent reactions, this decomposition step is to be carried out very carefully, taking all necessary precautions. The preparation of oxides containing metallic ions highly active in oxidation needs very stringent precautions and is generally not advisable. In particular, the possible detonation of copper and silver salts should be borne in mind. In these cases, the freshly formed metal particles could be powerful catalysts for some unexpected reactions, e.g. with ammonia. Also, secondary reactions can occur even at room temperature resulting in the formation of a small amount of lethal cyanogen gas. Clearly, this is not a method to be tried by students or inexperienced researchers.

The mechanisms of reactions occurring during preparation of mixed oxides by the citrate methods have been outlined in some detail [37]. In the dehydration under vacuum, extensive loss of nitrate ions (in the form of various nitrogen oxides and ammonium nitrate) occur together with the loss of water. Although easier in the presence of citric acid, the decomposition of nitrate does not involve extensive reaction with the latter below 380 K. The semidecomposed precursor obtained around 410 K is essentially a dehydrated, amorphous, highly porous mixed citrate. The higher temperature decomposition stage, mainly between 500 and 670 K, consists of the burning of citric acid by oxygen. It is facilitated because of the presence of nitrate ions in the initial precursor. As indicated above, this stage is catalyzed by the presence of metals whose oxides are oxidation catalysts. Additional details can be found in Refs 5 and 37.

Mixed oxides obtained by the above method are very lightweight powders of apparent density only  $<0.05 \text{ g cm}^{-3}$ , amorphous to X-rays, free flowing, and consist of aggregates of particles of 20–100 nm. Upon further heating, these oxides crystallize into various well-defined structures depending on the nature and composition of the starting materials: solid solutions, spinels, perovskites, garnets [3]. Variants of the citrate method consist of simply adding citric acid or other

hydroxymultifunction acids to solutions used by other methods (precipitation, impregnation, sol-gel, etc.). Although not leading to such excellent results as the original citrate method, the result of such a use of hydroxyacid corresponds to substantial improvement. An improved citrate method has been proposed in which a polyalcohol is added to the initial solution [38]. The polyalcohol is supposed to promote the reticulation in the transformation of the starting solution to the rigid foam. The reticulation or polymer formation is due to the esterification reaction between citric acid and the polyalcohol. This method has been used for the preparation of barium titanates doped by a large variety of ions, but apparently not for preparing catalysts.

Considering the case of crystalline complex salts and the amorphous precursor method, both chemical complexation methods have found important and innovative applications in recent years for the preparation of a wide variety of catalysts and of various perovskite-type catalysts and barium hexaaluminates, as required for high-temperature ( $>1500 \text{ K}$ ) applications such as catalytic combustion. It is therefore worthwhile describing some applications, in the next two subsections.

#### *c Citrate Method for the Preparation of Perovskite Catalysts*

A general introduction to perovskites and their catalytic properties is given in the reviews by Tejuca et al. [39] and Yamazoe and Teraoka [40]. In general, perovskites have been prepared by calcining a solid mixture of constituent metal oxides or carbonates (the method used in the ceramic industry), or by evaporating an aqueous solution of constituent metal nitrates or acetates and by subsequent calcination. The resulting oxides have relatively small surface areas. Some methods which can give higher specific surface areas are listed in Table 8. The guiding principle here is to attain as thorough a dispersion as possible, almost to a molecular level, of constituent components in the precursors prior to calcination. Once this is achieved, lower calcination temperatures can convert the precursors to the required perovskite structure of larger surface areas, as shown in Table 9.

Teraoka et al. [41, 42] have applied the amorphous citrate process to prepare unsupported (or neat) and supported perovskites of the type LaMn, LaCo, LaMnCu, LaCoFe, LaCaCo, LaCaMn, LaSrMn, LaSrCo, LaSrCoCu, and LaSrCoFe. The use of the citrate method for preparing atomically homogeneous oxides on supports has been a very important extension of the citrate method over the years. Nitrates of constituent metals of the required perovskite were dissolved in water and mixed with an aqueous solution of citric acid (molar ratio of citric acid to total metals 1:1). Water was evaporated from the mixed solution

**Table 8.** Methods of preparation of high-surface-area perovskites (adapted from Ref. 40).

Description	Preparation method
Control of evaporation (decomposition) process	freeze drying, spray drying, mist decomposition, explosion
Contrivance of precursor materials	coprecipitated oxalate decomposition, amorphous citrate decomposition, decomposition of solid solutions of cyanides and hydroxides

**Table 9.** Specific surface area of  $\text{LaCoO}_3$ , prepared by various methods (adapted from Ref. 40).

Preparation method	Final heat treatment <sup>a</sup>	Surface area ( $\text{m}^2 \text{g}^{-1}$ )
Ceramic methods	1523 K, 48 h	1.7
Oxalate decomposition	1273 K, 12 h	1.6
	1173 K, 15 h	4.5
Acetate decomposition	1123 K, 5 h	2.5
	1123 K, 5 h	2.2
Mist decomposition	973 K <sup>b</sup>	11.8
Citrate decomposition	973 K, 4 h	15.3
	873 K, 2 h	11.3
	973 K, 4 h	8.5
Cyanide decomposition	923 K, 4 h	37.5
Freeze drying	773 K, 10 h	36.2
Explosion	773 K, 10 h	34.6

<sup>a</sup>Temperature and period of calcination in air sufficient for obtaining a single perovskite phase.

<sup>b</sup>A mist of a mixed aqueous solution of cobalt and lanthanum nitrates was treated successively in a flow-type reactor equipped with three furnaces (443 K, 573 K, 973 K), and the residence time in a final furnace (973 K) was about 11 s.

using a rotary evaporator at 330–340 K until a sol was obtained. The sol was further dehydrated at the same temperature under vacuum for 5 h. Stabilized alumina of composition  $\text{La}_2\text{O}_3 \cdot 19\text{Al}_2\text{O}_3$  was used as the support for the perovskites. For comparison, Teraoka et al. also prepared the above perovskites by an acetate process, instead of by the citrate process. The specific surface areas of the perovskites by the citrate and the acetate processes are compared in Table 10. The amorphous citrate precursor decomposed in three steps, the third decomposition at 820–920 K already inducing crystallization of perovskite-type oxides. The acetate process needed a higher calcination temperature of 1120 K and consequently produced samples the surface areas of which were only 1/3 to 1/7 of those of samples from the citrate process. The higher-area perovskites from the citrate process had higher catalytic activity for methane oxidation. For the preparation of supported perovskite catalysts also, the citrate process was more effective than the acetate process.

An improvement of the oxalate precipitation method for the preparation of  $\text{LaSrCo}$  perovskites has been reported recently by Chang and Weng [43]. By substitut-

ing ethanol for water in the washing of the perovskite precursors, the problems of chemical inhomogeneity and cobalt elution are both eliminated. This method is claimed to be an easier and quicker way to prepare a large variety of perovskites having high surface area, pore volume, and catalytic oxidation activity.

#### d Complex Cyanide Method

Very recently Geus and co-workers [44, 45] have applied another method based on chemical complexes. This is the complex cyanide method to prepare both monocomponent (Fe or Co) and multicomponent Fischer–Tropsch catalysts. A large range of insoluble complex cyanides are known in which many metals can be combined, e.g. iron(II) hexacyanide and iron(III) hexacyanide can be combined with iron ions, but also with nickel, cobalt, copper, and zinc ions. Soluble complex ions of molybdenum(IV) which can produce insoluble complexes with metal cations are also known. Deposition precipitation (Section A.2.2.1.5) can be performed by injection of a solution of a soluble cyanide complex of one of the desired metals into a suspension of a suitable support in a solution of a simple salt of the other desired metal. By adjusting the cation composition of the simple salt solution, with a same cyanide, it is possible to adjust the composition of the precursor from a monometallic oxide (the case when the metallic cation is identical to that contained in the complex) to oxides containing one or several foreign elements.

Complex metal cyanides decompose at fairly high temperatures. Decomposition in an oxidizing atmosphere (up to 600 K) results in the corresponding oxides, that in an inert or in a reducing atmosphere (up to 900 K) results in the metals or alloys. In either case, reaction of the oxides or of the metals/alloy with the support is minimized. The complex cyanide method can thus establish homogeneity of the constituent ions on a molecular scale and also prevent undesired reactions of the active precursors with the support.

#### D Miscellaneous Methods for Obtaining Solid Precursors of Flexible Composition

There are still other ways to avoid segregation of phases during the decomposition of a solid precursor to form an oxide.

One such method uses soluble gums or polymers. The principle is the same as in previously described methods. A solution containing all the desired elements is made very viscous by dissolving gums, or functional polymers. Hydroxymethylcellulose and similar structures have been used for this purpose. Usually, the viscous solution can be concentrated (e.g. by evaporation) with little or no crystallization or segregation, and calcined to a mixed oxide containing all the elements finely interdispersed.

Another very interesting method, although of limited application, is a kind of self-gelation. This occurs in the

**Table 10.** Specific surface area of perovskite-type catalysts, prepared by the citrate process and the acetate process (adapted from Ref. 41).

Sample	Citrate process		Acetate process	
	Calcination temp. (K)	Surface area (m <sup>2</sup> g <sup>-1</sup> )	Calcination temp. (K)	Surface area (m <sup>2</sup> g <sup>-1</sup> )
LaMnO <sub>3</sub>	923	44.8	1123	7.3
LaCoO <sub>3</sub>	873	11.3	1123	2.2
LaCo <sub>0.4</sub> Fe <sub>0.6</sub> O <sub>3</sub>	823	22.7	1123	3.3
LaMn <sub>0.6</sub> Cu <sub>0.4</sub> O <sub>3</sub>	873	33.0	1123	7.5
La <sub>0.8</sub> Sr <sub>0.2</sub> MnO <sub>3</sub>	873	36.4	1123	8.2
LaCo <sub>0.8</sub> Cu <sub>0.2</sub> O <sub>3</sub>	823	24.7	-	-
La <sub>0.6</sub> Ca <sub>0.4</sub> MnO <sub>3</sub>	873	33.0	-	-
La <sub>0.4</sub> Ca <sub>0.6</sub> CoO <sub>3</sub>	873	14.3	-	-

case of amorphous hydrated precipitates with a strong hydrophilic character that favors their interaction with the solution and transformation through tridimensional reticulation to a homogeneous hydrogel retaining the solution in its net. The only well characterized example is iron molybdate gels (pure or with additives) which were developed for the production of catalysts for the oxidation of methanol to formaldehyde [46–51]. Figure 7 [5] shows that gel formation only occurs in a narrow range of composition and operating conditions. The main parameters are the Mo:Fe ratio, the nature of the starting salts, the nature and amount of additives, the temperature, the concentrations, and the intensity of stirring. Aging increases reticulation and homogeneity; the hydrogel becomes hard and brittle (the fractured surfaces exhibit the aspect of glass fractures also commonly found in hydrogels). Depending on the concentrations and Mo:Fe proportions, a precipitate first forms, then partly or totally dissolves to give a gel. A true metastable solution is transiently formed for atomic ratios Mo:Fe  $\leq 1.5$  [5]. The aged gel is then dried to give a brown transparent, homogeneous xerogel containing less than 1 wt% water which produces the activated catalyst after calcination. This preparation method permits the introduction of many elements as doping agents. The gel may incorporate a large excess of molybdenum compared to the stoichiometry of Fe<sub>2</sub>(MoO<sub>4</sub>)<sub>3</sub>.

It is not known whether this method can be extended to other systems. It could be speculated that all elements giving high molecular weight polyanions could form similar gels when combined with cations carrying three or more positive charges.

### E Solid-State Ion Exchange for Zeolite Catalysts

Impregnation and ion-exchange methods for preparation of supported catalysts are discussed in detail in Section 2.2.1.1. Only ion exchange in the solid state as a novel method to prepare zeolite catalysts is described here.

Modification of zeolite catalysts can be achieved by solid-state reactions between zeolite and other crystal-

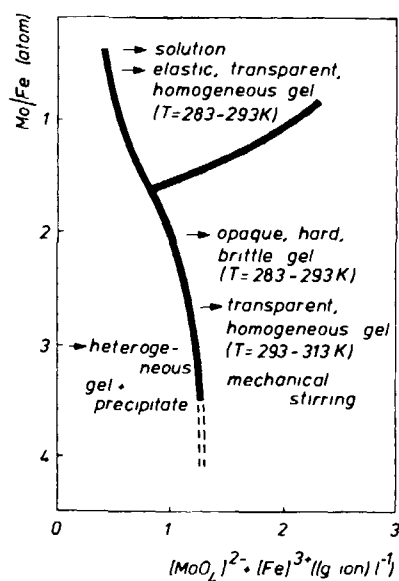
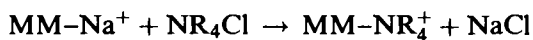


**Figure 7.** Formation of gels from iron molybdate precipitates [5]. A very fine colloidal precipitate forms in all cases but undergoes different changes suggested by the arrows, according to concentration and Mo:Fe proportions, as well as other conditions mentioned in the figure. In the upper part domain, the colloidal precipitate seems to dissolve to form a solution whose viscosity increases until formation of a gel. In the right-hand domain, the gel directly forms from the colloidal system but can become transparent if the reaction takes place in the temperature range 293–313 K.

line phases. Thus, alkaline earth, rare earth, and transition metal cations can be introduced into A, X, Y, ZSM-5, beta and mordenite molecular sieves by means of solid-state ion-exchange reactions [52]. Other variations of this approach are solid-state reactions to form host-guest (supramolecular) complexes [53] and the intercalation of polar organic molecules into smectite clays [54, 55]. Still another development is the preparation of organoammonium montmorillonites by room-temperature ion exchange between sodium montmorillonite (MM-Na<sup>+</sup>) and solid organoammonium halides [56]:



This methodology has also been extended [57] to high-valent metal cations such as  $\text{Al}^{3+}$  and  $\text{Fe}^{3+}$ : a simple ball-grinding with the corresponding metal nitrate at ambient temperature in air yields the Al- or Fe-exchanged montmorillonite. Such products are interesting acid-clay catalysts, their Brønsted acidity arising mainly from the dissociation of adsorbed water:



However, the large-scale preparation of such acid-clay catalysts was until recently hampered by two problems:

- (i) the tendency of clay suspensions to form gels at clay concentrations above about  $20 \text{ g l}^{-1}$ , which necessitates the use of a large volume of water;
- (ii) the difficulties of large-scale filtering of clay suspensions.

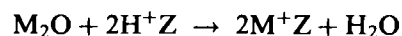
The solid-state ion-exchange reactions, which do not have such limitations, are proving to be an interesting, practical, and low-energy alternative to the preparation of clay catalysts.

Solid-state ion-exchange methods are also suitable for the preparation bifunctional catalysts, containing an acidic as well as a hydrogenation–dehydrogenation function. A typical example is Pd-loaded ZSM-5 [58]. Since a concomitant incorporation of  $\text{Ca}^{2+}$  gave a better catalyst, a two-step solid-state ion exchange could also be carried out, first with  $\text{CaCl}_2$  and then with  $\text{PdCl}_2$ . On subsequent reduction with  $\text{H}_2$ , a catalyst with a mean Pd particle size of about 2 nm was obtained with a strong and stable activity for both hydrogenation and hydroisomerization.

Ga-ZSM-5 catalysts have received considerable attention in recent years ever since the development of the Cyclar process by BP/UOP for aromatization of  $\text{C}_3$ – $\text{C}_4$  alkanes. Kanazirev et al. [59] have shown that this Ga-doping can be achieved by a mechanical mixing of  $\beta$ - $\text{Ga}_2\text{O}_3$  and HZSM-5 in the presence of hydrogen. The solid-state reaction proceeds through  $\text{Ga}_2\text{O}$  as an intermediate, which moves on to the HZSM-5 and gets trapped at the cationic positions in a still lower oxidation state, probably as Ga. This is a new route to high-quality catalyst preparation, without involving any wet-process step.

The above work prompted attempts [60] to incorporate other metals also into ZSM-5 by direct solid-state reactions. Thus, a long-distance transfer and fairly uniform distribution of indium in large ZSM-5 crystals occurs when powdered  $\text{In}_2\text{O}_3$  and ZSM-5 are loosely mixed and then subjected to reduction in hydrogen at a temperature as low as 623 K. Energy dispersive X-ray (EDX) analysis of  $\text{In}_2\text{O}_3$  distribution on ZSM-5 crystals varied between 2.8 and 3.6 wt%, with an average of 3.21 wt%. The reductive solid-state ion

exchange with both Ga and In is proposed [60] to proceed as follows ( $\text{M} = \text{Ga}$  or  $\text{In}$ ;  $\text{Z} = \text{HZSM-5}$ ):



## F Specific Methods: Example of Hydrotalcite-type Catalysts

The example of hydrotalcite catalyst can serve to illustrate the fact that solids of given structures containing several elements in rather flexible proportions can be obtained by different techniques. This example will also show that special techniques can be designed for the preparation of specific precursors.

Hydrotalcite (HT) is a clay mineral which on crushing becomes a fine powder, similar to talc. It is a hydroxycarbonate of Mg and Al, of the general formula  $\text{Mg}_6\text{Al}_2(\text{OH})_{16}\text{CO}_3 \cdot 4\text{H}_2\text{O}$ , and occurs in nature in foliated and controlled plates and/or fibrous masses. Anionic clays of the HT type have been of importance in catalysis since 1970. Their interesting properties for catalytic applications are:

- (i) large surface area;
- (ii) basic properties;
- (iii) formation of homogeneous mixtures of oxides with very small crystal size, which on reduction form small and thermally stable metal crystallites;
- (iv) a “memory effect”, which allows reconstruction under mild conditions of the original HT structure when the product of the thermal treatment is contacted with aqueous solutions containing various anions.

Cavani et al. [61], who reviewed this area extensively in 1991, emphasize that all the stages of preparation of a catalyst with a HT-type precursor need precise chemical control to avoid inhomogeneities and chemical segregation.

Three different methods of preparation have been tried so far for HT-type catalysts:

- (i) precipitation (increasing pH method or coprecipitation either at low or at high supersaturation);
- (ii) hydrothermal synthesis and treatments, also ageing;
- (iii) ion-exchange methods.

Since several cases and details for these preparation methods have been given in the review by Cavani et al. [61], only the preparation by Trifiro et al. [62] of a Ni catalyst for steam reforming will be cited here as an illustrative example. The HT-type precursors were prepared by coprecipitation at pH 8 by adding a solution of the nitrates of Mg and Al (or Cr) in the right proportions to a stirred solution of  $\text{NaHCO}_3$ . The precip-

itate was washed with distilled water till the  $\text{Na}_2\text{O}$  content in it was  $<0.02\%$  and then dried at 363 K. By heating the precipitate in air or vacuum in the range 623–1173 K, various catalysts could be prepared with average Ni crystallite sizes ranging from 2 to 100 nm. These catalysts contained a NiO phase, probably containing traces of  $\text{Al}^{3+}$  ions, a spine-type phase, and an alumina-type phase (doped with small amounts of  $\text{Ni}^{2+}$  ions), probably grafted onto the spinel-type phase. This last phase contributes significantly to the surface area of the catalyst samples, but it has little or no influence on their thermal stability or catalytic activity.

Applications of HT-type catalysts, prepared by the above methods, have been reported in recent years for basic catalysis (polymerization of alkene oxides, aldol condensation), steam reforming of methane or naphtha, CO hydrogenation as in methanol and higher-alcohol synthesis, conversion of syngas to alkanes and alkenes, hydrogenation of nitrobenzene, oxidation reactions, and as a support for Ziegler–Natta catalysts (Table 2).

### 2.1.6.3 Conclusions and Prospects

In this section, the main topic has been the use of solid-state transformations to prevent segregation of the composition of solid precursors in a final oxide catalyst. On the whole, crystalline precursors do not permit the desired composition to be achieved, but they can be excellent for some specific cases. Amorphous precursors, especially those using polyfunctional hydroxy acids, of almost any possible composition can be prepared, and can give the corresponding oxides. The initial aim of the method was to prepare solid solutions or oxides of two or several elements in well-defined structures, sometimes containing element substituted within the normal lattice structure. Only one other method has been claimed to offer similar flexibility. This is the sol–gel method (Section A.2.1.4). The two methods have still to be compared in detail. It seems, however, that the kinetics of hydrolysis change very much from one alkoxide to another, with the consequence that the different elements get incorporated in the gel sequentially during gel formation. This phenomenon has the same consequences as the successive precipitation of different elements mentioned above (Fig. 2), namely that the homogeneity of the gel at a molecular scale is not perfect.

When the objective is to prepare an extremely intimate mixture of two or more different oxides, each of them constituted of very small grains or particles, techniques such as spray calcination, oil drop, or freeze drying, the complexation methods (and generally all methods described in Sections B and C above) and the sol–gel method seem to have the same potential in principle. The

use of a particular technique is then dictated by other considerations, such as the availability of starting material (especially for alkoxides) or ease of decomposition.

Finally, a word of caution should be added. The successful transformation of the precursors to a homogeneous oxide or a finely interdispersed mixture of oxides demands that diffusion leading to segregation be made as difficult as possible. In particular, the formation of liquid phases during decomposition and calcination of the precursor should be completely avoided. What cannot be avoided is surface contamination.

Another important consideration in preparing mixed-oxide catalysts is the spontaneous monolayer dispersion of oxides and salts onto surfaces of support substrates on calcination. Both temperature and duration of calcination are important here, as discussed in the reviews by Xie and Tang [63] and by Knözinger and Taglauer [64]. If this dispersion step is inadequate or incomplete, the resulting oxide layer, and any reduced metal surface from it, will not be reproducible: from the same catalyst system therefore, one can then have different catalysts prepared at different times and, of course, from one laboratory to another. Spreading and wetting phenomena in preparation of supported catalysts is discussed in Section A.2.2.1.3.

Heterogeneous catalysts are not just chemicals in the ordinary sense of the word: they are performance chemicals or surface-active materials. Naturally, the performance of the catalyst will depend not so much on the initial composition or surface of it as on the real surface, which is formed and stabilized and then changing dynamically under the prevailing process conditions. Here one has to take into account known and controlled process parameters such as temperature, pressure, reactant concentration, and space velocity, as well as variable factors such as feed composition, and unpredictable or unsuspected factors such as impurities and poisons in the feed [65, 66].

## References

1. C. Marcilly, *Rev. Inst. Fr. Petr.* **1984**, *39*, 189–208.
2. C. Marcilly, J.-P. Franck, *Rev. Inst. Fr. Petr.* **1984**, *39*, 337–364.
3. P. Courty, H. Ajot, C. Marcilly, B. Delmon, *Powder Tech.* **1973**, *7*, 21–38.
4. P. Courty, C. Marcilly in *Preparation of Catalysts I* (Eds B. Delmon, P. A. Jacobs, G. Poncelet), Elsevier, Amsterdam, **1976**, pp. 119–145.
5. P. Courty, C. Marcilly in *Preparation of Catalysts III* (Eds G. Poncelet, P. Grange, P. A. Jacobs), Elsevier, Amsterdam, **1983**, pp. 485–519.
6. B. Delmon, N. de Keyser in *Chemical and Physical Aspects of Catalytic Oxidation*, (Eds. J. L. Portefaix, F. Figueras), CNRS, Lyon, **1978**, pp. 491–534.
7. B. Delmon, P. A. Jacobs, G. Poncelet (Eds), *Preparation of Catalysts I*, Elsevier, Amsterdam, **1976**.
8. B. Delmon, P. Grange, P. A. Jacobs, G. Poncelet (Eds), *Preparation of Catalysts II*, Elsevier, Amsterdam, **1979**.

- 9 G Poncelet, P Grange, P A Jacobs (Eds), *Preparation of Catalysts III*, Elsevier, Amsterdam, 1983
- 10 B Delmon, P Grange, P A Jacobs, G Poncelet (Eds), *Preparation of Catalysts IV*, Elsevier, Amsterdam, 1987
- 11 G Poncelet, P A Jacobs, P Grange, B Delmon (Eds), *Preparation of Catalysts V*, Elsevier, Amsterdam, 1991
- 12 G Poncelet, J Martens, P A Jacobs, P Grange, B Delmon (Eds), *Preparation of Catalysts VI*, Elsevier, Amsterdam, 1995
- 13 M Ruwet, B Delmon, unpublished results
- 14 P G Rouxhet, R E Sempels, *J Chem Soc, Faraday Trans I*, 1974, 70, 2021–2033
- 15 M Haruta, B Delmon, *J Chim Phys*, 1986, 83, 859–868
- 16 S H Overbury, P A Bertrand, G A Somorjai, *Chem Rev* 1975, 75, 547–560
- 17 G A Somorjai, *Chemistry in Two Dimensions Surfaces*, Cornell University Press, Ithaca, NY, 1981
- 18 B Delmon in *Reactivity of Solids* (Eds K Dyrek, J Haber, J Nowotny), Elsevier, Amsterdam, and PWN, Warszawa, 1982, pp 327–369
- 19 B Delmon, *J Chim Phys*, 1986, 83, 875–883
- 20 A M Efstathiou, D Boudouvas, N Vamvouka, X E Venikios, *J Catal* 1993, 140, 1–15
- 21 D Papagiorgio, A M Efstathiou, X E Venikios, *Appl Catal A* 1994, 111, 41–62
- 22 G S Lane, E Miro, E E Wolf, *J Catal* 1989, 119, 161–178
- 23 P Gherardi, O Ruggeri, F Trifiro, A Vaccari, G Del Piero, G Manara, B Notari in *Preparation of Catalysts III* (Eds G Poncelet, P Grange, P A Jacobs), Elsevier, Amsterdam, 1983, pp 723–733
- 24 G Petrini, F Montino, A Bossi, F Garbassi in *Preparation of Catalysts III* (Eds G Poncelet, P Grange, P A Jacobs), Elsevier, Amsterdam, 1983, pp 735–744
- 25 E B M Doesburg, R H Höppener, B de Koning, Xu Xiaoding, J J F Scholten in *Preparation of Catalysts IV* (Eds B Delmon, P Grange, P A Jacobs, G Poncelet), Elsevier Amsterdam, 1987, pp 767–783
- 26 B S Rasmussen, P E Højlund Nielsen, J Villadsen, J B Hansen in *Preparation of Catalysts IV* (Eds B Delmon, P Grange, P A Jacobs, G Poncelet), Elsevier, Amsterdam, 1987, pp 785–794
- 27 W D Kingery, *Introduction to Ceramics*, Wiley, New York, 1960, pp 291–305
- 28 P K Gallager, H M O'Bryan, F Schrey, F R Monforte, *Am Ceram Soc Bull* 1969, 48, 1053–1059
- 29 W F Kladnig, W Karner, *Ceram Bull* 1990, 69, 814–817
- 30 P Reynen, H Bastius, *Powder Metall Int* 1976, 8, 91
- 31 J Paris, R Paris, *Bull Soc Chim Fr* 1965, 1138–1141
- 32 Y Saikali, J M Paris, *Compt Rend (C)* 1967, 265, 1041–1043
- 33 G Paris, G Szabo, R A Paris, *Compt Rend (C)* 1968, 266, 554–556
- 34 C Marcilly, B Delmon, *Compt Rend (C)* 1969, 268, 1795–1797
- 35 P Courty, B Delmon, *Compt Rend (C)* 1969, 268, 1874–1875
- 36 C Marcilly, P Courty, B Delmon, *J Am Ceram Soc* 1970, 53, 56–57
- 37 B Delmon, J Droguest in *Fine Particles 2nd Intern Conf* (Eds W E Kuhn, J Ehretsmann) The Electrochemical Soc., Princeton, 1974, pp 242–255
- 38 M P Pechini, N Adams, US Patent 3 330 697, 1967
- 39 L G Tejuca, J L G Fierro, J M D Tascon, *Adv Catal* 1989, 36, 237–238
- 40 N Yamazoe, Y Teraoka, *Catal Today* 1990, 8, 175–199
- 41 Y Teraoka, H-M Zhang, N Yamazoe, *Proc 9th Internat Congr Catal, Calgary* 1988, pp 1984–1991
- 42 H-M Zhang, Y Teraoka, N Yamazoe, *Appl Catal* 1988, 41, 137–146
- 43 C C Chang, H S Weng, *Ind Eng Chem Res* 1992, 31, 1615–1621
- 44 E Boellaard, A M van der Kraan, J W Geus, in (Eds G Poncelet, J Martens, P A Jacobs, P Grange, B Delmon) *Preparation of Catalysts VI*, Elsevier, Amsterdam, 1995, pp 931–940
- 45 E Boellaard, *Supported Iron (Alloy) Catalysts from Complex Cyanides*, Ph D Thesis, Univ Utrecht, 1994
- 46 Ph Courty, H Ajot, B Delmon, *C R Acad Sc*, 1973, 276C, 1147–1150
- 47 Ph Courty, H Ajot, B Delmon (Institut Français du Pétrole), French Patent 1 600 128, 1970, Belgian Patent 743 578, 1970
- 48 Ph Courty, H Ajot, B Delmon (Institut Français du Pétrole), French Patent 2 031 818, 1970, Belgian Patent 745 024 1970
- 49 Ph Courty, H Ajot, B Delmon (Institut Français du Pétrole), German Patent 1 965 176, 1970
- 50 Institut Français du Pétrole French Patents 2 060 171 1969, 2 082 444, 1970, US Patents 3 716 497, (1973), 3 846 341 (1974), 3 975 302, (1976), 4 000 085, (1976), 4 141 861, (1979)
- 51 Ph Courty, H Ajot, B Delmon, unpublished results (1967)
- 52 S Beran, B Wichterlova, H G Karge, *J Chem Soc Faraday Trans* 1990, 86, 3033–3037, and references cited therein See also C Jia, P Massiani, P Beaunier, D Barthomeuf *Appl Catal A* 1993, 106, L185–L191
- 53 F Toda, K Nanaka, A Sekikawa, *J Chem Soc Chem Commun* 1987, 279–280
- 54 M Ogawa, K Kuroda, C Kato, *Chem Lett* 1989, 1659
- 55 M Ogawa, T Hashisume, K Kuroda, C Kato, *Inorg Chem* 1991, 30, 584–585
- 56 M Ogawa, T Handa, K Kuroda, C Kato, *Chem Lett* 1990, 71
- 57 M Crocker, R H M Herold, C A Emeis, M Krijger *Catal Lett*, 1992, 15, 339–345
- 58 H G Karge, Y Zhang, H K Beyer, *Catal Lett* 1992, 12, 147–156
- 59 V Kanazirev, G L Price, K M Dooley in *Zeolite Chemistry and Catalysis* (Eds P A Jacobs et al), Elsevier Amsterdam, 1991, p 277–285
- 60 V Kanazirev, V Valtchev, M P Tarassov, *J Chem Soc Chem Commun* 1994, 1043–1044
- 61 P Cavani, F Trifiro, A Vaccari, *Catal Today*, 1991, 11, 173–301
- 62 F Trifiro, A Vaccari, O Clause, *Catal Today* 1994, 21, 185–195
- 63 Y C Xie, Y Q Tang, *Adv Catal* 1991, 37, 1–43
- 64 H Knozinger, E Taglauer, *Catalysis*, The Royal Society of Chemistry, Cambridge, 1993, Vol 10, 1–40
- 65 P G Menon, *Catal Today* 1991, 11, 161–172
- 66 P G Menon, *Chem Rev* 1994, 94, 1021–1046

## 2.1.7 Heteropoly Compounds

K.-Y. LEE AND M. MISONO

### 2.1.7.1 Structure and Catalytic Properties

Heteropolyanions are polymeric oxoanions (polyoxo metalates) formed by condensation of more than two



kinds of oxoanions [1]. The term heteropoly compound (HPA) is used for the acid forms and the salts. Other HPA-related compounds are organic and organometallic complexes of polyanions.

Heteropolyanions are composed of oxides of addenda atoms (V, Nb, Mo, W, etc.) and heteroatoms (P, Si, etc.). Various elements which are shown in Table 1 can be the addenda atoms and heteroatoms [2]. The structures are classified into several groups based on the similarity of the composition and structure, for example: Keggin-type,  $\text{XM}_{12}\text{O}_{40}^{n-}$ ; Silverton-type,  $\text{XM}_{12}\text{O}_{42}^{n-}$ ; Dawson-type,  $\text{X}_2\text{M}_{18}\text{O}_{62}^{n-}$ ; Strandberg-type,  $\text{X}_2\text{M}_5\text{O}_{23}^{n-}$ ; Anderson-type,  $\text{XM}_6\text{O}_{24}^{n-}$ ; and Lindqvist-type,  $\text{XM}_6\text{O}_{24}^{n-}$ , where X is heteroatom and M is addenda atom [3]. Structural isomers and lacunary polyanions are also known. Keggin-type anions, of which the catalytic activity has been extensively examined, are the main subject of this chapter. For HPAs in the solid state, the primary structure (polyanions), the secondary (three-dimensional arrangement of polyanions, counter cations, water of crystallization, etc.) and the tertiary structures (particle size, pore structure, etc.) are differentiated (Fig. 1) [4, 5]. Not only the primary and secondary structures, but also tertiary and higher-order structures are influential in the catalytic function. In this respect, the preparation process and resulting structure are very important.

There are three prototypes of heterogeneous catalysis with heteropoly compounds as shown in Fig. 2 [4, 5]. Actual cases could be intermediate and vary by the kind of heteropoly compounds, reacting molecules, and reaction conditions. Ordinary heterogeneous catalysis is the surface type, where the catalytic reaction takes place on a two-dimensional surface. Bulk type I is the reaction in the pseudoliquid phase. The secondary structure (Fig. 1b) of certain HPAs is flexible and polar molecules are readily absorbed in interstitial positions of the solid bulk to form the pseudoliquid phase. Bulk type II has been demonstrated for several catalytic oxidations at relatively high temperatures. The reaction fields for the bulk types are three-dimensional.

For acid catalysis, the rates of bulk-type reactions show close correlations with the bulk acidity, while the catalytic activities for surface-type reactions are related to the surface acidity which is sensitive to the surface composition and often change randomly. Similarly, in the case of oxidation catalysis, good correlations exist between the oxidizing ability of catalyst and the catalytic activity for oxidation in both bulk-type and surface-type reactions. Acid and redox bifunctionality is another characteristic of HPAs. For example, the acidity and oxidizing ability work cooperatively for the oxidation of methacrolein, whereas they function competitively for the oxidative dehydrogenation of isobutyric acid [5]. Interestingly, the former is of surface type and the latter of bulk type.

Heteropoly compounds are useful as catalysts due to the following unique characteristics:

- (i) acidic properties and oxidizing ability are systematically controllable;
- (ii) Polyanions are well-defined oxide clusters, hence, catalyst design at the molecular level is possible;
- (iii) Unique reaction environment, such as the pseudoliquid phase, is available, and catalytically useful coordination is possible.

Some HPAs in the solid state are thermally quite stable and suitable for vapor-phase reactions conducted at high temperatures. The thermal stability is in the order  $\text{H}_3\text{PW}_{12}\text{O}_{40} > \text{H}_4\text{SiW}_{12}\text{O}_{40} > \text{H}_3\text{PMO}_{12}\text{O}_{40} > \text{H}_4\text{SiMO}_{12}\text{O}_{40}$  and can be enhanced by the formation of appropriate salts [5–8].

Attempts to utilize HPAs as catalysts have a long history [5]. A bench-scale test was reported for alkylation of aromatics in 1971. The first industrial process using a HPA catalyst was launched in 1972, for the hydration of propene in the liquid phase. The essential role of the Keggin structure for the oxidation of methacrolein was indicated in a patent in 1975. Systematic basic research into heterogeneous catalysis started in the mid 1970s to elucidate the quantitative correlations between the acid–redox properties and catalytic performance of HPAs. Pseudoliquid phase (bulk-type I catalysis) was reported in 1979 and the bulk-type II behavior in 1983 [5]. Similar efforts for homogeneous systems were also carried out in the same period. In the 1980s, several new large-scale industrial processes (e.g. the oxidation of methacrolein, the hydration of isobutene and *n*-butene, and the polymerization of tetrahydrofuran) were initiated by using HPA catalysts [4, 9]. Typical reactions catalyzed by HPAs are shown in Tables 2–6.

### 2.1.7.2 Heteropolyacids – Acid Forms in Solid State and in Solution

Heteropolyacids are also Brønsted acids in the solid state. Their acidities depend on the constituent elements and their structure.  $\text{H}_3\text{PW}_{12}\text{O}_{40}$  (Keggin type) and its acidic salts are especially strong acids. The color changes of indicators show that solid  $\text{H}_3\text{PW}_{12}\text{O}_{40}$  (anhydrous) is a very strong acid with Hammett acidity function  $H_0 < -8$  [10a], and a superacid,  $H_0 < -13.16$  [10b]. Thermal desorption of pyridine shows that a significant amount of pyridine (equal to the number of protons of the whole bulk) remains for  $\text{H}_3\text{PW}_{12}\text{O}_{40}$  at 573 K, while pyridinium ions adsorbed on  $\text{SiO}_2\text{--Al}_2\text{O}_3$  are completely removed at the same temperature (Fig. 3) [11, 12]. This strong acidity of the heteropolyacid can be attributed to the large size of



Table 2. Homogeneous acid-catalyzed reactions.

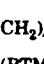
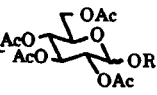
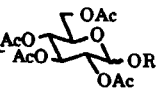


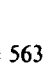
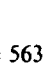




Reaction	Catalyst	Remarks	Reference
Hydration of olefins	$\text{H}_3\text{PW}_{12}\text{O}_{40}$	$T = 313\text{--}423\text{ K}$	102(a)
$n$  $\longrightarrow$ $\text{HO} \left[ (\text{CH}_2)_4\text{-O} \right]_n \text{H}$ (PTMG)	$\text{H}_3\text{PW}_{12}\text{O}_{40} \cdot n\text{H}_2\text{O}$ ( $n = 0\text{--}6$ )	$T = 333\text{ K}$ , $\text{MW} \approx 3000$	102(b)
 + $\text{ROH} \longrightarrow$ 	$\text{H}_3\text{PW}_{12}\text{O}_{40}$ $\text{H}_6\text{P}_2\text{W}_{18}\text{O}_{62}$	$T = 298\text{ K}$ , yield = 60–98% (2 h) $T = 315\text{ K}$ , selectivity $\approx 100\%$	102(c) 102(d)
 + $\text{CH}_3\text{OH} \longrightarrow$ 	$\text{H}_3\text{PW}_{12}\text{O}_{40}$ $\text{H}_3\text{PMO}_{12}\text{O}_{40}$	$T = 298\text{ K}$	102(e)
$3\text{ C}_2\text{H}_5\text{CHO} \longrightarrow$ trimer			

Table 3. Heterogeneous acid-catalyzed reactions.

Reaction	Catalyst	Remarks	Reference
$\text{CH}_3\text{COOH} + \text{C}_2\text{H}_5\text{OH} \longrightarrow \text{CH}_3\text{COOC}_2\text{H}_5 + \text{H}_2\text{O}$	$\text{H}_3\text{PW}_{12}\text{O}_{40}$	$T = 423\text{ K}$ , selectivity = 91% (90% conv.)	103(a)
Alkylation of aromatics	$\text{H}_3\text{PW}_{12}\text{O}_{40}$	$T = 303\text{--}373\text{ K}$ ,	103(b)
Alkylation of alkanes	$\text{Cs}_{2.5}\text{H}_{0.5}\text{PW}_{12}\text{O}_{40}$	$T = 293\text{ K}$ , $P = 5\text{ kg cm}^{-2}$	103(c)
Isomerization of alkanes	$\text{Pd}_{1.5}\text{PW}_{12}\text{O}_{40}$	$T = 483\text{ K}$	103(d)
$\text{CH}_3\text{OH}$ ( $\text{CH}_3\text{OCH}_3$ ) $\longrightarrow$ $\text{C}_1\text{--C}_6$ Hydrocarbons	$\text{H}_3\text{PW}_{12}\text{O}_{40}$ $\text{H}_3\text{PW}_{12}\text{O}_{40}$	$T = 348\text{ K}$ $T = 573\text{ K}$ ,	101, 103(e)
 + $\text{CH}_3\text{OH} \longrightarrow$ 	$\text{Cs}_{2.5}\text{H}_{0.5}\text{PW}_{12}\text{O}_{40}$	$T = 563\text{ K}$ , selectivity ( $\text{C}_2\text{--C}_4$ alkenes) = 74%	103(f)
 + $\text{HNO}_3 \longrightarrow$ 	$\text{H}_6\text{P}_2\text{W}_{18}\text{O}_{62}$	$T = 323\text{ K}$	103(g)
 + $(\text{CH}_3\text{CO})_2\text{O} \longrightarrow$ 	$\text{Cs}_{1.5}\text{H}_{1.5}\text{PMO}_{12}\text{O}_{40}$ $\text{Cs}_{2.5}\text{H}_{0.5}\text{PMO}_{12}\text{O}_{40}$	$T = 413\text{ K}$ , selectivity = 97% (94% conv.) $T = 573\text{ K}$	103(h) 103(i)

Heteropolyacids are much more active than mineral acids for several types of homogeneous reactions in both organic solvents and aqueous solution [4, 8]. The enhancement is generally greater in organic solvents. For the hydration of isobutene in a concentrated aqueous HPA solution (above  $1.5\text{ mol dm}^{-3}$ ), the reaction rate is about 10 times greater than for mineral acids [21]. This rate enhancement is attributed to the combination of stronger acidity, stabilization of protonated intermediates, and increased solubility of alkenes [21]. In this case, the selectivity is also much improved with HPA catalysts.

The catalytic behavior of HPA depends on the basicity of reactants [22]. For the decomposition of weakly basic isobutyl propionate, the catalytic activities of the heteropolyacids are 60–100 times higher than those of  $\text{H}_2\text{SO}_4$  and *p*-toluenesulfonic acid, and the catalytic activity decreases in the order of  $\text{H}_3\text{PW}_{12}\text{O}_{40} > \text{H}_4\text{SiW}_{12}\text{O}_{40} \approx \text{H}_4\text{GeW}_{12}\text{O}_{40} > \text{H}_5\text{BW}_{12}\text{O}_{40} > \text{H}_6\text{CoW}_{12}\text{O}_{40}$ . This is also the order of the acid strength in solution, which increases with the decrease in the negative charge of the polyanion [15, 16, 23, 24]. Izumi et al. [23] indicated that the catalytic activities in nonaqueous solutions were related to the acidity of the

Table 4. Homogeneous oxidation reactions.

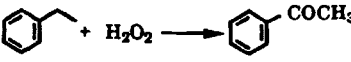
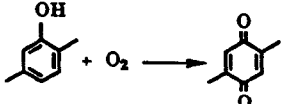
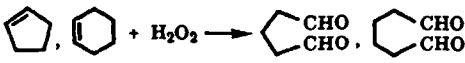
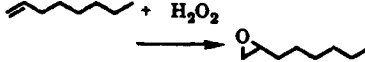
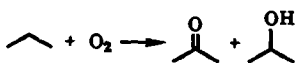
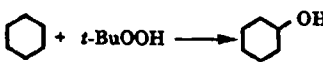
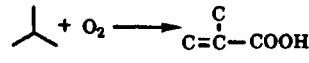
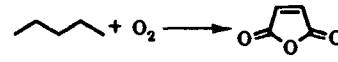
Reaction	Catalyst	Remarks	Reference
	H <sub>3</sub> PMo <sub>12</sub> O <sub>40</sub>	reflux, selectivity = 100%	104(a)
	H <sub>5</sub> PMo <sub>10</sub> V <sub>2</sub> O <sub>40</sub>	T = 333 K, O <sub>2</sub> = 1 atm, yield = 80%	104(b)
	H <sub>3</sub> PMo <sub>6</sub> W <sub>6</sub> O <sub>40</sub>	T = 303 K	2(b)
	H <sup>+</sup> /WO <sub>4</sub> <sup>2-</sup> /PO <sub>4</sub> <sup>3-</sup> /QX (CP) <sub>3</sub> PW <sub>12</sub> O <sub>40</sub> CP = cetylpyridinium ion	T = 343 K, yield = 82% T = 333 K, yield = 76%	104(c) 104(d)
	H <sub>7</sub> PW <sub>9</sub> Fe <sub>2</sub> NiO <sub>37</sub>	T = 423 K, turnover number = 9730 (3 h)	104(e)
	PW <sub>11</sub> CoO <sub>39</sub> <sup>5-</sup>	T = 298 K	67(c)

Table 5. Heterogeneous oxidation reactions.

Reaction	Catalyst	Remarks	Reference
$\text{CH}_2=\text{C}(\text{CH}_3)\text{CHO} + \text{O}_2 \longrightarrow \text{CH}_2=\text{C}(\text{CH}_3)\text{COOH}$	CsH <sub>3</sub> PVMo <sub>11</sub> O <sub>40</sub>	T = 553 K, selectivity = 80–85%	45, 105(a)
	H <sub>3</sub> PMo <sub>12</sub> O <sub>40</sub>	T = 623 K, selectivity = 45%	105(b)
$\text{CH}_3\text{CH}(\text{CH}_3)\text{COOH} \longrightarrow \text{CH}_2=\text{C}(\text{CH}_3)\text{COOH}$	H <sub>5</sub> PV <sub>2</sub> Mo <sub>10</sub> O <sub>40</sub>	T = 573 K, selectivity = 72% (52% conv.)	49, 105(c)
	H <sub>5</sub> PV <sub>2</sub> Mo <sub>10</sub> O <sub>40</sub>	T = 583 K, selectivity = 55%	105(d)

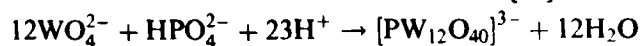
heteropolyacid solution and the softness of the polyanion. In dilute aqueous solutions, however, the softness becomes more important, since most heteropolyacids are nearly completely dissociated [23]. For some reactions involving basic molecules such as alcohols, no large differences in activity among these catalysts including H<sub>2</sub>SO<sub>4</sub> and *p*-toluenesulfonic acid are observed [22]. This is probably due to the leveling effect.

Heteropolyacids are good multielectron oxidants due to the presence of Mo<sup>6+</sup>, W<sup>6+</sup>, and V<sup>5+</sup> and the charge delocalizability in the polyanion structure. Generally, the oxidizing ability decreases in the order V- > Mo- > W-containing heteropolyanions [13]. The reduction potential decreases linearly with a decrease in the valence of the central atom or an increase in the negative charge of the heteropolyanions: PW<sub>12</sub>O<sub>40</sub><sup>3-</sup> >

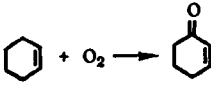
GeW<sub>12</sub>O<sub>40</sub><sup>4-</sup> ≈ SiW<sub>12</sub>O<sub>40</sub><sup>4-</sup> > FeW<sub>12</sub>O<sub>40</sub><sup>5-</sup> ≈ BW<sub>12</sub>O<sub>40</sub><sup>5-</sup> > CoW<sub>12</sub>O<sub>40</sub><sup>6-</sup> > CuW<sub>12</sub>O<sub>40</sub><sup>7-</sup> [13, 14]. This property is well reflected in their catalytic activities. For cyclohexene oxidation with hydrogen peroxide, the catalytic activity increased in the order B<sup>3+</sup> < Si<sup>4+</sup> < C<sup>4+</sup> ≤ P<sup>5+</sup> [25, 26]. Cetylpyridinium salts of HPA can be used as phase-transfer catalysts and catalyze epoxidation of alkenes very efficiently in a two-phase system comprising aqueous H<sub>2</sub>O<sub>2</sub> and CHCl<sub>3</sub> [27].

#### A Preparation

The typical method for the preparation of heteropolyacids is the acidification of aqueous solutions of oxoanions of addenda atoms and heteroatoms [1b]:



**Table 6.** Heteropoly-metal multifunctional catalysts.

Reaction	Catalyst	Reference
$RCH=CH_2 + 1/2O_2 \longrightarrow RCHOCH_3$	$PMo_{12-n}V_nO_{40}^{3+n} + PdSO_4$	13, 60
$C_6H_6 + 1/2O_2 \longrightarrow (C_6H_5)_2$	$PMo_{12-n}V_nO_{40}^{3+n} + Pd(OCOCH_3)_2$	13, 60
$PhNO_2 + 3CO + CH_3OH \longrightarrow PhNHCO_2CH_3 + 2CO_2$	$H_5PMo_{10}V_2O_{40} + PdCl_2$	63, 106a
	$[(n-C_4H_9)_4N]_5Na_3[(1,5-cod) \cdot IrP_2W_{15}Nb_3O_{62}]$	71
$\equiv C-OH + H_2 \longrightarrow \equiv C-OH$	$Li_4SiMo_{12}O_{40} + RhCl(PPh_3)_3$	64
$CH_3OH + CO \longrightarrow CH_3COOH$	$RhPW_{12}O_{40}/SiO_2$	106b

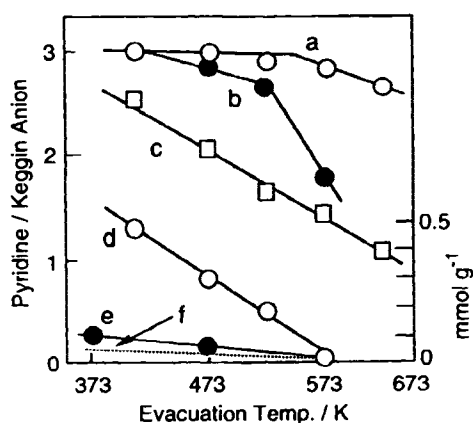


**Figure 3.** Thermal desorption of pyridine: (a)  $H_3PW_{12}O_{40}$ , (b)  $H_3PMo_{12}O_{40}$ , (c)  $NaH_2PW_{12}O_{40}$ , (d)  $Na_3PW_{12}O_{40}$ , (e)  $Cs_3PW_{12}O_{40}$ , (f)  $SiO_2-Al_2O_3$ . Pyridine ab(sorbed) at 298 K was desorbed at each temperature for 1 h by evacuation.

Acidification is generally achieved by the addition of mineral acids. The rates of formation are large, so that the polyanions can be crystallized from stoichiometrically acidified mixtures of the components at room temperature. Although the stoichiometry is often a good guide to the preparation, in some cases an excess heteroatom, the addition of small amount of oxidants, or careful control of temperature and pH is necessary.

The hydrolysis and condensation are usually fast and depend on the pH as well as on the solvent. For example,  $PW_{12}O_{40}^{3-}$  starts to decompose above pH 2 and coexists with  $PW_{11}O_{39}^{7-}$  and  $PW_9O_{34}^{9-}$  [28]. In this respect, pure  $PW_{12}O_{40}^{3-}$  should be isolated as free acid by the extraction by ether, the so-called etherate method. If a very acidic solution of the heteropolyanion is shaken with excess diethyl ether, three phases separate: a top ether layer, a middle aqueous layer, and a bottom

heteropoly-etherate. The bottom layer is drawn off, shaken with excess ether to remove entrained aqueous solution, and separated again. The etherate is decomposed by the addition of water, the ether is removed, and the aqueous solution of the heteropolyacid is allowed to evaporate until crystallization occurs [1].

By this general method, heteropolyacids containing various kinds of heteroatoms can be prepared:  $H_3PW_{12}O_{40} \cdot 30H_2O$  is prepared from  $Na_2WO_4 \cdot 2H_2O$  and  $Na_2HPO_4$  [29];  $H_4SiW_{12}O_{40} \cdot 22H_2O$  from  $Na_2WO_4$  and  $Na_2SiO_3 \cdot 9H_2O$  [30];  $H_4GeW_{12}O_{40} \cdot 7H_2O$  from  $Na_2WO_4 \cdot 2H_2O$  and  $GeO_2$  [22];  $H_5BW_{12}O_{40} \cdot 15H_2O$  from  $Na_2WO_4 \cdot 2H_2O$  and  $H_3BO_3$  [31]; and  $H_6CoW_{12}O_{40} \cdot 19H_2O$  from  $Na_2WO_4 \cdot 2H_2O$  and  $Co(OCOCH_3)_2 \cdot 4H_2O$  [22, 32]. The number of water molecules included in the crystal is variable in all these cases. The structure can be identified by IR, NMR, XRD, etc. [1b, 5].

### 2.1.7.3 Salts of Heteropolyacids – Cation-Exchanged Forms

Salts of heteropolyacids can be divided into two groups according to Niiyama et al. [5, 7]: the salts of small cations such as Na and Cu (group A salts) and salts of large cations like Cs, K, and  $NH_4$  (group B salts). The behavior of group A salts is similar to that of the acid forms, but is very different in several respects from group B salts. Group A salts can exhibit pseudoliquid behavior and are very soluble in water and other polar solvents, whereas group B salts are generally insoluble and have high surface areas. Organic salts also exist, but very few studies on their thermal stability and catalytic function have been reported. The thermal stability of group B salts is high (no decomposition occurs

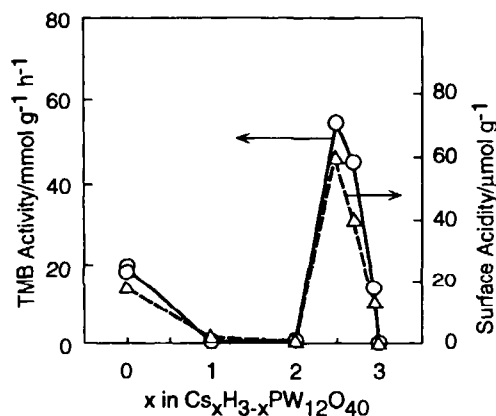


**Figure 4.** Changes in catalytic activity for the alkylation of 1,3,5-trimethylbenzene (TMB) with cyclohexene and surface acidity (number of protons on the surface) as a function of Cs content in  $\text{Cs}_x\text{H}_{3-x}\text{PW}_{12}\text{O}_{40}$ .

below their melting points, for example; the melting points of K and Cs salts of  $\text{H}_3\text{PMO}_{12}\text{O}_{40}$  are reported to be 913 and 963 K, respectively [6]). This is probably due to the absence of protons and water in the lattice of B salts, as the decomposition starts with the formation of water from oxygen of the polyanion and protons (or water) in the lattice.

The group B salts of  $\text{H}_3\text{PW}_{12}\text{O}_{40}$  are also strong acids unless they are stoichiometrically neutralized. These salts catalyze various kinds of reactions in the liquid phase as solid catalysts. For the alkylation of 1,3,5-trimethylbenzene with cyclohexene, the activity of  $\text{Cs}_{2.5}\text{H}_{0.5}\text{PW}_{12}\text{O}_{40}$  (abbreviated as  $\text{Cs}_{2.5}\text{W}$ ) is much higher than those of  $\text{SO}_4^{2-}/\text{ZrO}_2$  and Nafion. Here,  $\text{Cs}_{2.5}\text{W}$  is not soluble and the reactions take place on the surface of the solid.

For  $\text{Cs}_x\text{H}_{3-x}\text{PW}_{12}\text{O}_{40}$  (a typical group B salt), the catalytic activity changes dramatically with the extent of neutralization by Cs (Fig. 4).  $\text{Cs}_{2.5}\text{W}$  shows the highest catalytic activity, which is even higher than the acid form. This is in contrast to Na salts (group A salts), where the activity as well as the acidity decreases monotonically with the Na content [33]. The acid strength of  $\text{Cs}_{2.5}\text{W}$  is almost the same as that of  $\text{H}_3\text{PW}_{12}\text{O}_{40}$  according to temperature programmed desorption (TPD) of  $\text{NH}_3$  [34].  $\text{Cs}_{2.5}\text{W}$  consists of very fine particles (particle size 8–10 nm, surface area 100–200  $\text{m}^2\text{g}^{-1}$ ). Solid-state  $^{31}\text{P}$  NMR reveals that all protons in the salts are distributed randomly, indicating that nearly uniform acidic salts are formed [4]. The same  $^{31}\text{P}$  NMR spectrum is observed after heat treatment of a sample prepared by the impregnation of  $\text{H}_3\text{PW}_{12}\text{O}_{40}$  on the  $\text{Cs}_3\text{W}$  salt, indicating the formation of the same solid solution by the diffusion of Cs ion and proton. By assuming a uniform distribution of protons, the surface acidity (the number of protons on the surface) of the Cs salts can be estimated from the

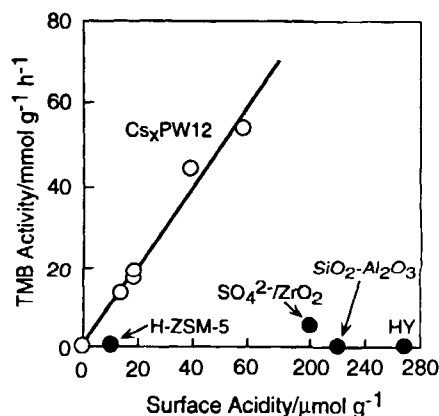


**Figure 5.** Catalytic activity of  $\text{Cs}_x\text{H}_{3-x}\text{PW}_{12}\text{O}_{40}$  for alkylation of 1,3,5-trimethylbenzene (TMB) with cyclohexene as a function of surface acidity. The surface acidity is the number of protons on the surface (external surface for zeolites).

proton content in the bulk and the specific surface area. When the catalytic activities are plotted against the surface acidity estimated in this way, a good linear correlation is found (Fig. 5) [10b], indicating that the high activity of  $\text{Cs}_{2.5}\text{W}$  is due to its high surface acidity. It is also noteworthy in Fig. 5 that the activities per unit acidity are much greater for Cs salts than for  $\text{SiO}_2\text{-Al}_2\text{O}_3$ ,  $\text{SO}_4^{2-}/\text{ZrO}_2$ , and zeolites. This indicates the presence of additional effects such as acid–base bifunctional acceleration by the cooperation of acidic protons and the basic polyanions.

The acid strength of the acid forms in the solid state usually reflects the one in solution, but the acidic properties of the salts in the solid state are more complicated in general. Five mechanisms are possible for the generation of acidity in metallic salts [5]:

- (i) protons in acidic salts, as for Cs salts as described above;
- (ii) partial hydrolysis of polyanions to form weakly acidic protons;
- (iii) acidic dissociation of water coordinated with multivalent metal ions;
- (iv) Lewis acidity of multivalent metal ions;
- (v) protons formed by the reduction of metal ions with hydrogen.

The redox properties can also be controlled by the formation of salts. However, the relationship between these properties and the catalytic activity for oxidation is not sufficiently clarified. For example, it was reported that the activity order for alkali salts was reversed by the reaction temperature [35]. Nevertheless, good correlations are obtained if the concept of surface- and bulk-type catalysis is appropriately considered [4, 36–38]. The reduction by  $\text{H}_2$  of free acid and group A salts proceeds both on the surface and in the

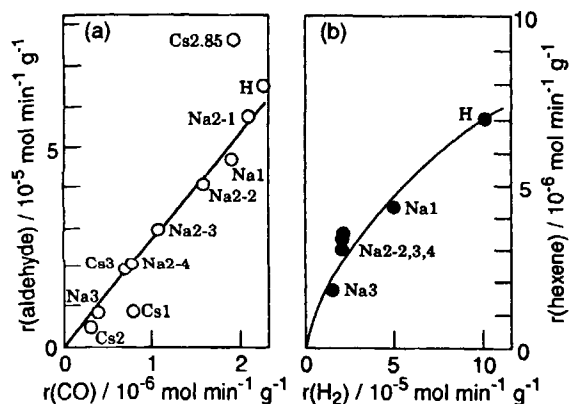


**Figure 6.** Correlations between catalytic activity and oxidizing ability: (a) oxidation of acetaldehyde (surface type) and surface oxidizing ability; (b) oxidative dehydrogenation of cyclohexene (bulk type) and bulk oxidizing ability [4, 38] ( $r(\text{aldehyde})$  and  $r(\text{hexene})$  are the rates of catalytic oxidation of acetaldehyde and cyclohexene, respectively).

bulk due to the diffusion of protons and electrons, whereas reduction by CO occurs only near the surface. Hence, the rate of reduction by  $\text{H}_2$  represents the oxidizing ability of the catalyst bulk ( $r[\text{H}_2]$ ), while the rate of reduction by CO expresses the oxidizing ability of the surface ( $r[\text{CO}]$ ). Figure 6(a) shows the correlation of the rates of oxidation of acetaldehyde (surface type) with the surface oxidizing ability ( $r[\text{CO}]$ ). In Fig. 6(b), a similar relationship between the rate of oxidative dehydrogenation of cyclohexene (bulk type) and the bulk oxidizing ability ( $r[\text{H}_2]$ ) is presented. Only a poor correlation exists if the former reaction (surface) is plotted against the bulk oxidizing ability. In this way, the catalytic activity and the oxidizing ability of Na salts decrease monotonically with the Na content for both reactions. However, for the oxidations over  $\text{Cs}_x\text{H}_{3-x}\text{PMo}_{12}\text{O}_{40}$ , activity patterns are similar to that in Fig. 4 due to differences in the surface area and secondary structures [4].

Redox properties of  $\text{H}_{3+x}\text{PMo}_{12-x}\text{V}_x\text{O}_{40}$  have been examined by many researchers in relation to selective partial oxidations. However, their oxidizing abilities remain controversial [5]. One reason is that these catalysts are unstable at high temperatures. For example, in the case of oxidative dehydrogenation of isobutyric acid over acidic Cs salts of 12-molybdovanadophosphoric acids ( $\text{Cs}_n\text{H}_{4-n}\text{PMo}_{11}\text{VO}_{40}$ ,  $\text{Cs}_n\text{Mo}_{11}\text{V}$ ),  $\text{Cs}_{2.75}\text{Mo}_{11}\text{V}$  was very efficient: 97% conversion and 78% selectivity to methacrylic acid (MAA) at 623 K, as compared to 40% conversion and 52% selectivity for  $\text{Mo}_{11}\text{V}$  (acid form) [39].  $\text{Mo}_{11}\text{V}$  is significantly decomposed during the pretreatment in  $\text{O}_2$  at 623 K, while  $\text{Cs}_{2.75}\text{Mo}_{11}\text{V}$  decomposes only slightly. The improved thermal stability probably enabled the use of the controlled redox ability.

Noble metal salts of heteropolyacids function in novel ways as catalysts.  $\text{Pd}_{1.5}\text{PW}_{12}\text{O}_{40}$  supported on

$\text{SiO}_2$  catalyzes the skeletal isomerization of hexane in the presence of hydrogen more efficiently than the parent compound  $\text{H}_3\text{PW}_{12}\text{O}_{40}$  [40, 41]. The isomerization rate depends reversibly on the hydrogen partial pressure. The role of hydrogen is thought to be twofold. It dissociates on the surface of metallic palladium and spilled-over hydrogen atoms not only become acidic protons but also suppress coke formation, thus ensuring higher steady activity and longer catalytic life.

Acid sites of  $\text{Ag}_3\text{PW}_{12}\text{O}_{40}$  are generated upon the reduction with hydrogen at 573 K [40, 42]. After the reduction, the catalytic activity (for example, for *o*-xylene isomerization) develops. The generation of acid sites has been confirmed by pyridine adsorption and solid state  $^1\text{H}$  NMR [42].

### A Preparation

Isolation of the polyanions from solution is generally achieved by the addition of an appropriate counter cation, usually alkali metal, ammonium or tetraalkylammonium ion [1].

Acidic Cs salts of  $\text{H}_3\text{PW}_{12}\text{O}_{40}$  are prepared from aqueous solutions of heteropolyacids and  $\text{Cs}_2\text{CO}_3$ . The compound  $\text{H}_3\text{PW}_{12}\text{O}_{40} \cdot 20\text{H}_2\text{O}$ , which is prepared as described above, is evacuated at 323 K to form  $\text{H}_3\text{PW}_{12}\text{O}_{40} \cdot 6\text{H}_2\text{O}$ . Commercial  $\text{Cs}_2\text{CO}_3$  is dehydrated by evacuation at 693 K for 2 h, prior to use for the preparation of an aqueous solution of  $\text{Cs}_2\text{CO}_3$ . The acidic cesium salts ( $\text{Cs}_x\text{H}_{3-x}\text{PW}_{12}\text{O}_{40}$ ,  $\text{Cs}_x\text{W}$ ) are prepared by the titration of aqueous solution of  $\text{H}_3\text{PW}_{12}\text{O}_{40}$  ( $0.08 \text{ mol dm}^{-3}$ ) with aqueous solution of  $\text{Cs}_2\text{CO}_3$  ( $[\text{Cs}^+] = 0.25 \text{ mol dm}^{-3}$ ), where the aqueous solution of  $\text{Cs}_2\text{CO}_3$  is added dropwise to the  $\text{H}_3\text{PW}_{12}\text{O}_{40}$  solution at room temperature at a controlled rate ( $1 \text{ ml min}^{-1}$ ) [34, 43]. The white colloidal solution obtained is evaporated to solid at 323 K. The surface area changes considerably with the Cs content and the method of preparation. For example, the surface area of  $\text{H}_3\text{PW}_{12}\text{O}_{40}$  is  $5 \text{ m}^2 \text{ g}^{-1}$ , whereas for  $\text{Cs}_x\text{H}_{3-x}\text{PW}_{12}\text{O}_{40}$  prepared as above it is 1, 1, 135, and  $156 \text{ m}^2 \text{ g}^{-1}$  for  $x = 1, 2, 2.5,$  and 3, respectively, after the treatment at 573 K. Just after evaporation,  $\text{Cs}_2\text{W}$  appears to be a mixture of nonacidic  $\text{Cs}_3\text{W}$  covered by the acid form whereas  $\text{Cs}_1\text{W}$  is a mixture of acid form and  $\text{Cs}_2\text{W}$ .  $\text{Cs}_{2.2}\text{W}$  and  $\text{Cs}_{2.5}\text{W}$  have basically the same structure as  $\text{Cs}_2\text{W}$ , except that the amount of acid form covering the  $\text{Cs}_3\text{W}$  surface is much lower for  $\text{Cs}_{2.2}\text{W}$  and  $\text{Cs}_{2.5}\text{W}$ , which brings about the high surface area and unique shape selectivity [44]. As described above, random distribution of  $\text{Cs}^+$  and  $\text{H}^+$  occurs during drying and calcination to form nearly uniform acidic salts.

#### 2.1.7.4 Mixed-Coordinated Heteropoly Compounds

Molybdenum–vanadium mixed-coordinated HPAs are active for several selective oxidations in both homo-

geneous and heterogeneous systems. The main component of commercial catalysts for the oxidation of methacrolein to methacrylic acid is an acidic Cs salt of  $H_{3+x}PMo_{12-x}V_xO_{40}$  ( $x = 1-2$ ) [9, 45, 46]. For the oxidative dehydrogenation of isobutyric acid over  $Cs_{2.75}H_{0.25+x}PMo_{12-x}V_xO_{40}$ , the activity increased in the order of  $x = 1 > x = 2 > x = 0$  and the methacrylic acid (MAA) selectivity was  $x = 1 \geq x = 2 > x = 0$  [39]. Although various studies of mixed-coordinated HPA catalysts have been reported, their stability and redox properties remain controversial [47-49]. The compound  $Na_5PMo_{10}V_2O_{40}$ , supported on active carbon, is active for the oxidative dehydrogenation of benzylic alcohols and amines without overoxidation of benzaldehyde and benzylamine [50]. The mechanism of the aerobic oxidative dehydrogenation of  $\alpha$ -terpinene to *p*-cymene in solution with mixed-coordinated  $PMo_{10}V_2O_{40}^{5-}$  has recently been reported [51].

Molybdenum-tungsten mixed-coordinated HPA shows a remarkable synergistic effect for, for example, the formation of dialdehydes from alkenes [26, 52]. Compounds of the type  $H_3PMo_{12-x}W_xO_{40}$  ( $Mo_{12-x}W_x$ ,  $x = 0-12$ ), prepared by the conventional method, are statistical mixtures of 13 mixed-coordinated heteropolyacids [26, 53]. For the oxidation of cyclopentene by  $H_2O_2$  in tri-*n*-butylphosphate solution,  $Mo_6W_6$  shows the highest yield of aldehyde, much higher than  $Mo_{12}$  and  $W_{12}$  alone or a mechanical mixture of them (Fig. 7). The selectivity of concurrent formation of diol increases with the ratio of W to Mo, reflecting the acidity. The synergistic effect is explained quantum chemically by the increase in the stability of reduced states of mixed-coordinated polyanions [54]. However, there is a possibility that active peroxy species are formed by partial degradation of the starting Keggin anion and the formation is easier with mixed coordinated HPA.

### A Preparation

Reproducible preparation of  $H_{3+x}PMo_{12-x}V_xO_{40}$  ( $x = 1-3$ ,  $Mo_{12-x}V_x$ ) was established by Tsigdinos and Hallada [55]. An aqueous solution of  $Na_2HPO_4$  and sodium metavanadate is acidified with a concentrated sulfuric acid. To this mixture is added an aqueous solution of  $Na_2MoO_4 \cdot 2H_2O$ . The detailed procedure is available in the literature. Note that excess sodium metavanadate is used.

Molybdenum-tungsten mixed-coordinated heteropolyacids,  $H_3PMo_{12-x}W_xO_{40}$ , are prepared from  $Na_2HPO_4 \cdot 12H_2O$ ,  $Na_2WO_4$ , and  $Na_2MoO_4 \cdot 2H_2O$  solutions. After the solutions are mixed at 353 K for 1 h, hydrochloric acid is added at room temperature. Then the heteropolyacids are extracted with diethyl ether and crystallized at room temperature;  $H_3PMo_{12}O_{40}$  and  $H_3PW_{12}O_{40}$  can also be used as the starting materials. The mixed aqueous solution is held at 353 K for 6 h, followed by extraction by diethyl ether and re-

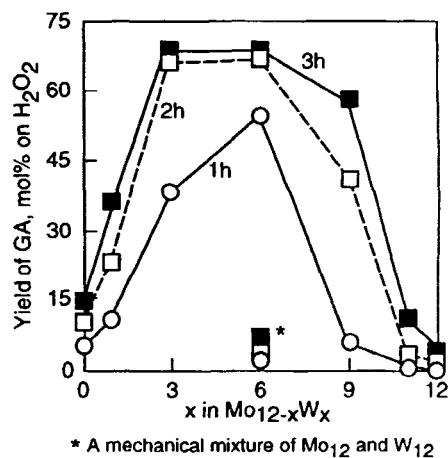


Figure 7. Synergistic effect of Mo-W mixed-coordinated heteropolyacids for the oxidation of cyclopentene with hydrogen peroxide [26]; 1 h, 2 h, and 3 h are the reaction times. GA = glutaraldehyde

crystallization. The heteropolyacids prepared by these methods are mixtures of mixed-coordinated heteropolyanions having a statistical distribution of  $x$ .

The synthesis of specifically Mo- or V-substituted positional isomers of tungstophosphates is achieved by the method of Massart or Domaille et al., but their catalytic activities are not as high [56, 57]. A requirement for these syntheses is isolation, or the in-place generation, of an appropriate defect polytungstate anion that is subsequently resubstituted with V or Mo: the ion  $[PVW_{11}O_{40}]^{4-}$  is derived from in-place generation of  $[PW_{11}O_{39}]^{7-}$ ;  $[\alpha-1,2,3-PV_3W_9O_{40}]^{6-}$  is prepared from preformed  $[\alpha-PW_9O_{34}]^{9-}$ ;  $[\beta-$  and  $\gamma-PV_2W_{10}O_{40}]^{5-}$  are isolated from  $[PW_{10}O_{36}]^{7-}$  [57];  $[\alpha-PW_9Mo_2O_{39}]^{3-}$  is prepared from  $[\beta-PW_9O_{34}]^{9-}$ ;  $[\alpha-PW_9Mo_3O_{40}]^{3-}$  is derived from  $[\alpha-PW_9Mo_2O_{39}]^{3-}$  [56]. Two important preparative details are emphasized [58]:

- (i) reproducible syntheses require accurate pH readings on a calibrated pH meter;
- (ii) vanadium (V) species are strong oxidants, particularly at low pH, and metallic spatulas are attacked, leaving an intense heteropoly "blue" vanadium (IV) product (ceramic spatulas are recommended).

Product identification relies on  $^{31}P$  NMR of their solutions. Details of  $^{31}P$  NMR measurements and preparation methods are available in the literature [59].

### 2.1.7.5 Metal-Coordinated Heteropolyanions

Metals can be coordinated with a heteropolyanion in three different ways to form metal-coordinated polyanions, which show unique catalytic activities for various reactions. The first method is the simple combina-



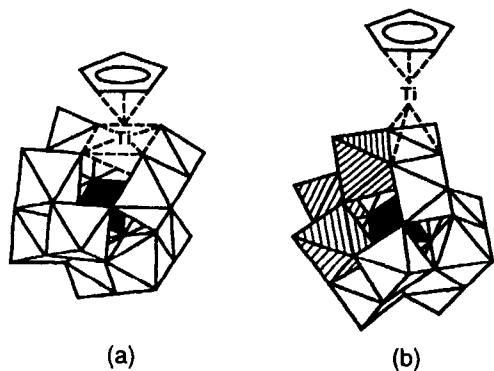


**Figure 8.** (a) Transition metal-substituted heteropolyanion  $[\text{PW}_{12}\text{O}_{39}(\text{TiCp})]^{4-}$ ; (b) heteropolyanion-supported transition metal  $[\text{TiCp} \cdot \text{SiW}_9\text{V}_3\text{O}_{40}]^{4-}$  [65]. The hatched octahedra represent  $\text{VO}_6$ , the central phosphate is shown by black tetrahedra,  $\text{Cp} = \text{C}_5\text{H}_5$ .

tion of metal salts with a heteropolyanion. The second is the use of lacunary anion as a ligand for transition metal ions, i.e. transition metal-substituted polyanion (TMSP; Fig. 8(a)). The third is to use a polyanion to support transition metals, i.e. heteropolyanion-supported transition metal (Fig. 8(b)).

### A Combination of Metal Salts with Heteropolyanions

The Wacker-type reaction is a good example in which the heteropolyanion plays a role as a reoxidizing reagent of  $\text{Pd}^0$  in the reaction [60]. It is reported that  $\text{PMo}_6\text{W}_6\text{O}_{30}^{3-}$  is an efficient reoxidant for this reaction and the rate determining step is the reoxidation of  $\text{Pd}^0$  to  $\text{Pd}^{2+}$  [61]. The pH and the concentration of  $\text{Cl}^-$  can be controlled by the use of  $\text{Na}_y\text{H}_{3+x-y}\text{PMo}_{12-x}\text{V}_x\text{O}_{40}$  ( $x = 2, 3$ ), so that the reaction rate and the stability of  $\text{Pd}^{2+}$  increase, and the concentration of  $\text{Cl}^-$  decreases to 1% of that in the conventional ethylene Wacker-type reaction [62]. The anion,  $\text{PMo}_{12-x}\text{V}_x\text{O}_{40}^{(3+x)-}$ , is considered to promote both the solubilization of high concentration of  $\text{V}^{5+}$  and the reoxidation of  $\text{V}^{4+}$  by  $\text{O}_2$ .

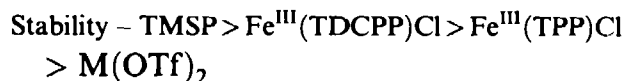
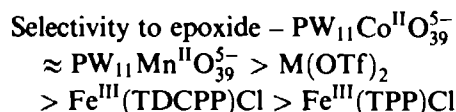
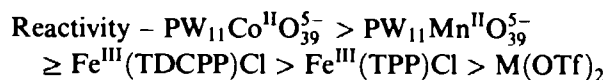
Terminal alkenes can be hydrogenated selectively in the presence of  $\text{PdCl}_2$  [63] or  $\text{RhCl}(\text{PPh}_3)_3$  [64] and heteropoly compounds. The catalytic system is also highly active for the production of urethane or isocyanate compounds by the reductive carbonylation of nitrobenzene. It is considered that polyoxometalate coordinating with  $\text{Pd}^{2+}$  in the reduced form is the active species, since easily reducible heteropolyanions are more active [63].

### B Transition Metal-Substituted Polyanions (TMSP)

Lacunary Keggin anions,  $\alpha\text{-XM}_{11}\text{O}_{39}^{n-}$ , have a "defect" Keggin structure, in which one addenda atom and one terminal oxygen are missing. These lacunary hetero-

polyanions, which are formed at relatively high pH, are used as ligands of 3d metal ions. The vacancy is the binding site; for example,  $\text{PW}_{11}\text{O}_{39}^{7-}$  acts as a pentadentate and tetradentate ligand of Co and Cu, respectively [1b, 65, 66]. Complexes of anions such as  $\text{XM}_{11}\text{O}_{39}^{n-}$  ( $X = \text{P, Si}$ ;  $M = \text{Mo, W, V, Nb}$ ) with metal ions are used as inorganic analogs of metalloporphyrins (inorganic synzyme) and have important advantages as catalysts, i.e. high resistance to oxidative degradation and thermal stability.

Hill and co-workers have reported that TMSP is effective for the epoxidation of alkenes and the oxygenation of alkanes by use of *t*-BuOOH and PhIO as oxidants [67]. The characteristics of TMSP in alkene epoxidation, compared with those of metalloporphyrins, Schiff base complexes, and triflate salts, are as follows [67]:



(TDCPP = tetrakis-2,6-dichlorophenylporphyrin;  
TPP = tetraphenylporphyrin; OTf = triflate ion)

Thus, the substituted heteropolyanion is stable and active even in the presence of oxidants such as *t*-BuOOH or PhIO. Note that the heteropolyanion is unstable with respect to hydrogen peroxide. Based on the high stability, TMSP can be used for alkane hydroxylation [67b]. Mansuy et al. have reported that  $\text{P}_2\text{W}_{17}\text{O}_{61}(\text{Mn}^{3+} \cdot \text{Br})^{8-}$  is oxidation resistant and more active for the epoxidation of cyclooctene with PhIO than those containing  $\text{Fe}^{3+}$ ,  $\text{Co}^{2+}$ ,  $\text{Ni}^{2+}$ , or  $\text{Cu}^{2+}$  [68]. The oxygenations of cyclohexane, adamantane, and heptane and the hydroxylation of naphthalene, are also catalyzed by TMSP.

Ruthenium has been used as the catalytic center in TMSP for the oxidations of cyclohexane, adamantane, and styrene with PhIO or *t*-BuOOH [69].

### C Heteropolyanion-Supported Metals

The organometallic cations can be supported on reduced heteropolyanions or more negatively charged polyanions such as  $\text{SiW}_9\text{M}_3\text{O}_{40}^{7-}$  and  $\text{P}_2\text{W}_{15}\text{M}_3\text{O}_{62}^{9-}$  ( $M = \text{V}^{5+}, \text{Nb}^{5+}$ ). The latter has three full units of anionic surface charge that enable tight and covalent bonding of transition metals [66].

Finke and co-workers have reported that a  $\text{P}_2\text{W}_{15}\text{Nb}_3\text{O}_{62}^{9-}$ -supported Ir catalyst,  $[(\eta\text{-C}_4\text{H}_9)_4\text{N}]_5\text{Na}_3\{(1,5-$

(cod)Ir · P<sub>2</sub>W<sub>15</sub>Nb<sub>3</sub>O<sub>62</sub>] (cod = cyclooctadiene), is active for both hydrogenation [70] and oxygenation [71] of cyclohexene. The turnover frequency is 100 times higher than that of its parent Ir compound, [(1,5-cod)IrCl]<sub>2</sub>. The supported structure probably remains intact during the reaction, while it is unstable under H<sub>2</sub> atmosphere [72].

#### D Preparation

The preparation of TMSPs (Keggin-type and Dawson-type) is described in detail by Walker and Hill [73] and Lyon et al. [74]. The tetrakis(tetra-*n*-butylammonium) salt of PMO<sub>11</sub>O<sub>39</sub><sup>7-</sup>, (*n*-Bu<sub>4</sub>N)<sub>4</sub>H<sub>3</sub>PMO<sub>11</sub>O<sub>39</sub> (**1**) is prepared and metalated to form the corresponding Keggin-type TMSP.

The compound **1** is prepared as follows: α-H<sub>3</sub>PMO<sub>12</sub>O<sub>40</sub> is dissolved in water; the pH of the solution is adjusted to 4.3 with Li<sub>2</sub>CO<sub>3</sub>; a precipitate is formed by adding solid *n*-Bu<sub>4</sub>NBr (14 equiv) to the solution with vigorous stirring; the crude product is collected, washed with H<sub>2</sub>O, evaporated to dryness, and allowed to air dry overnight at room temperature. In contrast to recrystallization from protic media [75], the light yellow-green crystalline product **1**, can be obtained by repeated recrystallization from organic solvents without decomposition. Recrystallization under nonprotic conditions involves dissolving the crude product in CH<sub>3</sub>CN by stirring without heating, followed by slow evaporation of the solvent at room temperature. After three recrystallizations the complex has >99% purity, as confirmed by <sup>31</sup>P NMR [73].

From the lacunary polyanion, for example, the Mn-substituted polyanion, (*n*-Bu<sub>4</sub>N)<sub>4</sub>HPMO<sub>11</sub>Mn<sup>II</sup>(CH<sub>3</sub>CN)O<sub>39</sub>, can be prepared [73]: **1** is dissolved in acetonitrile with stirring, and then toluene is added to produce a homogeneous light yellow-green solution; this solution is poured into a separatory funnel to which is added an aqueous solution of MnSO<sub>4</sub> · H<sub>2</sub>O (1.5 equiv); vigorous shaking of the heterogeneous mixture for ≈1 min results in an immediate color change of the organic layer to brown indicating that **1** has rapidly extracted the manganese ion into the organic layer; the water layer is drawn off, and the remaining organic layer is placed in a crystallizing dish and allowed to evaporate slowly at room temperature; the crude brown crystalline product is separated by filtration and recrystallized from acetonitrile. Unlike Co<sup>II</sup>, Mn<sup>II</sup>, or Cu<sup>II</sup>, metalation with Zn<sup>II</sup> induces the decomposition of **1** [73].

A heteropolyanion-supported metal, [(*n*-C<sub>4</sub>H<sub>9</sub>)<sub>4</sub>N]<sub>5</sub>-Na<sub>3</sub>[(1,5-cod)Ir · P<sub>2</sub>W<sub>15</sub>Nb<sub>3</sub>O<sub>62</sub>] (**2**) is prepared from (Bu<sub>4</sub>N)<sub>9</sub>P<sub>2</sub>W<sub>15</sub>Nb<sub>3</sub>O<sub>62</sub> and [(1,5-cod)Ir(CH<sub>3</sub>CN)<sub>2</sub>]BF<sub>4</sub> [76]. The choice of the metal–ligand combination Ir(1,5-cod)<sup>+</sup> and synthesis of (Bu<sub>4</sub>N)<sub>9</sub>P<sub>2</sub>W<sub>15</sub>Nb<sub>3</sub>O<sub>62</sub> are described in the literature [77, 78]. The synthesis and subsequent storage of **2** require strict oxygen-free

conditions. The key to obtaining **2** as a pure solid is the use of mixed Bu<sub>4</sub>N<sup>+</sup>/Na<sup>+</sup> salts and at least two reprecipitations from paper-filtered homogeneous CH<sub>3</sub>CN solution using EtOAc. Bu<sub>4</sub>NBF<sub>4</sub> is very soluble in EtOAc and thus is removed by this process. Analytically pure **2** is obtained as a bright yellow, very air-sensitive powder.

#### 2.1.7.6 Heteropolyanions Intercalated in Layered Double Hydroxides

Layered silicate clays intercalated by pillaring polyoxocations are precursors to an important class of microporous catalysts. Smectite clay was the only host structure known to be pillared by purely inorganic oxo ions. Recently, layered double hydroxides (LDH) pillaring oxo ions were reported by Pinnavaia and co-workers [79, 80].

The pillaring of LDH by Keggin-type heteropolyanions and their lacunary species has been attempted. The gallery heights are reported to be about 10 Å. The reactivity of [XM<sub>12</sub>O<sub>40</sub>]<sup>n-</sup> species for intercalative ion exchange depends strongly on both the net charge and polyhedral framework of the ion [80]. Since the cross-section of a Keggin anion (10 Å diameter) is ≈80 Å<sup>2</sup> and the area per unit positive charge is 16.6 Å<sup>2</sup> for the layer surface of an LDH, [Zn<sub>2</sub>Al(OH)<sub>6</sub>]NO<sub>3</sub> · 2H<sub>2</sub>O, Keggin ions with a charge less than -5 cannot be electrically balanced by the host LDH [80].

However, more study is needed to establish the catalytic properties, structures and thermal stabilities of the LDH-pillared HPAs.

#### A Preparation

The ion-exchange reactions are carried out by dropwise addition of a boiling suspension of [Zn<sub>2</sub>Al(OH)<sub>6</sub>]NO<sub>3</sub> · 2H<sub>2</sub>O to a 40% excess of the polyoxometalates in aqueous solution at room temperature. A nitrogen atmosphere is used to avoid possible reaction of the LDH with atmospheric CO<sub>2</sub>. The final products are stored under nitrogen [80]. The host LDH is prepared by the reaction of freshly precipitated aluminum hydroxide with an aqueous zinc chloride solution at pH 6.2, according to the general method of Taylor [81]. The reaction time at 373 K is 7 days.

#### 2.1.7.7 Supported Heteropoly Compounds

Supported heteropoly compounds, where heteropoly compounds are dispersed on the surface of porous solids, are important for applications, since the surface area of heteropolyacids is usually low. The structure, stabil-

ity, and catalytic properties are very much dependent on the support materials, the extent of loading, and the method of preparation [5, 82]. As supports for heteropoly compounds,  $\text{SiO}_2$ ,  $\text{Al}_2\text{O}_3$ , and  $\text{TiO}_2$ , active carbons, ion-exchange resins, and high surface area salts of HPA have been used. A silane coupling reagent has been tested for binding HPA on oxide support [83]. Insolubility is also an important property when HPA is applied to liquid-phase reactions.

Basic solids such as  $\text{Al}_2\text{O}_3$  and  $\text{MgO}$  tend to decompose HPAs [5, 84, 85], although significant activities have been reported in some cases. On the other hand,  $\text{SiO}_2$  and some carbons are relatively inert. In the cases of  $\text{H}_3\text{PW}_{12}\text{O}_{40}$  and  $\text{H}_3\text{PMo}_{12}\text{O}_{40}$  on  $\text{SiO}_2$ , HPAs are dispersed as thin layers on the support up to a certain quantity of HPA and above that quantity they form thick layers or separate particles [38]. Detailed studies of  $\text{H}_4\text{SiMo}_{12}\text{O}_{40}$  supported on  $\text{SiO}_2$  have been reported [86]. Spectroscopic as well as catalytic tests indicate that the Keggin structure is maintained and catalytic properties corresponding to the parent HPA are revealed at high loading levels [86a,c]. However, at a very low level of loading, strong interactions between the heteropolyacid and surface silanol groups suppress the acidity, and the redox catalysis predominates. It was also shown that the state in solution influences the dispersion after being supported on  $\text{SiO}_2$  [86b]. The thermal stability of HPA on  $\text{SiO}_2$  is usually comparable or slightly lower than the parent HPA [86c, 87], whereas it was reported that  $\text{H}_3\text{PMo}_{12}\text{O}_{40}$  was stable up to 853–873 K when supported on  $\text{SiO}_2$  [88]. Besides decomposition, reformation of the Keggin structure takes place under certain (wet) conditions [5, 89–91]. Silica-bound  $\text{Cs}_{2.5}\text{H}_{0.5}\text{PW}_{12}\text{O}_{40}$ , which is prepared by the hydrolysis of ethyl orthosilicate in the presence of colloidal  $\text{Cs}_{2.5}\text{H}_{0.5}\text{PW}_{12}\text{O}_{40}$  in ethanol, is catalytically more active than Amberlist-15 and H-ZSM-5 with respect to the turnover frequency, as based on the unit acid site [92].

Potassium and cesium salts of HPAs which have high surface areas are useful supports for HPAs. Increased stability as well as improved yield in selective oxidation of acrolein is observed when  $\text{H}_{3+x}\text{PV}_x\text{Mo}_{12-x}\text{O}_{40}$  compounds are supported on  $\text{K}_3\text{PMo}_{12}\text{O}_{40}$  [47, 48]. It was claimed that free acids covered epitaxially the surface of the support, but also the possible formation of a solid solution of  $\text{H}(\text{K}, \text{Cs})_3\text{PW}_{12}\text{O}_{40}$  [93] and  $\text{H}(\text{K}, \text{Cs})_3\text{PMo}_{12}\text{O}_{40}$  [94] due to the diffusion of  $\text{K}^+$ ,  $\text{Cs}^+$  and  $\text{H}^+$  need to be considered.

A certain kind of active carbon is an excellent support of HPAs to make HPAs insoluble [95]. It has been reported that proton transfer from HPAs to the carbon support tightens the binding [96]. High activity was reported for HPAs supported on ion-exchanged resin [97] and HPAs doped in polymers [98, 99].

Polyacetylene can be doped with large anions of  $\text{H}_3\text{PMo}_{12}\text{O}_{40}$ . The doping increases not only the conductivity of the polymer but also the catalytic activity. The HPA is distributed nearly uniformly over the cross-section of the polymer film. For the conversion of ethanol, the catalyst exhibits acid–base activity as well as redox activity. Through the pulse reaction, it has been shown that the rate of formation of ethylene and diethyl ether increased 10 times and the rate of formation of acetaldehyde increased 40 times [98].

Lee and co-workers have shown that the oxidation rate of ethanol was remarkably increased by using a  $\text{H}_3\text{PMo}_{12}\text{O}_{40}$ -blended porous polysulfone (PSF) film [99]. The selectivity for acetaldehyde was high (above 90% selectivity at  $\approx 10\%$  conversion, compared with 40% selectivity at 2% conversion without polymer at 433–463 K).

The coexistence of metal and HPA reveals a unique catalytic bifunctionality. For  $\text{Pt}-\text{Cs}_{2.5}\text{H}_{0.5}\text{PW}_{12}\text{O}_{40}$ , the activity of the *n*-butane isomerization is remarkably enhanced in the presence of  $\text{H}_2$ . The rate of isobutane formation at 573 K is comparable with or higher than those of  $\text{Pt}-\text{H}-\text{ZSM5}$  and  $\text{Pt}-\text{SO}_4^{2-}/\text{ZrO}_2$  while the selectivity of HPA is much higher [100, 101].

### A Preparation

Conventional methods such as incipient wetness impregnation are applicable to the preparation of supported HPAs [8].

The doping of polyacetylene with HPAs is performed via chemical oxidation in acetonitrile containing  $\text{H}_3\text{PMo}_{12}\text{O}_{40}$  and minute amount of suitable complexing reagent. Anodic oxidation in an  $\text{H}_3\text{PMo}_{12}\text{O}_{40}$ -acetonitrile electrolyte is also possible using polyacetylene film as the anode. After doping, the films are washed with dry acetonitrile and again vacuum-dried. The samples are stored in vacuum-sealed glass tubes [98].

For blending porous polysulfone (PSF) and HPAs, the choice of solvent is important; dimethylformamide (DMF) has been recommended [99]. A HPA–PSF film is prepared by casting the HPA–PSF–DMF solution on a glass plate, followed by drying in air for 4–5 h and subsequent evacuation for 2 h. The thickness of the HPA–PSF film is usually 0.1 mm [99].

The compound  $\text{Pt}-\text{Cs}_{2.5}\text{H}_{0.5}\text{PW}_{12}\text{O}_{40}$  is prepared as follows [100, 101]: An aqueous solution of  $\text{Pt}(\text{NH}_3)_4\text{Cl}_2$  is added dropwise to an aqueous solution of  $\text{H}_3\text{PW}_{12}\text{O}_{40}$  followed by the addition of an aqueous solution of  $\text{Cs}_2\text{CO}_3$  at 323 K; the resulting suspension is evaporated to solid at 323 K. The molar ratio of  $\text{Pt}^{2+}:\text{Cs}^+:\text{PW}_{12}\text{O}_{40}^{3-}$  is 0.25:2.5:1, where the amount of Pt corresponds to 1.5 wt %, and the surface area is  $112 \text{ m}^2 \text{ g}^{-1}$ . The palladium analog is obtained from  $\text{Pd}(\text{NO}_3)_2$  in a similar way.

## References

- 1 (a) G A Tsigdinos, *Topics Curr Chem* **1978**, *76*, 1, (b) M T Pope, *Heteropoly and Isopoly Oxometalates*, Springer-Verlag, Berlin, **1983**, (c) M T Pope, A Müller, *Angew Chem Int Ed Engl* **1991**, *30*, 34, (d) V W. Day, W G Klemperer, C Schwartz, R -C Wang in *Surface Organometallic Chemistry The Molecular Approach to Surface Science and Catalysis* (Eds J M Basset, B C Gates), Reidel, Dordrecht, **1988**, p 173
- 2 M Misono, M Hashimoto, *Shokubai (Catalyst)* **1992**, *34*, 152
- 3 Y Jeannin, M Fournier, *Pure Appl Chem* **1987**, *59*, 1529
- 4 M Misono, *Proc 10th Int Congr Catal* 1992, Akademiai Kiado Budapest, **1993**, p.69
- 5 M Misono, *Catal Rev Sci Eng* **1987**, *29*, 269, **1988**, *30*, 339
- 6 K Eguchi, N Yamazoe, T Seiyama, *Nippon Kagaku Kaishi*, **1981**, 336
- 7 H Niiyama, Y Saito, S Yoshida, E Echigoya, *Nippon Kagaku Kaishi*, **1982**, 569
- 8 Y Izumi, K Urabe, M Onaka, *Zeolite, Clay, and Heteropolyacid in Organic Reactions*, Kodansha, Tokyo, and VCH, Weinheim, **1992**
- 9 M Misono, N Nojiri, *Appl Catal* **1990**, *64*, 1
- 10 (a) M Otake, T. Onoda, *Shokubai* **1975**, *17*, 13, H Hayashi, J B Moffat, *J Catal* **1982**, *77*, 473, (b) M Misono, T Okuhara, *CHEMTECH*, **1993**, *Nov*, 23
- 11 M Misono, K Sakata, Y Yoneda, W Y Lee, *Proc 7th Int Congr Catal*, 1980, Kodansha, Tokyo, and Elsevier, Amsterdam, **1981**, p 1047
- 12 M Misono, N Mizuno, K Katamura, A Kasai, Y Konishi, K Sakata, T Okuhara, Y Yoneda, *Bull Chem Soc Jpn* **1982**, *55*, 400
- 13 I V Kozhevnikov, K I Matveev, *Appl Catal* **1983**, *5*, 135
- 14 J J Altenau, M T Pope, R A Prados, H So, *Inorg Chem* **1975**, *14*, 417
- 15 D E. Katsoulis, M T. Pope, *J Am Chem Soc* **1984**, *106*, 2737
- 16 T Okuhara, C Hu, M Misono, *Bull Chem Soc Jpn* **1994**, *67*, 1156
- 17 F Lefebvre, F X Liu-Cai, A Auroux, *J Mater Chem* **1994**, *4*, 125
- 18 K Y Lee, T Arai, S-I Nakata, S Asaoka, T Okuhara, M Misono, *J Am Chem Soc* **1992**, *114*, 2836
- 19 M Hashimoto, M Misono, *Acta Cryst* **1994**, *C50*, 231
- 20 J G Highfield, J B Moffat, *J Catal* **1985**, *95*, 108, **1986**, *98*, 245
- 21 A Aoshima, S Yamamatsu, T Yamaguchi, *Nippon Kagaku Kaishi* **1987**, 976
- 22 C Hu, M Hashimoto, T Okuhara, M Misono, *J Catal* **1993**, *143*, 437
- 23 Y Izumi, K Matsuo, K Urabe, *J Mol Catal* **1983**, *18*, 299
- 24 L Barcza, M T Pope, *J Phys Chem* **1975**, *79*, 92
- 25 N Mizuno, S Yokota, I Miyazaki, M Misono, *Nippon Kagaku Kaishi* **1991**, 1066
- 26 K Y Lee, K Itoh, M Hashimoto, N Mizuno, M Misono in *New Developments in Selective Oxidation II* (Eds V C Corberán, S V Bellón), Elsevier, **1994**, p 583
- 27 (a) Y Matoba, H Inoue, J Akagi, T Okabayashi, Y Ishii, M Ogawa, *Syn Commun* **1984**, *14*, 865, (b) Y Ishii, Y Kazumasa, T Ura, H Yamada, T Yoshida, M Ogawa, *J Org Chem* **1988**, *53*, 3587, 5549, (c) Y Ishii, K Yamawaki, T Yoshida, T Ura, M Ogawa, *J Org Chem* **1987**, *52*, 1868, (d) T Oguchi, Y Sakata, N Takeuchi, K Kaneda, Y Ishii, M Ogawa, *Chem Lett* **1989**, 2053
- 28 P Souchay, *Ions Minéraux Condensés*, Masson & Cie, Paris, **1969**
- 29 J C Bailar, *Inorg Synth* **1939**, *1*, 132
- 30 C Rocchiccioli-Deltcheff, M Fournier, R Franck, R Thouvenot, *Inorg Chem* **1983**, *22*, 207
- 31 P Souchay, *Bull Soc Chim Fr* **1951**, *18*, 365
- 32 L C W Baker, T P McCutcheon, *J Am Chem Soc* **1956**, *78*, 4503
- 33 T Okuhara, A Kasai, N Hayakawa, Y Yoneda, M Misono, *J Catal* **1983**, *83*, 121
- 34 T Okuhara, T Nishimura, H Watanabe, M Misono, *J Mol Catal* **1992**, *74*, 247
- 35 M Akimoto, K Shima, H Ikeda, E Echigoya, *J Catal* **1981**, *72*, 83
- 36 M Misono, N Mizuno, T Komaya, *Proc 8th Intern Congr Catal Berlin, 1984*, Verlag Chemie-Dechema, **1984**, Vol 5, p 487
- 37 N Mizuno, T Watanabe, M Misono, *J Phys Chem* **1985**, *89*, 80
- 38 N Mizuno, T Watanabe, H Mori, M Misono, *J Catal* **1990**, *123*, 157
- 39 K Y Lee, S Oishi, H Igarashi, M Misono, *Catal Today*, in press
- 40 Y Ono, *Perspectives in Catalysis* (Eds J M Thomas, K I Zamaraev), Blackwell London, **1992**
- 41 S Suzuki, K Kogai, Y Ono, *Chem Lett* **1984**, 699
- 42 T Baba, M Nomura, Y Ono in *Acid-Base Catalysis II* (Eds H Hattori, M Misono, Y Ono), Elsevier, Amsterdam, and Kodansha, Tokyo, **1994**, p 419
- 43 T Nishimura, T Okuhara, M Misono, *Appl Catal* **1991**, *73*, L7
- 44 T Okuhara, T Nishimura, M Misono, *Chem Lett* **1995**, No 2
- 45 S Nakamura, H Ichihashi, *Proc 7th Int Congr Catal Tokyo, 1980*, Kodansha, Tokyo, and Elsevier, Amsterdam, **1981**, p 755
- 46 N Simizu, M Ueshima, M Wada, *Shokubai* **1988**, *30*, 555
- 47 J B Black, N J Claydon, P L Gai, J D Scott, E M Serwicka, J B Goodenough, *J Catal* **1987**, *106*, 1
- 48 K Bruckman, J Haber, E M Serwicka, *Faraday Disc Chem Soc* **1989**, *87*, 173, K Bruckman, J Haber, E Lalik E M Serwicka, *Catal Lett* **1988**, *1*, 35, K Bruckman, J Haber, E M Serwicka, N Yurchenko, T P Lazarenko, *Catal Lett* **1990**, *4*, 181
- 49 M Akimoto, H Ikeda, A Okabe, E Echigoya, *J Catal* **1984**, *89*, 196
- 50 R Neumann, M Levin, *J Org Chem* **1991**, *56*, 5707
- 51 R Neumann, M Levin, *J Am Chem Soc* **1992**, *114*, 7278
- 52 H Furukawa, T Nakamura, H Inagaki, E Nishikawa C Imai, M Misono, *Chem Lett* **1988**, 877
- 53 M A Schwegler, M Floor, H van Bekkum, *Tetrahedron Lett* **1988**, *29*, 823
- 54 J K Burdett C K Nguyen, *J Am Chem Soc* **1990**, *112*, 5366
- 55 G A Tsigdinos, C J Hallada, *Inorg Chem* **1968**, *7*, 437
- 56 R Massart, R Contant, J-M Fruchart, J-P Ciabrin, M Fournier, *Inorg Chem* **1977**, *16*, 2916
- 57 P J Domaille, G Watunya, *Inorg Chem* **1986**, *25*, 1239
- 58 P J Domaille, *Inorg Synth* **1990**, *27*, 96
- 59 A Teze, G Herve, *Inorg Synth* **1990**, *27*, 85
- 60 K I Matveev, I V Kozhevnikov, *Kinet Katal* **1980** *21*, 1189

- 61 K Urabe, F Kimura, Y Izumi, *Proc 7th Intern. Congr Catal Tokyo, 1980*, Kodansha, Tokyo and Elsevier, Amsterdam, 1981, p 1418
- 62 J H Grate, D R Hamm, S Mahajan, *Preprint distributed at 14th Conference on Catalysis of Organic Reactions*, Albuquerque, NM, April 27-29, 1992
- 63 Y Izumi, Y Satoh, H Kondoh, K Urabe, *J Mol Catal* 1992, 72, 37
- 64 K Urabe, Y Tanaka, Y Izumi, *Chem Lett* 1985, 1595
- 65 N Mizuno, M Misono, *J Mol Catal* 1994, 86, 319
- 66 R K Ho, W G Klemperer, *J Am Chem Soc* 1978, 100, 6772
- 67 (a) M Faraj, C L Hill, *J Chem Soc, Chem Commun* 1987, 1487, (b) C L Hill, *Activation and Functionalization of Alkanes*, Wiley, New York, 1989, (c) C L Hill, R B Brown, Jr, *J Am Chem Soc* 1986, 108, 536
- 68 D Mansuy, J-F Bartoli, P Battioni, D K Lyon, R G Finke, *J Am Chem Soc* 1991, 113, 7222
- 69 R Neumann, C A-Gnim, *J Chem Soc, Chem Commun* 1989, 1324
- 70 D K Lyon, R G Finke, *Inorg Chem* 1990, 29, 1789
- 71 N Mizuno, D K Lyon, R G Finke, *J Catal* 1991, 128, 84
- 72 M Pohl, R G Finke, *Organometallics* 1993, 12, 1453
- 73 L A C-Walker, C L Hill, *Inorg Chem* 1991, 30, 4016
- 74 D K Lyon, W K Miller, T Novet, P J Domaille, E Evitte, D C Johnson, R G Finke, *J Am Chem Soc* 1991, 113, 7209
- 75 M Fourmer, R C R Massart, *Acad Sci Paris, Ser C* 1974, 279, 875
- 76 R G Finke, D K Lyon, K Nomiya, S Sur, N Mizuno, *Inorg Chem* 1990, 29, 1787
- 77 (a) M Green, T A Kuc, S H Taylor, *J Chem Soc A* 1971, 2334, (b) R R Schrock, J A Osborne, *J Am Chem Soc* 1971, 93, 3089
- 78 (a) D J Edlund, R J Saxton, D K Lyon, R G Finke, *Organometallics* 1988, 7, 1692, (b) R G Finke, D K Lyon, K Nomiya, T R J Weakley, *Acta Crystallogr C* 1990, 46, 1592
- 79 T Kwon, G A Tsigdinos, T J Pinnavaia, *J Am Chem Soc* 1988, 110, 3653
- 80 T Kwon, T J Pinnavaia, *Chem Mater* 1989, 1, 381
- 81 R M Taylor, *Clay Miner* 1984, 19, 591
- 82 K Tanabe, M Misono, Y Ono, H Hattori, *New Solid Acids and Bases*, Kodansha, Tokyo and Elsevier, Amsterdam, 1989, p 170
- 83 M Kamada, Y Kera, *Chem Lett* 1991, 1831
- 84 J A R van Veen, P A J M Hendricks, R R Andrea, E J M Romers, A E Wilson, *J Phys Chem* 1990, 94, 5282
- 85 K Nowinska, R Fiedorow, J Adamec, *J Chem Soc Faraday Trans* 1991, 87, 749
- 86 (a) J-M Tatibouet, M Che, M Amirouche, M Fournier, C Rocchiccioli-Deltcheff, *J Chem Soc Chem Commun* 1988, 1260, (b) M Fournier, R Thouvenot, C Rocchiccioli-Deltcheff, *J Chem Soc, Faraday Trans* 1991, 87, 349, (c) C Rocchiccioli-Deltcheff, M Amirouche, G Herve, M Fournier, M Che, J-M Tatibouet, *J Catal* 1990, 126, 591
- 87 M J Bartoli, L Monceaux, E Bordes, G Hecquet, P Courtine, *Stud Surf Sci Catal* 1992, 72, 81
- 88 S Kasztelan, E Payen, J B Moffat, *J Catal* 1990, 125, 45
- 89 C R Rocchiccioli-Deltcheff, M Amirouche, M Che, J M Tatibouet, M Fournier, *J Catal* 1990, 125, 292
- 90 A Ogata, A Kazusaka, A Yamazaki, M Enyo in *Acid-Base Catalysis* (Eds K Tanabe, H Hattori, T Yamaguchi, T Tanaka), VCH, Weinheim 1989, p 249
- 91 Y Konishi, K Sakata, M Misono, Y Yoneda, *J Catal* 1982, 77, 169
- 92 Y Izumi, M Ono, M Ogawa, K Urabe, *Chem Lett* 1993, 825
- 93 (a) T Nishimura, H Watanabe, T Okuhara, M Misono, *Shokubai* 1991, 33, 420, H Watanabe, T Nishimura, S Nakata, T Okuhara, M Misono, *63rd National Meetings of Chem Soc Jpn*, March 1992, (b) N Mizuno, M Misono, *Chem Lett* 1987, 967
- 94 M Misono, N Mizuno, H Mori, K Y Lee, J Jiao, T Okuhara in *Structure-Activity and Selectivity Relationships in Heterogeneous Catalysis*, (Eds R K Grasselli, A W Sleight), Elsevier, Amsterdam, 1991, p 87
- 95 Y Izumi, K Urabe, *Chem Lett* 1981, 663
- 96 M A Schwegler, P Vinle, M van der Eijk, H van Bekkum, *Appl Catal* 1992, 80, 41
- 97 T Baba, Y Ono, *Appl Catal* 1986, 22, 321
- 98 J Poznyczek, I Kulszewicz-Bajer, M Zagorska, K Kruczala, K Dyrek, A Bielanski, A Pron, *J Catal* 1991, 132, 311
- 99 I K Song, S K Shin, W Y Lee, *J Catal* 1993, 144, 348
- 100 K Na, T Okuhara, M Misono, *J Chem Soc, Chem Commun* 1993, 1422
- 101 K Na, T Okuhara, M Misono, *Chem Lett* 1993, 1141
- 102 (a) Y Onoue, Y Mizutani, S Akiyama, Y Izumi, *Chemtech* 1978, 8, 432, A Aoshima, S Yamamatsu, T Yamaguchi, *Nippon Kagaku Kaishi* 1990, 233, (b) A Aoshima, S Tonomura, S Yamamatsu, *Polymers Advan Tech* 1990, 2, 127, (c) Eu Patent, EP 263027 (Nippon Fine Chemical Co), (d) G Maksimov, I V Kozhevnikov, *React Kinet Catal Lett* 1989, 39, 317, (e) S Sato, C Sakurai, H Furuta, T Sodesawa, F Nozaki, *J Chem Soc, Chem Commun* 1991, 1327
- 103 (a) Y Izumi, R Hasebe, K Urabe, *J Catal* 1983, 84, 402, (b) T Nishimura, T Okuhara, M Misono, *Chem Lett* 1991, 1695, Y Izumi, N Natsume, H Takamine, I Tamaoki, K Urabe, *Bull Chem Soc Jpn* 1989, 62, 2159, (c) T Okuhara, M Yamashita, K Na, M Misono, *Chem Lett* 1994, 1450, (d) Y Ono, M Taguchi, Gerile, S Suzuki, T Baba, *Stud Surf Sci Catal* 1985, 20, 167, (e) Y Ono, T Baba, J Sakai, T Keii, *J Chem Soc, Chem Commun* 1982, 400 (f) T Okuhara, T Hibi, K Takahashi, S Tatematsu, M Misono, *J Chem Soc, Chem Commun* 1984, 697 (g) S Shikata, T Okuhara, M Misono, *Sekiyu Gakkaishi* 1994, 37, 632, (h) Jpn Patent 1991 300150, (i) Y Izumi, M Ogawa, W Nohara, K Urabe, *Chem Lett* 1992 1987
- 104 (a) D Attanasio, D Orru, L Suber, *J Mol Catal* 1989, 57, L1, (b) M Lissel, H Jansen, R Neumann, *Tetrahedron Lett* 1992, 33, 1795, (c) C Venturello, R D'Aloisio, *J Org Chem* 1988, 53, 1553, (d) Y Ishii, K Yamawaki, T Ura, H Yamada, T Yoshida, M Ogawa, *J Org Chem* 1988, 53, 3587, (e) J E Lyons, P E Ellis, Jr, V A Durante, *Stud Surf Sci Catal* 1991, 67, 99
- 105 (a) M Ueshima, H Tsuneki, A Shimizu, *Hyomen* 1985, 23, 69, (b) Jpn Patent 1988 145249 (Asahi Chem Ind), Jpn Patent 1991 106839 (Sumitomo Chem), (c) G B McGarvey, J B Moffat, *J Catal* 1991, 132, 100 (d) G Centi, J L Nieto, C Iapalucci, K Bruckman, E M Serwicka, *Appl Catal* 1989, 46, 197
- 106 (a) Y Izumi, Y Satoh, K Urabe, *Chem Lett* 1990, 795 (b) R W Wegman, *J Chem Soc Chem Commun* 1994, 947

## 2.1.8 High-Surface Transition Metal Carbides and Nitrides

S. T. OYAMA

### 2.1.8.1 General Properties of Transition Metal Carbides and Nitrides

The alloying of main group elements, such as C, N, or O, with early transition metals produces a class of materials known as carbides, nitrides, or oxycarbide/nitrides [1–3]. The materials have high melting points ( $> 3300$  K), hardness ( $> 2000$  kg mm<sup>-2</sup>) and strength ( $> 3 \times 10^5$  MPa) [1, 4] and are employed commercially in advanced structural and cutting tool applications. Interestingly, although their physical properties are those of refractory ceramics, their electronic and magnetic properties are typical of metals. Thus, they are good conductors of heat and electricity and have Hall coefficients, magnetic susceptibilities, and heat capacities in the metallic range [1].

The monometallic carbides and nitrides often adopt simple crystal structures (Fig. 1) with the metal atoms arranged in cubic close-packed (ccp), hexagonal close-packed (hcp) or simple hexagonal (hex) arrays. The nonmetallic elements, C, N, and O, occupy interstitial spaces between metal atoms, and for this reason the materials are also known as interstitial alloys.

The crystal structures adopted by the binary carbides and nitrides are similar to those found in noble metals. The resemblance is not coincidental, and has been explained using Engel–Brewer valence bond theory [5]. Briefly, the main group elements C and N increase the metal's effective *s*–*p* electron count, so that structures and chemical properties of the early transition metals resemble those of the Group 8 metals. This idea was first introduced by Levy and Boudart [6] who noted that tungsten carbide had platinum-like properties.

The carbides and nitrides have been found to be exceptional hydrogenation catalysts [7]. They have activity close to or surpassing those of the Group 8 noble metals for such diverse reactions as methanation [8], ammonia synthesis [9], ammonia decomposition [10], hydrocracking [11], hydrogenation of benzene and cyclohexene [12], and hydroisomerization of *n*-hexane [13], *n*-heptane [14], and methylcyclohexane [15]. Considerable work is also being done in the area of hydroprocessing [16], where the materials have been shown to have high activity for both hydrodesulfurization (HDS) [17, 18] and hydrodenitrogenation (HDN) [19, 21].

### 2.1.8.2 Thermodynamic Considerations in the Preparation of Carbides and Nitrides

Strategies for preparation are numerous and involve widely differing starting metallic compounds, as well as different carbon and nitrogen sources. It is therefore instructive to consider the thermodynamics [2] of various kinds of transformations. The heats and free energies of formation from the elements at 298 K and 1000 K are presented in Table 1 for carbides and Table 2 for nitrides. For illustration, different transformations to molybdenum carbide are presented at 298 K in Table 3 and at 1000 K in Table 4.

Carbide formation from elemental carbon and transition metals show a number of trends (Table 1). First, the free energy of formation is strongly negative for the early transition metals, and becomes less favorable in going to the Group 8 metals. As temperature is raised, carbide stability decreases slightly among the early transition metals, but increases markedly for the late transition metals. In general, trends in free energies are mirrored by values of the heats of reaction but, towards the right in the periodic table, entropic effects are important in stabilizing the compounds.

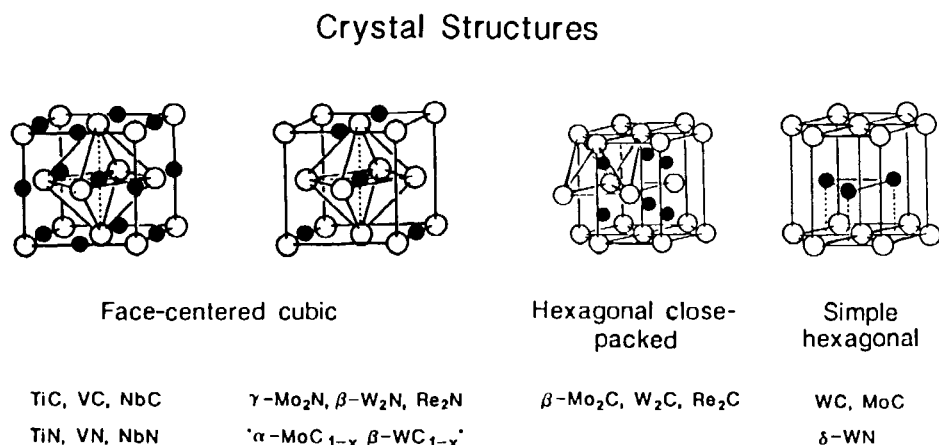


Figure 1. Typical crystal structures and compositions of carbides and nitrides (reproduced with permission from Ref. 3).

**Table 1.** Heat and free energy of formation from the elements of transition metal carbides ( $\text{kJ mol}^{-1}$ ) calculated from data in Ref. 22.

Transformation	$\Delta H_{298}^0$	$\Delta G_{298}^0$	$\Delta H_{1000}^0$	$\Delta G_{1000}^0$
Ti + C $\rightarrow$ TiC	-184.5	-181.0	-184.1	-173.6
Zr + C $\rightarrow$ ZrC	-207.1	-203.7	-208.3	-195.9
Hf + C $\rightarrow$ HfC	-225.9	-223.0	-225.0	-217.5
V + C $\rightarrow$ VC	-101.7	-99.08	-103.1	-92.21
Nb + C $\rightarrow$ NbC	-138.9	-136.9	-136.2	-134.4
Ta + C $\rightarrow$ TaC	-144.1	-142.6	-142.5	-140.8
Cr + $\frac{2}{3}$ C $\rightarrow$ $\frac{1}{3}$ Cr <sub>3</sub> C <sub>2</sub>	-85.35	-102.1	-25.17	-182.4
Mo + $\frac{1}{2}$ C $\rightarrow$ $\frac{1}{2}$ Mo <sub>2</sub> C	-49.45	-58.82	-27.82	-96.11
W + C $\rightarrow$ WC	-40.58	-39.49	-38.88	-38.48
Mn + $\frac{1}{3}$ C $\rightarrow$ $\frac{1}{3}$ Mn <sub>3</sub> C	-15.06	-33.24	+29.00	-108.75
Fe + $\frac{1}{3}$ C $\rightarrow$ $\frac{1}{3}$ Fe <sub>3</sub> C	+25.04	+3.69	+70.53	-83.21

**Table 2.** Heat and free energy of formation from the elements of transition metal nitrides ( $\text{kJ mol}^{-1}$ ) calculated from data in Ref. 22.

Transformation	$\Delta H_{298}^0$	$\Delta G_{298}^0$	$\Delta H_{1000}^0$	$\Delta G_{1000}^0$
Sc + $\frac{1}{2}$ C $\rightarrow$ ScN	-313.8	-283.8	-312.0	-213.6
Y + $\frac{1}{2}$ N <sub>2</sub> $\rightarrow$ YN	-299.2	-271.5	-296.6	-207.7
Ti + $\frac{1}{2}$ N <sub>2</sub> $\rightarrow$ TiN	-338.1	-309.4	-335.4	-243.0
Zr + $\frac{1}{2}$ N <sub>2</sub> $\rightarrow$ ZrN	-368.2	-339.6	-365.0	-274.1
Hf + $\frac{1}{2}$ N <sub>2</sub> $\rightarrow$ HfN	-373.6	-346.4	-369.8	-284.4
V + $\frac{1}{2}$ N <sub>2</sub> $\rightarrow$ VN	-217.2	-191.1	-213.6	-131.2
Nb + $\frac{1}{2}$ N <sub>2</sub> $\rightarrow$ NbN	-235.1	-206.0	-231.0	-138.8
Ta + $\frac{1}{2}$ N <sub>2</sub> $\rightarrow$ TaN	-252.3	-223.8	-245.0	-160.9
Cr + $\frac{1}{2}$ N <sub>2</sub> $\rightarrow$ CrN	-117.2	-92.8	-112.1	-37.97
Mo + $\frac{1}{4}$ N <sub>2</sub> $\rightarrow$ $\frac{1}{2}$ Mo <sub>2</sub> N	-40.7	-27.3	-35.8	+1.80
Fe + $\frac{1}{8}$ N <sub>2</sub> $\rightarrow$ $\frac{1}{4}$ Fe <sub>4</sub> N	-2.8	+4.37	-5.1	+8.57
Co + $\frac{1}{6}$ N <sub>2</sub> $\rightarrow$ $\frac{1}{3}$ Co <sub>3</sub> N	+2.8	+11.46	+3.22	+20.1

**Table 3.** Heat and free energy of reaction of molybdenum carbide at 298 K ( $\text{kJ mol}^{-1}$ ) calculated from data in Ref. 22.

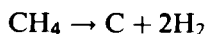
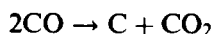
Transformation	$\Delta H_{298}^0$	$\Delta G_{298}^0$
Mo + $\frac{1}{2}$ C $\rightarrow$ $\frac{1}{2}$ Mo <sub>2</sub> C	-24.75	-25.2
Mo + $\frac{1}{2}$ CH <sub>4</sub> $\rightarrow$ $\frac{1}{2}$ Mo <sub>2</sub> C + H <sub>2</sub>	+12.7	+0.15
Mo + CO $\rightarrow$ $\frac{1}{2}$ Mo <sub>2</sub> C + $\frac{1}{2}$ CO <sub>2</sub>	-166.2	-170.0
MoO <sub>3</sub> + 3 $\frac{1}{2}$ C $\rightarrow$ $\frac{1}{2}$ Mo <sub>2</sub> C + 3 CO	+388.8	+231.1
CaMoO <sub>4</sub> + $\frac{1}{4}$ CaC <sub>2</sub> + $\frac{11}{6}$ Al $\rightarrow$ $\frac{1}{2}$ Mo <sub>2</sub> C + $\frac{5}{4}$ CaO + $\frac{11}{12}$ Al <sub>2</sub> O <sub>3</sub>	-786.1	-777.1
MoO <sub>3</sub> + 1 $\frac{1}{6}$ CH <sub>4</sub> $\rightarrow$ $\frac{1}{2}$ Mo <sub>2</sub> C + $\frac{2}{3}$ CO + 2 $\frac{1}{3}$ H <sub>2</sub> O	+170.0	+77.41
Mo(CO) <sub>6</sub> + $\frac{1}{2}$ H <sub>2</sub> $\rightarrow$ $\frac{1}{2}$ Mo <sub>2</sub> C + 5 $\frac{1}{2}$ CO + $\frac{1}{2}$ H <sub>2</sub> O	+162.4	-36.70
MoCl <sub>6</sub> + $\frac{1}{2}$ CH <sub>4</sub> + 2 H <sub>2</sub> $\rightarrow$ $\frac{1}{2}$ Mo <sub>2</sub> C + 6 HCl	-79.7	-192.8
MoS <sub>2</sub> + $\frac{1}{2}$ CH <sub>4</sub> + H <sub>2</sub> $\rightarrow$ $\frac{1}{2}$ Mo <sub>2</sub> C + 2 H <sub>2</sub> S	+247.7	+200.6

**Table 4.** Heat and free energy of reaction of molybdenum carbide at 1000 K ( $\text{kJ mol}^{-1}$ ) calculated from data in Ref. 22.

Transformation	$\Delta H_{1000}^0$	$\Delta G_{1000}^0$
Mo + $\frac{1}{2}$ C $\rightarrow$ $\frac{1}{2}$ Mo <sub>2</sub> C	-23.3	-27.2
Mo + $\frac{1}{2}$ CH <sub>4</sub> $\rightarrow$ $\frac{1}{2}$ Mo <sub>2</sub> C + H <sub>2</sub>	+21.8	-36.9
Mo + CO $\rightarrow$ $\frac{1}{2}$ Mo <sub>2</sub> C + $\frac{1}{2}$ CO <sub>2</sub>	-152.8	-186.8
MoO <sub>3</sub> + 3 $\frac{1}{2}$ C $\rightarrow$ $\frac{1}{2}$ Mo <sub>2</sub> C + 3 CO	+374.4	-135.4
MoO <sub>3</sub> + 1 $\frac{1}{6}$ CH <sub>4</sub> $\rightarrow$ $\frac{1}{2}$ Mo <sub>2</sub> C + $\frac{2}{3}$ CO + 2 $\frac{1}{3}$ H <sub>2</sub> O	+163.2	-140.1
Mo(CO) <sub>6</sub> + $\frac{1}{2}$ H <sub>2</sub> $\rightarrow$ $\frac{1}{2}$ Mo <sub>2</sub> C + 5 $\frac{1}{2}$ CO + $\frac{1}{2}$ H <sub>2</sub> O	+167.2	-570.4
MoCl <sub>6</sub> + $\frac{1}{2}$ CH <sub>4</sub> + 2 H <sub>2</sub> $\rightarrow$ $\frac{1}{2}$ Mo <sub>2</sub> C + 6 HCl	-95.7	-449.1
MoS <sub>2</sub> + $\frac{1}{2}$ CH <sub>4</sub> + H <sub>2</sub> $\rightarrow$ $\frac{1}{2}$ Mo <sub>2</sub> C + 2 H <sub>2</sub> S	+239.1	+95.9

The thermodynamics of nitride formation from molecular nitrogen and transition metals show similar trends to the carbides. Again, the free energies of formation are strongly negative towards the left in the transition series, and become less favorable on moving to the right. Nitride stability is lower at higher temperatures, and is dominated by the heat of reaction. Entropic effects do not stabilize the late transition metal nitrides as they do the carbides. In general, nitride formation is more favorable than carbide formation in the early transition metals, but this is reversed in the late metals.

Thermodynamic considerations are useful for determining conditions for carburization and nitridation. For example, in the nitridation of niobium the particular phase of the product (e.g. NbN,  $\beta$ -Nb<sub>2</sub>N, or  $\gamma$ -Nb<sub>4</sub>N<sub>3</sub>) will depend on temperature and pressure. This holds true also for carbides. However, for carbides, competing reactions such as



can cause deposition of free carbon. These side reactions can be controlled by properly adjusting gas composition by means of ratios of reactant gases such as (CO)/(CO<sub>2</sub>) or (CH<sub>4</sub>)/(H<sub>2</sub>)<sup>2</sup>. Examples are given for WC and Mo<sub>2</sub>C synthesis (Fig. 2).

The thermodynamic considerations above are useful guides to the preparation of carbides and nitrides, but are not limiting as the syntheses can be carried out at nonequilibrium conditions. For example, in the carburization or nitridation of oxides it is possible to lower the temperature of reaction by sweeping away the product gases [23]:



Water vapor produced during reduction is particularly problematic as it can inhibit the reaction or lead to hydrothermal sintering.

### 2.1.8.3 Survey of Preparative Methods

Many types of preparation are applicable for both carbides and nitrides, and these will be described in this section. General references for this section are Frad [24], Juza [25], Kosolopova [26], Toth [1], Santhanam [27], and Stoll and Santhanam [28].

Some of the methods described in this section are employed to produce metallurgical carbides and produce low specific surface area ( $S_g$ ) materials. Nevertheless, some of the compositions have been used in catalytic studies (especially prior to 1980), and their preparation is included in this section.

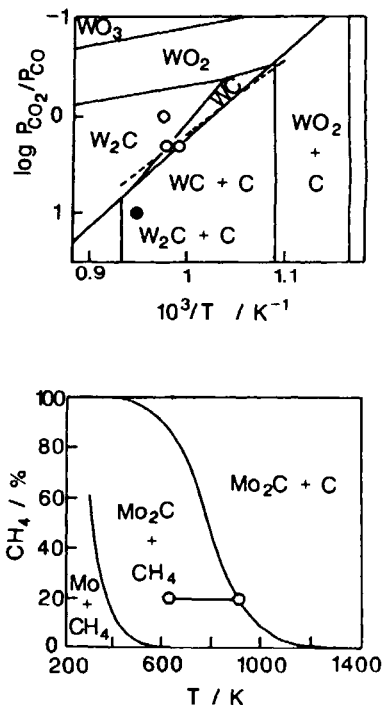
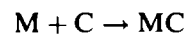


**Figure 2.** Equilibrium curves for the carburization of tungsten and molybdenum. The tungsten diagram shows experiment points for W<sub>2</sub>C (open circles) and WC (solid circle) [39]. The molybdenum diagram shows the operating line for synthesis with 20% CH<sub>4</sub> in H<sub>2</sub> [11] (reproduced with permission from Ref. 3).

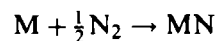
## A Direct Reaction of Metals and Nonmetals

### a Carbides



This method of preparation is carried out by contacting metallic powders and solid carbon, sometimes in the presence of gaseous hydrocarbons, at 1500–2300 K. Thermodynamics (Section A.2.1.8.2) indicate that carbide formation from the elements is favorable at low temperatures, but high temperatures are used to counter solid-state diffusion limitations [26]. Heating provided by conventional ovens or at higher temperatures in arc furnaces. The latter method is called the Moissan fusion method, after the originator [29, 30]. In the case of the fusion method, the carbides are produced in a molten form and cast shapes can be poured from the melt [31].

### b Nitrides



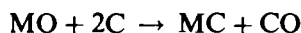
Thermodynamic calculations (Table 2) indicate that nitride formation from the elements is favorable, and indeed, many nitrides can be so prepared. For example, TiN, VN, and CrN can be made at 1 bar with mo



cular nitrogen. As with the carbides, the transformations are diffusion controlled and high temperatures are needed, usually between 1400 K and 1900 K [25]. Elements to the right of molybdenum cannot be nitrified with molecular nitrogen at pressures attainable in conventional facilities.

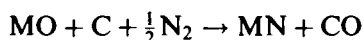
## B Reaction of Metal Oxides in the Presence of Solid Carbon

### a Carbides



This transformation is carried out by intimately mixing metal oxide powders with carbon, again as with the pure metals, at temperatures between 1500–2300 K, with or without the presence of a hydrocarbon gas. The reactions of oxides with carbon are thermodynamically favored, but high temperatures are again needed because the transformations are limited by diffusion. The direct transformation of oxides to carbides is economically advantageous over the use of metals since the need to separately reduce the oxide phases is avoided. Wide application is found for the commercial production of carbides of molybdenum, tungsten, and tantalum.

### b Nitrides



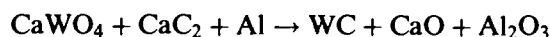
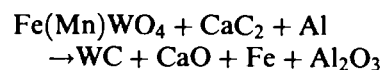
The carbothermal nitridation of oxides is a common method of preparation of nitrides that goes back to the work of Friederich and Sittig [32] in 1925. It is generally applicable to nitrides of high thermal stability such as TiN, VN and CrN. Its main drawback is that it produces impure phases.

## C Extraction of Carbides from Ferrous Alloys



This method involves extracting carbide precipitates from solid solution of steels and ferrous alloys. The method is reported by Shimer [33] in 1887 who prepared TiC by dissolving Fe from a titanium-bearing cast iron with hydrochloric acid. Commercial practice involves the use of minerals such as wolframite  $Fe(Mn)WO_4$  or microlite  $Ca_2Ta_2O_7$  in a high-temperature melt of auxiliary (menstruum) metal with carbon [28]. Carbides of vanadium, chromium, titanium, tantalum, tungsten, and molybdenum for use in machine tools have been produced in this way. Disadvantages of the method are the use of costly acids and the generation of considerable amounts of waste salts.

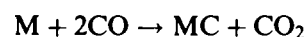
## D Reaction of Oxides with Calcium Carbide and Aluminum



Reactions such as the above have been used for the large-scale commercial production of WC by Kennametal, Inc. in a process called the Macro Process [28]. Thermodynamics for the analogous molybdenum reaction show that the reaction is highly exothermic (Table 3). The solid reactants are metered into a carbon-lined kiln to develop a self-sustained exothermic reaction. The reaction occurs in a pool of molten metal at temperatures above 2800 K. At the end of the run the kiln contents solidify into a lower heavy layer of carbide crystals and an upper slag layer of oxides.

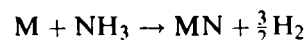
## E Reactions of Metals or Metal Oxides with Gas-Phase Reagents

### a Carbides



Carburization with gaseous carbon sources such as methane, higher hydrocarbons, and carbon monoxide was initially carried out mainly with metal wires such as tungsten or tantalum, and coarse tungsten powder. Clearly, contacting of the gas and the solid is a problem, and the method is not used commercially. However, it is very useful for the preparation of small-scale laboratory batches. For catalytic applications metals have been carburized with methane and ethane [34], propane [35], and carbon monoxide [36]. One approach to obtain higher surface area carbides has been to maximize the surface area of the precursor [37]. In this manner Palanker et al. [38] optimized the surface area of a tungstic acid precursor to obtain tungsten carbide of  $S_g$  up to  $30 \text{ m}^2 \text{ g}^{-1}$ . Similarly, Lemaître et al. carburized a hydrous oxide precursor with a CO/CO<sub>2</sub> mixture to obtain tungsten carbide with  $S_g$  of  $47 \text{ m}^2 \text{ g}^{-1}$  [39].

### b Nitrides



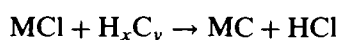
Flowing ammonia has been applied to the synthesis of the nitrides of iron, cobalt, and nickel compounds with very low enthalpies of formation (Table 2). Again, isothermal conditions were employed. Ammonia is preferable over the use of molecular nitrogen to nitride

metals or oxides because of the following favorable reaction that produces surface nitrogen,  $N^*$ , and eventually nitride:



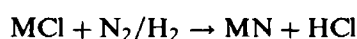
## F Decomposition of Metal Halide Vapors

### a Carbides



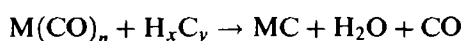
In this method metal chlorides or oxychlorides are made to react with gaseous hydrocarbons in the vicinity of a localized heat source (1400–2100 K). Clearly, the reaction is thermodynamically favorable (Tables 3 and 4). The method was first used by Van Arkel in 1923 with an incandescent tungsten filament to make carbides of tantalum and zirconium [40]. Although the reaction variables have been studied extensively, problems remain with control of the process and with low productivity. Application to catalyst synthesis has been moderate [41].

### b Nitrides



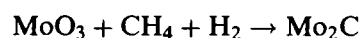
The Van Arkel process can also be used to make metal nitrides. Because of the tendency of  $NH_3$  to decompose at the temperatures needed for nitride formation (1300–1900 K), the gaseous reactant is a mixture of  $H_2$  and  $N_2$ . The nitride forms as a layer around the tungsten wire.

## G Decomposition of Gaseous Metal Carbonyls



This method is similar to that employing metal chlorides, except that it uses metal carbonyls. Both methods still receive attention [42]. In the case of the carbonyl compounds the heat of reaction is unfavorable, but the transformation is driven by the release of substantial amounts of carbon monoxide (Tables 3 and 4). The use of carbonyl compounds rather than metal chlorides may have some advantages since the carbon source is already included in the starting material [43]. For example, the reaction of  $WCl_6$  in an isobutane/hydrogen atmosphere produced a WC sample extensively contaminated by surface carbon, as seen by Auger electron spectroscopy. On the other hand, the reaction of  $Mo(CO)_6$  in hydrogen/CO mixtures gave a molybdenum oxycarbide,  $MoO_xC_y$ , with substantially improved surface properties [44], and good activity in ammonia synthesis [45].

## H Temperature-Programmed Methods (Carbides and Nitrides)



The temperature-programmed reaction (TPR) method of preparation [46] is a variation of the isothermal method described in Section E. The TPR method consists of treating an oxide precursor in a reactive gas stream while raising the temperature in a uniform manner. By monitoring changes in the exit gas-phase composition, the end of the reaction can be ascertained and the product quenched. Because the synthesis involves the direct transformation of an oxide to a carbide or nitride, it is possible to bypass the metallic state, which is the most prone to sinter (lowest Tamman temperature). In addition, the use of the temperature program allows an optimal balance between synthesis and sintering rates and results in product with high specific surface areas ( $S_g$ ).

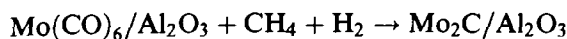
A typical synthesis [47] using the TPR method is exemplified by the preparation of  $\beta$ - $Mo_2C$  (hcp) from  $MoO_3$  using a  $CH_4/H_2$  reactant gas mixture. Gas chromatographic traces as a function of temperature and X-ray diffraction indicate that the transformation occurs through a  $MoO_2$  intermediate. The resulting product  $\beta$ - $Mo_2C$  is formed with  $S_g$  increasing from 50 to  $90 \text{ m}^2 \text{ g}^{-1}$  as the  $CH_4$  concentration is raised from 20 to 100 mol%.

If instead of the  $CH_4/H_2$  reactant, a pure  $NH_3$  stream is used; the product is  $\gamma$ - $Mo_2N$  (fcc) of surface area as high as  $225 \text{ m}^2 \text{ g}^{-1}$  [48]. This high value (the equivalent of a silica of  $800 \text{ m}^2 \text{ g}^{-1}$ ) is the result of a solid-state process known as a topotactic transformation [49]. In this process nitrogen replaces oxygen in the lattice with minimal disruption of the molybdenum atoms, so that the product  $\gamma$ - $Mo_2N(100)$  planes are produced parallel to the original parent  $MoO_3(010)$  planes. Because of density differences each original  $MoO_3$  crystallite of  $\mu\text{m}$  size is transformed into a sponge-like porous agglomerate of  $\gamma$ - $Mo_2N$  microcrystals, retaining the original external size and shape of the  $MoO_3$  parent. This retention of external morphology is known as pseudomorphism. Because of the gradual replacement of oxygen by nitrogen, there is no  $MoO_2$  intermediate phase but, rather, a continuous transformation through oxynitride compositions.

The same process can be repeated using  $WO_3$  as the starting material to produce  $\beta$ - $W_2N$  (fcc) of up to  $90 \text{ m}^2 \text{ g}^{-1}$ . Interestingly, both the  $\gamma$ - $Mo_2N$  and  $\beta$ - $W_2N$  can be converted by topotactic transformations to the corresponding carbides, but of the high-temperature cubic structure,  $\alpha$ - $MoC_{1-x}$  (fcc) and  $\alpha$ - $WC_{1-x}$  (fcc) with  $x \approx 0.5$ . These phases retain the high surface area of their parent nitrides [50, 51].

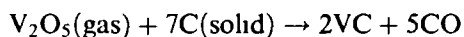
The TPR method has now been applied to  $TiN_xO_y$  [52], VN [23], and NbC [53]. Although the TPR method produces high surface area materials, the pore structure of these is usually not controllable. Often, the pores are in the micropore regime (< 3 nm). However, a number of the solid state transformations that lead to carbides and nitrides are topotactic and exhibit pseudomorphism (retention of external particle size and shape) This provides a possible means of engineering the pore structure by preparing oxide precursors with the desired external morphology.

## I Utilization of Supports



Highly dispersed carbide phases may be prepared by depositing a precursor on a support and carburizing it This was demonstrated by Lee et al [12] for molybdenum carbide using  $Mo(CO)_6$  deposited onto dehydroxylated alumina from the gas phase Carburization in a  $CH_4/H_2$  stream resulted in a highly dispersed material which X-ray absorption fine structure spectroscopy (EXAFS) confirmed to be  $\beta$ - $Mo_2C$ . Supported carbides and nitrides may also be obtained from supported oxide precursors [12, 54, 55], and supported nitrides may be converted to supported carbides [56] For example, a TiN coating on spherical  $SiO_2$  particles was prepared by nitriding  $TiO_2/SiO_2$  with ammonia [57] The use of supports offer the advantage of better usage of the active component and higher control of surface area and pore size distribution

## J Reaction Between Metal Oxide Vapor and Solid Carbon



A novel method of preparation of ultrahigh surface area carbides has been developed by the group of Ledoux It involves the reaction of solid carbon with vaporized metal oxide precursors such as  $MoO_3$  or  $WO_2$  [58] The synthesis uses high specific surface area-activated carbons and the final product appears to retain a "memory" of the porous structure of the starting material The carbon acts as a skeleton around which the carbides are formed Catalytically active carbides with surface areas between 100 and  $400\text{ m}^2\text{ g}^{-1}$  are generated.

## References

- 1 L E Toth *Transition Metal Carbides and Nitrides*, Academic Press, New York, 1971
- 2 E K Storms, *The Refractory Carbides*, Academic Press, New York, 1967

- 3 S T Oyama, *Catal Today* **1992**, *15*, 179
- 4 S T Oyama, Ed, *The Chemistry of Transition Metal Carbides and Nitrides*, Blackie Academic and Professional, London, 1996
- 5 S T Oyama, *J Solid State Chem* **1992**, *96*, 442
- 6 R B Levy, M Boudart, *Science* **1973**, *181*, 547
- 7 B Vidick, J Lemaitre, L Leclercq, *J Catal* **1986**, *99*, 439
- 8 G S Ranhotra, A T Bell, J A Reimer, *J Catal* **1987**, *108*, 40
- 9 M Boudart, S T Oyama, L Leclercq, *Proc 7th Int Cong Catal*, Tokyo, 1980, (Eds T Seiyama and K Tanabe) Kodansha, 1980, Vol 1 p 578
- 10 S T Oyama, *J Catal* **1992**, *133*, 358
- 11 J S Lee, S T Oyama, M Boudart, *J Catal* **1987**, *106*, 125
- 12 J S Lee, M H Yeom, K Y Park, I-S Nam, J S Chung, Y G Kim, S H Moon, *J Catal* **1991**, *128*, 126
- 13 M J Ledoux, C Pham Huu, J Guille, H Dunlop, *J Catal* **1992**, *134*, 383
- 14 F H Ribeiro, M Boudart, R A Dalla Betta, E Iglesia *J Catal* **1991**, *130*, 498
- 15 F H Ribeiro, R A Dalla Betta, M Boudart, J Baumgartner, E Iglesia, *J Catal* **1991**, *130*, 86
- 16 J C Schlatter, S T Oyama, J E Metcalfe, III, J M Lambert, Jr, *Ind Eng Chem Res* **1988**, *27*, 1648
- 17 E J Markel, J W Van Zee, *J Catal* **1990**, *126*, 643
- 18 M Nagai, T Miyao, *Catal Lett* **1993**, *18*, 9
- 19 K S Lee, H Abe, J A Reimer, A T Bell, *J Catal* **1993**, *139*, 34
- 20 D J Sajkowski, S T Oyama, *Appl Catal* **1996**, *134*, 339
- 21 C W Colling L T Thompson, *J Catal* **1994**, *146*, 193
- 22 O Knacke, O Kubaschewski, K Hesselmann, *Thermochemical Properties of Inorganic Substances*, 2nd ed, Springer-Verlag, Berlin, 1991
- 23 R Kapoor, S T Oyama, *J Sol St Chem* **1992** *99* 303
- 24 W A Frad in *Advances in Inorganic Chemistry and Radiochemistry* (Eds H J Emeleus, A G Sharpe) Academic Press, New York, 1968, Vol 2, p 153
- 25 R Jusa in *Advances in Inorganic Chemistry and Radiochemistry* (Eds H J Emeleus, A G Sharpe), Academic Press, New York, 1966, Vol 9, p 81
- 26 T Ya Kosolapova, *Carbides Properties Production and Applications*, Plenum Press New York, 1971
- 27 A T Santhanam in *Kirk Othmer Fncyclopedia of Chemical Technology* (Ed M E Howe Grant), 4th ed, John Wiley & Sons New York 1992 Vol 4, p 848
- 28 W M Stoll, A T Santhanam in *Kirk Othmer Encyclopedia of Chemical Technology* (Ed M E Howe-Grant), 4th ed, John Wiley & Sons, New York, 1992, Vol 4, p 861
- 29 H Moissan, *Compt Rend* **1893**, *116*, 1225
- 30 H Moissan, *The Electric Furnace* (Translated A T de Moulpied), Arnold, London, 1904
- 31 P Schwarzkopf R Kieffer *Refractory Hard Metals*, Macmillan, New York, 1953
- 32 E Friederich, L Sittig *Z Anorg Allgem Chem* **1925**, *143*, 293
- 33 P W Shimer, *Chem News* **1887**, *55*, 156
- 34 J S Sinfelt, D J C Yates, *Nature Phys Sci* **1971**, *229*, 27
- 35 M Saito, R B Anderson, *J Catal* **1980** *63* 438
- 36 B Vidick, J Lemaitre, B Delmon, *Acta Chim Acad Sci Hungar* **1982**, *111*, 449
- 37 E A Mazulevsky V Sh Palanker, E N Baybatyrov, A M Khisametdinov, E I Domanouskaya, *Kinet Katal* **1977**, *18*, 767
- 38 V Sh Palanker, D V Sokolsky, E A Mazulevsky, E N Baybatyrov, *J Power Sources* **1976/1977**, *1*, 169
- 39 J Lemaitre, B Vidick, B Delmon, *J Catal* **1986** *99* 415
- 40 A E Van Arkel, *Physica* **1923**, *3*, 76
- 41 L Leclercq, M Boudart, US Patent 4 107 282, Aug 15, 1978, (Stanford University)

42. J. Hojo, T. Oku, A. Kato, *J. Less-Common Met.* **1978**, *59*, 85.
43. L. Leclercq in *Surface Properties and Catalysis by Non-Metals* (Eds: J. P. Bonnelle, B. Delmon, E. Derouane), Reidel, Dordrecht, **1983**, p. 433.
44. L. Leclercq, K. Imura, S. Yoshida, T. Barbee, M. Boudart in *Preparation of Catalysts II* (Eds: B. Delmon, P. Grange, P. A. Jacobs, G. Poncelet), Elsevier, **1978**, p. 627.
45. M. Boudart, S. T. Oyama, L. Leclercq, *Proc. 7th Int. Cong. Catal.* (Eds: T. Seiyama, K. Tanabe), Kodansha, **1980**; Vol. 1, p. 578.
46. S. T. Oyama, PhD Thesis, Stanford University, **1981**.
47. J. S. Lee, S. T. Oyama, M. Boudart, *J. Catal.* **1987**, *106*, 125.
48. L. Volpe, M. Boudart, *J. Sol. St. Chem.* **1985**, *59*, 332.
49. L. Volpe, M. Boudart, *Catal. Rev.-Sci. Eng.* **1985**, *27*, 515.
50. L. Volpe, M. Boudart, *J. Sol. St. Chem.* **1985**, *59*, 348.
51. J. S. Lee, L. Volpe, F. H. Ribeiro, M. Boudart, *J. Catal.* **1988**, *112*, 44.
52. C. H. Shin, G. Bugli, G. Djega-Mariadassou, *J. Sol. State Chem.* **1991**, *95*, 145.
53. V. L. S. Teixeira da Silva, E. I. Ko, M. Schmal, S. T. Oyama, *Chem. Mat.* **1995**, *7*, 179.
54. L. H. Slaugh, R. J. Hoxmeier, US Patent 4326 992, **1982**, (Shell Oil Company).
55. D. E. Willis, *J. Catal.* **1983**, *84*, 344.
56. L. H. Slaugh, R. J. Hoxmeier, US Patent 4325 843, **1982**, (Shell Oil Company).
57. R. E. Partch, Y. Xie, S. T. Oyama, E. Matijevic, *J. Mater. Sci.* **1993**, *8*, 2014.
58. M. J. Ledoux, C. Pham-Huu, S. Marin, M. Weibel, J. Guille, *C. R. Acad. Sci. Paris*, **1990**, *310*, Série II, 707.

## 2.1.9 Carbons

R. SCHLÖGL

### 2.1.9.1 Introduction

The element carbon plays a multiple role in heterogeneous catalysis. In homogeneous catalysis it occurs as the most prominent constituent of ligand systems and will be treated as such there. Carbon-containing molecules are, in most catalytic applications, the substrates of the process under consideration. Deposits and polymers of carbon often occur as poisons on catalysts. Carbon deposition is the most severe problem in certain zeolite applications. In hydrogenation reactions carbon deposits are thought to act as modifiers of catalyst activity and to provide selectivity by controlling the hydrogenation–dehydrogenation activity of the metal part of the catalyst. Carbon deposits are even thought to constitute part of the active sites in some cases.

Carbon is a prominent catalyst support material as it allows the anchoring of metal particles on a substrate which does not exhibit solid acid–base properties. Carbon is finally a catalyst in its own right, enabling the activation of oxygen and chlorine for selective oxidation, chlorination, and dechlorination reactions.

These multiple roles operate in parallel with a complex structural chemistry giving rise to families of chemically vastly different modifications of the element. It is a special characteristic of carbon chemistry that many of these modifications cannot be obtained as phase-pure materials. This limits the exact knowledge of physical and chemical properties to a few archetype modifications, namely graphite and diamond.

The reason for this poor definition of materials is found in the process of their formation, namely difficult to control polymerization reactions. Such reactions also occur in catalytic reactions with small organic molecules. The nature of carbon deposits therefore reflect all the complexity of the bulk carbon materials. One aim of this article is to describe the structural and chemical complexity of carbon or “soot” in order to provide an understanding of the frequently observed complexity of the chemical reactivity (e.g. in reactivation processes aiming at an oxidative removal of deposits).

The surface chemistry of carbon which determines its interfacial properties is a rich field as a wide variety of surface functional groups are known to exist on carbon. By far the most important family of surface functional groups are those involving oxygen. Other prominent heteroatoms on the surface are hydrogen and nitrogen. This article focuses on the description and characterization of oxygen surface functional groups.

The final section discusses selected case studies of carbon chemistry in catalysis in order to illustrate characteristic properties of carbon materials as wanted or unwanted components in catalytic systems.

### 2.1.9.2 Structural Chemistry of Carbon

The chemistry of carbon is extremely complex, both in the molecules and in the solid state. The reason for this complexity lies in the pronounced tendency of the element to form homonuclear bonds in three bonding geometries. They can either occur uniformly or in almost unlimited combinations allowing a very large number of homonuclear structures of elemental carbon. The moderate electronegativity of carbon allows for strong covalent interactions with all main group elements. This adds enormously to the complexity of the solid-state chemistry of carbon. In the present context carbon–oxygen bonds will be treated in some detail as they determine to a large extent the stability and reactivity of carbon in typical catalytic environments.

A consequence of the wide choice of bonding situations for carbon atoms is that very few species can be prepared with any degree of purity, thus complicating the determination of structural, chemical, and physical properties. This is illustrated by the fact that even the

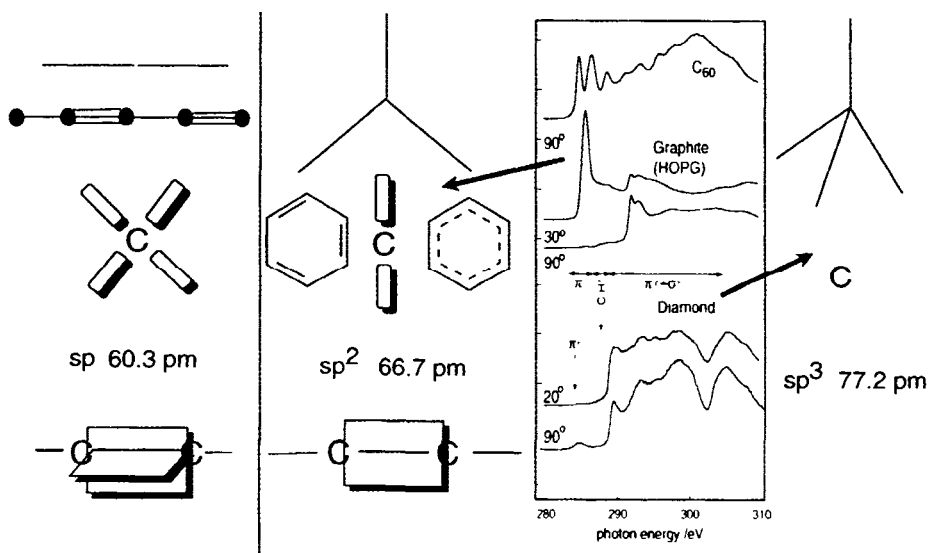


**Figure 1.** Connectivities and principle bonding properties of carbon. From top to bottom: connectivity, chemical bonding representation, distribution of  $\pi$  electrons, hybridization symbol, bond length, orientation of the  $\pi$  bonds relative to the carbon skeleton. The spectra represent polarization-dependent carbon 1s XAS data for  $sp^2$  and  $sp^3$  carbons. The angles denote the orientation of the  $E$  vector of the incident light relative to the surface normal of the oriented sample. The assignment of the spectral regions is given and was deduced from the angular dependence of the intensities of each feature. The graphite impurity in the CVD diamond film is less than 0.1 monolayers.

crystal structure of graphite is only an approximate model [1] as no single crystal with low enough defect concentrations has been found to allow a regular three-dimensional X-ray structure determination. In the context of catalysis it is important to note that “black carbon”, “coke”, “soot” or “carbonaceous deposit” is by no means a graphitic or even homogeneous material with reproducible properties. This leads to the wide variations in application profiles of synthetic carbon blacks (several thousand varieties) and to the difficulties in the determination of oxidation properties of “coke” on catalyst surfaces.

### 2.1.9.3 Overview

The carbon atom with its  $2s^2$ ,  $2p^2$  electron configuration can form a maximum of four bonds which can be either single, double or triple. As a consequence as three main connectivities result depicted in Fig. 1. The valence orbitals hybridize forming, in the elemental state,  $sp$ ,  $sp^2$  or  $sp^3$  hybrid orbitals. The data in Fig. 1 illustrate that the local bonding geometry and the carbon-carbon bond distances vary significantly with the connectivity as the bond order (and bond strength) increases from the  $sp^3$  to the  $sp$  hybridization state.

The tetrahedral connectivity leads to space-filling carbon polymers which are realized as defect-free ideal structures in diamond. The trigonal connectivity leads to sheets of carbon which are, in the defect-free variety, made up of hexagons leading to so-called graphene layers. The structures of graphite will result if these layers are regularly stacked in the third dimension. In

the trigonal connectivity the  $sp^2$  hybrid orbitals leave one nonbonding atomic orbital per carbon atom. These orbitals can interact with each other forming so-called weak bonds. These weak bonds can either interact as isolated or conjugated localized double bonds as in alkene molecules or as delocalized aromatic bonds providing metallic properties as in graphite. Any combination between these ideal interactions in defective carbons occurs within areas of double bond character and areas of aromatic character within one carbon sheet. In molecular chemistry this effect of varying degree of double bond localization is referred to as mesomerism. This is rarely observed experimentally (in certain polycyclic aromatic molecules) due to the limited size of organic molecules. A further consequence of the existence of the weak bonds is the action of strong dispersive forces (or van der Waals bonds) in successive layers allowing for the cohesion of graphene layers. These forces provide energy for chemisorption of both polar and nonpolar molecules on graphite surfaces. The bonding strength of the planar connectivity leads to a very poor chemical reactivity of graphene layers which are only reactive at their edges, where the lack of carbon atoms results in dangling bonds.

The trigonal connectivity leads not only to hexagons but enables the incorporation of triangles, pentagons, heptagons and larger cyclic structures as local defects into the basic honeycomb structure. A consequence of these defects is the strong localization of double bonds

around these defects and the deviation of the carbon sheet from planarity. Three-dimensional bends require the incorporation of non-hexagonal units in carbon layers. These form preferred centers of chemical reactivity as the localized double bonds will behave as alkene molecules in organic chemistry, showing pronounced reactivity towards addition and insertion as compared to the typical substitution chemistry of aromatic structures.

The linear connectivity of  $sp$  hybridization leads to chain-like polymers with conjugated triple bonds formed by the two sets of orthogonal nonbonding orbitals shown in Fig. 1. The resulting structure of cumulated electron density creates high chemical reactivity towards restructuring into the trigonal or tetragonal connectivity and towards addition of heteroatoms. A redistribution of the weakly bonding electrons, as found in molecular ketenes, does not occur in pure carbon materials. The inherent chemical instability of this arrangement causes the materials to occur, under ambient conditions, only rarely in pure form after rapid quenching from high-temperature carbon sources or in meteorites. These phases (e.g. chaotit) are thermodynamically metastable but can occur as part of more complex carbon polymers.

Figure 1 also shows how the different bonding situations are reflected in electron spectroscopy. Depicted are X-ray absorption spectra (XAS) [2] of  $C_{60}$ , graphite and diamond (as CVD film [3], with a trace impurity of graphite). The carbon 1s XAS method is chosen as it resolves clearly the presence of delocalized electrons from the  $\pi$  bonds shown in the connectivity diagrams. For oriented surfaces the polarization dependence of the excitation with synchrotron light allows direct determination of the orientation of the  $\pi$  bond relative to the carbon-carbon backbone bonding which accounts for the high-energy structures. Fullerene and graphite are dissimilar in their spectra mainly because of the molecular character of fullerene, giving rise to discrete bands of weakly interacting molecular orbitals, whereas in graphite a complete overlap of molecular states to broad bands of density of states gives rise to only a few structural features in the spectrum. The ordering of electronic states with energy is, however, very similar for the two carbons with the same connectivity.

#### 2.1.9.4 Basic Structures

The two allotropes of carbon with particularly well defined properties are hexagonal graphite, as thermodynamically stable modification at ambient conditions, and its high-pressure, high-temperature allotrope, cubic diamond. Although both well-crystallised forms with only very rarely be encountered in catalytic systems, it is important to recall some details about their prop-

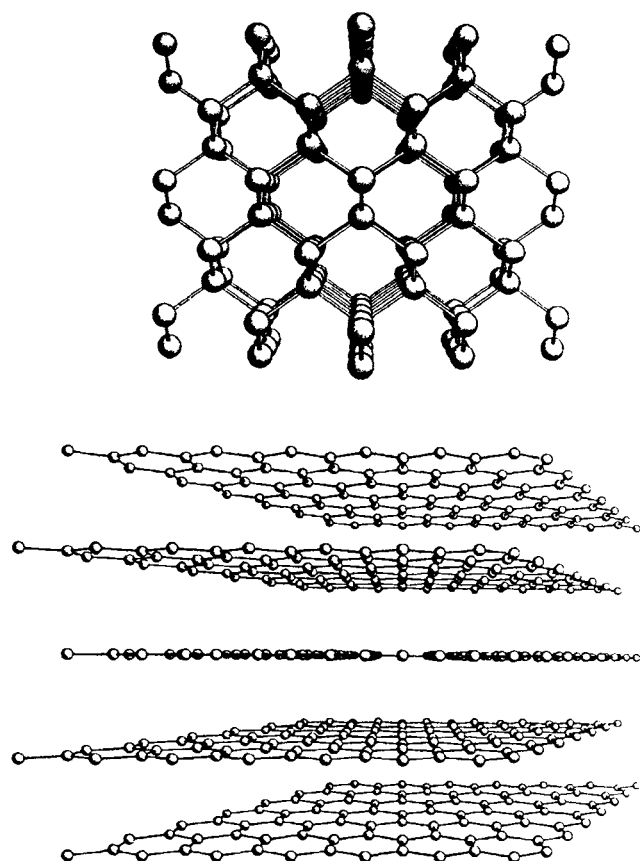


Figure 2. Idealized crystal structures of diamond and graphite

erties as these also prevail in the practical forms of carbon.

The idealized crystal structures are displayed in Fig. 2. The consequences of the different connectivities can be clearly seen. Diamond is an isotropic material consisting of corner-sharing tetrahedra, equivalent to a face-centred close-packed structure of carbon atoms with additional atoms in the centers of every other octant of the cubic unit cell. The ideal tetrahedral arrangement of carbon atoms leads to four equal bonds 154 pm in length. The long-range ordering can be described by layers of bent carbon hexagons with one additional interlayer bond per carbon atom. The bent hexagons are equivalent to cyclohexane with the in-plane bonds in equatorial and the interlayer bonds in axial positions. The resulting crystals are highly symmetric (space group  $Fd\bar{3}m$ ) with a preferred (111) cleavage plane. The historical classification of diamond is according to optical absorption properties, which are predominantly controlled by the abundance of substitutional nitrogen and boron atoms.

The structural properties are reflected in the physical properties selected in Table 1. Diamond is a superhard electrical insulator with an extremely good thermal conductivity. Phase transitions into the liquid state or

**Table 1.** Selected properties of hexagonal graphite and cubic diamond. Anisotropic data for graphite are given in directions first parallel to and then perpendicular to the graphene layers.

Property	Graphite	Diamond
Density ( $\text{g cm}^{-3}$ )	2.266	3.514
C–C bond length (pm)	142	154
Enthalpy of sublimation ( $\text{kJ mol}^{-1}$ )	715	710
Enthalpy of oxidation ( $\text{kJ mol}^{-1}$ )	393.51	395.41
Enthalpy of formation ( $\text{kJ mol}^{-1}$ )	0.0	1.90
Melting temperature (K)	2600/9 kbar	4100/125 kbar
Thermal expansion ( $\text{K}^{-1}$ )	$-1 \times 10^{-6}/+29 \times 10^{-6}$	$1 \times 10^{-6}$
Electrical resistivity ( $\Omega \text{ cm}^{-1}$ )	$5 \times 10^{-7}/1$	$10^{20}$
Mohs hardness	0.5/9	10

sublimation occur outside the range of conditions for catalysis (see Table 1). Its chemical reactivity is very limited, occurring mainly through a catalyzed transformation into graphite. From there oxidation and halogenation reactions will occur. An extensive report about structural, morphological and kinetic aspects is available [4].

The trigonal connectivity leads to a planar arrangement of carbon with stronger bonds between the carbon atoms within the planes, as seen from the reduced bond distance of 142 pm. The interplanar distance of 335 pm is significantly larger than the in-plane bonds, leading to a significant reduction of the bulk density of graphite as compared to that of diamond (Table 1). All physical properties are strongly anisotropic with a metallic character within the plane directions and an insulator behavior perpendicular to the planes.

The electrical properties are unusual in that a very small band overlap between valence and conduction band of the order of 0.004 eV allows a very small number of carriers (0.02 electrons per C atom) to move freely with extremely small scattering probability. This yields good electrical in-plane conductivity. Perpendicular to the graphene planes the conductivity is of the zero-band semiconductor type with an inverse temperature coefficient as for the metallic in-plane conductivity. As defects increase in the graphene layers the conduction mechanism gradually changes from metallic to semiconducting with only moderate changes in the absolute resistivity, which now cannot be measured as an anisotropic quantity. A high density of defect states on both sides of the Fermi level [5] accounts for this behavior, which makes carbon brushes and carbon filament lamps work. The determination of the temperature dependence of the electrical resistivity is a suitable method with which to determine the degree of graphitic medium range structure in nanocrystalline carbon materials. It also allows the structural effects to be followed of heat treatment during graphitization of nongraphitic precursors.

The interplanar bonding forces are of the order of  $5 \text{ kJ mol}^{-1}$ , and are so weak that small changes in

electronic structure of adjacent planes allow swelling of the structure and the incorporation of a very large number of heteroelements and molecular compounds. The electronic changes can be either (i) a weak chemical reduction of the graphene layers by donor compounds such as alkali atoms or (ii) a weak oxidation by bromine, halide salts or mineral acids. All these compounds form intercalation structures with complicated structural and physical properties which have been investigated extensively [6].

In ideal graphite the graphene layers are very large relative to their thickness and are free of intralayer defects. Furthermore, they are stacked in perfect periodicity either in ABAB or in ABCABC stacking sequences giving rise to hexagonal or rhombohedral graphite. Graphite in catalytic situations differs considerably from this ideal structural type – several types of defects give rise to different families of modifications.

Apart from reactivity towards intercalation, graphite is rather inert to other chemicals, except strong oxidizing agents which form covalent compounds such as graphite fluoride or graphite oxide. Total oxidation of graphite to CO and CO<sub>2</sub> is a highly complex gas–solid reaction which is strongly influenced by the defect structure of the graphite. The reason for this is the chemical inertness of the ideal graphene layer, which cannot be attacked by molecular or atomic oxygen at thermal energies. Reaction thus occurs only at defect sites, such as missing atoms or nonhexagons, and on the perimeter of the graphene layer which collectively form the prism faces of graphite crystal. As these faces occupy less than 0.1% of the graphite crystal faces the number of reactive centers for oxidation in graphite is small. Reactivity thus depends heavily on the additional sites provided by in-plane defects.

In summary, graphite and diamond are two modifications of carbon with similar strong bonds between the carbon atoms (difference in bond length 8.5%). The differing hybridization leads to a different orientation of the covalent interaction. The strong structural ani-

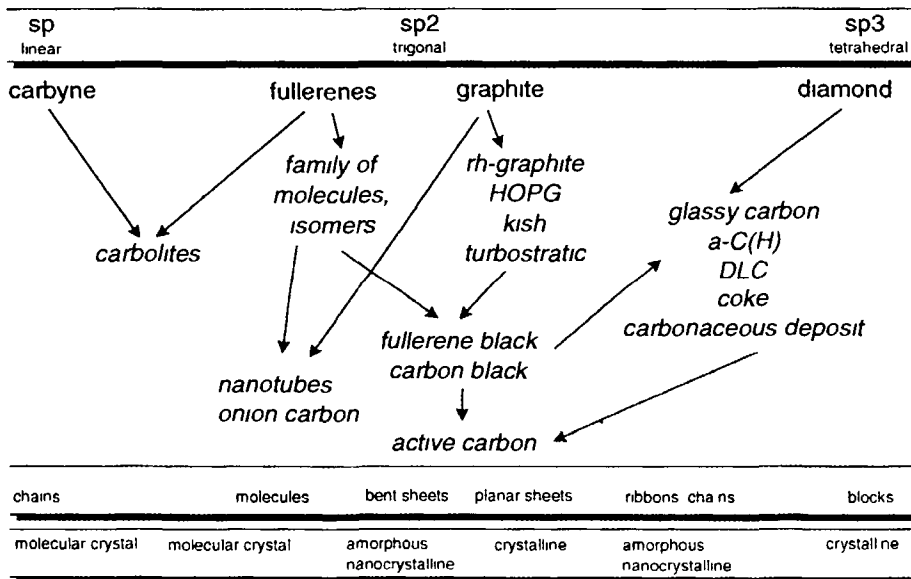


**Figure 3.** Families of carbon materials. The top line indicates the connectivity followed by the parent carbon materials representing according to present knowledge all allotrope phases of carbon. The range of materials in the center of the figure comprises carbons with distinct structural and chemical properties. Whether these are distinct phases or metastable phase mixture is not clear. The arrows mark structural relationships between the materials. The lower lines indicate the shape of the basic structural units and their organization in the solid state.

sotropy of graphite as compared to the perfectly isotropic diamond structure gives rise to fundamental physical and structural differences. The differing carbon-carbon bond strengths provide the handle with which to discriminate between the two modifications with a variety of spectroscopic methods. Such methods are of minor importance as long as crystalline materials are under discussion. In catalytic situations, however, multiphase amorphous carbon is frequently encountered which cannot be analyzed convincingly using diffraction techniques.

The fullerenes and carbynes, which are also well-defined forms of carbon, are very rare in their pure forms in catalytic materials. For this reason they will not be treated in detail in this work. Briefly, carbynes are molecular crystals of columns of carbon atoms linked with alternating single and triple bonds. The column length is variable but mass-spectral data suggest lengths of between 10 and 20 carbon atoms. A collection of properties of these silver-white carbons prepared by shock sublimation of graphite which seem stable only at temperatures above 2300 K but survive storage in natural conditions for thousands of years can be found in the literature [7].

Fullerenes [8, 9] are a large family of molecular carbon cage structures all with carbon atoms in the  $sp^2$  configuration. The three-dimensional structure is made possible by a controlled incorporation of pentagons [8] into the hexagon network. The high symmetry of the resulting ball-shaped molecules is the consequence of certain rules of combination, such as never combining two pentagons and including only 12 pentagons in

every molecule. In the frequent event of not following these rules, the bent carbon sheets polymerize to form complex amorphous carbons called fullerene black [10]. It is very important, in the present context, to note that the chemistry of these spherical  $sp^2$  carbons is substantially different from that of the planar allotrope graphite. The distinction arises from the "strain" in the weak bonds of the fullerenes. The non-planar geometry of the backbone reduces the orbital overlap of the  $\pi$  electrons (Fig. 1) causing localization of the double bonds and an overall chemistry of an electron-poor electrophilic polyalkene [11–13]. One consequence of this is an enhanced reactivity of fullerenes against oxygen compared to graphite [13–15]. Bends in graphene layers are thus the preferred centres of chemical reactivity even without the presence of coordinative undersaturation.

### 2.1.9.5 Loosely Defined Structures

Figure 3 summarizes some families of carbon materials which are defective variants of the basic allotropes shown in the top line of the scheme. These materials exhibit distinctly different properties compared to the idealized parent structures, so that they are often considered as carbon modifications in their own right. In the bottom lines the long-range ordering types and the crystal types are given for the families of materials.

Carbolites [7] are orange-colored transparent solids with a very low density of  $1.46 \text{ g cm}^{-3}$ . They can be prepared by graphite evaporation under conditions



**Table 2.** Characteristic structural data for various carbon forms.

Carbon	Unit Cell Parameters		
	<i>a</i> axis (pm)	<i>c</i> axis (pm)	$\gamma$ (deg)
Graphite hexagonal	246.2	676.8	120
Carbine	894.0	1536.0	120
Carbine II	824.0	768.0	120
Carbolite	11928	1062	120
Diamond cubic	356.7	—	—

**Table 3.** Raman data.

Carbon	Frequency (cm <sup>-1</sup> )	Appearance
Graphite	1582	sharp
Diamond	1332	sharp
Carbon black	1355	broad
a-CH	1332 + 1500	sharp + broad
Glassy carbon	1359 + 1600	broad + broad
Nanotubes (mixtures)	1566 + 1592	sharp + sharp

similar to fullerene formation but using argon or argon–hydrogen as quench gas at higher pressures than for fullerene formation. The structural properties are collected in Tables 2 and 3. Models of short chains of carbine structure with assumed interchain cross-links are controversial. The material is rather stable in ambient conditions. High-temperature processes and high temperature gradients are prerequisites for their formation.

The fullerenes [8, 9, 16] are well-defined molecular solids for the smallest compounds mainly for C<sub>60</sub>, C<sub>70</sub>, C<sub>72</sub> and C<sub>84</sub> which can be obtained in measurable quantities as purified materials. These molecules are soluble in solvents such as toluene or trichlorobenzene. They form deeply colored solutions which can be purified by liquid phase chromatography. The respective molecular solid needs careful sublimation to remove solvent and gas adducts. Fullerenes are air sensitive [17] and light sensitive [11] and decompose slowly by polymerization (becoming insoluble after storage in air).

The large number of predicted larger molecular structures [18] have not been observed as pure compounds, although evidence for the formation of larger cage molecules comes from TEM investigations of the residues of evaporated graphite after extraction of the small soluble fullerenes [19]. Such cage molecules may be present in amorphous carbon materials that have been subjected to sufficiently high temperatures for the skeletal rearrangement. These temperatures are reached in many combustion processes and in under-stoichiometric oxidation reactions of aromatic and aliphatic hydrocarbons [20]. These studies show that fullerenes can occur in many conventional reactions

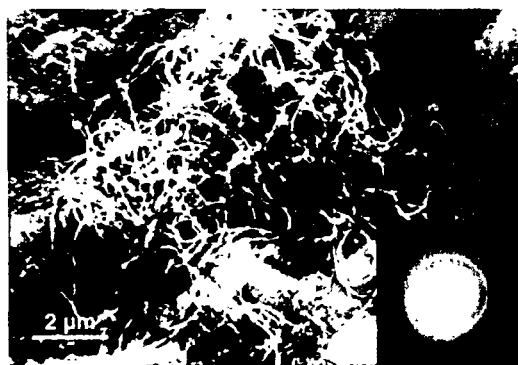
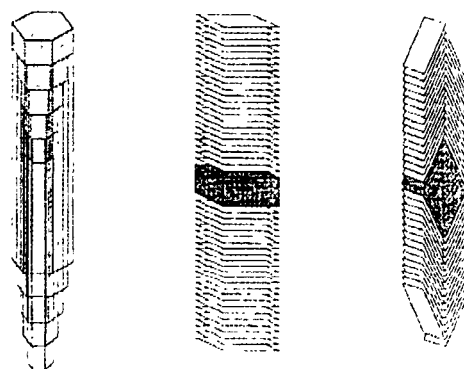


**Figure 4.** Carbon filaments [24] occur in several varieties, differing in the relative arrangement of the graphene units. The orientation is determined by the faceting of the metal catalyst particle (dark). The bottom SEM image shows a spaghetti pile of carbon fibers of tubular orientation. The reaction system was methanol on silver, the catalysts were particulate impurities of metals other than silver. The selected area of electron diffraction pattern shows the ring pattern for turbostratic graphite.

and not only in graphite evaporation processes which are not frequent in catalytic chemistry.

A class of intermediate compounds between graphite and fullerenes are the nanotube materials. Nanotubes are a special subgroup of graphite fiber materials [21] which can be formed by a wide variety of structure elements. Nanotubes consist of helical twisted [22] sheets of graphite capped with two half-shells of molecular fullerenes. This continuous arrangement of sp<sup>2</sup> carbons exhibits very special electronic properties [23] and is a highly desirable material which is still difficult to obtain in the pure form. Nanotubes frequently contain several layers of graphene sheets wrapped concentrically around each other. In catalytic chemistry this form of tubes or filaments is rather rare. They are very much in contrast to other forms of carbon filaments or tubes which are created under the influence of catalytic conversion of hydrocarbons (see below). Figure 4 summarizes common forms of graphitic filaments [24] which all consist of graphene sheets which are stacked

together without chemical bonds between the basic structural units [25]. This lack of continuous chemical bonding drastically affects the electronic properties and the chemical reactivity, which are comparable to that of planar graphite. The dark blocks in the figure symbolize the location of the catalyst which is most effective when it contains iron or nickel. A combination of catalytic metals, such as iron or nickel with phosphane impurities, leads to the growth of extremely unusual forms of carbon fibers such as helically wound graphite spirals from acetylene at 975 K [26]. Under catalytic conditions a wide variety of carbon filaments, which may not be linear but resemble spaghetti piles, are possible and may not be recognized as carbon. This is illustrated in Fig. 4 with a silver catalyst used for methanol dehydrogenation with a deposit as spaghetti pile. The identification of carbon was possible by selective area electron diffraction and by energy-dispersive X-ray analysis. From the diffraction pattern it is seen that the internal structure of the fibres is as displayed in the top left schematic drawing.

Onion carbon [27] is also a derivative of graphite which is made from concentric spherical graphene layers which are said to be continuous [28]. A more frequent form of polyhedral graphite particles is made from packages of concentric graphene layers which are bent but not closed by continuous chemical bonds. Such materials occur in graphitization processes of all kinds of precursors and can grow in size to several microns. As it has not been possible to isolate more than milligram quantities of onion carbon little is known about its chemical properties. Its existence in any carbon material indicates, however, a thermal prehistory of graphitization conditions, i.e. temperatures well above 1500 K with reducing or inert gas phase compositions.

A large group of carbon materials represent the disorder varieties of graphite. Figure 5 summarizes stacking schemes along the crystallographic *c*-axis. Figure 5(A) shows the stacking of large graphene layers which can be continuous up to lateral sizes of several hundred micrometers. The most frequently observed regular stacking of carbon atoms within the sheets are the hexagonal ABA stacking as in natural graphite and the rhombohedral ABCA stacking. Regular stacking of the graphene layers which are only very weakly bound to each other (by induced dipole moments of the aromatic  $\pi$  electrons) is given by a closest packing of the carbon atom spheres. This gives rise to the following dimensions for ideal hexagonal graphite:

in-plane distance 142.1 pm

in-plane lattice constant 246.2 pm

*c*-axis lattice constant 670.8 pm

interlayer distance 353.9 pm

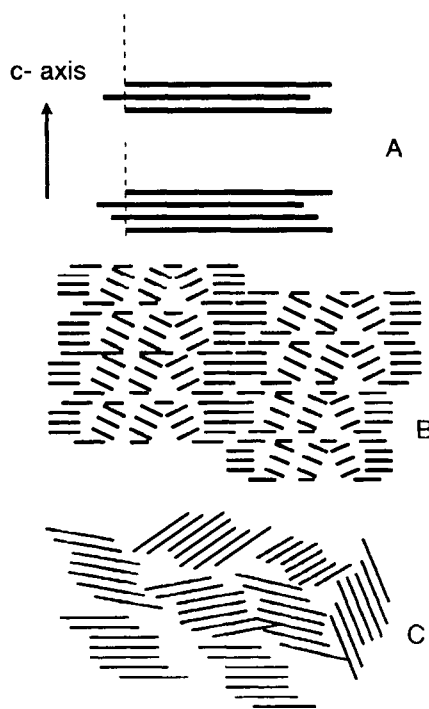


**Figure 5.** Stacking variants in graphitic carbon: (A) ideal graphite in ABA and ABCA stacking; (B) partly graphitized carbon with regions of angular inclined graphene stacks between parallel aligned graphene stacks; (C) irregular graphene stacks of nongraphitic  $sp^2$  carbons.

The rhombohedral graphite polymorph is slightly less stable than hexagonal graphite and converts during oxidation or even during mechanical treatment (ultrasonication, milling) into the hexagonal form. It can be discriminated by its powder X-ray diffractogram in the region of the cross-lattice reflections ( $h \neq 0, l \neq 0$ ), which are generally sensitive to the stacking order of a graphite material. The presence of rhombohedral reflections can be used as an absolute criterion with which to identify natural graphite.

As the interlayer bonding in graphite is so weak, it is easy to obtain graphite with little or no regular stacking order, which explains the extreme difficulty of obtaining single crystals of graphite. The interlayer distance increases up to 344 pm as a consequence of the absence of stacking. Even higher values have been reported, which are characteristic for nanocrystalline carbon in which the graphene layers are no longer parallel to each other (see Figure 15). A large number of graphitic materials exists between these two cases, in which the graphene layers become successively smaller and form packages of parallel layer fragments, known as basic structural units (BSUs) [235]. These packages can either be aligned in parallel or may be inclined towards each other. In Fig. 5(B) regular arrays of parallel and inclined stacks of BSUs can be seen. This alignment is characteristic of synthetic graphite used as catalyst

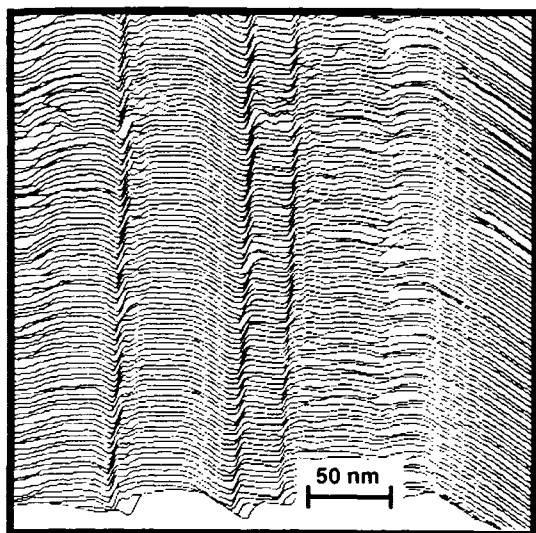


**Figure 6.** Low-resolution STM survey image of a partly oxidized graphite flake. The asymmetric V-shape of the deep trenches is a tip artefact. Conditions: Burleigh ARIS 6000, air, W tip, constant current mode, gap voltage 200 mV.

support materials. As the chemistry of the edges of the BSU stacks is very different from that of the basal planes, a patterned surface chemistry is observed. The patterning depends on the average angle of inclination. In synthetic graphite which is postannealed after its formation under high temperature and at hydrostatic pressure [29] highly oriented pyrolytic graphite (HOPG; Fig. 3) this angle is as low  $1^\circ$  for top quality samples used as graphite monochromators. At angles of  $5\text{--}30^\circ$  these materials are known as pyrographite. The absence of any preferential alignment is observed between the BSU stacks in pyrocarbons and some carbon black materials. Such a secondary structure is often observed when the process of carbon generation occurs at low temperatures or in large temperature gradients. The surface chemistry of these hard carbons is characterized by a hydrophilic nature, caused by the many terminating oxygen functionalities on these materials.

Kish graphite is a well-ordered variety of synthetic graphite obtained from exsolution of carbon out of liquid iron. Under certain conditions excess carbon, which is insoluble as FeC, crystallizes in a well-ordered platelet morphology and can be isolated by dissolution of the iron matrix in mineral acids. It is the macroscopic variety of the BSU which forms the graphene stacks in filamentous carbon, as shown in Fig. 4. Under certain cooling conditions of the iron melt these flakes can grow to 1 mm in diameter. They represent, by their extraordinarily high degree of ordering, the closest known approximation to graphite single crystals. In catalytic systems the microkish graphite particles are

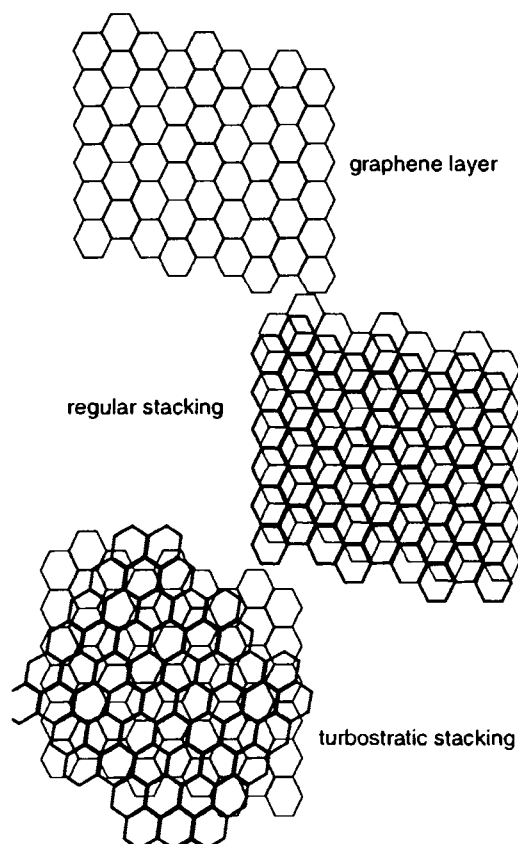


**Figure 7.** In-plane ordering of graphene layers. The turbostratic case gives rise to Moiré and pseudosymmetric superlattice structures, detectable in STM images. In many cases, however, no correlation exists between the individual layers. The turbostratic ordering has very little effect on the interplanar spacing. Enlarged  $c/2$  parameters arise from defects such as  $sp^3$  centers which accompany the turbostratic graphene layers.

also of highly crystalline, rendering them very resistant to chemical transformation in oxidising or reducing atmospheres.

An example of the lateral anisotropy of the surface chemistry which results from the partial alignment of BSUs according to Fig. 5(B) can be seen in Fig. 6. The STM wide scan shows a system of trenches in HOPG which was oxidized in air at 1000 K for 30 min. Smooth rectangular stripes of hydrophobic graphitic basal planes coexist with almost the same surface area of prismatic faces of the step surfaces. The wedge-shaped contours are imaging artefacts caused by the STM tip. As oxidation proceeds, mainly on the prismatic edges, a pattern results from high recession velocity in the valleys and a low reactivity at the basal planes.

The unidimensional disorder of graphene stacking has a two-dimensional counterpart in the relative angular orientation of the hexagons within adjacent graphene layers. Figure 7 shows schematically the two

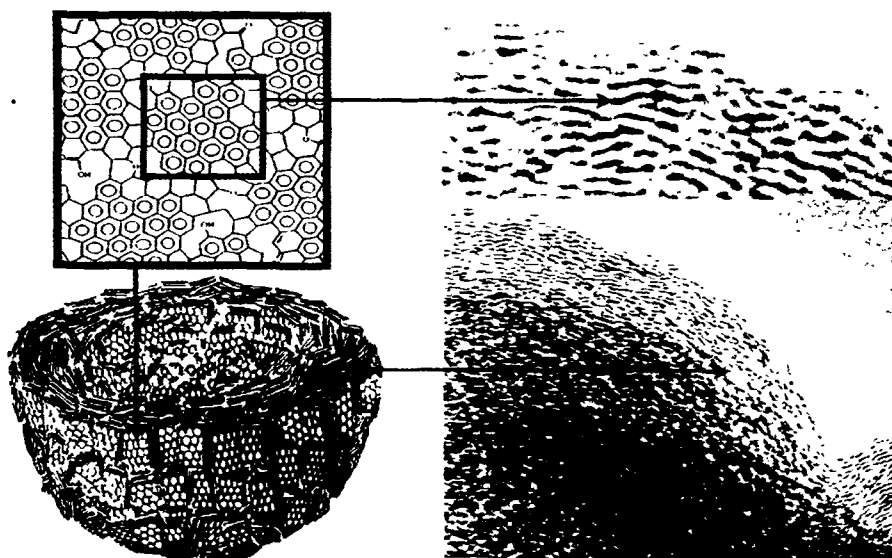


**Figure 8.** Microstructure of carbon black. The nested model is built from planar BSU stacks interconnected by covalent bonds (see top scheme). One BSU (central frame in top scheme) is resolved in high resolution TEM of a real carbon black particle (FW-1, Degussa, Phillips CM 20 FEG, 200 keV). The main image shows a projection through an agglomerate of spherical black particles. The distance between the BSU is 340 pm.

possibilities of stacking in two-dimensional registry (relative displacement of carbon atoms 0.5 and 0.5 unit cell lengths, hexagonal stacking) and without registry which is referred to as turbostratic disorder. This special state of crystalline disorder is characteristic of layered materials with weak interlayer bonding. Its detection indicates well-developed graphene layers with very little chemical impurity which would force the stacking of layers into a three-dimensional disordered state with no parallel orientation of adjacent BSUs. Nongraphitic carbons frequently exhibit this type of disorder with the consequence that all X-ray diffraction peaks other than the (002) line are absent or very broad.

These disordered carbons constitute a transition form, between graphite and carbon blacks, which are turbostratic materials with the additional complication that the lateral size of the BSU becomes very small with typical sizes of below 5 nm. Carbon blacks appear as chainlike aggregates of spherical particles of 10–50 nm diameter [30]. Elemental analysis reveals a significant hydrogen content of  $C_{8-12}H$ . Such materials are referred to as nanocrystalline carbon as the X-ray diffraction mechanism changes from Bragg diffraction to elastic scattering with the different physics of the scattering process [31, 32]. The broad peak in the range of the graphite (002) is no longer a Bragg peak but represents the absolute maximum of the pair correlation function which is dominated by the still parallel arrangement of small graphene layers of sizes comparable to large aromatic hydrocarbons [31].

Figure 8 represents models and high resolution transmission electron microscopy of the secondary

structure of carbon blacks forming spherical aggregates. The shell structure of stacks of graphene layers optimizes the interstack interaction, via heteroatoms located at the prism edges of each graphene layer. In many materials the shells are filled by smaller particles or grow around a noncarbon nucleus. The interstack interactions are mediated in many carbon blacks through hydrogen bonds of adjacent OH groups. The outer surface of a black particle also contains significant amounts of OH groups which control the aggregation of the primary spherical particles to fractal larger aggregates, often called the "structure" of carbon black. Modification of the ion strength (for example in aqueous solution) affects the strength of the interaction and influences the aggregation behavior. Thermal activation of the hydroxy groups creates dangling bonds and reorientation of the graphene packages so as to form a covalently cross-linked polymer. The process creates  $sp^3$  bonds and leads to an enormous decrease in chemical reactivity and an increase in mechanical strength. This important aspect of the reactivity of carbons with a high fractional prismatic surface area has the consequence that thermal treatment even under oxidizing conditions can transform the reactive carbon black material into highly stable glassy carbon (see below).

Fullerene black is of a similar constitution and secondary structure as normal carbon black, but with the important difference that its BSUs are composed of non-planar graphene layers. Additionally, the stacks are not straight but curved, giving rise to a more disordered and less dense carbon material. The chemical reactivity is higher as the stability of nonplanar graphene layers is reduced. In addition, the irregular shape

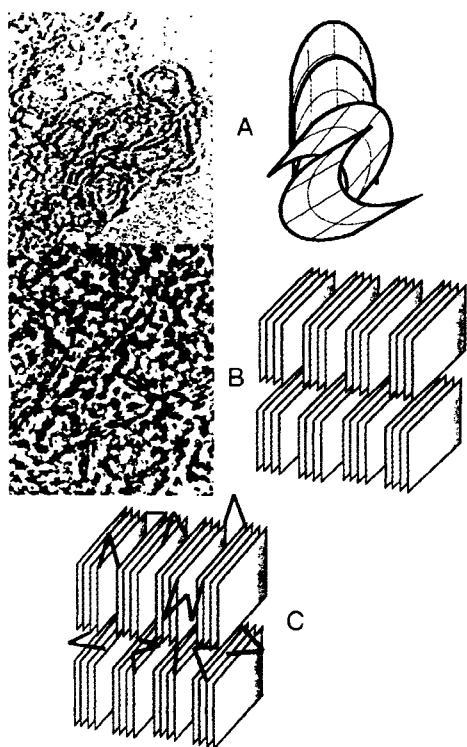


**Figure 9.** Organization of carbon sheets in nanocrystalline carbons. Case (A) represent bent sheets which are stacked concentrically and randomly. In the high-resolution TEM of fullerene black filamentous structures from carbon macrocycles which did not react to fullerene molecules can also be seen (weak contrasts). Case (B) shows the arrangement of stacks of planar graphene units. Only few of these stacks are oriented with the  $a$ -axis parallel to the electron beam and can be imaged as illustrated in the sketch, the majority are randomly orientated and give hence an amorphous contrast. Case (C) is the same as (B) with the addition of covalent bonding interactions between the stacks. These bonds are invisible by electron microscopy but influence the graphitizability of the carbon.

of each graphene layer prevents the formation of parallel stacks to a large extent. A fully amorphous array with a large surface fraction of prism faces with result which additionally increase the chemical reactivity.

Figure 9 summarizes these interactions in nanocrystalline carbons which constitute a large fraction of carbonaceous deposits on catalytic materials. It is important to note that these carbons exhibit a high reactivity towards polymerization under weakly oxidizing conditions (inert, vacuum, steam, reducing) and a high reactivity towards total oxidation under strongly oxidizing conditions. Both reactivity patterns are a consequence of the high ratio of prismatic to basal surface area of the carbon stacks. The materials in Figs 9(A) and 9(B) result from weak interactions between the various building blocks. A carbon with  $sp^2$  and  $sp^3$  local bond geometries is formed after polymerization by cross-linking with bonds, atoms or even molecules, as schematically illustrated in Figure 9(C).

The resulting hard carbon black is nongraphitizable by thermal treatment up to 3000 K. The  $sp^3$  bond cannot be rehybridised to  $sp^2$ . These hard carbons are often referred to in catalytic systems as carbonaceous deposit. The material contains some heteroatoms (usually hydrogen). It is chemically heterogeneous, structurally amorphous, mechanically hard, and exhibits no graphitic properties, although the large majority of all carbon-carbon bonds are  $sp^2$  hybridized. Higher contents of heteroatoms and the presence of nitrogen, sulfur and oxygen are characteristic properties of coke, the product from carbonization of coal or other hydrocarbon sources with larger molecular constituents. Carbonization is a polymerization process in which small molecules such as methane are liberated. Heteroatoms in the form of ammonia, water and hydrogen disulfide are removed and irregular stacks of small graphene layers (originating from the large organic molecules) are cross-linked by molecular fragments under preservation of the irregular orientation of the stacks (Fig. 9(C)).

In a-CH or diamond-like carbon (DLC) the hydrogen content is as high as  $CH_{0.4}$  and the carbon atoms are arranged in ribbons or chains with no discernible stack structure of graphene layers. Glassy carbon is a technical product made from carbonization of organic polymers and consists of ribbons of  $sp^2$  carbon with a significant contribution of nonhexagonal rings allowing a three-dimensional tangled structure. This creates the high mechanical hardness and the resistance against graphitization lending to this material excellent mechanical stability at high thermal and mechanical load (only under nonoxidizing conditions). Turbostratic stacks of 3 nm width and 10 nm length form the continuously bent BSU of this carbon, which can be formed in catalytic reactions allowing polymerization of molecular precursors followed by carbonisation at around 1000 K (in regeneration cycles for example). The content of  $sp^3$  bonds is low in this material but the hydrogen content which is required to saturate the high specific prismatic surface area of the ribbons, is significant.

Active carbon or charcoal is an important modification of carbon in catalysis. It consists of carbonized biopolymer material which is activated in a second step. This procedure creates a high specific surface area by oxidative generation of micropores of very variable size and shape distribution. A more controlled activation is achieved by the addition of phosphoric acid or zinc chloride to the raw product. The additive is incorporated during carbonization into the hard carbon and is subsequently removed by leaching creating the empty voids in a more narrow pore size distribution as achievable by oxidation. Other activation strategies

**Table 4.** Types of carbon supports and their geometric surface areas.

Carbon	Surface area ( $\text{m}^2 \text{g}^{-1}$ )
Natural graphite	0.1–20
Synthetic graphite	0.3–300
Graphitized carbon blacks	20–150
Carbon blacks	40–250
Activated carbon from wood	300–1000
Activated carbon from peat	400–1200
Activated carbon from coal (coke)	200–1000
Activated carbon from coconut shells	700–1500

employ liquid oxidants such as nitric acid to create large pores with a very wide size distribution. Today, many thousands of patents describe numerous ways to structurally activate carbon [33] from mostly natural sources.

A large number of oxygen functional groups are created during the activation process by saturation of dangling bonds with oxygen. This creates a rich surface chemistry which is used for selective adsorption. In addition, it determines the ion exchange properties that are relevant for catalyst loading with active components. A more detailed description of the surface chemical aspects which are most relevant for the catalytic uses of nanocrystalline and activated carbons follows below. The microstructure of activated carbon may be described by the archetypes depicted in Figs 9(B) and 9(C) and may even contain significant amounts of graphitic structure [34], depending on the temperature regime of activation. The micro-morphology is often characteristic of the biological origin of the raw material with shapes of cell arrays and even whole plant organs being detectable by SEM imaging. Active carbon contains significant amounts of inorganic matter (iron silicates, silicates, calcium oxides etc.) which is analyzed as ash content after complete combustion. Activated carbons are very heterogeneous materials and are difficult to characterize in micro-structure and reactivity. Recent reviews about this class of large-scale technical carbons are available [35, 36].

To summarize, a wide variety of forms of carbon can be found under catalytic conditions. In particular, during deposition and thermal post-treatments a very complex carbon material with unexpected chemical and structural properties can result, causing severe problems in catalyst regeneration and modification of its properties during deactivation. The group of carbons which specifically employed in catalytic systems is summarized in Table 4 together with its most important physical parameter, the specific geometric surface area. The values vary over three orders of magnitude and reach values between geometric surfaces of micron-size particles up to the surface area of the number of

carbon atoms in the sample. These latter values are unrepresentative if they are interpreted in terms of a monolayer coverage of the nitrogen probe molecules. Highly porous carbons exhibit pronounced capillary condensation phenomena requiring a full BET isothermal analysis for the determination of the true geometric surface area. Although this is widely known and described in detail in other sections of this handbook, it is still customary to present these very high numbers of BET surface area. Care must be taken in comparing data based on surface area measurements in carbon chemistry as some sources determine the monolayer sorption capacity, whereas others do not. For this reason surface area values determined with various adsorbents, such as nitrogen,  $\text{CO}_2$  or Kr, may also differ significantly as these probe molecules exhibit quite different condensation properties at the conditions of adsorption. The most useful contribution of sorption data to evaluate the nature and size distribution of porosity in carbon materials is not discussed here.

It is noted that in different areas the use of terminology to describe structure and properties of carbons is quite different. Within the carbon-science community a clear system of terminology and definitions was elaborated which is recommended whenever applicable [37, 38].

### 2.1.9.6 Formation of Carbon Materials, General Pathways

The technical synthesis of graphite, diamond and a variety of other forms of  $\text{sp}^2$  carbons (Fig. 3) is described in a review [39] and is not covered here. As the unintended formation of carbon in deactivation processes and the modification of primary carbon surfaces during chemical treatment (in catalytic service and during oxidative reactivation) and their chemical properties are frequent problems encountered in catalytic carbon chemistry, it seems appropriate to discuss some general mechanistic ideas which mostly stem from the analysis of homogeneous combustion processes (flame chemistry) and from controlled-atmosphere electron microscopy.

The source of all carbon relevant to the present context is the feedstock of hydrocarbon molecules (aliphatic, aromatic, with and without heteroatoms). Figure 10 summarizes the possibilities for their conversion into black carbon. The chemical route comprises polymerization into aromatic hydrocarbons with final thermal dehydrogenation. This process often includes a liquid crystalline phase immediately before final solidification. In this phase large aromatic molecules can self-organize into parallel stacks and form well-ordered precursors for graphitic structures with large planar graphene layers. This phase is referred to

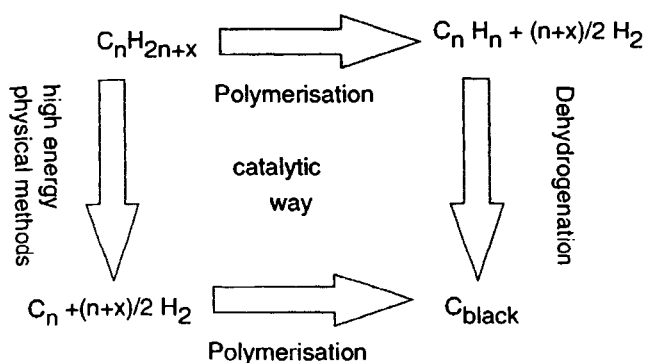


**Figure 10.** Reaction pathways from organic molecules to solid carbons. The fundamental processes of dehydrogenation and polymerization occur simultaneously in the catalytic pathway.

as mesophase and can be observed by polarized light optical microscopy.

The physical pathway requires activation of the molecules by high external energy input such as high-temperature flames, projectiles like accelerated and free electrons, or the presence of a plasma source. These conditions can also occur in analytical instruments such as electron spectrometers and microscopes which have the potential to create black carbon during analytical inspection of hydrocarbon layers [27]. In all these cases the molecules are fragmented and dehydrogenated in one process and represent a source of free carbon atoms or small fragments such as  $C_2$  dimers. These fragments condense into chains of carbon atoms which have a strong tendency to form small ring molecules by nucleophilic self-substitution of the end groups. Saturation of the dangling bonds of the primary rings by polymerization leads to graphene layers. These processes occur very rapidly compared to the slow activation along the chemical path. Little time is available for orientation of the rings into stacks, and cross-linking into nonplanar units can easily occur (see Fig. 9). Hard, nongraphitizable carbons are the final products of these processes in which all fullerenes and fullerene blacks are also formed.

A large number of intermediate pathways are possible when catalytic reactions interfere with the polymerization–dehydrogenation steps. A common scenario is the catalytic dehydrogenation of hydrocarbons on nickel surfaces followed by dissolution of the activated carbon atoms and exsolution of graphene layers after exceeding the solubility limit of carbon in nickel. Such processes have been observed experimentally [40] and used to explain the shapes of carbon filaments. In the most recent synthetic routes to nanotubes [41] the catalytic action of in situ-prepared iron metal particles was applied to create a catalyst for the dehydrogenation of either ethylene or benzene.

### 2.1.9.7 Formation of Carbon Materials, Mechanistic Aspects

A schematic correlation between reaction pathways and the principal structural properties of common carbon forms according to the classifications given in Fig. 3 is presented in Fig. 11. The literature [33] is rather controversial [42] allowing only a survey of chemically plausible pathways relevant to the present conditions of possible carbon formation.

Three main synthetic routes to carbon can be identified, none of which produces exclusively one phase or modification of carbon. In all cases, mixtures are produced, as indicated by the central box in Fig. 11. This complexity highlights the generally strong influence that kinetic aspects have on the formation reactions. The realization of a perfect  $sp^2$  local configuration is always energetically favourable and is reached in graphene layers with only hexagonal constituents. The saturation of the peripheral dangling bonds of graphenes can occur either by homonuclear cross-linking (resulting in macroscopic planes or irregular arrays of stacked graphenes) or by heteronuclear bonding (resulting in either polymers or surface functional groups). Metastable configurations contain mixtures of six-membered rings with other ring geometries causing strain in the  $sp^2$  bonds. Nonplanar structures of a wide variety result. These structures are chemically highly reactive and disappear in oxidizing or hydrogenating atmospheres, preferentially over planar structures. This explains an additional strong influence of the gas phase conditions on the distribution of carbon materials.

The group of synthesis routes at the top of Fig. 11 combines the chemistry of carbon formation in combustion processes [43, 42]. In high-temperature combustion reactions (above 1200 K) the general reaction occurs via the physical pathway indicated in Fig. 10 with initial fragmentation into neutral species and thermoions (without an additional source of energy).  $C_2$  fragments such as acetylene, or oligomers react to form carbon chains which result in predominantly aromatic molecular fragments (with dangling bonds) and to a lesser extent in combustion atmospheres as three-dimensional cage structures with both  $sp^2$  and  $sp^3$  bonds (becoming a dominant path in fullerene-generating conditions). In cooperation with ionic fragments these secondary building blocks condense to the graphene BSUs with a planar or bent layer structure. In a detailed analysis of the flame chemistry [44–46] a three-zone model of a flame was derived. The elementary building blocks for carbon are formed in the hottest oxidation zone. A surrounding zone with luminous

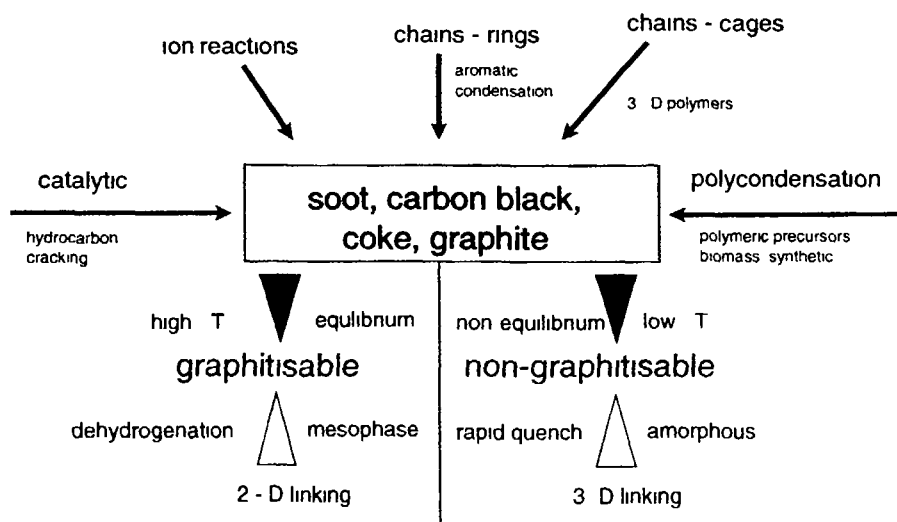


**Figure 11.** Reaction pathways to the mixed materials with  $sp^2$  connectivity. All these materials occur as either a reactive form (graphitizable) or as a nonreactive final product (see also Fig 9)

constituents is identified as the location of chain growth into polyalkyne molecules of the form  $C_nH_2$ . In the third dark zone these molecules rearrange into polycyclic hydrocarbons and finally into graphene layers. Ample evidence for this model comes from mass spectral analysis of the gas phase in various types of flames. This diagnostic method gives no indication about the reactive particles, as by the time of their detection they are energetically cold and represent the ground state of a mere species rather than the reaction intermediate. For this reason it is difficult to see that long linear chains could be important intermediates as they are never found in carbon products. A scenario in which these processes are modified by interaction of thermoions [47, 48] and/or aromatic radicals [49] and several independent repair mechanisms for a maximum yield of six-membered condensed rings seems more plausible [42]. The kinetic boundary conditions are of great importance in all these processes as large local temperature gradients are required to allow a significant accumulation of carbons from reactive intermediates. At constant high temperatures the unstable species decomposes effectively back into their constituents. This was studied in detail in several types of combustion reactions [45] and is the guiding principle of all technical processes for carbon black synthesis [39].

Another important aspect is the nature of the hydrocarbon source in relation to the efficiency of carbon formation. The idea that the structure of the molecule should be relevant for the carbon formation (aromatic molecules are better than aliphatic structures) is in correct in all situations where a pool of primary building blocks is formed (in flames, under oxidative polymerization conditions and under physical activation). However, it is confirmed that a decrease in the average

C–C bond energy allows easier chemical fragmentation, which enhances the rate of carbon formation [50].

The growth of carbon particles cannot occur in one synthetic step by condensation of small molecular units. However large an aromatic molecule may become [47–49] it will be too small to create a micron size carbon particle. Three major routes can lead to such large particles. The most unlikely case is a continuous polymerization process at the surface of a fullerene molecule [8]. Both the unfavourable kinetics [51] and the absence of structural evidence that fullerene-like structural elements (identified by characteristic C–C bond lengths) occur in the radial distribution function of black carbon material [31] are strong indicators that carbon particles, although of spherical morphology grow in a heterogeneous rather than in a homogeneous way. In a combined kinetic, statistical and microscopic analysis of the growth process [47, 52] a model of surface growth was put forward. According to this, the polyaromatic molecules are dehydrogenated and the dangling bonds are saturated by cocondensation of alkyne units. A mass growth of carbon particles of 90% of the total carbon inventory could be explained in this way, which is in excellent agreement with experimental flame studies [47]. The prediction of this model of a structureless agglomerate of aromatic molecules surrounded by a concentric array of graphene layers [52] is in excellent agreement with all HRTEM observations of homogeneously produced carbon particles. The spherical texture is assumed to be the consequence of droplet formation of aromatic molecule in the initial stages of carbon fragment supersaturation required for homogeneous nucleation. These droplets are not residues from the possible liquid initial fuel, but occur as a consequence of the very rapid



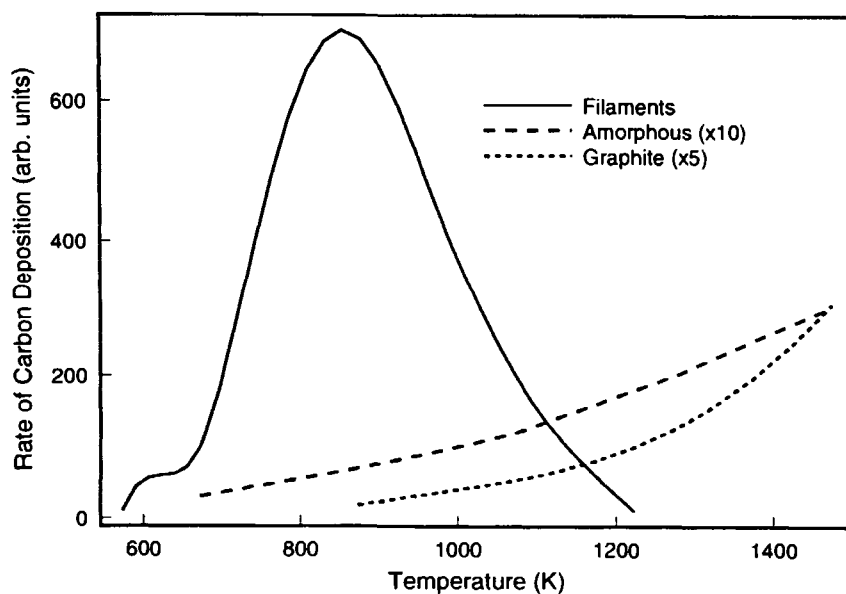


**Figure 12.** Carbon deposition on metal particles as a function of metal temperature. The dominating form is filamentous carbon, and more conventional forms occur in sizeable quantities only in extremely high-temperature catalytic processes. (After [24]).

initial polymerization of the highly active small carbon fragments.

In summary, all processes which homogeneously generate carbon from molecular precursors and from homogeneous activation lead to spherical particles made from graphene layers (see Figs 8, 9(B) and 9(C)). Spontaneous growth from supersaturated reservoirs of small molecular precursors (chains, alkyne structures, polyalkynes) of PAH and cocondensation with smaller molecular fragments lead to spherical carbon particles which aggregate to chains of spheres.

Carbons with much larger continuous graphene layers can be obtained from pyrolytic polymerization of prepolymerized hydrocarbons. Synthetic materials such as kapton or polyacrylonitrile (PAN), or biopolymers such as coconut shells, wood coal, rice husks and similar materials, can be used. Carbonization or "coking" involves the chemical removal of all heteroatoms such as nitrogen or sulfur and the cross-linking of the polymeric blocks via the dangling bonds created by the removal of the heteroatoms. In this way the texture of the precursor material is preserved in the final product. As no fragmentation of the precursor is required, this method of carbon generation is much less energy intensive. It leads further to a great variety of structural properties with extreme examples as shown in Figure 9. The possibility of retaining a portion of the heteroatoms, such as silicates in biomass carbon, makes it feasible to produce extra strong carbons (silicate reinforced). These can be useful for anchoring catalytically active metal components such as noble metal particles. The exact chemistry of carbonization is complex and depends on the nature of the precursor

and on the gas phase chosen (inert, oxidizing, steam, reducing). For this reason no general description is possible of this difficult to control process, which occurs between 500 K and 1000 K.

#### 2.1.9.8 Catalytic Formation of Carbon from Molecules

The catalytic generation of carbon (Fig. 11, left side) is of significance as the deactivation reaction in many processes involves the presence of hydrocarbons and of transition metal reaction sites. These catalyze dehydrogenation reactions or form solid acid-base centers catalyzing polymerization reactions (see Fig. 10). In a review [24] a large amount of kinetic data was compiled about the type of carbon deposited as a function of deposition temperature. Figure 12 shows that the predominant carbon form at most catalytically useful temperatures is filamentous carbon. The carbon source may be CO, methane, acetylene or other hydrocarbons. The metals for which this correlation is valid are either nickel or iron on all kinds of conventional supports and also as binary or Cu alloys. It is important to note that forms of carbon other than filaments rarely grow under the conditions required for steam reforming or Fischer-Tropsch synthesis.

The sequence of events for the growth of these filaments, which can destroy the whole catalyst bed, is now well understood [53-56]. Electron micrographs of the catalyst particles show that they are detached from

their support and form either the front or occasionally the centre of a growing carbon filament. In all cases the shape of the particle changes during its operation as the filament growth catalyst. The growth of an anisotropic carbon particle requires structure sensitivity from the process of carbon atom-to-graphite polymerization. Otherwise a shell of graphite would be produced around a core of metal which would then stop acting as a catalyst after completion of the carbon shell. Such morphologies have been observed but are not discussed here as they occur either at high temperatures (see Fig. 12) or under unusual gas phase conditions which are lean in carbon sources. The fact that very little amorphous carbon with uncontrolled polymerization of the BSU is produced further illustrates the relevance of the metal catalyst particle which not only generates the source for the solid carbon formation but also controls the geometry of the polymerization process.

The structure sensitivity of the catalyst is induced in an induction period in which carbon is dissolved into the metal. A flat surface with a subsurface carbide forms, which dissociates the molecular carbon source. The activated atoms diffuse through this layer and migrate to other faces where they exsolve, forming graphene layers. The reconstruction was observed by electron microscopy, revealing a deformation of spherical metal particles into droplet-like conical particles. The base forms the active surface for dissociative adsorption and is always directed away from the surface from which the filament grows. The conical mantels are faceted in various directions and allow the growth of graphene layers with different velocities and orientation. The structures of Fig. 4 result from different abundancies of different facet orientations. Coadsorption of impurities such as oxygen or sulfur strongly affects the growth kinetics by affecting the reconstruction. This sensitivity of the carbon generation process on surface orientation can be used advantageously by controlling the shape and rate of carbon filament growth. Inhibitions as well as enhanced production of carbon filaments can be achieved. Additives in the gas phase (oxygen, sulfides, phosphorus compounds) or the promotion with alkali or boron oxide affect the metal faceting. Additives of alloys of molybdenum, silicon or tungsten influence the migration kinetics and the thermodynamic solubility limits of the carbon atoms in the metal particles (10–300 nm diameter), which is often believed to be the rate-limiting step in the overall process. A number of models differ in the character of the carbide phase, which can be a solid solution or a distinct phase such as cementite in the Fe–C system. An additional source of discrepancy is the origin of the carbon concentration gradient, allowing continuous transport through the metal particle. Thermal gradients were excluded by several independent experiments and convincing circumstantial evidence.

### 2.1.9.9 Carbon on Noble-Metal Catalysts

In catalytic reactions of hydrocarbon conversions on noble metals (hydrogenation, isomerizations over platinum or rhodium are typical examples) it was found that submonolayer quantities of carbonaceous deposits exert a dominating influence on the sequence of events. This is also known in practical applications where it is noted that a little prereaction time in the hydrocarbon atmosphere is required to obtain a selective performance. The beneficial effect of the carbon overlayer is believed to arise from a moderation of the dehydrogenation activity of noble metal surfaces. Dehydrogenation reactions are the fastest reactions catalyzed by platinum, whereas skeletal rearrangements and hydrogenolysis reactions are about an order of magnitude slower on various single crystal surfaces of platinum at atmospheric pressure and at 573 K [57]. If the hydrocarbon is not adsorbed directly on the metal but is bound instead on a carbon material onto which hydrogen atoms can spill over, it is expected that hydrogenation occurs more selectively relative to all other processes. This idea of an intermediate inert surface with intimate contact to the hydrogen-activating metal, which was developed during the analysis of the coking behavior of supported Ni, Rh, Pd and Pt catalysts [58], requires complete chemical inertness of the carbon against hydrogenation and a suitable electronic structure to permit chemisorption of the organic substrate. In addition, the beneficial effect of structure sensitivity, which is prominent in platinum metal catalysis [57], is lost. Combined carbon radiotracer and temperature-programmed desorption experiments on platinum [59] have revealed that up to temperatures of 473 K a carbon species with the composition  $C_nH_{1.5n}$  prevails, which can be removed in excess hydrogen. At higher exposition temperatures the carbon to hydrogen ratio falls sharply to below 1:1 and the resulting carbon is no longer reactive in hydrogen. This more graphitic carbon fulfils the conditions required to act as stable adsorption intermediate. Above 750 K the layer converts into structurally identified graphite which is, however, inactive for hydrogen transfer as was shown by hydrogen isotopic exchange studies [60]. All reaction carried out with hydrocarbons below 473 K require a permanent readsorption of the hydrogen-rich carbon intermediate, whereas high-temperature treated platinum is permanently modified and passivated for hydrocarbon reactions above 750 K.

The structure of the hydrogen-poor carbon deposit has not been clarified by surface science and is referred to as the carbonaceous overlayer. The structural nature of the hydrogen-rich carbon deposit, however, was amenable to a suite of surface science techniques and the unique structure of alkylidines [61] was derived. These adsorbate species, which have molecular coun-

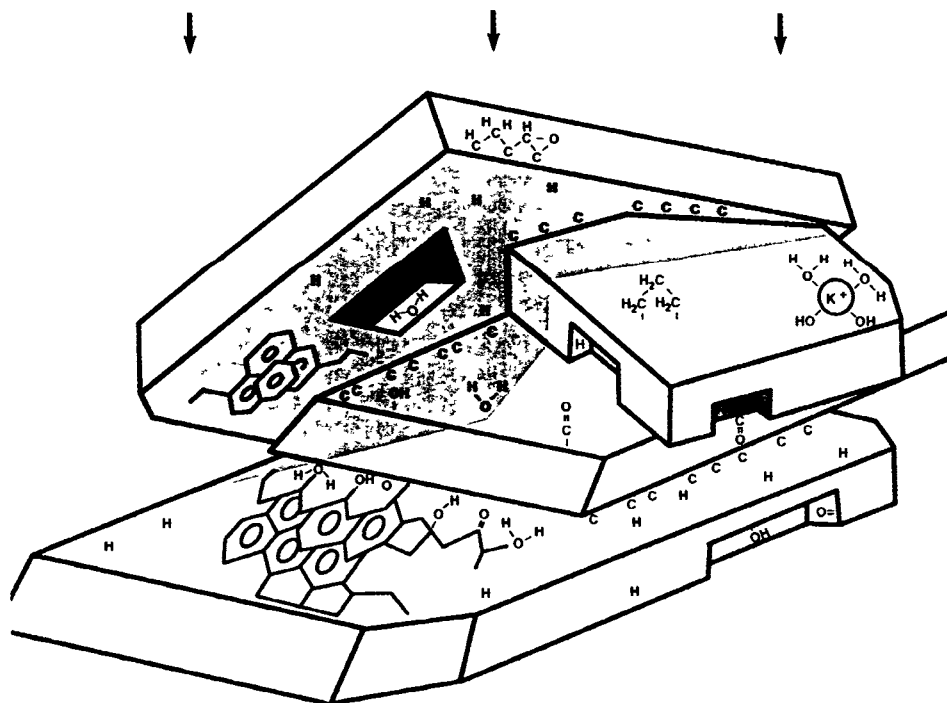


**Figure 13.** Schematic representation of the surface coverage of platinum crystallites as they are used in hydrogenation catalysis. The surface analysis instrument detects only the light parts and is affected by shadowing (grey zones; arrows indicate direction of illumination).

terparts in organometallic chemistry [62], consist of at least two carbon atoms one of which is bonded to three metal atoms. The other carbon atoms are fully hydrogenated alkyl groups with only C–C single bonds in-between. On reacting platinum surfaces no structure-sensitive effect is expected because 80–95 atom% of all platinum atoms are covered by the carbonaceous deposit, which can be of a different structure. According to the general scheme of Fig. 10 polymerization and dehydrogenation produce hydrogen-poor molecular species with multiple bonds at the surface. The alkyldiene species is a well-defined limiting structure occurring instantaneously on clean metal surfaces [63] upon exposure to pure small alkene molecules. With longer residence times and higher temperatures these still hydrogenated species carbonize to form graphene layers which deactivate the metal surface underneath.

Still controversial [64] is the function of the deposit. It could either act as a dynamic cover for nonselective active sites, which is compressed laterally upon substrate adsorption and reexpanded after desorption of the product. The alternative function is to serve as a weakly interacting surface for the substrate adsorption [65].

One way to clarify the role of the adsorbate is the *in situ* investigation of platinum catalysts with electron spectroscopy, which is capable of quantitatively determining the abundance and chemical structure of the carbon species present. This has been done for a platinum black [66] material used after various activation procedures in *n*-hexane conversion reactions. It was

found that pristine catalysts are significantly oxidized. These surface oxides are reduced by alkane decomposition into methane, carbon and ethylene. Selectivities to higher hydrocarbons and skeletal isomers of hexane were observed only after an initial induction period. Surface analysis at this stage revealed the presence of Pt metal, of adsorbed OH groups, and a variety of carbon species including carbidic carbon, graphite, amorphous hydrogenated carbon, and several partial oxidation products of this polymer. The total abundance of carbon varied between 15 atom% for purified Pt and 48 atom% after catalysis. This complex situation is summarized in Fig. 13. Only a small fraction of the carbon deposit is of a graphitic nature. Most carbon species are still in a state before carbonization. The nature of the catalytically active stable, but reactive, carbon deposit may be a layer of amorphous hydrogenated carbon which is sufficiently stable due to its complex network structure but which is still enough polar to provide active centers for hydrocarbon adsorption.

#### 2.1.9.10 Carbon Formation in Zeolites

Zeolites and other oxide-based solid acid catalysts are used in hydrocarbon conversion reactions with enormous economic impact. Their lifetime is, however, very

limited due to deposition of carbon which is referred to in the literature as coke formation. The definition of coke in zeolites is very much wider than in the sense of the present article as it is understood that coke is "a carbonaceous deposit which is deficient in hydrogen compared with coke forming molecules" [67]. Two types of coke are discriminated by several techniques amongst which are liquid phase extraction, thermal desorption and spectroscopies like UV-VIS and NMR. One type is white coke which covers naphthalene-type aromatic molecules including derivatives with alkyl chains and the second type is black coke which covers larger pericondensed aromatic molecules and alkylated derivatives. This latter type of coke would be referred to in carbon chemistry as a precursor to coke in the sense of Figs 10 and 11.

A significant problem in oxide coke analysis is the determination of the C:H ratio, the most important integral value for a structural characterization. The main problem is the interference of adsorbed or structural water and the structural change occurring during temperature-programmed analysis allowing for carbonisation and the formation of irreversible coke, which is structurally identical with black carbon from polymerization (Fig. 11). In a methodical review [67] the solutions to this problem which contributed a lot to the controversial descriptions of coke on oxide catalysts are described in detail. The absence of large amounts of graphitic carbon in zeolite coke was shown recently by using X-ray absorption spectroscopy at the carbon K-edge [68]. The spectra from an industrial zeolite which was treated with aliphatic and complex aromatic hydrocarbon feedstocks to generate coke showed in both cases the predominant presence of catacondensed aromatic molecules (naphthenes). The independence of the coke properties from the nature of the hydrocarbon feedstock being either methanol (in the MTG process) or small hydrocarbons such as ethylene or propylene or aromatic molecules such as mesitylene or heavy oil fractions, was demonstrated for a technical zeolite sample [69]. This showed that under the influence of the solid acid catalyst the feed is broken into small units from which catacondensed aromatics (with alkyl side chains or as bridging units) are formed. This process, which is similar to carbon formation in homogeneous systems (flames), occurs at comparatively very low temperatures, as low as 475 K. After this polymerization stage, according to the classification of Fig. 10, a step of dehydrogenation up to 700 K follows in which all molecules which can escape the micropore system react into pericondensed polycyclic aromatic molecules. Those molecules that remain in the micropores retain their shape and are not polymerized, which explains the simultaneous presence of both types of coke in zeolites [67]. In subsequent oxidative regeneration steps the pericondensed mole-

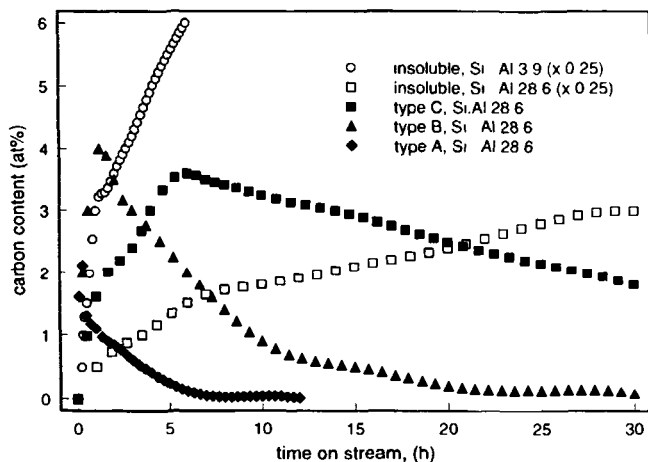


**Figure 14.** Abundance of various types of coke on zeolite H-Y during reaction with propene. The soluble fractions (A–C, black symbols) represent different aromatic structures which form during the first polymerization steps. The insoluble coke is the final product of polymerization which is affected by the solid state acidity of the zeolite, represented here as the Si:Al ratio.

cules at the outer surface carbonize and are eventually oxidized giving free all outer surface according to selective adsorption experiments [69]. The catacondensed deposits in the micropores cannot fully carbonize due to spatial constraints and remain partly intact as molecular pore blockers, reducing the micropore accessibility significantly [69].

The sequence of events in coke formation was studied in the model reaction [70] of H-Y zeolite with propene at 723 K. Under these drastic conditions the soluble white coke formed rapidly within 20 min and was converted into insoluble coke within 6 h under inert gas without losing carbon atoms in the deposit. Due to the larger pores in the Y-zeolites compared to the ZSM type zeolites used in the other studies mentioned so far, the structure of the aromatic molecules is somewhat different. The soluble coke in this system consisted of alkyl cyclopentapyrenes ( $C_nH_{2n-26}$ , Type A) as the hydrogen-rich primary product and of alkyl benzoperylene ( $C_nH_{2n-32}$ , Type B) and alkyl coronenes ( $C_nH_{2n-36}$ , Type C) as matured components. The temporal evolution of the various products is presented in Fig. 14. It clearly emerges that the soluble coke fractions are precursors for the insoluble coke and that within the soluble coke fraction the final steps of dehydrogenation–polymerization are very slow compared to the initial formation of smaller aromatic molecules from propene. The sequential formation of precursors with decreasing C:H ratio follows from the shift of the maximum in the abundance of each fraction on the time axis.

The formation of the insoluble coke occurs clearly in several kinetically well discernible stages which can be attributed to initial growth at the outside of the zeolite

crystallites and in a slow diffusion-limited growth inside the micropore system. The diffusion limitation will affect the migration of soluble coke molecules rather than the motion of the small precursor molecules. It can be further seen that the acidity of the zeolite is an important controlling parameter, which is summarized here rather crudely as the Si:Al ratio. The more acid sites the faster the kinetics and the higher the absolute amount of coke deposition.

The role of the acid sites may be either catalytic or they are consumed irreversibly during coke formation. In the propene coking study the abundance of coke molecules remained always significantly below the number of supercages in the zeolite which, together with the fact that insoluble coke formation was not saturated within 30 h on stream, points to a catalytic function. This was studied in great detail in a combined catalysis FT-IR study [71] which revealed the constant abundance of Bronsted acid sites in modernite with a Si:Al ratio of 12 during coke formation in ethylbenzene disproportionation. The fact that an IR-active band at  $1600\text{ cm}^{-1}$  can be assigned to coke shows that the structure of zeolite coke is certainly not comparable to coke from coal carbonization. This was incorrectly supposed in a study of coke formation from hexane and hexene in faujasite zeolites [72]. In this study it was found further that alkenic hydrocarbons are much more active than aliphatic which may, however, be interpreted as inhibition of the initial cleavage of the aliphatic feed molecules which becomes important for long-chain molecules. The ethylbenzene conversion [71] dropped with time on stream and the coke IR band increased proportionally to that without any change in the Bronsted acid band at  $3600\text{ cm}^{-1}$ . Moreover, after complete deactivation of ethylbenzene conversion the acid sites were still active for coke formation with a small precursor molecules as ethylene, which increased the coke band further when fed after ethylbenzene. These results are in line with observations from propene coking but are in conflict with other studies [67] which either claim the involvement of extremely hygroscopic Lewis acid sites (which are hydrolyzed by minute traces of water from hydrocarbon oxidation with lattice oxygen) or the consumption of acid sites during alkene polymerization (which may be an experimental artefact due to the extreme loss in IR transmittance of the samples in these highly reactive coking gas mixtures). It remains an intrinsic disadvantage of this type of study that IR can only detect various forms of soluble coke (the shifts and varying positions of the coke band are a direct consequence of the successive dehydrogenation-polymerization of polyaromatic molecules) and do not indicate the formation, transformation and absolute abundance of insoluble coke which is only detectable in Raman or NMR experiments.

### 2.1.9.11 Graphitization of Carbons

The various types of carbons obtained by one of the three routes shown in Fig. 11 can be discriminated with respect to their reactivity upon thermal treatment. The lower part of the figure shows the two categories of carbon which will either graphitize (further) upon thermal treatment (annealing) or remain nongraphitic even at temperatures up to 3000 K. The main reason for this distinction of reactivity is the dimensionality of the cross-linking of constituting BSUs. If they are linked in three-dimensional networks then, by thermal treatment, little possibility exists for rearrangement of the cross-linking into the two-dimensional network which is required to form the large planar graphene layers which constitute graphite. The larger the fraction of three-dimensional links in a carbon, the quicker is its formation as there is insufficient time to reach the equilibrium situation of an all  $\text{sp}^2$  carbon connectivity (which excludes three-dimensional networks). Synthesis conditions of rapid quenching from high temperatures are typical for this carbon. Alternatively, the reaction temperature is very low and thus insufficient to provide the activation energy for a rearrangement of the C-C bonds. In catalytic situations charcoals and activated carbons are the usual materials of this class.

Synthesis conditions of high temperatures, with dehydrogenation of hydrocarbons being rate-determining, and the intermediate formations of a liquid phase or even a liquid-crystalline phase (mesophase) of two-dimensional stacking of PAH molecules, are favorable for reaching the equilibrium situation. Pregraphitic structures are then formed which only require annealing for better stacking order and polycondensation of the BSUs by a final dehydrogenation step. The sequence of graphitization events [73] is summarized in Fig. 15. The end of the carbonization process leaves molecular structures consisting of polycyclic aromatic molecules with no heteroatoms other than hydrogen and some alkyl terminating groups. Their alignment is parallel to each other as in van-der Waals crystals of polycyclic molecules. The intermolecular dispersive forces between parallel ring systems are responsible for the alignment. At higher temperatures all non-six-membered structures and most of the alkyl groups are removed. At around 1900 K the large aromatic molecules start condensing to graphene layers. As some of the interconnections are not achieved by pericondensation but by the formations of C-C single bonds, considerably stained sheets with significant buckling will result. This state of graphitization can be observed experimentally by high resolution TEM [73]. The final step, the aromatization of all

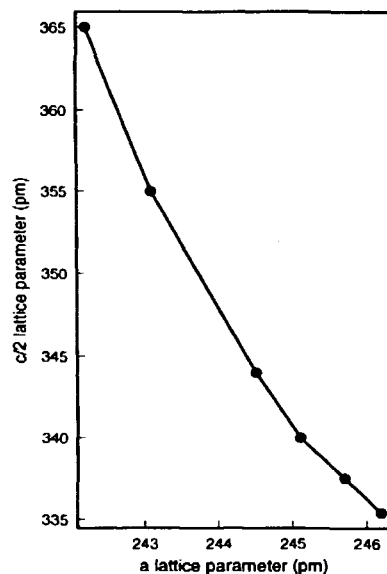
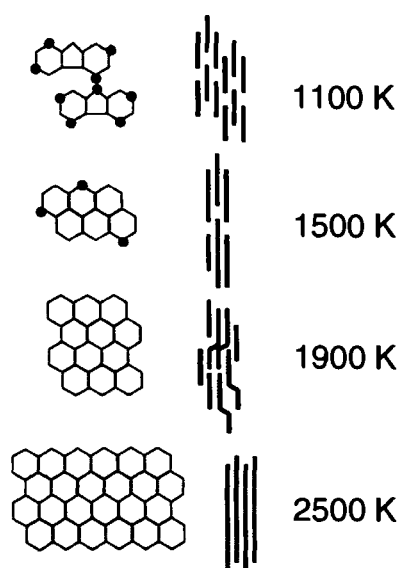


**Figure 15.** Graphitization of nanocrystalline graphene precursors (see Fig. 9). Chemical structures (dots represent heteroatoms or methyl groups) and stacking order are given as a function of characteristic temperatures. The polymerization and aromatization are reflected in the average lattice parameters which can be extracted from X-ray diffraction data. The correlation between the axis parameters indicates the shrinking of the cell volume [75].

C–C bonds, occurs only well above 2000 K. Only at such temperatures does the parallel alignment of the graphene layers and the formation of a regular stacking occur, as then the abundance of defective structures within the graphene layers becomes small enough to allow the dispersive forces between the graphene layers to direct the orientation of the BSUs. These sequences of events with the existence of intermediate stages of ordering between graphite and aromatic molecules has been derived conclusively by X-ray diffraction [74, 75]. The evolution of interplanar spacing with carbonization temperature and the kinetics of its equilibration served as tools for the analysis. The aromatization was detectable from a shrinking in the  $a$ -axis parameter, reflecting the shortening of the average C–C bond distance. Both changes lead to a shrinking in the cell volume which is reflected in the relationship between the lattice parameters shown in Fig. 15. The graphitization reaction proceeds through a series of metastable states [74] with an average change in the carbon–carbon bonding and not via a simple reorientation of turbostratic units into well-stacked units as is frequently assumed.

Good candidates for such solid-state phase transformations are carbons produced by polymerization of pitch, tar or other high-boiling fractions of fossil fuels [76]. Pyrocarbons from methane, which are generated under conditions of strongly understoichiometric oxidation, are also suitable candidates for highly ordered synthetic graphitic materials [29]. In catalytic situations most carbonaceous deposits, carbon blacks and synthetic graphite belong to this class of carbons.

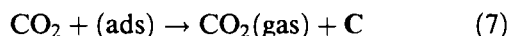
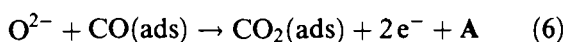
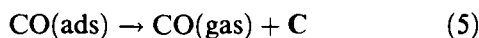
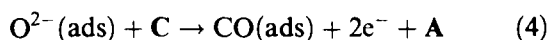
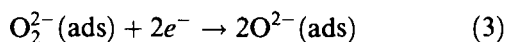
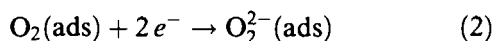
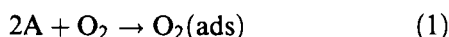
The range of temperatures in which graphitization occurs is between 1100 K and 2500 K with significant variations depending on the number and quality of structural defects in the material. In fullerene material the sequence of events of graphitization occurs at temperatures of about 1000 K below that for other carbons [77, 78]. The incorporation of large amounts of potential energy in the form of ring tension by the presence of non-six-membered  $sp^2$  carbon rings lowers the activation energy for the solid structural transformations drastically and allows graphitization at combustion temperatures. A similar low-temperature graphitization is also possible if the carbonaceous deposit on a hydrogenation catalyst has stored chemical energy in form of highly reactive organic molecular structures.

### 2.1.9.12 Reaction of Oxygen with Carbon

This apparently simple reaction is of multiple relevance in catalytic carbon chemistry. The reaction is used to activate carbon by the increase of surface area due to hole burning. It is further used to create surface functional groups (Section 2.1.9.5). Finally it is used to remove undesired carbon deposits in regeneration procedures.

The reaction is a gas–solid interface reaction which requires two independent types [79] of electronically different sites. One site should be electron-rich to activate molecular oxygen (site A); the other site should be electron-deficient to react with activated oxygen atoms

(site C). A minimal sequence of elementary steps is composed of the following processes:



This sequence of events was suggested by several authors [79, 80] with, however, different assignments to the nature of the two sites ranging from “ionic to covalent” [79] or to a distribution of sites with varying energy of oxygen chemisorption [81]. In these models it was assumed that the steps (5–7) are rate determining.

Steps 1–3 designate the activation of molecular oxygen into an oxidizing atomic species. This process requires the presence of weakly bound electrons in order to split the dioxygen double bond. Such catalytic sites are available on the basal planes of graphitic carbon. The notion that almost free electrons are also available at structural defect sites [82, 83] is only valid for extremely fast reaction rates, as otherwise stable surface complexes with oxygen, water or hydrogen deactivate such structural defects. The site A is thus at graphene planes of sufficient size to exhibit delocalized electrons more weakly bound than in aromatic molecules [84]. The oxygen atoms will diffuse on the surface [85] using their excess dissociation energy until they either recombine and desorb or find a structural defect C where they can form a covalent bond to carbon (step 4). This reaction is an oxidation reaction in which the directly bonding carbon atom C loses two electrons which flow back into the reservoir of almost free electrons of the graphene layer. It is a matter of ongoing debate to decide on the influence of the diffusion of activated oxygen on the overall kinetics [86]. Due to the extremely different reaction conditions and usually intentionally small conversions, at which experiments are made, it is difficult to decide this question at present. The main problem is the integrating effect of the large number of reactive sites present in an oxidizing carbon sample which precludes the identification of the influence of any particular reaction step, due to the convolution of the elementary step kinetic parameters with the energy distribution of the reactive sites.

The resulting CO complex can either desorb using its energy of formation for activation or survive due to insufficient activation energy. The amount of activation energy depends on the carbon skeleton onto which site C is bonded to. It is a structure-sensitive reaction [86,

87]. If the primary CO complex remains long enough at the surface where activated oxygen atoms are available (or if a sufficient flux of activated oxygen is available), then complete oxidation will occur, according to step 6. The desorption of the oxidation product leaves in any case an empty site for a new attack of an oxygen atoms (steps 5 and 7). The oxidation reactions (steps 4 and 6) leave an active site each for oxygen adsorption and dissociation. These sites are, however, not those at which the primary oxygen atoms are formed which changed their positions to diffuse from their location of generation on a graphene layer to the oxidation site.

From this scenario, which was developed from extensive experimental observations [84, 88–92], it is evident that efficient oxidation requires the presence of extended graphene layers for oxygen activation [84, 90] and sufficient defect sites for reaction of the activated oxygen. It was found necessary in an extensive formulation of hypothetical elementary steps to invoke the existence of stationary and mobile initial oxidation products (step 4) in order to explain the varying selectivity between CO and CO<sub>2</sub>. The experimental evidence showed different TDS peaks for carbon–oxygen compounds and not for dioxygen [83, 85, 91, 93] which led the authors to consider only the possibility that reaction products are mobile and not activated oxygen. The process of oxygen activation was assumed to be possible only at the reaction sites themselves (C in the reaction scheme). If the activation of molecular oxygen occurs by nonchemical means (glow discharge [83, 93] or radiolysis [82]) the sensitivity of the overall reaction kinetics to the presence of graphene layers for oxygen activation is lost and a fully structure-insensitive process occurs. In the other extreme of a dioxygen reaction on a perfect graphene layer, reaction of activated oxygen will always occur at the unavoidable external prism surfaces and very efficiently at the few intralayer defects.

One consequence of the reaction mechanism is that carbon burns with molecular oxygen in a layer-by-layer fashion at a decreasing rate as the perimeter of the graphene stack becomes progressively smaller with increasing burn-off. The defects present in variable abundance in each layers contribute significantly to the rate with an increasing tendency towards burn-off as the perimeter of the etch pits enlarges with ongoing reaction. The resulting net rate is an addition of a constant decreasing term and a fluctuating term with an unpredictable overall behavior with burn-off. The unusual dominating role of in-plane defects was established by microscopic studies on graphite oxidation [94, 95]. This effect precludes a definition of reactivity of carbon materials as their average structure is not sufficiently accurately determined to account for the defect

distribution in the carbon which controls the activity. This was established recently [96] for a very wide range of carbons containing most of the structural features shown in Fig. 3. A nonlinear compensation effect of the kinetic parameters was discussed. Several groups of carbons with different average structures (graphite, carbon blacks, coals) are differently affected by the rate-enhancing effect of defects which cause simultaneously a decrease in apparent activation energy and an increase in the preexponential factor. The correlation of the kinetic parameters of all carbons results in a nonlinear correlation due to the disregarded structural influence.

Alternative reaction scenarios for the activation of the aromatic graphenic layers may be considered. A plausible model with a period of increasing defect creation followed by a period of rapid gasification was discarded by in situ spectroscopic experiments, revealing that the average degree of graphitic chemical bonding does not change with burn-off [2]. The local electronic structure of graphitic  $sp^2$  configurations and the extended structural feature of parallel graphene planes is also not drastically changed with burn-off [2]. Disintegration of the well-ordered surface as preparation for oxidation at every surface site, as found for the reaction of atomic oxygen [83], is not observed with molecular oxygen.

Recent experiments with in situ X-ray diffraction [89, 97] revealed that defective parts of graphite crystals oxidize preferentially, leaving behind a more perfect structure until the total mass loss eliminates the most ordered parts of the crystal. These data are in agreement with the general experience of solid-state chemistry that an increase in defect density creates an increase in gas–solid reactivity. The increase in ordering of the residual graphite surface with progressive oxidation is documented in the STM survey images shown in Fig. 16. The rough surface of a graphite single crystal [89] which is covered by small crystallites [98] becomes smooth after about 10% burn-off with large terraces and few large step structures indicating the grain boundaries of the crystal. Studies at higher resolution show [99] that the terraces are atomically flat, with very few exceptions which are due to certain defects which are more difficult to oxidize than the matrix. A structure with sharp needles and small towers results. These observations confirm the complex influence of the defects on the oxidation kinetics which can either accelerate or decelerate by various types of defects. Elemental impurities such as boron are likely candidates for such inhibiting effects as boron compounds are well known for the inhibiting effect on carbon oxidation [100]. Other known inhibiting groups are C–H and certain C–O surface complexes [101].

The in situ X-ray diffraction [89, 97] data further excluded the possibility that oxygen intercalates between the graphene layers and starts the reaction in a

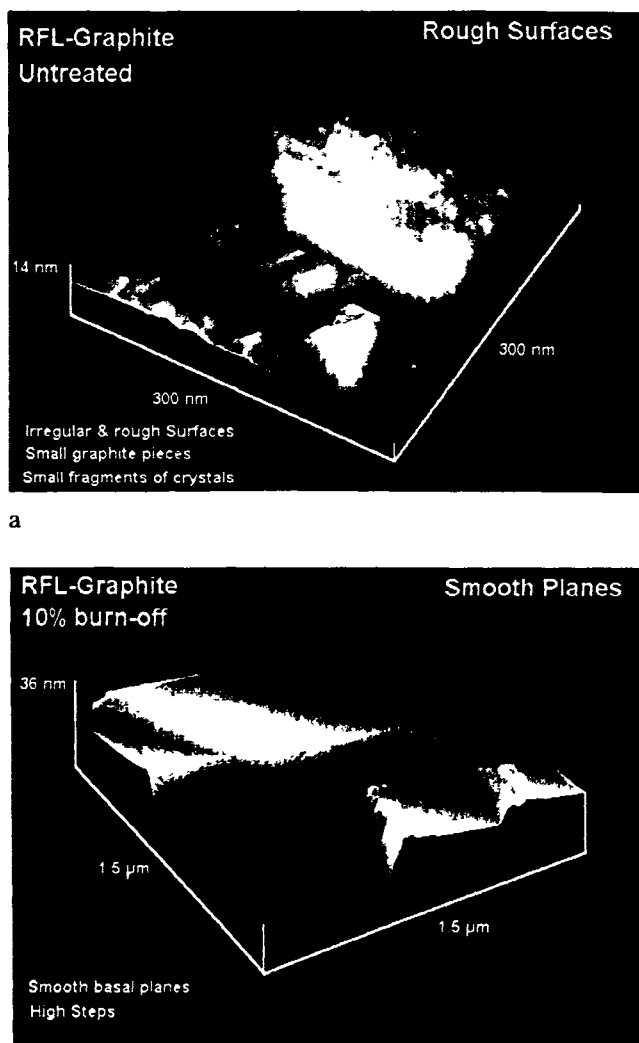


**Figure 16.** STM images (Burleigh ARIS 6000, air, W tip, constant current mode, 200 mV gap voltage, graphite natural single crystals, oxidation in air at 900 K) of (a) pristine and (b) oxidized graphite surfaces.

three-dimensional way at the internal surface. In-depth oxidation occurs only at structural defects with three-dimensional character such as at grain boundaries and interlayer defects [41, 102]. The contribution of this extra-oxidation activity to the overall rate is small, but severe consequences arise for the mechanical stability of all carbon materials under oxidative load. At very early stages of oxidation they disintegrate and fall into small particles of individual graphitic crystallites. Such mechanical disintegration has important implications for catalyst support materials where the active component falls off at the very beginning of any oxidative load on the system. An extensive review of the uncatalyzed and alkali-ion-catalyzed gasification at defect sites summarizes the present status of research in this highly relevant area [103].



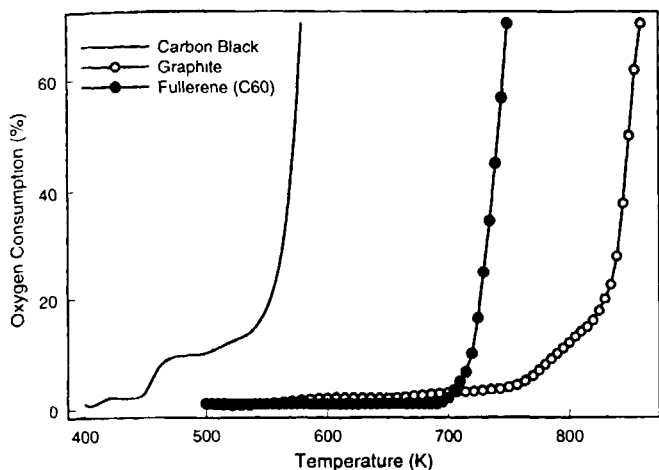


**Figure 17.** Reactivities of different forms of carbon against oxidation in 5% oxygen in Ar (100%) as function of temperature. The carbon black was FW-1 (Degussa), the graphite natural graphite powder AF (Kropfmühl).

In any practical consideration of carbon application or intended removal (regeneration) the oxidation reactivity is of importance. Figure 17 summarizes results of initial oxidation experiments. Different carbon materials which exhibit all the  $sp^2$  connectivity of carbon atoms exhibit a wide range of oxidation temperatures. The values of these temperatures depend on the definition of reactivity which can be either the first uptake of oxygen, the 50% line of oxygen consumption or even the 50% line of weight loss. Care has to be taken to compare literature values [81, 96, 104] as all these definitions are in use and the differences in temperatures are quite drastic.

The reactivity of the molecular fullerene solid resembles the expected pattern for a homogeneous material. Only a small preactivity at 700 K indicates that a fullerene-oxygen complex [12] is formed as an intermediate stoichiometric compound [15, 105]. At 723 K the formation of this compound and the complete oxidation are in a steady state [12, 106, 107] with the consequence of a stable rate of oxidation which is nearly independent of the burn-off of the fullerene solid. This solid transforms prior to oxidation into a disordered polymeric material. The process is an example of the alternative reaction scenario sketched above for the graphite oxidation reaction. The simultaneous oxidation of many individual fullerene molecules, leaving behind open cages with radical centers, is the reason for the polymerization.

The molecular nature of this carbon allows the spectroscopic identification [15, 108] of this intermediate and several oxocomplexes serving as precursor compounds [105, 109, 110]. On this basis the reactivity of fullerenes in oxidation is now understood in detail and the reaction scenario is secured by experimental verification [106, 107, 111].

The other two graphitic carbons oxidize, according to the data in Fig. 17, at quite different temperatures and with complex reactivity patterns. They show extensive prereaction activity. A significant oxygen consumption initiates at lower temperatures than the main reaction indicating gasification at extra reactive sites. The spread in temperature of this prereaction activity is very significant. It has been shown recently that the gasification activity at low temperatures is not a surface effect but can lead to a complete combustion of all the carbon [112]. This means for practical applications in catalysis that the minimum corrosion temperature of carbon in oxidative atmosphere can be very much lower than the bulk gasification temperature measured by thermogravimetry, which is too insensitive in most cases to indicate the prereaction activity. The distribution of the preactivity over reaction temperature is not a characteristic property of a carbon material, but depends in the same way as the main reactivity on the origin, storage and thermal history of the carbon. The oxidation rate as a function of the geometric carbon surface area (total surface area (TSA)) is a sensitive function of extrinsic sample properties [113].

The concept of the existence of an active surface area (ASA) representing a small fraction of the TSA was developed [114] in order to overcome this highly complicated situation. In full analogy with the concept of active sites in catalysis, it was concluded that a surface area measurement with dioxygen under defined conditions should measure the active sites in combustion (C sites in the reaction scheme). This technique allows the detection of the average change of the abundance of active sites with burn-off. The change in ratio between TSA and ASA by over an order of magnitude [114] for a graphitized carbon black highlights the relevance of surface modifications for the oxidation reactivity. A numerical example of the ratio TSA:ASA of  $76:0.24 \text{ m}^2 \text{ g}^{-1}$  (ratio 316) at the beginning of burn-off and of  $128:2.12 \text{ m}^2 \text{ g}^{-1}$  (ratio 60) at 35% burn-off of the graphitized carbon black illustrates the accuracy required to obtain meaningful results. This problem of large ratios may be the reason for the deviating numbers for carbon reactivities still quoted by different authors in the literature [86]. The same concept was further very successful in eliminating all the extrinsic influences on the carbon reactivity over ranges of materials with the consequence that a universal rate for the oxidation of  $sp^2$  carbon was established, deviating for various classes of materials only by a factor of about two [86, 113].

The method of determination of the ASA creates some carbon-oxygen surface complexes which are nonreactive and which cause the still significant dependence of the turn over frequency (TOF) on burn-off or

material property. A further improvement of this situation, reducing the dependence of the TOF on burn-off to below 10%, was achieved by introducing the concept of reactive surface area (RSA) [86] or active site density [115]. A simultaneous in situ measurement of rate and abundance of active sites allows the determination of the RSA without any assumptions on reactivity or energy spread of active sites to be incorporated in the method. The experiment is a transient kinetic measurement as it is well known in catalyst characterization [116].

The oxidation of carbon can also be catalyzed. Two fundamentally different cases should be discriminated. Transition metal oxides and carbides were found to be efficient local sources of atomic oxygen increasing its abundance much above the uncatalyzed case. Streams of diffusing oxygen atoms created decorated pathways of nonselective oxidation of basal plane sites as detected by transmission electron microscopy [117, 118].

Alkali and earth alkaline metal compounds (hydroxides and bicarbonates) were found to be efficient catalysts reducing the 50% weight loss temperature of all kinds of carbon materials by up to 200 K [103]. Two principally different modes of action have been proposed for this technologically and scientifically interesting effect. First, it was assumed that alkali graphite intercalation compounds could form and modify the surface electronic structure of the top graphene layer to enhance the sticking coefficient of molecular oxygen on carbon. This may, however, result from the action of the strong positive point electrostatic charge of a alkali cation residing chemisorbed at the carbon surface. Oxygen molecules still in the gas phase will become polarized which greatly enhances their sticking probability at the surface. The second effect is related to the set of elementary steps required to form a surface oxygen complex. Many of these structures involve the presence of charged oxygen species which require protons as counterions (carboxylic acids, alcohol, phenols etc.). Alkali ions provide ideal counterions in the situation of gasification where few protons are available. In addition, alkali ions do not only accelerate the formation of salts of surface functional groups but they also cannot act as site blockers such as hydrogen, which can form very stable surface hydrogen bonds and reduce the number of active sites. Finally, the alkali salts are all strong Bronsted bases which help desorbing surface functional groups forming during carbon oxidation. Using isotope labeling and other kinetic experiments it was established [119–122] that one very important function in alkali-catalyzed gasification (with  $\text{CO}_2$ ) is to enhance the amount of exchangeable oxygen between gas phase molecules and surface complexes. An alkali–oxygen cluster is envisaged at the active species, which is loaded with oxygen from the gas phase and unloaded by spillover of oxy-

gen to substrate. A fraction of carbon–oxygen–alkali always remains nonexchangeable which is seen as the “backbone” of the system, keeping the alkali at the surface (at high temperatures of about 1000 K where evaporation would be a problem) [103, 123].

A good indicator for the mode of operation of a catalyst in carbon gasification is the ratio of CO and  $\text{CO}_2$  which are formed according to the reaction scheme in independent reactions as simultaneous products. The possible postoxidation of CO to  $\text{CO}_2$  was excluded by a large number of observations and is a basic ingredient in the formulation of the reaction scenario described above. In uncatalyzed gasification reactions the product ratio is about unity with a factor of five deviations for different carbons. The presence of Ca as a catalytic impurity on the carbon from a sooting flame decreased the product ratio to less than 0.01 [81]. A kinetic analysis revealed that the addition of Ca enhanced the rate of  $\text{CO}_2$  formation without affecting CO production. The effect was attributed to a modification of the active sites of reaction step 6 which may be envisaged chemically as a Ca salt formation with a suitable surface complex. The suggested analytical value of the CO: $\text{CO}_2$  ratio [81] should, however, be taken with care, as other factors such as the basal:prism surface area ratio also affect the product ratio [86, 87].

The oxidation of graphitic carbon is a complicated gas–solid interaction with the unusual characteristic of a dependence of the reaction rate on conversion. Several independent factors with different dependencies on conversion cooperate in the control of the overall reaction rate. The most difficult part to control is the strong influence of atomic intralayer defects in the graphitic surface. It was made clear by electron microscopy that these unpredictably occurring reaction initiators can dominate the overall reaction rate [95]. The reaction rate expressed as the normalized mass loss per time as a function of burn-off is schematically shown in Fig. 18. In this figure the main controlling factors and their dependencies on burn-off are indicated. The dominating influence is exerted by the changes in TSA and in fractional active prismatic faces surface area of the graphene stacks. In the initial phase of burn-off the removal of surface defects and surface functional groups determines the rate. This was found experimentally by various techniques [89, 124] and is indicated in Fig. 16. The initially strongly changing rate led many researchers to exclude the first 10–20% of the burn-off curve from a kinetic analysis in order not to have to account of this initial effect. For catalytic purposes this effect is highly relevant as the stability of the surface functional groups and surface defects will determine the catalytic reactivity of a carbon sample. In applications where active species are bonded to carbon, the surface structure and its stability determine dispersion and stability of the metal–support system.

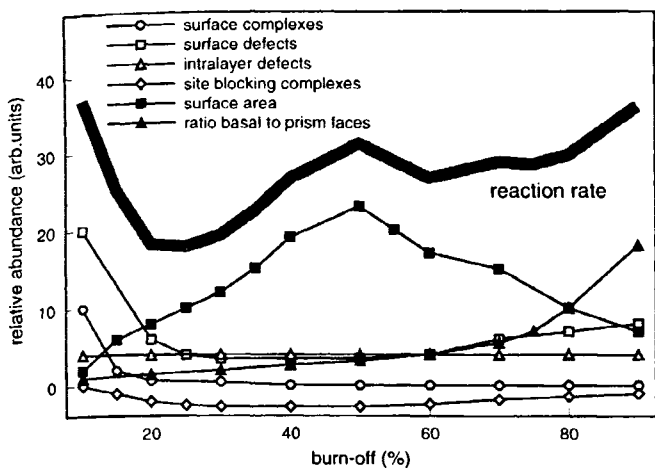


**Figure 18.** Schematic representation of the convolution of several influences on the observable oxidation rate as function of carbon burn-off. The broad line for the rate indicates that rapid fluctuations are superimposed on the slow trend.

All of the effects shown in Fig. 18 are accounted for if the carbon reactivity is given as TOF based on RSA. The only uncontrolled parameter remains the variation in intralayer defect density, which is statistical and not measurable by any reaction-based technique (as the technique modifies the number of intralayer defects). This is symbolized in Fig. 18 by the broad line for the rate which is a slow function of burn-off and a rapidly varying function of the intralayer defect density.

This information shows that the reactivity of a carbon material relevant in catalysis against oxygen (and other oxidizing gases such as  $\text{CO}_2$ ,  $\text{NO}_x$  and water) is not easily defined. As almost no experimental studies have ever applied the RSA-TOF concept it is not surprising that severe inconsistencies about kinetic parameters exist in the literature. A recent review highlights the merits of the transient kinetic technique which is the basis for a unified description of carbon oxidation [125].

The issue of carbon oxidation reactivity is further complicated in all cases where the oxidation of a carbonaceous deposit or a zeolite coke is involved. In these cases the solid carbon oxidation kinetics is superimposed on entirely different oxidation pathways involving organic molecules, and on the kinetics describing the carbonization reaction occurring simultaneously with the gasification reaction. The carbonization reaction system described in Fig. 10 is a sequence of polymerization dehydrogenation processes which leave essentially pure carbon with widely differing degrees of structural ordering. This carbon, which is responsible for the frequently reported conversion from coke into graphite, is not oxidized at moderate temperatures due to the inhibiting effect of the many surface defects precluding oxygen activation.

### 2.1.9.13 Surface Chemistry of Carbon

The surface chemistry of carbon is of relevance to all aspects of catalytic carbon chemistry. The two most important heteroelements are hydrogen and oxygen. Each element can undergo a variety of chemically different coordinations which need to be discriminated in analyses of the chemical function of the carbon-heteroatom bond. In the literature the term "surface complex" is often used to describe a group of chemically different bonds which could not be specified in detail.

The local connectivity of surface carbon atoms can be discriminated into  $\text{sp}^3$ , alkenic  $\text{sp}^2$  and aromatic  $\text{sp}^2$  for all kinds of carbon materials of catalytic relevance. Each of the three connectivities can form several types of heterobonds allowing for a broad distribution of carbon heteroatom interactions which coexist on any surface exhibiting structural defects. The surface chemistry of prismatic and basal planes of  $\text{sp}^2$  carbons is fundamentally different, which renders the surface area ratio between the two orientations one of the dominating factors for the description of carbon reactivity. One way of obtaining an estimate for this ratio is to assume that the abundance of hydrophilic sites on a carbon is due to surface functional groups at the prism faces, whereas the basal planes should be hydrophobic. The existence of both properties on a carbon can be verified and quantitatively determined by selective chemisorption of long chain aliphatic molecules ( $n\text{-C}_{32}\text{H}_{66}$ ) or metal salts such as  $\text{HAuCl}_4$  for the hydrophobic sites and alcohol molecules such as  $n$ -butanol for the hydrophilic sites. A practical procedure using microcalorimetry has been developed in the literature [126, 127].

The complexity of carbon materials together with the surface chemical anisotropy and the modifying effects of defects creates a highly complex situation for surface chemistry even when only one heteroelement is considered to be actively bonded. It is a characteristic of this branch of chemistry to describe surfaces in terms of distributions of properties rather than in sharp numbers.

The greatest attention in the literature has been paid to the carbon-oxygen-hydrogen interaction because of their enormous chemical relevance and the existence of a suite of chemical and physical tools for their characterization. Classes of carbons which are suitable for such studies are carbon blacks. These materials are of high elemental purity (no inorganic impurities) and sufficient specific surface area to allow a quantitative determination of the heteroelement content, which is the basis for any meaningful normalization of surface

Table 5. Heteroatoms in carbon black materials.

Property	Philblack A furnace	Philblack E furnace	Spheron C channel	Spheron 9 channel	Mogul colour
Surface area ( $\text{m}^2 \text{g}^{-1}$ )	45.8	135.1	253.7	115.8	308
Total H (g per 100 g C)	0.35	0.31	0.33	0.62	0.48
Total O (g per 100 g C)	0.58	1.01	3.14	3.49	8.22
CO <sub>2</sub> (g per 100 g C) <sup>a</sup>	0.187	0.401	0.575	0.536	2.205
CO (g per 100 g C) <sup>a</sup>	0.343	0.411	2.00	1.928	4.180
H <sub>2</sub> O (g per 100 g C) <sup>a</sup>	0.00	0.435	0.600	0.710	1.440
H <sub>2</sub> (g per 100 g C) <sup>a</sup>	0.209	0.137	0.152	0.321	0.132
H ( $\mu\text{mol m}^{-2}$ )	38.2	11.5	6.5	26.5	7.7
O ( $\mu\text{mol m}^{-2}$ )	7.9	4.7	7.7	18	16.7
CH <sub>x</sub>	0.48	0.15	0.08	0.33	0.1
CO <sub>x</sub>	0.1	0.06	0.1	0.23	0.21
C <sub>x</sub> R	1.72	4.76	5.55	1.79	3.25
Ratio H : O	4.8	2.5	0.8	1.43	0.48
Ratio CO : CO <sub>2</sub>	1.83	1.02	3.48	3.36	2.04

<sup>a</sup> Integral from thermal desorption up to 1475 K.

chemical reactions. In addition, the spectrum of industrial manufacturing processes [39] and the industrial production allows the comparison of data from homogeneous samples with distinctly different (but often unknown) microstructural properties.

A representative collection of surface chemical data of several carbon blacks is compiled in Table 5 which was collected from extensive data [33]. The specific surface area varies by an order of magnitude for the five samples. The total content of heteroatoms (determined by classical microanalytical techniques) amounts to between about 1 and 5 wt% which is a sizeable quantity for a material which is nominally pure carbon.

A technique used often in chemical speciation of the surface functional groups is temperature-programmed desorption (TPD) of all functionalities. The strength of the surface chemical bonds requires maximum temperatures of usually 1273 K with desorption profiles extending from 400 K to the upper limit of heating in inert atmosphere in a quartz tube furnace. Table 5 lists the integral abundance of all possible decomposition products of C–O–H functionalities. The data show that both absolute amounts and product distributions (CO to CO<sub>2</sub> ratios) vary significantly and exhibit no apparent correlation to surface area or synthesis method for the carbon. Reduction of the data per surface area reveals that carbon-hydrogen functions are abundant heterobonds on carbon black surfaces. Carbon-oxygen functions are always present and in samples 3 and 5 more frequent than hydrogen terminations. The importance of the heteroatoms for the description of the surface properties becomes apparent when the carbon to heteroatom ratios are considered. It occurs that about every other carbon atom exhibits in its connectivity one heteroatom. The ratio of carbon to heteroatom can be used to estimate the size of the basic structural units. Assuming the microstructure of

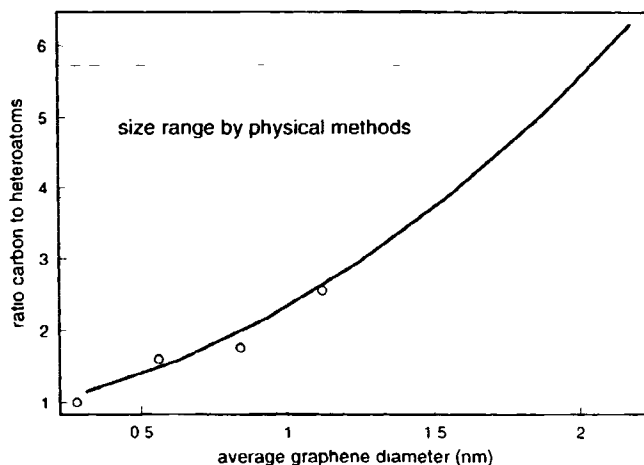


Figure 19. Calibration curve for the determination of the average size of a graphene unit in nanocrystalline carbon from its content in heteroatoms. The size range seen by physical methods stems from direct electron microscopic observation, from scattering models of X-ray diffraction and from NMR.

carbon to consist of small graphene platelets with few intralayer defects (Figs 5–9) one may estimate from the topology of pericondensed aromatic structures the ratio of carbon to heteroatoms. These are all located at the prism faces of the graphene layers and saturate the dangling bonds in the carbon  $\text{sp}^2$  configurations. This ratio is 1.0 for benzene, 1.25 for naphthalene, 1.6 for perylene, 1.76 for coronene and 2.56 for a  $n = 4$  pericondensed molecule. Such a molecule has a diameter of about 1.2 nm. A coarse correlation between the carbon to heteroatom ratio and the size of hypothetical circular graphene layer is presented in Fig. 19. HRTEM images of carbon blacks exhibit 1.5–2.0 nm as characteristic diameters [130], compatible with  $n = 5$ –8 ring pericondensed structures. Samples 2 and 3 from Table 5 exhibit an abundance of heteroatoms.

consistent with a graphene diameter as seen with physical methods. The other samples consist of significantly smaller BSUs which are, however, not observed by microscopy [128, 129]. This discrepancy together with the H:O ratio from Table 5 indicates that more than one heteroatom is bound frequently to one peripheral carbon atom, calling for more complex functional group structures than C–H or C=O terminations. Sample 3 is the best approximation to pure carbon in the selection of Table 5 with a large number of simple carbonyl functions as carbon termination groups (see CO to CO<sub>2</sub> ratio). Sample 4 with the lower surface area and the same synthesis history exhibits a much richer surface chemistry which could give rise to a strongly underestimated average size of the graphene layers. It is pointed out here that the physical method of determination of graphene layer diameters by X-ray diffraction [33, 39, 130] is critical. Smaller particles than the average do not contribute significantly to the overlapping and diffuse line profiles of the (*hk*) reflections used for the analysis. For this reason it remains valuable to compare physical data with chemical information such as that shown in Fig. 19.

Using refined X-ray diffraction techniques and the extraction of the radial distribution function from molecular X-ray scattering it has been possible to develop a model for a graphene layer [31]. This model is free of the difficulties mentioned above and predicts cluster sizes of between  $n = 3$  and  $n = 5$  for pericondensed rings (coronene, hexaperibenzo coronene) in full agreement with electron microscopic [25] and NMR [131] data which led to construction of Fig. 19. The model material [31] was a coal sample before carbonization containing, as well as the main fraction of sp<sup>2</sup> centres, about 20% carbon atoms in aliphatic connectivity. This one-dimensional structure analysis represents a real example of the scheme displayed in Fig. 9(C).

The data from Table 5 show clearly that a significant fraction of the total carbon surface which is chemically active (prism faces and defect sites) is covered by heteroatoms and many of these sites are not just passivated by C–H bonds. This situation is also characteristic of carbonaceous deposits with C<sub>x</sub>R values of 1.5–2.5 (corresponding to C:H ratios of 0.45–0.65) pointing to truly smaller average diameters of the BSU (see Fig. 19), as was determined by chemical extraction and mass spectrometry [70, 132, 133]. The situation is also typical for carbon materials resulting from dehydrogenation of organic polymers with a large abundance of prism faces and a significant presence of oxygen functional groups. For carbons with larger BSU diameters the dominance of prism sites is gradually reduced and defect sites at crystallite boundaries and intraplane defects become important locations for surface functional groups. The absolute abundance is, however, so much reduced that the accuracy

of elemental analytical data as used above is too low to allow a meaningful chemical and structural interpretation.

#### 2.1.9.14 Non-Oxygen Heteroelements on Carbon Surfaces

The most important non-oxygen heteroelement is hydrogen bound to a variety of different reaction sites. Thermal desorption experiments showed that weakly held hydrogen desorbs at 1000 K, and more strongly bound species desorb at 1270 K and 1470 K. Only above 1900 K all hydrogen is released from a carbon material [134]. As this especially stable hydrogen can be as much as 30% of all hydrogen present, it was suggested that this species should be bonded to alkene and alkane link structures within the graphene layers (see Fig. 9(C)) and represents hydrogen bonded to inner surfaces.

The chemical structure of the hydrogen groups is difficult to assess as they can be present either directly bonded to carbon or as protons together with other functional groups. In addition, at low temperatures, all hydrophilic carbons carry a layer of molecular water which needs to be desorbed first to allow a quantitative analysis. Thermal desorption with discrimination of water and carbon oxides can be used to control the desorption the unspecific water layer. It is observed, however, that the water desorption affects the surface chemistry of the carbon, as some labile groups are desorbed and the vacant surface sites can react with water to form C–O–H or C–H bonds [88, 135]. IR spectroscopy can be used to show that even after mild desorption of water from an oxidized carbon black a variety of hydrogen species is present at the surface. Figure 20 shows the corresponding transmission spectrum of two technical carbon blacks with hydrophilic and hydrophobic reaction against liquid water after in situ desorption of molecular water at 573 K. The absorption from carbon–hydrogen and carbon–hydroxy groups overlap to form a complex peak structure. A range of different O–H groups is present (see below) and the C–H frequencies occur also as convolution of signals from isolated C–H functions and shifted components due to C–H groups next to C–O bonds in various configurations. Figure 20 and the TPD experiments from the literature indicate that hydrogen is present not only in strongly bound C–H groups, which coexist with other functional groups, but also in a variety of C–O–H groups which cannot be removed at moderate temperatures up to 675 K. For the hydrophilic sample a broad structure of oligomeric OH group fundamental vibrations causes the strongly

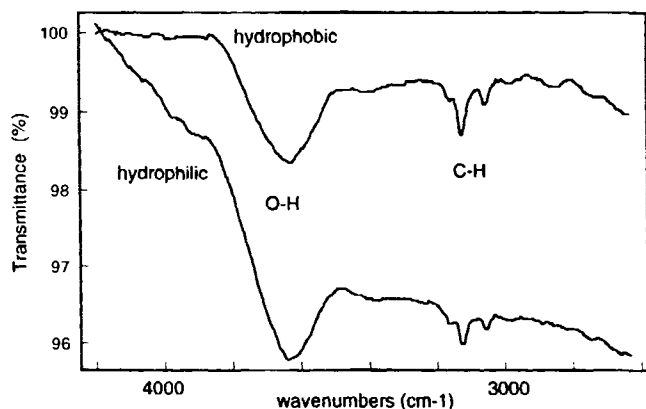


**Figure 20.** Transmission FT-IR data for two carbon blacks which were pretreated to desorb molecular water films. An in-situ reaction cell with specially prepurified KBr supports were used to accumulate the spectra in dry Ar. All sample handling was carried out in a glove box. A Bruker ISF 66 instrument was used to collect 1000 scans from each sample.

falling background at high wavenumbers. After more severe heat treatments the carbon surface is more uniform [136] but is modified in its defect properties and in its chemical reactivity.

The existence of several distinct C-H surface functional groups and the modification of the carbon surface during adsorption of hydrogen has been studied in detail [137]. Four different kinetic regimes of coverage versus reaction time have been identified, indicating the structural heterogeneity of the carbon surface. The material studied (graphon) is a graphitized carbon black with no inorganic impurities. This allows the deduction of the heterogeneity of the adsorption sites which was also reproduced by a variation in activation energy for adsorption as an intrinsic effect of the carbon material. The fact that temperatures above 700 K are required to saturate the carbon surface suggests that structural modifications (hydrogen etching) of the surface may significantly contribute to the surface reaction which seems to be more complex than adsorption of hydrogen atoms on (preexisting) chemisorption sites.

Carbon-nitrogen surface groups are not abundant in carbons made from hydrocarbon precursors. Carbons from nitrogen-containing natural and synthetic polymers contain structural C-N-C groups in aliphatic and aromatic coordination. Surface complexes such as amines, amides, or nitro groups are not very stable and are desorbed during heat treatment (manufacture, activation, precleaning). An extensive body of work has been assembled [135] concerning the intended incorporation of nitrogen from ammonia or cyanides using carbon surfaces prereacted with oxygen or halogens. Several structures of C-N and C-N-H have been identified with physical methods. The stability of the most abundant C-N-H groups is, however, rather limited in temperature.

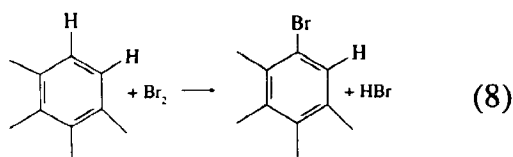
Most significant is the observation that the catalytic behavior of a carbon (from various sources) remains affected by the amination treatment, even when the nitrogen is desorbed from the surface. The explanation was put forward that nitrogen binding (and removal) occurs on defective sites and the nitrogen activation is in fact a mild version of preferential removal of defective surface sites, leaving behind a carbon surface with a more graphitic electronic structure than originally present. Some of the structural nitrogen (pyridine-like incorporation in the graphene layers) is thermally stable up to 1273 K [33, 135] without affecting the catalytic performance of the carbon material. This observation excludes the notion that the heterocyclic substitution injects additional electrons into the conduction band of the semimetal graphite and in doing so enhances its activity in electron transfer reactions (e.g. activation of molecular oxygen in liquid phase oxidation catalysis [138]).

Carbon-sulfur groups are extremely stable surface compounds which cannot be removed by thermal treatment up to 1470 K. Only by a reductive treatment with hydrogen it is possible to clean carbon from sulfur adsorbates. One source of sulfur is the fuel used for the generation of the carbon from which about 90% are covalently bonded to the carbon and 10% are segregated as adsorbate which can be removed by solvent extraction. The abundance of sulfur can amount to several wt%. Removal of the structural sulfur is possible by hydrogen reduction to H<sub>2</sub>S at about 1000 K. A collection of references on this subject is found in the literature [33]. In activated carbons sulfur can also be present in an oxidized form as sulfate or as C-S-O compounds.

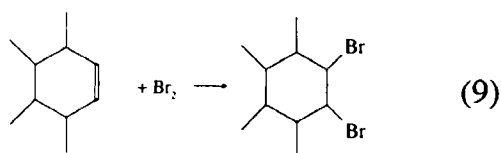
The generation of sulfur functional groups has been investigated in detail in order to prepare anchoring sites on surfaces used in rubber vulcanization (for tyre manufacture). Only those sulfur groups which are not incorporated in the graphene layers can be chemically active for cross-linking polymerization in vulcanization. In a broad study [139], carbon disulfide, hydrogen disulfide, thionyl chloride and sulfur dioxide were used at elevated temperatures to generate sulfided carbon surfaces on a variety of sp<sup>2</sup> substrates. Structural data revealed in all cases the absence of graphitization phenomena even though the reaction temperatures were up to 1173 K. XPS and IR data indicated that two types of species were formed. One type should be C=S bonded to aromatic rings and the other one a thiolactone.

Carbon-halogen groups are well known to exist for fluorine, chlorine and bromine. These groups can be attached by redox reactions involving the halogen elements either in aqueous solution or in the gas phase. At elevated temperatures bulk reactions occur under intercalation and eventually under formation of bulk covalent carbon-halogen materials (CF<sub>1.1</sub> solid, CCl<sub>4</sub>

gaseous) [140]. At lower chemical potentials of the halogens, substitution reactions into C–H bonds (reaction 8) or addition reactions onto in situ formed unsaturated bonds (reaction 9) occur. These two reactions are one of the most important analytical tools in describing the chemical reactivity of carbon materials. On the basis of extensive experiments with various carbons [141] the reaction of a carbon with aqueous bromine is suggested to serve as reference experiment for the quantification of the unsaturated carbon atoms which are mostly masked by oxygen surface groups (reaction 9).



The reaction with chlorine occurs, after high-temperature outgassing, directly as addition of halogen on the unsaturated C=C bonds. The strength of the carbon–halogen bonds is determined by using halogen-saturated carbons for halogenation of nucleophiles [33]. It occurs that iodine groups are fully reversibly adsorbed, whereas bromine and chlorine are partly irreversibly adsorbed and can only be removed by high temperature treatments under oxidizing or reducing conditions. This result led to the conclusion that aqueous iodine solutions should be used to determine the surface area of carbon as a selective adsorbent. Reaction with iodine vapor at elevated temperature (600 K) results in the same chemistry as shown in reactions 8 and 9 and is not suitable for carbon selective surface area determination.



Care has to be taken when interpreting results of halogen uptake on carbon at low temperatures, in aqueous solutions or at undefined surface states of the carbon (as received). A large number of reaction involving halogens and oxygen surface functional groups and of course between halogen hydrogen acids and basic functional groups occur simultaneously with the reactions mentioned above. They may thus perturb the analytical data (in particular the amount of HX as measure for reaction 8) to such an extent that no meaningful result can be obtained. The only method is to define the surface chemistry of the carbon by pre-annealing and treatment in the gas phase or by in situ cooxidation [142], forcing reaction 9 to dominate.

### 2.1.9.15 Surface Oxygen Groups

The abundance of oxygen atoms on carbons varies over a wide range with a maximum at about C<sub>4</sub>O (see Table 5). The surface chemical and hence many technical properties of carbon materials (including diamond [143]) depend, however, crucially on the carbon–oxygen chemistry which controls adsorption, adhesion and oxidation activities of the surfaces. From the reaction with liquid water acidic and basic surface complexes can be discriminated. Under almost all catalytic conditions both types of oxygen groups are present simultaneously and the pH value of an immersion of carbons in water is the result of protolysis of solid acids and solid base groups. The pH can be as low as weak mineral acids indicating that a significant solid acidity can be present on carbon. The basic reaction is rather more limited and rarely exceeds the value of pH 8. For this reason, an overall good quantitative correlation between pH in aqueous solution and analytical oxygen content for a carbon species has been established [144]. A consequence of the Bronsted acid functionality is that many of the carbon–oxygen groups exhibit a cation exchange capacity and a simultaneous anion exchange capacity (from the basic groups). These functions are most relevant for the application of carbon as catalyst support and provide a method for anchoring metal ions by the same method as used for oxide supports also on carbons. For the special case of protons (exchange on basic groups) the graphene layer in its unperturbed aromatic state is sufficiently basic to allow direct adsorption [145]. In catalytic situations this problem is of limited relevance because for high surface area material the abundance of graphitic surface patches is low and on graphitic materials the surface area is often low, so that a significant interference with the determination of basic functional groups is to be expected only in graphitized carbon blacks. However, when the hydrogen adsorption method is used to determine the dispersion of small metal particles the sorption capacity of the support for activated hydrogen (spill over) has to be taken into account.

The dominating importance of the oxygen functional groups has led to significant efforts to devise preparation routes to obtain only part of the wide pK<sub>a</sub> spectrum on the surface, i.e. to prepare either only acidic or only basic functional groups. This was, however, only partly successful with the result that in all circumstances a spectrum of neutralization equilibria rather than a single pK value characterized a carbon surface. Basic functional groups can be obtained when carbons are annealed in vacuum or inert gas (Ar, not nitrogen) at 875 K for several hours, cooled down under inert

conditions to 300 K and then exposed to air, water or oxygen [146]. The basic reactivity occurs only after contact with water molecules which contribute to the formation of the basic groups.

Predominantly acidic groups are obtained by heating carbon in air or oxygen to 600–900 K with a decrease in acidity with increasing temperature (self-gasification). Very strongly acidic groups can be obtained with low-temperature liquid phase oxidation using hydrogen peroxide, ozone, chromic acid or aqua regia.

The characterization of the resulting surfaces has been problematic ever since the early attempts [143, 147] by applying chemical means. The advent of many surface physical methods has not contributed significantly more information than that obtained with chemical probe reactions (derivatization as in the early days of organic chemistry). The reason for this is the small abundance of a wide variety of chemically different species. Most surface spectroscopies are too insensitive for the variations in chemical environment. Others require single crystal surfaces which cannot be functionalized. Vibrational spectroscopy is hampered by the strong bulk absorption of light. Nuclear magnetic resonance has relaxation problems with non-hydrogen-carrying surface groups bound to aromatic graphene structures. For these reasons the bulk of our knowledge about the structural details of carbon-oxygen functionalities stems from chemical experiments as collected in several reviews [32, 33, 146, 148–150]. A special series of publications is devoted to structure and reactivity of basic oxygen groups [151–154]. The following description is a critical summary from this large body of information which contains plenty of references to the original work with ample experimental details.

The analysis of the structural chemistry of oxygen groups with chemical methods is limited to stable configurations and misses by definition all metastable configurations which may, however, be present under *in situ* oxidation conditions. Chemical structures of reaction products of the reaction sequence provided by eqs 1–7 may be found in this description, but other less stable configurations may also exist. Care should be taken to transfer the knowledge reported here directly to the actual discussion about the atomic structure of oxidation reaction intermediates [86, 122, 155].

The acidic functional groups can be characterized by their neutralization reactions with a selection of bases differing in their *pK* values. The usual reagents are sodium hydroxide, sodium carbonate, sodium bicarbonate and, for very weak acids, sodium ethoxide in alcohol. An additional dimension of information can be obtained by pretreating the carbon prior to neutralization analysis [156].

Figure 21 shows the representations of the fundamental structures responsible for Brønsted acidity.

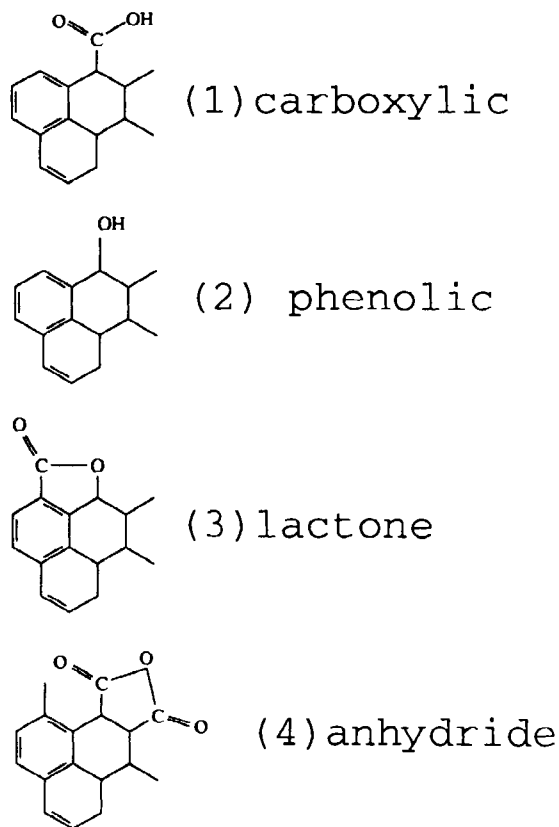


Figure 21. Chemical structures of acidic surface groups.

Only carboxylic and anhydride groups are strictly acidic in water, with the anhydride hydrolyzing to two carboxylic acid functions. These two groups contribute mainly to the reaction with sodium hydroxide but react with all weaker and stronger bases than hydroxide. The lactone groups need to undergo ring opening in a basic medium which can be achieved by 0.05 M sodium carbonate. Phenolic groups are supposed to be frequent due to their structural simplicity (reaction product of eq 4). Their acidity is limited in water and will depend strongly on neighbouring functional groups. Sodium ethoxide is a selective reagent for their detection.

Some oxygen functional groups do not react with water molecules and behave thus as neutral. Their fundamental structures are shown in Fig. 22. Some carbonyl groups can still react with sodium ethoxide. The ether or xanthene structure is fully inactive in aqueous media. Both neutral structures are believed to occur frequently due to their structural simplicity and the fact that in any oxidation reaction these structures have to occur as intermediates in ring destruction sequences. In quantitative studies where the oxygen content is compared to the sum of all neutralization reactions a significant excess of chemically unreactive oxygen is stated [149, 146] which is accounted for by these neutral functions.



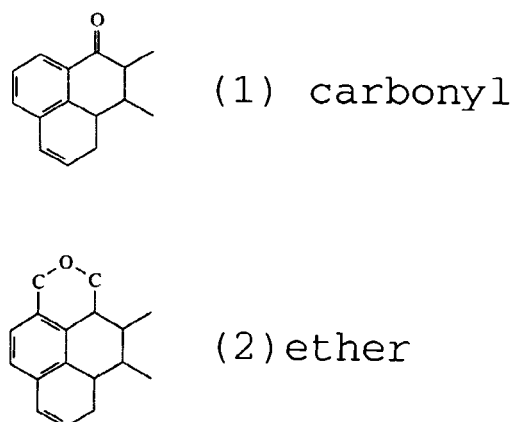


Figure 22. Chemical structures of neutral groups (weak acids in nonaqueous media).

Bronsted-basic groups are of complicated structure as can be seen from Fig. 23. They consist of two interacting oxygen centres [157], one of which is active in proton adsorption and the other one in anion exchange. The interrelation has been shown in a series of elegant chemical reactions [151–154]. The structure shown in Fig. 23 is tentative, representing the simplest configuration and may have more complicated isomer structures. It is interesting to note that during formation of the basic groups a nonstoichiometric amount of hydrogen peroxide is formed when the oxidized carbon is contacted with moisture or water. This reaction which was also discussed in conjunction with an oxidation of ether structures to chromene groups [157] is reminiscent of the anthraquinone catalysis of technical hydrogen peroxide synthesis. It should be taken into account that in all situations in which dry oxidized carbons are contacted with water a chemically detectable amount of hydrogen peroxide will be formed which may interfere with experimental observations.

Suitable reactions for the chemical identification of fundamental surface groups are collected in reactions 10–24 which summarize convenient reactions for chemical group identification. A large number of additional reactions with rather special applications can be found in the review literature. When these reactions are used, it is advisable to test the reaction conditions by several different reactions characteristic for the same functional group. It occurs that the neutralization kinetics can be slow, in particular with hydrophobic and porous carbons. Reaction times should not be under 24 h at ambient conditions. However, artefacts such as glass adsorption, reaction with traces of air and the intrinsic problem of conversion of the surface functional groups during chemical reaction limit the reaction time to an optimum for complete but artefact-free determination.

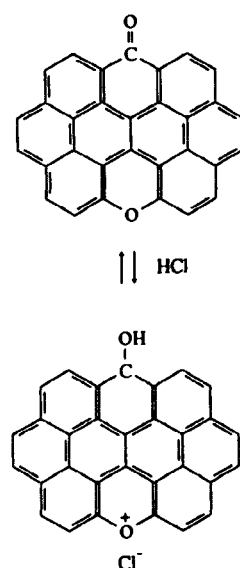
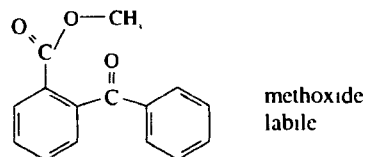
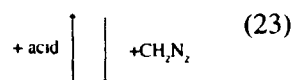
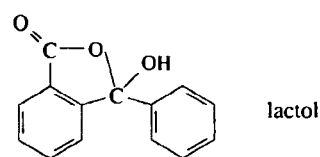
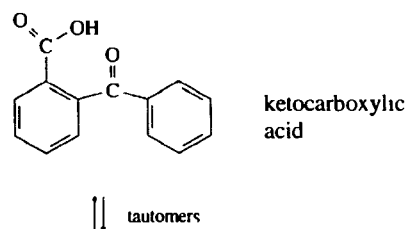
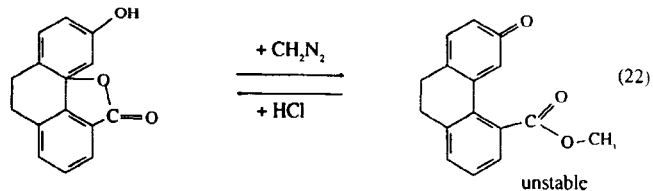
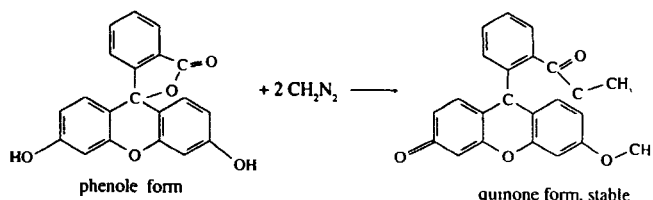
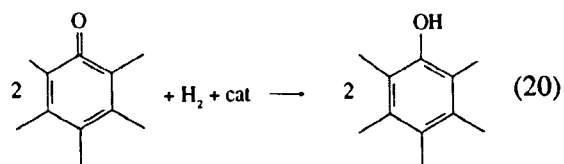
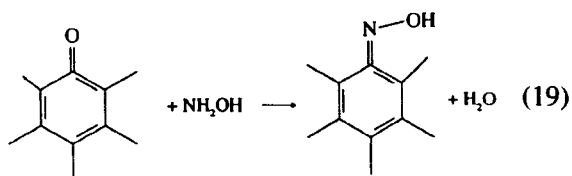
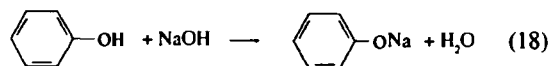
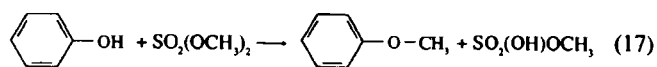
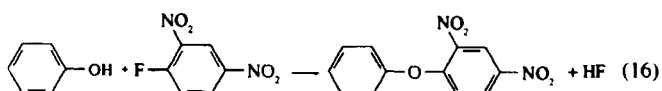
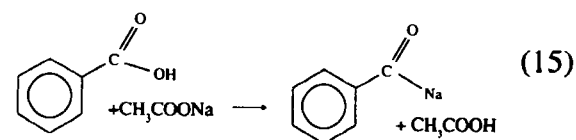
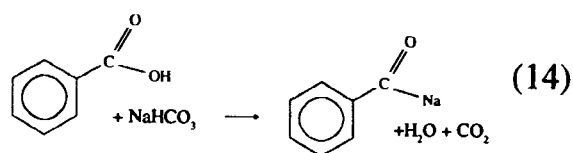
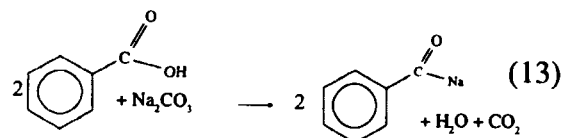
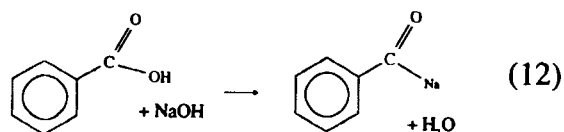
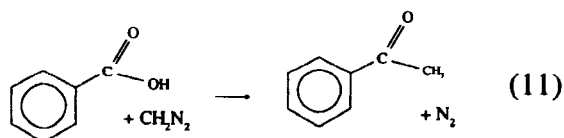
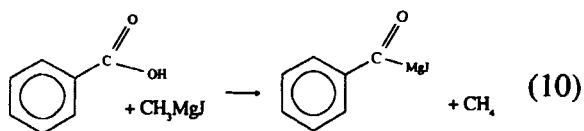


Figure 23. Chemical structure of basic functional groups. Both heteroatomic structures are required to explain the neutralization reactivity.

Reactions 12–15 describe the standard neutralization reaction for an organic carboxylic acid. The discrepancy in neutralization capacity for the different reagents can be used to estimate the pK distribution [88]. Amounts between 50 and 500  $\mu\text{eq}$  acid per gram of carbon are characteristic values which indicate the high degree of experimental perfection required to determine such surface acidity data. Reactions 10 and 11 form derivatives of the carboxylic acid and can be used to volumetrically detect their presence by monitoring the gaseous reaction products.

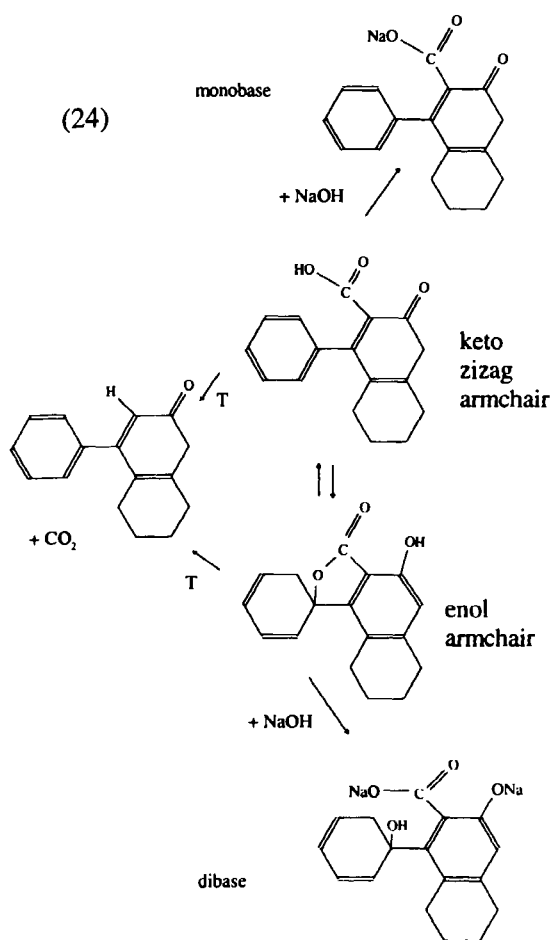
Phenol groups are determined by the difference of the neutralization reactions between sodium hydroxide and sodium carbonate which are common for carboxylic and phenolate groups. Oxidized carbons (typically in air at 700 K) contain equal amounts of these two functional groups. Activated carbons contain up to 800  $\mu\text{eq g}^{-1}$  carbon of phenolate groups. The volumetric determinations are also sensitive to both carboxylic and phenolate groups so that specific derivatization processes are needed to reliably discriminate the two types of groups.

With more complicated structures such as lactones the identification problems become more complex as the reaction of lactones in water result in the formation of a carboxylic acid group and a neighbouring phenol



group. Reactions 23–25 are only characteristic for lactones with the assumption that under the mildest possible reaction conditions the neighbourhood effects of the ring opening reaction will favor the derivation over the same reaction occurring on additionally present non-correlated functional groups.

The complexity of the chemical situation increases further when combinations of different surface groups start to react with each other. A prominent example is the lactol group originating according to reaction 23 from combination of a carboxyl group and a carbonyl group. This is a situation which is frequent due to the high abundance of both fundamental groups. The resulting structure, representing a complicated example of a coadsorption effect, can undergo a whole spectrum of reactions and interfere with several derivation reactions simultaneously.



Another type of complication arises from the chemical inequivalence of (110) and (110) terminating surfaces, referred to as zigzag and armchair configurations of the graphene layers. In reaction 24 an armchair configuration exhibiting two different functional groups at one six-membered ring is shown. The resulting structure, using the same fundamental groups as for the lactol reaction which are now in 1,2 configuration with respect to each other (1,1 configuration for the lactol), allows tautomerism with the result that upon neutralization either one or two equivalents of base will be consumed. The equilibrium between the two forms depends upon the base concentration of the base used for detection.

Reaction 24 is also a good example for the insensitivity of thermal desorption for such effects because the same molecule results after decarboxylation. Any quantitative correlation between neutralization and thermal desorption thus leads to inconsistencies, which is the historic reason for the intensive investigation into this surface chemical problem [33].

These few examples give an impression about the chemical complexity of the carbon-oxygen surface reaction. They illustrate that surface acidity as a single number of sample characterization is a very poor rep-

resentation of the spectrum of reactivity already present in aqueous media. It becomes apparent why in practical applications [130, 150, 158] only poor correlations are observed between such simplified surface chemical parameters and the observed reactivity.

In recent years a simplifying attempt to overcome this complexity was to analyze carbon by TPD and to integrate the total CO and CO<sub>2</sub> emission and to correlate the results with sample pretreatment and chemical reactivity [33]. The limited validity of such an approach is apparent. As is illustrated below, the chemically complex surfaces which are not described by such crude correlations are those with the highest catalytic activity. In applications of carbons as catalyst support it is immediately apparent that the details of the carbon-to-metal interaction depend crucially on such details of surface chemistry. This explains the enormous number of carbon supports commercially used (several thousands). A systematic effort to understand these relationships on the basis of modern analytical capabilities is still missing.

In this situation a variety of techniques can be used to obtain complementary and if possible quantitative information on the surface chemistry of a given carbon material. High sensitivity and chemical selectivity are characteristic for titration methods of the solid-acid surfaces. The most prominent technique in a one- or two-point titration with two fixed concentrations of e.g. 0.05 n and 0.5 n bases. The titration is usually carried out as back-titration after an adsorption experiment. The results usually differ from each other indicating the distribution of acid sites over one order of magnitude in pK values. Reactions 12 and 18 are associated with these two values. For a variety of different carbons the characteristic concentrations for the predominant analysis of carboxylic acids and phenols may differ due to variable distributions of local adsorption geometry. This affects, via neighbouring group effects, the dissociation constants of the surface groups and hence modifies the pK distribution. To avoid the possibly substantial errors, it is recommended practice to determine the adsorption isotherm of the neutralisation reagent on the carbon and to analyze the resulting data in terms of a multiple Langmuir chemisorption model.

The Langmuir model describes, for a uniform surface and a non-self-interacting adsorbate, the relationship between amount adsorbed and exposure concentration. The parameters of the model are the maximum amount adsorbed as a full monolayer and the equilibrium constant for the adsorption-desorption process which indirectly reflects the strength of the adsorbate-substrate interaction. For the present situation the analysis is modified in the following ways:

- it is assumed that several independent site types exist which represent acids with different  $pK$  values;
- the neutralization process is seen as an equilibrium reaction which occurs in an additive way on the different site types;
- no interaction between different site types is assumed (no effects as described in eqn 24),
- no complications with correlated equilibria for generation of the primary sites (e.g. hydrolysis of lactones or anhydrides) are taken into account.

Within these limitations the method supplies information on the absolute abundance of the fundamental solid acid sites and gives a qualitative indication about the  $pK$  average of each site. The procedure works in principle for acid and basic sites [88]. Figure 24 illustrates an example for acid sites on a carbon black sample (FW-1 from DEGUSSA). This sample was selected as the high purity allows an unambiguous assignment of the neutralization to carbon-bonded functional groups and the high surface area provides sufficient chemical heterogeneity for a realistic model. The top panel shows the experimental adsorption isotherms after 24 h equilibration in anaerobic conditions for the as-received sample and an extracted sample. Extraction was done with xylene and ether to remove polycyclic aromatic molecules which are chemisorbed in an abundance of less than a monolayer [39] on the carbon and passivate the genuine carbon surface. The strong effect of the extraction is clearly visible. The shape of the isotherm indicates, at least for the extracted material, some complications as a stepped curvature should not occur from a single Langmuir isotherm. As the reaction should occur in an additive way it is also not expected that the combination of several isotherms should give rise to such a feature, which is absent in the as-received sample. The discontinuity is ascribed to the generation of additional functional groups by chemical reactions between the NaOH with nominally unreactive functional groups during the adsorption–equilibration process.

The lower panel of Fig. 24 shows the analysis of the normalized isotherms. It occurs that two processes are superimposed in each isotherm. The break in the isotherm of the extracted carbon at around 0.1 n concentration indicates that in this regime the extra reactivity which consumes base outside an adsorption has probably occurred. The data can be quantified and provides the following information. The two adsorption sites differ in their acid strengths as can be concluded from the equilibrium constants ( $K = 14$  (17) for the majority site and  $K = 64$  (107) for the minority sites). The limiting values of coverage are  $2.32 \text{ mmol g}^{-1}$  ( $3.41 \text{ mmol g}^{-1}$ ) and  $1.24 \text{ mmol g}^{-1}$  ( $1.74 \text{ mmol g}^{-1}$ ) for the two species. The data in parentheses give the values for the extracted surface which indicate the sen-

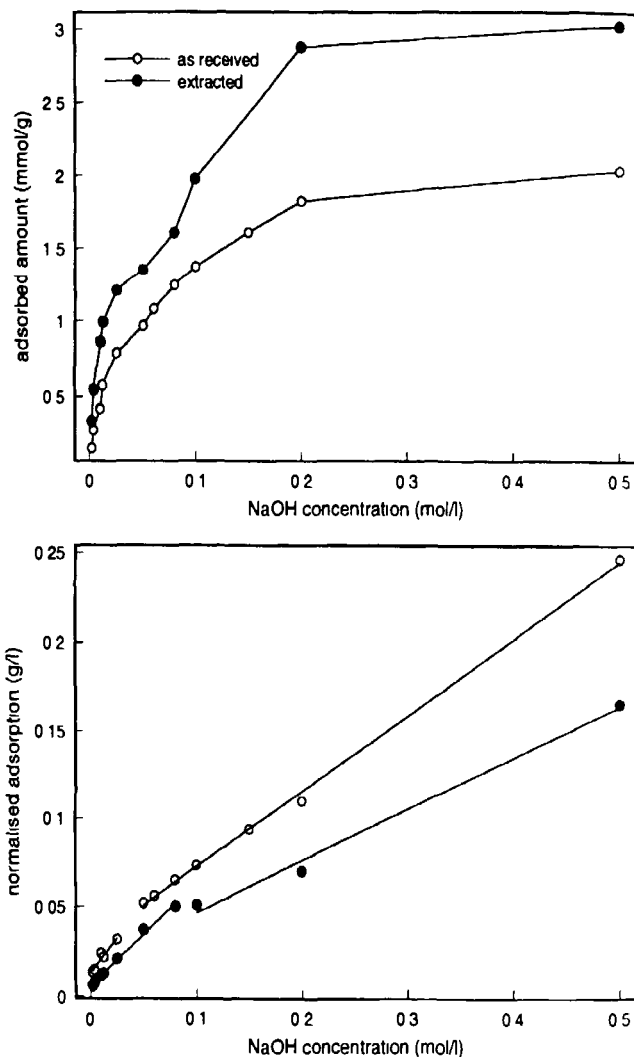


**Figure 24.** Neutralization isotherms (adsorption isotherm of  $\text{OH}^-$ ) for acidic surface groups on a carbon black. The lower plot represents the linearized isotherms according to a modified Langmuir adsorption model.

sitivity of the method and the drastic effect of the surface purification process. The purification also has a detectable effect on the acid strength of the sites, which may be explained by the operation of neighbor group effects (adsorbate–adsorbate interaction).

The suitability of this adsorption model to characterize quantitative aspects of surface acidic groups gives no indication, however, about the chemical structure of the reactive sites. Only in combination with the chemical probe reactions is it possible to assign the two types of acid sites to carboxylic acid and hydroxy groups, respectively. It is noted that such an approach can also be used to determine ion exchange capacities for metal ion loading required for the generation of dispersed metal–carbon catalyst systems.

For carbons with large amounts of surface groups per unit weight the method of direct titration can be

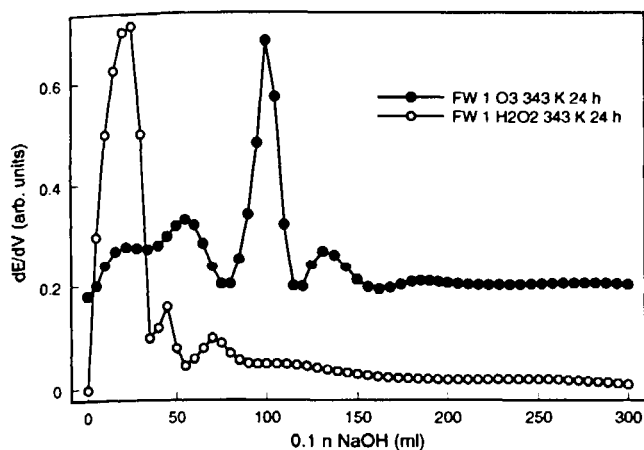


**Figure 25.** Direct titration of acidic groups on a carbon black. The curves represent the high-resolution first derivatives of the titration curves. The ordinate scales are identical for both experiments (offset).

used. In this method a suitable arrangement for potentiometric titration with slow neutralization, anaerobic conditions and good temperature stability of the experiment, is used to measure directly the titration curve of the solid acid. The first derivative shows the equivalence points of all stages of dissociation. The carbon is considered in this picture as an oligoprotic acid with a series of dissociation equilibria [33, 159]. Figure 25 illustrates the type of information obtained from such a direct titration experiment with a carbon black sample (FW-1) which was oxidized at low temperature in liquid phase to obtain acidic functional groups. Large differences in the abundance (proportional to the peak positions on the abscissa) and in the dissociation constant (peak profile representing the shape of the discontinuity at the equivalence point relative to the strong base 0.1 n NaOH) can be seen for the two oxidizing agents applied under identical conditions to the same carbon material. It is obvious that ozone treatment resulted in the formation of a large amount of very strongly acidic surface functional groups, as seen from the sharp peak in the derivative plot. Three to four other types of functional groups may be identified with widely varying abundance. Care must be taken in analyzing the derivative profiles, because for weaker acidic systems the effect of incomplete dissociation and the formation of a buffering system which all broaden the derivative peaks must be taken into account.

The direct titration of the parent carbon black which also carries significant amounts of functional groups is not possible. From this, it can be seen that the two alternative chemisorption techniques both have their relevance in carbon chemistry.

Another physical method which became popular in functional group analysis is photoelectron spectroscopy with X-ray excitation. The XPS or ESCA method is

**Table 6.** Selected carbon 1s chemical shift data for carbon-oxygen groups; common reference is C 1s = 284.6 eV for graphite.

Binding energy (eV)	Assignment	Surface	Reference
285.6	C-O-C	polyvinyl alcohol	234
286.5	C-O-H	polyvinyl alcohol	234
287.8	C=O	polyvinyl alcohol	234
289.2	CO <sub>2</sub> H	polyvinyl alcohol	234
286.2	C-O-R	polyethylene oxidized	174
287.5	C=O	polyethylene oxidized	174
289.0	CO <sub>2</sub> H	polyethylene oxidized	174
286.1	C-O-H	carbon fiber oxidized	172
287.6	C=O	carbon fiber oxidized	172
289.1	CO <sub>2</sub> H	carbon fiber oxidized	172
290.6	carbonate	carbon fiber oxidized	172

used in this context as a fingerprinting tool using empirically derived tables for the chemical shift to analyze the data. Oxygen functional groups can be analyzed either by the oxygen O 1s emission or by the carbon C 1s emission. Due to the much larger shift sensitivity, the carbon 1s range is used in almost all applications. In addition, the presence of a film of molecular water which is not removed in UHV creates a large oxygen 1s signal at 533 eV which overrides many structures in the functional group oxygen spectrum.

The issue of assigning carbon 1s data to chemical structures has been developed extensively in carbon polymer science and is exhaustively reviewed there [160–162]. The principle of the assignment resides on the following assumptions. All sp<sup>2</sup> and sp<sup>3</sup> C-C and C-H bonds give rise to one C 1s signal at 285 eV with a tendency towards lower binding energies for pure graphite which was located for defect-poor samples at 284.6 eV [2, 90, 163]. All carbon heterobonds shift the C 1s signal to higher binding energy. This shift is the larger the more electronegative the heteroelement is relative to carbon. Further increments are brought about by carbon-heteroatom double bonds and by 1,1 substitution of the C-C or C-H bonds. Table 6 reports a critical compilation of literature data on carbon-oxygen-induced shifts for several carbon materials. The table confirms the general trend outlined above. Other tabulations in the literature [33] are physically inconsistent and contain erroneous data. These discrepancies arise from three different sources of inconsistencies:

- Calibration of the binding energy scale for different experiments (see below).
- Influence of the defect structure on the absolute position of the main line which is often used as internal standard for calibration of the binding energy scale [163].

- Disregard of the asymmetric lineprofile of the graphitic carbon 1s signal. This asymmetry contradicts a physically meaningful spectral deconvolution into a set of Gaussian peaks as mostly done in the literature. The resulting inconsistencies in the positions of contributions and the variable linewidths used in these deconvolution procedures arise from the varying contribution of the line asymmetry to the total spectral weight of the carbon 1s profile. The asymmetry is mainly caused by the coupling of the core hole state created during photoemission to the semimetallic valence band states of graphite and by the convolution of the primary photoemission with the phonon and plasmon loss spectra [164, 165].
- Disregard of charging effects. Highly functionalized carbons are often not sufficiently metallic conducting to allow the photocurrent to flow through the sample without creating integral potential drops which affect the position of the binding energy scale. In difficult cases the charging up is locally variable (for example with a thick uneven specimen) and prevents correction by recalibration with an internal standard (the C-H + C-C line or the water line).

These three groups of effects shift all or part of the photoemission intensity into the range of the carbon-oxygen chemical shifts and can thus affect the interpretation in an undetected way. The same problems arise when carbon-nitrogen groups are analysed. Nitrogen-oxygen groups (nitrate, nitrite, nitrosyl) are well discernible (403–406 eV binding energy) from nitrogen-hydrogen bonds (around 401–400.5 eV for amino groups) and from carbon-nitrogen bonds (400.0–397 eV). The individual chemical configuration within the groups is, however, difficult to resolve [135]. In a recent publication [166] on the reactivity of nitrogen species with oxidized activated carbons a consistent series of nitrogen chemical shifts falling within the ranges specified above is established. This list of compounds is chemically self-consistent as the modifications used for their generation are fully in line with conventional nitrogen organic chemistry.

The C 1s line is less affected by the less electronegative nitrogen heteroatom and exhibits a much smaller shift range than for oxygen groups. In a recent publication aiming at the XPS analysis of the novel diamond-like  $C_3N_4$  material [167] all these problems are well documented. The authors did not consider charging effects, nor did they account for oxidation of the sputtered surfaces during transfer. In addition, they used Gaussian line profiles and arrived at significantly high carbon 1s chemical shifts for two different C-N bonding geometries which they see as diamond-like (aliphatic) and polypyridine-like (heterocyclic aromatic).

In a very detailed study of the chemical shifts of carbon 1s lines on the nature of the C-C bonding interaction [168] it was found that using the well-determined C 1s value of  $284.6 \pm 0.3$  eV [169] hydrogenated carbons exhibiting a binding energy of  $285.3 \pm 0.05$  eV and carbidic carbon in SiC were found to occur at  $283.4 \pm 0.05$  eV. Diamond and graphite were found to be fully indistinguishable from their shift data, which is in full agreement with a different study using compact [2] rather than film [169] samples. The significant uncertainty which is quoted for the value of graphite C 1s photoemission was clarified in a study on the dependence of the carbon 1s line position on the crystalline quality (nature and abundance of surface defects) [163]. For hydrogenated amorphous carbon films a complex influence of the substrate on the binding energy and probably also on the detailed atomic structure was detected in a study of a-C-H films on various GaAs surfaces. A carbon-rich species with a binding energy of 284.8 eV on GaAs and of 284.6 eV on Si was found in the near interface region of sputtered thin carbon overlayers [170]. These data indicate that a clear speciation of the chemical structure of a carbon species in a catalytic system can be quite ambiguous and that – contrary to chemical intuition – the connectivity of a carbon cannot be inferred from its carbon XPS spectrum. The reason for this failure of the ESCA effect lies in the complex convolution of ground state electronic properties of the carbons (which are all different [2] as expected by intuition) with final state effects [164, 165] (relaxation of the core hole) which produce a diffuse but intense structure in each peak, accounting for their apparent similarity. This became apparent in studies aiming at a discrimination of the KVV Auger spectrum of carbon into s-derived and p-derived valence band states which should be suitable for discrimination of  $sp^3$  and  $sp^2$  carbon connectivities by the Auger lineshape [171].

In summary, care must be taken in interpreting the main component of the carbon 1s line as fingerprint for the carbon connectivity. In the high binding energy side additional problems arise from plasmon satellites which can occur at 5.6–7.2 eV in  $sp^2$  carbons and at 11.3–12.5 eV in  $sp^3$  carbon above the main line [169]. These broad and weak structures interfere with chemical shift identifications of highly oxidized C-O functional groups [163].

A practical situation is shown in Fig. 26. The carbon 1s data of HOPG as reference are compared to those of a chemically etched graphitized carbon black sample. The defective graphitized carbon surface exhibits a significantly wider main line at almost the same position as the well-ordered graphite (cleaved and annealed in UHV [90]). It can be seen that the neglect of the line asymmetry invariably causes the erroneous detection of additional lines in the range 1–2 eV above the peak

maximum. The difference spectrum is mainly caused by the broadened main line. Only after removing the asymmetric main contribution a small structure (top in Figure 26) can be isolated revealing peaks at 286.0, 287.3, 288.7 and 290.0 eV which can be attributed to surface oxygen functional groups. Only 4.3% of the total intensity is due to the surface groups, in good agreement with 5.5 at% oxygen content. The comparison of these numbers indicates [172] that most functional groups can only carry one oxygen atom per carbon atom and that carboxylic groups, with the largest shift, must be a small minority. The data agree fairly well with those from oxidized carbon fibers [172] and are in agreement with the values from Table 6. A maximum of three different oxygen functionalities can be resolved by XPS. These are the basic chemical structures mentioned in Fig. 21. The more complex cases which were shown to exist with carbon–oxygen single bonds (peak at 286.0 eV in Fig. 26) can also not be resolved by this method with any degree of chemical selectivity.

A significant increase in the chemical specificity of XPS can be achieved when the surface sensitivity of the surface analytical detection is combined with the chemical specificity of the probe reactions discussed above. A highly specific analysis of the chemically reactive surface functional groups can be obtained using heteroatoms such as barium from barium hydroxide, chlorine from HCl or  $\text{SOCl}_2$  [173], or nitrogen and sulfur tags from complex functional reagents [174, 175]. These data reveal that a large number of oxygen functions detected by integral elemental analysis are chemically inert and exhibit no acid–base activity. Such behavior is consistent with keto functions or with oxygen heterocyclic functions (C–O–C in Table 6). From all chemical shift data in the literature and the spectrum in Fig. 26 it appears that the heterocyclic function is the dominating functional group. This accounts for much of the analytical oxygen content without contributing to the low-temperature chemistry. From the sequence of events in carbon oxidation this group is the primary reaction product and has thus also from the mechanistic point of view a high probability of survival in any oxidation treatment as the most abundant reaction intermediate.

At this point a characterization technique with a higher chemical resolution is desirable because such functionalization plus surface analytical combination experiments are extremely difficult to perform in a clean and reproducible way. Vibrational spectroscopy such as FT-IR has been developed into such a tool, after several methodical improvements concerning sample preparation and detector sensitivity. In situ oxidation experiments are still very difficult as heated black carbon is a perfect IR emission source and interferes with any conventional detection in the spectral range of carbon–oxygen fingerprint vibrations.

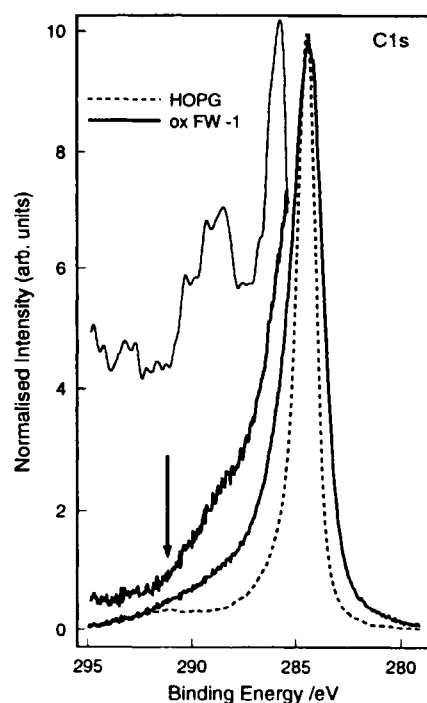


**Figure 26.** XPS data in the carbon 1s region for a UHV cleaved graphite reference (HOPG) and a carbon black sample used in the titration experiments of Fig. 25. The arrow marks the position of the graphite surface plasmon. The top section of the modified spectrum in the high-binding energy side reveals several weak peaks for oxygen functional groups after removal of the asymmetric line profile from the main peak.

A compilation of fingerprint vibrations for characteristic carbon–oxygen functions is found in Table 7. Data from a variety of organic molecules from spectra libraries are analyzed and grouped together. Only strong vibrations are tabulated and extreme positions are removed. The compilation shows that several regions of interest exist:

- The  $\text{OH}^-$  valence region which is due to combinations with molecular water is often difficult to resolve.
- The C=O region (1800–1650 wavenumbers).
- The region at 1650 wavenumbers, of C=C vibrations which are isolated from the graphene network (the graphene vibrations are only Raman active, see Table 2).
- The region of C–O single bond vibrations at 1300–1100 wavenumbers with a significant selectivity for different groups when combined with the simultaneously occurring C=O vibrations.

The practical observation of all these vibrations is difficult, as not all of the respective groups are present on a carbon with the same relative abundance. As the quality of the spectra is generally poor, weak charac-

**Table 7.** Characteristic group frequencies in IR absorption.

Functional group	Absorption frequency (cm <sup>-1</sup> )	Assignment
phenol groups		
O-H	3650-3590	valence
O-H	3500 b	valence polymer
C-OH	1220-1180	valence
C-OH	1350-1100	valence aliphatic
O-H	1390-1330	deformation
keto groups		
C=O	1745-1715	valence aliphatic
C=O	1700-1680	valence aromatic
C=O	1730-1705	valence $\alpha$ -diketo
quinones		
C-O, para	1690-1655	valence, two lines
C-O, ortho	1660	valence, one line
aldehyde groups		
C-H	2920-2880	valence, combined
C=O	1720-1715	valence, combined
carboxylic acids		
C=O (aliphatic)	1735-1700	valence
C=O (aromatic)	1700-1680	valence
C-O (anhydride)	1830, 1750	valence, two lines
O-H	3000-2700	valence
O-H	940-900	deformation
esters, lactones, ethers		
C=O	1730	valence, benzoic
C=O	1740	valence, lactones
C-O-C	1280-1100	valence, ester, lactones
C-O-C	1320-1250	valence, ethers

teristic peaks of a minority group may not be recognized. Strong peaks at 2355 cm<sup>-1</sup> and at about 2045 cm<sup>-1</sup> arise from chemisorbed CO<sub>2</sub> and carbon monoxide during in situ studies [176-178]. The diagnostic value of the data in Table 7 is enhanced by the search for combined absorptions for the more complex functions. Such combinations allow the resolution of the crowded spectral range between 1800 and 1700 cm<sup>-1</sup>. Two oxidized carbon samples are discussed as being representative for the many possible applications of Table 6. The discussion of characteristic IR

data on fullerenes and their oxidation products can be found in the literature [105, 106, 108, 111].

Table 8 lists the main absorption frequencies for the two samples. One is a disc of glassy carbon formed under electrochemical oxidation, the other is a powder sample of a high surface area carbon black (FW-1, 235 m<sup>2</sup> g<sup>-1</sup>). The in-situ electrochemical oxidation study [176] allows the tracing of several coexisting species by their respective fingerprints. It can be seen that several groups which remain undetected by chemical adsorption and XPS analysis can be found with the IR technique. No carbon-oxygen single bonds were found in this study. The oxidation potential may have been too high for the accumulation of a significant abundance of these still oxidizable groups. A technical reason may well be the poor spectral quality below 1600 cm<sup>-1</sup>, precluding the detection of any specific absorption besides the extremely strong background. The broad water hydroxy peak from the in situ reaction environment also does not allow the detection of hydrogen groups. For these reasons, not all species are identified. This is required, however, to derive a plausible oxidation mechanism suggested in this paper.

The oxidation reaction by dry ozone at 335 K leads to the formation of a large number of strongly acidic surface groups [179]. A whole spectrum of chemical changes occurs with the treatment leading finally to a breakdown of the carbon into soluble graphene fragments. The ozone reaction is also used to study the oxidation mechanism and its control by micromorphological effects of "hole burning" [180]. Finally, the ozone oxidation is also of influence in atmospheric chemistry, where it modifies carbon black particles which become efficient catalysts for the oxidation of SO<sub>2</sub> under ambient conditions [181].

The data from Table 8 and the spectra in Fig. 27 indicate that a wide variety of functional groups with single and double oxygen-carbon bonds are formed after mild ozonization at 335 K in aqueous medium. The agreement between the assignments of the absorptions in both samples is quite remarkable and agrees

**Table 8.** Observed IR absorption bands for oxidized carbons.

oxidized glassy carbon		oxidized carbon black	
Absorption frequency (cm <sup>-1</sup> )	Assignment	Absorption frequency (cm <sup>-1</sup> )	Assignment
2045	adsorbed CO	3425	C-OH
1780	lactones	2924	C-H aliphatic
1722	carboxylic acids	2355	CO <sub>2</sub> gas phase
1696	aromatic ketones	1760 sh	lactones
1678	quinones	1729	carboxylic acids
1611	isolated C-C bonds	1620	isolated C=C bonds
		1438	O-H deformation
		1399	C-O lactones
		1230 sh	C-O aromatic ether
		1210	C-O phenol



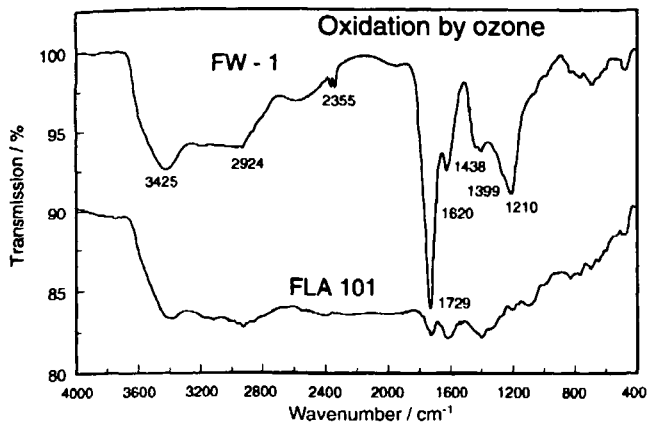


Figure 27. FT-IR data of heavily oxidized carbon blacks. The FLA sample is much more graphitic in the stacking order of the BSU and exhibits only 10% of the geometric surface area of the standard FW-1 sample.

also with the reference data in Table 7. The influence of neighborhood effects on vibrational data and the uncertainty of locating the position of absorptions in broad, overlapping and diffuse bands account for the minor discrepancies in the numerical values of the peak positions. The regions of characteristic absorptions mentioned above can be identified in the top spectrum of Fig. 27. A distribution of absorption band positions for each chemical structure causes the broad envelopes and indicates the structural heterogeneity of the oxidized carbon surface. The sharp double peak of gaseous  $\text{CO}_2$  arises from the large micropore volume of the sample which stores detectable amounts of  $\text{CO}_2$  in relation to the natural abundance of this gas in the ambient air.

The nature of the functional groups seems not to depend on the structure of the carbon substrate, as even on oxidized fullerenes the same bands can be found by IR spectroscopy [108]. The relative abundance is, however, significantly different as can be seen from the comparison of the two carbon black samples used for the data of Fig. 27. The FLA 101 sample is more graphitic with a significantly reduced surface area. The abundance of carbon-oxygen single bonds is greatly reduced with the predominant species being carboxylates after the same treatment which produced the broad variety of functional groups on FW-1. This is full agreement with the published mechanistic picture [180], which correlates velocity and depth of oxidation with microstructure and porosity of the carbon substrate.

Vibrational spectroscopy is a very versatile and, chemically, well-resolved technique for the characterization of carbon-oxygen functional groups. The immense absorption problems of earlier experiments seems to be overcome in present times with modern FT-IR, DRIFTS or photoacoustic detection instruments.

The physical technique of desorption spectroscopy of oxygen functional groups is much more frequently used. The conceptually simple experiment using a carrier gas and a nondispersive infrared detector for CO and  $\text{CO}_2$  is not in line with the theoretical complexity of the experiment. One group of complications is of a technical nature and refers to carrier gas purity, mass transport limitations, temperature gradients, nonlinear heating ramps and temperature measurement problems. More severe is the problem that the method is destructive in two ways. First, it removes the functional groups and has to break all adsorbate-substrate bonds in a distribution of local geometries. Second, it is a high-temperature process which activates functional groups to change their structure during the experiment and to interconvert between them. This is particularly complicated in situations with carbon-oxygen single and double bonds located adjacently (see for example lactone decomposition exemplified in reaction 24).

Despite these principal ambiguities the thermal desorption method is a standard characterization technique in carbon surface chemistry. Various examples and data about desorption profiles for a selection of carbon treatments can be found in the literature [88, 90, 155, 182, 183].

The general features of all these data can be discussed using the experiments shown in Fig. 28. A highly reactive carbon with complex amorphous structure was treated with ozone at 335 K in water and the dried product subjected to a temperature-programmed decomposition in flowing nitrogen using a special mass spectrometer (IMR-MS) as detector. This instrument [184] allows the suppression of the nitrogen signal and fully removes any fragmentation of  $\text{CO}_2$  into CO. This is a problem which is significant in conventional mass spectrometers, allowing only crude estimates of changing ratios of CO to  $\text{CO}_2$ . The acid groups (1), (3) and (4) in Fig. 21 result in  $\text{CO}_2$  as decomposition products, whereas all other surface groups produce mainly CO during their pyrolysis under non-oxidizing conditions. The more strongly oxidized  $\alpha$ -carbon atoms in acidic groups desorb from the graphene surface at lower temperatures than the CO from the basic groups. This behavior can be recognized in the IMR-MS traces of Fig. 28. The  $\text{CO}_2$  trace shows structures in three broad features with the first peak exhibiting some internal structure which is ascribed to the decomposition of free carboxylic acid groups and structures with other functions next to the acidic group (reaction 24). The poor resolution of the main features indicates significant kinetic effects at a heating rate of  $0.5 \text{ K s}^{-1}$  which

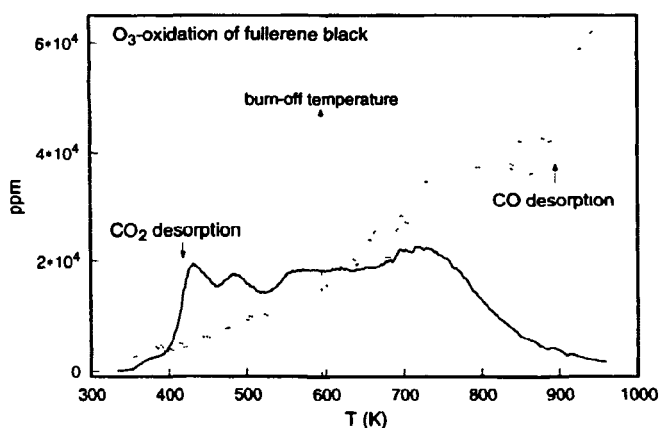


**Figure 28.** Thermal desorption (heating in flowing nitrogen, heating rate  $3 \text{ K s}^{-1}$ ) of  $\text{CO}_2$  and carbon monoxide from heavily oxidized fullerene black (treated in 10% ozone, oxygen at 333 K in water). An IMR-MS detector was used for unperturbed gas analysis and simultaneous detection of other desorption products (see text and Fig. 29). The value for the burn-off temperature is defined as the temperature where a weight loss of 3% had occurred.

points to a distribution of binding energies rather than to one specific desorption event. The occurrence of postdesorption reactions of the  $\text{CO}_2$  acting as oxidant for other functional groups has to be taken into account at temperatures above 650 K [112]. This finds its expression in the crossing-over of the (sensitivity-corrected) desorption traces around 650 K. The increased stability of the basic and neutral functional groups is seen in the high-temperature rise of the CO trace which peaks only above 1000 K. At these temperatures the structural rearrangement of the graphene layers in amorphous carbon becomes an important process, which prevents the observation of the complete desorption of all oxygen functional groups without changing the bulk structure of the substrate. Structural changes in the substrate give rise to the noisy appearance of the CO trace, which indicates eruptions of gas due to the beginning hole-burning process initiated by local concentration maxima of surface oxygen species which terminate quickly due to the lack of oxidant.

The desorption of oxygen functional groups is not correlated with the steady state burn-off of the material in molecular oxygen which begins at temperatures significantly above the desorption of predominantly highly oxidised functional groups.

The relative contributions of the different desorption processes changes with the average surface structure. Comparison of the data in Fig. 28 with those of an analogous oxidation experiment with a different carbon substrate (carbon black FW-1) shown in Fig. 29 reveals that the carbon black contains significantly more basic functional groups than the amorphous fullerene black. This can be traced back to a reduced

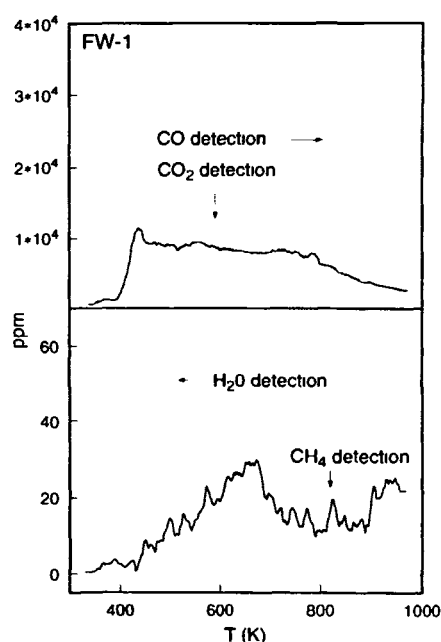


**Figure 29.** Thermal analysis of a carbon black under the same conditions as used for the experiment in Fig. 28. Note the different scales of the ordinates.

number of carbon atoms which could be highly oxidized (removed from the aromatic backbone of a graphene BSU) by ozone in the two materials. The presence of five-membered rings in the fullerene black and the organization into stacks of planar graphene units in the carbon blacks are consistent structural explanations. In the carbon black sample, the separation into regimes of stability for acidic and basic functional groups is much less resolved. This indicates a larger structural diversity of the functional groups in the carbon black relative to the pronounced maximum of acidic groups in the fullerene black.

The lower traces in Fig. 29 reveal that other desorption processes occur with the decomposition of oxygen functional groups. The polar oxygen groups bind a layer of water molecules which desorbs above 415 K, after the removal of water multilayers slightly above ambient temperature. The desorption of  $\text{CO}_2$  from acidic groups leaves behind a C-H function. If this function is in an alkenic or aliphatic environment, i.e. in a surface without a closed carbon hexagon termination, then desorption of methane can contribute to a stabilization of the surface by removal of the non-aromatic structures. The missing hydrogen atoms are taken from reactions of water with these defective carbon centres. The respectively small methane signal is displayed in Fig. 29. No higher hydrocarbons are detectable in this experiment. A desorption of molecular hydrogen at temperatures above 900 K from the terminating hydrogen atoms with aromatic carbon structure has been observed [33].

Thermal desorption data can be integrated and may be used to quantify the total number of oxygen functional groups on a carbon surface. When these data are compared with the sum of all chemically detected functional groups a significant excess of the desorption value over the chemical value is found. This excess is confirmation for the existence of chemically neutral oxygen functions which are, in part, strongly bound to the substrate (keto functions, see Fig. 22). These groups act as side blockers in surface reactions and are known in the carbon oxidation literature [86] as "stable complexes" which inhibit the oxidation.

The data in Figs 28 and 29 reveal that it is not possible to fully detect the oxygen desorption without reaching temperatures at which structural changes occur in the substrates. This is a significant problem for hydrocarbon-rich carbons in catalytic deposits. The application of thermal characterization methods has to be regarded with significant reservation, as severe carbonization and dehydrogenation will go along with the "analytical" desorption events. In subsequent adsorption or reaction experiments the presence of a stable graphitic carbon as second phase is stated. The second phase is, in fact, an artefact of the preceding thermal treatment. This feature, which also complicates surface science experiments with oxygen on carbons, has been investigated [88, 90].

### 2.1.9.16 Carbon as Catalyst Support

The application of carbons in catalysis is mainly as support for active phases in various reactions. Besides a wide variety of noble metal-carbon systems for hydrogenation reactions and fuel cell applications, the large-scale application in the synthesis of vinyl acetate and vinyl chloride are important technical applications [185]. An important application of carbon-supported oxides of silver and copper-chromium, known as whetlerite, is as the active mass in filters for gas masks. The complex chemistry occurring upon oxidation of hazardous gases requires the presence of the carbon surface besides the oxide particles, which is interpreted [186] as indication for a synergistic effect between carbon and oxides for chemisorption of the hazardous gases and simultaneous selective oxidation by activated oxygen. The special field of carbon gasification catalysis is not covered here as in this reaction the carbon is not only the support but also the substrate. The rare case of a desired consumption of the catalyst support creates a special situation [185, 187, 188]. The application of carbon-supported catalysts in synthetic organic chemistry has been reviewed [189].

In all synthetic catalytic applications, carbon is considered as a support with little reactivity towards sen-

sitive molecules with reactive functional groups which would be activated by either Bronsted or Lewis acidity of an oxidic substrate. This so-called weak metal-support interaction was questioned in a comparative study on metal-support interactions for platinum particles [190]. Unfortunately, the preparation conditions were chosen such that gasification of the support had occurred. For a detailed discussion see below. The extremely valuable advantage of an inert substrate consequently has the disadvantage that the active phase is difficult to anchor on the surface. It is hence difficult to create and maintain any useful dispersion of the active phase on carbon. An elegant way around this problem has been suggested [191]. A conventional oxide-supported catalyst may be, after its synthesis, covered with a deliberate carbon contamination layer on the support oxide to shield the free support surface by a carbonaceous deposit. Chemical vapor deposition of carbon from propene on alumina carrying a technical HDS system as active phase was used as demonstrator.

Two more classical ways to anchor the active phase [36] to the substrate are the fixation on oxygen functional groups or on surface defects such as steps in a basal plane of a graphitic structure. In a recent study [192] of the anchoring of the active phase on graphite, the hydrolysis of a platinum complex followed by an *in situ* reduction at low temperature allowed the grafting of platelets of platinum metal with a highly preferred (111) orientation and with high dispersion on a graphite substrate. It is not yet demonstrated that this attractive arrangement survives catalytic action under useful conditions for useful times. The system was, however, used to study the microstructure of the dispersed platinum. Figure 30 shows an STM image of a raft of platinum (area 1) on graphite (001) (area 2). It can be seen from the atomic resolution insets that both surfaces exhibit the same symmetry, indicating the (111) orientation of the platinum. The distinction between carbon and platinum was made possible by the differing lattice constants. The noise in the graphite image next to the platinum raft is attributed to a contamination of the STM tip which was collected from the metal. The thickness of the platinum raft is several metal monolayers, making any accurate analysis difficult due to the imaging artefacts. The genesis of this catalytically highly desirable structure is assumed to start from a molecular anchoring of the precursor at atomic defect sites. These act as nucleation centers for the metal platelets resulting from low-temperature chemical reduction and subsequent coagulation of initially formed metal clusters with no stable anchoring at the basal plane.

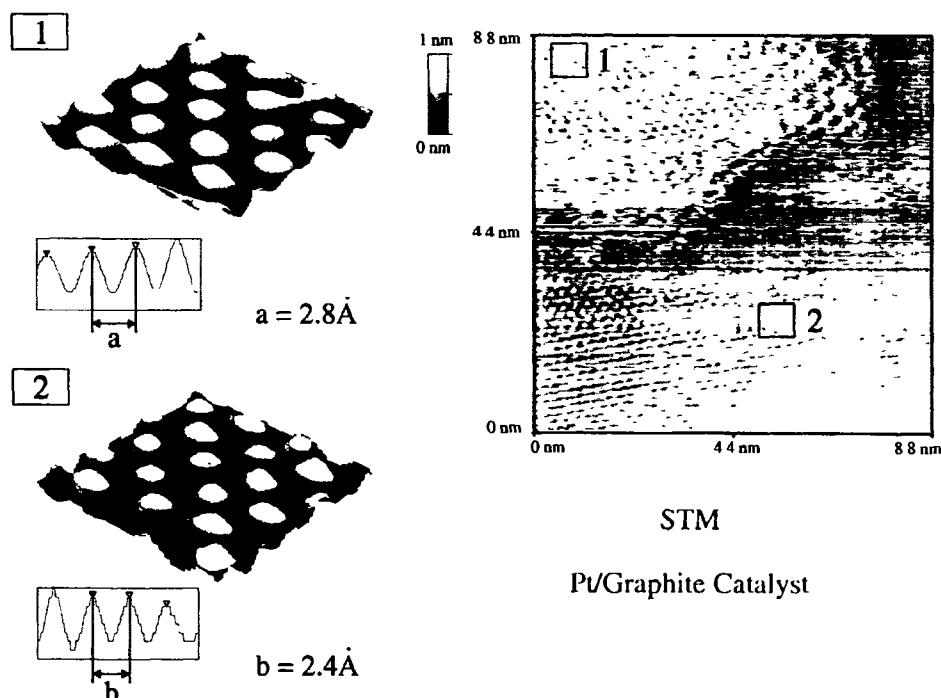


**Figure 30.** STM image of a platinum raft on a graphite powder particle. An organometallic route was used to deposit the metal at low temperatures. The discrimination of metal and graphite with the same lattice geometry is possible by the different lattice parameters

The more conventional strategy contains several steps of modification and activation [36, 189]:

- Use of a high surface area graphite with little pore structure in which the active component can be occluded.
- Creation of a maximum amount of acidic surface functional groups with cation exchange capacity.
- Cation exchange of protons by metal ions or hydrolysis of metal complexes by the surface acid groups.
- Chemical reduction of the metal at low temperatures.

This final activation step is often the difficult reaction step as the reduction of the active component should not reduce the anchoring sites at the carbon. This reduction can occur either chemically by hydrogen atom spill-over or thermally by decarboxylation of the anchoring group. Figure 29 reveals that this decarboxylation can occur at such low temperatures that the stability limit can easily be exceeded by a thermal reduction, with hydrogen for example. The section on surface groups reveals that it is not possible to use stable functional surface groups for anchoring as these groups are chemically inactive and all active groups are thermally unstable.

The inherent problem of limited thermal and chemical stability of metal anchoring sites on carbon limits not only the activation temperature but also the application conditions [185]. In oxidizing environments carbon supports are much less stable than the macroscopic burn-off temperature (see Figs 28 and 17). In order to

maintain the dispersion of the active phase, the limiting temperature should be less than the decarboxylation temperature of the anchoring groups. This temperature is equal to the initial  $\text{CO}_2$  evolution which sets a margin of stability of the initial dispersion to about 450–500 K. In hydrogenation applications the limiting temperature can be even lower as the active catalyst can produce a stream of active hydrogen which reacts with oxidized anchoring groups under hydrogenolysis/hydrogenation even below 500 K. As, however, most hydrogenation reactions are carried out at temperatures below 373 K to maintain high selectivities, the carbon-metal systems are usually not limited by thermal degradation in the case of hydrogenation reactions.

The reactivity of carbon surfaces without functional groups is low with respect to most elements [193]. Important exceptions are molecular oxygen dihalogens [185] and alkali metals. The redox-amphoteric behavior of  $\text{sp}^2$  carbon, which is the basis for the intercalation chemistry [140], allows for a significant charge transfer between adsorbed alkali (or halogen) atoms and even carbon on the graphite (001) surface. Thermodynamic properties of these adsorbates [194] predict that such adlayers with submonolayer coverage should be stable at high temperatures against desorption and should withstand even hydrolysis in liquid water. This is of significant relevance in applications where alkali is needed as catalyst promoter and the carbon substrate serves as reservoir for its storage [195].

Recent experiments [196] with high surface area carbons and iron particles strongly reduced in flowing hy-

drogen at 1173 K reveal an intimate contact between iron and carbon. It is further shown that an analogous charge transfer between iron and graphite as between alkali and graphite is operative when the iron particles are flat platelets with a high interface area.

These observations mark a transition from the anchoring strategy to the geometric fixation strategy for fixation of active components on carbon. This strategy relies on the assumption that chemically stable edge sites on carbon act as geometric barriers for the diffusion of catalyst particles at high temperatures where molecular anchors are already unstable. A possible additional chemical anchoring via metal carbon bonds to the dangling bonds of the terminating graphene layer reduces a possible lateral diffusion along the step edge. The best fixation is achieved when the catalyst particle digs a small hole in its fixating geometry where it uniquely fits. Such a selective etching may be achieved by the high temperature reductive treatment mentioned in literature reports about metal carbon catalyst systems [190, 195, 196].

The intuitive assumption that carbon surfaces with a high surface fraction of prismatic faces (110, 100 and higher indexed orientations of graphite) would be suitable to create metal-carbon (carbide) bonds is not supported by experimental evidence. These prismatic faces are chemically too reactive and undergo facile gasification in oxygen or hydrogen. This leads to a geometrically unstable situation for metal particles, which, at reaction conditions, frequently lose their specific adsorption site and become mobile with the chance for agglomeration and deactivation. Successful high-temperature carbon catalysts are always prepared from materials with a smooth and preferentially graphitic surface. Here, the average reactivity of the support is minimized while still providing sufficient structural defects to create mechanical anchoring sites for active metal particles. This has been rationalized by experiments with platinum particles on carbon and by an analysis of the dispersion versus carbon pretreatment [197, 198]. The two studies were carried out with different carbons and using different reaction conditions. Both concluded that the increase in smooth surface area (not in porosity) is an important factor for stabilizing small metal particles. An additional factor of increased surface heterogeneity is given, with different relative importance in both studies. In the present context, this influence is traced back to increasing surface defects allowing direct anchoring. For high temperature preparations (at 723 K) the marked increase in platinum stabilization [198] is traced back to the selective etch process.

The principle of mechanical fixation at step edges is illustrated in Fig. 31 which shows Ru particles on a graphite surface. The single crystalline flake is preferentially (001) oriented but exhibits a system of step structures as revealed by the Moiré fringes (weak line

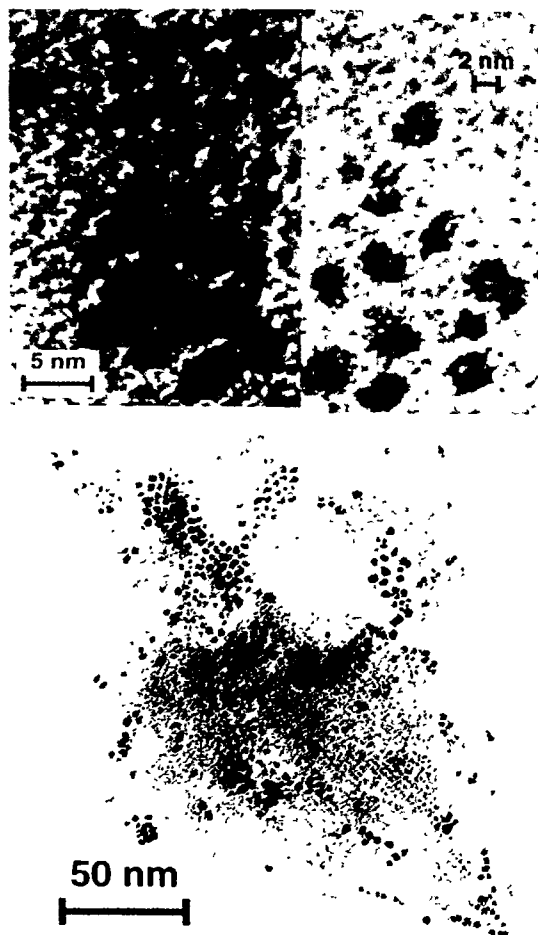


**Figure 31.** Ru metal particles on a flake of natural graphite (TEM, 100 keV)  $\text{Ru}_3\text{CO}_2$  was impregnated from toluene and calcined in an inert atmosphere at 375 K. EDX and the beam stability confirmed the metallic character of these particles. Note the regular arrangement at step edges occurring from crystallite edges causing the Moiré contrast in the main image

contrast in the main image). The metal particles of a few nm size are platelets which are occasionally stacked above each other (top left plate in Fig. 31). In the main image it can be seen how an almost regular array of particles is formed at step edges of the surface. This geometric arrangement is stable in hydrogen up to 725 K where the particles become efficient methanation catalysts for their substrate. Such geometric arrangements have led to speculations that intercalation compounds between metal and graphite may constitute an active catalyst with the particles seen in Fig. 31 being mechanically bound between adjacent graphene layers. The existence of such geometries is shown by TEM [199]. The investigation of other samples discounts the existence of a fixation by intercalation [200]. The activity of the materials is traced back to particles sitting only at external step edges.

The concept of mechanical fixation of metal on carbon makes catalytic applications at high temperatures possible. These applications require medium-sized active particles because particles below 2 nm in size are not sufficiently stabilised by mechanical fixation and do not survive the high temperature treatment required by the selective etching. Typical reactions which have been studied in detail are ammonia synthesis [195, 201–203] and CO hydrogenation [204–207]. The idea that the inert carbon support could remove all problems associated with the reactivity of products with acid sites on oxides was tested, with the hope that a thermally well-conducting catalyst lacking strong–metal support interactions, as on oxide supports, would result.

The picture which emerges from the studies of CO hydrogenation is that in addition to this “clean” case of large and active particles, a second class of small particles occurs on less graphitic surfaces. These particles exhibit different activity and more importantly a much more desirable product spectrum with a high alkene to paraffin ratio. These iron particles are superparamagnetic and may be partially oxidized [208]. The electron deficiency which is stated in all studies for the small particles is controversially discussed as pictures of different phases or a specific charge transfer with the carbon substrate.

This raises the question about the metal–support interaction in carbons. The term “wetting” has been used for the carbon–metal interaction [196, 206]. The usual geometry of spherical metal particles, as well as chemical arguments, render the formation of chemical bonds between each metal atom and the carbon substrate less likely. The case of alkali metals is an exception, but only in the limiting case of submonolayer coverages. The images in Figs 30 and 31 support the notion of metal rafts floating on carbon rather than resting as stable compounds. Such wetting interactions should be very stable and are in strong contradiction to the observed chemistry of metal–carbon catalysts. The raft structures occur only in cases of mild preparative conditions which allow the agglomeration of primary metal clusters in a predominant two-dimensional fashion. The existence of metal particles with supposed strong interaction [190, 196] is described as always being associated with very severe chemical activation conditions. It is suggested that under these conditions a combination of selective etching with a redeposition of carbon in the interface region between support structure and metal particle occurs in the same way as described above for the carbon filament synthesis. Under these conditions a reactive non-graphitic carbon binder material cements the active particle into the substrate and thus allows for a strong metal–carbon interaction with covalent bonds between the metal and the support mediated by the binder carbon. No microstructural data are available in the literature to support this hypothesis which would explain a large body of

	Fixation	Dispersion	Stability
mild	chemical	++	--
	mechanical	+	-
	etch	-	++
severe	chemical + etch	--	++

activation conditions

**Figure 32.** Schematic representation of the modes of fixation of metal particles on graphitic surfaces. A stack of graphene layers with a step edge is shown with a metal particle (granite pattern) and surface anchoring groups (black). Nongraphitic carbon deposits are shown in dark grey with fading contrast (bottom sketch).

partly conflicting results about location and stability of metal–carbon catalysts.

The whole range of carbon interactions with active phases is summarized in Fig. 32. In all cases no strong chemical interaction is assumed between the graphene (001) layers and the metal platelet. The weakest interaction with, however, the highest possible dispersion is obtained with surface anchoring via functional groups. Better stability at low loading with smaller dispersion can be obtained by mechanical fixation. This process requires a flat geometry and thus selective removal of all surface impurities which frequently cover basal planes of graphitic carbons. An example of the application of platinum particles on carbon in selective NO reduction was made [209]. It was concluded from kinetic arguments that the platinum behaves identically to model single crystals with preferred (110) orientation. This can be seen as an indication for the weak metal–support interaction and for the usefulness of non highly dispersed metal–supported systems in selective reactions.

Significantly higher stability is obtained when larger agglomerates are brought into shallow holes (monolayer etch pits) of the basal planes. The generation of such pits can be achieved by reductive gasification under catalytic influence. An alternative to the in situ generation is the strategy of using microporous carbons which involves depositing metal particles at the pore mouths. The usually broad distribution of pore sizes in carbons prevents, however, the complete use of all the metal loaded, as some particles disappear into deeper parts of larger pores and fail to be active in catalysis due to diffusional limitations. Redeposition of carbon from hydrocarbon sources (from either catalytic reactions or the ongoing reductive etching) at the

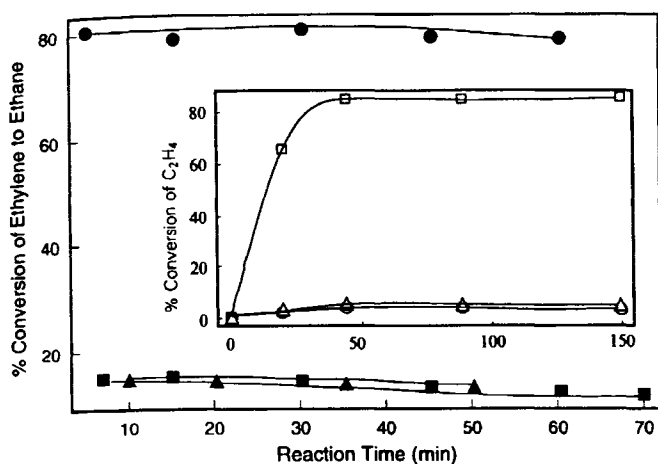


**Figure 33.** Catalytic activity of Fe–Cu bimetallic particles supported on alumina (squares), activated carbon (triangles) and carbon nanofibers (dots). The inset shows the activity of the metal particles on nanofibers in the decomposition of ethylene into solid carbon (squares), ethane (triangles) and methane (dots).

boundary between the metal particle and the carbon substrate occurs. This carbon may not be graphitic but can be of a more reactive connectivity (a-C–H for example) and thus provide chemical bonding between carbon and active particle.

The chemical fixation of metal particles onto carbon via covalent interaction is possible not only via reactive carbon entities as in the latter case but also directly on to a  $sp^2$  surface. This occurs, provided that the electronic structure is locally perturbed transforming the carbon from aromatic into a (poly)alkenic structure. Such a transformation can be achieved by either introducing controlled defect sites or by synthesizing carbons with structurally localized double bonds. Fullerene carbon is an example of the latter case. Oxidized nanotubes or catalytically synthesized carbon nanofibers are examples of the first case. The carbon nanofiber approach has been tested in several reactions [210] and the origin of the different chemical reactivities of the same active metal on planar carbon and on nanofibers was investigated in detail. Figure 33 reveals that the bimetallic iron–copper particles exhibit similar catalytic activities in ethylene hydrogenation on alumina and activated carbon but a considerably higher activity on nanotubes. The inset shows that these bimetallic particles are quite resistant against deactivation by carbon deposition when ethylene is decomposed to carbon filaments and methane plus ethane. The reference catalysts are fully deactivated by the time the nanofiber catalyst has reached a steady state. The most plausible explanation of a different particle size distribution of the bimetallic particles was investigated by TEM. Figure 34 shows the result. It occurs that the widest size distribution by far, with a maximum for the largest particles observed, is found for the most active nanofiber catalyst. The narrowest size distribution with

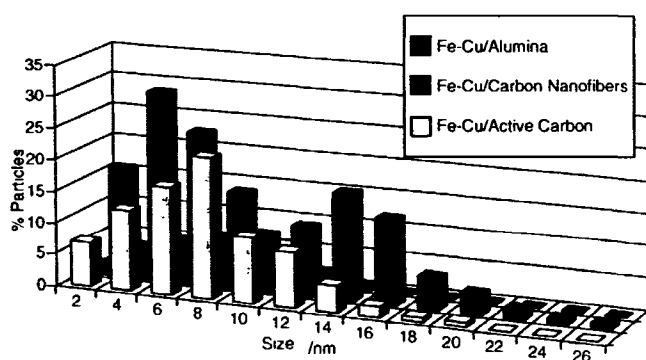


**Figure 34.** Particle size distributions derived from electron microscopy of the catalysts used for the experiments shown in Fig. 33.

the highest dispersion is achieved on the alumina support, whereas the metal-on-activated carbon catalyst still exhibits a wide distribution of intermediate sized particles. The authors claim the structure shown in Fig. 30 to be responsible for the effects. An epitactic relationship between graphite (001) and the metal close-packed structure is anticipated. The geometric data from Fig. 30 render a strong stabilization of an epitactic relationship surviving the activation step in hydrogen at 673 K less likely. The bonding of a broad spectrum of particles on defects situated or created by reductive etching on the graphene terminations of the discontinuous nanofibers (made by catalytic synthesis and not via the fullerene way) as shown in Fig. 4 seems considerably more plausible.

This example shows that a nonoxidic support can give rise to interesting properties in active particles. The catalytic performance is not simply correlated to size distributions. The experiments presented in this section reveal how few indisputable facts are yet known concerning the metal–support interaction for carbon substrates. Interactions of the type (metal d-states)–(carbon  $sp^3$ )–(carbon  $sp^2$ ) mediated via amorphous accommodation particles (Fig. 32) of intermediate layers should be considered in the prevailing picture of a yet unproved epitaxy between transition metals and graphite (001) surfaces.

### 2.1.9.17 Carbon as Catalyst

Carbon may also be used as a catalyst without an active component supported on it. This function may overlap with the widespread application of high surface area carbons and sorbents for selective chemisorption processes which are not considered here. The application of carbon as a catalyst in its own right has been reviewed [211–213]. All applications are based on the

simultaneous action of two functions. The first one is the selective chemisorption of an educt at the carbon through either ion exchange via oxygen functions or directly through dispersive forces involving the graphite valence electronic system. The other function is the production of atomic oxygen (or free organic radicals in dehalogenation reactions [211]) occurring on the graphene basal faces of every  $sp^2$  carbon material. Due to its central function in carbon chemistry this process is discussed in detail below. The conjecture that both processes play an important role in catalysis and that, in particular, surface patches with an intact graphene electronic structure act as sinks and sources of electrons in catalytic reaction steps, can be inferred from several observations [34, 135, 211]. The importance of the graphene layers in reactivity is still discussed rather controversially in the literature. The inertness of the basal planes in oxidation frequently dominates the chemical intuition about the stability of an "aromatic" surface.

The fact that carbon is already catalytically active at ambient conditions and in aqueous media has led to considerable efforts in applying carbon as a catalyst in the condensed phase [213]. In many of these applications the surface reactivity is given by the ion exchange capacity of the oxygen functional groups binding active ions (instead of particles) and by the simultaneous presence of delocalized electrons acting as redox equivalents. The widespread use of glassy carbon as an electrochemical surface is a special case of the use of this bifunctional property of carbon under mild chemical conditions. The irreversible oxidation under these conditions, and thus the decarboxylation-desorption of surface functional groups, limits drastically the application of carbon catalysts in gas phase reactions. The reactions are, in this case, very slow [214] and allow the extensive use of these functionalities and their broad chemical variation in catalytic applications.

### 2.1.9.18 Case Studies of Catalytic Applications

The catalytic oxidation of sulphurous acid in aqueous medium to sulphuric acid [138, 84] has been suggested as a probe reaction for the ability of a carbon to activate molecular oxygen at ambient conditions. Besides this remarkable property the reaction is of interest in atmospheric chemistry where it provides a sink for all nonphotochemically oxidized sulfur dioxide [215]. Carbon plays a special role in this environmental application as both pure carbon and active particles (iron oxide [84] for example) anchored to carbon can act as efficient catalysts. The detailed analysis of the reactivity of various types of carbon [138] reveal that basic surface oxides (see Fig. 23) are important to fix the educt  $HSO_3^-$  ion. It was found, in addition, that the

activation of molecular oxygen is of kinetic relevance. A variety of surface treatments which did not modify the surface basicity have drastic effects on the reaction kinetics and affect the oxygen activation. The degree of graphitic surface area, the content of nitrogen dopants and the overall electronic structure in terms of the surface perfection are found to be influencing factors. It is suggested [138] that doping of the conduction band of the carbon with free electrons from nitrogen atoms [211] is an important factor.

The selective oxidation of hydrogen disulfide to sulfur with oxygen in the gas phase at around 400 K is an important side reaction in hydrogen disulfide absorbers used for natural gas treatments. The activated carbons tolerate a high load of elemental sulfur but are eventually deactivated by a full coverage of the activated surface with sulfur. This can be removed by high-temperature steaming. Discussions about this reaction are quite controversial regarding the reaction kinetics [7, 216]. Different carbons with differing pretreatments and different testing conditions were applied. All papers agree on the relevance of the activation details of the carbon for the performance of the catalysts. The variation of the reaction orders between 0 and 1 for each educt makes it difficult to discuss a mode of action for the catalyst. Observations from other reactions make the model presented in a review [216] highly plausible. It is assumed that carbon produces atomic oxygen which oxidises  $HS^-$  anions present in the aqueous film residing on the polar carbon surface under reaction conditions. The promoters iodine and ferrous ions act to support the chemisorption of  $HS^-$ . A compensation effect is claimed with a perfect linear relationship between activation energy and preexponential factor. All these details point to a significant impact of kinetic limitations which are not given by the sequence of elementary reactions.

The reaction between phosgene and formaldehyde does not occur as a homogeneous reaction under conventional conditions. It proceeds, however, in the presence of a variety of carbons with ideal selectivity at 445 K [217]. Desorption experiments show that an intermediate adduct between the two educts is the most abundant surface intermediate. The existence of highly polar (acidic) surface groups and the absence of any d-states, which decompose both educts immediately at reaction temperature, are responsible for the success of carbon in this reaction. The reaction involves the selective breaking of a Cl-Cl bond in phosgene and is thus somewhat similar to the well-known action of charcoal in the synthesis of  $SOCl_2$  from chlorine and  $SO_2$ . Carbon further catalyzes the synthesis of phosgene from CO and chlorine. It should be mentioned that the existence of surface oxides is not sufficient to explain the reaction as OH groups on oxides do not catalyze the reaction.



The example of selective oxidation of creatinine by activated carbon and air in physiological environments [218] shows again the relationship between catalysis and chemisorption in carbon applications. The creatinine oxidation plays a role as an unwanted side reaction in artificial blood regeneration during dialysis. Creatinine is the ketone to the carboxylic acid creatine which is a heterocyclic nitrogen compound. Whereas the carboxylic acid is only chemisorbed on carbons, the ketone is slowly (time constant one day) oxidized to unknown products which may be toxic. This biologically relevant process occurs only in the presence of molecular oxygen and can be poisoned by chemisorption of thiosulfate. Both indications point again to the operating property of activation of molecular oxygen under very mild conditions.

#### 2.1.9.19 Catalytic Removal of NO by Carbon

One of the most interesting applications of carbon in the future may be the selective reduction of NO with a nonmetallic catalyst. Several highly selective and very active metal oxide catalyst systems exist for this application. They suffer, however, from lifetime and stability problems in mobile applications such as in advanced car systems. Carbon offers several unique possibilities. First, it exhibits a self-renewing surface in oxidizing and in reducing environments. This removes the problem of catalyst destruction due to sudden instabilities of the gas source. Second, it is less sensitive to irreversible poisoning by metal adsorbates (lead, arsenic, mercury). Finally it may be cultivated as an autoreducing agent and may allow NO removal without a second source of reducing agent, such as ammonia or propene. The technological advantage is that it is cheap and can be produced in large amounts. All this has been demonstrated through research effort, and two kinds of carbon, as SCR (selective catalytic reduction) catalyst [34, 219, 220] and as NO decomposition catalyst [221, 222], have been established. The general problem is to establish sufficient activity in a carbon which is not acting as catalyst support and which is not surface modified. Only then can the advantages of the system over oxide systems be fully exploited. Carbon as catalyst support for copper particles was also tested as a successful alternative to oxide supports [223].

In the SCR application a viable solution has been found [34] by activating the surface such that extremely temperature-resistant surface functional groups with nitrogen atoms are incorporated into the carbon. Complete conversion was achieved at 575 K in the presence of a significant excess of molecular oxygen. The successful modification is obtained from a controlled synthesis of carbons from organic precursors with glucosamine as the nitrogen donor. A variety of

carbon samples with other nitrogen donors and carbonization-activation procedures also enhances the SCR activity. There is, however, an unclear correlation between activity and characterization parameters. It is interesting to note that the nitrogen modification results in a change in the interaction of oxygen with the surface. The reaction order is zero with respect to the reductant and positive respect to NO and oxygen. The kinetic data, expressed as a rate constant of NO conversion as function of oxygen partial pressure, reveal a higher reaction order than the square-root dependence on oxygen partial pressure intuitively expected for dissociative activation. Such a square-root dependence was found in earlier experiments for unmodified carbons [138]. A second type of SCR activity is found over unmodified carbons in which the carbon acts only as adsorption platform for the reactants. This is indicated by a negative apparent activation energy [34].

The direct reaction of carbon as graphite or activated carbon [221, 222] with NO in the presence of excess oxygen is a high-temperature process operating with full NO conversion only at about 875 K. The parallel course of the activation curve for NO removal and for oxidation is taken as indication [224] that oxygen etches active sites into the carbon which decompose NO.

Mechanistic studies [225] lead to the conclusion that NO reacts with the carbon to form CO and surface nitrogen groups, which activate the carbon to react with molecular NO under formation of molecular nitrogen and oxygen. The similarity of the relevant nitrogen functional groups in the two reaction channels is striking as well as the importance of additional oxygen to maintain high catalytic activity. This effect is sacrificial in carbon but underlines the operation of a reaction in which defective surfaces are removed and fresh graphitic surfaces are regenerated. The relevance of the surface ordering is in line with the concept of graphene (001) surfaces acting as electron donor-acceptor sites for redox reactions. This unusual mode of catalyst operation in which no specific surface functional group is the key to activity, but rather the availability of a defect-poor free surface, has been substantiated in several studies with different kinds of carbon materials [226–228]. The question about the catalytic nature of this reaction, which is to a certain extent sacrificial, has been addressed in all studies and answered positively by the determination of a factor  $F$ . This is defined as the fraction of carbon consumed in the  $\text{NO} + \text{O}_2/\text{C}$  reaction. Values from about 0.25 down to 0.09 have been reported for a variety of materials ranging from activated carbon to coke and coal. The reaction is thus clearly a catalytic process. For practical considerations it should be mentioned that with this still “poor” cat-

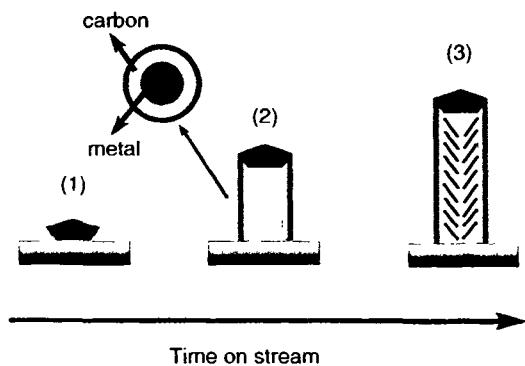


**Figure 35.** Mode of operation for the removal of a melt particle from an oxidic support by growing a carbon filament. Stage (1) initial saturation of the particle with carbon atoms from dissociation of a hydrocarbon and subsurface dissolution of the resulting free atoms. Stage (2) is after about 1 h on stream: the particle exsolves at the most active faces carbon which grow in a concentric set of graphene bands and remove the particle from the support. Stage (3) is after some time on stream: the particle has reshaped such that surfaces within the carbon tube also become active for graphene formation and are deposited as little flakes inside the tube.

alysis about 10 ml of solid carbon are sufficient to remove 100 l of gaseous NO in a 5 vol% oxygen–inert atmosphere at ambient pressure.

### 2.1.9.20 Removal of Carbon Deposits From Catalyst Materials

This subject is a special subsection of the carbon oxygen reaction system and has been treated in some detail above. The present section summarizes observations of the deactivation and possible regeneration of metal–oxide catalyst systems. It has long been rationalized [229] that in oxidative regeneration of carbonized catalysts the transport limitations play a more important role than the chemistry of carbon. The fact that part of the carbon is usually nonremovable under regeneration conditions is indication of the parallel carbonization reaction transforming disordered carbon of  $\text{CH}_x$  stoichiometry into graphitic carbon with much higher resistance to oxidation. To control this interplay between carbonization and oxidation a detailed analysis of the carbon deposit and a specific adjustment of the kinetic details of the regeneration are necessary for each catalytic system.

A second problem of catalyst regeneration is often the modification of the dispersion of the active component. Several studies [24, 230] clarify that carbon deposition originating from hydrocarbons not only covers an active particle but may remove it from its support. This mode of carbonization occurs effectively with metals catalyzing the formation of carbon filaments (see above). Figure 35 summarizes this effect. A metal

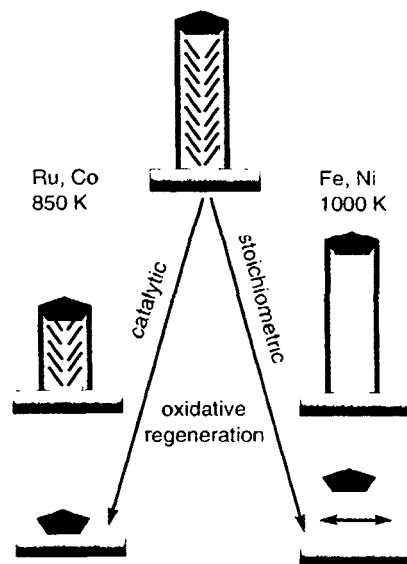


**Figure 36.** Oxidative decomposition of the carbon filaments grown in the mode described in Fig. 35. Catalytic metals lower the oxidation temperature and enable reversible removal; non-catalytic metals require higher temperatures which lead to spatial and structural modifications of the metal and finally to deactivation of the catalyst.

particle on an oxidic support (stage 1) is removed from it by the solution–exsolution mechanism creating carbon filaments. In the initial growth stage a hollow filament results (stage 2). At later stages (3) the particle restructures under the influence of the carbon–hydrogen dissolved in it and the filament is filled by the formation of graphene layers segregating from the side facets. This oversimplified growth history has been observed in a variety of case studies by electron microscopy [24].

In the later oxidative regeneration two cases of catalytic and stoichiometric gasification [230] have to be discriminated. In Fig. 36 the respective reaction pathways are depicted schematically. The catalytic path leads to a reversal of the filament generation with the effect that at comparatively moderate temperatures the initial stage of a metal particle supported on the oxide is restored. In the stoichiometric case the reaction temperature is higher, leading to a preferential oxidation of the inner filler graphene layers according to the layer-by-layer sequence of events described above. During the final stage of tube-wall oxidation the relationship between the metal particle and the carbon fixation is lost with the consequence that the metal particle floats on the support surface and has a chance to agglomerate and move on the support surface. Depending on the catalyst loading this loosening of the metal particle will lead to severe structural deactivation during the first or during subsequent regeneration cycles.

This simple sequence of events can be distilled out of the reviewed observations and detailed microscopic

studies available [24, 230]. It is in full agreement with the fundamental aspects of the topochemistry of carbon oxidation and the apparently difficult to understand wide variation of reported sensitivities of metal-oxide catalytic systems in carbon regeneration procedures.

### 2.1.9.21 Activation of Oxygen on Carbon Surfaces

The process of chemisorption and dissociation of molecular oxygen on carbon is fundamental to almost all aspects of carbon surface chemistry touched on here. It is also the basis of the application of carbon as a selective oxidation catalyst and is an essential part of the carbon gasification reaction (reactions 1-3). Despite this fundamental importance little reliable information is available on the mechanism, adsorption kinetics and sticking coefficient, and on the orientational dependence of such data. This is because reaction conditions and the preparation of well-defined surfaces of carbon are incompatible with conventional UHV systems. Data on polycrystalline samples or on poorly defined surfaces are available. The following cumulative assessment is given from a selection of these data. It is pointed out that similar arguments hold for the diamond surface. Only this interaction has been well researched with UHV surface science methods as the oxygen reaction controls the surface reconstruction of diamond surfaces [231, 232]. Little is known about the oxidation of diamond other than the fact that oxidation and graphitization occur hand in hand.

A set of well defined and quantitative experiments on oxygen chemisorption was carried out on a sample of preheated graphitized carbon black called graphon. This reference material is liberated from surface functional groups by annealing at 1000 K in UHV and subjection to oxygen exposures between 200 K and 550 K in a pressure range of  $10^{-4}$ – $10^2$  mbar [136]. These conditions are suitable for the formation of basic and neutral oxygen functional groups (see Figs 22 and 23). This leads to the conclusion that several chemically inequivalent species are formed. A cumulative analysis of the kinetics of adsorption reveal five inequivalent sorption processes with different time constants and activation energies between  $12 \text{ kJ mol}^{-1}$  and  $50 \text{ kJ mol}^{-1}$ . All species adsorbed are atomic oxygen, as shown by isotope scrambling. Their formation creates CO and CO<sub>2</sub> in the gas phase. The observations can only be rationalized as an indication for the reaction of prism faces with oxygen ending in basic functional groups. The desorption of adsorbed oxygen is only possible by destructive high temperature treatment, releasing CO and CO<sub>2</sub> at 1000 K. The adsorption and activation of molecular oxygen is undetectable because the surface is too reactive to bind the dissociation product atomic oxygen. These findings also

mean that molecular oxygen can be dissociated at 200 K on polycrystalline carbon with a small apparent activation energy of  $12 \text{ kJ mol}^{-1}$ .

According to these data no reactive atomic oxygen at low and intermediate oxygen concentrations should be present on carbon, which is in clear contradiction to many chemical facts reported above. Other forms of oxygen activation must co-exist with this immediate functionalization of prismatic faces.

A first XPS spectroscopic study was aimed at the chemisorption of oxygen at 300 K onto graphite (001) [213]. A "very small but unmistakably present" amount of oxygen was detected which we today interpret as oxygen chemisorbed at the surface defects of the sample which was not annealed prior to the experiment. A sticking coefficient for molecular oxygen at 300 K of  $10^{-14}$  is estimated. It is found that cleaning the surface by Ar ion bombardment, which destroys the graphite structure as we know today [163], enhances the sticking coefficient to measurable dimensions of  $10^{-7}$  on the basal plane at 673 K. Kinetic data reveals in analogy to the graphon experiments a variety of "at least four different" species with binding energies between 530 eV and 533 eV. As no C 1s data were reported, it is difficult today to assign these shifts to different species.

The authors [233] later reduced the number of surface species to two and assigned carbonyl and C–O–C species to the XPS lines. It is found that atomic oxygen, generated by a microwave discharge from NO, is effectively chemisorbed at basal planes of graphite giving rise to excessive bulk oxidation. In this study the disruption of the graphite structure upon Ar ion bombardment is demonstrated. The release of implanted Ar by subsequent oxidation is taken as an elegant measure for the oxidation kinetics. Oxidation experiments on natural diamond surfaces can be found in this paper. These surfaces are much more inert in the as-received state and are found to become similar to graphite upon Ar etching. This is explained by ion bombardment-induced graphitization of the diamond.

In a more recent set of experiments [84, 90, 163] a pre-annealed surface of pyrographite with an average (001) orientation was used to perform in situ oxidation experiments which showed measurable conversions at  $10^{-6}$  mbar and 900 K. The oxygen XPS data reveals at higher resolution the same two structures mentioned above. On the basis of the in situ observation it is shown conclusively that carbon-oxygen bonds give rise to several unresolved peaks between 532 eV and 529.9 eV. The structure at 533 eV is found after low-temperature chemisorption of molecular oxygen at 78 K and during in situ gasification at 900 K as a shoulder on the strong peak of carbon-oxygen func-

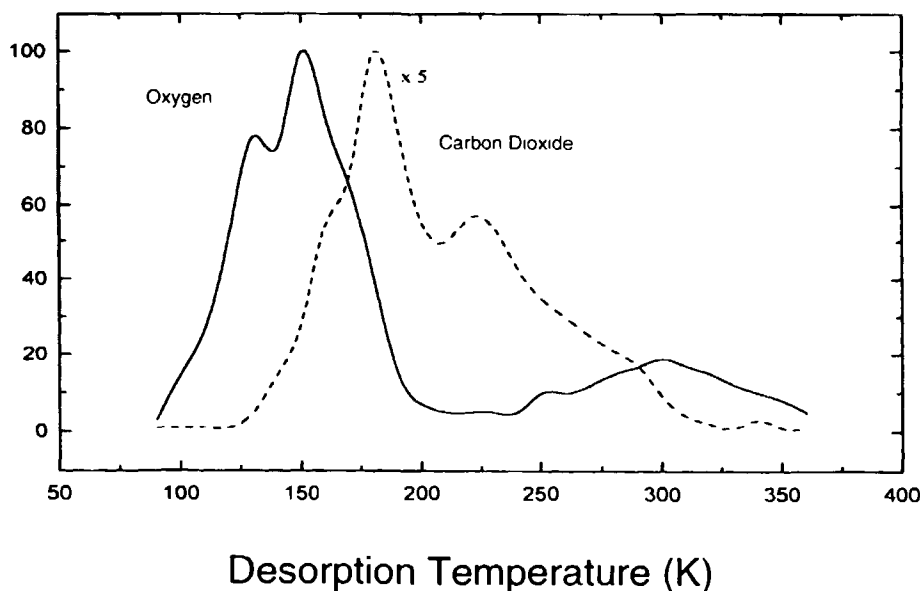


**Figure 37.** Temperature-programmed ( $10 \text{ K s}^{-1}$ ) of molecular oxygen from a cleaved and annealed (001) surface of HOPG graphite. 1000 L oxygen were admitted to the surface at 78 K and  $10^{-6}$  mbar pressure.

tions. This high binding energy feature is assigned to a peroxo-like molecular adsorbate species of oxygen weakly bonded to the basal planes of graphitic carbon.

Supporting evidence for the existence of such a weakly held precursor species to carbon-oxygen functions comes from TDS experiments on a well-characterized graphite (001) surface [90]. The material HOPG is not of single crystalline quality and contains an uncharacterized amount of surface defects. It is, however, the best approximation to a single crystal basal surface which technically can be handled. Figure 37 shows the desorption traces for molecular oxygen and  $\text{CO}_2$  recorded simultaneously after adsorption of molecular oxygen at 78 K. A structured desorption signal for molecular oxygen is seen at low temperatures which is associated with a chemisorbed molecular species. Variation of the heating rate does not cause a shift of the main peak, indicating a low formal reaction order. The detection of a second signal around ambient temperature exhibiting considerable structure was unexpected. These features are taken to indicate a structural heterogeneity of the adsorption sites, whereas the two peak systems at 150 K and at 300 K represent two chemically different oxygen species. The simultaneously recorded  $\text{CO}_2$  emission indicates the following facts:

- At temperatures as low 180 K oxygen is activated dissociatively and oxidizes (at defect sites) the carbon (001) plane.
- This is shown by a repetition of the experiment shown in Fig. 37 which is impossible on the once-reacted surface. Mechanical cleavage of the sample is required to repeat the experiment.

- No unspecific re-adsorption of oxygen can be detected for all sites from which chemisorbed oxygen in the first experiment was removed by warming to 360 K.
- The desorptions of oxygen and  $\text{CO}_2$  occur partly overlapping and partly alternating.
- The broad structure in  $\text{CO}_2$  desorption indicates the existence of a variety of different reaction sites, compatible with varying local geometries around the defect sites. The participation of prism faces is only possible at step edges as the large prism face area of the geometric sample block is passivated by the very first experiment with the sample. Valence band electronic spectra recorded simultaneously with the desorption experiment [90] reveal the transformation of the semimetallic surface into a fully insulating state, compatible with the creation of many surface defects on the (001) plane.
- Oxygen is activated on patches of relatively electron-rich graphitic structure and reacts at structural defects which are numerous on the mechanically cleaved surface.

These observations imply that no oxygen remains unreacted with carbon above 350 K, which is in line with the catalytic function of carbon exhibiting no oxidation activity at high temperatures. This precludes, however, the possibility that any of the species detected so far can act as efficient precursors for carbon oxidation which begins with the emission of CO at significantly higher temperatures.

Attempts were made with powdered carbons and enlarged oxygen exposure pressures to detect further

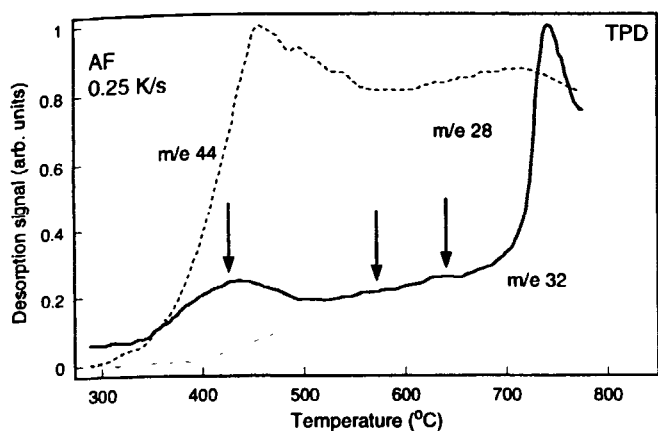
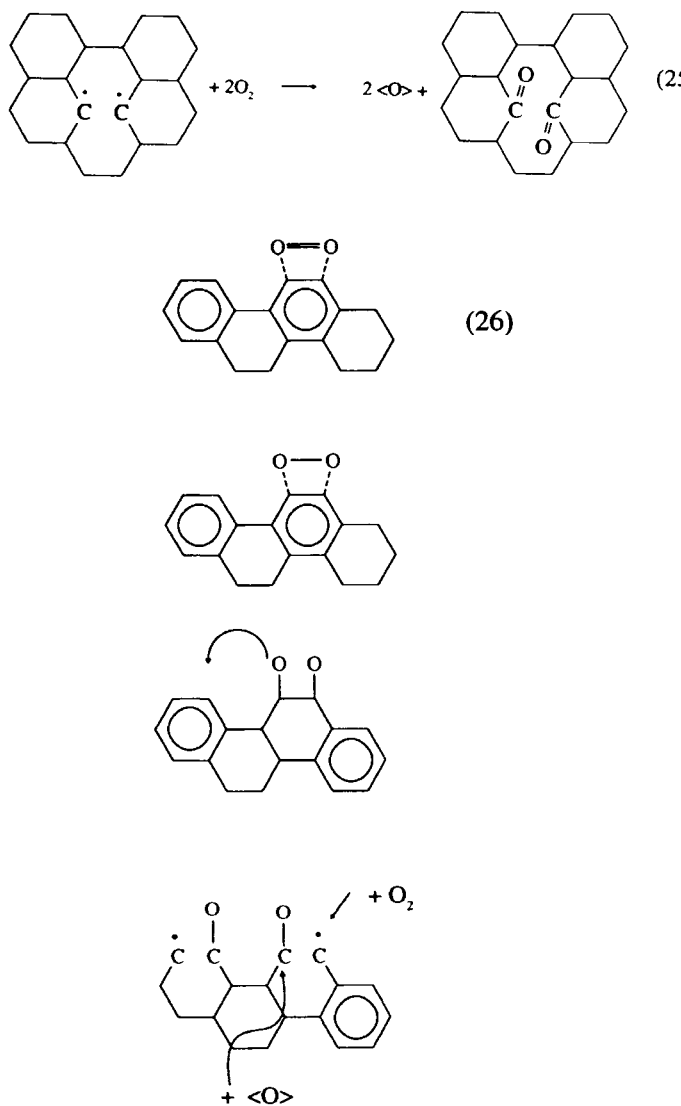


**Figure 38.** Temperature-programmed decomposition ( $0.25 \text{ K s}^{-1}$ ) of oxygen surface functional groups from a graphite powder. The simultaneous mass-spectroscopic analysis reveals the irreversible character of this experiment in which the substrate surface is removed during desorption of the adsorbate.

species of oxygen by thermal desorption (Fig. 38). The spectra were obtained from a powdered graphite with a low surface area. The arrows mark oxygen desorption peaks from a sample of high surface area carbon black (FW-1, DEGUSSA). It occurs that additional adsorbed species of oxygen exist which exhibit, during their thermal activation, a finite chance to desorb as oxygen rather than the more likely thermally activated reaction with carbon sites. A low-temperature process reacts specifically to acid sites releasing  $\text{CO}_2$ . A broad structure and the sharp high-temperature desorption peak generate increasingly more CO than  $\text{CO}_2$ . Only the high-temperature species has the chance to reach the prism faces and to react with freshly created defect sites. All other species react with very labile surface defects which terminate in their activity after a few reaction cycles. Considering the rough structure of carbon surfaces shown in Fig. 16, this seems likely for carbons with a small degree of total burn-off as is the case with all surface science experiments.

The experimental observations can be summarized in the following scenario of oxygen activation on carbon. Two independent pathways of activation have to be considered. Both require electron-rich adsorption sites for molecular oxygen. The electrons may be either delocalized on graphitic patches or may be localized in dangling bonds at coordinatively unsaturated defects (i.e. free radical centers). These latter sites exist only after high temperature treatment in inert conditions or as short-lived species during steady state gasification. The graphitic surface patches on carbon exist after mild burn-off (see Fig. 16) after the nitrogen activation procedure discussed above and after UHV cleavage and survive in reactive gas atmospheres such as water, air, NO or halogen-containing environments, provided



that the rate of defect formation via "hot" oxygen is low enough not to passivate the graphitic character.

Reaction scheme 25 summarizes the activation of oxygen on a radical center. This is exemplified here as an intralayer defect (one C-C bond missing). Two carbonyl groups are formed, eliminating the radical centers. Two atomic oxygen species O may either subsequently oxidize the former radical centers further to a carboxylic acid site or may diffuse to other sites on the carbon. This depends upon temperature and the local structural environment of the primary radical centers.

Reaction scheme 26 illustrates the chemisorption pathway in which, after a precursor state, first a hyperoxy species and then a peroxy species is formed. The dashed bonds indicate incomplete charge transfer. Only at the final step of dissociation of the molecular

precursor states is the aromatic character of the carbon adsorption site lost. The following steps can then be the diffusion of atomic oxygen, leaving behind a defective carbon site (localized double bonds), or straight reaction of the atomic oxygen with the carbons on which they are chemisorbed. In the boundary condition of high oxygen partial pressure and high temperatures or at very low temperatures, both reaction pathways may cooperate and thus explain the TDS observations discussed above.

Unfortunately, no quantitative data on any of these reaction steps exist, which are obtained under strict control of the experimental variables as in usual surface science experiments with metallic surfaces. Microkinetic modeling which could support in a quantitative way the picture derived so far has to await such well-defined experiments.

### 2.1.9.22 Conclusions

The surface chemistry of carbon is rather complex. At a single adsorption site several chemically inequivalent types of heteroatom bonds may form. Strong interactions between surface functional groups further complicate the list of surface chemical structures as derived for the most relevant carbon-oxygen system. An additional dimension of complexity is presented by the large variety of substrate structures of carbon which arise from anisotropic covalent bonding rather than by a isotropic metallic interaction.

It is not surprising that a very large body of seemingly conflicting experimental observations has been collected in the literature. A great deal of confusion can be traced back to inadequate analysis of the type of carbon under study, as exemplified by the use of the term "coke" in different fields of chemistry. Another general problem is the insufficient consideration of the reactivity of many carbon species during chemical treatment or even during analytical experiments (temperature-programmed methods). The underlying problem here is the insufficient distinction between thermodynamic phases (allotropes of carbon) and metastable structures. It is a matter of debate how many allotropes of carbon exist besides graphite and diamond. In this ill-defined situation a general description of "the chemistry" of carbon is difficult and is thus not even attempted here. The intention of this compilation of experimental data is to assist the reader in finding an adequate approach with which to analyse the situation for a particular problem with carbon chemistry.

A comprehensive review about particular case studies of carbon as a catalyst [236] provides detailed information and access to the original literature.

## References

- 1 J D Bernal, *Proc Roy Soc A* **1924**, *106*, 749-773
- 2 F Atamny, J Blocker, B Henschke, R Schlogl, T Schedel-Niedrig, M Keil, A M Bradshaw, *J Phys Chem* **1992**, *96*, 4522
- 3 T Schedel-Niedrig, D Herein, H Werner, M Wohlers, R Schlogl, G Francz, P Kania, P Oelhafen, C Wild, *Europhys Lett* **1995**, *31*(8), 461-466
- 4 R Berman, *Physical Properties of Diamond*, Academic Press, Oxford, **1965**
- 5 R Schlogl, *Surf Sci* **1987**, *189*, 861-872
- 6 R Schlogl in *Graphite Intercalation Compounds II*, (Eds H Zabel, S A Solin), Springer-Verlag, **1992**
- 7 V I Kasatochkin, A M Sladkov, Y P Kudryavtsev, M M Popov, J E Sterenberg, *Carbon* **1973**, *11*, 70-72
- 8 H Kroto, *Science* **1988**, *242*, 1139-1145
- 9 W Kratschmer, L D Lamb, K Fostiropoulos, D R Huffman, *Nature* **1990**, *347*, 354-358
- 10 H Werner, D Herein, J Blöcker, B Henschke, U Tegtmeyer, T Schedel-Niedrig, M Keil, A M Bradshaw, R Schlogl, *Chem Phys Lett* **1992**, *134*(1-2), 62-66
- 11 C Taliani, G Ruani, R Zamboni, R Danieli, S Rossini, V N Denisov, V M Burlakov, F Negri, *J Chem Soc Chem Commun* **1993**, 220
- 12 H S Chen, A R Kortan, R C Haddon, M L Kaplan, C H Chen, A M Mujser, H Chou, D A Fleming *Appl Phys Lett* **1991**, *59*(23), 2956
- 13 I M K Ismail, S L Rodgers, *Carbon* **1992**, *30*(2), 229-239
- 14 R A Assink, J E Schirber, D A Loy, B Morosin, G A Carlson, *J Mater Res* **1992**, *7*(8), 2136
- 15 H Werner, T Schedel-Niedrig, M Wohlers, D Herein, B Herzog, R Schlogl, M Keil, A M Bradshaw, *J Chem Soc, Farad Trans* **1994**, *90*(3), 403-409
- 16 H W Kroto, A W Allaf, S P Balm, *Chem Rev* **1991**, *91*, 1213-1235
- 17 H Werner, D Bublak, U Gobel, B Henschke, W Bensch R Schlogl, *Angew Chem* **1992**, *104*(7), 909-911
- 18 J D Fitzgerald, G H Taylor, L F Brunckhorst L S K Pang, M H Terrones, A L Mackay, *Carbon* **1992**, *30*, 1251-1260
- 19 T Belz, H Werner, F Zemlin, U Klengler, M Wesemann B Tesche, E Zeitler, A Reller, R Schlogl, *Angew Chem Int Ed Engl* **1994**, *33*(18), 1866-1869
- 20 T Baum, S Löffler, P Weilmunster, K-H Homann, *Ber Bunsenges Phys Chem* **1992**, *96*(7), 841-857
- 21 M Endo, H W Kroto, *J Phys Chem* **1992**, *96*, 6941-6944
- 22 M Monthieux, J G Lavin, *Carbon* **1994**, *32*, 335-343
- 23 R Saito, M Fujita, G Dresselhaus, M S Dresselhaus *Mater Sci Eng B* **1993**, *B19*, 185-191
- 24 R T K Baker, *Amer Chem Soc, Fuel Chem* **1996**, *41*(2), 521-524
- 25 M Audier, A Oberlin, M Coulon, L Bonnetain, *Carbon* **1981**, *19*, 217-224
- 26 S Motojima, I Hasegawa, S Kagiya, K Andoh, H Iwanaga, *Carbon* **1995**, *33*, 1167-1173
- 27 W A de Heer, D Ugarte, *Chem Phys Lett* **1993**, *207* (4-6), 480-486
- 28 M S Zwanger, F Banhart, *Philosophical Magazine B* **1995**, *72*(1), 149-157
- 29 A W Moore, in *Chemistry and Physics of Carbon* (Eds P L Walker Jr P A Thrower), Marcel Dekker New York **1981**, p 233
- 30 H-P Boehm, *Z Anorg Allg Chem* **1958**, *297*, 315-322
- 31 D L Wertz, M Bissell, *Fuel* **1995**, *74*(10) 1431-1435

- 32 W Ruland, *J Appl Phys* **1967**, *38*, 5585
- 33 J-B Donnet, R Ch Bansal, M-J Wang in *Carbon Black, Science and Technology*, Marcel Dekker, New York, **1993**
- 34 L Singoredjo, F Kapteijn, J A Moulijn, J-M Martin-Martinez, H-P Boehm, *Carbon* **1993**, *31*, 213-222
- 35 R Burmeister, B Despeyroux, K Deller, K Seibold, P Albers, *Stud. Surf Sci Catal* **1993**, *78*, 361-368
- 36 D Richard, P Gallezot, *Stud. Surf Sci. Catal* **1987**, *31*, 71
- 37 P B Weisz, R D Goodwin, *Carbon* **1982**, *20*, 445-449
- 38 P B Weisz, R D Goodwin, *Carbon* **1983**, *21*, 517
- 39 O Vohler, F von Sturm, E Wege, H von Kienle, M Voll, P Kleinschmit, *Ullmann's Encycl Ind. Chem.* **1986**, p 95-163
- 40 M S Kim, N M Rodriguez, R T K Baker, *J Catal* **1991**, *131*, 60-73
- 41 X X Bi, *J Mater Res* **1995**
- 42 H F Calcote, *Combustion and Flame* **1981**, *42*, 215-242
- 43 J Lahaye, G Prado in *Chemistry and Physics of Carbon* (Eds P L Walker Jr, P A Thrower), Marcel Dekker, New York **1978**, p 167-294
- 44 K H Homann, H G Wagner, *Proc Roy Soc A* **1968**, *307*, 141-152
- 45 J H Kent, H G Wagner, *Combustion Science and Technology* **1984**, *41*, 245-269
- 46 K H Homann, H G Wagner, *Ber Bunsenges* **1965**, *69*, 20-35
- 47 J Lahaye, G Prado, J B Donnet, *Carbon* **1974**, *2*, 27-35
- 48 G P Prado, J B Howard, in *Advances in Chemistry Series Evaporation-Combustion of Fuels* (Ed J T Zung), American Chemical Society, Washington, **1978**, p 153-166
- 49 C Bertrand, J-L Delfau, *Combustion Science and Technology* **1985**, *44*, 29-45
- 50 F Takahashi, I Glassman, *Combustion Science and Technology* **1984**, *37*, 1-19
- 51 M Frenklach, L B Ebert, *J Phys Chem* **1988**, *92*, 563-564
- 52 J Lahaye, *Polymer Degradation and Stability* **1990**, *30*, 111-121
- 53 R T K Baker, M A Barber, P S Harris, F S Feates, R J Waite, *J Catal* **1972**, *26*, 51-62
- 54 I Alstrup, *J Catal* **1988**, *109*, 241-251
- 55 A J H M Kock, P K de Bokx, E Boellaard, W Klop, J W Geus, *J Catal* **1985**, *96*, 468-480
- 56 J R Rostrup-Nielsen, *J Catal*, **1972**, *27*, 343-356
- 57 G A Somorjai, *Proc 8th International Congress on Catalysis*, Verlag Chemie, Weinheim **1984**, p 113
- 58 G F Taylor, S J Thomson, G Webb, *J Catal* **1968**, *12*, 191-197
- 59 S M Davis, F Zaera, B E Gordon, G A Somorjai, *J Catal* **1985**, *92*, 240-246
- 60 M Salmeron, G A Somorjai, *J Phys Chem* **1982**, *86*, 341-350
- 61 L H Dubois, D G Castner, G A Somorjai, *J Chem Phys* **1980**, *72*(9), 5234-5240
- 62 J R Fritch, K P C Vollhardt, *Angew Chem* **1980**, *92*(7), 570-572
- 63 B E Bent, C M Mate, J E Crowell, B E Koel, G A Somorjai, *J Phys Chem* **1987**, *91*, 1439-1502
- 64 S M Davis, F Zaera, G A Somorjai, *J Catal* **1982**, *77*, 439-459
- 65 S J Thomson, G Webb, *J Chem Soc Chem Commun* **1976**, 526-527
- 66 Z Paal, R Schlogl, G Ertl, *Faraday Trans* **1992**, *88*(8), 1179-1189
- 67 H G Karge in *Introduction to Zeolite Science and Practice* (Eds H van Bekkum, E M Flanigen, J C Jansen) Elsevier, Amsterdam **1991**, p 531-570
- 68 S M Davis, Y Zhou, M A Freman, D A Fischer, G M Meitzner, J L Gland, *J Catal* **1992**, *139*, 322-325
- 69 G P Handreck, T D Smith, *J Catal* **1990**, *123*, 513-522
- 70 K Moljord, P Magnoux, M Gussnet, *Appl Catal A* **1995**, *122*, 21-32
- 71 H G Karge, E P Boldingh, *Catal Today* **1988**, *3*, 53-63
- 72 D Eisenbach, E Gallei, *J Catal* **1979**, *56*, 377-389
- 73 H Marsh in *Carbon and Coal Gasification* (Eds J L Figueiredo, J A Moulijn), Martinus Nijhoff Publishers, Dordrecht **1986**, p 27
- 74 J Maire, J Mering, *Chem Phys Carbon* **1970**, *6*, 125-190
- 75 R W Henson, W M Reynolds, *Carbon* **1965**, *3*, 277
- 76 H Marsh, P L Walker Jr in *Chemistry and Physics of Carbon* (Eds P L Walker Jr, P A Thrower), Marcel Dekker, New York, **1979**, p 230
- 77 T Belz, J Find, D Herein, N Pfander, T Ruhle, H Werner, M Wohlers, R Schlogl, *Ber Bunsenges Phys Chem* submitted
- 78 M Kanowski, H-M Vieth, K Luders, G Buntkowsky, T Belz, H Werner, M Wohlers, R Schlogl, *Carbon* submitted
- 79 G Blyholder, H Eyring, *J Phys Chem* **1959**, *63*, 1004-1008
- 80 S Ahmend, M Back, J M Roscoe, *Combustion & Flame* **1987**, *70*, 1-16
- 81 Z Du, A F Sarofim, J P Longwell, *Energy & Fuels* **1991**, *5*, 214-221
- 82 F S Feates, *Trans Faraday Soc* **1968**, *64*, 3093-3099
- 83 H Marsh, T E O'Hair, R Reed, *Trans Faraday Soc* **1965**, *61*, 285-293
- 84 F Atamny, J Blocker, A Dubotzky, H Kurt, G Loose, W Mahdi, O Timpe, R Schlogl, *J Mol Phys* **1992**, *76*(4), 851-886
- 85 F J Vastola, P J Hart, P L Walker, *Carbon* **1964**, *2*, 65-71
- 86 L R Radovic, H Jiang, A A Lizzio, *Energy & Fuels* **1991**, *5*, 68-74
- 87 A A Lizzio, H Jiang, L R Radovic, *Carbon* **1990**, *28*, 7-19
- 88 B Henschke, H Schubert, J Blocker, F Atamny, R Schlogl, *Thermochimica Acta* **1994**, *234*, 53-83
- 89 D Herein, J Find, B Herzog, H Kollmann, R Schmidt, R Schlogl, *ACS Symp Ser* **1996**, *148*, 154
- 90 R Schlogl, G Loose, M Wesemann, *Solid State Ionics* **1990**, *43*, 183-192
- 91 J M Ranish, P L Walker Jr, *Carbon* **1993**, *31*, 135-141
- 92 L E C de Torre, J L Llanos, E J Bottani, *Carbon* **1991**, *29*(7), 1051-1061
- 93 H Marsh, T E O'Hair, W F K Wynne-Jones, *Trans Faraday Soc* **1965**, *61*, 274-283
- 94 J M Thomas, *Chem Phys Carbon* **1965**, *1*, 121
- 95 C Wong, R T Yang, B L Halpern, *J Chem Phys* **1983**, *78*(6), 3325-3328
- 96 A Cuesta, A Martinez-Alonso, J M D Tascon, *Energy & Fuels* **1993**, *7*, 1141-1145
- 97 B Herzog, D Bokern, T Braun, R Schlogl, *Materials Sci Forum* **1994**, *166-169*, 517-522
- 98 A Kavanagh, R Schlogl, *Carbon* **1988**, *26*(1), 23-32
- 99 R Schlogl, F Atamny, W J Wirth, J Stephan, *Ultra microscopv* **1992**, *42-44*, 660-667
- 100 D W McKee in *Fundamental Issues in Control of Carbon Gasification* (Eds J Lahaye, P Ehrburger), Kluwer Dordrecht, **1991**, p 484-514
- 101 K J Huttinger, J Adler, G Hermann, *Carbon and Coal Gasification* Nijhoff, Dordrecht, **1986**, p 213
- 102 S Amelinkx, P Delavignette, M Heerschap, *Chem Phys Carbon* **1965**, *1*, 2
- 103 H Marsh, N Murdie, I A S Edwards, H P Boehm, *Chem Phys Carbon* **1987**, *20*, 213
- 104 F M Lang, P Magnier, *Chem Phys Carbon* **1968**, *3*, 121

- 105 H Werner, M Wohlers, D Bublak, J Blocker, R Schlogl, *J Fullerene Sci Technol* **1993**, 1(4), 457-474
- 106 M Wohlers, A Bauer, T Ruhle, F Neitzel, H Werner, R Schlogl, *J Fullerene Sci Technol* in press
- 107 H Werner, M Wohlers, D Bublak, T Belz, W Bensch, R Schlogl in *Electronic Properties of Fullerenes* (Eds H Kuzmany, J Fink, M Mehring), Springer, Berlin **1993**, p 16-38
- 108 M Wohlers, H Werner, D Herein, T Schedel-Niedrig, A Bauer, R Schlogl, *Synth Met* **1996**, 77, 299-302
- 110 K L Yeung, E E Wolf, *J Catal* **1993**, 143(2), 409-429
- 111 M Wohlers, A Bauer, Th Belz, Th Ruhle, Th Schedel-Niedrig, R Schlogl, *ACS Symp Ser* **1996**, 108-112
- 112 I M K Ismail, P L Walker Jr, *Carbon* **1989**, 27(4), 549-559
- 113 R L Radovic, P L Walker, R G Jenkins, *Fuel* **1983**, 62, 849-856
- 114 N R Laine, F J Vastola, P L Walker Jr, *J Phys Chem* **1963**, 67, 2030-2034
- 115 H Freund, *Fuel* **1986**, 65, 63-66
- 116 P Biloen, *J Mol Catal* **1983**, 21, 17-24
- 117 R T Yang, C Wong, *J Catal* **1984**, 85, 154-168
- 118 B Pennemann, R Anton, *J Catal* **1989**, 118, 417-423
- 119 F Kapteijn, O Peer, J A Moulijn, *Fuel* **1986**, 65, 1371
- 120 S R Kelemen, H Freund, *J Catal* **1986**, 102, 80-91
- 121 M B Cerfontain, R Meijer, F Kapteijn, J A Moulijn, *J Catal* **1987**, 107, 173-180
- 122 J A Moulijn, F Kapteijn, *Carbon* **1995**, 33(8), 1155-1165
- 123 R Schlogl in *Physics and Chemistry of Alkali Metal Adsorption* (Eds H P Bonzel, A M Bradshaw, G Ertl), Elsevier Science, Amsterdam, **1989**, p 347-377
- 124 L Bonnetain, X Duval, M Letort in *Proc 4th Carbon Conference, Buffalo*, Pergamon Press, **1960**, p 107-112
- 125 F Kapteijn, R Meier, S C van Eyck, J A Moulijn in *Fundamental Issues in Control of Carbon Gasification* (Eds J Lahaye, P Ehrburger), Kluwer, Dordrecht, **1991**, p 221
- 126 A J Groszek, S Partyka, D Cot, *Carbon* **1991**, 29, 821-829
- 127 A J Groszek, *Carbon* **1987**, 25, 712-722
- 128 F Atamny, A Reller, R Schlogl, *Carbon* **1992**, 1123-1126
- 129 F Atamny, H Kollmann, H Bartl, R Schlogl, *Ultramicroscopy* **1993**, 48, 281-289
- 130 E Koberstein, E Lakatos, M Voll, *Ber Bunsenges* **1971**, 75(10), 1104-1114
- 131 J A Franz, R Garcia, J C Lineman, G D Love, C E Snape, *Energy & Fuel* **1992**, 6, 598-602
- 132 M Spiro, *Catal Today* **1990**, 7, 167-178
- 133 R C Bansal, N Bhatia, T L Dhami, *Carbon* **1978**, 16, 65-68
- 134 B R Puri, R C Bansal, *Carbon* **1964**, 1, 451-455
- 135 B Stohr, H P Boehm, R Schlogl, *Carbon* **1991**, 29(6), 707-720
- 136 R C Bansal, F J Vastola, P L Walker Jr, *J Colloid Interface Sci* **1970**, 32(2), 187-194
- 137 R C Bansal, F J Vastola, P L Walker *Carbon* **1971**, 9, 185-192
- 138 M Zuckmantel, R Kurth, H P Boehm, *Z Naturforsch* **1979**, 34b, 188-196
- 139 C H Chang, *Carbon* **1981**, 19, 175-186
- 140 R Schlogl in *Progress in Intercalation Research, Physics and Chemistry of Materials with Low-Dimensional Structures*, (Eds Muller-Warmuth), Kluwer, Dordrecht **1994**, p 83-176
- 141 B R Puri, R C Bansal, *Carbon* **1966**, 3, 533-539
- 142 W O Stacy, W R Imperial, P L Walker, *Carbon* **1966**, 4, 343-352
- 143 H-P Boehm, *Angew Chem* **1966**, 78(12), 617-628
- 144 M L Studebaker, *Rubber Chem Technol* **1957**, 30, 1400-1483
- 145 C A L Y Leon, J M Solary, V Calemma, L R Radovic, *Carbon* **1992**, 30, 797
- 146 H-P Boehm, E Diehl, *Z Electrochem* **1962**, 66(8/9), 642-647
- 147 U Hofmann, G Ohlerich, *Angew Chem* **1950**, 62(1), 16-21
- 148 H-P Boehm, E Diehl, W Heck, R Sappok, *Angew Chem* **1964**, 76(17), 742-751
- 149 H P Boehm, H Knozinger in *Catalysis, Science and Technology* (Eds J R Anderson, M Boudart), Springer Verlag Berlin, **1983**, Chapter 2
- 150 H P Boehm, *Adv Catal* **1966**, 16, 179-274
- 151 H-P Boehm, M Voll, *Carbon* **1970**, 8, 227-240
- 152 M Voll, H-P Boehm, *Carbon* **1970**, 8, 741-752
- 153 M Voll, H-P Boehm, *Carbon* **1971**, 9, 473-480
- 154 M Voll, H-P Boehm, *Carbon* **1971**, 9, 481-488
- 155 H Marsh, A D Foord, J S Mattson, J M Thomas, E L Evans, *J Colloid Interface Sci* **1974**, 49(3), 368-382
- 156 G M Badger, J E Campbell, J W Cook, R P Ruffael, A I Scott, *J Chem Soc* **1950**, 2526
- 157 V A Garten, D E Weiss, *Aust J Chem* **1957**, 10, 309-328
- 158 H P Boehm, U Hofmann, A Clauss in *Third Carbon Conference, Buffalo New York*, Pergamon Press Oxford **1957**, p 241-247
- 159 A S Arico, V Antonucci, M Minutoli, N Giordano *Carbon* **1989**, 27(3), 337-347
- 160 D T Clark, A Harrison, *J Polymer Sci Polym Chem Ed* **1981**, 19, 1945-1955
- 161 D T Clark, A Harrison, *J Polymer Sci Polymer Chem Ed* **1976**, 14, 533-542
- 162 A Diks in *Electron Spectroscopy Theory Techniques and Application* (C R Brundle, A D Baker) **1981**
- 163 R Schlogl, H P Boehm, *Carbon*, **1983**, 21(4), 345-358
- 164 Y Baer, *J Electr Spectrosc Rel Phen* **1981**, 24, 95-100
- 165 P M T M van Attekum, G K Wertheim, *Phys Rev Lett* **1979**, 43, 1896-1898
- 166 R J J Jansen, H V Bekkum, *Carbon* **1995**, 33, 1021-1027
- 167 D Marton, K J Boyd, A H Al-Bayati, S S Todorov, J W Rabalais, *Phys Rev Lett* **1994**, 73(1), 118-121
- 168 D N Belton, S J Schmieg, *J Vac Sci Technol* **1990**, A8(3), 2353-2362
- 169 F R McFeely, S P Kowalczyk, L Ley, R G Cavell, R A Pollak, D A Shirley, *Phys Rev B* **1974**, 9(12), 5268-5278
- 170 D Ugolini, J Eitle, P Oelhafen, M Wittmer, *Appl Phys* **1989**, A48, 549-558
- 171 M A Smith, L L Levenson, *Phys Rev B* **1977**, 16(6), 2973-2977
- 172 E Desimont, G I Casellas, A M Salvi, T R I Cataldi, A Morone, *Carbon* **1992**, 30, 527
- 173 P Denison, F R Jones, J F Watts, *J Mater Sci* **1985**, 20, 4647-4656
- 174 L J Gerenser, J F Elman, M G Mason, J M Pochan *Polymer* **1985**, 2026, 1162-1166
- 175 R H Bradley, E Sheng, I S P K Freakley, *Carbon* **1995**, 33(2), 233-241
- 176 Y Yang, Z G Lin, *J Appl Electrochem* **1995**, 25, 259-266
- 177 A M Vassallo, L S K Pang, P A Cole-Clarke, M A Wilson, *J Am Chem Soc* **1991**, 113, (7820-7821)
- 178 M Starsinic, Y Otake, P L Walker Jr, P C Painter *Fuel* **1984**, 63, 1002-1007
- 179 J B Donnet, P Ehrburger, A Voet, *Carbon* **1972**, 10, 757
- 180 V R Deiz, J L Bitner, *Carbon* **1972**, 10, 145
- 181 W R Cofer, D R Schryer, R S Rogowski, *Atmosph Environ* **1984**, 18, 243
- 182 L Bonnetain, *J Chem Phys* **1961**, 58, 34
- 183 S Matsumoto, H Kanda, Y Sato, M Setaka *Carbon* **1977**, 15, 299-302
- 184 U Tegtmeier, H P Weiss, R Schlogl, *Fresenius J Anal Chem* **1993**, 347, 263-268



- 185 H Juntgen, *Fuel* **1986**, *65*, 1436–1446
- 186 M S McIntyre, G R Mount, T C Lipson, B Harrison, S Liang, *Carbon* **1991**, *29*, 1071
- 187 A Linares-Solano, M Almela-Alarcon, C S-M de Lecea, *J Catal* **1990**, *125*, 401–410
- 188 D Cazorla-Amoros, A Linares-Solano, C S-M de Lecea, J P Joly, *Carbon* **1991**, *29*, 361
- 189 R L Augustine in *Heterogeneous Catalysis for the Synthetic Chemist*, Marcel Dekker, New York, **1996**
- 190 R T K Baker, E B Prestridge, R L Garten, *J Catal* **1979**, *56*, 390
- 191 S L Butterworth, A W Scaroni, *Appl Catal* **1985**, *16*, 375–388
- 192 F Atamny, D Duff, A Baker, *Catal Lett* **1995**, *34*, 305–311
- 193 R W Joyner, J B Pendry, K Saldin, S R Tennison, *Surf Sci* **1984**, *138*, 84–94
- 194 C E Milstead, A B Riedinger, L R Zumwalt, *Carbon* **1966**, *4*, 99–106
- 195 S R Tennison in *Catalytic Ammonia Synthesis Fundamentals and Practice, Fundamental and Applied Catalysis* (Ed J R Jennings), Plenum Press, New York, **1991**
- 196 E Hegenberger, N L Wu, J Phillips, *J Phys Chem* **1987**, *91*, 5067–5071
- 197 A Linares-Solano, F Rodriguez Reinoso, C S-M de Lecea, O P Mahajan, P L Walker Jr, *Carbon* **1982**, *20*(3), 177–184
- 198 P Ehrburger, O P Mahajan, P L Walker Jr, *J Catal* **1976**, *43*, 61–67
- 199 R Schlogl, P Bowen, G R Millward, W Jones, H P Boehm, *J Chem Soc Faraday Trans*, **1983**, *1*(79), 1793–1818
- 200 S Parkash, S K Charkrabartup, J G Hooley, *Carbon* **1978**, *16*, 231
- 201 K Aika, H Hori, A Ozaki, *J Catal* **1972**, *27*, 424–431
- 202 M E Vol'pin, Y N Novikov, V A Postnikov, V B Shur, B Bayerl, L Kaden, M Wahren, L M Dmitrienko, R A Stukan, A V Nefed'ev, *Z Anorg Allg Chem* **1977**, *428*, 231–236
- 203 K Kalueki, P W Morawski, *J Chem Tech Biotechnol* **1990**, *47*, 357
- 204 S Parkash, J G Hooley, *J Catal* **1980**, *62*, 187–188
- 205 A Sepulveda-Escribano, F Rodriguez-Reinoso, *J Mol Catal* **1994**, *90*, 291–301
- 206 A A Chen, M A Vannice, J Phillips, *J Phys Chem* **1987**, *91*, 6257–6269
- 207 V K Jones, L R Neubauer, C H Bartholomew, *J Phys Chem* **1986**, *90*, 4832–4839
- 208 H J Jung, M A Vannice, L N Mulay, R M Stanfield, W N Delgass, *J Catal* **1982**, *76*, 208–224
- 209 K J Lim, M Boudart, *J Catal* **1987**, *105*, 263–265
- 210 N M Rodriguez, M-S Kim, R T K Baker, *J Phys Chem* **1994**, *98*, 13108–13111
- 211 H P Boehm, G Mair, T Stoehr, A R de Rincon, B Tereczki, *Fuel* **1984**, *63*, 1061–1063
- 212 H Juntgen, H Kuhl, *Chem Phys Carbon* **1990**, *22*, 145
- 213 M Barber, E L Evans, J M Thomas, *Chem Phys Lett* **1973**, *18*(3), 423–425
- 214 M Pourbaix, *Atlas of Electrochemical Equilibria in Aqueous Solution*, Pergamon Press, Oxford, **1966**, p 450–457
- 215 O Timpe, R Schlogl, *Ber Bunsenges Phys Chem* **1993**, *97*(9) 1076–1085
- 216 J Klein, K-D Henning, *Fuel* **1984**, *63*, 1064–1067
- 217 T A Ryan, M H Stacey, *Fuel* **1984**, *63*, 1101–1106
- 218 E M Smith S Alfrossman, J M Courtney, *Carbon*, **1977**, *149*–152
- 219 T Okuhara, K Tanaka, *J Chem Soc Faraday Trans 1* **1986**, *82*, 3657–3666
- 220 H Yamashita, H Yamada, A Tomita, *Appl Catal* **1991**, *78*, L1–L6
- 221 H Teng, E M Sunberg, J M Carlo, *Energy & Fuel* **1992**, *6*, 398
- 222 H Yamashita, A Tomita, H Yamada, T Kyotani, L R Radovic, *Energy & Fuel* **1993**, *7*, 85–89
- 223 L Singoredio, M Slagt, J van Wees, E Kapteijn, J A Moulijn, *Catal Today* **1990**, *7*, 157
- 226 M J Illan-Gomez, A Linares-Solano, L R Radovic, C S-M de Lecea, *Energy & Fuels* **1995**, *9*, 97
- 227 M J Illan-Gomez, A Linares-Solano, L R Radovic, C S-M de Lecea, *Energy & Fuels* **1995**, *9*, 104
- 228 J Mochida, S Kishimori, M Hironaka, S Kawano, Y Matsumura, M Yoshikawa, *Energy & Fuels* **1994**, *8*, 1341
- 229 P B Weisz, R D Goodwin, *J Catal* **1963**, *2*, 397–404
- 230 J van Doorn, J A Moulijn, *Catal Today* **1990**, *7*, 257–266
- 231 A V Hamza, G D Kubiak, R H Stulen, *Surf Sci* **1990**, *237*, 35–52
- 232 T Frauenheim, U Stephan, P Blaudeck, D Porezag, H-G Busman, W Zimmermann-Edling, S Lauer, *Phys Rev B* **1993**, *48*(24), 18189–18202
- 233 S Evans, J M Thomas, *Proc R. Soc Lond A* **1977**, *353*, 103–120
- 234 S Akhter, K Allan, D Buchanan, J A Cook, A Campion, J M White, *Appl Surf Sci* **1988**, *35*, 241–258
- 235 A Oberlin, *Chem Phys Carbon* **1992**, *22*, 2
- 236 L R Radovic, F Rodriguez-Reinoso *Chem Phys Carbon* **1997**, *25*, 243

## 2.2 Supported Catalysts

### 2.2.1 Deposition of Active Component

#### 2.2.1.1 Impregnation and Ion Exchange

M CHE, O CLAUSE AND CH MARCILLY

#### A Introduction

Many practical catalysts consist of one or several catalytically active component(s) deposited on a high-surface-area support and the present article deals with only such catalysts. The main purpose of using a support is to achieve an optimal dispersion of the catalytically active component(s) and to stabilize it (them) against sintering. However, in a number of reactions, the support is not inert and the overall process is actually a combination of two catalytic functions: that of the active component(s) and that of the support. Fig 1 gives the number of papers dealing with catalyst preparation involving the supports most frequently studied during the period 1967–1993.

There are many definitions of catalyst preparation but the most revealing one seems to have been given by Richardson [1] "catalyst preparation is the secret to achieving the desired activity, selectivity and life time". This definition conveys the idea that catalyst preparation is a strategic procedure which should not be dis-

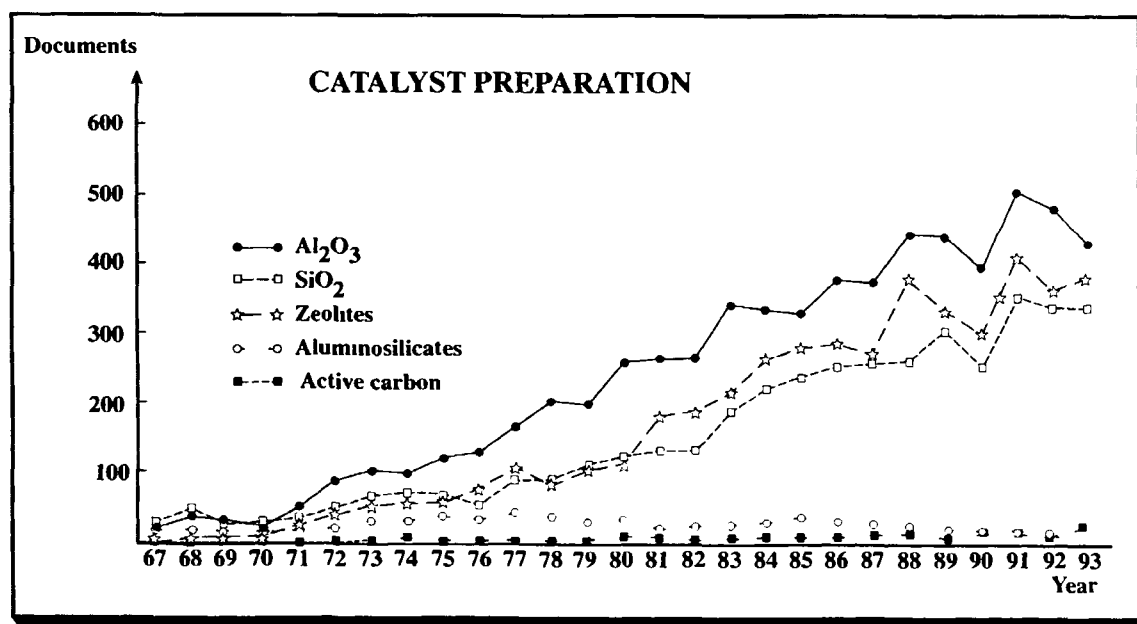


Figure 1 Number of papers concerned with catalyst preparation involving the most frequently used supports during the period 1967–1993

closed or, if published, should be protected in the form of patents

Although the preparation of supported catalysts is one, if not the most, important step in the course of a catalytic process, it is interesting to observe that little attention has been given to this subject in most textbooks written on catalysis. By contrast, the number of documents published on this subject is very large (Fig 2(a)). This apparent contradiction lies in the fact that most, if not all, papers and patents give preparation procedures rather than rationalizations and concepts, making any synthesis, usually required in textbooks, rather difficult. It is thus no surprise that the term “catalyst design” has been little used.

It is also interesting to observe that while the number of papers steadily increases, the number of patents is, by contrast, almost constant (Fig 2(a)). It is also important to note (Fig 2(b)) that the literature on catalyst characterization steadily increases but remains almost one order of magnitude less abundant than for catalyst preparation, explaining perhaps why our understanding of the latter domain is not satisfactory and is not well rationalized.

For these reasons, there now appears to be a general consensus that one should try to

- (i) investigate the basic aspects of catalyst preparation,
- (ii) identify the elementary steps and the related pertinent parameters so that new sequences of such steps can be proposed, making catalyst architecture possible,
- (iii) establish procedures for choosing the most appropriate method for industrial catalyst preparation

In recent years, major advances have been made on techniques for physically and chemically characterizing supported catalysts [2] and on the quantitative and qualitative aspects of catalyst preparation [3–12] so that the design of supported catalysts has begun to become a feasible activity.

The term “design” is most appropriate when the precise nature of the active center for a given reaction is known and can be reproduced at the molecular level including the oxidation state of the catalytically active element, the nature and symmetry of the environment (namely the nature and number of the different ligands (in particular the type of support and number of bonds with the latter, the number and nature of ancillary ligands) and the number of coordination vacancies).

A properly designed catalyst should have the essential attributes of activity, stability, selectivity and regenerability [13]. Such characteristics can be related to the physical and chemical properties of the catalyst which in turn can be related to the many parameters inherent to the method used to prepare the catalyst. In the past, much of the literature on supported catalysts has not included this information.

There are two main steps in catalyst preparation. The first consists of depositing the active component precursor, as a divided form, on the support and the second of transforming this precursor into the required active component which depending on the reaction to be catalyzed can be found in the oxide, sulfided or metallic state. A large majority of deposition methods involve aqueous solutions and the liquid/solid interface. In some cases, deposition can be also performed from the gas phase and involves the gas/solid interface.

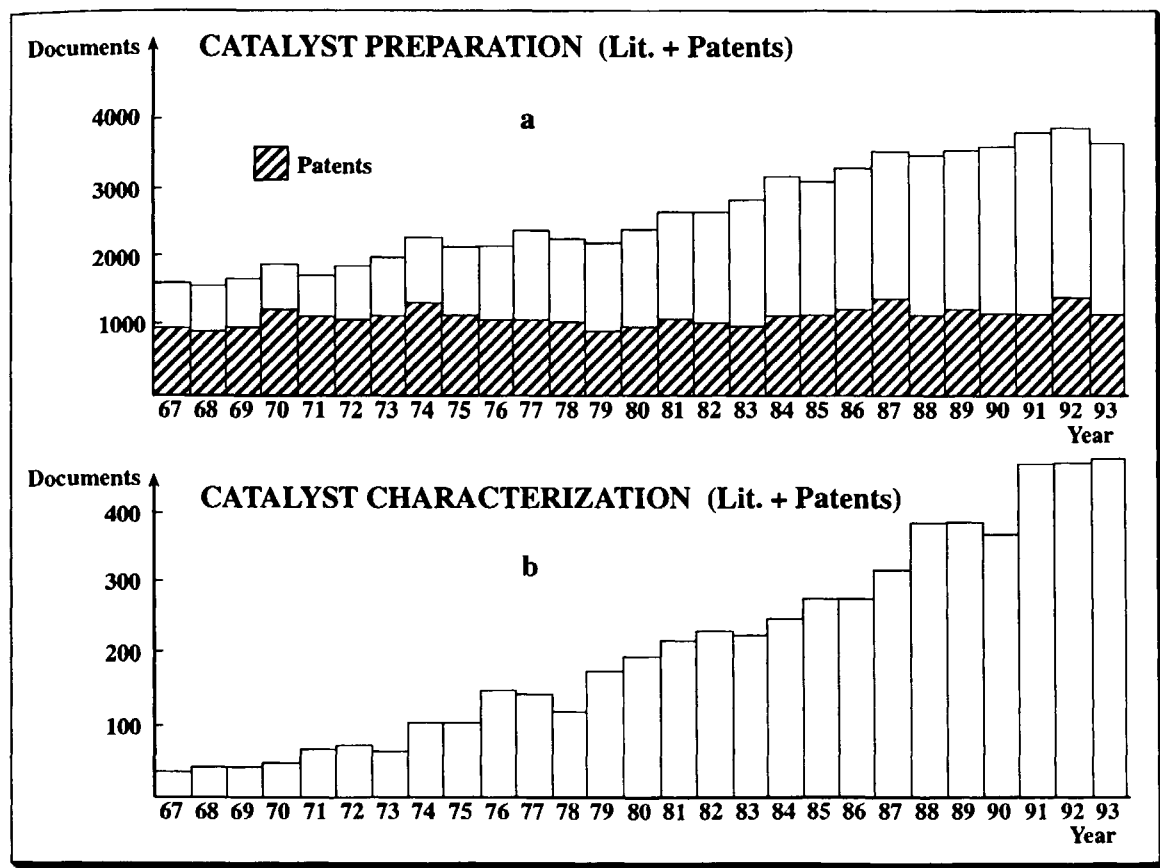


Figure 2. Comparison of the number of papers and patents found in the literature dealing with (a) catalyst preparation and (b) characterization during the period 1967–1993.

The methods most frequently used to achieve deposition of the active component precursor are impregnation, ion exchange, anchoring, grafting, spreading and wetting, heterogeneization of complexes, deposition–precipitation (homogeneous and redox) and adapted methods in the case of supported bimetallic catalysts. In some cases, the active component (not its precursor form) can be deposited directly on the support.

When a support is put in a solution containing a precursor of the active component, several phenomena can occur among which ion exchange, impregnation, dissolution of the support and formation of surface compounds are the most important. If the experimental parameters are not properly adjusted, there is a fair probability that these phenomena may occur simultaneously. In what follows, we shall therefore discuss, for the sake of simplicity, first ion exchange and then impregnation. We will then consider the problem of oxide dissolution.

### B Ion Exchange

Ion exchange consists of replacing an ion in an electrostatic interaction with the surface of a support by

another ion species. The support containing ion A is plunged into an excess volume (compared to the pore volume) of a solution containing ion B that is to be introduced. Ion B gradually penetrates into the pore space of the support and takes the place of ion A, which passes into the solution, until an equilibrium is established corresponding to a given distribution of the two ions between the solid and the solution.

#### a Types of Ion Exchangers

Almost all solid mineral supports are oxides. They behave like ion exchangers when their surface bears electric charges. Two categories may be distinguished: (i) natural exchangers and (ii) amphoteric oxides.

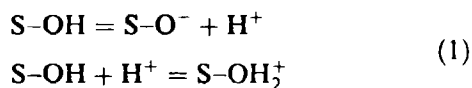
Natural exchangers are composed of a framework bearing electric charges neutralized by ions of opposite sign. For zeolites, for example, these charges are negative and are due to the particular environment of aluminum. Aluminum, just like silicon, is effectively situated in the center of a tetrahedron of four oxygen atoms, which provides it with four negative charges, whereas the aluminum itself has only three positive

charges. The tetrahedron ( $\text{AlO}_4$ ) is thus an overall bearer of a negative charge distributed over the oxygen atoms, and this charge is neutralized by the presence of various cations,  $\text{Na}^+$ ,  $\text{K}^+$ , etc.

These cations are not definitively linked to the framework but may be replaced by other cations during an ion-exchange operation. Whatever the exchange conditions, and in particular the pH, zeolites are cation exchangers and have a constant number of exchange sites, which is equal to the number of aluminum atoms in their framework.

There are natural ion exchangers other than zeolites. Clays and silicates are cation exchangers, whereas hydrotalcites are anion exchangers. As in the case of zeolites, the number of exchange sites is not pH dependent.

Oxide surfaces contacted with water are generally covered with hydroxy groups which can be schematically represented as  $\text{S-OH}$  where S stands for Al, Si, Ti, Fe etc. Some of these groups may behave as Brønsted acids, whereas other hydroxy groups may behave as Brønsted bases, giving rise to the following equations:



The resulting surface charge which arises from an excess of one type of charged site over the other, is a function of the solution pH. A given value of pH exists for which the particle is not charged overall. This value is characteristic of the oxide and is called the pristine point of zero charge (PPZC or simply ZPC) of the oxide. There is some variation in terminology in the literature in that ZPC sometimes means the isoelectric point (IEP) [14–16]. The ZPC values of oxides frequently used as catalyst supports have been reviewed by Parks [14] and Kung [15]. When oxide particles are suspended in aqueous solutions with  $\text{pH} > \text{ZPC}$ , the oxide particles tend to be negatively charged and to adsorb cations. Conversely, at  $\text{pH} < \text{ZPC}$ , anion adsorption is favored [16]. Reported values of the ZPC for  $\gamma$ -alumina range between 7 and 9, depending on thermal activation and impurities. This is illustrated in Fig. 3 which shows the variation of zeta potential as a function of pH for silica and alumina. Thus  $\gamma$ -alumina is amphoteric and may adsorb cations as well as anions. ZPC values for silica range between 1.5 and 3. Silica may only adsorb cations. It should be mentioned that cation adsorption is significant only above pH 7 [16, 17].

Many electrical double-layer and adsorption models have been proposed to account for experimental data dealing with the adsorption of ions on oxides. Stern suggested separation of the solution region near the surface into two parts, the first consisting of a layer of

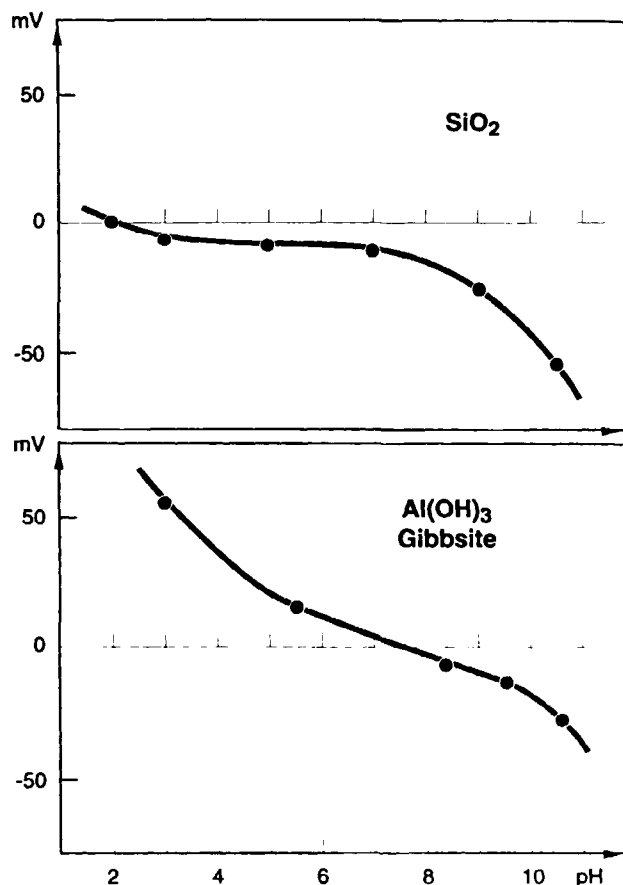


Figure 3. Variation of the zeta potential of silica and alumina (gibbsite) as a function of pH.

ions adsorbed at the surface (compact layer) and the second consisting of a diffuse Gouy layer [18]. More specifically the compact region can be structured as an inner Helmholtz plane (IHP) located at the surface of the layer of Stern adsorbed ions and an outer Helmholtz plane (OHP), located on the plane of centers of the next layer of ions [19, 20]. Specifically adsorbed ions are located in the IHP, whereas electrostatically adsorbed ions are located in the OHP (site binding models) [19, 21–26].

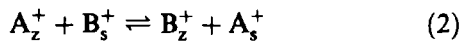
Assumptions underlying the adsorption models are not often discussed in the literature, since the exact nature of the relevant surface complexes or phases is difficult to identify. In particular, lateral interactions between adsorbed ions, site heterogeneity as well as phenomena involving the oxide dissolution or rehydration are not taken into account systematically. The latter phenomena are discussed in section D.d. Lateral interactions between adsorbed ions (ion coadsorption) have been reported [27, 28] and make questionable the use of mass action equations at interfaces. The effect of surface structure, site heterogeneity and surface composition, in particular on the ZPC value, were also pointed out [29, 30].

The adsorption of atomically dispersed ions generally allows for a much better dispersion of the active agent than does simple wetting without exchange [31–33]. Obviously, the high dispersions gained in the precursors have to be kept during the subsequent drying, calcination or reduction operations, which is frequently observed. For example, the metal dispersion on silica resulting from impregnating  $\text{Pt}(\text{NH}_3)_4\text{Cl}_2$  by ion exchange is excellent, even when the platinum loading reaches several weight percent, whereas incipient wetness impregnation with  $\text{H}_2\text{PtCl}_6$  solutions leads to the formation of large metal crystallites after reduction [34].

#### *b Elementary Background of Single Ion Exchange*

We have a single exchange when the solid-solution system makes only two ions intervene: ion  $\text{A}^+$  to be replaced on the solid Z, for instance a zeolite, by ion  $\text{B}^+$  present in the solution.

For the simple case of two monovalent cations, the exchange equilibrium can be written as



in which the subscripts S and Z represent the solution and the solid, respectively.

An exchange is characterized by an isothermal exchange curve representing the variation of the  $C_{\text{BZ}}$  concentration of ion  $\text{B}^+$  in the solid as a function of the  $C_{\text{BS}}$  concentration of  $\text{B}^+$  in the solution. The concentrations  $C_{\text{BZ}}$  and  $C_{\text{BS}}$  are expressed in ion-grams per unit of volume of the solid for the former and of the solution for the latter.

A simple equation between  $C_{\text{BZ}}$  and  $C_{\text{BS}}$  may be obtained by means of various simplifying assumptions. If we take the case of an ideal exchange (both the exchanger and the solution are ideal), and which has only a single category of site, the equilibrium constant  $K_a$  can be written as

$$K_a = \frac{C_{\text{BZ}}C_{\text{AS}}}{C_{\text{BS}}C_{\text{AZ}}} \quad (3)$$

with  $C_{\text{AZ}} + C_{\text{BZ}} = C_z$  and  $C_{\text{AS}} + C_{\text{BS}} = C_s$ .

With  $C_z$  and  $C_s$  being the total concentrations of cations in the solid and the solution respectively, it follows that

$$C_{\text{BZ}} = \frac{K_a C_z C_{\text{BS}}}{C_s + (K_a - 1)C_{\text{BS}}} \quad (4)$$

If the exchange is no longer ideal, eq 4 must be expressed in terms of concentrations and activity coefficients. The problem becomes even more complicated if the ions are not monovalent and if there are several types of sites on the solid surface. In such cases, often encountered in practice, theoretical predictions are no longer possible. It then becomes indispensable to have recourse to experiments to obtain isothermal

curves that can be used in predicting the number and conditions of successive exchanges required to replace a given fraction of ions A by ions B.

A simple and standard example of an exchange is that used to replace sodium ions in zeolite NaY by ammonium ions. Zeolite NaY, with the overall formula  $\text{Na}_2\text{O} \cdot \text{Al}_2\text{O}_3 \cdot 5\text{SiO}_2$ , contains 9.9 wt% sodium. Available isothermal exchange curves show that, at room temperature, only about 73% of the sodium ions can be exchanged and that, unless a very large volume of solution is used with an ammonium salt, a single exchange operation is not sufficient to eliminate all of the exchangeable sodium ions. To reach a high exchange degree, we thus adopt either a discontinuous technique, which involves several successive operations, or a continuous technique in which the exchange solution crosses the solid bed and is renewed by the progressive addition of fresh solution with the corresponding drain of the balanced solution.

#### *c Multiple or Competitive Ion Exchange Involving a Single Metal Ion*

This technique, which has been known for a long time with regard to anions [35, 36], was suggested for the first time with regard to cations by Benesi [37]. It proves to be particularly useful when trying to introduce and homogeneously distribute small amounts of a noble metal on a support with a large surface area. This situation is examined in detail by a simple example, that of introducing the ion  $\text{Pt}(\text{NH}_3)_4^{2+}$  by cation exchange into a zeolite  $\text{NH}_4\text{Y}$ .

##### *(i) Statement of the Problem*

In zeolite  $\text{NH}_4\text{Y}$ , about 73% of the ammonium ions are situated in large cavities and can be replaced by  $\text{Pt}(\text{NH}_3)_4^{2+}$  ions [38–40]. The saturation of all of these exchangeable sites corresponds to the fixing of more than 25 wt% of platinum in relation to the anhydrous zeolite. Yet, for obvious reasons of price, industrial catalysts must contain small amounts of noble metal, less than 1 wt% in relation to the zeolite, and the catalyst manufacturer will try to fix on the zeolite all the metal contained in the solution. This amount of metal contained thus represents 3–4% at the most of the exchangeable sites of the zeolite.

Let us consider a support composed of grains (beads, extrudates or others) several millimeters in diameter and containing a more or less large amount of zeolite Y (20–70 wt%, for example). After impregnation, question arises as to what is:

- the degree of metal fixation by the solid and hence, the residual quantity of metal ions in solution, and

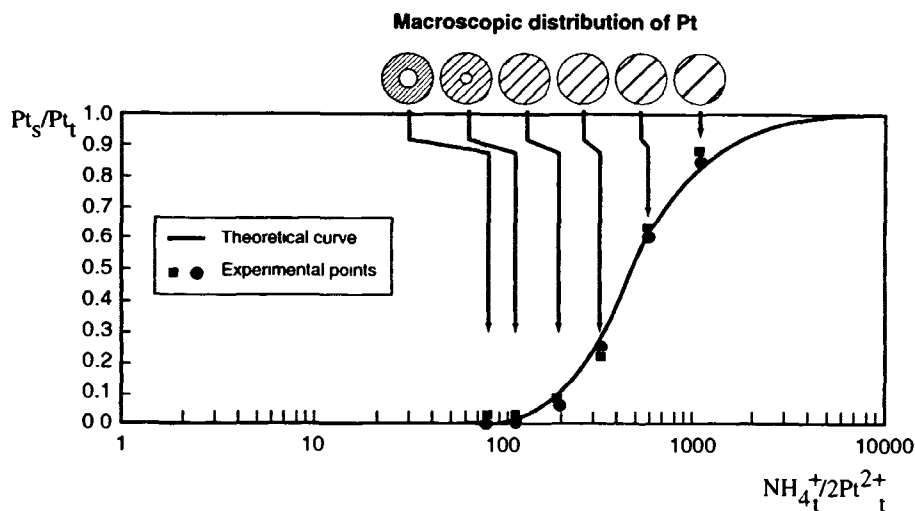
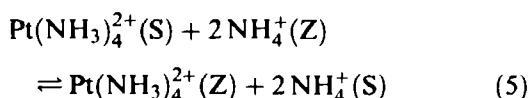


**Figure 4.** Residual fraction of Pt in the solution as a function of the  $\text{NH}_4^+_t \cdot 2 \text{Pt}^{2+}_t$  ratio of competition between  $\text{NH}_4^+$  and  $\text{Pt}^{2+}$  ions in the whole system.

- the macroscopic distribution of the metal inside the support.

The equilibrium between  $\text{NH}_4^+$  and  $\text{Pt}(\text{NH}_3)_4^{2+}$  ions is as follows:



The isothermal exchange curve between  $\text{NH}_4^+$  ions and  $\text{Pt}(\text{NH}_3)_4^{2+}$  suggests that zeolite Y has a strong affinity for the  $\text{Pt}(\text{NH}_3)_4^{2+}$  ion [39, 40]. Since the exchange velocity is limited by the diffusion inside the grain, tetrammine platinum ions will be quantitatively and strongly fixed on the first sites encountered, i.e. on the periphery of the grains. The concentration of the solution, which is almost the sole driving force behind the diffusion (adsorbed-phase diffusion may be neglected), will thus decrease rapidly. A state of pseudo-equilibrium is obtained which is characterized by a very heterogeneous metal deposit at the macroscopic scale (crust deposit) and which evolves only very slowly towards a state of true equilibrium corresponding to a homogeneous dispersion inside the volume of the grain [39, 40].

The only way of speeding up this evolution towards true equilibrium is to increase the amount of residual metal in solution  $\text{Pt}(\text{NH}_3)_4^{2+}(\text{S})$  or  $\text{Pt}_s$  (obviously while maintaining constant the total amount of platinum  $\text{Pt}_t = \text{Pt}_s + \text{Pt}_z$  in the system) so as to speed up diffusion. This result is obtained, as shown by Fig. 4, by adding an ionic agent, here  $\text{NH}_4^+$ , whose role is to make eq 5 regress towards the left, hence to increase  $\text{Pt}_s$ . Such ionic agents are called "competitors" and the resulting effect the "competition effect."

(ii) *Thermodynamic Aspect: Fixation Degree of Metal Ions on the Zeolite*

The thermodynamic constant of eq 5 can be written in terms of concentrations of the various ionic species:

$$K_a = \frac{[\text{Pt}]_z [\text{NH}_4]_s^2}{[\text{Pt}]_s [\text{NH}_4]_z^2} \quad (6)$$

If concentrations are replaced by the amounts of the corresponding ions in the system, for example  $[\text{Pt}]_z = \text{Pt}_z / V_z$ , eq 6 becomes

$$K_a = \frac{\text{Pt}_z (\text{NH}_4)_s^2}{\text{Pt}_s (\text{NH}_4)_z^2} \times \frac{V_z}{V_s} \quad (7)$$

where  $V_z$  and  $V_s$  are the volumes of the zeolite crystals and the solution, respectively. By replacing  $\text{Pt}_t$  by  $\text{Pt}_t - \text{Pt}_z$  and  $\text{NH}_{4s}$  by  $\text{NH}_{4t} - \text{NH}_{4z}$ , eq 7 becomes

$$K_a = \frac{\text{Pt}_z}{(\text{Pt}_t - \text{Pt}_z)} \times \left( \frac{\text{NH}_{4t} - \text{NH}_{4z}}{\text{NH}_{4z}} \right)^2 \times \frac{V_z}{V_s} \quad (8)$$

where  $\text{NH}_{4t}$  is the total amount of ammonium ions in the system.

If  $\text{Pt}_t$  is small compared to the total number  $N_z$  of exchangeable sites of the zeolite, we can write  $\text{NH}_{4z} \approx N_z$ . We can thus express the variation of the fraction of Pt fixed on the zeolite as a function of the total amount  $\text{NH}_{4t}$  of the competing ion:

$$\frac{\text{Pt}_z}{\text{Pt}_t} \approx \frac{1}{K_a} \times \frac{V_z}{V_s} \left( \frac{\text{NH}_{4t}}{N_z} - 1 \right)^2 + 1 \quad (9)$$

It can thus be seen that the value of the fixation level  $\text{Pt}_z/\text{Pt}_t$  can be adjusted to the desired value by adjusting the total amounts of the competing ammonium ion  $\text{NH}_{4t}$  in the system.

*(iii) Practical Aspects*

The importance of the competition technique lies in the possibility of speeding up the impregnation kinetics and of reaching, within a reasonable length of time, a homogeneous macroscopic distribution of the metal on the support. This is particularly important when the catalyst grains are larger than several millimeters, as would be the case of a Y zeolite-based catalyst in the form of cylindrical pellets about 3 mm in diameter and 2 mm long. In the absence of  $\text{NH}_4^+$  ions in the initial solution, the platinum is distributed in a peripheral crown about 0.5 mm thick. Castaing's microprobe shows that, inside this crown, the platinum concentration diminishes strongly from the outside to the inside. The choice of proper amount of  $\text{NH}_4^+$  ions per  $\text{Pt}^{2+}$  ion in the system must leave less than 5% of the initial platinum in equilibrium in the final solution, but it must also bring about a quasihomogeneous distribution of the metal within a few hours. Proper stirring of the medium is beneficial for the operation. In the absence of stirring, the kinetics is actually limited by diffusion in the bed of solid grains at the bottom of the recipient and of the boundary layer surrounding each grain.

The advantage of the competitive exchange technique is obviously much less evident when the zeolite is exchanged in the form of a fine powder. If no competition is used, various precautions must be strictly respected:

- very effective stirring of the powder;
- progressive addition of the metal ion to the solution (for about an hour);
- an exchange duration longer than or equal to about 5 hours.

Slight competition also speeds up the operation appreciably.

**C Impregnation without Precursor–Support Interaction**

Such techniques consist of introducing, into the pore space of a support, a solution of an inert precursor, i.e. one that does not interact with the solid surface. In principle, the precursor thus remains in the dissolved state in the solution and does not become fixed on the surface at this stage of preparation.

Two cases can be distinguished, depending on whether the pore space of the support contains only ambient air at the start or whether it is already filled by the solvent from the impregnation solution (usually water) or by another liquid. Impregnation is said to be capillary in the former case and diffusional in the latter.

*a Capillary Impregnation*

The operation consists of putting into contact with the previously dried support, with a pore volume  $V_p$ , a

volume  $V$  of solution containing the precursor selected [41, 42]. In almost all cases,  $V = V_p$ , so that at the end of the operation no excess solution remains outside of the pore space. This is called dry impregnation.

Capillary impregnation is mainly characterized by its exothermicity, by the capillary pressures developed in pores and by the speed with which the pore space is filled.

*(i) Exothermicity*

The replacement of the solid–gas interface by a solid–liquid interface generally causes a considerable decrease in the free enthalpy of the system. This causes a strong release of heat, which often has little effect on the quality of the impregnation, except in the following specific cases:

- The precursor has retrograde solubility and its concentration is about the same as the saturation.
- In a solution containing an unstable mixture of several metal precursors, the temperature rise risks causing the precipitation of a mixed compound poorly distributed on the surface.
- The impregnation solution is aggressive with regard to the support (very acid pH, for example), and an attack of the support surface may then occur, with accelerated alteration of its surface properties.

Solutions exist for avoiding these disadvantages, such as:

- Deactivation of the support by means of superheated steam to form a liquid surface film.
- Stabilization of the precursor(s), for example by complex formation.

*(ii) Pressures Developed in Pores upon Impregnation*

As soon as the support is placed in contact with the solution, the solution is sucked up by the pores [43–48]. Part of the air present in the pore space will be imprisoned and compressed under the effect of capillary forces. The pressures developed inside the imprisoned gas bubbles depend on the radii  $r$  of the curve of the liquid–gas menisci and may reach several MPa (or tens of bar) when  $r < 100$  nm, as a result of the Young–Laplace law:

$$\Delta P = P - P' = \frac{2\gamma}{r} \quad (10)$$

where  $\gamma$  is the liquid–gas interfacial tension.

Considerable forces will thus be exerted on the portions of the pore walls in contact with these bubbles. The walls that are not strong enough will break down,

causing a degradation of the mechanical properties, sometimes even bursting the catalyst grains.

The development of high pressures is a transitory phenomenon. When highly compressed, air becomes dissolved and progressively escapes from the solid. The filling of the pore space is thus far from being instantaneous.

Methods exist for preventing or limiting the bursting of the support upon impregnation, such as operating in vacuum and adding a surfactant to the solution.

### (iii) Capillary Impregnation Rate

Oversimplified calculations show that the time taken by the liquid to fill up the pores is of the order of a few seconds [49–53]. In reality, however, determination of impregnation time must take into consideration the imprisonment of air within the porosity and the elimination of this occluded air [48]. The impregnation process will be limited by the dissolution of the imprisoned and compressed air and its migration to the outside of the grain. The Young–Laplace law (eq 10) shows that the last bubbles to disappear are those present in the largest pores, because they are subjected to the lowest pressures.

### b Diffusional Impregnation

If the pore space of the support is filled with the same solvent as the impregnation solution, prior to being placed in contact with the latter, the characteristics defined above are valid only for the first phase of saturation by the solvent.

The second phase is generally an immersion phase that consists of plunging the solvent-saturated support into the impregnation solution. This second phase is no longer exothermic and does not cause the development of high pressures inside the pore space. The precursor salt migrates progressively from the solution into the heart of the grains of the support. The driving force at all times is the concentration gradient between the extragranular solution and the advancement front of the soluble precursor in the intragranular solution. The migration time is obviously much longer than for capillary impregnation.

The principle of diffusional impregnation is much simpler than when a precursor–support interaction occurs. Two cases may be distinguished:

- (i) when the concentration of the solution outside the grains remains constant;
- (ii) when this concentration varies from the start to the end of the diffusion process.

The first case has been dealt with by various authors [54–59]. Weisz [56] defines a relaxation time constant  $\tau$  for the system, which is representative of the time re-

quired to be very close to equilibrium (reaching uniform concentration theoretically requires an infinite time):

$$\tau = \frac{R^2}{D} \quad (11)$$

where  $R$  is a length parameter depending on the volume geometry ( $R$  is the radius in the case of a sphere or an extrudate) and  $D$  is the diffusion coefficient of the precursor in the solvent.

When volume  $V$  is occupied by a porous solid, eq 11 is generally made to include a tortuosity coefficient  $\beta$ , the pore fraction  $\varepsilon$  (fraction of the support grain volume occupied by the pore space) and an interaction coefficient  $K$  between the precursor and the support ( $K = 1$  if there is no interaction):

$$\tau = \frac{R^2}{D} \times \frac{\beta}{\varepsilon} \times K = \frac{R^2}{D_{\text{eff}}} \quad (12)$$

where  $D_{\text{eff}} = \varepsilon D / \beta K$  is the effective or apparent diffusion coefficient of the solute in the porous solid.

The values of  $\beta$  are generally between 1.3 and 10, more often between 2 and 6 (values determined from various gases [60]). The values of  $\varepsilon$  are mostly between 0.3 and 0.7 [60]. The values of  $D$  in the liquid phases are generally about  $10^{-5} \text{ cm}^2 \text{ s}^{-1}$  [55–60].

As an example, consider a support made up of beads with radius  $R = 2 \text{ mm}$ , and assume that  $K = 1$ ,  $D = 10^{-5} \text{ cm}^2 \text{ s}^{-1}$  and  $\varepsilon = 0.5$ . Time  $\tau$  calculated from eq 11 is:

$$\begin{aligned} \text{if } \beta &= 1.3, & \tau &\approx 3 \text{ h} \\ \text{if } \beta &= 5, & \tau &\approx 12 \text{ h} \end{aligned}$$

Since the value of  $\tau$  is proportional to the square of the radius, it can be appreciably reduced by diminishing the size of the particles. Thus with beads having a radius of 1 to 0.5 mm, the above values are divided by 4 and 16, respectively.

Diffusional impregnation is almost never used for preparing catalysts when there is no appreciable interaction between the precursor and the support.

## D Role of the Support During the Preparation Steps

Supported transition metal ions (TMI) which often are catalytic sites can also be used to probe the role of the support, via their own interaction with the latter. Because of their partly filled d orbitals, any change in their first coordination sphere immediately affects their optical and magnetic properties and can thus be detected by spectroscopy. In the context of interfacial coordination chemistry [12, 61], the approach has been to use transition metal complexes in aqueous solutions and to investigate the changes, occurring at the liquid–solid interface during deposition, in the interaction between the TMI engaged in the complex and the support.



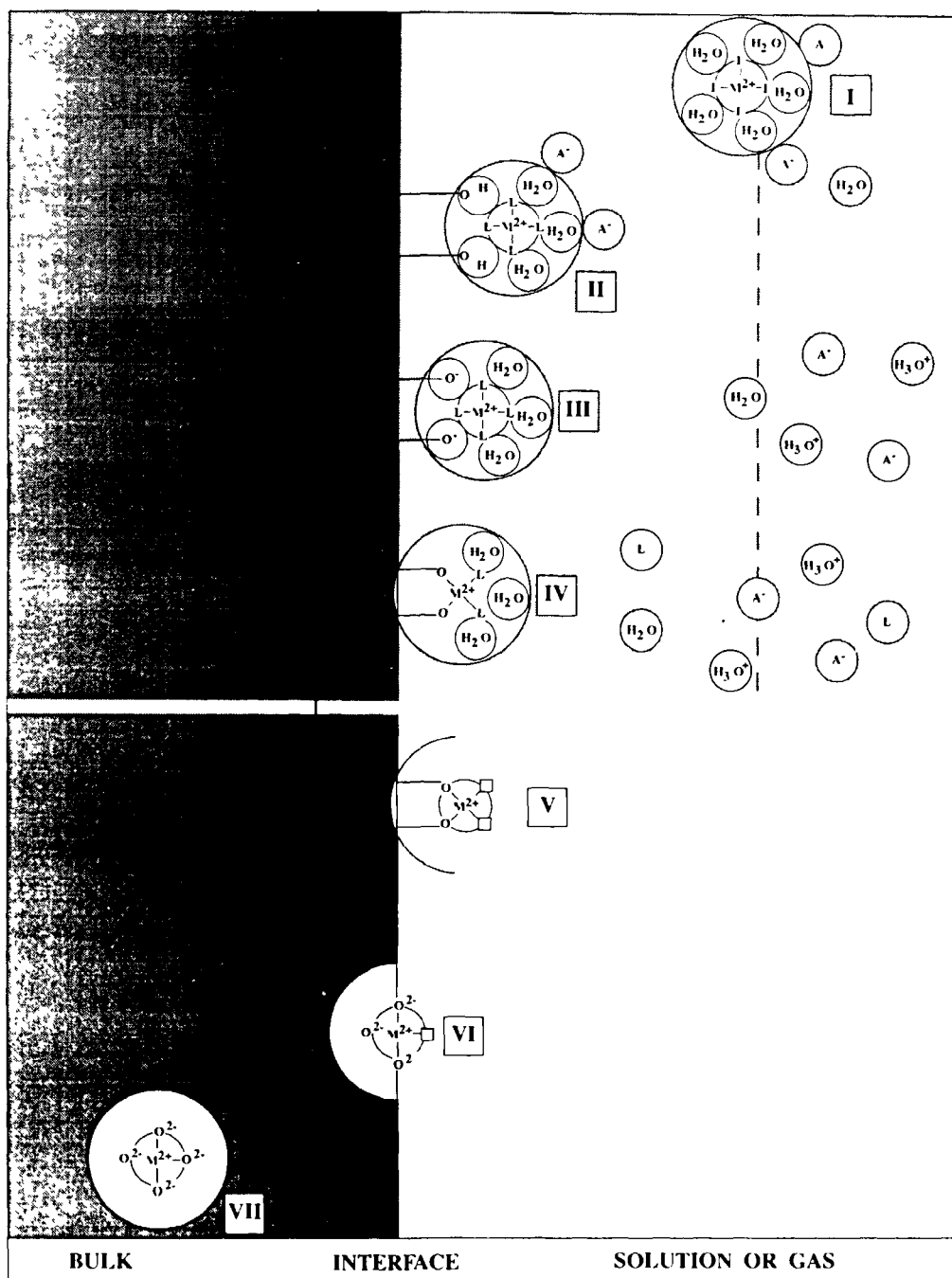


**Figure 5.** Interaction models between a TMI of a precursor complex and an oxide support (top) liquid; (bottom) gas. The left- and right-hand sides represent the solid oxide and fluid phase respectively. The vertical dotted lines represent the width of the interface, as explained in Ref 12.

By a careful control of the preparation parameters, it is possible to obtain the TMI successively in solution (Fig. 5, model I), on the surface in extraframework position (models II–V), then in the surface in framework position (model VI), to finally reach the bulk of the oxide (model VII). Models II–IV are pertinent to the deposition of the active component precursor.

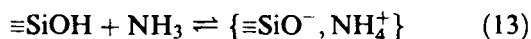
#### *a Physical Nature of the Oxide Surface*

When complexes involving TMI are put in microcontainers, such as the pores of amorphous solids or in the cavities of zeolites, their coordination chemistry is basically not changed and model I (Fig. 5) is applicable.

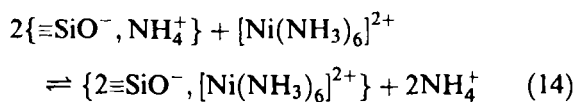
For pHs where surface functions are essentially OH groups, the oxide is able to enter the outer sphere of solvation of the complex in the same way as the solvent molecules (Fig. 5, model I) and thus acts as a solid solvent (Fig. 5, model II). When ligands have electro-negative donor atoms (N, O, Cl, F), there can be some hydrogen bonds (model II, assuming  $L = \text{NH}_3, \text{H}_2\text{O}$ ) between the ligands and the OH or/and oxygen ions of the oxide [62]. This aspect, which is little documented, is different from that encountered in zeolites which can act as solid ionic solvents [63] or in solvent oxides where TMIs come to rest after high temperature diffusion to form doped or mixed oxides (Fig. 5, model VII) [64].

#### b Oxide Surface as a Counter Ion

The role of the support has been studied further, essentially by diffuse reflectance spectroscopy, in the case of the Ni/SiO<sub>2</sub> system prepared by the competitive cation exchange method using nickel nitrate in water-ammonia solutions [12, 65]. In this method, the silica surface is first contacted with an ammonia solution at a pH above the ZPC of silica, leading to a negatively charged surface (subsection B.a):



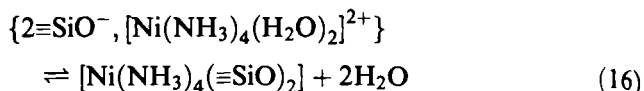
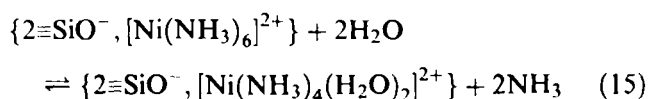
Upon contact of silica with a nickel nitrate ammoniacal solution, one observes that the purple blue colour, characteristic of nickel hexaammine  $[\text{Ni}(\text{NH}_3)_6]^{2+}$ , is transferred from the solution to the silica support, while the diffuse reflectance of the resulting wet powder is the same as that of the initial solution. These phenomena can be explained in terms of the following competitive cation exchange, where ammonium ions compete with nickel hexaammine complexes to occupy the  $\equiv\text{SiO}^-$  exchange sites of silica:



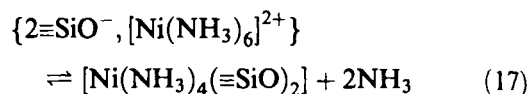
Reaction 14 shows an ion pair is formed with the oxide surface acting as a supramolecular counterion to which the TMI is bonded by ligand-screened electrostatic adsorption (Fig. 5, model III).

#### c From Electrostatic Adsorption to Grafting: the Oxide Surface as a Supramolecular Ligand

Upon washing with ammonia solutions, in conditions of pH and NH<sub>3</sub> concentration corresponding to the stability range of the complex  $[\text{Ni}(\text{NH}_3)_4(\text{H}_2\text{O})_2]^{2+}$ , it is suggested that grafting occurs via substitution of two NH<sub>3</sub> molecules by two surface  $\equiv\text{SiO}^-$  ligands according to the successive reactions



The intermediate tetraammine complex has not been detected so far and the actual process can in fact be written as the sum of the two preceding reactions as follows:



It appears that the ligand exchange NH<sub>3</sub>/H<sub>2</sub>O in the initial hexaammine complex weakens the coordination sphere making grafting possible via two surface bonds (Fig. 5, model IV), with formation of a neutral *cis*-octahedral complex. It is important to note that the oxide, entering into the coordination sphere of Ni<sup>2+</sup>, becomes a supramolecular bidentate ligand via vicinal  $\equiv\text{SiO}^-$  groups. The latter have been found to be the most probable grafting sites, on the basis of geometrical considerations [12, 65] and by analogy with silicate structure [66]. This also has been confirmed by EXAFS studies [67].

The chelating effect of the surface appears to be the driving force for the formation of the surface *cis*-octahedral complex. Equation 17, which is the sum of eqs 15 and 16, is accompanied by an entropy increase with the release of water molecules and the disappearance of charged species leading to a subsequent disordering of nearby solvent molecules. This aspect is well documented in solution coordination chemistry [68, 69].

Once TMI coming from complexes of the liquid phase (Fig. 5, model I) become bonded to the oxide surface (Fig. 5, model IV), they can remain attached to the support even though the liquid phase is eliminated and the remaining gas-solid system (Fig. 5, model V) heated at higher temperatures. It is then possible to produce vacant coordination sites. The reactivity of such sites towards ligand addition or substitution is the driving force for adsorption and catalysis. This constitutes one of the major differences with coordination compounds in solution [61].

Often, the active oxide forms oligomeric/polymeric species, a monolayer or tridimensional oxide particles, with the surface acting as a ligand. In some other cases, intermediate compounds or solid solutions are formed when the support becomes a reactant. This aspect is considered next.

#### d Support as a Chemical Reactant

The impregnations with or without interaction and the ion exchange techniques described in the previous sections involve bringing oxide surfaces in contact with aqueous solutions. The oxide-water system is thermo-

dynamically metastable and evolves slowly towards the oxide precursor, namely the hydrous oxide or hydroxide. Thus, a realistic description of oxide-water interfaces should take into account two phenomena, the oxide rehydration and the oxide dissolution.

On exposure to water, an anhydrous oxide can become hydrated by physical adsorption of water molecules without dissociation, dissociative chemisorption of water leading to new hydroxy groups, and finally to the formation of superficial oxyhydroxide or hydroxide, such as for MgO [14]. When silica groups are exposed to water for an extended time, their hydroxylation produces polymeric chains of  $-\text{Si}(\text{OH})_2-\text{O}-\text{Si}(\text{OH})_2-\text{OH}$  groups which can link up to form three-dimensional silica gel networks. Around 2 nm thick silica gel layers have been observed on silica surfaces prepared by evaporation of silica on mica which were exposed to humid air [70]. Thus, it may be postulated that surface groups are present not only in a two-dimensional oxide-liquid interface, but also in a bulk phase of finite thickness extending from the surface into the interior of the solid [71].

However, oxide dissolution has often been reported, in particular when impregnations were conducted far from the ZPC of the oxide, which is also the point of minimum solubility of the solid [72]. It is known that alumina dissolves in highly acidic impregnation solutions and that a fraction of dissolved aluminum may be re-adsorbed during impregnation or drying. Such an effect has been reported during the preparation of alumina-supported platinum [16, 73–76], nickel [77] or palladium [78] catalysts. Silica solubility is constant from pH 2–8, then increases very rapidly in basic medium [16]. For pH 9–10.7 amorphous silica is in equilibrium with the neutral  $\text{Si}(\text{OH})_4$  monomers as well as silicate ions. Above pH 10.7 silica dissolves to form soluble silicates [17]. Silica dissolution in basic media creates new hydroxy groups and hence new sites with chemical affinity for cations, which may explain the observed sharp increase of cation adsorption on silica at pH higher than 10.5 [79, 80].

Interestingly, impurities such as aluminum, calcium, magnesium or zinc were reported to reduce both the rate of dissolution and the solubility of silica at equilibrium. Nitric acid-cleaned silica was immersed in solutions of Al, Be, Fe, Ga or Gd ions at pH from 2 to 9. A drastic reduction of the solubility of silica was observed. In particular, the introduction of Al ions rendered silica insoluble at pH 9. This effect was attributed to the formation of a monolayer of insoluble silicate which lowered the silica solubility to that of the surface compound [17]. Seemingly, silicates involving metal ions are formed even at pH values apparently non-aggressive for silica. However, the amount of metal silicate is not specified and the formation of only a silicate monolayer is purely speculative.

Recently, the formation of layer-type silicates was demonstrated during the impregnation of silica with ammine  $\text{Ni}^{\text{II}}$  ions in the 8–9 pH range [80]. No epitaxy could be identified between the phyllosilicates and the carrier, inferring a monolayer description. This observation is consistent with experiments indicating the weathering at 100 °C of pyrex vessels by aqueous solutions containing  $\text{Ni}^{\text{II}}$  or  $\text{Mg}^{\text{II}}$  salts, leading to the formation of antigorite-type silicates [81, 82]. Likewise, the formation of hydrotalcite-type coprecipitates involving Al ions extracted from the support was observed during impregnation of  $\gamma$ -alumina with  $\text{Ni}^{\text{II}}$ ,  $\text{Co}^{\text{II}}$  and  $\text{Zn}^{\text{II}}$  ions under mild conditions, i.e. pH close to the ZPC, ambient temperature and reasonable contact times [83, 84]. Anions whose presence was required for the electroneutrality of the hydrotalcite-like structures were adsorbed simultaneously with the metal cations. Thus, the oxide supports should not be considered systematically as inert even during impregnations conducted at pH close to the isoelectric point.

The extent of phenomena such as coprecipitate formation during the preparation of industrial catalysts, i.e. during unit operations such as impregnation, separation, aging or ripening, and drying, needs to be investigated in detail. Spectroscopies allowing coprecipitate determination at the oxide-liquid interface, such as IR, Raman or XAS, should be used for systematic investigations of the role of parameters such as pH, ionic strength, or contact time. It should be realized that there is no need for significant solubility of the support for the formation of surface compounds. The dissolution of the support may be driven by a subsequent coprecipitation with metal ions. Nevertheless, gel-mediated pathways involving the diffusion of metal cations and anions through a hydrous gel layer, by analogy with phenomena occurring during the natural weathering of soils, cannot be excluded [85, 86].

As shown above, the oxide support may play several different roles and those may occur separately or simultaneously, depending on the preparation method [87].

## E Applications

The pertinent key parameters which may influence the interaction of a transition metal complex with an oxide support are first briefly discussed, before examples of important applications of ion exchange and impregnation are given.

### *a Key Experimental Parameters*

When dealing with metal complexes in solution and a preformed support, the main problem is to know how to control the interaction (physical or chemical) between the complexes and the support. The discussion

above distinguishes five main parameters, which can create or influence the strength of this interaction.

(i) *Isoelectric Point (IEP) of the Oxide Support: Influence of Temperature, Impurities and Selective Doping*

This is an essential parameter with which to initiate the electrostatic interaction between the metal complex and the oxide support. A number of papers have been devoted to the problem of regulating the IEP of oxides and the concentration of the charged surface groups. Two methods have been developed. The first one involves the change of temperature of the impregnating solution and the second involves the selective doping of the support surface with various types of ions [88]. Different behaviors were observed depending upon the support. For instance, the IEPs of  $\gamma\text{-Al}_2\text{O}_3$  and  $\text{TiO}_2$  were found to increase upon increasing the temperature of the impregnating solution, in contrast to that of  $\text{SiO}_2$  which was found to decrease. Selective doping of  $\gamma\text{-Al}_2\text{O}_3$  by very small amounts of  $\text{Na}^+$  ions brought about an abrupt increase of IEP, whereas doping with  $\text{F}^-$  ions caused a shift to lower IEP values. It should be mentioned that the selective doping method cannot be applied when the dopant leads to catalyst deactivation.

(ii) *Cationic and Anionic Metal Complexes*

Metal complexes may exist in essentially two forms: cationic and anionic. Neutral complexes, such as  $\text{Co}(\text{NH}_3)_3\text{Cl}_3$ , exist but are relatively rare and would not lead to an electrostatic interaction which requires entities (oxide surface and complex) of opposite charges. In an earlier review, Brunelle [16] gathered the complexes of metals belonging to Groups 7–11, most frequently used in supported catalysts preparation.

(iii) *Solution pH*

The pH appears to be a very versatile and important parameter in the preparation process with which to achieve the desired ion–support interaction. It is worth noting that it influences separately or simultaneously the liquid or/and solid part of the interface.

Qualitatively, the pH allows the sign of the surface charge to be selected as shown by Fig. 3. On the liquid side, it also determines the nature and nuclearity of the complex. For instance, upon decreasing the pH from 14, complexes change from hexaammine to hexa-aquametal (III) for many transition metals or from mononuclear  $\text{MoO}_4^{2-}$  to polynuclear  $\text{Mo}_8\text{O}_{26}^{4-}$  [89]. Finally, it controls the solubility of the oxide support. The dissolution of the latter is all the more important as the pH of the solution departs from the IEP [16].

Quantitatively, the pH determines on the solid side the value of the zeta potential related to the concentration of charged surface sites (Fig. 3). On the liquid side, it allows selection of the most abundant metal

complex from those coexisting at the same pH. Finally, it controls the amount of monomer produced in the solution upon oxide support dissolution [16].

Having emphasized the importance of the pH parameter, it should be recognized that its measurement is in itself a difficult task [90]. When the surface is charged, the overall ion concentrations are not constant close to the oxide–fluid interface. For instance, above the IEP, i.e. for negatively charged surfaces, there is an increase in cation and proton concentrations at the surface. Therefore, the pH is lower than in the bulk of the solution. The situation is reversed at a pH lower than the IEP. This is a typical compensation effect of the pH.

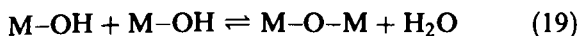
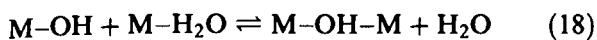
In colloidal solutions the measurement of the pH is always delicate, since it depends on the average distance between the oxide particles and the pH electrode. This explains why the latter is a function of the stirring rate of the solution. The best measure is the value obtained without stirring, the solid being far from the electrode and deposited at the bottom of the flask (a centrifugation is sometimes necessary). This measure can be considered as the pH of the bulk solution. This latter value, combined with the characteristics of the solution and the IEP of the oxide, allows calculation of the pH profile from the theory developed by Davis et al. [19]. Devices based on fiber-optic sensors [91] are being developed which might help resolve the difficult problem of the determination of pH of oxides in suspension.

(iv) *Ligand Nature*

The ligand type greatly affects both the nature and strength of the metal complex–surface interaction. Several structural and electronic aspects have to be considered for each ligand:

- The type of ligand (neutral molecules or anions) determines the charge of the transition metal complex and hence the conditions such as support nature and pH range, for which ion exchange can occur.
- The bulkiness of the ligand will tend to screen and decrease the electrostatic interaction between the charged surface and the transition metal complex [62].
- When the ligand possesses an appropriate element, such as nitrogen, oxygen or hydrogen, there is a possibility of forming hydrogen bonds with the surface via S–OH groups [62].
- The polydentate nature of the ligand, whether it be the solution mobile ligand such as ethylenediamine, or the rigid surface ( $=\text{SiO}$ )<sub>2</sub>, has a strong entropy effect on the stability of either the initial solution complex or the final grafted complex [61].
- Under conditions where oxide dissolution takes place, the monomers released in solution can react with the molecular species of the precursor compo-

ment and M–O–M bonds can be formed via olation and oxolation reactions:



where M is either the metal cation of the support monomer or of the metal complex. The result is that intermediate surface compounds are observed (see subsection D.d) [12, 92]. It is important to note that reactions 18 and 19 can take place because both OH and O are bridging ligands. By contrast, when the ligands of the metal complexes of the precursor component are nonbridging, such as ammonia or ethylenediamine, reactions (18) and (19) cannot occur and isolated grafted complexes are favored.

The understanding of what type of ligand the surface can be identified with, is an important aspect which has some practical consequences. It is well known for instance, that the standard redox potential of TMI can be largely modified depending upon the nature of its surrounding ligands [93]. It is thus expected that different supports will lead, for a given TMI, to different standard redox potentials.

#### (v) Competitive Ions

From a practical point of view, the reversibility of adsorption by means of competing ions, as shown by equilibria such as 5 and 14, is very important because it leads to a redistribution of the adsorbed metal complex ions among the charged surface sites, as discussed in subsection B.c. Competitive ions achieve a homogeneous deposition not only on the support surface but also, when pellets are used, throughout the catalyst grain volume [47]. In the latter case, it is possible to control [47, 94, 95] and to model [9] the exchange process and the distribution profile of the active phase along the radius of the grain as a function of time. Some important industrial applications are presented in section E.b.

#### (vi) Washing

It is known that washing has to be avoided after the component precursor has been deposited by impregnation. When other deposition methods are involved, the washing step has been reported to have various effects.

The fundamental aspects of washing have not been much studied in the past, although washing can have important consequences. The first is electrostatic in nature and refers to the oxide support as a charged surface (see subsection D.b). Washing can be accompanied by pH changes so that the surface and the adsorbed species can acquire charges of opposite sign, leading to repulsions [96]. The second consequence rests on the ligand nature of the surface. Here the pH changes accompanying washing may lead to grafting of

the component precursor and this aspect has been discussed in section D.c [65]. Yet another consequence of washing is connected with the role of reactant of the oxide support. The oxide dissolution will eventually lead to intermediate compound formation at the surface of the oxide support [80, 92].

### b Application Examples

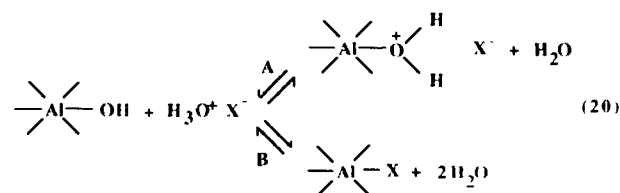
#### (i) Preparation of Monometallic Reforming Catalysts

Most conventional reforming catalysts are based on well-dispersed platinum on an alumina promoted by a halogen, usually chlorine. The two main alumina supports used are the two transition aluminas  $\eta$ - and, principally,  $\gamma$ - $\text{Al}_2\text{O}_3$  [75].

The deposition of platinum on alumina is usually carried out by immersing the alumina in an aqueous solution of chloroplatinic acid and hydrochloric acid as a competing agent [34, 75].

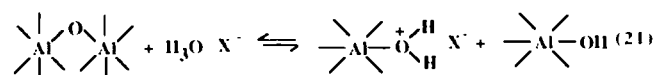
#### a Interactions Between Acid Solutions and the Surface of Alumina

Hydroxy groups present at the surface of a transition alumina behave like bases with respect to the protons of the acids [16, 97]. According to various authors, the reaction is represented by two different mechanisms A and B in eq 20.



In mechanism A, the OH group is protonated and its interaction with the anion is electrostatic [16, 19, 98–101]. In mechanism B [9, 13, 94, 100, 102, 103], the X<sup>-</sup> anion replaces the OH<sup>-</sup> group in the complexation sphere of the surface aluminum. Mechanism A is expected to predominate since the surface of the transition aluminas is mainly covered with OH groups [104–107], in presence of water.

Protonation of an oxygen atom of the surface can also occur and lead to the scission of an Al–O bond, according to reaction 21.



According to reactions 20A and 21,  $\text{Al}_2\text{O}_3$  behaves like an anion exchanger. The maximum quantity of anions that the surface can fix, or the anion exchange capacity, is related directly to the number of protonated OH

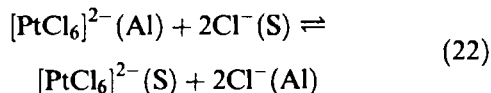
groups [16, 19, 98, 100, 108]. Logically, it depends on the equilibrium constant of reaction 20A. It rises as the pH of the aqueous solution decreases [16, 19, 98, 100, 108, 109]. The process of anion fixation on the surface is kinetically very fast [99], and rarely limits the overall kinetics. The rate limiting step is expected to be the diffusion of the ionic species in the pores of the alumina particle.

### b Platinum Deposition

The maximum amount of platinum fixed on alumina from  $\text{H}_2\text{PtCl}_6$  acid, without any significant attack of the support, differs widely according to various authors [16, 34, 35, 73, 95, 108, 110], varying between 2 and about 8 wt%. Most of the values obtained at saturation of  $\gamma$ -aluminas with surface areas ranging between 150 and  $250\text{ m}^2\text{ g}^{-1}$  are normally between 2 and about 4 wt% [16, 34, 95, 110]. The platinum content of industrial catalysts is much lower, varying between 0.2 and 0.6 wt%.

Many authors have observed a strong interaction between the chlorinated complex of platinum,  $\text{H}_2\text{PtCl}_6$ , and  $\gamma\text{-Al}_2\text{O}_3$  [16, 34–36, 94, 95, 111]. At impregnation conditions approaching those used for the preparation of reforming catalysts (i.e. small amounts of platinum, generally less than 0.6 wt% of platinum with respect to the support, and low pH, hence high anion exchange capacity), platinum tends to be fixed rapidly and strongly on the first sites encountered. This risk of a heterogeneous macroscopic distribution of platinum on the surface is similar to that described above in the case of the zeolite  $\text{NH}_4\text{Y}$  with  $\text{Pt}(\text{NH}_3)_4^{2+}$  cation.

To obtain homogeneously distributed platinum on alumina, it is necessary to add a competitor ion to the solution. The usual competitor is HCl [34, 47, 112] whose role is to act on the equilibrium between the platinum precursor in the solution S and that fixed on the alumina support Al according to the reaction



The quantity of  $\text{Cl}^-$  ions added to the system is usually adjusted to leave a sufficient quantity of  $[\text{PtCl}_6]^{2-}$  in the aqueous solution to ensure easy migration to the center of the grain so that, at the end of the operation, this residual nonadsorbed amount is only a small fraction of the total quantity of platinum involved.

The chemical phenomena in this case are more complicated than in competitive cation exchange on  $\text{NH}_4\text{Y}$  zeolite. HCl acts not only as a competitor but also as a stabilizing agent for the coordination sphere of platinum. It has been shown [113, 114] that the  $[\text{PtCl}_6]^{2-}$  anion can lose two to four chloride ligands after a few hours in the absence of hydrochloric acid.

Another level of complexity is caused by the chemical reactivity of the alumina surface, which can be altered in an acidic medium.

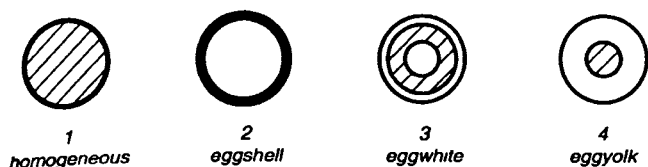
### c Chemical Alteration of Alumina

In an acidic media, simultaneously with the protonation reaction 20A of the OH groups, a process of attack and dissolution of the support also occurs [16, 31, 47, 101, 108, 111, 115]. This process occurs below about pH 4, and the solubility of the support rises rapidly with decreasing pH. Reaction 21 probably represents the first step of the formation of soluble compounds of the type  $[\text{Al}(\text{H}_2\text{O})_y(\text{OH})_x]^{(3-x)+}$  with  $x + y = 6$ . This is expected to occur only after reaction 20A is complete. Several experimental observations [31] support these considerations. If alumina beads are placed in contact with an HCl solution, the following sequence of events occurs: a rapid fixation of the  $\text{Cl}^-$  anion, probably due to reaction 20A; a subsequent slowdown of this fixation; a decrease in the quantity of chloride fixed probably due to the progressive dissolution of the external part of the alumina particle (reaction 21), where the pH is the lowest; and finally a slow fixation of the  $\text{Cl}^-$  anion. If the initial quantity of acid used is small (less than 4–5 wt% Cl), the final event (the slow chloride fixation) resumes after several minutes [31]. This happens because the situation at the particle scale is still far from equilibrium – the pH in the external solution is low but higher in the internal solution near the center of the particle. The pH progressively evolves toward equilibrium, which corresponds to a pH slightly higher than 3. At such a pH, chlorinated aluminum species, which were solubilized at the lower pH during the beginning of the reaction, will be redeposited on the support. Note that, at the concentrations used for the preparation of monometallic reforming catalysts, the solubility of  $\gamma\text{-Al}_2\text{O}_3$  is very low (no more than a few hundred ppm).

#### (ii) Metal Concentration Profiles in Supports

For deposition of chloroplatinic acid on alumina, competitors other than HCl can be used [36, 94, 95, 111, 112, 116–123]. Acids such as  $\text{HNO}_3$  and  $\text{H}_2\text{SO}_4$  are usually more effective than the corresponding salts, such as ammonium, aluminum and sodium nitrates [36]. Nitric acid is about five times more effective than acetic acid [120]. Hydrofluoric acid has a much stronger interaction with alumina than chloroplatinic acid [112] – HF blocks the alumina sites inhibiting the adsorption of the  $[\text{PtCl}_6]^{2-}$  anions. Among the other competitors used are  $\text{CO}_2$  [119], phosphoric acid [117, 118], organic acids such as formic, oxalic, propionic, lactic, salicylic, tartaric and citric acids [94, 116–118, 121–123], miscellaneous salts such as alkaline phosphate [95], alkaline halogenides [95, 118], alkaline benzoate [95], and amines such as monoethanolamine [94].

Precursor = metallic complex MC, competitor A



- 1 roughly same affinities of MC and A
- 2 high affinity of MC; no competition
- 3 high affinity of A, low affinity of MC, low A/MC ratio
- 4 high affinity of A, low affinity of MC, high A/MC ratio

**Figure 6.** The four main categories of macroscopic distribution of a metal within a support. A/MC is the ratio representing competition (with a proportionality factor depending upon the valence of the ions).

Some of these competitors, such as monoethanolamine, really act not by a competition effect on adsorption, but rather by a pH effect [94]. In fact a rise in the pH tends to lower the exchange capacity of alumina, causing a more uniform occupation of the surface by the metallic complex.

Careful selection of metal precursors and of competitors helps to obtain a large number of metal distribution profiles on the support surface between the periphery and the grain center [50, 95, 111, 124–127], depending on the strength of their interaction with the support. Four main types of profiles [50, 124–127] serve to describe all the others: uniform, film or eggshell, internal ring or egg white, central or egg yolk (Fig 6).

Hydrofluoric [112], oxalic, lactic, tartaric [121] and citric acids [121, 128], for example, help to obtain an egg-white or egg-yolk distribution of chloroplatinic acid. These competing agents, which have a high affinity for alumina, become irreversibly fixed on the external sites of the support and force the platinum precursor to migrate farther towards the center of the grain in order to find free sites.

The profile of the macroscopic distribution of the metal on the support depends not only on the competition and time but also on the more or less strong tendency of the metal ion to modify its sphere of coordination or to polymerize. Thus  $[\text{PtCl}_6]^{2-}$  can undergo, in neutral or slightly acid medium, various reactions of aquation and hydrolysis [16, 49, 129–131] which modify the metal environment, the ion charge and thus the affinity of the latter for the support. Molybdic and tungstic ions, present as monomers  $\text{MoO}_4^{2-}$  or  $\text{WO}_4^{2-}$  in basic medium, polymerize when put in neutral or acid medium. The polymerization of tungstic ions, for example, influences the distribution profile [132] via the diffusion rate of these ions. It can also lead to the blocking of part of the pores.

A number of theoretical models of migration and deposition of metallic ions with time in porous supports, with or without the presence of competitor compounds, based on competing liquid-phase diffusion and adsorption mechanisms, have been proposed to account for the experimental results [56–58, 112, 133–138].

## F Conclusions

This short review has tried to emphasize the molecular aspects of catalyst preparation, the role of the support and the different interactions taking place between the metal complex and the support. The case of ion exchange has been presented in more detail, because of the possibilities of varying such interactions in a large domain, ranging from weak physical interactions to stronger chemical interactions.

Although catalyst preparations are usually composed of several successive unit operations (e.g. ion exchange, washing and drying) which are clearly separated, the identification of the elementary steps taking place at the molecular level are far more difficult to detect and to separate. There seems, however, to be some hope, using experimental key parameters, to achieve a better identification and separation so that new sequences can be proposed, making catalyst architecture possible.

## References

- 1 J T Richardson, *Principles of Catalyst Development*, Plenum Press, New York, 1989, p. 134
- 2 B Imelik, J C Védrine (Eds) *Catalyst Characterization Physical Techniques for Solid Materials*, Plenum Press, New York, 1994
- 3 K Morikawa, T. Shirasaki, M Okada, *Adv Catal* 1969, 20, 97–133
- 4 L L Murrell in *Advanced Materials in Catalysis* (Eds J J Burton, R L Garten) Academic Press, New York, 1977, Chapter 8
- 5 D L Trimm, *Design of Industrial Catalysts*, Elsevier, New York, 1980
- 6 K Foger, *Catalysis, Science and Technology*, 1984, 6, 227–305
- 7 Y Iwasawa in *Tailored Metal Catalysts* (Ed Y Iwasawa), Reidel, Dordrecht, 1986, Y Iwasawa, *Adv Catal* 1987, 35, 187–264
- 8 B C Gates, L Guzzi, H Knozinger (Eds) *Metal Clusters in Catalysis*, Elsevier, Amsterdam, 1986
- 9 L L Hegedus, R Aris, A T Bell, M Boudart, N Y Chen, B C Gates, W O Haag, G A Somorjai, J Wei, *Catalyst Design*, Wiley, New York, 1987.
- 10 K I Tanaka, *Adv Catal* 1985, 33, 99–158
- 11 M Ichikawa, *Adv Catal* 1992, 38, 283–400
- 12 M Che, *Stud Surf Sci Catal* 1993, 75A, 31–68
- 13 G J K Acres, A J Bird, J W Jenkins, A King, *Catalysis (London)* 1981, 4, 1–30
- 14 G A Parks, *Chem Rev* 1965, 65, 177–198
- 15 H H Kung, *Transition Metal Oxides Surface Chemistry and Catalysis*, Elsevier, Amsterdam, 1989

- 16 J P Brunelle, *Pure Appl Chem* **1978**, *50*, 1211–1229
- 17 R K Iler, *The Chemistry of Silica*, Wiley, New York, **1979**, p 56
- 18 O Stern, *Z Elektrochem* **1924**, *30*, 508–514
- 19 J A Davis, R O James, J O Leckie, *J Colloid Interface Sci* **1978**, *63*, 480–499
- 20 A W Adamson, *Physical Chemistry of Surfaces*, Wiley, New York, **1982**, 185–231
- 21 D E Yates, S Levine, T W Healy, *J Chem Soc, Faraday Trans 1* **1974**, *70*, 1807–1818
- 22 J A Davis, J O Leckie, *J Colloid Interface Sci* **1978**, *67*, 90–107
- 23 T W Healy, L R White, *Adv Colloid Interface Sci* **1978**, *9*, 303–345
- 24 J Westall, H Hohl, *Adv Colloid Interface Sci* **1980**, *12*, 265–294
- 25 R Spryca, *J Colloid Interface Sci* **1984**, *102*, 173–185
- 26 W H van Riemsdijk, J C M de Wit, L K Koopal, G H Bolt, *J Colloid Interface Sci* **1987**, *116*, 511–522
- 27 K C Williams, J L Daniel, W J Thomson, R I Kaplan, R W Maatman, *J Phys Chem* **1965**, *69*, 250–253
- 28 N Spanos, A Lycourghiotis, *Langmuir* **1993**, *9*, 2250–2252
- 29 W H van Riemsdijk, G H Bolt, L K Koopal, J Blaakmeer, *J Colloid Interface Sci* **1986**, *109*, 219–228
- 30 C Contescu, J Jagiello, J A Schwarz, *Langmuir* **1993**, *9*, 1754–1765
- 31 C Marcilly, J P Franck, *Rev IFP* **1984**, *3*, 337–364
- 32 C N Satterfield, *Heterogeneous Catalysis in Industrial Practice*, McGraw-Hill, New York, **1991**, Chapter 7
- 33 C Perego, P Villa in *The Catalytic Process from Laboratory to the Industrial Plant* (Ed D Sanfilippo), **1994**, Chapter 2
- 34 J F Le Page, *Applied Heterogeneous Catalysis*, Technip, Paris, **1987**, p 12–122
- 35 R W Maatman, C D Prater, *Ing Eng Chem* **1957**, *49*, 253–257
- 36 R W Maatman, *Ind Eng Chem* **1959**, *51*, 913–914
- 37 H A Benesi, US Patent 3 527 835, **1970**
- 38 M El Malki, J P Franck, C Marcilly, R Montarnal, *C R Acad Sci Ser 2*, **1979**, *288 C*, 173–176
- 39 F Ribeiro, C Marcilly, *Rev IFP*, **1979**, *34*, 405–428
- 40 F Ribeiro, PhD Thesis, University of Poitiers, **1980**
- 41 L I Kheifets, A V Neimark, *Multiphase Processes in Porous Media*, Izd Khimiya, Moscow, **1982**, p 320
- 42 G A Aksel'rud, M A Al'tshuler, *Introduction to Capillary-Chemical Technology*, Izd Khimiya, Moscow, **1983**, p 264
- 43 R Montarnal, unpublished results, **1973**
- 44 M A Al'tshuler, *Kolloidny Zhurnal*, **1961**, *23*, 646–651, **1977**, *39*, 1142–1144
- 45 K M Adam, *Water Resources Research* **1969**, *5*, 840–870
- 46 P Leroux, unpublished results, **1978**
- 47 C Marcilly in *Catalyse par les Metaux* (Eds B Imelik, G A Martin, A J Renouprez), CNRS, Paris **1984**, p 121–150
- 48 V V Veselov, G A Chernaja, T A Levanjuk, *Kinet Katal* **1982**, *20*, 83–87
- 49 J R Anderson, *Structure of Metallic Catalysts*, Academic Press, London, **1975**, p 172
- 50 A V Neimark, L I Kheifets, V B Fenelonov, *Ind Eng Chem Prod Res Dev*, **1981**, *20*, 439–450
- 51 E W Washburn, *Phys Rev* **1921**, *17*, 273–283
- 52 C H Bosanquet, *Phil Mag* **1923**, *45*, 525–31
- 53 M A Lauffer, *J Chem Educ* **1981**, *58*, 250–256
- 54 J Crank, *Mathematics of Diffusion*, Clarendon Press, Oxford, **1964**
- 55 R Paterson, *An Introduction to Ion Exchange*, Heyden and Son, London, **1970**
- 56 P B Weisz, *Trans Faraday Soc* **1967**, *63*, 1801–1806
- 57 P B Weisz, J S Hicks, *Trans Faraday Soc* **1967**, *63*, 1807–1814
- 58 P B Weisz, H Zollinger, *Trans Faraday Soc* **1967**, *63*, 1815–1823
- 59 J Crank, G S Park, *Diffusion in Polymers* Academic Press, London, **1984**, Chapter 1
- 60 C N Satterfield, *Mass Transfer in Heterogeneous Catalysis*, MIT Press, London, **1970**
- 61 C Lepetit, M Che, *J Mol Catal* **1995**, *100*, 147–160
- 62 T Setoyama, M Che, unpublished results
- 63 J A Rabo, P H Kasai, *Prog Solid State Chem* **1975**, *9*, 1–19
- 64 A Davidson, M Che, *J Phys Chem* **1992**, *96*, 9909
- 65 L Bonneviot, O Legendre, M Kermarec, D Olivier M Che, *J Colloid Interface Sci* **1990**, *134*, 534–547
- 66 G W Brindley, G Brown, *Crystal Structures of Clay Minerals and their X Ray Identification*, 2nd edn, Mineralogy Society, London, **1980**, p 2
- 67 L Bonneviot, O Clause, M Che, A Manceau, H Dexpert, *Catal Today* **1989**, *6*, 39–46
- 68 K F Purcell, J C Kotz, *Inorganic Chemistry*, Saunders, Philadelphia, **1977**
- 69 F A Cotton, G Wilkinson, *Advanced Inorganic Chemistry*, 4th ed, Wiley, New York, **1980**
- 70 G Vigil, Z Xu, S Steinberg, J Israelachvili, *J Colloid Interface Sci* **1994**, *165*, 367–385
- 71 J Lyklema, *J Electroanal Chem* **1968**, *18*, 341–348
- 72 G A Parks, P L de Bruyn, *J Phys Chem* **1962**, *66*, 967–973
- 73 R W Maatman, P Mahaffy, P Hoekstra, C Addink, *J Catal* **1971**, *23*, 105–117
- 74 E Santacesaria, S Carra, I Adami, *Ind Eng Chem Prod Res Dev* **1977**, *16*, 41–44
- 75 J P Boitiaux, J M Deves, B Didillon, C R Marcilly, *Catalytic Naphta Reforming* (Eds G J Antos, A M Atani, J M Parera), Marcel Dekker, New York **1995**, Chapter 4
- 76 S Parkash, S K Chakraborty, T Koanigawa, N Berkowitz, *Fuel Process Technol* **1982**, *6*, 177–182
- 77 S L Chen, H L Zhang, J Hu, C Contescu, J A Schwarz, *Appl Catal*, **1991**, *73*, 289–312
- 78 S Subramanian, D D Obngkeit, C R Peters M S Chattha, *J Catal* **1992**, *138*, 400–404
- 79 D W Fuerstenau, K Osseo-Asare, *J Colloid Interface Sci* **1987**, *118*, 524–542
- 80 O Clause, M Kermarec, L Bonneviot, F Villain, M Che, *J Am Chem Soc* **1992**, *114*, 4709–4717
- 81 S Henin, *C R Acad Sci Ser 2* **1957**, *244*, 225–227
- 82 S Caillere, S Henin, H Besson, *C R Acad Sci* **1963**, *256*, 208–210
- 83 J L Paulhiac, O Clause, *J Am Chem Soc* **1993**, *115*, 11602–11603
- 84 J-B d Espinose de la Caillerie, C Bobin, B Rebours O Clause, *Preparation of Catalysts VI*, Elsevier Amsterdam **1995**, pp 169–184
- 85 W H Casey, J F Banfield, H R Westrich, L McLaughlin, *Chem Geol* **1993**, *105*, 1–15
- 86 W H Casey, H R Westrich, J F Banfield G Ferruzzi G W Arnold, *Nature*, **1993**, *366*, 253–256
- 87 M Che, L Bonneviot, *Stud Surf Sci Catal*, **1988**, *44*, 147–158
- 88 A Lyeourghiotis in *Acidity and Basicity of Solids Theory Assessment and Utility*, (Eds J Fraissard L Petrakis) NATO ASI Series 444c, Kluwer, Dordrecht **1994**, pp 415–444
- 89 C F Baes, R E Mesmer, *The Hydrolysis of Cations* Krieger, Malabar **1986**
- 90 M Che O Clause L Bonneviot in *Proc 9th Int Congr Catal* (Eds M J Phillips, M Ternan), Chemical Institute of Canada, Ottawa, **1988**, *4*, pp 1750–1757 and *5*, pp 534–537



- 91 W Tan, Z-Y Shi, S Smith, D Birnbaum, *Science* **1992**, 258, 778–781
- 92 M Kermarec, J Y Carnat, P Burattin, M Che, A Decarreau, *J Phys Chem* **1994**, 98, 12008–12017
- 93 F Basolo, R G Pearson, *Mechanisms of Inorganic Reactions*, 2nd edn, Wiley, New York, **1967**
- 94 A K Aboul-Gheit, *J Chem Tech Biotechnol* **1979**, 29, 480–486
- 95 Y-S Shir, W Ernst, *J Catal* **1980**, 63, 425–433
- 96 C Louis, and M Che, *J Catal* **1992**, 135, 156–172
- 97 E Borello, G Dalla Gatta, B Fubini, C Morterra, G Venturello, *J Catal* **1974**, 35, 1–10
- 98 J A Schwarz, *Catal Today* **1992**, 15, 395–405
- 99 M J D'Amelo, Jr, *J Catal* **1981**, 69, 9–17
- 100 A M Ahmed, *J Phys Chem* **1969**, 73, 3546–3555
- 101 L J Jacimovic, J Stevovic, S Veljkovic, *J Phys Chem* **1972**, 76, 3625–3632
- 102 H Hohl, W Stumm, *J Colloid Interface Sci* **1976**, 55, 281–288
- 103 S Sivasanker, A V Ramaswamy, P Ratnasamy, *Stud Surf Sci Catal* **1979**, 3, 185–196
- 104 H Knozinger, P Ratnasamy, *Catal Rev* **1978**, 17, 31–70
- 105 J B Peri, *J Phys Chem* **1965**, 69, 220–230, *J Phys Chem* **1965**, 69, 211–219, *J Phys Chem* **1965**, 69, 231–239
- 106 H Knozinger, *Adv Catal* **1976**, 25, 184–271
- 107 Z Vit, J Vala, J Malek, *Appl Catal* **1983**, 7, 159–168
- 108 E Santacesaria, D Gelosa, S Carra, *Ind Eng Chem Prod Res Dev* **1977**, 16, 45–47
- 109 R Poisson, J P Brunelle, P Nortier, *Catalyst Supports and Supported Catalysts*, (Ed A B Stiles), Butterworth, Boston, **1987**, pp 11–55
- 110 E I Gil'Debrand, *Intern Chem Eng* **1966**, 6, 449–480
- 111 Th Mang, B Breitscheidel, P Polanck, H Knozinger, *Appl Catal* **1993**, 106, 239–258
- 112 L L Hegedus, T S Chou, J C Summers, N M Potter, *Stud Surf Sci Catal* **1979**, 3, 171–183
- 113 J C Summers, S A Ausen, *J Catal* **1978**, 52, 445–452
- 114 G Lietz, H Lieske, H Spindler, W Hanke, J Volter, *J Catal* **1983**, 81, 17–25
- 115 F Umland, W Fischer, *Naturwiss* **1953**, 40, 439–440
- 116 H Lieske, G Lietz, H Spindler, J Volter, *J Catal* **1983**, 81, 8–16
- 117 V Haensel, US Patent 2 840 532, **1958**
- 118 M S Heise, J A Schwarz, *Stud Surf Sci Catal* **1987**, 31, 1–13
- 119 C T Kresge, A W Chester, S M Oleck, *Appl Catal* **1992**, 81, 215–226
- 120 G N Maslyanskiy, B B Zharkow, A Z Rubinov, *Kinet Katal* **1971**, 12, 699–701
- 121 W Jianguo, Z Jiayu, P Li, *Stud Surf Sci Catal* **1983**, 16, 37–46
- 122 T A Nuttal, *CSIR Report CENG 182*, CSIR, Pretoria, South Africa, **1977**
- 123 E R Becker, T A Nutall, *Stud Surf Sci Catal* **1979**, 3, 159–167
- 124 M Komiyama, *Catal Rev Sci Eng* **1985**, 27, 341–372
- 125 E R Becker, J Wei, *J Catal* **1977**, 46, 365–381
- 126 A Gavrilidis, A Varma, *Catal Rev* **1993**, 35, 399–456
- 127 R C Dougherty, X E Verykios, *Catal Rev* **1987**, 29, 101–150
- 128 J Papageorgiou, *J Catal* **1966**, 158, 439–451
- 129 W P Griffith *The Chemistry of the Rarer Platinum Metals* Interscience, London, **1967**
- 130 C M Davidson, R F Jameson, *Trans Faraday Soc* **1965**, 61, 2462–2467
- 131 G H Van Den Berg, H T Rijntjen, *Stud Surf Sci Catal* **1979**, 3, 265–277

- 132 L R Pizzio, C V Caceres, M N Blanco, *Catal Lett* **1995**, 33, 175–192
- 133 P Harnott, *J Catal* **1969**, 14, 43–48
- 134 R C Vincent, R P Merrill, *J Catal* **1974**, 35, 206–217
- 135 M Komiyama, R P Merrill, H F Harnsberger, *J Catal* **1980**, 63, 35–52
- 136 M Komiyama, R P Merrill, *Bull Chem Soc Jpn* **1984**, 57, 1169
- 137 S Y Lee, R Aris, *Stud Surf Sci Catal* **1983**, 16, 35–45
- 138 A A Castro, O A Scelza, E R Benvenuto, G T Barone, S R De Miguel, J M Parera, *Stud Surf Sci Catal* **1983**, 16, 47–56

### 2.2.1.2 Anchoring and Grafting of Coordination Metal Complexes onto Oxide Surfaces

C. LOUIS AND M. CHE

#### A Introduction

Many heterogeneous catalysts have been reported in the past to be prepared by anchoring or grafting, processes whereby stable, covalent bonds are formed between an homogeneous transition metal complex and an inert polymer or inorganic support [1–4]. The aim was to combine the potential versatility and selectivity of homogeneous catalysts with the practical advantages of a solid material [5].

According to the recommendations of the International Union of Pure and Applied Chemistry (IUPAC), “deposition involving the formation of a strong (e.g. a covalent) bond between the support and the active element is usually described as grafting or anchoring. This is achieved through a chemical reaction between functional groups (e.g. hydroxyl groups) on the surface of the support and an appropriately selected inorganic, or organometallic compound of the active element [6].” Anchored catalysts are not distinguished from grafted ones either in this definition or in the literature where the situation is made even more complicated since other terms (immobilized, heterogenized, attached, etc.) can be found for the same type of catalysts. Recently, Campbell [7] attempted to distinguish anchoring from grafting as follows: “An anchored catalyst is created by the binding of a species, without substantial change in its structure, to a solid surface. A grafted catalyst is produced when an initial structure bound to the surface is altered considerably by subsequent treatments. Here, the initially bound species is not usually an active catalyst.” Although it is difficult at times to estimate how “substantial” or “considerable” are the changes undergone by a species attached to a surface, we shall nevertheless use Campbell’s definition in what follows. These definitions imply that anchoring will necessarily occur before grafting can take place.

The next few examples are given to illustrate the distinction between anchoring and grafting. By means

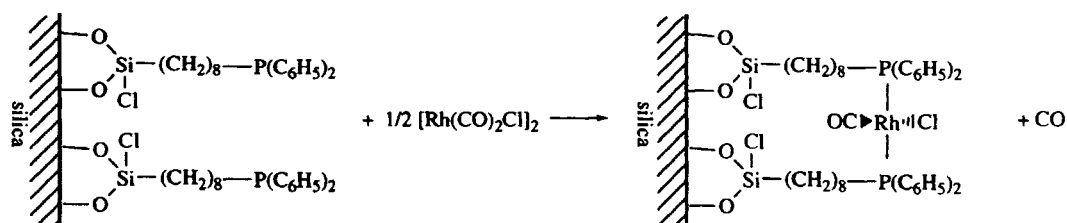


Figure 1. Example for the preparation of an anchored catalyst (from Ref. 1).

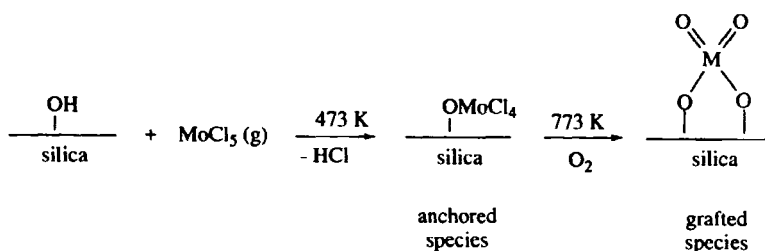


Figure 2. Example for the preparation of a grafted catalyst (from Ref. 7).

of Fig. 1, an anchored complex is obtained which is a close analog of *trans*-L<sub>2</sub>Rh(CO)Cl, an active catalyst in the homogeneous hydroformylation reaction [1]. The anchored catalyst also catalyzes hydroformylation.

The example used by Campbell to illustrate grafting concerns oxidation catalysts (Fig. 2) [7]: the formation of the grafted catalyst starts by reacting the silanol groups of a silica previously dehydrated at 473 K with MoCl<sub>5</sub>; an intermediate anchored species is obtained. With subsequent heating to 773 K in oxygen, the remaining chlorines are removed to finally produce a grafted species with terminal molybdenyl bonds [8, 9]. The final surface complex catalyzes methanol oxidation to produce methylformate with a 90–95% selectivity at about 500 K [10].

It is possible to classify the coordination metal complexes used as precursors for anchoring/grafting into three types:

- (i) metal halides and oxyhalides;
- (ii) metal alkoxides;
- (iii) organometallics, and especially metal allyls and metal carbonyls.

Only metals in carbonyl complexes are in the zero-valent state and can be polynuclear.

The history of the anchoring/grafting preparation may be found in Chapter 1 and Appendix 2 of Ref. 11. It appears that the first works have been performed to heterogenize transition metal complexes used as homogeneous catalysts of polymerization.

This method is not extensively used for the preparation of industrial catalysts although many patents have been issued. It is mainly developed in research laboratories for the preparation of model catalysts.

The present review deals with the anchoring/grafting of transition metal complexes (mononuclear, dinuclear, or polynuclear) on inorganic supports except zeolites, which are covered in Section A.2.3. Catalysts with anchored complexes which are the analogs of homogeneous catalysts are described in Section A.2.2.1.4.

## B Preparation: General Principles

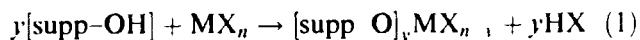
The preparation of supported catalysts by anchoring/grafting usually involves several basic steps.

### a Support Pretreatment

Prior to the reaction, the inorganic oxide support is thermally pretreated to remove physisorbed water and thus avoid spurious reactions which would not lead to anchoring/grafting. The support can be also dehydroxylated to various extents to control the amount and dispersion of the anchored/grafted species. Different types of hydroxy groups with different reactivities are present on supports. The structure of support surfaces and their reactivity have been extensively described in several reviews ([12–18] and references therein).

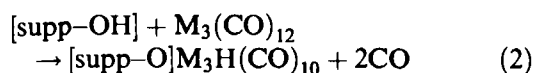
### b Anchoring

The chemical reaction usually occurs as soon as the coordination metal complex is in contact with the support. The anchoring involves a condensation reaction between the precursor and the surface OH groups of the support:



The metal oxidation state does not change. In the case of metal carbonyls, the anchoring involves an oxidative addition of a surface OH group to the zerovalent com-

plex (Eq. 2):



The coordination metal complexes are often air-sensitive, so preparations involving nonaqueous and inert solvents or vapor phase reactions (chemical vapor deposition (CVD), Section A.4.9) are required. The reactions are usually performed between room temperature and a maximum that is limited by the decomposition temperature of the precursor for vapor phase reactions, and the solvent reflux temperature for liquid phase reactions.

As shown in Eq. 1, the support acts as a macroligand for the metal. Depending on the number of bonds between the metal and the support ( $y = 1, 2$  or  $3$ ), the metal can be considered as singly, doubly, or triply bonded to the support. The value of  $y$  may vary with the reactivity, concentration, and nature of both the OH and the coordination metal complex, and also with the reaction temperature.

#### c Elimination of Physisorbed Metal Complexes

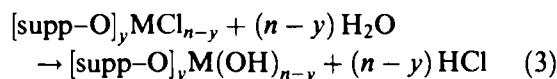
This treatment is obtained by purge under dry and inert gas, for catalysts prepared in the vapor phase, and by washing with pure solvent for catalysts prepared in the liquid phase.

Such anchored complexes with remaining original ligands may be directly used in reactions (Section A.2.2.1.4), such as alkene metathesis (Section E.a below).

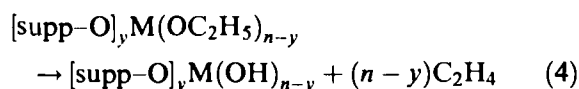
#### d Grafting

The remaining initial ligands are eliminated as follows:

- (i) By hydrolysis of the metal–ligand bond (e.g. chloride) of the anchored complex with water (in liquid or vapor phase at various temperatures):



- (ii) By decomposition of the anchored complexes (e.g. alkoxides, organometallics) under mild thermal conditions, for example:



The reaction stoichiometry may be determined from the amount of anchored metal and the number of ligands in the coordination sphere, or the amount of gas evolved (e.g. HCl or C<sub>2</sub>H<sub>4</sub>) during hydrolysis/decomposition, provided that it does not adsorb on the support.

The anchored/grafted metal species may be characterized by different spectroscopic methods: IR, UV-Vis diffuse reflectance (UV-Vis DRS), electron spin reso-

nance (ESR), X-ray photoelectron (XPS), Raman, X-ray absorption fine-structure (EXAFS), magic angle spinning–nuclear magnetic resonance (MAS NMR), low energy ion scattering (LEIS), etc.

The main advantage of anchoring/grafting over conventional impregnation is the deposition of transition metal elements in various given oxidation states, from zero to high oxidation states. It is theoretically possible to obtain:

- (i) highly dispersed ions with previously partially dehydroxylated supports;
- (ii) a monolayer if the reactive OH groups are close enough to each other.

Theoretically, the amount of metal chemically bonded to the support cannot exceed the monolayer; however, multilayers can be obtained by several cycles of anchoring–hydrolysis or anchoring–decomposition.

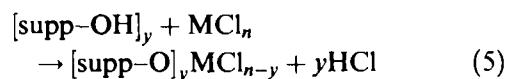
In addition, because of the chemical interaction between transition metal ions and the support established during anchoring, it is possible to prevent migration, sintering and agglomerate formation during subsequent thermal treatments, in contrast with species deposited by mere impregnation which are mainly physically adsorbed.

#### C Metal Chlorides and Oxychlorides

The anchoring/grafting may be performed with metal chlorides (TiCl<sub>4</sub>, VCl<sub>4</sub>, MoCl<sub>5</sub>, WCl<sub>6</sub>, SnCl<sub>4</sub>), and oxychlorides (VOCl<sub>3</sub>, WOCl<sub>4</sub>). Only grafted complexes are used as catalysts since chlorides must be eliminated before catalytic reactions.

After support dehydration and dehydroxylation, the preparation consists of three steps:

- (i) Anchoring between the (oxy)chloride and the hydroxy groups of the support:



- (ii) Elimination of the physisorbed metal complexes (as described in Section B).
- (iii) Hydrolysis of the M–Cl bond with water (liquid or vapor) to obtain grafted catalysts (see Eq. 3).

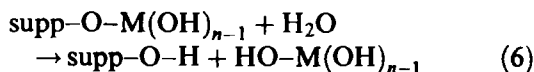
The determination of the stoichiometry of reaction 5 (most often leading to singly or doubly bonded species) is usually based on the measurement of the amounts of anchored metal and Cl on the catalyst, or HCl evolved during the reaction [19–24].

Based on the Cl:V ratio and ESR analysis, Fricke et al. [25] have shown that depending on the pretreatment temperature of the silica (523, 873, 1073K), VCl<sub>4</sub>

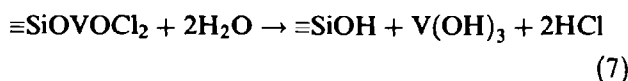
can be anchored on silica via three, two or one bonds at 333 K. Haukka and co-workers [26, 27] have also found that the reaction mechanism depends on the reaction temperature. For a reaction between  $\text{TiCl}_4$  and silica at 450 K, the Cl:Ti ratio indicates the presence of species anchored via one and two bonds to titania. The proportion of singly anchored species increases with the increase in the pretreatment temperature of the silica.

The structure of the anchored species may be also deduced from in situ characterization. However, to our knowledge, only a few attempts by ESR and UV-Vis DRS have been reported [8, 19, 24].

It may be also noted that, depending on the systems, the undesirable hydrolysis of the metal-support bond (supp-O-M) may occur:



Hanke et al. [28] and Khalif et al. [29] have shown that the  $\equiv\text{Si-O-V}$  bond is hydrolyzed during chloride hydrolysis of  $\text{VOCl}_3$  anchored on silica:



whereas the Ti-O-V bond is retained after anchoring of  $\text{VOCl}_3$  on titania [30]. Fricke et al. [24] show by ESR that reaction 6 also occurs during hydrolysis of  $\text{MoCl}_5$  anchored on silica.

When the supp-O-M bonds are hydrolyzed (Eq. 6), the released species must be removed by washing so as to keep only really anchored species in the catalyst [9, 31]. This washing step can advantageously replace step d of the preparation (Section B above) since both hydrolysis and elimination of the released metal species can take place simultaneously. This crucial step is barely mentioned in the literature. This may be the reason why some authors claim that the grafting of chloride complexes does not lead to homogeneously dispersed species on the support surface and forms three-dimensional oxide particles after calcination [29, 32, 33].

Highly dispersed grafted species can be obtained: after grafting of  $\text{MoCl}_5$  [8] or  $\text{SbCl}_5$  [34] on silica, the elimination of the released metal species during washing with ammonia solution and water, respectively, leads to the formation of highly dispersed isolated species.

The amount of grafted metal is usually low, for several possible reasons: low support OH reactivity, chlorination of the surface, and release of metal species during hydrolysis. Bond and Brückman [30] mentioned that it is difficult to obtain a monolayer of vanadium species on  $\text{TiO}_2$  because of the chlorination of the support surface by the HCl evolved during the anchoring of  $\text{VOCl}_3$  at 313 K.

Several cycles of anchoring reaction-hydrolysis can be performed in order to increase the metal loading. However, during the subsequent cycles, the metal chloride complexes can react with the OH groups of both the support and the grafted metal [35], and lead to the formation of two-dimensional or three-dimensional particles.

Hattori et al. [31] mentioned that after three cycles of vapor phase reaction between  $\text{SnCl}_4$  and silica pretreated at 453 K, followed by washing and calcination, the amount of grafted Sn is very close to that required for a monolayer coverage. However, transmission electron microscopy (TEM) and X-ray diffraction (XRD) studies show that not all the silica surface OH groups react with chlorides, and that  $\text{SnCl}_4$  prefers to react with the Sn-OH formed during the hydrolysis. After calcination at 773 K,  $\text{SnO}_2$  particles of 10–15 nm are formed, whereas high and uniform dispersion of  $\text{SnO}_2$  (<2 nm) is obtained for samples prepared by conventional impregnation. The reasons for this are not given in the paper but these results show that grafted catalysts do not always exhibit better characteristics than conventional impregnated samples.

A few authors have mentioned that the use of chloride metal complexes gives a reproducible amount of grafted metal: Benvenuti et al. [34] for the grafting of  $\text{SbCl}_5$  on silica in  $\text{CCl}_4$  at the solvent-reflux temperature, Lindblad and Lindfors [36] for the grafting of  $\text{WOC}_4$  on silica at 473 K, Haukka and Lakomaa [26] for the grafting of  $\text{TiCl}_4$  on silica at 450 K and 723 K.

The central ions in (oxy)chloride metal complexes are in a high oxidation state that is preserved during anchoring (Eq. 5) and grafting. Therefore, these grafted catalysts are mainly used to catalyze oxidation reactions, e.g. oxidative dehydrogenation of ethylbenzene [31], oxidation of acrolein [29], methanol [10], and *o*-xylene [30, 37].

For example, Khalif et al. [29] have observed that the rate of oxidation of acrolein at 593 K per vanadium atom is five times higher with a grafted sample than with an impregnated one because of the higher V dispersion. In the case of  $\text{Mo/SiO}_2$ , Louis et al. [10] have found that the grafted  $\text{Mo/SiO}_2$  exhibits a higher selectivity in methylformate for methanol oxidation than impregnated  $\text{Mo/SiO}_2$ , which is selective in formaldehyde. The differences in the selectivity were explained in terms of the Mo dispersion, which is higher on the grafted samples. Bond and Brückman [30] have shown that the activity and selectivity of  $\text{V/TiO}_2$  in the oxidation of *o*-xylene to phthalic anhydride are highest when the supported vanadium is close to a monolayer.

#### D Metal Alkoxides

The principle of preparation is as previously described. The anchoring is often performed in the vapor phase because of the high thermal stability of the alkoxide

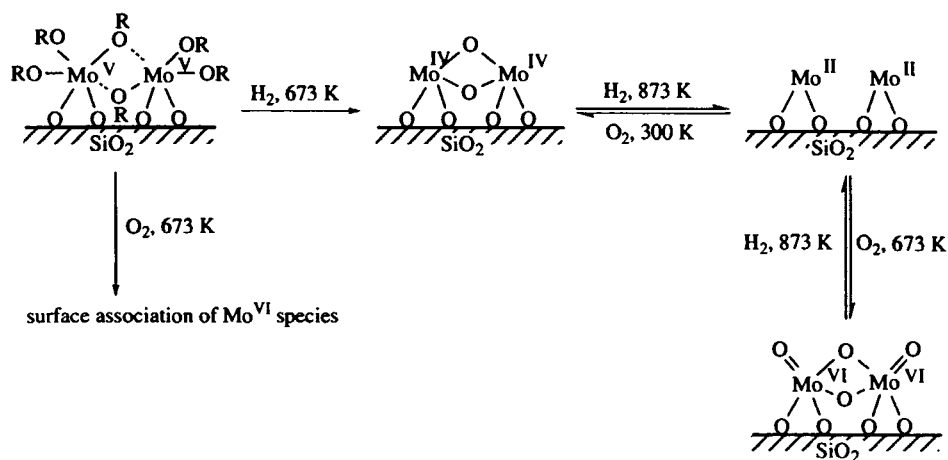
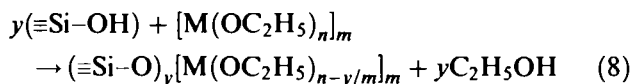


Figure 3. Anchoring/grafting of  $[\text{Mo}(\text{OC}_2\text{H}_5)_5]_2$  onto silica support (from Ref. 38).

complexes. The most studied precursors are the ethoxy and acetylacetonate ( $\text{acac} = \text{C}_5\text{H}_7\text{O}_2$ ) complexes.

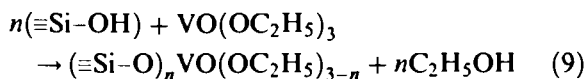
One of the earlier works using these precursors for catalyst preparation was performed by Kuznetsov et al. [38] and Yermakov et al. [11] with the anchoring of  $[\text{Mo}(\text{OC}_2\text{H}_5)_5]_2$  and  $[\text{Re}(\text{OC}_2\text{H}_5)_5]_3$  on silica:



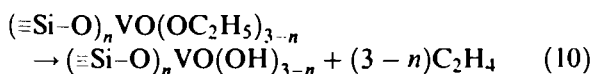
with  $y = 4$  for Mo and  $y = 2$  or 3 for Re. Further thermal oxidation–reduction treatments may take place, leading to the formation of grafted species with different oxidation states, characterized by XPS, EXAFS, ESR (Fig. 3).

The authors [11, 38] mention that the oxidation of anchored ethoxy complexes without preliminary reduction destroys some of the bonds between the metal ions and the silica. This also applies to allyl complexes [11] (see Section E.a below).

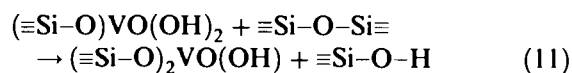
The control of the amount of reactants permits the deposition of highly dispersed species. This can be illustrated by the anchoring of  $\text{VO}(\text{OC}_2\text{H}_5)_3$  from vapor phase onto silica at 423 K, followed by a desorption at 723 K [39]. Singly and doubly anchored V species ( $n = 1$  or 2 in Eq. 9) can be obtained whose ratio depends on the pretreatment temperature of silica:



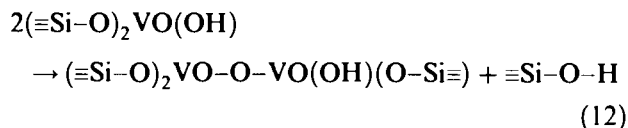
Grafted V is obtained upon thermal decomposition at 523–723 K:



Simultaneously, condensation reactions with other surface sites can also occur, leading to the regeneration of surface OH groups:

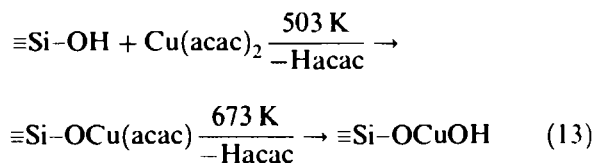


or



Several cycles of anchoring–decomposition may be performed since both the V–OH and the regenerated  $\equiv\text{Si}-\text{O}-\text{H}$  (Eqs 11 and 12) can again react with the precursors; Si–OH can take part in the lateral growth of the vanadium oxide layer along the silica surface, and V–OH in the thickening of the layer. XRD, Raman, EXAFS and XPS reveal that for a 19.4 wt%  $\text{V}_2\text{O}_5$  loading, a thin layer is obtained with the grafted sample, whereas  $\text{V}_2\text{O}_5$  crystallites are formed with the impregnated one [39, 40]. The grafted sample is three to four times more active in the reaction of oxidative dehydrogenation of ethanol to acetaldehyde than the impregnated one because of the higher surface area of vanadium oxide [40].

$\text{Cu}(\text{acac})_2$  in acetonitrile does not react at room temperature with  $\text{SiO}_2$ . Heated at 503 K, the physically adsorbed  $\text{Cu}(\text{acac})_2$  reacts with silanol groups and loses one acac per Cu. Subsequent calcination in air at 673 K removes fragments of acac and leaves only OH on the grafted complex [41]:



Anchoring can occur directly when the reaction is performed at higher temperature. Chromium acetyla-

acetate was found to react from the vapor phase at 473–553 K with the OH of silica, leading to the release of one acac ligand [42]. Depending on the intended use of the Cr/SiO<sub>2</sub> samples, the ligands can be removed either by water vapor at 588 K, which prevents the Cr<sup>III</sup> from oxidizing to Cr<sup>VI</sup>, or by air treatment at 673 K, which produces Cr<sup>VI</sup> species. The same type of study has been made with the Ni(acac)<sub>2</sub>–alumina system at 473 K [43].

It is suggested [41–43] that the steric hindrance due to the size of the anchored complexes determines the maximum amount of metal bonded to the support, and makes them atomically dispersed. The metal loading can be also controlled by the pretreatment temperature of the support which determines the number of OH groups, and by the reaction temperature. The preparations of Cr/SiO<sub>2</sub> and Ni/Al<sub>2</sub>O<sub>3</sub> described above give homogeneous and reproducible metal contents.

Several cycles of anchoring–air treatment can be made. It was found with the Ni(acac)<sub>2</sub>–alumina system [44] that the atomically dispersed Ni<sup>II</sup> species grafted during the first step act as nuclei for the growth of nickel particles during the subsequent preparation cycles.

## E Organometallics

Organometallic complexes are one of the most common types of precursors used in catalyst preparation by anchoring/grafting. Among them the allyls and the carbonyls are most used, but other ligands such as methyl, *n*-butyl, benzyl, neopentyl ( $\sigma$  ligands), cyclopentadienyl, arene ( $\pi$  ligands) can be also employed.

### a Metal Allyls

The metal allyls can provide a large variety of anchored/grafted species with different oxidation states after subsequent thermal treatments. They are involved as model catalysts in various catalytic reactions: hydrogenation, oxidation, metathesis, isomerization, or polymerization. The most widely studied metal allyls are Mo and Cr. A list of the metal allyls used as precursors for anchoring/grafting as well as their catalytic applications can be found in Table 5 of Ref. 15.

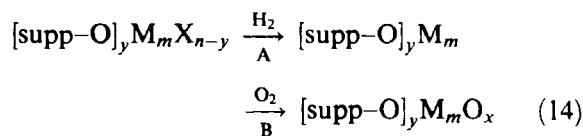
Earlier reviews devoted to the use of metal allyls and other organometallics for the preparation of supported catalysts have been written by Ballard [45], and Candlin and Thomas [46]; extensive work has been performed by Yermakov and co-workers [11, 47–50], and also by Iwasawa and co-workers [15, 16, 51, 52] on difficult-to-reduce elements (e.g. Ti, Zr, Hf, Cr, Mo, W) and, for example, by Basset and co-workers [53–55] on easy-to-reduce elements (e.g. Ni, Pd, Pt).

Typically, the anchoring consists of a reaction between an allyl metal complex, either mononuclear (e.g. Mo, or Cr( $\eta^3$ -C<sub>3</sub>H<sub>5</sub>)<sub>4</sub>) or binuclear (e.g. Mo<sub>2</sub> or Cr<sub>2</sub>( $\eta^3$ -C<sub>3</sub>H<sub>5</sub>)<sub>4</sub>), and the OH of the support, according to Eq. 1.

A doubly bonded anchored metal complex is usually obtained with Cr, Mo, and W, a singly bonded one with Ni, Pd, and Pt, and either one with Ti, Zr, and Rh (Table 5 of Ref. 15).

The reactions are usually performed at room temperature in pentane, but other solvents can be used, such as toluene. After reaction, the samples are washed several times with pure solvent in order to eliminate unreacted complexes (see step c in Section B); this step is not always mentioned in the related papers. Sometimes [54], the precursor may be sublimed under vacuum at room temperature.

The remaining organic ligands can be removed under mild reduction conditions (step A in Eq. 14), so as to lead to grafted metal catalysts.



After step A, the grafted species is in a low oxidation state, and exhibits catalytic activity. For example, the grafted Mo<sup>II</sup> dimers are more active in 1,3-butadiene hydrogenation at 273 K than the corresponding conventional impregnated Mo catalysts similarly reduced with H<sub>2</sub> – by two orders of magnitude when grafted on silica and by more than three orders when grafted on alumina [16].

During step A of Eq. 14, hydrides can be formed with Group 4 elements (Ti, Zr, Hf). For example, the anchored  $[\equiv\text{Si-O}]_2\text{Zr}^{\text{IV}}(\eta^3\text{-C}_3\text{H}_5)_2$  species is transformed into grafted zirconium dihydride  $[\equiv\text{Si-O}]_2\text{Zr}^{\text{IV}}\text{H}_2$  after treatment under hydrogen at 393 K [56]. The anchored Zr<sup>IV</sup> species is known to be active in ethylene polymerization [45], whereas the grafted zirconium hydrides are found to be the direct precursors of the propagation centers for ethylene polymerization [56]. These hydrides also exhibit high activity in alkene isomerization, especially of 1-butene, with higher rates at 300 K than homogeneous or other heterogeneous catalysts [57].

After oxidation (step B of Eq. 14), grafted oxidized species are obtained with a well-defined structure, characterized for example by EXAFS [16].

Highly dispersed grafted species can be obtained with metal allyls. Figure 4 shows an example of the change in the structure and oxidation state of isolated Mo grafted on silica after different oxidation-reduction treatments [16]. The different species obtained on silica have been characterized by Yermakov and co-workers [11, 47] and on alumina by Iwasawa [15, 16] using techniques such as EXAFS, UV-Vis DRS, and IR. Grafted Mo<sup>VI</sup> catalysts (species 4) are found to be 11 times more active than the corresponding catalyst obtained by impregnation in the selective oxidation of propene to acrolein [16]. Molybdenum(IV) (species 3)

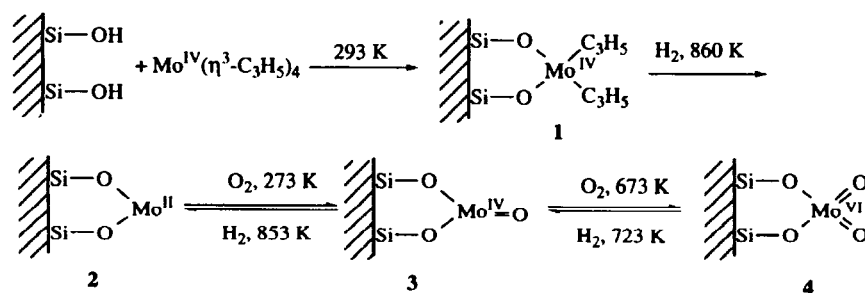


Figure 4. Anchoring/grafting of  $\text{Mo}(\eta^3\text{-C}_3\text{H}_5)_4$  onto silica support (adapted from Ref. 16).

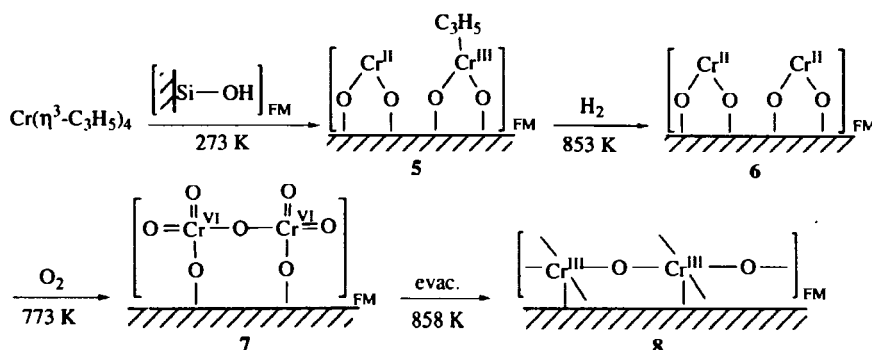


Figure 5. Stepwise transformation of  $\text{Cr}(\eta^3\text{-C}_3\text{H}_5)_3$  anchored onto silica to form a monolayer (from Ref. 15, FM = full monolayer).

exhibits activity for propene metathesis, but species 1 with allyl ligands is more effective.

A monolayer catalyst can be also obtained. For example, in the case of a reaction between excess  $\text{Cr}(\eta^3\text{-C}_3\text{H}_5)_3$  and a full monolayer of OH groups on silica, a two-dimensional layer of grafted  $\text{Cr}^{\text{III}}$  has been obtained (species 8 in Fig. 5; FM = full monolayer) [15]. After anchoring, the resultant species 5 has about one allyl ligand per two Cr atoms which can be readily removed by  $\text{H}_2$  treatment at 853 K to form a  $\text{Cr}^{\text{II}}$  monolayer 6. The latter is oxidized with  $\text{O}_2$  at 773 K into a  $\text{Cr}^{\text{VI}}$  monolayer 7 which can be transformed into a  $\text{Cr}^{\text{III}}$  monolayer 8 by treatment at 858 K under vacuum. Each  $\text{Cr}^{\text{III}}$  ion is square pyramidal and exhibits one vacant site in its coordination sphere, which makes it more active by two orders of magnitude for the catalytic oxidation of CO at about 473 K than a conventional impregnated Cr catalyst that usually exhibits a three-dimensional  $\text{Cr}_2\text{O}_3$  phase [15].

It is also possible to prepare supported metal catalysts from easy-to-reduce elements. For example,  $[\equiv\text{Supp-O}]\text{Rh}(\eta^3\text{-C}_3\text{H}_5)_2$  (with supp = Al, Si, or Ti) reacts with  $\text{H}_2$  at room temperature to give rhodium metal particles (1.5 nm) [54, 58]. Dialllyl compounds of Group 10 elements (Ni, Pd, Pt), forming species singly anchored onto silica or alumina, are transformed into small metal particles (<1 nm) after reduction under

$\text{H}_2$  at 300–373 K ( $\text{Pt}^0$ ,  $\text{Pd}^0$ ) and 573–673 K ( $\text{Ni}^0$ ) [11, 47, 59].

The metal allyls can be also used to prepare dispersed metal particles stabilized by the presence of low-valent ions (coming from hard-to-reduce transition elements) and produce bimetallic supported catalysts [47–50, 60] after the following sequence of steps:

- (i) Interaction of benzyl Ti, Hf, allyl Zr (Group 4) or allyl Mo, W complexes (Group 6) with a silica previously calcined at 773–873 K.
- (ii) Reduction at 773–873 K to obtain grafted low-valent ions.
- (iii) Treatment of the reduced catalyst with a solution of allyl Ni, Pd, or Pt complexes (Group 10) in pentane.
- (iv) Reduction with hydrogen.

These mixed catalysts exhibit a higher metal dispersion than monometallic catalysts as well as a stabilization of the metal particles against sintering. Difficult-to-reduce elements (Ti, Hf, Zr, Mo, W) are supposed to act as nucleation sites for the growth of metal particles. Because of the change in the electron density of the metal particles, these catalysts exhibit a higher specific activ-

ity than monometallic catalysts in benzene hydrogenation and ethane hydrogenolysis.

### b Metal Carbonyls

Many reviews have been devoted to the use of carbonyl metal complexes for the preparation of supported catalysts [2, 4, 17, 18, 61–67].

The main differences between the carbonyl metal complexes and the metal complexes previously described, are the following:

- (i) The reactivity of metal carbonyls with inorganic oxide surfaces appears more complex; indeed, several types of reaction with the support may be involved, depending on various parameters such as the carbonyl metal complex, the acid–base character of the support, the nature of the carrier gas, the reaction temperature; they lead to different metal complex–support bondings, from Van der Waals to iono-covalent [17, 18, 61, 67]; hence, the anchoring reaction cannot always occur.
- (ii) The metal in the carbonyl complexes is zerovalent; therefore, the anchoring reaction does not involve a condensation reaction with the surface OH groups (Eq. 1) but an oxidative addition of an OH group to the zerovalent complexes (Eq. 2).
- (iii) The complexes can be mononuclear [63], polynuclear, or heteronuclear (carbonyl clusters) [64, 67].

The main reasons for using carbonyl metal complexes as precursors for catalyst preparation are the following:

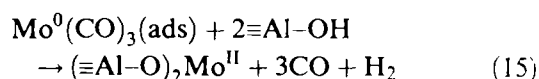
- (i) Anchored metal carbonyls can be used as heterogeneous analogs of the metal carbonyls used in homogeneous catalysis (see Section A.2.2.1.4).
- (ii) Grafted mononuclear or polynuclear entities can be produced upon decomposition of the anchored carbonyl species.
- (iii) Small metal particles can be easily produced by decomposition or low-temperature reduction of supported metal carbonyls.

A summary of the studies devoted to supported carbonyl metal complexes can be found in Table 2 of Ref. 2.

The anchoring/grafting of carbonyl metal complexes on a support may be ideally described as follows. After thermal pretreatment of the support, the carbonyl metal complex is introduced most often from the vapor phase or via organic solvents such as benzene, cyclohexane, and pentane. At this stage, the complexes are either anchored or physisorbed. When physisorbed, their decomposition as well as the elimination of the excess of physisorbed carbonyl metal complexes occur upon

heating the system under vacuum. Upon increasing temperature, ligands may be lost in a stepwise way, leading to subcarbonyl anchored species, and finally to grafted species.

Among monomeric metal carbonyls,  $\text{Mo}(\text{CO})_6$ ,  $\text{Cr}(\text{CO})_6$ ,  $\text{Fe}(\text{CO})_5$ , and  $\text{Ni}(\text{CO})_4$  have been most studied. Their stepwise decomposition on the support may lead to the formation of grafted species. For example,  $\text{Mo}(\text{CO})_6$  is first physically adsorbed onto hydroxylated alumina at room temperature [2, 62, 63, 68]. Thermal decomposition leads to the formation of adsorbed subcarbonyl species such as  $\text{Mo}(\text{CO})_5$  and then  $\text{Mo}(\text{CO})_3$  at 373 K. Complete decarbonylation at 573 K is observed upon oxidative addition of the metal on surface hydroxy groups:



Such grafted catalysts exhibit higher activity in alkene metathesis than conventional catalysts. More details concerning this example can be found in Refs. 2, 62, 63, 68, and references therein.

The deposition of polynuclear carbonyl complexes with metals of Groups 7–9 on oxide supports has been extensively studied as well as that of bimetallic complexes ([64, 67] and references therein). As mentioned above, the pathway leading to anchored/grafted cations or metal particles depends on the nature of the support, i.e. the nature and the amount of surface OH groups. Thus,  $\text{Ru}_3(\text{CO})_{12}$  exhibits stronger interaction with  $\gamma\text{-Al}_2\text{O}_3$  than with  $\text{SiO}_2$  [69, 70]. The EXAFS results show that at room temperature,  $\text{Ru}_3(\text{CO})_{12}$  is physisorbed on silica, whereas it reacts with the OH groups of alumina and forms the anchored  $[\text{HRu}_3(\text{CO})_{10}(\text{O}-\text{Al}\equiv)]$  species (Fig. 6). Upon treatment under vacuum at about 450 K,  $\text{Ru}_3(\text{CO})_{12}$  physisorbed on silica partially decomposes into “adsorbed”  $\text{Ru}_3(\text{CO})_6$  (no Ru–O–Si bonding), whereas Ru anchored on alumina transforms into  $[\text{Ru}(\text{CO})_2(\text{O}-\text{Al}\equiv)_2]$ . Reduction under  $\text{H}_2$  at 723 K leads to small metal particles  $[\text{Ru}]_{12}$  on silica and to grafted oxidized Ru entities  $[\text{Ru}_6(\text{O}-\text{Al}\equiv)_6]$  on alumina (Fig. 6).

This example shows that, in contrast to what is observed with the metal alloys, the formation of metal particles may not involve the formation of anchored species, i.e. cationic species.

It may be noted that other reactions can occur with polynuclear carbonyl complexes, such as oxidative fragmentation [17, 61, 66]. This is observed when  $[\text{HRu}_3(\text{CO})_{10}(\text{O}-\text{Al}\equiv)]$  is transformed into  $[\text{Ru}(\text{CO})_2(\text{O}-\text{Al}\equiv)_2]$  at 473 K (Fig. 6), leading to an oxidation of  $\text{Ru}^{\delta+}$  into  $\text{Ru}^{\text{II}}$ .

### F Conclusion

The anchoring of coordination metal complexes was first used to heterogenize homogeneous catalysts.



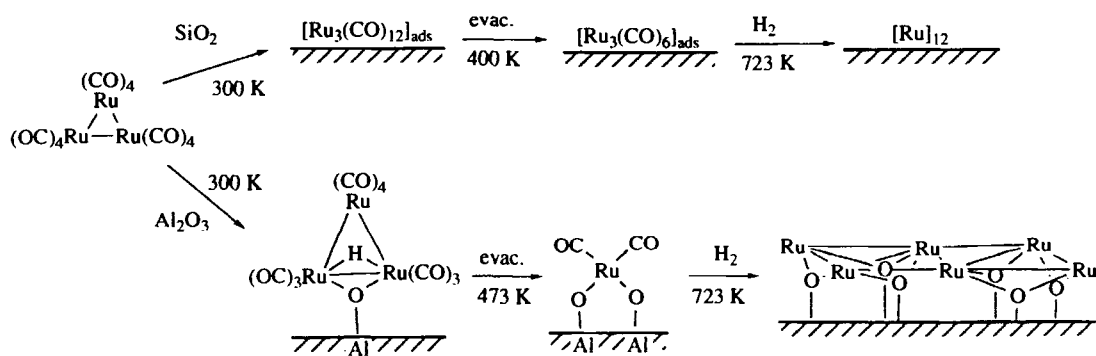


Figure 6. Transformation of  $\text{Ru}_3(\text{CO})_{12}$  supported on silica and alumina during thermal treatment (from Ref. 69, 70).

However, it was soon realized that the resulting anchored complexes exhibited unusual catalytic properties, and that the grafted catalysts could be obtained with controlled dispersion (isolated species, monolayers, multilayers). It appears that the nature of the catalysts obtained depends on many parameters such as the nature of the precursor.

The general problem for using these metal molecular precursors is the necessity of (i) using water- and air-free conditions, and (ii) synthesizing them when they are not commercially available.

In addition, the anchoring reaction does not permit the deposition of metal loadings higher than that corresponding to the monolayer. The metal loading mainly depends on the number of surface OH groups of the support provided that they all can react with the precursor. To get higher loading, i.e. multilayers, it is necessary to perform several cycles of anchoring/decomposition or hydrolysis, which require long and tedious procedures.

Up to now, the most used metal complexes to prepare catalysts by anchoring/grafting have been organometallics, and especially, metal allyls; it appears possible to obtain versatile catalysts containing metal ions with controlled dispersion, various coordination numbers, various ligands, and various but uniform oxidation states, in contrast with impregnated samples.

Metal carbonyls may be used as precursors for anchoring/grafting preparation but their reactivity is much more intricate, and it is uncertain which type of bonding will be predominant and therefore whether anchoring will occur.

Less systematically studied have been chloride metal complexes and those containing alkoxide ligands. Some studies suggest that they are less reliable for obtaining species as well-defined as with allyl precursors. However, recent works [26, 27, 36, 42–44, 71] devoted to the anchoring/grafting in vapor phase (CVD) (see Sections C and D), show that a well-defined supported phase may be obtained when each preparation parameter is carefully controlled and a systematic procedure is used.

However, one must be aware that (oxy)chloride metal complexes are only used for the preparation of grafted ions in a rather high oxidation state whereas alkoxide and allyl precursors can provide ions in various oxidation states (Figs. 3–5).

## References

1. L. L. Murrell in *Advanced Materials in Catalysis*, (Eds.: J. J. Burton, R. L. Garten), Academic Press, New York, 1977, Chapter 8.
2. D. C. Bailey, S. H. Langer, *Chem. Rev.* **1981**, *81*, 109–148.
3. H. Hirai, N. Toshima in *Tailored Metal Catalysts*, (Ed.: Y. Iwasawa), Reidel, Dordrecht, Holland, 1986, Chapter 2.
4. B. C. Gates, *Stud. Surf. Sci. Catal.* **1986**, *29*, 415–425.
5. K. G. Allum, R. D. Hancock, S. McKenzie, R. C. Pitkethly, *Catalysis* **1973**, *1*, 477–489.
6. J. Haber, *Pure Appl. Chem.* **1991**, *63*, 1227–1246.
7. I. M. Campbell, *Catalysis at Surfaces*, Chapman & Hall, London, 1988, p. 64.
8. C. Louis, M. Che, *J. Catal.* **1992**, *135*, 156–172.
9. C. Louis, M. Che, M. Anpo, *J. Catal.* **1993**, *141*, 453–464.
10. C. Louis, J.-M. Tatibouët, M. Che, *J. Catal.* **1988**, *109*, 354–366.
11. Y. I. Yermakov, B. N. Kuznetsov, V. A. Zakharov, *Stud. Surf. Sci. Catal.*, Vol. 8, Elsevier, Amsterdam, 1981.
12. H. Knözinger, R. Ratnasamy, *Catal. Rev.-Sci. Eng.* **1978**, *17*, 31–70.
13. H.-P. Boehm, H. Knözinger, *Catal. Sci. Technol.* **1983**, *4*, 40.
14. K. Foger, *Catal. Sci. Technol.* **1984**, *6*, 227.
15. Y. Iwasawa in *Tailored Metal Catalysts*, (Ed.: Y. Iwasawa), Reidel, Dordrecht, Holland, 1986, Chapter 1.
16. Y. Iwasawa, *Adv. Catal.* **1987**, *35*, 187–264.
17. H. H. Lamb, B. C. Gates, H. Knözinger, *Angew. Chem., Int. Ed. Engl.* **1988**, *27*, 1127–1144.
18. A. Zecchina, C. O. Arean, *Catal. Rev.-Sci. Eng.* **1993**, *35*, 261–317.
19. J. C. W. Chien, *J. Am. Chem. Soc.* **1971**, *93*, 4675–4684.
20. S. I. Kol'tsov, V. B. Aleskovskii, *Russ. J. Phys. Chem.* **1967**, *4*, 336–337.
21. S. I. Kol'tsov, V. B. Aleskovskii, *Russ. J. Phys. Chem.* **1968**, *42*, 630–632.
22. S. I. Kol'tsov, A. N. Volkova, V. B. Aleskovskii, *Russ. J. Phys. Chem.* **1970**, *44*, 1272–1274.
23. S. I. Kol'tsov, A. A. Malygin, A. N. Volkova, V. B. Aleskovskii, *Russ. J. Phys. Chem.* **1973**, *47*, 558–560.
24. R. Fricke, W. Hanke, G. Öhlmann, *J. Catal.* **1983**, *79*, 1–12.

- 25 R Fricke, H-G Jerschke, V B Kazanski, V A Shvets, G Ohlmann, *React Kinet Catal Lett* **1981**, *18*, 465–471
- 26 S Haukka, E-L Lakomaa, A Root, *J Phys Chem* **1993**, *97*, 5085–5094
- 27 S Haukka, E-L Lakomaa, O Jylhä, J Vilhunen, S Horntzkyj, *Langmuir* **1993**, *9*, 3497–3506
- 28 W Hanke, R Bienert, H-G Jerschke, *Z Anorg Allg Chem* **1975**, *414*, 109–129
- 29 V A Khahf, E L Aptekar, O V Krylov, G Ohlmann, *Kinet Katal* **1977**, *18*, 1055–1059
- 30 G C Bond, K Bruckman, *Faraday Discuss Chem Soc* **1981**, *72*, 235–246
- 31 T Hatton, S Itoh, T Tagawa, Y Murakami, *Stud Surf Sci Catal* **1987**, *31*, 113–122
- 32 Y V Plyuto, J Stoch, I V Babytch, A A Chuyko, *J Non-Cryst Sol* **1990**, *124*, 41–47
- 33 R Castillo, B Koch, P Ruiz, B Delmon, *J Mater Chem* **1994**, *4*, 903–906
- 34 E V Benvenuto, Y Gushkem, C U Davanzo, S C de Castro, I L Torriani, *J Chem Soc Faraday Trans* **1992**, *88*, 3193–3196
- 35 A N Volkova, S I Kol'tsov, V B Aleskovskii, N N Kushakova, *Russ J Phys Chem* **1977**, *51*, 251–252
- 36 M Lindblad, L P Lindfors in *Proceedings of the 10th International Congress on Catalysis*, Budapest, **1992**, (Eds L Guzzi, F Solymosi, P Tetenyis), Elsevier Science, Amsterdam, **1992**, Vol B, p 1763
- 37 G C Bond, P Konig, *J Catal* **1982**, *77*, 309–322
- 38 B N Kuznetsov, A N Startsev, Y I Yermakov, *J Mol Catal* **1980**, *8*, 135–145
- 39 K Inumaru, T Okuhara, M Misono, *J Phys Chem* **1991**, *95*, 4826–4832
- 40 T Okuhara, K Inumaru, M Misono, N Matsubayashi in *Proceedings of the 10th International Congress on Catalysis*, Budapest, **1992**, (Eds L Guzzi, F Solymosi, P Tetenyis), Elsevier Science, Amsterdam, **1992**, vol B, p 1767
- 41 J C Kevlin, M G White, *J Catal* **1991**, *130*, 447–458
- 42 S Haukka, E-L Lakomaa, T Suntola, *Appl Surf Sci* **1994**, *75*, 220–227
- 43 M Lindblad, L P Lindfors, T Suntola *Catal Lett* **1994**, *27*, 323–336
- 44 J-P Jacobs, L P Lindfors, J G H Reintjes, O Jylhä, H H Brongersma, *Catal Lett* **1994**, *25*, 315–324
- 45 D G H Ballard, *Adv Catal* **1973**, *23*, 263–325
- 46 J P Candlin, H Thomas, *Adv Chem Ser* **1974**, *132*, 212–239
- 47 Y I Yermakov, *Catal Rev -Sci Eng* **1976**, *13*, 77–120
- 48 Y I Yermakov, B N Kuznetsov, *Kinet Katal* **1977**, *18*, 1167–1178
- 49 Y I Yermakov, Y A Ryndin, O S Alekseev, V I Zaitkovskii, A V Pashis, *Appl Catal* **1986**, *26*, 313–326
- 50 Y I Yermakov, Y A Ryndin in *Homogeneous and Heterogeneous Catalysis*, (Eds Y I Yermakov, V A Likholobov), VNU Science Press, Utrecht, **1986**, p 1019
- 51 Y Iwasawa, H Sato, *Chem Lett* **1985**, 507–510
- 52 Y Iwasawa, *Catal Today* **1993**, *18*, 21–72
- 53 M Agnelli, P Louessard, A E Mansour, J P Candy, J P Bournonville, J M Basset, *Catal Today* **1989**, *6*, 63–72
- 54 P Dufour, C Houtman, C C Santini, J-M Basset, *J Mol Catal* **1992**, *77*, 257–272
- 55 S L Scott, J-M Basset, G P Niccolai, C C Santini, J-P Candy, C Lecuyer, F Quignard, A Choplin, *New J Chem* **1994**, *18*, 115–118
- 56 V A Zakharov, V K Dudchenko, E A Paukshtis, L G Karakchiev, Y I Yermakov, *J Mol Catal* **1977**, *2*, 421–435
- 57 J Schwartz, M D Ward, *J Mol Catal* **1980**, *8*, 465–469
- 58 H C Foley, S J DeCario, K D Tau, K J Chao, J H Onuferko, C Dybowski, B C Gates, *J Am Chem Soc* **1983**, *105*, 3074–3082
- 59 G Carturan, G Cocco, L Schiffini, G Strukul, *J Catal* **1980**, *65*, 359–368
- 60 Y I Yermakov, B N Kuznetsov, Y A Ryndin, *Kinet Katal* **1978**, *19*, 169–179
- 61 J M Basset, A Choplin, *J Mol Catal* **1983**, *21*, 95–108
- 62 J Phillips, J A Dumesic, *Appl Catal* **1984**, *9*, 1–30
- 63 R F Howe in *Tailored Metal Catalysts*, (Ed Y Iwasawa), Reidel, Dordrecht, Holland, **1986**, Chapter 3
- 64 M Ichikawa, in *Tailored Metal Catalysts*, (Ed Y Iwasawa), Reidel, Dordrecht, Holland, **1986**, Chapter 4
- 65 R Psaro, R Ugo, *Stud Surf Sci Catal* **1986**, *29*, 427–496
- 66 B C Gates, H H Lamb, *J Mol Catal* **1989**, *52*, 1–18
- 67 M Ichikawa, *Adv Catal* **1992**, *38*, 283–400
- 68 A Brenner, R L Burwell, *J Catal* **1978**, *52*, 353–363
- 69 K Asakura, K-K Bando, Y Iwasawa, *J Chem Soc Faraday Trans* **1990**, *86*, 2645–2655
- 70 K Asakura, Y Iwasawa, *J Chem Soc, Faraday Trans* **1990**, *86*, 2657–2662
- 71 E-L Lakomaa, *Appl Surf Sci* **1994**, *75*, 185–196

### 2.2.1.3 Spreading and Wetting

H KNOZINGER AND E. TAGLAUER

#### A Introduction

Many solid catalysts consist of several (at least two) solid phases which are brought into intimate contact. One of these phases is frequently the support with the catalytically active phases being dispersed on its surface. The most obvious examples of these types of heterogeneous catalysts are supported metals or oxides. Wetting and spreading phenomena frequently occur in such composite materials and may critically influence or determine the structure and morphology of the active phases and hence, their catalytic properties.

Wetting and spreading processes may play an important role in several steps of catalyst syntheses, in catalyst ageing, and rejuvenation. One example are supported metal catalysts which are typically prepared by impregnation from solutions containing suitable salt precursors. Dispersed metal particles are formed during subsequent reduction steps. The growth mechanisms of the metal particles, their sintering during use and their redispersion during regeneration processes are strongly influenced by the wetting properties between the participating metal and oxide phases. Metal support interactions (Section A 3.2.4) can be discussed on the basis of wetting properties. The encapsulation of small metal particles by an overlayer of support oxide which leads to the so-called strong metal-support interaction SMSI [1] is clearly due to the spreading of the support oxide material across the surface of the metal particles. Further, promoter effects are frequently, if not always, due to the formation of an intimate contact between, for example, a metal particle and an oxide promoter. In bimetallic catalysts containing two metals

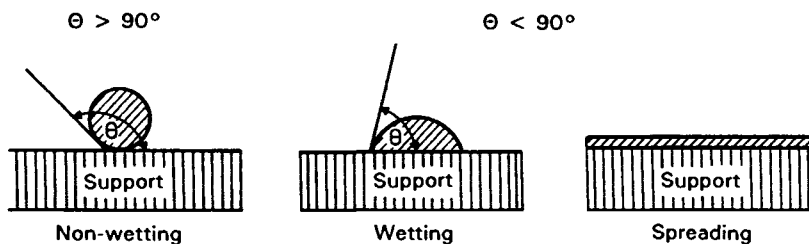


Figure 1. The solid–solid–gas interphase.

that are immiscible in the bulk (such as Cu and Ru), one metal may still wet the other and thus form an overlayer (Cu on Ru) which may ultimately lead to complete encapsulation [2].

Another example is the synthesis of supported oxide catalysts by spreading of one oxide across the surface of another (support) oxide in physical mixtures. Also, the phenomenon of solid-state ion exchange in zeolites may be discussed within the framework of the wetting and spreading concept.

Despite the significance of wetting and spreading processes in heterogeneous catalysis, they have not been considered very frequently in the catalytic literature. In a recent review [3], Ko argues that this may be due to the fact that the term wetting is attributed to the liquid–solid interface by most researchers and he raises the question as to whether the term wetting in its strictest sense can be used to describe solids that have low atomic mobility at ambient temperature. However, mobility may be induced in solid materials at catalytically relevant temperature conditions, and the general formalism of the thermodynamics of wetting can be applied to solid–solid interfaces [1]. This has been advocated by Haber and co-workers [4–7] in several articles, and the increasing awareness by catalytic chemists of the importance of wetting and spreading phenomena in heterogeneous catalysts is documented in three recent review articles by Xie and Tang [8], by Knözinger and Taglauer [9], and by Ko [3].

The present chapter first briefly discusses in general terms the formalism of the thermodynamics of wetting and spreading, and the dynamics of the spreading process. Experimental results related to supported metal catalysts including sintering, redispersion, encapsulation of a metal particle by oxide (SMSI) or by another metal are then presented. Finally, the spreading of one oxide on the surface of another oxide is discussed in some detail and solid-state ion exchange in zeolites are mentioned briefly.

## B Theoretical Considerations

### a Thermodynamics of Wetting and Spreading

The thermodynamics of wetting of a solid by a liquid is well established and discussed in detail in textbooks on colloid and interface chemistry. A schematic repre-

sentation of wetting and spreading is shown in Fig. 1 where  $\Theta$  is the contact angle between the two phases that are contacting each other.  $\Theta$  is defined by Young's equation,

$$\gamma_{ag} \cos \Theta = \gamma_{sg} - \gamma_{as} \quad (1)$$

where  $\gamma_{ij}$  denotes the specific interface free energy between phases  $i$  and  $j$ , and the subscripts a, s, and g denote active phase, support and gas phases, respectively. If under equilibrium conditions the contact angle is  $\Theta > 90^\circ$ , the supported active phase does not wet the support, whereas wetting occurs for  $\Theta < 90^\circ$ . Spreading of the supported phase across the support surface may occur for the limiting case when  $\Theta$  approaches zero.

When active phase material is brought into contact with an uniform support, the overall change in interfacial energy  $\Delta F$  is given by eq 2

$$\Delta F = \gamma_{ag} \Delta A_a - \gamma_{sg} \Delta A_s + \gamma_{as} \Delta A_{as} \quad (2)$$

The  $\Delta A$  are the changes in surface–interface areas. For spreading to occur of the active phase across the support surface,  $\Delta F$  must be negative. In the opposite case when  $\Delta F > 0$ , islands of the active phase will form on the support which will tend to coalesce into larger particles in order to decrease the free energy of the system.

To fulfil the condition for spreading, namely  $\Delta F < 0$ , the inequality

$$(\gamma_{ag} \Delta A + \gamma_{as} \Delta A_{as}) < \gamma_{sg} \Delta A_s \quad (3)$$

or

$$(\gamma_{ag} + \gamma_{as}) < \gamma_{sg} \quad (4)$$

if  $|\Delta A_a| = |\Delta A_s| = |\Delta A_{as}|$ , must hold.

The interfacial free energy  $\gamma_{as}$  is given by [10–13]

$$\gamma_{as} = \gamma_{ag} + \gamma_{sg} - U_{as} \quad (5)$$

where

$$U_{as} = U_{int} - U_{strain} \quad (6)$$

Here,  $U_{int}$  is the interaction energy per unit interfacial area between the two phases and  $U_{strain}$  is the strain

**Table 1.** Surface free energies, three-dimensional melting points ( $T_{\text{melt}}$ ) and Tammann temperatures ( $T_{\text{Tam}}$ ) of oxides [14].

Oxide	$\gamma$ ( $10^{-6}$ J cm $^{-2}$ )	$T^a$ (K)	$T_{\text{melt}}$ (K)	$T_{\text{Tam}}$ (K)
Al $_2$ O $_3$	68–70	2323	2327	1163
	90	2123		
MgO	110–115	298	3073	1536
	110	1870		
SiO $_2$	60	298	1986	993
	39	2063		
TiO $_2$	28–38	2125–2600	2173 (rutile)	1086
ZnO	90		2248	1124
ZrO $_2$	59–80	1423–2573	2988	1494
	113	< 1423		

<sup>a</sup>Temperatures at which surface free energies were measured.

energy per unit area which is generated by the mismatch of the lattices of the two phases. Combining eqs 4 and 5 gives

$$U_{\text{as}} > 2\gamma_{\text{ag}} \quad (7)$$

i.e.  $U_{\text{as}}$  must be greater than two times the surface free energy  $\gamma_{\text{ag}}$  of the active phase for spreading to occur.

For predictions to be made as to whether or not solid–solid wetting can in principal occur in a given system, surface free energies must be known for the experimental temperature and environmental conditions applied. Surface free energies of metals and pure binary oxides have been compiled by Overbury et al. [14]. The available data are typically measured near the melting point of the material and the temperature coefficients of the  $\gamma$  values (which are of the order of magnitude of  $-10^{-8}$  J cm $^{-2}$  K $^{-1}$  [14]) are not known in most cases. Surface free energies will also vary with the nature and composition of the gas phase in an unknown form. Therefore, tabulated values can only be used for order-of-magnitude considerations. Surface free energies of several metals and oxides, which bear relevance in heterogeneous catalysis, are summarized in Tables 1 and 2, respectively, together with their bulk melting points  $T_{\text{melt}}$  and Tammann temperatures  $T_{\text{Tam}} \approx 0.5T_{\text{melt}}$ .

The ratio  $U_{\text{as}}/2\gamma_{\text{ag}}$  is considered to be a measure for the tendency toward spreading of phase a across the surface of phase s (eq 7). In a microscopic picture, the same ratio must also be a measure of the relative strengths of interactions between the atoms of phase a and those of phase s in the interface and among the atoms of phase a themselves. The interactions between the two phases are complex in nature and may involve dispersion, polar, and covalent interactions depending on the chemical nature of the two phases.

Van Delft et al. [15, 16] have discussed the tendency of monolayer formation versus crystallite growth of a metal phase a on a substrate s. Deliberately ignoring entropy effects, they calculated the difference  $\Delta E$  in

binding energy per atom for an infinite number of adsorbate atoms in either a monolayer or a cubic crystallite:

$$\Delta E = \left( \sum_{\text{aa,as}} E_{ij} \right)^{\text{monolayer}} - \left( \sum_{\text{aa}} E_{ij} \right)^{\text{bulk}} \quad (8)$$

If  $\Delta E \leq 0$ , monolayer formation (spreading) will occur, whereas  $\Delta E \gg 0$  predicts the nucleation of crystallites (Volmer–Weber growth mechanism). For a small positive value of  $\Delta E$ , flat islands may be formed. For low coverages (finite number of adsorbate atoms), monolayer formation is favored over crystallite growth, since the crystallite would have a finite size so that the unfavorable contributions of the binding energies of adsorbate atoms at the surface, and particularly at edges and corners of the crystallite, would become relevant [15]. The same authors also proposed that similar considerations may determine whether a layer-by-layer growth (Frank–van der Merwe mechanism) or growth of crystallites on top of a monolayer (Stranski–Krastanov mechanism) will occur. They also pointed out that this simple broken-bond model cannot be applied to systems of ionic solids (oxide–oxide) [16].

It must be noted that the thermodynamic treatment of wetting and spreading given above, is strictly correct only if the thickness of a film produced on a support surface by spreading is large enough to be considered as a bulk phase. As shown by Ruckenstein [17, 18], the free energy change becomes dependent on film thickness when the range of the interaction forces between an atom at the exposed surface of the film and the support is comparable to the thickness of the film. The continuum approach of these authors shows that there exists a critical film thickness for which the free energy change assumes a maximum negative value, which is typically of the order of interatomic distances and hence corresponds to the thickness of a monolayer.

Ruckenstein [19] also analyzed the stabilities of small crystallites relative to film formation. They showed that there is a minimum crystallite radius  $r_m$  above which the crystallite state is thermodynamically more stable than a film. This minimum radius depends on the contact angle and hence, on the degree of wetting of the support by the active phase:

$$r_m = \frac{h}{1 - \cos \Theta} \quad (9)$$

In eq 9, which is valid for thick films,  $h$  denotes the film thickness. Note that  $r_m$  becomes very large for  $\cos \Theta = 1$  (wetting situation), suggesting that the film is always favored relative to crystallite formation. For situations relevant to supported catalysts, the loading of the support by active phase would generally be small and, hence, the films would be thin. In this case,  $r_m$  becomes dependent on a parameter  $\alpha$ , which is pro-

**Table 2.** Surface free energies and Tammann temperatures of selected metals [113] and their oxides [14].

Metal	$\gamma$ ( $10^{-6}$ J cm $^{-2}$ )	$T^a$ (K)	$T_{\text{Tam}}$ (K)	Oxide	$\gamma$ ( $10^{-6}$ J cm $^{-2}$ )	$T^a$ (K)	$T_{\text{Tam}}$ (K)	
Cu	135	1356	678	FeO	59–73	1573–1693	846	
Ir	225	2683	1342		105	1683		
Fe	185	1808	904		36–40	1811	906	
Mo	225	2890	1445	MoO <sub>3</sub>	5–7	1068	534	
Ni	180	1726	863	Re <sub>2</sub> O <sub>7</sub>	3–4	600–800	285	
Pd	150	1827	914					
Pt	180	2045	1023					
Rh	200	2239	1120	V <sub>2</sub> O <sub>5</sub>	8–9	963	482	
Ru	225	2583	1292		WO <sub>3</sub>	10	1746	873
					ZnO	9		988

\*Temperature of measurement.

portional to the difference of two quantities representing the strength of interactions between atoms of the active phase (a–a interactions) and the strength of interactions between a-atoms and s-atoms of the substrate (a–s interactions). For thin films, the minimum crystallite radius  $r_m$  is then given by

$$r_m = \frac{3h}{1 - \cos \Theta + \alpha/h^2\gamma_{ag}} \quad (10)$$

If the a–a interactions are stronger than the a–s interactions, the parameter will most likely be negative, and if  $h$  is sufficiently small,  $r_m$  can become negative. In this situation, the crystallite state is always thermodynamically favored over the film state. If, however, the denominator of eq 10 becomes positive, when a–s interactions are stronger than a–a interactions, then the radius  $r_m$  can become very large and positive. Under these conditions, the film state may be the thermodynamically preferred situation. For further details, the reader is referred to the detailed treatment by Ruckenstein [19].

Based on his thermodynamic treatment of wetting and spreading, Ruckenstein [20] concluded, that surface-phase transformations may occur. Below a critical loading of the support, a submonolayer of active phase exists on the support. Above the critical loading, large crystallites will form in addition to the submonolayer (or monolayer). It is most likely that submonolayer films always exist in equilibrium with crystallites, although the fractional coverage can be very low. Obviously, these situations are closely related to the growth mechanisms of particles on the support surface.

#### *b Qualitative Discussion of the Dynamics of Interfacial Processes*

The foregoing discussions on the thermodynamics of wetting and spreading are limited to systems which are

in their equilibrium state. This is not the case for many solid catalysts and in particular not for supported catalysts in which the support material is supposed to stabilize small particles of the active phase. Because of the resulting high dispersions and high surface areas, such systems are typically in a state of high surface free energy. During heating and/or during catalytic reactions, these materials therefore have a high tendency to sinter, thereby decreasing the exposed surface area and the surface free energy of the system. Especially, supported metals tend to age via crystallite growth. Under certain conditions and for certain combinations of active phase/support materials, the surface area of the active phase, especially oxides, being exposed to the chemical environment can be increased. Redispersion or spreading may occur. Sintering, redispersion and spreading are dynamic processes which drive a given system toward its equilibrium state. The extent of sintering or dispersion of a given catalytic material depends on several parameters including time of treatment or use, temperature, gas phase composition, presence of additional species on the support surface, and the properties of the support and of the active phase. Here, the surface free energies of the two components and the two-dimensional mobility (surface diffusion coefficients) of atoms, molecules or clusters of the active phase are of special importance.

The formation of highly dispersed particles or crystallites in the synthesis process of, for example, a supported metal catalyst, is governed by nucleation and growth mechanisms (vide supra) that have been described in the literature [15, 16, 21–23]. For sintering or redispersion (spreading and film formation) to occur, particles or atoms, molecules or clusters of the active

phase must become mobile. As a rule of thumb, the Tammann temperature (in degrees K)

$$T_{\text{Tam}} \approx 0.5T_{\text{melt}}^{\text{bulk}} \quad (11)$$

is considered to be sufficient to make atoms or ions of the bulk of a solid sufficiently mobile for bulk-to-surface migrations, whereas the Hüttig temperature (approximately one-third of the bulk melting temperature) is enough to make the species already located on the surface sufficiently mobile to undergo agglomeration or sintering. Ruckenstein [13, 24] has shown that the enhanced mobility can be associated with the two-dimensional melting of the surface of a solid particle that leads to a liquid-like behavior of the surface layer. A theory of two-dimensional melting has been advanced by Kosterlitz and Thouless [25] which is based on the dislocation pairs model of melting. The two-dimensional melting temperature is given by

$$T_{\text{melt}}^{2\text{-dim}} = (mk/8h^2)a^2\theta_D^2 \quad (12)$$

where  $m$  is the atomic mass,  $k$  the Boltzmann constant,  $h$  Planck's constant,  $a$  the lattice parameter, and  $\theta$  the Debye temperature. It turns out that  $T_{\text{melt}}^{2\text{-dim}}$  as given by eq 12 is proportional to the bulk melting temperature as obtained by Lindemann [26] with the proportionality constant being close to 0.5, the value used in the definition of the Tammann temperature. Values of bulk melting temperatures of catalytically relevant metals and oxides are summarized in Tables 1 and 2, respectively.

Baker [27] observed mobilization of small particles of several metal oxides on graphite at a temperature (the so-called mobility temperature) that was identical to the Tammann temperature. Thus, at least in systems exhibiting relatively weak interactions between active phase and support surface, particle mobility may be induced at this temperature. The particle migration may perhaps be described as a floating of the active phase particle on the liquid-like surface layer.

For the sintering of small (metal) particles situated on a support surface, several simple mechanisms have been proposed:

- (i) migration of crystallites and their coalescence [28, 29];
- (ii) emission of atoms from small crystallites and their capture by large ones by Ostwald ripening [30–34];
- (iii) a combination of the two previous mechanisms [32].

The theoretical treatment of these various mechanisms has been reviewed by Ruckenstein [35]. The essential features of sintering (of metal particles) can be qualitatively summarized on the basis of these simple processes. Consider a supported metal catalyst with a broad particle-size distribution ranging from single

atoms to large particles. Single atoms may migrate across the surface of the support at sufficiently high temperatures and be captured by particles. Simultaneously small particles can migrate across the surface and coalesce when they encounter each other or large ones. This process can be diffusion-controlled if the interaction between two particles in contact are so strong that they form a single particle within a time that is short compared to the time of migration. If, however, the coalescence of two particles into one is slow compared to the diffusion time, the process is said to be coalescence controlled or interface controlled.

The migration rate of particles is size (i.e. mass) dependent. Small particles, being the mobile ones, will therefore tend to be exhausted and further sintering can only occur if the remaining (slow or immobile) particles will emit atoms that migrate from smaller particles to larger ones by which they are captured. It can be shown that there exists a critical radius for the particles [32]. Those particles that have a radius  $r$  smaller than the critical radius  $r_c$  will loose atoms while particles with  $r > r_c$  will gain atoms and grow bigger. This is, of course, the mechanism of Ostwald ripening. As indicated in the previous section, monolayer or submonolayer films can coexist with particles. If there is a particle size distribution with small and large particles being present, atoms will be emitted to the film by the small particles and captured by the larger ones because the film is undersaturated relative to small ones but supersaturated with respect to the large ones. This process can be considered as global ripening and should preferentially be operative at high metal loadings. Alternatively, direct ripening may occur at low metal loadings whereby atoms are transferred directly from small particles to large ones without involving the two-dimensional film of single atoms.

It is clear that the sintering process can be globally dominated by either particle migration or single atom migration. The properties of the support and active phase of the considered catalyst system determine which of the two possible pathways will be dominantly chosen. Ruckenstein and Dadyburjor [32] considered a sintering mechanism in which single atoms and clusters of atoms are emitted from particles, particles of all sizes migrate at size-dependent rates, two particles (including single atoms) that collide, tend to coalesce. The theoretical treatment provided by Ruckenstein and Dadyburjor [32] takes into account the effects of metal loading, two-dimensional solubility, diffusional and interfacial processes for all sizes. All these models however, cannot fully describe the mechanisms of sintering because they still disregard the influence of wetting phenomena. Wetting determines the surface contact between support and active phase and therefore affects the migration of the active-phase particles across the support surface. Moreover, the two-dimensional film

servicing as a pool of single atoms in global ripening must be formed via the spreading of a submonolayer of atoms from the crystallites.

In all the models discussed so far, the support surface was assumed to be flat. In fact, very many case studies, particularly of supported metals, have used flat, low-surface-area substrates. However, Wynblatt and Ahn [36] have demonstrated that surface curvature does affect the surface free energy, the growth of particles (sintering) via particle migration and interparticle transport. Therefore, the sintering process of practical supported catalysts which frequently use high-surface-area, porous supports must be significantly more complex than described by the simple models.

Redispersion processes are very closely related to wetting and spreading phenomena. Inspection of the data accumulated in Table 2 shows that typically the surface free energies of metals are higher than those of the respective oxides. Hence, the thermodynamic condition for spreading (eq 7) on the surface of an oxide support is more likely to be fulfilled for supported metal catalysts in an oxidizing atmosphere, particularly when strong chemical interactions (compound formation) are occurring, thus increasing the value of  $U_{as}$ . It appears that smaller particles spread on the support surface more easily than larger ones do. This phenomenon has been interpreted by Ruckenstein and Chu [37], by introducing a critical radius  $r_c$  for spreading (which obviously is very closely related to the critical radius for particle growth by emission and capture of atoms (vide supra)). Smaller particles have a higher dissolution pressure than larger ones, and thus develop a higher tendency towards spreading. Particles with a radius smaller than  $r_c$  can spread completely across the support surface as a monolayer patch.

It is for the above reasons that rejuvenation of supported metal catalysts is typically performed in oxidizing atmospheres. However, redispersion mechanisms may be much more complex than indicated since fragmentation of particles may also occur during the thermal treatments in oxidizing atmospheres (see subsection C).

Several oxides which are used as active phases in supported oxide catalysts or catalyst precursors are also capable of spreading on typical support materials, such as alumina or titania [3, 8, 9]. Two driving forces may be principally involved in the spreading process. One is the concentration gradient of the active phase which might induce independent atom/molecule diffusion onto the support surface. Haber and co-workers [5, 38], however, argued that surface diffusion should be very slow in oxide systems in the temperature ranges frequently encountered in the solid state synthesis of oxide systems, because of the typically high values of the lattice energies of oxides. Therefore the variation of the surface free energy along the interface of a bi-

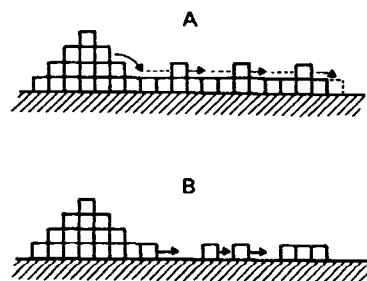


**Figure 2.** Schematic representation of surface transport processes: (A) unrolling-carpet mechanism; (B) transport by defect diffusion.

nary oxide system must be considered as the dominant driving force. The overall surface free energy in such a system can be minimized through the expansion of regions with a low surface free energy and contraction of those with high surface free energy. The gradient of the surface free energy along the surface creates a shear stress on the supported oxide phase and the molecules of this phase may then migrate under the action of this stress from regions of lower to those of higher surface free energy.

As discussed above, surface melting may occur at the Tammann temperature. The mechanism of spreading in powder mixtures of oxides has therefore been described [9] as a migration of species from a liquid-like surface layer of one solid across contact boundaries between grains onto the surface of the support, where they may be immobilized again if the interaction energy  $U_{int}$  is sufficiently high. A thin film (possibly a single atomic or molecular layer) may thus extend from the contact boundary between the particles onto the support surface. Further transport of the active oxide material can then be envisaged to occur via migration of the active species over the film surface toward the leading edge of the film where they would ultimately be trapped again on the support surface. This process may be described as an unrolling carpet mechanism [39] which is schematically represented in Fig. 2. One may expect that once a monolayer of active material has formed on the support, excess active phase is forming crystallites. Depending on the individual properties of the interacting oxide materials, formation of thick films (several molecular layers) or islands (particles) with finite contact angle may also occur [13] (vide supra).

Still another model for the spreading of an active oxide ( $V_2O_5$ ) under oxidizing conditions onto the surface of a support (anatase) was proposed by Haber et al. [40]. In this model, the active phase crystallite spreads spontaneously at the beginning of the thermal treatment (hot plate effect) which leads to amorphization of the active phase. Thereafter the spreading is

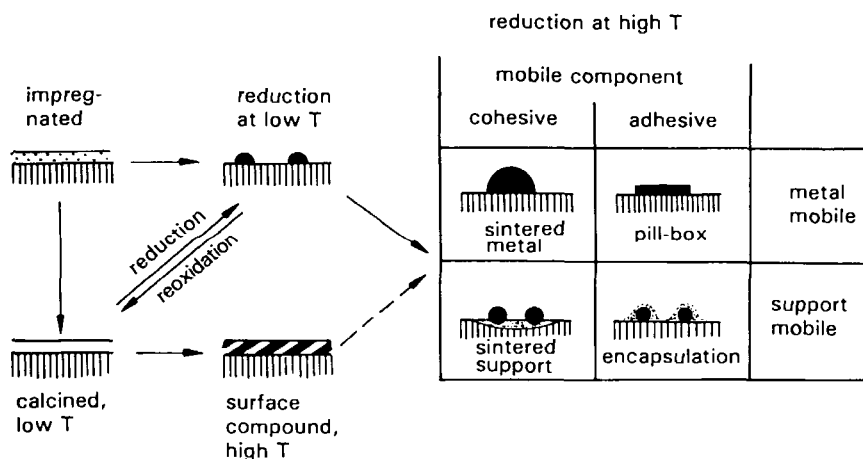


Figure 3. Schematic representation of metal-support interactions (adopted from Ref. 16).

assumed to be diffusion-controlled. Since migration of active phase across the monolayers already formed was found to be highly improbable, it was proposed that spreading in this second stage occurs by diffusion of defects (vacancies) through the monolayer [39], these defects being refilled at the interface between the monolayer and the amorphous active phase (see Fig. 2). Most probably this transport via vacancy diffusion can only occur if the interaction between active phase and support is sufficiently weak for vacancies in the monolayer to be formed under the applied thermal conditions.

It may be interesting to note that Neiman [41] has recently proposed a mechanism for cooperative transport processes in complex oxide materials involving V, Nb, Mo, and W. In this model, it is assumed that the mobile species are  $\text{MeO}_x$  complexes (because of the high covalence of the  $\text{Me-O}$  bonds) which migrate by rearrangement of the  $\text{Me-O}$  bonds in regions of local amorphization and quasi-melting of the lattice. It may be speculated that similar processes also occur during spreading of two-dimensional films across the surface of supports.

### C Supported Metal Catalysts

The various stages of the preparation and thermal treatments of supported metal catalysts are very schematically illustrated in Fig. 3. A very similar presentation was earlier given by van Delft et al. [16]. Typically, the support is impregnated with a metal salt (see Section A.2.2.1.1) which serves as the metal precursor and should be well dispersed. Small metal particles may be formed by either direct reduction under mild conditions or by reduction after an intermediate oxidation step. Mild oxidation will lead to thin oxide films spread out on the support or to small oxide particles, where particles and film may also coexist. More severe treatments in oxidative atmospheres can lead to the

formation of surface compounds (e.g. spinels) which again may coexist with oxide particles. Continued reduction or thermal treatment in reducing atmosphere under more severe conditions can induce several processes, depending on the nature of the metal and of the support. If the metal is mobile and strong cohesive interactions are operative sintering will occur, whereas the metal particles may spread out and form flat islands (pill-box) if the metal-support interactions are strong. If, in contrast, the support is mobile and strong adhesive interactions come into play, the metal particles can become encapsulated and the so-called SMSI state (strong-metal-support-interaction) may be induced.

It is clear that wetting and spreading phenomena are significantly involved in all steps indicated in Fig. 3. Rather than report on the many studies on sintering and redispersion in practical supported metal catalysts, the following discussion briefly highlights some model studies which have been nicely reviewed by Ruckenstein et al. [1].

#### a Sintering and Redispersion

Chen and Ruckenstein [42] have performed a mechanistic study of the sintering of Pd on alumina by transmission electron microscopy (TEM) using model catalysts. These consisted of thin self-supporting and electron-transparent  $\gamma\text{-Al}_2\text{O}_3$  films onto which Pd metal was vacuum evaporated. The resulting thin Pd film was transformed during treatment in flowing  $\text{H}_2$  into crystallites in the diameter range 1–7 nm. Starting from this situation, the effects of additional heat treatments in  $\text{H}_2$  at various temperatures and for increasing periods of time were studied by TEM. The time sequences of changes in size, shape and position of individual particles at 923 K indicated that the major processes occurring were large-scale crystallite migration and coalescence, because a large number of small crystallites were shown to disappear without change of



size with the average diameters of crystallites simultaneously growing. Interestingly, crystallites having diameters as large as 7.5 nm did migrate at 923 K, while some smaller ones appeared to be immobile. Thus, mobilities of crystallites are not only dependent on size. Small crystallites may be trapped in valleys or pits of a rough surface, whereas larger ones, which contact only the tips of the ridges on the surface may travel with greater ease. In addition, the local surface morphologies may affect the interaction forces between particles and support surface. Although the size of small particles did not in general decrease before they disappeared, the possibility of Ostwald ripening could not be excluded. In fact, in localized regions where a few small crystallites were located in close vicinity to larger ones, the former decreased in size and then disappeared. This observation was interpreted as being due to direct ripening (*vide supra*).

Under more severe H<sub>2</sub> treatment, facetting of crystallites larger than 12.5 nm also occurred.

Particle migration (up to 8 nm particles migrated over 25 nm at 773 K) was also observed for Pt on alumina [43]. The two major mechanisms of sintering of supported Pt crystallites appeared to be (i) short-distance, direction-selective migration of particles followed by either collision and coalescence or by direct transfer of atoms between the two approaching particles, or (ii) localized direct ripening between a few immobile, adjacent particles.

Chen and Ruckenstein [44] also investigated the behaviour of large Pd crystallites on  $\gamma$ -Al<sub>2</sub>O<sub>3</sub> model supports in O<sub>2</sub> atmospheres in the temperature range 623–1193 K. The Pd crystallites are oxidized to form PdO at temperatures below the decomposition temperature of 1143 K. Since the surface free energy of PdO is smaller than that of Pd metal (Table 2), the crystallites extended on the support surface to a smaller wetting angle as expected. Spreading under oxidizing conditions occurs because the surface free energy of the metal oxide  $\gamma_{ag}$  and the interface free energy  $\gamma_{as}$  between the oxidized palladium and the alumina support are smaller. As can be seen from eq 5,  $\gamma_{as}$  is smaller because  $\gamma_{ag}$  is smaller and the interaction energy  $U_{as}$  is larger for the metal oxide than for the metal.

However, additional much more complex phenomena have been observed. Depending on crystallite size and temperature conditions, the formation of porous structures, of torus-like particles, the extension of particles developing irregular leading edges with pits and cavities, and ultimately tearing and fragmentation was observed in 1 bar O<sub>2</sub> over the temperature range mentioned. The pit formation was explained as a surface tension gradient-driven phenomenon (perhaps enhanced by a wetting-produced stress), and/or as a consequence of crack propagation caused by stress, which was induced by wetting and enhanced by the oxidation of

the freshly exposed surface at the tip of the crack. The formation of the torus-like particle was attributed to incomplete oxidation of larger particles at lower temperatures.

It should be noted that, at temperatures higher than the decomposition temperature of bulk PdO in 1 bar O<sub>2</sub>, the palladium particles sintered and formed faceted crystallites.

Very similar phenomena were observed by Ruckenstein and Lee [45] when Ni supported on model alumina films was treated in O<sub>2</sub> atmospheres. Extension of the particles leading to a torus shape during heating was reported, the torus being divided into interlinked subunits and containing small crystallites within the ring. The extension of the oxidized Ni particles is obviously due to the lower surface free energy of NiO and to the lower interfacial free energy between the NiO and the alumina support as outlined above for the Pd-alumina system. However, the interfacial free energy  $\gamma_{as}$  can be extremely small (perhaps even negative under nonequilibrium conditions) when strong chemical interactions or surface compound formation increase the interaction energy  $U_{as}$  in eq 5. In contrast to PdO, NiO has a high tendency toward surface spinel formation in contact with alumina [46, 47], and hence  $U_{as}$  should be large. Therefore, under dynamic oxidation conditions, the large decrease in the dynamic value of  $\gamma_{as}$  and the simultaneous decrease of  $\gamma_{ag}$ , can very significantly increase the driving force for spreading. Spinel formation starts at the interface between the NiO particle and the alumina support and propagates into the latter. The surface spinel layer grows until the rate of formation is slowed down by a large diffusional resistance. The interaction energy  $U_{as}$  is only large during the formation of the surface compound and decreases again for the interaction of the NiO with the surface spinel. Therefore, when  $U_{as}$  is plotted against time, it passes through a maximum while, correspondingly,  $\gamma_{as}$  passes through a minimum (which can be negative) as illustrated schematically in Fig. 4. Although there may also be thermodynamic reasons for the appearance of the torus-shaped NiO particles, Ruckenstein and Lee [45] could also explain their formation as a kinetic phenomenon. They suggested that very rapid spreading takes place as soon as the surface spinel starts forming because of the resulting large driving force for wetting, and that this may lead to the formation of the torus shape by stress-simulated fracture of the crystallites.

In a similar study, Sushumna and Ruckenstein [48] demonstrated that the composition of gas atmosphere can be of critical importance for the detailed behaviour of Fe supported on alumina catalysts. Even trace impurities of O<sub>2</sub> and H<sub>2</sub>O in H<sub>2</sub> in the ppm range

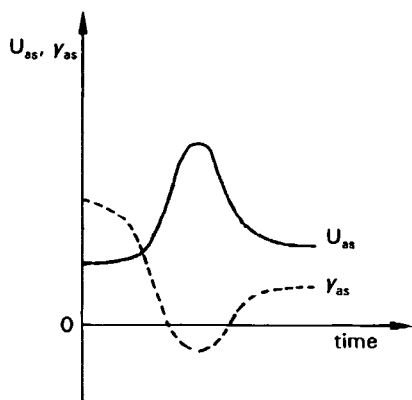


Figure 4. Time dependence of  $U_{sa}$  and  $\gamma_{sg}$  (adopted from Ref. 1).

had detectable effects on the sintering behavior of Fe particles.

Industrial regeneration techniques [49] of supported metal catalysts typically involve oxidation/reduction cycles. Redispersion is achieved during thermal treatments in oxidative atmospheres containing  $O_2$ , water, halogens and others [50] often as mixtures since the  $U_{sa}$ , interaction energies and, thus, the tendency towards wetting and spreading of the active phase onto the support surface is strongly enhanced under those conditions. As a consequence, highly dispersed metal particles may be formed under subsequent mild reduction conditions.

An interesting case of wetting–nonwetting transition under reaction conditions was recently described by Clausen et al. [51]. By measuring the changes of Cu–Cu coordination numbers by EXAFS for a Cu/ZnO catalyst, these authors inferred that small metallic Cu particles dynamically changed morphology, when the oxidation potential of the  $H_2O/CO/CO_2/H_2$  gas phase was varied by changing the partial pressure of the components. The morphology changes were attributed to wetting–nonwetting phenomena which were due to gas phase-induced changes of the interaction energy between Cu metal and the ZnO support. Essentially no changes of morphology were detected for Cu/SiO<sub>2</sub> catalysts.

#### *b Strong Metal Support Interactions (SMSI)*

As schematically shown in Fig. 3, two extreme situations may occur during thermal treatment at high temperature ( $>773$  K) in reducing atmospheres. If the support is immobile and strong interactions occur between metal particle and support, the metal may spread out on the support surface and form flat islands (pill-box model). If, however, the metal has a high melting point and the support is mobile, then encapsulation of the metal particle may occur by wetting of the metal by support oxide. Since Tauster and co-workers [52, 53] first reported that the chemisorption capacity for  $H_2$

and CO decreased dramatically for supported metal catalysts in the SMSI state, there has been continuing discussion as to whether the phenomenon was caused by electronic or by geometric/morphological effects [1, 54, 55] (see Section A.3.2.4). The encapsulation or decoration model was proposed because of the failure of the electron transfer models to explain the behavior of large particles supported on titania [56–58]. However, electron transfer effects may also be important contributions for the encapsulation to occur. The phenomenon of encapsulation can be explained in terms of wetting and spreading.

The SMSI effect has been observed for support materials such as TiO<sub>2</sub>, V<sub>2</sub>O<sub>5</sub>, Nb<sub>2</sub>O<sub>5</sub>, and Ta<sub>2</sub>O<sub>5</sub>. Inspection of the surface free energies of these oxides (see Table 1), show that they are smaller than those of other supports such as SiO<sub>2</sub>, Al<sub>2</sub>O<sub>3</sub>, ZrO<sub>2</sub>, MgO which do not manifest SMSI. Considering the unrealistic situation of the formation of a thick oxide film on the metal particle, low  $\gamma_{sg}$  values (the support must spread for encapsulation of the metal) would be favorable for spreading as the ratio  $U_{sa}/2\gamma_{sg}$  would increase. The driving force for spreading would even further increase if the interaction energy  $U_{sa}$  between the metal and the support oxide is large. It should be noted that the oxides that manifest SMSI are reducible, and it is generally accepted that partial reduction (possibly catalyzed by the metal) of the support is a prerequisite for encapsulation to occur [1, 54, 55]. Electron transfer from the oxide support to the metal may in fact occur with greater ease if the oxide is in a reduced state. This would increase  $U_{sa}$ , and significantly enhance the driving force for spreading. It should, however, also be noted that the surface free energies of reducible oxides increase if they become oxygen deficient, and that their melting points simultaneously increase. Therefore, the driving force for spreading and the mobility of the oxide decrease in the reduced state. These effects may influence the tendency toward encapsulation, although the enhancement of the interaction term  $U_{sa}$  seems to overcompensate them.

In reality, the strong interactions are short range, and therefore the oxide film forming on the metal particle is expected to be a monolayer or submonolayer film. The driving forces involved are therefore the concentration gradient of the oxide and the gradient of the surface free energy along the metal surface which leads to shear-stress-induced migration of oxide molecules across the metal surface, as already discussed above.

Several studies have been reported in which model TiO<sub>2</sub> thin films were used as supports, which clearly demonstrated the metal particle encapsulation [59, 60]. Linsmeier et al. [61] and Taglauer and Knözinger [62] have studied the behavior of Rh which was evaporated onto an electrochemically produced TiO<sub>2</sub> (anatase) film using low energy ion scattering (LEIS; see Section

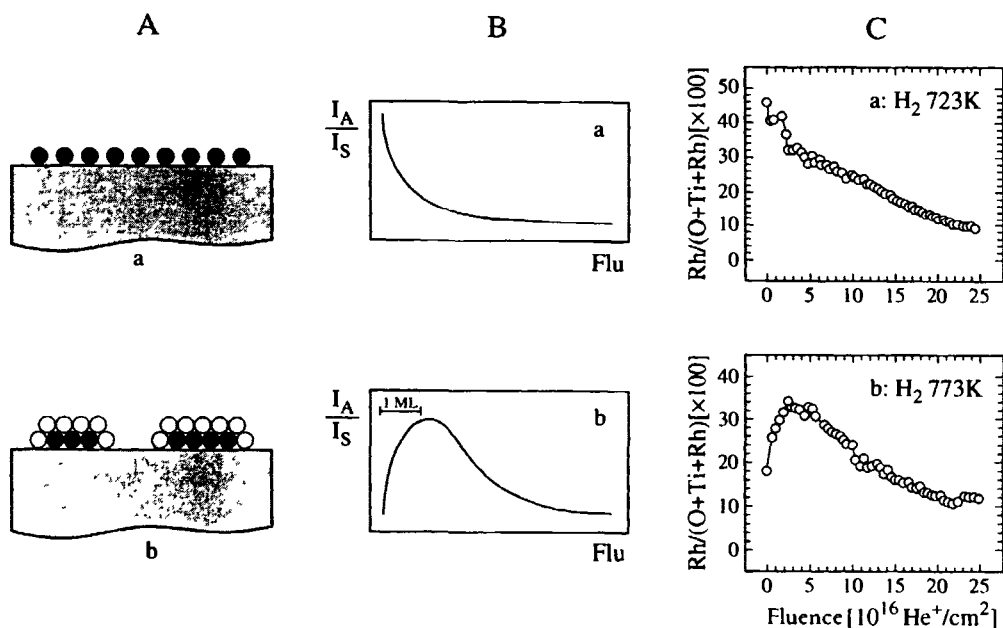


**Figure 5.** Low energy ion scattering on Rh/TiO<sub>2</sub> model catalysts: (A) structure models; (B) expected intensity profiles; (C) experimental intensity profiles (adopted from Ref. 62).

A.3.2.1.2) as a surface-sensitive analytical technique. Figure 5(A) shows two models for supported metal catalysts, namely (a) a monolayer of atoms A on the support surface S; and (b) small islands of atoms A which are encapsulated by support S. Figure 5(B) represents the corresponding profiles that are expected for the two models when the scattering intensity ratio  $I_A/I_S$  is plotted versus the fluence (total number of He<sup>+</sup> ions impinging on the surface). Experimental results for the Rh/TiO<sub>2</sub> model catalyst after mild H<sub>2</sub> treatment at 723 K (non-SMSI state) and after severe H<sub>2</sub> treatment at 773 K (SMSI state) are shown in Fig. 5(C). The experimental profile obtained after low temperature treatment resembles that of a highly dispersed metal film, whereas the profile after high temperature treatment passes through a maximum and clearly indicates the encapsulation of the Rh particles. A rough estimate showed that the fluence at the position of the maximum corresponds to the average value required to sputter one monolayer of oxide. This result nicely relates to the prediction made above for the expected film thickness.

### c Bimetallic Catalysts

Surface segregation phenomena and the surface composition of bimetallic catalysts are controlled by the surface free energies of the constituents of the bimetallic particles. The deposition of metal on metal in relation to bimetallic catalysts has been discussed by Dodson [63].

Particularly interesting systems in the context of wetting are bimetallic supported catalysts containing

two metals that are immiscible in the bulk, such as Ru and Cu. Sinfelt and co-workers [64, 65] first reported on a Cu-induced suppression of hydrogen chemisorption for SiO<sub>2</sub>-supported RuCu catalysts; this observation was consistent with the structural model of the bimetallic particles consisting of a Ru core encapsulated by a Cu layer, which was developed by Sinfelt et al. [66] on the basis of EXAFS results. Several surface science studies also demonstrated the formation of Cu films on the surface of Ru single crystal surfaces [67, 68] and infrared studies of CO chemisorption on RuCu/SiO<sub>2</sub> catalysts supported the encapsulation model [69]. The available experimental evidence therefore clearly demonstrates that – although the two metals do not form binary alloys – Cu does wet the Ru. The surface free energy  $\gamma_{Cu}$  of Cu is relatively small (see Table 2) and lower than that of Ru. Moreover, surface science studies on single crystal model systems [70] and infrared spectra of chemisorbed CO on RuCu/SiO<sub>2</sub> catalysts [69] showed that electron transfer occurs from Cu to Ru. This electron transfer contributes to the strength of interaction between the two metals at the interface and presumably leads to a ratio  $U_{RuCu}/2\gamma_{Cu} > 1$ , so that the spreading condition for Cu across the surface of Ru is fulfilled.

### D Supported Oxide Catalysts

Supported oxides of transition metals, particularly of groups Vb (V), VIb (Cr, Mo, W) and VIIb (Re) are widely used as catalysts or catalyst precursors for vari-

ous industrially important reactions. These so-called monolayer-type catalysts are formed when one metal oxide (mobile active phase) is dispersed on the surface of a second metal oxide (immobile support). Typical catalyst supports in industrial applications are transition aluminas, silica, and titania. Inspection of the data summarized in Table 1 indicates, that the surface free energies of these support oxides are higher than those of the mentioned transition metal oxides. Assuming the formation of thick films, the spreading condition of eq 7, namely  $U_{as}/2\gamma_{ag} > 1$ , must be fulfilled. Unfortunately the interaction energies  $U_{as}$  are practically always unknown. However, it has been argued [71] that chemical contributions to  $U_{as}$  should be high if the two components have a tendency to form a ternary oxide via solid-state reactions. In this case the spreading condition should be fulfilled. Based on these arguments, the experimentally observed spreading of  $\text{MoO}_3$  on alumina and titania could be explained [71] since both supports form bulk ternary oxide phases with  $\text{MoO}_3$  ( $\text{Al}_2(\text{MoO}_4)_3$  and  $\text{Ti}(\text{MoO}_4)_2$ , respectively) at higher temperatures, although these are not detected under the spreading conditions. In contrast,  $\text{MoO}_3$  is not known to undergo a solid-state reaction with silica, and consequently spreading of  $\text{MoO}_3$  on the surface of silica was not observed [71].

As already mentioned above, the interaction forces between active phase and support are short range and should be restricted to the interface. Therefore, the driving forces for spreading are expected to decrease significantly once a molecular monolayer is formed. As a consequence, oxide particles or crystallites of the active phase are expected to form when the loading by the active oxide exceeds the theoretical monolayer capacity of the support. Experimental evidence for this situation has in fact been reported in the literature [9].

These principles can be applied for the preparation of supported oxide monolayer catalysts from mechanical mixtures, the advantage of this route being that the handling of solutions for impregnation can be avoided. However, for efficient spreading to occur, the two components of a powder mixture must be brought into intimate contact and optimal mixing is required so as to obtain a homogenous product. Moreover, the active (and mobile) phase must be present as crystallites having diameters below a critical value (see eqs 9 and 10), since otherwise the crystallite state may be thermodynamically more stable than the film. Grinding or milling is therefore usually applied to the powder mixture prior to thermal treatments. Often these processes are not well controlled when powder mixtures are prepared for solid-state synthesis of bulk products or supported catalysts, although they must be expected to influence the reactivity of the powders very significantly.

Grinding will certainly influence the grain sizes and grain-size distributions, and thus the rates of spreading.

Also, the two-dimensional melting temperature should be dependent on the grain size (curvature). Several additional phenomena occur in the very complex grinding process that must influence the spreading and reactivity behavior of powder mixtures [72–74]. During grinding, several particles are simultaneously and repeatedly subjected to stress application in the grinding zone. With each stress application, several fractures may occur in each particle. Cracks will be initiated and will propagate; flaw interaction in a particle, secondary breakage, and interaction of particles with each other will occur. The physical and chemical interaction between particles and the grinding environment, and the transport of material through the grinding zone will also affect the nature of the product obtained. Occasionally material transport between chemically distinct particles may already lead to spreading during the grinding and milling procedure. This may particularly occur when crystallites are involved that have layer structures (e.g.  $\text{V}_2\text{O}_5$ ), so that stress application may lead to exfoliation processes. Even solid-state reactions in bulk phases can be induced by mechanical activation of solid materials and several tribochemical processes have found technological application [75]. For example, Angelov and Bonchev [76] have reported on the formation of a Cu-rich surface layer on  $\text{Co}_3\text{O}_4$  by mechanically treating a powder mixture of  $\text{CuO}$  and  $\text{Co}_3\text{O}_4$  in a friction grinder. These reactions are believed to occur due to strong local temperature increases which may lead to melting of microscopic zones within contact regions.

The effect of mechanical stress applied to  $\text{MoO}_3$  by grinding in a planetary mill have recently been studied by Mestl and co-workers [77–79]. It was shown that the crystallite sizes decreased from an initial value of about  $1\ \mu\text{m}$  to  $50\ \text{nm}$ , with some ultrafine amorphous material also being produced. The BET surface area simultaneously increased from an initial value of  $1.3\ \text{m}^2\ \text{g}^{-1}$  to  $32\ \text{m}^2\ \text{g}^{-1}$ . A substoichiometric  $\text{MoO}_3$  was formed during grinding. The presence of shear defects was indicated by XRD, and  $\text{Mo}^{5+}$  was detected by ESR and optical spectroscopy. When this milled  $\text{MoO}_3$  was gently mixed with alumina without applying additional mechanical stress, and then thermally treated in  $\text{O}_2$  at  $823\ \text{K}$  (melting point of bulk  $\text{MoO}_3$  is  $1068\ \text{K}$ ), in situ high temperature Raman spectroscopy demonstrated the existence of a surface melt of molybdenum oxide which transformed into a glassy  $\text{MoO}_3$  surface phase on quenching to room temperature [80]. The experiments described by Mestl et al. [80] clearly showed the higher reactivity of the milled  $\text{MoO}_3$  and its more efficient spreading on the alumina surface as compared to the initial low-surface-area material.

Since the reported literature has been summarized in several recent review articles [3, 8, 9], we will only briefly describe a few experimental studies on spreading in oxide mixtures.

### a Molybdenum-based Catalysts

The most thoroughly studied supported oxide systems are those involving molybdenum oxide as the mobile phase. As already mentioned, spreading of  $\text{MoO}_3$  in physical mixtures was observed on the surfaces of aluminas and titania (anatase) but not on silica; the reason for the different behavior of these support oxides was thought to be connected with the interaction energy  $U_{\text{as}}$  between  $\text{MoO}_3$  and the support materials [71]. Highly dispersed molybdenum oxide surface phases were also detected on  $\text{MgO}$  [81, 82] and on  $\text{SnO}_2$  [81]. It is interesting to note that  $\text{MoO}_3$  and  $\text{MgO}$  undergo a solid state reaction to form  $\text{MgMoO}_4$ .

The transport of  $\text{MoO}_3$  across the surface of alumina was demonstrated in several model experiments. Hayden et al. [83] prepared molybdenum oxide on a graphite support. Because of the weak interaction between these two components,  $\text{MoO}_3$  particles were formed. This material was then mixed with  $\text{Al}_2\text{O}_3$  and studied by controlled atmosphere electron microscopy.  $\text{MoO}_3$  particles were mobile on the graphite surface at 930 K and spontaneously disappeared when they contacted alumina grains. This observation was explained by rapid spreading of the  $\text{MoO}_3$  over the  $\text{Al}_2\text{O}_3$  surface, and related to the higher surface free energy of alumina as compared to graphite. It should, however, be emphasized that the large interaction energy  $U_{\text{as}}$  between  $\text{MoO}_3$  and  $\text{Al}_2\text{O}_3$  is crucial for the large driving force for spreading. Leyrer et al. [84] used model samples which consist of an alumina wafer in contact with a  $\text{MoO}_3$  wafer forming a sharp dividing line. Concentration profiles across the dividing line between the two oxides were measured by Raman microscopy with a lateral resolution of approximately 20  $\mu\text{m}$ . The results clearly demonstrated that  $\text{MoO}_3$  was in fact transported onto the  $\gamma\text{-Al}_2\text{O}_3$  surface at 800 K in streams of either dry or humid  $\text{O}_2$  whereby the initially sharp concentration profile became diffuse and reached widths of several hundred (up to 1000  $\mu\text{m}$ ) micrometers after 100 h. It was also shown that the presence of water vapor increased the rate of spreading, and led to the formation of a surface polymolybdate (vide infra). These model experiments also enabled gas phase transport and surface diffusion in a concentration gradient to be discounted as possible mechanisms for the migration of  $\text{MoO}_3$ , since no transport occurred onto a  $\text{SiO}_2$  wafer in an analogous experiment. This result again emphasizes the crucial importance of the interaction energy in fulfilling the spreading conditions given by eq 7.

Spreading of polycrystalline  $\text{MoO}_3$  in powder mixtures with  $\gamma\text{-Al}_2\text{O}_3$  and  $\text{TiO}_2$  (anatase) was indicated by the disappearance of the X-ray diffraction pattern of  $\text{MoO}_3$  after thermal treatment, provided that the  $\text{MoO}_3$  content remained below a certain limit [8, 85, 86]. This limiting  $\text{MoO}_3$  content was determined as

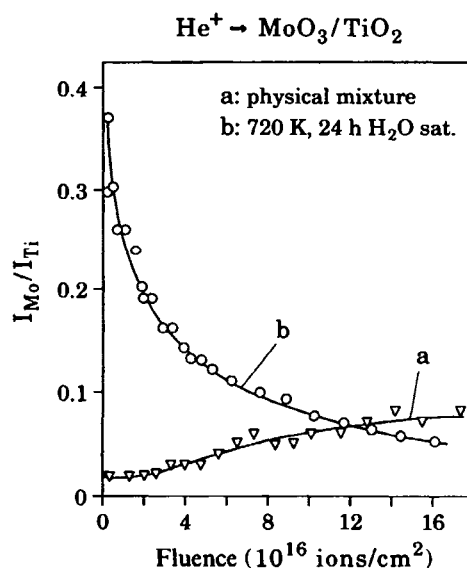
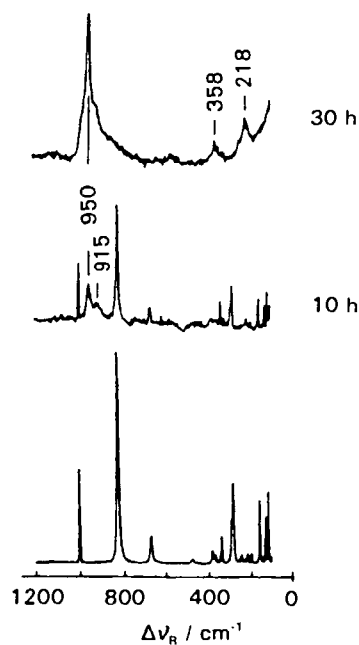


Figure 6. LEIS intensity profiles for  $\text{MoO}_3/\text{TiO}_2$  catalyst: (a) physical mixture prior to thermal treatment; (b) after thermal treatment for 24 h at 720 K in an  $\text{O}_2$  flow saturated with water vapor.

0.12 g  $\text{MoO}_3$  per 100  $\text{m}^2$  of both alumina and titania, and was interpreted as corresponding to the monolayer capacity. More direct evidence for spreading has been obtained by surface-sensitive techniques such as XPS [8, 9, 85–87] and LEIS [8, 9, 62, 71, 88, 89]. As an example, Fig. 6 shows ion scattering data which clearly support the spreading of  $\text{MoO}_3$  on  $\text{TiO}_2$  during thermal treatment at 720 K. In the figure, the intensity of  $\text{He}^+$  ions backscattered from Mo atoms relative to that of  $\text{He}^+$  backscattered from Ti atoms is plotted against the fluence (=total number of  $\text{He}^+$  ions that have impinged on unit surface area). Profile (a) represents the one characteristic of the physical mixture prior to thermal treatment; the second profile (b) was obtained after thermal treatment of the same mixture at 720 K for 5 h in a flow of oxygen saturated with 32 mbar  $\text{H}_2\text{O}$  vapor. The intensity ratios extrapolated to zero fluence are characteristic of the virgin surface being unaffected by sputtering processes. This value is very low for the starting physical mixture consisting of grains of  $\text{Al}_2\text{O}_3$  and small crystallites of  $\text{MoO}_3$ . Because of the surface sensitivity of the LEIS technique, the Mo/Ti intensity ratio extrapolated to zero fluence is expected to approach infinity if a monolayer of molybdenum oxide is formed on the  $\text{TiO}_2$  surface. Profile (b) indeed steeply rises near zero fluence and thus strongly supports the spreading of  $\text{MoO}_3$  on  $\text{TiO}_2$ . Similar results were obtained with alumina as the support. LEIS experiments also verified that spreading of  $\text{MoO}_3$  on both supports occurred in  $\text{O}_2$  in the presence and in the absence of water vapor.



**Figure 7.** Raman spectra of a physical mixture of 9 wt%  $\text{MoO}_3$ - $\text{Al}_2\text{O}_3$  prior to thermal treatment (bottom) and after calcination at 723 K in a stream of  $\text{O}_2$  saturated with water vapour for 10 and 30 h (adopted from Ref. 90).

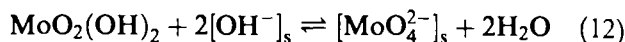
Neither XPS nor LEIS provide structural information of the molybdenum oxide overlayers on the support surfaces. Therefore, laser Raman spectroscopy (LRS) [9, 71, 81, 88–90] and X-ray absorption spectroscopy [91, 92] have been applied to elucidate the structural characteristics of the two-dimensional oxide films. LRS emphasized the role of water vapor for the structure formation. As a representative example, Fig. 7 shows spectra of  $\text{MoO}_3$ - $\text{Al}_2\text{O}_3$  mixtures [89]. The bottom spectrum is characteristic for the oxide mixture prior to thermal treatment and represents the signature of polycrystalline  $\text{MoO}_3$ . When the mixture was thermally treated in water-free  $\text{O}_2$ , the same spectrum was obtained for the dispersed oxide film, suggesting that the X-ray-amorphous film still preserved the structural characteristics of  $\text{MoO}_3$ . Figure 7 also shows the spectra of the  $\text{MoO}_3$ - $\text{Al}_2\text{O}_3$  mixture after thermal treatment in humid  $\text{O}_2$  obtained after 10 and 30 h. These spectra demonstrate the chemical transformation of  $\text{MoO}_3$  into a surface heptamolybdate (spectrum after 30 h) with an intermediate monomeric  $\text{MoO}_4^{2-}$  anion being detectable by the characteristic band at  $915\text{ cm}^{-1}$ . These conclusions were supported by X-ray absorption fine structure spectroscopy (EXAFS) [91] for the  $\text{MoO}_3$ - $\text{Al}_2\text{O}_3$  mixture and by the pre-edge and X-ray absorption near-edge (XANES) structure for the  $\text{MoO}_3$ - $\text{TiO}_2$  system [92].

The chemical transformation of  $\text{MoO}_3$  into a surface polymolybdate on  $\text{Al}_2\text{O}_3$  and  $\text{TiO}_2$  was described as being due to the intermediate formation of

$\text{MoO}_2(\text{OH})_2$ , a reaction which is known to occur under the experimental spreading conditions [93]:



This oxyhydroxide was assumed to react with basic surface hydroxy groups  $[\text{OH}^-]_s$  to yield the monomeric surface molybdate  $[\text{MoO}_4^{2-}]_s$  that was detected by LRS as an intermediate (see Fig. 7):



These intermediates subsequently undergo condensation with formation of the surface polymolybdate if the local concentration of the monomer becomes sufficiently high.

Since gas-phase transport and diffusion in a concentration gradient could be excluded (*vide supra*), transport of the molybdenum oxide via the unrolling carpet mechanism was proposed [9] (Fig. 2). However, migration via defect diffusion may still be an alternative. Recent in situ LRS studies [80] indicated the presence of a liquid-like layer containing monomers and oligomers of  $\text{MoO}_3$  which might be considered as the migrating species.

#### *b Vanadium-based Catalysts*

The spreading of  $\text{V}_2\text{O}_5$  on alumina and titania has been studied intensely because of the importance of these monolayer-type materials as catalysts for selective catalytic oxidation (see Sections B.4.6.2 and B.4.6.6) and for selective catalytic reduction of  $\text{NO}_x$  (Section B.1.2).  $\text{V}_2\text{O}_5$  has a low melting point, and hence high mobility under mild temperature conditions. It also has a low surface free energy and probably undergoes strong interaction with supports such as alumina since it forms the ternary oxide  $\text{AlVO}_4$ . Thus, the spreading condition  $U_{as}/2\gamma_{ag} > 1$  should be fulfilled. Moreover, in the presence of water vapor, highly volatile and reactive oxyhydroxides such as  $\text{V}_2\text{O}_3(\text{OH})_4$  [94] or  $\text{VO}(\text{OH})_3$  [95] are formed which permit an interpretation of surface chemical transformations of  $\text{V}_2\text{O}_5$ . The many studies on vanadia-based materials have been reviewed [3, 9].

Haber and co-workers [4–6, 38, 40, 96, 97] have demonstrated in several detailed investigations that spreading occurred in  $\text{V}_2\text{O}_5/\text{TiO}_2$  mixtures. They showed in particular [38] that migration of  $\text{V}_2\text{O}_5$  over the surface of anatase grains led to encapsulation of the latter by a thin overlayer, the properties of which were strongly modified by the interaction with the anatase support. On top of this inner layer on outer layer was detected, its properties being similar to those of  $\text{V}_2\text{O}_5$ . Centi and co-workers [98, 99] also reported on spreading of  $\text{V}_2\text{O}_5$  over the surface of titania with formation of an oxide monolayer of  $\text{V}^{4+}$  oxide species [98] on top of which amorphous multilayer patches of  $\text{V}^{5+}$  oxide were believed to grow [99].

In contrast to Haber and co-workers [4–6, 38], Centi et al. [98, 99] observed the spreading of  $V_2O_5$  not only on anatase but also on the rutile modification. Based on their results, Haber and co-workers [4–6, 38] proposed that spreading was dependent on the crystallographic modification of the support and on the type of crystal plane.

The migration mechanism of  $V_2O_5$  on the surfaces of alumina and titania is not yet understood in detail. As already mentioned, very recent results reported by Haber et al. [40] seem to indicate that a process of defect diffusion through the vanadia monolayer is involved.

### c Tungsten-based Catalysts

The thermodynamic spreading condition may be fulfilled for  $WO_3$  since its surface free energy is relatively low and it definitely forms a ternary oxide  $Al_2(WO_4)_3$  with alumina. However, the Tammann temperature is 873 K, leading to low mobility. Nevertheless, spreading of  $WO_3$  on  $\gamma$ - $Al_2O_3$ , although slow, was observed at 820 K by LEIS [71] and LRS, and EXAFS [100] provided evidence for the formation of a surface polytungstate in the presence of water vapor via an intermediate oxyhydroxide  $WO_2(OH)_2$ . An analogous surface chemistry was also reported for physical mixtures of  $WO_3$  with  $TiO_2$  (anatase) [100].

### d Zeolites as Supports

A few studies involving zeolites and layer silicates as supports for oxides are reported in the literature. Haase et al. [101] have provided experimental evidence for the spreading of  $V_2O_5$  on mordenite. Migration of  $Ga_2O_3$  in H-ZSM-5 zeolites was observed by Mériaudeau and Naccache [102]. Fierro et al. [103] proposed the incorporation of  $MoO_3$  into the intracrystalline cavities of Y-type zeolites by means of vaporization of  $MoO_3$  by reaction with water vapor at 623 K. It was claimed that the zeolite structure was largely retained under these conditions. At higher temperatures, however, a progressive loss of crystallinity was observed. Leyrer and Knözinger [104] have shown that complete degradation of the zeolite structure resulted, when incorporation of Mo into Y-zeolites was attempted via gas-phase transport of  $MoO_2(OH)_2$  at 720 K.

### D Solid-state Ion Exchange of Zeolites

Solid-state ion exchange may be related to phenomena of wetting and spreading in solid–solid systems. Rabo et al. [105–106] first reported that proton-containing samples of zeolite Y reacted with sodium chloride under evolution of HCl. Later, Karge and co-workers [107–111] developed solid-state ion exchange further as a synthetic route for the preparation of alkaline, alkaline earth, rare earth, and transition and noble-metal-containing zeolites starting from parent materials that

contain  $H^+$ ,  $NH_4^+$ , or  $Na^+$ . In several cases a 100% cation incorporation could be achieved in a one-step solid-state reaction. Very recently, even the large  $Cs^+$  ions could be driven into  $S_1$  sites of zeolite Y via solid-state ion exchange [112]. Such degrees of exchange are difficult to obtain by conventional methods.

### References

- 1 S A. Stevenson, J A. Dumesic, R T K Baker, E Ruckenstein, *Metal-Support Interactions in Catalysis, Sintering, and Redispersion*, Van Nostrand Reinhold, New York, 1987
- 2 J H Sinfelt, *Bimetallic Catalysts Discoveries, Concepts and Applications*, Wiley, New York, 1983
- 3 E I Ko in *Wettability* (Ed J C Berg), M. Dekker, New York, 1993, p 431
- 4 J Haber in *Surface Properties and Catalysis by Non-Metals* (Eds J. P. Bonnelle, B Delmon, E Derouane), Reidel, Dordrecht, 1983, p 1
- 5 J Haber, *Pure Appl Chem* 1984, 56, 1663
- 6 J Haber, *Proceedings of the 8th International Congress on Catalysis*, Berlin, 1984, Verlag Chemie, Weinheim, 1984, Vol 1, p 85
- 7 J Haber, J Ziolkowski in *Proceedings of the 7th International Symposium React Solids*, Bristol, 1972, Chapman and Hall, London, 1972, p 782
- 8 Y C Xie, Y Q Tang, *Adv Catal* 1990, 37, 1
- 9 H Knozinger, E Taglauer in *Catalysis* (Eds J J Spivey, S K Agarwal), Royal Society of Chemistry, Cambridge, 1993, Vol 10, p 1
- 10 E Ruckenstein, S H Lee, *J Catal* 1987 104, 259.
- 11 I Sushumna, E Ruckenstein, *J Catal* 1985, 94, 239
- 12 S A Stevenson, J A Dumesic, R T K Baker, E Ruckenstein, *Metal-Support Interactions in Catalysis, Sintering, and Redispersion*, Van Nostrand Reinhold, New York, 1987, p 141
- 13 E Ruckenstein in *Sintering and Heterogeneous Catalysis*, (Eds G C Kuczynski, A E Miller, G A Sargent), Plenum Press, New York, London, 1984, p 199
- 14 S H Overbury, P A Bertrand, G A Somorjai, *Chem Rev* 1975, 75, 547
- 15 F C M J M van Delft, A D van Langefeld, B E Nieuwenhuys, *Thin Solid Films* 1985, 123, 333
- 16 F C M J M van Delft, A D van Langefeld, B E Nieuwenhuys, *Solid State Ionics*, 1985, 16, 233
- 17 E Ruckenstein in S A Stevenson, J A Dumesic, R T K Baker, E Ruckenstein, *Metal-Support Interactions in Catalysis, Sintering, and Redispersion*, Van Nostrand Reinhold, New York, 1987, p 241
- 18 E Ruckenstein, *J Cryst Growth*, 1979, 47, 666
- 19 E Ruckenstein in S A Stevenson, J A Dumesic, R T K Baker, E Ruckenstein, *Metal-Support Interactions in Catalysis, Sintering and Redispersion*, Van Nostrand Reinhold, New York, 1987, p 236
- 20 E Ruckenstein in S A Stevenson, J A Dumesic, R T K Baker, E Ruckenstein, *Metal-Support Interactions in Catalysis, Sintering, and Redispersion*, Van Nostrand Reinhold, New York, 1987, p 247
- 21 G E Rhead, M G Barthes, C Argile, *Thin Solid Films* 1981, 82, 201
- 22 E Bauer, H Poppa, *Thin Solid Films* 1972, 12, 167
- 23 E Bauer, H Poppa, G Todd, P R Davis, *J Appl Phys* 1977, 48, 3773
- 24 E Ruckenstein in S A Stevenson, J A Dumesic, R T K Baker, E Ruckenstein, *Metal-Support Interactions in Catal-*

- ysis, *Sintering, and Redispersion*, Van Nostrand Reinhold, New York, 1987, pp 153
- 25 J M Kosterlitz, D J Thouless, *J Phys C* 1972, 5, L 124, 1973, 6, 1181
  - 26 F A Lindemann, *Z Phys* 1910, 11, 609
  - 27 R T K Baker, *J Catal* 1982, 78, 473
  - 28 E Ruckenstein, B Pulvermacher, *J Catal* 1973, 29, 224
  - 29 E Ruckenstein, B Pulvermacher, *AIChE J* 1973, 19, 356
  - 30 B K Chakraverty, *J Phys Chem Solids* 1967, 28, 2401
  - 31 P C Flynn, S E Wanke, *J Catal* 1974, 33, 233
  - 32 E Ruckenstein, D B Dadyburjor, *J Catal* 1977, 48, 73
  - 33 E Ruckenstein, D B Dadyburjor, *Thin Solid Films* 1978, 55, 89
  - 34 H H Lee, *J Catal* 1980, 62, 129
  - 35 E Ruckenstein in S A Stevenson, J A Dumesic, R T K Baker, E Ruckenstein, *Metal-Support Interactions in Catalysis, Sintering, and Redispersion*, Van Nostrand Reinhold, New York, 1987, pp 156, 187
  - 36 P Wynblatt, T M Ahn in *Sintering and Catalysis* (Ed G C Kuczynski), Plenum Press, New York, 1975, p 83
  - 37 E Ruckenstein, Y F Chu, *J Catal* 1979, 59, 109
  - 38 J Haber, T Machej, T Czeppe, *Surf Sci* 1985, 151, 301
  - 39 P von Blanckenhagen in *Structure and Dynamics of Surfaces II Phenomena, Models, and Methods* (Eds W Schommers, P von Blanckenhagen), Springer-Verlag, Berlin, 1987, p 73
  - 40 J Haber, T Machej, E M Serwicka, I E Wachs, *Catal Lett* 1995, 32, 101
  - 41 A Ya Neimann, *Solid State Ionics* 1996, 83, 263
  - 42 J J Chen, E Ruckenstein, *J Catal* 1981, 69, 254
  - 43 I Sushumna, E Ruckenstein, *J Catal* 1988, 109, 433
  - 44 J J Chen, E Ruckenstein, *J Phys Chem* 1981, 85, 1606
  - 45 E Ruckenstein, S H Lee, *J Catal* 1984, 86, 457
  - 46 M Lo Jacono, M Schiavello, A Cimino, *J Phys Chem* 1971, 75, 1044
  - 47 Y Chen, L Zhang, *Catal Lett* 1992, 12, 51
  - 48 I Sushumna, E Ruckenstein, *J Catal* 1985, 94, 239
  - 49 E Ruckenstein, D B Dadyburjor, *Rev Chem Eng* 1983, 1, 251
  - 50 M J D'Aniello, Jr, D R Monroe, C J Carr, M H Krueger, *J Catal*, 1988, 109, 407
  - 51 B S Clausen, J Schiøtz, L Gråbaek, C V Oveson, K W Jacobsen, J K Nørskov, H Topsøe, *Topics Catal* 1994, 1, 367
  - 52 S J Tauster, S C Fung, R L Garten, *J Am Chem Soc* 1978, 100, 170
  - 53 S J Tauster, S C Fung, *J Catal* 1978, 55, 29
  - 54 G L Haller, D E Resasco, *Adv Catal* 1989, 36, 173
  - 55 *Strong Metal Support Interactions* (Eds R T K Baker, S J Tauster, J A Dumesic), American Chemical Society, Washington, 1986
  - 56 S Engels, B Freitag, W Morke, W Roschke, M Wilde, *Z Anorg Allg Chem* 1981, 474, 209
  - 57 P Meriaudeau, J F Dutel, M Dufaux, C Naccache, *Stud Surf Sci Catal* 1982, 11, 95
  - 58 J Santos, J A Dumesic, *Stud Surf Sci Catal* 1982, 11, 43
  - 59 B-H Chen, J M White, *J Phys Chem* 1983, 87, 1327
  - 60 A D Logan, E J Braunschweig, A K Datye, D J Smith, *Langmuir* 1988, 4, 827
  - 61 Ch Linsmeier, H Knozinger, E Taglauer, *Nucl Instr Meth B*, in press
  - 62 E Taglauer, H Knozinger, *Phys Stat Sol (b)* 1995, 192, 465
  - 63 B W Dodson, *Surf Sci* 1987, 184, 1
  - 64 J H Sinfelt, Y L La, J A Cusumano, A E Barnett, *J Catal* 1976, 42, 227
  - 65 E B Prestridge, G H Via, J H Sinfelt, *J Catal* 1977, 50, 115
  - 66 J H Sinfelt, G H Via, F W Lytle, *J Phys Chem* 1980, 72, 4832
  - 67 K Christmann, G Ertl, H Shimizu, *J Catal* 1980, 61, 397, *Thin Solid Films* 1979, 57, 247
  - 68 J T Yates, C H F Peden, D W Goodman, *J Catal* 1985, 94, 321
  - 69 R Liu, B Tesche, H Knozinger, *J Catal* 1991, 129, 402
  - 70 J E Houston, C H F Peden, P J Feibelman, *Surf Sci* 1987, 192, 457
  - 71 J Leyrer, R Margraf, E Taglauer, H Knozinger, *Surf Sci* 1988, 201, 603
  - 72 P Somasundaran in *Ceramic Processing before Firing* (Eds G Y Onoda, Jr, L L Hensch), Wiley, New York, 1978, p 78
  - 73 K Shinohara in *Powder Technology Handbook* (Eds K Jinoya, K Gotoh, K Higashitani), M Dekker, New York, 1991, p 481
  - 74 K Miyamoto in *Powder Technology Handbook* (Eds K Jinoya, K Gotoh, K Higashitani), M Dekker, New York, 1991, p 595
  - 75 G Heimcke, *Tribochemistry*, Akademie Verlag, Berlin 1984
  - 76 S A Angelov, R P Bonchev, *Appl Catal* 1986, 24, 219
  - 77 G Mestl, B Herzog, R Schlogl, H Knozinger, *Langmuir* 1995, 11, 3027
  - 78 G Mestl, N F D Verbruggen, H Knozinger, *Langmuir* 1995, 11, 3055
  - 79 G Mestl, T K K Srinivasan, H Knozinger, *Langmuir* 1995, 11, 3795
  - 80 G Mestl, N F D Verbruggen, F C Lange, B Tesche, H Knozinger, *Langmuir* 1996, 12, 1817
  - 81 S R Stampfl, Y Chen, J A Dumesic, C Niu, C G Hill, Jr, *J Catal* 1987, 105, 445
  - 82 J M M Llorente, V Rives, *Solid State Ionics* 1990, 38, 119
  - 83 T F Hayden, J A Dumesic, R D Sherwood, R T K Baker, *J Catal* 1987, 105, 299
  - 84 J Leyrer, D Mey, H Knozinger, *J Catal* 1990, 124, 349
  - 85 Y Xie, L Gui, Y Liu, B Zhao, N Yang, Y Zhang, Q Guo, L Duan, H Huang, X Cai, Y Tang in *Proceedings of the 8th International Congress on Catalysis*, Berlin 1984 Dechema, Frankfurt, 1984, Vol V, p 147
  - 86 Y Xie, L Gui, Y Liu, Y Zhang, B Zhao, N Yang, Q Guo, L Duan, H Huang, X Cai, Y Tang in *Adsorption and Catalysis on Oxide Surfaces* (Eds M Che, G C Bond) Elsevier, Amsterdam, 1985, p 139
  - 87 B M Reddy, K Narsimha, P Kanta Rao, *Langmuir* 1991, 7, 1551
  - 88 R Margraf, J Leyrer, E Taglauer, H Knozinger, *Surf Sci* 1987, 189/190, 842
  - 89 R Margraf, J Leyrer, E Taglauer, H Knozinger *React Kinet Catal Lett* 1987, 35, 261
  - 90 J Leyrer, M I Zaki, H Knozinger *J Phys Chem* 1986, 90, 4775
  - 91 G Kisfaludi, J Leyrer, H Knozinger, R Prins *J Catal* 1990, 124, 349
  - 92 L M J von Hippel, F Hilbrig, H Schmelz, B Lengeler, H Knozinger, *Collect Czech Chem Commun* 1992, 57, 2456
  - 93 O Glemser, H G Wendland, *Angew Chem* 1973, 75, 949
  - 94 O Glemser, A Muller, *Z Anorg Allg Chem* 1963, 325, 220
  - 95 N L Yannopoulos, *J Phys Chem* 1968, 72, 3293
  - 96 M Gasior, J Haber, T Machej, *Appl Catal* 1987, 33, 1
  - 97 T Machej, J Haber, A M Turek, I E Wachs, *Appl Catal* 1991, 70, 115
  - 98 G Centi, E Giannelo, D Pinelli, F Trifiro, *J Catal* 1991, 130, 220
  - 99 G Centi, D Pinelli, F Trifiro, D Ghossoub, M Guelton, L Gengembre, *J Catal* 1991, 130, 238



100. F. Hilbrig, H. E. Göbel, H. Knözinger, H. Schmelz, B. Lengeler, *J. Phys. Chem.* **1991**, *95*, 6973.
101. R. Haase, J.-G. Jerschke, G. Öhlmann, J. Richter-Mendau, J. Scheve in *Book of Abstracts, 2nd International Symposium on Scientific Bases for the Preparation of Heterogeneous Catalysts*, Louvain-la-Neuve, Belgium, **1978**, paper F5.
102. P. Mériaudeau, C. Naccache, *Appl. Catal.* **1991**, *73*, L13.
103. J. L. G. Fierro, J. C. Conesa, A. Lopez Agudo, *J. Catal.* **1987**, *108*, 334.
104. J. Leyrer, H. Knözinger, unpublished results.
105. J. A. Rabo, P. H. Kasai, *Progr. Solid State Chem.* **1975**, *9*, 1.
106. J. A. Rabo in *Zeolite Chemistry and Catalysis* (Ed: J. A. Rabo), American Chemical Society, Washington, **1976**, p. 332.
107. H. K. Beyer, H. G. Karge, G. Borbély, *Zeolites* **1988**, *8*, 79.
108. H. G. Karge, H. K. Beyer, G. Borbély, *Catal. Today* **1988**, *3*, 41.
109. H. G. Karge, V. Mavrodinova, Z. Zheng, H. K. Beyer, in *Guidelines for Mastering the Properties of Molecular Sieves* (Eds: D. Barthomeuf, E. G. Derouane, W. Hölderich), Plenum Press, New York, **1990**, p. 157.
110. H. G. Karge, H. K. Beyer, in *Zeolite Chemistry and Catalysis* (Eds: P. A. Jacobs, N. I. Jaeger, L. Kubelková, B. Wichterlová), Elsevier, Amsterdam, **1991**, p. 43.
111. H. G. Karge, B. Wichterlová, H. K. Beyer, *J. Chem. Soc., Faraday Trans.* **1992**, *88*, 1345.
112. J. Weitkamp, S. Ernst, M. Hunger, T. Röser, S. Huber, U. A. Schubert, P. Thomasson, H. Knözinger in *Proceedings of the 11. International Congress on Catalysis* (Eds.: J. W. Hightower, W. N. Delgass, E. Iglesia and A. T. Bell) Baltimore 1996, Elsevier, Amsterdam, 1996, p. 731.
113. R. Anderson, *Structure of Metallic Catalysts*, Academic Press, New York, **1975**.

### 2.2.1.4 Heterogenization of Complexes and Enzymes

W. KEIM AND B. DRIEBEN-HÖLSCHER

#### A Heterogenization of Complexes

In the early 1960s, new processes embracing homogeneous solution catalysis of transition metal complexes emerged. Due to the built-in selectivity advantages and because of its promise to utilize the metals employed up to 100% efficiency – especially for noble metals – homogeneous catalysis advanced rapidly. It soon became obvious that catalyst recycling represented a major hurdle and had to be solved to give homogeneous catalysis a broader industrial future. In the search to combine the advantages of both heterogeneous and homogeneous catalysis, the field of heterogenizing homogeneous transition metal-based catalysts developed. The reasons are obvious: ease of separation of the catalyst from the products; molecular dispersion and accessibility of nearly all metal atoms; achievement of high selectivity; potential for ligand tailoring, mild reaction conditions, use of conventional equipment such as packed-bed or fluidized-bed reactors.

A number of different approaches developed to support homogeneous metal complex catalysts:

- (i) supported liquid-phase catalysis [1, 2];
- (ii) heterogenized metal complexes;
- (iii) porous material entrapped complexes (see Section A.2.3.5);
- (iv) use of membrane filtration;
- (v) use of oligomeric complexes (application of membranes) [3].

Many publications have appeared on the heterogenization of complexes. Reference is given to the reviews, which have appeared in this field over the last two decades [4].

The heterogenization of supported solid phase (SSP) catalysts has attracted considerable attention, and Fig. 1 summarizes the various approaches that have been used.

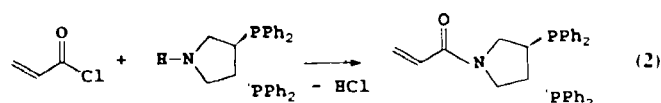
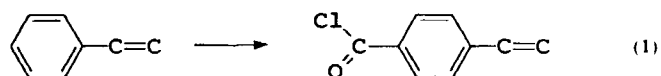
The chemically bound metal complex catalysts may be further subdivided into covalently attached complexes and those that are ionically bound. In all heterogenized catalysts the main feature of a homogeneous metal-based catalyst, namely ligand coordination and means to tailor-make a catalyst by ligand variation on a molecular level, are given. In this context the immobilization of organometallic compounds or clusters on inorganic supports followed by decomposition, which is used to achieve a high dispersion, must also be mentioned. Examples are chemical vapor deposition (CVD) and the thermal or photochemical decomposition of the complexes (clusters) supported [5]. They are outside of the scope of this chapter.

#### a Organic Supports

The use of organic supports (macroreticular/macroporous polymers) as carriers for an organometallic complex, which by itself may serve as the catalyst precursor complex, has been widely studied. The polymers must be macroporous, providing a highly accessible internal surface area.

In catalyst preparation the following steps can be distinguished: monomer synthesis → monomer polymerization → functionalization → metal attachment → activation.

In monomer synthesis it is possible to functionalize a monomer selected prior to polymerization, as exemplified in Eqs 1 and 2.



- ysis, *Sintering, and Redispersion*, Van Nostrand Reinhold, New York, 1987, pp 153
- 25 J M Kosterlitz, D J Thouless, *J Phys C* 1972, 5, L 124, 1973, 6, 1181
  - 26 F A Lindemann, *Z Phys* 1910, 11, 609
  - 27 R T K Baker, *J Catal* 1982, 78, 473
  - 28 E Ruckenstein, B Pulvermacher, *J Catal* 1973, 29, 224
  - 29 E Ruckenstein, B Pulvermacher, *AIChE J* 1973, 19, 356
  - 30 B K Chakraverty, *J Phys Chem Solids* 1967, 28, 2401
  - 31 P C Flynn S E Wanke, *J Catal* 1974, 33, 233
  - 32 E Ruckenstein, D B Dadyburjor, *J Catal* 1977, 48, 73
  - 33 E Ruckenstein, D B Dadyburjor, *Thin Solid Films* 1978, 55, 89
  - 34 H H Lee, *J Catal* 1980, 62, 129
  - 35 E Ruckenstein in S A Stevenson, J A Dumesic, R T K Baker, E Ruckenstein, *Metal-Support Interactions in Catalysis, Sintering, and Redispersion*, Van Nostrand Reinhold, New York, 1987, pp 156, 187
  - 36 P Wynblatt, T M Ahn in *Sintering and Catalysis* (Ed G C Kuczynski), Plenum Press, New York, 1975, p 83
  - 37 E Ruckenstein, Y F Chu, *J Catal* 1979, 59, 109
  - 38 J Haber, T Machej, T Czeppe, *Surf Sci* 1985, 151, 301
  - 39 P von Blanckenhagen in *Structure and Dynamics of Surfaces II Phenomena, Models, and Methods* (Eds W Schommers, P von Blanckenhagen), Springer-Verlag, Berlin, 1987, p 73
  - 40 J Haber, T Machej, E M Serwicka, I E Wachs, *Catal Lett* 1995, 32, 101
  - 41 A Ya Neimann, *Solid State Ionics* 1996, 83, 263
  - 42 J J Chen, E Ruckenstein, *J Catal*, 1981, 69, 254
  - 43 I Sushumna, E Ruckenstein, *J Catal* 1988, 109, 433
  - 44 J J Chen, E Ruckenstein, *J Phys Chem* 1981, 85, 1606
  - 45 E Ruckenstein, S H Lee, *J Catal* 1984, 86, 457
  - 46 M Lo Jacono, M Schiavello, A Cimino, *J Phys Chem* 1971, 75, 1044
  - 47 Y Chen, L Zhang, *Catal Lett* 1992, 12, 51
  - 48 I Sushumna, E Ruckenstein, *J Catal* 1985, 94, 239
  - 49 E Ruckenstein, D B Dadyburjor, *Rev Chem Eng* 1983, 1, 251
  - 50 M J D'Aniello, Jr., D R Monroe, C J Carr, M H Krueger, *J Catal*, 1988, 109, 407
  - 51 B S Clausen, J Schiøtz, L Gråbaek, C V Oveson, K W Jacobsen, J K Nørskov, H Topsøe, *Topics Catal* 1994, 1, 367
  - 52 S J Tauster, S C Fung, R L Garten, *J Am Chem Soc* 1978, 100, 170
  - 53 S J Tauster, S C Fung, *J Catal* 1978, 55, 29
  - 54 G L Haller, D E Resasco, *Adv Catal* 1989, 36, 173
  - 55 *Strong Metal Support Interactions* (Eds R T K Baker, S J Tauster, J A Dumesic), American Chemical Society, Washington, 1986
  - 56 S Engels, B Freitag, W Morke W Roschke, M Wilde, *Z Anorg Allg Chem* 1981, 474, 209
  - 57 P Meriaudeau, J F Dutel, M Dufaux, C Naccache, *Stud Surf Sci Catal* 1982, 11, 95
  - 58 J Santos, J A Dumesic, *Stud Surf Sci Catal* 1982, 11, 43
  - 59 B-H Chen, J M White, *J Phys Chem* 1983, 87, 1327
  - 60 A D Logan, E J Braunschweig, A K Datye, D J Smith, *Langmuir* 1988, 4, 827
  - 61 Ch Linsmeier, H Knozinger, E Taglauer, *Nucl Instr Meth B*, in press
  - 62 E Taglauer, H Knozinger, *Phys Stat Sol (b)* 1995, 192, 465
  - 63 B W Dodson, *Surf Sci* 1987, 184, 1
  - 64 J H Sinfelt, Y L La, J A Cusumano, A E Barnett, *J Catal* 1976, 42, 227
  - 65 E B Prestridge, G H Via, J H Sinfelt, *J Catal* 1977, 50, 115
  - 66 J H Sinfelt, G H Via, F W Lytle, *J Phys Chem* 1980, 72, 4832
  - 67 K Christmann, G Ertl, H Shimizu, *J Catal* 1980, 61, 397, *Thin Solid Films* 1979, 57, 247
  - 68 J T Yates, C H F Peden, D W Goodman, *J Catal* 1985, 94, 321
  - 69 R Liu, B Tesche, H Knozinger, *J Catal* 1991, 129, 402
  - 70 J E Houston, C H F Peden, P J Feibelman, *Surf Sci* 1987, 192, 457
  - 71 J Leyrer, R Margraf, E Taglauer, H Knozinger, *Surf Sci* 1988, 201, 603
  - 72 P Somasundaran in *Ceramic Processing before Firing* (Eds G Y Onoda, Jr., L L Hensch), Wiley, New York, 1978, p 78
  - 73 K Shinohara in *Powder Technology Handbook* (Eds K Jinoya, K Gotoh, K Higashitani), M Dekker, New York, 1991, p 481
  - 74 K Miyamoto in *Powder Technology Handbook* (Eds K Jinoya, K Gotoh, K Higashitani), M Dekker, New York, 1991, p 595
  - 75 G Heimcke, *Tribochemistry*, Akademie-Verlag, Berlin, 1984
  - 76 S A Angelov, R P Bonchev, *Appl Catal* 1986, 24, 219
  - 77 G Mestl, B Herzog, R Schlogl, H Knozinger, *Langmuir* 1995, 11, 3027
  - 78 G Mestl, N F D Verbruggen, H Knozinger, *Langmuir* 1995, 11, 3055
  - 79 G Mestl, T K K Srinivasan, H Knozinger, *Langmuir* 1995, 11, 3795
  - 80 G Mestl, N F D Verbruggen, F C Lange, B Tesche, H Knozinger, *Langmuir* 1996, 12, 1817
  - 81 S R Stampfl, Y Chen, J A Dumesic, C Niu, C G Hill, Jr., *J Catal* 1987, 105, 445
  - 82 J M M Llorente, V Rives, *Solid State Ionics* 1990, 38, 119
  - 83 T F Hayden, J A Dumesic, R D Sherwood R T K Baker, *J Catal* 1987, 105, 299
  - 84 J Leyrer D Mey, H Knozinger, *J Catal* 1990, 124, 349
  - 85 Y Xie, L Gui, Y Liu, B Zhao, N Yang, Y Zhang Q Guo, L Duan, H Huang, X Cai, Y Tang in *Proceedings of the 8th International Congress on Catalysis*, Berlin 1984 Dechema, Frankfurt, 1984, Vol V, p 147
  - 86 Y Xie L Gui, Y Liu, Y Zhang, B Zhao, N Yang Q Guo, L Duan, H Huang, X Cai, Y Tang in *Adsorption and Catalysis on Oxide Surfaces* (Eds M Che G C Bond) Elsevier, Amsterdam, 1985, p 139
  - 87 B M Reddy, K Narsimha, P Kanta Rao, *Langmuir* 1991, 7, 1551
  - 88 R Margraf, J Leyrer, E Taglauer, H Knozinger *Surf Sci* 1987, 189/190, 842
  - 89 R Margraf, J Leyrer, E Taglauer, H Knozinger *React Kinet Catal Lett* 1987, 35, 261
  - 90 J Leyrer, M I Zaki, H Knozinger, *J Phys Chem* 1986, 90, 4775
  - 91 G Kisfaludi, J Leyrer, H Knozinger, R Prins *J Catal* 1990, 124, 349
  - 92 L M J von Hippel, F Hilbrig, H Schmelz, B Lengeler H Knozinger, *Collect Czech Chem Commun* 1992, 57, 2456
  - 93 O Glemser, H G Wendland, *Angew Chem* 1973, 75, 949
  - 94 O Glemser, A Muller, *Z Anorg Allg Chem* 1963, 325, 220
  - 95 N L Yannopoulos, *J Phys Chem* 1968, 72, 3293
  - 96 M Gasior, J Haber, T Machej, *Appl Catal* 1987, 33, 1
  - 97 T Machej, J Haber, A M Turek, I E Wachs *Appl Catal* 1991, 70, 115
  - 98 G Centi, E Giamello, D Pinelli, F Trifiro *J Catal* 1991, 130, 220
  - 99 G Centi, D Pinelli, F Trifiro, D Ghossoub, M Guclton L Gengembre *J Catal* 1991, 130, 238

100. F. Hilbrig, H. E. Göbel, H. Knözinger, H. Schmelz, B. Lengeler, *J. Phys. Chem.* **1991**, *95*, 6973.
101. R. Haase, J.-G. Jerschkewitz, G. Öhlmann, J. Richter-Mendau, J. Scheve in *Book of Abstracts, 2nd International Symposium on Scientific Bases for the Preparation of Heterogeneous Catalysts*, Louvain-la-Neuve, Belgium, **1978**, paper F5.
102. P. Mériaudeau, C. Naccache, *Appl. Catal.* **1991**, *73*, L13.
103. J. L. G. Fierro, J. C. Conesa, A. Lopez Agudo, *J. Catal.* **1987**, *108*, 334.
104. J. Leyrer, H. Knözinger, unpublished results.
105. J. A. Rabo, P. H. Kasai, *Progr. Solid State Chem.* **1975**, *9*, 1.
106. J. A. Rabo in *Zeolite Chemistry and Catalysis* (Ed: J. A. Rabo), American Chemical Society, Washington, **1976**, p. 332.
107. H. K. Beyer, H. G. Karge, G. Borbély, *Zeolites* **1988**, *8*, 79.
108. H. G. Karge, H. K. Beyer, G. Borbély, *Catal. Today* **1988**, *3*, 41.
109. H. G. Karge, V. Mavrodinova, Z. Zheng, H. K. Beyer, in *Guidelines for Mastering the Properties of Molecular Sieves* (Eds: D. Barthomeuf, E. G. Derouane, W. Hölderich), Plenum Press, New York, **1990**, p. 157.
110. H. G. Karge, H. K. Beyer, in *Zeolite Chemistry and Catalysis* (Eds: P. A. Jacobs, N. I. Jaeger, L. Kubelková, B. Wichterlová), Elsevier, Amsterdam, **1991**, p. 43.
111. H. G. Karge, B. Wichterlová, H. K. Beyer, *J. Chem. Soc., Faraday Trans.* **1992**, *88*, 1345.
112. J. Weitkamp, S. Ernst, M. Hunger, T. Röser, S. Huber, U. A. Schubert, P. Thomasson, H. Knözinger in *Proceedings of the 11. International Congress on Catalysis* (Eds.: J. W. Hightower, W. N. Delgass, E. Iglesia and A. T. Bell) Baltimore 1996, Elsevier, Amsterdam, 1996, p. 731.
113. R. Anderson, *Structure of Metallic Catalysts*, Academic Press, New York, **1975**.

### 2.2.1.4 Heterogenization of Complexes and Enzymes

W. KEIM AND B. DRIEBEN-HÖLSCHER

#### A Heterogenization of Complexes

In the early 1960s, new processes embracing homogeneous solution catalysis of transition metal complexes emerged. Due to the built-in selectivity advantages and because of its promise to utilize the metals employed up to 100% efficiency – especially for noble metals – homogeneous catalysis advanced rapidly. It soon became obvious that catalyst recycling represented a major hurdle and had to be solved to give homogeneous catalysis a broader industrial future. In the search to combine the advantages of both heterogeneous and homogeneous catalysis, the field of heterogenizing homogeneous transition metal-based catalysts developed. The reasons are obvious: ease of separation of the catalyst from the products; molecular dispersion and accessibility of nearly all metal atoms; achievement of high selectivity; potential for ligand tailoring, mild reaction conditions, use of conventional equipment such as packed-bed or fluidized-bed reactors.

A number of different approaches developed to support homogeneous metal complex catalysts:

- (i) supported liquid-phase catalysis [1, 2];
- (ii) heterogenized metal complexes;
- (iii) porous material entrapped complexes (see Section A.2.3.5);
- (iv) use of membrane filtration;
- (v) use of oligomeric complexes (application of membranes) [3].

Many publications have appeared on the heterogenization of complexes. Reference is given to the reviews, which have appeared in this field over the last two decades [4].

The heterogenization of supported solid phase (SSP) catalysts has attracted considerable attention, and Fig. 1 summarizes the various approaches that have been used.

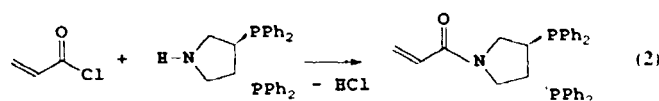
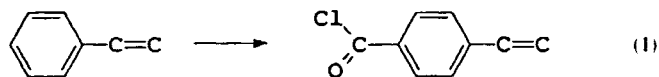
The chemically bound metal complex catalysts may be further subdivided into covalently attached complexes and those that are ionically bound. In all heterogenized catalysts the main feature of a homogeneous metal-based catalyst, namely ligand coordination and means to tailor-make a catalyst by ligand variation on a molecular level, are given. In this context the immobilization of organometallic compounds or clusters on inorganic supports followed by decomposition, which is used to achieve a high dispersion, must also be mentioned. Examples are chemical vapor deposition (CVD) and the thermal or photochemical decomposition of the complexes (clusters) supported [5]. They are outside of the scope of this chapter.

#### a Organic Supports

The use of organic supports (macroreticular/macroporous polymers) as carriers for an organometallic complex, which by itself may serve as the catalyst precursor complex, has been widely studied. The polymers must be macroporous, providing a highly accessible internal surface area.

In catalyst preparation the following steps can be distinguished: monomer synthesis → monomer polymerization → functionalization → metal attachment → activation.

In monomer synthesis it is possible to functionalize a monomer selected prior to polymerization, as exemplified in Eqs 1 and 2.



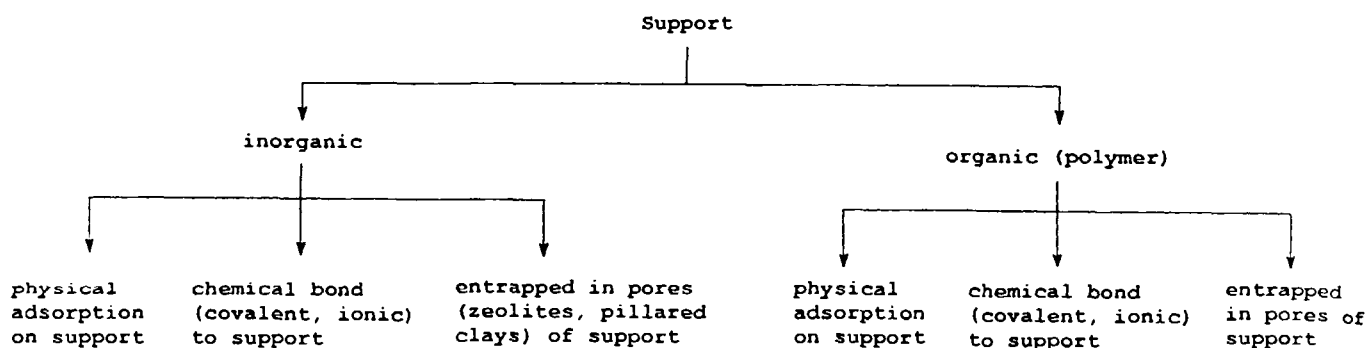


Figure 1. How to heterogenize complexes.

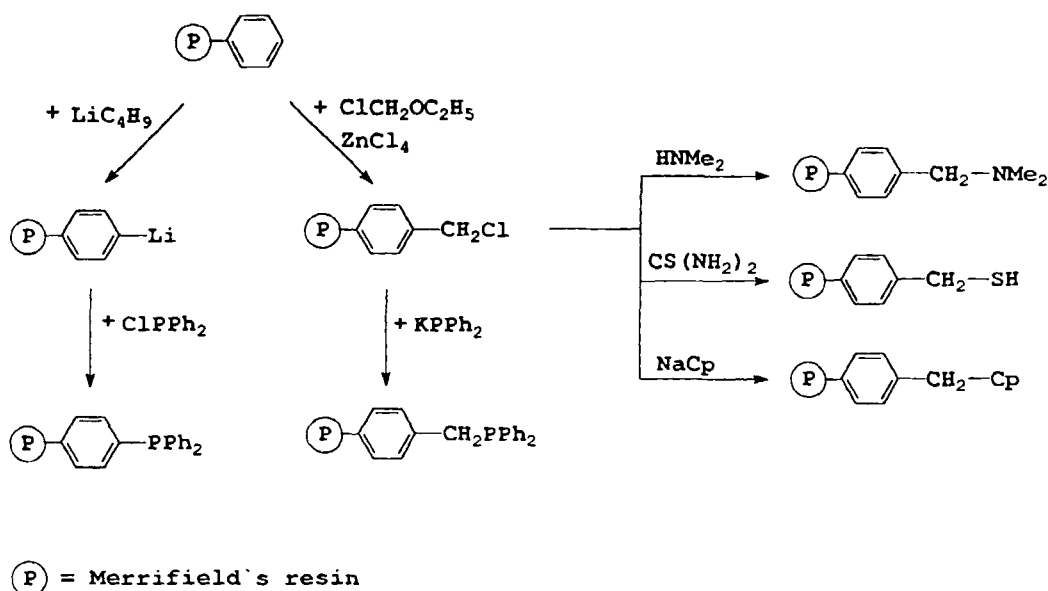


Figure 2. Functionalization of Merrifield's resin.

The monomers obtained can be polymerized by themselves or copolymerized with other monomers. The copolymerization route is effective for the synthesis of tailor-made polymer supports with precise control over functionality and other polymer characteristics, but it is laborious and requires specialized skills in polymer synthesis.

To be useful as a catalyst support, the gelular polymers must be swellable, the propensity of which can be controlled by the degree of cross-linking. Polymers can be tailor-made to swell in a particular solvent by appropriate selection of monomer and cross-linking agent.

The functionalization of a polymer can be effected by numerous synthetic procedures and can be achieved chemically or by grafting onto a polymeric material that can, by itself, be used to support metal complexes. Often, the grafting occurs via radiation.

A frequently investigated approach is based on Merrifield's resin, which is a polystyrene polymer [6].

The multiplicity of ways in which to functionalize these resins is shown in Fig. 2.

The functionalization method appears particularly convenient, because underivatized beaded resins of various types and many polymers (such as polyethylene, polystyrene, polyacrylates, polysaccharides, and many others) are commercially available. However, this method suffers from the possibility of side-reactions on the cross-linked polymer, and can yield poorly characterized polymer supports.

Another approach is the use of ion-exchanged resins. Figure 3 illustrates the principle.

Again P- or P-N-containing polymeric supports are commercially available [6]. They include:

- (i) Polystyrene cross-linked with typically 1–2% divinylbenzene, available with the following functional groups: aminomethyl ( $-\text{CH}_2\text{NH}_2$ ),  $\alpha$ -aminobenzyl ( $-\text{CH}(\text{NH}_2)\text{C}_6\text{H}_5$ ), chloromethyl ( $-\text{CH}_2\text{Cl}$ ), bromo (Br) and diphenylphosphino ( $-\text{P}(\text{C}_6\text{H}_5)_2$ ).

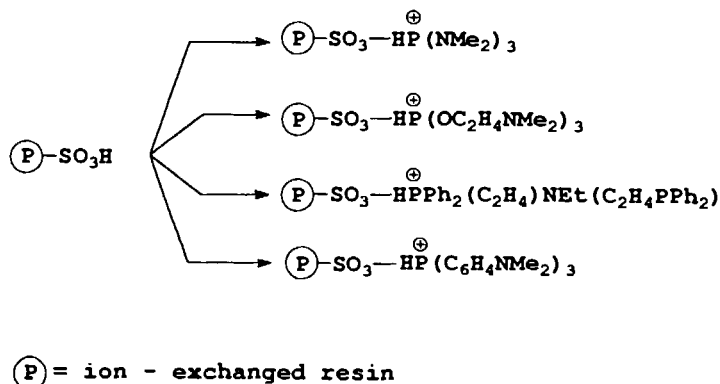
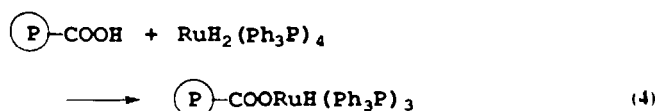
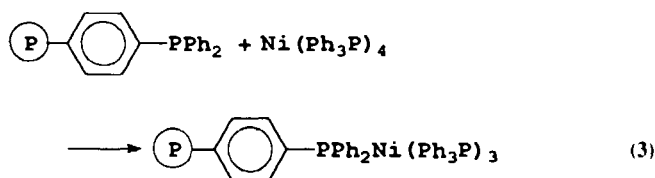


Figure 3. Ion-exchanged resin as a support.

- (ii) Amberlyst resins – macroreticular styrene–divinylbenzene ion-exchange resins (with a high divinylbenzene content) designed for use with organic solvents, functionalized with  $-\text{SO}_3\text{H}$ ,  $-\text{N}(\text{CH}_3)_2$ ,  $-\text{N}(\text{CH}_3)_3^+$ ,  $\text{CH}_3\text{COO}^-$ ,  $\text{CN}^-$ ,  $\text{NO}_2^-$ ,  $\text{SCN}^-$ , and  $\text{BH}_4^-$ .
- (iii) Poly-4-vinylpyridine and pyridinium resins cross-linked with (typically) 2% divinylbenzene. Pyridinium resins are available as the chloride ( $\text{Cl}^-$ ), toluene-4-sulphonate ( $\text{CH}_3\text{C}_6\text{H}_4\text{SO}_3^-$ ), tribromide ( $\text{Br}_3^-$ ), chlorochromate ( $\text{CrClO}_3^-$ ) and dichromate ( $\frac{1}{2}\text{Cr}_2\text{O}_7^{2-}$ ). Poly-4-vinylpyridine resins are available as poly-4-vinylpyridine–sulphur trioxide complex and poly-2-vinylpyridine–borane complex (Nafion) [7].

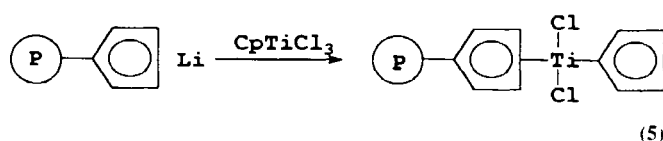
The functionalized polymers can react in a ligand exchange reaction as shown in Eqs 3 and 4, leading to the corresponding polymer-supported organometallic complexes. Figure 4 illustrates the broad versatility of this approach.



(P) = polymer chain

One of the most widely quoted examples of site isolation involves polymer-supported titanocene according to Eq. 5 [8].

Various attempts have been reported in which a complex containing a double bond amenable to poly-



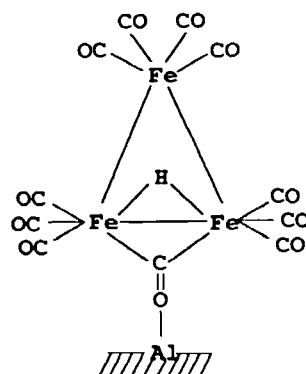
merization is polymerized: *cis*-[PdCl<sub>2</sub>(CN(CH<sub>2</sub>)<sub>3</sub>-OCO-CH=CH<sub>2</sub>)<sub>2</sub>] [9], vinyl ferrocene, and dimethyl acrylamide [10].

#### b Inorganic Supports

Various approaches to support complexes on inorganic supports are feasible:

- (i) the complexes are adsorbed on surfaces such as  $\text{SiO}_2$ ,  $\text{Al}_2\text{O}_3$ ,  $\text{Al}_2\text{O}_3-\text{SiO}_2$ ;
- (ii) the complexes are fixed by a chemical bond;
- (iii) the complexes are entrapped in cavities of zeolites or pillared clays [2].

Numerous papers deal with the immobilization of complexes physisorbed/chemisorbed on inorganic supports. In particular, the anchoring of clusters has attracted much attention. For instance, a structure such as **1** was proposed in which the adduct formation is reached by a CO–interaction of the cluster with the  $\text{Al}_2\text{O}_3$  surface [11].



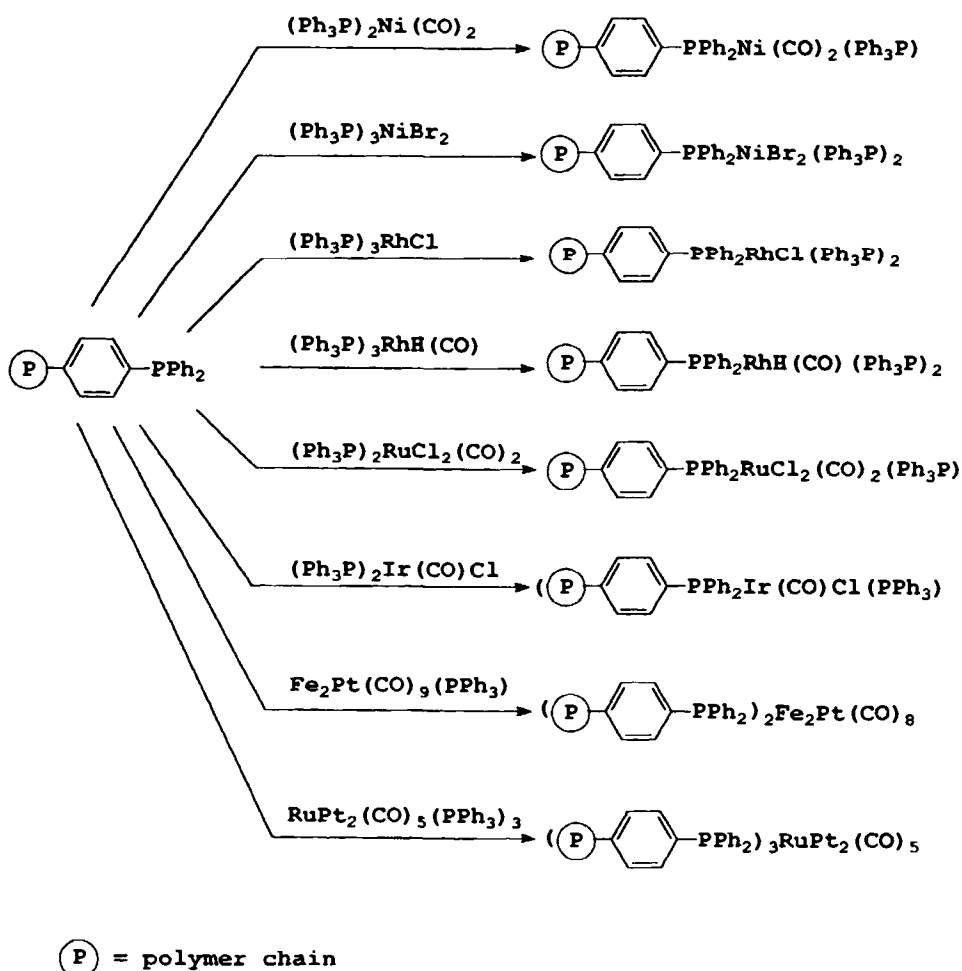
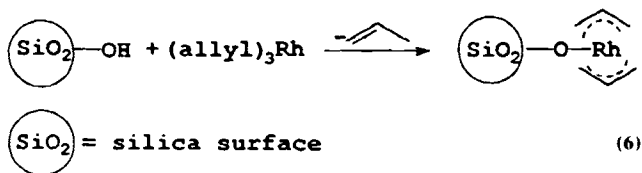


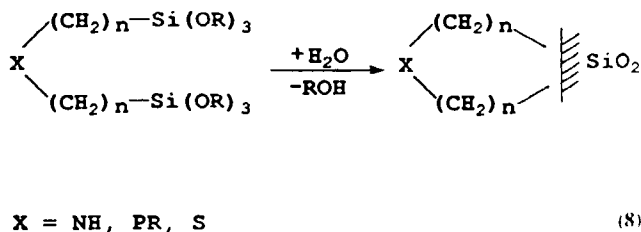
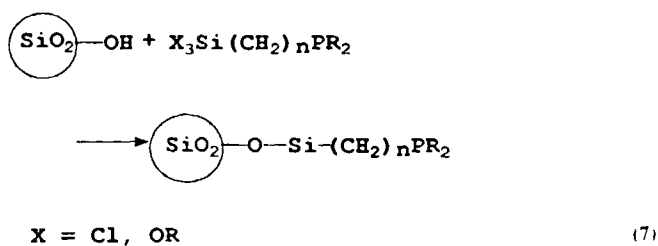
Figure 4. Attachment of metals to organic supports.

The reactive surface hydroxy groups can also react with organometallic compounds as exemplified in Eq. 6 [12].



Many authors have investigated the surface organometallic chemistry, which gives rise to a great variety of reaction pathways [13]. A second approach is based on ligand tailoring of inorganic surfaces. Inorganic matrices have reactive surface hydroxy groups, and common practice involves their reaction with organochlorosilanes which either contain the desired functional group according to Eq. 7 or can be subject to subsequent modification [14].

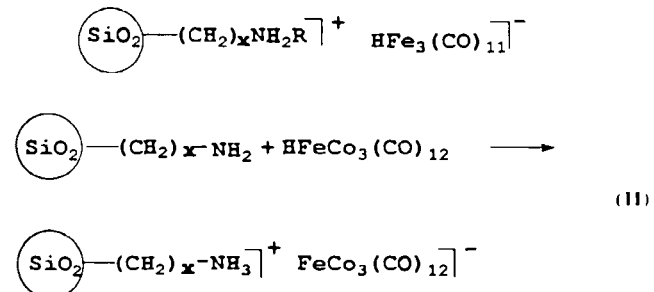
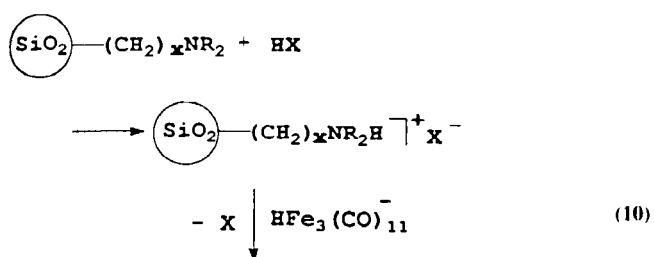
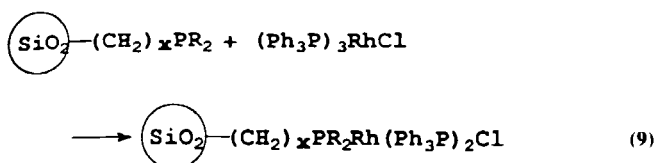
It is also feasible to proceed according to Eq. 8 using hydrolysis of the -Si(OR)<sub>3</sub>- units. Catalysts of this type



are commercially available under the tradename DEXLAN [15]. The silica used can be modified as is well known in heterogeneous catalysis.

Additionally, ion-exchanged structures can be tied to  $\text{SiO}_2$  as in  $[(\text{EtO})_3\text{Si}(\text{CH}_2)_3\text{PBU}_3]^+$ . It is also possible to synthesize a complex such as  $(\text{Ph}_3\text{P})_2\text{R}_2\text{P}-4(\text{CH}_2)_x\cdot\text{Si}(\text{OR})_3\text{RhCl}$  which, upon hydrogenolysis, yields a silica-supported rhodium catalyst.

The metals can be added by various routes: by ligand exchange reactions as in Eq. 9, by ion-exchange as in Eq. 10, or by an acid-base reaction as in Eq. 11 [17].



### c Chemical Reactions

Heterogenized complexes have been used to catalyze a great number of reactions, such as: hydrogenation [18], hydroformylation [19], ethylene oligomerization [20], hydrosilylation [21, 22], polymerization [23], telomerization [24], oxidation [25], oligomerization of monoalkene [26], methanol carbonylation [27], butadiene oligomerization [28], synthesis gas chemistry [29], and isomerization [30].

One of the most attractive fields of homogeneous catalysis is catalysis by chiral transition metal complexes, as the tool for preparing very valuable optically active products from prochiral reactants.

The use of heterogenized complexes looks promising due to the expected fixation of the prochiral reactant in the support matrix. The literature contains some examples, especially in hydrogenation [31], but also in telomerization [32].

To be commercially useful, a catalyst must possess several desirable features. It must exhibit high selectivity, reasonable activity per unit volume of reactor space, and its cost per unit mass of product produced should be low.

The principal disadvantages of organic polymers are their poor heat-transfer ability and in many cases their poor mechanical properties which prevent them from being used in stirred reactors in which they are pulverized. In this regard inorganic supports look more promising. In addition, one of the greatest difficulties in polymer-supported catalysts is their swelling.

One major consequence of confining a catalyst to the surface of a solid is that reagents have a reduced degree of freedom for access to and egress from the site of catalytic activity. Liquid-phase diffusion rates are generally  $\approx 10^{-5} \text{ cm s}^{-1}$ , whereas diffusion rates commonly experienced in polymer matrices are often an order of magnitude lower ( $\approx 10^{-6} \text{ cm s}^{-1}$ ). If the chemical reaction is fast compared with diffusion, the solid catalyst is not used effectively, and a reduced specific activity per site will be observed. This lower activity is expressed in terms of an effectiveness factor which is defined as the ratio of the observed to the intrinsic rate constants:  $\eta = k_{\text{obs}}/k_{\text{intr}}$ . This phenomenon has been described extensively for catalysis by ion-exchange resins and has also been observed for heterogenized catalysts.

Despite the large amount of work done in the field of support-bound metal catalysis, no important practical application has emerged. One explanation can be the need for a multidisciplinary approach. Various areas of competence in coordination chemistry, polymer science, and engineering must be combined. In addition, the flexible polymer chain can lead to a blocking of free coordination sites needed for catalysis, as shown in Fig. 5. Also metal bleeding represents a great problem. The covalently bonded ligands can easily dissociate, thus freeing the metal (Fig. 5).

Everyone working in the respective areas knows about the difficulties in characterizing catalysts and polymers. This certainly becomes no easier in the heterogenization of complexes.

### B Heterogenization of Enzymes

The heterogenization of complexes is directed towards immobilizing the catalytic centers which ensure the high activity and selectivity of the heterogenized complexes. In the case of immobilized enzymes the situation is quite different (see Section B4.15). Enzymes act in aqueous media under mild conditions very specifically. They are not always ideal catalysts for practical

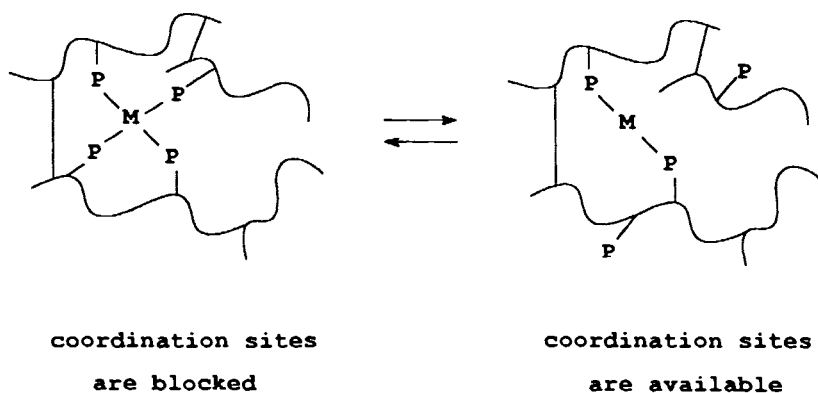


Figure 5. Dissociation of ligands.

applications, because they are generally unstable and can seldom be used in organic solvents or at elevated temperatures. As one of the methods employed to make enzymes more suitable in biocatalysis, the immobilization of enzymes has been studied since the late 1950s. The number of enzymes known with potential industrial application is impressive, and attempts to heterogenize enzymes have been numerous (Section B4.15). Therefore, within the framework of this article, it is impossible to cover all of them, and reference is given to various reviews in this field [33–46].

There are many advantages when using immobilized enzymes:

- (i) high stability and resistance to sheer stress and contamination;
- (ii) ease of developing continuous processes;
- (iii) fast reaction rate due to high catalyst concentration;
- (iv) easy separation of biocatalysts from fermentation media;
- (v) repetitive use of biocatalysts.

However there are also disadvantages:

- (i) the existence of mass transfer resistances;
- (ii) the necessity of immobilization processes;
- (iii) the additional costs of immobilization reagents.

#### a Enzyme Heterogenization Methods

Methods for the immobilization of enzymes – paralleling those for complexes shown in Figure 1 – can be classified into three categories, namely carrier binding, cross-linking, and entrapping methods. Carrier binding is based on linking enzymes to water-insoluble matrices. A further division can be made considering the binding mode: physical adsorption, ionic binding, and covalent binding. Figure 6 exhibits a schematic drawing of the important types of bonding. It is possible to use inorganic, organic, or biological carrier materials.

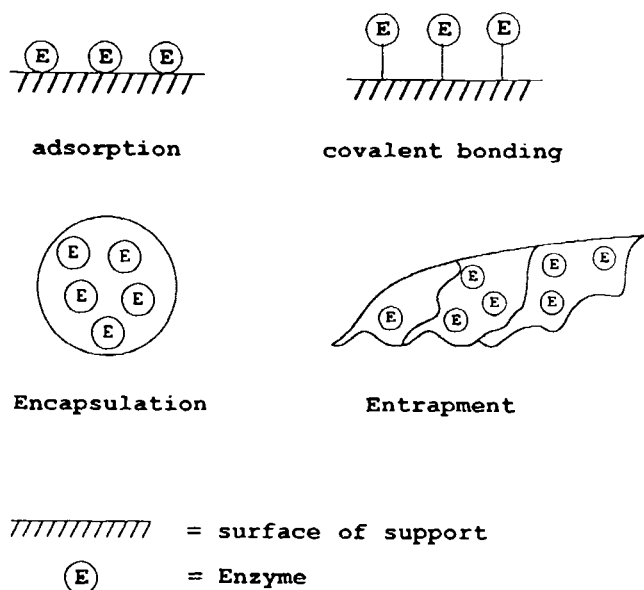


Figure 6. Schematic representation of enzyme immobilization.

Adsorption is the bonding of an enzyme to the surface of a carrier, which does not contain a functionalized group for covalent bonding. In theory the adsorption should be reversible, but in practice this is rarely the case. The adsorption is a simple and economic method but highly unreliable. In the following, carrier binding by chemical bonds will be predominantly considered.

#### Carrier Binding to Inorganic Supports

Inorganic carrier materials used for chromatography have been applied to covalent enzyme immobilization over the last 25 years [47]. The properties of the support must be adjusted to the enzyme. Several aspects, such as pore morphology, durability in the solvents, handling, compression strength, amount of loading, toleration of maximum pressure drop, and storage must be considered. Inorganic materials have an ad-



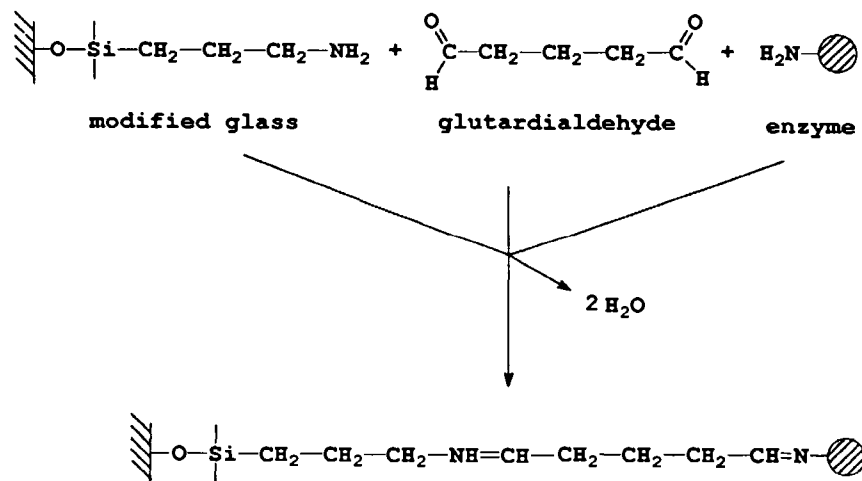
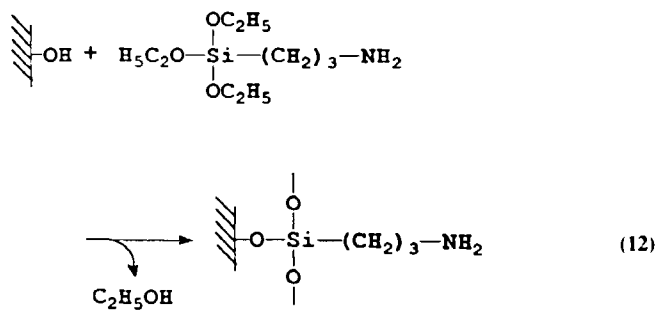


Figure 7. Covalent bonding of an enzyme with glutaraldehyde.

vantage in that they come as particles of all shapes and sizes as well as in the shape of monolithic porous supports or filter materials. They show no compression even at extremely high pressure drops. Other advantages are that they are not susceptible to microbial attack and that they do not shrink or swell in organic solvents or with pH changes. The most important aspect is their loading capacity which is high enough for a variety of applications.

Common industrial inorganic supports are [14] silica, porous glass, alumina, zeolites, ceramics, Aerosil, and glass balls. Prior to its use the porous silica glass, for instance, must be modified as shown in Eq. 12 with amino alkoxy silanes [14].

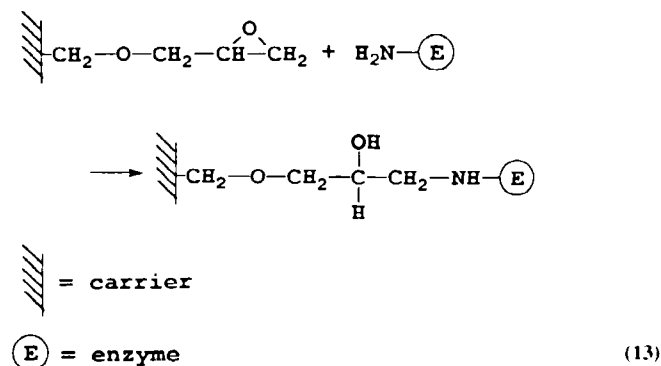


The amino group can be activated with bifunctional reagents. A commonly applied procedure is the introduction of an aldehyde function by the bifunctional reagent glutaraldehyde. The activated carrier can be used directly for the covalent bonding of the enzyme as shown in Fig. 7. Table 1 summarizes various examples of enzyme immobilization.

#### Carrier Binding to Organic Supports

Frequently used organic carrier materials are polymers such as polyacrylamide, polymethacrylamide, polyhydroxyethylmethacrylate, polyamide, vinylacetate-divinylethylene, and polystyrene [66]. Often applied

polymers contain hydroxy, amino, oxirane, and anhydride groups. Methods of covalent enzyme bonding [44] are azide, carbodiimide, isothiocyanate, and cyanogen bromide. Polymers with weakly active OH groups must be activated with bifunctional reagents such as cyanogen bromide, trichlorotriazine, tresylchloride, or tosylchloride. Acrylic bead polymers with oxirane groups show preferable properties and immobilization is shown in Eq. 13.



The following list may serve as an introduction to a variety of polymers used [41]: polyacrylamide [67], polyester [68], polyethylene [69], polystyrene [70], Nylon [71].

#### Carrier Binding to Biological Supports

Biological materials with OH- and NH<sub>2</sub>- groups for covalent enzyme coupling are agarose, cellulose, alginate, chitosan, dextran, and collagen. The polysaccharides agarose and cellulose, with their hydroxy

**Table 1.** Examples of enzymes covalently coupled to inorganic support materials through silane coupling agents.

Support material	Immobilized component	Reference
Silica	$\beta$ -galactosidase	49
Silica	cellulase	50
Silica	glucose oxidase	51
Porous silica	carbonic anhydrase	52
Porous silica	peroxidase, amyloglucosidase, urease	53
Porous silica	glucose isomerase, $\beta$ -galactosidase, cellulase	54 55
Silica gel	peroxidase, urease, amyloglucosidase	56
Magnetite	$\beta$ -galactosidase, cellulase	57 58
Alumina	alkaline protease, glucose oxidase, alcohol dehydrogenase	59
Ca-Ti phosphate	invertase	60
Controlled-pore glass	acetylcholinesterase	61
Controlled-pore glass	amyloglucosidase	62
Controlled-pore glass	glucose oxidase	63
Sintered glass	amyloglucosidase	64
Titanium oxide	hydrogenase	65

groups, are widely applicable to the covalent coupling of enzymes. The highly active  $\text{NH}_2$ - groups in chitosan can easily be activated with glutaraldehyde in a similar manner to that shown in Fig. 7.

#### *Entrapping/Encapsulation Methods*

Enzymes can be immobilized by physical entrapment without involving any chemical bonding. This route is somewhat more laborious but yields an enzyme that is least altered by the immobilization.

The enzyme can be entrapped into the growing polymer or gel materials or microcapsules (microencapsulation). The retention of enzymes in the reaction vessel can also be achieved by an ultrafiltration membrane. All these immobilization types have in common that the enzymes are not modified and are still acting in their soluble form, so that they should be freely mobile in their "cage". An older but good review of these techniques is given by Tramper [72]. Frequently used matrices for gel entrapment are polyacrylamide and collagen [41]. The membrane inclusion method is a broadly applicable one.

A number of single-enzyme reactions have also been described that function in an enzyme membrane reactor [73].

The main disadvantage is that entrapping methods can often be used for the conversion of low-molecular-weight substrates only, and there is always the possibility for losses of the enzyme to the surrounding environment.

When using the encapsulation method the enzyme is enclosed in a semipermeable membrane. Particles of 1-

100  $\mu\text{m}$  diameter are obtained during the immobilization procedure. The encapsulation method, similar to the entrapment method, is suitable only for enzymes acting on low-molecular-weight substrates. Applications of entrapped or encapsulated enzymes are limited.

#### *b Summary and Prospective Trends*

No single immobilization method is best for all enzymes or all applications of any given enzyme. The choice of a given immobilization method, an appropriate matrix, or even the best enzyme to use depends strongly on the application and must be checked from case to case. However, the number of immobilized enzymes with possible industrial application is impressive [74].

One would recommend the use of immobilized enzymes in industry when a novel product can be obtained, when the biotechnological process can compete with a corresponding known chemical process, and when the reaction shows regio- and/or stereo specificity. Developments are expected in the following areas. First, in the synthesis and separation of chiral drugs. One approach could involve a combination of enzyme-catalyzed and chemical asymmetric reactions. Secondly, processes involving enzyme-catalyzed reactions in nonaqueous media will develop further, thus circumventing one of the problems of enzymes associated with limited activity in organic solvents. Thirdly, the coenzyme regeneration may expand to increase the economic feasibility of these rather labile and expensive compounds. Finally, immobilized enzymes can be used

for the treatment of waste water, particularly when the water has been polluted by one or more well-characterized contaminants that can be specifically modified or eliminated by enzymes.

An interesting and quite new technique is the treatment of enzyme microcrystals with glutaraldehyde. The cross-linked enzyme crystals obtained remain active in otherwise hostile environments such as prolonged exposure to high temperatures, extreme pH values, or in organic solvents [75].

It can be expected that the use of immobilized enzymes and cells in the food, pharmaceutical, and chemical industries will continue to expand in the future.

## References

- 1 V Rao, R Datta, *J Catal* **1988**, *114*, 377–382
- 2 L A Gerritsen, J M Herrmann, J J F Scholten, *J Mol Catal* **1980**, *9*, 241–245
- 3 (a) E Bayer, V Schung, *CHEMTECH* **1976**, *5*, 484–487, (b) J S Kim, R Datta, *AIChE J* **1991**, *37*, 1657–1662, (c) D E Bergbreiter, *Functional Polymers*, Plenum Press, New York, **1989**, (d) J T Groves, R Neumann, *J Am Chem Soc* **1989**, *111*, 2900–2909
- 4 (a) Z M Michaska, D E Weber, *Platinum Met Rev* **1974**, *18*, 65–73, (b) B Delmon, G Jannes, *Catalysis Heterogeneous and Homogeneous*, Elsevier, New York, **1975**, (c) J P Candlin, H Thomas, *Adv Chem Ser* **1974**, *132*, 212–239, (d) Y I Yermakov, V Zakharov, *Adv Catal* **1975**, *24*, 173–219, (e) Y I Yermakov, *Catal Rev-Sci Eng* **1976**, *13*, 77–120, (f) F R Hartley, *Supported Metal Complexes*, Reidel, Dordrecht, **1985**, (g) J H Clark, S R Cullen, S J Barlow, T W Bastock, *J Chem Soc, Perkin Trans 2* **1994**, *6*, 1117–1130, (h) G Braca, *Chimicaoggi* **1988**, *2*, 23–27, (i) J J Crowley, H Rapoport, *Accounts of Chem Res* **1976**, *9*, 135–144, (j) F R Hartley, P N Vezev, *Adv Organomet Chem* **1977**, *15*, 189–234, (k) B C Gates, *Catalytic Chemistry*, Wiley, **1991**, p 182–254, (l) P Hodge, D C Sherrington, *Polymer-Supported Reactions in Organic Synthesis*, Wiley, Chichester, **1980**, (m) G Luft, *Chem-Ing-Tech* **1991**, *63*, 659–667
- 5 (a) H Knozinger, E Rumpf, *Inorg Chim Acta* **1978**, *30*, 51–58, (b) B C Gates, L Guzzi, H Knozinger, *Metal Clusters in Catalysis*, Elsevier, Amsterdam, **1986**
- 6 (a) R B Merrifield, *Angew Chem Int Ed Engl* **1985**, *24*, 799 (b) *SMPTECH*, Artillerigatan 4D, Abo, SF-20520 Finland (Supply Company)
- 7 K J Cavell, *Austr J Chem* **1994**, *47*, 769–797
- 8 R H Grubbs, C Gibbons, L C Kroll, W Bonds, C H Brubaker, *J Am Chem Soc* **1973**, *95*, 2373
- 9 B Corain, M Zecca, F O Sam, G Palma, L Silvano, *Angew Chem, Int Ed Engl* **1990**, *29*, 384–386
- 10 R Arshady, B Corain, S Lora, G Palma, U Russo, F O Sam *Adv Mater* **1990**, *2*, 412–413
- 11 H Knozinger in *Homogeneous and Heterogeneous Catalysis* (Eds Y Yermakov, V Likhobolov), VNU Science Press, Utrecht **1986**, p 789–818
- 12 J Schwartz in *Homogeneous and Heterogeneous Catalysis* (Eds Y Yermakov, V Likhobolov) VNU Science Press, Utrecht **1986**, p 661–691
- 13 (a) J Evans, B P Gracey, *J Chem Soc Dalton Trans* **1982**, 1123–1129, (b) J M Basset, J P Candy, A Choplin, C Santini, A Theolier, *Catal Today* **1989**, *6*, 1–26, (c) J M Basset, J P Candy, A Choplin, B Didillon, F Quignard, A Theolier in *Perspectives in Catalysis* (Eds J M Thomas, K I Zamarayev), Blackwell Scientific, London, **1992**, p 125–145, (d) B C Gates, H H Lamb, *J Mol Catal* **1989**, *52*, 1–18
- 14 M Capka, *Collect Czech Chem Commun* **1990**, *55*, 2803–2839
- 15 U Deschler, P Kleinschmit, P Panster *Angew Chem* **1986**, *98*, 237–253
- 16 I Tando, *J Am Chem Soc* **1982**, *104*, 6551
- 17 R Hemmerich, W Keim, M Roper, *J Chem Soc Chem Commun* **1983**, 428
- 18 (a) J M Brown, H Molinari, *Tetrahedron Lett* **1979**, *31*, 2933–2936, (b) F Sanchez, M Iglesias, A Corma, C del Pino, *J Mol Catal* **1991**, *70*, 369–379, (c) I E Uflyand, V N Sheinker, A V Bulatov, A D Pomogailo, *J Mol Catal* **1989**, *55*, 391–395, (d) E A Karakhanov, E B Neimerovets, A G Dedov, *Applied Organomet Chem* **1990**, *4*, 1–7, (e) R A Awe, E N Frankel, *J Am Oil Chem Soc* **1981**, 557–562, (f) T Okano, K Tsukiyama, H Konishi, J Kiji, *Chem Lett* **1982**, *5*, 603–606, (g) F Joo, M T Beck, *J Mol Catal* **1984**, *16*, 135, (h) A D Kim, D V Nadkarni, J L Fry, *Tetrahedron Lett* **1994**, *35*, 1507–1510, (i) A El Mansour, J P Candy, J P Bournonville, O A Feretti, J M Basset, *Angew Chem* **1989**, *101*, 360–362, (j) R J Card, C E Liesner, D C Neckers, *J Org Chem* **1979**, *44*, 1095–1098
- 19 (a) C Dossi, A Fusi, L Garlaschelli, D Roberto, R Ugo, *Catal Lett* **1991**, *11*, 335–340, (b) I Toth, B E Hanson, J Guo, M E Davis, *Catal Lett* **1991**, *8*, 209–214, (c) W Junfan, S Juntan, L Hong H Binglin, *React Polym* **1990**, *12*, 177–186, (d) L Alvila, T A Pakkanen, T T Pakkanen, O Krause, *J Mol Catal* **1992**, *71*, 281–290 (e) S C Tang, T E Paxson, L Kim, *J Mol Catal* **1980**, *9*, 313, (f) M E Ford, A N, Neogi, *J Mol Catal* **1983**, *9*, 99 (g) E Rode, M E Davis, B E Hanson, *J Chem Soc Chem Commun* **1985**, 1477–1478, (h) G Schmid, R Kupper, H Hess, J-O Malm, J-O Bovin, *Chem Ber* **1991**, *124*, 1889–1893, (i) A Fukuoka, L F Rao, N Kosugi, H Kuroda M Ichikawa, *Appl Catal* **1989**, *50*, 295–301, (j) M Ichikawa, *Polyhedron* **1988**, *7*, 2351–2367, (k) M Ichikawa, L Rao T Kimura, A Fukuoka, *J Mol Catal* **1990**, *62*, 15–35, (l) L A Gerritsen, A van Meerkerk, M H Vreugdenhil, J J F Scholten, *J Mol Catal* **1980**, *9*, 138–155 (m) J Hjortkjaer, M S Scurrel, P Simonsen, H Svendsen, *J Mol Catal* **1981**, *12*, 179–195
- 20 (a) W Keim, M Peuckert, *J Mol Catal* **1984**, *22*, 289–295, (b) G A Nesterov, G Fink, V A Zakharov, *Makromol Chem Rapid Commun* **1989**, *10*, 669–673, (c) G A Nesterov, V A Zakharov, G Fink, W Fenzl, *J Mol Catal* **1991**, *66*, 367–372 (d) I E Uflyand, A D Pomogailo, *J Mol Catal* **1989**, *55*, 302–310, (e) G Braca, M Di Girolamo, A M Raspolli Galetti, G Sbrana, M Brunelli, G Bertolini, *J Mol Catal* **1992**, *74*, 421–431
- 21 B Marcimec, Z W Konetka, W Urbaniak, *J Mol Catal* **1981**, *12*, 221–230
- 22 M Capka, M Czakoova, J Hjortkjaer, U Schubert, *React Kinet Catal Lett* **1993**, *50*, 71–74
- 23 (a) V A Zakharov, Y I Yermakov, *Cat Rev Sci Eng* **1979**, *19*, 67–103, (b) S Collins, W M Kelly, D V Holden, *Macromolecules* **1992**, *25*, 1780–1785, (c) G G Arzoumanidis, N M Karayannis, H M Khelghation, S S Lee *Catal Today* **1992**, *13*, 59–71, (d) F S Dyachkovskii, A D Pomogailo, *J Polym Sci Polym Symp* **1980**, *68*, 97–108
- 24 (a) K Kaneda, H Kurosaki, M Terasawa, T Imanaka, S Teranishi, *J Org Chem* **1981**, *46*, 2356–2362, (b) J P Bianchini, E Gaydou, B Wagell, A Eisenbeis, W Keim *J Mol Catal* **1985**, *30*, 197–212

- 25 (a) T Yokoyama, M Nishizawa, T Kimura, T M Susuki, *Chem Lett* **1983**, *11*, 1703–1706, (b) H Fischer, G Schulz-Ekloff, T Buck, D Wohrle, *Erdöl, Erdgas, Kohle* **1994**, *110*, 128–135, (c) A Sorakin, B Meunier, *J Chem. Soc., Chem. Commun* **1994**, 1799–1800
- 26 (a) B M Trost, J M Tour, *J Am Chem Soc* **1987**, *109*, 5268–70, (b) N Kawata, T Mizoroki, A Ozaki, *J Mol Catal* **1975**/*76*, *1*, 275–283
- 27 (a) M S Scurell, *La Chimica el Industria* **1979**, *61*, 652–655, (b) T-N Huang, J Schwartz, *J Mol Catal* **1984**, *22*, 389–93, (c) M S Scurell, R Howe, *J Mol Catal* **1980**, *7*, 535–537, (d) P Geln, G Coudurier, Y Ben Taarit, C Naccache, *J Catal* **1981**, *70*, 32–40
- 28 (a) C U Pittman Jr, S K Wu, S E Jacobson, *J Catal* **1976**, *44*, 87–100, (b) U Schuchardt, E N Dos Santo, F S Dias, *J Mol Catal* **1989**, *55*, 345–352
- 29 B Corain, M Basato, M Zecca, G Braca, A M R Galetti, S Lora, G Palma, E Guglielminotti, *J Mol Catal* **1992**, *73*, 23–41
- 30 L C Po, C B Hung, R H Grubbs, C H Brubaker, *J Organomet Chem* **1981**, *214*, 325–37, (b) A P Raje, R Datta, *J Mol Catal* **1992**, *72*, 97–116
- 31 (a) I Toth, B E Hanson, *J Mol Catal*, **1992**, *71*, 365–371, (b) G L Baker, S J Frtschel, I R Stille, J K Stille, *J Org Chem* **1981**, *46*, 2954–60, (c) A Corma, M Iglesias, C del Pino, F Sanchez, *J Organomet Chem* **1992**, *431*, 233–246, (d) U Nagel, E Kinzel, *J Chem Soc Chem Commun* **1986**, *14*, 1098–1099, (e) H B Kagan, T P Dang, W Dumont, J C Poulin, *J Am Chem Soc* **1973**, *95*, 8295
- 32 W Keim, D Schwarzer, D Vogt, *Chem-Ing-Techn* **1995**, *67*, 904
- 33 O R Zaborsky, *Immobilized Enzymes*, CRC Press, Cleveland, Ohio, **1973**
- 34 H H Weetall, *Immobilized Enzymes, Antigens, Antibodies and Peptides*, Dekker, New York, **1975**
- 35 I Chibata, *Immobilized Enzymes*, Wiley, New York, **1978**
- 36 K Buchholz, *Charakterization of Immobilized Biocatalysts*, Dechema Monographie 84, Verlag Chemie, Weinheim, **1979**
- 37 J C Johnson, *Immobilized Enzymes*, Noyes Data Corp., Park Ridge, NJ, **1979**
- 38 P Durnill, A Wisemann, N Blakebrough, *Enzymic and Nonenzymic Catalysis*, Ellis Horwood, Chichester, UK, **1980**
- 39 J F Kennedy, J M S Cabral, *Solid Phase Biochemistry* (Ed W H Scouten), **1983**, Wiley Interscience, New York, p 253
- 40 W Hartmeier, *Immobilisierte Biokatalysatoren*, Springer Verlag, Berlin, **1986**
- 41 K Mosbach, *Immobilized Enzymes and Cells*, Methods of Enzymology, Vol 135–137, Academic Press, New York, **1987**
- 42 H-J Rehm, G Reed, *Biotechnology*, 2nd ed, VCH, Weinheim, **1993**, 430–466
- 43 K Drauz, H Waldmann, *Enzyme Catalysis in Organic Synthesis*, VCH, Weinheim, **1994**
- 44 B P Sharma, L F Bailey, R A Messing, *Angew Chem* **1987**, *94*, 836–852
- 45 I Chibata, T Tosa, T Sato, *J Mol Catal* **1986**, *37*, 1–24
- 46 S Fukui, A Tanaka, *Ullmann's Encycl Ind Chem 5th ed* **1987**, Vol A9, p 382–388
- 47 H H Weetall, *Science* **1969**, *166*, 615
- 48 H H Weetall, *Appl Biochem Biotechnol* **1993**, *41*, 151–188
- 49 A Kozhukharova, K Batsalova, Y A Popova, N Kirova, D Klisurski, D Simeonov, *Biotechnologia* **1990**, *1*, 61
- 50 M Kitaoka, H Taniguchi, T Sasaki, *J Ferment Bioeng* **1989**, *67*, 182
- 51 A Kojuharova, Y Popova, N Kirova, D Klisurski, D Simeonov, L Spasov, *J Chem Technol Biotechnol* **1988**, *42*, 95
- 52 J P O'Daly, A L Crumbliss, R W Henkens, *Biotechnol Appl Biochem* **1990**, *12*, 11
- 53 J Lobarzewski, A Wojcik, T Blaszczyńska, *Acta Biotechnol* **1989**, *9*, 239
- 54 J E Sorensen, C Emborg, *Enzyme Microb Technol* **1989**, *11*, 26
- 55 K Shimizu, M Ishihara, *Biotechnol Bioeng* **1987**, *29*, 236
- 56 A Wojcik, J Lobarzewski, T Blaszczyńska, J Fiedurek, *Biotechnol Bioeng* **1987**, *30*, 983
- 57 F R H Dekker, *Appl Biochem Biotechnol* **1990**, *23*, 25
- 58 A Garcia, S Oh, C R Engler, *Biotechnol Bioeng* **1989**, *33*, 321
- 59 G A Kovalenko, V D Sokolovskii, *Biotechnol Bioeng* **1992**, *39*, 523
- 60 T Suzuki, M Tonyama, H Hosono, Y Abe, *J Ferment Bioeng* **1991**, *5*, 384
- 61 S Kumaran, H Meier, A M Danna, C Tran-Minh, *Anal Chem* **1991**, *63*, 1914
- 62 F Janowski, G Fisher, W Urbaniak, Z Foltynowicz B Macemec, *J Chem Technol Biotechnol* **1991**, 51
- 63 M M Hossain, D D Do, *Biotechnol Bioeng* **1985**, *27*, 842
- 64 J Fiedurek, J Lobarzewski, *Starch Staerke* **1990**, *42*, 358
- 65 P Cuendet, M Gratzel, K K Rao, D O Hall, *Photobiology Photobiophys* **1984**, *7*, 311
- 66 N F Mathur, C K Norang, R W Williams, *Polymers as Aids in Organic Chemistry*, Academic Press, New York, **1980**
- 67 J K Imman, H M Dintzis, *Biochemistry* **1969**, *8*, 4074
- 68 R S Franek, *Czech Epidemiol Mikrobiol Immunol* **1978**, 27
- 69 T T Ngo, K J Laider, C F Yam, *Can J Biochem* **1979**, *57*, 1200
- 70 N Grabhofer, L Schluth, *Naturwissenschaften* **1953**, *40*, 508
- 71 W E Hornby, L Goldstein in *Methods in Enzymology* (Ed K Mosbach), **1987**, Vol 44, p 118, Academic Press New York
- 72 J Tramper in *Solid Phase Biochemistry* (Ed W H Scouten) Wiley Interscience, New York, **1983**, p 393
- 73 U Kragl, D Vasic-Racki, C Wandrey, *Chem-Ing-Tech* **1992**, *64*, 499
- 74 J G Shewale, S R Naik, *J Scientific Ind Res* **1991**, *50*, 947
- 75 N L St Clair, M Navia, *J Am Chem Soc* **1992**, *114*, 7314–7316 This material is commercially available from Altus Biologies Inc, Cambridge, USA

### 2.2.1.5 Preparation of Supported Catalysts by Deposition–Precipitation

J W GEUS AND A J VAN DILLEN

#### A Introduction

The activity of solid catalysts is usually proportional to the active surface area per unit volume of catalyst. A high activity per unit volume consequently calls for (extremely) small particles. Since most active species

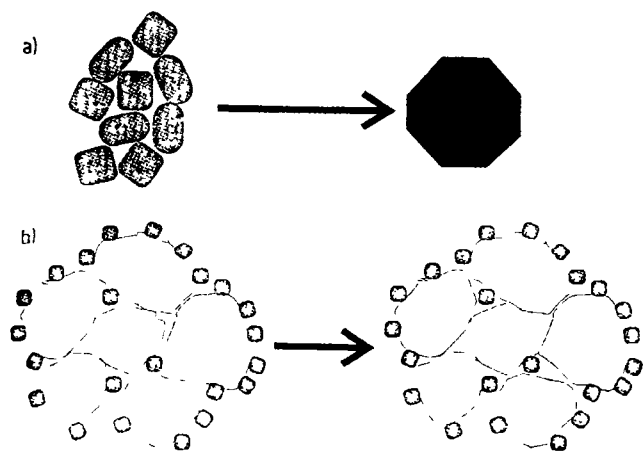


**Figure 1.** (a) Rapid sintering of unsupported active particles. (b) Supported thermostable active material.

sinter rapidly at the temperatures at which the thermal pretreatment and the catalytic reaction are performed [1], small particles of the active species alone do not provide thermostable, highly active catalysts. To provide solid catalysts with the desired thermal stability, a support is therefore generally utilized. A support is a highly porous, thermostable material onto which the active species is dispersed. As indicated in Fig. 1, sintering of small particles leads to a low active surface area; application on a support stabilizes the active surface area.

In view of the favorable bulk density, the price, and its thermal stability, the most frequently used support is alumina. The other supports often used are silica and active carbon. Silica has a lower bulk density, and is more liable than alumina to sintering at temperatures above about 900 K. Furthermore, silica can volatilize at high steam pressures and elevated temperatures. Active carbon supports usually offer very high surface areas. In an environment inert to carbon the thermal stability is extremely high. In an oxidizing environment, however, active carbon will rapidly react with oxygen, and with hydrogen or carbon dioxide, reaction to methane or carbon monoxide, respectively, can proceed. The mechanical strength of carbon supports is, moreover, often insufficient.

Depending upon the nature of the active component two different types of supported catalysts can be distinguished [2]. When the active component is highly expensive, as with precious metals, a maximum active surface area per unit weight of active component is aimed at. With less costly active components, such as base metals, base metal oxides, or sulfides, a maximum active surface area per unit volume is most attractive. The reason is that a high active surface area causes a relatively small catalytic reactor volume to be sufficient to achieve a technically satisfactory conversion. When

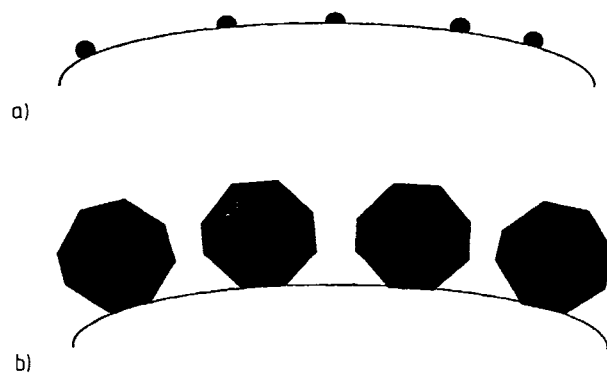


**Figure 2.** (a) Characteristic supported precious metal catalyst. (b) Characteristic supported base metal catalyst.

the costs of the reactor dominate the process, a high loading of the support maximizing the active surface area per unit volume will be attractive. Conversely, when the costs of the active component are most important, the maximum active surface area per unit weight of active component is desired. Expensive active components, therefore, will be applied to supports at low loadings leading to small or very small supported active particles, thus providing a high active surface area per unit weight of active component. Since the support is diluting the active component, much higher loadings of the support are generally utilized with base metals or base metal compounds. However, the mobility of the atoms of the active species over the surface of the active component is usually high under the conditions of the catalytic reaction or the thermal pretreatment of the catalyst. As a result, contacting active particles will rapidly decrease their surface area by sintering, which can lead at high loadings to very large bodies of the active component(s) exposing a small active surface area. Contact between the supported active particles must consequently be limited as much as possible. An even and dense distribution of small particles of (the precursor) of the active component over the surface of the support is therefore desired for catalysts containing base metal (compounds) as the active component. Figure 2 schematically indicates a supported precious metal catalyst and an active component consisting of a base metal applied at a high loading on a support.

When the surface area of the support is not affected by the active precursor, the maximum active surface area that can be achieved is of the same order of magnitude as the surface area of the support. A surface of the support thus covered with the active component in a way that the active particles are just not touching will



Figure 3. Usual supported, highly loaded base metal catalyst

provide an active surface area approaching that of the support. Usually such a coverage calls for small particles of the active component. However, the activity per unit surface area of the active component may vary with the size of the supported active moieties. When the activity per unit surface area drops with the size of the active species, the specific activity may be so low that the resulting activity is disappointing, in spite of a high catalytically active surface area per unit volume of catalyst. Reactions for which the surface structure of the catalytically active component is affecting the activity and/or the selectivity are known as structure-sensitive or demanding [3]. With structure-insensitive or facile reactions the structure of the surface of the active component is not affecting the catalytic properties. Small particles may not be favorable when the reaction is structure-sensitive; larger particles may exhibit a higher activity and/or selectivity per unit surface area. Although the active surface area is lower, the higher activity per unit surface area of the active phase results in a higher overall activity. With the selectivity the effect of the size of the active moieties may be even stronger, which causes small supported active particles to be very unfavorable. The most favorable size of supported active particles has, however, only rarely been established. The reason is that it is difficult to vary systematically the size of the active particles deposited on a support while maintaining a narrow particle size distribution. It is consequently desirable to be able to apply the active component(s) uniformly and densely over the surface of the support as particles of controlled size. This is one of the main goals in the preparation of supported catalysts by deposition-precipitation. In Fig. 3 a very highly loaded support surface is schematically indicated – such a loading of a support is difficult to achieve in practice.

After a general discussion of the production of supported catalysts, the theory of nucleation and growth of solids is surveyed. Next the interaction between supports and precipitating precursors of the active components, which is dominating the nucleation with precipitation onto suspended supports, is discussed. This is followed by a review of the loading of powdered supports suspended in an aqueous solution of the active precursor(s) by deposition-precipitation. Highly prom-

ising is a technique for the preparation of synthetic clay minerals by deposition-precipitation. A number of embodiments of the procedure are mentioned, including a technically attractive electrochemical precipitation method. Finally, the application of catalytically active precursors into preshaped support bodies is dealt with.

## B Production of Supported Catalysts

The procedures for the production of supported catalysts can be divided into two main groups, namely selective removal of one or more components out of usually nonporous bodies of a compound containing precursors of the support and the active component(s), and application of (a precursor of) the active component(s) onto a separately produced support [2]. Both procedures are carried out extensively on a technical scale.

### *a Selective Removal of One or More Components*

With highly loaded supports, the first procedure – selective removal, is often employed. The most successful example is the technical ammonia synthesis catalyst, which is produced from magnetite ( $\text{Fe}_3\text{O}_4$ ) containing some (up to about 4 wt%) alumina [4]. Selective removal of the oxygen of the magnetite by reduction leads to a highly porous material, in which metallic iron particles of about 40 nm are separated by the remaining alumina. In the reduced catalyst the loading of active component is no less than 96–98 wt%, while the mechanical strength is extremely high. With the copper-based catalysts for the methanol synthesis and for the low-temperature carbon monoxide shift conversion water, carbon dioxide, and oxygen bonded to the copper are selectively removed from a coprecipitate of copper(II), aluminum(III), and zinc(II). A last example is the removal of water and carbon dioxide from mixed oxalates, as with copper-magnesium or nickel-magnesium oxalates [5]. As shown in Fig. 4, selective removal can result in a porous body, as with the ammonia synthesis catalyst, or in a powder of the support loaded with the active component – as with mixed oxalate precursors.

Although with the selective removal procedure the active component and the support are usually very intimately mixed, it is difficult to control the porous structure and/or the mechanical strength of the resulting catalyst bodies. Nonetheless the procedure is difficult to beat for the production of highly loaded supports. The most well known example of selective removal, the preparation of Raney metals, where aluminum is selectively removed, leaves behind almost exclusively the desired active metal.

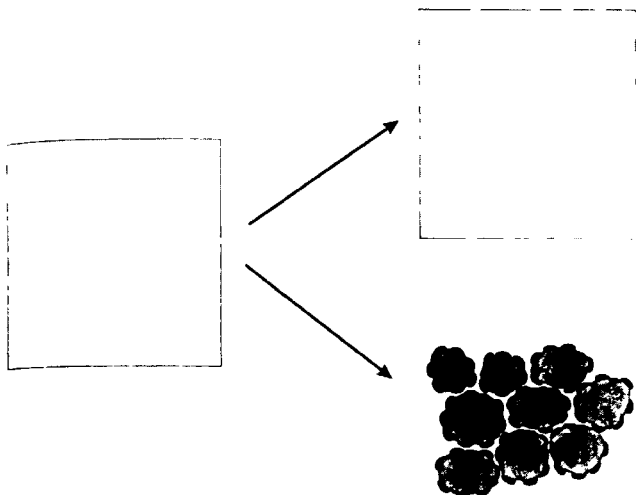


**Figure 4.** Production of supported catalysts by selective removal of components from nonporous precursor leading to porous bodies (above) or powder of supported active component (below).

#### *b Application on Separately Produced Supports*

Application of an active precursor onto a separately produced support can be performed with powdered supports and with preshaped support bodies. A powdered support minimizes transport problems during loading with the active component(s), but the subsequent shaping of the loaded support to mechanically strong artifacts may present difficulties. Also, control of the pore structure of the final catalyst can be difficult with loaded, finely divided supports. The most rapid procedure to prepare technical catalysts is to start from commercially available preshaped support bodies of the desired size, shape, porous structure, and mechanical properties. Applying the active component(s) uniformly and finely divided into the support bodies leads immediately to the technical catalyst. However, transport through the long pores of preshaped support bodies can prevent the establishment of a uniform, dense distribution of the active component(s).

*Impregnation of Supports and Drying.* Most obvious is incipient wetness impregnation of a support with a solution of an active precursor and subsequent drying and calcination of the thus loaded support [6]. Incipient wetness or pore-volume impregnation is especially attractive with preshaped support bodies. When the active component has to be in the metallic state, reduction can be carried out after the calcination step. Often, the catalyst is reduced after loading into the reactor to prevent a separate passivation step, in which the surface of the pyrophoric reduced catalyst is carefully oxidized. However, to achieve reproducible catalysts the catalyst manufacturer usually reduces the catalyst and delivers the passivated catalyst, which then only needs a short additional reduction.

It is advantageous if no waste water is produced with impregnation and drying, or if loss of active precursor can be prevented fairly easily. To produce supported precious metal catalysts impregnation and drying is therefore the procedure of choice. For the low loadings usual with precious metals, e.g. 0.5 wt %, adsorption of the precursor on the surface of the support can be used. With alumina, negatively charged precious metal complexes are applied at relatively low pH levels, whereas with silica positively charged ammine complexes are usually employed.

When high loadings are required, pore-volume impregnation is more difficult. First, the solubility of the precursor has to be sufficiently high to allow one to dissolve the required amount of the active component or its precursor in a volume of liquid equal to the pore volume of the support. Often the concentration of the active precursor in the liquid cannot be raised sufficiently. Consequently multiple impregnations are required to achieve the desired loading of the active component. The final distribution of the active component within the support bodies after drying is also often unfavorable. Extensive research has demonstrated that the active precursor is frequently deposited at the external edge of the impregnated support bodies. Boon [7] has shown that for supports with wide pores deposition at the external edge is due to the small crystallites of the active precursor deposited initially at the external edge. The interstices between the small crystallites are more narrow than the pores of the support, which causes a capillary flow of the impregnated liquid from the wide pores of the support to the small crystallites of the active precursor. The result is a porous crust of active precursor, deposited at the external edge of the support bodies. Sometimes no active precursor is deposited at all within the internal volume of the support bodies, as indicated in Fig. 5.

With supports having narrow pores, deposition of the active precursor appears to proceed usually at the external edge of the support bodies. The transport of the liquid to the external edge was found to be much faster than the transport of the water vapor through the pores of the support. When the pores of the support are completely filled, capillary flow transports the liquid to the external edge of the support bodies. Furthermore, Knijff [6] and van den Brink [8] have shown that with partly emptied pores the transport of the liquid proceeds through fluid elements capillary-condensed in necks present between the elementary particles of the support. The condition with filled necks bordering the regions of the pore system that have been emptied is known as the funicular state of the im-

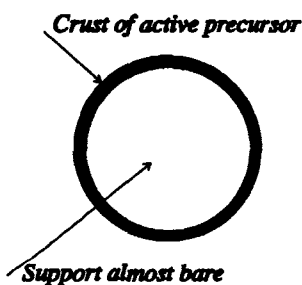


Figure 5. Unfavorable distribution of active precursor after impregnation and drying.

pregnated porous solid. As a result the active precursor is mainly deposited at the external edge of the support bodies, where the evaporation of the solvent proceeds and where consequently the concentration is highest.

To prevent migration of the main fraction of the active precursor to the external edge of the support bodies, an active precursor has to be utilized that does not crystallize readily and exhibits a high interaction with the surface of the support, preferably through hydrogen-bridge bonding. Solutions of citrates or ethylenediaminetetraacetic acid (EDTA) complexes have been found to be very effective at preventing deposition of the active precursor exclusively at the external edge of the support bodies [9–12]. With EDTA complexes especially, the pH of the solution being impregnated has to be considered carefully. Much information can be obtained by drying a drop on a microscope slide. If the dissolved material is deposited as a ring, impregnation of a preshaped support and drying is likely to lead to deposition of the precursor on the external edge of the support bodies. If, however, the area of the microscope slide initially covered by the liquid is almost equal to that covered by the dried solid, an even deposition throughout the pores of the support can be expected.

Nevertheless, high loadings often cannot be achieved by pore-volume impregnation, since the required amount of the active precursor cannot be dissolved in the pore-volume of the support. Suspension of the support in a volume of the solution of the active precursor larger than the pore-volume and subsequent drying does not lead to a uniform distribution of the active precursor over the internal surface of the support. The evaporation of the solvent proceeds essentially outside the pore system of the support and the active precursor is deposited where the solvent evaporates. With a powdered, finely divided support, however, that is continuously and intensively stirred, reasonable results can be obtained. Nonetheless the loading of the support is always inhomogeneous, and the procedure is very difficult to scale up satisfactorily.

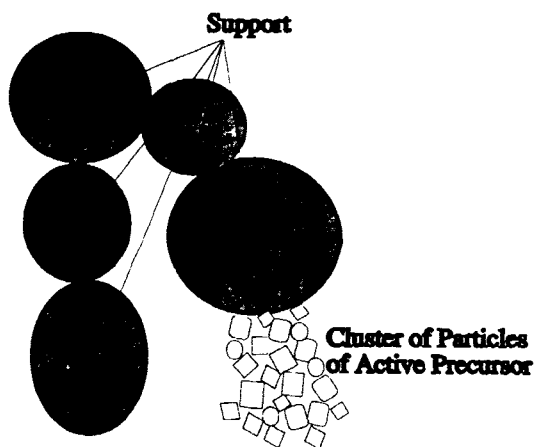


Figure 6. Clusters of particles of active precursor within support.

*Precipitation onto a Suspended Support.* Precipitation of an active precursor onto a support suspended in a solution of the precursor can provide high loadings, since the compound(s) dissolved in a liquid volume large as compared to the pore-volume of the support are concentrated on the support. Besides coprecipitation of the precursors of the support and the active material and subsequent selective removal of some components, precipitation in the presence of a suspended support is also often carried out to achieve high loadings of the support. The apparatus and the procedures do not differ significantly. However, the precipitation usually proceeds where the precipitating liquid is entering the suspension, and the precipitant necessarily does not enter the suspension within the porous conglomerates of the support. When nucleation and growth of the precipitate of the precursor are rapid, large crystallites of precursor result. With rapid nucleation and slow growth, which is usually encountered with poorly soluble compounds, clusters of small particles of the active precursor outside the pore system of the support are often obtained. At the high concentration at the point where the precipitant enters the suspension, the small particles rapidly and irreversibly flocculate, which leads to the above clusters of small particles. Thus prepared catalysts are liable to rapid deactivation during pretreatment or use at elevated temperatures, since the small elementary particles of the precursor are intimately connected and therefore sinter readily. Figure 6 schematically indicates the type of cluster often found with supported catalysts prepared by precipitation.

The above discussion has indicated that precipitation onto a suspended support is often required to produce catalysts in which the support is highly loaded. Highly loaded supports are especially desirable for catalysts containing (compounds of) base metals as mentioned



above. To be able to effect precipitation within the porous system of a suspended support we have to modify the precipitation process so as to enable the still soluble active precursor to migrate into the pores of the support. Since the diffusion of colloidal particles is fairly slow, we even have to prevent formation of colloidal particles of the active precursor outside the pore system of the support. To obtain the conditions required to achieve transport into the pores of a suspended support, the nucleation of insoluble solids within (aqueous) solution must be considered.

### C Theory of Nucleation

Only a simple review of the theory of nucleation and precipitation [13, 14], to assess the conditions to achieve precipitation exclusively on the surface of the support, is presented here. Consider first the formation of a spherical nucleus in the bulk of the solution. The change in the free enthalpy upon formation of the above nucleus is

$$\Delta G_{\text{tot}} = \Delta G_v - \Delta G_s$$

in which

$$\Delta G_v = \frac{4}{3} \pi r^3 (\mu_s - \mu_1) = \frac{4}{3} \pi r^3 \Delta \mu_{\text{sl}}$$

$$\Delta G_s = 4\pi r^2 \gamma$$

$$\Delta G_{\text{tot}} = \frac{4}{3} \pi r^3 \Delta \mu_{\text{sl}} + 4\pi r^2 \gamma$$

Here,  $\Delta G_v$  is the volume change in free enthalpy and  $\Delta G_s$  is the interfacial energy of the precipitating solid with the solution,  $2r$  is the diameter of the nucleus of the precipitate,  $\mu_s$  the molecular free enthalpy of the solid precipitate, and  $\mu_1$  of the dissolved solid, while  $\gamma$  is the interfacial energy. The term  $\Delta \mu_{\text{sl}}$ , the difference in molecular free enthalpy between the solid and the dissolved compound, is negative with the bulk solid being stable. For a small change in the size of the nucleus the change in free enthalpy is

$$\frac{d\Delta G_{\text{tot}}}{dr} = 4\pi r^2 \Delta \mu_{\text{sl}} + 8\pi r \gamma$$

A maximum in the free enthalpy is obtained when

$$\frac{\Delta G_{\text{tot}}}{dr} = 0$$

that is

$$4\pi r_c^2 \Delta \mu_{\text{sl}} + 8\pi r_c \gamma = 0$$

$$r_c = 2 \frac{\gamma}{\Delta \mu_{\text{sl}}}$$

Note that in the latter expression the negative quantity  $\mu_{\text{sl}}$  has been changed for  $\mu_{\text{ls}}$ , a positive value. When the size  $2r$  of the nucleus is greater than  $2r_c$ , the critical size

for nucleation, the free enthalpy drops when the size of the nucleus rises. The critical size of the nucleus corresponds to the maximum in free enthalpy that has to be crossed to arrive at a stable nucleus.  $\Delta \mu_{\text{sl}}$  strongly increases with the activity and thus with the concentration of the dissolved compound. The size of the critical nucleus therefore drops rapidly at growing concentration of the dissolved compound.

The rate of nucleation is generally assumed to be proportional to the incidence rate of elementary moieties of the crystallizing species onto the critical nuclei. The rate of nucleation is therefore proportional to the concentration of critical nuclei, which is proportional to

$$\exp\left(-\frac{\Delta G_{\text{tot}}}{RT}\right)$$

Provided that  $r\Delta \mu_{\text{sl}} \geq 3\gamma$ , the rate of nucleation is proportional to

$$\exp\left(-\frac{16}{3} \pi \frac{\gamma^2}{\Delta \mu_{\text{ls}}^2 RT}\right)$$

Insertion of the earlier derived expression leads to the latter relation to which the density of critical nuclei and, hence, the rate of nucleation is proportional. It can be seen that a higher activity and thus a higher concentration of the precipitating active precursor, which leads to a higher value of  $\Delta \mu_{\text{ls}}$ , causes the concentration of critical nuclei to increase exponentially. At a higher concentration the rate of nucleation thus rises sharply.

To account for the interaction with the support consider a hemispherical nucleus attached to the support. The change in free enthalpy upon crystallization to form cap-shape nuclei on the support is

$$\Delta G_{\text{tot}} = \frac{3}{2} \pi r^3 \Delta \mu_{\text{sl}} + 2\pi r^2 \gamma_{\text{ls}} + \pi r^2 \gamma_{\text{ss}}$$

where  $\gamma_{\text{ss}}$  is the interfacial energy with the support. The above equations indicate that interaction with the support causing a low value of  $\gamma_{\text{ss}}$  can decrease considerably the change in free enthalpy of the formation of a nucleus and hence the concentration of the dissolved active precursor at which a substantial rate of crystallization is exhibited.

We can survey the precipitation in the usual equilibrium diagram, in which the concentration and the temperature of the saturated solutions are represented. Figure 7 schematically indicates the solubility of a solid as a function of the temperature. It can be seen that at increasing temperatures the solubility increases. Since the rate of crystallization or precipitation in-

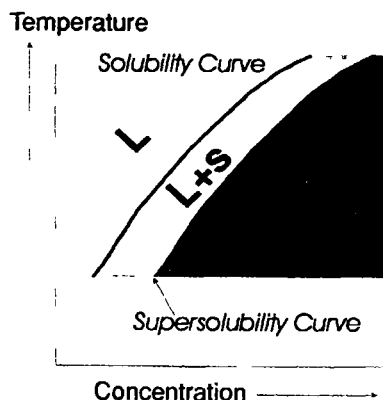


Figure 7. Solubility plot also showing the supersolubility curve.

creases rapidly over a narrow range of concentrations, the concentration as a function of the temperature can be indicated where the precipitation abruptly becomes measurable. The plot of the above concentrations is known as the supersolubility curve, which is also represented in the figure. It is important to note that at concentrations between the solubility and supersolubility curves precipitation within the bulk of the solution does not proceed, although large crystallites of the precursor are stable in the solution.

When the nuclei of the precursor to be precipitated interact significantly with the surface of the support, the rate of precipitation is measurable at much lower concentrations. Accordingly it is possible to perform precipitation exclusively on the surface of the support by maintaining the concentration of the precursor between that of the solubility and supersolubility curve. Control of the concentration of catalytically active precursors within the above range is the basis of the deposition-precipitation procedure. With sparingly soluble solids, the concentration difference between the solubility and supersolubility curves is small. The concentration therefore has to be controlled fairly accurately.

Figure 8 shows the case when the active precursor reacts with the surface of the support to yield a compound of a lower solubility. Now both the solubility and the supersolubility curve have been shifted to lower concentrations. We will see that reaction to form a compound with the support often takes place.

With the usual addition of a precipitant to a solution, as schematically represented in Fig. 9, the local concentration rises temporarily above that of the supersolubility curve, which causes rapid nucleation of the precipitate. When after homogenizing the liquid, the final concentration is lower than that of the supersolubility curve, nucleation has already proceeded and the crystallites precipitated are stable. Consequently, the concentration has to be maintained continuously

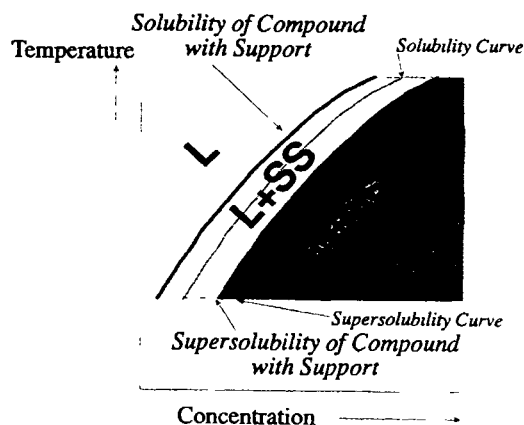


Figure 8. Reaction of precipitating active precursor with support to form a less soluble compound.

below that of the supersolubility curve. With deposition-precipitation this is achieved by performing precipitation from a homogeneous solution [15-17]. A homogeneous solution is most easily obtained by separating the mixing and the generation of the precipitant. This is usually brought about by mixing at a sufficiently low temperature that the reaction generating the precipitant does not proceed markedly, and subsequently raising the temperature to a level where the generation of the precipitant is rapid.

#### D Deposition-Precipitation onto Suspended Finely Divided Supports

As discussed above, sufficiently large interaction between the nuclei of an insoluble active precursor and the surface of a suspended support can bring about precipitation of the precursor exclusively at the surface of the support. Procedures have been developed to achieve deposition-precipitation by changing the pH level, or the valence state of the active precursor, or the concentration of a complexing agent. The complexing agent keeps the active precursor in solution under conditions where the (hydrated) metal ion alone precipitates. To ensure a sufficiently smooth transport of the precipitating species into the pore system of the support, a finely divided support is generally used. When the support after being loaded and separated from the liquid is dried, shaping is usually very easy. The hydroxy groups present in the loaded carrier substantially facilitate the shaping of the support by establishing hydrogen-bridge bonds.

##### a Change of pH Level

Precipitation by raising the pH level can be used with the preparation of many catalysts. Especially with tin, nickel and cobalt the procedure is fairly straightforward. The support to be loaded is suspended in a solution of the metal nitrate and a compound is added

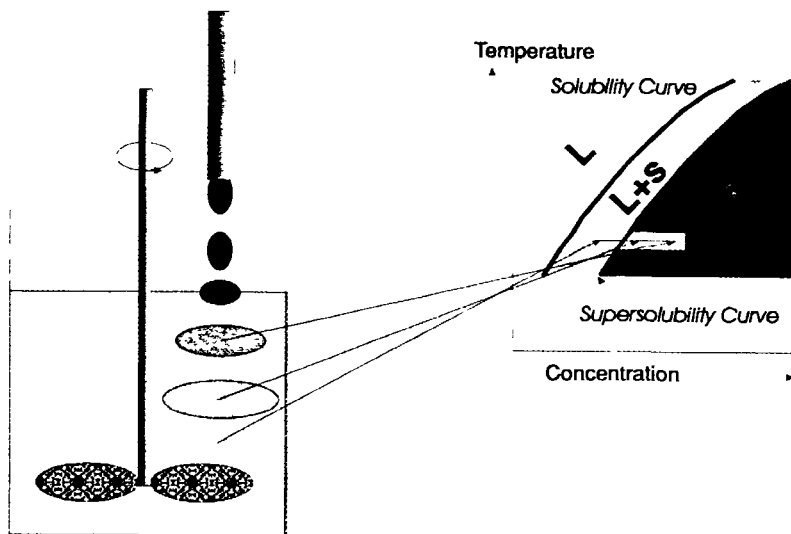
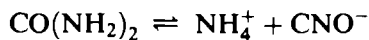


Figure 9. Usual addition of precipitant to suspension of support in solution of active precursor, rapid nucleation outside porous support.

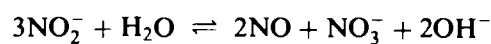
that is able to consume hydrogen ions. Urea can be utilized to increase the pH of the suspension. Usually the amount of urea is chosen to be 1.5–2.5 times the amount theoretically needed. Urea reacts according to



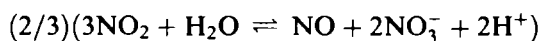
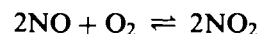
This reaction in which the urea first reacts to produce cyanate and subsequently to ammonium, carbon dioxide, and hydroxy groups, exhibits only a measurable rate at temperatures above about 330 K. It is the first of the above reactions that calls for a temperature of at least 330 K, because ammonium cyanate reacts rapidly at room temperature. Mixing can therefore be carried out at room temperature, while the generation of hydroxy groups proceeds at higher temperatures. When it is desired to perform the precipitation at lower temperatures, ammonium cyanate or a cyanate of an alkali metal can be used. Now, however, mixing has to be done with a suspension kept at about 273 K, to prevent rapid reaction during mixing. An enzyme, urease, has been tried to hydrolyze the urea at low temperatures. However, this enzyme did not work in the presence of usual dissolved catalytically active precursors.

When high loadings of the support have to be applied, the formation of ammonium ions leads to difficulties, because at the higher pH levels required to deposit nickel hydroxide or cobalt hydroxide onto its own lattice, the concentration of ammonium ( $\text{NH}_3$ ) is fairly high. As a result nickel(II) and cobalt(II) redissolve as ammonium complexes. The ammonia can be volatilized by keeping the suspension for a prolonged time at a temperature near 373 K, but then redissolution of nickel or cobalt is difficult to prevent. At high loadings, therefore, it is advantageous to use sodium nitrite,

which does not lead to formation of ammonium. Sodium nitrite reacts according to



Oxygen (air) has to be excluded, because oxidation of the NO released leads to the generation of hydrogen ions according to



Consequently the pH changes much less when the nitrogen oxide released can be oxidized by oxygen.

A problem with the use of urea or cyanate can be the production of waste water containing chemically bonded nitrogen, which is difficult to deal with. With the hydrolysis of urea the reaction can be significantly accelerated by performing the reaction at slightly elevated pressures and at temperatures above 373 K. Since the suspension of the support can be thoroughly mixed at a temperature where the reaction does not proceed, very concentrated solutions can be utilized with urea.

Also the NO released with the disproportionation of nitrite calls for special measures to avoid emission. The environmental problems and the lack of accurate control of the course of the pH level with time has led to the development of an additional deposition–precipitation method, namely the injection procedure. It has been observed that injection of an alkaline solution through a tube ending below the surface of the suspension of the support, avoids locally high concentrations. The reason is that high shear stresses can be established around the end of the injection tube, which is not possible at the surface of the suspension. The

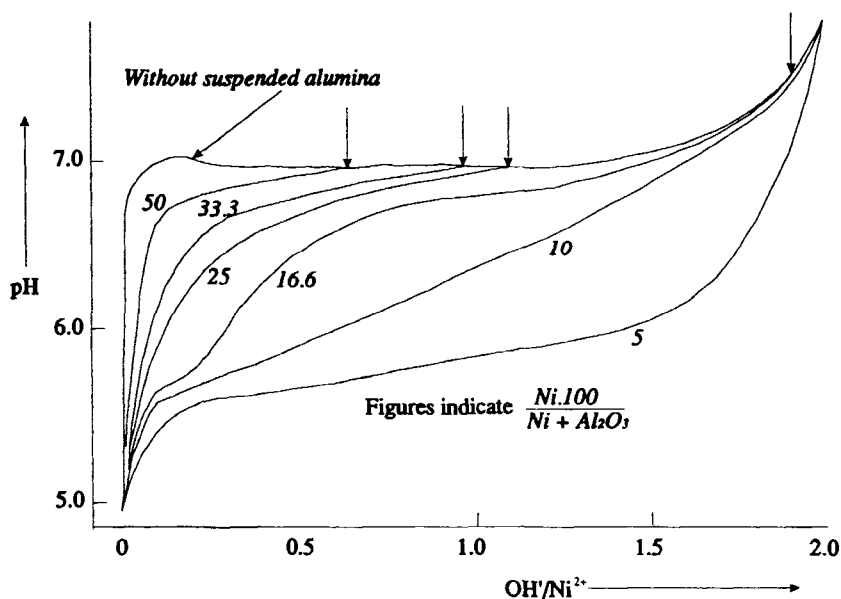


**Figure 10.** Precipitation of nickel(II) from a homogeneous solution by injection of sodium hydroxide at 293 K. A measurement without suspended alumina and measurement with suspended alumina are represented. The final nickel loading is indicated in the figure [18].

injection must be performed slowly and continuously to maintain the solution homogeneous. At a high rate of injection, elements of the solution being injected are brought rapidly in the bulk of the suspension, where the shear stresses are low. Although the injection procedure can be controlled more accurately than the methods using hydroxy ions generating reactants, the procedure calls for much more attention.

Scaling up of the deposition-precipitation procedure does not present any difficulty with urea or sodium nitrite. The preparation of tin oxide on silica catalysts has been scaled up from 1 l to a vessel of 2 m<sup>3</sup> without any difference in the final catalyst. The injection procedure has been scaled up by recirculating the suspension of the support from a large vessel through a small vessel in which the alkaline solution was injected into the vigorously agitated suspension. Provided the flow of the fluid being injected was kept slow and continuous, excellent results have thus been obtained.

Interaction with the support is a prerequisite to achieve the desired dense and uniform coverage of the surface of the support with the precursor of the active component. Precipitation from a homogeneous solution without interaction with the support leads usually to relatively large precipitated crystallites. The interaction with the support can be easily assessed by measuring the pH as a function of time or of the amount of alkali injected both with and without a suspended support. If there is a significant interaction with the support, the level of the pH remains with a suspended support considerably below that of the pH measured without a suspended support. Without a support, the concentration of the supersolubility curve is often apparent from the pH curve passing through a maximum.

When the concentration of the supersolubility curve has been attained, nucleation proceeds rapidly and the subsequent growth of the nuclei proceeds faster than the generation or addition of hydroxy ions.

Figure 10 shows the course of the pH during injection of alkali into a nickel nitrate solution kept at 293 K [18]. It can be seen that without a suspended alumina support, the pH passes through the maximum mentioned above. When alumina has been suspended in the solution, the pH remains below the pH level measured with nickel nitrate alone. At a low loading of the support, as with the loading of 5% in Fig. 10, the pH remains considerably below the level exhibited with only nickel nitrate. The low pH level indicates reaction of the surface of the suspended alumina support with nickel(II) ions to a hydrotalcite structure. At higher loadings of the alumina support the nickel ions can no longer be completely accommodated in the surface hydrotalcite and nickel hydroxide grows, which is evident from the pH curve merging the curve measured with nickel nitrate alone. In Fig. 10 a vertical arrow indicates the point where the curve measured with suspended alumina reaches the curve measured with nickel nitrate only. Using temperature-programmed reduction De Bokx et al. [18] demonstrated that the fraction of hydroxy ions consumed at pH levels lower than that observed with nickel nitrate alone measures the fraction of nickel hydrotalcite formed.

Figure 11 shows the course of the pH during the precipitation of zinc(II) with and without suspended alumina [19]. The pH is recorded during addition of alkali to the same volume of water, of a suspension of alumina in water, and of a solution of nickel nitrate. In the figure the curve obtained by addition of the hy-

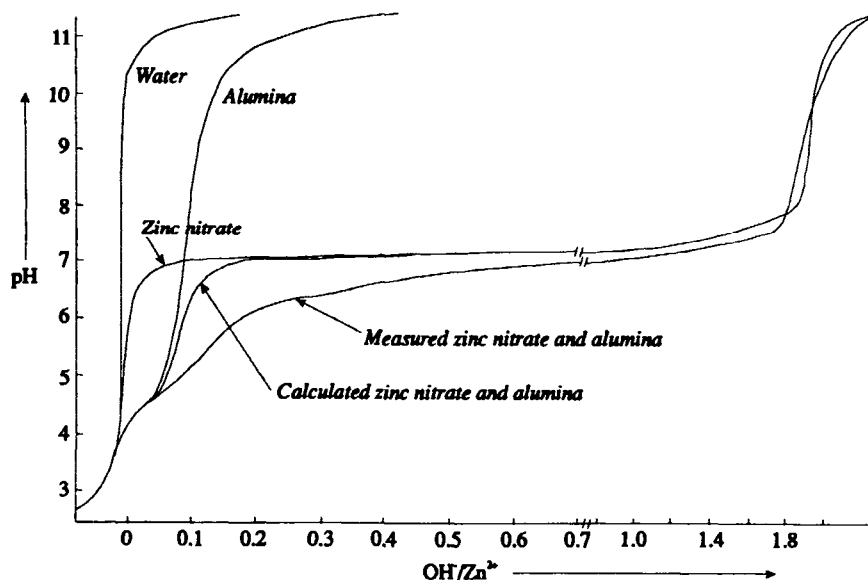


Figure 11. Precipitation of zinc(II) from a homogeneous solution by injection of sodium hydroxide at 293 K [19].

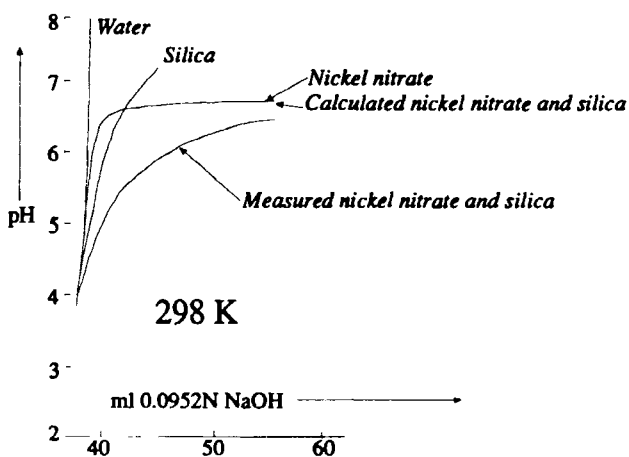


Figure 12. Precipitation of nickel(II) from a homogeneous solution by injection of sodium hydroxide at 298 K [20, 21].

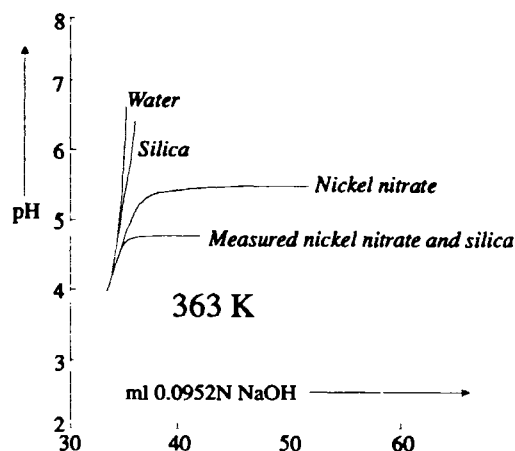


Figure 13. Precipitation of nickel(II) from a homogeneous solution by injection of sodium hydroxide at 363 K [20, 21].

droxy ions consumed in the above three measurements is compared with the pH curve experimentally measured with suspended alumina. It is evident that the calculated pH curve runs appreciably above the curve recorded experimentally. The interaction of the precipitating zinc ions with the alumina is evident from the consumption of hydroxy ions at a relatively low pH level.

Analogous experiments with silica as the support indicate the appreciable interaction of precipitating nickel(II) ions with silica [20, 21]. In the experiments represented in Fig. 12 the solutions or the suspension was kept at 298 K. The curve measured with suspended silica runs again considerably below the curve calculated from the curves recorded with water, suspended silica, and nickel nitrate alone. The interaction with the silica support causes a higher consumption of hydroxy ions at a low pH level. Burch and Flambard [22] per-

formed the same experiments with both silica and titania supports. They observed exactly the same behavior, namely a considerably lower pH level when the precipitation of nickel(II) was carried out in the presence of a silica or titania support.

Figure 13 represents measurements at 363 K with silica as a support. The curve measured with suspended silica in a nickel(II) solution at 363 K remains appreciably below the curve measured with nickel nitrate alone and does not approach the curve measured without suspended silica. The course of the pH with suspended silica indicates formation of a bulk compound with the support, as schematically indicated in Fig. 8. Formation of nickel antigorite (a 1 : 1 clay mineral) or nickel hectorite (a 1 : 2 clay mineral) is evident from X-

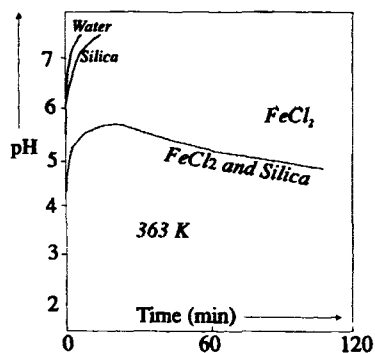


Figure 14. Precipitation of iron(II) from a homogeneous solution by injection of sodium hydroxide at 363 K [24].

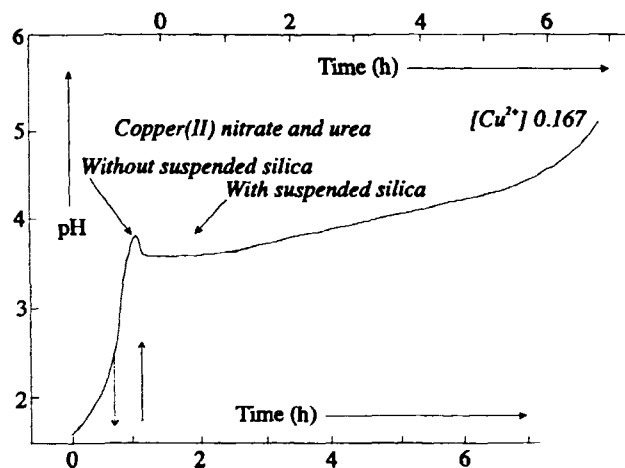


Figure 15. Precipitation of copper(II) from a homogeneous solution of copper nitrate by hydrolysis of urea both with and without suspended silica [25].

ray diffraction, electron microscopy, temperature-programmed reduction, and the considerable increase in BET surface area of the silica support after reaction with the nickel ions. Richardson et al. [23] have reported precisely the same results with the precipitation of nickel(II) ions from a homogeneous solution in the presence of a suspended silica (Cabosil) support.

Figure 14 indicates that iron(II) reacts analogously with silica upon precipitation from a homogeneous solution kept at 363 K [24]. Reaction to a new solid phase is also apparent from the maximum exhibited by the pH curve measured with suspended silica. Also with precipitating nickel and suspended silica a maximum in the pH level is often observed when the pH is homogeneously raised at 353 K or at a higher temperature (as shown in Fig. 18).

Figure 15 shows the course of the pH when the pH of a copper(II) nitrate solution is raised by the hydrolysis of urea [20, 25]. Curves with and without suspended silica are represented. Both curves show a distinct maximum and are almost identical. Consequently

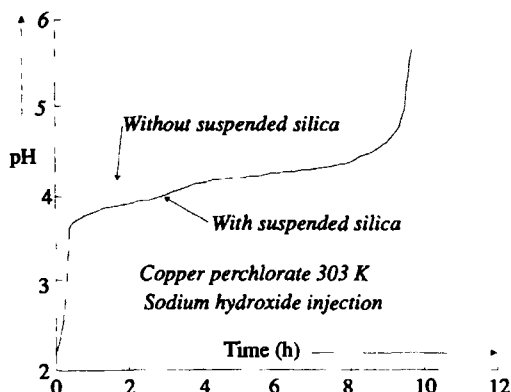


Figure 16. Precipitation of copper(II) from a homogeneous solution of copper perchlorate by injection of sodium hydroxide at 303 K [25].

copper(II) ions precipitating at a pH level below about 4 in the presence of nitrate ions exhibit no interaction with a suspended silica support. During the precipitation of copper(II) from a homogeneous solution of copper nitrate, the copper(II) precipitates as large thin platelets of basic copper nitrate,  $\text{Cu}_2(\text{OH})_3\text{NO}_3$ . Nucleation of the basic copper(II) nitrate and the subsequent rapid growth and consequent rapid consumption of hydroxy ions lead to the pronounced maximum exhibited in the curves of Fig. 15. In the presence of sulfate and chloride ions the corresponding basic salts are precipitating as relatively large crystallites upon precipitation from a homogeneous solution.

With perchlorate ions, which interact less strongly with precipitating copper(II) ions, nucleation of precipitated copper species proceeds at a significantly higher pH level, as can be concluded from Fig. 16. When more alkali has been added, reaction of the basic salt initially precipitated to (brown or black) copper oxide, which is more stable, takes place. Consequently, a drop in pH level is exhibited due to the exchange of perchlorate ions for hydroxy ions. With suspended silica the pH curve runs initially below the level measured without suspended silica. The stabilization of the copper species precipitated by interaction with the support is evident from the fact that now no copper oxide results when more alkali has been added. The loaded support displays still a blue color when the precipitation has finished which is maintained after drying at 383 K.

Figure 17 shows the precipitation of copper(II) at 363 K in the presence of suspended silica when more hydroxy ions are admitted and consequently higher pH levels are obtained [26]. It has been observed that the basic copper nitrate initially precipitated becomes unstable and reacts with the support at higher pH levels. The silica support reacts to a considerable extent with the copper(II) ions to a hydrosilicate, which has a

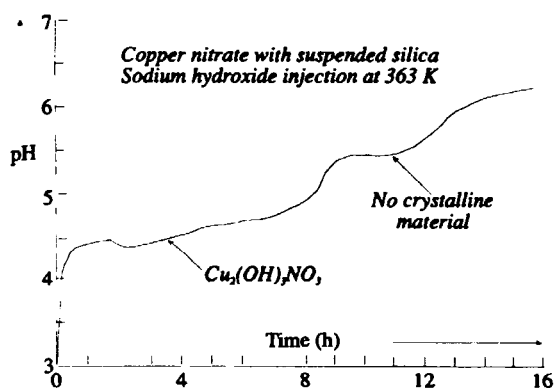


Figure 17. Deposition-precipitation of copper(II) onto suspended silica by injection of sodium hydroxide [26].

structure analogous to that of the mineral chrysocolla. Nickel hydrosilicate grows without nucleation on silica having reacted with copper(II) ions as is shown in Fig. 18 [27]. When nickel(II) ions are precipitating from homogeneous solution by hydrolysis of urea at 363 K in the presence of suspended silica, the pH passes through a maximum as can be seen in Fig. 18. Since the pH level remains much lower than with the precipitation of nickel(II) without suspended silica, nucleation of a nickel hydrosilicate (a clay mineral) is indicated. In the presence of suspended silica that has reacted with copper, the pH remains substantially lower than with pure silica as exhibited in Fig. 18. Accordingly, growth of a mixed hydrosilicate proceeds smoothly with copper(II) hydrosilicate.

It is important to consider the interaction with the support more closely. Often an electrostatic model has been used to account for the interaction of precipitating species with the support. It has been established that species having an electrostatic charge of the same sign as the support do not deposit onto the support. The isoelectric point of silica is, for instance, about 2, which implies that at lower pH levels the silica is positively charged due to the uptake of hydrogen ions, whereas at higher pH levels ionization of surface hydroxy groups leads to a negative charge:



If an electrostatic interaction alone would determine the interaction of precipitating species with the surface of a suspended support, the interaction with precipitating hydrated iron(III) oxide would be small, whereas the interaction with precipitating copper(II) hydroxide would be considerable. Indeed it was observed that hydrated iron(III) oxide, which reacts to form clusters of very small moieties at pH levels of 2, does not interact significantly with suspended silica. However, the precipitation of copper(II), which also proceeds at a pH level of about 3 with most anions, is not markedly affected by the presence of suspended

silica. As shown by the experimental results presented above, copper(II) precipitates with many anions as a basic salt of the anion being present during the precipitation without a significant interaction with the suspended silica support. Actually small silica particles are being supported by large crystallites of the basic copper salts after performing a deposition-precipitation. The above results with copper(II) were measured by Van der Meijden, who extensively studied the precipitation of copper(II) with and without suspended silica [20, 25]. His data show that a pH level above about 4 is required for interaction of precipitating copper(II) with suspended silica. Precipitation from copper(II) perchlorate solutions, which do not readily react to basic copper(II) perchlorate, and which proceeds at higher pH levels, leads to a significant interaction with the silica support.

We therefore feel that besides an electrostatic interaction a chemical interaction between the precipitating species and the support is also required. With colloidal silica solutions a reaction proceeds between the hydroxy groups present on different silica particles. Condensation of water leads to formation of oxygen bridges between the silica particles, which causes gelation of the silica sol. An analogous reaction will proceed between hydroxy groups present on the surface of silica particles and hydroxy groups of partially hydroxylated metal ions. The gelation of silica calls for a pH level of at least about 4, which agrees very well with the pH level at which hydroxylated metal ions are exhibiting interaction with silica. The reaction of the hydroxy groups is schematically indicated in Fig. 19.

Iron consequently has to be applied onto silica from iron(II) solutions, since iron(II) precipitates at a much higher pH level than iron(III) [28]. With iron(II) a high interaction with silica supports is observed. With iron(III) a reverse precipitation has to be carried out. An acid iron(III) solution is injected into a suspension of silica, kept at a pH level of about 6 by simultaneous hydrolysis of urea or simultaneous injection of an alkaline solution.

The behavior of copper(II) is interesting. At higher pH levels the initially precipitated basic salt becomes unstable and copper(II) is precipitating onto the suspended silica support. At higher temperatures without suspended silica, black copper(II) oxide results, whereas at lower temperatures without suspended silica blue copper hydroxide is formed. With urea, intermediate formation of malachite, basic copper(II) carbonate, is observed in the absence of suspended silica.

A number of catalytically important metals cannot be applied smoothly on silica, namely metals present in the most stable state as highly charged metal ions forming anions with oxygen. The most important in-

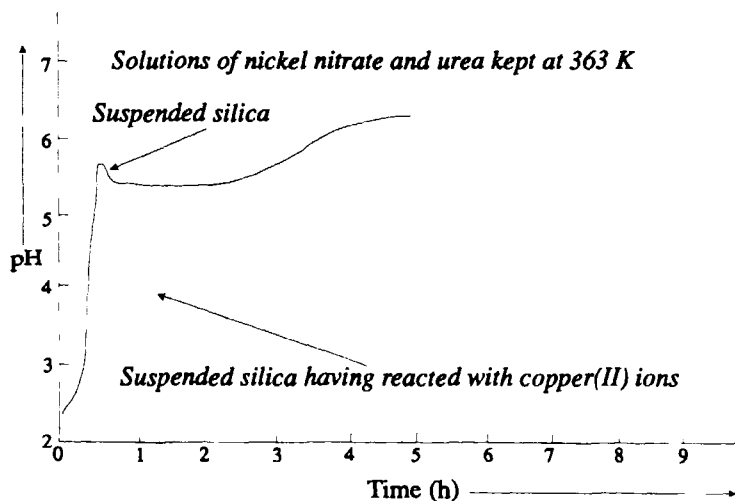


**Figure 18.** Comparison of deposition-precipitation of nickel(II) ions on silica and on silica having previously reacted with copper(II) ions [27].

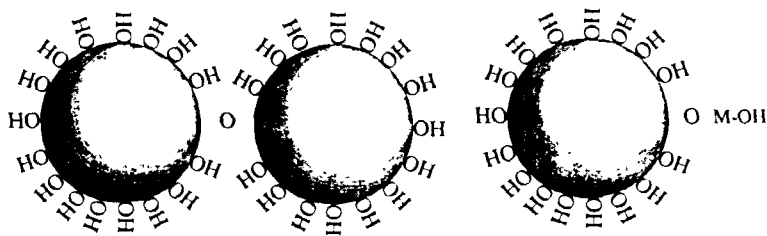


**Figure 19.** Schematic representation of the reaction between hydroxy groups on different silica particles leading to gelation of silica sols (left-hand side) and of the hydroxy group(s) on partially hydroxylated metal ions with surface hydroxy groups of silica.

stances of this group of metals are molybdenum, tungsten, and vanadium. The negatively charged  $\text{MoO}_4^{2-}$ ,  $\text{WO}_4^{2-}$ , and  $\text{VO}_3^-$  ions cannot be deposited on silica, which is also negatively charged. The electrostatic charges of the support and of the species to be deposited being opposite is a necessary, but not a sufficient condition to have a sufficient interaction with the support to enable one to perform deposition-precipitation. Vogt et al. [29, 30] have established that decreasing the valence of the metal ions caused the metal ions to be present as hydrated cations in an aqueous solution. Electrochemical reduction of vanadium(V) and molybdenum(VI) to trivalent metal ions can be performed smoothly. Overbeek [31] has carried out the scaling up of the electrochemical reduction and has achieved a very high current efficiency. With the lower valent metal ions the usual deposition-precipitation can be performed by raising the pH of a suspension of silica in a solution of the lower valent metal ion [30, 32, 33].

The behavior of vanadia and molybdena deposited very finely divided on silica is interesting. Vogt showed that vanadia applied as  $\text{V}^{\text{III}}$  and subsequently oxidized to  $\text{V}^{\text{V}}$  by calcination at 623 K for 72 h was deposited on silica as a monolayer; the infrared absorption due to vibrations of hydroxy groups of the silica surface

disappeared at a monolayer coverage of vanadia. Apparently the interaction of the precipitating vanadium(III) with the silica surface is strong. De Boer [33] accurately investigated the interaction of molybdena with silica. With molybdena deposited as  $\text{Mo}^{\text{III}}$  and oxidized to  $\text{Mo}^{\text{VI}}$  the vibrations of hydroxy groups of the silica surface did not disappear completely, which indicates that the molybdenum oxide species is not covering the silica surface completely. Low-energy ion scattering, Laser-Raman spectroscopy, and EXAFS have revealed that the molybdena species are present as small hydrated clusters on the silica surface. Upon dehydration, the molybdenum(VI) oxide moieties are spreading over the silica surface and covering the silica surface completely; rehydration leads again to clusters and to some bare silica. When the molybdenum(VI) oxide is finely divided, nucleation of  $\text{MoO}_3$  cannot proceed and the molybdenum oxide is strongly interacting with the silica. The uniform thin layer of molybdenum oxide can only be established by deposition from molybdenum(III) solutions.

The chemical interaction of metal ions precipitating from a homogeneous solution with silica at higher temperatures has been confirmed extensively. With finely divided silica, reaction with synthetic clay minerals



has been established. Consequently the reaction is not confined to the surface of silica, but involves also the bulk of small silica particles. Reaction with another solid phase was already concluded from the maximum through which the pH curve often passes during the deposition-precipitation of nickel at a temperature of about 350 K or higher. The complete reaction of the silica particles is also evident from electron micrographs [2], which show a complete disappearance of the silica particles initially present. When the amount of bivalent metal ions is not sufficient to convert the silica completely, growth of platelets of clay minerals out of the silica particles can be easily seen.

By precipitation from homogeneous solution in the presence of suspended silica a procedure for the production of synthetic clay minerals has thus been achieved that is much more favorable than the procedures used in the state of the art, which involves hydrothermal treatment at high temperatures and pressures for prolonged periods of time [34]. The clay minerals from bivalent metal ions are of the hectorite type; the bivalent metal ions are present within the octahedral holes of a central layer, which is covered at both sides by a layer containing  $\text{Si}_2\text{O}_5(\text{OH})$  groups. With magnesium very small platelets exhibiting a surface area of about  $700\text{ m}^2\text{ g}^{-1}$  are obtained, and with zinc much larger platelets having a surface area of about  $200\text{ m}^2\text{ g}^{-1}$ . The surface areas with nickel and cobalt are intermediate. The surface areas are considerably higher than the surface area of the original silica support. The reaction to clay minerals is also evident from the acid groups present within thus loaded silica supports after partial reduction of reducible metal ions, such as, nickel or copper. Addition of tetrahedrally coordinated aluminum during the deposition precipitation leads to reaction to saponite clay minerals, in which a fraction of the silicon ions present in the tetrahedral holes is substituted by aluminum ions. After exchange of the interlayer cations, usually ammonium after the preparation, acid protons are present in the saponite clay minerals. The above preparation procedure yields reproducible clay minerals, the properties of which can be accurately controlled within a wide range, offers interesting possibilities for the technical application of clay minerals in catalytic reactions.

Also, with alumina, reaction of the support to compounds with active precursors can proceed, although the reaction remains generally limited to the surface layer of the alumina. With bivalent metal ions reaction to compounds of a hydrotalcite structure occurs [18]. Hydrotalcite is a mixed magnesium-aluminum hydroxide ( $\text{Mg}_6\text{Al}_2(\text{OH})_{16}\text{CO}_3 \cdot 4\text{H}_2\text{O}$ ) and takovite ( $\text{Ni}_6\text{Al}_2(\text{OH})_{16}\text{CO}_3 \cdot 4\text{H}_2\text{O}$ ) is the analogous nickel compound. The metal ions are present in the octahedral sites of the brucite structure. Due to the presence of trivalent aluminum ions, the electrostatic charge

cannot be compensated by the hydroxy ions only and anions, such as carbonate ions, are accommodated in the interlayer between the hydroxy groups. Reaction to the analogous nickel-aluminum and cobalt-aluminum compounds has been observed with deposition-precipitation of nickel or cobalt on suspended alumina. Actually the reaction to the surface hydrotalcites (or Feitknecht compounds) is unfavorable, since nucleation of spinels of the bivalent metal ions, e.g.  $\text{NiAl}_2\text{O}_4$ , proceeds upon thermal treatment of the surface hydrotalcites.

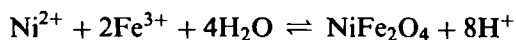
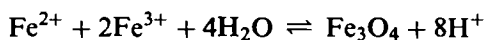
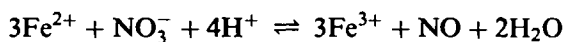
It is notable that when performing reactions within a homogeneous solution, interfacial inorganic reactions often take place that are completely analogous to geochemical reactions. Both the reactions with clay minerals and with hydrotalcites are also well known in geochemistry.

Effecting deposition-precipitation by decreasing the pH level is interesting with metal ions present in the stable state in aqueous solution as anions [35]. With silica no interaction is observed, which has led to the development of the electrochemical reduction procedure. To apply metal ions, such as, molybdenum or vanadium, on alumina, a homogeneous decrease in pH level is interesting. The pH level has been decreased by injection of nitric acid or perchloric acid and electrochemically. However, the rate of crystallization of the hydrated oxides of vanadium(V) and molybdenum(VI) was observed to be fairly low. To prevent dissolution of the alumina supports the pH cannot be decreased to levels below about 3, at which the crystallization of the hydrated metal oxides does not proceed rapidly.

Decreasing the pH levels of suspensions of a suitable support in a solution of an active precursor has therefore been studied much less than raising the pH level.

#### *b Changing the Valency of Precursor Ions*

Precipitation from a homogeneous solution by changing the valence of the metal ions to be precipitated can be performed very smoothly in some cases. An increase in valency has been used with iron and manganese. Iron(II) and manganese(II) are much more soluble than iron(III) and manganese(III) and -(IV). Oxidation with a dissolved oxidizing agent therefore leads to precipitation from a homogeneous solution. With iron(II) the oxidation can be carried out with nitrate ions [28]. Since hydrolysis of the resulting iron(III) ions releases hydrogen ions, the pH must be kept constant by simultaneous injection of an alkaline solution or by hydrolysis of urea. Usually, oxidation of iron(II) from a homogeneous solution leads to precipitation of magnetite,  $\text{Fe}_3\text{O}_4$ . When other suitable bivalent metal ions are present in the solution, other ferrites, such as, nickel or cobalt ferrite, result:



Finely divided magnetite deposited on a support is liable to oxidation and hydrolysis, which leads to hydrated supported iron(III) oxide. To prevent oxidation and hydration, the loaded support has to be dried in an inert gas. After being dried the supported magnetite is fairly stable on exposure to atmospheric air, although reaction to  $\gamma\text{-Fe}_2\text{O}_3$  may proceed.

Precipitation by reduction of metal ions has many applications [36]. Precipitation from a homogeneous solution of chromium by reduction of chromium(VI), which is soluble at pH levels around 7, to chromium(III), which is insoluble at this pH range, has been done. Also, reduction of metal ions, such as, silver, palladium or platinum, to the metallic state can lead to very finely divided metal particles. De Jong and Geus have studied precipitation by reduction of silver ions in the presence of a suspended silica support [37, 38]. A bimodal particle size distribution usually results. The silver complexes adsorbed on the support react with the reducing agent to very small silver particles (about 1 nm), whereas in the bulk of the solution the more difficult nucleation of metallic silver leads to relatively large particles (at least 10 nm). With other precious metals an analogous behavior has been observed. With suspended silica supports that were loaded at pH levels around 7, it was demonstrated that the electrostatic charge of the precursor complexes is determining whether precipitation by reduction to the metal on the support can proceed. Only positively charged complexes, such as the silver ammine complex, resulted in small silver particles deposited evenly over the silica support. The amount of silver complex that can be adsorbed on the silica support, however, was also found to be limited. A higher concentration of silver simply resulted in large silver particles formed in the bulk of the solution.

Controlled growth of previously deposited very small silver particles can also be performed. The procedure involves to establish first the minimum temperature at which reduction of the metal proceeds in the bulk of the solution. With the reduction of silver ammine complexes by formaldehyde, the temperature to effect reduction in the bulk of the liquid is about 310 K. It has been found that metallic silver particles catalyze the reduction of the silver ammine complexes. By suspension of a silica support covered with small silver particles in a solution of  $\text{Ag}(\text{NH}_3)_2^+$  cooling the suspension to 273 K and subsequently injection of formaldehyde, controlled growth of the silver particles can be achieved. It is interesting that the silver particles

grow to an elongated shape; apparently the electrostatic repulsion between the positively charged silver complexes brings about an approach from opposite sides. Thermal treatment at a moderate temperature in a reducing gas flow suffices to produce symmetrical metal particles. An analogous procedure can also be carried out with small particles of precious metals, such as platinum or palladium. It is also possible to grow different metals on small metallic nuclei, such as silver, onto platinum particles.

### c Removal of Complexing Agent

The best known procedure in which a complexing agent is removed involves the volatilization of ammonia from ammine complexes. It is important to start from an insoluble compound and to dissolve the metal ions of the solid compound by complexing with ammonia. An instance is nickel hydroxide, which is dissolved in a mixture of ammonium carbonate and ammonia; removal of the ammonia leads to precipitation of nickel carbonate. It is therefore difficult to achieve a sufficiently high concentration of dissolved nickel. Another problem is the relatively high pH level required to bring the ammonium concentration at the required level to dissolve the nickel completely. At the high pH levels due to the required ammonia concentration, supports such as alumina and silica dissolve.

Procedures have also been developed to oxidize complexing agents, such as EDTA or ethylenediamine. The oxidation was performed with hydrogen peroxide (perhydrol) at a pH level where the uncomplexed metal ions are insoluble [39]. With a number of metal ions, the procedure was successful. With copper, however, cautious operation was required. The oxidation of a copper EDTA complex exhibits an induction period of about 30 min. After this period of time very finely divided copper oxide is deposited onto the support, thus providing a very efficient catalyst for the decomposition of hydrogen peroxide. The hydrogen peroxide rapidly decomposes, releasing a large volume of oxygen, which results in a blowout of the contents of the reactor. To carry out the preparation procedure involving the oxidation of EDTA complexes by hydrogen peroxide on a large scale, a film reactor was utilized to enable the rapid evolution of gas.

### d Electrochemical Deposition-Precipitation

Base metals are generally cheaper than the corresponding metal salts. One reason is that production and transport of the salt, which is heavier per unit weight of metal than the pure metal, can be avoided. With the production of supported catalysts it is therefore often advantageous to start from the metal to be applied onto an appropriate support and not from a salt of the metal. According to the usual procedure the metal has to be dissolved in a suitable acid in the catalyst pro-

duction plant. To minimize environmental problems hydrochloric acid is often used, although nitric acid can be more easily removed from the catalyst by a thermal treatment. Precipitation of the metal as a hydroxide, hydrated oxide, or basic salt, calls for soda or other alkaline compounds and leads to the production of salts of the alkali metals used, which has to be disposed.

An attractive procedure is possible when a metal is applied without being completely dissolved. Van Stiphout and co-workers have developed a precipitation method in which a metal, such as copper, nickel, or cobalt, can be deposited onto a suspended support by anodic dissolution of the metal [19, 40, 41]. Metal rods or scrap are put into a polymeric basket and connected to an electrode. When the metal is the anode and the voltage for dissolution is lower than the voltage to produce oxygen from water, dissolution of the metal proceeds readily. However, deposition of the metal onto the cathode has to be prevented. At the cathode hydrogen and hydroxy ions should be produced. Van Stiphout and co-workers investigated two methods to prevent deposition of the catalytically active metal onto a platinum cathode. With a polymer membrane capable of a rapid transport of hydrogen ions and water, slow transport of hydroxy ions and copper, zinc, and cadmium ions, migration of anodically dissolved metal atoms to the cathode can be prevented or impeded. As an alternative, a thin chromia layer can be deposited onto the platinum. Apparently, nucleation of a metal on the chromia proceeds much more slowly than on platinum metal.

The above authors have established that the procedure with the polymeric membrane is not satisfactory. At high current densities, metallic nickel nucleates on the polymeric membrane. Although a reasonable loading of a suspended silica carrier could be achieved, a considerable fraction of the nickel was deposited on the polymeric membrane. The chromia layer method was observed to yield much better results.

Using the electrochemical precipitation procedure silica-supported catalysts having nickel, copper, and copper-nickel as the active components have been prepared. The thus prepared catalysts showed analogous characteristics as the catalysts prepared by deposition precipitation using urea. The copper-nickel catalysts are especially interesting. Measurement of the saturation magnetization and temperature-programmed reduction experiments indicated the formation of copper-nickel alloys after reduction of supports loaded simultaneously or sequentially with copper and nickel. Since the dissolution of nickel or copper is accompanied by the reaction of hydrogen ions to gaseous hydrogen, resulting in the formation of hydroxy ions, the pH level of the suspension does not vary provided that hydroxides or layered silicates containing  $\text{Si}_2\text{O}_5^{2-}$  species are

generated. When no suspended silica is present, anodically dissolved copper initially reacts to basic copper salts, which leads to a rapid rise in pH, since the loss of hydrogen ions is not compensated by an equivalent consumption of hydroxy ions. With suspended silica, however, the pH remains virtually constant, except when nitrate ions are present and reaction to nitrite or nitrogen oxide can proceed at the cathode. Both reactions consume hydrogen ions.

Electrochemical procedures can thus be used in the production of solid catalysts for the reduction of higher valent metal ions, usually present as oxyanions, to a lower valent state, where they are less acidic. Also, the above deposition-precipitation method can be extremely well controlled by electrochemical means.

### E Deposition-Precipitation within Preshaped Support Bodies

Application of one or more precursor(s) uniformly over the internal surface of preshaped support bodies is attractive for the development of industrial catalysts within a short period of time. Since impregnation and drying often leads to deposition more or less exclusively at the external edge of the support bodies, an improved procedure is highly desirable.

Knijff et al. have extensively studied deposition-precipitation within the pore-systems of preshaped support bodies [6, 42]. Impregnation was performed with a solution of the active precursor and urea or ammonium or sodium nitrite. Preferably, the support bodies were evacuated before the impregnating fluid was admitted. To prevent evaporation of the liquid while maintaining the impregnated support bodies at a temperature of about 350 K, their open container was placed in a vessel with an atmosphere of water saturated at 350 K. With the hydrolysis of urea and with the disproportionation of nitrite, gases are evolved. It is possible that gas bubbles generated within narrow pores push the liquid out of the pores, thus preventing deposition of the active precursor onto the pore walls. Some experiments showed that removal of the liquid out of (part of) the pore system by gas bubbles did not occur. Apparently, dissolution of the gases in the liquid present in the pore system effectively transports the evolved gases out of the pore system of the supports.

Extremely good distributions of the active precursor over the internal surface of the support bodies were obtained. The difficulty, however, is the loading that can be achieved. The limited pore volume of preshaped support bodies and the solubility of the precursor to be deposited and of the agent(s) for deposition-precipitation necessitate multiple impregnations in order to achieve loadings characteristic of base metal (compounds). With urea and simple nitrates, however, highly

concentrated solutions can be used, which allows the application of high loadings of the active component. The difficulty here is to fill the pore system completely with the highly viscous concentrated solution. Deposition-precipitation within the pores of preshaped support bodies is therefore attractive for supports with a very high pore volume and calls for additional research when high loadings are desired with supports of a low or intermediate pore volume

## F Concluding Remarks

The above procedures for catalyst preparation have generally provided excellent results. Especially important are surface-sensitive reactions. With supported catalysts in which the active components have a narrow particle-size distribution, the optimum particle size for a demanding reaction can be established. Major improvements of supported catalysts, e.g. with respect to carbon deposition and ammonia decomposition, can be achieved by preparing catalysts with a narrow particle-size distribution. Also, the preparation of catalysts in which the active components have a uniform chemical composition is highly important. One instance is the preparation of supported vanadium oxide phosphorus oxide (VPO) catalysts for the selective oxidation of *n*-butane to maleic anhydride, which has been carried out using vanadium(III) deposition onto silica [31]

Technically, the most desirable procedures are those that can use existing equipment for the commercial production of catalysts. Impregnation of preshaped support bodies, drying, and subsequent calcination and/or reduction are therefore attractive, since these techniques can usually be executed in existing equipment. It is interesting that the inorganic chemistry and the techniques to produce advanced catalysts can also be used for the production of magnetic materials, inorganic pigments, and finely divided metals.

Much of the material covered in this review has only been published in the patent literature. Reference is made to the relevant patent literature, since the patents contain accurately described experiments, that nicely exemplify the results dealt with in this review.

## References

- 1 J W Geus in *Sintering and Catalysis* (Ed G C Kuczynski), Plenum, New York, 1975, pp 29-61
- 2 J W Geus in *Preparation of Catalysts III* (Eds G Poncelet, P Grange, P A Jacobs) Elsevier, Amsterdam, 1983, pp 1-33
- 3 C N Satterfield, *Heterogeneous Catalysis in Practice*, McGraw Hill, New York, 1980, p 131
- 4 R Schlögl in *Catalytic Ammonia Synthesis Fundamentals and Practice* (Ed J R Jennings), Plenum Press, New York, 1991, p 19
- 5 W Langenbeck, H Dreyer, D Nehring, *Naturwissenschaften* 1954, 41, 332, W Langenbeck, H Dreyer, D Nehring, *Z Anorg Allgem Chem* 1955, 281, 90
- 6 L M Knijff, Ph D Thesis, Utrecht University, 1992
- 7 A Q M Boon Ph D Thesis, Utrecht University, 1990
- 8 P J van den Brink Ph D Thesis, Utrecht University, 1992
- 9 US Patent 4 783 434 1988 (DOW Chemical Company)
- 10 G R Meima, B G Dekker, A J Van Dillen, J W Geus, J E Bongaarts, F R Van Buren, K Delcour, J M Wigman in *Preparation of Catalysts IV* (Eds B Delmon, P Grange, P A Jacobs, G Poncelet) Elsevier, Amsterdam, 1987, p 83
- 11 P J Van den Brink, A Scholten, A van Wageningen, M D A Lamers, A J van Dillen, J W Geus in *Preparation of Catalysts V* (Eds G Poncelet, P A Jacobs, P Grange, B Delmon) Elsevier, Amsterdam, 1991
- 12 G R Meima Ph D Thesis, Utrecht University, 1987
- 13 A R West, *Solid State Chemistry and its Applications*, Wiley, Chichester, 1984, p 436
- 14 D Mealor, A Townshend, *Talanta* 1966, 13, 1069
- 15 H H Willard, N G Tang, *J Am Chem Soc* 1937, 59, 1190
- 16 H H Willard, N G Tang, *Ind Eng Chem, Analytical Edition* 1937, 9, 357
- 17 P F S Cartwright, E J Newman, D W Wilson, *The Analyst* 1967, 97, 663
- 18 P K De Bokx, W B A Wasserberg, J W Geus, *J Catal* 1987, 104, 86
- 19 P van Stiphout Ph D Thesis, Utrecht University, 1987
- 20 A J van Dillen, J W Geus, L A M Hermans, J van der Meijden in *Proceedings of the Sixth International Congress on Catalysis*, London, 1976, (Eds G C Bond, P B Wells and F C Tompkins) Chemical Society, Letchworth, England 1977, Vol 2, p 667
- 21 L A M Hermans, J W Geus in *Preparation of Catalysts II* (Eds B Delmon, P Grange, P Jacobs, G Poncelet) Elsevier, Amsterdam, 1979, p 113
- 22 R Burch, A R Flambard in *Preparation of Catalysts III* (Eds G Poncelet, P Grange, P A Jacobs) Elsevier, Amsterdam, 1983, p 311
- 23 J T Richardson, R J Dubus, J G Crump, P Desai, U Osterwalder, T S Calc in *Preparation of Catalysts II* (Eds B Delmon, P Grange, P Jacobs, G Poncelet) Elsevier, Amsterdam, 1979, p 131
- 24 W J J van der Wal Ph D Thesis, Utrecht University 1987
- 25 J van der Meijden Ph D Thesis, Utrecht University 1981
- 26 J van Beijnum Ph D Thesis, Utrecht University, 1991
- 27 C N A M Mesters Ph D Thesis, Utrecht University, 1984
- 28 J W Geus, *Appl Catal* 1986, 25, 313
- 29 E T C Vogt, M De Boer, A J van Dillen, J W Geus, *Appl Catal* 1988, 40, 255
- 30 E T C Vogt Ph D Thesis, Utrecht University, 1988
- 31 R A Overbeck Ph D Thesis, Utrecht University, 1994
- 32 M de Boer, A J van Dillen, D C Koningsberger, J W Geus, M A Vuurman, I E Wachs, *Catal Lett* 1991 11 227
- 33 M de Boer Ph D Thesis, Utrecht University, 1992
- 34 R J M J Vogels, M J H V Kerkhoffs, J W Geus in *Preparation of Catalysts VI* (Eds G Poncelet, J Martens, P A Jacobs, P Grange) Elsevier, Amsterdam, 1995, p 1153
- 35 German Patent 1 964 620 1970 (Stamicarbon)
- 36 Netherlands Patent 16 777 1968 (Stamicarbon)
- 37 K P de Jong J W Geus, *Appl Catal* 1982, 4, 41
- 38 K P de Jong Ph D Thesis, Utrecht University, 1982
- 39 German Patent 1 963 827 1970 (Stamicarbon)
- 40 P C M van Stiphout, C R Bayense, J W Geus, *Appl Catal* 1988, 37, 189

41. P. C. M. van Stiphout, H. Donker, C. R. Bayense, J. W. Geus, F. Versluis in *Preparation of Catalysts IV* (Eds: B. Delmon, P. Grange, P. A. Jacobs, G. Poncelet) Elsevier, Amsterdam, 1987, p. 55.
42. L. M. Knijff, P. H. Bolt, R. van Yperen, A. J. van Dillen, J. W. Geus in *Preparation of Catalysts V* (Eds: G. Poncelet, P. A. Jacobs, P. Grange, B. Delmon) Elsevier, Amsterdam, 1991, p. 165.

### 2.2.1.6 Redox Methods for Preparation of Bimetallic Catalysts

J. BARBIER

#### A Introduction

The main problem when preparing bimetallic catalysts is to create close interaction between the two metals [1–5].

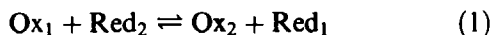
The classic co-impregnation or successive impregnation of two metallic salts often proves to be unsatisfactory and new techniques are being tried [6–10]. In all cases these techniques call for the preparation of a monometallic catalyst (i.e. parent catalyst) which is then modified by addition of the second metal. This modification occurs through a selective reaction which takes place solely on the monometallic particles of the parent catalyst.

Metal–metal interactions can result from surface redox reactions occurring in a liquid phase between a reducing agent present or adsorbed on the parent metal and the oxidized form of the second metal [2–10]. The nature of the reductant depends on the various method used:

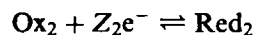
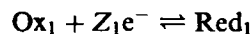
- (i) preparation of bimetallic catalysts by direct redox reaction – the reductant of the modifier is the parent metal;
- (ii) preparation of bimetallic catalysts by redox reaction of adsorbed reductant – the reductant is pre-adsorbed on the metallic surface of the parent catalyst (hydrogen is most commonly used);
- (iii) preparation of bimetallic catalysts by catalytic reduction – the catalytic properties of the parent metal are used to improve the rate of the reaction between a reductant and the modifier;
- (iv) preparation of bimetallic catalysts by under-potential deposition – in some cases deposition of adatoms or submonolayers of modifier can occur at a higher potential than the thermodynamic potential required for bulk deposition.

#### B Preparation of Bimetallic Catalysts by Direct Redox Reaction

A typical redox reaction can be expressed as



The evolution of the overall reaction is defined by comparing the equilibrium potentials of the two half reactions:



These potentials can be calculated from Nernst's law:

$$E_1 = E_1^0 + \frac{RT}{Z_1F} \ln \frac{a_{\text{Ox}_1}}{a_{\text{Red}_1}} \quad (2)$$

$$E_2 = E_2^0 + \frac{RT}{Z_2F} \ln \frac{a_{\text{Ox}_2}}{a_{\text{Red}_2}} \quad (2')$$

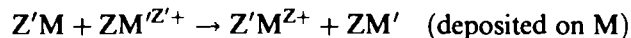
where  $a_{\text{Ox}}$  and  $a_{\text{Red}}$  are the activities of the oxidized and reduced species, respectively, and the other symbols have their usual meanings.

The difference in equilibrium potentials determines the value of the change in the free energy and, therefore, the direction of the overall reaction:

$$\Delta G = -Z_1Z_2F(E_1 - E_2) \quad (3)$$

shown here for eq 1 going from left to right. For  $E_1 > E_2$ ,  $\Delta G$  will be negative and the oxidized form  $\text{Ox}_1$  will be reduced by the reductant  $\text{Red}_2$ .

Direct redox reactions can be of great interest for the preparation of bimetallic catalysts, in cases where a parent monometallic catalyst is prepared and is modified by reaction with the oxidized form of a second metal. A typical reaction can be expressed as



where M is the parent metal and M' the modifier.

In practice the preparation of bimetallic catalysts using direct redox reactions can be extensively used for depositing a noble metal with a high standard electrochemical potential onto a non-noble metal with a lower standard electrochemical potential (eq 3).

From an experimental point of view a monometallic catalyst is reduced in a reactor, outgassed under a nitrogen flow and then immersed in an aqueous solution. The solution is continuously stirred by a counter-current of nitrogen. The modifier salt, which acts as precursor of the additive, is introduced as a solution. The concentration of the solution is adjusted to equal the number of modifier atoms required for the required composition of the bimetallic phase.

An example of the use of direct redox reactions in the preparation of bimetallic catalysts is the modification of copper catalysts by the addition of ruthenium, platinum, gold, or palladium [11–14]. Assuming the metallic state for copper atoms on the surface, the redox reaction with the noble metal salts is

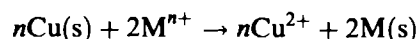


Table 1. Standard redox potentials.

Reaction	$E^0$ (V)
$\text{Cu}^{2+} + 2e^- \rightleftharpoons \text{Cu}$	0.34
$\text{PtCl}_6^{2-} + 4e^- \rightleftharpoons \text{Pt} + 6\text{Cl}^-$	0.74
$\text{AuCl}_4^- + 3e^- \rightleftharpoons \text{Au} + 4\text{Cl}^-$	1.00
$\text{Pd}^{2+} + 2e^- \rightleftharpoons \text{Pd}$	0.99
$\text{Ru}^{3+} + 3e^- \rightleftharpoons \text{Ru}$	0.38
$\text{ReO}_4^- + 8\text{H}^+ + 7e^- \rightleftharpoons \text{Re} + 4\text{H}_2\text{O}$	0.37
$\text{PdCl}_4^{2-} + 2e^- \rightleftharpoons \text{Pd} + 4\text{Cl}^-$	0.62

where (s) indicates surface location. Comparison of the standard electrochemical potentials (Table 1) shows that three redox reactions can occur.

Chemical analysis of solids and solutions indicate that in all cases metallic ruthenium, platinum, and gold are deposited on copper. Ruthenium, deposit is restricted to approximately 0.33 of the copper surface atoms, demonstrating that the redox reaction between Cu and  $\text{Ru}^{3+}$  can occur only on some special copper sites [11]. With platinum or gold, for the highest amount of modifier introduced ( $M^{n+}/\text{Cu}(s) > 100$ ), a deposit larger than a monolayer is obtained, indicating that all accessible copper atoms and subsurface copper atoms are involved in the redox reaction [13].

Particles of Raney copper, modified by redox deposition of ruthenium, platinum, or gold were characterized by energy dispersive spectroscopy. Ruthenium is deposited preferentially on the rims of the copper particles while low Miller-index planes are totally free of deposited ruthenium atoms. For platinum or gold the deposition can occur over the whole copper surface [11].

The extent of deposition of a metal M introduced as  $M^{n+}$  on a Cu catalyst (or on a metal of lower standard potential) depends on the redox reaction equilibrium constant:

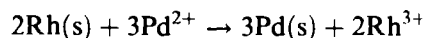
$$2nF \frac{(E_{\text{Cu}/\text{Cu}^{2+}}^0 - E_{\text{M}/\text{M}^{n+}}^0)}{RT} = \ln \frac{(a_{\text{M}^{n+}})^2 (a_{\text{Cu}})^n}{(a_{\text{M}})^2 (a_{\text{Cu}^{2+}})^n} \quad (4)$$

According to the standard electrochemical potentials (Table 1), with Cu/Cu<sup>2+</sup> and Ru/Ru<sup>3+</sup> couples, the amount of ruthenium deposited on metallic copper will be small, whereas the redox reaction carried out in presence of platinum or gold salts will occur to a large extent. On the other hand, for electrodes of first type (metal immersed in a solution of a salt of that metal), the standard electrochemical potentials as defined by thermodynamics are calculated with regard to a polycrystalline metallic phase of infinite size. However, in the case of small metallic particles, characterized by metallic atoms of different coordination numbers, the notion of a local potential can be introduced. That no-

tion is well known for corrosion reactions which occur preferentially on more oxidizable metal sites, such as faults, and generally on metallic atoms of low coordination numbers.

As a consequence when the difference between equilibrium potentials of the two half redox reactions is low, the modifying metal, during the preparation of a bimetallic catalyst by direct redox reaction, will be deposited selectively on specific sites of the parent metal (i.e. sites that are highly oxidizable such as corners, edges, etc.). However, the equilibrium potentials are defined by Nernst's law which provides facilities to fit the potential values by changing the concentrations of the oxidized and reduced forms (eqs 2 and 2') and so induces selective deposition of the modifier on the parent catalyst.

Finally, the redox properties can be modified by using different ligands which, by chelating metallic ions, alter the standard redox potentials and consequently the equilibrium potentials. As an example, a rhodium catalyst was modified by the surface deposition of palladium obtained when metallic rhodium ( $E_{\text{Rh}/\text{Rh}^{3+}}^0 = 0.79$  V) was exposed to palladium nitrate solution ( $E_{\text{Pd}/\text{Pd}^{2+}}^0 = 0.99$  V); the reaction is given by



However, in the presence of chloride ions which induce a complexation of the palladium ions ( $E_{\text{Pd}/\text{PdCl}_4^{2-}}^0 = 0.62$  V), the overall reaction is reversed and rhodium can be deposited on the surface of a metallic palladium catalyst according to the reaction



Identical results have been obtained with platinum and rhodium couples for preparation of model exhaust gas catalysts.

In summary, the direct redox reactions can be largely used in the preparation of bimetallic catalysts with a close interaction between the metallic constituents. In that case a metal with a high electrochemical potential is deposited on a metal with a lower potential. The applicability of the technique can be extended significantly by using different ligands which, by chelating metallic ions, modify the standard electrochemical potentials.

Finally, under well-defined experimental conditions (essentially the concentrations), the modifying metal can be deposited selectively on specific sites of the parent metal. Such deposition can significantly influence the selectivity of the bimetallic catalysts [12, 14].

### C Preparation of Bimetallic Catalysts by Redox Reaction of Adsorbed Reductant

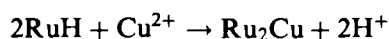
Bimetallic catalysts can be prepared by using a reductant that preadsorbs selectively on the parent metal.

The ions of the second metal (additive) are reduced by that reagent and the two metals interact. This technique was extensively studied by Szabo and co-workers who, using hydrogen as reductant, describe the technique as the "adsorption of metallic ions via ionization of adsorbed hydrogen" [15–19].

A simple example of using preadsorbed hydrogen as reductant was the preparation of a homodispersed Pt/Al<sub>2</sub>O<sub>3</sub> catalyst with increasing particle sizes prepared by platinum returning to the parent Pt/Al<sub>2</sub>O<sub>3</sub> catalyst saturated with irreversibly chemisorbed hydrogen [20].

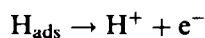
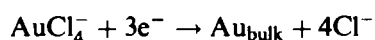
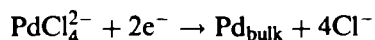
Hydrogen, preadsorbed on noble metals, is commonly used to prepare bimetallic catalysts by redox reaction. This requires the parent metal to chemisorb hydrogen (Pt, Pd, Rh, Ru, etc.) and to introduce a modifier that is reducible by hydrogen (Cu, Re, Ir, Rh, Pd, Pt, Au, etc.). All combinations of these metals have been prepared and characterized. For example, this technique has been used to prepare model Pt–Re reforming catalysts. Also, Pt–Rh and Pd–Rh were prepared to examine the interaction between platinum and rhodium in exhaust gas catalysts [8–10, 15–20, 21].

An interesting example is the preparation of Ru–Cu bimetallic catalysts by the reaction

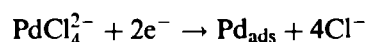
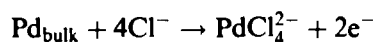


Previously, Cu–Ru was prepared by direct redox reaction, with Ru deposited on Cu. In this case, however, Cu is deposited on Ru. Comparison between the two bimetallic catalysts showed, during D-glucitol transformation that the two bimetallic phases, with same surface compositions, but prepared by two different techniques, had very different catalytic properties [22].

Szabo, Nagy, Margitfalvi, and co-workers [9, 23, 24] investigated the preparation of platinum–gold and platinum–palladium bimetallic catalysts using the ionization of hydrogen preadsorbed on platinum. The first step is the bulk deposition of additive according to the equations



In the presence of chloride ions, the first step is followed by the following spontaneous redistribution of the additive as adsorbed adatoms:



These reactions can also be written for AuCl<sub>4</sub><sup>−</sup>, which suggests that the chloride ions play an important role. Thus, the chelating power of the chloride ions in the transition metal complexes is critical in deposition and

redistribution on the parent catalyst surface of the metal additive. If there are few or no chloride ions (that is, in the absence of chloride ions other than those of the precursor or if a chloride-free precursor such as Pd(NO<sub>3</sub>)<sub>2</sub> is used) the bulk deposition–reoxidation reaction is negligible and the deposition of the additive is stable.

Furthermore preparation of Pt–Au bimetallic catalysts using hydrogen preadsorbed on platinum is a complex reaction involving simultaneously reduction of AuCl<sub>4</sub><sup>−</sup> by hydrogen but also direct oxidation of metallic platinum atoms by AuCl<sub>4</sub><sup>−</sup> (Table 1) [25].

A kinetic study of reduction of AuCl<sub>4</sub><sup>−</sup> by hydrogen adsorbed on platinum or by direct oxidation of bare reduced platinum demonstrated that the rate of reduction by hydrogen is 100 times higher than that of the direct redox reaction. Therefore, during preparation of Pt–Au bimetallic catalysts, for low gold coverages (when the quantity of adsorbed hydrogen is sufficient to reduce all the introduced gold ions), gold is reduced by preadsorbed hydrogen; however, for higher gold concentrations, reduction by preadsorbed hydrogen and by direct oxidation of platinum can occur simultaneously.

Different Pt–Au catalysts loaded by different amounts of gold were characterized by energy dispersive spectroscopy which allows the local elemental analysis of the two components [25]. It appeared that, at low gold coverage, the deposition of the additive occurs statistically on the whole surface of platinum. In that case gold is reduced by hydrogen atoms which are adsorbed on all accessible platinum atoms. For higher gold contents the deposition occurs by direct redox reaction and preferentially on high Miller-index planes of platinum particles.

At present considerable research is being carried out to investigate reductants other than hydrogen; the emphasis here is on possible structural sensitivity. For example, hydrazine and aldehydes (such as glucose) at low coverages are selectively adsorbed by particular sites of the basic metal, and can then be used to induce the deposition of additives on those sites [8].

In summary, the preparation of bimetallic catalysts by surface redox reaction using a reductant preadsorbed on the parent monometallic catalyst has been studied in detail. Unfortunately, the method is intricate and time consuming, especially if several successive operations are required. Furthermore, when the modifier has a standard electrochemical potential higher than that of the parent metal (AuCl<sub>4</sub><sup>−</sup> deposited on Pt<sup>0</sup>), the overall reaction is a complex one involving a reduction by adsorbed reductant but also direct oxidation of the metallic parent catalyst. The relative rate of the two parallel reactions determines the catalytic properties of the resulting bimetallic catalyst.

### D Preparation of Bimetallic Catalysts by Catalytic Reduction

The aim of this technique is to use the catalytic properties of the parent catalyst to increase the rate of reduction of the modifier. Thus the additive is deposited on the catalytic site that is active for the reduction reaction, and the two metals are closely situated.

The catalytic reduction of copper by hydrogen has been investigated on platinum, rhodium, ruthenium, and palladium. Thermodynamics show that  $\text{Cu}^{2+}$  in aqueous solution can be reduced by molecular hydrogen at room temperature. However, a copper solution under a hydrogen flow is perfectly stable because of the slow kinetics of the reaction. Metals such as platinum, palladium, and rhodium, which are able to activate hydrogen, can catalyze the reduction of copper.

The catalytic reduction of  $\text{Cu}^{2+}$  by hydrogen is faster on small platinum particles since the turn over number increases from 0.37  $\text{Cu}^{2+}$  ions reduced per accessible platinum atom per hour to 3.0 when the platinum dispersion increases from 11% to 54% [8]. Thus the catalytic hydrogenation of  $\text{Cu}^{2+}$  ions is a structure-sensitive reaction occurring preferentially on small platinum particles.

Analogous experiments have been performed with rhodium/alumina catalysts [26, 27]. Catalysts (monometallic  $\text{Rh}/\text{Al}_2\text{O}_3$  and modified  $\text{Rh-Cu}/\text{Al}_2\text{O}_3$ ) were characterized by IR spectroscopy using carbon monoxide as a probe molecule. The evolution of the relative intensity gem/linear bonds can be explained by assuming that copper is preferentially deposited on rhodium atoms of low coordination numbers. These results are in agreement with the kinetic study and confirm the view that copper, catalytically reduced by hydrogen, deposits preferentially on high Miller-index planes of the rhodium particles. Similar selective deposition of copper on parent metal particles was achieved by catalytic reduction of  $\text{Cu}^{2+}$  by hydrogen on a  $\text{Pd}/\text{SiO}_2$  catalyst. Such selective deposition of an inactive compound (Cu) on specific active sites of the parent metal (Pt, Rh, Pd, etc.) produces significant modifications of catalytic properties, particularly with regard to selectivity [27, 28].

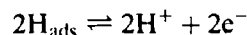
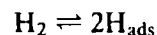
The technique of catalytic reduction can be extended to reducing agents other than hydrogen. The redox potentials of many organic compounds are well known and the most used system in electrochemistry is the quinone-hydroquinone system. According to Bodnar et al. [29], an organic oxidant-reductant system would irreversibly poison a metallic surface, causing loss of catalytic activity. However, hydrazine and hydroxylamine (in a slightly basic medium) or ascorbic acid were used at a working equilibrium potential less cathodic than hydrogen. Under these conditions, bulk deposition of the additive is limited, thus promoting the generation of submonolayers by underpotential deposition (see next section) [8].

A practical example of using a reductant other than hydrogen is the preparation of  $\text{Rh-Cu}/\text{Al}_2\text{O}_3$  bimetallic catalysts from catalytic reduction of copper by glucose on rhodium. A comparison of the catalytic properties of the two solids (reduction of copper by hydrogen and reduction of copper by glucose), in the conversion of methylcyclopentane shows that the two catalysts perform very differently with regard to hydrogenolysis, yielding low hydrocarbons. These results were explained by assuming that the glucose molecule, to be adsorbed, needs a large ensemble of rhodium atoms and induces deposition of copper on large planes, whereas reduction by hydrogen occurs selectively at the edges and corners of rhodium particles. In conclusion, the catalytic reduction of copper on rhodium is a structure-sensitive reaction which allows deposition of copper onto particular sites, but the structural sensitivity depends on the nature of the reductant [30].

The preparation of bimetallic catalysts by catalytic reduction ensures that the additive is deposited on the metallic site that is active for the reduction reaction. If the additive itself is not catalytically active, only one atom of additive metal would be deposited per active site. In fact, in the case of copper deposition on platinum, using hydrogen as the reducing agent, almost 200 atoms of copper can be deposited per accessible platinum atom. This property was used in the so-called electroless process which allows, for example, the preparation of supported copper catalysts. In this case the support is preactivated by impregnation of very low palladium loadings (almost 0.01%). Then the catalytic reduction of copper by hydrogen or formaldehyde, using the catalytic properties of the palladium atoms, yields almost 5% loaded copper catalysts [31].

In bimetallic catalysts prepared by catalytic reduction of copper by hydrogen, copper is deposited as three-dimensional agglomerates which are located, at low copper loadings, on the edges, corners, and rims of the parent metallic particles. The mechanism of deposition can be transferred from that proposed in corrosion and involving a local electrochemical cell:

- (i) the activation of hydrogen can occur on the free platinum surface area:



- (ii) then the reduction reaction, allowed by a transfer of electrons through the metallic phase, can occur on the copper surface:



Finally, at high copper loading (almost 200 copper atoms for one accessible platinum atom), the platinum



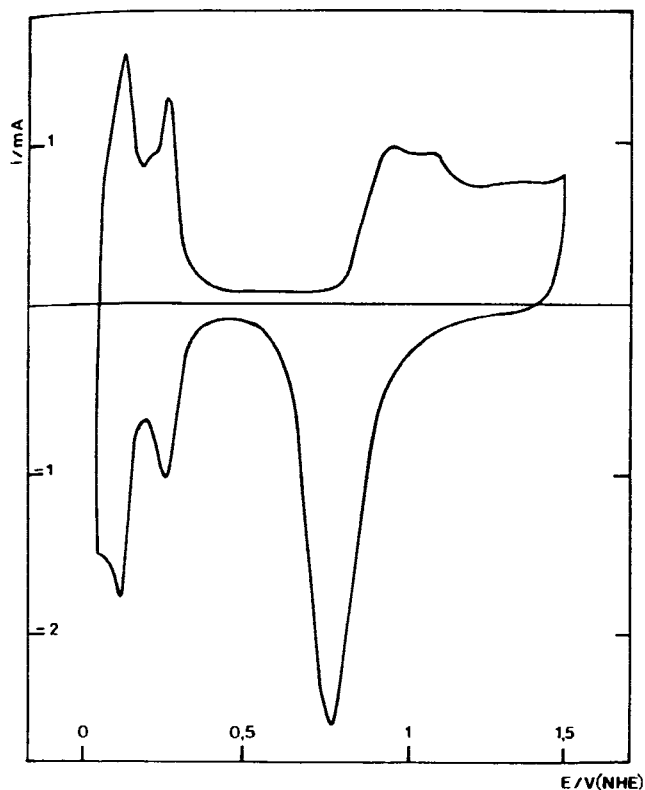


Figure 1. Stationary intensity potential curves: electroreduction of  $\text{ReO}_4^-$ ; electrooxidation of  $\text{H}_2$  (at two values of  $P_{\text{H}_2}$ ).

surface is totally covered and the deposition reaction is terminated.

The additive loading at saturation of the parent catalyst is dependent on the experimental conditions. So, different Pt-Re/ $\text{Al}_2\text{O}_3$  bimetallic catalysts were prepared by catalytic reduction of  $\text{ReO}_4^-$  by hydrogen.

On such bimetallic catalysts the rhenium loading at saturation of a 0.6% Pt/ $\text{Al}_2\text{O}_3$  catalyst depends on the hydrogen pressure. From a thermodynamic point of view the quantity of additive deposited at saturation is defined by the equilibrium conditions of the system under consideration. By taking into account the reduction of  $\text{ReO}_4^-$  to  $\text{Re}^0$  at 303 K (Table 1),

$$0.37 + \frac{0.06}{7} \log \frac{(\text{ReO}_4^-)(\text{H}^+)^8}{\Theta_{\text{Re}}(\text{H}_2\text{O})^4} = \frac{0.06}{2} \log \frac{(\text{H}^+)^2}{p_{\text{H}_2}}$$

where  $\Theta_{\text{Re}}$  is the coverage of platinum by rhenium. This relationship allows the calculation of  $\Theta_{\text{Re}}$  (over Pt) for different concentrations of  $\text{ReO}_4^-$ , different pH values, and different hydrogen pressures.

As an example, Fig. 1 introduces the stationary intensity-potential curves of the two redox systems ( $\text{H}_2 \rightleftharpoons 2\text{H}^+$  and  $\text{ReO}_4^- \rightleftharpoons \text{Re}^0$ ) and illustrates the effect of the experimental conditions on the nature of the deposit. It can be seen that at high hydrogen pressure the working point of the system  $E$ , (the potential at which

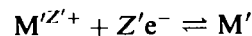
reduction of  $\text{Re}^{7+}$  and oxidation of  $\text{H}_2$  occur at the same rate (same intensity)) is close to the reversible potential of hydrogen (almost 300 mV more cathodic than the bulk deposition of Re). At low hydrogen pressure (with lower limiting diffusion intensity) the working potential  $E_2$  is close to the reversible potential of reduction of  $\text{ReO}_4^-$ . In electrodeposition it is known that the lower the potential of reduction (more cathodic) the higher the roughness of the deposit and the higher the extent of a three-dimensional electro-deposit.

In summary, the technique of catalytic reduction for the preparation of bimetallic catalysts can be extensively used with a variety of parent metals and reductants. However, some structure sensitivities of the reduction reactions become apparent and the modifying metal can be selectively deposited on specific sites of the parent-supported metal. Furthermore, such structure sensitivity depends on the nature of the reductant, and a given modifier can be deposited, according to the reductant used, selectively onto different parts of the metallic surface. In fact, a bimetallic catalyst can be tailored to provide the optimum activity, selectivity and lifetime for a given reaction.

### E Preparation of Bimetallic Catalysts by Underpotential Deposition

For the three techniques previously described, the deposition of the modifier occurs at electrochemical potentials (working potential of the system) which are lower than the equilibrium potential of the modifier (Fig. 1). Under such conditions the deposition of the modifier takes place as a three-dimensional deposit. By contrast, the underpotential deposition (UPD) characteristically forms submonolayer adatom structures [32, 33].

For the electroreduction of  $M'$  the equilibrium potential is



$$E_{M'/M'^{Z'+}} = E_{M'/M'^{Z'+}}^0 + RT/Z'F \ln(a_{M'^{Z'+}}/a_{M'})$$

For bulk deposition the activity of the deposited metal,  $a_{M'}$ , is assumed to be constant and equal to one. When the metal  $M'$  is reduced and deposited on a basic metal  $M$  (different to  $M'$ ), the activity of the deposit in the submonolayer is less than one until the coverage of  $M$  by  $M'$  is complete. The following linear relationship is assumed between the activity  $a_{M'}$  of the deposit and the coverage  $\Theta$  of  $M$  by  $M'$  [34–37]:

$$a_{M'} = \gamma_{M'} \Theta \quad (0 \leq \Theta \leq 1)$$

where  $\gamma_{M'}$  is the activity coefficient of  $M'$ . For  $\Theta = 1$ ,

$$a_{M'} = \gamma_{M'} = 1$$

**Table 2.** Underpotential shifts ( $\Delta E_p$ ) of metal ions deposited on platinum.

Metal ion	Supporting electrolyte	$\Delta E_p$ (V)
Ag <sup>+</sup>	0.5 M H <sub>2</sub> SO <sub>4</sub>	0.44
Cu <sup>2+</sup>	0.5 M H <sub>2</sub> SO <sub>4</sub>	0.41
Sb <sup>3+</sup>	0.5 M H <sub>2</sub> SO <sub>4</sub>	0.64
Ge <sup>4+</sup>	0.5 M H <sub>2</sub> SO <sub>4</sub>	0.75
Pb <sup>2+</sup>	1.0 M HClO <sub>4</sub>	0.87
Bi <sup>3+</sup>	0.12 M HClO <sub>4</sub>	0.59
Cd <sup>2+</sup>	1.0 M HClO <sub>4</sub>	0.96

For the deposition of a submonolayer the equilibrium potential is given by

$$E_{M'/M, z^{'+}}(\Theta) = E_{M'/M, z^{'+}}^0 + \frac{RT}{Z'F} \ln \frac{a_{M', z^{'+}}}{\Theta}$$

For  $\Theta < 1$  the equilibrium potential of the submonolayer  $E_{M'/M, z^{'+}}(\Theta)$  is always more positive than Nernst's potential of bulk deposition  $E_{M'/M, z^{'+}}$ . As a result, an underpotential deposition of M' over M may occur.

The electrochemical potential difference between  $E(\Theta)$  and  $E$  corresponds to a free energy difference:

$$\Delta G = -Z'e_0(E(\Theta) - E) = (\mu_{M'}^{\Theta} - \mu_{M'}) = Z'e_0\Delta E_p$$

where the chemical potentials of M' deposited in the submonolayer form and in the bulk are  $\mu_{M'}^{\Theta}$  and  $\mu_{M'}$ , respectively and where  $e_0$  is the elemental charge of the electron.

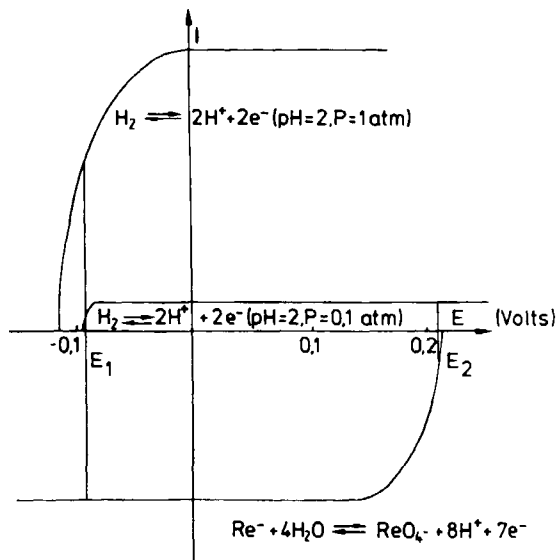
The difference between  $\mu_{M'}^{\Theta}$  and  $\mu_{M'}$ , is a direct measurement of the difference between the adatom binding energy of M' deposited on M and the binding energy of M' deposited on M'. Consequently, the potential at which UPD occurs for adatom M' varies depending on the substrate M. If  $\Delta E_p$  is known, the binding energy between the substrate M and the deposited atom M' can be determined [38–39] (this binding energy is in fact a free energy of chemisorption).

To describe these UPDs quantitatively, Kolb [32] proposed values of  $\Delta E_p$  for a series of substrate–adatom systems. Table 2 gives estimated values of underpotential shifts ( $\Delta E_p$ ) for various metal ions deposited on platinum. Based on these estimated values,  $\Delta E_p$  varies significantly, with the nature of the adatom.

Kolb, Gerischer and co-workers [34–39] showed that the excess energy ( $\Delta E_p$ ) due to UPD varies linearly with the difference between the work functions ( $\Delta\Phi$ ) of the substrate and of the adsorbate:

$$e_0\Delta E_p = 0.5\Delta\Phi$$

Note, however, that the work functions vary with the surface orientation. Thus, the structure of the crystal-

**Figure 2.** Typical voltammogram of polycrystalline Pt in H<sub>2</sub>SO<sub>4</sub> medium.

line metal (M) should lead to the preferential deposition of the additive M' on specific sites of M.

The simplest method to investigate UPD deposit is cyclic voltammetry. This technique, by a linear variation of potential, allows a direct observation of adsorption and desorption peaks of adatoms. As an example Fig. 2 shows a typical voltammogram obtained on polycrystalline platinum electrodes in acidic medium. The first area (between 0 to 0.4 V/RHE (Reference Hydrogen Electrode; the reversible potential of hydrogen at the given pH is taken as reference)) is related to hydrogen adsorption (at negative current, according to the electroreduction of protons:  $H^+ + e^- \rightarrow H_{ads}$ ) and with hydrogen desorption (at positive current, according to the electrooxidation of adsorbed hydrogen:  $H_{ads} \rightarrow H^+ + e^-$ ). The potential at zero current is the equilibrium potential corresponding to the redox equilibrium  $H_2 \rightleftharpoons 2H^+ + 2e^-$  and is given by the Nernst's law. At lower potential than this, equilibrium potential evolution of molecular hydrogen takes place, but at higher potential the peaks of hydrogen adsorption can be offered as a first example of underpotential deposition. At least two forms of adsorbed hydrogen are reflected by the two different peaks. These two forms (strongly and weakly bonded) correspond to the chemisorption of hydrogen on different sites of platinum.

The influence of structure on UPD for different metals adsorbed polycrystalline electrodes has been extensively studied in electrochemistry. One general conclusion [35, 37, 40, 49] is that the formation of a submonolayer of adatoms by UPD differs substantially, depending on the substrate structure and the crystal orientation. Indeed, with a heterogeneous poly-

crystalline surface, the deposition potential can be controlled so that adatoms adsorb preferentially on specific sites of the polycrystal.

In heterogeneous catalysis, the first tests on UPD were performed on bulk catalysts which allows, for the preparation of the bimetallic catalyst, easy control of the electrochemical potential by an external device (potentiostat). In the same way all electrochemical techniques, particularly the control of catalyst potential required for submonolayer deposition, can be extrapolated to metallic catalysts supported on conductive materials such as carbon or carbides [8].

However, in heterogeneous catalysis, metals are usually deposited on nonconducting supports such as alumina or silica. For such conditions electrochemical techniques cannot be used and the potential of the metallic particles is controlled by means of a supplementary redox system [8, 33]. Each particle behaves like a microelectrode and assumes the reversible equilibrium potential of the supplementary redox system in use. For example, with a platinum catalyst deposited on silica in an aqueous solution and in the presence of hydrogen, each particle of platinum takes the reversible potential of the equilibrium  $2\text{H}^+ + 2\text{e}^- \rightleftharpoons \text{H}_2$ , given by Nernst's law as

$$E = \frac{RT}{2F} \ln \frac{(\text{H}^+)^2}{P_{\text{H}_2}}$$

This potential, adjusted as a function of the pH of the solution and of the hydrogen pressure, is easily fixed between +0.1 V and -0.9 V/NHE (Normal Hydrogen Electrode). The  $\text{H}_2/\text{H}^+$  couple was used to prepare supported catalysts with platinum, palladium, ruthenium, and rhodium modified with deposits of tin, lead, iron, germanium, and bismuth [50–54]. These catalysts were proposed for their good selectivities for different reactions in specialize organic chemistry.

In fact the UPD technique has been used empirically by specialists of organic chemistry who, in order to increase the selectivity of liquid-phase hydrogenation catalysts, recommended the addition of metallic cations to the hydrogenating reactors. For example, during the selective hydrogenation of ethylenic aldehydes, cations such as  $\text{Co}^{2+}$ ,  $\text{Ru}^{3+}$ ,  $\text{Ag}^+$ ,  $\text{Zn}^{2+}$ ,  $\text{Fe}^{3+}$ , or  $\text{Fe}^{2+}$  were often added to the solvents to promote the selectivity of platinum [55–56]. Under the hydrogenating conditions used, in the presence of hydrogen, and in a protonic solvent, UPD of the additive adatom explains the changes in the selectivity.

Redox systems other than the  $\text{H}_2/\text{H}^+$  couple can be used to monitor the potential of the parent metal particles. For example, the quinone–hydroquinone system can be used to keep the electrochemical potential between 0.5 and 0.0 V/NHE by varying the pH from 0 to 7 for solutions of equal concentrations of quinone and of hydroquinone [57]. UPD clearly opens up a vast

field of research since few well-known organic redox systems have used it to date. Note, however, that such surface arrangements may be unstable due to the diffusion of adatoms on the surface or in the bulk of the metal. In some situations, such instability could exclude the use of the catalyst at high temperatures.

In conclusion, as deposition of adatoms can be controlled on well-defined fractions of the parent metal, the UPD technique, by a precise adjustment of the potential, allows a real tailoring of bimetallic catalysts.

## F Concluding Remarks

Surface redox reactions represent a relatively new approach for preparing supported bimetallic catalysts. Three main techniques have already been identified:

- (i) direct redox reactions between the parent metal and the modifier;
- (ii) redox reactions between a reductant and the modifier – the reductant can be previously adsorbed on the parent metal or introduced as a reagent in the reactor (if no homogeneous reaction can occur between the modifier and the reductant);
- (iii) underpotential deposition.

All these variants are complementary to one another and, by using different experimental conditions, ligands, reductants, and modes of preparation, this approach can apparently be used to prepare any type of bimetallic couple. However, the catalytic properties of the final catalyst will depend strongly on the technique used. The selection of one variant over another depends on the desired structure of the bimetallic phase.

In conclusion, redox reactions allow the surface to be tailored during catalyst preparation, which explains the exceptional catalytic properties, particularly in terms of selectivity, of bimetallic catalysts prepared by these techniques.

## References

1. V. Ponec, *Catal Rev Sci Eng* **1975**, *11*, 41
2. J. H. Sinfelt, *Bimetallic catalysts: Discoveries, concepts and applications*, John Wiley and Sons, New York, **1983**
3. J. H. Sinfelt US Patent 3 953 368 **1976** Exxon
4. H. E. Klusdahl US Patent 3 415 737 **1968** Chevron Corp
5. J. E. Weisang, P. Engelhard US Patent 3 700 588 **1972** C F R
6. R. Nuzzo, L. Dubois, N. Bowles, M. Tressoske, *J Catal* **1984**, *85*, 267
7. J. P. Candy, O. A. Feretti, G. Mabilon, J. P. Bournonville, A. E. E. Mansour, J. M. Basset, G. Martino, *J Catal* **1988**, *112*, 210
8. J. Barbier, Catalytica Studies Division, *Advances in Catalyst Preparation*, Study number 4191 CP (1992)
9. J. Margitfalvi, S. Szabo, F. Nagy, S. Gobolos, M. Hegedus in *Preparation of Catalysts III* (Eds G. Poncelet, P. Grange, P. A. Jacos) Elsevier, Amsterdam, **1983**

- 10 J Margitfalvi, S Szabo, F Nagy in *Catalytic hydrogenation* (Ed L Lerveny) Elsevier, Amsterdam, 1986
- 11 J Barbier, J C Menezo, C Montassier, J Naja, G Del Angel, J M Dominguez, *Catal Lett* 1992, 14, 37
- 12 J Barbier, J P Bottaux, P Chaumette, S Leporq, J C Menezo, C Montassier, EU Patent 380402 1990 Institut Français du Pétrole
- 13 C Montassier, J C Menezo, J Naja, J Barbier, J M Dominguez, P Sarrazin, B Didillon, *J Mol Catal* 1994, 91, 107
- 14 C Montassier, J C Menezo, J Naja, P Granger, J Barbier, P Sarrazin, B Didillon, *J Mol Catal* 1994, 91, 119
- 15 S Szabo, F Nagy, *J Electroanal Chem* 1976, 70, 357
- 16 S Szabo, F Nagy, *J Electroanal Chem* 1977, 84, 93
- 17 S Szabo, F Nagy, *J Electroanal Chem* 1978, 87, 261
- 18 S Szabo, F Nagy, *J Electroanal Chem* 1984, 160, 299
- 19 S Szabo, I Bakos, *J Electroanal Chem* 1987, 230, 233
- 20 J C Menezo, M F Denanot, S Peyrovi, J Barbier, *Appl Catal* 1985, 15, 353
- 21 P Marecot, J Barbier, G Mabilon, D Durand, M Prigent EU Patent 9290516-2 (1992) Institut Français du Pétrole
- 22 C Montassier, J C Menezo, L C Hoang, C Renaud, J Barbier, *J Mol Catal* 1991, 70, 99
- 23 I Bakos, S Szabo, *J Electroanal Chem* 1993, 344, 303
- 24 S Szabo, G Nagy, *J Electroanal Chem* 1977, 85, 339
- 25 J Barbier, P Marecot, J P Bottaux, B Didillon, G Del Angel, P Bosch, M Dominguez, I Schifter, *Appl Catal* 179 1994, 116 (1-2)
- 26 J Barbier, J M Dumas, C Geron, H Hadrane, *Appl Catal* 1990, 67, 1
- 27 J M Dumas, C Geron, H Hadrane, P Marecot, J Barbier, *J Mol Catal* 1992, 77, 87
- 28 C Geron, T Mbang, J Barbier, V Bertin, G Del Angel, *XIV Simposio Iberoamericano de Catalisis* 1994, 1, 7
- 29 Z Bodnar, T Mallat, S Szabo, J Petro in *Preparation of Catalysts V* (Eds G Poncelet, P Grange, P A Jacobs), Elsevier, Amsterdam, 1991
- 30 J Barbier, *XIV Simposio Iberoamericano de Catalisis* 1994, 1, VI-1
- 31 H F Chang, M A Saleque, *Appl Catal* 1993, 103 A, 233
- 32 D M Kolb in *Advances in Electrochemistry and Electrochemical Engineering* (Eds M Genscher, C N Tobias), John Wiley and Sons, New York, 1975
- 33 S Szabo, *Int Reviews Phys Chem* 1991, 10-12, 207
- 34 D M Kolb, M Przasnyski, H Genscher, *J Electroanal Chem* 1974, 54, 25
- 35 R R Adzic, E Yeager, B D Cahan, *J Electrochem Soc* 1974, 121, 474
- 36 R R Adzic, A V Trpkovic, R Atanososki, *J Electroanal Chem* 1978, 94, 231
- 37 R R Adzic, A V Trpkovic, N M Markovic, *J Electroanal Chem* 1980, 114, 37
- 38 H Genscher, D M Kolb, J K Sass, *Adv Phys* 1978, 27, 437
- 39 H Genscher, D M Kolb, M Przasnyski, *Surf Sci* 1974, 43, 662
- 40 A Hamelin, *J Electroanal Chem* 1979, 101, 285
- 41 A Hamelin, A Katayama, *J Electroanal Chem* 1981, 117, 221
- 42 A Hamelin, A Katayama, G Picq, P Vennecreau, *J Electroanal Chem* 1980, 113, 293
- 43 A M Abd El Hahm, K Juttner W J Lorenz, *J Electroanal Chem* 1980, 106, 193
- 44 G Kokkinidis, K Juttner, *Electrochim Acta* 1981, 26, 971
- 45 S Calde, S Brickenstein, *Anal Chem* 1971, 43, 1858
- 46 E Lamy, J Barbier, C Lamy, *J Chim Phys* 1980, 77 (10), 967
- 47 E Lamy J Barbier, *Electrochim Acta* 1982, 276, 713

- 48 R Amadelli, J A Molla, E Yeager, *J Electroanal Chem* 1981, 126, 265
- 49 R Amadelli, J A Molla, P Bindra, E Yeager, *J Electroanal Chem* 1981, 128, 2706
- 50 J C Menezo, L C Hoang, C Montassier, J Barbier, *React Kinet Catal Lett* 1992, 46-1, 1
- 51 E Lamy-Pitara, L El Ouazzani-Benhuma, J Barbier, *J Electroanal Chem* 1992, 335, 363
- 52 E Lamy-Pitara, L El Ouazzani-Benhuma, J Barbier, *Appl Catal* 1992, A-81, 47
- 53 I Bakos, S Szabo, F Nagy, T Mallat, Z S Bodnar, *J Electroanal Chem* 1991, 309, 293
- 54 S Szabo, I Bakos, F Nagy, T Mallat, *J Electroanal Chem* 1989, 263, 137
- 55 W F Tuley, R Adams, *J Am Chem Soc* 1925, 45, 3061
- 56 G Cordier, Y Colleuille, P Fouilloux (Eds), *Catalyse par les métaux*, CNRS, Paris 1984
- 57 M Kotter, L Riekert in *Preparation of Catalysts II* (Eds B Delmon, P Grange, P Jacobs, G Poncelet), Elsevier, Amsterdam, 1979

## 2.2.2 Formation of Final Catalyst

B. DELMON

### 2.2.2.0 Introduction and Background

#### A Introduction

In most cases, the solids prepared according to the methods described in Section A 2 2 1 are not catalytically active as such. The only exceptions are some grafted catalysts (2 2 1 2), most heterogenized complexes (2 2 1 4) and a large proportion of the catalysts prepared by redox methods (2 2 1 6). In the other cases, the substance deposited on the support must be transformed to a suitable compound (e.g. transformation of hydroxide or oxide to metal or to sulfide) in order to acquire the desired activity.

When a substance is supported on a carrier, its chemical reactivity is fundamentally altered. Comparing reactions of a nonsupported compound with those of the same compound dispersed on a carrier indicates that the kinetics in exactly the same conditions are always altered, and that they may even lead to different products, namely different catalytic materials.

Some of those changes are intuitively expected. This is the case when some chemical reaction has taken place between the active substance and the support. The reactivity then reflects that of the new compound. But other modifications are very often not properly recognized. One of the most common errors results from the ignorance that, beyond a certain threshold, the simple fact that a substance is more highly dispersed may not lead to increased, but rather diminished reactivity.

The present section will examine the phenomena taking place during the last stages of the formation of the active phase, namely calcination, reduction, or sul-

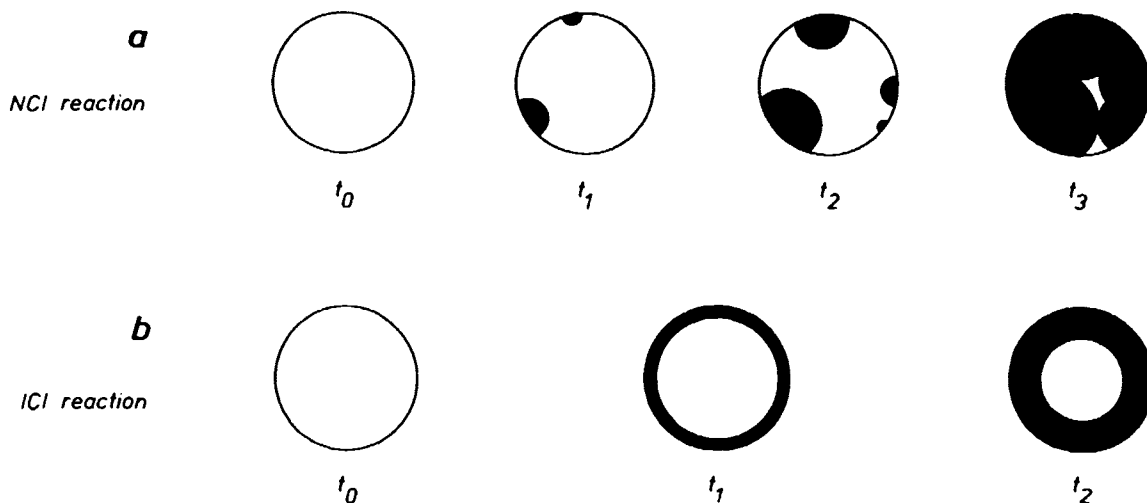


Figure 1. Nucleation-controlled interface reaction (NCI) and interface-controlled reaction (ICI) at various times  $t_0$ – $t_3$ .

fidation. These last stages, especially reduction and sulfidation, are usually called activation [1]: activation is defined by IUPAC as the transformation of the precursor solid to the active phase. This is a crucial operation. For a large part it determines or influences all the practical properties of catalysts: activity, selectivity, and resistance to ageing. Only a small proportion of the practical catalysts is used unsupported. Although the activation of such catalysts is important, much more space has to be allotted to supported precursors. This is why the present section belongs to Part A.2.2. of the *Handbook*. The reason for this importance is the already mentioned fact that the particular behavior of supported phases with respect to chemical transformation is poorly understood in general. Principally, two factors must be taken into account. The first is the state of dispersion of the precursor. The second is the interaction of the precursor with the support. Two sections are devoted to these aspects in what follows.

## B Particulars of Chemical Reactions for Supported Substances

### a General Kinetic Features of Solid-State Reactions

In the transformation of a dispersed supported precursor to its oxide (in calcination), and further to metal or sulfide, various types of reactions take place. It is necessary to recall briefly the different fundamental processes which are involved in such reactions.

In a general way, two main families of reactions involving solids must be distinguished:

- (i) Reactions taking place as a result of diffusion of a chemical species through the bulk of one of the solids involved (reactant or product). These are *solid-state diffusion* or *ssDC reactions*. Typical examples of such reactions are those of transition metal oxides, such as NiO or  $\text{Co}_3\text{O}_4$ , with an alu-

mina support, making a solid solution of the transition metal in  $\gamma\text{-Al}_2\text{O}_3$ , or even leading to the formation of a spinel,  $\text{NiAl}_2\text{O}_4$  or  $\text{CoAl}_2\text{O}_4$ .

- (ii) Reactions taking place at an interface and kinetically limited by processes occurring at this interface. These are *interface controlled* or *IC reactions*. This corresponds to the case of many dehydroxylations (transformation of hydroxides to oxides), reductions of oxides to metals (NiO to Ni) or reduction–sulfidation processes leading to sulfides (deposited “cobalt molybdate” bilayer, transforming to  $\text{Co}_9\text{S}_8 + \text{MoS}_2$ ).

IC reactions can be of two types. The nucleation of the new phase (e.g. Ni produced by the reduction of NiO) may be rate determining. In that case, separate nuclei of the new phase can be detected (Fig. 1(a)). These are called nucleation-controlled interface or NCI reactions. In other cases, all the surface of the initial solid reacts, and a continuous interface entirely covers the solid reactant. With respect to kinetics, the interfacial process entirely controls the reaction in this last case. This is an ICI reaction (Fig. 1(b)).

For interface-controlled reactions, the rate of reaction at the interface,  $r_i$ , is proportional to the area of the interface  $S_i$ , with a proportionality factor  $k_i$  which is the rate or velocity of interface movement:

$$r_i = k_i S_i$$

The factor  $k_i$  depends on the experimental conditions. For ICI reactions in constant conditions,  $r_i$  keeps decreasing during the whole reaction. Figure 1(b) suggests that the area of the interface between product (black) and reactant (white) steadily decreases. This is not the case for NCI reactions, where  $r_i$  first increases

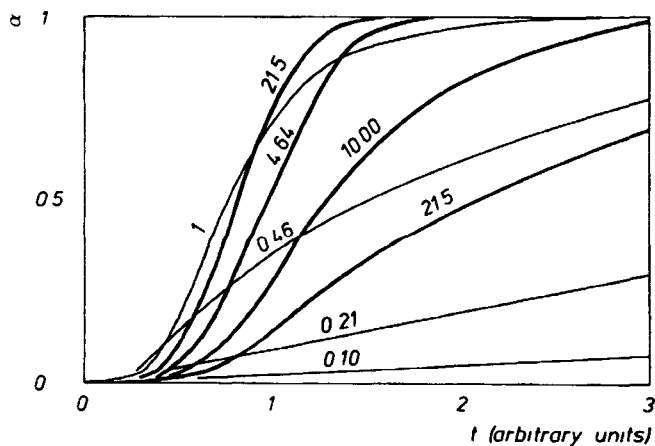


**Figure 2.** Comparison of the course of reaction (degree of reaction vs. time) of samples composed of identical spherical particles of various diameter. Conventionally, dimension unit is 1 for the curve at the left (adapted from Fig. XI.23, Ref. [7]).

and later decreases: this is suggested in Fig. 1(a) where the interface has considerably shrunk at time  $t_3$ . The overall phenomenon thus depends both on the rate of nucleation  $r_n$  (number of nuclei forming per unit surface area per unit time) and  $k_1$  [2, 3].

It is possible to calculate the variation of the overall rate  $r$ , due to the convolution of the kinetics of nucleation and interface movement [4–7]. The corresponding variation of the degree of transformation of the solid,  $\alpha$ , can be calculated from  $k_1$  and  $S_1$ . This can be done for different shapes of particles [7], but it is sufficient here to outline the result of calculations made with the assumption of spherical particles of identical diameter. Starting from large particles, a diminution of their size will lead to higher rates of overall reaction. But, contrary to intuitive expectation, the rate will diminish when the particles become very small. This is shown in Fig. 2, which is a plot of the degree of transformation against time (common scale for all curves) for samples composed of particles of diameter  $d$ ; in this figure, by convention,  $d = 1$  for the sample reacting with the highest rate at the lower  $\alpha$  values. The rate of reaction decreases dramatically by a factor of approximately 20 when the particles are one order of magnitude smaller in diameter. Particles with very different sizes, namely 0.46 and 21.5, surprisingly have comparable reactivities. It should be clear that the parameter governing those changes is the ratio of the rates of nucleation and interface movement; more details can be found in Ref. 7.

It should be noted that this phenomenon has to be taken into account in thermoprogrammed reactions (TPR, TPS, etc.) for correct interpretation. A shift of a reaction peak to higher temperature should not be automatically attributed to a change of chemical composition of the reactant or to the fact that it is less dispersed [8]. The contrary may be true.

**b Interaction Between Supported Phases and Supports**  
Generally, the observation that activation, or, more generally, the reactions of supported phases, occur differently compared to those of the corresponding pure unsupported material, is generally attributed to interactions between the supported phase and the support. This is of course true phenomenologically. But an essential concept is missing, namely the distinction between two different effects:

- (i) The first effect is merely brought about by the fact that the state of dispersion of the deposited phase is different; this was examined in the previous section.
- (ii) The second effect concerns the nature of the chemical or physico-chemical forces which act between the supported phase and the support and keep the former attached to the latter.

The error in many interpretations in the literature is that this distinction is not clearly made. This may have serious consequences with respect to the understanding of the activation mechanism and the efficient search for experimental parameters permitting the control of activation.

Considering now the chemical or physico-chemical interactions between the supported phase and the support, it is clear that a change of reactivity will be observed if the supported phase reacts chemically with the carrier: for example, nickel can combine with silica to make some hydroxysilicate compound when the deposition-precipitation method is used for preparation. The reactivity of the hydroxysilicate with hydrogen during activation by reduction is very different (actually lower) compared to that of nickel oxide. But careful analysis of the various examples mentioned in literature shows that quite different situations may exist.

Figures 3–10 reflect one way to classify the various categories of precursor-support interaction with emphasis on the chemical or physico-chemical nature of the interaction and the consequence with respect to the structure of the supported phase. Most of the possible situations are represented. Relevant examples can only be found if very different precursors are considered. It should, however, be clear, when considering these figures, that the precursor-support system taken as representative of one category may also correspond in specific cases to other categories. The reason is that the structure of a complex solid system depends strongly on the whole succession of phenomena having taken place during the preparation. In spite of the difficulty resulting from this effect, a clear distinction between the different possible situations definitely needs to be made for understanding the multiplicity of behaviors of precursors during activation. The classification presented in the succession of Figs 3–10 and the comments

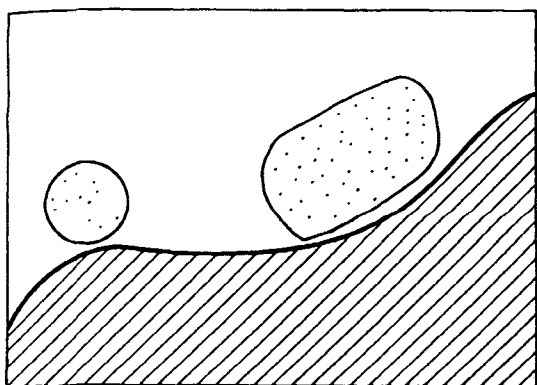


Figure 3. Supported phase-support interaction: very weak forces.

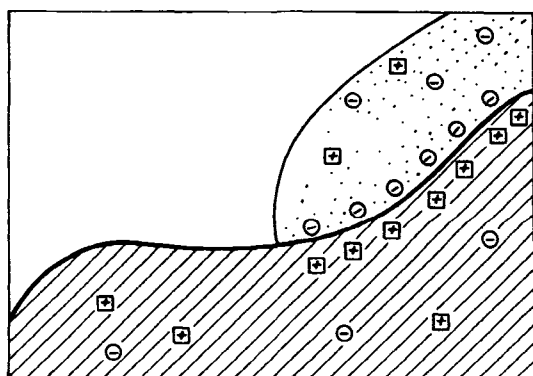


Figure 4. Supported phase-support interaction: electronic interaction.

below correspond to increasingly stronger chemical interactions between the supported phase and the support (see also Section A.3.2.4).

*Case 1: Very weak forces* (Fig. 3). This is the case of Van der Waals forces or hydrogen bonds. Such weak forces are probably insufficient for retaining an active phase attached to the support during an industrial process, but may be sufficient for handling a precursor. Organic precursors deposited from organic solutions are retained on the support by this sort of interaction in most cases. For hydrated salts, hydrogen bonds may also contribute to the attachment of the deposited substance. In both cases, the role of the support is only to disperse the precursor. In principle, weak forces could also be sufficient to bring about some preferential lattice orientation of the crystallites of the precursor. Graphite [9] and, perhaps, sometimes silica [10] could be examples of carriers which exert only a weak action on the supported substance. But care must be taken that carbon may have a functionalized surface and that the hydroxyls of silica can react with a precursor to form Si-O-R bridges (where R may represent many different organic or inorganic moieties: acyl or alkyl species, coordination compounds, etc.).

*Case 2: Electronic interaction* (Fig. 4). In principle, semiconducting or conducting substances deposited on a semiconducting support may form a *junction*, in the electronic sense, with the latter, even if no chemical bond as defined conventionally is formed. Electron transfer across the boundary can, in principle, change the electron density of deposited aggregates. The effect is expected to be more pronounced for small aggregates. This could change the reactivity of the deposited precursor.

*Case 3: Attachment through a thin transition layer* (Fig. 5). In adhesion or attachment of two solids together, by more or less strong forces, a whole spectrum

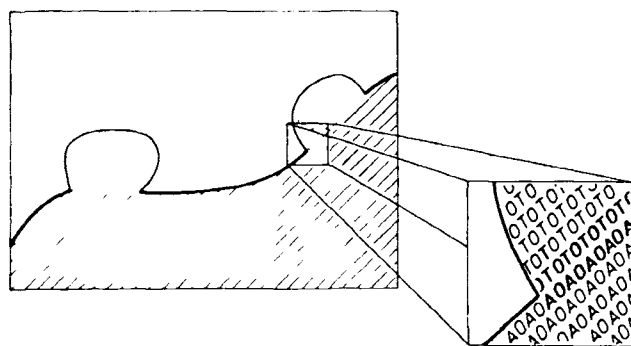


Figure 5. Supported phase-support interaction: attachment through a transition layer.

of mechanisms may explain the mutual interaction across the interface. However, except for the two cases mentioned above, the existence of a transition layer is always assumed. This transition layer may be a mixed compound of molecular thickness joining together the solids, or involve a thicker layer across which the composition progressively changes from that of one of the solids to that of the other [11]. Figure 5, for simplicity, represents the first situation. The mechanisms permitting adhesion are the same as those which will be discussed in the next cases of interaction (monolayers and bilayers). The main difference is that here the present surface energy of the deposited precursors is higher than the interface energy of the interface with the support, thus favoring the formation of deposited crystallites rather than that of covering layers. There is certainly a whole spectrum of possible situations between the weak or relatively weak interactions discussed above and very strong chemical interactions. This is reflected by the variety of situations observed in practice. A good example of a precursor which corre-

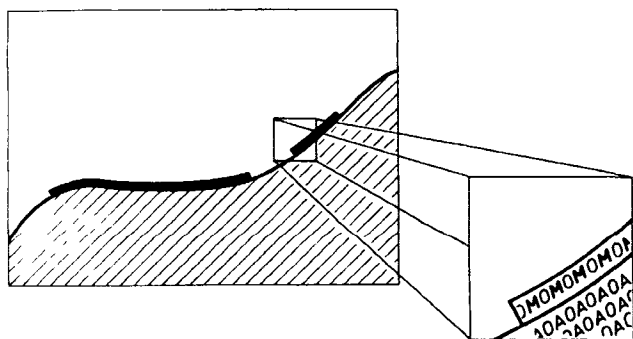


Figure 6. Supported phase-support interaction: patches of monolayer (rafts) or complete monolayer.

sponds to the present case is cobalt oxide (obtained from nitrate) on silica. In that case, there is a relatively strong interaction, as shown by the partial formation of a monolayer, but the stable situation corresponds to crystallites deposited on silica. The interface probably has the structure of a cobalt silicate but is certainly only a few angströms or nanometers thick. Another example, actually not corresponding to precursors but to the active phase, is  $\text{MoS}_2$  supported on alumina, where a molybdenum oxysulfide makes the transition. This compound may be considered as partly aluminum molybdate, on the alumina side, and molybdenum sulfide, on the other side.

With respect to reactivity in the activation reaction, the situation represented in Fig. 5 suggests that the features of the activation will initially resemble those of the above cases 1 or 2 (Figs 3 or 4), but that new processes will be necessary for making the reaction possible in the final stages. These are expected to be similar to those described for cases 4 through 9.

*Case 4: Chemical interaction: patches of monolayers or complete monolayer* (Fig. 6). This category corresponds to situations where all the atoms or molecules of the supported precursor are exposed on the surface. The upper limit is encountered when the precursor phase combines with the carrier surface as a continuous monolayer. Figure 6 represents a partial coverage with one-molecule-thick patches (also called rafts). A typical example corresponds to the formation of a monolayer of  $\text{MoO}_3$  on the surface of  $\gamma\text{-Al}_2\text{O}_3$  as follows:

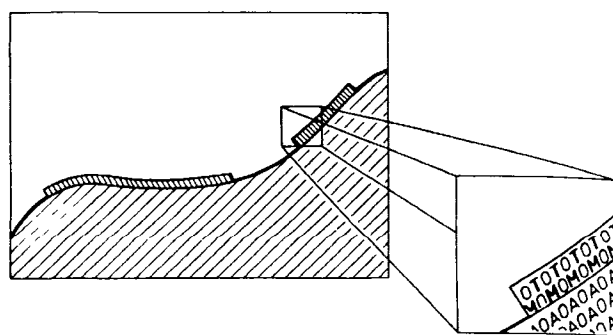
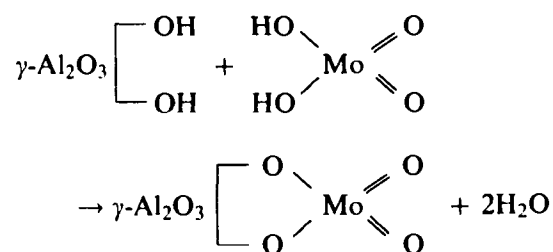


Figure 7. Supported phase-support interaction: formation of bilayers.

Much evidence of this phenomenon has been presented [12–17]. It is due to a real surface reaction, leading to the formation of a two-dimensional compound with well defined physico-chemical characteristics. The most conspicuous ones are electronic effects [18–24]: a shift of about 0.5 eV towards higher binding energies, of the  $\text{Mo } 3d^{3/2}$  and  $3d^{5/2}$  levels, has been reported.

Special structural features have also been detected using various spectroscopies (see, for example, Ref. 25 and the comprehensive review of Ref. 26). These results have been reproduced very frequently by many authors.

In such a case, one must conclude that a real two-dimensional aluminum molybdate is formed. As long as the quantity of aluminum molybdate corresponds to less than a monolayer, no three-dimensional aluminum molybdate forms.

The reactivity (and all chemical properties) of monolayers are very different from those of the pure supported precursor (here  $\text{MoO}_3$ ) or those of the bulk mixed compound of composition similar to the monolayer (here  $\text{Al}_2(\text{MoO}_4)_3$ ) (see Ref. 26).

*Case 5: Chemical interaction: formation of bilayers* (Fig. 7). The formation of a two-dimensional compound of molecular thickness is not limited to compounds of a single catalytically active element. The phenomenon also occurs when a precursor contains two elements. The most conspicuous example is that of the cobalt-molybdenum and nickel-molybdenum oxide bilayers on  $\gamma\text{-Al}_2\text{O}_3$  [26–28]. Much of the structure of these bilayers is known [26, 28–30]. They should be considered as two-dimensional cobalt or nickel molybdates; Ion scattering spectroscopy (ISS) studies show that the Group VIII element may, according to circumstances, sit on the outside (exposed to the exterior) or inside (between  $\gamma\text{-Al}_2\text{O}_3$  and the bilayer) [29, 30]. Bilayers have also been the object of innumerable studies reproducing the initial results or sometimes adding particular details.

Comments with respect to reactivity are essentially similar to those made for monolayers. As generally ex-



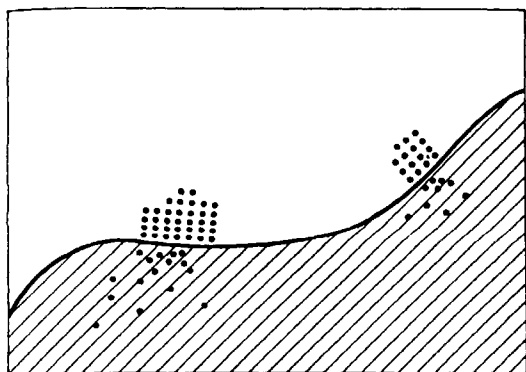


**Figure 8.** Supported phase-support interaction: partial formation of solid solutions.

pected with oxides containing two or several metallic elements [44], their reactivity is promoted by the presence of the element most easily reacted (e.g. Co or Ni in Co-Mo or Ni-Mo oxide monolayer with respect to reduction).

*Case 6: Partial formation of solid solutions* (Fig. 8). A more extensive reaction between a precursor and the support is often observed. This can lead to the formation of solid solutions of the supported element in the support. Other compounds of ill-defined stoichiometry can also form between the two partners. This can occur during the precipitation stage, by partial dissolution, and by precipitation, as shown in very recent work [31]. A still more extensive reaction can occur during calcination aimed at producing supported oxide precursors.

Depending on the temperature of calcination, the oxide and the carrier, when their structures are compatible, can dissolve in each other to different extents. The result may range from an ionic exchange confined to the near interface regions, to a multiple layer thick solid solution (or even, ultimately, a homogeneous one). Figure 8 presents a simple case, namely when a precursor, schematically indicated as possessing a well defined structure, can dissolve partially in the support. This is the most common case, but the other phenomena mentioned above can also occur. The occurrence of the different situations and their bearing on reactivity have been discussed in a case not related to supported catalysts, but quite illustrative, namely that of the NiO-CuO system [3, 32]. Instances of formation of homogeneous solid solution involving substances used as supports are abundant in literature. For example,  $\text{Cr}_2\text{O}_3$  can react with an alumina support [33] and a similar effect is observed when CoO is contacted with a magnesia support [34]. A technologically very important case is the partial dissolution of cobalt (or nickel) in  $\gamma\text{-Al}_2\text{O}_3$  in HDS catalyst precursors. For cobalt, this

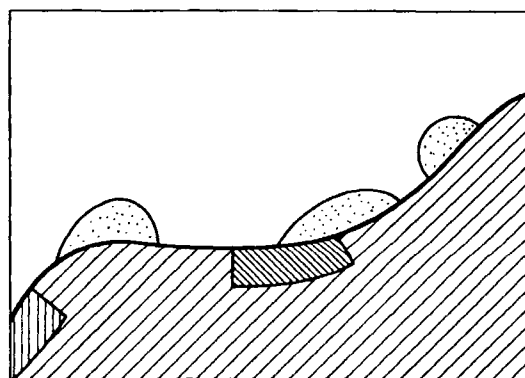


**Figure 9.** Supported phase-support interaction: partial formation of new compounds.

is easily explained by the fact that  $\text{Co}_3\text{O}_4$  and  $\gamma\text{-Al}_2\text{O}_3$  both have the spinel structure.

The changes in reactivity which may occur when solid solutions are formed are discussed in detail elsewhere [3]. The support is necessarily very inert with respect to activation conditions. The element trapped in the solid solution will therefore be much less reactive. Consequently, only part of the active element contained in the precursor gets activated. Indeed, the loss of part of cobalt or nickel by reaction with  $\gamma\text{-Al}_2\text{O}_3$  is of concern in hydrotreating reactions; regeneration by calcination, which increases the proportion of the active elements trapped in the support as solid solution, decreases the amount of cobalt or nickel which can play a catalytic role.

*Case 7: Partial formation of new compounds* (Fig. 9). The formation of a new compound can be either restricted to the near surface domains or extend to the bulk of the solid. It is likely that real spinels, rather than solid solutions (as in the present case) can form when oxide precursors containing transition metal elements such as copper or manganese (and also cobalt or nickel) are submitted to calcination when supported on alumina [35-38]. Other instances correspond unambiguously to the formation of a well defined new phase. Nickel hydroxysilicate is formed in the preparation of the precursor of Ni/SiO<sub>2</sub> catalysts. At high loading of MoO<sub>3</sub> (e.g. 20% MoO<sub>3</sub>) on  $\gamma\text{-Al}_2\text{O}_3$ , for example those used presently for very difficult hydrotreating reactions,  $\text{Al}_2(\text{MoO}_4)_3$  crystallites are formed [39, 40].

The comments concerning reactivity of precursors forming compounds with the support are identical to those of case 6. The general situation is also presented in Ref. 3.

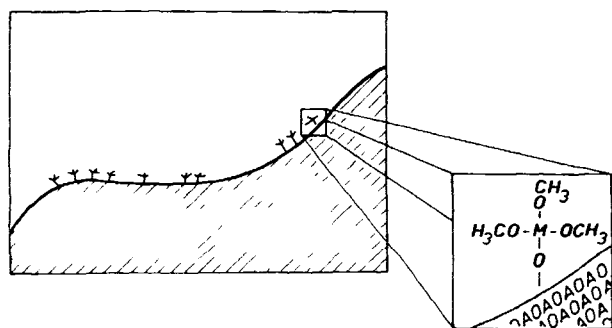


Figure 10. Supported phase-support interaction: grafted precursors.

*Case 8: Grafted precursors* (Fig. 10). Organometallic complexes are now very frequently anchored (or grafted) on inorganic surfaces. They may be used as catalysts without any further treatment. However, an increasing number of attempts are made to use these atomically dispersed species as precursors for all sorts of catalysts (oxides, bare metal crystallites, sulfides). This implies that these organometallic complexes also undergo an activation procedure. In parallel with these developments, other molecules attacking the surfaces through a chemical bond are also used. This is the case for chlorides which, by reacting with surface hydroxyls to release HCl, make a bond between the remaining oxygen and the metal. This has been used for dispersing vanadium pentoxide on anatase and for making other highly dispersed catalysts [41–43]. Recently, highly dispersed supported precursors have been successfully prepared using grafted alkoxides as precursors [41–43].

It could be expected that such precursors do not behave as solid reactants, but rather as molecular species. However, the resulting molecular product (bare metal atoms in the zero-valent state, oxide or sulfide monomers) aggregate very rapidly in most cases, leading to the formation of tiny crystallites, so that it is very difficult to clarify mechanisms or even to distinguish general trends. Although the chemical mechanisms concerning grafting are now investigated in detail (Sections A.2.2.1.2. and A.2.2.1.4.), it seems that the *transformation* for activation of the grafted species has not yet been explored in much detail.

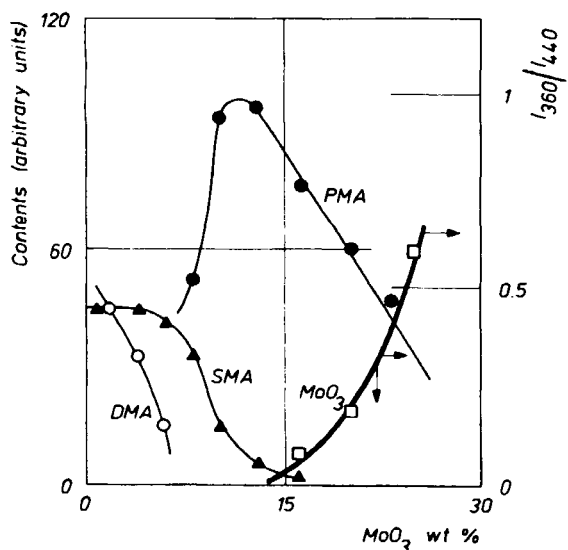
*Case 9: Intermediate cases.* There are two major difficulties in describing the supported oxide or, more generally, the precursor (e.g. oxychlorides, salts of various oxides or other compounds) which undergo activation. One is the fact that a same precursor may be involved in different types of interactions according to the nature of the support. The second is that several of the situations described above may coexist in a given catalyst. MoO<sub>3</sub> offers an excellent illustration of these two difficulties.

Table 1. Behavior of MoO<sub>3</sub> with respect to various supports or oxides involved in catalysis.

Support	Observed phenomena	References
Sb <sub>2</sub> O <sub>4</sub>	detaches completely	45–47
BiPO <sub>4</sub>	spontaneous segregation no MoO <sub>3</sub> or BiPO <sub>4</sub>	48 49
Co <sub>3</sub> O <sub>4</sub>	no spreading	50
SiO <sub>2</sub>	almost complete monolayer formation but weak interaction tendency to detach, especially when another ion (e.g. Co, Ni) is present	51, 52 53–55 56, 57
TiO <sub>2</sub>	monolayer up to 50% theoretical value spontaneous spreading of MoO <sub>3</sub> on TiO <sub>2</sub> above 50%: amorphous tridimensional and epitaxially grown MoO <sub>3</sub>	54, 58–61  50, 53 62
ZrO <sub>2</sub>	probably same as TiO <sub>2</sub>	54
MnO <sub>2</sub>	spontaneous spreading	50
SnO <sub>2</sub>	spontaneous spreading	53
MgO	spontaneous spreading	53, 54
Al <sub>2</sub> O <sub>3</sub>	extremely stable monolayer (almost complete coverage) spontaneous spreading strong modifications of properties of MoO <sub>3</sub>	innumerable 53 innumerable
Bi <sub>2</sub> MoO <sub>6</sub>	reaction to, respectively, Bi <sub>2</sub> MoO <sub>7</sub>	63, 64
Bi <sub>2</sub> MoO <sub>7</sub>	and Bi <sub>2</sub> Mo <sub>3</sub> O <sub>12</sub> via, probably, strong surface contamination with MoO <sub>3</sub>	

Table 1 summarizes the interaction between MoO<sub>3</sub> and various supports or oxides [44–64]. There is a whole range of situations. At one end is the extremely weak interaction with  $\alpha$ -Sb<sub>2</sub>O<sub>4</sub>. The MoO<sub>3</sub>/ $\alpha$ -Sb<sub>2</sub>O<sub>4</sub> interface energy is weaker than the surface energy of MoO<sub>3</sub>, so that MoO<sub>3</sub> detaches spontaneously from  $\alpha$ -Sb<sub>2</sub>O<sub>4</sub>. At the other end stays the MoO<sub>3</sub>/ $\gamma$ -Al<sub>2</sub>O<sub>3</sub> system, with a strong tendency to form a monolayer. Other oxides, such as bismuth molybdates, behave as  $\gamma$ -Al<sub>2</sub>O<sub>3</sub>.

With respect to coexistence of several types of interactions between given partners, this mainly concerns situations 3 through 7 above. This can be illustrated by the case of MoO<sub>3</sub> dispersed on silica. Silica is generally considered as an inert carrier. It is expected to have only weak interactions with the supported phase and to act merely as a dispersing agent. This is not the case [65, 66]. A series of MoO<sub>3</sub>/SiO<sub>2</sub> catalysts, prepared by pore volume impregnation, followed by drying at 383 K and calcination at 773 K, show a progressive shift towards higher values of the binding energy (BE) of the Si<sub>2p</sub> line, with increasing active phase loading from 0–20 wt% MoO<sub>3</sub>, where the positive shift reaches 1 eV [52]. This corresponds to a strong chemical interaction, which is substantiated by the formation of a monolayer [52, 56, 57]. This monolayer structure has limited stability and MoO<sub>3</sub> crys-



**Figure 11.** Product distribution in  $\text{MoO}_3/\text{SiO}_2$  catalysts as determined from acidimetric titrations: ( $\blacktriangle$ ) silicomolybdic acid; ( $\circ$ ) dimolybdates; ( $\bullet$ ) polymolybdates. The estimation of  $\text{MoO}_3$  ( $\square$ ) is derived from the intensity ratio of the reflectance bands at 360 and  $440\text{ cm}^{-1}$  [66].

tallites can form by spontaneous detachment of the monolayer. As a consequence, the following species are found in  $\text{MoO}_3/\text{SiO}_2$  precursors:  $\text{MoO}_3$ ; dimolybdates (DMA); polymolybdates (PMA); silicomolybdic acid (SMA); molybdenum bound to the surface of the support as a monolayer [14]. As shown in Fig. 11, the proportion of the various species changes according to composition [66].

As a consequence of the coexistence of several species, the  $\text{MoO}_3/\text{SiO}_2$  precursor contains:

- (i) monolayer patches (situation 4 above);
- (ii)  $\text{MoO}_3$  crystallites (situation 3 above);
- (iii) silicomolybdic compounds (situation 7 above).

The situation for the oxidic form of HDS catalysts supported on alumina is still more complicated, as was shown very early [35, 39, 67] and confirmed later by a very large number of authors. The system contains or may contain, according to the situation: free cobalt oxide; cobalt pseudoaluminate or  $\text{CoAl}_2\text{O}_4$ ; free  $\text{MoO}_3$ ; the  $\text{Co}_x\text{-Mo}_y\text{-O}_z$  bilayer; possibly  $\text{Al}_2(\text{MoO}_4)_3$  at high loading.

The temperature of calcination of a support before impregnation understandably modifies the interaction between the precursor and the support, as shown in the above case and that of alumina-supported nickel catalysts [68].

Another additional complication arises when two or several different oxides are deposited on a support, namely the possibility that they combine together. In this respect, cobalt molybdate  $\text{CoMoO}_4$ , although rarely found, can be added to the above list.

The examples selected for supporting the comments on the different types of interactions correspond to samples obtained after calcination. However, it is easy to see that most of these types of interactions can also occur in systems involving a precursor salt (to be decomposed to a catalytic active oxide) or a metal (e.g. to be sulfided) and a support (oxide or otherwise).

### C Article Structure

This article covers the activation of *supported* catalysts. It examines the formation of the final catalysts, as achieved by three categories of treatment: calcination, reduction, and sulfidation (more precisely reduction-sulfidation). Detailed studies of these three categories of processes did not lead to an equally detailed analysis. Outside very general (phenomenological) observations, very little is known concerning the calcination of supported precursors. By contrast, some particular systems have been studied in some detail in reduction (e.g.  $\text{NiO}/\text{support}$  for activation to  $\text{Ni}/\text{support}$ ) or sulfidation ( $\text{Co}_x\text{Mo}_y\text{O}_z/\gamma\text{-Al}_2\text{O}_3$  to sulfides).

The discussion is based on the main distinctions between calcination, reduction, sulphidation, and other reactions. Within each of these topics, the unsupported and supported situation will be examined individually if necessary. More emphasis is given to explaining these effects by using typical examples rather than by giving an inventory of the literature. The important point is to understand the general rules, the general trends that are to be observed when the activation parameters are modified, and the various structural and textural changes that activation may bring about.

These subsections will show why activation is such an important process, by demonstrating that it can alter most, probably all, the properties of catalysts.

#### 2.2.2.1 Activation of Supported Catalysts by Calcination

Some catalyst activation processes are extremely important: this is the case for oxides used as catalysts and supports ( $\text{Al}_2\text{O}_3$ ,  $\text{SiO}_2$ ,  $\text{TiO}_2$ ,  $\text{ZrO}_2$ , silica-aluminas), and zeolites. Extremely elaborate procedures are used. This concerns bulk, not supported systems, and is dealt with in Section A.2.1. The case of  $\text{SiO}_2$  mixed with active phases (e.g. in oxidation) has little relevance to the subject of the present section, as it seems that  $\text{SiO}_2$  does not play the role of a real support, but rather that of a diluent or spacer. An electron microscopy study coupled with microanalysis on a typical oxidation catalyst (propene to acrolein) shows that only a small fraction of the active phases is attached to silica or is situated in its immediate proximity [69]. There are not many cases

of truly supported catalysts whose final active form is obtained through calcination. The only notable and important instances are  $V_2O_5$ /anatase, used for the oxidation of *o*-xylene to phthalic anhydride, and  $V_2O_5$  deposited on  $TiO_2$  (or various modified supports) used for the selective catalytic reduction of  $NO_x$ . In all these cases, the literature has given much attention to details of impregnation or grafting, in particular the pretreatment of the support, the influence of support modifiers, and the mechanism by which the active element can be attached to the support (e.g. by grafting, by reaction with surface hydroxyls, etc.). However, only general information on calcination has been given.

Literature does not mention any systematic attempt to analyze the process taking place in the transformation of a supported precursor to the corresponding catalytically active supported oxide. Only scattered and too specific information is available. It is thus only possible to mention general ways which, according to circumstances, could be used to provide a better understanding and control of activation by calcination. This is the object of the following paragraphs.

The overall changes in the transformation of the supported precursor to the supported active oxide should obviously be understood. The supported initial precursor and the supported final oxide each correspond to one of the types of supported phase-support interactions described in Figs 3–9. It is very important to identify changes from one picture to another during calcination. The general tendency will be to reach higher thermodynamic stability through:

- (i) the situation of Fig. 3, corresponding to very weak interaction if the oxide and the support have no affinity to each other. The example (Table 1) is  $\alpha$ - $Sb_2O_4$ - $MoO_3$  where the oxides detach from each other during calcination irrespective of the precursors used;
- (ii) the formation of a monolayer or a bilayer (Fig. 6 or 7);
- (iii) the extensive formation of a solid solution or new compounds. These may contribute to anchor the active oxide crystallites to the support. This is approximately the case of the  $V_2O_5$ /anatase catalysts, where one observes very highly dispersed species (perhaps as patches of monolayers), small rafts which are several  $V_2O_5$  lattice units thick, and some dissolution of vanadium in anatase. There are good arguments suggesting that the formation of a solid solution or a compound between the support and the active phase keeps the latter in a higher dispersion state (Section 2.2.2.2).

The simple identification of supported phase-support interaction suggests many ways to control the calcination step: favoring the spreading of the precursor

thanks to adequate additives, inhibiting or promoting the formation of solid solutions or new compounds with the support by adequate doping of the latter, ramping increase of temperature or modification of calcination atmosphere (for controlling oxidation states of elements, which in turn modify the interactions with the support), etc.

A second approach to the understanding of calcination is to suppose that there is an analogy between activation of the supported precursor and the decomposition in the presence of oxygen of the corresponding bulk unsupported phase. Thermal decompositions have been the object of very intensive studies since the early 1940s, and rich information can be found in the classic books [2, 3, 70], in the proceedings of the International Symposia on the Reactivity of Solids, and in journals such as *Solid State Ionics* or *Thermochimica Acta*. With respect to the symposia, we give here reference to the 7th, 8th, 9th and 10th [71–74]; the two subsequent ones (1988, 1992) were published in *Solid State Ionics*. When using analogies with the reaction of bulk compounds, the factors mentioned in Section 2.2.2.0 should be taken into account. These could suggest modifications of the calcination procedure such as previous handling in vacuum or in a reducing atmosphere, or use of a succession of different reaction conditions in order to influence nucleation. The role of water vapor in the calcination furnace is very important: according to the circumstances, it can be detrimental (in particular to dispersion), or favorable (e.g. if it is wished to introduce vacancies into the activated supported oxide).

It is also possible to take advantage of studies dealing with the preparation of supported oxide precursors (namely, oxides to be further activated to produce active metals or sulfides by reduction or sulfidation, respectively). Although there is limited information in this field, some scattered information has been published, essentially for  $MoO_3$  and  $V_2O_5$ . Infrared and Raman spectroscopies have provided data concerning various steps in the transformation of precursor salts to oxides.

Summarizing, it is surprising that activation by calcination and, more generally, the calcination of precursor salts to oxides, has not been the object of more systematic studies. For supported catalysts working in the oxide state, the activation step has the same crucial importance as for metals or sulfides. Although the field is mostly unexplored, understanding calcination is certainly possible, on the basis of the general knowledge on reactions of solids, and using analogies with similar reactions of bulk or supported materials. The physico-chemical techniques now available in catalysis laboratories could provide a wealth of useful information, and allow a better control. These are, among others, the spectroscopic techniques (IR, UV, Raman), XPS, electron transmission microscopy and microanalysis with high spatial resolution.

### 2.2.2.2 Activation of Supported Catalysts by Reduction

In the majority of cases, the last step in the preparation of catalytically active metals is a reduction. The precursor is very frequently an oxide. An oxychloride is the real precursor of active platinum and some noble metals if chlorometal complexes (e.g. chloroplatinic acid) are used. It may be advantageous to use still other precursors and to reduce them directly without any intermediary transformation to oxide. On the other hand, nearly all catalytic metals are used as supported catalysts. The only notable exception is iron for ammonia synthesis, which is a very special case and then the huge body of industrial experience renders scientific analysis of little relevance. The other important metals are Raney nickel, platinum sponge or platinum black, and similar catalysts, but they are obtained by processes other than reduction. This shows the importance of understanding the mechanisms involved in activation by reduction.

Reduction is a typical reaction of a solid. It has been investigated in detail with bulk unsupported materials. The necessary background for the present section, namely that concerning unsupported oxides, can be found in general books [3, 7, 75, 76], the latter for more chemical engineering oriented problems. The backbone of the discussion will be provided by results on the activation of supported nickel catalysts. These catalysts constitute a good example, because the interpretation can benefit from the result of studies dealing with unsupported NiO. The reduction of NiO has been the object of the most extensive fundamental investigation. In addition, the activation of supported nickel catalysts has also been studied in comparatively more detail than other systems.

We shall examine in succession the effect of the dispersion of the precursor, calcination temperature in the preparation of the precursor, nature and amount of precursor, formation of compounds between precursor and supports, nature of support, effect of modifiers, and activation conditions.

#### A General: Effect of Precursor Dispersion

The general tendency is clearly that a more dispersed precursor will correspond to a higher rate of reduction and the production of a more dispersed activated metal, provided chemical interactions do not cause side-effects. This is indeed the trend, for all reactions which are not nucleation limited. However, care should be taken that diffusion limitations in the pores may limit activation in the interior of catalyst particles (beads, pellets, tablets).

As previously mentioned, the situation is more complicated in nucleation-limited (NCI) reactions, where extreme dispersion brings about a diminution of reac-

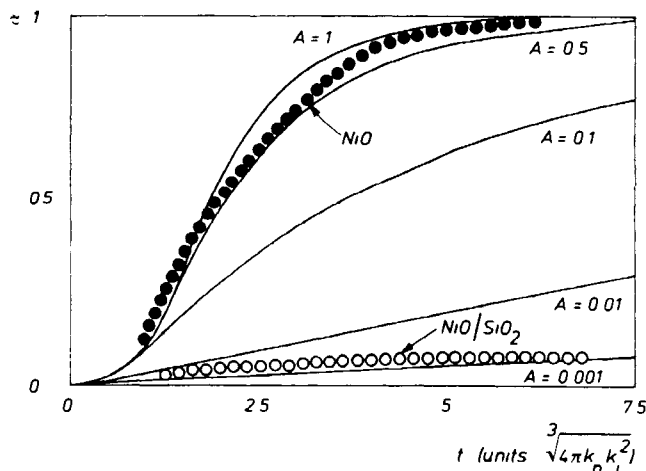


**Figure 12.** Quantitative comparison of the reduction ( $\alpha$  = fraction reduced) of bulk and silica-supported NiO at 538 K in a flow of pure H<sub>2</sub> [78]. The parameter  $A$  characterizes the relative rates of nucleation (constant  $k_n$ ) and interface progress (constant  $k_i$ ). Assuming spherical particles,  $A$  corresponds to the average number of nuclei being formed on each NiO particle in the time necessary for the interface to travel a distance equal to the radius  $a$  of the particle [7]:  $A = 4\pi k_n \times k_i^{-1} a^3$ .

tivity. This effect is illustrated and confirmed by Fig. 12, where the continuous curves correspond to the theory on which Fig. 2 is based and points correspond to experimental data. Electron microscopy data give an average diameter of 500 nm (0.5  $\mu$ m) for bulk NiO [7], and 80–100 nm for NiO/SiO<sub>2</sub> [77]. Figure 12 [78] indicates that the diminution of reactivity of NiO/SiO<sub>2</sub> is due to a reduction of NiO particle size by a factor of about 6 (cube root of the ratio of  $A = 0.5$  for bulk to  $A = 0.002$  for supported NiO). This is about the figure given by electron microscopy (factor of 5–6.3).

The conclusion that nucleation limited the rate of activation by reduction of NiO/SiO<sub>2</sub> precursor was simultaneously proposed following the above deductions [79] and by Coenen, using an impressive series of converging arguments [80].

#### B Overall Effects: Influence of Calcination Temperature in Precursor Preparation

Figure 13 shows the influence of the calcination temperature on the reactivity of NiO supported on silica. The effect is very important [81]. Such effects are often found [82]. These are still more dramatic if the support has not been calcined before impregnation [68].

However, calcination temperature may influence several characteristics of the supported precursor: dispersion, extent of formation of a compound by reaction with the support, etc. The curve giving the fraction of NiO reduced after 40 min suggests the general trends:

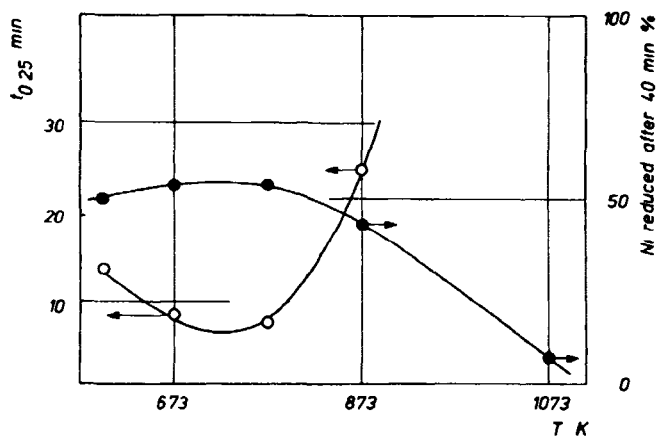


**Figure 13.** Influence of calcination temperature on the reduction of NiO/SiO<sub>2</sub> at 598 K by pure H<sub>2</sub> [81]. SiO<sub>2</sub> 334 m<sup>2</sup> g<sup>-1</sup>, 18.9% wt Ni, calcined at 773 K, 5 h,  $t_{0.25}$  is the time necessary to reduce 25% of the NiO, the degree of reduction obtained after 40 min is indicated on the right-hand axis

between 570 and 770 K, dispersion of NiO diminishes and the reaction rate increases as indicated in the previous subsection. Above 770 K, NiO reacts with silica so that the rate of reduction ( $1/t_{0.25}$ ) and the amount reduced decrease

The various parameters are analyzed separately in the following subsections

### C Role of Precursors

Not surprisingly, the reduction depends on the nature of the precursors, because their overall chemical reactivities are different. Some aspects of the changes, among others, are differences in pure chemical reactivity between compounds (as measured, for example, by rate of interface progress), different states of dispersion, and intervention or not of rate-limiting nucleation processes. As a consequence, the characteristics of the activated catalysts are also different. An interesting illustration of these changes concerns nickel catalysts prepared by incipient wetness impregnation of silica with an aqueous solution of nickel nitrate. One sample was simply dried at 393 K, the other one calcined at 723 K. In neither of these catalysts was nickel silicate detected, but the calcined sample exhibited very sharp X-ray diffraction peaks of NiO [83]. Figure 14 shows the TPR profiles of these samples, together with those of a bulk NiO. Referring to Fig. 2 and Section 2.2.2.2 A, the lower reactivity of supported "calcined" NiO compared to bulk NiO is due to its high dispersion. The temperature programmed reduction (TPR) peak consists of two components, very likely corresponding to two collections of crystallites of different particle size (bimodal size distribution). As shown independently, nickel combined with silica would reduce at temperatures 160–180 K higher [83, 84]. The dried sample reacts 70–90 K lower. The bulk NiO sample

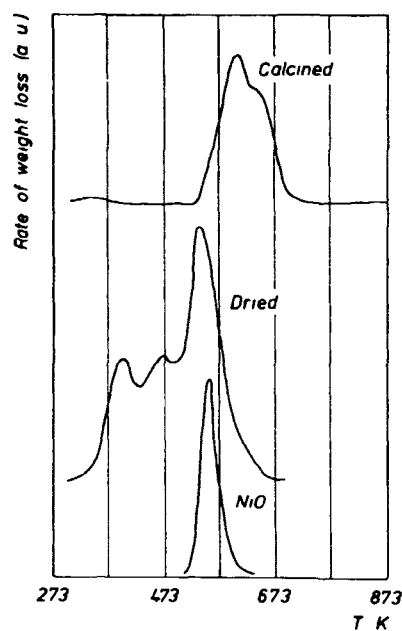


**Figure 14.** Comparison of the TPR profiles of samples of NiO/SiO<sub>2</sub>. SiO<sub>2</sub> surface area 275 m<sup>2</sup> g<sup>-1</sup>, pore volume 0.80 cm<sup>3</sup> g<sup>-1</sup>, pore distribution maximum 8 nm, incipient wetness impregnation by Ni(NO<sub>3</sub>)<sub>2</sub> solution, drying 393 K, 16 h (dried), calcination at 723 K, 16 h (calcined), NiO weight content, on the basis of SiO<sub>2</sub> + NiO, 10.6%, TPR, measured as weight loss, was performed in deoxygenated, predried H<sub>2</sub>, with a heating rate of 10 K min<sup>-1</sup>. The two peaks at 403 and 468 K for the dried sample probably correspond, respectively to dehydroxylation of Ni(OH)<sub>2</sub> and decomposition–reduction of ill-defined compounds containing nitrate ions [83]

used for comparison had been shown to correspond approximately to the maximum reactivity permitted by dispersion (curve 1 of Fig. 2). Nevertheless, the dried sample, with a much higher dispersion than the calcined sample, reacts 25 K lower than bulk NiO (peak at the highest temperature). The dispersion of reduced supported nickel (measured by hydrogen chemisorption, on the assumption of 2 atoms per Ni atom and a surface area of 6.33 Å<sup>2</sup> occupied by one Ni atom) was 20.1% for the dried sample, and only 2% for the calcined sample, after reduction at 773 K for 6 h. This result, which concerns samples which are as comparable as possible, dramatically shows the influence of the chemical nature of the precursor.

This conclusion prompts two observations. The first underlines the difference of reactivity of Ni(OH)<sub>2</sub> or partially decomposed Ni(NO<sub>3</sub>)<sub>2</sub>, on the one hand, and NiO, on the other hand, when used as supported precursors. The second suggests that it is advantageous in many cases to start from uncalcined samples for activation by reduction if deeper reduction and higher dispersion are wanted.

The case of cobalt catalysts supported on silica also suggests interesting differences when either the nitrate

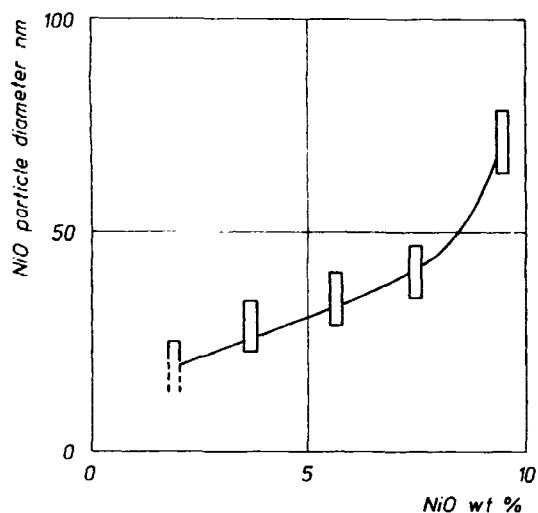


**Figure 15.** Increase in size of crystallites supported on  $\text{SiO}_2$  with increasing amount of NiO [83]. The  $\text{SiO}_2$  used had a surface area of  $415 \text{ m}^2 \text{ g}^{-1}$ , pore volume  $1.12 \text{ cm}^3 \text{ g}^{-1}$ . The samples were obtained by pore volume impregnation with an aqueous solution of nickel nitrate. Calcination was at 773 K for 4 h. The size of the crystallites was determined by electron microscopy.

acetate or chloride is used [82]. The corresponding study, however, did not isolate the effect on impregnation from that on activation.

#### D Influence of the Loading of Deposited Precursor

The influence of the amount of supported precursor is very easy to understand when this precursor mainly forms crystallites. The size of the crystallites tends to increase with the amount deposited (Fig. 15) [68, 79]. The effect on the rate of reduction by hydrogen can easily be inferred from this figure, taking account of Section A.

When the supported phase can form both partial monolayer patches and crystallites, as does  $\text{MoO}_3/\text{SiO}_2$  (case 9), the situation is more complicated, as indicated in Fig. 16. The decrease of reactivity for low loadings is due both to the fact that the reduction of  $\text{MoO}_3$  crystallites to  $\text{MoO}_2$  is nucleation limited (as mentioned in Section A) and that the monolayer patches which coexist with crystallites may have a lower reactivity than the latter. The decrease of reactivity for loadings exceeding 14% is due to the fact that the  $\text{MoO}_3$  crystallites increase in size in a range of dimensions where the role of interface progress is more rate-limiting than nucleation. These effects have been analyzed in some detail [3, 85].

#### E Effect of the Formation of Compounds Between the Precursor of the Active Metal and the Support

Impregnation of  $\text{SiO}_2$  by nickel nitrate brings about very little chemical interaction when calcination is made at low temperature (below 770 K). But the ne-

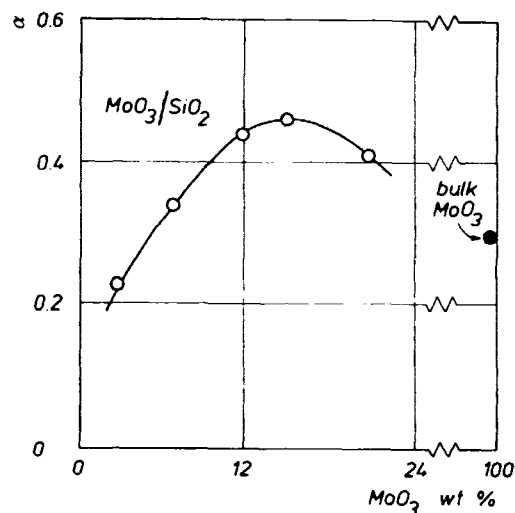


**Figure 16.** Degree  $\alpha$  of reduction of  $\text{MoO}_3/\text{SiO}_2$  to  $\text{MoO}_2/\text{SiO}_2$  after 10 h at 673 K,  $\text{H}_2$  pressure 100 kPa [78].

cessity to increase dispersion leads to the use of other methods [80, 87], in particular the highly successful deposition-precipitation technique (Section 2.2.1.5). This brings about the formation of large amounts of nickel hydroxysilicate, which appear as filaments in electron micrography [80, 83, 87]. Compared with Fig. 14, this corresponds to a considerable decrease of reducibility (Fig. 17), as shown by various authors [83, 84].

The reduction of samples impregnated with nickel hexammine  $[\text{Ni}(\text{NH}_3)_6]^{2+}$  also shows a dramatic decrease in the reduction rate and ultimate degree of reduction, compared to the nitrate-impregnated catalysts [79]. The explanation in that case must take into account two factors which have a parallel influence, namely the formation of a small amount of nickel silicate (or hydroxysilicate) and a much higher dispersion: for a NiO loading of 9.43%, the ratio of the  $\text{Ni}_{2p}$  to  $\text{Si}_{2p}$  XPS bands is multiplied by a factor of about 14 [79].

#### F Nature of the Support

At the end of sub-Section 2.2.2.0.B, we underlined the fact that the state of dispersion and magnitude of the interaction with the support depend strongly on the support. This has necessarily an influence on activation, as shown by a comparison of  $\text{SiO}_2$ ,  $\text{TiO}_2$ , and  $\text{Nb}_2\text{O}_5$  in the case of nickel [86]. Figure 18, taken from a study of the reduction of NiO supported on a range of silica-aluminas [88], illustrates this point. All catalysts were prepared in identical conditions. The reducibility reflects the change in the chemical interaction of NiO with the support, as indicated

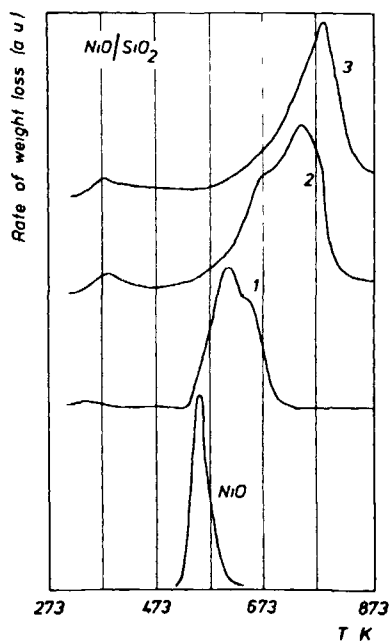


**Figure 17.** Comparison of TPR profiles of samples of NiO/SiO<sub>2</sub> prepared by nitrate impregnation (legend of Fig. 14) or by deposition-precipitation on the same support [83]. The NiO loadings were almost identical (10.6 and 10.9 wt%, on the basis of SiO<sub>2</sub> + NiO): (1) nitrate impregnated, calcined at 723 K (same as in Fig. 14); (2) deposition-precipitation, dried at 393 K for 16 h; (3) same precursor, calcined in the same conditions as the nitrate-impregnated sample. The curve for bulk NiO is added.

- (i) by UV reflection spectra – the presence of Ni<sup>2+</sup> in an octahedral environment on alumina-rich samples (especially SA-15 and SA-40);
- (ii) by XPS – a strong change in the binding energy of nickel, silicon and surface oxygen.

In addition, the dispersion of nickel oxide on the surface increases as expected when the alumina content increases, as indicated by XPS [88, 89].

### G Effect of Modifiers (Promoters)

It can be expected that modifiers considerably alter the course of the activation of catalysts by reduction.

The role of common additives, such as alkali metals used for depressing support acidity, and other additives oppositely promoting acidity, can be inferred from a series of studies using alumina as a support, and cobalt or molybdenum oxide as the supported phase [90–109]. The phenomena are very complex. They result from complicated reactions during its impregnation step, leading to changes of dispersion, migration of species inside pores, and formation of compounds involving the supported phase and the modifier. This considerably alters the reducibility of the supported precursor and the distribution and dispersion of the reduced metal. To our knowledge, this has only been shown

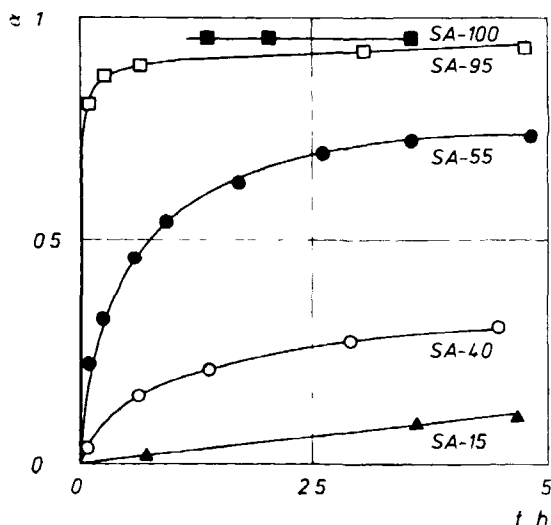


**Figure 18.** Influence of the nature of the support on the reducibility of NiO. Silica aluminas (SA) containing the percentage of SiO<sub>2</sub> indicated in the designation of the sample (e.g. SA-55: 55 wt% SiO<sub>2</sub>) were impregnated by nickel nitrate using pore volume impregnation; NiO content 10 wt%. The samples were dried for 2 h at 383 K, and calcined at 773 K for 6 h. Reduction in pure H<sub>2</sub> (100 kPa) was carried out at 598 K;  $\alpha$  represents the fraction of NiO reduced [88].

quantitatively but not analyzed in detail. One such example is the role of Ba and La for Ni/ $\gamma$ -Al<sub>2</sub>O<sub>3</sub> [110].

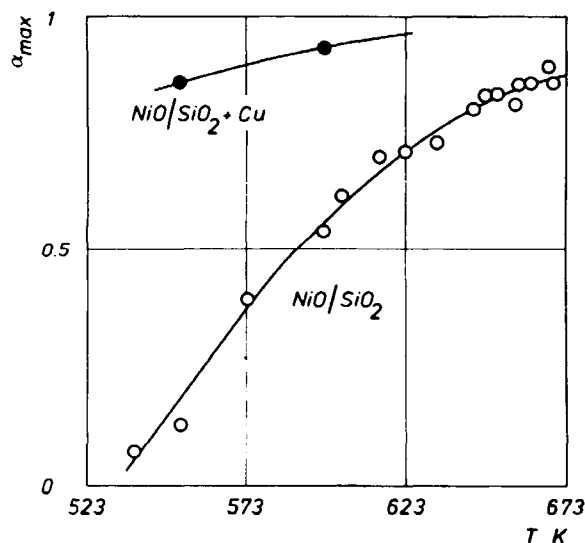
One case deserves special consideration. This is the role of metal additives such as platinum, copper, or donors of spillover hydrogen used in small quantities in comparison with the supported precursor. Figure 19 shows that the maximum degree of reduction,  $\alpha_{\max}$ , of NiO/SiO<sub>2</sub> increases very much when 0.5 wt% copper (as Cu) is added [81]. Platinum and palladium bring about the same kind of effect [81].

Figure 20 compares the amount of NiO reducible at 598 K without ( $\alpha_{\max}$ ) and with copper, for samples of different NiO loading containing 5.3 wt% Cu on the basis of the Ni content. Copper brings about a substantial increase of ultimate reducibility. The proportion of NiO which becomes reducible, thanks to the action of Cu, diminishes as the overall NiO loading increases [81].

The explanation is that Cu (or Pt, or Pd) produces spillover hydrogen which considerably accelerates the nucleation of nickel metal in the reduction conditions. At low loading, the high dispersion of NiO makes that nucleation is rate-limiting if NiO is pure; copper permits nucleation and, consequently, reduction. The effect is proportionally smaller for high NiO loading, because the NiO crystallites are larger and can nucleate more easily (see Sections 2.2.2.0.B.a and 2.2.2.1, and Ref. 3).

This effect had been discovered with unsupported oxides. A review of the results obtained is available





**Figure 19.** Influence of copper as a promoter on the reduction of NiO/SiO<sub>2</sub>. The NiO/SiO<sub>2</sub> sample is the same as for the experiments of Fig. 13. Part of the sample was subjected to a second impregnation with copper nitrate (total Cu added 0.4 wt%) calculated on the total NiO + SiO<sub>2</sub> weight) and calcined at 773 K in air for 5 h. The apparent (or conventional) maximum degree of reduction,  $\alpha_{\max}$ , corresponds to that obtained after 40 min. Reduction in pure hydrogen (100 kPa) [81].

elsewhere [3, 81, 113], as is more data [81, 113–115]. Some publications mention the use of platinum [111, 112] to promote the activation of supported catalysts by reduction.

Let us mention, incidentally, that experiments concerning the influence of other promoters and additives on the reduction of bulk oxide [3, 113–115] can sometimes give pieces of information which are useful for understanding the behavior of supported oxides.

#### H Influence of Activation Conditions

Very few systematic studies have been done concerning the influence of the conditions in which the activation by reduction is carried out. Very notable exceptions are two studies concerning NiO/SiO<sub>2</sub> [80, 116].

A higher temperature always brings about a higher degree of reduction [117], as shown in the preceding section. However, this is accompanied by a loss of dispersion, unless this increase permits the reaction of a *compound* of the active metal. For example, nickel from hydroxy silicates is usually more dispersed and less prone to sintering than nickel from NiO. Extremely high reduction temperatures may lead to the so-called strong metal support interaction (SMSI) effect, or alloying of the active metal with the reduced metallic element of the support, e.g. Ni and Si [118, 119].

The overwhelming majority of activation procedures use hydrogen as reducing gas. Other gases (e.g. CO) can indeed produce carbon deposits. There do not seem

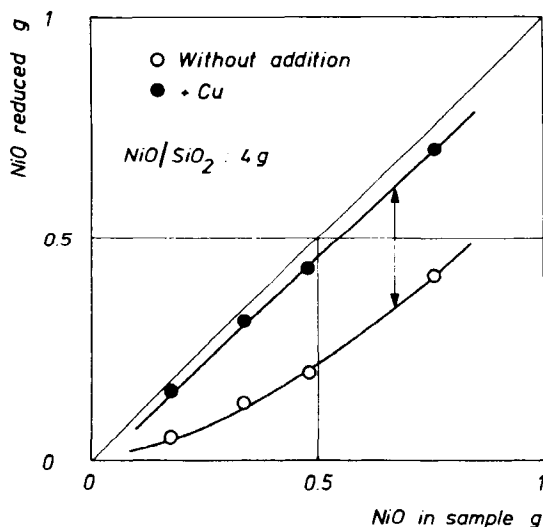


**Figure 20.** Additional reduction of NiO due to copper in NiO/SiO<sub>2</sub> catalysts. Samples of different NiO loadings (wt% of total sample, upper scale; or wt in gram in a 4 g NiO/SiO<sub>2</sub> sample, lower scale) prepared on the same silica and with the same procedure as the samples used for Figs 13 and 19. Copper was introduced as explained in the legend of Fig. 19, in the proportion Cu : Ni = 5.3 wt%. Reduction by pure H<sub>2</sub> (100 kPa) at 598 K. The weight of NiO reduced corresponds to  $\alpha_{\max}$  after 40 min. The double arrow indicates the magnitude of the additional reduction due to copper [81].

to have been studies on the influence of hydrogen pressure on activation. The influence of water seems to be always unfavorable [80, 120], and this for two reasons. The first is that water has an inhibitory effect. Working in the presence of water necessitates higher temperatures, with the consequence of an increased danger of loss of metal surface area by purely thermal sintering. The second reason is that water usually promotes sintering for reasons which are not clarified yet.

It is the opinion of the present contributor that some well-selected additives in the reducing gas could favorably modify dispersion and resistance to sintering of the activated metal, but there are no undebatable proofs of such effects.

#### I Overall View

The actual activation process is the result of all the factors mentioned above and, consequently, relatively complicated. A short article [121] and another one cited above [81], however, suggest that the fundamental approach presented above is very useful in understanding the overall phenomenon and controlling the activation process. Because of this complexity, no single method can provide all the information necessary for optimizing activation by reduction. Temperature programmed reduction used in previous examples and

in many other studies [84, 122] is valuable for providing a first set of data, but it must be completed by techniques adapted to the system (e.g. Mössbauer spectroscopy if Fe is the active phase [123]).

Although nickel catalysts have served as examples, articles dealing with other metals show that the same concepts apply. This is the case for Co deposition on silica or alumina [82], Cu/ $\gamma$ -Al<sub>2</sub>O<sub>3</sub> [124], and Ag/ $\eta$ -Al<sub>2</sub>O<sub>3</sub> and Ag/TiO<sub>2</sub> [125], for example. The preparation of bimetallic catalysts is more complicated because of possible preferential reduction of one metal before the other, a phenomenon well known with the bulk oxides [3]. A few studies suggest that approaches similar to those mentioned above can also be used in these cases [122].

This section, by focussing on the solid-state aspect of activation by reduction, shows the main parameters which are involved, and hence suggests methods for better control, but many aspects remain unclear. One of the strongest phenomena is the increase of thioreistance of Ni/Al<sub>2</sub>O<sub>3</sub> catalysts thanks to controlled partial reduction [126].

### 2.2.2.3 Reduction–Sulfidation

The hydrotreating reactions (hydrodesulfurization, hydrodenitrogenation, hydrodeoxygenation, hydrodemetalation) (Section B.3.8) and some hydrocracking reactions (Section B.3.1.3) use sulfided catalysts. Until very recently, these catalysts contained, as main active species, molybdenum (or sometimes tungsten). They also contained promoters (cobalt or nickel, or sometimes iron). These are the traditional hydrotreating catalysts. Only very recently have noble metals been used for deep hydrodesulfurization or deep dearomatization. The traditional catalysts are prepared by different techniques which all produce, in a more or less perfect way, bilayers containing active metals (Mo or W) and promoters (Co, Ni or Fe) in the oxide state. This corresponds to the precursor structure shown in Fig. 7. The formation of the active sulfided catalysts necessitates a deep reduction–sulfidation of the oxide precursor. This operation, always called *activation* in the field of hydrotreating, is absolutely crucial. Changes in temperature, rate of temperature increase or composition of the reducing–sulfiding medium can bring about variations of activity by factors exceeding 2 or 3, alter the selectivity, and also extend or diminish catalyst life [127].

In the early days of hydrotreating, the precursors were simply contacted with hydrogen and a sulfur-containing feed, usually an ordinary petroleum fraction to which sulfur-containing compounds were added (a so-called “spiked” feed). Later, the catalysts, charged in the reactor, were treated by a special mixture con-

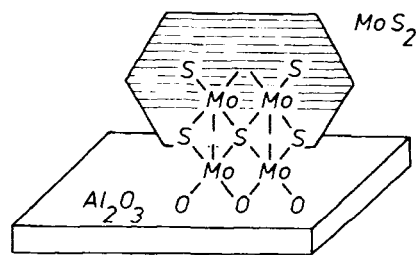


**Figure 21.** Schematic representation of a tiny crystallite of MoS<sub>2</sub> (diameter typically 5–10 nm) attached on the alumina surface in a sulfided hydrotreating catalyst.

taining, in addition to hydrogen, either H<sub>2</sub>S or a sulfur-containing compound very easily decomposed to H<sub>2</sub>S in the presence of hydrogen (e.g. dimethyl disulfide or a mercaptan). However, the operation in a large reactor is still difficult to control. For this reason, it seems that presulfidation outside the reactor may be the solution for the future.

Except for a part of the recent attempts to avoid in situ sulfidation, the activation of traditional hydrotreating catalysts always corresponds to the reaction of hydrogen and sulfur-containing compounds with the oxide precursor. Innumerable recipes are proposed for use in industry and have been described in literature. One article, among many, gives a still valuable overview of the possible procedures [128].

The present section deals only with the traditional catalysts, because too little is known presently on catalysts whose formulation includes noble metals. The objective will be to outline general trends, without attempting the almost impossible task of examining all the various recipes mentioned in the technical or scientific literature. The next section examines some fundamental aspects; subsequent sections outline the influence of various parameters.

### A Fundamental Data

Reduction–sulfidation corresponds to a drastic change of the structure of the active species. The starting bilayer is a two-dimensional oxide adhering to the support (usually alumina) along a continuous interface. The active catalyst is constituted of tiny crystallites attached to this support by small patches of transition interfaces (Fig. 21). The whole reduction–sulfidation reaction involves many simultaneous or successive processes: reduction of Mo<sup>6+</sup> to Mo<sup>4+</sup>, sulfidation of Mo<sup>4+</sup> to MoS<sub>2</sub>, sulfidation of the Group VIII metal initially in an oxide state to a sulfide, destruction of the bilayer, and formation of crystallites. The Group VI and VIII metals, initially associated in the bilayer, segregate to a large extent in the sulfided state (the extent of segregation is still being debated [129–132]). The existence of strong coupling effects in reactions of sol-

ids [3, 133] makes the full analysis of the process difficult, but suggests that many parameters can have a strong influence on the structure and texture of the final sulfided catalyst.

The most striking result of these coupling effects appears at a macroscopic scale, when reduction and sulfidation as a whole are considered.  $\text{MoO}_3$  is reduced at much lower temperatures (sometimes 200 K lower) in a  $\text{H}_2\text{S}/\text{H}_2$  mixture than in pure  $\text{H}_2$  [134, 135]. Starting from already reduced molybdenum, namely  $\text{Mo}^{4+}$  in  $\text{MoO}_2$ , sulfidation takes place at a lower rate than when reduction and sulfidation are simultaneous (namely when starting from  $\text{Mo}^{6+}$ , i.e.  $\text{MoO}_3$ ). The presence of cobalt (or nickel) probably has a slightly promoting effect on the reduction [136–138] because the corresponding oxides are more easily reduced and sulfided than molybdenum (or tungsten).

The explanation of the coupling effect is probably the following. The reduction of  $\text{MoO}_3$  to  $\text{MoO}_2$  is nucleation rate-limited [139]. Spillover hydrogen accelerates the reaction [115, 140, 141]. Because it adsorbs dissociatively on the surface [139, 142],  $\text{H}_2\text{S}$  probably also produces a reactive H species, promoting nucleation of lower Mo oxides at low temperature and, as a consequence, further reduction. The tiny nuclei of the thus-formed suboxide react easily to sulfides because of their high state of dispersion. In contrast,  $\text{MoO}_2$  produced by separate reduction has a well organized lattice and is much less reactive.

The above conclusions are based on fundamental studies of Steinbrunn and co-workers [139, 143]. The results of these authors also shed some light on the origin of the coupling effect. Upon reduction–sulfidation with pure  $\text{H}_2\text{S}$ , the surface of  $\text{MoO}_3$  is first reduced to  $\text{MoO}_2$ , then sulfided at a much slower rate to  $\text{MoS}_2$  [143]. During reaction with  $\text{H}_2\text{S}/\text{H}_2$  mixtures, a more complicated mechanism sets in, which leads to the formation of highly dispersed  $\text{MoS}_2$  clusters [139, 144].  $\text{MoS}_2$  crystals are formed only at a later stage. The reduction step (to  $\text{MoO}_2$ ) turns out to be slower with  $\text{H}_2\text{S}/\text{H}_2$  than with  $\text{H}_2\text{S}$ . Some refinements were obtained with  $\text{MoO}_3$  thin films [145]. Studies with composite thin films of  $\text{MoO}_3$  evaporated on a freshly cleaned CoO surface indicate that these observations are still valid in the presence of cobalt [146]. The success of the reduction–sulfidation is due to the better balance between reduction and sulfidation rates. Thanks to this better balance, the formation of much smaller  $\text{MoS}_2$  domains (cluster, instead of crystallites) is possible. This is very important for the activation of hydro-treating catalysts, because smaller crystallites of the active phase are finally formed.

A comparison with studies on supported catalysts containing only cobalt or molybdenum [19, 20, 147–149] shows that the simultaneous presence of both elements profoundly alters the processes. This is linked to

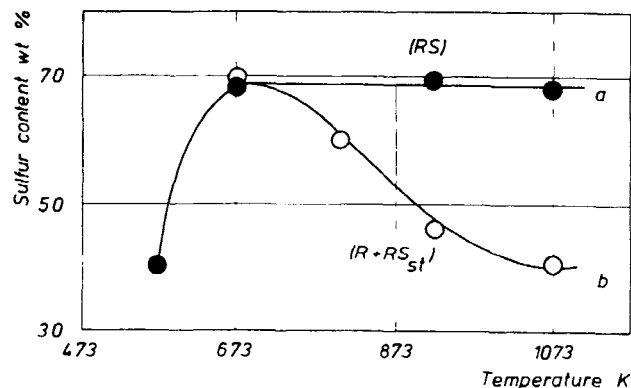


**Figure 22.** Comparison of the sulfur content of a commercial CoMo catalyst (Procatalyse HR 306) activated by simultaneous reduction–sulfidation (RS) or by reduction followed by sulfidation ( $\text{R} + \text{RS}_{\text{st}}$ ). (a) Simultaneous reduction–sulfidation by a  $\text{H}_2\text{S}/\text{H}_2$  mixture (15%  $\text{H}_2\text{S}$  by volume). Except for the experiment at 573 K, the samples were first reacted for 4 h at 673 K, then progressively heated to the reaction temperature indicated in the figure and maintained at that temperature for 4 h. (b) Reduction at the indicated temperature for 4 h, followed by sulfidation with the  $\text{H}_2\text{S}/\text{H}_2$  mixture at 673 K for 4 h ( $\text{RS}_{\text{st}}$  subscript denotes standard temperature) [138].

the existence of the CoMo oxide bilayer, and partly due to the interaction of both elements in the reduction–sulfidation, partly also to the segregation of cobalt from molybdenum in this process. The reduction sulfidation of cobalt molybdate  $\text{CoMoO}_4$  seems of little relevance [144, 150]; the reason is perhaps that it gets sulfided *before* sufficient reduction, as shown by gravimetry [151].

## B Influence of the Sequence of Steps in Reduction–Sulfidation

The coupling between reduction and sulfidation brings about complex phenomena in the activation of hydro-treating catalysts. A very direct consequence of the above discussion is the different degree of sulfidation reached if the precursor is, on the one hand, simultaneously reduced and sulfided or, on the other hand, reduced first and sulfided afterwards (Fig. 22). Sulfidation of the prerduced catalyst becomes increasingly less efficient as reduction temperature increases. This is presumably due to the growth of  $\text{MoO}_2$  crystallites which become increasingly more refractory to sulfidation. When carried out at low temperature (below about 600 K), a preliminary reduction step is much less harmful. Such a prerduction has even been recommended. The reason is probably that the Group VIII metal gets reduced, segregates and, in the form of sulfide, enhances the production of spillover hydrogen in the subsequent reduction–sulfidation.

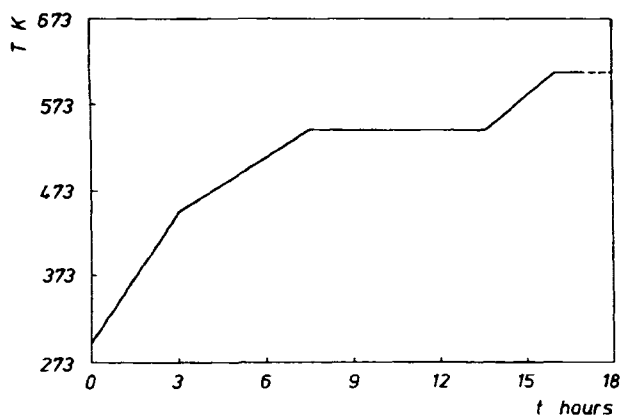


**Figure 23.** Typical modification of reactor temperature versus time in the activation of a  $\text{CoMo}/\gamma\text{-Al}_2\text{O}_3$  catalyst with a spiked feed.

The crucial experiment of Fig. 22 can be analyzed in more detail [138].  $\text{Mo}^{5+}$  species can be detected by XPS in series (R + RS), not in series (RS), indicating incomplete reduction. The gain in weight due to sulfidation takes place more rapidly in (RS) than in the (RS) step of (R + RS) experiments. This is paradoxical, as oxygen is removed in (RS), thus partially compensating the weight gain due to the introduction of sulfur by a weight loss. This demonstrates that sulfidation is more rapid when starting from  $\text{Mo}^{6+}$  than from reduced forms of molybdenum. NO adsorbed on Mo ions exhibits a special IR band at  $1680\text{--}1700\text{ cm}^{-1}$ , the position of which is characteristic of the reduction state of Mo. After the (R + RS) treatment, some deeply reduced Mo ions are present on the surface, whereas in (RS) catalysts only  $\text{Mo}^{4+}$  ions are observed. This proves that sulfidation is difficult when starting from  $\text{Mo}^{4+}$  ions [134, 138].

### C Influence of Activation Temperature

The changes in activation procedure lead to very large modifications of the activity and selectivity of catalysts, as could be expected from the data of the previous subsection. In view of the previous comments, it is not surprising that activation of HDN or HDS catalysts in the industrial plant must be conducted according to well controlled procedures. The temperature being a major parameter, as suggested by Fig. 22, it is recommended in all in situ activation procedures that the temperature be raised stepwise. Figure 23 is an example of such a temperature vs. time heating procedure. However, the precise procedure to use depends on the catalyst, the nature of the sulfur-containing compound used for sulfidation, and all other operating conditions [128]. The objective of the present discussion is to outline the fundamental phenomena which could justify these procedures.

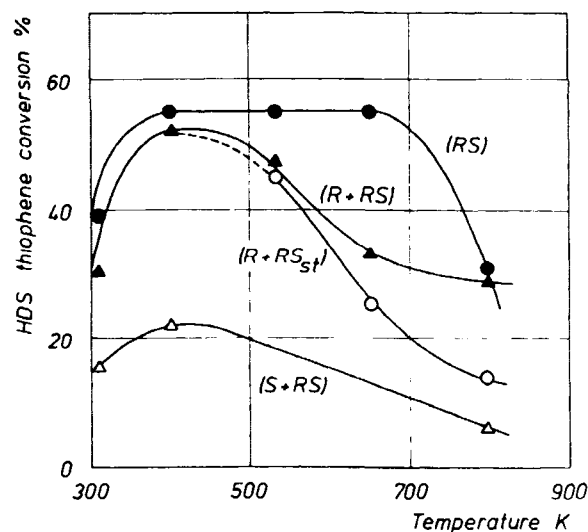


**Figure 24.** Hydrodesulfurization activity of catalysts (Procatalyse HR 306) activated according to different procedures at different temperatures: (RS) simultaneous reduction–sulfidation (15%  $\text{H}_2\text{S}$  in  $\text{H}_2$ ) – except for the experiment at 573 K, the samples were first reacted for 4 h at 673 K, then progressively heated to the temperature indicated in the figure and maintained at this temperature for 4 h; (R + RS) successive reduction in  $\text{H}_2$  (4 h) and reduction–sulfidation, as above (4 h), both at the temperature indicated; (R + RS<sub>st</sub>) reduction at the temperature indicated (4 h) followed by reduction–sulfidation at 673 K (4 h) as above; (S + RS) sulfidation by pure  $\text{H}_2\text{S}$  (4 h) followed by reduction–sulfidation as above (4 h), both steps at the temperature indicated. The reaction with hydrogen with a feed containing 0.5% thiophene and 30% cyclohexene in cyclohexane was made under a total pressure of 3 MPa [138, 152].

The dramatic influence of temperature is always conspicuous, without consideration of the reduction–sulfidation procedure used. Figures 24 and 25 correspond to activity in hydrodesulfurization and hydrogenation, respectively, where both reactions (HDS of thiophene and hydrogenation of cyclohexene) occurred simultaneously in a continuous flow equipment under a pressure of 3 MPa [138, 152]. In addition to the procedures used for the results of Fig. 22, samples were also successively reduced and then sulfided at the same temperature (procedure R + RS; note that there is here no subscript) or, alternatively, were sulfided by pure  $\text{H}_2\text{S}$  and subsequently reduced–sulfided, at the same temperature (S + RS). The activities change dramatically. A careful examination of the figure shows that the HDS/hydrogenation selectivity also changes. For the (RS) series, the selectivity varies by a factor larger than 2. Selectivity to HDS is the lowest after activation at 673 K; similar high selectivities are observed for both 573 K and 1073 K [153].

Understandably, the  $\text{MoS}_2$  crystallites grow larger as the activation temperature increases. Electron microscopy shows that the ratio of the total edge plane area to that of the basal planes changes little (by about

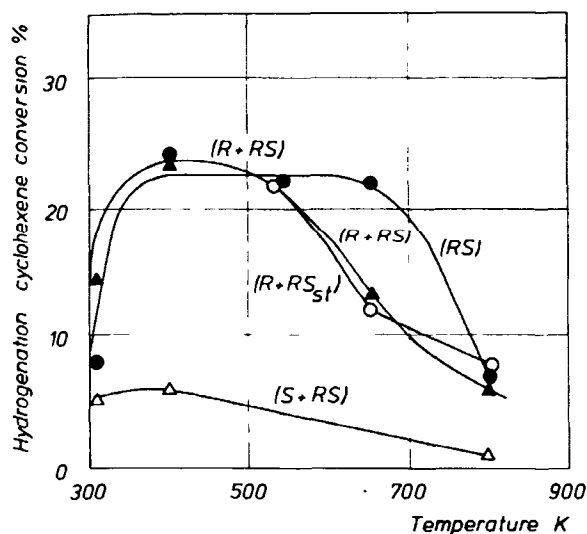


**Figure 25.** Hydrogenation activity of catalysts activated according to different procedures. The experimental conditions are described for Fig. 24 [138, 152].

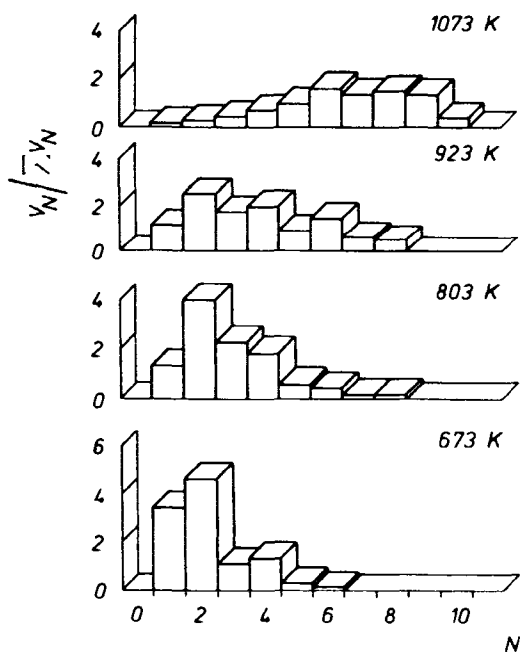
$\pm 20\%$ ). The area of the edge planes relative to the volume of the crystallites decreases considerably (by a factor of 5) for activation temperatures growing from 673 to 1073 K [153]. This reflects a proportional change of both the diameter and thickness of the crystallites. Figure 26, which shows the distribution in thickness of the  $\text{MoS}_2$  stacks, indicates how the repartition in size varies with temperature [153]. Infrared studies of adsorbed NO, ISS studies [138, 152, 154] as well as  $^{57}\text{Co}$  Mössbauer emission studies have also been made. When the activation temperature increases, the signal of cobalt pseudoaluminate (or cobalt aluminate-like species) diminishes, indicating that part of the cobalt strongly bound to alumina reacts. The signal attributed to the so-called "Co–Mo–S" phase gets strongly decreased at 923 K, although the catalytic activity remains high (Fig. 27) [152, 155, 156].

Among many studies, three additional systematic studies of the influence of temperature must be cited here [157–159].

#### D Influence of the Sulfiding Molecule

It has long been known that the nature of the feed, the spiking of the feed, and the chemical nature of the sulfiding molecules generally, are of considerable importance [128, 160, 161]. This is illustrated by Figs 28 and 29 concerning the hydrodesulfurization of thiophene and the hydrogenation of cyclohexene [160]. The optimal temperature for activation is different according to the sulfur containing molecule. As in Figs 24 and 25, it is noteworthy that changing the activating molecule modifies the selectivity.

There is no explanation yet for this effect, except that the very delicate coupling effects between the various



$$V_N = \frac{1}{n} N D_n^2$$

**Figure 26.** Variation of the size of the  $\text{MoS}_2$  crystallites on supported CoMo catalyst (Procatalyse HR 306) obtained after activation at different temperatures (procedure RS, see captions for the above figures) as determined by high resolution electron microscopy. The figure considers the collection of crystallites (number  $n$ ) with the same number  $N$  of  $\text{MoS}_2$  layers (thickness  $N$ ). The total volume of each collection can be calculated as indicated in the figure. The fraction in volume (or weight) that each collection represents in the overall sample,  $V_N / \sum V_N$  gives the height of the corresponding bar in the figure [153].

elementary reactions mentioned in subsection A are modified when a different source of sulfur is used. The possible formation of highly dispersed carbon in the case of some organic molecules could also explain some differences.

#### E Other Results

Other notable data on the reduction–sulfidation of  $\text{CoMo}/\text{Al}_2\text{O}_3$  catalysts can be found in articles not mentioned yet [162, 163]. In a work using supports calcined at various temperatures, incomplete reduction or reduction–sulfidation according to several procedures and characterization of used samples, an attempt has been made to obtain a more in-depth understanding of activation. The merit of the article is to show that accepted conclusions still hold when the activation is conducted in a wider investigation range than in previous studies [164]. The activation of hydrodesulfurization or hydrodenitrogenation catalysts other

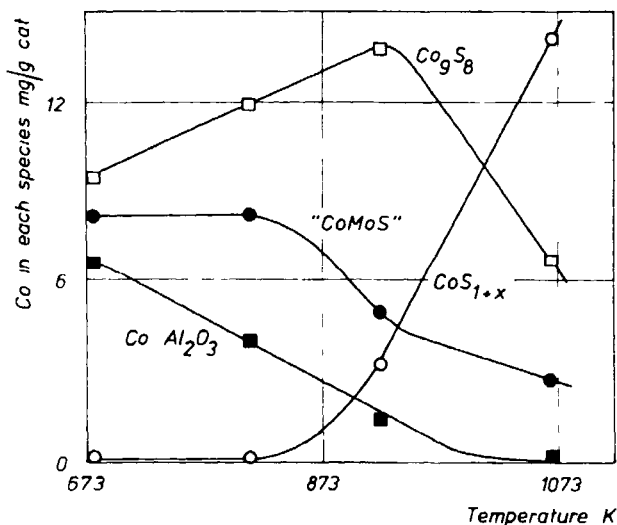


**Figure 27.** Distribution of cobalt among the various species of an activated HDS catalyst, as determined by emission Mössbauer spectroscopy. The catalyst, prepared by impregnation of ammonium heptamolybdate and  $^{57}\text{Co}$  nitrate, was as similar as possible to the commercial one used for obtaining the results presented in the previous figures (3 wt% as  $\text{CoO}$ , 13 wt% as  $\text{MoO}_3$  on  $\gamma$ -alumina). All precautions were taken to avoid possible errors due to noninstantaneous charge compensation in the sequence of nuclear events in  $^{57}\text{Co}$  decay (this has to be taken into account in the nonconducting  $\text{MoS}_2$  matrix) [155, 156].

than  $\text{CoMo}$  has also been the object of various studies:  $\text{NiMo}$  [165–168],  $\text{NiW}$  [163, 169],  $\text{FeMo}$  [170].

## F Outlook

The tendency at present is to presulfide the catalyst before loading the reactor. This is logical, as it permits a better control of the activation. The control of the activation process is easier in a dedicated plant than in gigantic reactors where temperature control is problematic and uniformity of composition of the sulfiding mixture is practically impossible to achieve.

A new technology is emerging for avoiding the pitfalls of in situ activation. It essentially consists in coating the precursor (oxide) catalyst with a mixture of organic sulfides or polysulfides. The technique had its origin in in situ soaking techniques developed in the late 1970s [128]. Some data are available on some of these new techniques [171]. The effect of this sort of presulfiding with alkylpolysulfides has been discussed [172]. The decomposition of the polysulfides at low temperature releases active species which permit sulfidation at low temperature. We speculate that these active species responsible for the efficiency of the process are not only sulfur but also hydrogen.

### 2.2.2.4 Other Methods of Activation

Some steps at the end of catalyst manufacture are sometimes called activation. This is the case, for ex-

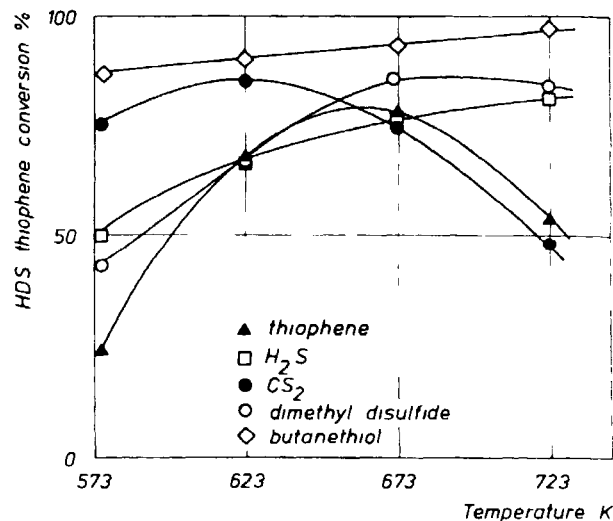


**Figure 28.** Influence of the nature of the sulfiding agent on HDS activity. The catalyst was Procatalyse HR 306. The amount of sulfiding agent was calculated in order to obtain a sulfur content of 3 wt% in the charge (hexane). The precursor samples (2 g) were heated in argon ( $36 \text{ L h}^{-1}$ , 3 MPa) up to the desired activation temperature. The argon was then replaced by hydrogen ( $36 \text{ L h}^{-1}$ ) and the feed introduced (liquid hourly space velocity  $42 \text{ h}^{-1}$ ). Activation time was 4 h. Activity measurements were made as explained for Fig. 24 [160].

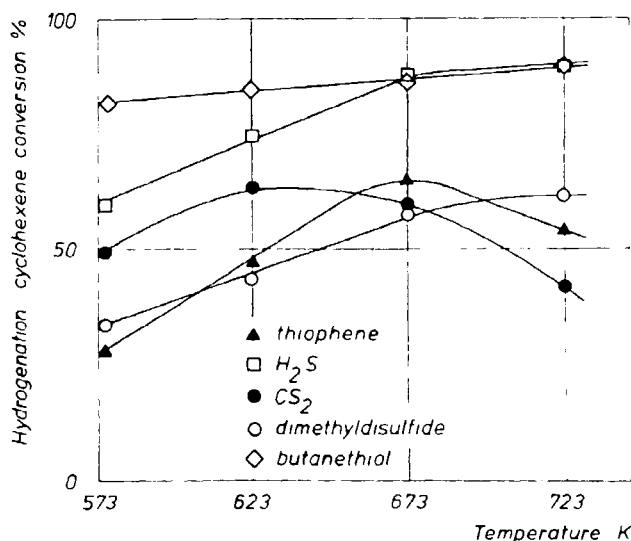


**Figure 29.** Influence of the nature of the sulfiding agent on hydrogenation activity. Conditions as indicated for Fig. 28 [160].

ample, for the leaching step in the preparation of Raney nickel (Section A.2.1.2); however, this is a special case. A situation which is closer to the topics discussed in the present section is the spontaneous activation which takes place when precursors are contacted with the reacting mixture or feed. It was mentioned in the previous subsection that catalysts were activated in this way in the early development of hydrotreatments.

Another example is the activation of vanadium phosphate (VPO) catalysts in the oxidation of butane to maleic anhydride: the fixed-bed VPO catalyst has to be contacted for several days with air-butane mixture before reaching normal activity. This case and that of Raney nickel (both unsupported) fall outside the scope of the present discussion

### 2.2.2.5 Conclusions

Although crucial for activity, selectivity, and sustained activity for long periods (catalyst life), the activation of catalysts has not yet been systematically investigated. This article suggests that a methodical study of activation is possible. Scientific interpretation is very often possible and leads to the design of improved procedures. The equipment generally available in most catalysis laboratories, in industry, university, and research institutes, is sufficient for gathering the necessary information. Well established mechanisms explain the phenomena observed. Unfortunately, the science of the reactivity of solids is often ignored, and this hampers proper interpretation and limits the development of improved activation procedures. This article hopefully shows that a better multidisciplinary approach can provide a much clearer picture of the various facets of activation of supported catalysts.

## References

- J Haber *Pure Appl Chem* **1991**, *63*, 1227-1246
- A K Galwey, *Chemistry of Solids*, Chapman and Hall, London, **1967**, Chapter 5
- V V Boldyrev, M Bulens, B Delmon, *The Control of the Reactivity of Solids*, Elsevier, Amsterdam, **1979**, Chapter 2
- W A Johnson, R F Mehl, *Trans Amer Inst Min Metall Engrs* **1939**, *135*, 416-459
- K L Mampel, *Z Phys Chem* **1940**, *A187*, 43-57
- K L Mampel, *Z Phys Chem* **1940**, *A187*, 235-248
- B Delmon, *Introduction a la cinetique heterogene*, Ed Technip, Paris, **1969**, Chapter 11
- J L Lemaître in *Characterization of Heterogeneous Catalysts* (Ed F Delannay), Marcel Dekker, New York, **1984**, p 29-70
- G C Stevens, T Edmonds in *2nd International Symposium on Preparation of Catalysts* (Eds B Delmon, P Grange, P A Jacobs, G Poncelet), Louvain, la-Neuve, **1978**, 507-517
- A Cimino, B A Angelis, *J Catal* **1975**, *36*, 11-22
- B Delmon in *Interfaces in New Materials* (Eds P Grange, B Delmon), Elsevier, London, **1991**, pp 1-11
- J Sonnemans, P Mars, *J Catal* **1973**, *31*, 209-219
- J M J G Lipsch, G C A Schuit, *J Catal* **1969**, *15*, 174-178
- M Dufaux, M Che, C Naccache, *J Chim Phys* **190**, *67*, 527-534
- V H J De Beer, T H M van Sint Fiet, J F Engelen, A C van Haandel, M V J Wolfs, C H Hamberg, G C A Schuit, *J Catal* **1972**, *27*, 357-368
- G C A Schuit, B C Gates, *AI Chem J* **1973**, *19*, 417-438
- W K Hall, M Lojaco, in *6th International Congress on Catalysis*, (Eds G C Bond, P B Wells, E C Tompkins), The Chemical Society, London, **1977**, 246-254
- P Gajardo, R I Declerck-Grimee, G Delvaux, P Olodo, J M Zabala, P Canesson, P Grange, B Delmon, *J Less Common Met* **1977**, *54*, 311-320
- R I Declerck-Grimee, P Canesson, R M Friedman, J J Fripiat, *J Phys Chem* **1978**, *82*, 885-888
- R I Declerck-Grimee, P Canesson, R M Friedman, J J Fripiat, *J Phys Chem* **1978**, *82*, 889-894
- P Canesson, C Defosse, R I Declerck-Grimee, B Delmon, *5th Ibero-American Symp on Catalysis*, Lisbon, **1976**, paper A3-8
- G C Stevens, T Edmonds in *Chemistry and Uses of Molybdenum* (Eds P C H Mitchell, A Seamen), Clmax, **1976**, 155-159
- A Miller, W Atkinson, M Barber, P Swift, *J Catal* **1971**, *22*, 140-142
- A W Armour, P C H Mitchell, B Folkesson, R Larsson, *J Less-Common Met* **1974**, *36*, 361-365
- A Lycourghiotis, C Defosse, F Delannay, B Delmon, *J Chem Soc Faraday Trans 1* **1980**, *76*, 2052-2064
- H Knozinger in *Proceedings 9th International Congress on Catalysis* (Eds M J Phillips, M Ternan), The Chemical Institute of Canada, Calgary, **1988**, 20-53
- B Delmon, P Grange, M A Apecetche, P Gajardo, F Delannay, *C R Acad Sci Sér C* **1978**, *287*, 401-403
- P Gajardo, P Grange, B Delmon, *J Catal* **1980**, *63*, 201-216
- F Delannay, E N Haeussler, B Delmon, *J Catal* **1980**, *66*, 469-472
- H Knozinger, H Jeziorowski, E Taglauer, *Proc 7th Intern Congr Tokyo* (Eds T Seiyama, K Tanabe), Kodansha and Elsevier, Tokyo and Amsterdam, **1981**, Vol 1, 604-615
- J B d'Espinose de la Callere, C Bobin, B Rebours, O Clause in *Preparation of Catalysts VI* (Eds G Poncelet, J Martens, B Delmon, P A Jacobs, P Grange) Elsevier, Amsterdam, **1995**, 169-184
- P Grange, H Charcosset, Y Trambouze, *J Thermal Anal* **1969**, *1*, 311-317
- Ch Marcellis, B Delmon, *J Catal* **1972**, *24*, 336-346
- A P Hagan, C O Arean, F S Stone, in *Reactivity of Solids* (Eds J Wood, O Lindqvist, C Helgesson, N G Vannerberg), Plenum Press, New York, **1977**, 69-74
- M Lojaco, A Cimino, G C A Schuit, *Gazz Chim Ital* **1973**, *103*, 1281-1295
- M Lojaco, M Schiavello, A Cimino, *J Phys Chem* **1971**, *75*, 1044-1050
- M Lojaco, M Schiavello, D Cordischi, G Mercati, *Gazz Chim Ital* **1975**, *105*, 1165-1176
- M Lojaco, M Schiavello in *Preparation of Catalysts* (Eds B Delmon, P A Jacobs, G Poncelet), Elsevier Amsterdam, **1976**, 473-484
- N Giordano, J C J Bart, A Vaghi, A Castellan, G Matinotti, *J Catal* **1975**, *36*, 81-92
- G N Asmolov, O V Krylov, *Kinet Katal* **1970**, *11*, 1028-1033
- X L Xiong, L T Weng, B Zhou, B Yasse, E Sham, L Daza, F Gil-Llambias, P Ruiz, B Delmon in *Preparation of Catalysts V* (Eds G Poncelet, P Grange, P A Jacobs, B Delmon) Elsevier Amsterdam, **1991**, p 537-546
- R Castillo, B Koch, P Ruiz, B Delmon, *J Mater Chem* **1994**, *4*, 903-906
- R Castillo, B Koch, P Ruiz, B Delmon in *Preparation of Catalysts VI* (Eds G Poncelet, J Martens, B Delmon, P A Jacobs, P Grange) Elsevier, Amsterdam, **1995**, 291-298
- B Delmon, *J Mol Cat* **1990**, *59*, 179-206

- 45 B Zhou, B Doumain, B Yasse, P Ruiz, B Delmon in *Proc 9th Int Congr Catalysis* (Eds M J Phillips, M Ternan), Ottawa, **1988**, 4, 1850–1857
- 46 B Zhou, E Sham, P Bertrand, T Machej, P Ruiz, B Delmon *J Catal* **1991**, 132, 157–182
- 47 L T Weng, B Zhou, B Yasse, B Doumain, P Ruiz, B Delmon in *Proc 9th Int Congr Catalysis* (Eds M J Phillips, M Ternan), Ottawa **1988** 4 1609–1616
- 48 M V E Rodriguez, B Delmon, J P Damon in *Proc 7th Int Congr on Catalysis* (Eds T Seiyama, K Tanabe), Kodansha and Elsevier, Tokyo and Amsterdam **1981**, 1141–1153
- 49 J M D Tascon, P Bertrand, M Genet, B Delmon *J Catal* **1986**, 97, 300–311
- 50 J Haber *Pure Appl Chem* **1984** 56, 1663
- 51 F Delannay, P Gajardo, P Grange, *J Microsc Spectrosc Electron* **1978**, 3, 411–426
- 52 P Gajardo, D Pirotte, C Defosse, P Grange, B Delmon, *J Electron Spectroscop Relat Phenom* **1979** 17 121–135
- 53 S R Stampfl, Y Chen, J A Dumesic, Chunming Niu, C G Gill Jr, *J Catal* **1987**, 105, 445–454
- 54 DuSung Kim, I E Wachs, K Segawa, *J Catal* **1994**, 146, 268–277
- 55 M A Beñares, Hangchun Hu, I E Wachs, *J Catal* **1994**, 150, 407–420
- 56 P Gajardo, P Grange, B Delmon, *J Phys Chem* **1979**, 83, 1771–1779
- 57 P Gajardo, D Pirotte, P Grange, B Delmon, *J Phys Chem* **1979**, 83, 1780–1786
- 58 K Y S Ng, E Gulari, *J Catal* **1985**, 92, 340–354
- 59 Y C Liu, G L Griffin, S S Chan, I E Wachs, *J Catal* **1985**, 94, 108–119.
- 60 G C Bond, S Flamerz, L van Wijk, *Catal Today* **1987**, 1, 229–243
- 61 J G Eon, E Bordes, A Vejux, P Courtine, in *Proc 9th Int Symp Reactivity of Solids* (Eds K Dyrek, J Haber, J Nowotny), Cracow, PWN, Warsaw, **1982**, Vol 2, 603–612
- 62 T Machej, B Doumain, B Yasse, B Delmon, *J Chem Soc Faraday Trans 1* **1988**, 84, 3905–3916
- 63 M El Jamal, PhD Thesis, Université Claude Bernard, Lyon, **1987**
- 64 M El Jamal, M Forissier, G Couduner, J C Vadrine, in *Proc 9th Int Congr Catalysis* (Eds M J Phillips, M Ternan), Ottawa, **1988**, 4, 1617–1623
- 65 P Biloen, G T Pott, *J Catal* **1973**, 30, 169–174
- 66 A Castellán, J C J Bart, A Vaghi, N Giordano, *J Catal* **1976**, 42, 162–172
- 67 V H J De Beer, M J M Van der Aalst, C J Machiels, G C A Schuit, *J Catal* **1976**, 43, 78–89
- 68 S Narayanan, K Uma, *J Chem Soc Faraday Trans 1* **1985**, 81, 2733–2744
- 69 F Delannay, *Characterization of Heterogeneous Catalysts*, Marcel Dekker, New York, **1984**, 113–115
- 70 W E Garner, *Chemistry of Solids*, Butterworth, London, **1955**
- 71 J S Anderson, M W Roberts, F S Stone, *Reactivity of Solids*, Chapman and Hall, London **1973**
- 72 J Wood, O Lindqvist, C Helgesson, N-G Vannerberg, *Reactivity of Solids*, Plenum Press, New York and London, **1977**
- 73 K Dyrek, J Haber, N Nowotny, *Proc 9th Int Symp Reactivity of Solids*, Elsevier, Amsterdam, **1982**
- 74 P Barret, L C Dufour, *Reactivity of Solids*, Elsevier, Amsterdam, **1985**
- 75 P Barret, *Cinétique hétérogène*, Gauthier-Villars, Paris, **1973**
- 76 J Szekeley, J W Evans, Hong Yong Sohn, *Gas-solid reactions*, Academic Press, New York, **1976**
- 77 M Montes, Ph D Thesis, Université Catholique de Louvain **1984**
- 78 B Delmon, M Houalla in *Preparation of Catalysts II* (Eds B Delmon, P Grange, P A Jacobs, G Poncelet) Elsevier Amsterdam **1979**, 439–464
- 79 M Houalla, F Delannay, I Matsuura, B Delmon *J Chem Soc Faraday Trans 1* **1980**, 76, 2128–2141
- 80 J W E Coenen in *Preparation of Catalysts II* (Eds B Delmon, P Grange, P A Jacobs, G Poncelet) Elsevier Amsterdam **1979** 89–111
- 81 A Roman, B Delmon *J Catal* **1973** 30 333–342
- 82 M P Rosynek, C A Polansky *Appl Catal* **1991** 73 97–112
- 83 M Montes, Ch Penneman de Bosscheyde, B K Hodnett, F Delannay, P Grange, B Delmon *Appl Catal* **1984** 12 309–330
- 84 J A Moulijn, P W N M van Leeuwen, R A van Santen *Catalysis* Elsevier, Amsterdam, **1993**, 355
- 85 J Masson, J Nechtschein, *Bull Soc Chim Fr* **1968** 3933
- 86 E I Ko, J M Hupp, F H Rogan, N J Wagner *J Catal* **1983** 84, 85–94
- 87 L A M Hermans, J W Geus in *Preparation of Catalysts II* (Eds B Delmon, P Grange, P A Jacobs, G Poncelet) Elsevier Amsterdam **1979**, 113–142
- 88 M Houalla, B Delmon in *Reactivity of Solids* (Eds K Dyrek, J Haber, J Nowotny), Elsevier, Amsterdam **1982**, 923–926
- 89 M Houalla, B Delmon, *J Phys Chem* **1980** 84 2194–2199
- 90 M Houalla, B Delmon, *CR Acad Sci Paris Ser C* **1980** 290, 301–303
- 91 M Houalla, J Lemaître, B Delmon, *J Chem Soc Faraday Trans 1* **1982** 78, 1389–1400
- 92 M Houalla, B Delmon, *CR Acad Sci Paris Ser C* **1979** 289 77–80
- 93 A Lycourghiotis, C Defosse, B Delmon, *Rev Chim Minerale* **1979**, 16, 473–476
- 94 A Lycourghiotis, C Defosse, F Delannay, J Lemaître, B Delmon, *J Chem Soc, Faraday Trans 1* **1980** 76 1677–1688
- 95 A Lycourghiotis, C Defosse, F Delannay, B Delmon *J Chem Soc Faraday Trans 1* **1980**, 76, 2052–2064
- 96 A Lycourghiotis, C Defosse, B Delmon, *Bull Soc Chim Belg* **1980**, 89, 929–935
- 97 M Houalla, F Delannay, B Delmon, in *Preprints 7th Canadian Symp on Catalysis* (Eds S E Wanke, S K Chakrabarty), Chemical Institute of Canada, **1980** 158–165
- 98 M Houalla, F Delannay, B Delmon, *J Phys Chem* **1981** 85, 1704–1709
- 99 J M Porto Lopez, S Ceckiewicz, C Defosse, P Grange, B Delmon, *Appl Catal* **1984**, 12, 331–346
- 100 F M Mulcahy, M Houalla, D M Hercules, *J Catal* **1987**, 106, 210–215
- 101 Ch Papadopoulou, A Lycourghiotis, P Grange, B Delmon, *Appl Catal* **1988**, 38, 255–271
- 102 H K Matralis, A Lycourghiotis, P Grange, B Delmon *Appl Catal* **1988**, 38, 273–287
- 103 M Houalla, B Delmon, *Appl Catal* **1981** 1, 285–289
- 104 M Houalla, F Delannay, B Delmon, *J Electron Spectroscop Relat Phen* **1982**, 25, 59–95
- 105 H Lafiteau, E Neel, C Clement in *Preparation of Catalysts* (Eds B Delmon, P A Jacobs, G Poncelet), Elsevier, Amsterdam, **1976**, 393–404
- 106 J P R Vissers, S M A M Bouwens, V H J de Beer, R Prins in *Proc Symp on Fundamental Chemistry of Promoters and Poisons in Heterogeneous Catalysis*, American Chemical Society, New York, April 13–18 **1986** 227



- 107 A Stanislaus, M Absi-Halabi, K Al-Dolama, *Appl Catal* **1988**, *39*, 239–253
- 108 P Atanasova, R Halachev, *Appl Catal* **1988**, *38*, 235–240
- 109 M M Ramirez de Agudelo, A Morales in *Proc 9th International Congress on Catalysis* (Eds M J Phillips, M Ternan), The Chemical Institute of Canada, Calgary, **1988**, Vol 1, 42–49
- 110 S Narayanan, K Uma, *J Chem Soc, Faraday Trans I* **1988**, *84*, 521–527
- 111 E J Novak, R M Koros, *J Catal* **1967**, *7*, 50–56
- 112 E J Novak, *J Phys Chem* **1969**, *73*, 3790
- 113 W Verhoeven, B Delmon, *Bull Soc Chim* **1966**, 3065–3073
- 114 W Verhoeven, B Delmon, *Bull Soc Chim* **1966**, 3073–3079
- 115 H Charcosset, B Delmon, *Ind. Chim Belg* **1973**, *38*, 481–495
- 116 J T Richardson, R J Dubus, J G Crump, P Desai, U Osterwalder, T S Cale, in *Preparation of Catalysts II* (Eds B Delmon, P Grange, P A Jacobs, G Poncelet), Elsevier, Amsterdam, **1979**, 131–142
- 117 E B Doesburg, S Orr, J R H Ross, L L van Rijen, *J Chem Soc, Chem Comm* **1977**, *20*, 734–735
- 118 H Pralraud, G A Martin, *J Catal* **1981**, *72*, 394–396
- 119 R Frety, L Tournayan, M Primet, G Bergeret, M Guenin, J B Baumgartner, A Borgna, *J Chem Soc, Faraday Trans* **1993**, *89*, 3313–3318
- 120 G A Martin, C Mirodatos, H Pralraud, *Appl Catal* **1981**, *1*, 367–382
- 121 J Cosyns, M-T Chênebaux, J F Le Page, R Montarnal in *Preparation of Catalysts* (Eds B Delmon, P A Jacobs, G Poncelet), Elsevier, Amsterdam, **1976**, 459–472
- 122 Sun-Hua Chen, Hsiau-Wen Huang, Kuang-Lieh Lu, *Bull Inst Chem Acad Sinica* **1985**, *32*, 9
- 123 B S Clausen, H Topsøe, S Mørup, *Appl Catal* **1989**, *48*, 327–340
- 124 J M Dumas, C Géron, A Kribbi, J Barbier, *Appl Catal* **1989**, *47*, L9–L15
- 125 L M Strubinger, G L Geoffroy, M A Vannice, *J Catal* **1985**, *96*, 72–81
- 126 D Duprez, M Mendez in *Catalyst Deactivation* (Eds B Delmon, G F Froment), Elsevier, Amsterdam, **1987**, 525–534
- 127 D S Thakur, M G Thomas, *Appl Catal* **1985**, *15*, 197–225
- 128 H Hallie, *Oil Gas J*, **1982**, Dec 20, 69–74
- 129 B Delmon in *Catalysts in Petroleum Refining 1989* (Eds D L Trimm, S Akashah, M Absi-Halabi, A Bishara), Elsevier, Amsterdam, **1990**, 1–40
- 130 B Delmon, *Latin American Appl Res*, **1995**, in press
- 131 B Delmon, *Bull Soc Chim Belg*, **1995**, *104*, 173–187
- 132 K Inamura, R Prins, *TOCAT2*, Tokyo, August 7–11, **1994**, Abstracts, 111–112
- 133 B Delmon in *Reactivity of Solids* (Eds K Dyrek, J Haber, J Nowotny), Elsevier, Amsterdam, **1982**, 327–369
- 134 J M Zabala, P Grange, B Delmon, *C R Acad. Sc Paris Ser C* **1974**, *279*, 725–728
- 135 H Zahradnikova, V Karnik, L Beranek, *Coll Czech Chem Comm* **1985**, *50*, 1573
- 136 J M Zabala, P Grange, B Delmon, *C R Acad Sc Paris Ser C* **1974**, *279*, 561–563
- 137 J M Zabala, P Grange, B Delmon, *C R Acad Sc Paris Ser C* **1975**, *280*, 1129–1132
- 138 R Prada Silvy, J L G Fierro, P Grange, B Delmon in *Preparation of Catalysts IV* (Eds B Delmon, P Grange, P A Jacobs and G Poncelet), Elsevier, Amsterdam, **1987**, 605–617
- 139 A Steinbrunn, C Lattaud, *Surf Sci* **1985**, *155*, 279–295
- 140 D K Lambiev, T T Tomova, G V Samsonov, *Powder Metall Intern* **1972**, *4*, 17
- 141 J Masson, B Delmon, J Nechtschein, *C R Acad. Sci Paris*, **1968**, 266, 428
- 142 A Steinbrunn, J C Colson, C Lattaud, C G Gachet, L de Mourgues, M Vrnat, J P Bonnelle in *Reactivity of Solids* (Eds P Barret, L C Dufour), Elsevier, Amsterdam, **1985**, 1079–1080
- 143 A Steinbrunn, C Lattaud, H Reteno, J C Colson in *Physical Chemistry of the solid state applications in metals and their compounds* (Ed P Lacombe), Elsevier, Amsterdam, **1984**, 551–563
- 144 G L Schrader, C P Cheng, *J Catal* **1984**, *85*, 488–498
- 145 P A Spevak, N S McIntyre, *J Phys Chem* **1993**, *97*, 11031–11036
- 146 A Steinbrunn, M Bordignon, *Bull Soc Chim Belg* **1987**, *96*, 941–949
- 147 R Thomas, E M van Oers, V H J de Boer, J A Moulijn, *J Catal* **1983**, *84*, 275–287
- 148 B Scheffer, P Arnoldy, J A Moulijn, *J Catal* **1988**, *112*, 516–527
- 149 B Scheffer, N J J Dekker, P J Mangnus, J A Moulijn, *J Catal* **1990**, *121*, 31–46
- 150 T I Koranyi, I Manninger, Z Paal, O Marks, J R Gunter, *J Catal* **1989**, *116*, 422–439
- 151 D Pirotte, P Grange, B Delmon in *Reactivity of Solids* (Eds K Dyrek, J Haber, J Nowotny), Elsevier, Amsterdam, **1982**, 973–977
- 152 R Prada Silvy, P Grange, B Delmon in *Catalysts in Petroleum Refining 1989* (Eds D L Trimm, S Akashah, M Absi-Halabi, A Bishara), Elsevier, Amsterdam, **1990**, 233–260
- 153 R Prada Silvy, F Delannay, B Delmon, *Indian J Technol* **1987**, *25*, 627–638
- 154 R Prada Silvy, J M Beuken, J L G Fierro, P Bertrand, B Delmon, *Surf Interf Anal* **1986**, *8*, 167–172, **1986**, *9*, 247
- 155 J Ladriere, R Prada Silvy, *Hyperfine Interactions* **1988**, *41*, 653–656
- 156 R Prada Silvy, Ph D Thesis, Université Catholique de Louvain, **1987**
- 157 V Stuchly, K Klusacek, *Appl Catal* **1987**, *34*, 263–273
- 158 Seo Il Kim, Seong Ihl Woo, *Appl Catal* **1991**, *74*, 109–123
- 159 P J Mangnus, E K Poels, J A Moulijn, *Ind Eng Chem Res* **1993**, *32*, 1818–1821
- 160 R Prada Silvy, P Grange, F Delannay, B Delmon *Appl Catal* **1989**, *46*, 113–129
- 161 T I Koranyi, I Manninger, Z Paal, *Solid State Ionics* **1989**, *32–33*, 1012–1018
- 162 M W J Craje, V H J de Beer, J A R van Veen, A M van der Kraan, *J Catal* **1993**, *143*, 601
- 163 P J Mangnus, A Bos, J A Moulijn, *J Catal* **1994**, *146*, 437–448
- 164 T I Koranyi, M Schikorra, Z Paal, R Schlogl, J Schutze, M Wesemann, *Appl Surf Sci* **1993**, *68*, 307–317
- 165 R Badilla-Ohlbaum, D Chadwick in *Catal Proc 7th Intern Congress* (Eds T Seiyama, K Tanabe), Kodansha and Elsevier, Tokyo and Amsterdam, **1981**, *2*, 1126–1140
- 166 J Abart, E Delgado, G Ertl, H Jeziorowski, H Knozinger, N Thiele, X Zh Wang, E Taglauer, *Appl Catal* **1982**, *2*, 155–176
- 167 F Mauge, J C Duchet, J C Lavalley, S Housseny E Payen, J Grmblot, S Kasztelan, *Catal Today*, **1991**, *10*, 561–577
- 168 V L S Teixeira da Silva, R Frety, M Schmal *Ind Eng Chem Res* **1994**, *33*, 1692–1699
- 169 M Breyse, M Cattinot, T Decamp, R Frety, C Gachet, M Lacroix, C Leclercq, L de Mourgues, J-L Portefaix, M Vrnat, M Houari, J Grmblot, S Kasztelan, J P Bonnelle, S Housni, J Bachelier, J-C Duchet, *Catal Today*, **1988**, *4*, 39–55

## 2.4 Solid Superacids

K. TANABE AND H. HATTORI

A solid superacid is defined as a solid material which shows an acid strength higher than the acid strength ( $H_0 = -11.9$ ) of 100% sulfuric acid [1]. The acid strength is measured by use of basic indicators having different  $pK_a$  values [2]. However, this method is not suitable for colored materials and may have some problems when pore sizes of a solid are too small for large molecules of the indicators and if there exist any interactions between the indicators and any sites (basic or redox sites) other than acid sites. The catalytic activity for the skeletal isomerization of *n*-butane is a measure of superacidity, since the reaction does not take place in the presence of 100% sulfuric acid at room temperature. Superacidity can be estimated also by utilizing the temperature-programmed desorption (TPD) method using ammonia or pyridine, provided that the relative value in TPD is related to the absolute value ( $H_0$ ) and the interaction of ammonia or pyridine with basic sites on solid surfaces is confirmed to be negligible.

Recently, various kinds of solid superacids have been developed. The first group is metal oxides and mixed oxides containing a small amount of sulfate ion, and those modified with platinum. The second group is metal oxides, mixed oxides, graphite, metal salts, etc. treated or combined with antimony fluoride or aluminum chloride. The third group is perfluorinated polymer sulfuric acid (Nafion-H). The fourth and fifth groups are H-ZSM-5 and a type of heteropolyacids, respectively. The last group is simply mixed oxides.

The solid superacids of the second group which have a possibility of leaching or evaporating of halogen compounds seem to be environmentally undesirable as catalysts. These superacids and Nafion-H have been extensively reviewed [1–5]. H-ZSM-5 and heteropolyacids are discussed in Sections 2.3.3 and 2.1.7 of this handbook, respectively. Therefore, the superacids of the first group for which many papers have been contributed recently and the industrial application of which is promising, are mainly described here and the other superacids are dealt with only briefly.

### 2.4.1 Sulfate-Treated Metal Oxides, Mixed Oxides, and Those Modified with Platinum

Preparation of these kinds of solid superacids is described first and the effects of the preparation method on the morphology, surface properties, structure of superacid sites, and catalytic performance are discussed.

#### 2.4.1.1 Preparative Methods

The solid superacids such as  $SO_4^{2-}/ZrO_2$ ,  $SO_4^{2-}/TiO_2$ , and  $SO_4^{2-}/Fe_2O_3$  are easily prepared by impregnating  $Zr(OH)_4$ ,  $TiO_2 \cdot nH_2O$ , and  $Fe(OH)_3$ , respectively, with  $(NH_4)_2SO_4$  or  $H_2SO_4$  followed by calcination at 773–923 K [2, 6]. As an example, the preparation of  $SO_4^{2-}/ZrO_2$  is described in more detail. Commercially available  $ZrOCl_2$ ,  $ZrO(NO_3)_2$ , or  $Zr(NO_3)_4$  is hydrolyzed with 28% aqueous ammonia and the precipitates formed are washed thoroughly with distilled water and dried at 373 K overnight to obtain  $Zr(OH)_4$ . The pH in the precipitation of  $Zr(OH)_4$  strongly influences the surface property, the structure of  $ZrO_2$ , and the catalytic activity of  $SO_4^{2-}/ZrO_2$ . Variation of the surface areas of hydrous and calcined  $ZrO_2$  and  $SO_4^{2-}/ZrO_2$  with pH in the precipitation of  $Zr(OH)_4$  is shown in Fig. 1 [7]. The higher the pH, the higher the surface area. The time required for precipitation also affects the surface areas. The hydroxide,  $Zr(OH)_4$ , is immersed into an aqueous solution of  $(NH_4)_2SO_4$  or  $H_2SO_4$ , and the suspended solution is evaporated to dryness, followed by heat treatment in air or in a vacuum at 773–923 K to obtain  $SO_4^{2-}/ZrO_2$ . When  $H_2SO_4$  was used, the concentration in aqueous solution affects the catalytic activity of  $SO_4^{2-}/ZrO_2$  for the isomerization of *n*-butane [8]. The optimum content of  $SO_4^{2-}$  in  $SO_4^{2-}/ZrO_2$  changes from 1 to 8 wt % depending on the type of reaction. For the isomerization of *n*-butane, maximum activity was observed when the intrinsic sulfur content corresponds to roughly the mondoyer [8]. In the case of acylation of chlorobenzene with chlorobenzoyl chloride, 8 wt % of  $SO_4^{2-}$  was optimum [9]. Waqif et al. [10] point out that  $ZrO_2$  and  $TiO_2$  containing a large amount of sulfate form sulfur complexes different from those in the samples containing a small amount of sulfate.

The optimum temperature of calcination changes, depending on the  $SO_4^{2-}$  source ( $H_2SO_4$  or  $(NH_4)_2SO_4$ ), the type of metal oxide in  $SO_4^{2-}/$ metal oxides, and the type of reaction. In the acylation reaction, the optimum temperatures are 823 and 873 K for  $H_2SO_4$ -treated  $ZrO_2$  and  $(NH_4)_2SO_4$  treated  $ZrO_2$ , respectively, as shown in Fig. 2 [9]. For the isomerizations of *n*-butane and *n*-pentane, the optimum calcination temperature of  $SO_4^{2-}/ZrO_2$  at which the highest acid strength is observed is 923 K, while that of  $SO_4^{2-}/TiO_2$  is 773 K [11].

An important point is to use metal hydroxides instead of metal oxides as adsorbents of  $SO_4^{2-}$ . Since solid superacids lose superacidity by absorbing moisture and carbon monoxide [12], calcination in Pyrex glass tubes and storage in sealed tubes are recommended.

As in the case of  $(NH_4)_2SO_4$  or  $H_2SO_4$ , the addition of  $SO_3$  to  $ZrO_2$ ,  $TiO_2$ , and  $Fe_2O_3$  causes the generation of superacidity [13]. However, the addition of  $SO_2$  or

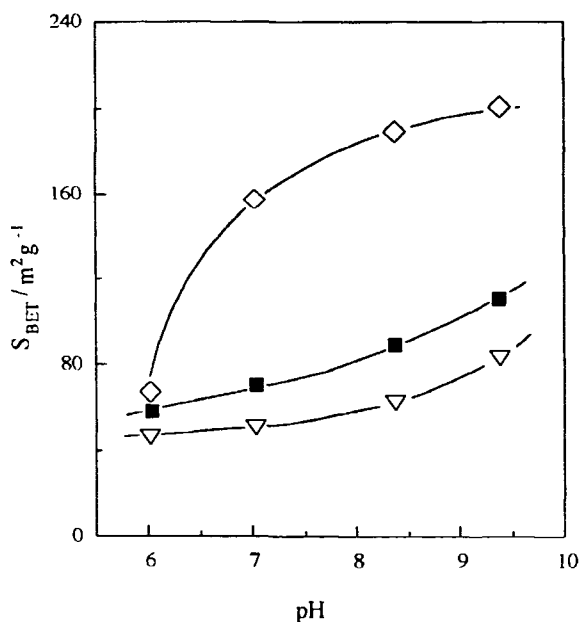


**Figure 1.** Variation of surface area of  $\text{ZrO}_2 \cdot n\text{H}_2\text{O}$  ( $\diamond$ ),  $\text{ZrO}_2$  ( $\nabla$ ), and  $\text{SO}_4^{2-}/\text{ZrO}_2$  ( $\blacksquare$ ) with pH change in precipitation of  $\text{Zr}(\text{OH})_4$ .

such as hydrogen, alcohols, etc. at high temperatures (above 673 K).

In the preparation of  $\text{Zr}(\text{OH})_4$ , the homogeneous precipitation method using urea can be applied. Namely,  $\text{Zr}(\text{OH})_4$  is prepared by hydrolyzing with an aqueous solution of 10% urea at 368–370 K to precipitate the hydroxide [15]. In the next section the morphology and surface properties are compared with  $\text{Zr}(\text{OH})_4$  prepared by the usual heterogeneous method using aqueous ammonia.

A  $\text{SO}_4^{2-}/\text{TiO}_2\text{-ZrO}_2$  superacid is prepared similarly as  $\text{SO}_4^{2-}/\text{ZrO}_2$  except that  $\text{TiO}_2 \cdot n\text{H}_2\text{O-Zr}(\text{OH})_4$  is obtained from a mixed solution of  $\text{TiCl}_4$  and  $\text{ZrOCl}_2$  by coprecipitation with aqueous ammonia [3]. Fe, Mn,  $\text{SO}_4^{2-}/\text{ZrO}_2$  superacids are prepared by impregnating dried  $\text{ZrO}_2$  with aqueous  $\text{Fe}(\text{NO}_3)_3$ ,  $\text{Mn}(\text{NO}_3)_2$  and  $(\text{NH}_4)\text{SO}_4$ , containing 1.5 wt% Fe, 0.5 wt% Mn and 4.0 wt%  $(\text{NH}_4)_2\text{SO}_4$  and by calcining at 998 K for 1 h [16, 17].

The  $\text{SO}_4^{2-}/\text{ZrO}_2$  modified with Pt is prepared by impregnating  $\text{SO}_4^{2-}/\text{ZrO}_2$  with an aqueous solution of  $\text{H}_2\text{PtCl}_6$ , followed by drying at 383 K and calcining at 873 K in air [18, 19]. For example, the amounts of Pt and S are 0.5 and 1.5 wt%, respectively [18].

The  $\text{SO}_4^{2-}/\text{metal oxides}$  supported on  $\text{SiO}_2$  are prepared as follows. The required amount of  $\text{ZrO}_2$  is mounted on  $\text{SiO}_2$  (surface area =  $299 \text{ m}^2 \text{ g}^{-1}$ , calcined at 773 K) from a methanol solution of  $\text{ZrO}(\text{NO}_3)_2$ , decomposed in air at 673 K and finally activated by admitting  $\text{SO}_3$  gas at room temperature, calcining at 873 K and then oxidizing at 573 K [3, 20]. The  $\text{SO}_4^{2-}/\text{Fe}_2\text{O}_3/\text{SiO}_2$  is obtained by anchoring various iron compounds such as  $[\text{Fe}_3(\text{CH}_3\text{COO})_7\text{OH}]\text{NO}_3$ ,  $\text{Fe}(\text{NO}_3)_3$ ,  $\text{NH}_4\text{Fe}(\text{SO}_4)_2$ , and  $\text{Fe}(\text{CO})_3$  on a  $\text{SiO}_2$  surface and by activating with  $\text{SO}_3$  [21]. The amount of Fe compound is important for generation of strong acidity, about 3 mmol of Fe per gram of  $\text{SiO}_2$  being used.

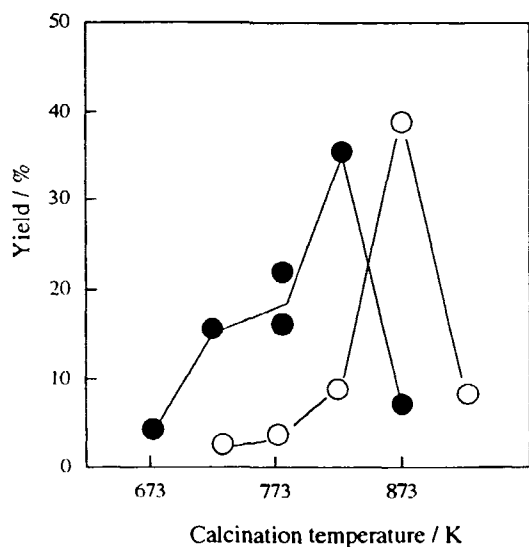


**Figure 2.** Catalytic activities of  $\text{SO}_4^{2-}/\text{ZrO}_2$  prepared by use of  $\text{H}_2\text{SO}_4$  ( $\bullet$ ) and  $(\text{NH}_4)_2\text{SO}_4$  ( $\circ$ ) vs calcination temperature. Yield % of dichlorobenzophenone in acylation of chlorobenzene with *o*-chlorobenzoyl chloride at 403 K in 3 h.

$\text{H}_2\text{S}$  (adsorption at 673 K) does not generate superacidity. It is interesting that  $\text{SO}_2/\text{Fe}_2\text{O}_3$  or  $\text{H}_2\text{S}/\text{Fe}_2\text{O}_3$  does not show any acidity, but exhibits superacidity when oxidized with  $\text{O}_2$  at 773 K [14]. On the other hand,  $\text{SO}_4^{2-}/\text{Fe}_2\text{O}_3$  loses its acidity when reduced with  $\text{H}_2$  at 773 K. These facts indicate that oxidation and reduction influence the acidity of sulfur-containing superacids. It should be noted that the solid superacids cannot be used in the presence of reducing reagents

### 2.4.1.2 Morphology and Surface Properties

The exothermic peak of  $\text{ZrO}_2$  in a differential thermal analysis profile is shifted from 693 to 813–885 K by  $\text{SO}_4^{2-}$  treatment [15]. Crystallographic phase compositions of various  $\text{SO}_4^{2-}/\text{ZrO}_2$  is shown in Table 1 [22]. It is evident that a metastable tetragonal phase is stabilized when a small amount of  $\text{SO}_4^{2-}$  is present. The development of a monoclinic form in  $\text{ZrO}_2$  and the transformation of tetragonal to monoclinic in  $\text{SO}_4^{2-}$ -promoted  $\text{ZrO}_2$  are almost independent of the preparation method (heterogeneous or homogeneous, with  $\text{H}_2\text{SO}_4$  or  $(\text{NH}_4)_2\text{SO}_4$ ). However, the ratio of the tetragonal to the monoclinic phase changes with changes of the pH in the precipitation of  $\text{Zr}(\text{OH})_4$ .

**Table 1.** Crystallographic phase transformation in various ZrO<sub>2</sub> samples.

Sample	Calcination temperature (K) <sup>a</sup>			
	623	773	923	1073
ZrO <sub>2</sub> -A	<u>M</u>	M	M	M
H <sub>2</sub> SO <sub>4</sub> /ZrO <sub>2</sub> -A	Amor.	<u>T</u>	T	T, <u>M</u>
(NH <sub>4</sub> ) <sub>2</sub> SO <sub>4</sub> /ZrO <sub>2</sub> -A	Amor.	<u>T</u>	T	<u>T</u> , <u>M</u>
ZrO <sub>2</sub> -U	<u>M</u>	M	M	M
H <sub>2</sub> SO <sub>4</sub> /ZrO <sub>2</sub> -U	Amor.	<u>T</u>	<u>T</u>	T, <u>M</u>
(NH <sub>4</sub> ) <sub>2</sub> SO <sub>4</sub> /ZrO <sub>2</sub> -U	Amor.	<u>T</u>	T	<u>T</u> , <u>M</u>

<sup>a</sup> Amor. = amorphous; M = monoclinic; M = monoclinic (not well developed); T = tetragonal; T = tetragonal (not well developed); ZrO<sub>2</sub>-A = prepared by hydrolysis of ZrO(NO<sub>3</sub>)<sub>2</sub> · 2H<sub>2</sub>O with aqueous ammonia; ZrO<sub>2</sub>-U = prepared by hydrolysis of ZrO(NO<sub>3</sub>)<sub>2</sub> · 2H<sub>2</sub>O with urea.

**Table 2.** Surface areas of SO<sub>4</sub><sup>2-</sup>/ZrO<sub>2</sub> (Table 1 gives the definition of ZrO<sub>2</sub>-A and ZrO<sub>2</sub>-U).

Sample	Surface area (m <sup>2</sup> g <sup>-1</sup> )
ZrO <sub>2</sub> -A	47.1
ZrO <sub>2</sub> -U	41.7
(NH <sub>4</sub> ) <sub>2</sub> SO <sub>4</sub> /ZrO <sub>2</sub> -A	119.5
(NH <sub>4</sub> ) <sub>2</sub> SO <sub>4</sub> /ZrO <sub>2</sub> -U	119.2
H <sub>2</sub> SO <sub>4</sub> /ZrO <sub>2</sub> -A	85.2
H <sub>2</sub> SO <sub>4</sub> /ZrO <sub>2</sub> -U	65.1

When the pH is increased from 6 to 9.4, the percentage of the tetragonal form in SO<sub>4</sub><sup>2-</sup>/ZrO<sub>2</sub> increases from 73 to 100%, although that in pure ZrO<sub>2</sub> increases from 33 to 70%, only [7].

There is little change in surface area with change of precipitating reagents; ZrO<sub>2</sub>-A prepared with ammonia has a slightly larger area than ZrO<sub>2</sub>-U prepared with urea as shown in Table 2 [15]. An H<sub>2</sub>SO<sub>4</sub> treatment caused a considerably lower surface area than in the case of a (NH<sub>4</sub>)<sub>2</sub>SO<sub>4</sub> treatment. The surface area of SO<sub>4</sub><sup>2-</sup>/ZrO<sub>2</sub> changes not only with the pH (Fig. 1), but also with the time of preparation of ZrO<sub>2</sub>. For example, the surface areas of SO<sub>4</sub><sup>2-</sup>/ZrO<sub>2</sub> in which Zr(OH)<sub>4</sub> was prepared at precipitation times of 0.5, 1, and 8 h at constant pH = 8.3 were reported to be 92, 127, and 132 m<sup>2</sup> g<sup>-1</sup>, respectively [7].

The highest acid strengths of SO<sub>4</sub><sup>2-</sup>/ZrO<sub>2</sub> and SO<sub>4</sub><sup>2-</sup>/TiO<sub>2</sub> measured in sulfuryl chloride by the indicator method are H<sub>0</sub> ≤ -16.0 [22] and H<sub>0</sub> ≤ -14.5 [23], respectively, being higher than that of 100% H<sub>2</sub>SO<sub>4</sub>. However, the acid strength of SO<sub>4</sub><sup>2-</sup>/ZrO<sub>2</sub> was reported to be H<sub>0</sub> ≤ -13.16 according to recent study by Ishikawa et al. [24] and H<sub>0</sub> ≈ -12 by a spectrophotometric method [25]. The difference may be due to the difference in the preparation method and the

**Table 3.** Acid strength of supported solid superacid (SO<sub>3</sub>/ZrO<sub>2</sub>/SiO<sub>2</sub>).

Amount of ZrO <sub>2</sub> (mmol g <sup>-1</sup> )	Acid strength in H <sub>0</sub> acidity scale <sup>a</sup>			
	-11.4	-13.2	-13.8	-14.5
0.58	+	+	-	-
1.31	+	+	-	-
2.57	+	+	-	-
3.00	+	+	-	-
3.50	+	+	+	+
SO <sub>3</sub> /SiO <sub>2</sub>	-	-	-	-

<sup>a</sup> +, present; -, absent.

measurement method. As mentioned above, the preparation method changes the surface property. Concerning the measurement method using indicators, measurement in a vacuum system [26] seems necessary. Recently, the acid strengths of SO<sub>4</sub><sup>2-</sup>/TiO<sub>2</sub> (73 mol %)-SiO<sub>2</sub> [27] and SO<sub>4</sub><sup>2-</sup>/ZrO<sub>2</sub> (85 mol %)-SiO<sub>2</sub> [28] are reported to be H<sub>0</sub> = -14.5 according to the indicator method in benzene. The acid strengths of SO<sub>4</sub><sup>2-</sup>/Fe<sub>2</sub>O<sub>3</sub> and Fe<sub>2</sub>O<sub>3</sub>-MnO<sub>2</sub>-SO<sub>4</sub><sup>2-</sup>/ZrO<sub>2</sub> cannot be measured by color change of indicators because of their dark colors. However, these are regarded as superacids, judging from their catalytic activities for the isomerization of *n*-butane at room temperature [29, 16]. The Fe<sub>2</sub>O<sub>3</sub>-MnO<sub>2</sub>-SO<sub>4</sub><sup>2-</sup>/ZrO<sub>2</sub> superacid is reported to be about three orders of magnitude more active than SO<sub>4</sub><sup>2-</sup>/ZrO<sub>2</sub> for the isomerization reaction [16]. Its superacidity was ascertained to be higher than that of SO<sub>4</sub><sup>2-</sup>/ZrO<sub>2</sub> on the basis of the TPD data using very weak bases such as benzene, monofluorobenzene, difluorobenzene, etc. and the amount of superacid sites being also larger [17]. Fe<sub>2</sub>O<sub>3</sub>-MnO<sub>2</sub>-SO<sub>4</sub><sup>2-</sup>/ZrO<sub>2</sub> shows the highest acid strength among solid superacids containing SO<sub>4</sub><sup>2-</sup>.

The acid strength of Pt-SO<sub>4</sub><sup>2-</sup>/ZrO<sub>2</sub> is determined to be H<sub>0</sub> ≤ -12.7 [30]. Sulfated zirconia supported on silica shows superacidity (Table 3) and the amount of SO<sub>4</sub><sup>2-</sup> is important for exhibiting the highest superacidity [20].

The type of superacid sites on SO<sub>4</sub><sup>2-</sup>/metal oxides evacuated at 773 K is only a Lewis type according to the IR absorption bands of adsorbed pyridine [31]. Morterra et al. [32] have shown that pyridine adsorbed on Lewis acid sites dominated the spectra of samples evacuated at 673 K and that the addition of water at 300 K significantly increased the amount of Brønsted acidity. Nascimento et al. [8] report that both Brønsted and Lewis acid sites exist on SO<sub>4</sub><sup>2-</sup>/ZrO<sub>2</sub> treated at 723 K and the ratio of Brønsted to Lewis sites changes with the change of sulfur content. Recently, Lunsford et al. revealed by use of <sup>31</sup>P MAS NMR spectra of adsorbed trimethylphosphine that three types of Lewis

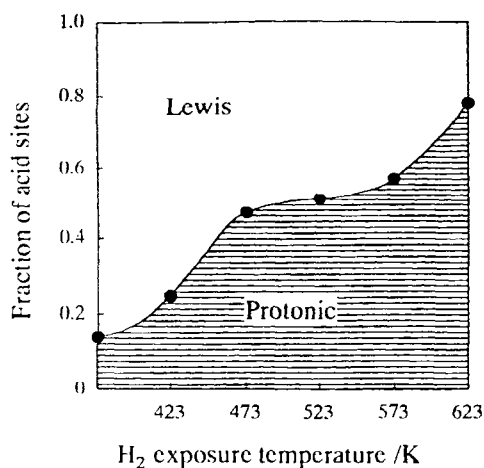


**Figure 3.** Change in fraction of P-Py (proton acid site-pyridine) and L-Py (Lewis acid site-pyridine) caused by exposure to hydrogen at different temperatures.

acid sites exist on the surface of  $\text{SO}_4^{2-}/\text{ZrO}_2$  treated at 593 K [33].

In the case of  $\text{Pt-SO}_4^{2-}/\text{ZrO}_2$ , molecular hydrogen converts into Brønsted acid sites on the surface with concomitant decrease in Lewis acid sites at temperatures above 423 K, as shown in Fig. 3. Molecular hydrogen in the gas phase seems to dissociate on platinum to form hydrogen atoms which migrate onto the oxide and lose their electrons at Lewis acid sites to convert into Brønsted acid sites [18].

According to an ESR study, the adsorption of perylene gave the typical signal of its cation radical on  $\text{SO}_4^{2-}/\text{ZrO}_2$ , while no signal was found on  $\text{ZrO}_2$  [15]. This indicates that an oxidizing property (single-electron accepting property) also appears on the solid superacid.

### 2.4.1.3 Structure of Superacid Sites

Infrared spectroscopic investigation revealed that the  $\text{SO}_4^{2-}/\text{ZrO}_2$ ,  $\text{SO}_4^{2-}/\text{TiO}_2$ , and  $\text{SO}_4^{2-}/\text{Fe}_2\text{O}_3$  gave a common characteristic strong absorption at 1375–1390  $\text{cm}^{-1}$  which indicates high double bond nature of S=O [31]. This band is missing after hydration and the magnitude of the shift after pyridine adsorption is correlated with catalytic activity; the larger the shift, the higher the catalytic activity.

The X-ray photoelectron spectrum of S 2P<sub>3/2</sub> for  $\text{SO}_4^{2-}/\text{Fe}_2\text{O}_3$  showed that the oxidation state of sulfur was S<sup>6+</sup> which is necessary for high catalytic activity of the superacid [34].

From these results, a model structure of the superacid was proposed, which is shown in Fig. 4 [31]. A characteristic feature of the structure is the presence of two S–O bonds. The superacid sites are considered to

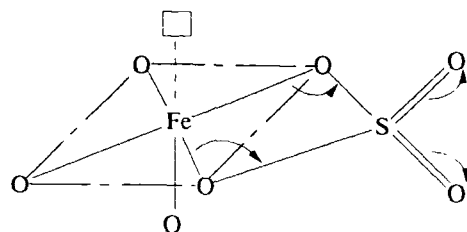


**Figure 4.** Model structure of a superacid,  $\text{SO}_4^{2-}/\text{Fe}_2\text{O}_3$ .

be metal ions (Lewis acid sites) whose acid strength is enhanced by an inductive effect of S=O. IR spectroscopy of CO adsorbed on  $\text{SO}_4^{2-}/\text{TiO}_2$  also suggests the enhancement of Lewis acid ( $\text{Ti}^{4+}$ ) strength by an inductive effect of the sulfate group [35]. Brønsted acid sites may be generated by the interaction of the Lewis acid sites with water molecules or reacting organic molecules. Whatever the starting materials of sulfur are, once they are oxidized on the metal oxide surfaces, they form the structure shown in Fig. 4 [13].

Saur et al. proposed a sulfite structure having only one S=O which shows a band at 1180–1250  $\text{cm}^{-1}$  [36]. Recently, Clearfield proposed a model which is shown by structures (1)–(3) in Fig. 5 [37]. The uncalcined  $\text{SO}_4^{2-}/\text{ZrO}_2$  contains protons as bisulfate groups and as hydroxyl groups bridging two zirconium ions. During calcination, water is lost to form (2) and (3). In both structures, Lewis acid sites are formed, but in (3) the bisulfate group remains intact, which results in a Lewis acid site adjacent to an S–O–H group. These bisulfate groups act as Brønsted acid sites and account for the strong acidity. Lunsford et al. suggest that water acting as a weak Lewis base may be nondissociatively adsorbed via its nonbonding electrons as shown by (4) of Fig. 5 [33] and the strong acidity requires the presence of adjacent Lewis acid sites, namely, through an inductive effect, electrons are withdrawn from O–H bonds by coordinatively unsaturated zirconium, thus giving rise to more strongly acidic protons. By use of Raman, <sup>1</sup>H MAS NMR, and IR spectroscopies, Riemer et al. [38] recently proposed a model structure of  $\text{SO}_4^{2-}/\text{ZrO}_2$  calcined at 873 K which is similar to (3) in Fig. 5, namely, the model contains only one S=O group and OH groups linked to the sulfate which develop high Brønsted acidity and zirconium cations which are responsible for Lewis acids. Babou et al. presented several models of sulfated zirconia on the basis of an ab initio quantum mechanical study [39].

The structure containing only one S=O group does not explain the XPS data indicating the existence of S<sup>6+</sup>. The metal oxides which show superacidity by introducing sulfur compounds are considered to have cations of high electronegativity and high coordination number.

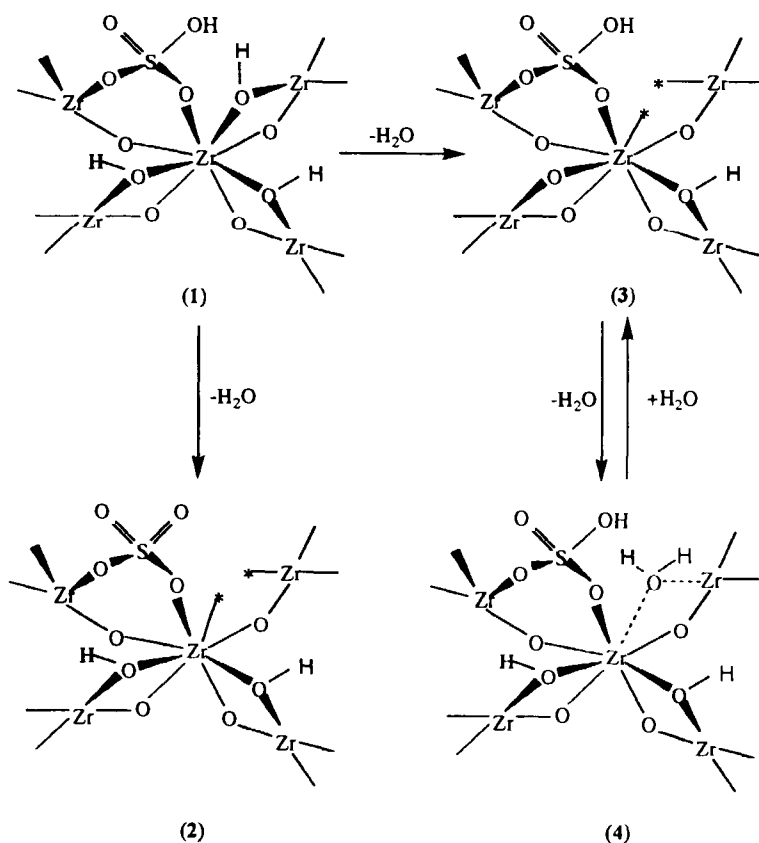


Figure 5. A model of superacidity generation on  $\text{SO}_4^{2-}/\text{ZrO}_2$ .

Also, the importance of coordinative unsaturation of the cations suggests that the cations in Figs 4 and 5 may reside at the edge or corner of the metal oxide surfaces [3].

Platinum on sulfated zirconia remains mostly in a cationic state, even after hydrogen reduction at 673 K according to the XPS study by Ebitani et al. [40, 41]. Thus, the platinum species in sulfated zirconia do not show typical metallic properties such as high olefin hydrogenation activity and chemisorption of CO [42, 43]. On the basis of XAFS data, however, Ebitani et al. [42] reported that platinum particles on sulfated zirconia are a mixture of platinum metal and platinum oxides and/or sulfide. On the contrary, Sayari and Dicko reported on the basis of X-ray photoelectron spectroscopy (XPS), X-ray diffraction (XRD), and TPR measurements that upon air calcination of  $\text{Pt-SO}_4^{2-}/\text{ZrO}_2$  at 873 K, platinum species were reduced to the metallic state [44]. Zao et al. [45] also reported from XAFS data that platinum species in  $\text{Pt-SO}_4^{2-}/\text{ZrO}_2$  existed in the metallic state following calcination in air at 998 K. There is a controversy on the state of platinum in  $\text{Pt-SO}_4^{2-}/\text{ZrO}_2$ . If the state of platinum were metallic, the catalyst would have shown a high hydrogenation activity and significant chemisorptive property for CO. Careful study of the state of platinum by XRD, X-ray absorption fine-structure spectroscopy

(XAFS), and XPS leads to the conclusion that in the core of the particles, metallic platinum exists and in the outer layer of the particles cationic platinum exists in the forms of oxides and/or sulfides.

#### 2.4.1.4 Catalytic Properties

The isomerization of *n*-butane is not catalyzed even by 100%  $\text{H}_2\text{SO}_4$  at room temperature. However,  $\text{SO}_4^{2-}/\text{ZrO}_2$  [22],  $\text{SO}_4^{2-}/\text{TiO}_2$  [23],  $\text{SO}_4^{2-}/\text{Fe}_2\text{O}_3$  [23], and  $\text{Fe}_2\text{O}_3\text{-MnO}_2\text{-SO}_4^{2-}/\text{ZrO}_2$  [16] were found to catalyze the isomerization at 293–323 K, the main product being 2-methylpropane. Among these solid superacids, the one which showed the highest catalytic activity and was most stable is  $\text{Fe}_2\text{O}_3\text{-MnO}_2\text{-SO}_4^{2-}/\text{ZrO}_2$  [16, 46]. However, the activities are lowered as the reaction proceeds, mainly due to coke formation. To prevent the catalysts from their deactivation, a  $\text{SO}_4^{2-}/\text{ZrO}_2$  containing a small amount of Pt or Ni was developed. Over a  $\text{Pt-SO}_4^{2-}/\text{ZrO}_2$ , no deactivation was observed in the isomerization of pentane at 413 K under  $20\text{ kg cm}^{-2}$  of hydrogen pressure, the lifetime being more than 6000 h [47]. Even if Pt is not added, the deactivation of  $\text{SO}_4^{2-}/\text{ZrO}_2$  is reported to be greatly decreased if the hydrogen pressure is high enough [48].

50]. The isomerization of alkanes over  $\text{Pt-SO}_4^{2-}/\text{ZrO}_2$  is limited to  $\text{C}_4\text{-C}_6$ , since *n*-hexane isomerizes to iso-hexanes at 437 K with 99% selectivity, but *n*-heptane isomerization selectivity is only about 50% even at low conversions. Iglesia et al. [51] found that the addition of small amounts of adamantane, a hydride transfer species, to *n*-heptane increased the isomerization rates by a factor of 3 and inhibited undesirable cracking reactions. The intermediates for *n*-butane isomerization catalyzed by liquid superacids such as  $\text{SbF}_5\text{-FSO}_3\text{H}$  and  $\text{SbF}_5\text{-HF}$  are carbonium ions formed by proton transfer from the superacids [52]. Although the mechanisms of *n*-butane isomerization over  $\text{SO}_4^{2-}/\text{ZrO}_2$  are not definite yet, as to whether the carbenium ions or the carbonium ions are involved, Adeeva et al. [53] studied the mechanism of butane isomerization over Fe, Mn-promoted  $\text{SO}_4^{2-}/\text{ZrO}_2$  at 353 K by tracer method in which dual  $^{13}\text{C}$  labeled butane was used. They proposed that the isomerization involves oligomerization and  $\beta$ -fission of a chemisorbed  $\text{C}_8$  carbenium ion to iso- $\text{C}_4$  fragments. On the other hand, Garin et al. [54] proposed the monomolecular mechanism for butane isomerization on  $\text{SO}_4^{2-}/\text{ZrO}_2$  at 523 K by tracer study.

Over  $\text{SbF}_5/\text{metal oxides}$ , it was proposed that *n*-butane isomerization proceeded via carbenium ion intermediates formed by hydride ion transfer from *n*-butane to the Lewis acid sites [55]. The details of sulfated zirconia as a hydrocarbon conversion catalyst have been summarized by Davis et al. [56].

The alkylation of isobutane with 2-butene takes place over  $\text{SO}_4^{2-}/\text{ZrO}_2$  [57, 58] and  $\text{SO}_4^{2-}/\text{TiO}_2$  [58]. The selectivity of a  $\text{SO}_4^{2-}/\text{ZrO}_2$  catalyst for the formation of trimethylpentanes is 91% at 273 K, which is much higher than 16% in the case of zeolite  $\beta$ . The lower selectivity over zeolite  $\beta$  is due mainly to the formation of dimethylhexanes by dimerization of butenes [55]. For alkylation of benzene with propylene at 443 K, the activities of superacids are in the order of  $\text{SO}_4^{2-}/\text{TiO}_2\text{-ZrO}_2 > \text{SO}_4^{2-}/\text{ZrO}_2 > \text{SO}_4^{2-}/\text{TiO}_2 > \text{SO}_4^{2-}/\text{Fe}_2\text{O}_3$  [3]. No activity was observed over  $\text{TiO}_2\text{-ZrO}_2$ ,  $\text{ZrO}_2$ , and  $\text{TiO}_2$ . The activities of  $\text{SiO}_2\text{-Al}_2\text{O}_3$  and H-ZSM-5 were lower than that of  $\text{SO}_4^{2-}/\text{TiO}_2\text{-ZrO}_2$ , but comparable to  $\text{SO}_4^{2-}/\text{ZrO}_2$ . The alkylation of aromatics and naphthenes with alkanes occurs at 433–523 K in the presence of  $\text{Pt-SO}_4^{2-}/\text{ZrO}_2$  and hydrogen, the products varying with the nature of aromatics and the length of the alkane chain [59].

Acylation of aromatics which had been known to be catalyzed only by  $\text{AlCl}_3$  was found to be effectively catalyzed by solid superacids. As shown in Table 4,  $\text{SO}_4^{2-}/\text{ZrO}_2$  exhibited a high activity for the acylation of chlorobenzene with *o*-chlorobenzoyl chloride in the liquid phase. The yield is 100% at 406 K in 10 h, while the yields over H-ZSM-5 and  $\text{SiO}_2\text{-Al}_2\text{O}_3$  are 0 and 0.17%, respectively [9].

**Table 4.** Activities of solid acid catalysts for acylation.

Catalyst	Amount (g)	Reaction time (h)	Yield (%)
$\text{ZrO}_2$	3.0	3	0
$\text{SO}_4^{2-}/\text{ZrO}_2$	3.0	1	26
$\text{SO}_4^{2-}/\text{ZrO}_2$	6.1	10	100
$\text{SiO}_2\text{-Al}_2\text{O}_3$	2.5	1	0.2
H-ZSM-5	3.0	3	0
$\text{H}_2\text{SO}_4$	2 ml	3	0

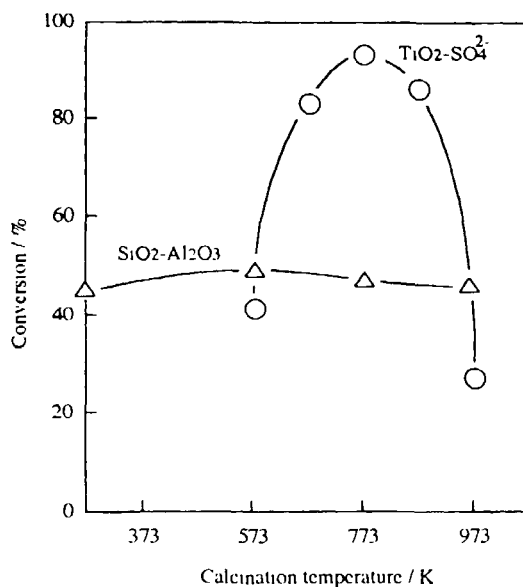
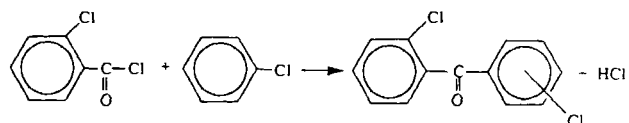


**Figure 6.** Esterification of terephthalic acid with ethylene glycol: reaction temperature 473 K, reaction time 90 min.

For the esterification of terephthalic acid with ethylene glycol at 473 K,  $\text{SO}_4^{2-}/\text{TiO}_2$  calcined at 773 K is much more active than  $\text{SiO}_2\text{-Al}_2\text{O}_3$  as shown in Fig. 6 [60]. The  $\text{SO}_4^{2-}/\text{TiO}_2$  showed a maximum activity when calcined at 573 K for the esterification of oleic acid with glycerol and of propionic acid with butanol at 403 K [61], where the active sites were attributed to Brønsted acid sites from a correlation between the activity and the Brønsted acidity. The esterification of phthalic anhydride with 2-ethylhexanol to form dioctyl phthalate is also efficiently catalyzed by solid superacids, the selectivity being more than 90% [62]. The

**Table 5.** Reactions of CH<sub>4</sub> with C<sub>2</sub>H<sub>4</sub> on solid superacid catalysts

Catalyst	Product composition (percentage C) <sup>a</sup>						
	C <sub>2</sub>	C <sub>3</sub>	<i>i</i> -C <sub>4</sub>	<i>n</i> -C <sub>4</sub>	<i>i</i> -C <sub>5</sub>	<i>n</i> -C <sub>5</sub>	C <sub>6</sub>
TaF <sub>5</sub> /Al <sub>2</sub> O <sub>3</sub>	13.2	13.8	38.6	6.5	12.7	5.3	-
SO <sub>4</sub> <sup>2-</sup> /ZrO <sub>2</sub> <sup>b</sup>	-	10.9	51.2	-	13.4	-	-

<sup>a</sup> Products excluding CH<sub>4</sub> and C<sub>2</sub>H<sub>4</sub> <sup>b</sup> Reaction conditions GHSV = 960, temperature = 573 K, C<sub>1</sub>/C<sub>2</sub> = 2.35 mol mol<sup>-1</sup>, pressure = 1.95 MPa, time on stream = 305 min

catalytic activity was in the order SO<sub>4</sub><sup>2-</sup>/ZrO<sub>2</sub> > SO<sub>4</sub><sup>2-</sup>/Fe<sub>2</sub>O<sub>3</sub> > HPA (dodecatungstophosphoric acid)/SiO<sub>2</sub> > HPA/Al<sub>2</sub>O<sub>3</sub> > HPA/TiO<sub>2</sub> > HPA/ZrO<sub>2</sub>. The activity of SO<sub>4</sub><sup>2-</sup>/Fe<sub>2</sub>O<sub>3</sub> for the esterification of propionic acid with butanol at 383 K becomes maximum when the catalyst is treated at 573–773 K [63], the catalyst structure being studied by ESR and Mossbauer spectroscopy.

For the activation of methane, SO<sub>4</sub><sup>2-</sup>/ZrO<sub>2</sub> was found to be active for the reaction of methane with ethylene to form C<sub>3</sub>, *i*-C<sub>4</sub>, *i*-C<sub>5</sub> [64]. In Table 5, the product distribution is compared with that of the other solid superacid, TaF<sub>5</sub>/Al<sub>2</sub>O<sub>3</sub> [65]. For the chlorination of methane, the selectivity of SO<sub>4</sub><sup>2-</sup>/ZrO<sub>2</sub> for the formation of methyl chloride exceeds 90% with 30% of chlorine conversion at 473 K and is above 80% with 70–90% conversion at 439 K. The selectivity is enhanced by adding Pt, while Fe<sub>2</sub>O<sub>3</sub>–MnO<sub>2</sub>–SO<sub>4</sub><sup>2-</sup>/ZrO<sub>2</sub> exhibits excellent selectivities (99–100%) at lower conversions [66]. The electrophilic insertion is said to involve electron-deficient metal-coordinated chlorine at the methane C–H bond.

Sulfated zirconia showed the highest activity for the disproportionation of diethyldimethylsilane [67]. For the catalytic combustion of propane at low temperatures Pt–SO<sub>4</sub><sup>2-</sup>/ZrO<sub>2</sub> and Pt–SO<sub>4</sub><sup>2-</sup>/Al<sub>2</sub>O<sub>3</sub> showed higher activities than Pt/SiO<sub>2</sub>–Al<sub>2</sub>O<sub>3</sub>, Pt/SiO<sub>2</sub>–ZrO<sub>2</sub>, Pt/Al<sub>2</sub>O<sub>3</sub>, Pt/ZrO<sub>2</sub>, etc., the conversion being 100% at 600 K [24]. The SO<sub>4</sub><sup>2-</sup>-doped oxides having higher acid strengths are suggested to be superior support materials for platinum catalyst for low-temperature combustion of propane.

A MoO<sub>3</sub>–SO<sub>4</sub><sup>2-</sup>/TiO<sub>2</sub> catalyst is much more active than MoO<sub>3</sub>/TiO<sub>2</sub> for the reduction of NO with NH<sub>3</sub>. The addition of 0.5 wt% SO<sub>4</sub><sup>2-</sup> increased the conversion from 58 to 84% at 573 K [68]. The higher activity is due to the acidity enhanced by the interaction of TiO<sub>2</sub> with SO<sub>4</sub><sup>2-</sup>. The selective catalytic reduction of NO with NH<sub>3</sub> at higher temperatures (673–798 K) is achieved by use of SO<sub>4</sub><sup>2-</sup>/TiO<sub>2</sub> [69]. The use of MoO<sub>3</sub> or V<sub>2</sub>O<sub>5</sub> causes the oxidation of NH<sub>3</sub> at the high temperatures. For the isomerization of 2-pinene to camphene and tricyclene SO<sub>4</sub><sup>2-</sup>/TiO<sub>2</sub> showed the highest activity and SO<sub>4</sub><sup>2-</sup>/ZrO<sub>2</sub> the lowest activity. SO<sub>4</sub><sup>2-</sup>/Fe<sub>2</sub>O<sub>3</sub> being in-

termediate [70]. A SO<sub>4</sub><sup>2-</sup>/Fe<sub>2</sub>O<sub>3</sub> catalyst shows high activities for the reactions such as the dehydration of alcohol, the double-bond isomerization of 1-butene, the isomerization of cyclopropane to propylene [71], and is also active for coal liquefaction [72]. The other reactions, are reviewed elsewhere [4, 6].

## 2.4.2 Other Solid Superacids

Besides sulfated metal oxides and sulfated mixed oxides, there are several kinds of solid superacids as mentioned in introduction.

SbF<sub>5</sub>/SiO<sub>2</sub>, Al<sub>2</sub>O<sub>3</sub>, SbF<sub>5</sub>/SiO<sub>2</sub>–TiO<sub>2</sub>, etc. whose acid strength is in the range from –13.16 to –14.52 are more active than SO<sub>4</sub><sup>2-</sup>/metal oxides for the isomerization of *n*-butane in the gas-phase reaction [26]. In the liquid-phase reaction of pentane, it is confirmed that SbF<sub>5</sub> does not dissolve into the liquid phase at room temperature [73]. In the gas-phase reaction of *n*-butane, SbF<sub>5</sub> is not removed if SbF<sub>5</sub>/metal oxide is preliminarily evacuated at 573 K. Thus, these solid superacids are also promising for the application as catalysts for particular reactions. These types of solid superacid have been described elsewhere [1, 4, 6].

AlCl<sub>3</sub>–CuSO<sub>4</sub>, AlCl<sub>3</sub>–CuCl<sub>2</sub>, etc. with H<sub>0</sub> values from –13.16 to –14.52 are active for the isomerization of alkanes Gatterman–Koch reaction, etc. [2, 4]. These solid superacids have also some disadvantages because they contain halogen atoms.

Nafion-H whose acid strength is –12 is active for diversified organic reactions such as alkylation, isomerization, disproportionation, transalkylation, acylation, nitration, hydration, rearrangement, etc. [1, 5]. Since Nafion-H can be used in aqueous solution, it is a useful catalyst.

A heteropolyacid H<sub>3</sub>PW<sub>12</sub>O<sub>40</sub>, and its C<sub>75</sub> salt calcined at 573 K were found recently to have a superacidity of ≤ –13.16 [74]. The catalytic activities of the heteropolyacids and the other solid superacids for the alkylation of 1,3,5-trimethylbenzene with cyclohexene are in the order Cs<sub>25</sub> salt ≫ H<sub>3</sub>PW<sub>12</sub>O<sub>40</sub> > SO<sub>4</sub><sup>2-</sup>/ZrO<sub>2</sub> > Nafion-H > H-ZSM-5 [75].

A well known zeolite, H-ZSM-5, calcined at 808 K was shown also to have superacidity of –12.70 [74]. The order of acid strength measured by the TPD method using ammonia is SO<sub>4</sub><sup>2-</sup>/ZrO<sub>2</sub> > H<sub>3</sub>PW<sub>12</sub>O<sub>40</sub> > Cs<sub>25</sub> salt > H-ZSM-5 > SiO<sub>2</sub>–Al<sub>2</sub>O<sub>3</sub>. The characteristic of H-ZSM-5 is to stabilize pentacoordinated carbonium ions. Thus, in the case of *n*-hexane reaction, the cracking occurs to form H<sub>2</sub>, CH<sub>4</sub>, etc. [76, 77]. According to the acidity estimation based on the in situ <sup>13</sup>C chemical shift measurement of mesityl oxide, however, the acid strength of H-ZSM-5 is reported to be comparable to that of a solution of 70% H<sub>2</sub>SO<sub>4</sub> [78].



Some mixed oxides are solid superacids according to measurement by the indicator method  $\text{WO}_3/\text{ZrO}_2$  calcined at 1073 to 1123 K shows an acid strength of  $\leq -14.5$  and is active for the acylation of toluene with benzoic anhydride at 303 K in liquid phase and the isomerizations of butane and pentane [79]. The mechanism of superacidity generation is said to be similar to that of  $\text{SO}_4^{2-}/\text{ZrO}_2$ , namely, the inductive effect of the double bond of  $\text{W}=\text{O}$  (like  $\text{S}=\text{O}$ ) enhances the acidity of zirconium cation. The acid strength of  $\text{SiO}_2\text{-Al}_2\text{O}_3$  is  $-13.16$  [26] or  $-12.70$  [74]. Very recently,  $\text{SiO}_2\text{-ZrO}_2$  was reported to show superacidity of  $-11.4$  to  $-13.8$ , which changes depending on the composition, although the measurement was made in isooctane [80]. Even  $\text{Al}_2\text{O}_3$  itself is known to show superacidity of  $\leq -14.5$  when prepared by hydrolysis of aluminum isopropoxide followed by calcination at 773 K [81].

Thus, there are now many solid superacids and the term superacidity is no longer unusual. It seems necessary to define solid superacids by judging their reactivities against not only indicators and TPD of ammonia or pyridine, but also test reactions such as the skeletal isomerization of *n*-butane, etc. The controversy concerning the mechanism of superacidity generation needs further research. Some examples have been given which show no correlation between acid strengths of superacids and their catalytic activities. For an interpretation, a concept of concerted acid-base bifunctional catalysis may have to be taken into consideration, since even superacids must have weak basic sites. The geometrical fit between a superacid site and a reacting molecule seems to be another important factor for influencing catalytic activity.

## References

- G A Olah, G K S Prakash, J Sommer, *Superacids*, Wiley, New York, 1985
- K Tanabe, M Misono, Y Ono, H Hattori, *New Solid Acids and Bases*, Kodansha, Tokyo, Elsevier, Amsterdam, 1989
- K Tanabe, H Hattori, T Yamaguchi, *Critical Rev in Surface Chem* 1990, 1, 1
- T Yamaguchi, *Appl Catal A*, 1990, 61, 1
- G K S Prakash, G A Olah, *Acid-Base Catalysis* (Eds K Thanabe, H Hattori, T Yamaguchi, T Tanaka), Kodansha, Tokyo, VCH, Weinheim, 1989, 59
- K Arata, *Adv Catal* 1990, 37, 165
- A Corma, V Fornes, M I Juan-Rajadell, J M Lopez Nieto, *Appl Catal A*, 1994, 116, 151
- P Nascimento, C Akrotopoulou, M Oszgyan, G Coudrner, C Travers, J F Joly, J Vedrner, *Proc 10th Intern Congr Catalysis*, Elsevier, Amsterdam, 1993, 1185
- K Tanabe, T Yamaguchi, K Akiyama, A Mitoh, K Iwabuchi, K Isogai, *Proc 8th Intern Congr Catal*, Berlin, 1984, Verlag Chemie, Weinheim, 5, 601
- M Waqif, J Bachelier, O Saur, J-C Lavalley, *J Mol Catal* 1992, 72, 127
- Z Gao, J Chen, W Hua, Y Tang, in *Acid-Base Catalysis III* (Ed H Hattori, et al), Kodansha, Tokyo, VCH, Weinheim, 1994, 26
- F Pinna, M Signoreto, G Strukul, G Cerato, C Morterra, *Catal Lett* 1994, 26, 339
- T Yamaguchi, T Jin, K Tanabe, *J Phys Chem* 1986, 90, 3148
- Y Nagase, T Jin, H Hattori, T Yamaguchi, K Tanabe, *Bull Chem Soc Jpn* 1985, 58, 916
- T Yamaguchi, K Tanabe, Y C Kung, *Mater Chem Phys* 1986, 16, 67
- C-Y Hsu, C R Heimbuch, C T Armes, B C Gates, *J Chem Soc, Chem Commun* 1992, 1645
- C-H Lin, C-Y Hsu, *J Chem Soc, Chem Commun* 1992, 1479
- K Ebitani, H Hattori, K Tanabe, *Langmuir* 1990, 6, 1743
- K Ebitani, J Konishi, H Hattori, *J Catal* 1991, 130, 257
- T Ishida, T Yamaguchi, K Tanabe, *Chem Lett* 1988, 1869
- T Yamaguchi, T Jin, T Ishida, K Tanabe, *Mater Chem Phys* 1986, 17, 3
- M Hino, K Arata, *J Chem Soc, Chem Commun* 1980, 851
- M Hino, K Arata, *Chem Lett* 1979, 1259, *J Chem Soc Chem Commun* 1979, 1148
- A Ishikawa, S Komai, A Satsuma, T Hattori, Y Murakami, *Appl Catal A* 1994, 110, 61
- B Umansky, J Engelhardt, W K Hall, *J Catal* 1991, 127, 128
- H Hattori, O Takahashi, M Takagi, K Tanabe, *J Catal* 1981, 68, 132
- J R Sohn, H J Jang, *J Catal* 1992, 136, 267
- J R Sohn, H J Jang, *J Mol Catal* 1991, 64, 349
- K Arata, M Hino, *Chem Lett* 1979, 1259
- S Baba, Y Shibata, H Takaoka, T Kimura, K Takasaka, Japanese Patent, 61-153 140, 1986
- T Jin, T Yamaguchi, K Tanabe, *J Phys Chem* 1986, 90, 4794
- C Morterra, G Cerrato, C Emanuel, V Bolis, *J Catal* 1993, 142, 349
- J H Lunsford, H Sang, S M Campbell, C-H Liang, R G Anthony, *Catal Lett* 1994, 27, 305
- T Jin, M Machida, T Yamaguchi, K Tanabe, *Inorg Chem* 1984, 23, 4396
- F Lange, K Hadjuvanov, H Schmelz, H Knozinger, *Catal Lett* 1992, 16, 97
- O Saur, M Bensitel, A B Mohammed Saad, J C Lavalley, C P Tripp, B A Morrow, *J Catal* 1986, 99, 104
- A Clearfield, G P D Serrette, A H Khazi-Syed, *Catal Today*, 1994, 20, 295
- T Riemer, D Spielbauer, M Hunger, G A H Mekhemer, H Knozinger, *J Chem Soc Chem Commun* 1944, 1181
- F Babou, B Bigot, P Sautet, *J Phys Chem* 1993, 97, 11501
- K Ebitani, H Konno, T Tanaka, H Hattori, *J Catal* 1992, 135, 60
- K Ebitani, H Konno, T Tanaka, H Hattori, *J Catal* 1993, 143, 522
- K Ebitani, T Tanaka, H Hattori, *Appl Catal* 1993, 102, 79
- K Ebitani, J Tsuji, H Hattori, H Kita, *J Catal* 1992, 135, 609
- A Sayari, A Dicko, *J Catal* 1994, 145, 561
- J Zhao, G P Huffman, B H Davis, *Catal Lett* 1994, 24, 385
- A Jatia, C Chang, J D MacLeod, T Okubo, M E Davis, *Catal Lett* 1994, 25, 21

- 47 S Baba, T Shimizu, H Takaoka, T Imai, S Yokoyama, Preprint of Disc Meeting of Petrol Chem of Jpn Petrol Inst., 1986, No 2-I-17 Private communication for catalyst life time
- 48 F Garin D Andriamasinoro, A Abdulsamad, J Sommer, *J Catal* 1991, 131, 199
- 49 F R Chen G Coudurier, J-F Joly, J Vadrine *J Catal* 1993, 143, 616
- 50 F Babou, B Bigot, G Coudurier, Ph Sautet, J C Vadrine Preprints of Acid-Base Catalysis II Symposium, Dec 2-4, 1993, Sapporo, p 34
- 51 E Iglesia, S L Soled, G M Kramer, *J Catal* 1993, 144, 238
- 52 G A Olah, Y Halpern, J Shen, Y K Mo *J Am Chem Soc* 1973, 95, 4960
- 53 V Adeeva, G D Lei, W M H Sachtler, *Appl Catal A* 1994, 118, L-11
- 54 F Garin, L Seyfried, P Girard, G Manre, A Abdulsamad J Sommer, *J Catal* 1995, 151, 26
- 55 O Takahashi, H Hattori, *J Catal* 1981, 68, 144
- 56 B H Davis, R A Keogh, R Srinivasan, *Catal Today* 1994, 20, 219
- 57 A Corma, M I Juan-Rajadell, J M Lopez-Nieto, A Martinez, C Martinez, *Appl Catal A* 1994, 111, 175
- 58 C Guo, S Yao, J Cao, Z Qian, *Appl Catal A* 1994 107 229
- 59 J Hu, K R Venkatesh, J W Tierney, I Wender, *Appl Catal A*, 1994, 114, L179
- 60 K Tanabe, H Hattori, Y Ban'i, A Mitsutani, Japanese Patent, 1980, 55-115570
- 61 L Rongsheng, C Jingfeng, Z Wuyang, Y Hua, Z Zhiming W Quan, *React Kinet Catal Lett* 1992, 48, 483
- 62 T S Thorat, V M Yadav, G D Yadav, *Appl Catal A* 1992, 90, 73
- 63 R-S Li, J-F Chen H Yang, W-Y Zhang, *Catal Lett* 1993, 18, 317
- 64 M S Scurrel, *Appl Catal* 1987, 32, 1
- 65 G A Olah, *Eur Pat Appl* 1983, 73673
- 66 P Batamack, I Bucsi, A Molnar G A Olah, *Catal Lett* 1994, 25, 11
- 67 H Fujisawa, T Yamaguchi, *Catal Lett* 1993 17, 319
- 68 S Okazaki, M Kumasaka, J Yoshida, K Kosaka, K Tanabe, *Ind Eng Chem, Product Res and Develop* 1981, 20, 301
- 69 J P Chen, R T Yang, *J Catal* 1993, 139, 227
- 70 R Ohnishi, T Monkawa, Y Hiraga, K Tanabe, *Z Phys Chem Neue Folge* 1982, 130, 205
- 71 K Tanabe, A Kayo, T Yamaguchi, *J Chem Soc Chem Commun* 1981, 602, A Kayo, T Yamaguchi, K Tanabe, *J Catal* 1983, 83, 99
- 72 K Tanabe, H Hattori, T Yamaguchi, S Yokoyama, J Umematsu, Y Sanada, *Fuel* 1982, 61, 389
- 73 O Takahashi, T Yamauchi, T Sakuhara, H Hattori, K Tanabe, *Bull Chem Soc Jpn* 1980, 53, 1807
- 74 T Okuhara, T Nishimura, H Watanabe, M Misono, *J Mol Catal* 1992, 74, 247
- 75 M Misono, T Okuhara, *Chemtech* 1993, 23, 23
- 76 W O Haag, R M Dessau *Proc 8th Intern Congr Catalysis* Dechema, Frankfurt, 1984, 2, 305
- 77 J A Lercher, R A van Santen, H Vinek, *Catal Lett*, 1994, 27, 91
- 78 J Sommer, M Hachoumy, F Garin, *J Am Chem Soc* 1994, 116, 5491
- 79 K Arata, M Hino, *Proc 9th Intern Congr Catalysis Chem Inst Canada, Ottawa, 1988, 4, 1727*
- 80 H J M Bosman, E C Kruijsink, J V D Spoel, F V D Brink *J Catal*, 1994, 148, 660
- 81 K Tanabe, M Uchiyama, H Hattori, *Proc Symp Sci Catalysis Appl Ind*, FPDIL Sindrı 1979 Paper No 46

## 2.5 Catalyst Forming\*

J F LE PAGE

The order in which the calcining and forming operations are carried out varies from case to case. If calcination causes much textural change, it will destroy the results of an earlier forming operation. This happens with crystallized precursors that are better formed after calcining, and then possibly recalcined after forming to improve mechanical resistance. If calcining does not radically change the texture, it can precede forming. This happens with certain xerogels that are shaped like balls or beads and whose mechanical resistance is enhanced by a well-run calcination.

Two extreme types of forming can be distinguished, depending on whether the desired product is powder microgranules or granules on the order of one to several millimeters.

### 2.5.1 Forming Microgranules

Crushing and grinding often serve only to prepare a charge for forming into granules. As a general rule, crushing and grinding is done by generating successive shocks between the product to be crushed and a very hard mass making up the grinder or crusher. The necessary kinetic energy is either furnished by the product, as in cyclone-pulverizers, or more usually by the equipment, as in ball-crushers and mixer-grinders. The lower limit of size for the powder is a few microns (Such a powder is not usable in fluidized beds because its mechanical resistance is too low).

Spray-drying, shown schematically in Fig 1, accomplishes forming and drying at the same time. It consists of spraying microdroplets of the product to be dried into a hot gas current. It is suitable only for making small-diameter beads (7-700  $\mu\text{m}$ ), because the violence of the treatment provokes local superheating in the solids, leading to difficulty in releasing steam that is suddenly produced, with consequent mechanical degradation of large beads.

Spray drying is used for obtaining cracking catalysts in the form of microbeads (silica-alumina or silica-alumina doped with 5-15% of X or Y molecular sieves exchanged with rare earth). Figure 2a and 2b show two different kinds of particle obtained by different atomizations of a given feed to a spray dryer.

Drop coagulation results from metastable sols suspended in a different liquid phase, and can simulta-

\* Reprinted with permission from J F Le Page *Applied Heterogeneous Catalysis: Design, Manufacture, Use of Solid Catalysts* Editions Technip Paris 1987

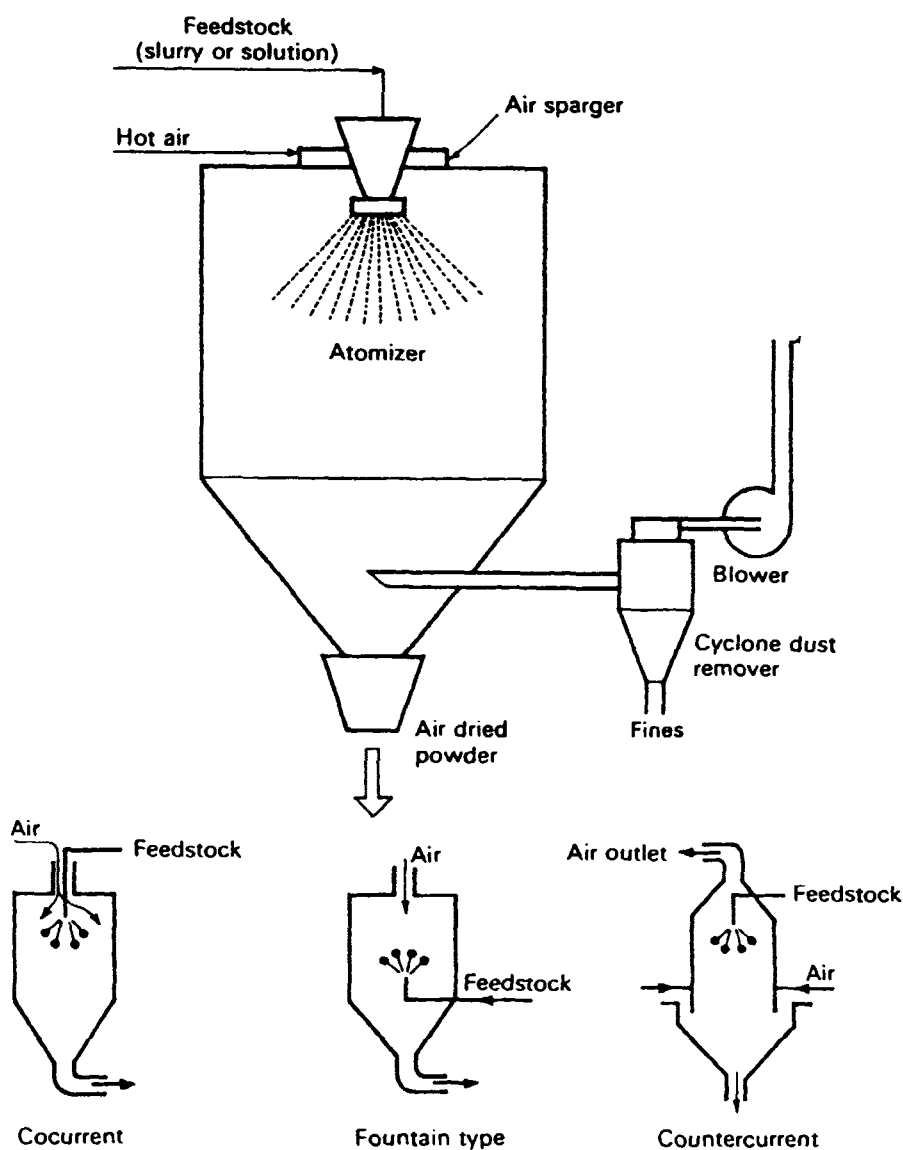


Figure 1. A typical air drier system for various flow patterns.

neously achieve gelling, ripening and forming. Figure 3 illustrates a reactor of the oil-drop type. The aqueous sol is distributed in the form of droplets by a sparger whose orifices are sized to give the desired diameter of bead. The droplets settle through the water-immiscible solvent, whose temperature is raised to around  $100^{\circ}\text{C}$ . The surface tension created on the droplets during passage through the solvent permits formation of gel spheres that must be ripened and ultimately dried. During drying, a contraction of the bead without deterioration is observed as long as the diameter is not too large. Accordingly, this treatment is suitable for producing either microbeads or beads on the order of a few millimeters, such as the silica-alumina beads used in thermoform catalytic cracking (TCC) shown in Fig. 2c.

The operating variables for drop coagulation are: temperature, contact time, sol composition, pH, and

the nature of the continuous phase (density, surface tension, etc.). The injection can be done at the top or bottom of the column (oil-drop or oil-up) depending on relative densities.

In drop-coagulation to form beads of alumina hydroxide, the top of a column holding oil and  $100^{\circ}\text{C}$  is fed with a blend of a sol of aluminium oxychloride and hexamethylene tetramine. Under the influence of the temperature, the amine is decomposed to liberate ammonia, which neutralizes the chloride ions. The product is then ripened, dried, calcined and can be used as a support for reforming catalysts or hydrodesulfurization catalysts [2]. In the same way, a silica sol feeding the bottom of a column of trichloroethylene at around  $75^{\circ}\text{C}$  permits obtaining silica beads at the top.

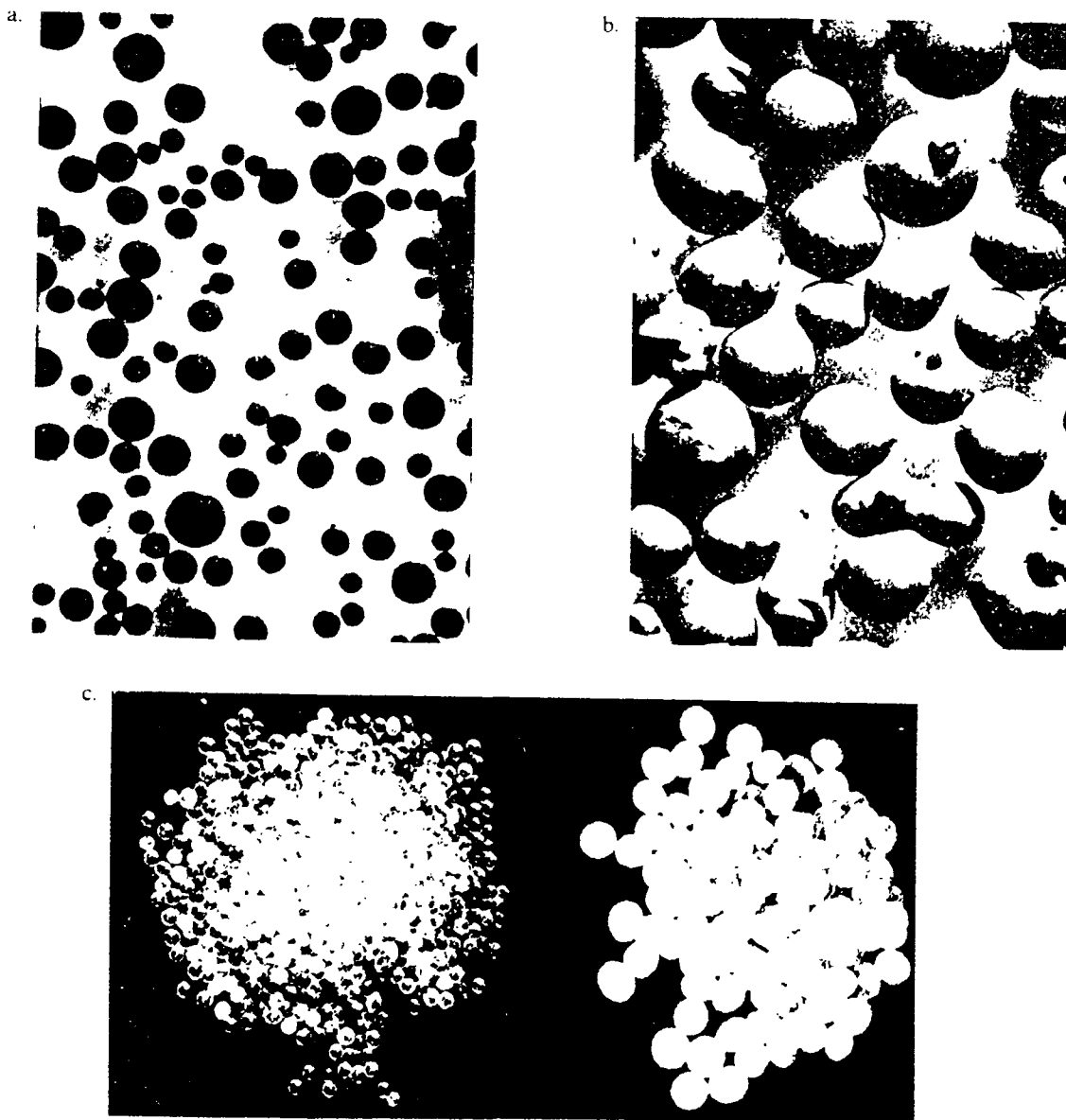


**Figure 2.** Production of micrograins. a. Atomized product 70–160  $\mu\text{m}$ . b. Atomized product 380–570  $\mu\text{m}$ . c. 1C catalyst formed in an oil-drop. On the left, after thermal activation,  $d_p = 3$  mm. On the right, before drying,  $d_p = 8-9$  mm.

## 2.5.2 Forming Granules

The raw material comprises a calibrated powder or paste with suitable rheological properties. No matter what method is to be used, the charge should show properties of fluidity and adhesiveness. Table 1 summarizes methods used for making granules according to the nature of the original charge, whether pelletizing, extrusion, pan granulation, or miscellaneous methods.

### 2.5.2.1 Pelletizing

This consists of compressing a certain volume of usually dry powder in a die between two moving

punchers, one of which also serves to eject the formed pellet. Fluidity of the powder is required to assure homogeneous filling of the die; a certain amount of plasticity is desirable in the granules to create the maximum contact between them; and the quality of the intergranular contacts will depend, after compression, on the adhesive properties of the powder.

If a powder does not have all the required qualities, one can add lubricants to aid the sliding and positioning of the microgranules. Such lubricants can be liquid (water, mineral oil) or solid (talc, graphite, stearic acid, and various stearates). Binders are also added to increase the post-compression adhesion, as for example starch is added for pelletizing active carbon. An increase in the adhesive forces due to chemical bonds resulting from contact between the granules can also be

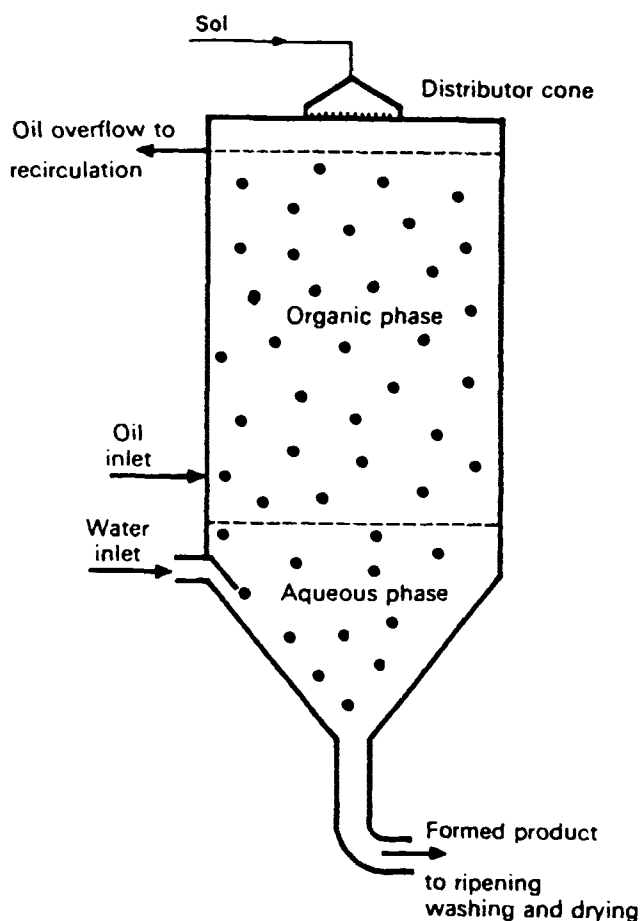
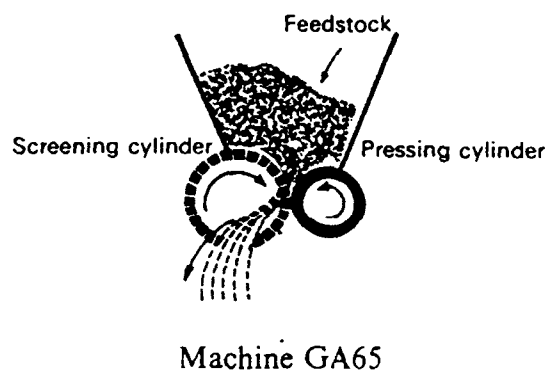
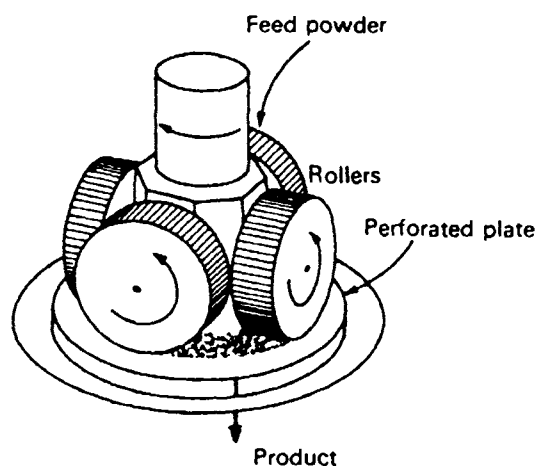


Figure 3. The oil-drop coagulation system.



Machine GA65



Roller press

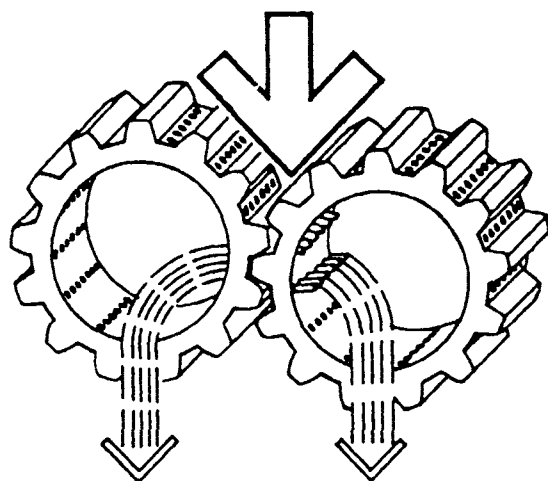
Table 1. Influence of starting material on the choice of a grain-forming process.

Starting material	Process
Monolithic blocks	Crushing and grinding
Powders	Pelletizing
	Granulation
Pastes, hydrogels	Extrusion
Sols	Extrusion
Melted solids	Drop coagulation
	Spray-drying

achieved by peptizing the microgranules, whose surfaces are thus made more chemically reactive.

Some of the operating variables are characteristic of the equipment (i.e., pressure, rhythm, and frequency of vibration to accelerate the flow of powder into the die), while others depend on the charge and, for a given powder, on the granulometry, the kind and concentration of binders, and the lubricants. The ratio of the diameter of the powder particles to that of the final granules should fall between  $1/20$  and  $1/50$ .

A conventional industrial pelletizer equipped with around thirty dies can produce 5–10 liter/h of pellets a few millimeters in diameter. Such pellets are usually cy-



Gear press

Figure 4. Operating principles of extrusion machines.

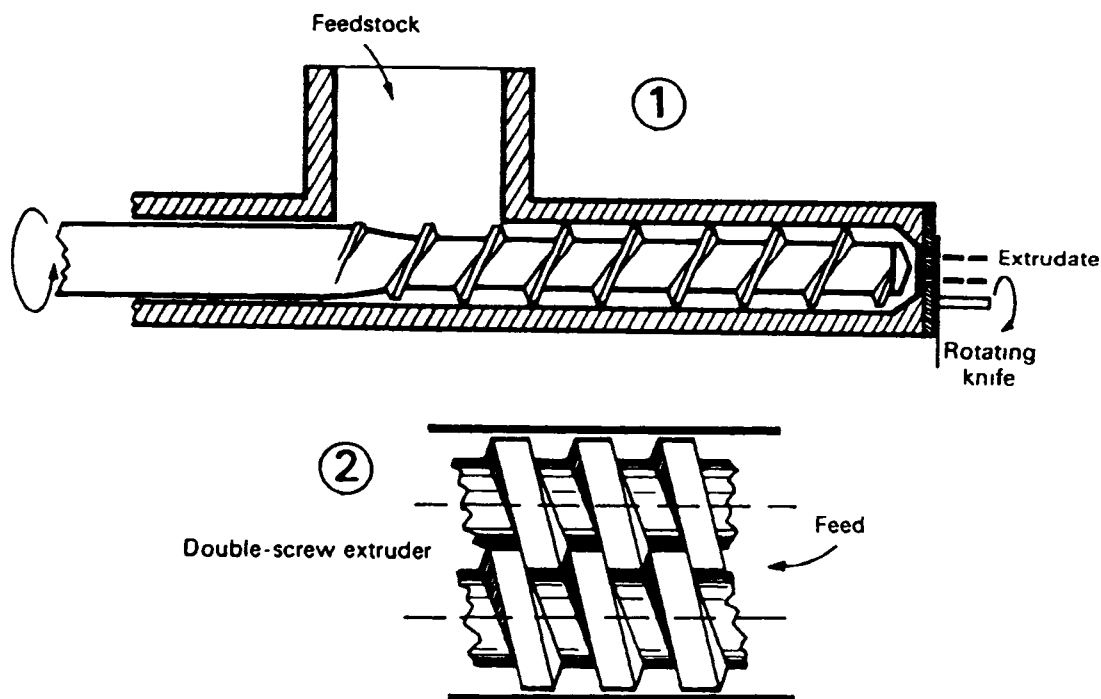


**Figure 5.** Operating principles of screw-extruders (1) Single screw extruder (2) Double turning screws, which permit a better mix higher compression and higher shear

lindrical with flat or rounded base surfaces (better distribution of the compression forces), however spheres, hollow cylinders, and toroids can also be obtained

### 2.5.2.2 Extrusion

Extrusion is a rather general technique applied to pastes, one device forces the paste through a die, while another cuts off the extruded material at the desired length. The ease of extrusion and quality of the product depend on the following properties of the paste

- Viscosity** A non-thixotropic product that is too viscous will block the extruder. A product that lacks in viscosity can not be extruded with a screw and will give extrudates without mechanical resistance when extruded by a press.
- Thixotropy** Certain substances become less viscous under shearing forces, and then recover their initial state after the forces have been released for a time called the relaxation time. The existence of such thixotropic properties is eminently favorable for the flow of a paste and formation of a solid granule at the exit of a die, providing the relaxation time is short enough.
- Stability** Under extrusion conditions there should be no dynamic sedimentation of the product through exuding water and forming a paste that is too viscous.
- Homogeneity** The paste must be homogeneous to assure that the quality of the product is constant.

When necessary, the paste is homogenized in a mixer-kneader under controlled conditions of temperature, time, and pH. An excess of kneading can in fact compact the material and suppress potential macropores. Screw extruders partially knead the paste as it travels along the screw.

Extruding equipment can be classed in one of two categories: press extruders (Fig. 4) and screw extruders (Fig. 5). Press extruders are used principally for pastes that are viscous, screw extruders are preferred for thixotropic products.

Even for a given charge with specific properties the operating variables are rather poorly defined and are closely related to the type of equipment. Generally they include temperature, addition of binders and lubricants to modify viscosity and thixotropy, as for example additions of alginates, starch, kaolinite and montmorillonite.

Extrusion granules generally occur as cylinders 0.5–10.0 mm in diameter. Hollow cylinders can also be obtained with special dies.

It should be borne in mind that the conditions of extrusion sometimes lend themselves well to certain hydrothermal transformations.

### 2.5.2.3 Pan Granulation

This consists of agglomerating a powder into beads by moistening it as it rolls about in a rotating pan (Fig. 6). Seed granules are coated with humidified powder under

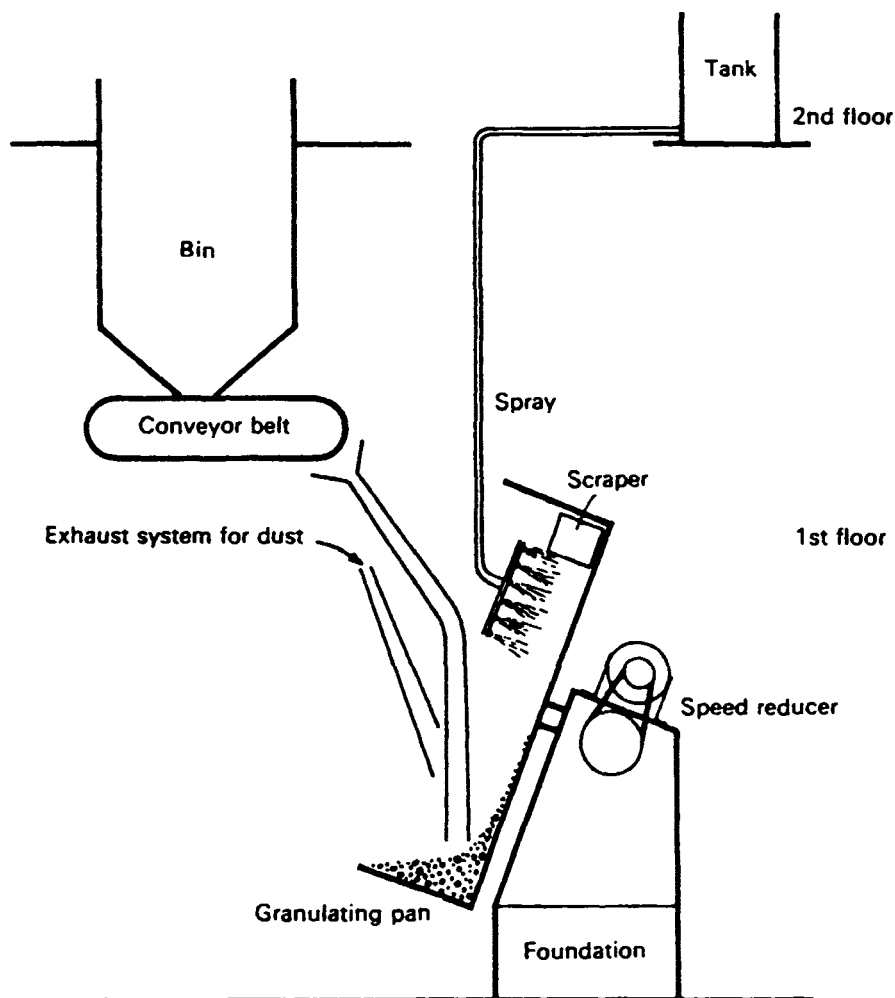


Figure 6. Operating principles of a pan granulator.

the effect of capillary tensions to give a bead of increasing diameter, by a kind of snow-ball phenomenon. The discharge of the beads in the desired size is accomplished through centrifuging. The granulation operation is followed by a ripening period that starts in the bowl. To achieve good granulation the powder must be rather fine ( $d_p < 50 \mu\text{m}$ ). For a powder with given internal properties the operating variables are: speed of rotation, inclination of the pan, rate of flow of water, and nature and quantity of the added binders.

Pan granulation is not expensive but has the drawback that the product has a rather wide size distribution, necessitating a screening operation afterwards. The diameter of the beads can vary from 1 mm to 20 mm.

#### 2.5.2.4 Miscellaneous Forming Operations

Leaching by chemically dissolving the aluminum from Rancy alloys (Ni, Co, Fe, and Cu) can be mentioned here (see this Handbook, Part A, chapter 2.1.2). Melt-

ing followed by pulverizing in an air jet comprises a method for preparing certain catalysts for the synthesis of ammonia. As for monolithic supports used particularly in catalytic mufflers, they are produced through special technology such as dry chemical oxidation of aluminum honeycomb, or through the extrusion of mixtures of oxides.

### 2.5.3 Organizing a Catalyst-Manufacturing Process

The location of different unit operations in catalyst-manufacturing production lines does not lend itself to debate. Precipitation occurs at the beginning of a fabrication process; calcination then activation, which will be treated later, are the final operations. Certain operations can be repeated in some processes; but the final calcination will come after the last drying. On the other

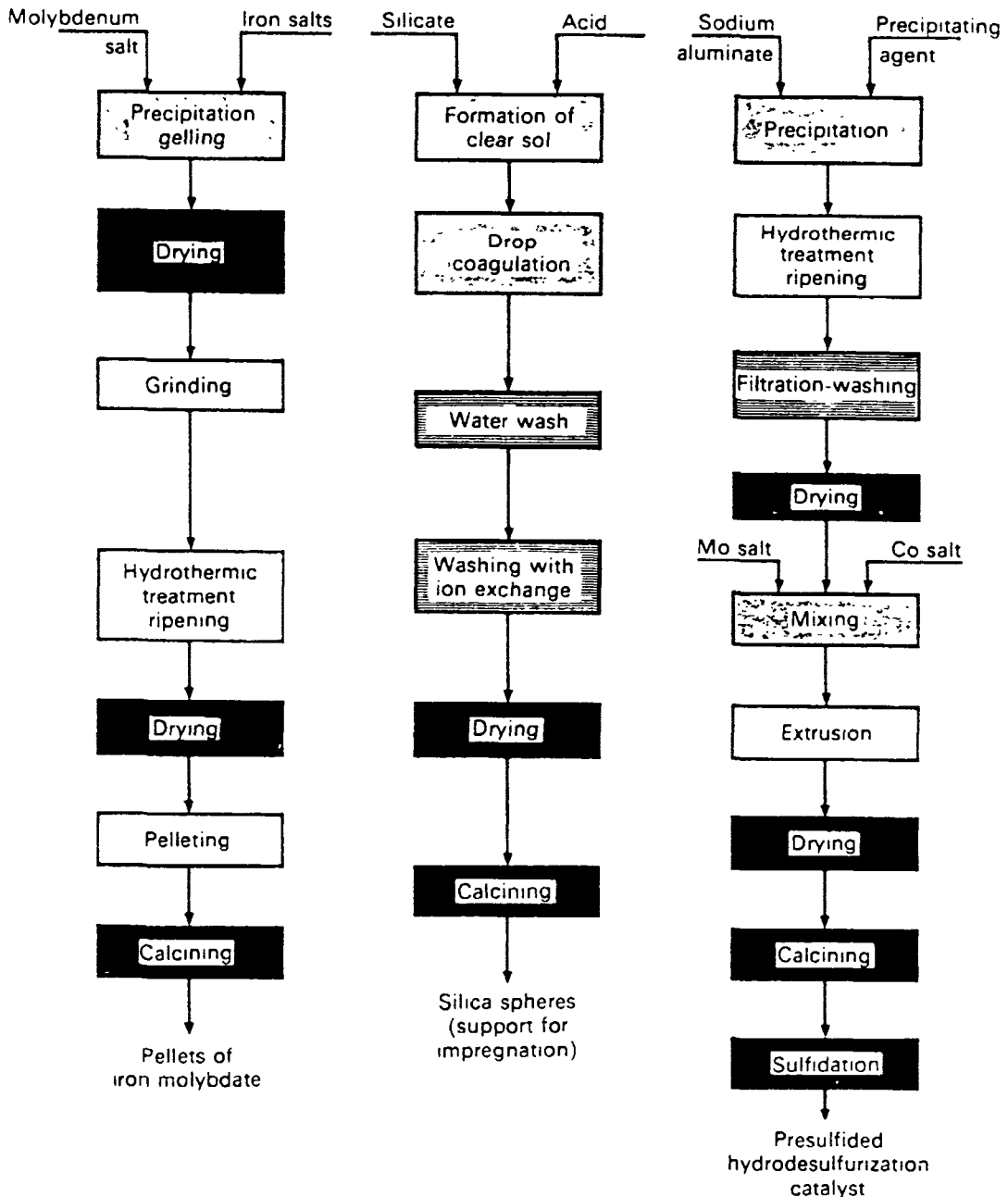


Figure 7. Typical arrangements of the unit operations for manufacturing catalysts.

hand, the location of forming operations can vary according to the circumstances; the operation can take place at the beginning (coagulation of sols) or penultimately (pelletizing of dry powders or even colloidal powders). Some of the operations require more than a particular piece of equipment, as often occurs with hydrothermal transformations.

In summary, numerous processes are possible, depending on the starting products, the composition, the structure and texture of the desired product, and frequently on the available equipment in the manufacturing shop. There will often be several processes that can

lead to catalysts with very similar characteristics and properties.

Figure 7 illustrates three types of processes corresponding to three different catalysts: a bulk catalyst of iron molybdate for the oxidation of methanol into formaldehyde; a support made of silica beads; and a kneaded and coagglomerated hydrodesulfurization catalyst based on cobalt and molybdenum on an alumina support. Kneading salts with a xerogel powder having a low water content does in fact correspond to an impregnation operation that will affect the properties of the final catalyst, although the overall process,



aside from this operation, remains the same as that which would be used for fabrication of the support alone.

Finally, the importance of choosing the precursor salts and the precipitating agents before any operation should be emphasized; general principles for this cannot be set forth, only some practical suggestions can be made, as follows:

The precursor salts should be decomposable in such a way as to eliminate the ions or useless constituents through washing or calcination. Use of gelling salts or precipitating agents (binders and lubricants) containing potential poisons of the catalyst must be avoided. Thus it is that in the preparation of catalysts based on copper chromite (used in CO conversion at low temperature) the use of copper chloride or sulfides, which are difficult to reduce and are generators of chlorine and sulfur, must be avoided, because  $\text{Cl}^-$  and  $\text{S}^{2-}$  are catalyst poisons. The same is true for hydrogenation catalysts based on reduced metals. For coprecipitation, compatible salt solutions that give a true coprecipitation must be chosen, and not those that give parallel or consecutive precipitations. Similarly, for certain catalysts obtained from crystallized precursors, one must think about choosing those anions capable of creating the best texture. Apart from these general considerations and certain considerations of economics, one must depend on experimentation for making the best selection of starting chemical compounds.

## References

1. Ph. Courty and P. Duhaut, *Rev. Inst. Française du Pétrole* 1974, XXIV-6, 861.
2. J. P. Fort and M. Graulier, *Actualité Chimique* 1973, 2, 7.

## 2.6 Computer-Aided Catalyst Design

M. BAERNS AND E. KÖRTING

### 2.6.1 Introduction

In the past, catalyst design has been mainly based on heuristics; more recently, deterministic methods have started to evolve. Heuristics describes methods by which knowledge is acquired in a logical but non-mathematical manner. In this way also, trial-and-error procedures may be considered to be of the heuristic

type as long as they are based on some rational, which is usually the case in catalyst design. Both, heuristic as well as deterministic methods employ computational methods [1, 2]. This article relates to these methods and explains their inherent bases. Before doing so, some necessary definitions and descriptions of the terminology common in computational catalyst design are given.

Heuristic catalyst design is based on a knowledge of:

- catalytic chemistry including inorganic, organic, physical as well as analytical chemistry;
- materials, e.g. their synthesis, characterization, texture and structure;
- chemical reaction engineering principles, i.e. thermodynamic equilibrium and kinetics of the catalytic reaction and of transport processes as well as their interplay; although applicable to deterministic considerations, these qualitative aspects nevertheless affect heuristic searches for an optimum catalyst.

Although some of these aspects are of a quantitative nature, the catalyst expert using his overall knowledge cuts through the complexity in inventing and/or improving a catalyst by handling it in a provisional and intuitive way combining heuristics, experimentation and qualitative modeling. This process is illustrated by Figure 1 which summarizes the various stages of traditional catalyst development.

The reasoning process may be modeled by a computer algorithm (see Section 2.6.2.1). In order to propose catalyst components for a given reaction on a more fundamental basis, reaction steps have to be identified which lead to the desired products or which should be avoided because they are not selective or because they result in deactivation of the catalyst. These reaction steps ought to be elementary reactions steps; however, in the case that such elementary reaction steps are not known, simplified reaction schemes may be useful, too.

From experience it is known which types of materials catalyze which reaction steps. It is desirable to relate their activity to solids properties which are measurable or which can be related to measurable quantities. In this way, it is possible to identify substance properties which are required for catalyst components or which should be avoided.

Then, catalyst components can be selected which presumably provide all necessary properties and functions but which do not catalyze undesired reactions or do not lose their activity due to deactivation. For different selection criteria, it will be necessary to find some optimum between possibly contradictory patterns. Since the process is heuristic, no guarantee can be given that

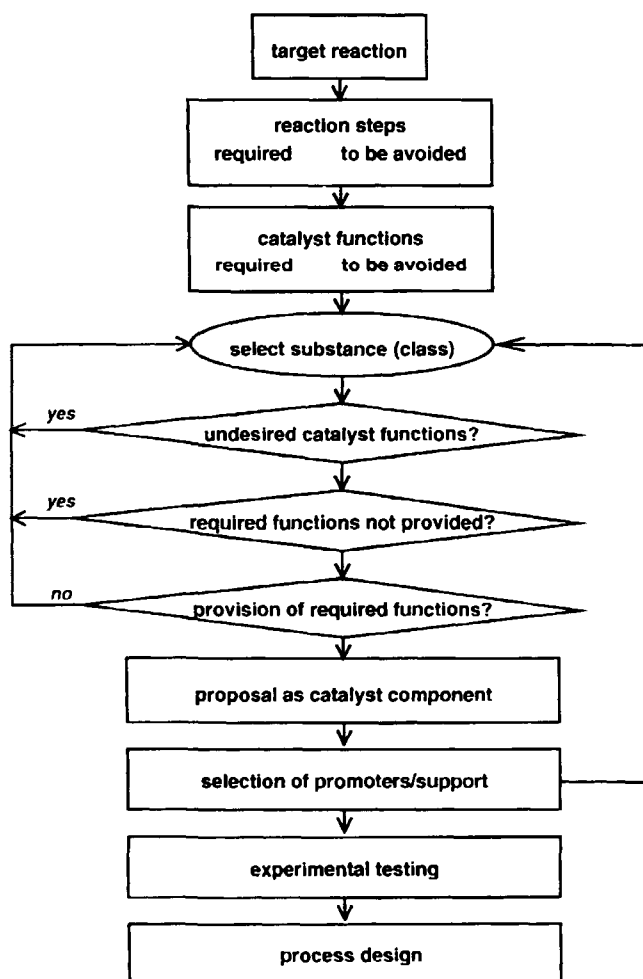


Figure 1. Modeling the reasoning process of catalyst experts by a computer algorithm.

the optimum catalyst is found. This is the reason why a set of promising materials has to be prepared and to be tested experimentally; the preselection of catalytic materials may also be based on different assumptions on elementary reaction steps and required solids properties and catalytic functions. The results of these tests will then be fed back in order to further improve selection criteria. Such an iterative process will also help to better understand the catalytic system in general.

Deterministic catalyst design is slowly supplementing the traditional heuristic approaches, comprising:

- Deriving and applying quantitative relationships for predicting chemical and physico-chemical properties of potential catalytic materials and relating them to the energetic and dynamic interactions of reacting molecules with the catalyst surface.
- Modeling and describing the time course of the catalytic reaction, i.e. their kinetics on an elementary-step basis and relating the reaction scheme and the respective rate constants and activation energies to

- the physical and chemical properties of the catalytic solid as a basis for further catalyst development [3].
- Combining the kinetics of the catalytic reaction and its interplay with transport phenomena as well as with the hydrodynamics of the chemical reactor to be used as the basis of shaping and operating the final catalyst.
- Relating porosity, pore diffusional processes and kinetics of the catalytic reaction and of the deactivation process to one another with the aim of minimizing apparent catalyst deactivation [4].

In its broadest application deterministic catalyst design will eventually also include molecular dynamics calculations and computer graphics which are both being used for simulating the behavior of molecules on catalytic surfaces and, in particular, on active sites. Although these methods have, in principal, a tremendous potential for predicting and/or improving the catalytic performance of catalytic materials [5–9], they will not be dealt with in detail since their comprehensive application to catalyst design in practice is still in its infancy. Only some selected cases are described.

Very striking results on the interactions of molecules with a catalyst have been recently reported in zeolite catalysis because of the well ordered structure of these materials; it is worth mentioning the subjects of zeolite design [10] and of acidic properties of metallosilicates [11]. In other areas where polycrystalline or even amorphous materials are applied, highly interesting results are now numerous emerging (such as hydrocarbon oxidation on vanadium-based catalysts [12]; location of transition metal cations on Si(100) [13]; CO molecules on MgO surfaces [14]; CH<sub>4</sub> and O<sub>2</sub> interaction with sodium- and zinc-doped CaO surfaces [15]; CO and NO on heavy metal surfaces [16]). An illustration of the computerized visualization of molecular dynamics of Pd clusters on MgO(100) and on a three-dimensional trajectory of Ar in Na mordenite, is the recent publication of Miura et al. [17].

Since chemical reaction engineering considerations apply to nondeterministic as well as deterministic methods they will be briefly dealt with separately. The interaction of chemical kinetics and transport processes and their effect on catalyst activity and selectivity in reaction networks will be emphasized. Some attention will be also paid to catalyst deactivation.

## 2.6.2 Heuristics in Catalyst Design

Heuristics are relationships between variables of qualitative nature. They may be supported by theoretical concepts, or just rules-of-thumb learned from experience. Since it is up to now impossible to predict the catalytic behavior of a solid only by deterministic

**Table 1.** Expert systems for catalyst design.

Approach	Reaction	Name	References
Levels of abstraction	CO hydrogenation	DECADE	19
Standard catalysts	hydrogenation	ESKA	20
Activity patterns	oxidative dehydrogenation	INCAP, INCAP-Muse	21–26
Optimization of catalysts	alcohol synthesis		27, 28
General applicability	different	ESYCAD	29, 30

methods, the application of heuristics is crucial in catalyst design.

Knowledge-based systems, frequently also called expert systems, for supporting catalyst development belong to the heuristic methods; emphasis is put on the wording “supporting” because such a system is not able to suggest the catalyst from the knowledge stored. (see Section 2.6.2.1). Another application of heuristics are neural networks which have been only very recently introduced as a means of supporting catalyst design (see Section 2.6.2.2).

### 2.6.2.1 Knowledge-Based Systems

Knowledge-based systems are computer programs which apply knowledge about a specific domain in order to derive new conclusions. These conclusions are on the level of a human expert in this field, but constrained by the field of expertise. Applied to catalysis, the knowledge base contains heuristics about relationships between chemical and physico-chemical properties of solids and their catalytic properties, as well as known properties for such solids which may be used as components of catalysts [2, 18]. An expert system is able to combine this knowledge about different catalyst properties which may be necessary to catalyze the required reaction steps, or which should be avoided because they catalyze side reactions.

Several expert systems of this type have been described in the literature (Table 1). In DECADE (Design expert for Catalyst Development) Bañares-Alcántara et al. [19] used knowledge processing methods (the expert system shell) of an expert system which was previously used for other problems, and added information about CO hydrogenation catalysis. Proposals for the selection of a catalyst and reaction conditions are reached on different levels of fundamental knowledge:

- (i) on the most abstract level known catalysts are selected for the desired reaction;
- (ii) catalysts are selected which are known to catalyze a reaction which belongs to the same reaction class as the desired reaction;

- (iii) on the most detailed level of knowledge, reaction steps are postulated by formal analysis of necessary breaking or formation of bonds, and catalyst components are selected on the basis of knowledge about the ability of different metals for the steps of hydrogen and carbon monoxide dissociation.

The system also provides recommendations for the selection of reaction conditions (pressure, temperature and  $H_2 : CO$  ratio).

The system ESKA (Expert System for Selection and Optimization of Catalysts [20]) was designed at BASF specifically for hydrogenation reactions. The main component of a catalyst is proposed on the basis of activity patterns which describe the applicability of catalysts for different types of hydrogenations. The system also is able to propose secondary catalyst components and, if necessary, a support material which is stable under reaction conditions and does not have any undesired catalytic properties. Based on heuristics for required as well as undesired side reactions and for different catalytically active components, the system also proposes reaction conditions as temperature, pressure, the solvent or the pH.

Kito and Hattori et al. have described INCAP (Integration of Catalyst Activity Patterns [21–23]), an expert system which rates the applicability of catalyst components for the desired reaction based on known activity patterns for different catalyst properties. The system was successfully applied for the selection of promoter components for the oxidative dehydrogenation of ethylbenzene to styrene. An improved version INCAP-MUSE (INCAP for Multi-Component catalyst Selection [24–26]) selects as many catalyst components until all required catalyst properties are present. Although the system was successfully applied to oxidation reactions, more recently better results have been obtained by neural network methods (Section 2.6.2.2).

Hu and co-workers have developed an expert system especially for the optimization of higher alcohol synthesis catalysts [27, 28]. The knowledge base contains data about experimental work and heuristic rules about

the relationships between preparation parameters, results of characterization, and higher alcohol selectivity. If the user queries the system for an alcohol catalyst with some required selectivity, starting with the best catalyst, the program proposes modifications, i.e. in composition or operating conditions, in order to improve the performance of the catalyst by application of heuristic rules.

Although the systems described above were designed specifically for one reaction or one reaction class, the system ESYCAD (Expert SYstem for Catalyst Design [29, 30]) has been applied to such different reaction types as CO hydrogenation, acid-catalyzed dehydrogenation of alkanes, or oxidative coupling of methane. The system has recently been extended by incorporating a knowledge acquisition facility which allows the user to enter his own knowledge and to apply the program to catalytic systems of his interest. In order to select catalyst components the system and/or the user proposes reaction steps which are required for a given reaction or which should be avoided as side reactions. Then catalyst properties are determined which are necessary for required reaction steps or which should be avoided because they catalyze undesired reactions or lead to deactivation of the catalyst. On the basis of a database containing chemical and physico-chemical properties of solids, the system selects catalyst components which provide all necessary properties, but do not catalyze undesired reactions. Optionally, secondary components can be selected (see Fig. 1).

As an illustration, the results of the application of the ESYCAD program to the oxidative coupling of methane are explained. For this reaction, methane may be activated at strong basic sites of the catalyst by heterolytic chemisorption, resulting in methyl anions which may be oxidized to radicals. In the selective reaction, these radicals dimerize to ethane as the primary product. Acid sites or  $n$ -conductivity should be avoided because they lead to total oxidation. Under reaction conditions the catalyst should be stable, i.e. not be oxidized or reduced or volatilize, which can be checked by thermodynamics.

By doping a primary catalyst component with lower-valent metal cations, additional oxygen vacancies will be created which facilitate the incorporation of electrophilic oxygen species chemisorbed on the surface into the bulk where they will not oxidize adsorbed methyl radicals. Also, the promoter oxide should be basic, not be reducible, oxidizable, or easily volatilizable. It should form a mixed oxide with the main component which may be possible if the ionic radii are similar. According to these rules, the expert system proposes as potential catalyst components combinations of substances with appropriate chemical and physico-chemical properties (Table 2). Many of these systems already have been described in the literature

**Table 2.** Proposals of the expert system ESYCAD for the oxidative coupling of methane.

primary	secondary	primary	secondary
Li <sub>2</sub> O			
MgO <sup>a</sup>	Li <sub>2</sub> O <sup>a</sup>		
CaO <sup>a</sup>	Na <sub>2</sub> O <sup>a</sup>	Dy <sub>2</sub> O <sub>3</sub> <sup>a</sup>	Na <sub>2</sub> O
SrO <sup>a</sup>	Na <sub>2</sub> O		CaO
BaO <sup>a</sup>	Na <sub>2</sub> O	Tb <sub>2</sub> O <sub>3</sub> <sup>a</sup>	SrO
Y <sub>2</sub> O <sub>3</sub> <sup>a</sup>	Cs <sub>2</sub> O		Na <sub>2</sub> O
	Na <sub>2</sub> O		CaO
	CaO <sup>a</sup>	Gd <sub>2</sub> O <sub>3</sub> <sup>a</sup>	SrO
	SrO <sup>a</sup>		Na <sub>2</sub> O
La <sub>2</sub> O <sub>3</sub> <sup>a</sup>	Na <sub>2</sub> O <sup>a</sup>		CaO
	CaO <sup>a</sup>		SrO
	SrO <sup>a</sup>	Eu <sub>2</sub> O <sub>3</sub> <sup>a</sup>	BaO
	BaO <sup>a</sup>		Na <sub>2</sub> O
Yb <sub>2</sub> O <sub>3</sub> <sup>a</sup>	Li <sub>2</sub> O		CaO
	Na <sub>2</sub> O		SrO
	CaO	Sm <sub>2</sub> O <sub>3</sub> <sup>a</sup>	BaO
	SrO		Na <sub>2</sub> O <sup>a</sup>
Er <sub>2</sub> O <sub>3</sub> <sup>a</sup>	Li <sub>2</sub> O		CaO <sup>a</sup>
	Na <sub>2</sub> O		SrO
	CaO	Tm <sub>2</sub> O <sub>3</sub> <sup>a</sup>	BaO
	SrO		Li <sub>2</sub> O
Ho <sub>2</sub> O <sub>3</sub> <sup>a</sup>	Na <sub>2</sub> O		Na <sub>2</sub> O
	CaO		CaO
	SrO		SrO
		Nd <sub>2</sub> O <sub>3</sub> <sup>a</sup>	Na <sub>2</sub> O
			CaO
			SrO
			BaO

<sup>a</sup> System already known as catalyst.

for the oxidative coupling, whereas others have not been tested yet.

### A Data Procurement for Knowledge-based Systems

Progress in analytical characterization of catalysts plays an important role in their further development and improvement. Synergistic effects of complimentary characterization tools by which different properties of the catalytic materials are determined are claimed to be beneficial in catalyst design. If this is so, then an expert system for assisting in catalyst selection should be designed in such a way that it accounts for different chemical and physico-chemical properties and their relation to catalytic performance of solid materials.

The catalytic behavior of solid materials is certainly largely governed by the nature of their few topmost atomic layers. However, it can be assumed that these layers are frequently related to the bulk properties of the materials. If one goes along with this preposition, catalytic performance should also be related at least partly to these properties. Then in turn, an expert system should not only incorporate surface but also bulk properties, such as crystallographic structure, lattice parameters, cluster sizes, electronic conductivity and concentration of ion defects.

Against the above background some important questions arise: How should bulk and surface properties be determined for a specific material considered to be a potential catalytic compound? What is the optimum procedure for procuring the required data? This problem is being dealt with in developing a standard Multi-Technique Approach (MTA) and in interpreting the information obtained [31]. To this end the authors emphasize the necessity of a structural model for computer-aided characterization of solid samples by bulk and surface properties. Such a model may then serve as a basis for optimization by selecting the most suitable characterization technique by artificial-intelligence methods. For example, an expert system has been developed for simultaneous interpretation of data gained from XPS and TEM on the surface topology of two-component supported catalysts, i.e. mainly surface-particle size.

### 2.6.2.2 Neural Networks

The basic idea behind an artificial neural network is a simplified model of the human brain which is said to be able to correlate output data (results) with input data (factors). It is anticipated that neural network technology could also contribute significantly to analyzing, predicting, and optimizing the performance of chemical manufacturing units and plants [32]. In the context of predicting the catalytic performance of inorganic solids, neural networks have been applied particularly to estimating or predicting structure-activity relationships and structure-spectrum correlations [33-36].

In heterogeneous catalysis the applicability of this method has been demonstrated. The method is explained below for the acid-catalyzed oxidative dehydrogenation of ethylbenzene as used by Kito et al. [37-41] aiming at maximizing the selectivity to styrene by promoting SnO<sub>2</sub> with various inorganic compounds.

Applied to catalysis, input data are properties of catalyst components, whereas output data is the observed catalytic performance such as activity and selectivities towards the products. Commonly, an intermediate hidden layer of neurons is included between the input layer and the output layer (Fig. 2), and the

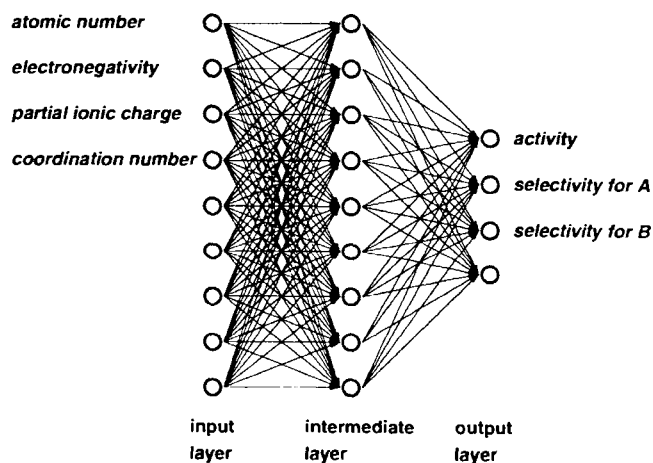


**Figure 2.** Modeling relationships between chemical and physico-chemical properties of catalyst components and their catalytical behavior by a neural network.

artificial neural network is set up this way that the activity of a neuron is calculated as a linear combination of the activity of the neurons of the preceding layer. The artificial neural network is trained with a given set of experimental data, by adjusting the weights for the linear combinations so that it describes the experimental data with a minimum error. The network may be tested if, for learning, one experiment is left out, and the catalytic performance is predicted from the catalyst properties as input data.

When applying a series of promoted and unpromoted SnO<sub>2</sub> catalysts for the oxidative dehydrogenation of ethylbenzene, the artificial neural network was able to predict the observed selectivities with an average absolute error of only 1.5% (Fig. 3). These results are much better than those obtained by the expert system INCAP (see Section 2.6.2.1), where the average absolute error for the styrene selectivity was about 20%.

In another example, a neural network was applied successfully to the prediction of conversion and yields in the decomposition of NO into N<sub>2</sub> and O<sub>2</sub> over Cu/ZSM-5 catalysts [42]. This shows that artificial neural networks are able to describe a complex catalytic system quite well if an appropriate numerical representation is found for the input and output data. The problem in their application may be the availability of a representative set of experimental data for learning, as well as the interpretation of the weights obtained for neuron interconnections which do not enable direct derivation of guidelines for the optimization of a catalytic system.

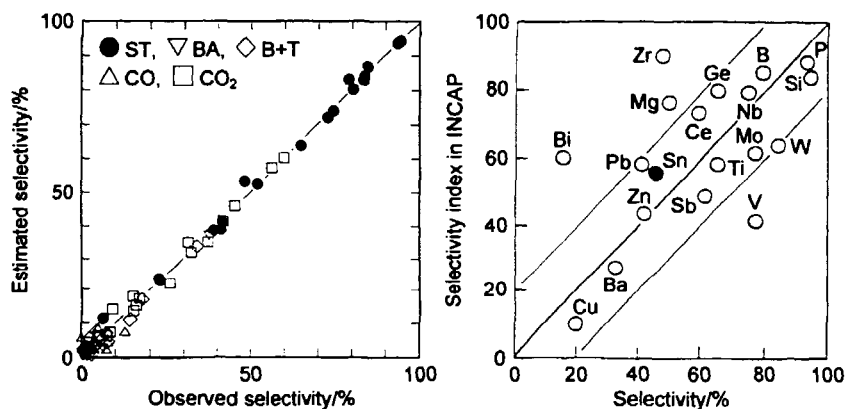


**Figure 3.** Accuracy of estimation of the selectivities for styrene (ST), benzaldehyde (BA), benzene + toluene (B + T), CO and CO<sub>2</sub> by a neural network (left) in comparison with the selectivity for styrene as estimated by an expert system, INCAP (right) (reproduced by kind permission of T. Hattori).

### 2.6.3 Deterministic Methods in Catalyst Design

More recently a hybrid approach to computer-assisted catalyst synthesis, based on a microkinetic analysis of the catalytic reaction, has been put forward which comprises essentially deterministic but also some non-deterministic features. For the synthesis of a catalyst with high activity and selectivity for a given reaction, the application of a microkinetic analysis has been suggested by Dumesic and co-workers [43–45]. The derivation of the microkinetics is not necessarily based on detailed kinetic experimentation but, by analogy, to similarities with other known catalytic processes. In an ideal situation, the microkinetics of a catalytic reaction are completely defined according to Dumesic and his collaborators when:

- all of the chemical species on and above the catalytic surface have been identified unambiguously;
- the elementary reaction steps involving the formation and cleavage of chemical bonds have been established uniquely;
- the rate constants for each elementary reaction have been measured independently;
- the rate constants for each elementary reaction are known as a function of the catalyst formulation.

Unfortunately, these requirements have not yet fully been met for any catalytic reaction, although for some simple catalytic reactions reasonable approaches are known. Such reactions are the oxidation of CO over a supported Rh catalyst [46, 47], ammonia synthesis over iron [48, 49], and the HCN synthesis over a Pt gauze catalyst. More recently Wolf [50] carried out a microkinetic analysis of the primary reaction steps in the oxidative coupling of methane and also related the rate

constants of the various surface steps to different compositions of various  $(\text{CaO})_{1-x} \cdot (\text{CeO}_2)_x$  catalysts and their resulting electronic properties.

In support of catalyst synthesis for a new reaction, a microkinetic simulation is performed using rate constants of the postulated elementary reactions which have been either independently measured or estimated. The applied mechanistic and kinetic models should be consistent with experimentally identified gas-phase products and surface intermediates observed by, for example, infrared spectroscopy. By using these models and kinetic parameters having physical and chemical meaning such as sticking coefficients, surface bond energies, preexponential factors and activation energies for surface reactions, surface bonding geometries, active sites densities and ensemble sizes, the general trend of the kinetic relationships is expected to be in agreement with experimental evidence. By changing the various parameters of the model which are assumed to be related to the catalytic compound(s) used an optimized catalyst composition should eventually evolve.

Dumesic and co-workers have presented various case studies in which they have applied the above concept of microkinetic analysis in order to propose new catalysts or to explain the different catalytic performance of different catalyst formulations for given reactions:

- (i) Oxidation of CO with NO and N<sub>2</sub>O decomposition into its elements on Y-zeolites and mordenite exchanged with different first-row transition metals (Cr, Mn, Fe, Co, Ni, Cu).
- (ii) Partial oxidation of methane to methanol and formaldehyde on exchanged Y-zeolites (Cr, Fe/Cu, Co, Mn/Ni).
- (iii) Ethane hydrogenolysis on silica-supported metal catalysts (Fe, Co, Ni, Ru, Rh, Pd, Re, Os, Ir, Pt).

The authors conclude that a coordinated effort involving experimental studies and microkinetic analysis of-

fers an opportunity for determining the factors that limit catalyst performance and for suggesting strategies that alter these limitations. If by microkinetic simulation a similarity is found to a known catalytic system, knowledge about this system may be transferred to the system of interest by analogy [43]. The combination of these ideas with semiempirical correlations of chemical bonding properties with catalyst structure and composition provides directions in the search for new materials.

The microkinetic analysis is certainly a scientifically interesting approach which will contribute to the identification and selection of catalytic compounds even in more complex situations as described above. One problem still to be solved is the experimental procurement and/or estimation of the parameters used in microkinetic simulations, which limits the wide applicability of the method. Providing kinetic parameters for a complex reaction network from kinetic experiments for an "analogous" catalyst is a time-consuming process. Despite the availability of modern experimental equipment and efficient computers, a complex reaction demands at least one man year of work [51]. The estimation of parameters by *ab initio* or semiempirical methods has to be considered with caution because ideal surfaces are usually assumed.

Nevertheless, *ab initio* or semiempirical quantum chemical calculations, with clusters to represent the catalytic solid material, can help build up a model of the catalytic system and study effects of modifications [52]. Even simulation of the molecular dynamics of the interaction between reactants or intermediates, together with replication of the unit cell of the catalytic solid in a simple force field, may describe observed effects in a catalytic system and may be able to predict the effect of catalyst modifications [53].

## 2.6.4 Chemical Reaction Engineering Aspects

The preceding discussion has concentrated on the selection of catalytically active components. Although this is an essential task, this is just one aspect of the whole catalytic process, which also includes selection of catalyst support and the design of the overall catalyst in relation to reaction engineering requirements, so that not only activity and selectivity but also mechanical and chemical stability are ensured. For catalyst supports, the design variables are the degree and the form of the dispersion of the catalytic active components, and the porosity of the support.

Deterministic computational methods have been applied to the description of deactivation processes [54]; models also exist for inter- and intraparticle diffusion as well as reactor hydrodynamics. For pore diffusion,

which influences catalyst effectivity and can also influence selectivity, the classical approach which uses equations for the Thiele modulus, relating the rate of chemical reaction to the rate of pore-diffusional processes [55], may be derived in analytical form by Berthe network models of randomly interconnected cylindrical pores. Alternatively, Monte Carlo methods may be applied as well for setting up a model of the solid, and for random walk simulation of diffusing reactants and intermediates [56].

Expert systems have been applied to reactor design, design of separation units, and over-all process design. These design tasks conflict with each other. For example the conversion and selectivity of the catalyst have consequences for the separation units, and the shape and mechanical properties of the catalyst are constrained by the reactor type and the operating conditions. Therefore an integrated approach may be useful, where specialized modules are supervised by a general control program, as proposed by Simmrock et al. for process synthesis [57].

## 2.6.5 Conclusions

The examples given above show that catalyst design requires an integrated approach, which considers heuristic relationships as well as deterministic methods. Computers can help to organize the huge amount of data. Knowledge about one reaction or reaction type and related methods is applicable also to other types of questions and related reaction classes, where similar reaction steps probably take place and so the same substance properties are involved. In this way a generalization may take place from empirical data about a specific reaction to reaction classes, opening the possibility for reasoning by analogy.

The more surface- and bulk-related properties of solid materials and their relevance to catalysis are incorporated into an expert system for assisting in catalyst design, the more effective such a system will be. Results and experience may be preserved in the knowledge base. Since such information may be applicable to other reaction types, if some reaction steps or relevant material properties are common, knowledge bases describing particular fields of interest may even be licensed to third parties, and so become tradable items.

## References

1. M. Misono, *Catal. Today* **1995**, *23*, 301.
2. H. C. Foley, E. E. Lowenthal, *CHEMTECH* **1994**, *24(8)*, 23.
3. J. A. Dumesic, B. A. Milligan, L. A. Greppi, V. R. Balse, K. T. Sarnowski, C. E. Beall, T. Kataoka, D. F. Rudd, A. A. Trevino, *Ind. Eng. Chem. Res.* **1987**, *26*, 1399.

- 4 S C Reyes, E Iglesia in *Computer Aided Design of Catalysts* (Eds E R Becker, C J Pereira), Marcel Dekker, New York, 1993, Chapter 5
- 5 A Miyamoto, T Hattori, T Inui, *Appl Surf Sci* 1992, 60, 660
- 6 A Miyamoto, T Hattori, T Inui, *Physica C* 1991, 190, 93
- 7 A Miyamoto, T Hattori, M Kubo, T Inui, *Jpn J Appl Phys* 1992, 31, 4463
- 8 A Miyamoto, M Kubo, *J Jpn. Petrol Inst* 1993, 36, 282
- 9 A Miyamoto, H Himeji, Y Oka, E Maruya, M Katagiri, R Vetrivel, M Kubo, *Catal Today* 1994, 22, 87
- 10 M E Davis, *CHEMTECH* 1994, 24(9), 22
- 11 T Inui, K Matsuba, Y Tanaka, *Catal Today* 1995, 23, 317
- 12 J Haber, M Witko, *Catal Today* 1995, 23, 311
- 13 M Ishida, M Yoshida, M Takashima, K Sawara, *Catal Today* 1995, 23, 341
- 14 H Kobayashi, D R Salahub, T Ito, *Catal Today* 1995, 23, 357
- 15 N Zhanpeisov, V Staemmler, M Baerns, *J Molec Catal* 1995, 101, 51
- 16 N Watari, S Ohnishi, *Catal Today* 1995, 23, 371
- 17 R Miura, H Yamano, R Yamauchi, M Katagiri, M Kubo, R Vetrivel, A Miyamoto, *Catal Today* 1995, 23, 409
- 18 Y H Sun, S W Li, S Y Chen, M Y Cheng, S Y Peng in *Computer Aided Innovation of New Materials II Part 1*, (Eds M Doyama, J Kihara, M Tanaka, R Yamamoto), Elsevier, Amsterdam, 1993, p 1111
- 19 R Bañares-Alcantara, A W Westerberg, E I Ko, M D Rychener, *Comput Chem Engng* 1987, 11, 265, 1988, 12, 923
- 20 H Speck, W Holderich, W Himmel, M Irgang, G Koppenhofer, W-D Mroß, *DECHEMA monographs* 1989, 116, 46
- 21 T Hattori, S Kito, Y Murakami, *Chem Lett* 1988, 1269
- 22 S Kito, T Hattori, Y Murakami, *Appl Catal* 1989, 48, 107
- 23 T Hattori, H Niwa, A Satsuma, S Kito, Y Murakami, *Appl Catal* 1989, 50, L11
- 24 S Kito, T Hattori, Y Murakami, *Chem Eng Sci* 1990, 45, 2661
- 25 S Kito, T Hattori, Y Murakami in *Catalytic Science and Technology* (Eds S Yoshida, N Takezawa, T Ono), VCH, New York, 1991, Vol 1, p 285
- 26 T Hattori, H Niwa, A Satsuma, S Kito, Y Murakami, *Stud Surf Sci Catal* 1993, 75, 489
- 27 X D Hu, H C Foley, A B Stiles, *Ind Eng Chem Res* 1991, 30, 1419
- 28 H C Foley, E E Lowenthal, X-D Hu in *Computer Aided Innovation of New Materials II* (Eds M Doyama, J Kihara, M Tanaka, R Yamamoto), Elsevier, Amsterdam, 1993, Part 1, p 1101
- 29 E Korting, M Baerns, *Chem -Ing -Tech* 1990, 62, 365
- 30 E Korting, M Baerns in *Computer Aided Innovation of New Materials II Part 1*, (Eds M Doyama, J Kihara, M Tanaka, R Yamamoto), Elsevier, Amsterdam, 1993, p 1107
- 31 D P de Bruijn, H P C E Kuipers, *Catal Today* 1991, 10, 131
- 32 S P Chitra, R J Bulson III, D G Morell, *CHEMTECH* 1995, 25(2), 18
- 33 J Gasteiger, J Zupan, *CICSJ Bulletin* 1991, 9, 15
- 34 J Zupan, G Gasteiger, *Anal Chim Acta* 1991, 248, 1
- 35 P C Jurs, *CICSJ Bulletin* 1991, 11(5), 2
- 36 J Zupan, J Gasteiger, *Neural Network for Chemists*, VCH, Weinheim, 1993
- 37 S Kito, T Hattori, Y Murakami, *Anal Sci* 1991, 7, 761
- 38 S Kito, T Hattori, Y Murakami, *Ind Eng Chem Res* 1992, 31, 979
- 39 S Kito, T Hattori, Y Murakami in *Computer Aided Innovation of New Materials II Part 1*, (Eds M Doyama, J Kihara, M Tanaka, R Yamamoto), Elsevier, Amsterdam, 1993, p 901
- 40 S Kito, T Hattori, Y Murakami, *Appl Catal* 1994 114 L173
- 41 T Hattori, S Kito, *Catal Today* 1995, 23, 347
- 42 M Sasaki, H Hamada, Y Kintaichi, T Ito, *Appl Catal A* 1995, 132, 261
- 43 D F Rudd, J A Dumesic, *Catal Today* 1991 10, 147
- 44 M G Cardenas-Galindo, L M Aparicio, D F Rudd, J A Dumesic in *Computer Aided Design of Catalysts* (Eds E R Becker, C J Pereira), Marcel Dekker, New York, 1993, Chapter 2
- 45 J A Dumesic, D F Rudd, L M Aparicio, J E Rekoske, A A Treviño, *The microkinetics of heterogeneous catalysis*, American Chemical Society, Washington, DC, 1993
- 46 S H Oh, G B Fisher, J E Carpenter, D W Goodman, *J Catal* 1986, 100, 360
- 47 G B Fisher, S H Oh, J E Carpenter, C L DiMaggio, S J Schmieg, D W Goodman, T W Root, S B Schwartz, L D Schmidt, *Stud Surf Sci Catal* 1987, 30, 215
- 48 P Stoltze, J K Nørskov, *J Catal* 1988, 110, 1
- 49 J A Dumesic, A A Treviño, *J Catal* 1989, 116, 119
- 50 D Wolf, *Catal Lett* 1994, 27, 207
- 51 R W Wojciechowski, N M Rice, *Chem Eng Sci* 1993 48, 2881
- 52 H Kobayashi, *Catal Today* 1991, 10, 167
- 53 J M Newsam, Y S Li, *Catal Today* 1995, 23, 325
- 54 R Christoph, M Baerns, *Stud Surf Sci Catal* 1987 34 355
- 55 G F Froment, K B Bischoff, *Chemical reactor analysis and design*, 2nd ed., Wiley, New York, 1979
- 56 S C Reyes, E Iglesia in *Computer Aided Design of Catalysts* (Eds E R Becker, C J Pereira), Marcel Dekker New York, 1993, p 89
- 57 K H Simmrock, B Fried, A Fried, *Chem Ing Tech* 1992 62, 1018



---

# 5 Elementary Steps and Mechanisms

---

## 5.1 Chemisorption

## 5.2 Microkinetics

## 5.3 Factors Influencing Catalytic Action

## 5.4 Organic Reaction Mechanisms

## 5.5 Computer Simulation

---

## 5.1 Chemisorption

### 5.1.1 Principles of Chemisorption

H.-J. FREUND

#### 5.1.1.1 Introduction

The term chemisorption was coined in order to classify the interaction between a particle in the gas phase and a solid surface, i.e. the result of the adsorption process [1]. If the interaction leads to the formation of a chemical bond the adsorbate formed is called a chemisorbate. Where chemical bond formation is not important the process is classified as physisorption. There are several conceptual problems with such a differentiation which we briefly address in the following, and which indicate that a more detailed look at the entire process of adsorbate formation is needed before a reliable classification may be carried out. In fact, as it turns out, for a conclusive classification one would need the full theoretical and experimental understanding of the system under investigation. Such an approach must include the static aspects, i.e. the energies involved, as well as the dynamic aspects, i.e. the processes involved in the formation of the adsorptive interactions.

Irving Langmuir in 1916 introduced and investigated the idea that there can exist strong, short-range forces between adsorbates and a substrate [2, 3]. Previously, it

was generally believed that more or less unspecified long-range forces – we would today call this physisorption – draw gases towards a solid. Langmuir, shortly after the introduction of the concept of an ordered lattice for the arrangement of the atomic constituents of a bulk solid by von Laue [4], considered an arrangement of atoms at the surface, a surface lattice, that defines a specific density of adsorption sites. Atoms from a gas phase, for example, striking the surface may either bounce back into the gas phase or establish a bond to one of these sites. This process is equivalent to the formation of a surface chemical bond and was termed chemisorption [5–7]. Chemisorption lowers the free energy of the closed system containing the uncovered, “clean” surface and atoms or molecules from the gas phase. This lowering in energy can be measured via calorimetry or – less well defined – by a Clausius–Clapeyron analysis of isostere data. It was therefore tempting to differentiate chemisorption with respect to physisorption via the energy that is deliberated in bond formation [1]. Such a definition involves a limiting energy which separates chemisorption and physisorption regimes. It was put in the neighborhood of  $40 \text{ kJ mol}^{-1}$  [1]. Obviously, such a definition is rather artificial, and today one generally disregards this kind of differentiation solely on the basis of the enthalpy of formation. The accepted definition of chemisorption today is independent of thermochemical data and rests on the concept of a short-range chemical bond, which only forms when there is direct intermingling of the substrate and the adsorbate charge densities. In order then to differentiate between chemisorption and physisorption one has to understand the electronic structure of the system [6, 8]. Experimentally, this means that we cannot rest the definition on a single measurement of the heat of adsorption but rather on an as complete as possible spectroscopical characterization of the surface interacting with the adsorbate in comparison with the same measurements of the separated systems.

The interaction between say a gas phase, containing molecules AB, and a surface is discussed by considering various aspects of the process of AB–surface bond formation. We cover the dynamic aspects connected with the sticking of AB such as its dependence on the

population of internal and external degrees of freedom of AB in the collision, mobility on the surface, i.e. surface diffusion etc., and the energetics, which will be the starting point, all as a function of the surface coverage. We shall discuss associative versus dissociative chemisorption and its dependences on surface structure. Consideration of coadsorption and cooperativity in the adsorption process is as important as invoking the structure of the adsorbate, as well as the restructuring of the surface as it interacts with an adsorbate.

### 5.1.1.2 Thermodynamics and Energetics

As this point it is important to differentiate between macroscopic and microscopic surface phenomena. Surface phenomena can be treated macroscopically by chemical thermodynamics, in which atomic concepts are not necessary. Accordingly, the thermodynamic relationships can be derived on the basis of pressure, volume, surface area, composition, and temperature, which can be measured in a straightforward manner. Historically, therefore, the thermodynamic approach was pursued first. Before discussing the atomic aspects of the energy content of an adsorbate phase we shall briefly summarize the important thermodynamic aspects noting, however, that this cannot be a comprehensive treatment. For the latter we refer to the literature [1, 7, 9–12].

Consider an adsorbate phase consisting of  $n_a$  moles of a nonvolatile adsorbent (surface) and  $n_s$  moles of an adsorbate (gas phase). They are assigned internal energy  $U$ , entropy  $S$  and volume  $V$ . The surface  $A$  of the adsorbent is assumed to be proportional to the adsorbent volume. The Gibbs fundamental equation for the full system is then

$$dG = -S dT + V dP + \mu_a dn_a + \mu_s dn_s \quad (1)$$

For the pure adsorbent,

$$dG^0 = -S_a dT + V_a dP + \mu_a^0 dn_a \quad (2)$$

Consequently, for the interacting adsorbate–adsorbent system, the difference  $dG^s = dG - dG^0$  gives

$$dG^s = -S_s dT + V_s dP + \Phi dn_a + \mu_s dn_s \quad (3)$$

where  $S_s = S - S_a$ ,  $V_s = V - V_a$ , and  $\Phi = \mu_a - \mu_a^0$ . Using the above mentioned proportionality between adsorbent volume and adsorbent surface,

$$\Phi dn_a = f \Phi dA \quad (4)$$

where  $f$  is a proportionality factor, the surface tension  $\varphi$  is given by

$$f \Phi = \varphi = \left( \frac{\partial G^s}{\partial A} \right)_{T,P,n} \quad (5)$$

which has the dimension of a two-dimensional pressure. This leads to the final equation

$$dG^s = -S_s dT + V_s dP + \varphi dA + \mu_s dn_s. \quad (6)$$

This equation refers to a system where the adsorbate resides on a truly inert substrate. In other words, eq 6 can only rigorously be applied to weakly interacting physisorbate systems. For chemisorbates this equation is not strictly applicable because the thermodynamic parameters of adsorbate and adsorbent cannot be separated.

Bearing this restriction in mind, and assuming that the adsorbate phase is in equilibrium with the gas phase, a Clausius–Clapeyron analysis yields

$$\left( \frac{\partial \ln P}{\partial T} \right)_\varphi = \frac{(s_g - s_s)}{RT} = \frac{(h_g - h_s)}{RT^2} = -\frac{\Delta h_{ads}}{RT^2} \quad (7)$$

where we have changed to molar quantities  $s$ ,  $v$ , and the enthalpy  $h$ . The slope of a semilogarithmic plot of the equilibrium pressure versus the inverse temperature at constant  $\varphi$  yields the adsorption enthalpy,  $\Delta h_{ads}$ , released upon adsorption of one mole of gas. The problem, of course, arises because the surface tension is hard to determine in general. However, the problem may be circumvented by considering the so-called surface coverage  $\Theta$  instead:

$$\Theta = \frac{n_s}{n_a} \quad (8)$$

and resorting to partial molar quantities, e.g.

$$\tilde{v}_s = \left( \frac{\partial v}{\partial n_s} \right)_{T,P,n_a} \quad (9)$$

Then, a similar Clausius–Clapeyron analysis leads to

$$\left( \frac{\partial \ln P}{\partial T} \right)_\Theta = \frac{(s_g - \tilde{s}_s)}{RT} = \frac{(h_g - \tilde{h}_s)}{RT^2} = \frac{-q_{st}}{RT^2} \quad (10)$$

where  $q_{st}$  is the isosteric heat of adsorption. This quantity can be measured quite easily because constant coverage is not too difficult to establish experimentally. However,  $q_{st}$  represents the difference between molar enthalpy in the gas phase and partial molar enthalpy in the adsorbed phase, a quantity not easily connected to microscopic considerations.

In order to directly see how the isosteric heat of adsorption is measured, eq 10 is written in the form

$$\frac{dP}{P} = \left( \frac{-q_{st}}{RT^2} \right) dT \quad (11)$$

and integrated for a reasonably small pressure and temperature interval so that we can assume the isosteric heat to be constant. This yields

$$\ln \left( \frac{P_1}{P_2} \right) = \frac{q_{st}}{R} \left( \frac{1}{T_1} - \frac{1}{T_2} \right) \quad (12)$$

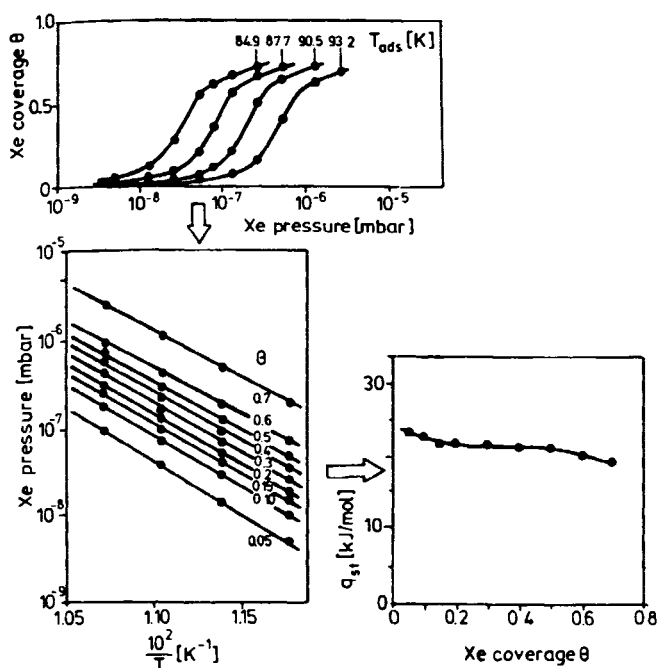


**Figure 1.** Determination of the isosteric heat of adsorption from the measurement of adsorption isotherms for the system Xe/Ni(100) [13].

for two pairs of temperatures and pressures that produce the same surface coverage. For true equilibrium conditions, a straight line with negative slope should be obtained for the semilogarithmic plot, which in turn yields the isosteric heat of adsorption. Repeating this procedure for various coverages allows the coverage dependence of the heat of adsorption to be determined. It is obvious that the isosteric heat is a differential quantity, in contrast to the equilibrium heat of adsorption. Both are, of course, isothermal quantities. From the differential heats of adsorption the integral heat of adsorption can be obtained as

$$Q_{\text{integr}} = \int_0^{n_s} q_{\text{st}} dn_s \quad (13)$$

In the following we present an example of isosteric heat determination [13]. Figure 1 shows, in the upper panel, a set of four isotherms for the physisorption system Xe/Ni(100). The second panel contains the data set in the upper panel as a plot of  $\ln p_{\text{Xe}}$  versus reciprocal temperature for various values of  $\Theta_{\text{Xe}}$ . From the shape of the individual straight lines the isosteric heat has been determined and plotted in the third panel as a function of  $\Theta_{\text{Xe}}$ . From the plot we see that the isosteric heat slowly varies with temperature, the decrease indicating repulsive interactions.

As mentioned above, the application of an isosteric heat analysis to a chemisorption system is rather problematic, because inherently the analysis starts from the

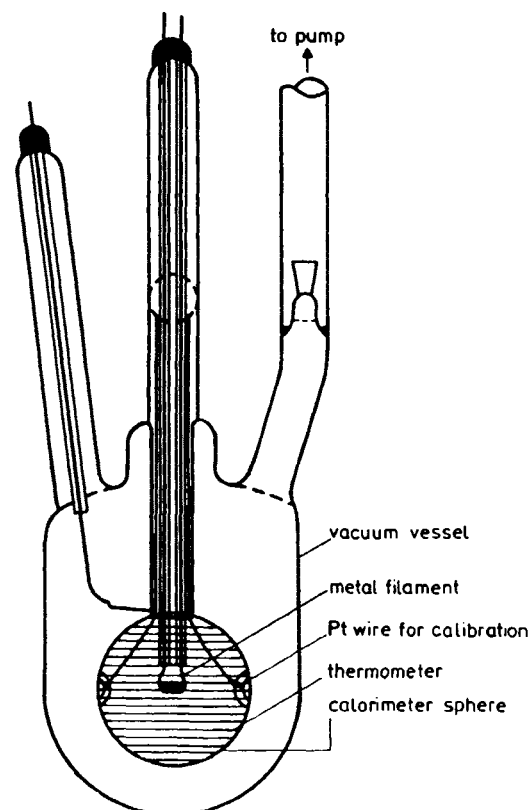


**Figure 2.** Schematic drawing of the spherical calorimeter [19].

assumption of truly separable subsystems. Therefore, for such systems it is more appropriate to resort to a direct calorimetric measurement of the adsorption enthalpy. Until very recently, it has not been possible to undertake such measurements for thin-film systems [1, 14–19]. The reason was that the increase in temperature of the calorimeter depends on the heat capacity of the system and the absolute number of adsorbed particles. The most complete set of data for such thin-film systems has been reported by Wedler and co-workers [1, 20]. They used the so-called “spherical calorimeter” shown in Fig. 2 [17]. Briefly, the calorimeter sphere is located inside an ultrahigh-vacuum glass recipient and temperatures change of less than  $10^{-5}$  K are registered with a thermometer connected to the calorimeter sphere. The metal film is evaporated onto the sphere and gas is admitted. The change in temperature measured by the thermometer surrounding the calorimeter sphere upon gas exposure is plotted versus time in Fig. 3. The heat of adsorption is determined from the integral of the  $T$  versus  $t$  curve. The example here is the adsorption of  $\text{H}_2$  onto a Pd film [21]. Converting the temperature–time curve into a heat of adsorption yields  $88 \text{ kJ mol}^{-1}$  [21].

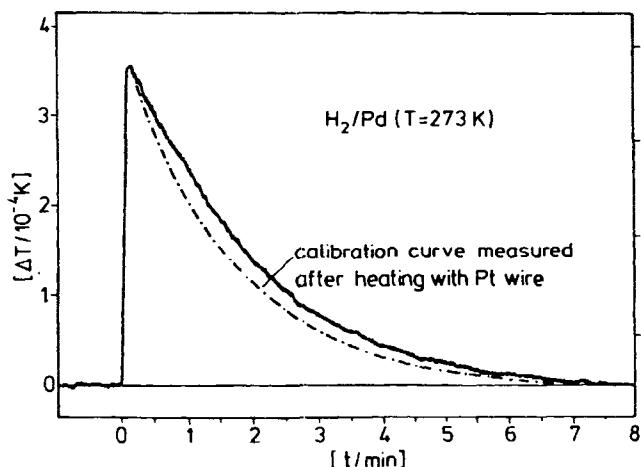


Figure 3. Temperature-time curve of a calorimetric measurement for the system  $\text{H}_2/\text{Pd}$  [21].

In Table I are assembled the heats of adsorption for various adsorbate systems on different substrates determined via isosteric heat measurement as well as calorimetric measurements. In some cases the heat of adsorption for one system has been measured using different techniques. This allows an estimation of the error involved in using those values based on different measurements. It is clear that the value for CO adsorption on Fe, for example, is considerably higher than values for other CO-adsorbate systems. In order to judge this, it must be understood that at room temperature CO partly dissociates on polycrystalline Fe which contributes to the observed calorimetric value. This is a useful reminder that consecutive processes have to be considered in calorimetric measurements.

King and co-workers have recently extended calorimetric measurements to single-crystal surfaces by applying molecular beam techniques in combination with IR radiation emission measurements (Fig. 4) [23, 38, 46–48]. There are three important parts of the experiment. First, there is a molecular beam source to provide accurate determination of coverage. Secondly, the sample consists of a unsupported single-crystal thin film to reduce the thermal mass to a minimum. Finally, an infrared detector is used to sense the heat radiated as the gas adsorbs. In order to reduce white noise experiments are performed using a pulsed molecular beam, which must be capable of producing a significant enthalpy change per pulse upon adsorption. A set of results is included in Table I where it is compared with results from other thermodynamic measurements. It is interesting to note that the results for the single crystal surfaces are situated in the region of those determined for the polycrystalline films, indicating that the latter consist of many crystallites exposing low-index planes.

The free enthalpy of adsorption is determined by the enthalpy as well as the entropy of adsorption. The

entropy of adsorption, which is the quotient of the reversibly exchanged heat and the temperature, may be calculated from the equilibrium heat of adsorption, if the surface tension is known, or from the isosteric heat of adsorption. Prerequisite is the knowledge of the corresponding equilibrium gas pressure. Table 2 collects typical values for the entropy of adsorption of several adsorbate systems.

The number of values available is much smaller than for the enthalpies of adsorption. The interpretation of entropies is considerably more involved than the interpretation of enthalpies. Often the observed values and, in particular, the coverage dependences, cannot be reconciled on the basis of theoretical predictions. It appears that the predictions as to how the various degrees of freedom of the adsorbate contribute are not accurate enough to date. However, in most cases large entropy values are found when the mobility of the adsorbate was expected or known (from other methods) to be large.

However, the most popular method by which to deduce the heat of adsorption of an adsorbate system is thermal desorption spectrometry (TDS) [53–57]. A schematic setup for a TDS measurement is shown in Fig. 5 [58]. The sample is heated resistively and the temperature is monitored by a thermocouple. If the sample is a single crystal it responds rather rapidly to heating so that relatively high heating rates may be used. The concentration of desorbing species is measured with a quadrupole mass spectrometer (QMS). Pumping capacity is important in thermal desorption, because only if it is high enough, readsorption of the desorbing species back onto the surface is excluded. If the pumping speed is infinitely high we can ignore readsorption and the change in adsorbate coverage per unit time; a measure for the desorption rate ( $r_{\text{des}}$ ), is given by the Wigner-Polanyi equation [7, 59]:

$$r_{\text{des}} = -\frac{d\Theta}{dt} = k_{\text{des}}\Theta^n = v(\Theta)\Theta^n \exp\left\{-\frac{E_{\text{des}}(\Theta)}{RT}\right\} \quad (14)$$

where  $T = T_0 + \beta t$ . This is the basis for the analysis of thermal desorption spectra.

Figure 6 schematically shows a set of TD spectra for various initial coverages  $\Theta_0$  and a given heating rate  $\beta$  [7, 58]. The first step is the integration of the spectra starting from highest temperature, i.e. coverage  $\Theta = 0$ , to a given coverage  $\Theta'$ , say 0.15. This yields a pair of ( $r, T$ ) values for each initial coverage larger than  $\Theta' = 0.15$ . A plot of  $\ln r$  versus  $1/T$  yields  $E_{\text{des}}(\Theta')$  from the slope and  $v(\Theta')$  from the intercept, which is given by  $n \ln \Theta' + \ln v(\Theta')$ , if the order  $n$  of the desorption reaction is known. However, for coverages above 0.1, the second term is much larger than the first.

Table 1. Enthalpies of adsorption.

Adsorbate	Substrate	$q$ (kJ mol <sup>-1</sup> )	Remarks	References	
CO	Ni(111)	111 ( $\pm 5$ )	WF <sup>1)</sup>	22	
		130	Microcalorimetry	23	
	Ni(100)	125 ( $0 \pm 5$ )	WF	24	
		115	TDS <sup>2)</sup>	25	
		119	TDS	26	
		138	TDS	27	
		109	isosteric $E_{ad}$	28	
		123	isosteric $E_{ad}$	24	
		130	isosteric $E_{ad}$	29	
		134	isosteric $E_{ad}$	30	
		123	Microcalorimetry	23	
		133	Microcalorimetry	23	
	Ni(110)	133	Microcalorimetry	23	
	Pd(100)	150 ( $\pm 5$ )	WF	31	
		161 ( $\pm 8$ )	WF, TDS, LEED	32	
	Pd(111)	142 ( $\pm 3$ )	WF	33	
	Ru(0001)	160 ( $\pm 10$ )	WF	34	
	Ru(10 $\bar{1}0$ )	157 ( $\pm 10$ )	Contact-pot., TDS	35	
	Cu(100)	58 ( $\pm 10$ )	WF	36	
	Fe(111)	325	273 K (dissociative)	37	
Fe(111)	200	195 K (partially diss.)	37		
Fe(111)	100	(not dissociative)	20		
CO/K	Ni(100)	190	Microcalorimetry	38	
		300	195 K (dissociative)	37	
CO <sub>2</sub>	Fe	300	195 K (dissociative)	37	
H <sub>2</sub>	Ni(100)	96.3 ( $\pm 5$ )	WF	39	
		90.0 ( $\pm 5$ )	WF	39	
	Ni(110)	96.3 ( $\pm 5$ )	WF	39	
		85 ( $\pm 5$ )	WF	40	
	Ni	75 ... 176		1	
	Pd(111)	88 ( $\pm 5$ )	WF	41	
	Pd(110)	103 ( $\pm 5$ )	WF	42	
	Pd(100)	102 ( $\pm 5$ )	WF	41	
	Rh(110)	92 ( $\pm 5$ )	WF, TDS	43	
	Ru(10 $\bar{1}0$ )	80 ( $\pm 5$ )		44	
	Co(10 $\bar{1}0$ )	80 ( $\pm 5$ )		45	
	Ta	188.1		1	
	W	188.1		1	
	Cr	188.1		1	
	Fe	133.8		1	
	Fe	100	dissociative (273 K)	20	
	Fe	97 ( $\pm 3$ )		37	
	Pd	80/96		21	
	Na	W	133.8		1
	Cs		267.5		1
O	Ni(100)	532 ( $\pm 5$ )	IR (300 K)		
		$\approx 432$	IR (100 K)		
		532 ( $\pm 5$ )		23	
	Ni(111)	470 ( $\pm 15$ )		23	
	Ni(110)	498 ( $\pm 5$ )		23	
O <sub>2</sub> /CO	Fe(111)	490	273 K	20	

<sup>1)</sup> WF, work function; <sup>2)</sup> TDS, thermal desorption spectroscopy

so the latter may be neglected without large errors. It should be noted that there are methods to determine the order rigorously. This analysis, called the "complete analysis" was first proposed by King in 1975 [55]. The preexponential factor  $\nu(\Theta)$  can be regarded as representing the frequency of attempts of the adsorbed particle to escape the chemisorptive potential. The values determined vary by at least four orders of magnitude, from  $10^{12}$  to  $10^{16}$  s<sup>-1</sup> [7]. If we adopt the

simplest picture and set  $\nu(\Theta)$  equal to the frequency of vibration of the adsorbed particle, values near  $10^{13}$  s<sup>-1</sup> are expected. The problems become even more involved if we consider the number of successful attempts, i.e. after multiplication of  $\nu(\Theta)$  by the exponential in eq 14. Here, the activation energy for desorption  $E_{des}(\Theta)$  comes into play; both  $\nu(\Theta)$  and

References see page 938

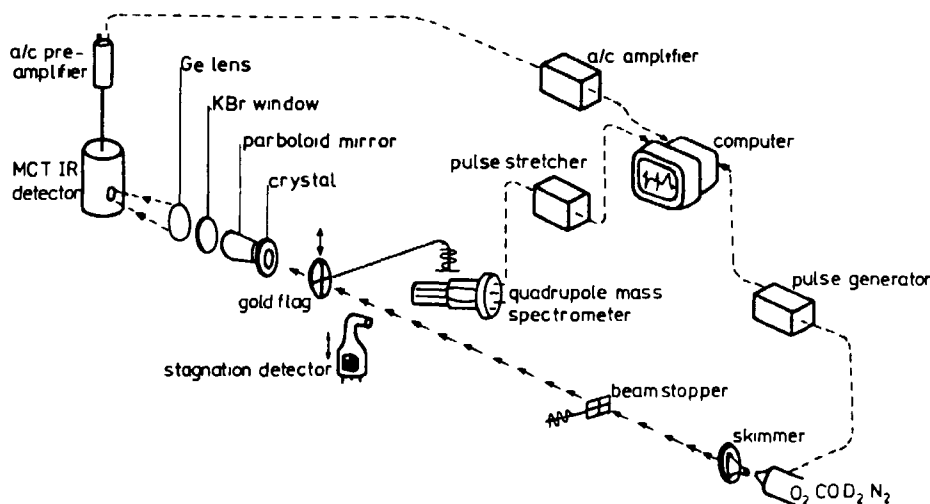


Figure 4. Schematic drawing of the setup for microcalorimetric measurements on single crystals [46]

Table 2. Entropies of adsorption

Adsorbate	Substrate	$\Delta S_{ad}^0$ (JK <sup>-1</sup> mol <sup>-1</sup> )	References
Xe	Ni(100)	≈ 56	13 49
	Pd(100)	≈ 58	50
H	Pd(100)	≈ 263	49
N <sub>2</sub>	Ni(100)	≤ 50	51
	Ni(110)	112 (± 5)	52

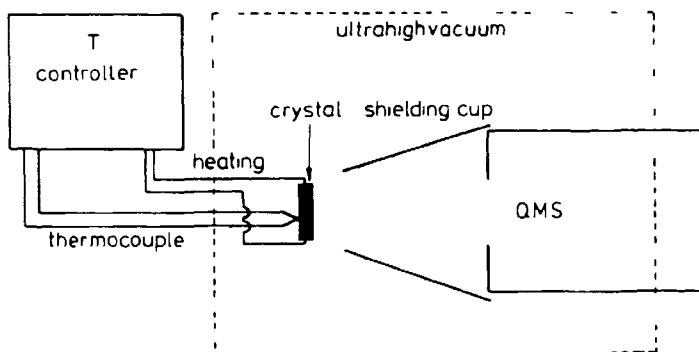


Figure 5. Schematic drawing of the experimental setup for a thermal desorption experiment

$E_{des}(\Theta)$  depend on coverage. These coverage dependences partly compensate each other for certain systems in the sense that high values of  $\nu(\Theta)$  are associated with large values of  $E_{des}$  [7]. This has to be considered when dealing with predictions and interpretations of desorption rates. It is therefore important to resort to a complete or close to complete analysis of desorption data. Simplified analyses were published much earlier. The most popular one is the so-called Redhead analysis, based on the peak maximum temperature observed in a thermal desorption spectrum [54]

$$E_{des} = RT_{max} [\ln(\nu T_{max}/\beta) - 3.46] \quad (15)$$

It results in reliable values only for first-order desorption and provided that a reliable value for  $\nu$  is available. The Redhead equation can be directly derived from the Wigner–Polanyi equation by determining the temperature derivative of the rate, and realizing that it must vanish at the peak maximum temperature [7]. Additional procedures are given in the literature [58, 60–63]. In connection with the initial question concerning the heat of adsorption, it must be realized that the desorption energy may be directly related to the heat of adsorption if adsorption is a nonactivated process. In other words, the adsorption process is energetically, continuously “downhill”. A detailed understanding, however, necessitates an understanding of the dynamics of adsorption.

A connection exists between the phenomenological view of the energetics from the standpoint of thermodynamics, and the microscopic view of adsorbate energetics. In this context, the question as to whether a process is activated or nonactivated may already have been answered.

This approach goes back to Lennard-Jones who discussed adsorption energetics in a landmark paper in 1932 applying a quasi-one-dimensional approach [64]. Neglect for the moment all problems connected with the question as to how a gas-phase particle is actually trapped in a bound state at the surface of a solid and simply consider the interaction potential between the gas-phase particle and a surface. Figure 7(a) shows the well known Lennard-Jones potential energy diagram. It represents the superposition of attractive (longer range) and repulsive (short range) forces according to

$$L(z) = -Az^{-6} + Bz^{-12} \quad (16)$$

where  $A$  and  $B$  are empirical constants and  $z$  is the distance between the adsorbed particle and the surface. To describe this interaction on the basis of *ab initio*

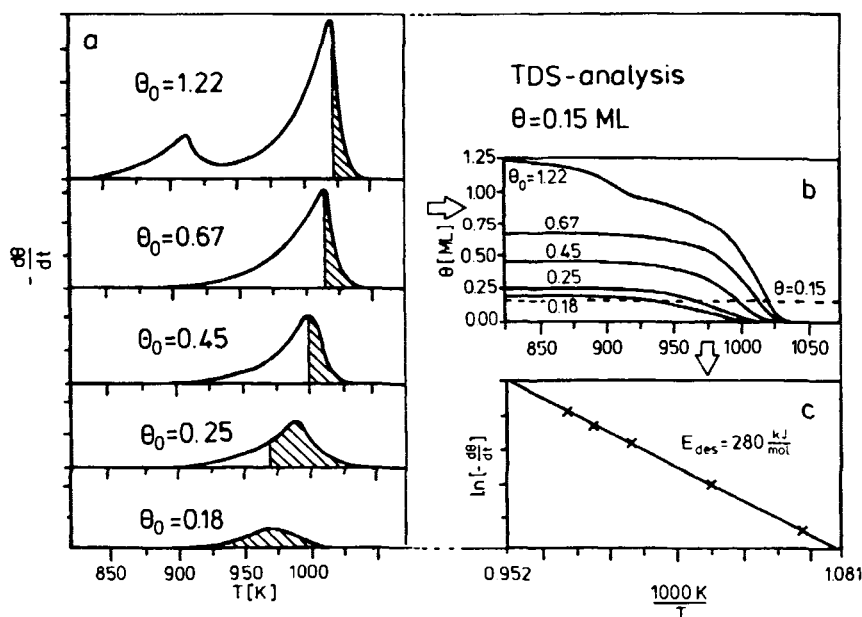


**Figure 6.** Determination of the desorption energy  $E_{des}$  from a model-independent analysis of thermal desorption data. The analysis is carried out for an artificially chosen coverage of  $\Theta = 0.15$ : (a) TDS data; (b) integration of the TDS data to give  $\Theta$  versus  $T$  plots; (c) plot of  $\ln(-d\Theta/dt)$  versus  $1/T$  to determine  $E_{des}$  according to eq 14. The basis for the diagram are data for Ag/Ru(0001) [58].

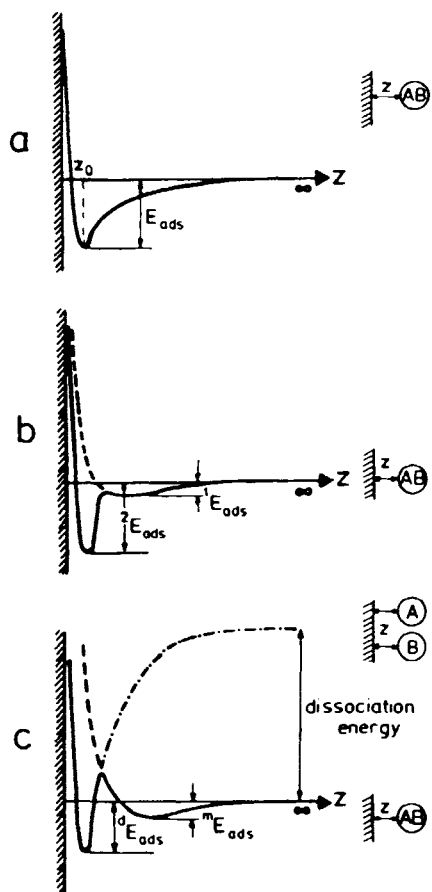


**Figure 7.** Schematic potential energy diagrams for a molecule AB approaching a surface: (a) associative chemisorption ( $E_{ads}$ ); (b) associative chemisorption ( $^2E_{ads}$ ) with precursor ( $^1E_{ads}$ ); (c) dissociative chemisorption ( $^dE_{ads}$ ) with molecular precursor ( $^mE_{ads}$ ).

quantum mechanical calculations it would be necessary to consider a semiinfinite solid interacting with an atom or a molecule. This can be done in favorable, simple cases using various approaches [65–68]. The most prominent one, at least for metal surfaces, is the density functional approach with which one can come close to the exact solution [65, 67]. Another approach is the so-called embedded cluster ab initio approach where the solid surface is represented by a cluster of atoms, augmented by an embedding scheme to represent more accurately the infinite extension of the two-dimensional system [68]. Assume for the moment that this problem has been solved. Then, the potential energy curve in Fig. 7(a) represents the case where the particle incident from the gas phase “sees” a continuously “downhill” energy change until it reaches the equilibrium position at  $z_0$ . (Note that, for the present, the dynamics of the trapping process is being neglected.) In such a case the desorption energy, as determined from thermal desorption data, is equivalent to the heat of adsorption. It is this situation that is often considered for associative molecular adsorption. However, the situation becomes more difficult if either a molecule which is associatively adsorbed may assume different adsorption geometries on the surface, or the molecule may dissociate upon adsorption and – to increase complexity – may do so via a molecularly adsorbed precursor state. Figures 7(b) and 7(c) schematically show the corresponding quasi-one-dimensional

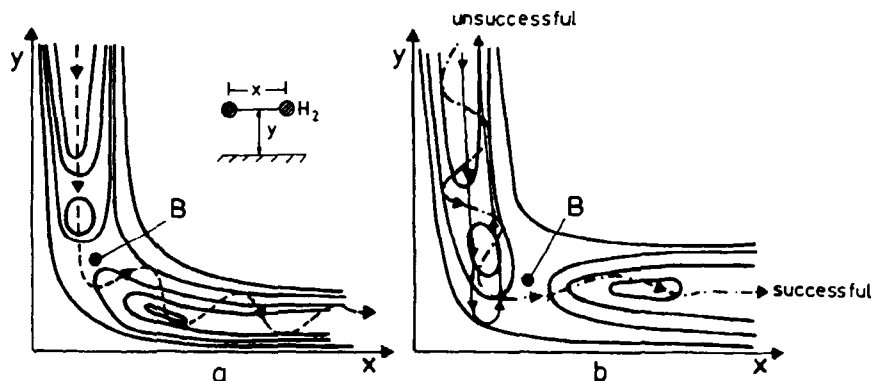


**Figure 8.** Two-dimensional potential energy surfaces (schematic) for (a) early and (b) late barrier (B) of dissociation of  $H_2$  on a transition metal surface.

potential energy diagrams. In Fig. 7(b) there is a second minimum in the potential energy diagram representing the two possible adsorption geometries. It is already obvious that, in this case, the use of such a quasi-one-dimensional diagram becomes very problematic because only a single spatial coordinate is used to represent the molecule-surface interaction. Therefore, such a situation calls for a multidimensional potential energy diagram, and we shall come back to this more general requirement later on. For the moment, however, Fig. 7(b) already allows us to visualize the transformation between the two inequivalent molecular adsorption geometries as an activated process. It is immediately clear that a desorption experiment will probe this more complicated potential energy curve, and thus a simple interpretation of the measured desorption energy as the heat of adsorption will not be possible in general.

The situation becomes even more complicated if, upon interaction with the surface, the molecule dissociates. This is depicted in Fig. 7(c). In this case it is necessary to consider two intersecting potential energy curves which refer to two different zero-energy levels, namely the diatomic molecule being infinitely separated from the surface for the associative interaction, as well as the two constituent atoms being infinitely separated from the surface. The difference between the reference levels, of course, represents the heat of formation of the diatomic molecule in the gas phase. In this case, the above-mentioned difficulty with the quasi-one-dimensional representation becomes particularly clear, in the sense that here the coordinate representing the separation between the two constituent atoms has not been considered at all. Nevertheless, it can be seen that there may be a rather large activation energy between the molecularly adsorbed precursor and the dissociatively adsorbed atoms, which is very crudely represented by the energy near the crossing point with respect to the potential energy minimum of the molecular precursor. Clearly, the point of intersection may

be situated well above the reference level corresponding to the infinitely separated molecule and surface, which in turn has strong consequences for the ability to populate the dissociative adsorbate. As will become clearer considering multidimensional potential energy surfaces in such a situation, the molecule has to have a certain impact energy to be able to surmount the activation barrier. Whether this impact energy should be represented by translational degrees of freedom or internal (rotational or vibrational) degrees of freedom cannot be concluded on the basis of the quasi-one-dimensional potential energy surface. However, it is already fully transparent that the shape of the potential energy surfaces will determine the kinetics as well as the dynamics of the system, and thus the probability to chemisorb. Experimentally, we measure (for example) the sticking probability of a particle from the gas phase into a particular adsorbate channel by probing the number of adsorbed species as a function of gas pressure and surface temperature. In other words, a relatively complex scenario is condensed into basically a single number. As the next section shows, it is far from easy to resolve the details.

Before tackling the problem of sticking consider, as alluded to above, potential energy diagrams that allow the incorporation of some essential additional features such as simultaneous motion along several coordinates (often normal coordinates). Clearly, the situation becomes very complicated as soon as many such coordinates come into play. Consider therefore, for simplicity the most simple case of a hydrogen molecule interacting with a transition metal surface. In recent years, this problem has been treated experimentally as well as theoretically in great detail so that a clear picture of the factors influencing the activation process has emerged. A good review for the case of  $H_2/Cu$  can be found in Ref. 69.

Figures 8(a) and 8(b) show potential energy diagrams for such a system [70]. The potential energy is plotted as equipotential lines in a coordinate system



where the ordinate represents the surface–molecule (center of mass) distance, and the abscissa the interatomic distance of the diatomic molecule, i.e. the hydrogen molecule in this case. Denoting the intermolecular distance in the molecule by  $x$  and the distance of the center of gravity of the bond to the surface by  $y$ , small  $x$  values are found for large  $y$  values, indicating the intact bond between the hydrogen atoms. As the molecule gets closer to the surface, i.e.  $y$  decreases,  $x$  finally increases to large values that are characteristic of the bond-breaking process. It is the exact position of the barrier, indicated by the letter B at the top of the saddle point in the potential energy diagram, that now governs the dynamics of the process. Two different situations are depicted. In Fig. 8(a) the activation barrier is located in the entrance channel. A molecule entering the entrance channel with sufficiently high translational energy can surmount the barrier, as indicated by the trajectory. However, it may well move up the wall before it can follow the bend (as if on a “bobsleigh” course) and the system will consequently come out the exit channel vibrationally excited (i.e. the hydrogen surface modes are excited) as indicated by the curved trajectory. In Fig. 8(b) the activation barrier is located more towards the exit channel. Here a vibrationally excited molecule has a better chance to surmount the activation barrier as indicated by the full trajectory. An unsuccessful attempt with a translationally excited molecule is shown for comparison. Once the vibrationally excited molecule has crossed the barrier, the hydrogen atoms formed will move across the surface with relatively high translational energy. The whole problem outlined so far can be mapped almost perfectly onto the so-called Polanyi rules [71], whereafter an exergonic reaction of type  $A + BC \rightarrow AB + C$  with an early barrier request translational energy, whereas, if the reaction has a late barrier, it requires vibrational excitation of the reactants.

Molecular beam studies [72] have been undertaken in recent years to prepare selectively translationally or vibrationally excited molecules before they were scattered off the surface, and a great deal has been learned about how the molecules stick to a metal surface, specifically for hydrogen–transition metal systems [65–73]. In the case of hydrogen absorption on Cu, the barrier [74–77] is in an intermediate position, so that both translational as well as vibrational excitation helps to surmount the barrier. There are still a lot of open questions as to which role rotational excitation plays [69]. However, even with a full understanding of the processes occurring on the potential energy surfaces shown in Figs. 8(a) and 8(b), there are still some important ingredients missing. This has particularly to do with the fact that in the discussion so far the geometric and electronic structure of the surface has not been considered. It is known that chemisorption is structure

sensitive, and therefore these aspects have to be considered. It should be pointed out that hydrogen adsorption on Cu surfaces may not be typical for interaction with transition metals in general [78]; in particular, remember that  $H_2$  dissociates with almost no barrier on metals such as Ni, Pd, etc. [73]. It is clear that in order to understand the barrier heights electronic structure calculations must be resorted to [79, 80]. However, the difference between Cu and Ni may be argued on a qualitative basis [79, 80]. Cu has the electronic configuration  $3d^{10}4s^1$ , with the rather diffuse 4s orbitals occupied. If a closed-shell  $H_2$  molecule approaches the Cu surface it will be repelled by the diffuse 4s electrons so that it is hard for the  $H_2$  to come in close to dissociate. Ni has the electronic configuration  $3d^94s^1$  in which the 4s orbital is occupied, which again leads to Pauli repulsion with the  $H_2$  molecule. However, in Ni the 4s electron may be promoted into the hole within the d shell, forming a  $3d^{10}4s^0$  configuration – this reduces the repulsion dramatically and allows the  $H_2$  molecule to come in close and dissociate. Therefore, the barrier for Ni is much lower than for Cu where it is in the range of 1 eV [69].

Another aspect that is important in connection with the discussion of adsorbate thermodynamics and energetics, so far neglected, is the aspect of interaction between adsorbed species. In Langmuir’s picture of adsorption [2, 3], mentioned in the introduction, the adsorbed particles occupy the lattice points of a two-dimensional substrate with equal probability and with hard wall potentials between them, preventing double or multiple occupancy of any particular site, and with well defined adsorption energies typical of the site. (Note that at this point structure sensitivity comes into the picture; however, this aspect is deferred until later.) As a result of this view of adsorption, saturation would be characterized by complete coverage and the formation of a true  $1 \times 1$  adsorbate layer. Obviously, the formation of ordered layers with coverages far below complete coverage are more the rule than the exception, and are a direct consequence of the existence of interaction potentials. Such an interaction potential is shown in Fig. 9 for the system CO/Pd(100) reported by Tracy and Palmberg in 1969, compared with a CO–CO interaction potential in the gas phase [31]. Interaction potentials may be either attractive or repulsive and may be classified into direct and indirect interactions [81–83]. Direct interactions involve dipole–dipole (multipole–multipole) and orbital-overlap interactions, and are often repulsive. On the other hand, indirect interactions mediated through the metal surface may be either attractive or repulsive depending on distance and surface sites, i.e. the kind of charge modification of the electronic structure of the substrate by

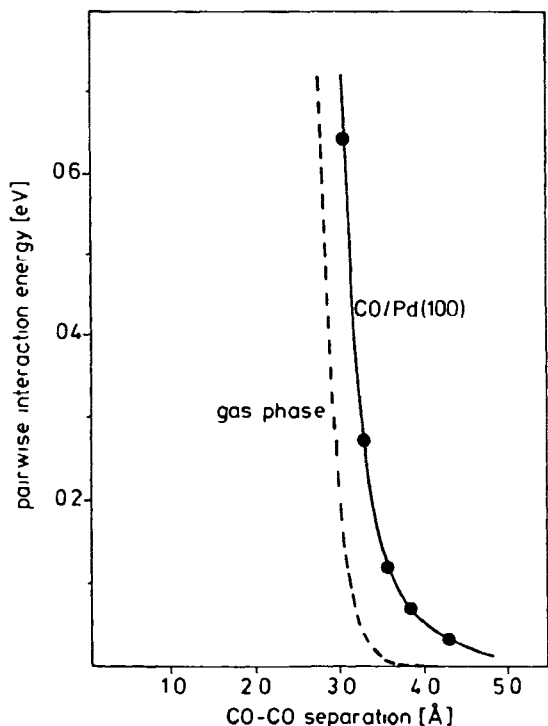


**Figure 9** Intermolecular potential for CO in the gas phase and CO adsorbed on a transition metal surface

the adsorbate. The interplay of the interaction potential and the adsorption energy of the isolated particle with the clean surface finally determines the observed properties of the adsorbed layer. In other words, the structure of the adsorbed layer depends on the heat of adsorption as well as on the coverage [5].

The situation again may be depicted in the form of a potential energy diagram, however we have to include the existence of different surface sites [84]. Figure 10(a) [7] shows a one-dimensional potential energy diagram where the spatial coordinate extends parallel to the surface. It has been assumed that every surface site provides identical binding conditions. All identical

adsorption sites are separated by a small activation energy if compared with the activation energy for desorption, which gives rise to a sinusoidal energy dependence across the surface. At low enough temperature the adsorbed particles will reside within the potential wells because their thermal energy is too small to overcome the activation barrier for diffusion. Correspondingly, for higher thermal energies, particles will site exchange resulting in a mobile adsorbed layer with short residence times in the individual wells. We shall discuss this situation in more detail further below. The potential energy diagram parallel to the surface changes significantly if the interaction between adsorbed particles is taken into account. This is schematically depicted in Fig. 10(b) where we have added an attractive as well as a repulsive potential to the one-dimensional diagram of Fig. 10(a). The consequences are energetic heterogeneities, weakening the adsorbate surface bond in the case of the repulsive interaction and strengthening the adsorbate surface interaction in the case of attractive interaction potentials. As mentioned above, phenomenologically this leads to the formation of ordered phases on surfaces. In fact, there may be several different ordered structures depending on both temperature and coverage, because surface diffusion may act against the formation of ordered structures, i.e. favoring disordered layers while for example, coverage increase locks in certain structures. A way to represent the various structures is to plot a so-called phase diagram [85]. An example is shown in Fig. 11. For the system CO/Cu(100), two ordered phases are found in the given temperature range [86]. These are denoted by I and II<sub>+</sub>, and they occur at coverages 1/2 and 4/7. Phase I is a  $c(2 \times 2)$  structure while phase II<sub>+</sub> consists of stripes of the  $c(2 \times 2)$  structure of width  $n = 3$  separated by domain walls. The main part of the phase diagram is filled by a disordered phase. A very interesting and frequently studied aspect of such phase diagrams are the two-dimensional phase transitions. In two dimensions, similar to

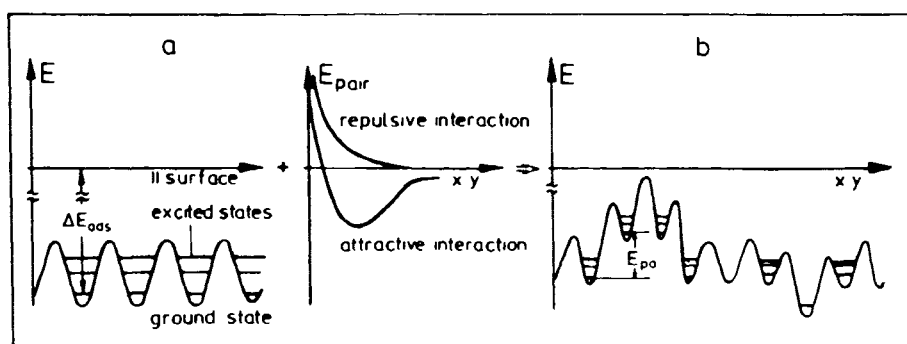


**Figure 10** One-dimensional potential energy parallel to the surface (a) empty surface with a single particle bound with adsorption energy  $E_{\text{ads}}$  (b) superposition of the potential energy in (a) with a pairwise interaction potential of particles on the surface ( $F_{\text{pair}}$ ) which may be either attractive or repulsive

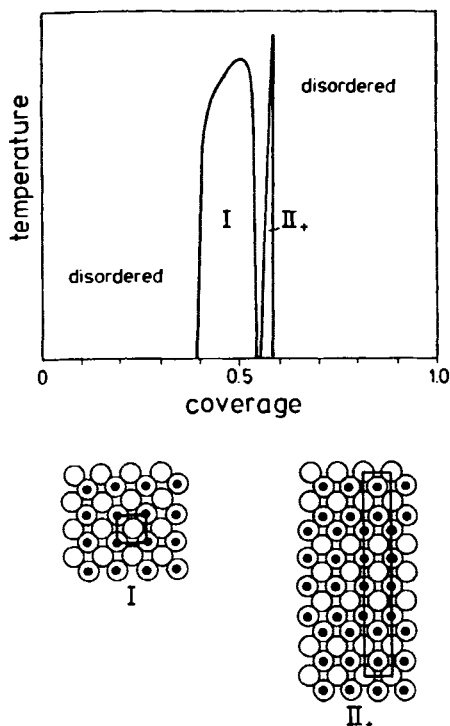


**Figure 11.** Phase diagram for the system CO/Cu(100), also showing the ordered structures [86].

three dimensions, phase transitions may be classified as discontinuous first-order, and continuous higher order. In general, phase transitions may be evaluated according to the temperature dependence of the thermodynamic functions. This subject is considered in greater detail elsewhere [87–90].

More important with regard to the heat of adsorption are the particle–particle interactions. As stated above, according to the Langmuir picture of adsorption [2, 3] we would expect constant adsorption energy until saturation of the surface is reached. In reality, this is never the case [85]. Rather, the adsorption energy generally decreases at medium and high coverages due to interactions between the adsorbed particles. It is possible to estimate the interactions from the coverage dependence of the isosteric heat of adsorption. In Fig. 12 [7] are several examples [22, 32, 39] where the work function has been used as a measure for the coverage (which may be sometimes dangerous). It is obvious from Fig. 12 that in all cases the adsorption energy sharply decreases as saturation is approached. At low coverage, however, the isosteric heat turns out to be either constant, decreasing, or increasing with coverage. The observed changes are a consequence of the particle–particle interactions on the surface, in the sense that increase means attractive interactions, as for example in the case of hydrogen for low coverage [39], decrease repulsive interaction, as in the case of CO on Ni(111) [22]. The step-like decrease of the heat of ad-

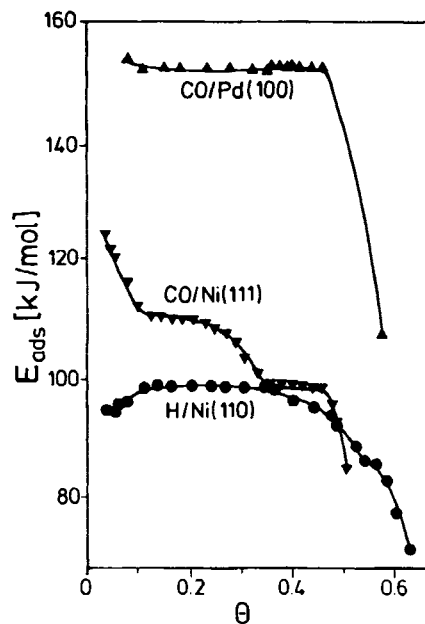


**Figure 12.** Adsorption energy ( $E_{\text{ads}}$  as a function of surface coverage  $\Theta$  [7]: ( $\blacktriangle$ ) CO/Pd(100) [32]; ( $\blacktriangledown$ ) CO/Ni(111) [22]; ( $\bullet$ ) H/Ni(110) [39].

sorption close to saturation for CO/Pd(100) [32] is due to the population of additional weakly bound species on the surface [91, 92]. These weakly bound species may be rather reactive. Owing to their small heat of adsorption they may react rather easily with co-adsorbed, neighboring functional groups. At high reactant pressures and not too elevated substrate temperatures this kind of scenario may play a significant role.

### 5.1.1.3 Sticking

This section considers the traditional description of the process where a molecule approaches a solid surface and eventually is trapped by the potential. A convenient way to gain access to this problem is through the consideration of the rate of adsorption. In the most simple case, the rate of adsorption is proportional to the number of molecules impinging per unit time on the surface, the so-called particle flux, and to the (dimensionless) efficiency with which an impinging particle actually sticks to the surface, i.e. the so called sticking probability. The initial sticking coefficient  $s_0$  is the ratio of the number of adsorbed particles  $\sigma_s$  and the number of impinging particles for the uncovered surface. Therefore,

$$0 < s_0 < 1 \quad (17)$$

In principle, determination of this quantity is straightforward. In an adsorption experiment a clean surface held at temperature  $T$  is exposed to a well defined pressure  $P$  for a given time  $t$  (exposure is measured in Langmuir:  $1\text{ L} = 10^{-6}$  torr for 1 s), and the amount of gas taken up by the surface (by a suitable surface science technique) is compared with the total amount of gas that has struck the surface. A method frequently used is the one proposed by King and Wells [93, 94]. In this case a molecular beam strikes the surface and the change in the background pressure of a given gas is measured by a mass spectrometer. The procedure is calibrated with respect to a gold sample that is known not to adsorb any molecules in the considered temperature range.

Knowing how  $s$  is measured experimentally, we can turn to further conceptual considerations. The rate of adsorption, i.e. the change of the number of adsorbed particles with time is given by [7]

$$r_{\text{ad}} = \frac{d\sigma_s}{dt} = \frac{P}{\sqrt{2\pi mkT}} s_0 f(\sigma_s) \quad (18)$$

where the flux of impinging particles has been treated according to the kinetic theory of ideal gases, and a function  $f(\sigma_s)$  accounts for the loss of empty sites as the adsorption process proceeds. The term  $s_0$  may be written in terms of a preexponential  $^{\circ}s$  and an activation energy  $^{\text{ads}}E_{\text{act}}$  as

$$s_0 = ^{\circ}s \exp\left(-\frac{^{\text{ads}}E_{\text{act}}}{kT}\right)$$

There is a different adsorption probability depending on whether the adsorption site is occupied or not. From what has been said before, the sticking coefficient must also depend on the population of internal and external degrees of freedom of the impinging molecule. This can be done in a closed form by assuming the sticking probability  $s$  to be composed of terms for the vibrational states involved, each weighted by a Boltzmann factor ( $F_B$ ) representing the population of the corresponding vibrational state [69]:

$$s(v, E_c, T) = \sum_v F_B(v, T) s_a(v, E_c) \quad (19)$$

where  $v$  represents the vibrational quantum state under consideration, which is populated according to the Boltzmann factor depending on the temperature  $T$  of the gas (effectively the nozzle temperature in a molecular beam experiment). The effective translation energy  $E_c$  is given by [74]

$$E_c = E_i \cos^n(\vartheta_i) \quad (20)$$

in which  $E_i$  is the translation energy of the incident particle, and  $\vartheta_i$  is the angle of incidence with respect to the surface normal. If  $n = 2$  then the effective trans-

lation energy shows a typical "normal energy scaling", in other words an exclusive dependence of the sticking probability on the normal component of the energy of the incident particle, which has been found rather frequently [95–100], and in particular for hydrogen adsorption on transition metals.

With this in mind we can go back to equation (18) and analyse the rate of adsorption further. First, write the rate in terms of coverage and not in terms of the absolute number of particles:

$$r_{\text{ad}}(\Theta) = \frac{d\Theta}{dt} = \frac{P}{\sqrt{2\pi mkT}} s_0 f(\Theta) \quad (21)$$

In the case of the most simple treatment according to Langmuir [2, 3], where it is assumed that each adsorbed particle occupies only one surface site, the adsorbed species does not interact with other adsorbed particles present on the surface. It is further assumed that the adsorption energy is completely exhausted as soon as one monolayer has been formed; the function  $f(\Theta)$  reduces to  $(1 - \Theta)$ . If the particle dissociates upon adsorption – it occupies two sites – the function  $f(\Theta)$  becomes  $(1 - \Theta)^2$ . Remembering that under equilibrium conditions the rate of adsorption must equal the rate of desorption

$$r_{\text{ad}} = r_{\text{des}} \quad (22)$$

we arrive at the following condition for the coverage:

$$(\Theta) = \frac{b(T)P}{1 + b(T)P} \quad (23)$$

which is the famous Langmuir adsorption isotherm [2]. In its derivation we have employed eq 14 for the desorption rate assuming a first-order process, and consecutively just solved for  $\Theta$ . In addition, we have used an abbreviation for a constant  $b(T)$  which only depends explicitly on temperature once the adsorbate parameters are known.  $b(T)$  is given by

$$b(T) = \frac{^{\circ}s}{v\sqrt{2\pi mkT}} \exp\left(-\frac{^{\text{ads}}E_{\text{act}} - ^{\text{des}}E_{\text{act}}}{kT}\right) \quad (24)$$

In this case the preexponential factor  $^{\circ}s$  should not depend on coverage because it has been assumed for the derivation that there is no intermolecular interaction.

Many different adsorption isotherms may be derived where all or some of the basic assumptions going into the derivation have been released or relaxed [101–105]. It should be stated, however, that the general form of the Langmuir isotherm, which is shown for two temperatures in Fig. 13, may be used for a phenomenological description of many processes. It is clear, from the adsorption isotherm, the sticking probability  $s_0$  may also be determined given that all other parameters are known [1, 7].

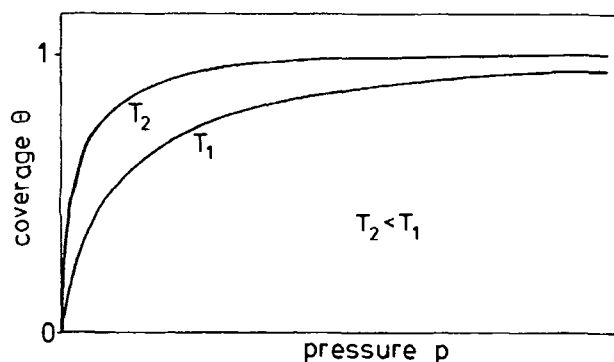


Figure 13. Plot of the Langmuir isotherm for two temperatures ( $T_1$  and  $T_2$ ).

Table 3 collects a set of sticking probabilities determined for various adsorbate systems. The values vary between unity and  $10^{-8}$ , although the range is usually between 0.15 and 1. Obviously, there is a clear trend that sticking is higher for atomically rough surfaces as compared with atomically smooth surfaces depending on the nature of the gas. It seems that energy accommodation is particularly easy on the rough surfaces as compared to the smooth ones. Carbon monoxide and nitric oxide stick quite effectively on many transition

metal surfaces regardless of their crystallographic orientation. On open surfaces they even tend to dissociate. The tendency to dissociate increases when going from the right to the left in the periodic table. Co is approximately on the border line.

We note at this point that in addition to the surface crystallography, surface defects (point defects as well as steps) are important to accommodate chemically active species [112, 127, 128]. Initial sticking probabilities are interesting, but for real systems it is important to consider the coverage dependence of the sticking coefficient. Of course, a model-free discussion of this aspect is very difficult. It is therefore common practice to assume a set of possible kinetic processes which are important in connection with sticking to a surface. A possible scenario is shown in Fig. 14 separately for adsorption and desorption [7]. We introduce precursor states which may be classified as either intrinsic or extrinsic precursor states [129, 132]. The former exist at empty surface sites and the latter at sites already occupied. While trapped into such a precursor state the particle is only weakly held to the surface. Thus it can diffuse across the surface and be eventually trapped into an empty surface site. Given a precursor lifetime of  $10^{-6}$  s, the molecule probes the surface for a sufficiently long time to find an empty site, if the pre-

Table 3. Initial sticking coefficients.

Adsorbate	Substrate	Sticking coefficient	Remarks	References
H	Ni(100)	0.06		106, 107
	Ni(111)	$\geq 0.01$		108
	Ni(110)	$\approx 1$		109
		0.96		110
	Pt(111)	0.1		111
		$\leq 0.0001$		112, 113
	Rh(110)	$\approx 1$		43
	Ru(10 $\bar{1}$ 0)	$\approx 1$		44
	Co(10 $\bar{1}$ 0)	0.75 ( $\pm 20\%$ )		45
	W(100)	1		114
O	Cu(100)	0.03	300 K	115
	Ni(100)	1		116
	Pt(111)	0.2		117
CO	Ni(111)	1		22, 118
	Ni(110)	0.89		119
	Pd(100)	0.6		32
	Pd(111)	0.96		120
	Ru(10 $\bar{1}$ 0)	1		35
N	Pt(111)	1		121
	W(100)	0.2-0.6	see Figure	94
	W(110)	$1-5 \times 10^{-3}$	$\beta$ -N <sub>2</sub>	122, 123
N <sub>2</sub>		0.22	$\gamma$ -N <sub>2</sub>	124
	W(111)	0.08		93
	Fe(100)	$10^{-6}-10^{-7}$		125
	Fe(111)	$10^{-6}-10^{-7}$		126
	Fe(111) > (100) > (110)	$10^{-6}-10^{-8}$		126

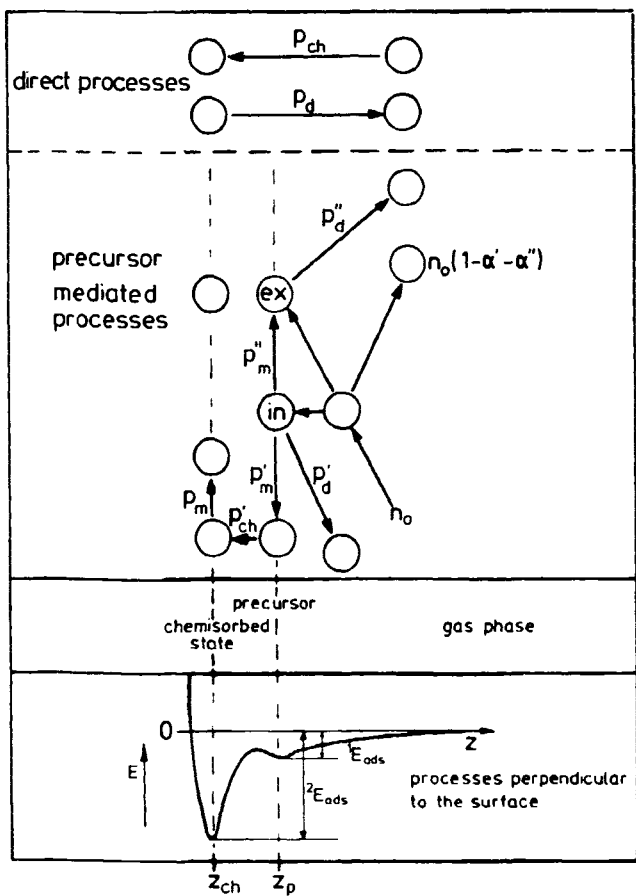


**Figure 14.** Schematic representation of direct and precursor-mediated processes on a surface [129, 130]. Processes occurring along the surface normal are plotted along the abscissa. The processes are correlated with the potential energy diagram of Fig. 7(b) (ex = extrinsic precursor, in - intrinsic precursor,  $n_0$  = number of impinging particles from the gas phase,  $\alpha'$  and  $\alpha''$  are fractions of trapped molecules,  $p$  = probabilities,  $p'_m$  = migration probability along the surface).

coverage is not too large. In order to set up a scheme we have to define probabilities ( $p_i$ ) with which the various states at the surface are populated. On the basis of this (Fig. 14), it is possible to arrive at equations for the rate of adsorption and desorption. However, in the present case, different from the situation discussed above for direct sticking, the sticking probability  $s(\Theta)$  will be dependent on the surface coverage. Kisliuk, as one of the first, has proposed a coverage dependent sticking coefficient based upon such considerations [131, 132]:

$$s(\Theta) = \frac{s_0}{1 + \frac{\Theta}{(1 - \Theta)} K} \quad (25)$$

The constant  $K$  is connected with the probabilities to populate a chemisorptive state via the various precursor states or desorb from them, respectively (Fig. 14):

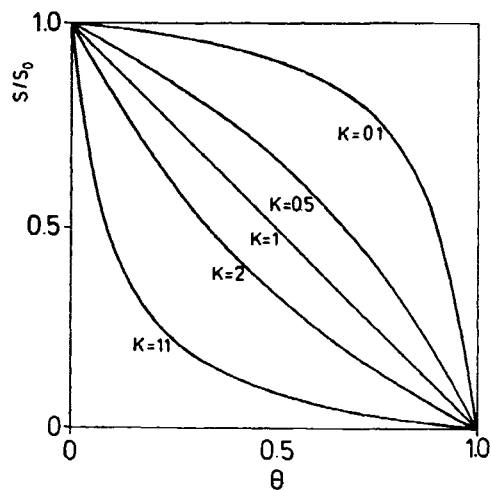


**Figure 15.** Relative sticking probabilities as a function of surface coverage according to the Kisliuk model [131, 132]. For an explanation of  $K$  see text.

$$K = \frac{p''_d}{p'_ch + p'_d} \quad (26)$$

The Kisliuk model for a coverage-dependent sticking coefficient contains the linear Langmuir behavior as well as the coverage-independent sticking probability as limiting cases. Clearly, as  $K = 0$ ,  $s(\Theta) = s_0$ . Also, as  $K = 1$ ,  $s(\Theta) = s_0(1 - \Theta)$ , i.e. the linear Langmuir behavior is retained. As  $K$  is always larger than zero, we have to consider two cases, namely for  $K > 1$ , and for  $0 < K < 1$ . The result is a convex curve for the former, and a concave curve for the latter case (Fig. 15) [131, 132]. Which behavior is actually encountered is largely determined by the probability  $p''_d$ , i.e. the probability for desorption out of the extrinsic precursor. It has to become smaller than the sum of probabilities to desorb out of the intrinsic precursor and the probability to chemisorb out of the intrinsic precursor, in order to achieve  $K < 1$ . Under ultrahigh-vacuum conditions, the population of extrinsic precursors is only easy to realize at low substrate temperatures. Therefore, concave sticking probabilities are generally found, as demonstrated for some examples in Fig. 16 [39, 120, 133, 134]. However, at higher pressures, the population of weakly bound precursor states may be of importance, so that the population of the chemisorbed state through the precursor becomes rate limiting. In such cases we may find a convex curve of the sticking probabilities. Of course, additional complications may arise if the structure of the surface changes upon changes of coverage [135]. Then the dependences may become very different altogether. Oscillatory surface chemical reactions are connected with such behavior in some cases [136].

To end the section on sticking we would like to describe a very interesting development that has recently become more visible, namely the experimental in-

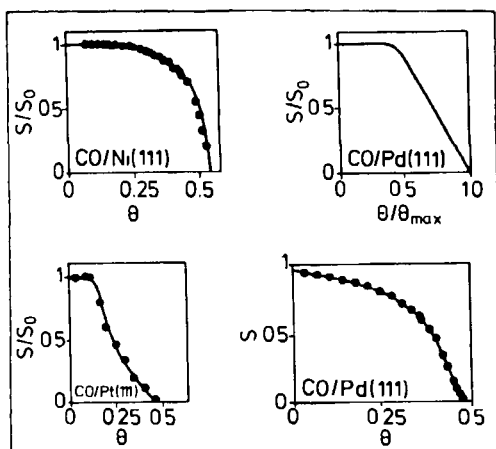


Figure 16. Relative and absolute sticking probabilities for carbon monoxide as a function of surface coverage [39, 120, 133, 134].

investigation of the dependence of sticking on the orientation of the particle, in particular a molecule, upon surface impact. Kleyn and co-workers [137, 138], as well as Heinzmann and co-workers [139–141] have shown that a molecule such as NO can be state selected and focused by taking advantage of a hexapolar electric field, and subsequently oriented in a homogeneous electric field, as schematically indicated in Fig. 17 [140],

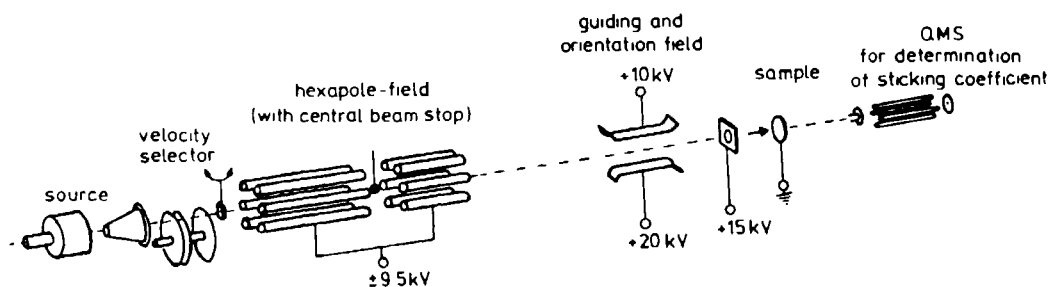


Figure 17. Experimental setup to study sticking probabilities of oriented NO molecules [139].

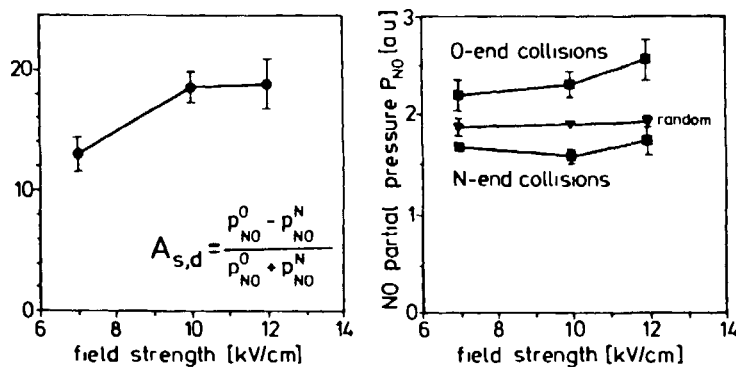


Figure 18. (Right) NO partial pressure after scattering from a Pt(100) surface as a function of field strength and NO orientation [141]. (Left) Corresponding orientation asymmetry of the partial pressure of NO [142].

before colliding with the substrate. Depending on the polarity of the electric field in front of the surface, two different orientations can be achieved: preferential N-end and preferential O-end collisions. The rotational temperature of the colliding molecules determines the degree of orientation of the molecules. Therefore seeded pulsed nozzle beams are used to cool the particles before collision. The integral number of molecules leaving the surface after scattering is detected from the NO partial pressure with a quadrupole mass spectrometer located behind the target and thus shielded from the direct beam [93]. Figure 18 shows a typical result in terms of partial pressures (right panel) for the scattering of NO from Pt(100) as a function of field strength and orientation of the NO molecule [142]. The observed asymmetry, which is plotted in the left panel, is very high. Note that the degree of orientation, given as the averaged cosine ( $\cos \vartheta$ ) of the angle between molecular axis and external electric field  $\vartheta$ , is 30%. The result documents the strong preference for trapping in the chemisorptive potential if the molecules approach the surface with the N-end. At higher surface temperatures the asymmetry decreases as expected, because the number of molecules that do not stick increases for both orientations. It seems that for a detailed understanding of the temperature dependence a kinetic model involving precursor states has to be

invoked. A fit to a Kisliuk model [131, 132] (see above) indicates that not only chemisorption is favored for N-end oriented molecules but also trapping into a presursor state. If we change the adsorbate system from a chemisorptive system such as NO on Pt(100) to a more weakly interacting system such as NO/Ag(111) [137] we realize that the observed symmetries are actually much smaller even at low temperature, and indeed, slightly favor trapping of NO molecules with the O-end approaching the surface even at lower coverage.

#### 5.1.1.4 Surface Diffusion

The motion of adsorbed particles obviously plays an important role for adsorbates and for surfaces in general, because this process enables the system to achieve its equilibrium structure. Particularly, at elevated temperatures the atoms of the substrate material can move, lowering the free energy content of the surface. The process of diffusion of substrate atoms has been investigated frequently in the past. Applying various methods such as scattering methods, field emission and contact potential measurements Bonzel and co-workers [143–145], Butz and Wagner [146, 147], Ehrlich [148], and Hölzl and co-workers [149, 150] have contributed to this area. Due to the rather high activation energies required for the substrate atom displacements, temperatures up to 1000 K have to be employed in order to obtain reasonable rates of diffusion of substrate atoms. In connection with the discussion of chemisorption, however, we are more concerned with a different type of surface diffusion, namely when diffusion occurs within the adsorbate phase. Such processes may be separated from the motion of substrate atoms because much lower temperatures are needed to induce diffusion. Typical diffusion coefficients are given in Table 4.

Diffusion within the adsorbed layer is instrumental to establish long-range order and to obtain optimal experimental conditions to perform diffraction experi-

ments, for example, via low energy electron diffraction (LEED). Furthermore, surface diffusion helps to overcome lateral concentration gradients due to non-equilibrium clustering phenomena often found at low temperatures. There is a large amount of information available on surface diffusion [129, 148, 149], both on the experimental methods to measure diffusion coefficients as well as on the theoretical aspects of the problem. We shall only give a brief, nonexhaustive overview of the situation [7].

Conceptually, the process is thought to occur as a random walk where adparticles hop between adjacent sites, i.e. from an occupied to an adjacent empty site. The hopping frequency depends then exponentially on the temperature of the system which leads to the following form of the diffusion coefficient:

$$D = D_0 \exp\left(-\frac{\Delta E_{\text{diff}}}{RT}\right) \quad (27)$$

with the preexponential factor  $D_0$  and the activation energy for diffusion  $\Delta E_{\text{diff}}$ . It is correlated with the height of the energy barrier in Fig. 10 parallel to the surface. An expression for  $D_0$  may be derived from transition state theory and depends on the activation entropy of the process. The important quantity for surface diffusion is the activation energy. Its magnitude is about a tenth of the adsorption energy for a typical chemisorbate such as CO/Pd, i.e. it amounts to approximately 15–20 kJ mol<sup>-1</sup>. For physisorbates it is probably considerably lower.

The diffusion coefficient may be measured via several experimental techniques. The most prominent ones at present are the direct observation of a diffusion boundary in either a field electron microscope [159, 160] or a photoelectron emission microscope [158] or via laser desorption experiments [161, 162]. In the latter case a short laser pulse is used to heat the surface to momentarily desorb the adsorbate from a well defined region of the crystal. Subsequent laser pulses with well defined time delays with respect to the first one, and measurement of the number of particles leaving the surface, allow one to determine the rate of diffusion into the depleted zone. Other methods to determine surface diffusion are spectroscopic measurements which cover the proper time window, for example magnetic resonance-based methods [163, 164]. In favorable cases these methods may even be applied to single crystal surfaces [165].

As mentioned above, the diffusion process is thought to be a random walk across the surface. Then the mean-square displacement of the adparticles is related to the diffusion coefficient via the relation

$$\langle x^2 \rangle = 4Dt \quad (28)$$

where it is understood that the surface itself only contains a very low concentration of adparticles which do

Table 4. Diffusivities of adsorbates.

Adsorbate	Substrate	$D_0$ (cm <sup>2</sup> s <sup>-1</sup> )	References
Cs	W(110)	0.23	151
K	W(tip)	10 <sup>-4</sup> –10 <sup>-6</sup>	152
N	W(110)	0.014	153
O	W(110)	0.04–0.25	154
H	Ni(100)	2.5 × 10 <sup>-3</sup>	155
D	Ni(100)	8.5 × 10 <sup>-3</sup>	155
H	W(tip)	1.8 × 10 <sup>-5</sup>	156
D	Pt(111)	8 × 10 <sup>-2</sup>	157
CO	Pt(111)	10 <sup>-2</sup> –10 <sup>-3</sup>	157
CO	Pt(110) [1 $\bar{1}$ 0]	2.7 × 10 <sup>-9</sup>	158
CO	Pt(110) [001]	0.8 × 10 <sup>-9</sup>	158



not interfere with each other. In other words, the model so far is coverage independent. However, we know from previous considerations that coverage dependence has to be considered. For example, if a particle wants to move to an empty site the probability to hop clearly depends on the number of empty sites in the neighborhood, or even on the concerted motion of adparticles. Coverage dependences may be introduced by using the general transport equations, or specifically Fick's law [166]. The solution of Fick's law again yields an exponential dependence of the diffusion coefficient as in equation (27):

$$D(\Theta) = D_0 \exp\left(-\frac{\Delta E_{\text{diff}}(\Theta)}{RT}\right) \quad (29)$$

where the coverage dependence of the process enters through a coverage dependence of the activation energy:

$$E_{\text{diff}}(\Theta) = E_{\text{diff}}(\Theta = 0) + \frac{ZE_{\text{pair}}}{2} \left[ \frac{1 - 2\Theta}{\sqrt{1 - 4\Theta(1 - \Theta)B}} \right] \quad (30)$$

where  $B$  is the short-range order parameter,  $B = 1 - \exp(E_{\text{pair}}/RT)$ ,  $Z$  is the number of nearest neighbor sites, and  $E_{\text{pair}}$  is the nearest neighbor interaction energy. Using this approach Fick's equation may be solved numerically.

Table 4 contains a collection of diffusion coefficients determined experimentally for a variety of adsorbate systems. It shows that the values may vary considerably, which is of course due to the specific bonding of the adsorbate to the surface under consideration. Surface diffusion plays a vital role in surface chemical reactions because it is one factor that determines the rates of the reactions. Those reactions with diffusion as the rate-determining step are called diffusion-limited reactions. The above-mentioned photoelectron emission microscope is an interesting tool to effectively study diffusion processes under reaction conditions [158]. In the world of real catalysts, diffusion may be vital because the porous structure of the catalyst particle may impose stringent conditions on molecular diffusivities, which in turn leads to massive consequences for reaction yields.

### 5.1.1.5 Structure Sensitivity

So far we have neglected the fact that the substrate has a particular geometric structure which influences, as we shall see further below, the adsorption behavior in a very pronounced way. Furthermore, in practical cases the macroscopic geometric structure is rather complex. Consider, for example, a real catalyst used in heterogeneous reactions. It may consist of bimetallic precipitates, or of thin films supported on alumina, silica, or

titania, or highly dispersed metals such as platinum black. However, even these materials possess a regular geometric structure on the microscopic scale. Often, microscopically analyzed, these materials expose regular crystallographic planes, which may be characterized via scattering methods or real-space imaging. In catalysis, the correlation between surface geometric and electronic structure, the geometric shape and electronic structure of a molecule, and the observed macroscopic reactivity represents a very important and long discussed, but not yet solved problem. One distinguishes between structure-sensitive and structure-insensitive reactions. Special site requirements have been discussed in terms of the so-called ensemble effect [167–169] whereafter a molecule can only adsorb if a certain group of adjacent surface atoms is available. Studies on bimetallic alloy surfaces have often been used as examples for such ensemble effects [167, 168].

The present section enters into the discussion of the electronic and geometric structure by considering first an example where we can vary the strength of interaction between a given adsorbate and various metal and metal-oxide surfaces. We have chosen carbon monoxide as the adsorbate because it offers the largest available data set, including structure determination. Photoelectron spectroscopy (PES) is a very sensitive tool with which to monitor the change in the electronic structure, which is why it is the method of choice to shed light on this question [170]. Figure 19 shows a set of photoelectron spectra of CO adsorbates on four different hexagonally close packed metal surfaces [171] as well as on two transition metal-oxide surfaces [172–173]. For comparison we show the spectrum of gaseous [174] and condensed CO [175]. The binding energy ( $E_b = E_{\text{kin}} - hv$ ) refers to the vacuum level, which allows us to put adsorbates on metals, on insulators, and molecular solids on the same energy scale. (Often the binding energy is referenced to the Fermi level ( $E_F$ ) of the system. The binding energy with respect to the vacuum level and the binding energy with respect to the Fermi level are connected via the work function  $\Phi$  of the system.) The region where we expect photoelectron emission from the three outer valence levels of CO, i.e.  $5\sigma$ ,  $1\pi$ , and  $4\sigma$  levels, is shown, and most of the following discussion will concentrate on these levels. From the bottom to the top the heat of adsorption increases from  $19 \text{ kJ mol}^{-1}$  to  $142 \text{ kJ mol}^{-1}$  for the metal surfaces. This is accompanied by clearly recognizable changes in the photoelectron spectra. There are several interesting differences in binding energies, line intensities and line shapes between gas phase [174], condensed phase [175] and adsorbate phases [172, 173, 176–179], which we shall comment on in the following. We shall start with the adsorbates on the metal surfaces

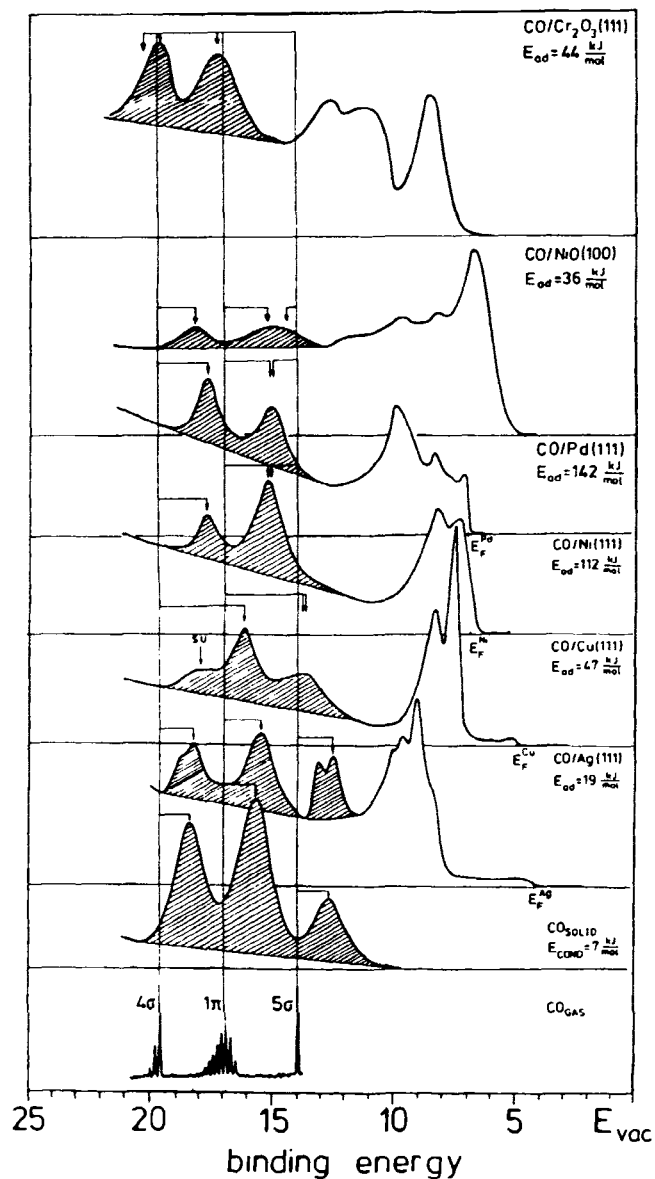


**Figure 19.** Photoelectron spectra of CO adsorbed on metal and metal oxide surfaces in comparison with gaseous and condensed CO. The spectra are taken in normal electron emission.

[176–179], and later turn to the oxide surfaces [172, 173] because bonding considerations are rather different for these systems.

In order to systematically approach an understanding of molecule–metal bonding and to relate the conceptual considerations to experiment we briefly refer to Fig. 20 [171]. In this figure the molecule–metal as well as the molecule–molecule interaction effects are illustrated on the basis of a one-electron level diagram for the valence electrons. It shows on the right-hand side a diagram for an isolated CO molecule correlated with a one-electron level diagram for a CO molecule interacting with a single metal atom. On the left-hand-side the band structure of an isolated CO overlayer is

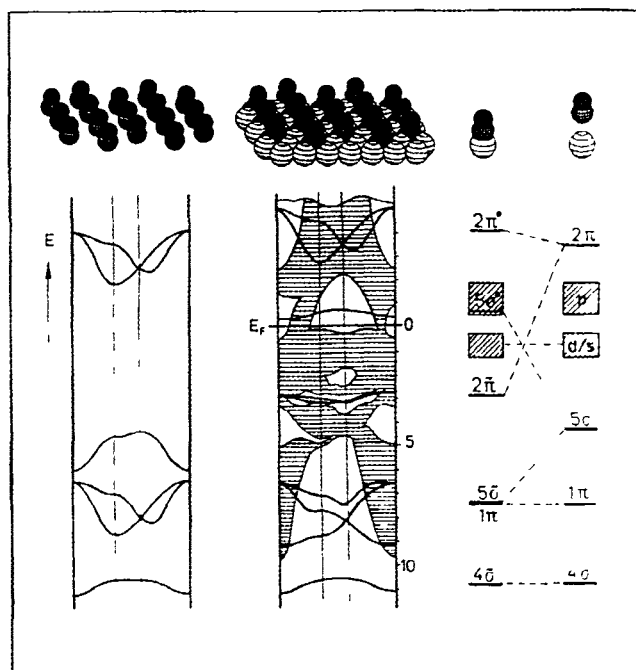


**Figure 20.** Schematic diagram for the bonding of an isolated CO molecule to a metal atom (right hand side) and a free two-dimensional array of CO molecules (left panel) to a metal surface (middle).

displayed, and compared in the middle with the full band structure of the CO adsorbate interacting with the compact metal substrate with (111) orientation. Both aspects, the molecule substrate as well as the intermolecular interactions, have consequences for the observed spectra, but the main effect we shall dwell on first is the molecule–metal interaction. What happens electronically can easily be explained in the so-called Blyholder model [180]. The carbon lone pair of CO is donated into empty d or s levels of the metal atom, establishing a  $\sigma$ -metal–molecule interaction; synergistically, metal d electrons are donated into empty molecular orbitals ( $2\pi$ ) of CO forming a  $\pi$ -metal–molecule interaction. From the view point of the molecule we can look at this charge exchange process as a  $\pi$ -donation– $\pi$ -backdonation process. This means that the distribution of electrons among the subsystems, i.e. CO molecule and metal atom, in the CO–metal cluster is considerably different to the noninteracting subsystems. For example, the electron configuration of the metal atom in the cluster may be different from the isolated metal atom, or the electron distribution within the CO molecule bonded towards the metal atom may look like the electron distribution of an “excited” CO molecule rather than the ground state CO molecule [181]. This scheme has been used to explain the well known changes in the vibrational properties of adsorbed CO as compared with the gas phase. In addition to the loss of the rotational fine structure upon ad-

sorption, the CO stretching frequency often shifts by more than  $100\text{ cm}^{-1}$  to lower values [182–185]. It is the filling of the CO antibonding  $2\pi$  orbital via the back-donation contribution which weakens the CO bond in the adsorbate and concomitantly shifts the stretching frequency to lower values [186]. Also, as a consequence of this interaction certain electronic levels of the subsystems are strongly influenced. Naturally, the distortions of the molecular as well as the metal levels are reflected by changes in the ionization energies, their ionization probabilities, and the line shapes of the ionization bands. In CO/Ag(111) [176] at  $T = 20\text{ K}$  CO is physisorbed as documented by the small adsorption energy of  $19\text{ kJ mol}^{-1}$ . This explains why a spectrum so similar to condensed CO is observed for this adsorbate. The splittings in the  $4\sigma$  and  $5\sigma$  ionizations are connected with the formation of a two-dimensional layer and will not be discussed at this point [187]. If compared with the gas phase, however, rather dramatic changes are found. The bands are shifted by about  $1\text{ eV}$  to lower binding energy and the line widths increase, which destroys to a large extent the vibrational fine structure observed in the gas phase, too. Theories have been developed that allow one to understand these processes on the basis of hole hopping and relaxation, i.e. effects in the ionized state, within the quasi-two-dimensional solid but for the present review we refer to the literature for details [188–193]. If the heat of adsorption increases to about  $47\text{ kJ mol}^{-1}$  [194], as for example in the case of CO on Cu(111) [177], the features in the spectrum shift and the intensities are altered. Three lines are still found but their assignment is very different as compared with the physisorbate [177].

We only briefly state here that many-particle effects in the ionized state of the adsorbate due to the presence of the highly polarizable metal electrons dominate the spectrum, and this alters the assignment considerably [177]. If we later turn to the oxide surfaces where such effects do not occur as strongly but the bond strength is comparable, we shall see that the interaction may be directly deduced from the spectrum. We note in passing that the assignment of the bands to states of different symmetry has been made on the basis of experimental investigations using angle resolved photoelectron spectroscopy (ARUPS) [170]. Reviews on this subject exist in the literature [170, 195, 196]. The next step is the study of the strongly chemisorbed systems with adsorption energies larger than  $100\text{ kJ mol}^{-1}$ . Out of a wealth of experimental data [197–214] we have shown here only two systems, i.e. CO/Ni(111) and CO/Pd(111). In these cases the spectra show two bands, whose binding energies are almost independent of the particular system under consideration as long as intermolecular interaction does not play an important role. The bands are shifted by more than  $2\text{ eV}$  with respect

to the gas phase. Via angle resolved photoelectron spectroscopy [170] it has been shown that the two bands really contain three components as indicated in the figure as well as expected from the simple bonding considerations made above [197]. The carbon lone pair is shifted close to the  $1\pi$  ionization due to the strong charge exchange and is actually located at higher binding energy. The overall shift of the bands to lower binding energy is a consequence again of the relaxation in the ionized state of the adsorbate due to the presence of the highly mobile metal electrons. Therefore, the experimental observation are in line with our simple charge-exchange model for CO–metal bonding but one has to be careful in the interpretation not to forget the effects of the probe, in the case of PES the creation of a hole in the system [170].

We now come to the comparison of the electronic structure of the adsorbates on the metal surfaces with those on the oxide surfaces [215, 216]. Very detailed electronic structure calculations [217–224] have recently shown that the interaction of molecules with oxide surfaces differs considerably from the interaction with metal surfaces in the sense that in the latter case interaction, at least on the regular surfaces, is much weaker. However, it is not necessarily a physisorptive interaction. Briefly, on the (100) surface of the strongly ionic NiO the interaction of a CO molecule is not governed by short-range charge-exchanges processes as in the case of the metal surface but rather by electrostatic interaction between the multipolar moment of the molecular electron density and the multipolar moment of the ionic surface. The reason for this behavior is that due to the presence of the closed shell oxygen ions in the (100) surface the molecule cannot approach the Ni site close enough to exchange charge. Pauli repulsion sets in at rather large distances from the surface and repels the molecule. The balance between the electrostatic attractive forces and the Pauli repulsion results in a rather weak chemisorptive bond of CO on a typical oxide surface. In addition, due to the rather weak interaction there is no longer a strong preference for one given orientation of the molecule with respect to the surface. For example, the molecular axis may be either perpendicular or tilted, or there may be interaction either with the carbon end or the oxygen end of the molecule with the surface. In other words, from an experimental point of view, we have to check in each case individually which situation is adopted by the system [172].

To a certain extent, the vibrational spectra [225, 226] again provide a clue towards a verification of the general statement made above. On oxide surfaces, in general, the observed shifts of the stretching frequencies

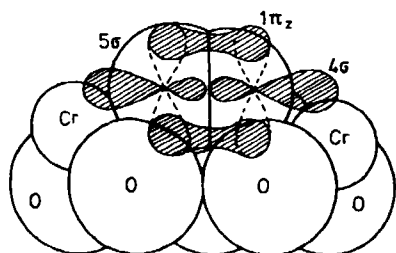


Figure 21. Schematic proposed arrangement of CO on a  $\text{Cr}_2\text{O}_3$  surface [173].

are considerably smaller as compared to adsorbates on metals [183–185]. The vibrations may be either red or blue shifted depending on the interaction. The small red shift observed in some cases may be interpreted by a limited charge transfer from the oxide to the adsorbed molecule in the same sense as for adsorbates on metal surfaces. The often observed blue shift, however, has a different origin. It can be explained by the so called “wall effect” [219, 220] in which the weakly held CO molecule vibrates against the hard wall of the substrate which shifts the stretching frequency to higher values, thus leading to a blue shift. The statement made above concerning the interaction of CO with the oxide surface can now also be verified via the photoelectron spectra in Fig. 19 [172]. We find the binding energy of the oxygen lone pair located very close to the energy in the condensed CO film indicating that there is no strong intermingling between the oxygen long-pair density and the surface electrons. The same is true for the CO  $\pi$ -bond electrons. However, we see a pronounced shift of the carbon lone pair electrons originating from the strong Pauli repulsion with the surface electronic charge. The relaxation shift found for the metal oxide systems is rather small also because the response of the oxide surface towards the creation of holes on the molecule in the ionization process is less pronounced than with the metal surface. Comparing the spectrum for the CO/NiO(100) system with the last example, i.e. CO/ $\text{Cr}_2\text{O}_3$ (111) [173] indicates a similar situation as far as the overall position of the adsorbate induced features are concerned. However, a detailed analysis of this  $\sqrt{3} \times \sqrt{3}$ -ordered adsorbate system shows that the individual ionizations are considerably shifted with respect to the CO/NiO(100) system. The reason is simple, and it can be proved by angle resolved photoelectron measurements or X-ray absorption measurements, that the orientation of the molecule with respect to the surface has changed. CO is no longer vertically oriented on the surface but rather strongly inclined. A schematic model of the local bonding situation is shown in Fig. 21. The analysis of the chromium oxide system underlines the necessity of determining individually the orientation of the molecular axis before we discuss the

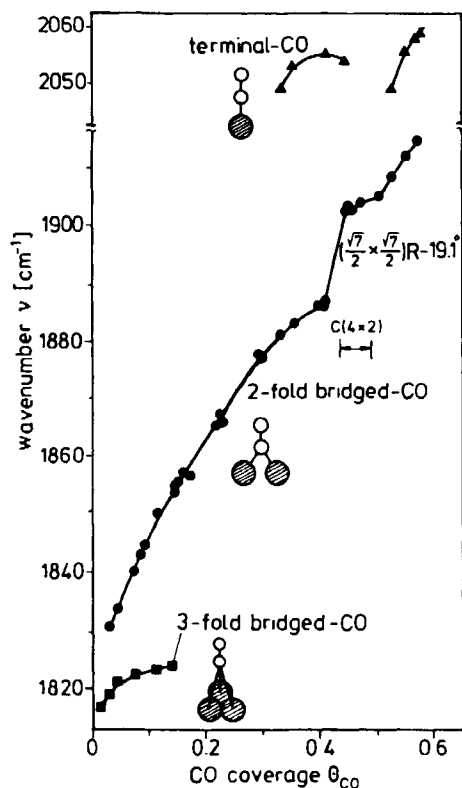


Figure 22. Stretching frequency of CO adsorbed on Ni(111) as a function of CO coverage. The surface was dosed at 90 K and subsequently annealed to 240 K [184].

details of the electronic structure of a system, in particular on an oxide surface.

The next step in the discussion of structure sensitivity of chemisorption is to consider the site of adsorption on a given surface and to answer the question as to whether and how the site changes as the coverage of the adsorbate is increased. Figure 22 shows the famous dependence of the CO stretching frequency on coverage for the system CO/Ni(111) [184]. This dependence has been interpreted as being due to two effects, namely a change of adsorbate site upon increase of coverage and additionally a shift caused by the coupling of the dynamic dipoles which depends on intermolecular distance [183–185]. Figure 22 indicates the adsorbate geometry deduced for the various coverage ranges based on the stretching frequency data. In recent years it has become more and more clear, however, that a structural assignment based on vibrational data has to be taken with caution. At low coverage a CO stretching vibration at  $1816\text{ cm}^{-1}$  shows up. This is replaced by a band at  $1831\text{ cm}^{-1}$  if the coverage increases and eventually shifts to  $1905\text{ cm}^{-1}$  at  $\Theta = 0.5$  corresponding to a  $c(4 \times 2)$  structure. On the basis of the suggestions by Eischens and Pliskin [182] the band at  $1816\text{ cm}^{-1}$  has been interpreted to be due to adsorption in a threefold hollow site at low coverage and the band shifting in the

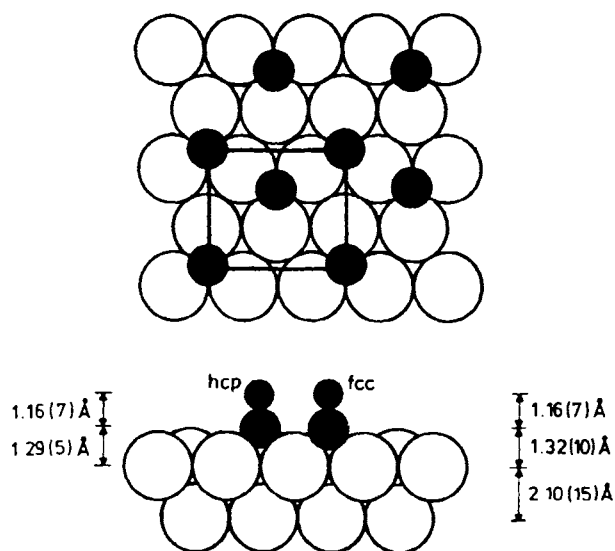


Figure 23. Schematic drawing of the geometric arrangement CO on Ni(111) in the  $c(4 \times 2)$  superstructure. Values are distances as determined by XPD [228].

range  $1831\text{--}1905\text{ cm}^{-1}$  to a CO bridge site. In a very convincing study based on the analysis of X-ray photoelectron diffraction data Bradshaw and coworkers [227–229] have shown that the adsorbate site over the whole coverage regime remains the same and is a threefold hollow site as indicated in Fig. 23. The observed shift in the stretching frequency is then purely due to intermolecular dynamic dipole coupling. Note that both the inequivalent threefold hollow sites (fcc and hcp) are occupied in this structure [228]. Another important factor in chemisorption becomes obvious by looking at the structures in Fig. 23, namely the cooperativity of the process. There is a 3% expansion ( $+0.07\text{ \AA}$ ) of the outermost Ni–Ni lattice spacing. This is meant here to stress the finding that although the surface provides a particular site for adsorption, the final geometry is determined via the interaction with the adsorbate and therefore depends on its chemical identity. This phenomenon is important in connection with the well known adsorbate induced reconstructions of surfaces [135]. If the reactivity of the surface towards another adsorbate changes through the reconstruction then cooperative phenomena are essential for the overall chemical reactivity in the system.

Whereas in the above example the local structure remains the same for increasing coverage, there are other cases where intermolecular interaction changes the geometry of the adsorbate. In the case of CO on Ni(110) at low coverage CO molecules adsorb in two different adsorption sites, namely on atop and on bridge sites with vertically oriented axis, as shown in Fig. 24 [230–233]. The molecule–substrate bond in this case is so strong that the system can tolerate even large lateral intermolecular stress. At a coverage of  $\Theta = 1$

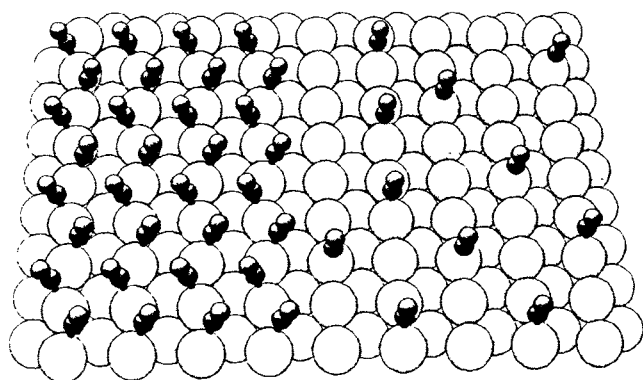
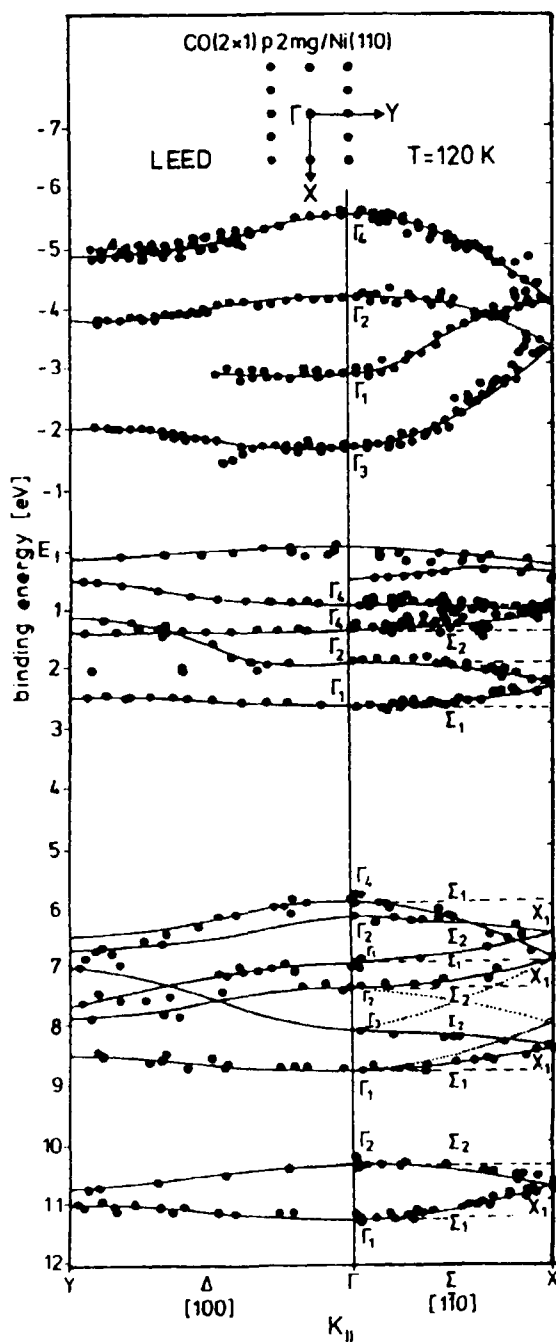


Figure 24. Geometric arrangement of CO molecules on a Ni(110) surface at low coverage (right) and high coverage (left).

the intermolecular distance would be  $2.5\text{ \AA}$  if the molecular axis remained perpendicular. Therefore the molecular axis tilts from the normal orientation in order to enlarge the average distance between molecules [234–236]. The equilibrium structure assumed is shown in Fig. 24, on the left. This system has been studied in some detail in order to understand the electronic structure of the system [237–240]. In line with Fig. 20 where the schematic band structure of an adsorbate system is shown, the present system has been studied with angle resolved photoelectron spectroscopy and the band structure has been experimentally determined [187]. Figure 25 shows the complete experimental band structure in the occupied region, i.e. of the  $5\sigma$ ,  $1\pi$ , and  $4\sigma$  levels [237, 239, 240]. Included is the band structure in the unoccupied region as determined by inverse photoemission. The  $5\sigma$ ,  $1\pi$ , and  $4\sigma$  levels lead to twice the number of bands due to the non-symorphic space group symmetry of the system with two molecules per unit cell [234]. Following the bands through the Brillouin zone shows that the energetically close  $5\sigma$  and  $1\pi$  bands hybridize. Also, one can clearly identify the  $\text{CO}(2\pi)\text{--Ni}(3d)$  backbonding states below the Fermi edge. The unoccupied  $2\pi$  derived levels are located above the Fermi edge. It is interesting to note the different magnitudes of the band dispersions for the different levels. This is clearly due to the variations in interaction strength for the different molecular orbitals depending on directionality and spatial extent. The largest dispersions are exhibited by the  $\pi$  orbitals. In fact, the  $2\pi$  orbital shows the largest effects because they are most diffuse and show large electron density off the molecular axis. To summarize, the strong intermolecular interaction is reflected in the adsorbate band structure and mainly due to  $\pi\text{--}\pi$  interaction.

We now turn to the question of how the adsorption properties of a given molecule changes when we change the geometric structure of the surface keeping its



**Figure 25.** Measured band structure in the range of occupied and unoccupied levels for  $\text{CO}(2 \times 1)p2\text{mg}/\text{Ni}(110)$ . The wave vector  $K$  is determined along the two orthogonal directions in the surface Brillouin zone as shown at the top and its energy dependence according to  $K_{\parallel} = (2m_e \hbar^{-2} E_{\text{kin}})^{1/2} \sin \theta$ .

chemical constitution constant. There are many examples in the literature. Again CO adsorption could be chosen [241]. Also, hydrogen chemisorption [73] or oxygen chemisorption [242, 243], which has been studied and reviewed in detail by Christmann [73], Wandelt [242], Brundle [243] and others are prominent examples for the structure sensitivity of chemisorption on metal

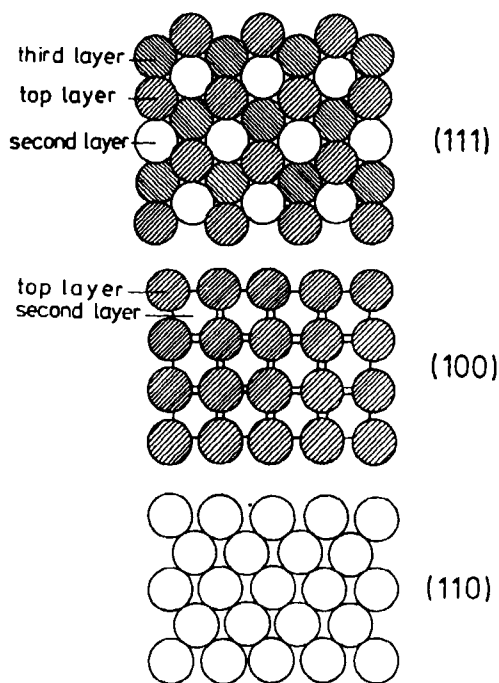


**Figure 26.** Structure of the close packed surfaces of iron (bcc).

surfaces. The adsorption of nitrogen on iron is chosen because of its importance in connection with ammonia synthesis [244]. In particular, Ertl and co-workers [125, 126] have investigated the structure sensitivity of dissociative nitrogen adsorption on the low-index surfaces of iron, i.e. the (100), (110) and (111) surface orientations. Figure 26 shows the arrangement of these surface structures on top of the body-centered cubic iron crystal. The (110) surface has a very low sticking coefficient for dissociative adsorption while the most open (111) surface has a much higher sticking coefficient [125, 126]. With a combination of photoelectron spectroscopy [245] and vibrational spectroscopy [246–248] the important factors influencing this face specificity have been uncovered. Briefly, on Fe(111) high resolution electron energy loss spectra (HREELS) [248] are observed as a function of temperature (Fig. 27). At about liquid nitrogen temperature a dominant feature with a stretching frequency at  $2100 \text{ cm}^{-1}$  is found. With angle resolved photoelectron spectroscopy [245] it has been shown that this species is oriented perpendicular to the surface. It is most likely to be bound to an atop site. The same species is found on all low-index iron surfaces [244]. It is weakly held by the surface. Upon heating the system slightly above 100 K a second molecular nitrogen species shows up in the vibrational spectra of  $\text{N}_2/\text{Fe}(111)$  at a lower stretching frequency ( $1415 \text{ cm}^{-1}$ ). Again, photoelectron spectroscopy has been used to show that this species is bound in a strongly tilted geometry, in line with the low stretching frequency typical for side-on bonded dini-

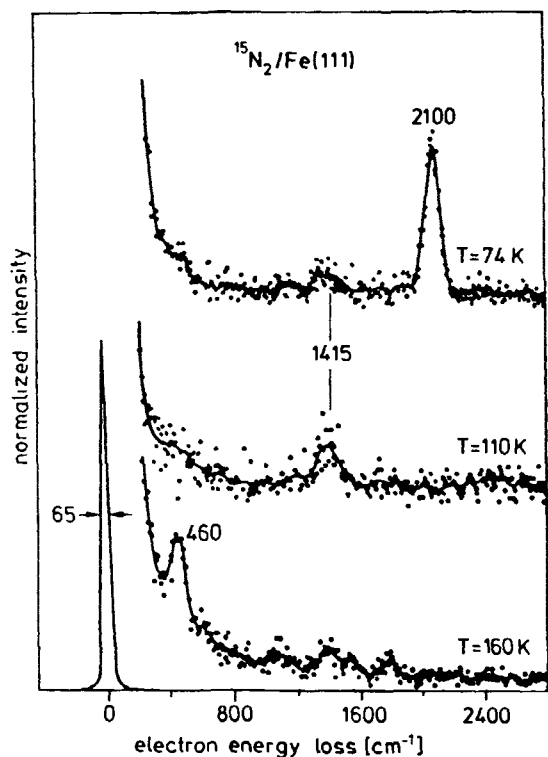


Figure 27. Electron energy loss spectra of  $^{15}\text{N}_2$  on Fe(111) as a function of surface temperature [248].

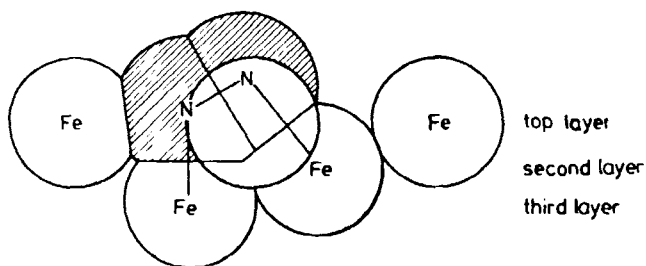


Figure 28. Proposed arrangement of  $\text{N}_2$  on Fe(111) [245].

nitrogen complexes. This species only exists on the surface within limited temperature range. Above 160 K the stretching frequency typical for molecular nitrogen species disappears and only atomic nitrogen ( $460\text{ cm}^{-1}$ ) is present on the surface. This scenario is typical for the (111) surface, while the existence of the intermediate species cannot be detected on the other low-index planes, i.e. (110) and (100) [244]. It is now generally accepted that the intermediate with the low stretching frequency is a precursor to nitrogen dissociation, and it is thought that the (111) surface provides the sites, necessary to assume the strongly tilted geometry [244]. Figure 28 shows the bonding geometry for the intermediate species [245]. The nitrogen molecule can donate both its lone pair as well as the  $1\pi$  electrons into empty metal orbitals, and at the same time establish a

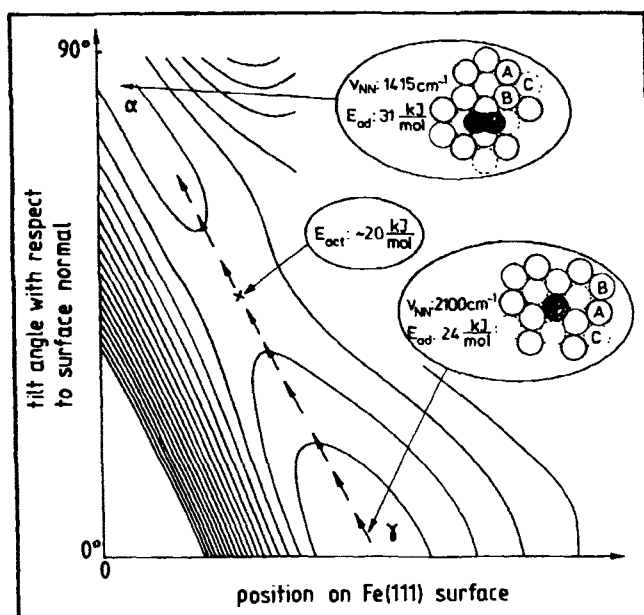


Figure 29. Two-dimensional potential energy diagram for the conversion of  $\gamma\text{-N}_2$  (vertically adsorbed) to  $\alpha\text{-N}_2$  (side-on bonded) [246–248] on the Fe(111) surface [249].

back-donative bond via the unoccupied  $\pi$  orbital. The back donation will weaken the nitrogen–nitrogen bond which finally leads to dissociation. Since both nitrogen atoms are already in close contact with the metal surface, this picture appears to provide a natural pathway to dissociation. It is believed to explain the observed strong face specificity of dissociative nitrogen chemisorption on Fe surfaces. Figure 29 shows a semi-empirical potential energy diagram for  $\text{N}_2/\text{Fe}(111)$  where the pathway from the molecular precursor to the dissociative adsorption is shown [249]. The value for the activation barrier is based on experimental data [250].

Finally, we would like to have a look at the structure sensitivity of transition metal oxide surfaces [215]. For such systems [251, 252] it is necessary to resort to some basic considerations about the electrostatics of ionic or partly ionic systems with respect to surface stabilities. Figure 30 schematically shows the arrangements of planes in a crystal of rock salt (AB) structure for the termination of (100) type on the left and of (111) type on the right [254]. The (100) surface of an AB-type solid is the typical case for a nonpolar surface with vanishing dipole moments between the planes and full charge compensation within the planes. This arrangement leads to a converged, finite electrostatic surface energy. Upon going to the (111) surface of an AB-type lattice we create a polar surface. In this case there is no charge compensation within each layer and there is also a dipole moment within the repeat unit perpen-

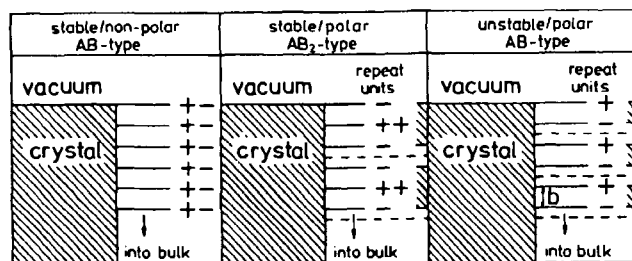


Figure 30. Stable and unstable surfaces of AB-type and AB<sub>2</sub>-type ionic crystals [253].

pendicular to the surface. Consequently, the surface energy does not converge but increases unbound as the number of repeat units increases. In general, polar surfaces are not unstable, as illustrated for the AB<sub>2</sub>-type solids. Even though there is no charge compensation in the plane, the dipole moment in the repeat unit perpendicular to the surface vanishes, thus leading to a stable situation. Returning to polar surfaces of the AB-type to consider the surface potential  $V$  in more detail [253],

$$V = \frac{2\pi}{S} [Nb(2\sigma - 1) + (1 - \sigma)b] \quad (31)$$

where  $S$  is the area of the unit cell. Equation 31 gives the surface potential as a function of the number of layers  $N$ , their separation  $b$ , and the parameter  $\sigma$  which describes the difference in charge of the surface layer with respect to the bulk layer. It is quite obvious that the reduction of the surface charge such that  $\sigma = 1/2$  leads to the disappearance of the first term in eq 31, and thus to a converging surface potential independent of the number of layers. While this is only a qualitative argument, it shows possible routes for the system to respond in order to stabilize polar AB-type surfaces. Surface-charge reduction may be accomplished by reconstructing [254], i.e. removing half of the ions, or by the creation of steps. The latter leads to the coexistence of A-terminated and B-terminated patches on the same surface and thus to a microscopic charge compensation. Also, relaxations in the layer distance are expected to occur in the near surface region which could help to reduce the surface potential. In certain cases other causes of stabilization may be considered. Upon adsorption of H<sup>+</sup>, provided by exposure to water, for example, OH<sup>-</sup> may form on an oxygen terminated surface thus effectively reducing the surface charge [252]. Thus one would predict a strong structure sensitivity of water adsorption on oxide surfaces which, indeed, has been observed [254, 255] and is exemplified in Fig. 31. The O(1s) XP spectra are shown for three different samples [255]. The lower trace shows the spectrum of a cleaved NiO(100) surface with very low defect concentration (sharp LEED pattern). The feature is symmetric after cleavage and it remains symmetric even after exposure to water at room temper-

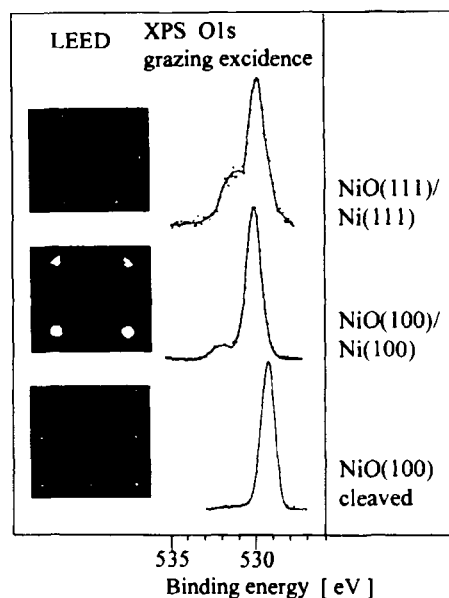


Figure 31. O(1s) XP spectra of a cleaved NiO(100) crystal: (a) a grown NiO(100) film; (b) a grown NiO(111) film. The corresponding LEED patterns are shown [254, 255].

ature [256]. At low temperature an ice layer forms which can be removed without residue by heating to room temperature. This indicates that a NiO(100) surface does not dissociatively chemisorb water. The situation is different for a NiO(100) surface containing defects, as indicated by the much broader LEED spots as compared with the cleaved surface [252, 255]. Here a small feature is found at 2.2 eV higher binding energy. It becomes particularly pronounced in the spectra if they are recorded at grazing electron excidence in order to amplify the surface sensitivity of the method. EELS investigations have shown that the feature is due to hydroxyl groups on the surface. These hydroxyl groups may be removed from a NiO(100) surface by thermal treatment. Exposure of the cleaned surface to water leads to the reappearance of hydroxyl, indicating that water dissociatively chemisorbs on defect sites of a NiO(100) surface. Dissociative chemisorption becomes even more pronounced on the NiO(111) surface. The



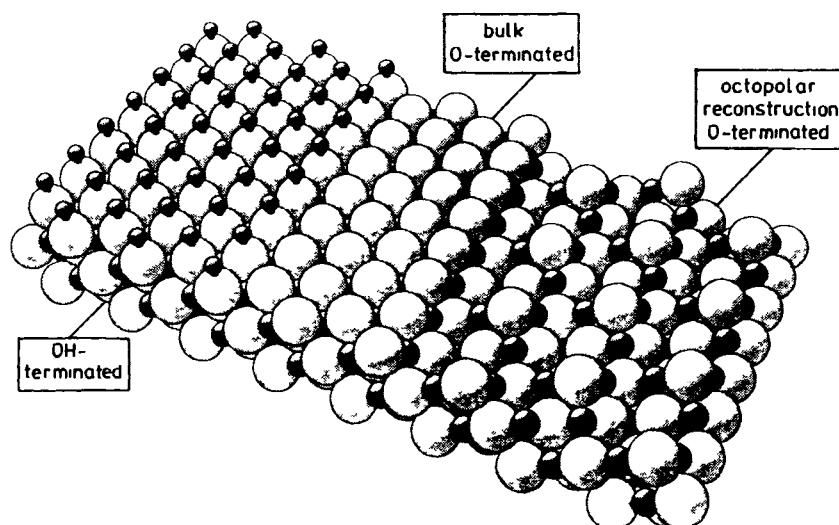


Figure 32. Schematic drawing of OH-terminated (left), bulk-terminated (middle) and octopolar reconstructed (right) NiO(111) surfaces

upper trace in Fig. 31 indicates a rather high concentration of hydroxyl groups at the surface. When (111) polar surfaces are prepared they often become OH stabilized, due to the electrostatic instability discussed above. In favorable cases such as NiO(111), the hydroxyl groups can be removed from the NiO(111) surface as water by thermal treatment. As a consequence, the OH-free unstable surface reconstructs. The most stable reconstruction of a polar surface of an ionic crystal is, according to Lacman [257] and to Wolf [258], the so-called octopolar arrangement, shown in Fig. 32 in comparison to the ideal  $(1 \times 1)$  surface. The octopolar reconstruction leads to  $p(2 \times 2)$  unit cell on the surface and is characterized by the removal of three out of four oxygen ions in the first layer (in the case of an oxygen terminated surface) and one out of four nickel ions within the second layer [254, 259]. The third layer contains then again a complete hexagonally close packed oxygen layer. A  $p(2 \times 2)$  reconstruction has been observed for iron oxide and nickel oxide but only in the latter case are there clear indications that an octopolar reconstruction has actually taken place [255].

Readsorption of water leads to a lifting of the reconstruction and the reoccurrence of the  $(1 \times 1)$  structure [254]. Note for completeness that the reconstructed surface exhibits a considerably higher chemical activity, for example in the  $\text{DcNO}_x$  reaction, than the hydroxyl-covered surface which is basically inactive towards further chemisorption [256]. In other words, water desorption and readsorption leads to a strong change in the chemical activity of certain crystallographic planes of oxide surfaces which may be relevant with respect to the catalytic activity of powders of real samples.

Previous sections have discussed the interaction between adsorbed species in connection with the coverage

dependence of adsorbate properties and especially energetics. Coadsorption of different chemical species is the general case in connection with the discussion of intermolecular interaction. Intermolecular interaction, however, is the basis for the understanding of chemical reactions between adsorbed species. There is such a vast literature on the subject [260] that a comprehensive and exhaustive review of the field cannot be provided here. Nevertheless, we would like to briefly address two coadsorbate systems where a broad knowledge has been accumulated over the years. To represent the limiting cases we resort again to carbon monoxide as one component and study its coadsorption with an electropositive additive, and also with electronegative additives. Needless to say, all aspects discussed above for chemisorbate systems in general are important, even at a more complex level, for coadsorbate systems. In the latter case it is necessary to consider the different chemical identities of the adsorbed species, and more importantly their influence on the electronic structure of the substrate, and on each other. In other words, the aspect of cooperativity that adsorbates and substrate interfere and determine each others properties becomes particularly noteworthy.

The most prominent and most frequently studied electropositive additives are alkali metals. Several comprehensive reviews have been published on the subject which provide more detailed information [260–262]. Characteristically, adsorption of alkali leads to dramatic changes of the work function of the system [260–262]. An example, K on Pt(111), is shown in Fig. 33 [263]. In general, small alkali coverages already lower the workfunction considerably before monolayer coverage is reached (in the present case more than

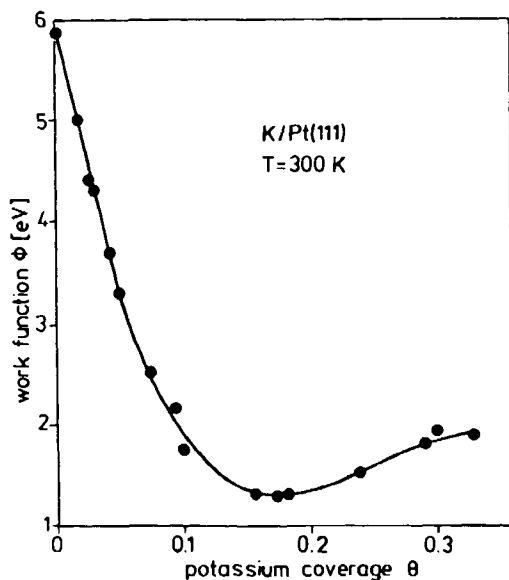


**Figure 33.** Work function of Pt(111) as a function of potassium coverage at 300 K [263].

4 eV). Before completion of the first monolayer coverage the work function reaches a minimum, turns around and then approaches, for increasing coverages, the value of the work function of the bulk alkali [260–262]. We are concerned only with the regime of alkali coverages below or close to monolayer coverage. It is generally accepted that in the low coverage regime the alkali atoms transfer charge towards the substrate, setting up a strong adsorbate–surface dipole which lowers the work function, hinders the alkali atoms to cluster on the surface, and allows them to adsorb as isolated atoms well separated from each other [264]. The energy needed to remove the alkali from the surface has been determined from TDS and calorimetric investigations to vary between 130 and 250 kJ mol<sup>-1</sup>. Co-adsorption of CO onto such an alkali-precovered surface leads to considerable effects on the energetics of the CO–substrate interaction as compared with the pure CO adsorbate. TD spectra of the pure and the coadsorbate system are shown in Fig. 34 [265]. The molecule still adsorbs associatively on the surface but note that the dissociative sticking coefficient increases considerably in the coadsorbate as has been observed for several CO–alkali coadsorbates [260]. The adsorption enthalpy increases for a typical CO–metal system from 130 kJ mol<sup>-1</sup> to 197 kJ mol<sup>-1</sup> for the alkali-adsorbed system [266]. There are coverage dependences as well, but we shall concentrate here on a single coverage. To learn more about how the observed energetic changes come about, consider the vibrational spectra of the system shown in Fig. 35 [267]. As compared with the pure CO adsorbate the CO stretching frequency in the coadsorbate is lowered by several hundred wavenumbers, indicating a weaker C–O bond in the co-

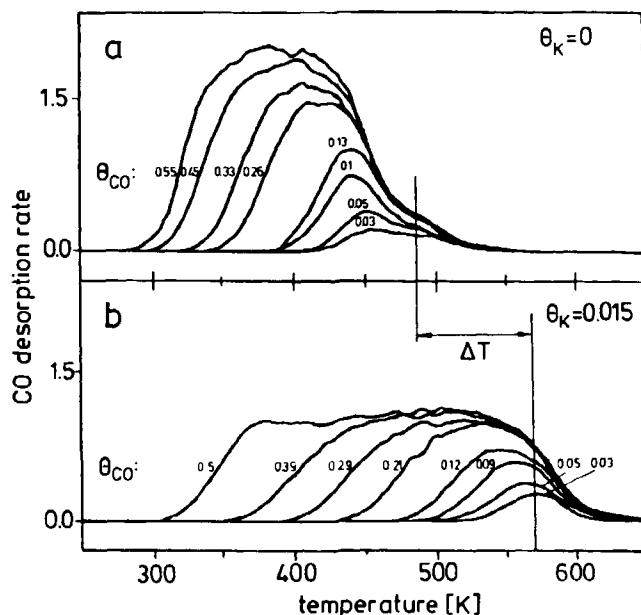


**Figure 34.** Thermal desorption spectra of (a) clean and (b) potassium covered ( $\Theta_K = 0.015$ ) Pt(111). Various CO coverages are plotted indicating the population of sites close to the alkali at low CO coverage. On the unmodified Pt(111) surface at higher coverages similar sites are observed [265].

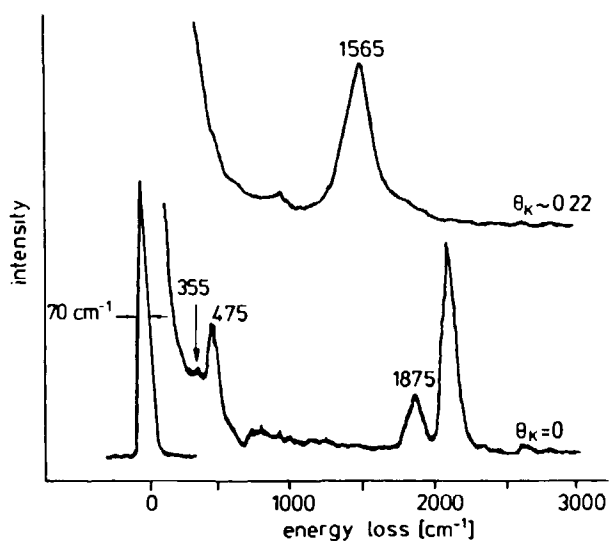


**Figure 35.** Electron energy loss spectra of CO on clean (lower trace) and K-modified (upper trace,  $\Theta_K = 0.02$ ) Pt(111) [267].

adsorbate. The explanation is straightforward: electrons from the electropositive additive are transferred either directly or via the substrate surface into the unoccupied CO antibonding orbitals thus weakening the CO bond [261]. Simultaneously, this stabilizes the CO–alkali interaction on the substrate surface and enhances the CO–substrate interaction. It turns out, however, to be rather difficult to exactly partition the interaction strength between CO–alkali and CO–substrate. It was

Table 5. Desorption energies for some transition metal surfaces modified by electronegative additives.

Adsorbate	Surface	Modifier	$E_d^0$ (kJ mol <sup>-1</sup> )	References
CO	Ni(100)	-	140	270
		P(2 × 2)S	90	
			110	
		C(2 × 2)S	≈ 30	
		P(2 × 2)O	120	
		P(2 × 2)N	≈ 90	
	Ni(111)	(2 × 2)p4gC	93	272
		-	140	273
		P(2 × 2)S	91	273
	Pd(100)	P(2 × 2)O	105	274
		-	160	275
		P(2 × 2)S	86	
	Pt(111)		60	
		-	154	276
		P(2 × 2)S	106	276
Ru(0001)	P(2 × 2)Se	110	277	
	-	170	278	
	P(2 × 2)S	105	278	
H	Ni(100)	-	102 ± 5	279
		P(2 × 2)S	84 ± 10	
		C(2 × 2)S	48 ± 16	
	Fe(100)	-	87 ± 50	280
		P(1 × 1)O	60 ± 10	280
	Pd(100)	-	85	281
	0.15S	49	281	

believed for some time that in the coadsorbate the CO-substrate interaction changes dramatically, leading to a change in the CO bonding geometry on the surface, i.e. from a vertically bound CO in the pure adsorbate to a side-on-bonded CO in the coadsorbate [268]. Near edge X-ray absorption fine structure (NEXAFS) has again been instrumental in showing that this is not the case [269]. In fact, CO remains vertically bonded on the surface and possibly interacts side-on with the coadsorbed alkali atom. The side-on geometry was particularly attractive because, similar to the case of nitrogen adsorption, this geometry could easily explain the increased dissociative sticking coefficient [260]. However, as it stands today, either the molecules transiently pass through such a side-on geometry before dissociation, and the concentration is so low that it cannot be identified, or dissociation can also start from vertically oriented, but electronically strongly modified CO. The described interaction between alkali and CO in a coadsorbate may be considered as special case of alkali promoter action, which is well established in catalysis [260].

A completely different situation is encountered when we coadsorb carbon monoxide with an electronegative species. Table 5 [260] collects desorption energies for carbon monoxide absorbed on transition metals modified by electronegative additives. In general, and opposite to the effect observed for the electropositive modifier, coadsorption with electronegative modifiers

leads to a decrease in the desorption energy. This may have different reasons. It could be due to repulsive modifier-CO interaction, or it could be due to the fact that the modifier blocks those sites of the surface leading to the strong CO-substrate interaction for the clean surface [260]. As judged from the vibrational data the influence of an electronegative additive onto the CO stretching frequency is much less pronounced if compared to the electropositive additives [282]. Often, instead of a strong red shift as observed for electropositive coadsorbates, a weak blue shift is observed which in certain cases may even lead to stretching frequencies higher than in the gas phase [282]. In this case it is even more difficult to disentangle the various contributions, i.e. direct and substrate-mediated interactions. The wealth of data presently available suggest that an electronegative additive mainly influences the substrate locally, i.e. in its direct vicinity, in the sense that (a) the adsorption sites which involve substrate atoms directly coordinated to the modifier are blocked, and (b) the adsorption sites sharing some substrate atoms with the modifier are substantially perturbed. This means, as schematically shown in Fig. 36 [260], that for a fcc(100) plane and a modifier residing in a fourfold site four atop sites and four bridge sites are blocked, and eight bridge sites, four close and four remote fourfold sites are perturbed. With increasing

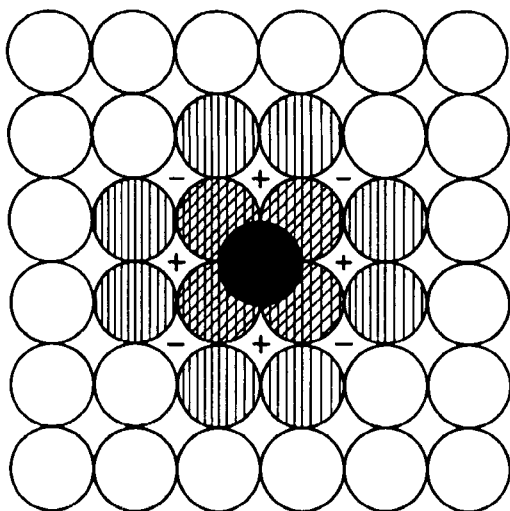


**Figure 36.** Schematic representation of the influence of an adsorbed electronegative modifier in a fourfold hollow site (black circle) on the neighboring sites. Neighboring fourfold hollow sites which are strongly (+) or less strongly (-) influenced are indicated [260].

modifier coverage, the number of affected sites per modifier atom decreases, because of overlap of effects. Following this simple model, obviously the most tightly bound states of the coadsorbate associated with the unaffected surface should be rapidly removed with increasing modifier coverage. In the case of Ni(100) where CO favors the atop site on the clean surface, one S atom, for example, is found to remove four atop CO molecules [270]. In addition, as evidenced by EELS data and TD spectra [270], CO is pushed to occupy the close bridge sites and the close fourfold hollow sites, in which the coupling with the substrate is reduced. Generalizing this observation it can be stated that coadsorption of electronegative additives often leads to a situation where a coadsorbate accesses the less strongly bound surface sites, which in turn leads to a strong modification of the reactivity in the presence of the modifier [260]. In catalysis such coadsorbate-induced effects are summarized as poisoning, particularly in connection with sulfur. However, as we have tried to indicate, due to the complexity arising from the specificity of the modified systems and the variety of possible interactions in the coadsorbed layer, there is still no uniform model for the mechanism of the poisoning action, even for the idealized model systems considered in this section [260]. The situation becomes even more complex if the additive induces surface reconstruction or even surface compound formation. Also, if there is a lack of a tendency to ordering and occupation of a definite adsorption site, coadsorption phenomena become increasingly complicated. In the case of modifying the surface with C, N, or O as opposed to S, P etc., transition metal surfaces may reconstruct or carbides,

nitrides, and oxides are formed [260]. Then, of course, the activity of the surface is determined by the properties of the new types of compounds formed. Often island formation is encountered in these systems which leads to a considerable reduction in the relative number of modified surface sites because the effect is restricted to the neighbors of the modifier island boundary. Summarizing, in such systems the problem of cooperativity, i.e. the phenomenon that the adsorbate and coadsorbate create their own active sites which are not present on the clean surface becomes particularly important. The future study of these effects in chemisorption is essential, even under ambient conditions, in order to identify which are the key effects that operate during catalysis at a microscopic level.

## References

1. G. Wedler, *Adsorption*, Chemische Taschenbücher, Vol. 9, Verlag Chemie, Weinheim, 1970.
2. I. Langmuir, *J. Amer. Chem. Soc.* **1916**, *38*, 2221.
3. I. Langmuir, *J. Amer. Chem. Soc.* **1918**, *40*, 1361.
4. W. Friedrich, P. Knipping, M. v. Laue, *Sitzungsber. Bayer. Akad. Wiss.* **1912**, *303/367*.
5. T. N. Rhodin, G. Ertl (Eds), *The Nature of the Surface Chemical Bond*, North-Holland, Amsterdam, 1979.
6. A. Zangwill, *Physics at Surfaces*, Cambridge University Press, Cambridge, 1988.
7. K. Christmann, *Introduction to Surface Physical Chemistry*, Topics in Physical Chemistry, Vol. 1, Steinkopff Verlag, Darmstadt, 1991.
8. G. Ertl, J. Küppers, *Low Energy Electrons and Surface Chemistry*, 2nd ed. Verlag Chemie, Weinheim, 1985.
9. A. Clark, *The Theory of Adsorption and Catalysis*, Academic Press, New York, 1970.
10. J. G. Dash, *Films on Solid Surfaces*, Academic Press, New York, 1975.
11. S. Cerny in *The Chemical Physics of Solid Surfaces and Heterogeneous Catalysis* (Eds: D. A. King, D. P. Woodruff), Elsevier, Amsterdam, 1983, Vol. 2, pp 1-57.
12. W. A. Steele, *The Interaction of Gases with Solid Surfaces*, Pergamon Press, Oxford, 1974.
13. K. Christmann, J. E. Demuth, *Surf. Sci.* **1982**, *120*, 291.
14. O. Beeck, W. A. Cole, A. Wheeler, *Discuss. Faraday Soc.* **1950**, *8*, 314.
15. J. Bagg, F. C. Tompkins, *Trans. Faraday Soc.* **1955**, *51*, 1071.
16. D. Brennan, D. O. Hayward, B. M. W. Trapnell, *Proc. Roy. Soc. A (London)* **1960**, *256*, 81.
17. G. Wedler, *Z. Phys. Chem. (Frankfurt/M.)* **1960**, *24*, 73.
18. F. J. Bröcker, G. Wedler, *Discuss. Faraday Soc.* **1966**, *41*, 87.
19. G. Wedler, H. Strothenk, *Ber. Bunsenges. Phys. Chem.* **1966**, *70*, 214.
20. G. Wedler, I. Ganzmann, D. Borgmann, *Ber. Bunsenges. Phys. Chem.* **1993**, *97*, 293.
21. C. Pluntke, G. Wedler, G. Rau, *Surf. Sci.* **1983**, *134*, 145.
22. K. Christmann, G. Ertl, O. Schober, *J. Chem. Phys.* **1974**, *60*, 4719-4727.
23. D. A. King, *Phys. Scr.* **1993**, *T49*, 560-562.
24. J. C. Tracy, *J. Chem. Phys.* **1972**, *56*, 2736-2747.
25. J. B. Benziger, R. J. Madix, *Surf. Sci.* **1979**, *79*, 394.
26. M. Kiskinova, D. W. Goodman, *Surf. Sci.* **1981**, *108*, 64.

- 27 B E Koel, D E Peebles, J M White, *Surf Sci* **1983**, *125*, 709
- 28 K Klier, A C Zettelmoyer, H Leidheiser Jr, *J Chem Phys* **1970**, *52*, 589
- 29 R S Bordoli, J C Vickerman, J Wolstenholme, *Surf Sci* **1979**, *85*, 244
- 30 F Labohm, C W R Engelen, O L J Gijzeman, J W Geus, G A Bootsma, *J Chem Soc, Faraday Trans* **1982**, *I* **78**, 2435
- 31 J C Tracy, P W Palmberg, *J Chem Phys* **1969**, *51*, 4852-4862
- 32 R J Behm, K Christmann, G Ertl, M A van Howe, *J Chem Phys* **1980**, *73*, 2984-2995
- 33 G Ertl, J Koch, *Z Naturforsch* **1970**, *25a*, 1906-1911
- 34 H Pfnur, P Feulner, H A Engelhardt, D Menzel, *Chem Phys Lett* **1978**, *59*, 481-486
- 35 G Lauth, T Solomun, W Hirschwald, K Christmann, *Surf Sci* **1989**, *210*, 201-224
- 36 J C Tracy, *J Chem Phys* **1972**, *56*, 2748-2754
- 37 G Wedler, I Ganzmann, D Borgmann, *Appl Surf Sci* **1993**, *68*, 335-340
- 38 N Al-Sarraf, J T Stuckless, C E Wartnaby, D A King, *Surf Sci* **1993**, *283*, 427-437
- 39 K Christmann, O Schober, G Ertl, M Neumann, *J Chem Phys* **1974**, *60*, 4528-4540
- 40 H Rinne, PhD thesis, Universität Hannover, **1974**
- 41 H Conrad, G Ertl, E E Latta, *Surf Sci* **1974**, *41*, 435-446
- 42 R J Behm, K Christmann, G Ertl, *Surf Sci* **1980**, *99*, 320-340
- 43 M Ehsasi, K Christmann, *Surf Sci* **1988**, *194*, 172-198
- 44 G Lauth, E Schwarz, K Christmann, *J Chem Phys* **1989**, *91*, 3729-3743
- 45 K H Ernst, PhD thesis Freie Universität Berlin, **1990**
- 46 C E Borroni-Bird, N Al-Sarraf, S Andersson, D A King, *Chem Phys Lett* **1991**, *183*, 516
- 47 C E Borroni-Bird, D A King, *Rev Sci Instr* **1991**, *62*, 1
- 48 H J Dixon-Warren, M Kovar, C E Wartnaby, D A King, *Surf Sci* **1994**, *16*, 307-309
- 49 R J Behm, K Christmann, G Ertl, *Surf Sci* **1980**, *99*, 320-340
- 50 R Miranda, S Daiser, K Wandelt, G Ertl, *Surf Sci* **1983**, *131*, 61
- 51 M Grunze, P A Dowben, R G Jones, *Surf Sci* **1984**, *141*, 455
- 52 M Golze, M Grunze, W Unertl, *Progr Surf Sci* **1986**, *22*, 101
- 53 G Ehrlich, *Adv Catal* **1963**, *14*, 255
- 54 P A Redhead, *Vacuum* **1962**, *12*, 203
- 55 D A King, *Surf Sci* **1975**, *47*, 384
- 56 D Menzel in *Interactions on Metal Surfaces*, Topics in Applied Physics Vol 4, Springer, Heidelberg, **1975**
- 57 L A Petermann, *Progr Surf Sci* **1972**, *1*, 2
- 58 J W Niemantsverdriet, *Spectroscopy in Catalysis An Introduction*, Verlag Chemie, Weinheim, **1993**
- 59 M Polanyi, *Trans Faraday Soc* **1932**, *28*, 314
- 60 C M Chan, R Aris, W H Weinberg, *Appl Surf Sci* **1978**, *1*, 360
- 61 E Habenschaden, J Kuppers, *Surf Sci* **1984**, *138*, L147
- 62 A M de Jong, J W Niemantsverdriet, *Surf Sci* **1990**, *233*, 355
- 63 J L Falconer, R J Madix, *Surf Sci* **1975**, *48*, 393
- 64 J E Lennard-Jones, *Trans Faraday Soc* **1932**, *28*, 333
- 65 V Bortolani, N H March, M P Tosi (Eds) *Interaction of Atoms and Molecules with Solid Surfaces*, Plenum Press, New York, **1990**
- 66 M C Derjougues, D Spanjaard *Concepts in Surface Physics*, Springer Series in Surface Science Vol 30, Springer, Heidelberg **1993**
- 67 M Scheffler, K Horn (Eds) *Handbook of Surface Science*, in preparation
- 68 P S Bagus, G Pacchioni *J Electron Spectrosc Relat Phenom* **1994**, *69*, 1-109
- 69 H A Michelsen, C T Rettner, D J Auerbach in *Surface Reactivity* (Ed R J Madix), Springer Series in Surface Science Vol 34, Springer, Heidelberg, **1994**, p 185
- 70 G Ertl, *Ber Bunsenges Phys Chem* **1982**, *86*, 425
- 71 J C Polanyi, *Science* **1987**, *236*, 680
- 72 G Comsa, R David, *Surf Sci Rep* **1985**, *5*, 145
- 73 K Christmann, *Surf Sci* **1988**, *9*, 1
- 74 M Balooch, M J Cardillo, D R Miller, R E Stuckney, *Surf Sci* **1974**, *46*, 358-392
- 75 G D Kubiak, G O Sitz, R N Zare, *J Chem Phys* **1985**, *83*, 2538-2551
- 76 P Anger, A Winkler, K D Rendulic, *Surf Sci* **1989**, *220*, 1-17
- 77 H F Berger, M Leisch, A Winkler, K D Rendulic, *Chem Phys Lett* **1990**, *175*, 425-428
- 78 J K Nørskov, P Stolze, *Surf Sci* **1987**, *189/190*, 91-105
- 79 J Harris, S Andersson, *Phys Rev Lett* **1985**, *55*, 1583-86
- 80 J Harris, *Appl Phys* **1988**, *A47*, 63-71
- 81 J Koutecky, *Trans Faraday Soc* **1958**, *54*, 1038
- 82 (a) T B Grimley, *Adv Catal* **1960**, *12*, 1, (b) T B Grimley, *Ber Bunsenges Phys Chem* **1971**, *75*, 1503
- 83 T L Einstein, J R Schrieffer, *Phys Rev* **1973**, *B7*, 3629
- 84 G Ertl in Ref 5
- 85 R L Park, T L Einstein, A R Kortan, L D Roelofs in *Ordering in Two Dimensions* (Ed S K Sinha), North Holland, Amsterdam, **1980**, p 17-24
- 86 B N J Persson, *Surf Sci* **1991**, *258*, 451
- 87 T L Hill, *Introduction to Statistical Thermodynamics*, Addison Wesley, Reading, **1962**
- 88 W Gebhardt, U Krey, *Phasenubergänge und kritische Phänomene*, Vieweg, Braunschweig, **1980**
- 89 G Kortum, *Einführung in die chemische Thermodynamik*, 6th ed, Vandenhoeck und Ruprecht, Göttingen, **1972**
- 90 E Bauer in *Phase Transitions on Single Crystal Surfaces and in Chemisorbed Layers in Structure and Dynamics of Surfaces II*, (Eds W Schommers, P von Blankenhagen) Springer, Berlin, **1987**, p 115-179
- 91 J P Biberian, M A van Hove, *Surf Sci* **1982**, *118*, 443
- 92 J Pritchard, *Surf Sci* **1979**, *79*, 231
- 93 D A King, M G Wells, *Surf Sci* **1972**, *29*, 454
- 94 D A King, M G Wells, *Proc Roy Soc London Ser A* **1974**, *339*, 245
- 95 K D Rendulic, G Anger, A Winkler, *Surf Sci* **1989**, *208*, 404
- 96 C T Rettner, L A DeLonise, D J Auerbach, *J Phys* **1986**, *85*, 1131
- 97 C T Rettner, H E Pfnur, D J Auerbach, *Phys Rev Lett* **1985**, *54*, 2716
- 98 M B Lee, Q Y Yang, S T Ceyer, *J Chem Phys* **1987**, *87*, 2724
- 99 A K Hamza, H-P Steinruck, R J Madix, *J Chem Phys* **1987**, *86*, 6506
- 100 A C Luntz, D S Bethune, *J Chem Phys* **1989**, *90*, 1274
- 101 M J Temkin, V Pyshev, *Acta physicochim USSR* **1940**, *12* 327
- 102 S Brunauer, P H Emmett, E Teller, *J Amer Chem Soc* **1938**, *60*, 309
- 103 H Freundlich, *Colloid and Capillary Chemistry* Methew London, **1926**
- 104 J Zeldowitsch, *Acta physicochim USSR* **1934**, *1*, 961
- 105 D M Young, A D Crowell, *Physical Adsorption of Gases* Butterworth, London, **1962**
- 106 J Lapujoulade, K S Neil, *Surf Sci* **1973**, *35*, 288-301
- 107 K Christmann, *Z Naturforsch* **1979**, *A34*, 22-29

- 108 J Lapujoulade, K S Neil, *Chem Phys* **1972**, *57*, 3535–3545  
 109 V Penka, K Christmann, G Ertl, *Surf Sci* **1984**, *136*, 307–318  
 110 H J Robota, W Vielhaber, M C Lin, J Segner, G Ertl, *Surf Sci* **1985**, *155*, 101–120  
 111 K Christmann, G Ertl, T Pignet, *Surf Sci* **1976**, *54*, 365–392  
 112 B Poelsema, L K Verheij, G Comsa, *Surf Sci* **1985**, *152/153*, 496–504  
 113 B Poelsema, K Lenz, L S Brown, L K Verheij, G Comsa, *Verhandl DPG* **1986**, *5* 1378  
 114 T E Madey, *Surf Sci* **1973**, *36*, 281  
 115 P Hofmann R Urwin, W Wyrobisch, A M Bradshaw, *Surf Sci* **1978**, *72*, 635–644  
 116 P J Holloway, J B Hudson, *Surf Sci* **1974**, *43*, 123–140  
 117 F P Netzer, R A Wille, *Surf Sci* **1978**, *74*, 547–567  
 118 J Benzinger, R J Madix, *Surf Sci* **1980**, *94*, 119  
 119 R J Behm, G Ertl, V Penka, *Surf Sci* **1985**, *160*, 387  
 120 T Engel, *J Chem Phys* **1978**, *69*, 373–385  
 121 G Ertl, M Neumann, K M Streit, *Surf Sci* **1977**, *64*, 393–410  
 122 T E Madey, J T Yates, *Nuovo Cimento* **1969**, *5*, 483  
 123 B J Hopkins, S Usamin in *The Structure and Chemistry of Solid Surfaces*, (Ed G A Somorjai), Wiley, New York, **1968**  
 124 M Bowker, D A King, *J Chem Soc Faraday Trans 1*, **1979**, *75*, 2100  
 125 F Boszo, G Ertl, M Grunze, M Weiss, *J Catal* **1977**, *49*, 18  
 126 G Ertl, *J Vac Sci Technol* **1983**, *A1*, 1247  
 127 K D Rendulic, *Appl Phys* **1988**, *A47*, 55  
 128 J N Russel Jr, I Chorkendorff, A M Lanzilotto, M D Alvey J T Yates Jr, *J Chem Phys* **1986**, *85*, 6186–6191  
 129 M A Morris, M Bowker, D A King in *Simple Processes at the Gas Solid Interface* (Eds C H Bamford, C F H Tipper, R G Compton), Elsevier, Amsterdam, **1984**, p 1–179  
 130 W H Weinberg in *Kinetics of Interface Reactions*, Springer Series in Surface Sciences Vol 8, Springer, Heidelberg, **1987**, p 94  
 131 P J Kisluk, *J Phys Chem Solids* **1957**, *3*, 95  
 132 P J Kisluk, *J Phys Chem Solids*, **1958**, *5*, 78  
 133 G Ertl, J Koch, *Z Naturforsch* **1970**, *25a*, 1906  
 134 C T Campbell, G Ertl H Kuipers, J Segner, *Surf Sci* **1981**, *107*, 207  
 135 K Heinz, *Progr Surf Sci* **1988**, *27*, 239, *Vacuum* **1990**, *41*, 328  
 136 G Ertl *Science* **1991**, *254*, 1750  
 137 M G Tenner, E W Kuipers, A W Kleyn, *J Chem Phys* **1979**, *89*, 6552  
 138 E W Kuipers, M G Tenner, A W Kleyn, S Stolte, *Nature* **1988**, *334*, 420  
 139 G H Fecher, N Bonsering, M Volkmer, B Pawlitzky, K Heinzmann, *Surf Sci Lett* **1990**, *230*, L169  
 140 G H Fecher, M Volkmer, B Pawlitzky, M Bowering, K Heinzmann, *Vacuum* **1993**, *41*, 265  
 141 H Muller, B Dierks, F Hamza, G Zagatta, G H Fecher, N Bowering K Heinzmann, *Surf Sci* **1992**, *269/270*, 207  
 142 H Muller, G Zagatta, N Bowering, K Heinzmann, *Chem Phys Lett* **1994**, *223*, 197  
 143 H P Bonzel, *Surf Sci* **1971**, *27*, 387  
 144 H P Bonzel, R Ku, *J Chem Phys* **1973**, *59*, 1641  
 145 H P Bonzel, E E Latta, *Surf Sci* **1978**, *76*, 275  
 146 R Butz, H Wagner, *Surf Sci* **1979**, *87*, 6984  
 147 R Butz, H Wagner, *Surf Sci* **1979**, *87*, 85  
 148 G Ehrlich, in T S Jayadanaah, R Vanselow (Eds), *Surface Science Recent Progress and Perspectives*, CRC Press, Cleveland, Ohio, **1974**  
 149 J Hölzl, G Porsch, *Thin Solid Films* **1975**, *28*, 93  
 150 P Schrammen, J Hölzl, *Surf Sci* **1983**, *130*, 203  
 151 H M Love, H D Wiedrenck, *Can J Phys* **1969**, *47*, 657–663  
 152 L Schmidt, R Gomer, *J Chem Phys* **1965**, *42*, 3573–3598  
 153 A Polak, G Ehrlich, *J Vac Sci Technol* **1977**, *14*, 407  
 154 M Bowker, D A King, *Surf Sci* **1980**, *94*, 564–580  
 155 D R Mullins, B Roop, S A Costello, J M White, *Surf Sci* **1987**, *186*, 67–74  
 156 R Lewis, R Gomer, *Surf Sci* **1969**, *14*, 333–345  
 157 E G Seebauer, A C F Kong, L D Schmidt, *J Chem Phys* **1988**, *88*, 6597–6604  
 158 H Rothermund, S Nettesheim, A von Oertzen, G Ertl, *Surf Sci Lett* **1922**, *275*, L645  
 159 J R Chen, R Gomer, *Surf Sci* **1979**, *79*, 413  
 160 S C Wang, R Gomer, *J Chem Phys* **1985**, *83*, 4193  
 161 A A Deckert, J L Brand, M V Arena, S M George, *Surf Sci* **1989**, *208*, 441  
 162 Z Rosenzweig, I Farbman, M Asscher, *J Chem Phys* **1993**, *98*, 8277  
 163 B Boddenberg, V Grundke, G Auer, *Ber Bunsenges Phys Chem* **1990**, *94*, 348  
 164 L Kevan, M K Bowman, *Modern Pulsed and Continuous-wave Electron Spin resonance*, Wiley, New York, **1990**  
 165 H Schlenz, M Beckendorf, U J Katter, Th Risse, H -J Freund, *Phys Rev Lett* **1995**, *74*, 761  
 166 L Boltzmann, *Wien Ann* **1904**, *53*, 53  
 167 W M H Sachtler, *Le Vide* **1973**, *164*, 67  
 168 V D Planck, W M H Sachtler, *J Catal* **1967**, *7*, 300, *J Catal* **1968**, *12*, 35  
 169 A A Balandin, *Adv Catal* **1958**, *10*, 86  
 170 S D Kevan (Ed), *Angle Resolved Photoemission Theory and Current Applications*, Studies in Surface Science and Catalysis Vol 74, Elsevier, Amsterdam, **1982**  
 171 H -J Freund, M Neumann, *Appl Phys* **1988**, *A47*, 3  
 172 D Cappus, J Klinkmann, H Kuhlenbeck, H -J Freund, *Surf Sci Lett* in press  
 173 C Xu, B Dillmann, H Kuhlenbeck, H -J Freund, *Phys Rev Lett* **1991**, *67*, 3551  
 174 D W Turner, C Baker, A D Baker, C R Brundle, *Molecular Photoelectronic Spectroscopy*, Wiley, New York **1970**  
 175 W Eberhardt, H -J Freund, *J Chem Phys* **1983**, *78*, 700  
 176 D Schmeisser, F Greuter, E W Plummer, H -J Freund, *Phys Rev Lett* **1985**, *54*, 2095  
 177 H -J Freund, W Eberhardt, D Heskett, E W Plummer *Phys Rev Lett* **1983**, *50*, 786  
 178 C L Allyn, Thesis, University of Pennsylvania, **1978**  
 179 G Odorfer, Diplomarbeit, Universität Erlangen-Nürnberg, **1987**  
 180 G Blyholder, *J Phys Chem* **1968**, *68*, 2772, *J Vac Sci Technol* **1974**, *11*, 865  
 181 C M Kao, R P Messmer, *Phys Rev* **1985**, *B31*, 4835  
 182 R P Eischens, A W Pliskin, *Adv Catal* **1958**, *10*, 1  
 183 A M Bradshaw, F Hoffmann, *Surf Sci* **1978**, *72*, 513  
 184 C Surner, F Xu, J T Yates, *Surf Sci* **1988**, *201*, 1  
 185 J G Chen, W Erley, H Ibach, *Surf Sci* **1989**, *223*, L891  
 186 G McElhiney, H Papp, J Pritchard, *Surf Sci* **1976**, *54*, 617  
 187 H -J Freund, H Kuhlenbeck in *Applications of Synchrotron Radiation* (Ed W Eberhardt), Springer Series in Surface Sciences Vol 35, Springer Verlag, Heidelberg, **1995**, p 9  
 188 T C Chiang, G Kandl, A E Eastman, *Solid State Commun* **1980**, *36*, 25  
 189 C B Duke, *Surf Sci* **1978**, *70*, 675  
 190 C B Duke, W R Salaneck, F -J Fabisch, J J Ritsko, H R Thomas, A Paton, *Phys Rev* **1978**, *B18*, 5717

- 191 J W Gadzuk, S Holloway, K Horn, C Mariani, *Phys Rev Lett* **1982**, *48*, 1288
- 192 U Hofer, M J Breitschäfer, E Umbach, *Phys Rev Lett* **1990**, *64*, 3050
- 193 M Bertolo, W Hansen, K Jacobi, *Phys Rev Lett* **1991**, *67*, 1898
- 194 J Kessler, F Thieme, *Surf Sci* **1977**, *67*, 405
- 195 N V Richardson, A M Bradshaw in *Electron Spectroscopy* (Eds C R Brundle, A D Baker), Academic Press, New York, **1982**, Vol 4
- 196 E W Plummer, W Eberhardt, *Adv Chem Phys* **1982**, *49*, 533
- 197 C L Allyn, T Gustafsson, E W Plummer, *Chem Phys Lett* **1977**, *47*, 127
- 198 K Horn, A M Bradshaw, K Jacobi, *Surf Sci* **1978**, *72*, 719
- 199 H Kuhlenbeck, M Neumann, H-J Freund, *Surf Sci* **1986**, *173*, 194
- 200 F Greuter, D Heskett, E W Plummer, H-J Freund, *Phys Rev* **1983**, *B27*, 7117
- 201 E S Jensen, T N Thodin, *Phys Rev* **1983**, *B27*, 3338
- 202 N D Shinn, *J Vac Sci Technol* **1986**, *A4*, 1351
- 203 R Miranda, K Wandelt, D Rieger, R D Schnell, *Surf Sci* **1984**, *139*, 430
- 204 K Horn, A M Bradshaw, K Hermann, I P Batra, *Solid State Commun* **1979**, *31*, 257
- 205 G Borstel, M Neumann, G Seitz, W Braun, *Proc 4th Intern Conf Solid Surfaces*, Cannes, **1980**, Vol 1, p 357
- 206 P Hoffmann, J Gossler, A Zartner, M Glanz, D Menzel, *Surf Sci* **1985**, *161*, 303
- 207 D Heskett, E W Plummer, R A DePaola, W Eberhardt, F M Hoffman, *Surf Sci* **1985**, *164*, 490
- 208 M Steinkilberg, Thesis, Technische Universität München, **1977**
- 209 W Braun, G Meyer-Ehmsen, M Neumann, E Schwarz, *Surf Sci* **1979**, *89*, 354
- 210 H Kuhlenbeck, Diplomarbeit, Universität Osnabrück, **1984**
- 211 CW Seabury, T N Rhodin, M Traum, R Benbow, Z Hurych, *Surf Sci* **1979**, *97*, 363
- 212 D Rieger, R D Schnell, W Steinmann, *Surf Sci* **1984**, *143*, 157, P Hoffmann, S R Bare, D A King, *Surf Sci* **1982**, *117*, 245
- 213 G Apar, R S Wehner, R W Williams, J Stohr, D A Shirley, *Phys Rev Lett* **1976**, *37*, 1497
- 214 R J Smith, J Anderson, G J Lapeyre, *Phys Rev Lett* **1976**, *37*, 1081 G J Lapeyre, J Anderson, R J Smith, *Surf Sci* **1979**, *89*, 304
- 215 H-J Freund, E Umbach (Eds), *Adsorption on Ordered Surfaces of Ionic Solids and Thin Films*, Springer Series in Surface Sciences Vol 33, Springer, Heidelberg, **1993**
- 216 V E Hennrich, P A Cox, *The Surface Science of Metal Oxides*, Cambridge University Press, Cambridge, **1994**
- 217 M Pohlchen, V Staemmler, *J Chem Phys* **1992**, *97*, 2583
- 218 V Staemmler in *Adsorption on Ordered Surfaces of Ionic Solids and Thin Films* (Eds H-J Freund, E Umbach), Springer Series in Surface Sciences Vol 33, Springer, Heidelberg, **1993**, p 169
- 219 G Pacchioni, G Cogliandro, P S Bagus *Surf Sci* **1991**, *225*, 344 G Pacchioni, T Minerva, P S Bagus *Surf Sci* **1992** *275*, 450
- 220 G Pacchioni, *Surf Sci* **1993**, *281*, 257, G Pacchioni, P S Bagus in *Adsorption on Ordered Surfaces of Ionic Solids and Thin Films* (Eds H-J Freund, E Umbach), Springer Series in Surface Sciences Vol 33, Springer Heidelberg, **1993**, p 180
- 221 G Pacchioni, K M Neymann, N Rosch, *J Electron Spectrosc Relat Phenom* **1994**, *69*, 13
- 222 K M Neymann, N Rosch, *J Chem Phys* **1992**, *168*, 267, *Surf Sci* **1993**, *297*, 223, *Chem Phys* **1993**, *177*, 561
- 223 C Pisani, R Dovesi, R Nada S Tamiro, *Surf Sci* **1989**, *216*, 267
- 224 M A Nygren, L G M Petterson, *J Electron Spectrosc Relat Phenom* **1994**, *69*, 43
- 225 S M Vesecky, X Xu, D W Goodman, *J Vac Sci Technol* **1994**, *A12*, 2114, M C Wu, C M Truong, D W Goodman, *J Phys Chem* **1993**, *97*, 4182, C M Truong, M C Wu, D W Goodman, *J Amer Chem Soc* **1993**, *115*, 3647
- 226 J Heidberg, L Cabigon, E Kampshoff, M Kandel, R Kühnemuth, D Meine, B Redlich, O Schonekas, M Suhren, H Weiss, D Wetter in *Adsorption on Ordered Surfaces of Ionic Solids and Thin Films* (Eds H J Freund, E Umbach), Springer Series in Surface Sciences Vol 33, Springer, Heidelberg, **1993**, p 46
- 227 D P Woodruff, A M Bradshaw, *Rep Progr Phys* **1994**, *57*, 1029
- 228 K M Schindler, Ph Hofmann, V Frische, S Bao, S Kul-karni, A M Bradshaw, D P Woodruff, *Phys Rev Lett* **1993**, *71*, 2045
- 229 A M Bradshaw, D P Woodruff in *Applications of Synchrotron Radiation* (Ed W Eberhardt), Springer Series in Surface Sciences Vol 35, Springer, Heidelberg, **1995**, p 127
- 230 B A Gurney, W Ho, *J Vac Sci Technol* **1985**, *A3*, 1541
- 231 J C Bertolini, B Terdy, *Surf Sci* **1981**, *102*, 131
- 232 M Nishijima, S Masuda, Y Sakisaka, M Onchi, *Surf Sci* **1981**, *107*, 31
- 233 P R Mahaffy, M J Dignam, *Surf Sci* **1980**, *97*, 377
- 234 R M Lambert, *Surf Sci* **1975**, *49*, 325
- 235 R J Behm, G Ertl, V Penka, *Surf Sci* **1985**, *160*, 367
- 236 D A Wesner, F P Creuen, H P Bonzel, *Phys Rev Lett* **1988**, *60*, 1045, *Phys Rev* **1989**, *B39*, 10770
- 237 H Kuhlenbeck, M Neumann, H-J Freund, *Surf Sci* **1986**, *173*, 194
- 238 H Kuhlenbeck, H B Schalfeld, U Buskotte, M Neumann, H-J Freund, E W Plummer, *Phys Rev* **1989**, *B39*, 3475
- 239 N Memmel, G Rangelov, E Bertel, V Dose, K Kometer, N Rosch, *Phys Rev Lett* **1989**, *63*, 1884
- 240 G Rangelov, N Memmel, E Bertel, V Dose, *Surf Sci* **1991**, *251/252*, 965
- 241 D A King, D P Woodruff (Eds), *The Chemical Physics of Solid Surfaces and Heterogeneous Catalysis*, Elsevier, Amsterdam, **1990**, Vol 3
- 242 K Wandelt, *Surf Sci Reports* **1982**, *2*, 1
- 243 C R Brundle, J Q Broughton in Ref 241, p 131
- 244 R Reval, M A Harrison, D A King in Ref 241, p 39
- 245 H-J Freund, B Bartos, R P Messmer, M Grunze, H Kuhlenbeck, M Neumann, *Surf Sci* **1987**, *185*, 187
- 246 M Grunze, M Gloze, W Hirschwald, H-J Freund, H Pulm, U Seip, N C Tsai, G Ertl, J Kuppers, *Phys Rev Lett* **1984**, *53*, 850
- 247 M C Tsai, U Seip, F C Bassignana, J Kuppers, G Ertl, *Surf Sci* **1985**, *155*, 387
- 248 L J Whitman, C E Beartosch, W Ho, G Strasser, M Grunze, *Phys Rev Lett* **1986**, *56*, 1984
- 249 D Tomanek, K H Bennemann, *Phys Rev B* **1985**, *31*, 2488
- 250 M Grunze, M Golze, J Fuhler, M Neumann, E Schwarz, *Proceedings of the 8th Intern Congr on Catalysis*, Berlin, **1984**, Vol IV, p 233
- 251 F Winkelmann, S Wohlrab, J Libuda, M Baumer, D Cappus, M Menges, K Al-Shamery, H Kuhlenbeck, H-J Freund, *Surf Sci* **1994**, *307-309*, 1148
- 252 D Cappus, C Xu, D Ehrlich, B Dillmann, C A Ventrice, K Al-Shamery, H Kuhlenbeck, H-J Freund, *Chem Phys* **1993**, *177*, 533

253. P. W. Tasker, *J. Phys. C* **1978**, *12*, 4977; *Phil. Mag. A* **1979**, *39*, 119.
254. F. Rohr, K. Wirth, J. Libuda, D. Cappus, M. Bäumer, H.-J. Freund, *Surf. Sci.* **1994**, *315*, L299.
255. D. Cappus, M. Haßel, E. Neuhaus, M. Heber, F. Rohr, H.-J. Freund, *Surf. Sci.*, **1995**, *337*, 268.
256. G. Illing, Thesis, Ruhr-Universität Bochum, **1990**.
257. R. Lacman, *Colloq. Int. CNRS* **1965**, *152*, 195.
258. D. Wolf, *Phys. Rev. Lett.* **1992**, *68*, 3315.
259. C. A. Ventrice Jr., H. Hannemann, Th. Bertrams, H. Neddermeyer, *Phys. Rev. B* **1994**, *49*, 5773.
260. M. P. Kiskinova, *Poisoning and Promotion in Catalysis Based on Surface Science Concepts and Experiments*, Studies in Surface Science and Catalysis Vol. 70, Elsevier, Amsterdam, **1992**.
261. H. P. Bonzel, *Surf. Sci. Rep.* **1987**, *8*, 43.
262. H. P. Bonzel, A. M. Bradshaw, G. Ertl (Eds), *Physics and Chemistry of Alkali Metal Adsorption*, Material Science Monographs Vol. 57, Elsevier, Amsterdam, **1989**.
263. M. P. Kiskinova, G. Pirug, H. P. Bonzel, *Surf. Sci.* **1983**, *133*, 321.
264. M. Scheffler, Ch. Droste, A. Fleszar, F. Máca, G. Wachutka, G. Barzel, *Physica* **1991**, *172B*, 143.
265. L. J. Whitman, W. Ho, *J. Chem. Phys.* **1989**, *90*, 6018.
266. H. Pfnür, P. Feulner, D. Menzel, *J. Chem. Phys.* **1983**, *79*, 4613.
267. J. E. Crowell, E. L. Garfunkel, G. A. Somorjai, *Surf. Sci.* **1982**, *121*, 303.
268. T. E. Madey, C. Benndorf, *Surf. Sci.* **1985**, *164*, 602.
269. F. Sette, J. Stöhr, E. B. Kollin, D. J. Dwyer, J. L. Gland, J. L. Robbins, A. L. Johnson, *Phys. Rev. Lett.* **1985**, *54*, 935.
270. J. L. Gland, R. J. Madix, R. W. McCabe, C. DiMaggio, *Surf. Sci.* **1984**, *143*, 46.
271. W. M. Daniel, J. M. White, *Surf. Sci.* **1986**, *171*, 289.
272. J. C. Bertolini, B. Tardi, *Surf. Sci.* **1981**, *102*, 131.
273. M. Trenary, K. J. Uram, J. T. Yates, Jr., *Surf. Sci.* **1985**, *157*, 512.
274. Xu Zi, L. Surnev, J. T. Yates, Jr., unpublished results.
275. T. Yamada, Z. Runsheng, Ya. Iwisawa, K. Tamaku, *Surf. Sci.* **1988**, *205*, 82.
276. M. Kiskinova, A. Szabo, J. T. Yates, Jr., *J. Chem. Phys.* **1988**, *89*, 7599.
277. M. Kiskinova, A. Szabo, J. T. Yates, Jr., *Surf. Sci.* **1990**, *226*, 237.
278. J. L. Brand, M. V. Arcna, A. A. Deckart, S. M. George, *J. Chem. Phys.* **1990**, *92*, 4483.
279. S. Johnson, R. D. Madix, *Surf. Sci.* **1981**, *108*, 77.
280. J. Benziger, R. J. Madix, *Surf. Sci.* **1980**, *94*, 119.
281. M. L. Burke, R. J. Madix, *Surf. Sci.* **1990**, *237*, 1.
282. J. G. Chen, W. Erley, H. Ibach, *Surf. Sci.* **1989**, *224*, 215.

## 5.1.2 Chemisorption Theory

R. A. VAN SANTEN AND M. NEUROCK

### 5.1.2.1 Introduction

Computational quantum chemistry and solid state physics have reached the stage where quantitatively reliable predictions on the interaction of small and moderate sized molecules with transition metal clusters or surfaces are now possible. Computation therefore be-

gins to enrich experimental information by providing results of model systems that are not easily accessible to experiment. In addition they allow us to probe the nature of transient surface species such as short-lived intermediates and activated complexes. Nonetheless, the qualitative theoretical framework that has been established over the past 50 years remains highly relevant. It provides a sound framework for conceptual analysis and interpretation. Computation and experiment then can be used to test ideas on the electronic and structural parameters which control the geometry, energetics, and dynamics of the chemisorbed molecule.

Two different schools of thought in chemisorption theory can be distinguished. The first is born out of the solid-state physics community, while the second originates from the theoretical chemistry community. Formal chemisorption theory dates back to the 1950s and 1960s where the relevant electronic factor for chemisorption was considered to be the local electron density of states at the Fermi level. This is especially true in catalysis. Magnetic and conductivity measurements were usually interpreted in these terms. With progress in solid state physics, theory became more refined and surface physicists developed a more physically realistic view of the surface chemical bond. Koutecky [1], Newns [2], Grimley [3], and Schieffer [4] are considered to be the founders of formal chemisorption theory. Many of their concepts remain today and are the basis of our current views on chemisorption. Formal chemisorption theory is therefore the subject of the first section. One of the most important results derived from formal chemisorption theory was the rationalization of strength of adsorbate-surface interaction in terms of the ratio of adsorbate-surface-atom strength versus the interaction energy between the surface atoms. It raised the issue of the existence of the concept of a surface adsorption complex, hence identifying chemisorption physics with surface complex chemistry.

The theoretical chemical application of surface chemical bonding theory, highlighted next, is related to formal chemisorption theory as developed in surface physics, but concentrates on quantum chemical concepts as the electron distribution over bonding and antibonding orbital fragments [5, 6]. It will be seen that both approaches complement each other. The notion of a surface molecule relates to the surface physicists' concept of surface state.

The final section provides an overview of the current understanding of the factors that govern the physical chemistry of chemisorption. Our understanding of the factors that determine the site preference of surface dependence of chemisorption is summarized. We demonstrate many of those concepts through a series of first-principle quantum chemical results on different example systems. The results allow us to specifically quantify different aspects of the interaction, such as



---

# 6 Kinetics and Transport Processes

- 
- 6.1 Rate Procurement and Kinetic Modeling
  - 6.2 Simultaneous Heat and Mass Transfer and Chemical Reaction
  - 6.3 Determination of Diffusion Coefficients in Porous Media
- 

## 6.1 Rate Procurement and Kinetic Modeling

F. KAPTEIJN AND J. A. MOULIJN

### 6.1.1 Introduction

Knowledge of the rate of a catalytic reaction and its selectivity is essential for its application in practice. More precisely, the kinetics of the reaction is required in the form of a rate expression, i.e. the function that tells how the reaction rate varies with temperature, pressure and composition of the reacting system. The kinetics determine the size of the catalytic reactor for a given overall production rate and without it, design would be highly speculative.

$$r = f(p_i, \dots, T, N_T, k_i, \dots, K_i, \dots, K_{eq}) \quad (1)$$

Kinetic studies focus on the selection of an adequate rate expression and determination of the unknown rate parameters it contains (eq 1). Generally, the rate is not measured directly but is derived from a measured quantity, conversion or concentration, at given operating conditions such as catalyst amount and feed rate. Apart from kinetic studies to determine the rate equation, other purposes of measuring rates are comparison of various catalyst formulations in screening of new catalysts, the time-dependent behavior of the catalyst activity to predict its long term performance and to characterize catalysts such as in temperature programmed reduction (TPR) or sulphidation (TPS) studies.

In this sense rate procurement is one of the core businesses of catalysis. It should, however, be carried out in the correct way. Rate measurements can be disguised by slow mass or heat transport phenomena inside and outside the catalyst particle or by the reactor configuration, through which not intrinsic rates are determined, thus rendering the data and efforts useless [1].

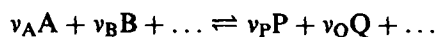
In this chapter the emphasis is on the methods to obtain data relevant for kinetic modeling and comparison of catalyst activities for the ultimate purpose of engineering applications. Some laboratory reactor types will be discussed, the procedure for kinetic modeling outlined together with the related parameter estimation and the determination of the rate constants in the rate expression. It should serve as a comprehensive reference to this type of activity in catalysis. Most of it comes from authoritative reviews [2–14].

### 6.1.2 Rate Procurement – Laboratory Reactors

Rates of catalytic reactions are obtained by measurement of the conversion of a key component, often the rate limiting reactant, in laboratory reactors and relating this to the amount of catalyst used and the amount or flow rate of reactants used, to obtain an intrinsic quantity,  $\text{mols}^{-1} \text{ amount}^{-1}$ . For practical application the mass or volume of a catalyst is most relevant as the amount but, for comparative studies the amount of active phase on a supported catalyst, its specific surface area or the number of active sites may be preferred. In the latter case this yields the turnover frequency (TOF) [3], which is quite relevant for fundamental studies. The number of active sites is, however, usually hard to determine and the mass of the catalyst  $W$  will be used, resulting in a rate dimensions of  $\text{mols}^{-1} \text{ kg}^{-1}$ . Other quantities are easily derived from this.

Three ideal reactor types are relevant from reactor theory [15], the two continuous flow types, the plug flow reactor (PFR) and continuous flow stirred tank reactor (CSTR), and the well-stirred batch reactor. The

first two are generally operated under steady state conditions, yielding time-independent relations for the conversion, whereas the batch reactor operates under transient conditions, the conversion level changes as a function of the elapsed reaction time. The relationships that hold for component A in a reaction such as



in these reactors are given by eqs 2–4:

$$\text{PFR : } \frac{dx_A}{d\left(\frac{W}{F_A^0}\right)} = v_A \times r \quad (2)$$

$$\text{CSTR : } \frac{x_A}{\left(\frac{W}{F_A^0}\right)} = v_A \times r \quad (3)$$

$$\text{batch : } N_A \frac{dx_A}{dt} = v_A \times r \quad (4)$$

All expressions contain the reaction rate  $r$ , but only in eq 3 can the rate can be calculated directly from the observed conversion. The differential equation (2) describes the conversion as a function of the space time (a kind of residence time),  $W/F_A^0$ , which can be considered as the reactor coordinate for a given feed rate. Only the exit conversion is measured and not a reaction rate, which varies with the conversion over the bed length. Only for low conversion levels, where the rate can be assumed to be constant over the bed length, does eq 2 reduce to eq 3. Therefore, the CSTR and the PFR at low conversion are referred to as differential reactors, in contrast to the integral PFR. Often people calculate rates for the latter on the basis of (3), but this will be an average value depending on the conversion level.

In eq 4 the rate is the time derivative of the conversion curve, which can be constructed from the observed conversion–time behavior by mathematical treatment, such as differentiation formulae or polynomial or spline interpolation, provided the product analysis is fast enough to follow the reaction. The same approach can be followed in principle for the plug flow reactor if data is collected at various space–time values.

In kinetic studies it is not necessary to use rates for determination of the rate parameters. In eqs 2–4  $r$  represents the rate expression for the reaction under consideration, whatever its mathematical form. This can be inserted in eq 2, and subsequently integrated after separation of variables, leading to eq 5. The result may be an implicit expression, containing the rate parameters, describing the relationship between space-time and conversion. It will be shown later that this relationship can also be used for parameter determination.

$$\frac{W}{F_A^0} = \int_0^{x_A} \frac{dx}{v_A r} \quad (5)$$

The plug flow reactor is increasingly being used under transient conditions to obtain kinetic data by analysing the combined reactor and catalyst response upon a stimulus. Mostly used are a small reactant pulse (e.g. in temporal analysis of products (TAP) [16] and positron emission profiling (PEP) [17, 18]) or a concentration step change (in step-response measurements (SRE) [19]). Isotopically labeled compounds are used which allow operation under overall steady state conditions, but under transient conditions with respect to the labeled compound [18, 20–23]. In this type of experiments both time- and position-dependent concentration profiles will develop which are described by sets of coupled partial differential equations (PDEs). These include the concentrations of proposed intermediates at the catalyst. The mathematical treatment is more complex and more parameters are to be estimated [17].

Basically, kinetic studies consist of:

- (i) the acquisition of rate versus space-time data or of conversion versus space-time data sets for various conditions of pressure, temperature and composition;
- (ii) derivation and selection of adequate rate expressions;
- (iii) determination of the unknown parameters in the rate expression by nonlinear least-squares methods for which the basic eqs 2–5 are applied.

This will form the main body of what follows.

### 6.1.2.1 Laboratory Reactors

Several reactor types have been described [5, 7, 11, 12, 24–26]. They depend mainly on the type of reaction system that is investigated: gas–solid (GS), liquid–solid (LS), gas–liquid–solid (GLS), liquid (L) and gas–liquid (GL) systems. The first three are intended for solid or immobilized catalysts, whereas the last two refer to homogeneously catalyzed reactions. Unless unavoidable, the presence of two reaction phases (gas and liquid) should be avoided as far as possible for the ease of data interpretation and experimentation. Premixing and saturation of the liquid phase with gas can be an alternative in this case. In homogeneously catalyzed reactions continuous flow systems are rarely encountered, since the catalyst also leaves the reactor with the product flow. So, fresh catalyst has to be fed in continuously, unless it has been immobilized somehow. One must be sure that in the analysis samples taken from the reactor contents or product stream that the catalyst does not further affect the composition. Solid catalysts are also to be fed continuously in rapidly deactivating systems, as in fluid catalytic cracking (FCC).

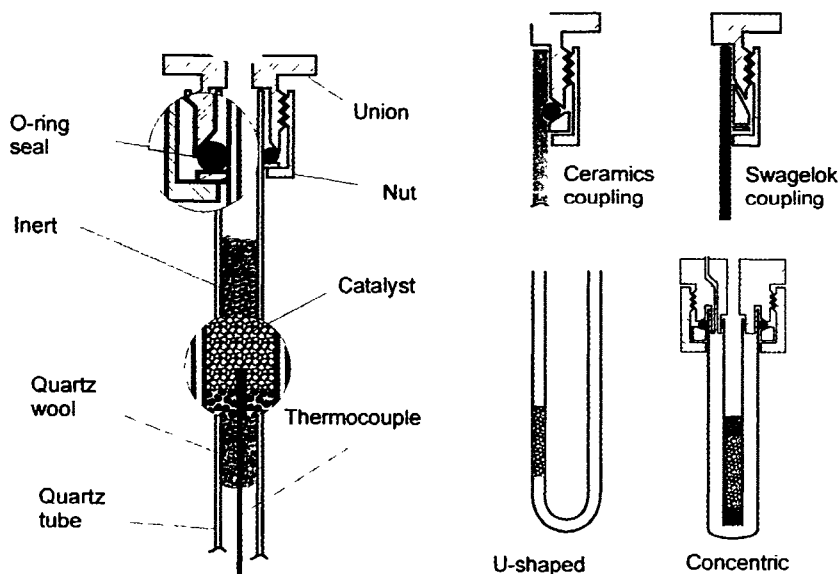


Figure 1. Packed bed reactor designs – examples of geometries and connections.

In spite of the differences in construction all reactors suited for kinetic studies can be classified into the three ideal reactor types mentioned above. It is stressed here that kinetic data should be acquired in laboratory reactors that are suited for kinetic studies and should not be a small-scale replica of the reactor intended to be used in practice.

The most commonly used and simplest type for gas–solid reaction systems is the packed bed reactor, Fig. 1. It simply consists of a reaction tube in which the catalyst is held between plugs of quartz wool, on a sintered frit or wire mesh gauze. Depending on the reaction conditions the tube consists of glass, quartz, a steel or ceramics (SiC, alumina). For low temperatures and pressure glass satisfies, high pressure requires steel, high temperatures quartz or ceramics. The latter are especially suited for high pressure–high temperature applications [27] where most steel alloys already lose their strength. Its optimal internal diameter is 4–6 mm, predominantly to ensure good heat transport to or from the catalyst [28]. The reactor may have a straight or U-shape, or a concentric geometry, with the catalyst in the inner tube [27]. The porous catalyst may be diluted with an inert well heat-conducting material (SiC) to improve this heat transfer and to satisfy plug flow criteria [1]. Before and after the bed, inert material can be placed for preheating the fluid phase and avoiding fluidization in upflow configurations.

To have a good temperature indication a thermocouple should be directly inserted in the catalyst bed or, when there is a chance of undesired catalytic action of the thermocouple, be surrounded by an insert. Under conditions of good wetting [1, 29] this reactor type can be used in trickle flow (GLS).

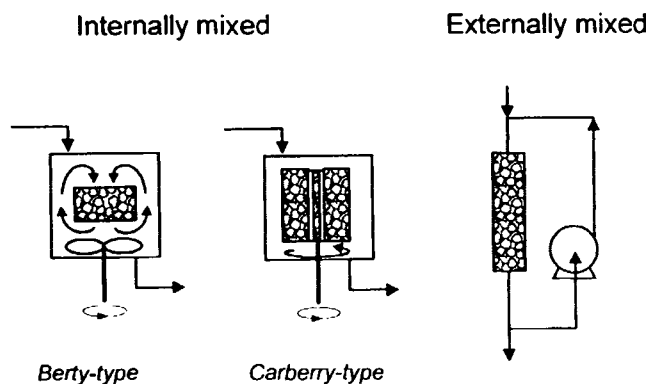


Figure 2. Schematics of CSTRs for heterogeneous catalysis applications.

Various designs exist to approach the ideal CSTR (Fig. 2). Berty reviewed them up to 1984, but new designs have been published [24, 30, 31]. Various configurations are commercially available. For GS systems two approaches are followed: either the catalyst is placed in baskets and stirred, the Carberry type [32], or the gas phase is circulated at a high rate internally, the Berty type [24], or externally by means of a gas pump (membrane, piston, plunger or centrifugal types) [24]. A major problem is the good contact between the two phases. Therefore, the Carberry-type reactors are restricted to larger particles (few mm), since the flow rate of the fluid through the bed of particles is not known. Various basket designs have been proposed to optimize this fluid–catalyst contact. Figure 3 gives the original Carberry basket in the form of a four-bladed stirrer

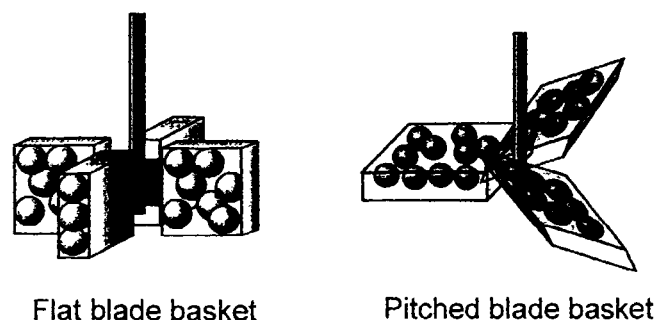


Figure 3. Basket designs for Carberry-type reactors.

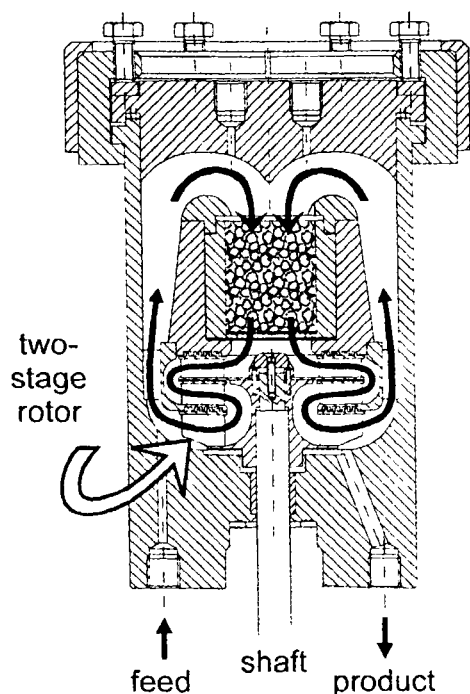


Figure 4. Layout of the RotoBerty reactor.

and a recent pitched-type stirrer, claimed to have good mixing properties [30, 33, 34]. The temperature of the catalyst bed cannot be measured in the Carberry-type reactor, and highly endo- or exothermal reactions are to be avoided. An example of the Berty type, the RotoBerty reactor, is given in Fig. 4. The catalyst is packed in the inner tube to avoid local maldistribution and catalyst bypassing. Monolithic catalysts can be ideally applied in these reactors because of their intrinsic low pressure drop. Various stirrer designs exist to create a good mixing, and even two-stage impellers are applied for gaseous reactions. These stirrers, of speeds up to 10 000 rpm, are usually actuated via a feedthrough of the stirrer axis or by a magnetic coupling. Since most magnets have their Curie point at relatively low temperatures, i.e. lose their magnetism,

this coupling occurs outside the oven section. Ticonal 500 magnets (Philips) are stable up to 700 °C. Feedthroughs may result in leakages, whereas magnetic coupling may give problems with the ideal mixing due to areas without convection. Due to the low conversion over the catalyst bed isothermal conditions are approached more easily than in packed bed reactors.

In LS systems the mixing is less problematic and the catalyst is not necessarily held in a packed bed, but can be suspended in the fluid with measures to prevent washing out of the reactor and accumulation at the exit.

Compared to the simple packed bed reactor the reactor volume of CSTRs is much larger, often >100 ml, while the amount of catalyst to volume ratio is at least two or three times smaller. This implies that upon changing the conditions one should take into account the physical residence time of the reactor before considering the system to have reached a new steady state. This may be appreciable, depending on the pressure used and feed flow rates. Also, deactivation of the catalyst is not so directly noticed for the same reason.

It is self-evident that all the CSTR systems may work as a batch reactor when the inlet and outlet lines are closed. An example is the determination of the *cis-trans* equilibrium determination for 2-butene by means of the metathesis reaction in an externally recirculated (membrane pump) system [35]. An elegant solution for internally mixed reactors that avoids the use of feedthroughs or voluminous magnetic couplings is the swinging capillary stirrer [36] (Fig. 5). A capillary is welded in the lid of the reactor and sealed at the bottom and equipped with a stirrer blade. From the top a bended rod (piano string) is inserted in this capillary and turned around. This yields a swinging movement and an effective mixing, and can be used in LS and GLS reactors under high pressures. The compact design reduces the reaction volumes to 10 ml and enhances the safety.

A disadvantage of the batch operation is that catalyst deactivation cannot be followed, unless the experiment can be repeated with the same catalyst sample.

A special case in kinetic studies is the modeling of catalyst deactivation. For moderately decaying systems sequential experimental design is recommended (see later). Here, new experiments are carefully planned on the basis of previous results, using a packed bed reactor. In case of rapidly deactivating catalysts these have to be fed continuously to the reactor together with the feed. A new development is the lab-scale riser reactor for FCC [37]. It consists of a folded tubular reactor to which the catalyst and evaporated reactants are cofed and both travel through the system in plug flow (Fig. 6). Various reactor elements can be con-

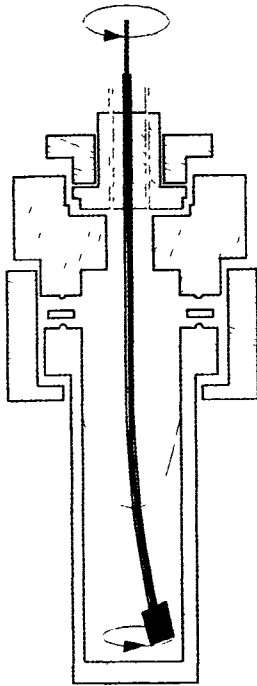


Figure 5. Layout of a microautoclave with the swinging capillary stirrer.

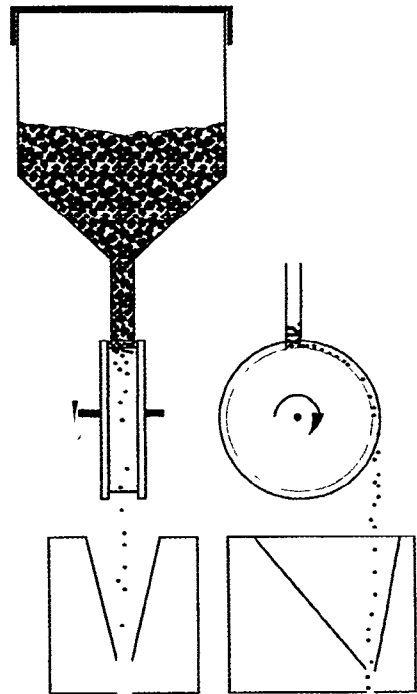


Figure 7. Layout of a continuous catalyst feeder.

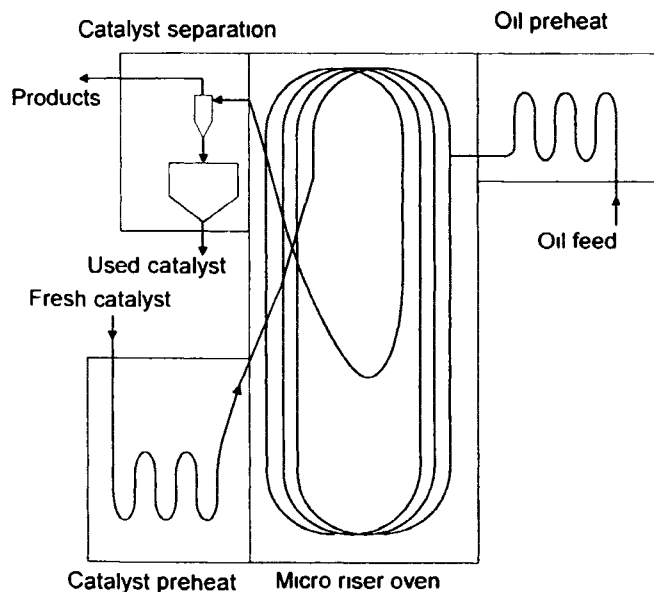


Figure 6. Schematics of a laboratory scale micro riser reactor setup for FCC investigations.

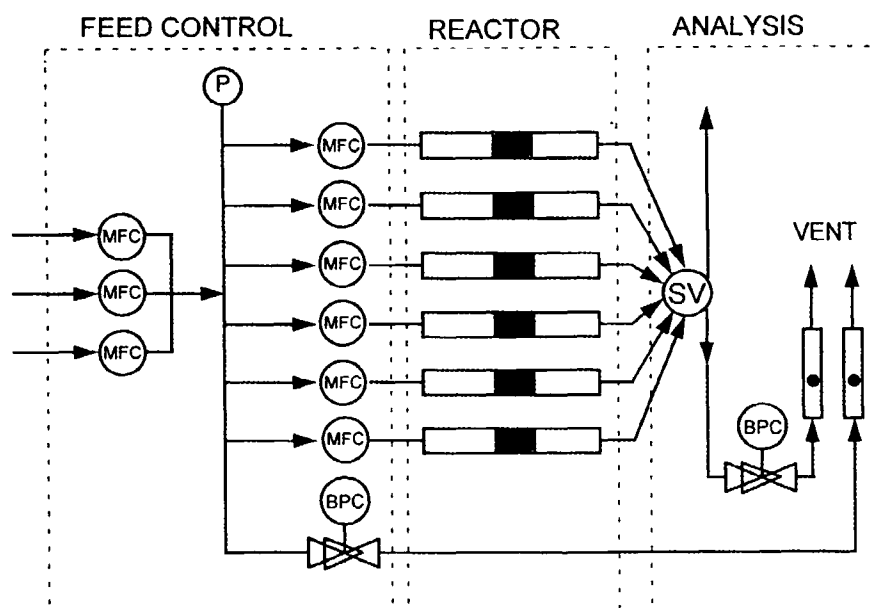
connected to vary the length. It is intended that this system gives more representative data than the so-called micro-activity test (MAT) of ASTM [12], whereby a certain amount of liquid feed is pushed through a packed bed of catalyst. The catalyst flowrate is controlled by a feeder, depicted in Fig. 7. The catalyst is

situated in a container with a bottom exit that ends just above a groove in a wheel, which rotates at a controlled speed. The rotation speed determines the feed rate of the catalyst. When it stands still the catalyst cannot flow out of the container freely, but when it rotates the wheel transports the catalyst which falls into a funnel where it is entrained by a sweep gas to the reactor inlet. The catalyst should flow out of the container without plugging for what kind of reason. Frequently encountered problems are a too broad particle size distribution and static electricity (very dry zeolite samples). These can be overcome by a narrower size distribution and humidification of the sample.

Another approach for FCC kinetics is described by Kraemer et al. [38]. They use an internally recirculated reactor containing the catalyst in a basket in which it is fluidized by the recirculating gas. A small pulse of reactant is allowed to react for a short time after which the reactor is purged. This procedure is repeated various times to map the catalyst activity as a function of time, intended to give a mapping of that along the length of a riser reactor. It is noted here that small-scale fluidized bed reactors are not suited for kinetic studies since their behavior is too complex to allow a straightforward data interpretation. They can only be used to heat up samples at a high rate.

**Table 1.** Summary of relative reactor ratings (L = low, M = medium, H = high).

Aspect	Reactor type						
	PFR differential fixed bed	PFR integral fixed bed	PFR solids transport (riser)	CSTR external recirculation	CSTR internal fluid recirculation	CSTR spinning catalyst basket	Batch internal fluid recirculation
Ease of use	H	H	H	M-H	M	L-M	M
Ease of construction	H	H	L	M	M	L-M	M
Cost	L	L	H	L-M	M-H	M-H	M
Sampling and analysis ease	M	H	L	H	H	H	M
Approach ideal type	H	H	M	H	M-H	L-M	H
Fluid-catalyst contact	H	H	M	H	M-H	L-M	H
Isothermicity	H	M-H	H	M-H	H	M	H
Temperature measurement	H	H	H	H	M-H	L	H
Kinetics	H	H	M	M	M-H	L-M	M
Deactivation noticed	H	H	L	M	M	M	L
GLS use	L-M	M-H	L	M-H	M-H	M	H

**Figure 8.** Six-flow reactor setup for fast catalyst screening and kinetic studies.

More exotic reactor types for special purposes have also been described [7, 12]. Table 1 gives a generalized comparison of the various reactor models.

A typical setup for kinetic measurements is given in Fig. 8. Basically a feed, a reactor and an analysis section are required. Nowadays mass flow controllers for both liquid and gas result in stable molar flowrates, ideally for kinetic studies. Pressure controllers maintain a constant feed pressure for the flow controllers, while backpressure controllers maintain the pressure in the reactors. Various methods of product analysis are available and depend highly on the system under investigation.

In view of the determination of the effect of sometimes several independent variables (temperature, par-

tial pressures, and space-time) on the conversion or reaction rate a fast screening is desired. Several ways of achieving this can be considered:

- look for a fast analysis method;
- build PC-controlled equipment, running unattended;
- put several reactors in parallel;
- perform temperature programmed experiments;
- apply sequential experimental design.

An example of a successful implementation of some of these ideas was the kinetic study of the selective catalytic reduction of NO over alumina-supported manganese oxide [39]. Product analysis was performed by a mass spectrometer, six reactors were placed parallel in one oven, one of them served as the reference

filled with inert particles, the other were filled with different amounts of catalyst. This yielded data at five different space-times. The equipment was PC-controlled and predesigned kinetic runs (pressure and temperature variation) could be carried out automatically within a short period of time. The feed composition to all reactors is the same and only the cost of additional flow controllers to divide the feed mixture and a selection valve is required. The tremendously increased speed of data generation completely outweighs the relatively small additional investment.

The temperature scanning reactor [40] idea goes even further. Here the data collection grid is so dense that interpolations are allowed and even isothermicity along the reactor axis is in principle not a strict requirement any more.

Further reduction of the experimental effort is obtained by sequential experimental design, carefully planning the new experimental conditions [9, 10].

It will be clear that stable catalyst activity is required for kinetic studies, unless deactivation is the subject.

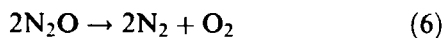
### 6.1.3 Kinetic Modeling

Many different types of rate expressions exist [41]. Well known are the power rate law expressions, which are in principle purely empirical and only valid in the range of conditions for which they were established. A better choice for rate expressions are the Langmuir–Hinshelwood–Hougen–Watson models [9, 15] which allow more extrapolation freedom. They are based on a sequence of elementary steps, the (micro)kinetic model, that constitute the overall catalytic process. The breakdown to elementary processes should preferably be based on known information of the reaction mechanism. From the kinetic model a rate expression can be derived where several assumptions are introduced. We focus here on the kinetics first developed by Hinshelwood, based on Langmuir adsorption, and later by Hougen and Watson [42] to become a systematized tool for process applications. The rate expressions have become known as Langmuir–Hinshelwood–Hougen–Watson (LHHW) expressions.

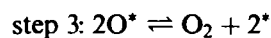
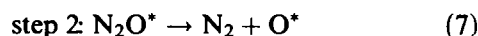
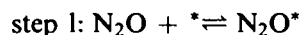
Much has been discussed about the fundamental validity of these kinetic models [3, 4, 13, 14], in view of the underlying assumptions, but their usefulness in engineering applications is undoubted. Here the procedure is presented for the derivation of the rate expressions.

#### 6.1.3.1 Rate Expression

As an example, consider the well-documented decomposition of nitrous oxide into nitrogen and oxygen [43]:



This irreversible reaction is proposed to proceed according to eq 7 over many transition metal oxides, whereby steps 1 and 3 are reversible and (b) is irreversible.



Since steps (a)–(b) are all elementary processes the rate expression can be based directly on the rate equation, resulting in eq 8. In these expressions  $s$  represents the nearest neighbours of an active site.

$$r_1 = r_{+1} - r_{-1} = k_1 N_T p_{\text{N}_2\text{O}} \times \theta_* - k_{-1} N_T \theta_{\text{N}_2\text{O}}$$

$$r_2 = r_{+2} = k_2 N_T \theta_{\text{N}_2\text{O}} \quad (8)$$

$$r_3 = r_{+3} - r_{-3} = k_3 N_T s \theta_{\text{O}}^2 - k_{-3} N_T s p_{\text{O}_2} \theta_*^2$$

Since steps 1 and 2 must proceed two times per overall reaction and step 3 once, the stoichiometric numbers of the steps are two, two and one, respectively, and the net rate of each step equals the overall net rate  $r$  of  $\text{N}_2\text{O}$  conversion, as in eq 9:

$$r = r_1 = r_2 = 2r_3 \quad (9)$$

The three unknown fractional occupancies of empty sites  $*$ , oxidized sites  $\text{O}^*$ , and sites occupied by  $\text{N}_2\text{O}$  must be eliminated from eq 8. This is achieved by the *steady state assumption*, namely that the concentration of these species do not vary in time:

$$0 = \frac{d\theta_*}{dt} = k_{-1} \theta_{\text{N}_2\text{O}} + 2k_3 s \theta_{\text{O}}^2 - k_1 p_{\text{N}_2\text{O}} \theta_* - 2k_{-3} s p_{\text{O}_2} \theta_*^2 \quad (10)$$

$$0 = \frac{d\theta_{\text{O}^*}}{dt} = k_2 \theta_{\text{N}_2\text{O}} + 2k_{-3} s p_{\text{O}_2} \theta_*^2 - 2k_3 s \theta_{\text{O}}^2$$

$$0 = \frac{d\theta_{\text{N}_2\text{O}}}{dt} = k_1 p_{\text{N}_2\text{O}} \theta_* - k_{-1} \theta_{\text{N}_2\text{O}} - k_2 \theta_{\text{N}_2\text{O}}$$

Equations 10 are equivalent to those of eq 9, in which only two are independent. Using this steady state assumption, generally one or more of these unknowns can be eliminated, but one remains. The second assumption is the *site balance*. The total concentration of active sites is constant and equal to  $N_T$ :

$$N_T = [\text{N}_2\text{O}^*] + [\text{O}^*] + [*]$$

or,

$$1 = \theta_{\text{N}_2\text{O}} + \theta_{\text{O}^*} + \theta_* \quad (11)$$

This yields generally a too complex expression for the rate [4, 44] and it is therefore assumed that some of the

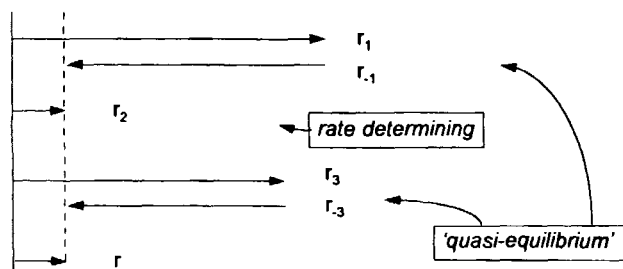


Figure 9. Visualisation of the rate determining step and quasi-equilibrium steps.

steps are in quasi-equilibrium, the forward and backward rates are much larger than their difference, e.g.  $r_i \ll r_{+i}, r_{-i}$ . The other step(s) that remain(s) are called the rate-determining step(s). In the example (Fig. 9) the adsorption of  $N_2O$  and desorption of  $O_2$ , steps 1 and 3, are considered in quasi-equilibrium and step 2 rate determining. For the former two,

$$K_1 = \frac{k_1}{k_{-1}} = \frac{\theta_{N_2O^*}}{p_{N_2O}\theta_*}; \quad \theta_{N_2O^*} = K_1 p_{N_2O} \theta_* \quad (12)$$

$$K_3 = \frac{k_3}{k_{-3}} = \frac{p_{O_2} \theta_*^2}{\theta_{O_2}^2}; \quad \theta_{O_2} = \sqrt{p_{O_2}/K_3} \times \theta_*$$

and the overall rate is now given by eq 13:

$$r = r_2 \quad (13)$$

It is implicitly assumed that all adsorption sites are energetically uniform and can accommodate only one species, as was first suggested by Langmuir.

This simplifies the treatment. Using eqs 11 and 12 in 13 yields the relationship between the rate and the partial pressures of  $N_2O$  and  $O_2$ :

$$r = \frac{k_2 N_T K_1 p_{N_2O}}{1 + K_1 p_{N_2O} + \sqrt{p_{O_2}/K_3}} \quad (14)$$

The denominator here represents the distribution of the sites which are empty, oxidized and occupied by  $N_2O$ . The dissociative adsorption of  $O_2$  (step 3 backward) gives rise to a square-root dependency on the  $O_2$  partial pressure.

Further simplification is obtained by the *initial reaction rate* consideration, i.e. that the product concentrations are so small that they can be neglected in the rate expression. In our example this yields a first-order reaction in  $N_2O$ :

$$r = k_2 N_T K_1 p_{N_2O} \quad (15)$$

Various rate expressions may be derived from a kinetic model, depending on the assumptions of quasi-equilibrium and rate determining step. Experimental data should provide information which expression describes best the rate dependency.

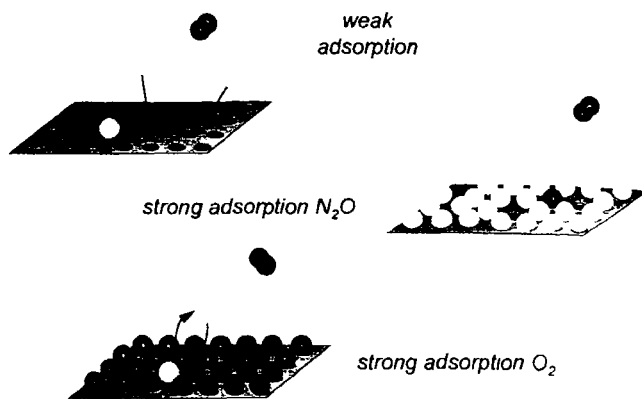


Figure 10. Visualisation of some limiting cases in  $N_2O$  decomposition. Light spheres  $N_2O$ , dark spheres  $O$ ,  $N_2$  not represented.

This approach has been followed successfully for many reactions. Extensive examples have been described [9, 14, 15]. One of the most elegant illustrations is the cracking of *n*-alkanes in ZSM-5 [45], where the sites can be considered to approach much better uniform energetics than in other amorphous porous catalysts.

A general rate expression of the LHHW type for a reaction  $A + B \rightleftharpoons C$  is of the form

$$r = \frac{k_{rds} N_T K_i \dots \{p_A p_B - p_C / K_{eq}\}}{\left(1 + K_A p_A + K_B p_B + K_C p_C + \sum_j K_j p_j\right)^n}$$

$$= \frac{\text{rate factor} \times \text{driving force}}{\text{inhibition term}} \quad (16)$$

where the numerator is a product of an apparent rate constant factor, containing the rate constant of the rate determining step and the active site concentration, and the driving force for the reaction, a measure of how far the overall reaction is from thermodynamical equilibrium. The overall equilibrium constant  $K_{eq}$  can be calculated from thermodynamics.

The denominator is a kind of inhibition term, always lowering the rate. It expresses the distribution of the active site over the different surface species, including components *j* that simply adsorb on the sites but which do not partake in the reaction, called inhibitors. The power *n* of the denominator is generally 0, 1 or 2 and indicates how many surface species are involved in the rate determining step. Pure fitting values up to 8 have been reported for *n*.

Considering some limiting cases of the example rate expression (14) one can recognize power rate dependencies (Fig. 10):

- (i) Weak adsorption of  $N_2O$  and  $O_2$  (or low partial pressures of both) - first order in  $N_2O$  and zero in  $O_2$

$$r = k_2 N_T K_1 p_{N_2O} \quad (17)$$



- (ii) weak adsorption of  $N_2O$  (or low partial pressures) and strong dissociative adsorption of  $O_2$  – first order in  $N_2O$  and minus half in  $O_2$

$$r = \frac{k_2 N_T K_1 p_{N_2O}}{\sqrt{p_{O_2}/K_3}} \quad (18)$$

- (iii) strong adsorption  $N_2O$  or high partial pressures, weak adsorption of oxygen – order in  $N_2O$  and  $O_2$  both zero, the observed rate is constant.

$$r = k_2 N_T \quad (19)$$

So, power rate expressions may be considered as special cases of the LHHW models, but valid over a limited range of conditions.

Some remarks can also be made about the temperature dependency of the reaction rate, as expressed in an apparent activation energy,  $E_a^{app}$ . It is assumed that the rate constant has an Arrhenius-type dependency, and that the equilibrium constant follows Van't Hoff and the active site concentration is constant:

$$k_i = k_{0i} \exp\left(-\frac{E_{ai}}{RT}\right) \quad (20)$$

$$K_i = K_{0i} \exp\left(-\frac{\Delta H_i}{RT}\right)$$

For the three cases above the following can be distinguished:

- (i) The apparent activation energy is lower than that of the rate determining step,

$$E_a^{app} = E_{a2} + \Delta H_1 \quad (21)$$

since an adsorption enthalpy  $\Delta H_1$  has a negative thermodynamic value.

- (ii) The apparent activation energy is given by

$$E_a^{app} = E_{a2} + \Delta H_1 + \frac{1}{2} \Delta H_3 \quad (22)$$

and its magnitude will be larger than in case *i* because the desorption enthalpy is a positive quantity. Oxygen has to desorb first before  $N_2O$  can adsorb and react.

- (iii) In this case the real activation energy of the rate determining process is observed:

$$E_a^{app} = E_{a2} \quad (23)$$

A salient example of case (i) is the cracking of *n*-alkanes over ZSM-5. The apparent activation energy of the initial reaction rate decreases as a function of the chain length, and for  $C_{16}$  and higher the apparent activation energy becomes even negative, due to the larger negative value of the adsorption enthalpy [45].

Because of the temperature dependencies of the parameters the rate expression may change depending on the operation temperature. Strongly adsorbing components occupy less sites with increasing temperatures

and the apparent rate expression may change from eq 18 to 17 or from eq 19 to 17.

More detailed treatments of the microkinetics of catalytic reactions and examples can be found [2, 9, 15].

### 6.1.3.2 Deactivation Kinetics

The deactivation of catalysts concerns the decrease in concentration of active sites on the catalyst  $N_T$ . This should not be confused with the reversible inhibition of the active sites by competitive adsorption, which is treated above. The deactivation can have various causes, such as sintering, irreversible adsorption and fouling (for example coking or metal depositions in petrochemical conversions). It is generally attempted to express the deactivation in a time-dependent expression in order to be able to predict the catalyst's life time. An important reason for deactivation in industry is coking, which may arise from a side path of the main catalytic reaction or from a precursor that adsorbs strongly on the active sites, but which cannot be related to a measurable gas phase concentration. For example for the reaction  $A \rightleftharpoons B$  the site balance contains also the concentration of blocked sites  $C^*$ . A deactivation function is now defined by eq 24, which is used in the rate expression.

$$\Phi = \frac{N_T - [C^*]}{N_T} \quad (24)$$

When the deactivation follows from a consecutive reaction of product **B** into **C** according to (25),



a LHHW approach could lead to the following rate of formation of **C**:

$$r_C = \frac{k_C^0 N_T K_B \Phi_C p_B}{1 + K_A p_A + K_B p_B} \quad (26)$$

The parallel reaction of  $A^* \rightarrow C^*$  can be treated similarly.

Now the rate expression for the reaction  $A \rightarrow B$  together with (26) indicates that the deactivation depends on the composition of the reaction mixture and may vary along the length of the reactor. Under integral reactor conditions this leads to a nonuniform catalyst deactivation in a packed bed. So differential conditions are to be preferred to study this phenomenon. Various empirical activity functions have been proposed [15] whereby using  $\Phi_C = f(t)$  instead of  $\Phi_C = f(c_C)$  has the advantage of being independent of

the concentration of reacting species, otherwise from eq 26 it follows that:

$$\frac{d\Phi_C}{dt} = -\frac{k_C^0 N_T K_B \Phi_C p_B}{1 + K_A p_A + K_B p_B} \quad (27)$$

so that

$$\Phi_C = \exp \left[ -\int_0^t \frac{k_C^0 N_T K_B p_B}{1 + K_A p_A + K_B p_B} dt \right] \quad (28)$$

which is much more difficult to handle than relationships such as eq [15]:

$$\begin{aligned} \Phi_C &= 1 - \alpha t \\ \Phi_C &= \exp(-\alpha t) \\ \Phi_C &= \frac{1}{1 + \alpha t} \end{aligned} \quad (29)$$

although it is clear that the fitting 'constant'  $\alpha$  is really a function of the operating conditions determining the coke deposition.

### 6.1.4 Parameter Estimation – Model Discrimination

The rate expressions contain a number of unknown parameters with a physical meaning. Their values are estimated by using on the one hand the experimental data and on the other hand the calculated values predicted from the rate expressions in the reactor and optimising a certain objective function. This is called data regression [8]. Several techniques exist to achieve this goal.

For a given rate expression this yields the optimal parameter values, but it has to be decided whether the rate expression is the most adequate one. This selection can be based on statistical analysis and on physical significance of the parameter values (for example they should be positive in many cases). Additional experimental effort can be used towards further model discrimination by carefully planning experiments – a kind of experimental design method.

The treatment below is initially restricted to single-response models in which only one dependent variable is considered. At the end of this section some remarks on the treatment of multiresponse models are given.

#### 6.1.4.1 Data Regression

In the parameter estimation theory it is generally assumed that the experimental errors are normally distributed with zero mean and a constant variance  $\sigma^2$ . The parameter values can then be estimated by max-

imizing the likelihood function of the parameters. If the errors are also statistically independent this likelihood function reads

$$L(\beta|y) = \frac{1}{(\sqrt{2\pi})^n} \exp \left\{ -\frac{1}{2\sigma^2} \sum_{i=1}^n (y_i - \eta_i)^2 \right\} \quad (30)$$

Under these conditions this is identical to minimizing the sum of squares of residuals  $Res_i$ , the factor  $SSR$  defined in eq 31. This is called the objective function for the parameter estimation:

$$\begin{aligned} SSR &= S(\beta) = \sum_{i=1}^n Res_i^2 \\ &= \sum_{i=1}^n (y_i - \eta_i)^2 \xrightarrow{\beta_1, \beta_2, \dots, \beta_p} \text{Min} \end{aligned} \quad (31)$$

In this equation  $\beta_i$  represents the true, but unknown parameter value and  $\eta_i$  the true, but unknown value of the response variable, the measured variable. The latter is also called the dependent variable, representing conversion or product concentrations, in contrast to the independent variables  $x_i$ , which represent the experimental settings like temperature, pressure and concentrations. Since the true values of  $\beta_i$  and  $\eta_i$  are unknown the estimated or calculated values will be denoted by  $b_i$  and  $\hat{y}_i$ .

#### A Linear Regression

If the model for the response variable is linear in the parameters, for each observation at chosen settings of the independent variables  $x_i$ , then for the set of  $n$  observations and  $p$  parameters one can write [8]:

$$\begin{aligned} y_1 &= \beta_1 x_{11} + \beta_2 x_{12} + \dots + \beta_p x_{1p} = \eta_1 + Res_1 \\ y_2 &= \beta_1 x_{21} + \beta_2 x_{22} + \dots + \beta_p x_{2p} = \eta_2 + Res_2 \\ &\cdot \\ &\cdot \\ y_n &= \beta_1 x_{n1} + \beta_2 x_{n2} + \dots + \beta_p x_{np} = \eta_n + Res_n \end{aligned} \quad (32)$$

In matrix notation this reads as

$$\mathbf{y} = \mathbf{X}\boldsymbol{\beta} + \mathbf{Res} \quad (33)$$

and the least-squares criterion as

$$\mathbf{Res}^T \mathbf{Res} \xrightarrow{\boldsymbol{\beta}} \text{Min} \quad (34)$$

The solution of this linear least-squares problem is exact and the estimate vector  $\mathbf{b}$  for the parameter values  $\beta_i$  is given by the matrix notation [8]

$$\mathbf{b} = (\mathbf{X}^T \mathbf{X})^{-1} \cdot \mathbf{X}^T \mathbf{y} \quad (35)$$

Under the conditions mentioned above  $\mathbf{b}$  is an unbiased estimate of the real parameter values, and its variance-covariance matrix is given by

$$\mathbf{V}(\mathbf{b}) = (\mathbf{X}^T \mathbf{X})^{-1} \sigma^2 \quad (36)$$

and the estimate of the error variance  $\sigma^2$  is given by the mean *SSR*, the minimum sum of squares of residuals divided by its corresponding number of degrees of freedom:

$$\sigma^2 \approx s^2 = \frac{\mathbf{Res}^T \mathbf{Res}}{n-p} = \frac{\sum_{i=1}^n (y_i - \hat{y}_i)^2}{n-p} \quad (37)$$

When the errors are distributed with zero mean, but do not have a constant variance and/or are interdependent, represented by a variance-covariance matrix  $\mathbf{V}$ , i.e.

$$\mathbf{Res} \sim N(\mathbf{0}, \mathbf{V}\sigma^2) \quad (38)$$

then a weighted least-squares minimization has to be applied, with the following results:

$$SSR = S(\mathbf{b}) = \mathbf{Res}^T \mathbf{V}^{-1} \mathbf{Res} \rightarrow \text{Min} \quad (39)$$

with vector of residuals  $\mathbf{Res}$  having elements of

$$Res_i = y_i - \hat{y}_i \quad (40)$$

The maximum likelihood estimates are then given by

$$\mathbf{b} = (\mathbf{X}^T \mathbf{V}^{-1} \mathbf{X})^{-1} \cdot \mathbf{X}^T \mathbf{V}^{-1} \mathbf{y} \quad (41)$$

and the variance covariance matrix by

$$\mathbf{V}(\mathbf{b}) = (\mathbf{X}^T \mathbf{V}^{-1} \mathbf{X})^{-1} \sigma^2 \quad (42)$$

The unknown factor  $\sigma^2$  is now obtained from

$$s^2 = \frac{S(\mathbf{b})}{n-p} = \frac{\mathbf{Res}^T \mathbf{V}^{-1} \mathbf{Res}}{n-p} = \frac{(\mathbf{y} - \mathbf{Xb})^T \mathbf{V}^{-1} (\mathbf{y} - \mathbf{Xb})}{n-p} \quad (43)$$

Based on the (symmetric) variance-covariance matrix of the parameter estimates  $\mathbf{V}(\mathbf{b})$ , one can determine confidence limits of the parameter estimates. The diagonal elements  $v_{ii}$  contain the parameter estimate variances, and the off-diagonal elements the covariances between the parameter estimates. The interval of parameter values that are statistically not significantly different from the estimated value  $b_i$  at a selected probability level  $(1 - \alpha)$  is defined by

$$b_i - t_{n-p, 1-\alpha/2} \sqrt{v_{ii}} < \beta_i < b_i + t_{n-p, 1-\alpha/2} \sqrt{v_{ii}} \quad (44)$$

Here,  $t_{n-p, 1-\alpha/2}$  represents the Student's *t*-value at  $n-p$  degrees of freedom and a confidence level of  $100(1 - \alpha)\%$ . Usual values of  $\alpha$  are 0.05 and 0.01. This relationship is valid if all other parameters are kept at their optimal estimate  $b_j$ .

Since the parameters are in fact correlated, a joint confidence region of the estimates  $\mathbf{b}$  can be defined, which accounts for the simultaneous variation of all the parameters:

$$S(\beta) \leq S(\mathbf{b}) [1 + [p/(n-p)] F(p, n-p, 1-\alpha)] \quad (45)$$

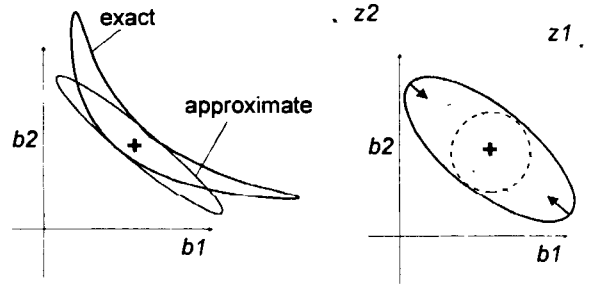


**Figure 11.** Confidence contours for two parameters,  $b_1$  and  $b_2$ . The optimal value is indicated by the + sign: (left) the linearized contour, eq 46, and the banana-shaped exact contour, eq 45; (right) examples of parameter improvement designs.

Here  $F(p, n-p, 1-\alpha)$  is the  $\alpha$  percentage point of the Fischer's *F* distribution at  $p$  and  $(n-p)$  degrees of freedom. The boundary of the joint confidence region is defined by all values of  $\beta$  which satisfy the hyper-ellipsoid in the  $p$ -dimensional parameter space around  $\mathbf{b}$ ,

$$(\mathbf{b} - \beta)^T \mathbf{X}^T \mathbf{X} (\mathbf{b} - \beta) = p s^2 F(p, n-p, 1-\alpha) \quad (46)$$

All parameter combinations enclosed by the ellipsoidal surface do not deviate significantly from the maximum likelihood estimates  $\mathbf{b}$  at the probability level  $(1 - \alpha)$ . Examples for a two-dimensional case are given in Fig. 11, to be discussed later.

### B Nonlinear Regression

Most kinetic expressions, however, are not linear in the parameters and two approaches can be followed. The first is to rewrite the expression in a linear form and apply the linear least-squares minimization to obtain parameter values. Expression 14 can be reformulated into eq 47.

$$\frac{1}{r} = \frac{1}{k_2 N_T} + \frac{1}{k_2 N_T K_1} \left( \frac{1}{p_{N_2O}} \right) + \frac{1}{k_2 N_T K_1 \sqrt{K_3}} \left( \frac{\sqrt{p_{O_2}}}{p_{N_2O}} \right) = b_0 + b_1 x_1 + b_2 x_2 \quad (47)$$

where three parameters are present and there are two independent variables. Similarly, exponential relationships are 'linearized' by taking the logarithm. It is noted that the error distributions change due to these types of transformations and the error limits provided by the equations given above are incorrect [10].

Therefore it is better to use the nonlinear model directly in a nonlinear regression of the observed variable, the nonlinear least-squares method. Because of the nonlinearity minimization is an iterative process.

Various more-or-less efficient optimization strategies have been developed [46, 47] and can be classified into direct search methods and gradient methods. The direct search methods, like those of Powell [48], of Rosenbrock and Storey [49] and of Nelder and Mead ('Simplex') [50] start from initial guesses and vary the parameter values individually or combined thereby searching for the direction to the minimum *SSR*.

The gradient methods, like those of Newton, Gauss-Newton, Fletcher, and Levenberg-Marquardt, use the derivative vector of the *SSR* with respect to the parameter directions to determine the direction where this gradient changes most, the steepest-descent direction.

$$\Delta \mathbf{b}_k = a_k \mathbf{X}_k^T \mathbf{Res}_k = a_k \mathbf{X}_k^T (\mathbf{y} - \hat{\mathbf{y}}_k) \quad (48)$$

$$x_{ij} = \frac{\partial \hat{y}_i}{\partial b_j} \quad \text{for } i = 1 \dots n \quad \text{and } j = 1 \dots p$$

The methods differ in the determination of the step length factor  $a_k$  at the  $k$ th iteration, since the direction of the steepest descent is, due to nonlinearities, not necessarily the optimal one, but only for quadratic dependencies. Some methods therefore use the second derivative matrix of the objective function with respect to the parameters, the 'Hessian' matrix, to determine the parameter improvement step-length and its direction:

$$\mathbf{H} = \nabla^2 SSR, \quad \text{where } h_{ij} = \frac{\partial^2 SSR}{\partial b_i \partial b_j} \quad i, j = 1 \dots p \quad (49)$$

$$\Delta \mathbf{b}_k = \mathbf{H}_k^{-1} \cdot \mathbf{X}_k^T \mathbf{Res}_k = \mathbf{H}_k^{-1} \cdot \mathbf{X}_k^T (\mathbf{y} - \hat{\mathbf{y}}_k)$$

In least-squares minimization, where it is assumed that the residuals are small, this Hessian can be approximated by the earlier encountered first derivative matrix multiplication:

$$h_{ij} = \frac{\partial^2 SSR}{\partial b_i \partial b_j} = \frac{\partial}{\partial b_i} \left( 2 \mathbf{Res}^T \frac{\partial \mathbf{Res}}{\partial b_j} \right)$$

$$= 2 \frac{\partial \mathbf{Res}^T}{\partial b_i} \frac{\partial \mathbf{Res}}{\partial b_j} + 2 \mathbf{Res}^T \frac{\partial^2 \mathbf{Res}}{\partial b_i \partial b_j}$$

$$\mathbf{H} \approx \mathbf{X}^T \mathbf{X} \quad (50)$$

However, the Hessian or its approximation has to be inverted to determine the parameter step-change for the next iteration and, especially when far from the real minimum of the *SSR*, the matrix is not positive definite, a requirement for inversion. Levenberg [51] and Marquardt [52] therefore added a diagonal matrix to it and allowed this contribution to vary according to a parameter  $\lambda$ , the Marquardt parameter. For the  $k$ th iteration this yields

$$\Delta \mathbf{b}_k = (\mathbf{X}_k^T \mathbf{X}_k + \lambda_k \mathbf{I})^{-1} \cdot \mathbf{X}_k^T \mathbf{Res}_k \quad (51)$$

For large values this takes the direction of the steepest descent, while for  $\lambda \rightarrow 0$  this has the Gauss-Newton

direction. During the parameter estimation procedure the value of  $\lambda$  is adapted (generally decreased to finally zero), so this Levenberg-Marquardt method is an optimal compromise between the steepest descent, efficient far from the minimum, and the Gauss-Newton method, efficient when close to the minimum [47].

Generally, the models are so complex that analytical derivatives cannot be provided, and they are calculated numerically by a small variation of the parameter value. It is noted that the gradient techniques directly provide the parameter variance-covariance matrix, eq 36 or 42, since this is already used in the calculation of the parameter step-changes at each iteration. Also, the relationships for the estimates of the parameter error limits, eq 44 and the joint confidence region, eqs 45 and 46, can be used. These are only approximations due to the nonlinearity of the model. So, eq 46 gives an approximate joint confidence region, a hyperellipsoid, while eq 45 defines the contour of the real confidence region at an approximate confidence level of  $100(1 - \alpha)\%$ . This gives often a banana shaped contour (Fig. 11).

Sometimes, a very strong correlation exists between the parameters, and their confidence contour has a strongly elongated shape [10]. This makes convergence during minimization difficult. This is especially the case for the relationships of rate or equilibrium constants, such as eq 20. In these cases a reparametrization is recommended, as eq 20(a), which yields a more spherical shape of the confidence contour and facilitates convergence [10].

$$k = k_{\text{ref}} \exp \left[ -\frac{E_a}{R} \left( \frac{1}{T} - \frac{1}{\bar{T}} \right) \right]$$

where

$$k_{\text{ref}} = k_0 \exp \left( -\frac{E_a}{R\bar{T}} \right) \quad (20a)$$

Here  $\bar{T}$  represents an average temperature over the temperature range investigated.

All methods need good initial guesses for the parameters, otherwise they may not converge or end in a local minimum. Here, the linearization technique is useful to provide these. The parameter iteration continues until a certain criterion is satisfied or the maximum number of function evaluations is exceeded. These criteria may be that the relative change in the *SSR* value, or in the parameter values is below a preset value or the norm of the gradient is less than a certain value (in the minimum this gradient norm vanishes).

Nowadays these minimization techniques are well implemented in computer codes [53]. Most of them can be found at Netlib World Wide Web site on Internet at URL: [www.netlib.org](http://www.netlib.org).

### 6.1.4.2 Kinetic Data Handling

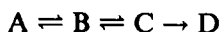
The observations in kinetic studies are usually concentration or conversion measurements. CSTRs and differential PFRs yield rate data directly, so the experimentally observed rate can be directly fitted on the rate expression and its parameters estimated.

Integral PFR data cannot be used directly in this way, since one has a differential equation that describes the conversion profile along the catalyst bed (eq 2). For simple cases this can be integrated analytically, yielding an implicit expression in the observed variable (eq 5). Sometimes the independent variable  $W/F_i^0$  is now used as observed variable and its *SSR* minimized [9], but this interchange of dependent and independent variable destroys the error properties and the parameter error limits are not correct. Often the parameter estimates correspond well [9] and can be used as starting guesses for more robust minimization to determine the real error bounds.

Alternatively the implicit relationship of eq 5 can be solved numerically, for example by the fast and powerful 'memory' method [54], allowing the proper minimization of the residual sum of squares of the conversion.

When the quadrature of eq 2 cannot be performed analytically the integration should be carried out numerically by robust routines such as the Runge–Kutta, Adams–Moulton predictor–corrector or Bulirsch–Stoer methods with step size and error control [53, 55, 56]. These routines can also be found in computer codings at Netlib and in standard books on computer codes [53].

A similar approach holds for the interpretation of batch reactor data. Here, the spatial integration has to be replaced by a time integration of eq 4. A nice example of such an application is the catalyzed hydrodemetallization of Ni-porphyrins [57], a reaction of the type



which is a multiresponse system (see later).

In combining the numerical integration with nonlinear parameter estimation one should be aware of the nesting of errors in the procedures. One should not demand a high accuracy in the *SSR* determination if the numerical integration has not sufficient accuracy. The most inner level, the integration, requires the highest numerical accuracy; the next level, the numerical derivatives calculation, the next highest, and the stopping criteria the lowest, otherwise the procedure will fail to converge. It is clear that one has to play around with the numerical accuracies to develop a feeling for the proper settings of these values.

Most challenging are kinetic studies by transient techniques. Here, one has a set of coupled partial differential equations (PDE) to be solved that describe the

concentration profiles along the catalyst bed as a function of time, embedded in the parameter estimation routine. Good results have been obtained by the relatively easy implementable numerical method of lines (NUMOL) [58]. In this method the spatial derivatives are replaced by an algebraic approximation in  $ng$  grid points along the catalyst bed length. For each PDE this results in a set of  $ng$  coupled ordinary differential equations (ODE). These initial value problems can be solved by robust explicit integrators mentioned above. The use of implicit integrators, such as LSODE [59], can have certain advantages. These use the Jacobian of the dependent variables, i.e. the derivative with respect to all grid point positions. This Jacobian is rather sparse and a reduced calculation effort can be obtained by application of a program that take this sparsity into account, such as LSODES [59]. After initialization, setup of the Jacobian, the implicit methods are rather fast in their time integration. However, when parameter values change much during parameter estimation in every iteration a new Jacobian has to be calculated and this advantage is lost. Therefore, in parameter estimation explicit routines have some preference and have much lower memory requirements. A more detailed discussion and examples can be found in Ref. 17.

### 6.1.4.3 Model Testing

A kinetic expression that is selected should satisfy certain statistical tests and physicochemical constraints, before it can be indicated as an adequate model. These tests often cannot be applied together, due to lack of information, but should be considered as far as possible in the evaluation and selection of the best rate expression. When still a set of competitive expressions are left some model discrimination techniques may be applied or additional experiments should be conducted, based on a careful, efficient planning.

#### A Statistical Testing – Model Adequacy

The residual sum of squares (*SSR*) contains contributions of a pure error *PE* due to pure experimental errors, and a lack-of-fit *LF* due to the inadequacy of the model. The pure error sum of squares *PE* can be obtained by, for example  $n_c$  replicated experiments at a number of, at least one, experimental settings. The relationships that hold are given in eq 52:

$$PE = \sum_{r=1}^{n_c} (y_r - \bar{y})^2 \quad \text{degrees freedom } n_c - 1$$

$$s_c^2 = \frac{PE}{n_c - 1} \quad (52)$$

$$LF = SSR - PE \quad \text{degrees freedom } n - p - n_c + 1$$

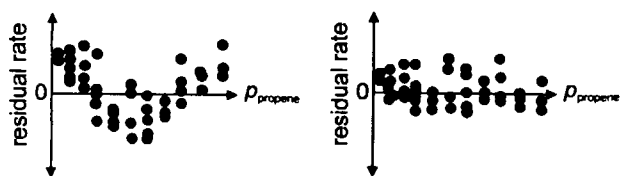


**Figure 12.** Residual rate distribution for the metathesis of propene: (left) Langmuir-Hinshelwood model; (right) model based on the carbene mechanism [60].

$$s_{\text{fr}}^2 = \frac{LF}{n - p - n_e + 1}$$

These variances of  $PE$  and  $LF$ ,  $s_e^2$  and  $s_{\text{fr}}^2$ , can be used in an  $F$ -test for lack-of-fit. If

$$F_c = \frac{s_{\text{fr}}^2}{s_e^2} > F(n - p - n_e + 1, n_e - 1, 1 - \alpha) \quad (53)$$

then there is a chance of  $(1 - \alpha)$  that the model is inadequate. The model is retained if the calculated value does not exceed the  $F$ -value. This test is only sparsely applied [60], since often there is little replicated data available.

### B Statistical Testing – Parameter Significance

Certain parameters have badly determined values and it is questionable whether they should be retained in the rate expression. This is simply achieved by the  $t$ -test, implicitly present in eq 44. If the interval of the estimated parameter contains zero then it does not statistically deviate from zero, at the applied confidence level  $(1 - \alpha)$ .

### C Statistical Testing – Residual Distribution

The error model used in the minimization is based on the hypothesis that the residuals have zero mean and are normally distributed. The first is easily checked, the latter is only possible when sufficient data points are available and a distribution histogram can be constructed. An adequate model also follows the experimental data well, so if the residuals are plotted as a function of the dependent or independent variable(s) a random distribution around zero should be observed. Nonrandom trends in the residuals mean that systematic deviations exist and indicate that the model is not completely able to follow the course of the experimental data, as a good model should do. This residual trending can also be evaluated numerically by correlation calculations, but visual inspection is much more powerful. An example is given in Fig. 12 for the initial rate data of the metathesis of propene into ethene and 2-butene [60]. One expression was based on a dual-site Langmuir-Hinshelwood model, whereas the other

**Table 2.** Physicochemical constraints of kinetic parameters [62–64, 67].

Feature	Constraint
Adsorption	$K_{\text{ads}} = \exp(-\Delta S_{\text{ads}}^0/R) \exp(-\Delta H_{\text{ads}}^0/RT)$
Unimolecular surface reaction	$k = k_0 \exp(-E_a/RT)$
Rule I	$0 < -\Delta S_{\text{ads}}^0 < S_{\text{gas}}^0$
Rule II	$-\Delta H_{\text{ads}}^0 > 0$
Rule III	$E_a > 0$
Guideline I	$-\Delta S_{\text{ads}}^0 > \sim 40 \text{ (J mol}^{-1} \text{ K}^{-1}\text{)}$
Guideline II	$-\Delta S_{\text{ads}}^0 < 51.2 - 0.0014\Delta H_{\text{ads}}^0 \text{ (J mol}^{-1} \text{ K}^{-1}\text{)}$
Site density	$10^{-9} < L < 10 \text{ (sites nm}^{-2}\text{)}$

was based on the carbene mechanism, which is nowadays generally accepted as the reaction mechanism. From the residual plots the latter model is clearly the best.

### D Physicochemical Testing – Kinetic Parameters

The kinetic parameters in the rate models all have a positive value, and negative values resulting from the parameter estimation have no physical meaning.

The same holds for the temperature dependency. Activation energies should be positive, unless a combination of parameters is fitted and apparent values are obtained. Due to their composition even negative values may be obtained, see eqs 21–23. Moreover, from thermodynamics it follows that adsorption enthalpies are negative and desorption enthalpies positive. The same holds for the associated entropy changes. A molecule loses degrees of freedom upon adsorption, at least one translational degree when mobile adsorption occurs. These entropy losses can be estimated pretty well [2, 61, 62]. In an analysis of kinetic modeling parameters Boudart and co-workers [63, 64] found a correlation between the enthalpy and entropy of adsorption that may serve as a guideline, rather than a constraint. Table 2 gives a summary of the physicochemical constraints.

It should be emphasized that the LHHW kinetic rate expressions are derived with assumptions of energetic uniformity and if this is violated then these constraints should be used with caution. In a transient kinetics study Dekker et al. [21] have shown that an occupancy dependent CO adsorption enthalpy on Pt results in very low values of the reaction activation energy, and might even become negative.

Much more can be said about the magnitude of pre-exponential factors and activation energies of elementary processes based on statistical thermodynamics applied to collision and reaction-rate theory [2, 61], but in view of the remark above one should be cautious in their application and limit it to well-defined model reactions and catalyst surfaces.

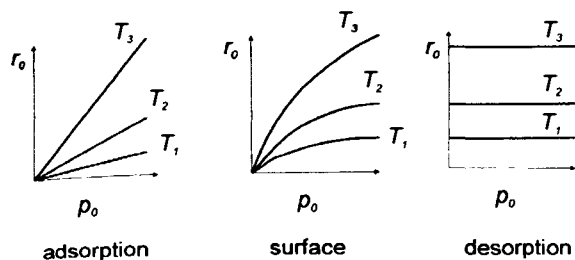


**Figure 13.** Examples of initial rate dependencies on the partial reactant pressure for different rate determining steps.

### E Physicochemical Testing – Site Density

Steady state kinetic modeling does not yield the value of the site density  $N_T$  separately, but always in combination with rate parameters, see eqs 14–19. Only selective poisoning experiments and transient kinetic techniques can yield this information [65, 66]. Maatman [67] has analyzed many catalytic systems and gives a (broad) range of acceptable values for site densities  $L$  (sites per  $\text{cm}^2$ ), included in Table 2.

#### 6.1.4.4 Discrimination Between Rival Models

After fitting data to the various rate expressions that have been derived it will often appear that several models do not differ much in their mean  $SSR$  value. Statistical tests, such as an  $F$ -test, cannot be directly performed on these mean  $SSR$  values since they are based on the same data set and are therefore not statistically independent. Therefore, other approaches have been devised to allow further selection between the possible candidates, and some of them are mentioned below [9].

#### A Model Discrimination – Initial Rate Expressions

Hougen and Watson [42] suggested analysis of the rate dependency on the partial reactant or the total pressure at low conversion levels, where the product concentrations can be neglected and so-called initial rates are measured. Depending on the assumed rate determining step in the kinetic model a different pressure dependency is predicted, as exemplified in Fig. 13. This allows a direct discrimination between possible rate expressions of different models.

#### B Model Discrimination – Diagnostic Parameters

Suppose a selection has to be made between two rival models, both of which have already been fitted to the experimental data and their parameters estimated. Then a new dependent variable is defined [68] containing a nonintrinsic diagnostic parameter  $\lambda$  and the cal-

culated predictions of the two models:

$$\hat{y} = \frac{1}{2}(\hat{y}_1 + \hat{y}_2) + \lambda(\hat{y}_1 - \hat{y}_2) \quad (54)$$

Now a linear least-squares minimization is used to determine  $\lambda$ . If  $\lambda$  takes the value 0.5 then model 1 is preferred, whereas for  $-0.5$  model 2 is the best. The confidence limits should be evaluated to be taken into account since it should not include the value of the other model.

For  $m$  models Wilks [69] proposed the following new dependent variable

$$\hat{y} = \lambda_1 \hat{y}_1 + \lambda_2 \hat{y}_2 + \dots + \lambda_m \hat{y}_m \quad (55)$$

with

$$0 \leq \lambda_i \leq 1 \quad \text{and} \quad \sum_{i=1}^m \lambda_i = 1$$

The diagnostic parameters  $\lambda_i$  are scaled and their estimation is also a (constrained) linear least-squares problem. These parameter values represent the fraction of  $y$  that is accounted for by model  $i$ .

#### C Model Discrimination – Bartlett's Chi-Square Test

The  $m$  rival models with their mean  $SSR$  or error variances,  $s_i^2$ , are pooled to a set of variances that are tested upon homogeneity. The following random variable is therefore defined [70]:

$$\chi_c^2 = \frac{\ln s^2 \sum_{i=1}^m (d.f.)_i - \sum_{i=1}^m (d.f.)_i \ln s_i^2}{1 + \frac{1}{3(m-1)} \left[ \sum_{i=1}^m \frac{1}{(d.f.)_i} - \frac{m}{\sum_{i=1}^m (d.f.)_i} \right]} \quad (56)$$

with

$$\bar{s}^2 = \frac{\sum_{i=1}^m (d.f.)_i \times s_i^2}{\sum_{i=1}^m (d.f.)_i}$$

This variable is distributed like  $\chi^2$  with  $m-1$  degrees of freedom ( $d.f.$ ). If its value exceeds  $\chi^2(m-1, 1-\alpha)$  the  $m$  models do not form a homogeneous set at a probability of  $(1-\alpha)$ . Now the model with the highest  $s_i^2$  value is rejected and the test is repeated with the remaining  $m-1$  models until the  $\chi^2$  is not exceeded any more. The remaining set of  $s_i^2$  is homogeneous and the models competitive. These models are not yet guaranteed to be adequate, this should be based on the statistical tests given above.

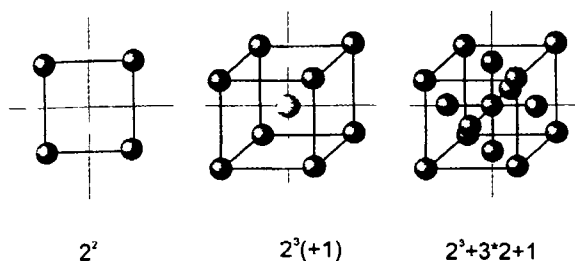


Figure 14. Factorial designs for initial sets of experiments (left) and (middle)  $2^n$  designs for linear models of two and three independent variables, (right) and (middle) reduced designs for nonlinear models of three independent variables

### 6.1.4.5 Sequential Experimental Design

Optimal planning of kinetic experiments is crucial for an efficient experimental effort in this time-consuming activity. Initially experiments will be conducted to determine the effect of the various independent variables (experimental conditions), which can be carried out according to a classical factorial design (Fig 14). If linear relationships are to be tested then only two conditions for each independent variable should be tested at the lowest and at the highest possible setting, and this for each independent variable. Also, cross-correlations are taken into account in this way. For  $q$  independent variables this leads to  $2^q$  experimental settings. If nonlinearity is assumed to be involved, at least three conditions should be taken per independent variable, leading to a  $3^q$ -factorial design. A picture of these designs is given in Fig 14. Intermediate designs can be devised to reduce the rapidly increasing number of experiments, for example by the introduction of a centre point, through which nonlinearities can be determined with less effort than a complete  $3^q$ -factorial design.

After this initial stage the selection of the best model and accurate parameter values are the two major goals in kinetics. Next experiments are carried out at the optimal conditions for further discrimination or parameter improvement. In both goals one should distinguish the criterion to achieve the goal, i.e. the discrimination criterion or parameter accuracy criterion, and the design criterion that determines the experimental settings. The experiments are limited by the experimental range of conditions that can be achieved in the equipment. Usually the experimental conditions are represented by a grid of combinations. In each grid point the design criterion is evaluated to determine the optimal experimental setting. This grid search is easier and faster than application of the optimization routines described above.

After each new experiment the parameter estimation procedure is repeated, the new information extracted,

and a new design is made until a satisfactory goal is reached. With all the power present nowadays in PCs it will be clear that the most time-consuming step is conducting the experiment, which motivates this approach.

### A Discrimination Between Rival Models – Design Criteria

The various approaches to discriminate between models and to test a given model's adequacies have been treated above, and focus is given here on the design criterion.

A simple approach can be followed to determine the maximum divergence between model predictions. Based on statistical considerations for two models, a simple expression was derived to measure the divergence  $D(\mathbf{x}_k)$  at the experimental settings  $\mathbf{x}_k$  of the experimental grid

$$D(\mathbf{x}_k) = [\hat{y}^{(1)}(\mathbf{x}_k) - \hat{y}^{(2)}(\mathbf{x}_k)]^2 \quad (57)$$

The set of conditions that yields the largest value of the divergence is chosen at which to conduct the next experiment. The criterion is easily extended to  $m$  models, as follows

$$D(\mathbf{x}_k) = \sum_{i=1}^{m-1} \sum_{j=i+1}^m [\hat{y}^{(i)}(\mathbf{x}_k) - \hat{y}^{(j)}(\mathbf{x}_k)]^2 \quad (58)$$

The double summation is used to take each of the models as a reference in order to avoid mislocations of optimal discrimination conditions.

Since the model adequacy criteria and the design criterion are independent of each other, any type of design criterion can be used. An alternative one is [9] given by eq 59

$$D(\mathbf{x}_k) = \sum_{i=1}^{m-1} \sum_{j=i+1}^m |\hat{y}^{(i)}(\mathbf{x}_k) - \hat{y}^{(j)}(\mathbf{x}_k)| \quad (59)$$

The divergence is, however, not only determined by the values of the response variable  $\hat{y}$  but also by their statistical uncertainties. Large differences between the model predictions are not necessarily important when their associated uncertainty is important. This is illustrated in Fig 15, which shows the predictions and their confidence limits. An experiment that is conducted at conditions where the confidence limits do not overlap has more power than one where the difference between the models is maximum, but where the confidence regions overlap. The variance of a model  $\hat{y}$  at settings  $\mathbf{x}_k$  is given by eq 60 [8]

linear models

$$V(\hat{y}(\mathbf{x}_k)) = \sigma_k^2 = \mathbf{x}_k^T (\mathbf{X}^T \mathbf{X})^{-1} \mathbf{x}_k \sigma^2 \quad (60)$$

nonlinear models

$$V(v(\mathbf{x}_k)) = \sigma_k^2 = \mathbf{v}_k^T (\mathbf{X}^T \mathbf{X})^{-1} \mathbf{v}_k \sigma^2$$

For a nonlinear model the matrix  $\mathbf{X}$  represents the matrix of partial derivatives of the dependent variable



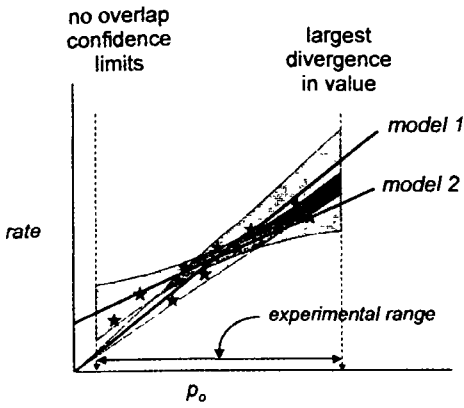


**Figure 15.** Illustration of discrimination between two rival models. Models (solid lines) are plotted as a function of a pressure, together with their confidence areas and the experimental data (stars). At the highest pressure the largest difference in rate values exists, but confidence regions overlap. At the lowest pressure these regions do not overlap, an optimal location for the next experiment.

with respect to the parameters in all data points (eq 48) and  $\mathbf{v}_k$  the vector of the partial derivatives taken at settings  $\mathbf{x}_k$  of the independent variables.

Box and Hill [71] derived the following expression for the divergence between  $m$  rival models

$$D(\mathbf{x}_k) = \sum_{i=1}^{m-1} \sum_{j=i+1}^m \pi_{i,n} \pi_{j,n} \left[ \frac{\sigma_{ki}^2 - \sigma_{kj}^2}{(\sigma^2 + \sigma_{ki}^2)(\sigma^2 + \sigma_{kj}^2)} - \{\hat{y}^{(i)}(\mathbf{x}_k) - \hat{y}^{(j)}(\mathbf{x}_k)\}^2 \cdot \left\{ \frac{1}{\sigma^2 + \sigma_{ki}^2} + \frac{1}{\sigma^2 + \sigma_{kj}^2} \right\} \right] \quad (61)$$

After  $n$  experiments the data are analysed and the next ( $n+1$ )th experiment has to be conducted at those conditions  $\mathbf{x}_k$  which maximise  $D(\mathbf{x})$ .  $\pi_{i,n}$  is the probability or degree of adequacy reached after  $n$  experiments. Initially all models start with equal probabilities. After the ( $n+1$ )th experiment this probability is updated by the Bayesian posterior probabilities of the models:

$$\pi_{i,n+1} = \frac{\pi_{i,n} p_i}{\sum_{j=1}^m \pi_{j,n} p_j} \quad i = 1, 2, \dots, m$$

in which: (62)

$$p_i = p_i(y_{n+1}) = \frac{1}{\sqrt{2\pi(\sigma^2 + \sigma_{n+1,i}^2)}} \exp \left\{ -\frac{(y_{n+1} - \hat{y}_{n+1}^{(i)})^2}{2(\sigma^2 + \sigma_{n+1,i}^2)} \right\}$$

is the probability density of the ( $n+1$ )th observation  $y_{n+1}$  under model  $i$ . Discrimination is achieved as soon as the posterior probability of a model approaches the value of 1. Inspection of eq 61 shows that:

- experimental conditions that result in large divergence in model predictions contribute strongly to  $D$  due to the squared term;
- predictions which are highly unreliable, with large variances contribute less due to the inverse proportionality;
- greater weight is given to the models which approximate the results best.

Several application examples are given by Froment and Hosten [9].

### B Improved Parameter Estimation

Once a model is selected it is often important to improve the precision of the estimated parameters. The cornerstone of the theory is the covariance matrix of the parameter estimates. The covariance matrix defines a hyperellipsoid around the optimal parameter combination; the joint confidence region (eq 46) can be written as

$$(\mathbf{b} - \beta)^T \mathbf{X}^T \mathbf{X} (\mathbf{b} - \beta) = \delta \quad (63)$$

which can be transformed to

$$\left( \frac{z_1}{\sqrt{\delta/\lambda_1}} \right)^2 + \left( \frac{z_2}{\sqrt{\delta/\lambda_2}} \right)^2 + \dots + \left( \frac{z_p}{\sqrt{\delta/\lambda_p}} \right)^2 = 1 \quad (64)$$

where  $\lambda_i$  represent the eigenvalues of the matrix  $\mathbf{X}^T \mathbf{X}$  and  $z_i$  the coordinates of the eigenvectors. This is indicated in Fig. 11. Various criteria can be used to improve the parameter estimates [9].

### C Improved Parameter Estimation – Minimum Volume Criterion

The volume of the hyperellipsoid represents the total parameter uncertainty, so a minimization of it is a valid goal. The volume can be determined by

$$\begin{aligned} \text{Vol.} \Theta &= \text{const} \times \prod_{k=1}^p \sqrt{\delta/\lambda_k} \\ &= \text{const} \times \frac{\delta^{p/2}}{\sqrt{\lambda_1 \lambda_2 \dots \lambda_p}} \sim \frac{1}{\sqrt{\det \mathbf{X}^T \mathbf{X}}} \quad (65) \end{aligned}$$

The experimental conditions are now chosen by a grid search such that the  $\det \mathbf{X}^T \mathbf{X}$  is maximized. To this purpose each new condition is individually added to the set of existing data settings and the determinant of the matrix  $\mathbf{X}^T \mathbf{X}$  is evaluated. This is done for each grid point to determine the highest value.

### D Improved Parameter Estimation – Shape Criterion

An alternative objective is to render the confidence region as spherical as possible, this means that the long-

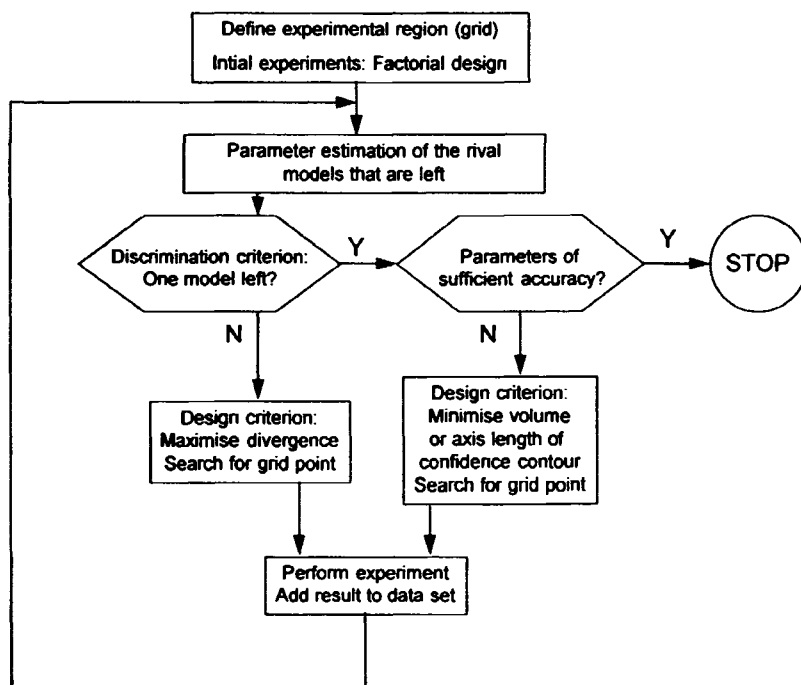


Figure 16. Flowchart of sequential experimental design in the process of model selection, followed by parameter improvement.

est axis of the hyperellipsoid has to be reduced (Fig. 11). Mathematically, the length of the axes is inversely proportional to the eigenvalues, so the smallest eigenvalue of  $\mathbf{X}^T\mathbf{X}$  has to be maximized.

### E Improved Parameter Estimation – Other Criteria

More criteria can be found in the literature. The variance of the parameter estimates can be minimized, which means the minimization of the trace of  $(\mathbf{X}^T\mathbf{X})^{-1}$

$$\sum_{i=1}^p (\mathbf{X}^T\mathbf{X})_{ii}^{-1} \xrightarrow{x_k} \text{Min} \quad (66)$$

One might try to improve the least accurate parameter estimate, or minimize the correlation between the parameters by minimizing the sum of squares of the correlation coefficients between the parameters which are also calculated from the elements of  $(\mathbf{X}^T\mathbf{X})^{-1}$ :

$$\sum_{i=1}^p \sum_{j=1}^p \rho_{ij}^2 \xrightarrow{x_k} \text{Min} \quad (67)$$

$$\{\rho_{ij}\} = \frac{(\mathbf{X}^T\mathbf{X})_{ij}^{-1}}{\sqrt{(\mathbf{X}^T\mathbf{X})_{ii}^{-1}(\mathbf{X}^T\mathbf{X})_{jj}^{-1}}}$$

Also in the improvement of parameter estimates several interesting case studies can be found in Ref. 9.

A typical flow diagram of the application of sequential experimental design is given in Fig. 16. It should be noted that both in the case of model discrimination and parameter improvement experimental settings at

the borders of the realizable conditions are often selected. In a way this is not surprising since at these locations the models often diverge most from each other or from the data, so they have the highest new information content. For one independent variable this location is easy to recognize, but with several independent variables this will be achieved more easily by the techniques described above.

### 6.1.4.6 Multiresponse Models

All treatments above are given for single response data, but often several dependent variables are to be considered simultaneously [9]. Assume that in each of the  $n$  experiments  $v$  dependent variables are determined then each has an associated error  $\epsilon_{ij}$  ( $i = 1 \dots n$ ,  $j = 1 \dots v$ ). These errors may be interdependent and the objective function for minimization is dependent on the information that one has about this dependency. All treatments are generally based on the following assumptions:

- All errors are normally distributed with zero mean.
- The  $n$  errors corresponding to the  $n$  observations of the  $j$ th response are statistically independent and have a constant variance  $\sigma_{jj}$ .
- The  $v$  errors within the  $i$ th experiment are statistically interdependent with a covariance matrix  $\Sigma$ . When the errors are independent the matrix reduces to a diagonal matrix.

**Table 3.** Objective functions to be minimized in parameter estimation of multiresponse data and conditions for application [9].

Objective function	Conditions for application
$\sum_{k=1}^v \sum_{l=1}^v \sigma^{kl} \sum_{i=1}^n (y_{ik} - \eta_{ik})(y_{il} - \eta_{il})$	experimental errors interdependent with known covariance matrix $\sum$ . $\sigma^{kl}$ are elements of the inverted matrix $\sum^{-1}$
$\sum_{k=1}^v \frac{1}{\sigma_{kk}} \sum_{i=1}^n (y_{ik} - \eta_{ik})^2$	experimental errors interdependent with unequal known variances
$\sum_{k=1}^v \sum_{i=1}^n (y_{ik} - \eta_{ik})^2$	experimental errors independent with equal (known or unknown) variances
$\det S$ , where	experimental errors interdependent with unknown covariance matrix $\sum$ ; no missing observations
$S = \{s_{kl}\} = \left\{ \sum_{i=1}^n (y_{ik} - \eta_{ik})(y_{il} - \eta_{il}) \right\}$	

- The covariance matrix  $\Sigma$  is the same for all  $n$  experiments.

In Table 3 several conditions for application of the various criteria are summarized. Special treatment will be required when some observations of response variables are missing, such as when an analysis was only partially successful [9]. It is noted that the determinant criterion is not a sum of squares criterion, so the minimization routines based on the Hessian approximation are not applicable and the other techniques have to be applied.

### 6.1.5 Concluding Remarks

In this chapter focus has been given to the derivation and application of the so-called Langmuir–Hinshelwood–Hougen–Waston models to describe catalyzed reactions. In spite of objections that can be made against their underlying assumptions these expressions have been proved to be quite successful. An important reason is probably the fact that it contains intrinsically a capacity, a limited number of catalytically active centers where the reaction takes place and which are distributed among the different adsorbing components.

Detailed knowledge of the reaction kinetics is important, especially when high conversions and/or high selectivities are to be achieved in industrial reactors. Recycles are often present in processes and some components will accumulate. The effect of such components on activity and selectivity should be carefully taken into account, otherwise reactor sizes or deactivation rates may be tremendously underestimated.

Kinetic studies are laborious, the most time consuming part being nowadays the experimental work. Optimal design of the experiments that are carried out is a challenge and directions have been outlined above. The mathematical expressions are relatively simple and it

can be easily incorporated in parameter estimation programs. Its application is, however, not frequently encountered in literature, probably due to the lack of dedicated, user-friendly software packages that follow this philosophy. It certainly deserves more attention from a viewpoint of efficiency.

### 6.1.6 Symbols

Quantity	Description	Units
A	component or species	–
$a_k$	steplength improvement factor at $k$ th parameter iteration (steepest descent)	–
$b_i$	estimated value parameter $i$	*
<b>b</b>	vector of estimated parameters	–
<i>d.f.</i>	number of degrees of freedom	–
$D(\mathbf{x}_k)$	divergence between rival models at experimental settings vector $\mathbf{x}_k$	*
$E_{a_i}$	activation energy of step $i$	J mol <sup>-1</sup>
$F(p, n - p, 1 - \alpha)$	$F$ -value of Fischer's distribution at $p$ and $n - p$ degrees of freedom and confidence level $(1 - \alpha)$	–
$F_A^o$	molar flow of A	mol.s <sup>-1</sup>
$h_{ij}$	element of Hessian matrix	*
<b>H</b>	Hessian matrix	–
$\Delta H_i$	enthalpy change for step or proces $i$	J.mol <sup>-1</sup>
<b>I</b>	unity matrix	–
$k_i$	rate constant of step or process $i$	*
$k_{0i}$	preexponential factor of $k_i$	*
$k_i^o$	rate constant value without deactivation	*
$k_{ref}$	rate constant defined through eq 20(a)	*
$K_i$	equilibrium constant of step or process $i$	*
$K_{eq}$	overall equilibrium constant of a reaction	*
$L$	site density (Table 2)	nm <sup>-2</sup>
$L(\beta y)$	likelihood function of parameter vector $\beta$ in model $y$	–

References see page 1208

$m$	number of rival models	-
$N_A$	amount of A	mol
$N_T$	site concentration	mol kg <sup>-1</sup>
$n$	number of experiments	-
$p$	number of parameters	-
$p_A$	partial pressure of A	Pa
$p_i$	probability density under model $i$ , eq 62	-
$r$	reaction rate	mol s <sup>-1</sup> kg <sup>-1</sup>
$r_i$	reaction rate of step $i$	mol s <sup>-1</sup> kg <sup>-1</sup>
$R$	universal gas constant	J mol <sup>-1</sup> K <sup>-1</sup>
$Res_i$	residual, observed minus calculated value of dependent variable at $i$ th experiment	*
<b>Res</b>	vector of residuals	*
$s^2$	estimated variance	*
$SSR$	sum of squares of residuals	*
$S(\mathbf{b})$	SSR function as a function of parameter vector $\mathbf{b}$	*
<b>S</b>	matrix defined in Table 3	
$\Delta S_i$	entropy change for step or process $i$	J mol <sup>-1</sup> K <sup>-1</sup>
$t$	time	s
$t_{n-p-1-\alpha/2}$	$t$ -value of Student's distribution at $n-p$ degrees of freedom and $(1-\alpha)$ probability level	-
$T$	temperature	K
$\bar{T}$	average temperature of experimental range	K
$W$	amount of catalyst	kg
$v_{ij}$	element $i, j$ of variance matrix	*
$\mathbf{V}(\mathbf{b})$	variance-covariance matrix of parameter estimates $\mathbf{b}$	*
$V(\hat{y}(\mathbf{x}_k))$	variance of predicted value of $y$ at experimental settings vector $\mathbf{x}_k$ of grid point $k$	*
$x_A$	conversion of A	-
$x_i$	setting of independent variable $i$	*
$\mathbf{x}_k$	vector of independent variables at the $k$ th grid point	*
<b>X</b>	matrix of independent variable settings of experiments	*
$y_i$	value of dependent (observed) variable of $i$ th experiment	*
$\mathbf{y}$	vector of dependent variable values	*
$\tilde{z}_p$	eigenvector coordinate	*
$\alpha$	deactivation constant or $\alpha$ percentage point in $F$ or $t$ distribution	s <sup>-1</sup>
$\beta_i$	real (unknown) value of parameter $i$	*
$\boldsymbol{\beta}$	vector of real (unknown) values of parameters	*
$\delta$	constant	*
$\epsilon_{ij}$	error of the $j$ th dependent (observed) variable at the $i$ th response (experiment)	*
$\eta_i$	real (unknown) value of dependent variable $y_i$	*
$\pi_{i,n}$	probability of model $i$ after $n$ experiments	-
$\theta_A$	surface occupancy of species A	-
$\Theta$	hyperellipsoid function (confidence contour)	-
$\lambda_i$	Wilks' diagnostic parameter in model discrimination	-
$\lambda_k$	Levenberg-Marquardt parameter after the $k$ th iteration	-
$\lambda_p$	the $p$ th eigenvalue	*
$\Phi_C$	catalyst deactivation function due to species C	-

$\rho_{ij}$	correlation coefficient between parameter $i$ and $j$	-
$\sigma^2$	real variance of a model	*
$\Sigma$	matrix of error variances in multiresponse experiments	*
$\nu_A$	stoichiometric number of A in reaction	-
$\chi_C^2$	function defined for model discrimination, eq 56	-
$\partial$	operator for partial derivatives	-
$\hat{\phantom{x}}$	referring to calculated value	-

\* dimensions of these variables depends on the systems considered

## References

- 1 F Kapteijn, J A Moulijn, Section A9 1 in *Handbook of Heterogeneous Catalysis* (Eds G Ertl, H Knozinger, J Weitkamp), VCH, Weinheim, 1997
- 2 M Boudart and G Djega-Mariadassou, *Kinetics of heterogeneous catalytic reactions*, Princeton University Press, Princeton, 1984
- 3 M Boudart, Section A5 2 1 in *Handbook of Heterogeneous Catalysis* (Eds G Ertl, H Knozinger, J Weitkamp), VCH, Weinheim, 1997
- 4 M Boudart, *Kinetics of chemical processes*, Butterworth-Heinemann, Boston, 1991
- 5 E G Christoffel, *Laboratory studies of heterogeneous catalytic processes*, Elsevier, Amsterdam, 1989
- 6 E Alpay, L S Kershenbaum, N F Kirkby, *Chem Engng Sci* 1995, 50, 1063
- 7 L K Doraiswamy, D G Tajbl, *Cat Rev Sci Eng* 1974, 10, 177
- 8 N Draper, H Smith, *Applied regression analysis*, Wiley, New York, 1981
- 9 G F Froment, L Hosten, in *Catalysis, Science and Technology* (Eds J R Anderson, M Boudart), Springer, Berlin, 1981, p 97
- 10 J R Kittrell in *Advances in Chemical Engineering* (Eds T B Drew, G R Cokelet, J W Hoopes, T Vermeulen) Academic Press, New York, 1970, Vol 8, p 97
- 11 K C Pratt in *Catalysis, Science and Technology* (Eds J R Anderson and M Boudart), Springer, Berlin, 1980, p 174
- 12 J R Anderson, K C Pratt, *Introduction to characterization and testing of catalysts*, Academic Press, Sydney, 1985
- 13 S W Weller, *Catal Rev -Sci Eng* 1992, 34, 227
- 14 M I Temkin, *Adv Catal* 1979, 28, 173
- 15 G F Froment, K B Bischoff, *Chemical reactor analysis and design*, Wiley, New York, 1979
- 16 J T Gleaves, J R Ebner, T C Kuechler, *Catal Rev -Sci Eng* 1988, 30, 49
- 17 S C V Linde, T A Nijhuis, F H M Dekker, F Kapteijn, J A Moulijn, *Appl Catal A* 1997, in press
- 18 K A Vonkeman, Thesis, Eindhoven University of Technology, 1990
- 19 F H M Dekker, Ph D Thesis, University of Amsterdam 1995
- 20 J Happel, *Isotopic assessment of heterogeneous catalysis* Academic Press, Orlando, 1986
- 21 F H M Dekker, J G Nazloomian, A Bliet, F Kapteijn, J A Moulijn, P L Mills, J J Lerou, *Appl Catal A* 1997 in press
- 22 C Mirodatos *Catal Today* 1991, 9, 83
- 23 R H Nibbelke, J Scheerova, M H J M de Croon, G B Marin, *J Catal* 1995, 156, 106

24 J M Berty, *Plant/Operation Progress* **1984**, *3*, 163  
 25 V W Weekman, *AIChE J* **1974**, *20*, 833  
 26 F Kapteijn, P Coevert, J A Moulijn, *J Phys E* **1982**, *15*, 1064  
 27 R Meijer, F Kapteijn, J A Moulijn, *Fuel* **1994**, *73*, 723  
 28 J A Moulijn, A Tarfaoui, F Kapteijn, *Catal Today* **1991**, *11*, 1  
 29 S T Sie, *The Chemical Engineering Journal* **1993**, *53*, 1  
 30 P C Borman, A N R Bos, K R Westerterp, *AIChE J* **1994**, *40*, 862  
 31 H P Calis, Ph D Thesis, University of Delft, **1995**  
 32 J J Carberry in *Catalysis, Science and Technology* (Eds J R Anderson and M Boudart), Springer, Berlin, **1980**, p 131  
 33 P Trambouze, H V Landeghem, J P Wauquier in *Chemical reactors* Editions Technip, Paris, **1988**, p 539  
 34 G B Tatterson, *Scaleup and design of industrial mixing processes*, McGraw-Hill, New York, **1994**  
 35 F Kapteijn, A J V Steen, J C Mol, *J Chem Thermodyn* **1983**, *15*, 137  
 36 S Tajik, P J V Berg, J A Moulijn, *Meas Sci Technol* **1990**, *1*, 815  
 37 M P Helmsing, Ph D Thesis, Delft University of Technology, **1996**  
 38 D W Kraemer, U Sedran, H I D Lasa, *Chem Engng Sci* **1990**, *45*, 2447  
 39 F Kapteijn, L Singoredjo, N J J Dekker, J A Moulijn, *Ind Eng Chem Res* **1993**, *32*, 445  
 40 B W Wojciechowski, N M Rice, *Chem Engng Sci* **1993**, *48*, 2881  
 41 R Mezaki, H Inoue, *Rate equations of solid-catalysed reactions*, University of Tokyo Press, Tokyo, **1991**  
 42 O A Hougen, K M Watson *Chemical Process Principles*, John Wiley, New York, Vol III **1947**  
 43 F Kapteijn, J J Rodriguez-Mirasol, J A Moulijn, *Appl Cat B* **1996**, *9*, 25–64  
 44 F Kapteijn, J A Moulijn R A V Santen in *Catalysis an integrated approach to homogeneous heterogeneous and industrial catalysis* (Eds J A Moulijn, P W N M Leeuwen R A V Santen), Elsevier, Amsterdam, **1993**, p 69  
 45 J Wei, *Ind Eng Chem Res* **1994**, *33*, 2467  
 46 Y Bard, *Nonlinear parameter estimation*, Academic Press, New York, **1974**  
 47 D M Himmelblau, *Applied nonlinear programming*, McGraw-Hill, New York, **1972**  
 48 M J D Powell, *Comput J* **1964**, *7*, 155  
 49 H H Rosenbrock, C Storey, *Computational techniques for chemical engineers*, Pergamon Press, New York, **1966**  
 50 J A Nelder, R Mead, *Comput J* **1965**, *7*, 308  
 51 K Levenberg, *Q Appl Math* **1944**, *2*, 164  
 52 D Marquardt, *SIAM J Appl Math* **1963**, *11*, 431  
 53 W H Press, S A Teukolsky, W T Vetterling, B P Flannery, *Numerical recipes The art of scientific computing*, Cambridge University Press, Cambridge, **1992**  
 54 M Shacham, E Kehat, *Chem Engng Sci* **1972**, *27*, 2099  
 55 R Bulirsch, J Stoer, *Num Math* **1966**, *8*, 1  
 56 C W Gear L R Petzold, *SIAM J Numer Anal* **1984**, *21*, 367  
 57 R L C Bonne, Ph D Thesis, University of Amsterdam, **1990**  
 58 W E Shesser, *The numerical method of lines*, Academic Press San Diego, **1991**  
 59 A C Hindmarsh, *ODEPACK A systematized collection of ODE solvers*, Elsevier, Amsterdam **1983**  
 60 F Kapteijn L H G Bredt, E Homburg J C Mol *Int Eng Chem Prod Res Dev* **1981**, *20*, 457  
 61 R A V Santen, J W Niemantsverdriet, *Chemical kinetics and Catalysis*, Plenum Press, New York, **1995**  
 62 M A Vannice, S H Hyum, B Kalpacki, W C Liah, *J Catal* **1979**, *56*, 358

63 M Boudart, D E Mears M A Vannice, *Ind Chim Belge* **1967**, *32*, 281  
 64 M Boudart, *AIChE J* **1972**, *18*, 465  
 65 F Kapteijn, R Meijer, J A Moulijn, *Energy and Fuels* **1992**, *6*, 494  
 66 P Biloen, *J Mol Catal* **1983**, *21*, 17  
 67 R W Maatman, *Adv Catal* **1980**, *29*, 97  
 68 R Mezaki, J R Kittrell, *Can J Chem Eng* **1966**, *44*, 285  
 69 S S Wilks, *Ann Math Stat* **1946**, *17*, 257  
 70 M S Bartlett, *Proc Roy Soc A* **1937**, *160*, 268  
 71 G E P Box, W J Hill, *Technometrics* **1967**, *9*, 57

## 6.2 Simultaneous Heat and Mass Transfer and Chemical Reaction

G. EMIG AND R. DITTMAYER

### 6.2.1 Introduction

Heterogeneous catalytic reactions, by their nature, involve a separate phase of catalyst, embedded in a phase of reacting species. Therefore, the chemical transformation relies on a number of physical transport processes which may have a strong influence on the rate of the overall process and which may introduce an additional dependence on the operating conditions. In the industrially important situation that the catalyst is a porous solid and the reactants form either a gaseous or a liquid phase, the following seven steps can be observed (Fig 1)

- 1 Diffusion of the reactants through a boundary layer or film adjacent to the external surface of the catalyst (film diffusion or interphase diffusion)
- 2 Diffusion of the reactants through the porous interior of the catalyst to the point at which the chemical transformation occurs (pore diffusion or intraparticle diffusion)
- 3 Adsorption of the reactants on the inner surface
- 4 Surface reaction at specific active sites
- 5 Desorption of the products from the inner surface
- 6 Diffusion of the products through the porous structure to the external surface (intraparticle diffusion)
- 7 Diffusion of the products through the external boundary layer into the bulk fluid phase (interphase diffusion)

Adsorption, surface reaction, and desorption are sequential steps, these constitute the chemical transformation. Interphase and intraparticle diffusion occur in a serial manner as well. However, intraparticle diffusion and chemical transformation (adsorption, surface re-

References see page 1251

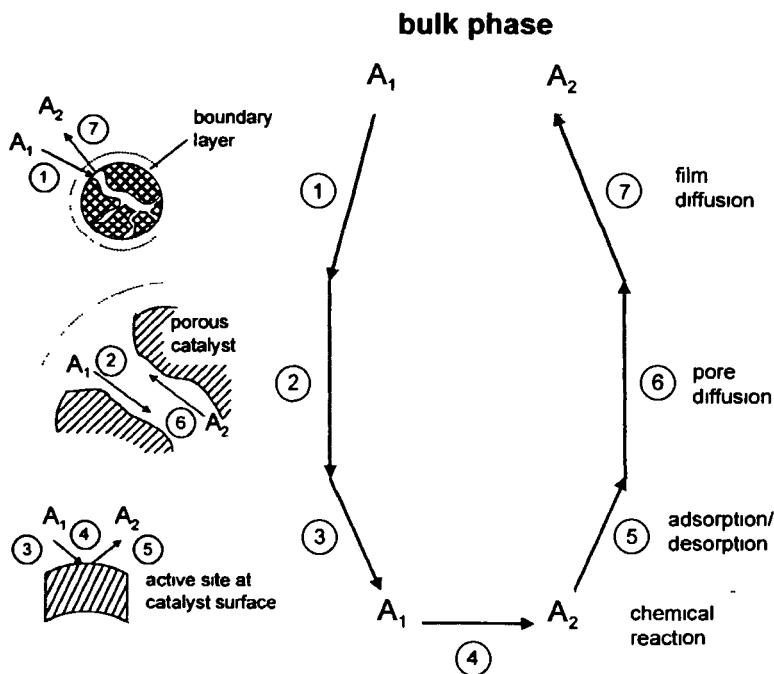


Figure 1. Individual steps of a simple, heterogeneous catalytic fluid–solid reaction  $A_1 \rightarrow A_2$  carried out on a porous catalyst

action, and desorption) take place simultaneously. Most chemical reactions are accompanied by heat effects. Thus, in addition to film and pore diffusion, also interphase and intraparticle heat transfer occurs.

The net kinetics of the overall reaction (steps 1–7) are normally called effective kinetics or macrokinetics, in contrast to the kinetics of the chemical transformation (steps 3–5) which are termed intrinsic kinetics or microkinetics.

Heat and mass transfer processes always proceed with finite rates. Thus, even when operating under steady state conditions, more or less pronounced concentration and temperature profiles may exist across the phase boundary and within the porous catalyst pellet as well (Fig. 2). As a consequence, the observable reaction rate may differ substantially from the intrinsic rate of the chemical transformation under bulk fluid phase conditions. Moreover, the transport of heat or mass inside the porous catalyst pellet and across the external boundary layer is governed by mechanisms other than the chemical reaction, a fact that suggests a change in the dependence of the effective rate on the operating conditions (i.e. concentration and temperature).

Normally, the intrinsic chemical rate is an exponential function of temperature, according to the Arrhenius law, whereas the mass transfer rate is less strongly influenced by a temperature change. The intraparticle effective diffusivity  $D_e$  is proportional to  $T^{3/2}$  when molecular diffusion dominates, and proportional to  $T^{1/2}$  for the case of governing Knudsen diffusion. The interphase mass transfer coefficient  $k_f$  ex-

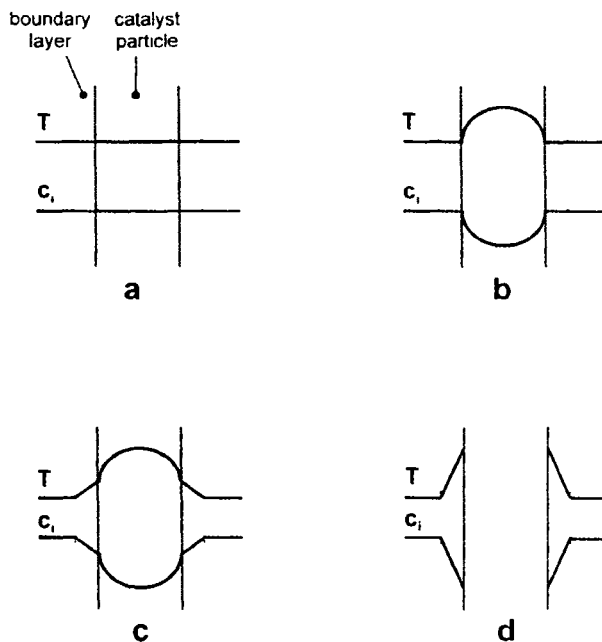
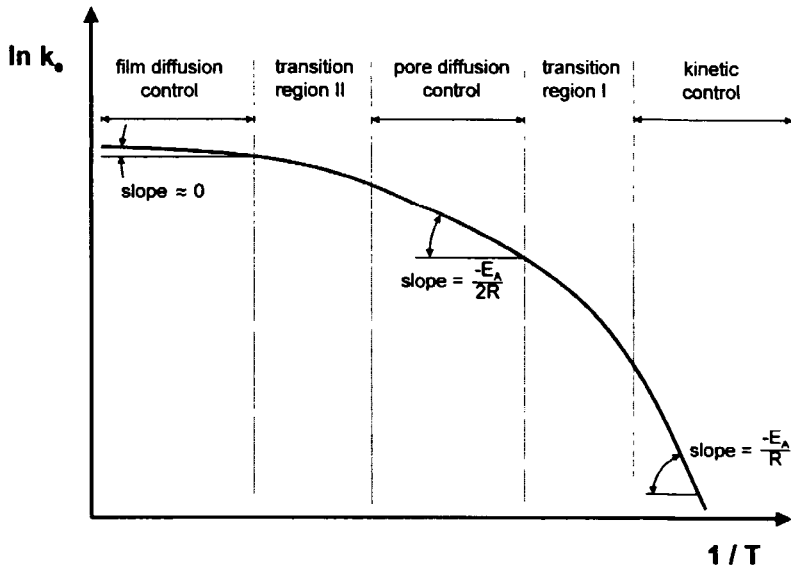


Figure 2. Stationary concentration (reactant) and temperature profiles inside and around a porous catalyst pellet during an exothermic, heterogeneous catalytic fluid–solid reaction (a) without transport influence, (b) limited only by intraparticle diffusion, (c) limited by interphase and intraparticle diffusion, (d) limited only by interphase diffusion (dense pellet)

hibits basically the same temperature dependence as the molecular diffusivity ( $k_f \sim T^{3/2}$ ).

When plotting the natural logarithm of the effective rate constant  $\ln(k_e)$  against the inverse of temperature



**Figure 3.** Transition from the kinetic regime to the diffusion-controlled regime of a heterogeneous catalytic fluid–solid reaction carried out on a porous catalyst.

(Arrhenius diagram), the general curve depicted in Fig. 3 is obtained. At a lower temperature the chemical reaction is slow and thereby rate controlling. Concentration and temperature remain constant over the entire cross-section of the catalyst pellet (see Fig. 2a). In this region, the slope of the curve in Fig. 3 is proportional to the intrinsic activation energy  $E_A$ .

By increasing the temperature, the intrinsic chemical rate is accelerated more strongly than the rate of intraparticle diffusion. When both of these simultaneous steps occur with a rate of about the same order of magnitude, a transition region is passed where the slope changes with temperature. As the intraparticle diffusion finally becomes rate determining, the concentration inside the porous catalyst pellet drops markedly (see Fig. 2b). The effective activation energy in this regime is roughly one half of the true value. Upon further increasing the temperature a second transition regime is passed. Finally, interphase mass transfer becomes the rate controlling step. As a consequence, the reactant concentration already falls off steeply across the external boundary layer (see Fig. 2c). Here, the slope of the curve in Fig. 3 tends towards zero, corresponding to an effective activation energy in the range of less than  $5\text{--}10\text{ kJ mol}^{-1}$ .

In general, not only the effective activation energy but also the effective order of reaction is changed during the transition from kinetic to diffusion control. According to Fick's first law, the rate of diffusion (interphase and intraparticle) is proportional to the concentration gradient, i.e. it is first order. The effective reaction order observed under severe intraparticle diffusion control approaches a value of  $(n + 1)/2$ , where  $n$  is the intrinsic order of reaction. In the case that

interphase mass transfer controls the overall rate, the effective concentration dependence of the reaction rate is close to first order. Changes of the effective reaction rate, the apparent activation energy, and the apparent order of reaction during the transition from the kinetic regime to the diffusion-controlled regime are of great importance for the technology of heterogeneously catalyzed reactions. These effects must be considered in practical situations, as otherwise wrong predictions with respect to selectivity and yield of the catalyst may result.

This chapter is concerned with the mathematical modeling of coupled chemical reaction and heat and mass transfer processes occurring in porous catalysts. It focuses primarily on steady state catalyst operation which is the preferred industrial practice. Stationary operation may be important for the startup and shutdown of an industrial reactor, or with respect to dynamic process control. However, these effects are not discussed here in great detail because of the limited space available. Instead, the interested reader is referred to the various related monographs and articles available in the literature [6, 31, 46–49].

The engineering implications of the interaction between the diffusional transport and chemical reactions were first identified by Damköhler [28], Zeldovich [114], and Thiele [98] in the late 1930s, and then by Wheeler [113], and Weisz and Prater [108] in the early 1950s. Since then the authors of numerous chemical engineering textbooks have addressed this problem within one or two separate chapters. The most comprehensive treatment of the subject has been given by

Aris [5, 6], although this is a more theoretical treatment. Practical aspects have been ably treated for example by Satterfield [91, 92] and Carberry [18, 19].

The contents of the present contribution may be outlined as follows. Section 6.2.2 introduces the basic principles of coupled heat and mass transfer and chemical reaction. Section 6.2.3 covers the classical mathematical treatment of the problem by example of simple reactions and some of the analytical solutions which can be derived for different experimental situations. Section 6.2.4 is devoted to the point that heat and mass transfer may alter the characteristic dependence of the overall reaction rate on the operating conditions. Section 6.2.5 contains a collection of useful diagnostic criteria available to estimate the influence of transport effects on the apparent kinetics of single reactions. Section 6.2.6 deals with the effects of heat and mass transfer on the selectivity of basic types of multiple reactions. Finally, Section 6.2.7 focuses on a practical example, namely the control of selectivity by utilizing mass transfer effects in zeolite catalyzed reactions.

Note that Section A.6.3 is concerned in detail with the modeling of diffusion and the determination of diffusivities.

## 6.2.2 Mathematical Description

The mathematical description of simultaneous heat and mass transfer and chemical reaction is based on the general conservation laws valid for the mass of each species involved in the reacting system and the enthalpy effects related to the chemical transformation. The basic equations may be derived by balancing the amount of mass or heat transported per unit of time into and out of a given differential volume element (the control volume) together with the generation or consumption of the respective quantity within the control volume over the same period of time. The sum of these terms is equivalent to the rate of accumulation within the control volume:

$$\begin{aligned} & \text{accumulation within control volume/time} \\ &= \text{in/time} - \text{out/time} + \text{generation or} \\ & \quad \text{consumption/time} \end{aligned}$$

The region over which this balance is invoked is the heterogeneous porous catalyst pellet which, for the sake of simplicity, is described as a pseudohomogeneous substitute system with regular pore structure. This virtual replacement of the heterogeneous catalyst pellet by a fictitious continuous phase allows a convenient representation of the mass and enthalpy conservation laws in the form of differential equations. Moreover, the three-dimensional shape of the catalyst pellet is replaced by assuming a one-dimensional model

geometry (sphere, infinite cylinder, infinite flat plate) in order to simplify the mathematical treatment.

For the case of a sphere, the control volume is given by a thin spherical shell of thickness  $dr$  and radius  $r$ . If we assume that the complex diffusion process inside the porous structure can be represented by Fick's first law, and we additionally suppose that the volume change due to reaction is negligible (i.e. the total number of moles is constant), we arrive at the following form of the mass conservation law for the reacting species  $i$ :

$$4\pi r^2 \delta r \frac{\partial c_i}{\partial t} = 4\pi r^2 D_{i,e} \frac{\partial c_i}{\partial r} \Big|_r - 4\pi (r + \delta r)^2 D_{i,e} \frac{\partial c_i}{\partial r} \Big|_{r+\delta r} + 4\pi r^2 \delta r R_i \quad (1)$$

Here,  $R_i$  is the pseudohomogeneous rate of production or disappearance of species  $i$  per unit volume which in the general case of a network of multiple reactions may be the result of  $M$  different chemical transformations. Therefore,

$$R_i = \sum_{j=1}^M v_{i,j} r_j \quad (2)$$

In eq 1  $D_{i,e}$  is the effective diffusivity of species  $i$  in the reaction mixture which can be determined on the basis of various models of the diffusion process in porous solids. This aspect is discussed more fully in Section A.6.3.  $D_{i,e}$  is affected by the temperature and the pore structure of the catalyst, but it may also depend on the concentration of the reacting species (Stefan–Maxwell diffusion [9]). As  $D_{i,e}$  is normally introduced on the basis of more or less empirical models, it may not be considered as a physical property, but rather as a model-dependent parameter.

The concentration gradient  $\partial c_i / \partial r$  at the position  $r + \delta r$  in eq 1 may be expanded as a Taylor series:

$$\frac{\partial c_i}{\partial r} \Big|_{r+\delta r} = \frac{\partial c_i}{\partial r} \Big|_r + \frac{\partial^2 c_i}{\partial r^2} \Big|_r \delta r \quad (3)$$

The resulting approximation is substituted in eq 1. The terms, which then include the expression  $\delta r^2$  in the numerator, can be neglected ( $\delta r$  is already small). After rearranging, the following mass balance is finally obtained:

$$\frac{\partial c_i}{\partial t} = D_{i,e} \left( \frac{\partial^2 c_i}{\partial r^2} + \frac{2}{r} \frac{\partial c_i}{\partial r} \right) + R_i \quad (4)$$

Equation 4 is equivalent to Fick's second law (non-stationary diffusion), expanded by an additional source term which accounts for the production or consumption of species  $i$  caused by chemical transformations. Similar to this mass balance, an enthalpy balance may be also derived:

$$\rho c_p \frac{\partial T}{\partial t} = \lambda_c \left( \frac{\partial^2 T}{\partial r^2} + \frac{2}{r} \frac{\partial T}{\partial r} \right) + H_R \quad (5)$$



Equation 5 is an expansion of Fourier's second law (nonstationary heat conduction), where the additional term  $H_R$ , in analogy to  $R_i$  in eq 4, gives the total heat of reaction produced or consumed per unit volume and time. This gives

$$H_R = \sum_{j=1}^M r_j(-\Delta H_{R,j}) \quad (6)$$

Although it is clear from eq 6 that  $H_R$  can be negative (endothermic) as well as positive (exothermic), in the following it is always considered as the heat release term, for notational simplicity.

In the general case, eqs 4 and 5 constitute a system of nonlinear coupled second-order partial differential equations. To specify the boundary conditions for this problem, it is necessary to include the external (interphase) heat and mass transfer, as both the concentration and the temperature at the external surface of the catalyst pellet may differ from the corresponding values in the bulk of the surrounding fluid phase.

To avoid unnecessary complications, the view is restricted here to the symmetric case. This means, that the catalyst pellet is assumed to be located in a homogeneous concentration and temperature field, i.e. the surrounding fluid phase is perfectly mixed. A consequence of this assumption is that uniform reaction conditions prevail at the pellet surface. Concentration or temperature gradients, which might occur on the surface in extreme situations [31], are neglected here. At the phase boundary no discontinuity of the mass and heat fluxes can occur. Therefore, the mass flux density of species  $i$  from the bulk fluid phase to the external catalyst surface, determined by the interphase mass transfer, must equal the mass flux density of this species attributed to intraparticle effective diffusion. The external mass flux density is given by the product of the mass transfer coefficient  $k_f$  and the concentration difference between the bulk fluid phase and the external surface ( $c_{i,b} - c_{i,s}$ ), whereas the mass flux density towards the center of the porous pellet is obtained by multiplying the effective diffusivity  $D_{i,e}$  by the concentration gradient at the external pellet surface ( $\partial c_i / \partial r$ )<sub>s</sub>. Equating both expressions (pellet surface:  $r = R$ ) yields the first boundary condition (eq 7). An analogous equation (eq 8) can be derived for the heat transfer.

$$k_f(c_{i,b} - c_{i,s}) = D_{i,e} \left. \frac{\partial c_i}{\partial r} \right|_s \quad (7)$$

$$h_f(T_b - T_s) = \lambda_c \left. \frac{\partial T}{\partial r} \right|_s \quad (8)$$

The second boundary condition is dictated by the symmetry of the (idealized) pellet geometry, i.e. the concentration and temperature gradients must disappear at the pellet center ( $r = 0$ ; eqs 9 and 10).

$$\left. \frac{\partial c_i}{\partial r} \right|_0 = 0 \quad (9)$$

$$\left. \frac{\partial T}{\partial r} \right|_0 = 0 \quad (10)$$

If the external heat and mass transfer resistances are negligible, eqs 7 and 8 can be simplified by replacing the unknown surface values  $c_{i,s}$  and  $T_s$  with the known conditions in the bulk fluid phase, and then transform to the following simple boundary conditions at the external pellet surface:

$$c_{i,s} = c_{i,b} \quad (11)$$

$$T_s = T_b \quad (12)$$

The condition of symmetry at the center of the pellet remains uninfluenced by a change of the boundary condition at the external pellet surface.

The solution of the above system of partial differential equations (eqs 4–12) yields the concentration and temperature profiles inside the catalyst pellet, and if necessary across the external boundary layer, as a function of time. However, there are only few cases of practical importance where this complete solution is required, as for instance startup and shutdown periods, dynamic process control options such as the so-called "Matros concept" with flow reversals (for redox processes), or situations where the catalyst is rapidly deactivated.

In most day to day operations only the stationary solution will be of interest. Hence, all partial derivatives with respect to time in eqs 4–12 can be set to zero, which leads to the following equations for the stationary case:

$$\text{Mass balance: } \frac{d^2 c_i}{dr^2} + \frac{2}{r} \frac{dc_i}{dr} = \frac{-R_i}{D_{i,e}} \quad (13)$$

$$\text{Enthalpy balance: } \frac{d^2 T}{dr^2} + \frac{2}{r} \frac{dT}{dr} = \frac{-H_R}{\lambda_c} \quad (14)$$

This is a system of ordinary differential equations. Its solution is subject to the same boundary conditions (eqs 7–12) as the solution of eqs 4 and 5. However, the variables involved are no longer time-dependent, which means that the partial derivatives  $\partial c_i / \partial r$  and  $\partial T / \partial r$  can be replaced by the ordinary derivatives  $dc_i / dr$  and  $dT / dr$ .

For simultaneous treatment of interphase and intraparticle transport resistances, the boundary conditions at the external pellet surface are now given by eqs 15 and 16, whereas eqs 11 and 12 still hold for the case of negligible interphase transport resistance. The bound-

any conditions at the pellet center, for both cases, are defined by eqs 17 and 18

$$k_f(c_{i,b} - c_{i,s}) = D_{i,e} \left. \frac{dc_i}{dr} \right|_s \quad (15)$$

$$h_f(T_b - T_s) = \lambda_e \left. \frac{dT}{dr} \right|_s \quad (16)$$

$$\frac{dc_i}{dr} = 0 \quad (17)$$

$$\frac{dT}{dr} = 0 \quad (18)$$

However, for a basic design or a detailed simulation of chemical reactors, profiles of the concentrations and the temperature inside the catalyst pellet are not of primary interest, but rather the effective rates of production or disappearance of the reacting species and the effective heat release or consumption as well. Both are defined according to eqs 19 and 20 as averaged values, related to the pellet volume.

$$R_{i,e} = \frac{1}{V_p} \int_{V_p} R_i dV \quad (19)$$

$$H_{R,e} = \frac{1}{V_p} \int_{V_p} H_R dV \quad (20)$$

To calculate  $R_{i,e}$  and  $H_{R,e}$ , one will normally not use their definition as given in eqs 19 and 20. Instead, it is more convenient to utilize the condition that, during stationary operation, the amount of heat and mass converted inside the catalyst pellet per unit time must meet the flux of the respective quantity across the external pellet surface. For the mass of the reacting species  $i$ , this gives the following relationship:

$$\frac{4}{3} \pi R^3 (-R_{i,e}) = 4 \pi R^2 D_{i,e} \left. \frac{dc_i}{dr} \right|_{r=R} \quad (21)$$

When both sides of eq 21 are divided by the pellet volume, we arrive at the final equation for determining  $R_{i,e}$ :

$$R_{i,e} = -\frac{3}{R} D_{i,e} \left( \frac{dc_i}{dr} \right)_{r=R} \quad (22)$$

In the same way, for  $H_{R,e}$ :

$$H_{R,e} = -\frac{3}{R} \lambda_e \left( \frac{dT}{dr} \right)_{r=R} \quad (23)$$

According to eqs 22 and 23, the concentration and temperature gradients at the external pellet surface must be known to evaluate  $R_{i,e}$  and  $H_{R,e}$ . As soon as the concentration and temperature profiles over the pellet radius are available, the gradients at the pellet surface can be determined by differentiation. However, full analytical solution of the coupled mass and enthalpy

balances is achieved only when the system can be described properly by just a single key reaction (the conversion problem) which, in addition, obeys a simple power law or Langmuir–Hinshelwood type kinetics. On the contrary, when several key reactions must be considered simultaneously (the selectivity problem), or when it is necessary to use a complex kinetic expression, then the solution in general requires the use of numerical methods.

For didactical reasons, a detailed discussion of the first case, the analytically solved (simple) conversion problem, is given initially. The main purpose of this is to demonstrate how the reaction rate under certain conditions is fundamentally influenced by heat and mass transfer. Attention is then given to the more complicated case in which several key reactions have to be considered and selectivity in addition to conversion becomes an issue.

### 6.2.3 Single Reactions (Conversion Problem)

Whenever the kinetics of a chemical transformation can be represented by a single reaction, it is sufficient to consider the conversion of just a single reactant. The concentration change of the remaining reactants and products is then related to the conversion of the selected key species by stoichiometry, and the rates of production or consumption of the various species differ only by their stoichiometric coefficients. In this special case, the combined influence of heat and mass transfer on the effective reaction rate can be reduced to a single number, termed the catalyst efficiency or effectiveness factor  $\eta$ . From the pioneering work of Thiele [98] on this subject, the expressions “pore-efficiency concept” and “Thiele concept” have been coined.

As a typical example of this type of reaction, the transformation  $A_1 \rightarrow$  products may be considered, where the kinetics are described by a simple power rate law of the order  $n$ . Since this reaction is completely characterized by specifying the conversion of reactant  $A_1$ , the above system of differential equations (eqs 11–18) may be readily expressed in a convenient, nondimensional form. For this purpose, the reactant concentration and the temperature are related to their corresponding values in the bulk fluid phase (eqs 24 and 25), and the radius coordinate  $r$  is divided by the pellet radius  $R$  to introduce a dimensionless coordinate (eq 26).

$$f = \frac{c}{c_b} \quad (24)$$

$$\theta = \frac{T}{T_b} \quad (25)$$

$$x = \frac{r}{R} \quad (26)$$

**Table 1.** Dimensionless representation of the stationary mass and enthalpy balance equations for combined interphase and intraparticle transport and reaction (single,  $n$ th order, irreversible reactions).

Parameter	Relationship
Mass balance	$\frac{d^2f}{dx^2} + \frac{b}{x} \frac{df}{dx} - \phi^2 f^n e^{\gamma(1-f)} = 0$ (32)
Enthalpy balance	$\frac{d^2\theta}{dx^2} + \frac{b}{x} \frac{d\theta}{dx} + \beta \phi^2 f^n e^{\gamma(1-f)} = 0$ (33)
Pellet center ( $x = 0$ )	$\frac{df}{dx} = 0$ (34)
	$\frac{d\theta}{dx} = 0$ (35)
Pellet surface ( $x = 1$ ) with interphase gradients	$\left. \frac{df}{dx} \right _s = Bi_m(1 - f_s)$ (36)
	$\left. \frac{d\theta}{dx} \right _s = Bi_h(1 - \theta_s)$ (37)
Pellet surface ( $x = 1$ ) without interphase gradients	$f_s = 1$ (38)
	$\theta_s = 1$ (39)

With these definitions, eqs 11–18 yield a structure which suggests a grouping of the different variables to several nondimensional numbers:

1. The well known Thiele modulus  $\phi$  of the reaction. This is defined as the ratio of the intrinsic chemical rate, calculated at bulk fluid phase conditions, to the maximum rate of effective diffusion at the external pellet surface. For spherical catalyst pellets, the Thiele modulus is given by

$$\phi = R \sqrt{\frac{k(T_b) c_b^{n-1}}{D_c}} \quad (27)$$

2. The Biot number  $Bi_m$  for mass transport. This can be interpreted as the ratio of internal to external transport resistance (intraparticle diffusion versus interphase diffusion):

$$Bi_m = \frac{k_f R}{D_c} \quad (28)$$

3. The Biot number  $Bi_h$  for heat transport. Analogous to  $Bi_m$ , this is defined as the ration of the internal to external heat transfer resistance (intraparticle heat conduction versus interphase heat transfer).

$$Bi_h = \frac{h_f R}{\lambda_c} \quad (29)$$

4. The Arrhenius number, which is a dimensionless representation of the intrinsic activation energy, related to the bulk temperature:

$$\gamma = \frac{E_A}{RT_b} \quad (30)$$

5. The Prater number, defined as the maximum observable temperature difference between the pellet

surface and the pellet interior, related to the bulk temperature:

$$\beta = \frac{c_b D_c (-\Delta H_R)}{\lambda_c T_b} \quad (31)$$

Substituting these nondimensional numbers into eqs 11–18, and after some rearrangement, the general dimensionless representation of the problem is obtained as depicted in Table 1. These equations are valid not only for spherical pellet geometry, but also for the infinite cylinder and the infinite flat plate (slab). The dimensionless numbers  $x$ ,  $\phi$ ,  $Bi_m$  and  $Bi_h$  must then be calculated on the basis of the respective characteristic length, i.e. the cylinder radius or the plate thickness. Moreover, the parameter  $b$  in eqs 32 and 33 is a factor depending on the pellet geometry. It is 2 for the sphere, 1 for the cylinder, and 0 for the flat plate.

An overall catalyst effectiveness factor of the reaction may now be defined as the ratio of the observed effective rate, averaged over the pellet volume, divided by the intrinsic chemical rate which would be expected in absence of concentration and temperature gradients in the system (i.e. under bulk fluid phase conditions)

$$\eta = \frac{r_c}{r_b} \quad (40)$$

When eqs 22, 24 and 26 are substituted into this relationship, the following expression for the effectiveness factor of a spherical catalyst pellet is obtained:

$$\eta = \frac{3 D_c \left( \frac{df}{dx} \right)_{x=1}}{R^2 k c_b^{n-1}} \quad (41)$$

Using the definition of the Thiele modulus according to eq 27 finally yields

$$\eta = \frac{3}{\phi^2} \left( \frac{df}{dx} \right)_{x=1} \quad (42)$$

This equation is valid for the general case, where the effective rate is influenced by external as well as internal heat and mass transfer. In real situations, however, one or more of the transport steps involved frequently proceed at a rate substantially above that of the chemical reaction. If this happens, these steps may be neglected without significantly affecting the observable reaction rate. Hence, the system may be simplified. The extent of simplification depends on which of the transport steps can be neglected. In the following, the different cases, which occur in practical situations, are discussed separately.

### 6.2.3.1 Pore Diffusion in an Isothermal Pellet

The simplest case is given when the effective reaction rate is influenced by pore diffusion only, whereas the interphase heat and mass transfer resistances as well as the effective heat conduction resistance inside the porous pellet may be neglected. Despite its simplicity, this case is of great practical importance, as it is often found when the reaction is associated only with a small heat release (or consumption), and/or when the catalyst exhibits a good thermal conductivity (e.g. metals). The pellet temperature is assumed to be constant and equal to the temperature of the surrounding fluid phase. Hence, the solution of the enthalpy balance is trivial. Moreover, the concentration at the external pellet surface is identical to the concentration in the bulk fluid phase. Therefore, the mass balance (eq 32) and the corresponding boundary conditions (eqs 34 and 38) are governed by a single parameter, namely the Thiele modulus  $\phi$ .

For single, irreversible reactions obeying simple, integer order power rate laws, this problem can generally be solved analytically. In the case of a first-order reaction in a spherical pellet, the following mass balance is found:

$$\frac{d^2f}{dx^2} + \frac{2}{x} \frac{df}{dx} = \phi^2 f \quad (43)$$

Introducing a new variable  $y = fx$  allows this differential equation to be rewritten in the simple form

$$\frac{d^2y}{dx^2} = \phi^2 y \quad (44)$$

A general solution of eq 44 is

$$y = fx = C_1 e^{\phi x} + C_2 e^{-\phi x} \quad (45)$$

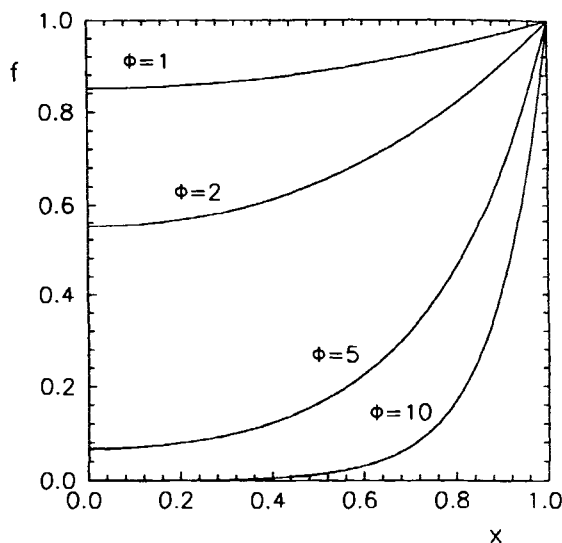


**Figure 4.** Normalized concentration profiles of reactant  $A_1$  versus the pellet radius, calculated from eq 49 for different values of the Thiele modulus  $\phi$  (isothermal, first order, irreversible reaction in a sphere).

From the condition of symmetry at the pellet center (eq 34), it can be easily deduced that the absolute values of the constants  $C_1$  and  $C_2$  must be equal:

$$C_1 = -C_2 \quad (46)$$

Therefore,

$$f = \frac{2C_1}{x} \sinh(\phi x) \quad (47)$$

The constant  $C_1$  is obtained from the boundary condition at the external pellet surface (eq 38):

$$C_1 = \frac{1}{2 \sinh(\phi)} \quad (48)$$

Combining eqs 47 and 48 leads to the final relationship for the change of the dimensionless concentration  $f$  across the pellet radius:

$$f(x) = \frac{\sinh(\phi x)}{x \sinh(\phi)} \quad (49)$$

To illustrate the decrease of the reactant concentration towards the pellet center, Fig. 4 shows a plot of the concentration profiles for few selected values of the Thiele modulus.

By differentiation eq 49, the concentration gradient at the outer pellet surface is obtained as

$$\left. \frac{df}{dx} \right|_{x=1} = \frac{\phi}{\tanh(\phi)} - 1 \quad (50)$$

Substituting eq 50 into eq 42 yields the final expression (eq 51) which gives the effectiveness factor  $\eta$  of a first

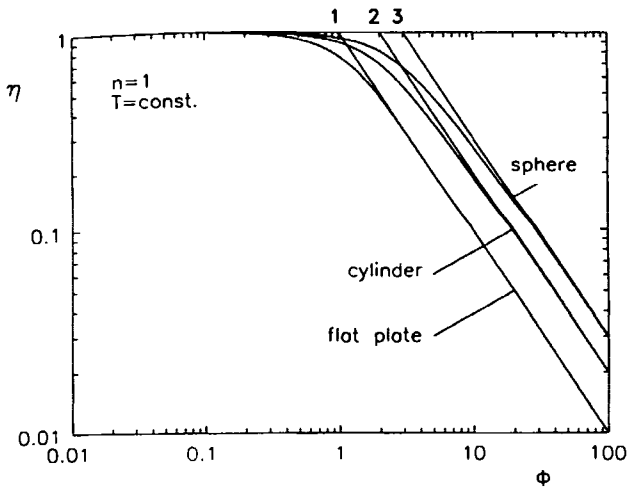


**Figure 5.** Effectiveness factor  $\eta$  as a function of the Thiele modulus  $\phi$  for different pellet shapes. Influence of intraparticle diffusion on the effective reaction rate (isothermal, first order, irreversible reaction).

order, irreversible reaction in a spherical pellet as a unique function of the Thiele modulus:

$$\eta = \frac{3}{\phi} \left( \frac{1}{\tanh(\phi)} - \frac{1}{\phi} \right) \quad (51)$$

Equation 51 has been derived for a spherical catalyst pellet. The corresponding solution for the cylinder is

$$\eta = \frac{2 I_1(\phi)}{\phi I_0(\phi)} \quad (52)$$

and for the flat plate is

$$\eta = \frac{\tanh(\phi)}{\phi} \quad (53)$$

where  $I_1(\phi)$  and  $I_0(\phi)$  denote the modified Bessel functions of first and zero order, respectively [12].

Figure 5 shows the dependence of the effectiveness factor on the Thiele modulus for the different pellet shapes. At small values of  $\phi$  the effectiveness factor approaches unity in all cases. Here, the chemical reaction constitutes the rate determining step—the corresponding concentration profiles over the pellet cross-section are flat (see Fig. 4). This situation may occur at low catalyst activity ( $k$  is small), large pore size and high porosity ( $D_c$  is large), and/or small catalyst pellets ( $R$  is small, i.e. in fluidized bed reactors  $R$  is typically around  $50 \mu\text{m}$ ).

At large values of  $\phi$ , the function  $\eta(\phi)$  for the sphere approaches the asymptotic solution  $\eta = 3/\phi$  which, on the double logarithmic scale of Fig. 5, is a straight line with a slope of  $-1$ . The asymptotes for the cylinder and the flat plate obey the same slope (logarithmic scale), but cross the line  $\eta = 1$  not at  $\phi = 3$ , as for the spherical case, but at values of  $\phi = 2$  and  $\phi = 1$ , respectively

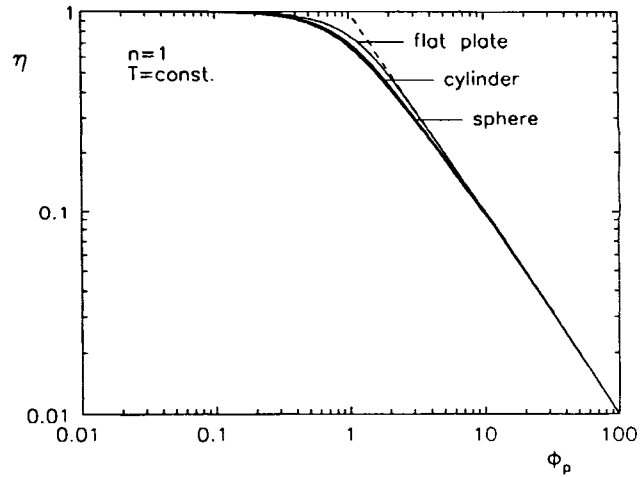


**Figure 6.** Effectiveness factor  $\eta$  as a function of the generalized Thiele modulus  $\phi_p$  for different pellet geometries. Influence of intraparticle diffusion on the effective reaction rate (isothermal, first order, irreversible reaction).

(see eqs 51–53). In this range of the Thiele modulus pore diffusion controls the overall reaction rate. As a consequence, the concentration of reactant  $A_1$  tends to approach zero towards the center of the pellet (see Fig. 4). This situation is typical for very active catalysts or catalysts with small pore size, low porosity, and/or large pellet diameter.

The observation that the slope of the asymptotic solution for  $\eta(\phi)$  in Fig. 5 seems to be unaffected by the catalyst geometry, suggests that the dependence of the effectiveness factor on the Thiele modulus might be described by a single asymptotic relationship, valid for arbitrary pellet shapes. In fact, Aris [3] could show that the curves of  $\eta(\phi)$  for sphere, infinite cylinder, and infinite flat plate fall together almost perfectly when a generalized Thiele modulus  $\phi_p$  is introduced, which is related to the ratio of the pellet volume to the external pellet surface (corresponding to the Sauter diameter) as a characteristic length scale of diffusion:

$$\phi_p = \frac{V_p}{S_p} \sqrt{\frac{k_c c_b^{n-1}}{D_c}} \quad (54)$$

Figure 6 shows the effectiveness factor for any of the three different pellet shapes as a function of the generalized Thiele modulus  $\phi_p$ . It is obvious that for larger Thiele moduli (i.e.  $\phi_p > 3$ ) all curves can be described with acceptable accuracy by a common asymptote  $\eta = 1/\phi_p$ . The largest deviation between the solutions for the individual shapes occurs around  $\phi_p \approx 1$ . However, even for the extremely different geometries of the flat plate and the sphere, the deviation of the efficiency

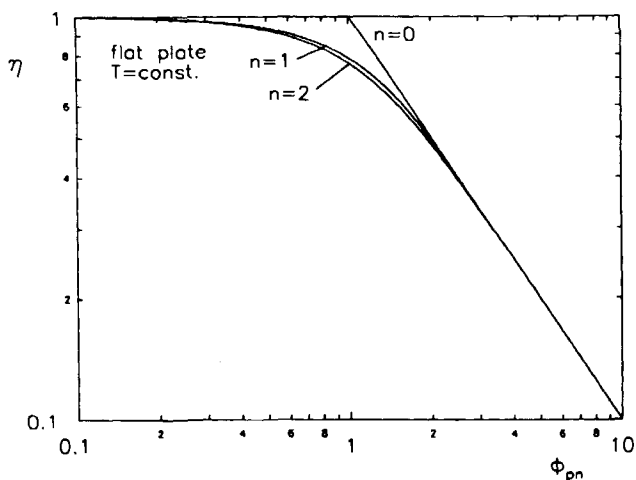


**Figure 7.** Effectiveness factor  $\eta$  as a function of the generalized Thiele modulus  $\phi_{pn}$  for different reaction orders. Influence of intraparticle diffusion on the effective reaction rate (isothermal, irreversible reaction in a flat plate).

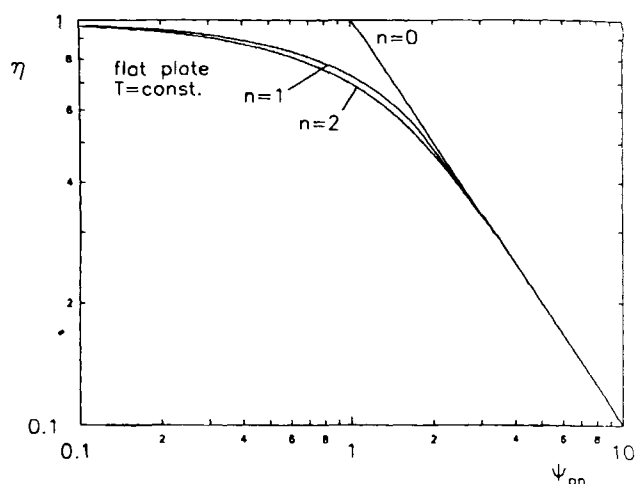


**Figure 8.** Effectiveness factor  $\eta$  as a function of the generalized Weisz modulus  $\psi_{pn}$  for various reaction orders. Influence of intraparticle diffusion on the effective reaction rate (isothermal, irreversible reaction in a flat plate).

factor is still below 10%. From a physico-chemical point of view, this can be explained by the fact that in the range of strong intraparticle diffusion limitation only a thin layer of the outer pellet shell participates in the chemical reaction. In this situation, the local surface curvature is relatively unimportant [31].

The above considerations can also be extended in a simple way to different reaction orders, if the modulus  $\phi_p$  is further modified. In this sense Petersen [85] defined a generalized Thiele modulus  $\phi_{pn}$  which takes into account the effects of the pellet shape as well as the influence of the reaction order:

$$\phi_{pn} = \frac{V_p}{S_p} \sqrt{\frac{n+1}{2} \frac{k c_b^{n-1}}{D_c}} = \phi_p \sqrt{\frac{n+1}{2}} \quad (55)$$

In Fig. 7 the effectiveness factor is shown as a function of the generalized Thiele modulus  $\phi_{pn}$  for different reaction orders (flat plate). From this figure, it is obvious that, except for the case of a zero order reaction, the curves agree quite well over the entire range of interest. The asymptotic solution  $\eta = 1/\phi_{pn}$  is valid for any reaction order and for values of the modulus  $\phi_{pn} > 3$ .

However, in many practical situations the problem exists that effective rate constants and activation energies have been derived on the basis of laboratory experiments. The question arises then as to whether or not these parameters are influenced by transport effects. With the relations given so far, this question cannot be answered yet, since according to its definition by eq 27 the Thiele modulus is based on the intrinsic rate constant  $k$ . This problem can be solved by introducing a new modulus, which in contrast to  $\phi$  only contains observable (effective) quantities, and thus can

be determined without any knowledge of the intrinsic kinetics. This modulus is known as Weisz modulus  $\psi$ . It is defined as the ratio of the effective pseudohomogeneous reaction rate versus the maximum effective rate of diffusion at the external pellet surface (eq 56). Physically, the Weisz modulus can be looked at as the ratio of the time constants of diffusion  $\tau_D = R^2/D_c$  and reaction  $\tau_R = c_b/r_c$ .

$$\psi = \frac{r_c R^2}{D_c c_b} \quad (56)$$

Equation 56 can be used only for spherical catalyst pellets and first order, irreversible reactions. However, for convenience, and in analogy to the Thiele modulus, a generalized modulus  $\psi_{pn}$  can be defined as well which applies to arbitrary pellet shape and arbitrary reaction order. This is defined as

$$\psi_{pn} = \left( \frac{V_p}{S_p} \right)^2 \frac{m+1}{2} \frac{r_c}{D_c c_s} \quad (57)$$

Comparing eqs 56 and 27, and recalling the definition of the effectiveness factor according to eq 40, yields the following simple relationship between the Thiele modulus and the Weisz modulus:

$$\psi = \eta \phi^2; \quad \psi_{pn} = \eta \phi_{pn}^2 \quad (58)$$

A plot of the effectiveness factor from eq 53 against the Weisz modulus  $\psi_{pn}$  from eq 58 gives the curve depicted in Fig. 8 for a first order reaction (flat plate). On the basis of this diagram, the effectiveness factor can be determined easily once the effective reaction rate and the effective diffusivity are known.

### 6.2.3.2 Film and Pore Diffusion in an Isothermal Pellet

The situation becomes more complicated when the reaction rate is already high enough to cause the reactant concentration to drop significantly across the external boundary layer. In this case, the combined effects of intraparticle and interphase mass transfer must be considered. If we again restrict our considerations to reactions that are accompanied only by minor heat effects, we may still assume a constant temperature inside the catalyst pellet, and within the boundary layer. Hence, no solution of the enthalpy balance (eq 33) is required. Moreover, the mass balance (eq 32) takes exactly the same form as in the previous case of negligible interphase concentration gradients, thus giving rise to an identical general solution (see Section 6.2.3.1). Again, for the simplest case of a first order, irreversible reaction, the solution is given by eq 47.

However, the boundary condition at the external pellet surface is now defined by eq 36 instead of eq 38. As a consequence, a different expression for the integration constant  $C_1$  results, which is not only a function of the Thiele modulus  $\phi$ , but also depends on the Biot number for mass transport  $Bi_m$ . Hence, a complete characterization of this problem already requires two parameters.

After determining  $C_1$  from eq 36 and rearranging, the following solution for the normalized concentration inside the pellet is obtained:

$$f = \frac{\sinh(\phi x)}{x \sinh(\phi)} \left[ \frac{Bi_m \tanh(\phi)}{\phi + (Bi_m - 1) \tanh(\phi)} \right] \quad (59)$$

Differentiation of this expression with respect to  $x$ , and substitution of the derivative at the point  $x = 1$  into eq 42 yields the final relationship for determining the catalyst efficiency:

$$\eta = \frac{3}{\phi} \left[ \frac{1}{\tanh(\phi)} - \frac{1}{\phi} \right] \left[ \frac{Bi_m \tanh(\phi)}{\phi + (Bi_m - 1) \tanh(\phi)} \right] \quad (60)$$

By comparing this relationship with the solution for the effectiveness factor in absence of interphase concentration gradients (eq 51), it becomes obvious that the overall effectiveness factor  $\eta$  can be expressed as the product of separate pore and external (film) effectiveness factors:

$$\eta = \eta_{\text{pore}} \eta_{\text{ext}} \quad (61)$$

where

$$\eta_{\text{pore}} = r_c/r_s \quad \text{and} \quad \eta_{\text{ext}} = r_s/r_b$$

The first term in parentheses in eq 60, together with the preceding factor  $3/\phi$ , is equivalent to eq 51; this represents the pore effectiveness factor  $\eta_{\text{pore}}$ , whereas the second expression in parentheses denotes the external effectiveness factor  $\eta_{\text{ext}}$ .

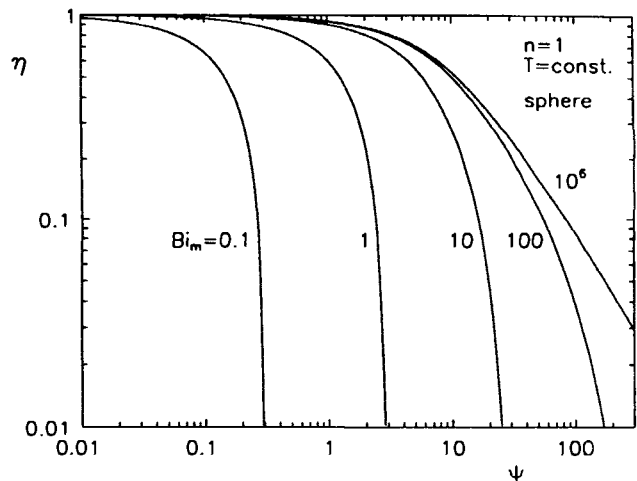


**Figure 9.** Effectiveness factor  $\eta$  as a function of the Weisz modulus  $\psi$ . Combined influence of intraparticle and interphase mass transfer on the effective reaction rate (isothermal, first order, irreversible reaction in a sphere, Biot number  $Bi_m$  as a parameter).

For practical purposes however, eq 60 again suffers from the disadvantage that the Thiele modulus must be specified in order to calculate the catalyst efficiency. Thus, the intrinsic rate constant must be known. In this situation, instead of directly plotting eq 60, it is more convenient to relate the effectiveness factor to the Weisz modulus, calculated from eq 58. For selected values of the Biot number  $Bi_m$ , such a diagram is given in Fig. 9.

From this figure, it can be concluded that the reduction of the effectiveness factor at large values of  $\psi$  becomes more pronounced as the Biot number is decreased. This arises from the fact that the reactant concentration at the external pellet surface drops significantly at low Biot numbers. However, a clear effect of interphase diffusion is seen only at Biot numbers below 100. In practice,  $Bi_m$  typically ranges from 100 to 200. Hence, the difference between the overall and pore effectiveness factor is usually small. In other words, the influence of intraparticle diffusion is normally by far more crucial than the influence of interphase diffusion. Thus, in many practical situations the overall catalyst efficiency may be replaced by the pore efficiency, as a good approximation.

### 6.2.3.3 Film and Pore Diffusion Together with Interphase Heat Transfer

When treating fast reactions which are accompanied by a substantial release or consumption of heat (e.g. oxidation or dehydrogenation reactions), one often has

to take into account a possible limitation of the heat transfer between the catalyst-pellet and the surrounding fluid phase, besides the combined effects of film and pore diffusion, since this may cause the catalyst to operate at a temperature significantly above or below the temperature of the bulk fluid phase.

However, if the effective thermal conductivity of the catalyst material is high enough, intraparticle temperature gradients will be absent, irrespective of whether or not external temperature differences exist, and the pellet itself may still be treated as isothermal. Assuming a constant temperature inside the pellet, it is sufficient to focus on the heat transfer across the external boundary layer instead of solving the general enthalpy balance given by eq 33. Therefore, we utilize the condition that the amount of heat generated (or consumed) inside the catalyst pellet per unit time, in a stationary mode of operation, must equal the amount of heat transported through the external fluid film per unit time. For a spherical catalyst,

$$\frac{4}{3}\pi R^3 r_e(-\Delta H_R) = 4\pi R^2 h_f(T_s - T_b) \quad (62)$$

Replacing the effective reaction rate  $r_e$  in eq 62 with the effectiveness factor, multiplied by the intrinsic reaction rate under bulk fluid phase conditions, and dividing both sides of the resulting equation by  $4\pi R^2$  yields the relationship

$$T_s = T_b + \frac{R}{3} \frac{\eta k c_b^n (-\Delta H_R)}{h_f} \quad (63)$$

which allows the unknown temperature at the external pellet surface to be determined. With the nondimensional numbers already introduced, this equation can be rewritten in dimensionless form:

$$\theta_s = 1 + \frac{\beta}{3 Bi_h} \eta \phi^2 = 1 + \frac{\beta}{3 Bi_h} \psi \quad (64)$$

Supposing that heat and mass are transported by an identical convective mechanism, the catalyst temperature, given by eq 64, can also be expressed as a function of the Biot number for mass transport  $Bi_m$ . For this purpose, the equivalence of the heat and mass transport factors ( $j$ -factors) is utilized [19]:

$$j_h = j_m = \frac{h_f}{\rho c_p} Pr^{2/3} = \frac{k_f}{u} Sc^{2/3} \quad (65)$$

Here,  $Pr$  is the Prandtl number:

$$Pr = \frac{\nu}{a} \quad (66)$$

where  $a = \lambda/\rho c_{pl}$  and  $Sc$  is the Schmidt number:

$$Sc = \frac{\nu}{D} \quad (67)$$

The quotient, Schmidt number divided by Prandtl number, which is known as the Lewis number, can be

interpreted as the ratio of the thermal diffusivity to the molecular diffusivity of the fluid:

$$Le = \frac{Sc}{Pr} = \frac{a}{D} \quad (68)$$

According to eqs 65 and 68, the ratio  $h_f/k_f$  can be expressed using the Lewis number:

$$\frac{h_f}{k_f} = \rho c_p Le^{2/3} \quad (69)$$

By substituting  $h_f$  from eq 69 into eq 64, the Biot number for heat transport can be replaced by the Biot number for mass transport, when additionally a modified Prater number  $\beta^*$  is introduced:

$$\beta^* = \frac{c_b(-\Delta H_R)}{\rho c_p T_b Le^{2/3}} \quad (70)$$

The unknown normalized pellet temperature  $\theta_s$  is now given by

$$\theta_s = 1 + \frac{\beta^*}{3 Bi_m} \psi \quad (71)$$

According to eq 71 the temperature of the catalyst pellet can be calculated as a function of the Weisz modulus, for given values of the modified Prater number and the Biot number for mass transport.

To derive an equation for determining the overall effectiveness factor, we first introduce a Thiele modulus  $\phi^*$  which is related to the unknown surface temperature  $T_s$ :

$$\begin{aligned} (\phi^*)^2 &= R^2 \frac{k(T_s) c_b^{n-1}}{D_c} = R^2 \frac{k(T_b) c_b^{n-1}}{D_c} \frac{k(T_s)}{k(T_b)} \\ &= \phi^2 e^{\gamma(1-(1/\theta_s))} \end{aligned} \quad (72)$$

Replacing  $\phi$  in eq 32 with  $\phi^*$  transforms the mass balance into the same form as in the isothermal case. For a first-order irreversible reaction the solution of the isothermal problem has already been derived (see Section 6.2.3.2). The reactant concentration is obtained analogous to eq 59 as a function of the radial coordinate, for given values of  $\phi^*$  and  $Bi_m$ . We then have:

$$f = \frac{\sinh(\phi^* x)}{x \sinh(\phi^*)} \left[ \frac{Bi_m \tanh(\phi^*)}{\phi^* + (Bi_m - 1) \tanh(\phi^*)} \right] \quad (73)$$

The derivative of  $f$ , calculated at the point  $x = 1$ , is now substituted into eq 42, resulting in the following expression for the catalyst efficiency:

$$\eta = \frac{3}{\phi^2} \left[ \frac{\phi^*}{\tanh(\phi^*)} - 1 \right] \left[ \frac{Bi_m \tanh(\phi^*)}{\phi^* + (Bi_m - 1) \tanh(\phi^*)} \right] \quad (74)$$

By substituting  $\phi^*$  from eq 72 into eq 74,  $\phi$  can be eliminated. The overall effectiveness factor can then be expressed in a more illustrative form:



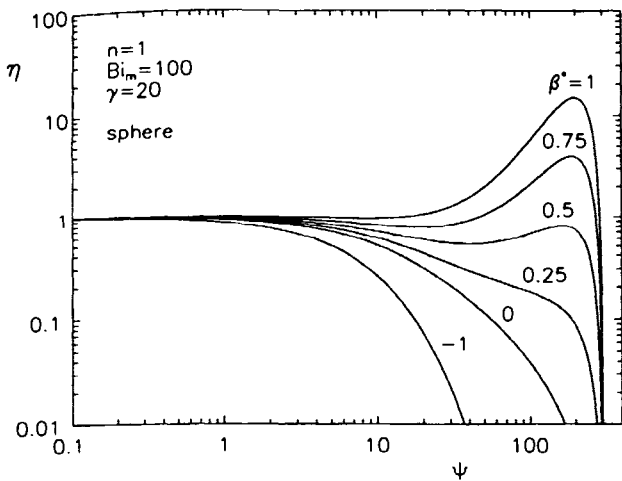


**Figure 10.** Effectiveness factor  $\eta$  as a function of the Weisz modulus  $\psi$ . Combined influence of intraparticle and interphase mass transfer and interphase heat transfer on the effective reaction rate (first order, irreversible reaction in a sphere, Biot number  $Bi_m = 100$ , Arrhenius number  $\gamma = 20$ , modified Prater number  $\beta^*$  as a parameter).

$$\eta = \frac{3}{\phi^*} \left[ \frac{1}{\tanh(\phi^*)} - \frac{1}{\phi^*} \right] e^{\gamma(1-1/\theta_s)} \times \left[ \frac{Bi_m \tanh(\phi^*)}{\phi^* + (Bi_m - 1)\tanh(\phi^*)} \right] \quad (75)$$

The first term in parentheses in eq 75, together with the preceding factor  $3/\phi$ , denotes the isothermal intraparticle effectiveness factor (see eq 51). The second term in parentheses is identical to the isothermal interphase effectiveness factor (see eq 60). The exponential factor between the two terms describes the influence of the deviating catalyst temperature.

Again, eq 75 cannot be used immediately to calculate the overall effectiveness factor, since the modulus  $\phi^*$ , which is related to the unknown catalyst temperature, can only be determined when the overall efficiency has been specified (see eqs 71 and 72). Therefore, both sides of eq 74 are multiplied by  $\phi^2$ , resulting in an expression which relates the Weisz modulus  $\psi$  to the modulus  $\phi^*$ . Then, for a given value of  $\phi^*$ , the corresponding value of  $\psi$  is calculated, and from  $\psi$  the unknown catalyst temperature  $\theta_s$  (eq 71). This temperature is substituted into eq 72 to obtain the corresponding value of the Thiele modulus  $\phi$ . Dividing  $\psi$  by  $\phi^2$  finally yields the overall effectiveness factor which is then plotted against  $\psi$ .

This procedure yields the curves depicted in Fig. 10 for fixed values of  $Bi_m$  and  $\gamma$ , and the modified Prater number  $\beta^*$  as a parameter. From this figure, it is obvious that for exothermal reactions ( $\beta^* > 0$ ) and large values of the Weisz modulus, effectiveness factors well above unity may be observed. The reason for this is that the decline of the reactant concentration over the

external boundary layer and further towards the center of the catalyst pellet might be overcompensated by an increase of temperature. This happens when the heat flux transferred from the pellet surface across the boundary layer to the surrounding fluid per unit time is considerably smaller than the amount of heat generated inside the pellet per unit time. Then, the effective reaction rate is higher than it would be expected under the conditions in the bulk fluid phase.

Whether or not such an effect occurs in a practical situation and if so, how pronounced it will be, depends basically on the modified Prater number  $\beta^*$  (see eq 71), that is on the maximum amount of heat effectively produced inside the pellet, as compared to the maximum amount of heat transported across the external boundary layer. Additionally, the Arrhenius number plays an important role which, as a normalized form of the activation energy, is a measure for the increase of the reaction rate due to an increase of temperature.

With the Thiele modulus, the Biot number for mass transport, the modified Prater number, and the Arrhenius number, four dimensionless numbers are necessary to fully characterize this problem.

Any of the curves in Fig. 10, which refer to different values of the modified Prater number  $\beta^*$ , tend to approach a certain limiting value of the Weisz modulus for which the overall effectiveness factor obviously becomes infinitely small. This limit can be easily determined, bearing in mind that the effective reaction rate can never exceed the maximum interphase mass transfer rate (the maximum rate of reactant supply) which is obtained when the surface concentration approaches zero. To show this, we formulate the following simple mass balance, analogous to eq 62:

$$\frac{4}{3} \pi R^3 r_c = 4 \pi R^2 k_f (c_b - c_s) \quad (76)$$

Dividing the above equation by the external pellet surface  $4\pi R^2$  and the bulk concentration  $c_b$ , and solving for  $c_s/c_b$  gives

$$\frac{c_s}{c_b} = 1 - \frac{r_c}{k_f \frac{3}{R} c_b} = 1 - \frac{\eta k(T_b) c_b^n}{k_f \frac{3}{R} c_b} \quad (77)$$

Substituting the second Damköhler number  $Da_{II}$ , which is defined as the ratio of the intrinsic reaction rate to the maximum rate of reactant supply,

$$Da_{II} = \frac{k(T_b) c_b^n}{k_f \frac{3}{R} c_b} \quad (78)$$

into eq 77, yields

$$\frac{c_s}{c_b} = 1 - \eta Da_{II} \quad (79)$$

The maximum effective reaction rate is obtained for the limiting value of  $c_s = 0$ . This means that the product of the effectiveness factor and the second Damköhler number can never exceed unity. A comparison of the definition of the Weisz modulus (eq 56) with the definition of  $Da_{II}$  (eq 78) gives the equivalence

$$\psi - \eta\phi^2 - \frac{r_c R^2}{c_b D_c} - \frac{r_c}{k_f \frac{3}{R} c_b} \frac{3 k_f R}{D_c} = \eta Da_{II} 3 Bi_m \quad (80)$$

or shorter:

$$\eta Da_{II} = \frac{\psi}{3 Bi_m} \quad (81)$$

Hence, as an alternative to Fig. 10, the overall effectiveness factor can also be plotted against the product  $\eta Da_{II}$ , which again contains only measurable quantities, and which, as already stated, can never exceed unity. This leads to the representation shown in Figs. 11 and 12 for two different values of the Arrhenius number.

#### 6.2.3.4 Film and Pore Diffusion Together with Interphase and Intraparticle Heat Transfer

When a fast reaction is highly exothermic or endothermic and, additionally, the effective thermal conductivity of the catalyst is poor, then significant temperature gradients across the pellet are likely to occur. In this case the mass balance (eq 32) and the enthalpy balance (eq 33) must be simultaneously solved using the corresponding boundary conditions (eqs 34–37), to obtain the concentration profile of the reactant and the temperature profile inside the catalyst pellet. The exponential dependence of the reaction rate on the temperature thereby imposes a nonlinear character on the differential equations which rules out an exact analytical treatment. Approximate analytical solutions [83, 99] as well as numerical solutions [13, 100, 110] of eqs 32–37 have been reported by various authors.

In the most general case, i.e. when intraparticle and interphase transport processes have to be included in the analysis, the effectiveness factor depends on five dimensionless numbers, namely the Thiele modulus  $\phi$ , the Biot numbers for heat and mass transport  $Bi_h$  and  $Bi_m$ , the Prater number  $\beta$ , and the Arrhenius number  $\gamma$ . Once external transport effects can be neglected, the number of parameters reduces to three, because the Biot numbers then approach infinity and can thus be discarded.

In Fig. 13, typical curves for the effectiveness factor as a function of the Thiele modulus  $\phi$  are given for a first order, irreversible reaction in a spherical catalyst pellet. These curves have been obtained numerically by Weisz and Hicks [110], for the case of negligible inter-

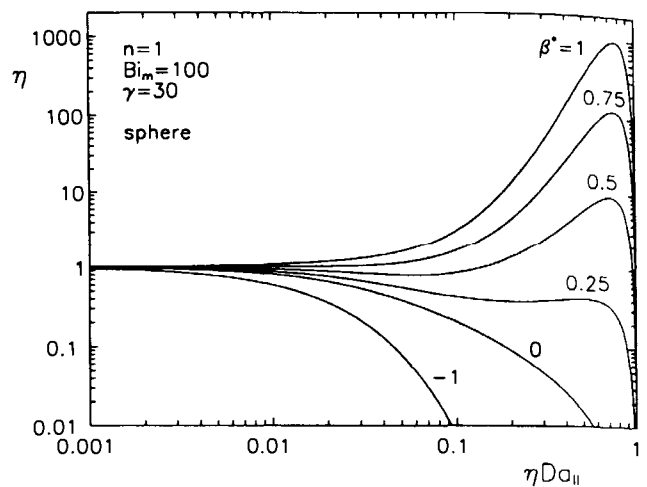


Figure 11. Effectiveness factor  $\eta$  as a function of the observable variable  $\eta Da_{II}$ . Combined influence of intraparticle mass transfer and interphase heat and mass transfer on the effective reaction rate (first order, irreversible reaction in a sphere, Biot number  $Bi_m = 100$ , Arrhenius number  $\gamma = 30$ , modified Prater number  $\beta^*$  as a parameter).

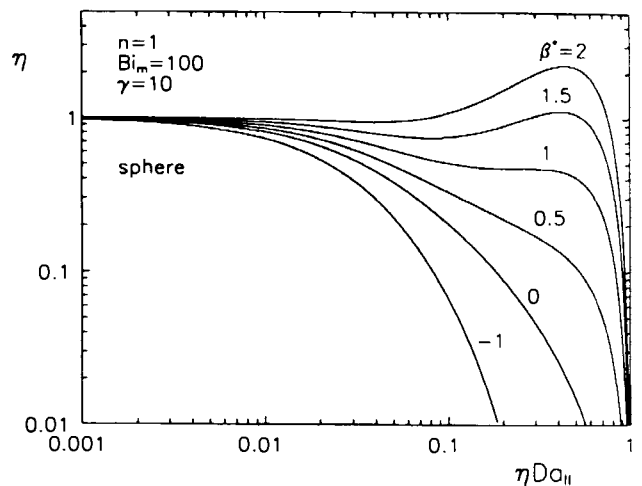
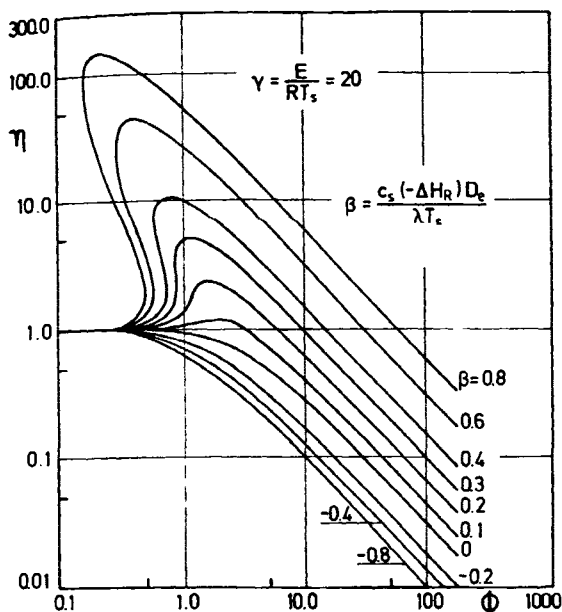


Figure 12. Effectiveness factor  $\eta$  as a function of the observable variable  $\eta Da_{II}$ . Combined influence of intraparticle mass transfer and interphase heat and mass transfer on the effective reaction rate (first order, irreversible reaction in a sphere, Biot number  $Bi_m = 100$ , Arrhenius number  $\gamma = 10$ , modified Prater number  $\beta^*$  as a parameter).

phase concentration and temperature gradients. In the light of the previous results, it comes as no surprise that under nonisothermal conditions inside the catalyst pellet effectiveness factors above unity are encountered (exothermic reactions). This happens when the heat of reaction, generated inside the porous pellet, accumulates due to a poor thermal conductivity of the catalyst material. The temperature inside the pellet then increases until finally a steady state between heat generation and heat removal is reached, at a temperature



**Figure 13.** Effectiveness factor  $\eta$  as a function of the Thiele modulus  $\phi$ . Combined effects of intraparticle heat and mass transfer on the effective reaction rate (first order, irreversible reaction in a sphere, Arrhenius number  $\gamma = 20$ , Prater number  $\beta$  as a parameter, adapted from Weisz and Hicks [110]).

level somewhat above the temperature at the external pellet surface. The corresponding rise of the reaction rate towards the center of the catalyst pellet may overcompensate the influence of the decreasing reactant concentration, thus producing a net increase of the reaction rate over the intrinsic rate which would be expected under the conditions in the bulk fluid phase.

This effect will be particularly emphasized at small values of the Thiele modulus where the intrinsic rate of reaction and the effective rate of diffusion assume the same order of magnitude. At large values of  $\phi$ , the effectiveness factor again becomes inversely proportional to the Thiele modulus, as observed under isothermal conditions (Section 6.2.3.1). Then the reaction takes place only within a thin shell close to the external pellet surface. Here, controlled by the Arrhenius and Prater numbers, the temperature may be distinctly higher than at the external pellet surface, but constant further towards the pellet center.

However, whereas effectiveness factors above unity under nonisothermal conditions can be explained quite easily, the observation of multiple steady states is a new and unexpected feature. These arise at small values of  $\phi$ , provided the reaction is substantially exothermic and, additionally, has a high activation energy. This means that, for a single value of the Thiele modulus, several possible solutions for the steady state overall effectiveness factor may exist (operating points), usually up to three. The middle operating point is normally unstable. Whenever the temperature and/or the

reactant concentration is increased by small-scale fluctuations of the operating conditions, the reaction is accelerated and the amount of heat additionally produced by the reaction inside the pellet per unit time surpasses the amount of heat that can be transported to the external pellet surface via effective heat conduction. The consequence is a further rise of the temperature inside the pellet. The system will reach a new stationary state between heat production and heat removal when finally approaching the upper operating point. The opposite case is observed when a sudden drop of the temperature and/or the reactant concentration occurs. The temperature decreases steadily until the lower operating point is reached.

Whether the upper or the lower operating point will prevail under stationary conditions, depends on the direction from which the stationary state is approached. When the system reaches the stationary point from higher temperatures, it will arrive at the upper operating point. If, however, the approach comes from lower temperatures, the system will operate at the lower stationary point. In the case that the operating points are rather close together, a cyclic switching between the upper and lower operating points is also possible (ignition/quenching behavior).

Whether or not multiple steady states will appear, and how large the deviation of the effectiveness factors between both stable operating points will be, is determined by the values of the Prater and Arrhenius numbers. Effectiveness factors above unity generally occur when  $\beta > 0$  (exothermal reactions). However, for the usual range of the Arrhenius number ( $\gamma = 10\text{--}30$ ), multiple steady states are possible only at larger Prater numbers (see Fig 13). For further details on multiple steady states, the interested reader may consult the monograph by Aris [6] or the works of Luss [69, 70].

As stated above, instead of plotting the effectiveness factor against the Thiele modulus  $\phi$  which contains the unknown, intrinsic rate constant, it is often more convenient to relate it to the observable Weisz modulus  $\psi$ . This leads to the representation given in Fig. 14 for the same situation as depicted in Fig. 13. The dashed portions of the curves indicate the regions in which a unique solution of the effectiveness factor does not exist, corresponding to the regions of multiple solutions in Fig. 13.

Figures 13 and 14 refer to the situation where only intraparticle transport effects influence the observable reaction rate. However, a similar behavior is observed if, besides intraparticle heat and mass transport processes, the heat and mass transfer between the catalyst pellet and the bulk fluid phase is also considered. More information about this situation can be found, for example, in the works of Cresswell [26], McGreavy and

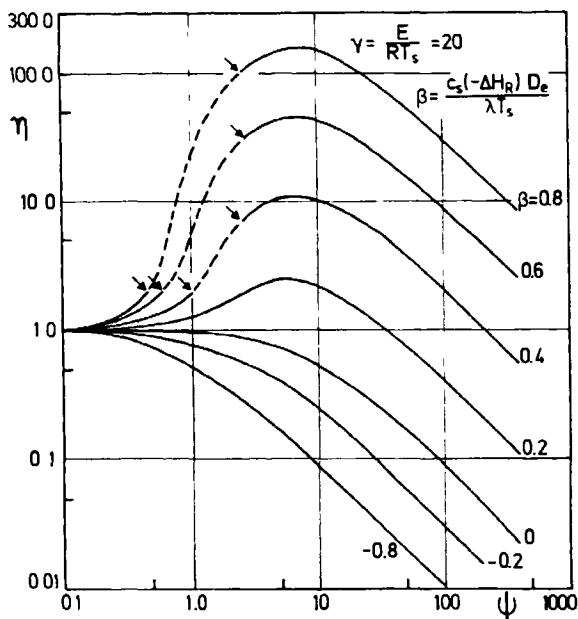


**Figure 14.** Effectiveness factor  $\eta$  as a function of the observable Weisz modulus  $\psi$ . Combined effects of intraparticle heat and mass transfer on the effective reaction rate (first order, irreversible reaction in a sphere, Arrhenius number  $\gamma = 20$ , Prater number  $\beta$  as a parameter, adapted from Weisz and Hicks [110]).

Cresswell [72, 73], Kehoe and Butt [62], Butt [11, 12], and Hatfield and Aris [43].

Although multiplicities of the effectiveness factor have also been detected experimentally, these are of minor importance practically, since for industrial processes and catalysts, Prater numbers above 0.1 are less common. On the contrary, effectiveness factors above unity in real systems are frequently encountered, although the dominating part of the overall heat transfer resistance normally lies in the external boundary layer rather than inside the catalyst pellet. For mass transfer the opposite holds: the dominating diffusional resistance is normally located within the pellet, whereas the interphase mass transfer most frequently plays a minor role (high space velocity).

The fact that the effective heat conduction within the catalyst pellet normally is not the crucial process in determining the excess temperature of the catalyst pellet can be illustrated by analyzing the contribution of the interphase temperature gradient to the total excess temperature. To demonstrate this, we first eliminate the common reaction term occurring in the mass and enthalpy balances (eqs 32 and 33):

$$\frac{d^2\theta}{dx^2} + \frac{b}{x} \frac{d\theta}{dx} = -\beta \left( \frac{d^2f}{dx^2} + \frac{b}{x} \frac{df}{dx} \right) \quad (82)$$

Upon introducing the new variables  $u = fx$  and  $v = \theta x$  (see eqs 43 and 44), this equation simplifies to

$$\frac{d^2v}{dx^2} = -\beta \frac{d^2u}{dx^2} \quad (83)$$

Integrating eq 83 twice and utilizing the boundary conditions at the pellet center,

$$\left. \frac{du}{dx} \right|_{x=0} = x \left( \frac{df}{dx} \right)_{x=0} + f = f \quad (84)$$

$$\left. \frac{dv}{dx} \right|_{x=0} = x \left( \frac{d\theta}{dx} \right)_{x=0} + \theta = \theta \quad (85)$$

and, at the external pellet surface,

$$u(x=1) = f_s \quad (86)$$

$$v(x=1) = \theta_s \quad (87)$$

gives the following simple relation between  $\theta$  and  $f$ :

$$\theta - \theta_s = \beta(f_s - f) \quad (88)$$

From eq 88 we conclude that the maximum temperature difference inside the pellet is related to the point at which the maximum concentration difference is observed, i.e. where the reactant concentration drops to zero ( $f = 0$ ). Therefore, we have a maximum internal temperature difference  $\Delta T_{\text{pore}}$  of

$$\Delta T_{\text{pore}} = \beta T_b \frac{c_s}{c_b} \quad (89)$$

The concentration ratio  $c_s/c_b$  in eq 89 can be expressed as a function of the observable variable  $\eta Da_{11}$  (eq 79). Hence,

$$\Delta T_{\text{pore}} = \beta T_b (1 - \eta Da_{11}) \quad (90)$$

The interphase temperature difference is given by eq 71 as

$$\Delta T_{\text{ext}} = T_b \frac{\beta^*}{3 Bi_m} \psi = T_b \beta^* \eta Da_{11} \quad (91)$$

If we denote by  $r_{\Delta T}$  the ratio of the interphase temperature difference  $\Delta T_{\text{ext}}$  versus the total excess temperature of the catalyst  $\Delta T_{\text{ext}} + \Delta T_{\text{pore}}$ , we finally obtain, after some rearrangement,

$$r_{\Delta T} = \frac{\Delta T_{\text{ext}}}{\Delta T_{\text{ext}} + \Delta T_{\text{pore}}} = \frac{r_\beta \eta Da_{11}}{1 + \eta Da_{11} (r_\beta - 1)} \quad (92)$$

where  $r_\beta$  is the ratio of the Prater numbers or Biot numbers:

$$r_\beta = \frac{\beta^*}{\beta} = \frac{Bi_m}{Bi_h} \quad (93)$$

The term  $r_{\Delta T}$  from eq 92 is depicted in Fig. 15 as a function of the observable variable  $\eta Da_{11}$ , for different values of  $r_\beta$ . When  $r_\beta = 1$ , a linear rise of the curve is obtained. However, with increasing  $r_\beta$ , the external temperature difference dominates already at low values of  $\eta Da_{11}$ .

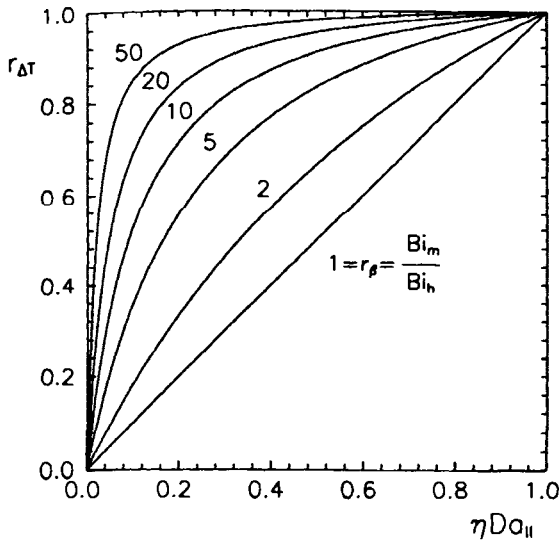


**Figure 15.** Ratio of interphase temperature difference versus total intra-interphase temperature difference  $r_{\Delta T}$  as a function of the observable variable  $\eta Da_{II}$  (spherical catalyst, ratio of Biot numbers  $r_{\beta} = Bi_m / Bi_h$  as a parameter, after Carberry [19]).

In reality, the Biot number for mass transport in most cases is considerably higher than the Biot number for heat transport, i.e. the ratio  $r_{\beta}$  is frequently larger than 40–50 [19]. This means that the catalyst pellet can usually be treated as isothermal, at a temperature level which is controlled by the interphase heat transfer resistance. However, this leads to a reduction of the general problem to the case which has already been treated in the previous section.

### 6.2.3.5 External Heat and Mass Transfer

A special type of fluid–solid catalyzed reaction is obtained when either the reaction rate is so fast that the reactants become completely exhausted at the external catalyst surface (i.e. at very high reaction temperatures) or when the catalyst is nonporous. Then, pore diffusion and effective heat conduction inside the pellet need not be considered. Thus, the problem is reduced to a treatment of the coupled interphase heat and mass transfer.

The conservation equations for mass and enthalpy for this special situation have already been given with eqs 76 and 62. As there is no diffusional mass transport inside the pellet, the overall catalyst effectiveness factor is identical to the film effectiveness factor  $\eta_{ext}$  which is defined as the ratio of the effective reaction rate under surface conditions divided by the intrinsic chemical rate under bulk fluid phase conditions (see eq 61). For an  $n$ th order, irreversible reaction we have the following expression:

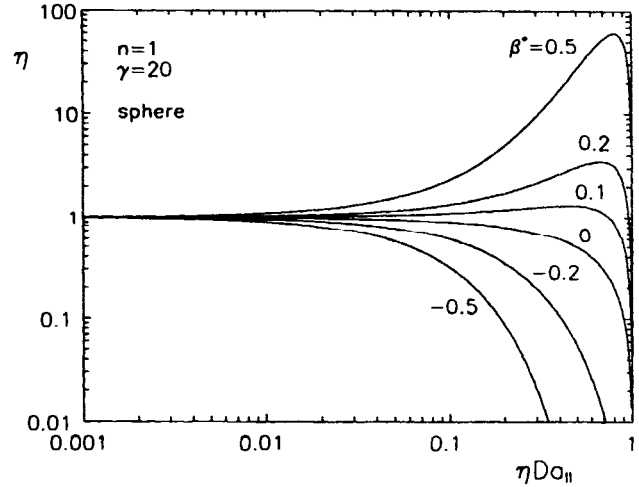


**Figure 16.** Effectiveness factor  $\eta$  as a function of the observable variable  $\eta Da_{II}$ . Combined influence of interphase heat and mass transfer on the effective reaction rate (first order, irreversible reaction in a sphere, modified Prater number  $\beta^*$  as a parameter).

$$\eta = \eta_{ext} = \frac{k(T_s)c_s^n}{k(T_b)c_b^n} = \left( \frac{k(T_s)}{k(T_b)} \right) \left( \frac{c_s}{c_b} \right)^n \quad (94)$$

According to this equation, the effectiveness factor is controlled by two terms, namely the ratio of the rate constants  $k_s/k_b$ , governed by the temperature difference over the external fluid film, and the ratio of the surface concentration versus the bulk concentration  $c_s/c_b$ . Defining equations for both of these terms have already been given with eqs 71 and 79. Substituting these into eq 94 and using eq 81, we obtain the effectiveness factor for arbitrary reaction order as a function of the observable variable  $\eta Da_{II}$ :

$$\eta = (1 - \eta Da_{II})^n e^{\gamma(1 - 1/(1 + \beta^* \eta Da_{II}))} \quad (95)$$

Figure 16 shows an effectiveness factor diagram for a first order, irreversible reaction which has been calculated from eq 95 for various values of the modified Prater number  $\beta^*$ . From this figure, it can be seen that for exothermal reactions ( $\beta^* > 0$ ) effectiveness factors above unity may be observed when the catalyst operates at a temperature substantially above the bulk fluid phase temperature. This is caused by the limited heat transfer between the pellet and the surrounding fluid. The crucial parameters controlling occurrence and size of this effect are again the modified Prater number and the Arrhenius number.

The reaction order also has a great influence on the effectiveness factor. This is illustrated in Fig. 17 for the isothermal case ( $\beta^* = 0$ ). Obviously, the effectiveness factor drops with increasing reaction order at a given value of  $\eta Da_{II}$ . For reactions with a negative order,

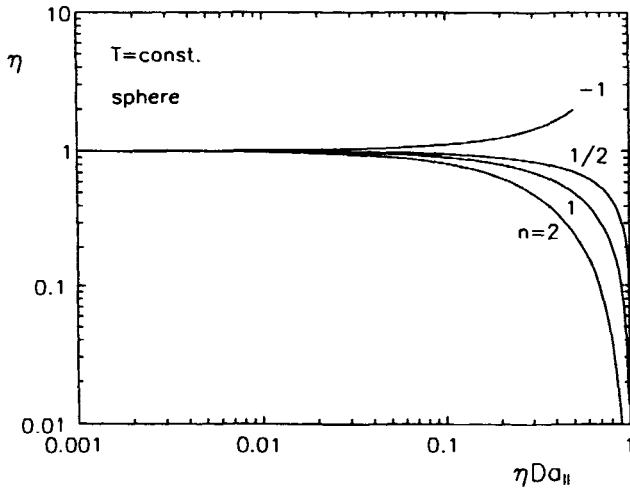


**Figure 17.** Effectiveness factor  $\eta$  as a function of the observable variable  $\eta Da_{II}$ . Influence of interphase mass transfer on the effective reaction rate (isothermal, irreversible,  $n$ th order reaction in a sphere, reaction order  $n$  as a parameter).

effectiveness factors above unity are possible even under isothermal conditions.

### 6.2.3.6 Use of Complex Rate Expressions

In the previous sections, only simple, irreversible reactions have been considered whose kinetics were assumed to obey a simple power rate law of the type  $r = kc^n$ . The reason for this assumption was to have analytical solutions for most of the important problems in order to demonstrate the key effects in a clear manner. Moreover, many heterogeneously catalyzed reactions, although not strictly obeying a power rate law, can nevertheless be described by this kind of rate expression for practical purposes, at least when the concentration range to be covered is not too wide.

In reality however, situations also exist where a more complex form of the rate expression has to be applied. Among the numerous possible types of kinetic expressions two important cases will be discussed here in more detail, namely rate laws for reversible reactions and rate laws of the Langmuir–Hinshelwood type. Basically, the purpose of this is to point out additional effects concerning the dependence of the effectiveness factor upon the operating conditions which result from a more complex form of the rate expression. Moreover, without going too much into the details, it is intended at least to demonstrate to what extent the mathematical effort required for an analytical solution of the governing mass and enthalpy conservation equations is increased, and how much a clear presentation of the results is hindered whenever complex kinetic expressions are necessary.

To keep the discussion as simple as possible, the view is restricted to the isothermal case without interphase concentration and temperature gradients (i.e. intraparticle diffusion and reaction only). For a more detailed treatment of complex kinetic expressions the monographs by Satterfield [91], Aris [5], and Emig [31] may be consulted.

### A Simple Reversible Reaction

We start with the simplest reversible reaction  $A_1 \rightleftharpoons A_2$ , where both the forward and the reverse reaction follow a first-order rate law. The net reaction rate of such a process is given by

$$r = k^+ c_1 - k^- c_2 \quad (96)$$

This type of reaction has been investigated by Smith and Amundsen [95] and Carberry [14]. Without derivation it may be stated that under isothermal conditions the same solution for the effectiveness factor is obtained as in the case of an irreversible reaction if a modified Thiele modulus  $\phi_{\text{rev}}$  is introduced [91]:

$$\phi_{\text{rev}} = R \sqrt{\frac{k^+}{D_{1,e}} + \frac{k^-}{D_{2,e}}} \quad (97)$$

If the effective diffusivities  $D_{1,e}$  and  $D_{2,e}$  do not differ markedly, then eq 97 can be expressed in a simplified form by introducing the equilibrium constant  $K_{\text{cq}} = k^+/k^-$ :

$$\phi_{\text{rev}} = R \sqrt{\frac{k^+(1 + 1/K_{\text{cq}})}{D_c}} \quad (98)$$

From this expression it can be seen that the modulus  $\phi_{\text{rev}}$  transforms to the standard Thiele modulus  $\phi$  (eq 27) when the equilibrium constant approaches infinity. Additionally, it is obvious that the effectiveness factor decreases when, at a given value of the forward rate constant  $k^+$ , the reverse reaction becomes increasingly important (Fig. 18). This holds for all types of reversible reactions [31, 91]. Therefore, the effectiveness factor of a truly reversible reaction might be considerably overestimated if the reaction is treated as irreversible.

This problem arises even at low conversion, because although the product concentration may then be negligible at the external pellet surface, in general this is not the case inside the pellet, unless diffusion effects upon the effective reaction rate are absent. Therefore, a difference normally exists between the effectiveness factor of irreversible and reversible reactions which becomes increasingly important as the equilibrium constant  $K_{\text{cq}}$  of the reaction is shifted to smaller values.

At large values of  $\phi_{\text{rev}}$  (i.e.  $\phi_{\text{rev}} > 10$ ), the proportionality  $\eta \sim 1/\phi_{\text{rev}}$  (see eq 51) for the given example of

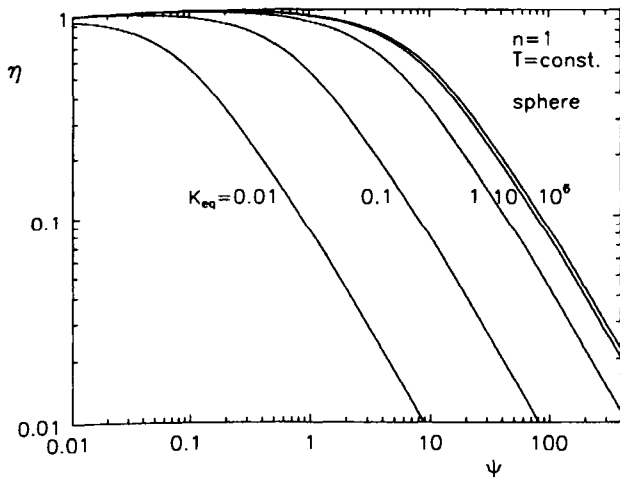


**Figure 18.** Effectiveness factor  $\eta$  of a first-order reversible reaction versus the Weisz modulus  $\psi$  (related to the forward rate constant  $k^+$ ). Influence of intraparticle diffusion on the effective reaction rate (isothermal reaction in a sphere, equal diffusivities  $D_{1,e} = D_{2,e}$ , equilibrium constant  $K_{eq}$  as a parameter).

a first-order reaction (eq 98) dictates a decrease of the catalyst efficiency by the factor  $(1 + 1/K_{eq})^{1/2}$ .

The mathematical effort increases considerably when the influence of a second reactant is considered. We then have a reaction of the type  $A_1 + A_2 \rightleftharpoons A_3 + A_4$ . According to eq 99 the net reaction rate for this general case of a bimolecular equilibrium reaction is a function of four different concentrations:

$$r = k^+ c_1 c_2 - k^- c_3 c_4 \quad (99)$$

Assuming a flat plate geometry Maymo and Cunningham [75] developed a relationship for calculating the effectiveness factor for reactions of the above type. This depends on the Thiele modulus and the equilibrium constant of the reaction, but additionally also on the stoichiometric ratio of the reactants and their effective diffusivities. In the most general case eight parameters have to be specified to determine the effectiveness factor. Even if a single common effective diffusivity can be used to describe the diffusion of the various reactants inside the porous pellet with sufficient accuracy, there still remains a five-parameter equation. Therefore, a graphical representation of the results is not very illustrative and hence has been omitted here. Moreover, the dependence of the effectiveness factor on the Weisz modulus and the equilibrium constant is very similar to the previously treated case of a first-order reversible reaction.

The main contribution of the work of Maymo and Cunningham [75] therefore is a criterion allowing a decision on whether or not a reversible reaction obeying a truly second-order rate law may be represented in simplified form by an irreversible, pseudofirst-order expression. It turns out that the error in the effective-

ness factor, associated with such a simplification, will be smaller than 10% whenever the product of the normalized concentration and the normalized diffusivity of the second reactant  $E_2 D_2$  is larger than or equal to 2, where  $E_2$  and  $D_2$  are defined by  $E_2 = c_{2,s}/c_{1,s}$  and  $D_2 = D_{2,e}/D_{1,e}$ .

Finally, it is worth noting that, according to Carberry [19], heat transfer effects are only of minor importance in reversible reactions, since the effect of temperature on the equilibrium constant compensates at least partly for the effect of temperature on the rate constants. As an example, the temperature rise towards the pellet center, which is observed for exothermic equilibrium reactions, leads to a decrease of the equilibrium constant, but in addition also to an increase of the forward rate constant [91].

### B Simple Irreversible Reactions with Langmuir-Hinshelwood-Type Kinetics

Similar to reversible reactions, the mathematical treatment becomes more complicated if a Langmuir-Hinshelwood (Hougen-Watson) type kinetic expression is used. For the most simple case of an irreversible, monomolecular reaction  $A_1 \rightarrow$  products, the following rate law holds:

$$r = \frac{k p_1}{1 + K_1 p_1 + \sum_{i \neq 1} K_i p_i} \quad (100)$$

Roberts and Satterfield [87, 88] analyzed this type of reaction. On the basis of numerical calculations for a flat plate, these authors presented a solution in the form of effectiveness factor diagrams, from which the effectiveness factor can be determined as a function of the Weisz modulus as well as an additional parameter  $K p_{1,s}$  which considers the influence of the different adsorption constants and effective diffusivities of the various species [91]. The constant  $K$  involved in this parameter is defined as follows:

$$K = \frac{K_1 - D_{1,e} \sum_{i \neq 1} \frac{K_i v_i}{D_{i,e}}}{\omega} \quad (101)$$

where  $\omega$  is given by

$$\omega = 1 + \sum_{i \neq 1} K_i \left[ p_{i,s} + p_{1,s} v_i \frac{D_{1,e}}{D_{i,e}} \right] \quad (102)$$

Here,  $p_{1,s}$  is the partial pressure of reactant  $A_1$  at the external pellet surface and  $v_i$  is the stoichiometric coefficient of species  $i$  which is positive for all products and negative for the reactants. When the adsorption constant  $K_1$ , as well as all other adsorption constants

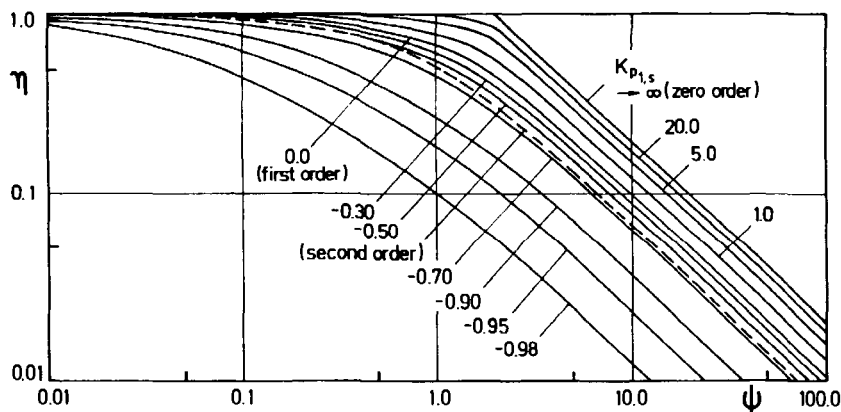


Figure 19. Effectiveness factor  $\eta$  of an irreversible monomolecular reaction with Langmuir–Hinshelwood-type kinetics versus the Weisz modulus  $\psi$ . Influence of intraparticle diffusion on the effective reaction rate (isothermal reaction in a flat plate,  $Kp_{1,s}$  as a parameter, adapted from Satterfield [91]).

$K_i$ , tend towards zero, the parameter  $Kp_{1,s}$  also approaches zero. We then have a simple first-order reaction. On the other hand, when  $Kp_{1,s}$  tends towards infinity, we get a simple zero-order expression. If at least one of the products is strongly adsorbed at the surface, negative values of  $Kp_{1,s}$  (i.e.  $K$ ) may result, which means that the reaction rate is inhibited. The smallest possible value of  $Kp_{1,s}$  is  $-1$ .

In Fig. 19, calculated curves of the effectiveness factor versus the Weisz modulus are shown for different values of  $Kp_{1,s}$  [91]. For comparison, this diagram also contains the curves corresponding to the results which apply to simple, irreversible power rate laws of zeroth, first and second order. From this figure it is obvious that a strong adsorption of at least one of the products leads to a similar decrease of the effectiveness factor as it is observed in the case of a reversible reaction.

Beside the convenient representation of the effectiveness factor as a function of the observable Weisz modulus, this diagram has the additional advantage that the error arising from an approximation of the truly hyperbolic form of the rate expression by a simple power rate law with integer order can be estimated.

Roberts and Satterfield [87, 88] also treated bimolecular reactions of the type  $A_1 + bA_2 \rightarrow$  products, described by Langmuir–Hinshelwood-type models. In this case, we have the rate expression

$$r = \frac{k p_1 p_2}{1 + K_1 p_1 + K_2 p_2 + \sum_{i \neq 1,2} K_i p_i} \quad (103)$$

Compared with the previous case of a monomolecular reaction, an additional parameter  $E$  is required to take into account the influence of the stoichiometric ratio of the reactants on the effectiveness factor. This is defined as

$$E = \left( \frac{-D_2 \epsilon p_{2,s}}{v_2 D_1 \epsilon p_{1,s}} \right) - 1 \quad (104)$$

In practice,  $A_1$  is chosen to designate that reactant that permits  $E$  to be zero or positive.  $E$  will be large whenever reactant  $A_2$  is present in large excess and/or has an effective diffusivity substantially larger than reactant  $A_1$ . It is therefore called the modified stoichiometric excess.

A special feature of bimolecular reactions is that  $\omega$ , defined by eq 102 and normally positive, might become negative when reactant  $A_2$  is adsorbed much more strongly than reactant  $A_1$  and when, additionally, the value of  $D_2 p_{2,s} / v_2$  is very small. For  $\omega < 0$ , the method of Roberts and Satterfield cannot be applied [91].

Inspection of the curves of the effectiveness factor versus the Weisz modulus for different values of  $Kp_{1,s}$  and  $E$  reveals two interesting phenomena when  $E > 0$  (Fig. 20) [87, 88, 91]. At first, for large values of  $Kp_{1,s}$  (10–100) effectiveness factors above unity may occur even though isothermal conditions prevail. This can be explained by the fact that the reaction rate given by eq 103 has a maximum for certain combinations of  $p_1$  and  $p_2$ . This maximum results from the assumption that the rate is proportional to the concentration of the adsorbed reactants  $A_1$  and  $A_2$  which compete for adsorption sites on the active (inner) surface. When, for example,  $A_1$  is adsorbed more strongly than  $A_2$ , then a raised partial pressure of  $A_1$ , at constant partial pressure of  $A_2$ , will lead to a displacement of  $A_2$  from the surface, and hence to a lowered reaction rate. By a quantitative analysis, it can be shown that effectiveness factors above unity will appear whenever  $Kp_{1,s}$  is greater than  $(E + 2)/E$  [91].

The second effect concerns the phenomenon that, for large values of  $E$  and  $Kp_{1,s}$ , a region is observed where



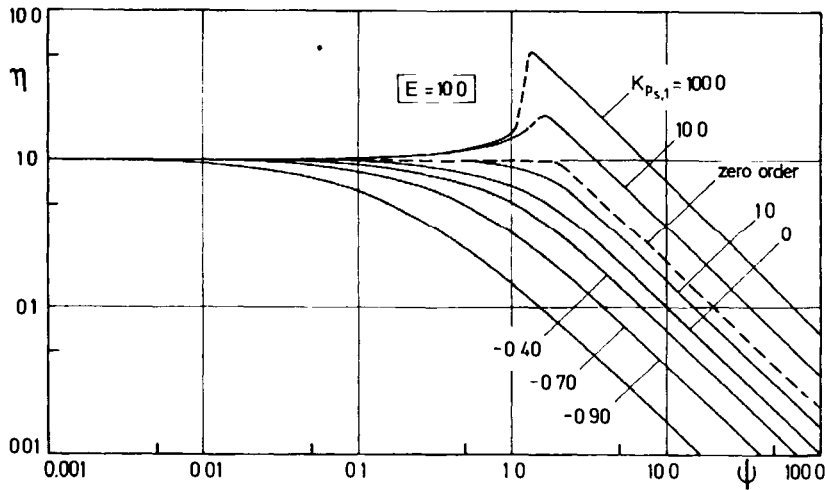


**Figure 20.** Effectiveness factor  $\eta$  for a bimolecular irreversible reaction with Langmuir–Hinshelwood-type kinetics versus the Weisz modulus  $\psi$ . Influence of intraparticle diffusion on the effective reaction rate (isothermal reaction in a flat plate, modified stoichiometric excess  $E = 10$ ,  $Kp_{1,s}$  as a parameter, adapted from Satterfield [91]).

the effectiveness factor is no longer a unique function of the Weisz modulus. This is in analogy to the multiplicities observed in the nonisothermal case for simple integer-order power rate laws (see Figs 13 and 14).

To give an example, Fig. 20 shows a diagram for  $E = 10$  and various selected values of  $Kp_{1,s}$ . The dashed lines indicate the range over which multiple steady states of  $\eta(\psi)$  occur. Here, by means of numerical methods it is not possible to determine a unique solution of the effectiveness factor of the pellet for given conditions at the external pellet surface [91]. Which operating point will be observed in a real situation again depends upon the direction from which the stationary state is approached [91].

### C Simple Reversible Reactions with Langmuir–Hinshelwood-Type Kinetics

The same approach as for irreversible Langmuir–Hinshelwood-type models can be extended to reversible reactions. Kao and Satterfield [61] developed a graphical method for monomolecular reversible reactions of the type  $A_1 \rightleftharpoons A_2$ , which is presented here as our last example. The method is based upon the following formulation of the net reaction rate:

$$r = \frac{k[p_1 - p_2(p_{1,\text{eq}}/p_{2,\text{eq}})]}{1 + K_1p_1 + K_2p_2 + \sum_{i \neq 1,2} K_i p_i} \quad (105)$$

where  $p_{1,\text{eq}}$  is the equilibrium partial pressure of reactant  $A_1$ , and  $\sum K_i p_i$  represents the inhibition of the reaction rate by adsorption of inert species. Compared to the irreversible case (eqs 100–102), which is unambiguously characterized by the Weisz modulus and the parameter  $Kp_{1,s}$ , two new parameters  $B$  and  $C$  are now required. Of these,  $B$  is an extension of the parameter

$Kp_{1,s}$  to the reversible case, whereas  $C$  is truly an additional parameter. They are defined as follows:

$$B = \frac{K(p_{1,s} - p_{1,\text{eq}})}{1 + Kp_{1,\text{eq}}} \quad (106)$$

$$C = \frac{p_{1,\text{eq}}}{p_{1,s}} \quad (107)$$

For  $p_{1,\text{eq}} = 0$  we have an irreversible reaction.  $B$  is then equivalent to the parameter  $Kp_{1,s}$ . Consequently,  $B$  ranges from a minimum value of  $-1$  to infinity (as well as  $Kp_{1,s}$ ), where  $B$  can never exceed  $Kp_{1,s}$ . Possible values of  $C$  range from 0 for an irreversible reaction to 1 when the reaction reaches the equilibrium and the net reaction rate approaches zero.

The effectiveness factor versus the Weisz modulus according to Kao and Satterfield [61] is shown in Fig. 21 for  $C = 0.5$  and different values of  $B$ . From this diagram, a similar behavior is seen as in the case of a simple, first order, reversible reaction (see Fig. 18): with decreasing value of  $B$ , the effectiveness factor is reduced. A decline of the effectiveness factor is also observed for a rise of the parameter  $C$ , which corresponds to a shift towards the chemical equilibrium, and hence to a reduction of the net reaction rate [91].

### 6.2.4 Temperature Dependence and Reaction Order of Transport-Limited Reactions

As stated in the introduction to this chapter, the observable activation energy and normally also the ob-

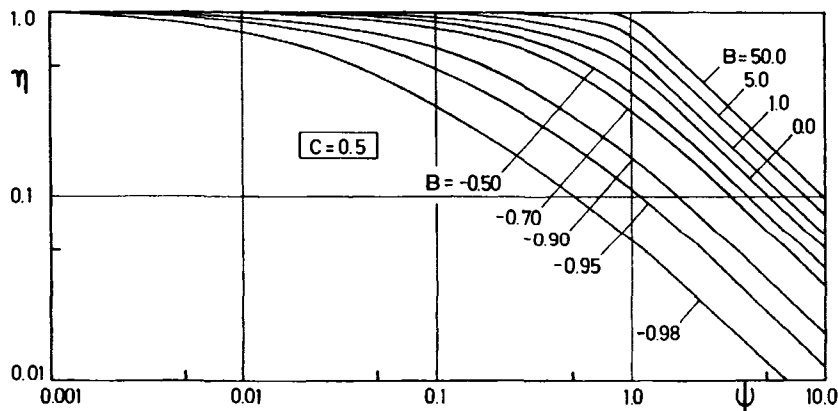


**Figure 21.** Effectiveness factor  $\eta$  of a monomolecular reversible reaction with Langmuir-Hinshelwood-type kinetics versus the Weisz modulus  $\psi$ . Influence of intraparticle diffusion on the effective reaction rate (isothermal reaction in a flat plate, equilibrium parameter  $C = 0.5$ ,  $B$  as a parameter, adapted from Satterfield [91]).

servable order of a heterogeneously catalyzed fluid-solid reaction, carried out on a porous catalyst, may differ from the respective properties of the intrinsic chemical reaction, whenever notable heat and mass transfer resistances exist (see Fig. 3). Therefore, the observable quantities are frequently termed effective or apparent properties, in order to provide a clear distinction from the true or intrinsic parameters of the pure chemical reaction. This aspect is now discussed in more detail, since it is of great importance for practical situations.

Two important restrictions must be introduced to allow a general representation of the temperature and concentration dependence of the effective reaction rate in the diffusion controlled regime. The first concerns the restriction to simple reactions, i.e. which can be described by only one stoichiometric equation. Whenever several reactions occur simultaneously, it is obvious that the individual activation energies and reaction orders may be influenced quite differently by transport effects. Thus, how the coupled system in such a case finally will respond to a change of temperature or concentration cannot be specified in a generally valid form.

The second necessary condition is isothermal operation. This is apparent from the results of Sections 6.2.3.3 and 6.2.3.4 where it has been shown that heat and mass transport may drive the effective reaction rate in opposite directions. Normally, mass transfer control of a reaction means a drop of the effective reaction rate (for positive reaction order), whereas a limited heat transfer in the case of an exothermal reaction will cause the temperature inside the catalyst pellet to rise, and will thus increase the effective reaction rate. When both effects occur simultaneously, an increase as well as a decrease of the effective rate may be observed, indicating either a lower or a higher apparent activation

energy (or reaction order). Again, this rules out a generalized treatment.

However, when the view is restricted to simple, irreversible reactions obeying an  $n$ th order power rate law and, if additionally, isothermal conditions are supposed, then—together with the results of Section 6.2.3—it can be easily understood how the effective activation energy and the effective reaction order will change during the transition from the kinetic regime to the diffusion controlled regime of the reaction.

#### 6.2.4.1 Intraparticle Diffusion

When the effective reaction rate is controlled by pore diffusion, then the asymptotic solution of the catalyst effectiveness factor as a function of the generalized Thiele modulus can be utilized (eq 108). This (approximate) relationship has been derived in Section 6.2.3.1. It is valid for arbitrary order of reaction and arbitrary pellet shape.

$$\eta = \frac{1}{\phi_{pn}}; \quad (\phi_{pn} > 3) \quad (108)$$

Combining eq 108 with the definition of the effectiveness factor (eq 40), the following expression for the effective reaction rate is obtained:

$$r_c = \eta r_b = \eta k c_b^n = (1/\phi_{pn}) k c_b^n \quad (109)$$

Substituting the generalized Thiele modulus from eq 55 yields

$$r_c = \frac{k c_b^n}{\frac{V_p}{S_p} \sqrt{\frac{n+1}{2} \frac{k c_b^{n-1}}{D_c}}} \quad (110)$$

The temperature dependence of the rate constant  $k$  is normally expressed by an Arrhenius law with the intrinsic activation energy  $E_A$ . In contrast, the temperature dependence of the effective diffusivity  $D_e$  is much weaker. Normally,  $D_e$  is obtained from

$$D_e = \frac{\varepsilon_p}{\tau} D \quad (111)$$

where  $\varepsilon_p$  denotes the void fraction (porosity) of the catalyst, and  $\tau$  is the empirical tortuosity factor. In practice, the diffusivity  $D$  is most often approximated either by the bulk diffusivity  $D_M$  or the Knudsen diffusivity  $D_K$ , depending on whether the diffusion process is governed by bulk or Knudsen diffusion, i.e. the characteristic pore size of the catalyst is substantially larger than or close to the mean free path of the molecules (see Section A.6.3). The dependence of  $D_M$  and  $D_K$  on temperature is usually described by

$$D_M \sim T^{3/2}; \quad D_K \sim T^{1/2} \quad (112)$$

As both  $\varepsilon_p$  and  $\tau$  are virtually uninfluenced by the temperature, the temperature dependence of  $D_e$  equals the temperature dependence of  $D_M$  or  $D_K$ , respectively. If we then formally introduce, instead of eq 112, and Arrhenius law with  $E_D$  representing the activation energy of the diffusion process, after some rearrangement, we obtain from eq 110 the following solution:

$$r_e = C e^{-(E_A + E_D)/2RT} c_b^{(n+1)/2} \quad (113)$$

where

$$C = \frac{k_0 D_{0,e}}{V_p / S_p \sqrt{(n+1)/2}} \quad (114)$$

From this relationship, it is obvious that the effective activation energy is given by the mean of the intrinsic activation energy of the catalyzed reaction  $E_A$  and the activation energy of the effective diffusion  $E_D$ . Additionally, it can be noticed that the effective reaction order  $(n+1)/2$  also tends to the average of the intrinsic reaction order  $n$  and the order of the diffusion process  $n_D = 1$ .

Because of the weak dependence of the effective diffusivity upon temperature (eq 112), which corresponds to an activation energy of less than 5–10 kJ mol<sup>-1</sup>,  $E_D$  can normally be neglected compared to  $E_A$ . Therefore, we obtain, as a rule of thumb, that the observable activation energy of an isothermal, simple,  $n$ th order, irreversible reaction will drop to roughly one half of the true value when the reaction is carried out under intraparticle diffusion control.

#### 6.2.4.2 Interphase Mass Transfer

If the effective rate is controlled by interphase mass transfer, then we may utilize the equivalence between the effective rate and the mass transfer rate:

$$r_e = \eta k c_b^n = k_f a (c_b - c_s) \quad (115)$$

Provided the interphase mass transfer resistance ( $1/k_f$ ) is sufficiently large, the reactant concentration at the external pellet surface will drop almost to zero. Thus, we may neglect the surface concentration  $c_s$  compared to the bulk concentration  $c_b$ . With  $c_s \rightarrow 0$  in eq 115, it is obvious that in this case the reaction will effectively follow a first-order rate law. Moreover, it is also clear that the temperature dependence of the effective reaction rate is controlled by the mass transfer coefficient  $k_f$ . This exhibits basically the same temperature dependence as the bulk diffusivity  $D_M$ , since the boundary layer thickness  $\delta$  is virtually not affected by temperature ( $k_f = D_M/\delta$ ). Thus, we have the rule of thumb that the effective activation energy of an isothermal, simple,  $n$ th order, irreversible reaction will be less than 5–10 kJ mol<sup>-1</sup> when the overall reaction rate is controlled by interphase diffusion.

### 6.2.5 Diagnostic Criteria and Experimental Methods for Estimating the Influence of Heat and Mass Transfer on the Effective Reaction Rate

In real situations, the question arises frequently as to whether or not a marked influence of heat and mass transfer on the observable reaction rate may be expected under certain reaction conditions. Quite often then, one has to deal with reactions obeying complex kinetics where either none or only a very cumbersome analytical solution is possible based upon the methods described in Section 6.2.3. For such cases a number of useful diagnostic criteria have been developed in the past, either derived from asymptotic solutions of the governing differential equations or from perturbation methods [86]. Most of these criteria have been explained in a detailed review by Mears [76]. More recent surveys of diagnostic transport criteria have been given by Butt [12] and by Madon and Boudart [74].

Typically, a criterion is derived on the premise that the net transport effect should not alter the true chemical rate by more than some arbitrarily specified amount, normally 5%. Because of the uncertainty involved in knowing some of the necessary parameters, and since they are based on approximate rather than exact solutions, the philosophy of using the criteria should be conservative. As a general rule, a clear decision on whether a reaction takes place under kinetic or diffusion control is possible only when the calculated value of a criterion is significantly above or below the respective limiting value (i.e. an order of magnitude), otherwise a more detailed analysis is recommended.

**Table 2.** Experimental diagnostic criteria for the absence of intraparticle transport effects in simple, irreversible reactions (power law kinetics only).

Application	No.	Criterion	Reference
Pore diffusion ( $T = \text{const.}$ )	1	$\frac{R^2 r_c}{D_c c_s} < 1; n = 1$	108
	2	$\frac{R^2 r_c}{D_c c_s} \begin{cases} < 6; & n = 0 \\ < 0.6; & n = 1 \\ < 0.3; & n = 2 \end{cases}$	109
	3	$\frac{R^2 r_c}{D_c c_s} < \frac{1}{ n }; n > 0$	50
Heat conduction ( $c = \text{const.}$ )	4	$\frac{R^2  \Delta H_R  r_c}{\lambda_c T_s} < \frac{R T_s}{E_A}$ less than 5% deviation of $\eta$ from $\eta_{\text{iso}}$	1
Pore diffusion and heat conduction (combined effect)	5	$\frac{R^2 r_c}{D_c c_s} < \frac{1}{ n - \gamma\beta }; n \neq \gamma\beta$	65
	6	$\frac{R^2 r_c}{D_c c_s} < 13; n \approx \gamma\beta$	76
	7	$ \gamma\beta  < 0.05n$ less than 5% deviation of $\eta$ from $\eta_{\text{iso}}$	76
	8	$\frac{R^2 r_c}{D_c c_s} e^{\left(\frac{n}{1-n}\right)} < 1$	110

Corresponding to the different use of the criteria, a subdivision into two groups appears to be useful. Experimental criteria are needed when the kinetics of the reaction under consideration are still unknown, i.e. neither the type of rate law nor the intrinsic values of the kinetic parameters have yet been identified. This may be the case during an early stage of a laboratory kinetic study when a new reaction is analyzed for the first time. Experimental criteria in general contain only directly observable quantities, i.e. the measured effective rate of reaction as well as some (effective) physical properties of the catalyst and the reaction mixture ( $R$ ,  $D_c$ ,  $\lambda_c$ , etc.). Therefore, these can be easily applied. However, experimental criteria suffer from the disadvantage to be sometimes less conservative when more complex kinetics prevail.

Theoretical criteria normally contain an explicit expression of the intrinsic chemical rate, and optionally also a measured value of the observed reaction rate. Thus, these criteria are useful only when the intrinsic kinetics are available, and one is, for example, interested in whether or not transport effects are likely to influence the performance of the catalyst as the operating conditions are changed. If it is not possible to generate a numerical solution of the governing differential equations, either due to a lack of time or to other reasons, then the use of theoretical criteria will not only save experimental effort, but also provide a more reliable estimation of the net transport influence on the observable reaction rate than simple experimental criteria can give, which do not contain any explicit

information about the true concentration and temperature dependence of the intrinsic rate.

### 6.2.5.1 Experimental Criteria

Table 2 lists most of the available experimental criteria for intraparticle heat and mass transfer. These criteria apply to single reactions only, where it is additionally supposed that the kinetics may be described by a simple  $n$ th order power rate law. The most general of the criteria, 5 and 8 in Table 2, ensure the absence of any net effects (combined) of intraparticle temperature and concentration gradients on the observable reaction rate. However, these criteria do not guarantee that this may not be due to a compensation of heat and mass transfer effects (this point has been discussed in the previous section). In fact, this happens when  $\gamma\beta \approx n$  [12].

As the most conservative policy, it may therefore be recommended to analyze separately whether the necessary conditions of isothermicity inside the pellet are met, for example by criteria 4 or 7. Then, when isothermal conditions can be ensured, criterion 3 may be used to check for concentration gradients.

A similar situation occurs when interphase transport effects are considered. Table 3 gives a survey of experimental criteria for the estimation of interphase transport effects. The most general relationship here is criterion 4. However, again it may be suggested that the separate isothermicity criterion 5 be used first, and

**Table 3.** Experimental diagnostic criteria for the absence of interphase, and combined intraparticle and interphase transport effects in simple, irreversible reactions (power law kinetics only).

Application	No.	Criterion	Reference
Interphase mass transfer ( $T = \text{const.}$ )	1	$\frac{\eta k_e}{k_f a} < 0.1; n = 1$	13
	2	$\frac{Rr_e}{k_f c_b} < \frac{0.15}{ n }; n \neq 0$	76
Interphase heat transfer ( $c = \text{const.}$ )	3	$ \chi  \frac{R \Delta H_R  r_e}{h_f T_b} < \frac{0.15 R T_b}{E_A}$ less than 5% deviation of $\eta$ from $\eta_{\text{iso}}$	77
Intra-/interphase heat and mass transfer (combined effect)	4	$\frac{R^2 r_e}{D_e c_b} < \frac{1 + 0.33 \gamma \chi}{ n - \gamma \beta (1 + 0.33 n w)}$ $w = \frac{Rr_e}{k_f c_b}$	77
	5	$ \gamma \beta + 0.3 n \gamma \chi  < 0.05 n$ less than 5% deviation of $\eta$ from $\eta_{\text{iso}}$	76

then, if isothermal conditions prevail, look for concentration gradients using relation 1 or 2 of Table 3 or, if necessary, the respective criteria of Table 2. The criteria given in Tables 2 and 3 apply to spherical catalyst pellets. If other geometries have to be treated, then the sphere radius may be replaced by the ratio of the pellet volume divided by the external pellet surface  $V_p/S_p$  [12].

At this point, it should be mentioned that there may be some doubt about how successful the nonisothermal criteria are at involving observable quantities only. This concerns the fact that in the nonisothermal case one has to specify the Arrhenius number which contains the true activation energy of the catalyzed reaction. The above statement would obviously define the true activation energy as a directly observable quantity in the nonisothermal criteria. However, this would presumably be an experimental value derived from studies in which intraparticle transport effects were absent, which is precisely what one is attempting to define [12].

### 6.2.5.2 Theoretical Criteria

Table 4 summarizes a number of well-known theoretical diagnostic criteria for the estimation of intraparticle transport effects on the observable reaction rate. Table 5 gives a survey of the respective criteria for interphase transport effects. It is quite obvious that these are more difficult to use than the simple experimental criteria given in Tables 2 and 3. In general, the intrinsic rate expression has to be specified and, additionally, either the first derivative of the intrinsic rate with respect to concentration (and temperature) at surface

conditions is required, or an integration of the rate expression must be performed.

In contrast to the experimental criteria of Tables 2 and 3, which apply to power law kinetics only, the criteria of Tables 4 and 5 can be used for arbitrary forms of rate expressions, although normally not for systems with more than one reaction. It is interesting to note that, in a recent publication, Gonzo [40] reports on the use of general theoretical criteria for the estimation of transport effects in networks of multiple catalyzed reactions.

Finally, at this point it should be recalled that when applying theoretical criteria one has to be aware of the fact that if concentration and temperature gradients occur simultaneously inside the catalyst pellet, both effects may compensate each other, and thus a combined heat and mass transport criterion alone may not be able to recognize that, in this case, the observed kinetics are actually influenced by transport effects.

### 6.2.5.3 Experimental Methods for Estimating the Influence of Heat and Mass Transfer Effects

To use the various criteria given in the previous section, some experimental data on the reacting system are necessary. These are the effective diffusivity of the key species in the pores of the catalyst, the heat and mass transfer coefficients at the fluid–solid interface, and the effective thermal conductivity of the catalyst. The accuracy of some of these parameters, which are usually obtained from known correlations, may sometimes be subject to question. For example, under labo-

**Table 4.** Theoretical diagnostic criteria for the absence of intraparticle transport effects (simple reactions with arbitrary kinetics).

Application	No.	Criterion	Reference
Pore diffusion ( $T = \text{const.}$ )	1	$\frac{R^2 r_e}{D_e} \left  \frac{dr(c)/dc}{r(c_s)} \right _{c=c_s} < 1$	50
Pore diffusion and heat conduction (combined effect)	2	$R \sqrt{\frac{r(c_{1,s}, c_{2,s}, \dots, T_s)}{D_e c_s}} < \sqrt{2} \left( \left  \int_0^1 r^*(\xi) d\xi \right  \right)^{1/2}$ $r^*(\xi) = \frac{r(c_1, c_2, \dots, T)}{r(c_{1,s}, c_{2,s}, \dots, T_s)}$	
	3	$\frac{R^2 r_e g(c_s)}{2 \int_{c_{eq}}^{c_s} D_e(c) g(c) dc} < 1$ $g(c)$ is an arbitrary rate expression without the pre-exponential factor of the main rate constant (but including the temperature variable part).	8
	4	$R < \frac{1}{2} \sqrt{\frac{3 D_e(1)}{100  dr(c, T)/dc _{(1)}}}$ The subscript (1) denotes the conditions at the external pellet surface.	4
	5	$R^2 \left  \frac{1}{D_e} \left( \frac{dr(c, T)}{dc} \right)_{c=c_s} - \frac{(-\Delta H)}{\lambda_e} \left( \frac{dT}{dT} \right)_{T=T_s} \right  < 1$	76
	6	$\left  \alpha \frac{R^2 r(c_s, T_s)}{D_e c_s} \left( \frac{dF(c/c_s)}{d(c/c_s)} \right)_{(c/c_s)=1} \right  < 0.05$ $\alpha = - \int_0^1 (n+1) f(x) A(x) x^n dx$ $F(c/c_s)$ denotes the dimensionless form of an arbitrary rate expression. $f(x)$ is a nonuniform, normalized catalyst activity distribution inside the pellet. $A(x)$ is an auxiliary function, subject to the following linear differential equation: $\frac{d^2 A}{dx^2} + \frac{n}{x} \frac{dA}{dx} = f(x)$ $n = 0, 1$ or $2$ for slab, cylinder or spherical catalyst geometry respectively.	39

**Table 5.** Theoretical diagnostic criteria for the absence of interphase transport effects (simple reactions with arbitrary kinetics).

Application	No.	Criterion	Reference
Interphase mass transfer ( $T = \text{const.}$ )	1	$\frac{R r_e}{k_f} \left  \frac{dr(c)/dc}{r(c_b)} \right _{c=c_b} < 0.15$	51
Interphase heat and mass transfer (combined effect)	2	$\left  \frac{\psi}{(n+1) Bi_m} \left( \frac{dF(c_s/c_b)}{d(c_s/c_b)} \right)_{(c_s/c_b)=1} \right  < 0.05$ $F(c_s/c_b)$ denotes the dimensionless form of an arbitrary rate expression. $n = 0, 1$ or $2$ for slab, cylinder or spherical catalyst geometry	39

ratory conditions of low particle Reynolds numbers the available correlations for estimating  $h_f$  and  $k_f$  are known to be less certain [22, 74]. To specify the effective diffusivity, not only the bulk and Knudsen diffusivities are required, but also the porosity and the tortuosity factor of the catalyst which normally have to be determined by separate experiments. Moreover, the diffusion process in the pores of the catalyst may be more complex than the usual assumption of a constant effective diffusivity throughout the pellet. That is, the catalyst may have a bimodal pore size distribution, the diffusional characteristics may change inside the pellet, or the diffusivity may depend on the concentration of the various species (see Section A.6.3).

Therefore, besides using diagnostic criteria, experimental tests are often carried out to estimate the influence of heat and mass transfer on the observed kinetics. Normally, to detect intraparticle diffusion effects, the catalyst pellet size is altered while the remaining operating conditions are kept unchanged. If a change of the catalyst activity is encountered, then this is said to be influenced by pore diffusion. However, if there is no change in activity upon increasing or decreasing the pellet size, one cannot say for sure that there are negligible intraparticle concentration gradients. A changing pellet size might cause distortions in the flow field which could affect contacting [74]. Moreover, if the catalyst has a bimodal pore size distribution, then the test may just indicate that there is no diffusional influence in the larger pores, but there still might be a concentration gradient in the small pores. Finally, when the reaction is strongly exothermic, concentration and temperature gradients may compensate each other.

To check for interphase transport effects in a flow system, the flow velocity is normally altered at constant space velocity. Then, if the reaction rate (or the conversion) remains constant, the influence of interphase diffusion is said to be negligible. A similar test is carried out in slurry reactors, where the constancy of the reaction rate is checked as the agitation of the slurry is increased. However, this test also suffers from several disadvantages. Again, if no change in the global reaction rate is observed, this might be due to a compensation of interphase heat and mass transfer effects, or even to the combined effect of interphase and intraparticle transport processes. In addition, at the low particle Reynolds numbers frequently encountered in laboratory reactors, the heat and mass transfer coefficients are quite insensitive to a change of the flow velocity, and hence the above diagnostic test may fail to indicate that the reaction rate actually is influenced by interphase concentration gradients.

To circumvent these disadvantages, Koros and Nowak [64] suggested a different type of criterion, which does not require any knowledge of the effective diffusivity or the rate expression, nor does it suffer from

the stated problems of the experimental tests. This criterion is based on making rate measurements on catalyst samples in which the concentration of the catalytically active material has been changed. The reaction rate, in the kinetic regime, is directly proportional to the concentration of the active material. Depending on the type of catalyst, this concentration may be defined as (a) the weight fraction, (b) the surface area, or (c) the surface moles of the active material per unit weight of catalyst. The Koros–Nowak criterion can then be explained by noting that in the kinetic regime the ratio of the measured reaction rate must equal the respective ratio of (a) weight fractions, (b) surface areas, or (c) turnover frequencies (defined as moles reacted per second per surface mole of the active material).

However, this criterion also has its limitations, as it is not always easy or possible at all to prepare catalyst samples with different concentration of the active material without simultaneously changing some other important properties of the catalyst, for example its diffusional characteristics. Details about the application of the Koros–Nowak criterion, as well as some methods how to prepare the required catalyst samples, can be found in the original paper by Koros and Nowak [64] or in a more recent article by Madon and Boudart [74].

### 6.2.6 Multiple Reactions (Selectivity Problem)

So far we have been concerned with simple reactions only, which can be properly described by specifying the conversion of a single key species. For this type of reaction it is possible to take into account the influence of heat and mass transport effects on the overall reaction rate by introducing a single factor, namely the catalyst effectiveness factor. The task then is to establish a functional or graphical relationship which allows determination of the effectiveness factor depending on the reaction conditions. This procedure apparently is successful when treating single reactions obeying simple integer power law kinetics, where an analytical solution of the governing differential equations can be achieved. However, when more complex kinetics must be considered, analytical treatment becomes increasingly difficult, and thus the main benefit of the effectiveness factor concept appears to be lost. The same holds for situations where additional effects, as for example a volume change due to reaction, or a more detailed description of the diffusion process (i.e. Stefan–Maxwell diffusion) have to be considered.

This becomes essentially evident when systems with more than one reaction have to be treated, where several products are formed from one or several reactants, and/or the desired product is unstable and will be further reacted by the catalyst. In all these cases, besides conversion, the selectivity of the catalyst becomes an issue, since the yield of the desired product is given finally by multiplying conversion and selectivity.

The question of selectivity, as influenced by diffusion effects, was addressed first by Wheeler [113], and has subsequently been subject to numerous studies which cannot be discussed in detail within the limited space available here. The books by Aris [5] and Butt [12] as well as a more recent chapter on diffusion–reaction interactions by Luss [70] may be consulted for a collection of relevant works in this field.

This section focuses on three basic types of catalyst selectivity, termed Type I, Type II, and Type III after Wheeler [113]. The main purpose of this is to demonstrate the fundamental effects of diffusion on the apparent selectivity of the catalyst, and to explain briefly the different situation, which is found when there is no longer a single functional, the effectiveness factor, to characterize the system, but the important questions concern the relative rates of reaction and how they are affected by diffusion.

### 6.2.6.1 Type I Selectivity

This may be explained by the following scheme:



where the catalyst promotes the conversion of two different reactants,  $A_1$  and  $A_2$  of which only conversion of  $A_1$  is desired. For the sake of simplicity we assume that both reactions are first order, isothermal conditions may prevail, and that no volume change due to reaction occurs. With  $k_1$  and  $k_2$  as the intrinsic rate constants, we may write the rate equations governing the reactor performance in absence of heat and mass transfer limitations as follows:

$$-\frac{dc_1}{dt} = k_1 c_1 \quad (116)$$

$$-\frac{dc_2}{dt} = k_2 c_2 \quad (117)$$

Dividing eq 116 by eq 117 yields

$$\frac{dc_1}{dc_2} = \frac{k_1 c_1}{k_2 c_2} \quad (118)$$

The ratio of the rate constants  $k_1/k_2$  in eq 118 is known as the intrinsic selectivity factor  $\Delta k$ . Integration of eq 118 yields an expression which relates the conversion of  $A_1$  to the conversion of  $A_2$ :

$$X_1 = 1 - \frac{c_1}{c_{1,0}} = 1 - \left( \frac{c_2}{c_{2,0}} \right)^{\Delta k} = 1 - (1 - X_2)^{\Delta k} \quad (119)$$

The point selectivity for Type I reactions is defined as the relative rate of the desired reaction, divided by the total rate of both reactions:

$$s_1 = \frac{r_1}{r_1 + r_2} = \frac{k_1 c_1}{k_1 c_1 + k_2 c_2} = \frac{1}{1 + \frac{1}{\Delta k} \frac{c_2}{c_1}} \quad (120)$$

Analogous to eq 120, the overall selectivity is given in terms of the number of moles of reactant  $A_1$  transformed into the desired product  $A_2$ , divided by the total number of moles converted ( $A_1$  and  $A_2$ ):

$$S_1 = \frac{c_{1,0} - c_1}{(c_{1,0} - c_1) + (c_{2,0} - c_2)} \quad (121)$$

Substituting eq 119 into this definition, and introducing the ratio of the initial concentrations  $\Delta c_0 = c_{2,0}/c_{1,0}$  for convenience, the following expression is obtained which relates the intrinsic overall selectivity to the conversion of reactant  $A_1$ :

$$S_1 = \frac{X_1}{X_1 + \Delta c_0 \left[ 1 - (1 - X_1)^{1/\Delta k} \right]} \quad (122)$$

If we now turn to the situation where intraparticle diffusion controls the overall reaction rate, eq 118 has to be rewritten in terms of the effective rather than the intrinsic reaction rates. However, because the two reactions are independent of each other, these may be treated separately. Hence, the intrinsic rate constants  $k_1$  and  $k_2$  are multiplied by the corresponding separate effectiveness factors. Instead of eq 118, this gives

$$\frac{dc_1}{dc_2} = \Delta k \frac{\eta_1 c_1}{\eta_2 c_2} \quad (123)$$

Assuming a spherical catalyst pellet and that interphase heat and mass transfer resistances can be neglected, substitution of eq 51 into eq 123 gives, upon rearrangement,

$$\frac{dc_1}{dc_2} = \Delta k \frac{\phi_2}{\phi_1} \left( \frac{\phi_2 \tanh(\phi_2) [\phi_1 - \tanh(\phi_1)]}{\phi_1 \tanh(\phi_1) [\phi_2 - \tanh(\phi_2)]} \right) \frac{c_1}{c_2} \quad (124)$$

We are interested mainly in how the selectivity will change when intraparticle diffusion controls the overall rate. Thus, we make use of the assumption  $\phi_j > 10$  which transforms eq 124 into the following simplified relationship:

$$\frac{dc_1}{dc_2} = \sqrt{\Delta k} \frac{c_1}{c_2} \sqrt{\frac{D_{1,c}}{D_{2,c}}} \quad (125)$$

Comparing eqs 118 and 125, we note that both share the same solution (eq 119) if we introduce an appar-



ent selectivity factor  $\Delta k_e$ , as defined in eq 126, and substitute this back into eq 125.

$$\Delta k_e = \sqrt{\Delta k} \sqrt{\frac{D_{1,e}}{D_{2,e}}} \quad (126)$$

Thus, we obtain the point and overall selectivities observed under intraparticle diffusion control by simply replacing the intrinsic selectivity factor  $\Delta k$  in eqs 120 and 122 with the apparent selectivity factor  $\Delta k_e$  given by eq 126.

If we now suppose that the effective diffusivities  $D_{1,e}$  and  $D_{2,e}$  are approximately the same, we have a selectivity factor  $\Delta k_e$  equal to the square root of the intrinsic selectivity factor  $\Delta k$ . The physical reason for this is that a smaller fraction of the internal surface of the catalyst is available to the faster of the two reactions, whereas a larger fraction is available to the slower reaction [55]. Therefore, provided the desired reaction is faster than the undesired one, Type I selectivity will be reduced when the reaction rate is influenced by intraparticle diffusion, otherwise it will be increased.

Similar results are obtained when, in addition to intraparticle diffusion, interphase mass transfer is considered. Instead of eq 51, in this case eq 60 may be substituted into eq 123, which then introduces the Biot numbers for mass transport of the reactants  $A_1$  and  $A_2$  as additional parameters. For large values of  $\phi_1$  and  $\phi_2$  (i.e.  $>10$ ) and, after some rearrangement,

$$\Delta k_e = \Delta k \frac{\phi_2}{\phi_1} \left( \frac{\phi_2/Bi_{m,1} + 1}{\phi_1/Bi_{m,2} + 1} \right) \quad (127)$$

Finally, when interphase mass transfer controls the overall rate, the ratio  $\phi/Bi_m$  may be sufficiently larger than unity, and hence eq 127 transforms to

$$\Delta k_e = \Delta k \left( \frac{\phi_2}{\phi_1} \right)^2 \frac{Bi_{m,2}}{Bi_{m,1}} = \frac{k_{f,2}}{k_{f,1}} \quad (128)$$

which indicates that the apparent point and overall selectivities, given by eqs 120 and 122, respectively, are no longer a function of the intrinsic rate constants  $k_1$  and  $k_2$ , but instead depend on the ratio of the mass transfer coefficients  $k_{f,1}/k_{f,2}$ . However, this is usually close to unity, which means that the overall selectivity is only affected by the ratio of the initial concentrations  $\Delta c_0$ . Figure 22 illustrates the influence of mass transfer effects on Type I selectivity by plotting the overall selectivity from eq 122, obtained under kinetic and diffusion control, respectively, versus the conversion of reactant  $A_1$ , for selected values of  $\Delta k$  and  $\Delta c_0$ .

An interesting opportunity is offered by eq 126. This concerns the dependence of the apparent selectivity factor on the ratio of the effective diffusivities. It has been stated above that this ratio in most practical cases

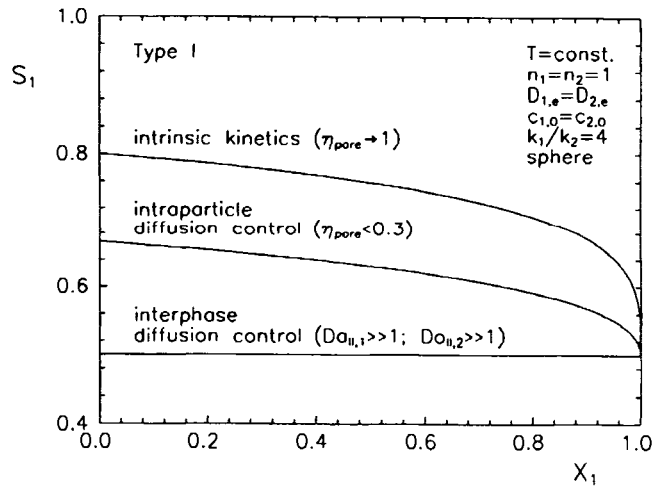


Figure 22. Variation of the apparent selectivity of a Type I reaction with conversion. Comparison of the results obtained under kinetic and diffusion control (isothermal operation, intrinsic selectivity factor  $\Delta k = 4$ , ratio of initial concentrations  $\Delta c_0 = 1$ , equal diffusivities  $D_{1,e} = D_{2,e}$ ).

using conventional catalysts, where bulk diffusion or Knudsen diffusion will govern the mass transport inside the porous pellet, will be more or less close to unity, depending on whether or not the molecular dimensions of the two reactants  $A_1$  and  $A_2$  will differ significantly. However, when the diffusion process is ruled by other mechanisms, i.e. configurational diffusion in zeolites, then the effective diffusivities of different reactants may vary by several orders of magnitude, a fact which suggests a great influence on selectivity (see Section 6.2.7).

So far it has been assumed that both reactions are first order and the pellet can be treated as isothermal. It may be obvious to note that under nonisothermal conditions the ratio of the intrinsic activation energies and, if necessary, the ratio of the external heat transfer coefficients will also affect the apparent selectivity of the catalyst. In addition, if the kinetic orders of the two reactions are different, this will also influence selectivity.

### 6.2.6.2 Type II Selectivity

This case is characterized by the following parallel reactions:



Again, we assume isothermal conditions and the absence of a volume change due to reaction. The governing rate equations for the disappearance of reactant  $A_1$

and the formation of the desired product  $A_2$  are then given by

$$-\frac{dc_1}{dt} = k_1 c_1^{n_1} + k_2 c_1^{n_2} \quad (129)$$

$$\frac{dc_2}{dt} = k_1 c_1^{n_1} \quad (130)$$

where  $k_1$  and  $k_2$  again denote the intrinsic rate constants of the two reactions. The point selectivity in this case is defined as the rate of formation of the desired product  $A_2$  divided by the total rate of consumption of reactant  $A_1$ :

$$s_{2,1} = \frac{k_1 c_1^{n_1}}{k_1 c_1^{n_1} + k_2 c_1^{n_2}} = \frac{1}{1 + \frac{1}{\Delta k} c_1^{n_2 - n_1}} \quad (131)$$

The overall selectivity is given in terms of the number of moles of product  $A_2$  formed from reactant  $A_1$  versus the total number of moles of reactant  $A_1$  consumed:

$$S_{2,1} = \frac{c_2 - c_{2,0}}{c_{1,0} - c_1} \quad (132)$$

In the following, we have to distinguish between two different cases, depending on whether the kinetic order of the two competing reactions is identical or not.

In the first case, when  $n_1 = n_2$ , the point selectivity, defined according to eq 131, becomes independent of the reactant concentration. Thus, the overall selectivity, obtained by integration of eq 131 over a range of conversions, will be identical to the point selectivity:

$$S_{2,1} = \frac{1}{X} \int_0^X \frac{k_1}{k_1 + k_2} dX' = \frac{k_1}{k_1 + k_2} \quad (133)$$

From eq 129 we note that if we define a new rate constant  $k'$  according to:

$$k' = k_1 + k_2 \quad (134)$$

and substitute this into eq 129, we essentially have a simple  $n$ th order, irreversible reaction describing the consumption of reactant  $A_1$ . Moreover, from eq 134 it is obvious then that a common effectiveness factor applies to both of the two reactions which can be obtained from the relations given in Section 6.2.3. Therefore, in this special case, Type II selectivity will not be affected by intraparticle diffusion. Instead, at each point in the pore structure both reactions will proceed with the same relative rate  $k_1/k_2$ , independent of the reactant concentration. The same holds for interphase concentration gradients.

In the second case, when  $n_1 \neq n_2$ , the point selectivity will be a function of the reactant concentration (see eq 131). Therefore, the apparent selectivity may be influenced by intraparticle diffusion, since a decrease of the reactant concentration towards the pellet center will have a different effect on the observable rates of

the two reactions. A higher order of reaction means a stronger influence of diffusion, hence Type II selectivity will be reduced as intraparticle diffusion becomes important whenever the desired reaction has a kinetic order higher than the undesired one; otherwise it will be improved.

Isothermal Type II problems with different orders of the two reactions have been treated by Roberts [89]. To give a rather simple example, which can be fully developed in terms of elementary functions, in the following we discuss the situation where the desired reaction is first order ( $n_1 = 1$ ), and the undesired reaction is zero order ( $n_2 = 0$ ). The intrinsic point selectivity, as obtained from eq 131, is then given by

$$s_{2,1} = \frac{1}{1 + \frac{1}{\Delta k} \frac{1}{c_1}} \quad (135)$$

When the catalyst operates under intraparticle diffusion control, the point selectivity can be expressed in terms of the net number of moles of product  $A_2$  effectively produced inside the pellet per unit time, divided by the net number of moles of reactant  $A_1$  consumed inside the pellet per unit time. Thus, we may write

$$\begin{aligned} s_{2,1} &= \frac{R_{2,e}}{-R_{1,e}} = \frac{r_{1,c}}{r_{1,e} + r_{2,e}} = 1 - \frac{r_{2,e}}{r_{1,e} + r_{2,e}} \\ &= 1 - \frac{\eta_2 r_{2,b}}{\eta_1 r_{1,b} + \eta_2 r_{2,b}} \end{aligned} \quad (136)$$

However, in contrast to the Type I selectivity problem treated in the previous section, the effectiveness factors  $\eta_1$  and  $\eta_2$  here cannot be determined separately, since the two parallel reactions share a common reactant, and do not obey the same kinetic order. Hence,  $\eta_1$  and  $\eta_2$  are not independent of each other. Therefore, instead of eq 40, we may define a more general effectiveness factor which is related to the rate of disappearance of reactant  $A_1$ :

$$\eta = \frac{R_{1,e}}{R_{1,b}} = \frac{\eta_1 r_{1,b} + \eta_2 r_{2,b}}{r_{1,b} + r_{2,b}} \quad (137)$$

Substituting this definition together with eq 20 into eq 136, we may express the apparent point selectivity in a more useful form:

$$S_{2,1} = 1 - \frac{k_2 \frac{1}{V_p} \int_{V_p} c_1^{n_2} dV'_p}{\eta(r_{1,b} + r_{2,b})} \quad (138)$$

We note that to determine the effectiveness factor  $\eta$ , we have to solve the mass balance for reactant  $A_1$  inside the porous pellet, which for the above chosen example ( $n_1 = 1$ ,  $n_2 = 0$ ) takes the following form:

$$\frac{d^2 f_1}{dx^2} + \frac{b}{x} \frac{df_1}{dx} = \phi_1^2 f_1 - \phi_2^2 \quad (139)$$

where  $\phi_1$  and  $\phi_2$  denote the Thiele moduli of the two reactions:

$$\phi_1 = R\sqrt{\frac{k_1}{D_{1,e}}}; \quad \phi_2 = R\sqrt{\frac{k_2}{D_{1,e}c_{1,b}}} \quad (140)$$

To keep the mathematics as simple as possible, we treat the catalyst pellet as an infinitely flat plate ( $b = 0$  in eq 139). The solution of eq 139 depends on whether the reactant concentration will drop to zero at some point  $x_0$  inside the pellet, in the case that the reaction rate is strongly influenced by diffusion, or will be finite everywhere in the pellet interior, if there is only a moderate effect of diffusion. This is a general feature of zero-order reactions which arises from the assumption that the reaction will proceed at a constant rate until the reactant is completely exhausted.

When  $f_1(x_0) = 0$  at  $0 < x_0 < 1$ , the rate of diffusion past the point  $x_0$  must be zero. Hence, we have to modify the boundary condition at the pellet center by replacing eq 34 with eq 142. For pellet surface ( $x = 1$ ),

$$f_1 = 1 \quad (141)$$

and, for pellet interior ( $x = x_0$ ),

$$\frac{df_1}{dx} = 0 \quad (142)$$

The general solution of eq 139, subject to the above boundary conditions, then becomes

$$f_1 = [1 + \Delta\phi] \frac{\cosh(\phi_1[x - x_0])}{\cosh(\phi_1[1 - x_0])} - \Delta\phi \quad (143)$$

where  $\Delta\phi$  denotes the ratio of the squared Thiele moduli  $\phi_2^2/\phi_1^2$ , which is equivalent to

$$\Delta\phi = \frac{\phi_2^2}{\phi_1^2} = \frac{k_2}{k_1 c_{1,b}} \quad (144)$$

By letting  $x_0 = 0$ , we note from eq 143 that  $f_1(x_0)$  will drop to zero at some point  $0 < x_0 < 1$  in the pellet interior only if the following condition is satisfied:

$$\phi_1 > \cosh^{-1}\left(1 + \frac{1}{\Delta\phi}\right) \quad (145)$$

For  $\phi_1$  in excess of this limiting value, we let  $f_1 = 0$  in eq 143 and solve for  $x_0$ . This leads to the following relationship for determining  $x_0$ :

$$x_0 = 1 - \frac{1}{\phi_1} \cosh^{-1}\left(1 + \frac{1}{\Delta\phi}\right) \quad (146)$$

For the case that eq 146 is not satisfied,  $x_0$  is equal to zero.

So far, we have obtained an explicit expression for the normalized concentration of reactant  $A_1$  inside the pellet. Analogously to eq 42, which relates the effectiveness factor of a spherical catalyst pellet to the nor-

malized concentration gradient of reactant  $A_1$  at the external pellet surface, and with eq 137, we have, for the flat plate geometry in our example,

$$\eta = \frac{1}{\phi_1^2(1 + \Delta\phi)} \left(\frac{df_1}{dx}\right)_{x=1} \quad (147)$$

To determine  $df_1/dx(x = 1)$ , we differentiate eq 143 with respect to  $x$ , and let  $x = 1$ :

$$\frac{df_1}{dx} \Big|_{x=1} = (1 + \Delta\phi)\phi_1 \tanh(\phi_1[1 - x_0]) \quad (148)$$

which is then substituted into eq 147. Hence, the effectiveness factor is given by

$$\eta = \frac{\tanh(\phi_1[1 - x_0])}{\phi_1} \quad (149)$$

If we substitute eq 149 into eq 138, and consider that the numerator on the right-hand side of this equation in the present case ( $n_2 = 0$ ) is equal to  $k_2(1 - x_0)$ , we obtain, for the point selectivity,

$$s_{2,1} = 1 - \frac{\phi_1(1 - x_0)}{\tanh(\phi_1[1 - x_0])} \frac{\Delta\phi}{(1 + \Delta\phi)} \quad (150)$$

As we are mainly interested in the situation where eq 145 is true, we eliminate  $x_0$  by substituting eq 146 into eq 150 and obtain

$$s_{2,1} = 1 - \frac{\cosh^{-1}\left(1 + \frac{1}{\Delta\phi}\right)}{\tanh\left[\cosh^{-1}\left(1 + \frac{1}{\Delta\phi}\right)\right]} \frac{\Delta\phi}{(1 + \Delta\phi)} \quad (151)$$

This expression can be simplified by utilizing the identity

$$\cosh^{-1}(y) = \operatorname{arctanh}[(y^2 - 1)^{1/2}/y]$$

which leads to the final equation for calculation of the apparent point selectivity under severe intraparticle diffusion control:

$$s_{2,1} = 1 - \frac{\Delta\phi \cosh^{-1}\left(1 + \frac{1}{\Delta\phi}\right)}{\sqrt{1 + 2\Delta\phi}} \quad (152)$$

If we now ask for the relative change in selectivity that occurs during the transition from the kinetic to the diffusion controlled regime, we divide eq. (152) by eq. (135), which specifies the point selectivity in absence of diffusion effects and obtain:

$$\Delta s_{2,1} = (1 + \Delta\phi) \left[ 1 - \frac{\Delta\phi \cosh^{-1}\left(1 + \frac{1}{\Delta\phi}\right)}{\sqrt{1 + 2\Delta\phi}} \right] \quad (153)$$

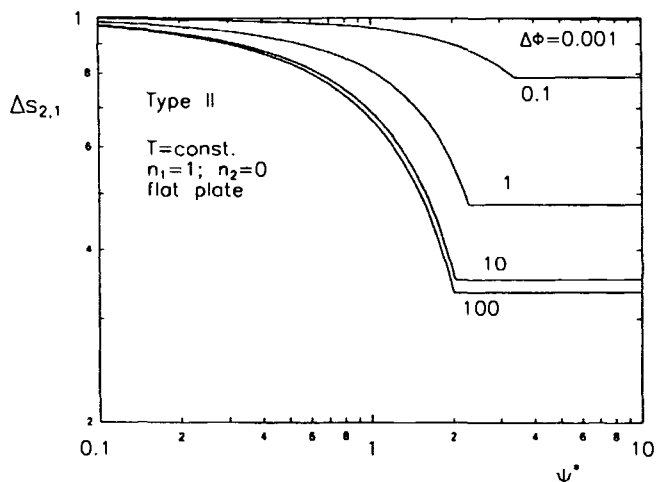


Figure 23. Relative selectivity  $\Delta s_{2,1}$  of a Type II reaction (first and zero order) plotted against the observable modulus  $\psi^* = \eta\phi_1^2(1 + \Delta\phi)$  (isothermal conditions, ratio of squared Thiele moduli  $\Delta\phi$  as a parameter, after Roberts [89]).

From eq 152 it follows that the apparent point selectivity will approach unity as the ratio  $\Delta\phi$  tends to zero. This is expected, since  $\Delta\phi \rightarrow 0$  means that the rate of the undesired reaction essentially becomes zero. Conversely, from eq 153 it can be derived that when  $\Delta\phi$  tends towards infinity, then the relative selectivity will approach a limiting value of  $1/3$  (see Roberts [89]). This means that the maximum loss of point selectivity is by a factor of 3.

To compare the change in overall selectivity, eqs 135 and 152 would have to be integrated over a range of conversions. However, the resulting lengthy expressions are not given here. Instead, Fig. 23 shows a plot of the relative point selectivity obtained from eq 153 versus the Weisz modulus

$$\psi^* = \eta\phi_1^2(1 + \Delta\phi)$$

for different values of the ratio  $\Delta\phi$ .

At this point it is worth noting that Roberts [89] also developed approximate relationships for arbitrary combinations of reaction orders which allow a rapid estimation of the effectiveness factor and the relative change in selectivity to be expected during the transition from the kinetic to the diffusion controlled regime. These are

$$\eta = \frac{\sqrt{2} \left( \frac{1}{n_1 + 1} + \frac{\Delta\phi}{n_2 + 1} \right)^{1/2}}{\phi_1(1 + \Delta\phi)} \quad (154)$$

$$\Delta s_{2,1} = \frac{n_2 + 1}{2n_1 - n_2 + 1} \quad (155)$$

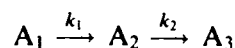
These equations apply to intraparticle diffusion effects only. Relationships similar to eqs 152 and 153 may be

derived for the case that both interphase and intraparticle concentration gradients occur, when instead of eq 141 the boundary condition at the external pellet surface is expressed according to eq 34.

So far, only isothermal operation has been considered. Under nonisothermal conditions, in Type II reactions a change of the apparent selectivity, caused by temperature variations across the pellet and/or the interphase boundary layer, may also be expected once the two reactions exhibit different activation energies. This holds irrespective of whether the kinetic order of the two reactions is equal or not. Nonisothermal Type II problems have been analyzed, for example, by Østergaard [81].

### 6.2.6.3 Type III Selectivity

Type III selectivity can be explained by the following sequence of two irreversible reactions:



where the desired product  $A_2$  is not stable, but further reacts on the catalyst to given an undesired product  $A_3$ . For convenience, again we assume that both reactions are first order and, additionally, unaffected by a change of volume, with  $k_1$  and  $k_2$  being the intrinsic rate constants. The governing rate equations for the above system then are:

$$-\frac{dc_1}{dt} = k_1 c_1 \quad (156)$$

$$\frac{dc_2}{dt} = k_1 c_1 - k_2 c_2 \quad (157)$$

Dividing eq 157 by eq 156, and rearranging:

$$s_{2,1} = -\frac{dc_2}{dc_1} = 1 - \frac{1}{\Delta k} \frac{c_2}{c_1} \quad (158)$$

where  $\Delta k = k_1/k_2$  again denotes the intrinsic selectivity factor. Equation 158 directly gives the point selectivity observed in the absence of transport limitations. Its integration therefore yields the intrinsic overall selectivity (see eq 132) as a function of the conversion of reactant  $A_1$ . For  $c_{2,0} = 0$ , we have

$$S_{2,1} = \frac{\Delta k}{\Delta k - 1} (1 - X_1) [(1 - X_1)^{(1/\Delta k - 1)} - 1] \quad (159)$$

If we now focus on the situation where the effective reaction rate is influenced by intraparticle diffusion effects, similar to the previously treated Type II problem, we first have to solve the mass balances for the reactant  $A_1$  and the desired product  $A_2$ . Again, to

avoid unnecessary complications, the catalyst is treated as an infinitely flat plate. This leads to the following expressions:

$$\frac{d^2 f_1}{dx^2} = \phi_1^2 f_1 \quad (160)$$

$$\frac{d^2 f_2}{dx^2} = \phi_2^2 \left[ f_2 - \Delta k \frac{c_{1,b}}{c_{2,b}} f_1 \right] \quad (161)$$

Equation 160 is independent of eq 161 and thus can be solved separately. The result is

$$f_1 = \frac{\cosh(\phi_1 x)}{\cosh(\phi_1)} \quad (162)$$

Substituting this into eq 161 yields

$$\frac{d^2 f_2}{dx^2} = \phi_2^2 \left[ f_2 - \Delta k \frac{c_{1,b}}{c_{2,b}} \frac{\cosh(\phi_1 x)}{\cosh(\phi_1)} \right] \quad (163)$$

The solution of this differential equation was given by Wheeler [113]:

$$f_2 = \left( 1 + \frac{c_{1,b}}{c_{2,b}} \frac{\Delta k}{(\Delta k - 1)} \right) \frac{\cosh(\phi_2 x / \sqrt{\Delta k})}{\cosh(\phi_2 / \sqrt{\Delta k})} - \frac{c_{1,b}}{c_{2,b}} \frac{\Delta k}{(\Delta k - 1)} \frac{\cosh(\phi_2 x)}{\cosh(\phi_2)} \quad (164)$$

We now ask for the point selectivity of the catalyst. This can be expressed by the net number of moles of  $A_2$  being released from the external surface per unit time, divided by the net number of moles of  $A_1$  entering the pellet per unit time, which is equivalent to the ratio of the concentration gradients of product  $A_2$  versus reactant  $A_1$  at the external pellet surface. By differentiating eqs 160 and 162, we obtain the following expression:

$$-\frac{dc_2}{dc_1} \Big|_{x=1} = \frac{\Delta k}{(\Delta k - 1)} - \left( \frac{c_{2,b}}{c_{1,b}} + \frac{\Delta k}{(\Delta k - 1)} \right) \times \frac{1}{\sqrt{\Delta k}} \frac{\tanh(\phi_2 / \sqrt{\Delta k})}{\tanh(\phi_2)} \quad (165)$$

For large diffusional effects (i.e.  $\phi_2 > 3$ ), this may be simplified, to give

$$s_{2,1} = -\frac{dc_2}{dc_1} \Big|_{x=1} = \frac{\sqrt{\Delta k}}{1 + \sqrt{\Delta k}} - \frac{1}{\sqrt{\Delta k}} \frac{c_{2,b}}{c_{1,b}} \quad (166)$$

Finally, the apparent overall selectivity is obtained by integration of eq 166 over a range of conversions. For  $c_{2,0} = 0$ , the result is

$$S_{2,1} = \frac{\Delta k}{\Delta k - 1} (1 - X_1) [(1 - X_1)^{(1/\sqrt{\Delta k} - 1)} - 1] \quad (167)$$

By comparing eqs 159 and 167, and assuming that  $\Delta k$  should be greater than unity, we note that Type III overall selectivity is reduced when the catalyst operates under intraparticle diffusion control.

An equation similar to eq 167 has been derived by Carberry [16] for the case of combined intraparticle and interphase concentration gradient (isothermal conditions). Without reproducing the details of its derivation, it turns out that the apparent overall selectivity can be calculated as follows:

$$S_{2,1} = \frac{\Delta k}{\Delta k - 1} (1 - X_1) [(1 - X_1)^{\Delta\psi - 1} - 1] + \Delta c_0 (1 - X_1)^{\Delta\psi} \quad (168)$$

where  $\Delta c_0 \neq 0$  corresponds to the most general case of a finite concentration of the desired species  $A_2$  at zero conversion. The parameter  $\Delta\psi$  is given by

$$\Delta\psi = \frac{1}{\sqrt{\Delta k}} \frac{\tanh(\phi_2) [1 + \phi_1 \tanh(\phi_1) / Bi_{m,1}]}{\tanh(\phi_1) [1 + \phi_2 \tanh(\phi_2) / Bi_{m,2}]} \quad (169)$$

At large values of the Thiele moduli  $\phi_1$  and  $\phi_2$ , i.e. when  $\phi_i > 3$ , the hyperbolic tangent approaches unity, and eq 169 then may be rewritten in a simplified form:

$$\Delta\psi = \frac{1}{\sqrt{\Delta k}} \frac{\left( \frac{Bi_{m,1}}{\phi_2} + \sqrt{\Delta k} \right) Bi_{m,2}}{\left( \frac{Bi_{m,2}}{\phi_2} + 1 \right) Bi_{m,1}} \quad (170)$$

If we assume that the Biot numbers of the two species are roughly the same, we note from eq 170 that when the ratio  $Bi_{m,1}/\phi_2$  is sufficiently large (i.e. compared to  $\Delta k^{1/2}$  and to unity), indicating that interphase diffusion effects are not likely to influence the effective reaction rate, then, with  $c_{2,0} = 0$ , eq 170 essentially transforms to eq 167. However, if this is not the case, the overall selectivity will be further reduced with decreasing value of  $Bi_{m,1}/\phi_2$ .

Figure 24 illustrates the dependence of Type III selectivity on intraparticle and interphase diffusion effects by plotting the apparent overall selectivity from eqs 159, 167 and 168 for  $Bi_{m,1}/\phi_2 = 1$ , against the conversion of reactant  $A_1$ . From this figure, it appears that the influence of intraparticle diffusion may reduce the overall selectivity in Type III reactions by a factor of about two. Wheeler [113] reported that this degree of reduction is independent of the intrinsic selectivity factor  $\Delta k$ . It may therefore serve as a general rule of thumb.

Again, this was for isothermal conditions. In non-isothermal Type III reactions, a deviating temperature will also impose additional effects on selectivity, once the activation energies of the two reactions differ sig-

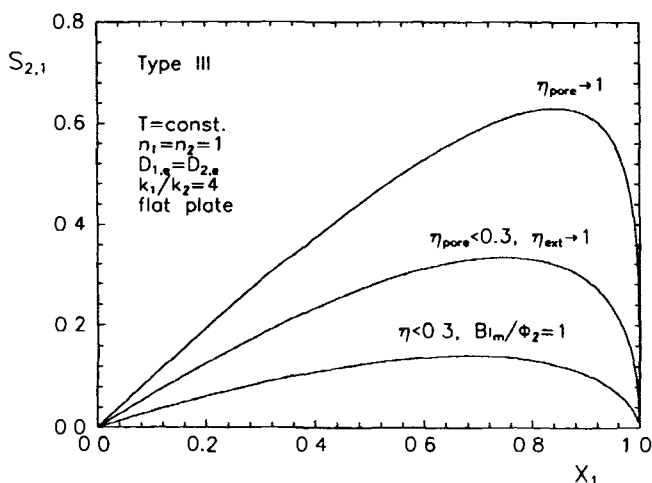


**Figure 24.** Variation of the apparent selectivity with conversion for a Type III reaction. Comparison of the results obtained under kinetic and diffusion control (isothermal conditions, intrinsic selectivity factor  $\Delta k = 4$ , equal Biot numbers  $Bi_{m,1} = Bi_{m,2}$ , initial concentration  $c_{2,0} = 0$ ).

nificantly. The same holds for the case that the two reactions obey different kinetic orders. For further details on the treatment of nonisothermal Type III reactions, the reader may consult the work of Butt [11].

## 6.2.7 Control of Selectivity in Zeolite Catalyzed Reactions by Utilizing Diffusion Effects

So far, the basic principles of the interaction of chemical reaction and heat and mass transfer have been introduced, which date back to the pioneering work of Damköhler [28], Thiele [98], and Zeldovich [114] in the late 1930s. Although not claiming to have exhaustively covered all important aspects of this field, which were developed mainly from the late 1950s to the early 1970s, the present state of knowledge is described in several separate sections so as to illustrate the various effects which can be observed in different experimental situations. Thereby, not only the problem of conversion has been addressed, but also questions concerning the selectivity in multiple reaction networks.

To complete this more general discussion by giving an illustrative example, the last section is devoted to a special application of current interest, namely the control of selectivity by utilizing diffusion effects in zeolite catalyzed reactions.

### 6.2.7.1 Shape-Selective Catalysis

Maximizing the selectivity (and the yield) to certain valuable products is beyond any doubt an important

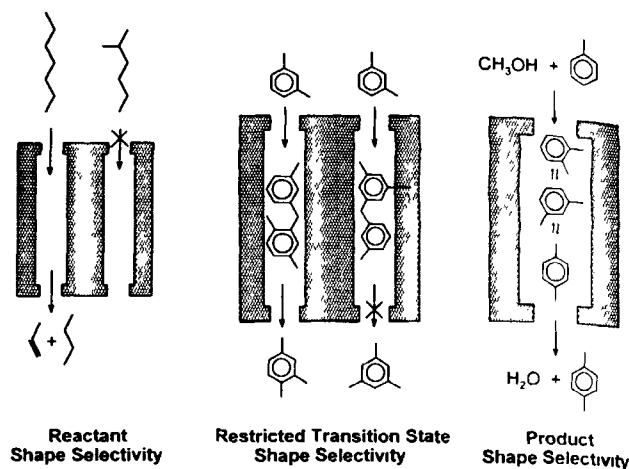


**Figure 25.** Classification of shape-selective effects according to Weisz [111] and Csicsery [27].

issue in the catalysis of multiple reactions. However, classical attempts at tailoring catalyst properties in order to meet this demand quite often come up against severe difficulties. In this sense, shape-selective catalysis using zeolites or related materials with a regular pore structure opens up a fascinating field to catalysis scientists and reaction engineers, as this allows a control of selectivity based on the geometry of the catalysts pore structure, which offers new opportunities to develop materials with tailor-made catalytic properties.

Shape-selective effects may occur whenever the pore size of a microporous catalyst is in the same range as the diameter of the molecules or transition states involved in the reacting system. Common microporous materials are zeolites and related materials (aluminophosphates, pillared clays, etc.) which possess a regular crystal lattice together with a well defined pore size. According to Weisz [111] and Csicsery [27], shape-selective effects may be classified into three types (Fig. 25).

#### A Reactant Shape Selectivity

This is found when only the tallest of several reactants is able to diffuse into the pore structure of the catalyst and is reacted.

#### B Product Shape Selectivity

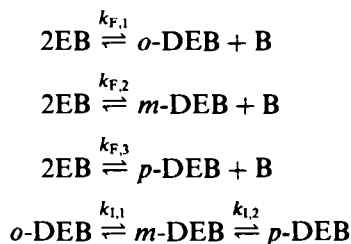
This is given when several products are formed from the reactants inside the crystallite, but those with a rather bulky structure cannot diffuse out. These molecules may be reacted further on the active surface to give either the desired products (e.g. by isomerization) or other, smaller molecules (e.g. by cracking) which then can readily leave the pore system. In the worst case, the bulky molecules will be trapped inside the cavities or channels, block the pores, and prevent other reactant molecules from entering (deactivation by coking).

### C Restricted Transition State Shape Selectivity

This means that in a network of multiple reactions those products are suppressed which require the intermediate formation of a bulky transition state, whenever the size of the cavities or channels is too narrow for this to be established.

Basically, reactant and product selectivities are mass transfer effects, where the diffusivities of the various species in practice frequently do not differ that extremely as indicated above. Instead, in most cases only a preferred diffusion of certain species is observed, a fact which often hinders a clear understanding of product shape selectivity. This is because the various products, during their way through the pore system, may be reacted when contacting the catalytically active surface of the wall. This combined effect of diffusion and reaction will be discussed in detail in the following, as it is of great importance for the product distribution in zeolite-catalyzed reactions.

The disproportionation of ethylbenzene (EB) to benzene (B) and diethylbenzenes (DEB) serves as a case study. This reaction has been introduced by Karge et al. and Weitkamp et al. to compare the activity of different zeolite catalysts [58, 59], and to distinguish between medium- and large-pore zeolites [112, 60]. Moreover, since 1994, it has been further developed as a standardized test reaction by the International Zeolite Association (IZA) [55]. A general representation of the individual transformations which occur in this type of reaction, is given in the following scheme:

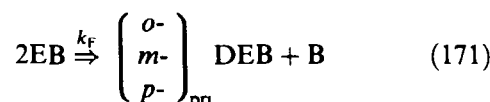


where the prefixes *o*-, *m*- and *p*- indicate the *ortho*, *meta*, and *para* isomers, respectively. It may be obvious to note that the effects to be discussed here will basically apply to similar reacting systems, such as the alkylation of other monoalkylbenzenes using various alkenes or alcohols, or the disproportionation of toluene.

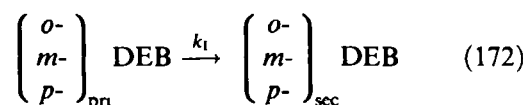
Olson and Haag [80] in 1983 showed that the yield of *p*-xylene observed during the disproportionation of toluene on various modified and unmodified ZSM-5 catalysts is actually influenced by product shape selectivity. The authors attributed the observed effects to an interaction of diffusion and reaction, characterized by means of a dimensionless modulus similar to the classical Thiele modulus  $\phi$ . The mathematical treatment of shape selectivity in zeolite catalysts, which will be applied in this section, is largely based on the theory of Olson and Haag [80], although some modifications and extensions to this are given.

### D Microkinetics

As an essential requirement for the fundamental effects of shape selectivity to be developed in an instructive manner, we first simplify the above general reaction scheme. In this sense, we restrict our considerations to a sufficiently small reactant conversion, where we may replace the separate formation reactions of the three isomers with a single pseudoirreversible reaction, described by a common rate constant  $k_F$ . This is justified by the fact that all three reactions obey the same kinetic order, and the backward reactions, due to the small isomer concentration at low level of conversion, may be neglected. Moreover, according to Wei [107] we treat the isomerization, which actually involves two reversible reactions, also as a single pseudoirreversible reaction. This may be interpreted in a sense that the reacting system globally approaches the chemical equilibrium with a rate characterized by a common rate constant  $k_I$ . Thus, we have two consecutive reactions: disproportionation



followed by isomerization



where the subscripts *pri* and *sec* denote the primary and secondary isomer distribution, respectively.

The primary isomer distribution, which is the result of the disproportionation reaction, may deviate significantly from the thermodynamic equilibrium composition, for two reasons. First, the reaction may be controlled by the kinetics rather than the thermodynamics, i.e. mechanistic reasons may exist which cause the reaction to proceed along a certain path. Second, in the case that the reaction obeys a bimolecular mechanism, it may pass through a transition state which would presumably favor the (taller) *para* isomer. Hence, it is possible that the primary product contains an enhanced fraction of the *para* isomer. The departure from the equilibrium composition then gives the driving force for the subsequent (monomolecular) isomerization reaction. This will reduce the fraction of the *para* isomer, provided the formation of the bulky *ortho* and *meta* isomers are not inhibited by sterical effects, i.e. when the micropore diameter is sufficiently large or there is a chance for the isomerization reaction to take place at the outer surface of the crystallites. Thus, the secondary isomer distribution may approach the thermodynamic equilibrium composition, as a limiting case.

### E Macrokinetics

As discussed in Section 6.2.6, the apparent selectivity of the catalyst in a network of multiple reactions may be affected by interphase and intraparticle heat and mass transfer. In zeolites or other microporous materials, the intraparticle diffusion process is normally governed by two different mechanisms. To illustrate this, the zeolite catalyst pellet may be visualized as consisting of a large number of individual crystallites, typically around 1–100  $\mu\text{m}$  in diameter. The void space between these crystallites constitutes the macropores of the pellet, whereas the micropores are given by the cavities or channels inside the zeolite crystals. Hence, these materials show a bimodal pore size distribution. The mass transport inside the macropores is governed by bulk (and/or Knudsen) diffusion, whereas the mass transport inside the micropores is controlled by configurational diffusion. However, as we are concerned here primarily with the investigation of product shape selectivity, which is basically something that happens inside the zeolite crystals, for the subsequent discussion we may neglect any concentration and temperature gradients along the macropores of the pellet and across the external boundary layer surrounding the pellet as well. Moreover, to keep the discussion as simple as possible, temperature gradients inside the crystallites will also be ignored. Hence, we have to consider the following steps, which are similar to the steps 1–7 described in the introduction, for the case of a macroporous pellet.

1. Adsorption of the reactant on the outer surface of the crystallite.
2. Disproportionation of the reactant at the catalytically active sites on the outer surface.
3. Diffusion of the reactant into the microporous structure.
4. Disproportionation of the reactant and isomerization of the products at the catalytically active sites inside the pore system.
5. Diffusion of the products out of the microporous structure.
6. Isomerization of the products at the catalytically active sites on the outer surface.
7. Desorption of the products from the outer surface.

At this point, it should be emphasized that steps 2–6 are not linked in a sequential manner. Instead, diffusion and reaction inside the pore system, steps 3–5, occur simultaneously, as observed in the macroporous pellet as well. Moreover, the opportunities for a reactant molecule either to be converted at the outer surface of the crystallite or to enter the porous structure also represent parallel reaction paths.

Although both the microporous (crystallite) and the macroporous (pellet) problem share instructive sim-

ilarities, they nonetheless differ in some aspects. These differences have important implications with respect to selectivity control. These include the fact that the boundary conditions at the outer surface of the crystallite are controlled by the laws of adsorption, whereas the boundary conditions at the external surface of the pellet are governed by interphase diffusion. Thus, a different adsorption behavior of the various species may have a significant effect on selectivity. In contrast, the interphase mass transfer coefficients of the various species are not likely to differ that extremely, and hence in the case of an isothermal, macroporous pellet interphase diffusion is not likely to have a marked influence on selectivity.

Moreover, in the case of a crystallite, there will be a difference in selectivity depending on whether the reaction takes place at the outer surface or inside the pore system. This is because in the first case the reaction will proceed unaffected by geometrical restrictions, whereas in the latter case shape-selective effects may control the selectivity. It is obvious that such a difference will not be observed in the macroporous pellet.

#### 6.2.7.2 Modeling of Shape-Selectivity Effects

In the light of the previous discussion it is quite apparent that a detailed mathematical simulation of the combined chemical reaction and transport processes, which occur in microporous catalysts, would be highly desirable to support the exploration of the crucial parameters determining conversion and selectivity. Moreover, from the treatment of the basic types of catalyst selectivity in multiple reactions given in Section 6.2.6, it is clear that an analytical solution to this problem, if at all possible, will presumably not favor a convenient and efficient treatment of real world problems. This is because of the various assumptions and restrictions which usually have to be introduced in order to achieve a complete or even an approximate solution. Hence, numerical methods are required. Concerning these, one basically has to distinguish between three fundamentally different types, namely molecular-dynamic models, stochastic models, and continuous models.

Molecular-dynamic simulations are characterized by a solution of Newton's laws of motion for the molecules travelling through the zeolite pore system under control of the force field given by the properties of the host lattice, by interactions between the host and the molecules, and by interactions between the molecules. To date this has been possible only for the diffusion of simple molecules (e.g. methane or benzene) inside a zeolite lattice of limited dimensions [29, 37, 54]. To take into account the effects of a chemical reaction as well would require quantum-mechanical considerations; however, such simulations are in their infancy.



In stochastic models, the regular zeolite lattice is projected onto a rectangular grid, where each grid element corresponds to the adsorption sites located either inside a certain cavity or crossing of channels, depending on the type of the zeolite. The site-to-site movement (jumping) of the adsorbed molecules is described in these models by the probability of jumping. In Monte Carlo methods, which may be considered as a special class of stochastic models, a random generator serves to initialize the activated adsorption sites and the directions of movement of the activated molecules. By additionally introducing the probability of reaction, chemical transformations may be included in such simulations. Theodorou and Wei [97] in 1983 were the first to report about the application of a Monte Carlo method to the modeling of combined diffusion and reaction in zeolite catalysts. Since then several related papers on this subject have appeared in the literature, for example the works of Tsikoyiannis and Wei [101] in 1991, Frank et al. [36] in 1993, and Wang et al. [106] in 1994. However, most of these simulations use rather simple model reactions, for example systems of the type  $A \rightleftharpoons B$ ,  $A \rightleftharpoons B \rightleftharpoons C$ , or  $A \rightarrow B \rightarrow C$ .

The principles and basic equations of continuous models have already been introduced in Section 6.2.2. These are based on the well known conservation laws for mass and energy. The diffusion inside the pores is usually described in these models by the Fickian laws or by the theory of multicomponent diffusion (Stefan–Maxwell). However, these approaches basically apply to the mass transport inside the macropores, where the necessary assumption of a continuous fluid phase essentially holds. In contrast, in the microporous case, where the pore size is close to the range of molecular dimensions, only a few molecules will be present within the cross-section of a pore, a fact which poses some doubt on whether the assumption of a continuous phase will be valid.

Wei [107] in 1982 was the first to come up with a continuous pseudohomogeneous model which allowed to simulate shape-selective effects observed during the alkylation of toluene using methanol to yield xylene isomers on a HZSM-5 catalyst. He treated diffusion and reaction of the xylene isomers inside the pores in a one-dimensional model. The isomer concentration at the pore mouth was set to zero, as a boundary condition. This allowed the model equations to be solved analytically, but it also limited the application of the results to small conversions.

Do [30] in 1985 then used a method based on the approach of Wei [107] to simulate again the alkylation of toluene on a HZSM-5 catalyst, but in contrast to Wei, for a fixed bed reactor where it was assumed that concentration gradients exist only inside the crystallites and along the axial coordinate of the catalyst bed.

Liang et al. [67] in 1990 extended the original model of Wei [107] by taking into account the adsorption at the outer surface of the crystallite. They assumed that the adsorption takes place at the pore mouth, and that the reaction and the diffusion into the microporous structure proceed in an adsorbed state.

A further improvement of the approach of Wei [107] was reported in 1989 by Hashimoto et al. [42], which considered not only adsorption effects, but also the nonselective reactions occurring at the outer surface of the crystallites. The nonselective influence of these reactions has also been recognized by Fraenkel [35] in 1990, who studied the formation of xylene from toluene on a HZSM-5 catalyst. Fraenkel assumed that inside the crystallite only *p*-xylene is formed, whereas the *ortho* and *meta* isomers are sterically inhibited there. Hence, he concluded that the amount of *o*- and *m*-xylene observed during his experiments must be due to the isomerization of *p*-xylene at the outer surface of the crystallites. This two-step mechanism was first suggested in 1987 by Paparetto et al. [82] for the ethylation of toluene. It may also be worth noting that Fraenkel's model took into account not only the isomerization but also the nonselective alkylation at the outer crystallite surface.

Finally, Emig et al. [32] in 1994 presented a continuous model, which uses a versatile numerical solver, and thus allows simulation of a variety of situations occurring when different steps of the overall process are significant (see steps 1–7 above). In the following, the mathematics and the use of this model will be explained.

### A Simplifying Assumptions

1. The model equations are based on the assumption that the disproportionation of EB, the present case study, is carried out in a gradientless recycle reactor (Fig. 26), where neither concentration gradients

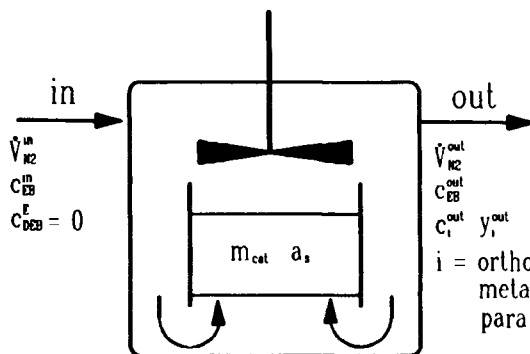


Figure 26. Schematics of a gradientless recycle reactor.

nor temperature gradients exist throughout the entire reacting volume. Moreover, such gradients may be absent inside the macropores of the zeolite pellet and across the external boundary layer as well. Finally, the crystallites may be isothermal. Hence, we have to treat only the coupled adsorption, diffusion and reaction inside the micropores of the crystallite.

- The disproportionation of EB is treated as a first order, irreversible reaction, making use of the simplifications described earlier. Thus, the rate of formation of the three DEB isomers is given by

$$R_{F,i} = y_{i,pr} k_F c_{EB} \quad (173)$$

where  $y_{i,pr}$  denotes the primary isomer distribution which is precisely the ratio of the mole fractions of the various isomers. This may be chosen arbitrarily. Hence, by varying the primary isomer distribution, restricted transition state shape selectivity as well as mechanistic aspects of the disproportionation reaction may be included in the simulations.

- The isomerization reaction is described in analogy to the approach of Wei [107]:

$$R_1 = K_1 c \quad (174)$$

where  $c$  denotes the isomer concentration vector,  $R_1$  is the vector of the rates of production or disappearance of the isomers due to the isomerization reaction, and  $K_1$  is the isomerization rate matrix, which is defined as follows:

$$K_1 = k_1 \begin{pmatrix} \kappa_{1,1} & \kappa_{1,2} & \kappa_{1,3} \\ \kappa_{2,1} & \kappa_{2,2} & \kappa_{2,3} \\ \kappa_{3,1} & \kappa_{3,2} & \kappa_{3,3} \end{pmatrix} \quad (175)$$

The elements  $\kappa_{i,j}$  are obtained by letting  $R_1(c^{eq}) = 0$ , which essentially means the condition that the isomerization rate must tend to zero as the isomer concentration approaches the thermodynamic equilibrium concentration  $c^{eq}$ . At this point, it should be noted that a direct transformation of *o*- into *p*-DEB is not possible, thus the elements  $\kappa_{1,3}$  and  $\kappa_{3,1}$  are zero.

- Reactions at the outer surface of the crystallites are neglected.
- The diffusion of the various species inside the micropores is described according to the Fickian laws, i.e. neither multicomponent diffusion nor a concentration dependence of the diffusivities are taken into account.
- An inert gas ( $N_2$ ) is assumed to be present in large excess. As a matter of the small partial pressures of the reacting species under these conditions, the adsorption isotherms may be approximated by linear relationships (eq 176); the volume change due to reaction may be neglected.

$$c_{i,s} = K_i c_i^{out} \quad (176)$$

- The individual crystallites are assumed to be of spherical shape and of the same size (radius  $R$ ).

## B Model Equations

With these assumptions, the mass conservation laws for the reactant EB and the three DEB isomers inside the crystallite may be written as follows:

$$\frac{d^2 c_{EB}}{dr^2} + \frac{2}{r} \frac{dc_{EB}}{dr} = \frac{k_F c_{EB}}{D_{EB,e}} \quad (177)$$

$$\frac{d^2 c_i}{dr^2} + \frac{2}{r} \frac{dc_i}{dr} = - \frac{y_{i,pr} k_F c_{EB} + k_1 \sum_{k=1}^3 \kappa_{i,k} c_k}{D_{i,e}} \quad (178)$$

$i = o-, m-, p\text{-DEB}$

This is a system of four coupled, second-order ordinary differential equations. The solution of each equation must satisfy two boundary conditions. The first is dictated by the symmetry of the crystallite (sphere) which requires the concentration gradients of all species to disappear at the center of the crystallite:

$$\left. \frac{dc_i}{dr} \right|_{r=0} = 0 \quad i = EB, o-, m-, p\text{-DEB} \quad (179)$$

The second condition can be derived from the overall mass balance (reactor) for the reacting species. As we have assumed a gradientless recycle reactor (see Fig. 26), the fluid inside the reactor is supposed to be perfectly mixed. Thus, we have an ideal CSTR for which the mass balance of species  $i$  takes the form:

$$q(c_i^{in} - c_i^{out}) - m_{cat} S_m D_{i,c} \left. \frac{dc_i}{dr} \right|_{r=R} = 0 \quad (180)$$

$i = EB, o-, m-, p\text{-DEB}$

In this equation,  $q$  denotes the volumetric flow rate to the reactor,  $m_{cat}$  means the catalyst weight, and  $S_m$  the outer surface area of the crystallites per unit mass. Substituting the linear adsorption law of eq 176 into eq 180, and rearranging yields the following expression for the concentration gradient at the outer surface of the crystallite:

$$\left. \frac{dc_i}{dr} \right|_{r=R} = \frac{q \left( c_i^{in} - \frac{c_{i,s}}{K_i} \right)}{m_{cat} S_m D_{i,c}} \quad i = EB, o-, m-, p\text{-DEB} \quad (181)$$

Inspection of the above equations shows that the EB mass balance (eq 177) together with the corresponding boundary conditions (eqs 179 and 181) is independent of the respective equations for the DEB isomers (eqs 178, 179 and 181). Hence, eq 177 may be solved separately. The solution of the nondimensional form of eq

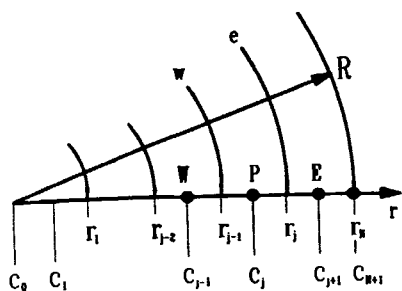


Figure 27. Subdivision of the crystallite into finite volumes and indexing of the finite volumes.

177 has already been given in Section 6.2.3 (eq 49). Thus, for convenience, we introduce the generalized Thiele modulus  $\phi_F$  related to the disproportionation reaction (see eq 54) which gives

$$\frac{c_{EB}(r)}{c_{EB,s}} = \frac{\sinh(3\phi_F r/R)}{r/R \sinh(3\phi_F)} \quad (182)$$

The unknown surface concentration  $c_{EB,s}$  can be determined by differentiating eq 182 and substituting the result into eq 181. After rearranging, this yields

$$\frac{c_{EB,s}}{c_{EB}^{in}} = \left( \frac{1}{K_{EB}} + \frac{D_{EB,e} m_{cat} S_m}{qR} \left[ \frac{3\phi_F}{\tanh(3\phi_F)} - 1 \right] \right)^{-1} \quad (183)$$

Hence, if we substitute eqs 182 and 183 into eq 178, we have reduced the system to three second-order ordinary differential equations.

This boundary value problem is then solved numerically by applying a (mass-conservative) finite volume method. In this, the crystallite is divided into a number of small volumes, i.e. thin spherical shells of thickness  $h$ , over which the isomer mass balances are separately invoked. The thickness of the shells may either be constant throughout the entire crystallite (evenly spaced nodes) or vary with the steepness of the actual concentration gradients (dynamic spacing). A dynamic node spacing, depending on the absolute values of the concentration gradients, provides an efficient control of the approximation error, i.e. the solution becomes virtually independent of the node spacing already at a smaller number of nodal points, which leads to significant savings in computation time.

Figure 27 illustrates the subdivision of the crystallite into finite volumes. Volume  $j$  is limited by coordinate  $r_j$  to the east (e), and by coordinate  $r_{j-1}$  to the west (w). The concentration of species  $i$  inside volume  $j$  is assigned to the geometrical center of the volume (P). Towards the edges of the crystallite, i.e. the outer surface and the center, the node spacing is cut to one half.

The mass balance for an arbitrary volume element inside the crystallite can be formulated as

$$N_{i,w} A_w - N_{i,e} A_e + R_i \delta V = 0 \quad (184)$$

where  $N_{i,w}$  denotes the molar flux density of isomer  $i$  at the western boundary and  $N_{i,e}$  is the same at the eastern boundary;  $A_w$  and  $A_e$  denote the respective boundary areas;  $R_i$  is the rate of production or disappearance of species  $i$  per unit volume and time;  $\delta V$  denotes the capacity of the volume element.

The molar flux densities  $N_{i,w}$  and  $N_{i,e}$  can be expressed according to Fick's first law:

$$N_{i,w} = -D_{i,e} \left. \frac{dc_i}{dr} \right|_w \quad N_{i,e} = -D_{i,e} \left. \frac{dc_i}{dr} \right|_e \quad (185)$$

The rate of production or disappearance of species  $i$  is given by

$$R_i = y_{i,pn} k_F c_{EB} + k_1 \sum_{k=1}^3 \kappa_{i,k} c_k \quad (186)$$

The boundary areas and the capacity of the volume element are calculated as follows:

$$A_w = 4\pi r_{j-1}^2; \quad A_e = 4\pi r_j^2; \quad \delta V = \frac{4}{3}(r_j^3 - r_{j-1}^3) \quad (187)$$

Substituting eqs 185–187 into eq 184, and rearranging, finally yields

$$\begin{aligned} & \frac{3}{(r_j^3 - r_{j-1}^3)} \left( r_j^2 \left. \frac{dc_i}{dr} \right|_e - r_{j-1}^2 \left. \frac{dc_i}{dr} \right|_w \right) + \frac{k_1}{D_{i,e}} \sum_{k=1}^3 \kappa_{i,k} c_k \\ & = y_{i,pn} \frac{k_F}{D_{i,e}} c_{EB} \end{aligned} \quad (188)$$

The derivatives in eq 188 are approximated by central differences. This leads to a discrete representation of the problem in the form of linear equations. For  $j=1$  and  $j=N$  we have slightly modified equations, since here the boundary conditions have to be considered. Because the concentration of three isomers has to be calculated for each of the  $N$  volume elements as a whole, we have a system of  $N \times 3$  linear equations. This can be expressed in matrix notation:

$$Ac = b \quad (189)$$

where the coefficient matrix  $A$  has a heptadiagonal structure. Such problems are solved very efficiently by means of LU decomposition [96].

### C Simulation Results

As already stated, the model was applied to simulate the effects of product shape selectivity during the disproportionation of EB on a HY-zeolite. The various parameters required for the simulations, i.e. the adsorption constants and diffusivities were taken from the

Table 6. Parameter range used for the simulation of the disproportionation of EB on a HY zeolite.

Parameter	Symbols	Units	Numerical values
Primary isomer distribution	$y_{o,pri}, y_{m,pri}, y_{p,pri}$	—	0.067, 0.638, 0.295
Adsorption constants	$K_{EB}, K_o, K_m, K_p$	$10^3 \text{ m}^3 \text{ m}^{-3}$	9, 14, 14, 14–1400
Effective diffusivities	$D_{EB,e}, D_{o,e}, D_{m,e}, D_{p,e}$	$10^{-14} \text{ m}^2 \text{ s}^{-1}$	0.5, 1, 1, 1–1000
Thiele modulus	$\phi_F$	—	0.01–100
Isomerization rate constant	$k_i$	$\text{s}^{-1}$	$10^{-8}$ – $10^4$
Reactant concentration	$c_{EB}$	$\text{mol m}^{-3}$	1.5
Flow rate	$q$	$\text{ml s}^{-1}$ (STP)	8
Catalyst weight	$m_{cat}$	g	0.35
Crystallite radius	$R$	$\mu\text{m}$	20

<sup>a</sup>  $\text{m}^3$  gas per  $\text{m}^3$  zeolite.

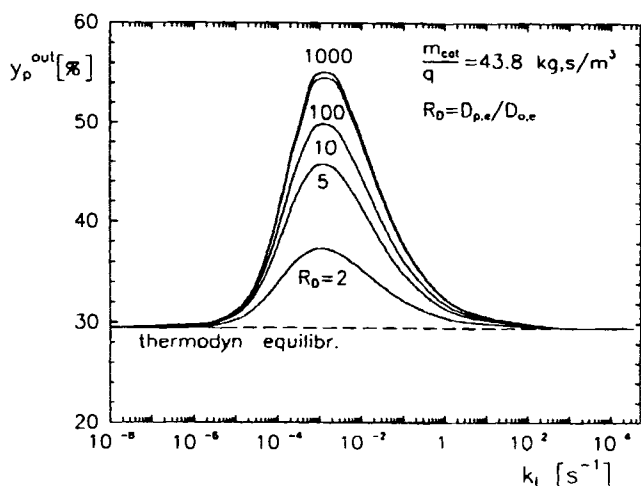


Figure 28. Simulated *para* selectivity  $y_p^{out}$  at the reactor outlet as a function of the isomerization rate constant  $k_i$ . Dependence on the ratio of effective diffusivities  $R_D = D_{p,e}/D_{o,e}$ .

literature [45]. The remaining simulation conditions were chosen to be similar to the operating conditions of related experimental studies on this reaction [63]. Table 6 gives the range of the respective variables covered in the simulations.

#### a Product Shape Selectivity (Unaffected by Other Factors)

For these simulations, the primary isomer distribution is chosen according to the thermodynamic equilibrium (see Table 6). Such a situation would be encountered in practice when neither the reaction mechanism kinetically favors a particular isomer nor restricted transition state shape-selectivity effects occur. The disproportionation reaction is assumed to be unaffected by diffusion (i.e.  $\phi_F < 0.01$ ). The effective diffusivities of the *ortho* and *meta* isomers are fixed, and assumed to be equal, but by a factor of  $R_D$  smaller than the effective diffusivity of the *para* isomer.

Figure 28 shows the simulated, normalized fraction of the *para* isomer in the DEB product stream at the reactor outlet. In the subsequent discussion, this will be

called the *para* selectivity for notational simplicity. From Fig. 28, it is clear that the observable *para* selectivity passes a maximum as the isomerization rate constant is increased. This may be explained as follows. On the left side of the maximum, where the isomerization reaction is slow compared to the rate of diffusion of the *para* isomer, an increased isomerization rate will cause the fast diffusing *para* isomer to be more readily supplied. However, as the isomerization rate is increased beyond a certain limit, the *para* isomer will be converted faster than it can diffuse out of the pore structure. Thus, at a given value of the effective diffusivity of the *para* isomer, the *para* selectivity will begin to drop upon further increasing the isomerization rate constant.

The maximum gain of the *para* selectivity, which gives the size of the product shape selective effect, naturally increases as the ratio of the diffusivities  $R_D$  becomes larger, although not to 100%, but instead to a limiting value which is approached at  $R_D > 100$ . This is controlled by several other factors, namely the absolute values of the diffusivities.

The simulation results also show that the product shape-selective effect does not depend on the inlet concentration of EB, nor on the rate of the disproportionation reaction (i.e. the rate constant  $k_F$ ). Instead, it is affected by the ratio of the catalyst weight, divided by the total flow rate,  $m_{cat}/q$ , which may be interpreted as a modified residence time. This is illustrated in Fig. 29, where the *para* selectivity is plotted against the isomerization rate constant for different values of  $m_{cat}/q$ .

A reduced residence time leads to an increase of the *para* selectivity. However, at the same time the conversion drops, and thus the *para* concentration at the reactor outlet is reduced. In addition, the maxima of the curves shown in Fig. 29 become less distinct. In the limiting case of zero conversion, the *para* selectivity increases steadily with increasing values of the isomerization rate constant. Then a maximum is no longer observed. This is exactly the result obtained by Wei [107]. However, it is true only for small conversions. As soon as the conversion increases, the assumption of a

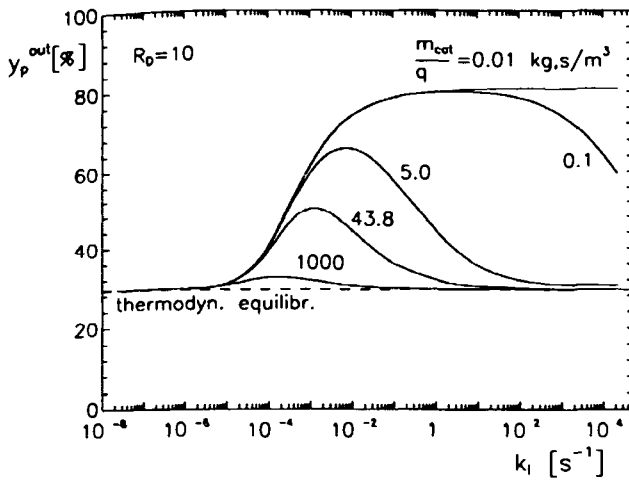


**Figure 29.** Simulated *para* selectivity  $y_p^{\text{out}}$  at the reactor outlet as a function of the isomerization rate constant  $k_i$ . Dependence on the modified residence time  $m_{\text{cat}}/q$  ( $c_{\text{EB}} = \text{const.}$ ).

negligible isomer concentration at the pore mouth, which has been introduced as a boundary condition in the approach of Wei [107], is no longer valid. Figure 29 shows that in this case the *para* selectivity begins to drop when the isomerization rate exceeds some limit. This has the important consequence that an increased activity of the zeolite does not automatically produce an enhanced yield of the *para* isomer. Instead, an optimum range of  $k_i$  is observed where the *para* yield is at maximum.

#### *b Product Shape Selectivity and Reactant Diffusion Limitation (Combined Effect)*

When the diffusion of the reactant begins to influence the effective rate of the disproportionation reaction, the observable product shape-selective effect is reduced. This is obvious from Fig. 30 which shows the *para* selectivity as a function of the isomerization rate constant  $k_i$  for various values of the Thiele modulus  $\phi_F$  (by variation of the rate constant  $k_F$ ). In the limiting case of  $\phi_F$  approaching infinity, no shape selective effect at all is encountered. This comes as no surprise, since the penetration depth of the reactant into the porous structure of the crystallite in this case approaches zero. Hence, the distance for the isomer molecules to pass from the point where they are formed until they reach the outer surface of the crystallite tends to zero, which is precisely the range where differences of the diffusivities of the isomers—together with the isomerization reaction taking place—at all generate product shape selectivity.

It may be obvious from this explanation that the *para* selectivity will become virtually independent of the size of the crystallites when the disproportionation rate is severely affected by a limited diffusivity of the reactant EB.

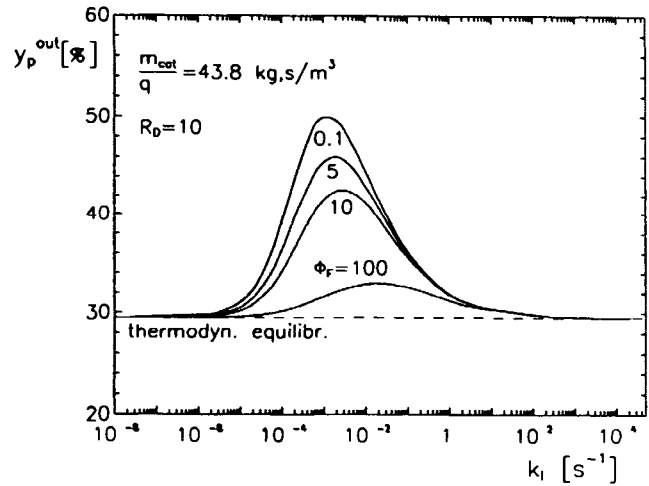


**Figure 30.** Simulated *para* selectivity  $y_p^{\text{out}}$  at the reactor outlet as a function of the isomerization rate constant  $k_i$ . Dependence on the Thiele modulus of the disproportionation reaction  $\phi_F$ .

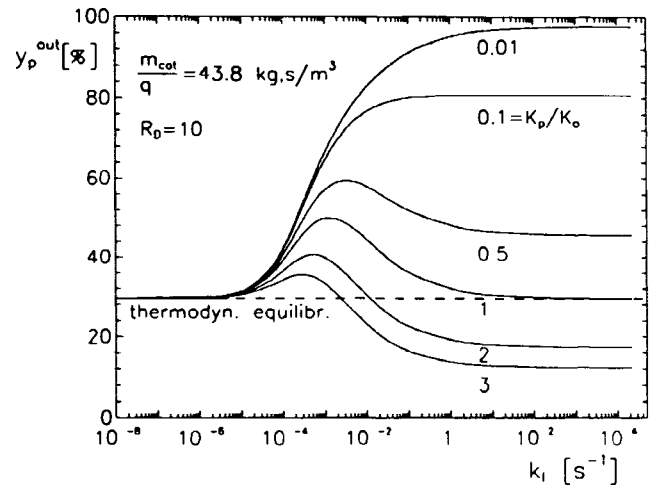


**Figure 31.** Simulated *para* selectivity  $y_p^{\text{out}}$  at the reactor outlet as a function of the isomerization rate constant  $k_i$ . Dependence on the ratio of the adsorption constants  $R_K = K_p/K_o$  ( $K_o = K_m = \text{const.}$ ).

#### *c Product Shape Selectivity and Selective Adsorption (Combined Effect)*

The effect of different adsorption constants of the isomers is illustrated in Fig. 31 where the *para* selectivity is plotted against the isomerization rate constant for different ratios of the adsorption constants  $R_K = K_p/K_o$  ( $K_o = K_m = \text{const.}$ ). From this we note that the maximum *para* selectivity increases as the adsorption constant of the *para* isomer is reduced below the respective constants of the other isomers. This effect is most pronounced at large values of  $k_i$ . Moreover, when the ratio of the adsorption constants  $R_K$  tends to zero, the *para* selectivity increases steadily with increasing values of

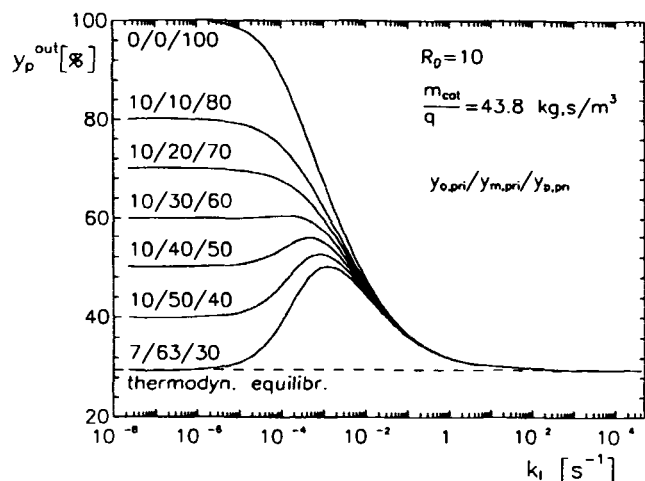


Figure 32. Simulated *para* selectivity  $y_p^{\text{out}}$  at the reactor outlet as a function of the isomerization rate constant  $k_1$ . Dependence on the primary isomer distribution  $y_i^{\text{pri}}$ .

the isomerization rate constant  $k_1$ . A maximum is no longer observed. For  $R_K$  above unity, where the *para* isomer is more strongly adsorbed than the others, the *para* selectivity drops below the thermodynamic equilibrium composition once the isomerization rate constant becomes sufficiently large.

This can be explained by the fact that, if the isomerization reaction is very fast, then the isomer concentration will approach the thermodynamic equilibrium at any point inside the crystallite. Thus, the isomer distribution in the surrounding fluid is controlled only by the adsorption of the various species.

#### d Product Shape Selectivity and Restricted Transition State Shape Selectivity (Combined Effect)

Finally, in Fig. 32 the influence of the primary isomer distribution on the observable *para* selectivity is shown by plotting the *para* selectivity versus the isomerization rate constant for different primary isomer distributions.

It is apparent that an increase of the fraction of the *para* isomer produced by the disproportionation will only lead to a net increase of the observable *para* selectivity when the isomerization rate is not too high. Otherwise most of the *para* isomer, which is selectively formed by the primary disproportionation reaction, will be converted to the other isomers by the secondary isomerization reaction. As  $k_1$  approaches infinity, in any case the thermodynamic equilibrium distribution of the isomers must be obtained.

### 6.2.7.3 Controlled Modification of the Pore Structure

The observation of shape-selective effects in zeolite catalysis suggests the possibility of tailoring catalyst properties, in the sense that selectivity towards certain

products could be maximized. So far, a variety of methods have been developed to modify the pore structure and the catalytic activity of zeolites and related materials. These may be divided into two groups, namely methods applied during the synthesis, and actions to be taken after the zeolite material has been synthesized (post-synthesis modification). The following brief discussion of such methods focuses on the case of zeolites applied to acid catalyzed reactions, where the activity of the material is due to Brønsted acid sites, stoichiometrically linked to the Al atoms of the host lattice, and also to Lewis acid sites.

The choice among the variety of different types of zeolites and related materials in a practical situation will depend on the characteristics of the reacting system and the types of selectivity effects to be expected. The pore size, the deactivation behavior and the chemical and thermal stability of the zeolite material determine whether or not a particular catalyst is attractive. The necessary condition for shape-selectivity effects to occur is that the pore size has to meet the dimensions of the reacting molecules. The radius of the crystallites as well as the strength and the number of the acid sites may then be adapted to the actual requirements during synthesis.

Post-synthesis methods (pore-size engineering) allow an existing shape-selectivity effect to be intensified, and also a new one to be established. However, normally not only the pore size will be influenced by most of these methods, but also the catalytic activity. Vansant [104] gives a classification of post-synthesis modification methods which covers the entire range of zeolite applications (gas separation, gas purification, encapsulation of gases and catalysis).

Of particular interest for shape-selective catalysis is the modification of the zeolite by means of cation exchange as well as the modification of the inner and/or outer crystallite structure by a treatment with chemically reacting agents which leads to a deposition of additional functional groups or compounds. This can be done either in the gas phase (i.e. chemical vapor deposition (CVD)) or in the liquid phase.

By means of ion exchange using metal cations of different size and specific charge, the geometrical restrictions, the number and the strength of the Brønsted acid sites, as well as the adsorption properties of the zeolite material can be influenced. Investigations of this kind have been reported in the literature, for example for ZSM-5 and mordenite catalysts [20, 105].

During a treatment with chemically reacting agents, these may penetrate into the pore system where they react to form deposits, which may lead to a narrowing of the pores as well as to a change in the catalytic activity. Boric acid, trimethylborate, phosphoric acid and triphenylphosphine may serve as examples for suitable reacting agents. Such methods have been applied successfully to the selective production of *p*-xylene by

disproportionation of toluene on a ZSM-5-zeolite, where *para* selectivities in excess of 90% were claimed [56, 93].

Chemical vapor deposition of silanes, along with a subsequent calcination using steam, can be utilized to deposit silica (SiO<sub>2</sub>) inside the pore system. By variation of the temperature, the partial pressure of the silane and the duration of the treatment, location and amount of the deposited material can be controlled [104]. When, for example, tetraethoxy- or tetramethoxysilane are used as reacting agents on a mordenite, ZSM-5, or  $\beta$ -zeolite, then a controlled deactivation of only the external crystallite surface is possible [23, 44]. This is because these are rather bulky molecules which are not able to diffuse into the pore system of the crystallite. Alternatively, an irreversible adsorption of bulky bases may serve to destroy the undesired external acidity. Suitable basic compounds are 4-methylquinoline for ZSM-5 [2] and tributylphosphite for mordenites [71].

Finally, a controlled precoking, as well as the undesired coking during reaction, may cause a change of selectivity. Coke in this general sense here is meant to include any type of undesired higher hydrocarbons which may be formed from an organic reactant [41]; however, polycondensed aromatics are of particular importance. The blocking of the catalytically active surface by coking may be traced back to basically two reasons. Either the hydrocarbon due to its size is trapped inside the zeolite cage or channel crossing, or its vapor pressure at the reaction conditions is too low. The latter may also cause a deactivation of the external surface of the crystallite. During the deposition of coke inside the pores either pore blockage or site coverage [41] may occur. In the case of pore blockage, the deactivation, at the same level of coke deposited, is more pronounced than in the case of site coverage. Analogous to the chemical vapor deposition, an appropriate choice of precoking agent along with the precoking conditions (temperature), allows control of whether the deposits will be placed at the outer surface of the crystallites or inside the microporous structure.

Investigations concerning the effects of precoking have been carried out for example on ZSM-5 catalysts for xylene production by disproportionation or alkylation of toluene [102]. During these experiments, an increase of the *p*-xylene selectivity could be observed. By a defined precoking, it is also possible to generate product-selectivity effects initially not present, as has been shown for the disproportionation of ethylbenzene on HY-zeolites [63].

## References

1. J. B. Anderson, *Chem. Eng. Sci.* **1963**, *18*, 147.
2. J. R. Anderson, K. Foger, T. Mole, R. A. Rajadhyaksha, J. V. Sanders, *Zeolites* **1993**, *13*, 518.
3. R. Aris, *Chem. Eng. Sci.* **1957**, *6*, 262.
4. R. Aris, *Ind. Eng. Chem., Fundam.* **1965**, *4*, 227; R. Aris, *Ind. Eng. Chem., Fundam.* **1965**, *4*, 487.
5. R. Aris, *The Mathematical Theory of Diffusion and Reaction in Permeable Catalysts*, Vol. 1: *The Theory of the Steady State*, Clarendon Press, Oxford, **1975**.
6. R. Aris, *The Mathematical Theory of Diffusion and Reaction in Permeable Catalysts*, Vol. 2: *Questions of Uniqueness, Stability and Transient Behavior*, Clarendon Press, Oxford, **1975**.
7. M. Baerns, A. Renken, H. Hofmann, *Chemische Reaktionstechnik*, 2nd ed., Thieme-Verlag, Stuttgart, **1992**, Chapter 6.
8. K. B. Bischoff, *Chem. Eng. Sci.* **1967**, *22*, 525.
9. R. B. Bird, W. E. Stewart, E. N. Lightfoot, *Transport Phenomena*, Wiley, New York, **1960**.
10. J. B. Butt, *AIChE J.* **1965**, *11*, 106.
11. J. B. Butt, *Chem. Eng. Sci.* **1966**, *21*, 275.
12. J. B. Butt, *Reaction Kinetics and Reactor Design*, Prentice-Hall, Englewood Cliffs, **1980**, Chapter 7.
13. J. J. Carberry, *AIChE J.* **1961**, *7*, 350.
14. J. J. Carberry, *AIChE J.* **1962**, *8*, 557.
15. J. J. Carberry, *Chem. Eng. Sci.* **1962**, *17*, 675.
16. J. J. Carberry, *Catal. Rev.* **1969**, *3*, 61.
17. J. J. Carberry and A. A. Kulkarni, *J. Catal.* **1973**, *31*, 41.
18. J. J. Carberry, *Chemical and Catalytic Reaction Engineering*, McGraw-Hill, New York, **1976**, Chapter 5.
19. J. J. Carberry, *Catalysis Science and Technology* (Eds: J. R. Anderson, M. Boudart), Springer-Verlag, Berlin, **1987**, Vol. 8, Chapter 3.
20. P. Cartaud, A. Cointot, M. Dufour, N. S. Gnep, M. Guisnet, G. Joly, J. Tejada, *Appl. Catal.* **1986**, *21*, 85.
21. G. Cassiere, J. J. Carberry, *Chem. Eng. Educ.* **1973**, *7*, 22.
22. R. M. Chambers, M. Boudart, *J. Catal.* **1966**, *6*, 141.
23. Y. Chun, X. Chen, A.-Z. Yan, Q.-H. Xu, *Stud. Surf. Sci. Catal.* **1994**, *84*, 1035.
24. N. Y. Chen, T. F. Degman, Jr., C. M. Smith, *Molecular Transport and Reaction in Zeolites - Design and Application of Shape Selective Catalysts*, VCH, New York, **1994**.
25. E. L. Cussler, *Diffusion - Mass Transfer in Fluid Systems*, Cambridge University Press, Cambridge, **1984**.
26. D. L. Cresswell, *Chem. Eng. Sci.* **1970**, *25*, 267.
27. S. M. Csicsery, *J. Catal.* **1970**, *19*, 394.
28. G. Damköhler, *Chemieingenieur*, **1937**, *3*, 359.
29. P. Demontis, G. B. Suffritti, *Stud. Surf. Sci. Catal.* **1994**, *84*, 2107.
30. D. D. Do, *AIChE J.* **1985**, *31*, 574.
31. G. Emig, *Top. Curr. Chem.* **1970**, *13*, 451.
32. G. Emig, E. Klemm, H. Sciler, *Chemie Ingenieur Technik* **1994**, *66*, 956.
33. F. Fitzer, W. Fritz, G. Emig, *Technische Chemie*, 4th ed., Springer-Verlag, Berlin, **1995**, Chapters 12 and 13.
34. H. S. Fogler, *Elements of Chemical Reaction Engineering*, Prentice Hall, Englewood Cliffs, **1990**, Chapters 10 and 11.
35. D. Fraenkel, *Ind. Eng. Chem., Res.* **1990**, *29*, 1814.
36. B. Frank, K. Dahlke, G. Emig, E. Aust, R. Broucek, M. Nywlt, *Micropor. Mater.* **1993**, *1*, 43.
37. S. Fritzsche, R. Haberlandt, J. Kärger, H. Pfeifer, M. Waldherr-Teschner, *Stud. Surf. Sci. Catal.* **1994**, *84*, 2139.
38. G. F. Froment, K. B. Bischoff, *Chemical Reactor Analysis and Design*, Wiley, New York, **1979**, Chapter 3.
39. E. E. Gonzo, J. C. Gottifredi, *J. Catal.* **1983**, *83*, 25.
40. E. E. Gonzo, *Latin. Am. Appl. Res.* **1993**, *23*, 1.
41. M. Guisnet, P. Magnoux, *Stud. Surf. Sci. Catal.* **1994**, *88*, 53.
42. K. Hashimoto, T. Masuda, and M. Kawase, *Stud. Surf. Sci. Catal.* **1989**, *46*, 485.
43. B. Hatfield, R. Aris, *Chem. Eng. Sci.* **1969**, *24*, 1213.
44. T. Hibino, M. Niwa, Y. Murakami, *Zeolites* **1993**, *13*, 518.

45. W. Hilgert, PhD Thesis, University of Erlangen-Nürnberg, 1991.
46. V. Hlaváčzek, M. Marek, *J. Catal.* **1969**, *15*, 17.
47. V. Hlaváčzek, M. Marek, *J. Catal.* **1969**, *15*, 31.
48. V. Hlaváčzek, *Chem. Eng. Sci.* **1970**, *25*, 1517.
49. V. Hlaváčzek, *J. Catal.* **1971**, *22*, 364.
50. R. R. Hudgins, *Chem. Eng. Sci.* **1968**, *23*, 93.
51. R. R. Hudgins, *Can. J. Chem. Eng.* **1972**, *50*, 427.
52. R. R. Hudgins, *Chem. Eng. Sci.* **1981**, *36*, 1579.
53. J. Hutchings, J. J. Carberry, *AIChE J.* **1966**, *12*, 20.
54. T. Inui, Y. Nakazi, *Zeolites* **1991**, *11*, 434.
55. P. A. Jacobs, E. Ma, *IZA Newsletter*, **1994**, *3*.
56. W. W. Kaeding, C. Chu, L. B. Young, B. Weinstein, S. A. Butter, *J. Catal.* **1981**, *67*, 159.
57. J. Kärger, D. M. Ruthven, *Diffusion in Zeolites and other Microporous Solids*, Wiley, New York, **1992**.
58. H. G. Karge, J. Ladebeck, Z. Sarbak, K. Hatada, *Zeolites* **1982**, *2*, 94.
59. H. G. Karge, K. Hatada, Y. Zhang, R. Fiedorow, *Zeolites* **1983**, *3*, 13.
60. J. Karge, S. Ernst, M. Weihe, U. Weiß, J. Weitkamp, *Stud. Surf. Sci. Catal.* **1994**, *84*, 1805.
61. H. S.-P. Kao, C. N. Satterfield, *Ind. Eng. Chem., Fundam.* **1968**, *7*, 664.
62. J. P. Kehoe, J. B. Butt, *Chem. Eng. Sci.* **1970**, *25*, 345.
63. E. Klemm, Ph D Thesis, University of Erlangen-Nürnberg, 1995.
64. R. M. Koros, E. J. Nowak, *Chem. Eng. Sci.* **1967**, *22*, 470.
65. H. Kubota, Y. Yamanaka, *J. Chem. Eng. (Jpn)* **1969**, *2*, 238.
66. H. H. Lee, *Heterogeneous Reactor Design*, Butterworth, Boston, **1985**, Chapter 4.
67. W. Liang, S. Y. Chen, S. Y. Peng, *Proceedings of the 9th International Zeolite Conference, 1992*, Montreal, Canada, Paper RP31.
68. D. Luss, *AIChE J.* **1968**, *14*, 966.
69. D. Luss in *Dynamics and Modeling of Reactive Systems* (Eds: W. E. Stewart, W. H. Ray, C. C. Conley), Academic Press, New York, **1980**.
70. D. Luss in *Chemical Reaction and Reactor Engineering* (Eds: J. J. Carberry, A. Varma), Marcel Dekker, New York, **1987**, Chapter 4.
71. T. Matsuda, E. Kikuchi, *Stud. Surf. Sci. Catal.* **1993**, *83*, 295.
72. C. McGreavy, D. L. Cresswell, *Chem. Eng. Sci.* **1969**, *24*, 608.
73. C. McGreavy, D. L. Cresswell, *Can. J. Chem. Eng.* **1969**, *47*, 583.
74. R. J. Madon, M. Boudart, *Ind. Eng. Chem. Fundam.* **1982**, *21*, 438.
75. J. A. Maymo, R. E. Cunningham, *J. Catal.* **1966**, *6*, 186.
76. D. E. Mears, *Ind. Eng. Chem., Proc. Design. Devel.* **1971**, *10*, 541.
77. D. E. Mears, *J. Catal.* **1971**, *20*, 127.
78. M. Morbidelli, A. Varma, *Chem. Eng. Sci.* **1981**, *36*, 1211.
79. E. B. Naumann, *Chemical Reactor Design*, Wiley, New York, **1987**, Chapter 10.
80. D. Olson, W. Haag, *ACS Symp. Ser.* **1984**, *248*, 275.
81. K. Østergaard, *Proceedings of the 3rd International Congress on Catalysis*, North Holland, Amsterdam, **1965**, 1348.
82. G. Papareto, E. Moretti, G. Leofanti, F. Gatti, *J. Catal.* **1987**, *105*, 227.
83. E. E. Petersen, *Chem. Eng. Sci.* **1962**, *17*, 987.
84. E. E. Petersen, *Chem. Eng. Sci.* **1965**, *20*, 587.
85. E. E. Petersen, *Chemical Reaction Analysis*, Prentice-Hall, Englewood-Cliffs, **1965**, Chapter 4.
86. E. E. Petersen, *Chem. Eng. Sci.* **1968**, *23*, 94.
87. G. W. Roberts, C. N. Satterfield, *Ind. Eng. Chem., Fundam.* **1965**, *4*, 288.
88. G. W. Roberts, C. N. Satterfield, *Ind. Eng. Chem., Fundam.* **1966**, *5*, 317.
89. G. W. Roberts, *Chem. Eng. Sci.* **1972**, *27*, 1409.
90. C. N. Satterfield, T. K. Sherwood, *The Role of Diffusion in Catalysis*, Addison-Wesley, Reading, **1963**.
91. C. N. Satterfield, *Mass Transfer in Heterogeneous Catalysis*, MIT Press, Cambridge, **1970**, Chapters 3 and 4.
92. C. N. Satterfield, *Heterogeneous Catalysis in Practice*, McGraw-Hill, New York, **1980**, Chapter 11.
93. M. Sayed, J. Vedrine, *J. Catal.* **1995**, *101*, 43.
94. J. M. Smith, *Chemical Engineering Kinetics*, 2nd ed., McGraw-Hill, New York, **1970**, Chapters 10 and 11.
95. N. L. Smith, N. R. Amundsen, *Ind. Eng. Chem.* **1951**, *43*, 2156.
96. J. Stoer, R. Bulirsch, *Numerische Mathematik*, 3rd ed., Springer-Verlag, Berlin, **1990**.
97. D. Theodorou, J. Wei, *J. Catal.* **1983**, *83*, 205.
98. E. W. Thiele, *Ind. Eng. Chem.* **1939**, *31*, 916.
99. J. D. Tinkler, R. I. Pigford, *Chem. Eng. Sci.* **1961**, *15*, 326.
100. J. D. Tinkler, A. B. Metzner, *Ind. Eng. Chem.* **1961**, *53*, 663.
101. J. Tsikoyiannis, J. Wei, *Chem. Eng. Sci.* **1991**, *46*, 223.
102. M. A. Uguina, D. P. Serrano, R. van Grieken, S. Venes, *Appl. Catal.* **1993**, *99*, 97.
103. J. G. Van de Vusse, *Chem. Eng. Sci.* **1966**, *21*, 645.
104. E. F. Vansant, *Pore Size Engineering in Zeolites*, Wiley, New York, **1990**.
105. H. Vinek, M. Derewinski, G. Mirth, J. A. Lercher, *Appl. Catal.* **1991**, *68*, 277.
106. J. G. Wang, Y. W. Li, S. Y. Chen, S. Y. Peng, *Stud. Surf. Sci. Catal.* **1994**, *88*, 525.
107. J. Wei, *J. Catal.* **1982**, *76*, 433.
108. P. B. Weisz, C. D. Prater, *Adv. Catal.* **1954**, *6*, 143.
109. P. B. Weisz, *Z. Physik. Chem.* **1957**, *11*, 1.
110. P. B. Weisz, J. S. Hicks, *Chem. Eng. Sci.* **1962**, *17*, 265.
111. P. B. Weisz, V. J. Frilette, R. W. Maatman, E. B. Mower, *J. Catal.* **1962**, *1*, 307.
112. J. Weitkamp, S. Ernst, P. Jacobs, H. G. Karge, *Erdöl und Kohle-Erdgas-Petrochemie*, **1986**, *39*, 13.
113. A. Wheeler, *Adv. Catal.* **1951**, *3*, 249.
114. Y. B. Zeldovich, *Acta Phys. Chim. USSR*, **1939**, *10*, 583.

## 6.3 Determination of Diffusion Coefficients in Porous Media

J. KÄRGER

### 6.3.1 Definitions

Diffusion is the process of molecular transport associated with the stochastic movement of the individual diffusants. Diffusion coefficients in porous media may be defined on the basis of the generalized Fick's first law

$$j_{z,i} = - \sum_j D_{ij} \partial c_j / \partial z \quad (1)$$

where  $j_{z,i}$  and  $c_i$  denote, respectively, the flux density in the  $z$  direction and the concentration of the  $i$ th com-



45. W. Hilgert, PhD Thesis, University of Erlangen-Nürnberg, 1991.
46. V. Hlaváčzek, M. Marek, *J. Catal.* **1969**, *15*, 17.
47. V. Hlaváčzek, M. Marek, *J. Catal.* **1969**, *15*, 31.
48. V. Hlaváčzek, *Chem. Eng. Sci.* **1970**, *25*, 1517.
49. V. Hlaváčzek, *J. Catal.* **1971**, *22*, 364.
50. R. R. Hudgins, *Chem. Eng. Sci.* **1968**, *23*, 93.
51. R. R. Hudgins, *Can. J. Chem. Eng.* **1972**, *50*, 427.
52. R. R. Hudgins, *Chem. Eng. Sci.* **1981**, *36*, 1579.
53. J. Hutchings, J. J. Carberry, *AIChE J.* **1966**, *12*, 20.
54. T. Inui, Y. Nakazi, *Zeolites* **1991**, *11*, 434.
55. P. A. Jacobs, E. Ma, *IZA Newsletter*, **1994**, 3.
56. W. W. Kaeding, C. Chu, L. B. Young, B. Weinstein, S. A. Butter, *J. Catal.* **1981**, *67*, 159.
57. J. Kärger, D. M. Ruthven, *Diffusion in Zeolites and other Microporous Solids*, Wiley, New York, **1992**.
58. H. G. Karge, J. Ladebeck, Z. Sarbak, K. Hatada, *Zeolites* **1982**, *2*, 94.
59. H. G. Karge, K. Hatada, Y. Zhang, R. Fiedorow, *Zeolites* **1983**, *3*, 13.
60. J. Karge, S. Ernst, M. Weihe, U. Weiß, J. Weitkamp, *Stud. Surf. Sci. Catal.* **1994**, *84*, 1805.
61. H. S.-P. Kao, C. N. Satterfield, *Ind. Eng. Chem., Fundam.* **1968**, *7*, 664.
62. J. P. Kehoe, J. B. Butt, *Chem. Eng. Sci.* **1970**, *25*, 345.
63. E. Klemm, Ph D Thesis, University of Erlangen-Nürnberg, **1995**.
64. R. M. Koros, E. J. Nowak, *Chem. Eng. Sci.* **1967**, *22*, 470.
65. H. Kubota, Y. Yamanaka, *J. Chem. Eng. (Jpn)* **1969**, *2*, 238.
66. H. H. Lee, *Heterogeneous Reactor Design*, Butterworth, Boston, **1985**, Chapter 4.
67. W. Liang, S. Y. Chen, S. Y. Peng, *Proceedings of the 9th International Zeolite Conference, 1992*, Montreal, Canada, Paper RP31.
68. D. Luss, *AIChE J.* **1968**, *14*, 966.
69. D. Luss in *Dynamics and Modeling of Reactive Systems* (Eds: W. E. Stewart, W. H. Ray, C. C. Conley), Academic Press, New York, **1980**.
70. D. Luss in *Chemical Reaction and Reactor Engineering* (Eds: J. J. Carberry, A. Varma), Marcel Dekker, New York, **1987**, Chapter 4.
71. T. Matsuda, E. Kikuchi, *Stud. Surf. Sci. Catal.* **1993**, *83*, 295.
72. C. McGreavy, D. L. Cresswell, *Chem. Eng. Sci.* **1969**, *24*, 608.
73. C. McGreavy, D. L. Cresswell, *Can. J. Chem. Eng.* **1969**, *47*, 583.
74. R. J. Madon, M. Boudart, *Ind. Eng. Chem. Fundam.* **1982**, *21*, 438.
75. J. A. Maymo, R. E. Cunningham, *J. Catal.* **1966**, *6*, 186.
76. D. E. Mears, *Ind. Eng. Chem., Proc. Design. Devel.* **1971**, *10*, 541.
77. D. E. Mears, *J. Catal.* **1971**, *20*, 127.
78. M. Morbidelli, A. Varma, *Chem. Eng. Sci.* **1981**, *36*, 1211.
79. E. B. Naumann, *Chemical Reactor Design*, Wiley, New York, **1987**, Chapter 10.
80. D. Olson, W. Haag, *ACS Symp. Ser.* **1984**, *248*, 275.
81. K. Østergaard, *Proceedings of the 3rd International Congress on Catalysis*, North Holland, Amsterdam, **1965**, 1348.
82. G. Papareto, E. Moretti, G. Leofanti, F. Gatti, *J. Catal.* **1987**, *105*, 227.
83. E. E. Petersen, *Chem. Eng. Sci.* **1962**, *17*, 987.
84. E. E. Petersen, *Chem. Eng. Sci.* **1965**, *20*, 587.
85. E. E. Petersen, *Chemical Reaction Analysis*, Prentice-Hall, Englewood-Cliffs, **1965**, Chapter 4.
86. E. E. Petersen, *Chem. Eng. Sci.* **1968**, *23*, 94.
87. G. W. Roberts, C. N. Satterfield, *Ind. Eng. Chem., Fundam.* **1965**, *4*, 288.
88. G. W. Roberts, C. N. Satterfield, *Ind. Eng. Chem., Fundam.* **1966**, *5*, 317.
89. G. W. Roberts, *Chem. Eng. Sci.* **1972**, *27*, 1409.
90. C. N. Satterfield, T. K. Sherwood, *The Role of Diffusion in Catalysis*, Addison-Wesley, Reading, **1963**.
91. C. N. Satterfield, *Mass Transfer in Heterogeneous Catalysis*, MIT Press, Cambridge, **1970**, Chapters 3 and 4.
92. C. N. Satterfield, *Heterogeneous Catalysis in Practice*, McGraw-Hill, New York, **1980**, Chapter 11.
93. M. Sayed, J. Vedrine, *J. Catal.* **1995**, *101*, 43.
94. J. M. Smith, *Chemical Engineering Kinetics*, 2nd ed., McGraw-Hill, New York, **1970**, Chapters 10 and 11.
95. N. L. Smith, N. R. Amundsen, *Ind. Eng. Chem.* **1951**, *43*, 2156.
96. J. Stoer, R. Bulirsch, *Numerische Mathematik*, 3rd ed., Springer-Verlag, Berlin, **1990**.
97. D. Theodorou, J. Wei, *J. Catal.* **1983**, *83*, 205.
98. E. W. Thiele, *Ind. Eng. Chem.* **1939**, *31*, 916.
99. J. D. Tinkler, R. I. Pigford, *Chem. Eng. Sci.* **1961**, *15*, 326.
100. J. D. Tinkler, A. B. Metzner, *Ind. Eng. Chem.* **1961**, *53*, 663.
101. J. Tsikoyiannis, J. Wei, *Chem. Eng. Sci.* **1991**, *46*, 223.
102. M. A. Uguina, D. P. Serrano, R. van Grieken, S. Venes, *Appl. Catal.* **1993**, *99*, 97.
103. J. G. Van de Vusse, *Chem. Eng. Sci.* **1966**, *21*, 645.
104. E. F. Vansant, *Pore Size Engineering in Zeolites*, Wiley, New York, **1990**.
105. H. Vinek, M. Derewinski, G. Mirth, J. A. Lercher, *Appl. Catal.* **1991**, *68*, 277.
106. J. G. Wang, Y. W. Li, S. Y. Chen, S. Y. Peng, *Stud. Surf. Sci. Catal.* **1994**, *88*, 525.
107. J. Wei, *J. Catal.* **1982**, *76*, 433.
108. P. B. Weisz, C. D. Prater, *Adv. Catal.* **1954**, *6*, 143.
109. P. B. Weisz, *Z. Physik. Chem.* **1957**, *11*, 1.
110. P. B. Weisz, J. S. Hicks, *Chem. Eng. Sci.* **1962**, *17*, 265.
111. P. B. Weisz, V. J. Frilette, R. W. Maatman, E. B. Mower, *J. Catal.* **1962**, *1*, 307.
112. J. Weitkamp, S. Ernst, P. Jacobs, H. G. Karge, *Erdöl und Kohle-Erdgas-Petrochemie*, **1986**, *39*, 13.
113. A. Wheeler, *Adv. Catal.* **1951**, *3*, 249.
114. Y. B. Zeldovich, *Acta Phys. Chim. USSR*, **1939**, *10*, 583.

## 6.3 Determination of Diffusion Coefficients in Porous Media

J. KÄRGER

### 6.3.1 Definitions

Diffusion is the process of molecular transport associated with the stochastic movement of the individual diffusants. Diffusion coefficients in porous media may be defined on the basis of the generalized Fick's first law

$$j_{z,i} = - \sum_j D_{ij} \frac{\partial c_j}{\partial z} \quad (1)$$

where  $j_{z,i}$  and  $c_i$  denote, respectively, the flux density in the  $z$  direction and the concentration of the  $i$ th com-

ponent. The parameters  $D_{ij}$  denote the generalized diffusion coefficients (or diffusivities). They depend on the given porous medium and the temperature, as well as on the diffusants involved and their concentrations. In using eq 1, the porous medium is considered as quasi-homogeneous. Concentrations and fluxes must be defined, therefore, with respect to sufficiently large volume elements and areas, so that the averages over all volume elements and areas are identical. In the case of intracrystalline diffusion in porous crystallites this is ensured by considering volume elements substantially exceeding the unit cell dimensions. In amorphous materials and beds of porous crystallites, much larger volume elements must be considered. The structure of such volume elements can clearly only be compared in a statistical sense. Diffusivities defined on the basis of eq 1 for inhomogeneous systems are sometimes called "apparent" diffusivities [1], since with this definition the system under study appears to be homogeneous with respect to its transport properties, even, though it is not really homogeneous.

Equation 1 says nothing about the underlying mechanisms, nor does it imply anything about the dependence of the diffusivities on the concentration of the relevant components. For diffusivities, which vary considerably with concentration, the concentration range covered within a sample during diffusivity measurement should be kept as small as possible. Otherwise only "integral" diffusivities may be determined, from which it is difficult to extract the "differential" diffusivities [2].

In a complex system such as a catalyst particle, a variety of processes may contribute to the diffusion fluxes [1-3] (see Section A.6.2). In general, the diffusants within the pore system of a catalyst particle coexist in two phases, a gas phase and an adsorbed phase. In the vicinity of the external surface, the gas phase concentration in the catalyst particle is determined by that of the surrounding atmosphere. If there are no additional resistances (e.g. film resistances), both concentrations are identical. Since the external gas phase concentration is easily accessible experimentally, molecular fluxes through the catalyst particle are often related to the gas phase concentration, even though this is at variance with the understanding of Fick's first law as formulated by eq 1. The "effective" diffusivities [1] defined in this way are clearly different from those introduced by eq 1. Obviously, if the density of molecules in the adsorbed phase is negligibly small in comparison with the gas phase within the particle pores, the ratio between the concentrations (referred to unit volume of the catalyst particle and of the gas phase, respectively) is given by the porosity. Consequently, the ratio between the effective diffusivities and the diffusivities introduced by eq 1 is also given by the porosity. In comparison with the gas phase, the diffusivities are ad-

ditionally reduced by the effect of the tortuosity factor [1-3].

Depending on the conditions of the diffusion experiment, the diffusivities defined by eq 1 are given particular names. For one-component diffusion under the influence of a concentration gradient, eq 1 reduces to

$$j_z = -D \, dc/dz \quad (2)$$

with  $D$  denoting the transport diffusivity.

Single-component diffusion under equilibrium conditions can be monitored either by labeling some of the molecules or by following their trajectories. Considering the diffusion flux of the labeled molecules, again a proportionality relation of the type of eq 2 may be established. The factor of proportionality is called the coefficient of self-diffusion (or tracer diffusion). In a completely equivalent way [2], the self-diffusion coefficient may be determined on the basis of Einstein's relation

$$\langle z^2(t) \rangle = 2Dt \quad (3)$$

as the factor of proportionality between the mean-square displacement of the diffusants and the observation time, provided that—for sufficiently large observation times—this proportionality is established (see Section A.5.5.2).

Self-diffusion under equilibrium conditions may also be monitored in multicomponent systems. Again, with both eqs 2 and 3 a self-diffusion coefficient (of a particular component) may be defined. This coefficient depends on the nature and the concentration of all molecular species involved as well as on the nature of the catalyst particle.

Mass transfer in catalysis proceeds under non-equilibrium conditions with at least two molecular species (the reactant and product molecules) involved [4, 5]. Under steady state conditions, the flux of the product molecules out of the catalyst particle is stoichiometrically equivalent (but in the opposite direction) to the flux of the entering reactant species. The process of diffusion of two different molecular species with concentration gradients opposed to each other is called counter diffusion, and if the stoichiometry is 1:1 we have equimolar counter diffusion. The situation is then similar to that considered in the case of self- or tracer diffusion, the only difference being that now two different molecular species are involved. Tracer diffusion may be considered, therefore, as equimolar counter diffusion of two identical species.

The process of diffusion of (generally two) components with concentration gradients pointing in the same direction is called codiffusion. According to eq 1, the flux density of each individual component may depend

on the concentration gradients of both species. The factors of proportionality are called coefficients of codiffusion. Obviously, any component in a two-component system is described by two coefficients of codiffusion, relating the flux of this component to the concentration gradient of the same component and of the other component, respectively. The diffusivities depend, in general, on the concentrations of both components.

## 6.3.2 Measurement of Transport Diffusion

### 6.3.2.1 Steady State Measurements

Steady state experiments have their origin in the classical permeation measurements of Darcy [1, 2]. In a typical experimental set-up a pressure drop is imposed across a porous plug (often a single cylindrical pellet) of catalyst by maintaining a constant (known) pressure on one side while the pressure on the other side is maintained at a lower constant value or allowed to increase with passage of the diffusant through the plug. In the latter case, monitoring the downstream pressure provides a simple and convenient way of measuring the flux. More recently, this technique has even been successfully applied to transport diffusion studies in zeolite crystallites by incorporating them in impermeable membranes [6–8]. In general, however, the method suffers from the disadvantage that the permeability rather than the diffusivity is measured. The two quantities are directly correlated only in the regimes of intracrystalline and Knudsen diffusion [1, 3, 9, 10].

This limitation is overcome in the Wicke–Kallenbach method [11]. This method differs from the original permeability experiment in that, by applying a carrier gas, the flux is measured under constant pressure conditions with a known concentration difference maintained across the membrane or pellet. In this way, any nondiffusive contribution (Poiseuille flow) to the observed fluxes may be excluded.

### 6.3.2.2 Time Lag Measurements

Information about transport diffusion in catalyst particles can also be deduced during the initial, unsteady state period of a permeation experiment. In this stage, the number of molecules passing the plug of catalyst per unit time will increase from zero until the rate of permeation characterizing the steady state behavior is attained. In the limit  $t \rightarrow \infty$ , the total amount of molecules which have permeated in the time interval  $0 \dots t$  is given by the relation [1, 2, 12]

$$Q(t \rightarrow \infty) = cD/L \times (t - L^2/(6D)) \quad (4)$$

with  $c$ ,  $D$ , and  $L$  denoting, respectively, the concentration and diffusivity of the diffusants within the porous system under study and its extension in the direction of the concentration gradient. The time intercept of a plot of  $Q(t \rightarrow \infty)$  versus time gives a time lag

$$\tau = L^2/(6D) \quad (5)$$

which may be used for the determination of the transport diffusivity.

Procedures to remove the restrictions of the permeation technique, also inherent in the time lag method, have been described by Grachev et al. [13] and Gibilaro et al. [14]. As with the Wicke–Kallenbach method, they are based on the application of a carrier gas. Details of these methods may be found in Ref. 1.

### 6.3.2.3 Sorption Rate Measurements

The most widely used unsteady state method for determining diffusivities in porous solids involves measuring the rate of adsorption or desorption when the sample is subjected to a well defined change in the concentration or pressure of sorbate. The experimental methods differ mainly in the choice of the initial and boundary conditions and the means by which progress towards the new position of equilibrium is followed. The diffusivities are found by matching the experimental transient sorption curve to the solution of Fick's second law. Detailed presentations of the relevant formulae may be found in the literature [1, 2, 12, 15–17]. For spherical particles of radius  $R$ , for example, the fractional uptake after a pressure step obeys the relation

$$\begin{aligned} \gamma(t) &= [m(t) - m(0)]/[m(\infty) - m(0)] \\ &= 1 - 6/\pi^2 \sum_{n=1}^{\infty} 1/n^2 \times \exp(-n^2\pi^2Dt/R^2) \end{aligned} \quad (6)$$

where the concentration in the surrounding atmosphere after the pressure step is assumed to be constant. This is a valid approximation if the system volume is large. The series converges rapidly for large values of time, and for  $\gamma > 0.7$  it is sufficient to retain the first term only:

$$\gamma(t) \approx 1 - 6/\pi^2 \times \exp(-\pi^2Dt/R^2) \quad (7)$$

Alternatively, in the short-time range ( $\gamma(t) < 0.3$ ) the uptake may be approximated by the  $\sqrt{t}$  law

$$\gamma(t) \approx 6 \sqrt{(Dt/\pi R^2)} \quad (8)$$

For sufficiently short times, eq 8 holds for any particle size. In this case,  $R$  is understood as an equivalent radius being equal to three times the ratio between the particle volume and the external surface.

If the uptake measurements are carried out in a small volume, the concentration in the surrounding atmosphere will decrease after the pressure step. Equation 6 is then replaced by

$$\gamma(t) = 1 - \sum_{n=1}^{\infty} 6\lambda(\lambda + 1)/(9 + 9\lambda + q_n^2 k^2) \times \exp(q_n^2 D t / R^2) \quad (9)$$

with  $\lambda = p(\infty)/(p(0) - p(\infty))$ , and  $q_n$  denoting the nonzero roots of

$$\tan q_n = 3q_n/(3 + \lambda q_n^2) \quad (10)$$

For sufficiently short times, the  $\sqrt{t}$  law may again be applied, with an additional factor

$$[p(0) - p(-0)]/[p(\infty) - p(-0)]$$

on the right-hand side of relation 8. The quantities  $p(-0)$ ,  $p(0)$  and  $p(\infty)$  denote, respectively, the sorbate pressure (and hence the concentration) in the surrounding atmosphere before the uptake experiment, at the beginning of the uptake experiment, and after attaining the new equilibrium value.

Conventionally, molecular uptake is recorded gravimetrically [18–20]. Alternatively, for a limited supply of adsorbate, molecular uptake may also be calculated from a knowledge of the time dependence of the pressure (piezometric method [21, 22]) or composition of the gas phase. Changing the sorbate pressure by a step change of the gas volume has proved to be a very efficient method for following fast sorption processes (single step method [23, 24]). The sorption uptake may also be measured volumetrically by means of a gas burette arrangement [25].

In principle, the determination of molecular uptake may be based on any experimentally accessible quantity which is a function of the amount adsorbed. Being directly sensitive to a certain molecular species, in this respect the application of spectroscopic methods is particularly suitable. IR spectroscopy has been successfully applied to studying molecular uptake by beds of zeolite catalysts [26–28] as well as—in combination with IR microscopy [29, 30]—on individual crystallites. Similarly, NMR spectroscopy has also been used to monitor the time dependence of the sorbate concentration within porous media [31]. Moreover, recent progress in NMR imaging allows the observation of concentration profiles within porous media with spatial resolution below the mm region [32–34].

Unambiguous information about molecular transport may clearly only be deduced from sorption experiments if the applied model correctly reflects the multitude of processes accompanying molecular uptake. This may be checked by varying a characteristic parameter of the system, for example the crystallite size

for the study of intracrystalline diffusion in beds of crystallites [35, 36]. As a necessary condition for the validity of the model, the measured dependency must coincide with the theoretical prediction.

Among the external processes possibly influencing the rate of overall adsorption, the access of the diffusants into the sorption vessel and the dissipation of the adsorption heat deserve special attention. A substantial number of models have been developed to quantify these influences, which are generally referred to as the valve effect [37–39] and the heat effect [2, 40–42]. In turn, in Ref. 43 a novel method for uptake measurements has been based on the heat effect during molecular sorption. By IR monitoring of the surface temperature it has become possible to acquire a second, independent source of information about the internal processes within the sample, yielding useful information in particular for fast processes.

#### 6.3.2.4 Frequency Response Measurements

As an alternative approach to conventional uptake measurements, in the frequency response technique [44–48] one follows the response of the sample to a regular periodic perturbation, e.g. a sinusoidal variation of the system volume. Using complex notation, one may write for the time dependence of the system volume,

$$V(t) = V_0(1 - v \exp\{i\omega t\}) \quad (11)$$

For sufficiently small perturbations, both the induced pressure variation  $P(t)$  and the amount adsorbed  $A(t)$  are also sinusoidal functions of time:

$$P(t) = P_0\{1 + p \exp[i(\omega t + \varphi)]\} \quad (12)$$

$$A(t) = A_0\{1 + a \exp[i(\omega t + \phi)]\} \quad (13)$$

The pressure variation,  $\Delta P(t) = P_0 p \exp(i\omega t) \times \exp(i\varphi)$ , and the variation of the amount adsorbed,  $\Delta A(t) = A_0 a \exp(i\omega t) \times \exp(i\phi)$ , must be correlated, therefore, by a proportionality relation of the type

$$\Delta A(t) = (\alpha_c - i\alpha_s)\Delta P(t) \quad (14)$$

with  $\alpha_c$  and  $\alpha_s$  representing the real and imaginary parts of the complex factor of proportionality. They may be interpreted, therefore, as the in-phase and out-of-phase components of the adsorbed species with respect to the pressure variation and are commonly called the in-phase and out-of-phase characteristic functions. By using the equation of material balance,  $d/dt[P(t)V(t)/RT + A(t)] = 0$ , the in-phase and out-of-phase characteristic functions may be easily shown

to be determined through the experimentally accessible quantities  $p$  and  $\varphi$  by the relationships

$$\alpha_c = (v/p) \cos \varphi - 1 \quad (15)$$

$$\alpha_s = (v/p) \sin \varphi \quad (16)$$

Theoretical expressions for the frequency dependence of the characteristic functions may be calculated by solving the relevant diffusion equation under oscillating boundary conditions [44–48]. The diffusivities are determined by matching the experimental curves to the theoretical expressions for the given model. As a rule of thumb, the out-of-phase characteristic function may be expected to pass through a maximum at  $\omega \approx D/l^2$  (where  $l$  is the characteristic diffusion length for the particles under study), approaching zero for frequencies both much larger and much smaller than this “resonance” frequency.

A fundamental advantage of the frequency response method is its ability to yield information concerning the distribution of molecular mobilities. For example, a bimodal distribution of diffusivities, which is difficult to detect by conventional sorption measurements, leads to two different resonances [49]. Moreover, from an analysis of the frequency response spectrum it is even possible to monitor molecular diffusion in combination with chemical reactions [45]. As in conventional sorption experiments, however, the intrusion of heat effects limits the information provided by this technique for fast adsorption–desorption processes [50].

This limitation may be circumvented in the thermal frequency response method [51, 52]. By applying the IR temperature monitoring technique [43], in this method one is able to record the temperature response of the sample as a consequence of the adsorption heat released or consumed during the adsorption–desorption process. Thus, in addition to the pressure response a second, independent quantity becomes experimentally accessible. Since the sample temperature is influenced in a completely different way by the rates of molecular uptake and heat release, any confusion between these two influences is excluded. Moreover, by referring the temperature response to the variation of the pressure rather than to the variation of the volume, the influence of disturbing effects like adsorption by the vessel walls or temperature changes accompanying the changes of the volume may be excluded.

### 6.3.2.5 Chromatographic and Flow Methods

The influence of heat effects and of external mass transfer resistances (film resistance) may be significantly reduced by the application of flow methods. In the usual chromatographic experiment, a steady flow of an inert (nonadsorbing) carrier is passed through a

small column packed with the catalyst under study. A small pulse of sorbate is injected at the column inlet, and the effluent concentration is monitored continuously. While the retention volume is a measure of the adsorption equilibrium, the dispersion of the response peak is determined by mass transfer resistance and axial mixing within the column. A particularly convenient way of analyzing the experimental data may be based on the moments of the response curves of the chromatographic column. The first and second moments,  $\mu$  and  $\sigma^2$ , are defined by the relationships

$$\begin{aligned} \mu \equiv \bar{t} &= \int_0^\infty ct \, dt / \int_0^\infty c \, dt \quad \text{and} \\ \sigma^2 &= \int_0^\infty c(t - \mu)^2 dt / \int_0^\infty c \, dt \end{aligned} \quad (17)$$

for the pulse response, and by

$$\begin{aligned} \mu \equiv \bar{t} &= \int_0^\infty (1 - c/c_0) dt \quad \text{and} \\ \sigma^2 &= \int_0^\infty (1 - c/c_0)t \, dt - \mu^2 \end{aligned} \quad (18)$$

for the step response where  $c$  denotes the concentration of the adsorbate in the effluent. For the step response,  $c$  approaches the equilibrium value  $c_0$ . For a biporous adsorbent model [1–3], when the equilibrium constant  $K$  is large, the second moment is given by the relation:

$$\frac{\sigma^2}{2\mu^2} = \frac{D_L}{vL} + \frac{\varepsilon v}{L(1 - \varepsilon)} \left( \frac{R_p}{3k_f} + \frac{R_p^2}{15\varepsilon_p D_p} + \frac{R_c^2}{15KD_c} \right) \quad (19)$$

with the following notations:  $D_c$  and  $D_p$  are the diffusivities in the micro- and macroparticles with the respective radii  $R_c$  and  $R_p$ ;  $\varepsilon$  is the external void fraction of the adsorbent bed;  $\varepsilon_p$  the porosity of the adsorbent particle;  $D_L$  the axial dispersion coefficient;  $L$  the column length;  $v$  the interstitial fluid velocity;  $k_f$  the external mass transfer coefficient of the macroparticle;  $K$  the dimensionless Henry’s law constant. Equation 19 includes the important result that the second moment is simply the sum of the moments of the different transport resistances (see Section A.6.1.3). The method of moments has also been successfully applied to the analysis of sorption rate [12, 53] and steady state [54] measurements. It follows from eq 19 that by varying characteristic parameters of the experiment such as the flow rate  $v$  or the size  $R_p$  of the macroparticles, the contributions of the different mechanisms may, in principle, be discriminated. In reality, however, various deviations from the ideal behavior which was assumed in the derivation of eq 19 may become relevant. Such deviations include the influence of a pressure drop over the column [55, 56], nonlinearities in the adsorption isotherm, heat transfer resistances [57] and the influence of the finite pulse width [58]. More detailed

accounts of the application of chromatography to the study of diffusion in porous media may be found in several reviews [1, 2, 59, 60].

While in chromatographic methods external heat and mass transfer resistances can be eliminated more easily than in a static system, the response may be additionally affected by axial dispersion, as represented by the first term on the right hand side of eq 19. In the zero length column (ZLC) method the basic advantages of the chromatographic method are retained while eliminating the limitations imposed by axial dispersion [61, 62]. In this technique, which has proved to be particularly useful for the observation of fast sorption phenomena, a small sample of adsorbent (in general only consisting of microparticles of radius  $R$ ) is equilibrated at a uniform sorbate concentration and then desorbed by purging with an inert gas at a flow rate high enough to maintain essentially zero sorbate concentration at the external surface of the particles. By following the composition of the effluent, it is possible to measure the rate of desorption which may be attributed to the transport diffusion within the particles. Analytical solutions for various models may be found in the literature [62–64]. For sufficiently large purge flow rates and small sorbate concentrations (Henry's law range), the adsorbate concentration  $c(t)$  in the outgoing gas flow obeys the following relation in the long-time limit

$$c(t) \propto \exp(-\pi^2 D t / R^2) \quad (20)$$

This expression may be easily deduced from the corresponding relation for the desorption experiment (eq 7) by differentiation with respect to time.

### 6.3.3 Measurement of Self-Diffusion

#### 6.3.3.1 Elementary Steps of Diffusion

The process of molecular diffusion may be viewed conceptionally as a sequence of jumps with statistically varying jump lengths and residence times. Information about the mean jump length  $\sqrt{\langle l^2 \rangle}$  and the mean residence time  $\tau$ , which might be of particular interest for a deeper understanding of the elementary steps of catalysis, may be provided by spectroscopic methods, in particular by quasielastic neutron scattering (see next Section) and nuclear magnetic resonance (NMR).

NMR spectroscopy has been applied to the determination of the mean residence time of adsorbed molecules in essentially two different ways, namely by proton magnetic relaxation studies and deuterium magnetic resonance line shape analysis. In the case of adsorbed molecules, proton magnetic relaxation is mainly determined by magnetic dipole interactions with protons of the same molecule (intramolecular proton–proton

coupling), with protons of other molecules (intermolecular proton–proton coupling), and with paramagnetic iron. Separating the different contributions by a relaxation analysis [65, 66] it is, in principle, possible to determine the correlation time for any of these interactions, and from this, under appropriate conditions, the mean residence time between successive jumps.

The deuterium magnetic line shape is determined by the gradient of the electric field brought about by the surroundings. Molecular reorientation with rate constants of the order of or larger than the line width of the rigid molecule leads to an averaging of the effective electric field gradient which is reflected in characteristic changes of the measured NMR spectrum. Attributing the observed spectra to the results of model calculations allows an estimate of the rates of reorientation and with them of the mean residence time [67, 68]. By assuming a molecular jump length comparable with the separation between adjacent large cavities as a reasonable estimate of the molecular mean jump length, deuterium NMR has been used in refs. [69, 70] to predict zeolitic diffusivities on the basis of the relation

$$D = \langle l^2 \rangle / 6\tau \quad (21)$$

Equation 21 is the microscopic equivalent of the Einstein equation (3) and implies that succeeding jumps are uncorrelated. In general, however, backward jumps will take place with a higher probability (the correlation effect [2]), so that eq 21 provides an upper limit of the diffusivity. Alternatively, with known values for  $D$  and  $\tau$ , eq 21 allows an estimate of the lower limit of the mean-square jump length [67, 68].

#### 6.3.3.2 Quasielastic Neutron Scattering

Diffusion measurement by thermal neutron scattering is based on an analysis of the (quasielastic) broadening in the energy distribution of the outgoing neutron beam (for the application of neutron scattering for the investigation of structural properties of catalysts, see Section A.3.1.3.7). This broadening may be conceptionally understood as a Doppler broadening, caused by energy transfer between the incident wave and the scattering centers (in general the protons of the molecules under study). Since the energy transfer corresponding to a diffusive motion is very small, the term quasielastic neutron scattering (QENS) is used for such studies. For a diffusive motion with infinitely small diffusion steps, the half width at half maximum of the energy distribution of the outgoing beam (quasielastic and incoherent part [71, 72]), is determined by

$$\Delta E \equiv \hbar \Delta \omega(\kappa) = \hbar \kappa^2 D \quad (22)$$

with  $\kappa$  and  $\omega$  denoting, respectively, the differences in the wave vectors and the frequencies between the incident and scattered neutron beams. On the basis of eq 22, the self-diffusivity may be easily determined from a plot of  $\Delta\omega$  vs.  $\kappa^2$ . For diffusion steps of finite length, one obtains [73]

$$\Delta E \equiv \hbar\Delta\omega(\kappa) = \hbar[1 - \exp(-\kappa^2\langle l^2 \rangle/6)]/\tau \quad (23)$$

which allows the determination of both the mean residence time (for large values of  $\kappa$ ) and the self-diffusivity (for small values of  $\kappa$ , where eqs 22 and 23 coincide). Moreover, using eq 21 the mean jump length may also be estimated from these two quantities. QENS has been applied to several zeolitic adsorbate-adsorbent systems [68, 71, 74, 75]. Its range of application is limited to relatively large diffusivities ( $\geq 10^{-10} \text{ m}^2 \text{ s}^{-1}$ ). The diffusion paths covered during observation by QENS are of the order of a few nanometers maximum.

### 6.3.3.3 Pulsed Field Gradient NMR

In the pulsed field gradient (PFG) NMR method, molecular transport is studied by making use of the spatial dependence of the nuclear magnetic resonance frequency in an inhomogeneous magnetic field [32, 33, 66, 68]. Superimposing the constant magnetic field over two short time intervals of duration  $\delta$  and separation  $t$  by a well defined inhomogeneous magnetic field  $\Delta B = gz$  (the field gradient pulses), the NMR signal (spin echo) generated by an appropriate sequence of rf pulses is attenuated by a factor

$$\Psi(t, \gamma\delta g) = \int P(z, t) \cos(\gamma\delta gz) dz \quad (24)$$

Here,  $P(z, t)$  (the mean propagator [32, 76]) denotes the probability (density) that during the time interval  $t$  a molecule within the sample is shifted over a distance  $z$  in the direction of the applied field gradient. The quantity  $\gamma$  denotes the magnetogyric ratio, a characteristic quantity of the given nucleus. In a homogeneous system of diffusivity  $D$ , the propagator is given by the relation

$$P(z, t) = (4\pi Dt)^{-1/2} \exp(-z^2/4Dt) \quad (25)$$

In this case eq 24 becomes

$$\Psi(t, \gamma\delta g) = \exp(-\gamma^2\delta^2 g^2 Dt) \quad (26)$$

and  $D$  results straightforwardly from a plot of  $\ln \Psi$  versus  $(\gamma\delta g)^2$ . Molecular displacements covered in PFG NMR measurements are typically of the order of a micrometer. Owing to the large magnetogyric ratio, protons offer the best conditions for PFG NMR diffusion studies with respect to both signal intensity and sensitivity towards molecular displacements. However,

PFG NMR studies in porous media have also been carried out using  $^{13}\text{C}$  [77],  $^{15}\text{N}$  [78],  $^{19}\text{F}$  [79] and  $^{129}\text{Xe}$  NMR [78]. The lower limit of diffusivities accessible by  $^1\text{H}$  PFG NMR is of the order of  $10^{-13} \text{ m}^2 \text{ s}^{-1}$ . However, such low diffusivities may only be measured under suitable conditions, in particular for large nuclear magnetic relaxation times  $T_1$  and  $T_2$  [32].

Owing to the quite general correlation between the primary experimental data and molecular propagation as provided by eq 25, PFG NMR is particularly suitable for diffusion studies in heterogeneous systems. It allows the determination of a variety of parameters characterizing molecular transport in porous media. In the investigation of beds or granules of zeolite crystallites it is possible to measure directly the rates of intracrystalline diffusion and of long-range diffusion, i.e. of the rate of molecular propagation through the bed or the granule [66, 68]. So far, it has been possible to observe five different patterns of concentration dependence for intracrystalline diffusion [80]. Further transport-related phenomena observable in such studies include diffusion anisotropy [81], the formation of transport resistances (surface barriers) by coke deposits [68] or deterioration of the crystal structure [82], deviations from ordinary diffusion following Einstein's relation (e.g. single-file diffusion [83-86] or diffusion in fractals, see Section A.3.1.6 and Ref. 87) and the influence of the pressure of compaction and of inert gases [88]. Being able to distinguish between intracrystalline and external coke deposits [89], PFG NMR may be very helpful in tracing the microdynamics of catalyst deactivation and regeneration (see Section A.7). As a noninvasive technique, sensitive to a particular nucleus or even (by applying Fourier transform NMR [90]) to a particular molecular species, PFG NMR may be applied to study the diffusivity of any individual component in a multicomponent system [91, 92]. Moreover, by this method the in situ observation of the diffusion of the reactant and product molecules during catalytic reactions has become possible [93].

### 6.3.3.4 Tracer Techniques

The methods described so far for studying self-diffusion are essentially based on an observation of the diffusion paths, i.e. on the application of Einstein's relation (eq 3). Alternatively, molecular self-diffusion may also be studied on the basis of the Fick's laws by using isotopically labeled molecules. As in the case of transport diffusion, the diffusivities are determined by comparing the measured curves of tracer exchange between the porous medium and the surroundings with the corresponding theoretical expressions. As a basic assumption of the isotopic tracer technique for studying self-diffusion, the isotopic forms are expected to have

identical properties. For small percentage differences in the atomic masses, this is a reasonable assumption. Differentiation between the isotopes may be based on the differences in their mass (gravimetry [94] and mass spectroscopy [95]), in their nuclear magnetization (NMR spectroscopy [66]), or in their IR frequencies [26]. If one of the isotopes is radioactive, the activity provides a particularly simple and sensitive measure of the labeled species [96]. In principle, by applying labeled components, the various concepts of measuring transport diffusion may be correspondingly applied to the measurement of self-diffusion, provided that the exchange process between the labeled and unlabeled molecules is determined by diffusion rather than being masked by other phenomena. For the investigation of fast processes, a tracer variant of the ZLC method [97] has proved to be of particular relevance.

### 6.3.4 Diffusion in Multicomponent Systems

In principle, any of the techniques described for studying self-diffusion may be applied to both single- and multicomponent systems. So far, however, most self-diffusion measurements of multicomponent systems have been carried out by PFG NMR. Such measurements are possible by applying a set of samples with deuterated compounds with only one species (namely that to be measured) in the protonated form [98], by simultaneously considering different nuclei (e.g.  $^1\text{H}$  and  $^{19}\text{F}$  [79]), and by Fourier transform PFG NMR [91, 92].

Diffusion measurements under nonequilibrium conditions are more complicated due to the difficulties in ensuring well defined initial and boundary conditions. IR spectroscopy has proved to be a rather sensitive tool for studying simultaneously the intracrystalline concentration of different diffusants, including the occupation density of catalytic sites [28]. By choosing appropriate initial conditions, in this way both co- and counterdiffusion phenomena may be followed. Information about molecular transport diffusion under the conditions of multicomponent adsorption may also be deduced from flow measurements [99]. As in the case of single-component adsorption, the diffusivities are determined by matching the experimental data (i.e. the time dependence of the concentration of the effluent or the adsorbent) to the corresponding theoretical expressions.

A rather special possibility to attain information about molecular diffusion is provided by catalytic reactions if they proceed in the range of medium Thiele moduli (i.e. in the transition range between intrinsically and transport controlled reactions) [100]. By analyzing the dependence of the effective reaction rate on the catalytic particle size [101, 102] and/or the intrinsic re-

activity [103] it is possible to determine the rate of counter-diffusion of the reactant and product molecules. Similarly, as with the flow techniques (Section 6.2.2.1), also in this case the diffusivities are determined under stationary conditions.

### 6.3.5 Correlation Between the Different Diffusivities

Diffusivities are often measured under conditions which are far from those of catalytic reactions. Moreover, corresponding to their different nature, the various measuring techniques are limited to special ranges of application. The possibility of a mutual transformation of the various diffusivities would therefore be of substantial practical relevance. Since each of the coefficients of self-diffusion and transport diffusion in single-component and multicomponent systems refers to a particular physical situation, one cannot expect that the multitude of information contained in this set of parameters can in general be adequately reflected by a smaller set of parameters. Any correlation which might be used in order to reduce the number of free parameters must be based on certain model assumptions.

In general, the coefficients of transport diffusion ( $D$ ) and self-diffusion ( $D^*$ ) under the conditions of single-component adsorption are assumed to be correlated by the equation

$$D = D^* \partial \ln p(c) / \partial \ln c \quad (27)$$

where  $p(c)$  denotes the external gas-phase pressure of the adsorbate that is necessary to maintain the adsorbate concentration  $c$ . Equation 27 may be shown by both thermodynamic [104, 105] and statistical [106] arguments to be valid only under the assumption that the correlation of the motion of different molecules may be assumed to be negligibly small. For a number of systems this assumption seems to be justified, since there are various comparative studies of transport and self diffusion [107–109] as well as MD simulations [106, 110] which are in reasonable agreement with eq 27. The generalization of eq 27 to multicomponent adsorption yields for the transport diffusivities (see eq 1)

$$D_{ij} = D_i^* c_i / c_j \times \partial \ln p_i / \partial \ln c_j \quad (i, j = 1 \dots n) \quad (28)$$

with  $p_i$  denoting the set of partial pressures necessary to maintain the set of sorbate concentrations  $c_j$ . Hence, if one knows the corresponding multicomponent adsorption isotherms, the elements of the  $n \times n$  matrix of transport diffusivities can be determined from the multicomponent self-diffusivities by using eq 28.



Another attempt to correlate transport and self-diffusivities has been based on a generalization of the Stefan–Maxwell formulation of irreversible thermodynamics [111–113]. By introducing various sets of parameters describing the facility of exchange between two molecules of the same and of different species, the resulting equations are more complex than eqs 27 and 28. They may be shown, however, to include these relations as special cases.

## References

- H W Haynes, *Catal Rev-Sci Eng* **1988**, *30*, 563–627
- J Karger, D M Ruthven, *Diffusion in Zeolites and Other Microporous Solids*, Wiley, New York, **1992**
- C S Satterfield, *Mass Transfer in Heterogeneous Catalysts*, MIT Press, Cambridge, **1970**
- R Ans, *The Mathematical Theory of Diffusion and Reaction in Permeable Catalysts*, Clarendon Press, Oxford, **1975**
- N Y Chen, T F Degnan, C M Smith *Molecular Transport and Reaction in Zeolites*, VCH, New York, **1994**
- D L Wernick, E J Osterhuber in *Proceedings of the Sixth International Zeolite Conference*, (Eds D Olson, A Bisio) Butterworths, Guildford, **1984**, p 122
- A Paravar, D T Hayhurst in *Proceedings of the Sixth International Zeolite Conference*, (Eds D Olson, A Bisio) Butterworths Guildford, **1984**, p 217
- M Noack, P Kolsch, D Venzke, P Toussaint, J Caro, *Micropor Mater* **1994**, *3*, 201–206.
- P Schneider, *Chem Eng Sci* **1978**, *33*, 1311–1319
- M Novak, K Ehrhardt, K Klusacek, P Schneider, *Chem Eng Sci* **1988**, *43*, 185–193
- E Wicke, R Kallenbach, *Kolloid-Z* **1941**, *97*, 135–141
- R M Barrer, *Zeolites and Clay Minerals as Sorbents and Molecular Sieves*, Academic Press, London, **1978**
- R A Grachev, K G Ione, R A Barshev, *Kinet Catal* **1970**, *11*, 445–455
- L G Gibilaro, F Gioia, G Greco, *Chem Eng J* **1970**, *1*, 5–9
- J Crank, *Mathematics of Diffusion*, Oxford University Press, London, **1956**
- H S Carslaw, J C Jaeger, *Conduction of Heat in Solids*, Clarendon Press, Oxford, **1959**
- H Tautz, *Wärmeleitung und Temperaturausgleich*, Akademie-Verlag, Berlin, **1971**
- D M Ruthven, R I Derrah, *J Chem Soc., Faraday Trans 1* **1975**, *71*, 2031–2044
- H-J-Doelle, L Rieker, *Angew Chem* **1979**, *91*, 309–316
- A Zikanova, M Bulow, H Schlodder, *Zeolites* **1987**, *7*, 115–118
- M Bulow, W Mietk, P Struve, P Lorenz, *J Chem Soc., Faraday Trans 1* **1983**, *79*, 2457–2466
- A Mücke, M Bulow, M Kocirk, *J Phys Chem* **1994**, *98*, 924–929
- N van den Begin, L V C Rees, J Caro, M Bulow, *Zeolites* **1989**, *9*, 265–269
- D Shen, L V C Rees, J Caro, M Bulow, B Zibrowius, H Jobic, *J Chem Soc Faraday Trans* **1990**, *86*, 3943–3948
- E T Nelson, P L Walker, *J Appl Chem* **1961**, *11*, 358–365
- H G Karge, W Niessen, *Catal Today* **1991**, *8*, 451–456
- W Niessen, H G Karge, *Micropor Mater* **1993**, *1*, 1–8
- W Niessen, H G Karge in *Zeolites and Related Microporous Materials State of the Art 1994*, (Eds J Weitkamp, H G Karge, H Pfeifer, W Holderich), Elsevier, Amsterdam **1994**, part B, p 1191
- F Schuth, D Demuth, S Kallus in *Zeolites and Related Microporous Materials State of the Art 1994*, (Eds J Weitkamp, H G Karge, H Pfeifer, W Holderich), Elsevier, Amsterdam **1994**, part B, p 1223
- M Hermann, W Niessen, H G Karge in *Catalysts by Microporous Materials*, (Eds H K Beyer, H G Karge, I Kincsi, J B Nagy), Elsevier, Amsterdam, **1995**
- C Forste, A Germanus, J Karger, H Pfeifer, J Caro, W Pilz, A Zikanova, *J Chem Soc., Faraday Trans 1* **1987**, *83*, 2301–2309
- P T Callaghan, *Principles of Nuclear Magnetic Resonance Microscopy*, Clarendon, Oxford, **1991**
- B Blumich, W Kuhn (Editors), *Magnetic Resonance Microscopy*, VCH, Weinheim, **1992**
- G Guillot, G Kassab, J P Hulin, P Rigord, *J Phys D Appl Phys* **198**, *24*, 763–773
- J Karger, M Bulow, V I Ulin, A M Voloshchuk, P P Zolotarev, M Kocirk, A Zikanova, *J Chem Techn Biotechn* **1982**, *32*, 376–381
- M Goddard, D M Ruthven, *Zeolites* **1986**, *6*, 283–289
- P Struve, M Kocirk, M Bulow, A Zikanova, A G Bezus, *Z Phys Chem (Leipzig)* **1983**, *264*, 49–60
- M Kocirk, G Tschurch, P Struve, M Bulow, *J Chem Soc., Faraday Trans 1* **1988**, *84*, 2247–2257
- A Mücke, M Kocirk, J Caro, *J Chem Soc Faraday Trans* **1990**, *86*, 3087–3091
- L-K Lee, D M Ruthven, *J Chem Soc., Faraday Trans 1* **1979**, *75*, 2406–2422
- M Kocirk, J Karger, A Zikanova, *J Chem Techn Biotechnol* **1979**, *29*, 339–345
- R Haul, H Stremming, *J Coll Interf Sci* **1984**, *97*, 348–355
- Ph Grenier, F Meunier, P G Gray, J Karger, Z Xu, D M Ruthven, *Zeolites*, **1994**, *14*, 242–249
- Y Yasuda, A Yamamoto, *J Catal* **1985**, *93*, 176–181
- Y Yasuda, *J Phys Chem* **1989**, *93*, 7185–7190
- Y Yasuda, *Heterogen Chem Rev* **1994**, *1*, 103–124
- D Shen, L V C Rees, *Zeolites* **1991**, *11*, 666–671
- D Shen, L V C Rees, *Zeolites*, **1991**, *11*, 684–689
- Y Yasuda, K Matsumoto, *J Phys Chem*, **1989**, *93*, 3195–3200
- M L Sun, F Meunier, J Karger, *Chem Eng Sci* **1993**, *48*, 715–722
- V Bourdin, Ph Grenier, F Meunier, L M Sun *AIChE J.*, **1996**, *42*, 700–712
- V Bourdin, A Germanus, Ph Grenier, J Karger *Adsorption*, **1996**, in press
- M Kocirk, A Zikanova, *Ind Eng Chem Fundam* **1974**, *13*, 347–350
- D Armost, P Schneider, *Chem Eng Sci* **1994**, *49*, 393–399
- O Pazdermik, P Schneider, *J Chromatogr* **1981**, *207*, 181–187
- A G Dixon, Y H Ma, *Chem Eng Sci* **1988**, *43*, 1297–1300
- H W Haynes, *AIChE-J* **1986**, *32*, 1750–1756
- H Boniface, D M Ruthven, *Chem Eng Sci* **1985**, *40*, 1401–1409
- J Valus, P Schneider, *Chem Eng Science* **1985**, *8*, 1457–1462
- A S Chiang, A G Dixon, Y H Ma *Chem Eng Sci* **1984**, *39*, 1451–1459, 1461–1468
- M Eic, D M Ruthven, *Zeolites* **1988**, *8*, 40–45
- M Eic, D M Ruthven in *Zeolites Facts Figures Future* (Eds P A Jacobs, R A van Santen), Elsevier, Amsterdam **1989**, p 897

63. A. Micke, M. Kocirik, M. Bülow, *Micropor. Mater.* **1993**, *1*, 363–371.
64. S. Brandani, D. M. Ruthven, *Chem. Eng. Sci.*, **1995**, *50*, 2055–2059.
65. H. Pfeifer, *Physics Reports* **1976**, *26*, 293–338.
66. J. Kärger, H. Pfeifer in *NMR Techniques in Catalysis*, (Eds: A. T. Bell, A. Pines), Marcel Dekker, New York, **1994**, p. 69.
67. J. Kärger, H. Pfeifer, M. Rauscher, A. Walter, *J. Chem. Soc., Faraday Trans. 1* **1980**, *76*, 717–737.
68. J. Caro, M. Bülow, H. Jobic, J. Kärger, B. Zibrowius, *Adv. Catal.* **1993**, *39*, 351–414.
69. B. Boddenberg, R. Burmeister, *Zeolites* **1988**, *8*, 480–487.
70. B. Boddenberg, R. Burmeister, *Zeolites* **1988**, *8*, 488–494.
71. H. Jobic in *Catalyst Characterization: Physical Techniques for Solid Materials*, (Eds: B. Imelik, J. C. Vedrine), Plenum, New York, **1994**, p. 347.
72. R. K. Thomas, *Progr. Solid State Chem.* **1982**, *14*, 1–93.
73. P. L. Hall, D. K. Ross, *Mol. Phys.* **1981**, *42*, 673–688.
74. E. Cohen de Lara, R. Kahn, F. Mezei, *J. Chem. Soc., Faraday Trans. 1* **1983**, *79*, 1911–1920.
75. H. Jobic, M. Bée, G. J. Kearly, *J. Phys. Chem.*, **1994**, *98*, 4660–4665.
76. J. Kärger, W. Heink, *J. Magn. Reson.*, **1983**, *51*, 1–7.
77. J. Kärger, H. Pfeifer, F. Stallmach, N. N. Feoktistova, S. P. Zhdanov, *Zeolites* **1993**, *13*, 59–55.
78. P. L. McDaniel, C. G. Coe, J. Kärger, J. D. Moyer, *J. Phys. Chem.*, **1996**, *100*, 16263–16267; N.-K. Bär, P. L. McDaniel, C. G. Coe, G. Seifbert, J. Kärger, *Zeolites*, in press.
79. J. Kärger, H. Pfeifer, S. Rudtsch, W. Heink, U. Groß, *J. Fluorine Chem.*, **1988**, *39*, 349–356.
80. J. Kärger, H. Pfeifer, *J. Chem. Soc., Faraday Trans.*, **1991**, *87*, 1989–1996.
81. U. Hong, J. Kärger, H. Pfeifer, U. Müller, K. K. Unger, *Z. Phys. Chem.* **1991**, *173*, 225–234.
82. J. Kärger, W. Heink, H. Pfeifer, M. Rauscher, J. Hoffmann, *Zeolites* **1982**, *2*, 275–278.
83. J. Kärger, M. Petzold, H. Pfeifer, S. Ernst, J. Weitkamp, *J. Catal.* **1992**, *136*, 283–299.
84. J. Kärger, *Phys. Rev.*, **1992**, *A 45*, 4173–4172; *E 47*, 1427–1428.
85. K. Hahn, J. Kärger, V. Kukla, *Phys. Rev. Lett.*, **1996**, *76*, 2762–2765; V. Kukla, J. Kornalowski, D. Demuth, I. Girnus, H. Pfufer, L. V. C. Rees, S. Sehunk, K. K. Unger, J. Karger, *Science*, **1996**, *272*, 702–704.
86. J. Kärger, W. Keller, H. Pfeifer, S. Ernst, J. Weitkamp, *Microp. Mat.* **1995**, *3*, 401–408.
87. J. Kärger, H. Pfeifer, G. Vojta, *Phys. Rev.*, **1988**, *A 37*, 4514–4517.
88. J. Kärger, A. Zikanova, M. Kocirik *Z. Phys. Chem. (Leipzig)* **1984**, *265*, 587–592.
89. J. Völter, J. Caro, M. Bülow, B. Fahlke, J. Kärger, M. Hunger, *Appl. Catal.* **1988**, *42*, 15–27.
90. K. P. Datema, C. J. J. den Ouden, W. D. Ylstra, H. P. C. E. Kuipers, M. Post, J. Kärger, *J. Chem. Soc., Faraday Trans.*, **1991**, *87*, 1935–1943.
91. U. Hong, J. Kärger, H. Pfeifer, *J. Am. Chem. Soc.* **1991**, *113*, 4812–4815.
92. S. S. Nivarthi, A. V. McCormick, *J. Phys. Chem.* **1995**, *99*, 4661–4666.
93. U. Hong, J. Kärger, B. Hunger, N. N. Feoktistova, S. P. Zhdanov, *J. Catal.* **1992**, *137*, 243–251; H. B. Schwarz, S. Ernst, J. Kärger, B. Knorr, G. Leiffert, R. Q. Snurr, B. Sbaudle, J. Weitkamp, *J. Catal.*, in press.
94. M. Goddard, D. M. Ruthven, *Zeolites* **1986**, *6*, 445–448.
95. A. Cornu, R. Massot, *Compilation of Mass Spectral Data*, Heyden, London, **1966**.
96. R. B. Cundall, A. Dyer, J. O. McHugh, *J. Chem. Soc., Faraday Trans. 1* **1981**, *77*, 1039–1048.
97. J. R. Hufton, S. Brandani, D. M. Ruthven in *Zeolites and Related Microporous Materials: State of the Art 1994*, (Eds: J. Weitkamp, H. G. Karge, H. Pfeifer, W. Hölderich), Elsevier, Amsterdam, **1994**, part B, p. 1323.
98. P. Lorenz, M. Bülow, J. Kärger, *Coll. Surf.* **1984**, *11*, 353–364.
99. R. Krishna, L. J. P. van den Broeke, *Chem. Eng. J.* **1995**, *57*, 155–162.
100. P. Schneider, *Chem. Engin. Sci.*, **1991**, *46*, 2376–2381.
101. W. O. Haag, R. M. Lago, P. B. Weisz, *Disc. Faraday Soc.*, **1982**, *72*, 317–330.
102. M. F. M. Post, J. van Amstel, H. W. Kouwenhoven in *Proceedings of the Sixth International Zeolite Conference*, (Eds: D. Olson, A. Bisio) Butterworths, Guildford, **1984**, p. 517.
103. S. F. Garcia, P. B. Weisz, *J. Catal.* **1993**, *142*, 691–696.
104. R. Ash, R. M. Barrer, *Surf. Sci.* **1967**, 461–467.
105. J. Kärger, *Surf. Sci.* **1973**, *36*, 797–801.
106. E. D. Maginn, A. T. Bell, D. N. Theodorou, *J. Phys. Chem.* **1993**, *97*, 4173–4181.
107. R. M. Barrer, B. E. F. Fender, *J. Phys. Chem. Solids* **1961**, *21*, 12–21.
108. J. Kärger, J. Caro, *J. Chem. Soc. Faraday Trans. 1*, **1977**, *73*, 1363–1376.
109. M. Bülow, W. Mietk, P. Struve, A. Zikanova, *Z. Phys. Chem. (Leipzig)* **1983**, *264*, 598–602.
110. S. Fritzsche, R. Haberlandt, J. Kärger, *Z. Phys. Chem.*, **1995**, *189*, 211–220.
111. R. Krishna, *Chem. Eng. Sci.* **1990**, *45*, 1779–1781.
112. R. Krishna, *Chem. Eng. Sci.* **1993**, *48*, 845–861.
113. R. Krishna, *Gas Separat. Purif.* **1993**, *7*, 91–104.

of the other SCFs examined. The high hydrophobicity led to a higher water concentration in the micro-environment surrounding the enzyme, and hence higher rates.

A subfield in this area is using SCFs to control the stereoselectivity of biologically active chiral compounds. For example, supercritical CO<sub>2</sub> has been used to do the lipase-catalyzed enantioselective esterification of ibuprofen. Enantiomeric purities exceeding 90% at an ibuprofen conversion of 25% have been reported [20].

### 8.4.5 Other Applications of SCFs and Catalysis

This chapter has focused on heterogeneous catalysis in supercritical media, but the relationship between supercritical fluids and catalysis is much broader. There have been numerous studies of homogeneous catalysis in SCFs. Examples include hydroformylation via cobalt carbonyl complexes in supercritical CO<sub>2</sub>, oxidation via metal salts dissolved in supercritical water, and acid-catalyzed dehydration of alcohols in supercritical water.

Motivation for the dehydration studies grew out of the desire to use biomass, a renewable resource, for the production of chemicals and fuels. Biomass can be biochemically processed (fermentation) to produce ethanol. This bioprocessing occurs in an aqueous phase, and the ethanol concentration is low. The ethanol is traditionally recovered via a train of distillation columns. This scheme leads to a concentrated ethanol stream that can be sold, but the separation is not a simple one since it involves an azeotropic distillation. The capital cost and energy requirements for the distillation sequence is high. Antal and co-workers [11] reasoned that the expensive separation processes could be eliminated if ethanol could be converted to a different chemical that was easily separated from water. This observation led them to investigate the feasibility of doing the acid-catalyzed dehydration of ethanol in supercritical water to form ethylene. The advantages of using supercritical conditions in this application are the presence of a single phase at reaction conditions, high temperatures and hence fast reactions, the possibility of having simple postreactor processing to separate ethylene and water, and the potential to produce a polymerization-grade ethylene stream that is already at a high pressure and hence ready to feed to a polymerization reactor.

This group's early work demonstrated the feasibility of this concept. They showed that ethanol and other alcohols could be converted to ethylene or the corresponding alkene in high yields. Reaction conditions

were typically around 380 °C and 34.5 MPa. They subsequently measured the reaction kinetics and postulated sets of elementary reaction steps for the dehydration reactions. They found that both ethanol and propanol dehydration were consistent with an E2 mechanism, but not with an E1 mechanism. Additional investigations into propanol dehydration revealed that the apparent net rate constant decreased by a factor of three as the system pressure increased from about 22 to about 35 MPa. That pressure can have a strong effect on reaction rate constants in SCFs was noted earlier in this chapter. The investigators opted to explain this pressure effect by postulating that the reaction rate constant for this acid-catalyzed reaction was a function of the solvent's dielectric constant. The dielectric constant of supercritical water is a strong and increasing function of pressure for a given temperature. That the rate constant decreased as the pressure increased (dielectric constant increased) suggested that the transition state for the reaction was less polar than the reactants. This finding was fully consistent with the proposed E2 mechanism. The authors also found that changing the ionic strength of the solvent did not alter the rate constant. This research broke new ground by showing that acid catalysis normally conducted in a liquid aqueous phase can also be accomplished at supercritical conditions with the attendant advantages. This particular chemistry and process proved to be economically unattractive, however, compared with the alternative of distillation to recover ethanol.

Another application of SCFs in catalysis is in the preparation or synthesis of catalytic materials and supports. For example, high-surface-area materials can be produced using supercritical processes. Moreover, supercritical processing is being explored as an alternative to sol-gel and subcritical hydrothermal processing. The adjustable properties of SCFs allow one to control the properties of the medium with small changes in temperature or pressure. This control of the medium's properties intimates the possibility of thereby controlling the particle size and morphology. Applications of SCFs in materials synthesis and processing have been reviewed [2].

### 8.4.6 Concluding Remarks

Supercritical fluids continue to attract interest as media for catalysis and chemical reactions because of their unique properties. They offer possible strategies for more economical chemical processes by increasing reaction rates, prolonging catalyst lifetime, and simplifying downstream processing. In addition to these considerations, the current trend towards pollution prevention in the chemical processing industry and the attendant search for environmentally benign solvents is

focusing attention on compounds such as carbon dioxide and water. When in the supercritical state, these nontoxic compounds are very good solvents for many organic compounds and hence attractive media for chemical reactions and catalysis.

## References

1. *The ASME Handbook on Water Technology for Thermal Power Systems* (Ed.: P. Cohen), American Society of Mechanical Engineers, New York, 1989.
2. P. E. Savage, S. Gopalan, T. I. Mizan, C. J. Martino, E. E. Brock, *AIChE J.* 1995, 41, 1723–1778.
3. K. A. Connors, *Chemical Kinetics: The Study of Reaction Rates in Solution*, VCH, New York, 1990.
4. V. M. Shmonov, R. J. Sadus, E. U. Franck, *J. Phys. Chem.* 1993, 97, 9054–9059.
5. J. M. H. Levelt Sengers, *J. Supercrit. Fluids* 1991, 4, 215–222.
6. M. McHugh, V. Krukoni, *Supercritical Fluid Extraction*, 2nd ed., Butterworth-Heinemann, Boston, 1994.
7. S. I. Sandler, *Chemical and Engineering Thermodynamics*, 2nd ed., John Wiley & Sons, New York, 1989.
8. H. Black, *Env. Sci. Technol.* 1996, 30, 124A–127A.
9. K. P. Johnston, *Nature* 1994, 368, 187–188.
10. P. G. Jessop, T. Ikariya, R. Noyori, *Nature* 1994, 368, 231.
11. X. Xu, C. P. De Almeida, M. J. Antal, Jr., *Ind. Eng. Chem. Res.* 1991, 30, 1478–1485.
12. H. Tiltcher, H. Wolf, J. Schelchshorn, *Ber. Bunsenges. Phys. Chem.* 1984, 88, 897.
13. J. A. Amelse, N. A. Kutz, US Patent 5030 788 1991.
14. F. Niu, G. Kolb, H. Hofmann, *Chem. Eng. Technol.* 1995, 18, 278–283.
15. K. Yokota, K. Fujimoto, *Ind. Eng. Chem. Res.* 1991, 30, 95.
16. N. A. Collins, P. G. Debenedetti, S. Sundaresan, *AIChE J.* 1988, 34, 1211.
17. D. M. Ginosar, B. Subramaniam in *Catalyst Deactivation: Proc. Int. Symp. on Catalyst Deactivation* (Ed.: B. Delmon, G. F. Froment), Elsevier, Amsterdam, 1994.
18. M. C. Clark, B. Subramaniam, *Chem. Eng. Sci.* 1996, 51, 2369–2377.
19. S. V. Kamat, J. Barrera, E. J. Beckman, A. J. Russell, *Biotech. Bioeng.* 1992, 40, 158.
20. O. Aaltonen, M. Rantakylä in *Proceedings of the 2nd International Symposium on Supercritical Fluids* (Ed. M. A. McHugh), 1991, p. 146.

## 8.5 Microwave Heating in Catalysis

R. B. MOYES AND G. BOND

Microwave heating has apparent benefits in catalytic systems where reactions occur on solid surfaces, because, using appropriate devices, the heating can be concentrated on the catalyst's mass. The advantage is that the surroundings remain relatively cool which can enhance selectivity. For microwave heating to be applied to catalytic systems, the catalyst must itself absorb the microwave energy, or be mixed with an ab-

sorber. Many active phases of known catalytic materials absorb microwave energy readily to different, sometimes large, extents, while the supports in common use, silica and alumina, do not. There has been some speculation of a "microwave effect" which produces different products from those expected from conventional heating. The consensus is, however, that such an effect does not exist, and that all differences can be explained in terms of selective heating. As this section of the Handbook is restricted in length, readers requiring a more general review of the applications of microwave dielectric heating effects to synthetic problems in chemistry are referred to that published by Mingos and Baghurst [1]. This extensive work provides a first recourse for readers who seek detail of the heating process. Additionally, Ovenston and Walls have examined the AC electrical characteristics of heterogeneous catalysts [2] in relation to radiofrequency (RF) heating using impedance spectroscopy. The frequency range used was 100 Hz to 10 MHz, (well below microwave frequencies) and in the temperature range 300–1000 K.

### 8.5.1 Microwave Energy and Microwave Heating

Microwaves are electromagnetic energy corresponding to wavelengths of 1 cm to 1 m (frequencies of 30 GHz to 300 MHz, respectively). To avoid interfering with other transmissions such as telecommunications, the industrial heating applications have been allocated the ISM (industrial, scientific, and medicine) frequency bands of 13.56, 27.12,  $915 \pm 15$ , and  $2450 \pm 50$  MHz [3]. The transformation of electric energy to thermal energy in this frequency range by dielectric heating arises from the interaction between the electromagnetic waves and the irradiated material [4].

Materials can be classified into three groups according to their interaction with the electromagnetic field. *Reflective* materials are mostly metals which do not heat in the presence of microwave energy. Instead, the electric field creates surface currents that penetrate some few microns into the material. The primary components of microwave applicators, which apply microwave energy to a system, are constructed from reflective materials. *Transparent* materials (low-loss) such as glass, silica, alumina, and plastics, do not absorb microwave energy but allow transmission of the radiation, thus making them good insulators. However, there is a host of *absorbing* materials, which include catalytic materials, that absorb microwaves (high-loss) and become heated [5, 6]. This comes about through

the interaction of the electromagnetic force fields with the material's molecular and electronic structure [4].

### 8.5.2 Dielectric Polarization

The heating effect relies upon dielectric polarization [1], itself containing components of electronic, atomic, dipolar, and interfacial polarization, of which the last two have timescales which allow them to contribute to the overall heating effect at these frequencies. The loss tangent,  $\tan \delta$ , consists of two components,  $\epsilon'$ , the dielectric constant, and  $\epsilon''$ , the dielectric loss, where

$$\tan \delta = \frac{\epsilon''}{\epsilon'}$$

The ability of microwave energy to affect dipoles depends upon their relaxation time constant, and this value must be comparable with the frequency of the exciting radiation, i.e. near 2.45 ps for the commonly used 2450 MHz radiation. Measurements of  $\epsilon''$  and  $\epsilon'$  for catalytic materials are relatively rare, and is currently an area in which research is required. The heating effect is mostly seen in solid or liquid materials, where free rotation is restricted, so that heating effects depend upon density (and upon viscosity in liquid systems). It is known that some liquids can be superheated to temperatures some tens of degrees above their normal atmospheric boiling point, because microwave heating occurs by a different mechanism [7].

### 8.5.3 Interfacial Polarization

Conducting particles held in a nonconducting medium form a system which has a frequency-dependent dielectric constant. The dielectric loss in such a system depends upon the build-up of charges at the interfaces, and has been modeled for a simple system by Wagner [8]. As the concentration of the conducting phase is increased, a point is reached where individual conducting areas contribute and this has been developed by Maxwell and Wagner in a two-layer capacitor model. Some success is claimed for the relation

$$\epsilon'' = \text{constant } f^{-k}$$

where  $f$  is the frequency and  $k$  is a constant, approaching unity at high concentrations of the conducting phase [9]. The interfacial polarization (Maxwell-Wagner effect) is particularly relevant in catalytic systems. Clearly such a system is related to the familiar active particles on a support which form many catalytic systems. Vannice and co-workers [10] measured the electrical conductivity of small particles by micro-

wave absorption. They claim that such measurements can provide fundamental information about adsorption and catalytic processes on semiconductor surfaces.

### 8.5.4 Ionic Conduction

The second microwave heating mechanism arises from the migration of ions in the electric field. The resulting current from the oscillating ions gives rise to heat in the familiar way, following the  $i^2r$  law, where  $i$  is the current and  $r$  reflects the resistance or impedance to ionic movement through collisions with other ions and molecules present in the medium. Ionic conduction is important in situations where the ions are free to move to some extent.

### 8.5.5 Microwave Heating

Microwave heating involves the application of substantial microwave power to the system. In this it differs from microwave spectroscopy, or the measurement of fundamental dielectric properties, where powers applied are in the milliwatt region. For microwave heating, magnetrons producing kilowatts are available. A number of microwave applicator designs are in use, including the familiar kitchen microwave oven (a multimode device) and the single-mode device where a standing wave is set up in a tuned cavity. Industrial scale methods are well developed in the polymer area, where microwave heating has been in use for decades.

The rate of temperature rise due to an microwave electric field is given by the equation

$$\frac{dT}{dt} = \text{constant } \frac{\epsilon'' f E_{\text{rms}}^2}{\rho C_p}$$

where  $f$  = frequency,  $E_{\text{rms}}^2$  = r.m.s. field intensity,  $\rho$  = density, and  $C_p$  = specific heat capacity.

The radiative losses can be calculated using the conventional equations [11]. The temperature rise dependence contains terms for the electric field strength, dielectric loss factor, heat capacity, and emissivity, and many of these are also temperature dependent. As a result, the complete theoretical analysis of dielectric heating is mathematically very complex [1].

Control of heating may raise substantial problems, in that temperature measurement itself has difficulties, since most probes for temperature measurement themselves interact with the electromagnetic field, and are at best unreliable. Remote sensing is the best available, but has its own difficulties, in that sensors detect the surface temperature rather than that of the bulk. If the temperature of a body within a microwave field is to be

controlled, then the control loop has to be fast enough to deal with the "runaway" situation. This arises because an increase in temperature results in an increase in absorption efficiency and hence further increase in temperature, and so the runaway situation develops.

Mingos [1] has listed the effect of microwave heating from ambient on a number of substances, including materials with catalytic activity such as CuO, carbon,  $\text{Co}_2\text{O}_3$ , Ni, NiO, CaO,  $\text{CeO}_2$ ,  $\text{Fe}_2\text{O}_3$ ,  $\text{La}_2\text{O}_3$ ,  $\text{MnO}_2$ ,  $\text{SnO}$ ,  $\text{PbO}_2$ ,  $\text{TiO}_2$ ,  $\text{V}_2\text{O}_5$ , and  $\text{WO}_3$ . Many other catalytic substances are absorbers of microwave radiation, but many more remain to be investigated.

### 8.5.6 Current Research

The majority of work carried out using microwave energy in the field of catalysis has centered around the stimulation of catalytic reactions. However, some use has been made in the area of catalyst preparation. The novel drying properties of microwave radiation has been used to produce supported metal catalysts with improved dispersion [12]. When microwave heating is employed in the preparation of zeolites, results show that a material with a far superior crystallinity is obtained in a greatly reduced time when compared with that from conventional heating techniques [13]. In the area of catalytic reactions two distinctly different approaches have been adopted. Wan in Canada has used high-power pulses of microwave radiation to stimulate reactions and only latterly has paid some attention [14] to the measurement of the catalyst temperature, perhaps because of the difficulty in obtaining a meaningful estimate. The two groups working in Europe, namely those of Maire, Roussy, and co-workers and Moyes, Bond, and co-workers, have adopted an approach of continuously irradiating the catalyst while making efforts to measure and control the temperature.

Wan and co-workers have demonstrated that a range of catalyzed processes are speeded up when exposed to microwave energy, no doubt through the high temperatures achieved. These reactions include the catalytic conversion of cyclohexene to benzene [15], catalytic cracking [16], decomposition of organic halides [17], decomposition of methane to ethene and hydrogen [18], microwave-induced catalytic conversion of methane to ethene and hydrogen [19], and water-gas shift reaction [16]. When heated conventionally, most of these reactions require relatively high temperatures compared with those reported for the microwave-heated systems.

Maire and co-workers have published detailed papers on reforming catalysts, particularly on the platinum-catalyzed cracking of 2-methyl pentane [20, 21]. These latter again suggests that the catalyst is

at a higher temperature than that expected from the bulk measurements. Roussy et al. [22] has published a detailed account of the drying of zeolites with microwaves which suggests a conduction mechanism for the accelerated process.

Moyes, Bond and co-workers have demonstrated that the oxidative coupling of methane to form ethene and ethane can be achieved at apparent bulk temperatures 300–400 K less than in the conventionally heated systems [23]. The work covers a range of coupling catalysts including  $\text{Sm}_2\text{O}_3$  and  $\text{La}_2\text{O}_3$ , both alone and supported on beta-alumina. Some of the lanthana catalysts were promoted by addition of SrO. In each case the product distributions were substantially the same with the microwave-heated case and with conventional heating, which suggests that the catalytic centers in the materials are operating at a higher temperature than the bulk. This observation is supported by more recent work on the selective conversion of isopropanol to acetone or to propene, catalyzed by basic catalysts such as potassium-doped carbon [24]. In this case the selectivity to one or other product depends upon the acidity or basicity of the surface. Both processes are accelerated by microwave heating when compared with conventional heating, but some changes in selectivity occur under microwave heating. This has led the authors to suggest that there are specific sites on the catalysts which are preferentially heated by microwave energy, while the bulk of the solid is at a lower temperature. Temperature measurement has its difficulties but reasonably reliable systems are available which indicate that there cannot be an error in the measurement which explains the difference in apparent reaction temperature.

In order to test this theory, Moyes, Bond, and Bool [25] have examined the steam reforming of methane catalyzed by a nickel catalyst and have shown that the microwave-heated equilibrium constant behavior reflects that of the conventionally heated counterpart, but at measured temperatures some 150 K less than expected. They interpret this observation as indicating that a small number of sites exist within the catalyst mass which are at the expected temperature but that they are insufficient to raise the whole mass to the normal temperature for such a value of the equilibrium constant. Clearly, this suggests methods of calculating the number of available sites in the catalyst sample. Furthermore, it holds out the possibility of directing energy in endothermic reactions at the catalyst sites themselves, with consequent efficiency gains. Different authors have contributed in alternative areas, particularly in accelerated organic reactions. There is a Mobil

patent on the microwave catalytic stripping of cracking catalysts [26]. In the field of organic chemistry there has been an extensive development of "dry" organic reactions, where the reactants are adsorbed at hydroxylated surfaces and react on irradiation with microwave energy. These include a one-pot synthesis of indoles catalyzed by montmorillonite [27] and clay-catalyzed barbituric acid condensation with aldehydes [28].

## References

1. D. M. P. Mingos, D. R. Baghurst, *Chem. Soc. Rev.* **1991**, *20*, 1
2. A. Ovenston, J. R. Walls, *J. Catal.* **1993**, *140*, 464.
3. International Radio Regulations, Geneva, **1959**.
4. A. C. Metaxas, R. J. Meredith, *Industrial Microwave Heating*, Peter Peregrinus and IEE, London, **1983**, Chapters 1–4.
5. E. D. Neas, M. J. Collins in *Introduction to Microwave Sample Preparation* (Ed.: H. M. Kingston, L. B. Jassie), American Chemical Society, Washington, DC, USA, **1988**, Chapter 2.
6. T. Ohlsson, Notes from Short Course on Microwave and High Frequency, Goteburg, **1993**.
7. D. R. Baghurst, D. M. P. Mingos, *J. Chem. Soc. Chem. Comm.* **1992**, *9*, 674.
8. K. W. Wagner, *Arch. Elektrotech.* **1914**, *2*, 371.
9. L. K. H. van Beek, *Prog. Dielectrics* **1967**, *7*, 69.
10. C. Lui, B. Na, A. B. Walters, M. A. Vannice, *Cat. Lett.* **1994**, *26*, 9.
11. J. M. Thomas, W. J. Thomas, *Introduction to the Principles of Heterogeneous Catalysis*, Academic Press, New York, **1967**, p. 483.
12. G. Bond, R. B. Moyes, D. A. Whan, *Proc. 10th Intern. Congr. Catal.* (Ed.: L. Gucci, F. Solymosi, P. Tetenyi), Akademiai Kiado, Budapest, **1993**, p. 1805.
13. A. Arafat, J. C. Jansen, A. R. Ebaid, H. van Bekkum, *Zeolites* **1993**, *13*, 162.
14. J. K. S. Wan, M. S. Ioffe, *Res. Chem. Intermed.* **1994**, *20*, 115.
15. K. Wolf, H. K. J. Choi, J. K. S. Wan, *Alberta Oil Sands Technology Research Agency J. Res.* **1986**, *3*, 53.
16. J. K. S. Wan, K. Wolf, R. D. Heyding, *Catalysis on the Energy Scene* **1984**, 561.
17. T. R. J. Dinesen, M. Y. Tse, M. C. Depew, J. K. S. Wan, *Res. Chem. Intermed.* **1990**, *15*, 15.
18. J. K. S. Wan, M. Tse, H. Husby, M. C. Depew, *J. Microwave Power Electromagnetic Radiation*, **1990**, *25*, 1.
19. J. K. S. Wan, Canadian Patent 1 241 293, **1988**.
20. J. M. Thiebaut, G. Roussy, M. Medjram, L. Seyfried, F. Garin, J. Maire, *J. Chim. Phys.* **1992**, *89*, 1427.
21. L. Seyfried, F. Garin, J. Maire, J. M. Thiebaut, G. Roussy, *J. Catal.* **1994**, *148*, 281.
22. G. Roussy, A. Zoualalian, M. Charreyre, J. M. Thiebaut, *J. Phys. Chem.* **1984**, *88*, 5702.
23. G. Bond, R. B. Moyes, D. A. Whan, *Catalysis Today*, **1993**, *17*, 427; *Catal. Lett.* **1993**, *21*, 133; Ref. 12 p. 1076.
24. G. Bond, R. B. Moyes, I. Theaker, D. A. Whan, *Topics in Catalysis*, **1994**, *1*, 177.
25. R. B. Moyes, G. Bond, C. J. Bool, unpublished work.
26. US Patent 4 968 403, **1988**.
27. D. Villemin, B. Labiad, Y. Ouhilal, *Chem. Ind.* **1989**, 60.
28. D. Villemin, B. Labiad *Synthetic Comm.* **1990**, *20*, 3333.

## 8.6 Sonocatalysis

K. S. SUSLICK

### 8.6.1 Introduction and the Origins of Sonochemistry

Research on the chemical effects of ultrasound has undergone a renaissance during the past decade and has had a significant impact in a variety of areas [1, 2]. Applications of sonochemistry have been developed in virtually all areas of chemistry and related chemical technologies [3, 4]. We can conceptually divide the effects of ultrasonic irradiation on heterogeneous catalysis into those that alter the formation of heterogeneous catalysts, those that perturb the properties of previously formed catalysts, and those that affect catalyst reactivity during catalysis. In practice, these three classes of effects are often deeply intertwined in reported experimental results.

No direct coupling of the acoustic field with chemical species on a molecular level can account for sonochemistry. Ultrasound spans the frequencies of roughly 20 KHz to 10 MHz, with associated acoustic wavelengths in liquids of roughly 100 to 0.15 mm: these are not on the scale of molecular dimensions. Instead, the chemical effects of ultrasound derive from several nonlinear acoustic phenomena, of which cavitation is the most important. Acoustic cavitation is the formation, growth, and implosive collapse of bubbles in a liquid irradiated with sound or ultrasound. When sound passes through a liquid, it consists of expansion (negative pressure) waves and compression (positive pressure) waves. These cause bubbles (which are filled with both solvent and solute vapor and with previously dissolved gases) to grow and recompress. Under proper conditions, acoustic cavitation can lead to implosive compression in such cavities. Such implosive bubble collapse produces intense local heating, high pressures, and very short lifetimes. As discussed elsewhere, these hot spots have temperatures of roughly 5300 K, pressures of about 1720 bar, and heating and cooling rates above  $10^9 \text{ K s}^{-1}$  [5–7]. Cavitation is an extraordinary method of concentrating the diffuse energy of sound into a chemically useable form.

When a liquid–solid interface is subjected to ultrasound, cavitation still occurs, but with major changes in the nature of the bubble collapse. If the surface is significantly larger than the cavitating bubble ( $\approx 100 \mu\text{m}$  at 20 kHz), spherical implosion of the cavity no longer occurs, but instead there is a markedly asymmetric collapse which generates a jet of liquid directed at the surface, as seen directly in high speed

# 9 Laboratory Reactors

---

## 9.1 Laboratory Catalytic Reactors: Aspects of Catalyst Testing

### 9.2 Ancillary Techniques in Laboratory Units for Catalyst Testing

### 9.3 Catalytic Membrane Reactors

---

## 9.1 Laboratory Catalytic Reactors: Aspects of Catalyst Testing

F. KAPTEIJN AND J. A. MOULIJN

### 9.1.1 Introduction

In the development of catalysts for a new process or the improvement of existing catalytic systems various stages can be distinguished. This development process covers the whole range from the new idea for a process or catalyst via the catalyst preparation, catalyst screening, establishing reaction networks, kinetic studies, and life tests to scale-up on pilot plant level, before a new or modified process is introduced. Figure 1 indicates the order of activities, although during the advancement of the development there will be a continuous feedback to other stages to optimize the catalyst and the process. The number of catalyst formulations will decrease during the progress, but the time taken and size both increase and, consequently so do the costs involved. This demands an efficient and proper approach for laboratory scale experimentation.

The objectives of the different development stages vary:

- Screening must give the first data about the activity and selectivity of the various catalyst formulations as a function of their composition and preparation and pretreatment history. As there are many variables, numerous catalysts should be screened at a high throughput rate. This yields the activity per unit of catalyst mass, active phase, or volume, depending

on the specific goals. Often, a first insight into the deactivation behavior, i.e. the catalyst stability, is obtained simultaneously.

- Establishing the reaction network, using the wealth of techniques at the disposal of catalyst researchers, gives insight into how the catalyst works and provides the basis for the kinetic modeling studies.
- Time consuming kinetic studies are indispensable for the design, operation and process control. A description is needed of the catalytic rate as a function of the process variables, i.e. temperature, pressure, and composition of the reaction mixture.
- Life studies are intended to test the catalysts during a longer time on stream, often on a bench or pilot scale with real feeds and recycle streams. The latter allow investigation of the effect of trace impurities or accumulated components, not observed in laboratory-scale experiments. Often, it is desired to test the catalyst at the same time in its shape for practical application. Here, the need exists for experimental results that can be directly linked to commercial applications.

Although they may be part of a catalyst testing [1–3] programme, investigations focused on revealing the reaction mechanism, such as in-situ Fourier transform infrared (FTIR) in transmission or reflection mode, nuclear magnetic resonance (NMR), X-ray diffraction (XRD), X-ray absorption fine-structure spectroscopy (EXAFS), X-ray photoelectron spectroscopy (XPS), electron microscopy (EM), electron spin resonance (ESR), and UV-visible (UV-vis) and the reaction cells used are not included. For the correct interpretation of the results, however, this chapter may also provide a worthwhile guide.

Various types of reactors can be applied, and it is of primary importance to select the proper reactor to obtain the required information, which generally means that one should not mimic the reactor type in which the process will be carried out. Other criteria apply for practical reactor selection than for catalyst testing. Downscaling, as far as possible, is desirable because of lower equipment costs, lower material consumption, and disposal, lower utility requirements, reduced demands



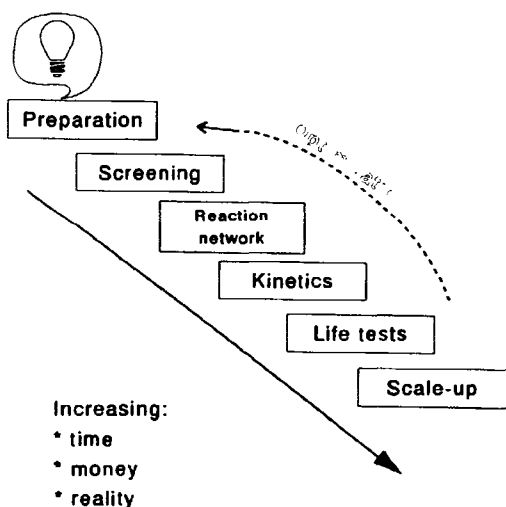


Figure 1. Stages in a catalyst development programme.

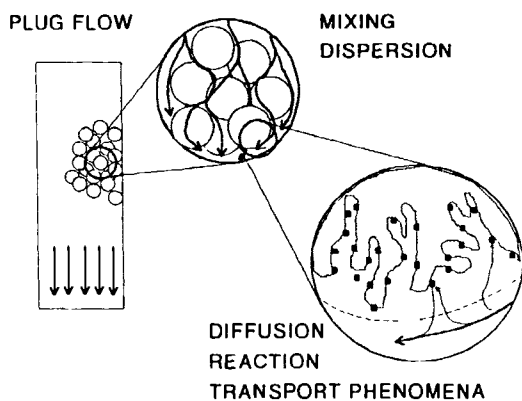


Figure 2. Transport phenomena in a catalytic packed bed reactor on different levels.

on laboratory infrastructure and increased intrinsic safety (reduced hazards of toxic emissions, explosions, or fires). Smaller scale requires, in addition, more accurate experimentation and the use of representative samples.

In the laboratory, catalysts are often tested using a packed bed contained in a reactor through which a reaction mixture flows (Fig. 2). On the reactor level the fluid seems to flow as a front through the bed (plug flow), but due to the flow around the catalyst particles a mixing (dispersion) may occur on the particle size level. This may affect the reactor performance. Along the length of the bed reactants will be gradually converted. Reactants have to diffuse from the bulk of the fluid through a stagnant layer around the particles to the exterior surface, and subsequently through the pore system to an active site where they can react. Products proceed the opposite way. Heat produced or consumed will have to be removed or supplied at a sufficient rate, otherwise temperature gradients may develop locally to

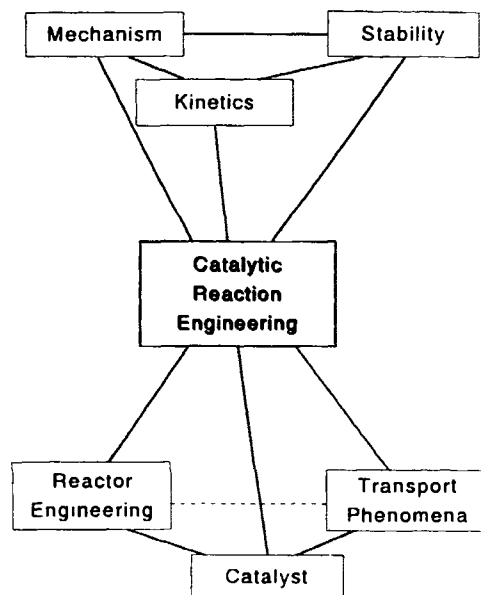


Figure 3. Catalytic reaction engineering.

an undesired level. The description of these phenomena is given by catalytic reaction engineering [4–10], which integrates catalysis, reactor analysis, and transport phenomena to aid in procuring and interpreting data on catalyst activity, stability, kinetics and reaction mechanisms (Fig. 3).

With the goal of obtaining intrinsic catalyst properties (reaction kinetics and selectivities) from experimental data without being disguised by the above-mentioned phenomena, the following conditions should be fulfilled:

- good contact between reactants and catalyst;
- no limitations due to mass and heat transport inside and outside the catalyst particle;
- good description of reactor characteristics (ideal systems).

Generally, this implies the use of ideal reactors of the plug flow or well stirred tank type with well defined residence times and residence time distributions under isothermal conditions (with some exceptions, as will be indicated). By-passing part of the catalyst by channeling in a packed bed or uneven flow distributions must be avoided. In three-phase systems (gas/liquid/solid), the even distribution of both fluid phases over the catalyst is crucial.

In this Chapter, criteria will be derived that can be used to check whether one operates under conditions that result in deviations of not more than 5% in reaction rate from the ideal situation. This can be expressed as

$$\frac{\text{rate}_{\text{observed}}}{\text{rate}_{\text{ideal}}} = 1 \pm 0.05 \quad (1)$$

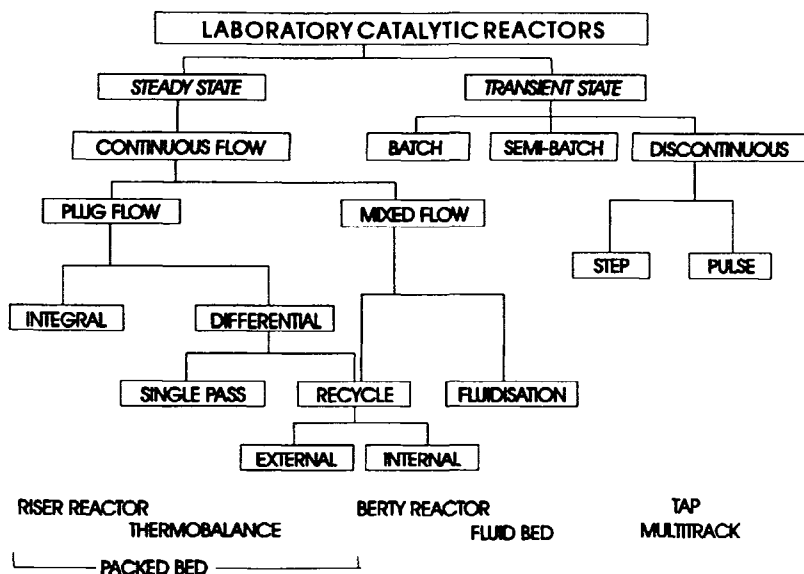


Figure 4. Classification of laboratory reactors according to the mode of operation.

The various aspects that are to be considered to achieve a proper and efficient catalyst testing approach are presented. This applies to heterogeneous systems in which the catalyst is the solid phase and the reactants are in the gaseous and/or the liquid phase. The presence of a solid phase introduces complicating phenomena on which this chapter focuses. In this respect, homogeneous catalysis is a limiting case and does not need separate treatment. The solid catalyst can be present as either a packed bed of particles, a wash-coated monolith, a fluid bed, an entrained bed, or in a liquid-phase slurry.

## 9.1.2 Reactor Systems

Various laboratory reactors have been described in the literature [3, 11–13]. The most simple one is the packed bed tubular reactor where an amount of catalyst is held between plugs of quartz wool or wire mesh screens which the reactants pass through, preferably in 'plug flow'. For low conversions this reactor is operated in the *differential mode*, for high conversions over the catalyst bed in the *integral mode*. By recirculation of the reactor exit flow one can approach a well mixed reactor system, the continuous flow stirred tank reactor (CSTR). This can be done either externally or internally [11, 12]. Without inlet and outlet feed, this reactor becomes a batch reactor, where the composition changes as a function of time (transient operation), in contrast with the steady state operation of the continuous flow reactors.

Catalysts are not necessarily kept fixed in the reactor. In slurry reactors, CSTR operation is easily

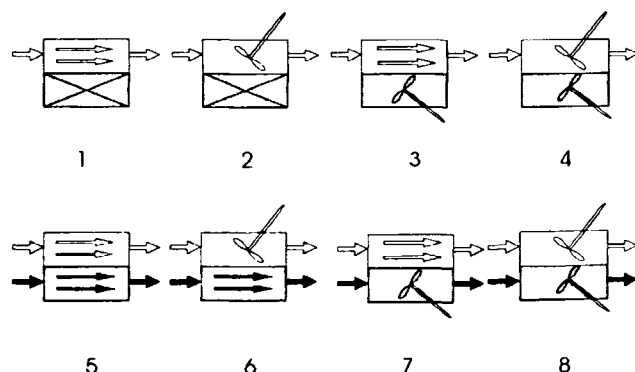


Figure 5. Classification of laboratory reactors according to the contacting mode.

achieved by a catalyst suspended in the liquid by efficient stirring. In fluid bed systems the catalyst is suspended by an upflow of fluid, having a higher catalyst density than slurry reactors. In riser reactors catalyst particles are also fed continuously to the reactor and withdrawn with the product mixture, and these are especially suited for rapidly deactivating catalysts (FCC).

### 9.1.2.1 Classification

Catalytic reactors can be classified globally according to their mode of operation: under steady state or transient conditions, as indicated in Fig. 4, or according to the contacting/mixing mode, as indicated in Fig. 5 for

a fluid–solid system. In both schemes a good contact between catalyst and reaction mixture is assumed.

Figure 4 represents a classical classification in operation forms. Steady state reactors, especially packed bed reactors, are most widely used in catalyst testing, predominantly because of the ease of operation and low costs. Transient operation is being used less and has some disadvantages for the mere goal of catalyst testing. In batch reactors the possible deactivation during the course of the experiment cannot be traced, except for the verification afterwards by repeating the experiment. In pulse reactors (TAP, Multitrack) the catalyst conditions are quite different from a continuous operation. Only transient operation by using isotopically labelled species under steady state conditions, such as positron emission profiling [14] is compatible. Transient operation is mainly applied for establishing reaction networks and detailed kinetic information, although in these cases care must also be taken to obtain intrinsic kinetic information [15].

The classification in Figure 5 serves the description of the reactors used. Here, two ideal contacting types are used, the plug flow mode and the ideally mixed mode, both for the fluid and the solid phase. By application of the design equations of these ideal reactor types the experimental results are interpreted in a straightforward manner. For two phases, two contacting types and two operation modes (batch and flow) eight combinations arise:

1. plug flow fixed bed reactor (PFR);
2. internal or external recirculation reactor (CSTR);
3. (circulating) fluid bed reactor (FBR);
4. fluid bed with recycle, slurry reactor;
5. riser reactor;
6. riser reactor with recycle;
7. (circulating) fluid bed reactor with continuous catalyst feed;
8. slurry reactor or fluid bed with recycle of fluid and continuous catalyst feed.

### 9.1.2.2 Balance Equations

To relate the reaction rate or conversion, pressure drop, and temperature variation over a catalyst bed with the operating variables of a reactor, flow rate, catalyst amount etc., so-called mass-, heat- and impulse balances are used in catalytic reaction engineering [4, 8]. This chapter assumes, however, that the catalyst bed is isothermal and the pressure drop over the bed is negligible. This leaves only mass balances for each reactant or product to be considered. For a component  $i$  this can be written for part of a catalyst bed or the whole bed as

$$\text{input}_i - \text{output}_i + \text{production}_i = \text{accumulation}_i \quad (2)$$

where the production refers both to production and consumption (negative) contributions. Under steady state conditions the accumulation terms vanishes, simplifying the resulting expression. This approach yields the following expressions for a component  $i$  and a single reaction: For PFR,

$$\frac{dx_i}{d\left(\frac{W}{F_i^0}\right)} = -v_i r_w \quad (3)$$

and, for CSTR,

$$\frac{W}{F_i^0} = \frac{x_i^{\text{out}} - x_i^{\text{in}}}{-v_i r_w} \quad (4)$$

Since the conditions in the CSTR are everywhere the same the mass balance is considered over the whole reactor, resulting in an algebraic expression relating the reaction rate directly to the measured conversion.

For the PFR only a small slice of the bed can be considered to have constant conditions, leading to a differential equation which describes the conversion as a function of the amount of catalyst. For low conversions the rate can be considered to be constant over the bed and the expression can be simplified to that of a CSTR (differential reactor). At high conversion the rate varies over the bed length and the reactor operates under integral conditions. Variation of the space time  $W/F_i^0$  yields the corresponding conversion data. Using numerical differentiation, rates can be estimated that can be compared for different catalysts. Differential conditions at high conversions, especially of interest for practical applications, can be achieved by using an up-wind reactor to attain the desired conversion level, followed by a differential reactor. This requires highly accurate analyses to determine the minor differences in composition. In general, catalyst activities are compared by comparison of the conversion levels at equal space times preferably at low conversion levels ('initial reaction rates'). At high conversions this is much less sensitive, and especially with respect to selectivities wrong conclusions may be drawn (see later).

The CSTR and PFR are the two extremes of continuous reactor types, one with an extremely good mixing, the other without. Some criteria or methods exist to judge whether one can use one of these reactor models.

### 9.1.2.3 Continuous-Flow Stirred-Tank Reactor (CSTR)

The most applied CSTRs are recirculation reactors in heterogeneous catalysis and well stirred vessels in slurry or liquid-phase systems. Injection of a  $\delta$ -pulse of a tracer should give an exponentially decaying output concentration:

$$c(t) = c_0 \exp(-t/\tau) \quad (5)$$

where  $\tau$  represents the average physical residence time in the reactor system ( $= N_{\text{tot,R}}/F_{\text{tot,out}}$ ), which should not be confused with the space time used in the mass balance equation ( $= W/F_{i,\text{in}}$ ). This exponential behavior can be easily verified experimentally.

In recirculation reactors, a recirculation ratio  $R_c$  (ratio of the total flow returned to the inlet and the total outlet flow) larger than 20 is frequently recommended [11, 16]. This criterion is not complete as is apparent from the literature [17–19]. One can demand that the rate over the catalyst bed may not change more than 5%, thus for an  $n$ th order isothermal reaction,

$$\frac{\text{rate at the inlet of the bed}}{\text{rate at the outlet of the bed}} = \frac{r(c^{\text{in}}, T^{\text{in}})}{r(c^{\text{out}}, T^{\text{out}})} = \left(\frac{c^{\text{in}}}{c^{\text{out}}}\right)^n$$

$$= \left(1 + \frac{x}{(1-x)(1+R_c)}\right)^n = 1 \pm 0.05 \quad (6)$$

which yields

$$\frac{x}{(1-x)(1+R_c)} < \frac{0.05}{n} \quad (7)$$

This implies that the necessary recirculation ratio is not a fixed value, but depends on the reaction under consideration and the conversion level. At low conversions, the recirculation rate need not be high according to this criterion (good mixing, eq 5, is still required to avoid dead zones in the reactor), and a differential PFR model can be used. At high conversions, the recirculation rate must increase. It can easily be seen that a recirculation ratio of 20 limits the conversion for a first-order and a second-order reaction to 50% and 25%, respectively.

The problem in the verification of these criteria is the calculation of the recirculation ratio. No general relationship is valid, and it must be estimated for each reactor configuration by experimentation (see Refs 16 and 18).

#### 9.1.2.4 Plug-Flow Reactor (PFR)

PFR systems can be described by an infinite number of CSTRs in series. A packed bed can be considered as a finite number of CSTRs, each corresponding to a certain height of a slice of the catalyst bed, also indicated as equivalent height of mixing. Making the bed length shorter will increase the deviation from plug flow towards more axial mixing. This is also described by the axial dispersion model where the dimensionless Péclet number  $Pe$  is used as parameter. The relation between  $Pe$  and the number  $N$  of mixers in series is, for large  $N$ ,

$$2N = Pe = \frac{L_b \times u}{D_{\text{ax}}} = \frac{L_b}{d_p} Pe_p \quad (8)$$

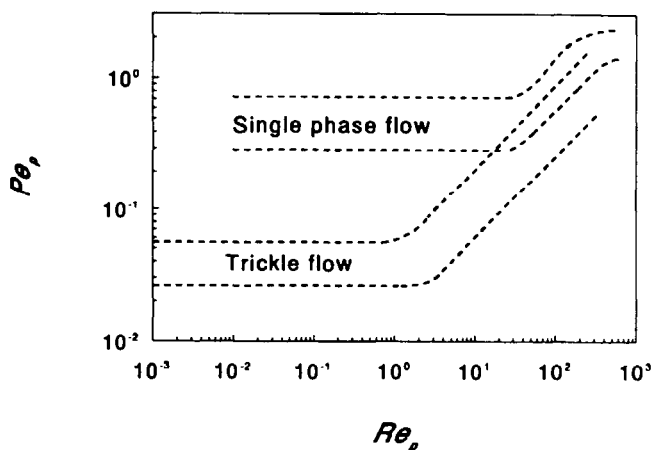


Figure 6. Relationship between the Péclet particle and Reynolds particle numbers for single and trickle phase flow (adapted from Ref. 20).

For a sufficiently close approach to an ideal plug flow reactor,  $N$  or  $Pe$  should exceed a certain value which depends on the degree of conversion and reaction order. Gierman [20] refined the criterion of Mears [21] and arrived at eq. 9, which can also be used for monoliths. In the latter case the axial dispersion coefficient should be replaced by the smaller molecular diffusivity, thus relaxing the criterion for monolithic elements as compared to packed beds:

$$Pe > 8n \times \ln\left(\frac{1}{1-x}\right) \quad (9)$$

Evaluation of literature data on the correlation between the particle Péclet number (also referred to as Bodenstein number) and particle Reynolds number for single phase and trickle flow yielded Fig. 6. At low  $Re_p$  ( $< 20$ ) a value between 0.3 and 0.7 holds for single phase flow, whereas for trickle flow this is one order of magnitude lower. These conditions are usually encountered in small scale laboratory reactors.

Combining these results yields a criterion for the ratio of the bed length and the particle size:

$$\frac{L_b}{d_p} > \frac{8n}{Pe_p} \times \ln\left(\frac{1}{1-x}\right) \quad (10)$$

Taking  $Pe_p = 0.5$  for the low Reynolds region of interest it is possible to calculate the minimum reactor length for a given reaction order, conversion, and particle size. A maximum allowable particle diameter can be calculated for a reactor of a given length. Figure 7 gives the maximum allowable particle diameters for a first-order reaction and various reactor lengths. For trickle flow reactors the reactor lengths are ten times larger at the same particle size.

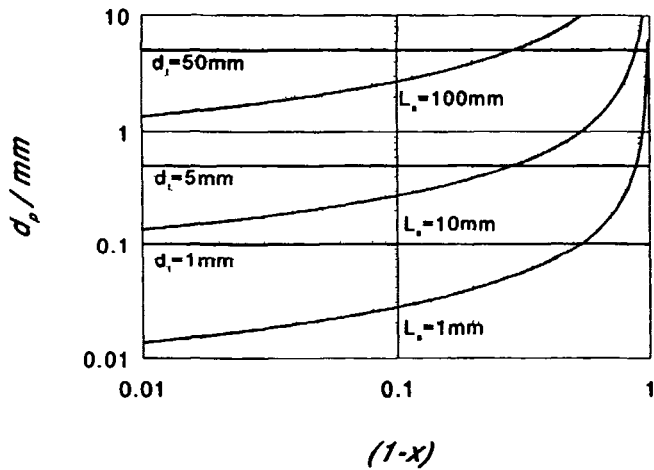


Figure 7. Maximum allowable particle diameters as a function of  $(1-x)$  for plug flow behavior (first-order reaction, single phase) at different bed lengths and for a flat velocity profile for different reactor diameters.

In PFRs not only the reactor length but also the diameter plays a role in its plug flow performance. Close to the wall, the packing density is lower than that in the interior because of the presence of a flat wall surface. The higher voidage implies a lower resistance to flow and higher local velocities are to be expected. However the radial mixing effects in the packed bed may relax this influence. To avoid these phenomena the following condition should be satisfied [22]:

$$\frac{d_t}{d_p} > 10 \quad (10)$$

The maximum allowable particle diameters for typical reactor diameters are included in Figure 7. Especially at low conversion levels, the last criterion is more severe at a given reactor length, whereas with increasing conversion the axial dispersion criterion should be satisfied.

In ideal trickle flow reactors, all particles in the catalyst bed take part in the overall reactor performance, since each is surrounded (wetted) by the liquid phase that flows around it. Situations in which the liquid flows preferentially through a certain part of the bed, while the gas phase flows predominantly through another part, should be avoided [23]. In this case, part of the bed is not contacted by the liquid reactant at all and does not contribute to the overall conversion. To avoid this maldistribution, Gierman [20] proposed the following criterion for the wetting number  $W_{tr}$  for concurrent downflow operation:

$$10^6 W_{tr} = 10^6 \times \frac{v_l \times u_l}{d_p^2 \times g} > 5 \quad (12)$$

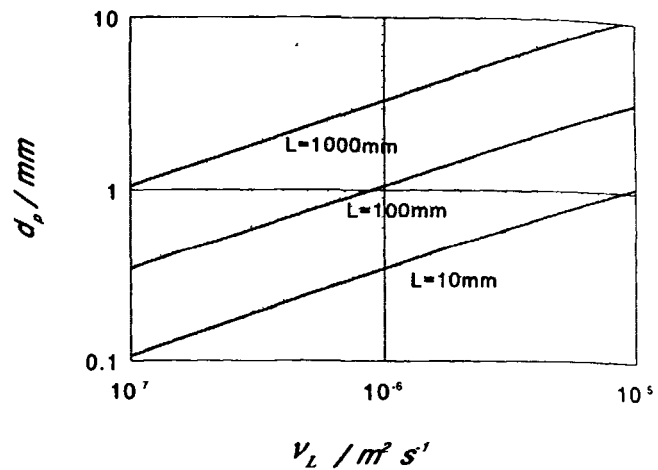


Figure 8. Maximum allowable particle diameters as a function of the kinematic viscosity for complete wetting in trickle flow reactors.



Figure 9. Testing of full sized catalyst particles by dilution with small inerts (adapted from Ref. 23).

The main variables that dictate the uniformity of catalyst irrigation are the liquid velocity, the particle diameter and the kinematic viscosity of the liquid. Figure 8 gives the maximum allowable particle diameters for several reactor lengths as a function of the kinematic viscosity.

From the foregoing it will be clear that the particle size is a major factor to be considered in the application of small reactors. In addition, it will be clear that a catalyst in the commonly used form of extrudates, for example of 1–3 mm diameter can only be tested in a large reactor on pilot-plant scale. Although these particles can be crushed to the size suitable for testing in laboratory reactors, this is not always desired. Sometimes, performance data are needed under conditions where internal diffusion gradients exist, to be able to predict industrial operation. Alternatively, the catalyst is of the egg-shell type or another defined concentration profile of the active phase that is not to be destroyed. A way to satisfy these criteria of small particle and yet to use the full-size catalyst is to dilute the large catalyst particles with fine inert particles, as schematically represented in Fig. 9. In this way, the hydrodynamics and kinetics are decoupled [23]. The fine particles dictate the hydrodynamic performance, i.e. the plug flow and wetting behavior, and the catalyst particles the kinetic behavior. Needless to say that bed dilution is also applicable in the case of small catalyst particles to obtain

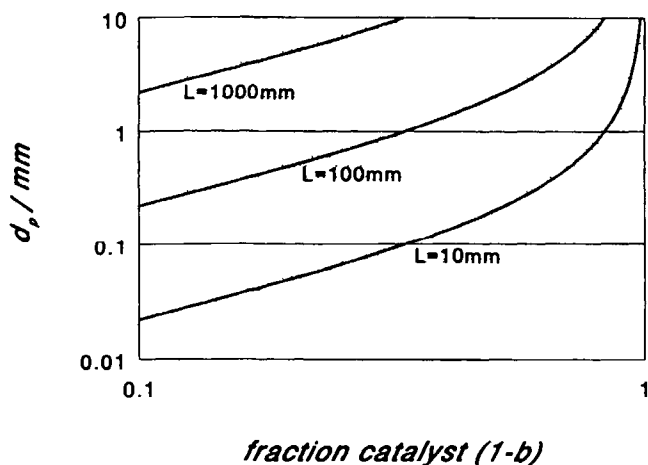


Figure 10. Maximum allowable particle diameters as a function of the fraction catalyst  $(1 - b)$  in a diluted bed.

sufficient bed length. This dilution technique has been successfully applied for years in hydrotreating research using trickle flow reactors [23].

The optimal and reproducible way of packing a reactor with large and fine particles is the dry method. Firstly, the reactor is packed with the large particles, followed by packing this prepacked bed with the fine particles while vibrating the reactor, and with a sufficiently low flow rate to avoid segregation [24].

One should be careful, however, in the degree of dilution. A too diluted system, especially in the case of equal sized particles, may lead to uneven distribution and bypassing of the catalyst. Van den Bleek et al. [25] evaluated this problem and advanced the following criterion for an inert bed fraction  $b$  and a 5% deviation of the ideal situation ( $L_0$  is the undiluted bed length):

$$\frac{2.5 \times b \times d_p}{(1 - b) \times L_b} = \frac{2.5 \times b \times d_p}{L_0} < 0.05 \quad (13)$$

This criterion imposes constraints on the maximum particle size as a function of the bed dilution and vice versa, which is graphically represented by Fig. 10 for various bed lengths. In general, samples should not be diluted more than 5–10 times.

One should also be cautious about too high dilutions, for reasons of sample inhomogeneity. Catalyst batches may contain particles of different activities, due to incomplete wetting during preparation or more times of impregnation. If too few particles are being used statistically the sample may not be representative. This imposes limits on the particle size at large fractions of inerts. It is recommended, however, that the preparation method should be improved. Visual inspection of the sample batches often already indicate its (in)homogeneity.

### 9.1.2.5 Laboratory Systems

Usually, small amounts of catalyst, ranging from 10 to 1000 mg, and gas flow rates between 10 and 1000 ml min<sup>-1</sup> (STP) are applied in laboratory reactors. This depends largely on the reactor type used. PFRs cover the whole spectrum with diameters ranging from a few to 20 mm, whereas CSTRs generally need more catalyst and higher flow rates due to their dimensions. Using packed beds in the latter necessitates the use of larger particles to overcome the pressure drop problem and to obtain high recirculation rates [16]. This is not always acceptable. In this respect, monolithic catalysts are easier to apply in CSTRs due to their intrinsic low pressure drop.

Some practical advantages and disadvantages of frequently used reactors are the following:

- PFR: deactivation noted directly; small amounts of catalyst needed; simple; yields primarily conversion data, not rates.
- CSTR: larger amounts of catalyst and flows needed; deactivation not immediately determined; direct rate from conversions.
- FBR: no ideal reactor behaviour; continuous handling of solids possible.
- TGA: limited to weight changes; careful data interpretation needed; often mass transfer limitations.
- Batch: Catalyst deactivation hard to detect; quickly yields conversion and selectivity data over a large conversion range.

More detailed treatment of laboratory reactors can be found elsewhere [3, 12, 13, 26].

## 9.1.3 Mass and Heat Transfer

Due to the consumption of reactants and the production or consumption of heat, concentration and temperature profiles can develop in the stagnant zone around and in the particle itself (Fig. 11). In the following paragraphs, criteria are derived to ensure that the effect of these gradients on the observed reaction rate is negligible [4, 27, 28]. In gas/liquid/solid slurry reactors, the mass transfer between the gas and liquid phase has to be considered, too (see Refs 9 and 29).

### 9.1.3.1 Extraparticle Gradients

Extraparticle mass and heat transfer is most conveniently analyzed by means of the so-called film model, in which the flux from the bulk fluid to the

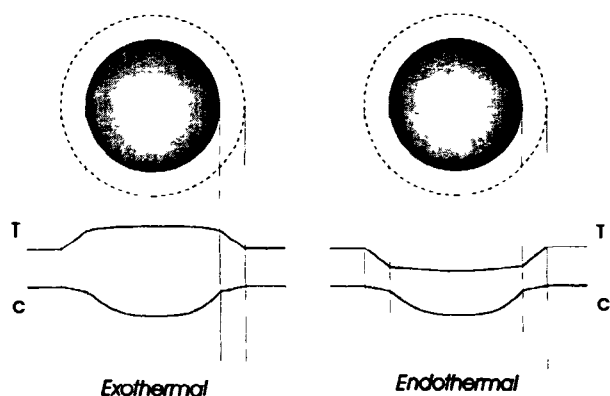


Figure 11. Temperature and concentration gradients in and around a catalyst particle for exothermal and endothermal reactions.

particle is defined in terms of mass and heat transfer coefficients  $k_f$  and  $h$ , respectively.

A mass balance over the film layer yields:

$$k_f(c_b - c_s)A_p = r_v V_p \quad (14)$$

This expression shows that the mass transfer rate is proportional to the concentration difference over the film. This rate is maximal when the surface concentration equals zero. Thus,

$$r_{\max} = k_f a' c_b \quad (15)$$

where  $a' = A_p/V_p$  is the specific particle area.

A dimensionless number  $Ca$ , the Carberry number [8], is introduced as follows:

$$Ca = \frac{r_{v, \text{obs}}}{k_f a' c_b} = \frac{c_b - c_s}{c_b} \quad (16)$$

$Ca$  relates the concentration difference over the film to procurable quantities and is therefore a so-called observable [4]. A criterion for the absence of extraparticle gradients in the rate data can be derived from the definition of an effectiveness factor for a particle. This should not deviate more than 5% from unity:

$$\eta_c = \frac{\text{observed reaction rate}}{\text{rate without gradients}} = \frac{r_{v, \text{obs}}}{r_{v, \text{chem}}(c_b, T_b)} = 1 \pm 0.05 \quad (17)$$

The minus sign applies to positive reaction orders and endothermal reactions, the plus sign to negative reaction orders and exothermal reactions. For an isothermal,  $n$ th-order irreversible reaction this gives

$$Ca < \frac{0.05}{|n|} \quad (18)$$

Analogously to mass transfer, the following equation is used for external heat transfer:

$$h \times a' \times (T_s - T_b) = r_v (-\Delta H_r) \quad (19)$$

Combination with eq 14 yields

$$\frac{T_s - T_b}{T_b} = \frac{k_f \times c_b \times (-\Delta H_r)}{h \times T_b} \times \frac{c_b - c_s}{c_b} = \beta_e \times Ca \quad (20)$$

where  $\beta_e$  is called the external Prater number. This represents the maximum relative temperature difference over the film or the ratio of the maximum heat production and heat transfer rates.

For rather general kinetics the effectiveness factor definition can be approximated as

$$\begin{aligned} \eta_c &= \frac{r_v(c_s, T_s)}{r_v(c_b, T_b)} = \frac{k_v(T_s)}{k_v(T_b)} \times \frac{f(c_s)}{f(c_b)} \approx \frac{k_v(T_s)}{k_v(T_b)} \\ &= \exp\left[-\frac{E_a}{RT_b} \left(\frac{T_b}{T_s} - 1\right)\right] = 1 \pm 0.05 \quad (21) \end{aligned}$$

under the assumption that heat effects dominate the transport disguises, so for small  $Ca$  values. Series expansion of the exponential leads to the simple result

$$\begin{aligned} |\gamma_b \times \beta_e \times Ca| &= \left| \left(\frac{E_a}{RT_b}\right) \times \left(\frac{(-\Delta H_r) \times k_f \times c_b}{h \times T_b}\right) \right. \\ &\quad \left. \times \left(\frac{r_{v, \text{obs}}}{k_f \times a' \times c_b}\right) \right| < 0.05 \quad (22) \end{aligned}$$

A result such as this is logical since it contains the three groups that determine the overall process.  $Ca$  determines the concentration drop over the film, the Prater number the maximum temperature rise or drop (exothermal or endothermal reaction), and the dimensionless activation energy expresses the sensitivity of the reaction to a temperature change.

Both criteria for extraparticle gradients contain observables and can be calculated based on experimental observations of reaction rates. For heat and mass transfer coefficients in packed beds various correlations exist in terms of dimensionless numbers. In Table 1 the most appropriate ones for laboratory reactors are given [5, 7, 30, 31]. Values of  $k_f$  and  $h$  for gases in laboratory systems range between  $0.1\text{--}10 \text{ m s}^{-1}$  and  $100\text{--}1000 \text{ J K}^{-1} \text{ s}^{-1} \text{ m}^{-2}$ , respectively. In the case of monoliths, other correlations should be used because of the different geometry [32–34].

### 9.1.3.2 Intraparticle Gradients

While the reactants have to diffuse to the active sites in the interior of catalyst particles, they can react, and a concentration profile over the particle diameter can develop. Mathematically, this is described by a differential equation derived from a mass balance over a small shell of the catalyst particle. This reads, for a slab geometry and first-order irreversible reaction,

$$D_{\text{eff}} \frac{d^2 c}{dz^2} - k_v c = 0 \quad (23)$$

**Table 1.** Correlations to calculate mass and heat transfer coefficients in packed beds [5, 7, 30, 31] and monoliths [32–34].

Mass transfer	Heat transfer	Range of validity
<i>Packed beds</i>		
$Sh = \frac{k_f \times d_p}{D_{if}}$	$Nu = \frac{h \times d_p}{\lambda_f}$	$Re_p = \frac{\rho_f \times u \times d_p}{\mu_f}$
$Sc = \frac{\mu_f}{\rho_f \times D_{if}}$	$Pr = \frac{\mu_f \times \bar{C}_{pf}}{\lambda_f}$	
<i>Gases</i>		
$Sh = \frac{0.357}{\epsilon_b} \times Re_p^{0.641} \times Sc^{1/3}$	$Nu = \frac{0.428}{\epsilon_b} \times Re_p^{0.641} \times Pr^{1/3}$	$3 < Re_p < 2000$
$Sh \approx 0.07 \times Re_p$	$Nu \approx 0.07 \times Re_p$	$0.1 < Re_p < 10$
<i>Liquids</i>		
$Sh = \frac{0.250}{\epsilon_b} \times Re_p^{0.69} \times Sc^{1/3}$	$Nu = \frac{0.300}{\epsilon_b} \times Re_p^{0.69} \times Pr^{1/3}$	$55 < Re_p < 1500$
$Sh = \frac{1.09}{\epsilon_b} \times Re_p^{1/3} \times Sc^{1/3}$	$Nu = \frac{1.31}{\epsilon_b} \times Re_p^{1/3} \times Pr^{1/3}$	$0.0016 < Re_p < 55$
<i>Monoliths</i>		
$Sh = Nu_\infty \left(1 + B_1 \times Re \times Sc \frac{d_H}{L}\right)^{0.45}$	where	$Re = \frac{\rho_f \times u \times d_H}{\mu_f}$
$Nu = Nu_\infty \left(1 + B_1 \times Re \times Pr \frac{d_H}{L}\right)^{0.45}$		$d_H = \frac{\sqrt{\epsilon_M \times \bar{\delta}_w}}{1 - \sqrt{\epsilon_M}} = \frac{4A_{ch}}{O_{ch}}$
and:	$Nu_\infty = 2.976$ 3.657 3.660 $B_1 = 0.095$	(square) (circular) (hexagonal) (catalytic monoliths)

in which  $D_{eff}$  is the effective diffusion coefficient and  $k_v$  the rate constant based on the unit volume of catalyst. The effective diffusion coefficient depends on the morphology of the porous material. For large pores ( $> \approx 10$  nm) the diffusivity is determined by the molecular diffusivity ( $\approx 10^{-4}$ – $10^{-5}$  m<sup>2</sup> s<sup>-1</sup> for gases), in case of small pores by the Knudsen diffusivity ( $\approx 10^{-6}$ – $10^{-7}$  m<sup>2</sup> s<sup>-1</sup>). The molecular diffusivity can be calculated by correlations [5, 6], or from extrapolation from a known value at other conditions of temperature and pressure, using the dependency

$$D_{if} \propto p^{-1}, T^{1.75} \quad (24)$$

The Knudsen diffusivity of component  $i$  for a cylindrical pore of radius  $r_0$  is

$$D_{K,i} = 97 \times r_0 \sqrt{\frac{T}{M_i}} \quad (25)$$

In a transition region, the Bosanquet formula can be used that accounts for both contributions:

$$\frac{1}{\bar{D}} = \frac{1}{D_{if}} + \frac{1}{D_K} \quad (26)$$

In zeolitic materials, where the molecules are of pore size dimensions, activated configurational diffusion

takes place for which even lower diffusivity values below  $10^{-8}$  m<sup>2</sup> s<sup>-1</sup> hold [35]. In this case diffusion description resembles that of surface diffusion, migration over the surface in the adsorbed phase, which explains sometimes the unexpected high diffusional flux [36].

A more rigorous approach for the combined effect of the various diffusion modes is based on the Maxwell–Stefan approach [36], for porous materials often referred to as the ‘dusty gas model’.

Additionally, due to the presence of solid material the volume in which diffusion can take place is reduced by a factor  $\epsilon_p$ , the particle porosity. The tortuous path increases the diffusion length for a molecule relative to the spatial coordinate by a factor  $\tau_p$ . The effective diffusivity can therefore be expressed as

$$D_{eff} = \frac{\epsilon_p}{\tau_p} \bar{D} \approx 0.05 - 0.1 \bar{D} \quad (27)$$

The form of mass balance 23 will depend on the particle shape (sphere, cylinder, trilobe, slab, etc.). For any geometry the characteristic length should be defined as

$$L = \frac{V_p}{A_p} = \frac{1}{a'} \quad (28)$$



to obtain essentially the same result as for the slab geometry of thickness  $2L$  given below. The solution of the concentration profile is

$$\frac{c}{c_s} = \frac{\cosh\left(\phi \frac{x}{L}\right)}{\cosh(\phi)} \quad (29)$$

in which  $\phi$  is known as the Thiele modulus and is the square root of the ratio of the reaction rate and the diffusional rate in the particle:

$$\phi = L \sqrt{\frac{k_v}{D_{\text{eff}}}} \quad (30)$$

When the Thiele modulus is small no internal concentration profile exists. In case of large values, due to the existence of a concentration profile, the catalyst is not effectively used, and an effectiveness factor is defined as

$$\begin{aligned} \eta_i &= \frac{\text{observed reaction rate}}{\text{rate without gradients}} = \frac{r_{v,\text{obs}}}{r_{v,\text{chem}}(c_s, T_s)} \\ &= \frac{\int r_v(c, T) dV}{r_{v,\text{chem}}(c_s, T_s) \times V_p} \end{aligned} \quad (31)$$

An analytical expression for the effectiveness factor can only be given for simple reaction kinetics, such as a first-order reaction in a slab (eq 32).

For a comparison of catalyst activities and in kinetic studies, one needs data that are not disguised by concentration gradients. For a 5% tolerance level the criterion for the effectiveness factor for the absence of internal diffusion limitations reads

$$\eta_i = \frac{\tanh(\phi)}{\phi} = 1 \pm 0.05 \quad (32)$$

While it is the purpose of a study to determine, for example, the intrinsic rate one cannot determine whether this criterion is satisfied. Therefore, the following combination is introduced that yields a procurable quantity (an observable) which is referred to as the Wheeler-Weisz modulus [4, 8]. From series expansion, and since  $\eta_i$  is close to 1, the following criterion follows for an  $n$ th-order reaction [27]:

$$\eta_i \phi_G^2 = \frac{r_{v,\text{obs}} \times L^2}{D_{\text{eff}} \times c_b} < 0.15 \left( \frac{2}{n+1} \right) \quad (33)$$

Here, the generalized form of the Thiele modulus is used, in order to be independent of the reaction kinetics, which is defined such that for the limit  $\phi_G \rightarrow \infty$   $\eta_i \rightarrow 1/\phi_G$  [8, 37]:

$$\phi_G = \frac{L \times r_v(c_s)}{\sqrt{\left(2 \times \int_{c_{\text{eq}}}^{c_s} D_{\text{eff}} \times r_v dc\right)}} \quad (34)$$

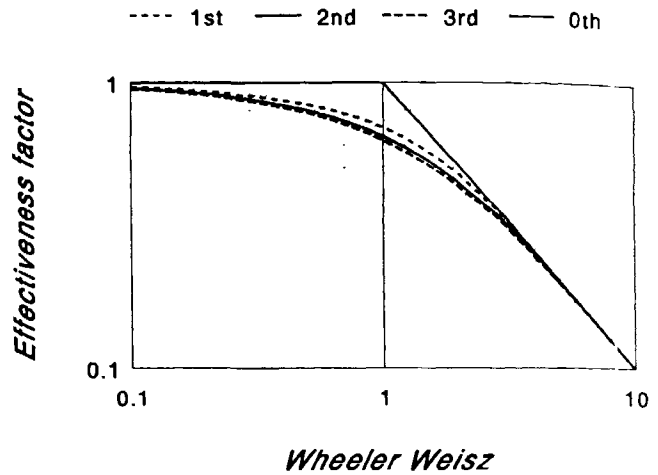


Figure 12. Isothermal internal effectiveness factor as a function of the Wheeler-Weisz modulus for different reaction orders.

This yields, for an  $n$ th order irreversible reaction,

$$\phi = L \sqrt{\left(\frac{k_v}{D_e} \times \frac{(n+1)}{2} \times c_s^{n-1}\right)} \quad (35)$$

Figure 12 shows the effectiveness factor as a function of the Wheeler-Weisz modulus for different reaction orders, indicating that criterion (33) holds for the generalized Thiele modulus. Due to the definition of  $L$  it is fairly independent of the catalyst geometry.

The derivation of the internal temperature gradient can only be performed numerically, even for simple kinetics. Again the 5% criterion is used for the internal effectiveness factor. Assuming that the rate can be simplified into a temperature and concentration dependent part, this yields

$$\begin{aligned} \eta_i &= \frac{r_v(c_i, T_i)}{r_v(c_s, T_s)} = \frac{k_v(T_i)}{k_v(T_s)} \times \frac{f(c_i)}{f(c_s)} \approx \frac{k_v(T_i)}{k_v(T_s)} \\ &= \exp\left[-\frac{E_a}{RT_s} \left(\frac{T_s}{T_i} - 1\right)\right] = 1 \pm 0.05 \end{aligned} \quad (36)$$

where the concentration effects are assumed to be negligible in order to derive a criterion for the temperature effects only.

In the nonisothermal case the reaction temperature in the center of the particle will be higher than  $T_s$  at the external surface for exothermal reactions and lower for endothermal reactions. Since we focus on small deviations from the isothermal behavior, the rates in the particle center will be higher or lower, respectively, than at the surface conditions. An expression for the temperature rise in the particle is obtained from the mass (eq. 23) and heat balance for a particle:

$$-\lambda_{p,\text{eff}} \frac{d^2 T}{dz^2} = r_v(-\Delta H_r) \quad (37)$$

Effective thermal conductivity values of porous materials  $\lambda_{p,\text{eff}}$  range between 0.1 and 0.5 J s<sup>-1</sup> K<sup>-1</sup> in gaseous atmospheres [6] and are only slightly larger than those for the gas phase. Straightforward combination of eqs 23 and 37 and integration leads to a simple general result that relates the temperature and concentration profile over a particle:

$$\frac{T - T_s}{T_s} = \beta_1 \times \frac{c_s - c}{c_s} \quad (38)$$

where

$$\beta_1 = \frac{(-\Delta H_r) \times D_{\text{eff}} \times c_s}{\lambda_{p,\text{eff}} \times T_s} = \frac{\Delta T_{\text{max}}}{T_s} \quad (39)$$

is the internal Prater number, which represents the maximum relative temperature difference across the particle or the ratio of the heat production rate and the heat conduction rate in the particle. Series development and combination of eqs 36 and 38 yields the following criterion for absence of temperature effects on the experimental data [21, 27]:

$$|\gamma_s \times \beta_1 \times \eta_1 \phi^2| = \left| \left( \frac{E_a}{R \times T_s} \right) \times \left( \frac{(-\Delta H_r) \times D_{\text{eff}} \times c_s}{\lambda_{\text{eff}} \times T_s} \right) \times \left( \frac{r_{v,\text{obs}} \times L^2}{D_{\text{eff}} \times c_s} \right) \right| < 0.1 \quad (40)$$

This criterion also contains ‘observables’, and so an estimation can be made about the presence of temperature gradients. This result is not unexpected and is quite similar to that for external transport. The Wheeler–Weisz parameter represents the concentration profile, the Prater number the maximum heat production relative to the heat removal by conduction, and the dimensionless activation energy the sensitivity of the rate for a temperature change. It can be shown that  $|\beta_1| \times \eta \phi^2$  represents the relative temperature gradient over the particle, similar to  $|\beta_c| \times Ca$  for that over the film. In the application of the criterion,  $c_s$  and  $T_s$  are not always known. Using the values for the bulk phase yields generally a good estimate. However, they can be calculated from the external transport balances, eqs 16 and 20.

It will be clear that in case of exothermal reactions the effectiveness factor can become larger than one. This is indicated by the numerical solution for the effectiveness factor in Fig. 13 for various values of  $\beta_1$  and  $\gamma_s$ . In these cases situations may arise that the temperature effect is counterbalanced by the concentration effects, resulting in an effectiveness factor around one. However, the temperature effect in the case of endothermal reactions only adds to the lowering of the effectiveness factor by a concentration profile.

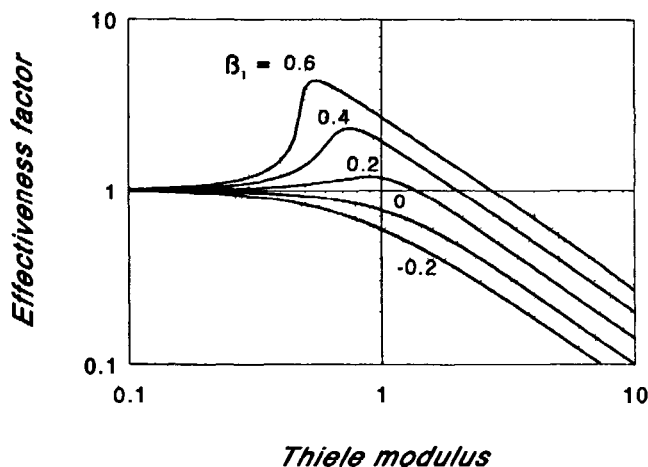


Figure 13. Internal effectiveness factor as a function of the Thiele modulus for nonisothermal reactions at different values for the Prater number and  $\gamma_s = 10$  (numerical solutions for a first order reaction).

### 9.1.3.3 Catalyst Bed Gradients

In the catalyst bed, temperature gradients can develop, analogously to those in a particle. In the axial direction the conversion increases under reaction conditions, causing a temperature gradient. These temperature gradients should be kept as small as possible, otherwise the rate data may not have the value attributed to them.

The heat produced or consumed by the reaction can be removed or supplied, respectively, by the fluid phase flowing through the bed, or by axial and radial conduction through the bed itself. Especially in the case of gas phase reactions, the heat capacity of the fluid may be insufficient to keep the temperature change within acceptable limits.

Axial conduction contributions are negligible in the case of packed beds due to the large  $L/d_i$  ratio imposed by the various criteria. Radial conduction to the wall of the reactor has the largest effect to minimize the temperature gradients. Heat conduction through packed beds, however, is poor. The porous particles themselves already have a poor conductivity, and the heat transfer between the particles is by their contact points and via the fluid phase. Radiation is only important at higher temperatures, in reactions like the reforming of methane by steam or carbon dioxide or the methane coupling reaction. Additionally, due to the lower porosity in the wall region the heat transfer from the bed to the reactor wall might be even worse.

Mears analyzed this problem for a plug flow reactor [28] and obtained an approximate solution for the maximum temperature rise in the catalyst bed. Based

**Table 2.** Correlations to calculate the effective heat conductivity in a catalyst bed and heat transfer coefficient to the reactor wall [8, 39].

$$\lambda_{b,\text{eff}} = \lambda_{b,\text{eff}}^0 + \frac{0.14 \times C_{p,g} \times \rho_g \times u}{1 + 46 \times \left(\frac{r_p}{r_t}\right)^2} \quad (44)$$

$$h_w = h_w^0 + 0.0115 \times \left(\frac{r_t}{r_p}\right) \times Re_p \quad (45)$$

with the static contributions:

$$\lambda_{b,\text{eff}}^0 = \varepsilon_b \lambda_g + (1 - \varepsilon_b) \times \lambda_{p,\text{eff}} \times \left(\frac{1}{\left(\phi_b \frac{\lambda_{p,\text{eff}}}{\lambda_g} + \frac{2}{3}\right)}\right) \quad (46)$$

$$h_w^0 = \frac{\lambda_{w,\text{eff}}^0}{r_p} \quad (47)$$

on this result a criterion for a less than 5% deviation from the isothermal rate could be given by Taylor series expansion of the rate and considering the whole cross section of the reactor to obtain an average reaction rate. This gave

$$\frac{E_a}{RT_w} \times \left| \frac{r_{v,\text{obs}} \times (-\Delta H_r) \times r_t^2}{\lambda_{b,\text{eff}} \times T_w} \right| \times \left( \frac{1}{8} + \frac{1}{Bi_w} \times \frac{r_p}{r_t} \right) < 0.05 \quad (41)$$

where the reaction rate  $r_{v,\text{obs}}$  based on the whole bed volume can be expressed as

$$r_{v,\text{obs}} = r_{v,\text{obs}} \times (1 - \varepsilon_b) \times (1 - b) \quad (42)$$

which includes the fraction of inert material  $b$ , from a possible bed dilution.

This criterion resembles much those for the temperature gradients on a particle level. The first term again represents the dimensionless activation energy  $\gamma_w$ , based on the reactor wall temperature  $T_w$ . The second term represents the ratio of the heat production rate and the heat conduction rate in radial direction. The last term accounts for the relative contributions of the radial conductivity and the heat transfer at the reactor wall. The latter contains the particle to bed radius ratio and the Biot number for heat transport at the wall, defined as:

$$Bi_{h,w} = \frac{h_w \times d_p}{\lambda_{b,\text{eff}}} \quad (43)$$

For  $Re_p < 100$  and  $0.05 < r_p/r_t < 0.2$ , wall Biot numbers range between 0.8 and 10 [28], so this means that wall effects cannot be neglected *a priori* [38]. Also this criterion contains procurable parameters. For the wall heat transfer coefficient  $h_w$  and the effective heat conductivity in the bed  $\lambda_{b,\text{eff}}$ , the correlations in Table 2, eqs. 44–47 can be used [8, 39]. These variables are assumed to be composed of a static and a dynamic (i.e. dependent on the flow conditions) contribution. Thermal heat conductivities of gases at 1 bar range from 0.01 to  $0.5 \text{ J s}^{-1} \text{ m}^{-1} \text{ K}^{-1}$ , depending on the nature of the gas and temperature.

The effective heat conduction at the wall  $\lambda_{w,\text{eff}}^0$  is calculated by eq 46 for the outer bed region of  $r_p$  thickness and its corresponding wall porosity  $\varepsilon_w$ . Values for the parameters  $\phi_b$  and  $\phi_w$  are given in Ref. 39 as a function of  $\lambda_{p,\text{eff}}/\lambda_g$ . Values of their product range between 1 and 100, and mostly between 2 and 10. Therefore, the last part in eq 46 is smaller than unity, decreasing the contribution of the solids. Other correlations may be used for the calculation of these parameters, including the radiation contribution [8, 40, 41].

Gradients in the catalyst bed will mainly occur in catalyzed gas-phase reactions due to the low heat capacity of the gases ( $\approx 1\text{--}5 \text{ kJ kg}^{-1} \text{ K}^{-1}$  at 1 bar). Bed dilution offers in this case the possibility to mitigate the situation. If an inert and good heat conducting material such as SiC ( $\lambda = 40 \text{ J m}^{-1} \text{ s}^{-1} \text{ K}^{-1}$ ) is used various effects contribute:

- the heat conduction in the bed is improved;
- the heat production is spread over a larger volume;
- the heat exchange area with the wall is enlarged.

When reactors are heated in ovens and not in intimate contact with the oven wall (radiative heating), it is found that temperature gradients may exist due to uneven heating. This temperature profile can be avoided by surrounding the reactor tube by a good conducting material with a high thermal conductivity, e.g. aluminum, silver, or copper.

In CSTRs one has one degree of freedom more available to minimize the temperature gradients, the recirculation ratio  $R_c$ . Increasing the total flow rate through the bed enhances the rate of heat supply or removal. If the temperature gradient over the bed is only affected by the heat production (consumption) through reaction and heat removal (supply) by the total flow through the bed, the criterion for sufficient isothermal behavior (less than 5% deviation in reaction rate, eq 6) is

$$\begin{aligned} \frac{E_a}{RT_b} \times \left| \frac{r_{\text{obs}} \times (-\Delta H_r)}{\tilde{C}_{pf} T_b} \right| \times \frac{W}{F_{\text{tot}}} \\ = \gamma_b \times \left| \frac{(-\Delta H_r)}{\tilde{C}_{pf} T_b} \right| \times \frac{y_0 \times x}{(R_c + 1)} < 0.05 \quad (48) \end{aligned}$$

As the criterion for concentration effects, this one also imposes larger recirculation rates at higher conversion than the thumb rule of 20, see the examples in Refs. 17–19.

### 9.1.4 Comparison Criteria

It is interesting to determine which criterion for the avoidance of mass and heat transport disguises is most severe, in order to have a quick impression whether all criteria are satisfied.

### 9.1.4.1 Mass Transport

Rearranging the parameters in the Wheeler–Weisz observable leads to

$$\eta_i \varphi^2 = \frac{r_{v,obs} L^2}{D_{eff} \times c_s} \approx \frac{k_f \times d_p}{D_{eff}} \times \frac{1}{s} \times \frac{r_{v,obs} \times L}{k_f \times c_b} = \frac{Bi_m}{s} \times Ca \quad (49)$$

where  $s$  equals 1, 2 or 3 for slab, cylinder or sphere geometry, respectively. Since most values for the Biot mass number range between 20 and 100 for conditions in laboratory reactors, the Wheeler–Weisz criterion is more severe than the Carberry criterion, i.e. internal mass transport limitations are expected to occur earlier than external limitations.

### 9.1.4.2 Heat Transport

Comparing the criteria for intra- and extraparticle heat transport the ratio of these criteria yields, globally,

$$\frac{\gamma_s \times |\beta_i| \times \eta_i \varphi^2}{\gamma_b \times |\beta_e| \times Ca} \approx \frac{D_{eff} \times h}{k_f \times \lambda_{p,eff}} \times \frac{Bi_m}{s} = \frac{h \times d_p}{\lambda_{p,eff} \times s} = \frac{Bi_h}{s} \quad (50)$$

The limits of the Biot heat number  $Bi_h$  are 0.01 and 50 [8], so it will depend on the particular conditions which criterion is the most severe. In the laboratory reactors it is often  $< 1$ . It is obvious that decreasing the particle size will shift the largest gradient to the film layer around the particle.

Under the assumption that inside a particle the reactant concentration becomes zero it can easily be shown that the ratio of the external and internal temperature gradients is

$$\frac{\Delta T_e}{\Delta T_i} = \frac{Bi_m}{Bi_h} \times \left( \frac{Ca}{1 - Ca} \right) \quad (51)$$

where [4]  $Bi_m/Bi_h$  is  $10^{-10^4}$  for gas–solid or  $10^{-4}-10^{-1}$  for liquid–solid interaction. This indicates that for liquid–solid reactions the external gradient is negligible, whereas in gas–solid reactions this will depend on the specific parameter values. Unlike in industrial operations (high flows, large particles) where, as a rule of thumb, the internal temperature gradient is assumed to be the largest [42], this is just the opposite in laboratory operation.

Comparing the criteria for intraparticle and for bed behavior, eqs 40 and 41, and neglecting the wall contribution and bed dilution, one sees immediately that their ratio results in

$$\frac{\gamma_w \times \left[ \frac{r_{v,obs} \times (-\Delta H_r) \times r_t^2 (1 - \varepsilon_b)}{8 \lambda_{b,eff} \times T_w} \right]}{\lambda_b \times \beta_e \times Ca} \approx \left( \frac{r_t}{r_p} \right)^2 \times \left( \frac{\lambda_{p,eff}}{\lambda_{b,eff}} \right) \times \left[ \frac{s^2 (1 - \varepsilon_b)}{8} \right] \gg 1 \quad (52)$$

The criterion for a flat velocity profile requires that the first term  $> 100$ , the second term is also larger than one since the effective conductivity of the bed is smaller than that of a particle, and the last term is only slightly smaller than one. Therefore, the temperature gradient in the catalyst bed will be the first that develops to an unacceptable extent and should be verified first. In case of concern, bed dilution with a well conducting inert material will improve the situation considerably.

Whether the criteria for intra- or extraparticle heat transport limitations are more severe than the corresponding ones for mass transport depends on the absolute value of the products  $\gamma_s \times \beta_i$  and  $\gamma_b \times \beta_e$ , respectively. In some cases the former product exceeds unity, but more often not [8], so internal temperature gradients do not occur frequently. The latter product is a factor  $Bi_m/Bi_h$  larger, generally  $> 10$  (gases), which means that in this case the extraparticle temperature gradient occurs earlier than an extraparticle concentration gradient.

For laboratory-scale operation the following order in relative importance of the various gradients can be indicated:

$$(T - \text{grad})_{\text{bed}} > (T - \text{grad})_{\text{ext}} > (c - \text{grad})_{\text{int}}, \\ (T - \text{grad})_{\text{int}} > (c - \text{grad})_{\text{ext}} \quad (53)$$

## 9.1.5 Effect of Particle Transport Limitations on the Observed Behavior

The observed reaction rate can be expressed as follows:

$$r_{v,obs} = \eta \times r_{v,chem}(c_b, T_b) = \eta_e \times \eta_i \times r_{v,chem}(c_b, T_b) \quad (54)$$

If external mass transport limitations strongly dominate, the rate becomes equal to the mass transfer rate, (eq 15). Hence, a first-order dependency is observed and, since the mass transfer coefficient is fairly independent of the temperature the apparent activation energy is negligible. However, due to the existing correlations, the observed rate constant is dependent on the flow rate and particle size.

If internal diffusion limitations dominate,  $\eta_i \rightarrow 1/\varphi$  and, for an  $n$ th order reaction,

$$r_{v,obs} \propto L^{-1} \sqrt{k_v \times D_{eff} \times c_s^{n+1}} \propto L^{-1} \\ \times c^{(n+1)/2} \exp\left(\frac{E_a}{2RT_s}\right) \quad (55)$$

The reaction is therefore dependent on the particle size, has an apparent order of  $(n + 1)/2$ , and has an apparent activation energy which is half the true activation energy.

**Table 3.** Apparent catalyst rate behavior depending on rate controlling regime (isothermal case).

Controlling process	Apparent order	Apparent activation energy	Dependency <sup>a</sup> $L$	Dependency <sup>a</sup> $u$
Kinetics	$n$	$E_a(\text{true})$	—	—
Internal diffusion	$(n + 1)/2$	$\frac{1}{2}E_a(\text{true})$	$1/L$	—
External mass transfer	1	$\approx 0$	$L^{m-2}$	$u^m$

<sup>a</sup> $m$  represents the power of the Reynolds number in the Sherwood correlation in Table 1.

At low temperatures reaction rates are generally kinetically controlled. With increasing temperature one first enters the diffusion limited region, and at even higher temperatures the film (extraparticle) diffusion limited region. In so-called Arrhenius plots this is nicely seen as a changing slope of the rate versus  $1/T$  dependency, which can be used as an indication for the presence of limitations. Good examples of this behavior can be found in the literature, for example the Fischer–Tropsch synthesis of middle distillates [43] and the catalyzed gasification of carbon [44]. This also demonstrates the applicability of the theory.

Changing activation energies are, however, not always indicative for the presence of limitations. The approach of thermodynamic equilibrium in the case of exothermal reactions can cause this phenomenon, as for hydrogenation reactions [44]. Also, changes in rate determining steps and catalyst deactivation might be causes. The same holds for reaction orders. Table 3 gives the various observations that can be made when mass transfer affects the isothermal kinetic behavior of catalyst particles.

Temperature gradients in endothermal reactions amplify the effects of concentration gradients. In exothermal reactions the thermal effects can compensate the concentration effects or dominate completely. In the latter cases the apparent activation energy can become higher than the true one due to a kind of ignition [5]. Also in this case at the highest temperatures the apparent  $E_a$  approaches zero.

## 9.1.6 Diagnostic Experimental Tests

Apart from the criteria based on the observable quantities derived above, some other experimental tests exist to verify the presence or absence of transport limitations.

### 9.1.6.1 Extraparticle Concentration Gradients

Since the mass transfer coefficient  $k_f$  is dependent of the fluid velocity in the catalyst bed, one can vary the flow rate and amount of catalyst simultaneously, while keeping the space time  $W/F_1^0$  constant, as indicated in

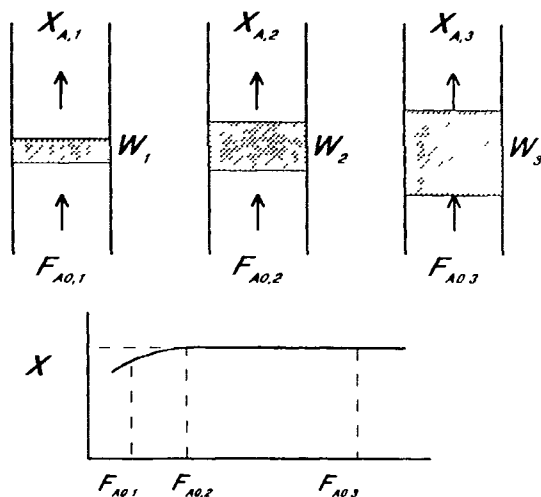


**Figure 14.** Diagnostic test for extraparticle concentration gradients keeping  $W/F^0$  constant

Fig. 14. If no limitations exist the resulting conversions should be the same. If temperature effects also interfere, however, they might (over)compensate concentration effects, so this method should be used with caution.

### 9.1.6.2 Intraparticle Concentration Gradients

More attention should be paid to the diffusion limitations, as was shown before. Under strongly limited conditions the observed rate becomes particle-size dependent,  $\propto 1/L$ . Variation of the particle size, for example by crushing and sieving the catalyst, and tests under identical conditions should give a proper answer whether diffusion interferes or not. Figure 15 exemplifies this. At small particle sizes the reaction is chemically controlled and independent of the particle size. Only for larger particles a decrease in the observed rate occurs. Be aware of the fact that extraparticle limitations also induce a particle-size dependency. The flow rate through the bed should not give any effect (Table 3). Also in this case, temperature effects should be avoided.

Koros and Nowak [45] designed a more complex test based on the fact that the intrinsic reaction rate is proportional to the concentration of active sites in the

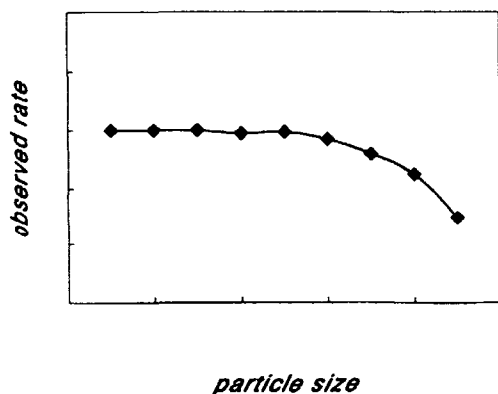


Figure 15. Dependency of the observed reaction rate on increasing particle size.

kinetic regime, to its square root in the diffusion limited regime, and independent in the external transport limited regime. The idea is to crush a catalyst and dilute it with inert support to various concentrations and pelletize to identical particle sizes. The dependency of the observed rate as a function of the concentration should indicate the regime in which one operates. This test is not conclusive, some reactions are structure sensitive, or diffusion limitations occur on a very small scale, as in zeolite crystals. Madon and Boudart discussed this test in detail [46]

### 9.1.6.3 Temperature Gradients

The best way to investigate the possible disguise by temperature gradients is to dilute the catalyst bed with an inert, good heat-conducting material, such as SiC. Lower conversions should result for exothermal reactions, and higher for endothermal reactions, if gradients were present. The presentation of crude rate data in 'Arrhenius plots' to inspect the temperature behavior can give indications of the presence of limiting transport processes by the changing slope ( $\propto$  activation energy). However, be aware of the fact that other phenomena can also induce this: changing rate determining step, catalyst deactivation or fouling, approach of thermodynamic equilibrium, and ignition phenomena.

### 9.1.7 Proper Catalyst Testing and Kinetic Studies

During the experimental investigations one should carry out a proper testing of the catalysts, in order to obtain the relevant information with regard to intrinsic activity, selectivity, deactivation, and kinetic behavior. The following guidelines should be applied:

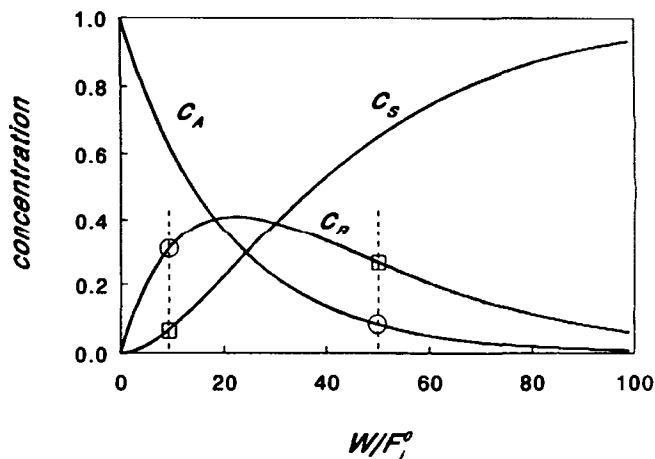


Figure 16. Product distribution for a consecutive irreversible first order reaction  $A \rightarrow R \rightarrow S$  as a function of the space time.

- adhere to criteria – ideal reactor behavior (plug flow or CSTR), isothermal bed, absence of limitations (observables, diagnostic tests);
- compare at low conversions to get insight into real activity differences (PFR);
- compare selectivities at same conversion levels.

In diagnostic tests crushing of the particles will not always be conclusive. Egg-shell catalysts or other types, zeolites and washcoated monoliths are exceptions. In washcoated monoliths the layer thickness is generally already quite low ( $< 50 \mu\text{m}$ ) and crushing will not yield smaller sizes. Cracking catalysts consist often of zeolitic crystals of  $\mu\text{m}$  dimensions and a binder yielding particles of about  $50 \mu\text{m}$ . If diffusion limitations exist in the zeolitic crystals, crushing will not eliminate these.

Low conversion levels are recommended to compare intrinsic activities or deactivation rates in PFRs since these are disguised due to the integral reactor behavior. For example, a factor of two in activity yields, for a first order irreversible reaction, pairs of conversion levels of 90 and 99%, 30 and 51% or 5 and 9.75%, depending on the used space velocity.

In this respect it is recommended that a good definition is given of this activity, preferably in terms of (i) reaction rate per unit mass or volume of catalyst or per unit mass of active phase or (ii) a turnover frequency (reaction events per site and per unit time).

Selectivities may depend strongly on the conversion level, as is exemplified for irreversible consecutive reactions in Fig. 16. If the intermediate product R is the desired one, then different apparent selectivities are obtained at different space times (corresponding to different conversion levels). A more active catalyst may therefore appear to be less selective, which is not nec-

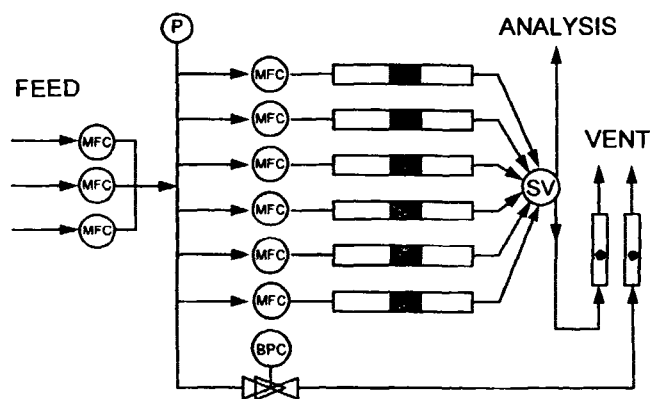


Figure 17. Six-flow reactor setup for simultaneously testing of catalyst samples.

essarily true. For catalyst selection it is important to have a good model of the reaction network. This determines the selectivity performance of a catalyst. On the basis of the rate parameters obtained and their temperature dependencies, one can explore the optimal conditions under which a catalyst should work and use this for the further catalyst selection. The experimental range of conditions that have been investigated is not necessarily sufficient, and useful catalyst formulations might otherwise be rejected. Transport limitations and deactivation phenomena also affect reaction selectivities [4, 5, 8] and should therefore be avoided.

Generally, during the course of a catalyst development programme procuring rate data is a laborious task. Many catalyst formulations are investigated and compared. Kinetic modeling requires data of conversion as a function of space time  $W/F_i^0$ , of temperature, of pressure and of composition, whereby competitively adsorbing components should not be forgotten. In all cases any improvement to speed up the process is helpful. For an efficient programme the following aspects can be considered to be implemented:

- Computer-controlled microreactor arrangements – these enable a stand-alone continuous operation and data collection over a predefined set of experimental conditions.
- Parallel reactors with individual flow control in one oven. For example, the six-flow reactor set-up that shown in Fig. 17. Often, one reactor serves as the reference containing only inerts or a reference catalyst. The others may contain different catalysts, different amounts, or duplicates. This enhances enormously the throughput of tested catalysts and lowers the time for kinetic studies [47], all at only moderately higher costs compared to a single reactor.
- Experimental design (for example for kinetic studies). This method searches for optimal experimental settings for the next data point [5, 8, 48], especially

useful in further discrimination between rival kinetic models or improvement of kinetic parameter estimates.

The computer(PC)-controlled equipment, especially when using the six-flow system, yields a wealth of results that should be properly processed and interpreted. The time involved in the latter should not be underestimated, and one should not lose oneself in experimentation only.

An interesting idea that was recently put forward in relation to PC-controlled equipment is the temperature scanning reactor [49] for kinetic studies. The basic idea is to release the requirement of isothermal operation in the axial direction in a PFR, but measuring the temperature at the exit of the catalyst bed. The conversion levels at various experimental settings of temperature and space time is investigated by temperature programmed experiments. Generally, one is interested only in a limited temperature range of about 100 K. Computer control of the reactor set-up and analysis equipment does the job. This yields data sets of conversion and exit temperatures at the same inlet temperature (or ‘clock time’ [49]) as a function of the space time  $W/F_i^0$ . By polynomial interpolation one can numerically differentiate the  $x$  versus  $W/F_i^0$  curve to obtain the reaction rate (eq 3) at different values of the corresponding space time. From the temperature–space time correlation the corresponding reaction temperature is known. This can be repeated for several pressures and compositions. Finally one obtains a large dataset of  $(W/F_i^0, x, r, T)$  points, that can be used for a thorough kinetic analysis.

In principle this looks a promising approach, especially when combined with the six-flow setup, provided the catalyst does not suffer from too much deactivation during the whole experimental process.

Sometimes the occurrence of a temperature profile along the reactor axis cannot be avoided, as in the study of exhaust gas monolithic catalysts. A possible approach can be to measure the temperature profile along the catalyst length, and use this for the data interpretation. It requires, however, a complete analysis of the mass and heat balances for a correct interpretation [50].

## 9.1.8 Notation

Symbol	Quantities	Units
$d$	specific surface area of catalyst particle	$\text{m}^{-1}$
$A_p$	external surface area of particle	$\text{m}^2$
$A_{ch}$	cross-sectional area of monolith channel	$\text{m}^2$
$b$	fraction inert in catalyst bed	

Symbol	Quantities	Units	Symbol	Quantities	Units
$c$	concentration	$\text{mol m}^{-3}$	<i>Dimensionless numbers</i>		
$\bar{C}_p$	molar heat capacity	$\text{J mol}^{-1} \text{K}^{-1}$	$Bi_m$	Biot number of mass	
$\hat{C}_p$	mass heat capacity	$\text{J kg}^{-1} \text{K}^{-1}$	$Bi_h$	Biot number of heat	
$d_H$	hydrodynamic channel diameter monolith	m	$Bi_w$	Biot number heat transfer at wall	
$d_p$	particle diameter	m	$Ca$	Carberry number	
$d_t$	diameter of reactor tube	m	$Nu$	Nusselt number	
$D_{ax}$	axial dispersion coefficient	$\text{m}^2 \text{s}^{-1}$	$Pe_p$	Péclet particle number	
$D_{K,i}$	Knudsen diffusivity of component $i$	$\text{m}^2 \text{s}^{-1}$	$Pr$	Prandtl number	
$D_{if}$	molecular diffusivity of $i$ in fluid phase $f$	$\text{m}^2 \text{s}^{-1}$	$Re$	Reynolds number	
$\bar{D}$	average diffusivity	$\text{m}^2 \text{s}^{-1}$	$Re_p$	Reynolds particle number	
$D_{\text{eff}}$	effective diffusivity in particle	$\text{m}^2 \text{s}^{-1}$	$Sc$	Schmidt number	
$E_a$	activation energy	$\text{J mol}^{-1}$	$Sh$	Sherwood number	
$f(c)$	concentration function in rate expression	–	$W_{tr}$	wetting number in trickle flow	
$F_i^0$	molar flow of $i$ at reactor inlet	$\text{mol s}^{-1}$	<i>Greek</i>		
$F_{\text{tot}}$	total flow through catalyst bed	$\text{mol s}^{-1}$	$\beta$	Prater number	–
$g$	gravitational acceleration	$\text{m s}^{-2}$	$\gamma$	dimensionless activation energy	–
$h$	heat transfer coefficient	$\text{J m}^{-2} \text{s}^{-1} \text{K}^{-1}$	$\delta_w$	wall thickness in monolith	m
$h^0$	static heat transfer coefficient	$\text{J m}^{-2} \text{s}^{-1} \text{K}^{-1}$	$\Delta H_T$	heat of reaction	$\text{J mol}^{-1}$
$k_v$	rate constant per unit particle volume	–	$\varepsilon$	porosity	–
$k_f$	mass transfer coefficient	$\text{m s}^{-1}$	$\varepsilon_M$	porosity of monolith	–
$L$	characteristic catalyst dimension	m	$\eta$	overall effectiveness factor	–
$L_b$	bed length	m	$\eta_i$	internal effectiveness factor	–
$L_0$	undiluted bed length	m	$\eta_e$	external effectiveness factor	–
$M_i$	molar mass of component $i$	$\text{kg kmol}^{-1}$	$\lambda_f$	thermal conductivity of fluid phase	$\text{J m}^{-1} \text{s}^{-1} \text{K}^{-1}$
$n$	reaction order	–	$\lambda_{\text{eff}}$	effective thermal conductivity	$\text{J m}^{-1} \text{s}^{-1} \text{K}^{-1}$
$N$	number of tanks in series	–	$\lambda_{\text{eff}}^0$	stationary effective thermal conductivity	$\text{J m}^{-1} \text{s}^{-1} \text{K}^{-1}$
$N_i$	number of moles of component $i$	mol	$\mu$	dynamic viscosity	$\text{kg m s}^{-1}$
$O_{\text{ch}}$	periphery of monolith channel cross section	m	$\nu_l$	kinematic viscosity of liquid	$\text{m}^2 \text{s}^{-1}$
$p$	pressure	Pa	$\nu_i$	stoichiometric coefficient of $i$ in reaction	–
$r_0$	average pore radius	m	$\rho$	density	$\text{kg m}^{-3}$
$r_p$	particle radius	m	$\tau$	average residence time CSTR	s
$r_t$	reactor tube radius	m	$\tau_p$	particle tortuosity factor	–
$r_v$	reaction rate per unit particle volume	$\text{mol s}^{-1} \text{m}_p^{-3}$	$\phi$	Thiele modulus	–
$r_{v,\text{chem}}$	intrinsic reaction rate per unit particle volume	$\text{mol s}^{-1} \text{m}_p^{-3}$	$\phi_G$	generalized Thiele modulus	–
$r_{v,\text{obs}}$	observed reaction rate per unit particle volume	$\text{mol s}^{-1} \text{m}_p^{-3}$	$\varphi$	parameter in effective thermal conductivity equation	–
$r_{V,\text{obs}}$	observed reaction rate per unit bed volume	$\text{mol s}^{-1} \text{m}_p^{-3}$	<i>Subscripts</i>		
$r_W$	reaction rate per unit catalyst mass	$\text{mol s}^{-1} \text{kg}^{-1}$	app	apparent	
$R$	universal gas constant	$\text{J mol}^{-1} \text{K}^{-1}$	b	in bulk phase; also bed	
$R_c$	recirculation ratio	–	chem	chemically controlled	
$s$	geometry parameter	–	e	external	
$t$	time	s	eff	effective	
$T$	temperature	K	f	fluid phase	
$u$	superficial velocity	$\text{m s}^{-1}$	i	intraparticle	
$V_p$	particle volume	$\text{m}^3$	M	monolith	
$W$	catalyst mass	kg	obs	observed	
$x$	conversion	–	p	particle	
$y_0$	molar fraction of reactant in reactor feed gas	–	s	at external particle surface	
$z$	coordinate	m	t	tube	
			w	at the reactor wall	



## References

- 1 *Applied Catalysis*, **1988**, Vol 43
- 2 *Catalysis Today*, **1991**, Vol 11
- 3 J R Anderson, K C Pratt, *Introduction to Characterization and Testing of Catalysts*, Academic Press, Sydney, **1985**, Chapter 6
- 4 J J Carberry in *Catalysis Science and Technology*, (Eds J R Anderson, M Boudart), Springer-Verlag, Berlin, **1987**, Vol 8, pp 131–171
- 5 L K Doraiswamy, M M Sharma in *Heterogeneous Reactions Analysis, Examples and Reactor Design*, Vol 1 *Gas-Solid and Solid-Solid Reactions*, Wiley, New York, **1984**
- 6 C N Satterfield, *Mass Transfer in Heterogeneous Catalysis*, MIT Press, Cambridge, **1970**
- 7 P Trambouze, H van Landeghem, J-P Wauquier, *Chemical Reactors Design/Engineering/Operation*, Editions Technip, Paris, **1986**, Chapter 11
- 8 G F Froment, K B Bischoff, *Chemical Reactor Analysis and Design*, 2nd ed., Wiley, New York, **1990**
- 9 F Kapteijn, G B Marin, J A Moulijn, in *Catalysis, an Integrated Approach to Homogeneous, Heterogeneous and Industrial Catalysis* (Eds J A Moulijn, P W N M van Leeuwen, R A van Santen) Elsevier, Amsterdam, **1993**, pp 251–306
- 10 J C R Turner in *Catalysis Science and Technology*, (Eds J R Anderson, M Boudart), Springer-Verlag, Berlin, **1981**, Vol 1, pp 43–86
- 11 J M Berty, *Plant Oper Progr* **1984**, 3, 163–168
- 12 K C Pratt in *Catalysis Science and Technology*, (Eds J R Anderson, M Boudart), Springer-Verlag, Berlin, **1987**, Vol 8, pp 174–226
- 13 L K Doraiswamy, D G Tjabl, *Catal Rev -Sci Eng* **1974**, 10, 177–219
- 14 K Tamaru, Section A 5 2 5
- 15 F H M Dekker, F Kapteijn, J A Moulijn, A Blek, *Chem Eng Sci*, **1995**, 50, 3573–3580
- 16 P C Borman, A N R Bos, K R Westerterp, *AIChE J* **1994**, 40, 862–869
- 17 R Broucek, *Chem Eng Sci* **1983**, 38, 1349–1350
- 18 R Dumpelmann, A Baiker, *Chem Eng Sci* **1992**, 47, 2665–2670
- 19 S Wedel, J Villadsen, *Chem Eng Sci* **1983**, 38, 1346–1349
- 20 H Gierman, *Appl Catal* **1988**, 43, 277–286
- 21 D E Mears, *Chem Eng Sci* **1971**, 26, 1361–1366
- 22 C F Chu, K M Ng, *AIChE J* **1989**, 35, 148–158
- 23 S T Sie, *Rev Inst Franc Petrole* **1991**, 46, 501–515
- 24 S S E H Elnashaie, M E Abashar, *Chem Eng Sci* **1990**, 45, 2964–2967
- 25 C M van den Bleek, K van der Wiele, P J van den Berg, *Chem Eng Sci* **1969**, 24, 681–694
- 26 V W Weekman jr., *AIChE J* **1974**, 20, 833–840
- 27 J A Moulijn, A Tarfaoui, F Kapteijn, *Catal Today* **1991**, 11, 1–12
- 28 D E Mears, *J Catal* **1971**, 20, 127–131
- 29 A A C M Beenackers, W P M van Swaaij, *Chem Eng Sci* **1993**, 48, 3109–3139
- 30 A Cybulski, M J van Dalen, J W Verkerk, P J van den Berg, *Chem Eng Sci* **1975**, 30, 1015–1018
- 31 C N Satterfield, *Heterogeneous Catalysis in Industrial Practice*, 2nd ed., McGraw-Hill, New York, **1992**, Chapter 11
- 32 R D Hawthorn, *AIChE Symp Ser* **1974**, 70, 428–438
- 33 R K Shah, A L London, *AIChE J* **1976**, 22, 344–353
- 34 A Cybulski, J A Moulijn, *Catal Rev -Sci Eng* **1994**, 36, 179–270
- 35 J Karger, D M Ruthven, *Diffusion in Zeolites*, John Wiley, New York, **1992**
- 36 R Krishna, *Gas Sep Purif* **1993**, 7, 91–104
- 37 P Schneider, *Catal Rev -Sci Eng* **1975**, 12, 201–278
- 38 J R Rostrup-Nielsen, L J Christiansen, J-H Bak Hansen, *Appl Catal* **1988**, 43, 287–303
- 39 D Kunii, O Levenspiel, *Ind Eng Chem Res* **1991**, 30, 136–141
- 40 M G Freiwald, W R Paterson, *Chem Eng Sci* **1992**, 47, 1545–1560
- 41 R J Wijngaarden, K P Westerterp, *Chem Eng Sci* **1993**, 48, 1273–1280
- 42 F M Dautzenberg in *Characterization in Catalyst Development*, American Chemical Society, Washington DC, **1989**, Vol 411, pp 99–119
- 43 M F M Post, A C van't Hoog, J K Minderhout, S T Sie, *AIChE J* **1989**, 35, 1107–1114
- 44 C A Bernardo, D L Trimm, *Carbon* **1979**, 17, 115–120
- 45 R M Koros, E J Nowak, *Chem Eng Sci* **1967**, 22, 470
- 46 R J Madon, M Boudart, *Ind Eng Chem Fundam* **1982**, 21, 438–447
- 47 F Kapteijn, L Singoredjo, N J J Dekker, J A Moulijn *Ind Eng Chem Res* **1993**, 32, 445–452
- 48 G F Froment, L H Hosten in *Catalysis Science and Technology*, (Eds J R Anderson, M Boudart) Springer-Verlag, Berlin, **1981**, Vol 2, pp 97–170
- 49 B W Wojciechowski, *Chem Eng Sci* **1993**, 48, 2881–2887
- 50 J A F Kunst, A Cybulski, X D Xu, P J T Verheijen, J A Moulijn in *Precision Process Technology, Perspectives for pollution prevention*, (Eds M P C Weijnen, A A H Drn kenburg), Kluwer, Dordrecht, **1993**, Vol 1, pp 197–206

## 9.2 Ancillary Techniques in Laboratory Units for Catalyst Testing

J. WEITKAMP

### 9.2.1 Introduction

All research in the field of heterogeneous catalysis ultimately aims at a more detailed understanding of the various chemical and mass transfer steps involved in the overall reaction and, based on this knowledge, at the formulation and preparation of improved catalysts. Testing the performance of a solid catalyst in the conversion of gaseous or liquid substrates is usually carried out on a small scale, in a laboratory apparatus accommodating typically 0 l to 10 g of catalyst. To make sure that meaningful and reproducible results are obtained in such laboratory-scale units, they must be properly designed and constructed, and parts which are prone to cause malfunctions should be avoided. It is the intention of the present Chapter to discuss critical building blocks of laboratory-scale catalytic units which are frequently designed in an inadequate manner. Since the core part of such units, viz the catalytic reactor, has been the subject of the preceding Chapter [1], this con

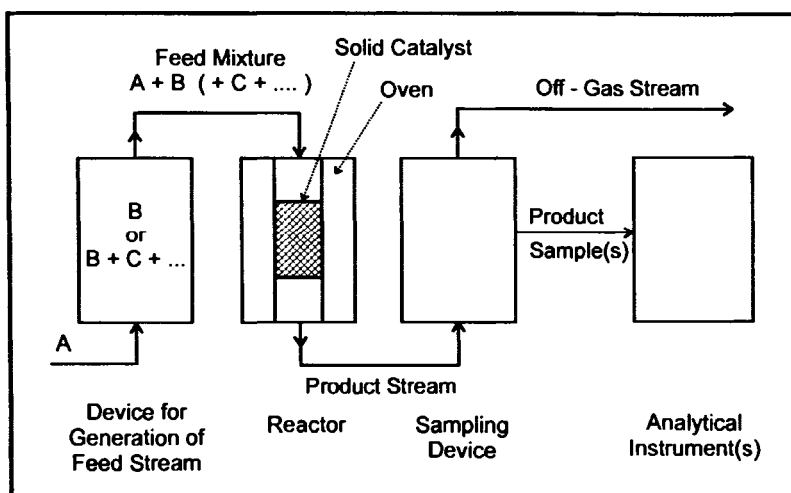


**Figure 1.** Scheme of a continuously operated flow-type unit with a fixed-bed reactor for studying a gas phase reaction on a solid catalyst (A is a carrier gas, B and C are solids or liquids at room temperature and vaporizable at elevated temperature).

tribution will focus on the peripheral building blocks, i.e., the devices for preparation of the feed mixtures to be sent to the reactor and the systems downstream of the reactor for transferring product samples into an analytical instrument. Furthermore, appropriate techniques for the elemental analysis of coke which, in many instances, deposits on the catalyst during the conversion of organic substrates, will be discussed.

## 9.2.2 Overall Equipment

The overall equipment used for catalytic studies is usually classified into (i) batch methods, (ii) semi-batch methods (e.g., a hydrogenation reaction, in which hydrogen gas bubbles continuously through a batch reactor containing the liquid substrate and the suspended solid catalyst), (iii) transient methods (including the pulse reactor), and (iv) continuous flow methods. While all these methods have their specific advantages and disadvantages [2], continuously operated flow-type units are strongly prevailing in practice. The reasons are obvious: Such units are not only well suited for measuring the kinetics of the catalytic reaction, but they also enable the experimentalist to detect readily and quantitatively whether the catalyst, while working, preserves a constant activity, deactivates (which happens frequently) or, conversely, is getting more active (which happens sometimes).

A rough scheme of a continuously operated flow-type unit for studying a gas phase reaction on a solid catalyst is depicted in Figure 1. Arbitrarily, a fixed-bed reactor [3] was chosen. In fact, fixed-bed reactors are most popular in heterogeneous catalysis, because they are easy to construct, relatively inexpensive (even if designed for high pressure), robust (since there are no

moving parts) and a downscaled image of the most frequently employed reactor type in industrial catalysis.

Ideally, the fixed-bed reactor behaves as a plug flow (or, synonymously, piston flow) reactor (PFR) with no radial gradients of partial pressures or gas velocity and with a complete absence of axial mixing. In a PFR, the reactant and product partial pressures are thus only a function of the reactor length coordinate. Its antipode is the continuous stirred tank reactor (CSTR) which also plays an important role in heterogeneous catalysis, especially in kinetic measurements. Ideally, the content of a CSTR is perfectly mixed, i.e., the partial pressures or concentrations of all reactants and products are uniform everywhere and equal to those in the effluent stream. Both the ideal PFR and the ideal CSTR behavior can be approximated to a large extent in real laboratory reactors. The description of the various reactor types developed for the study of heterogeneously catalyzed reactions is beyond the scope of this Chapter. For their pros and cons, their suitability for a rapid catalyst screening and the experimental strategies for collecting kinetic data in these reactors, reference can be made to an abundant number of valuable textbooks, monographs and review articles [2, 4–15].

By contrast, the problems associated with the ancillary building units, e.g., the proper design of devices for the generation of well defined and stationary feed streams or of good devices for product sampling (cf. Fig. 1) have received very scarce attention in the literature [16, 17]. From a critical evaluation of the pertinent literature, one is led to conclude that these problems tend to be overlooked by too many experimentalists and that unduly simple and inappropriate methods are

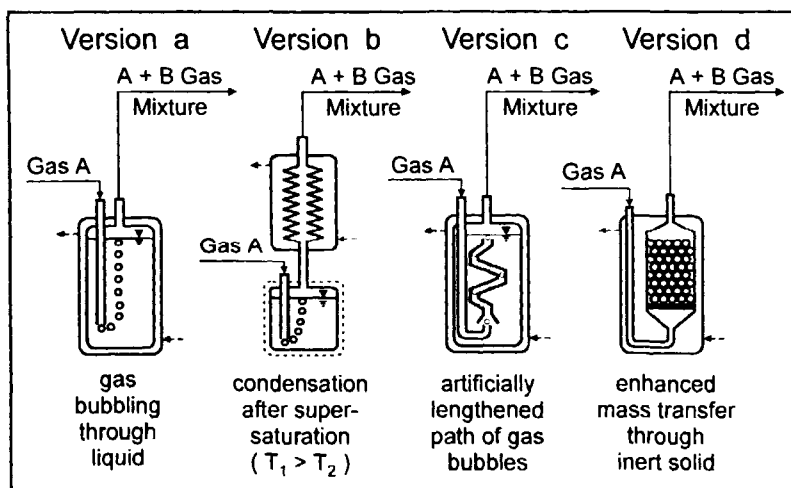


**Figure 2.** Design of saturators for the generation of gaseous feed mixtures consisting of a carrier gas A and vapors of another component B.

often employed. In the subsequent sections, selected problems encountered in the author's own group and examples for the solution of these problems will be discussed.

### 9.2.3 Generation of Feed Streams

The device for generating a gaseous feed stream consisting of vapors of one (B) or several (B + C + ...) component(s) in a permanent gas A (cf. Fig. 1) must meet a number of requirements: (i) The composition of the mixture must be strictly constant (stationarity requirement) during the whole experiment. (ii) The partial pressure(s) of the higher molecular weight component(s), i.e., B or B + C + ..., in the gas mixture to be generated should be variable independently from each other, preferentially over a wide range. (iii) The device should be reliable, durable (preferentially without moving parts) and inexpensive.

Let us first restrict to the simpler and more frequently encountered case that the feed mixture consists of vapors of a single component B in the carrier gas A. The optimum device, both at ambient and elevated pressure, will then be a saturator which contains component B in the solid or liquid state (Fig. 2). On its way through the saturator, the carrier gas A is loaded with vapors of B. Since its vapor pressure depends exponentially on the temperature, the saturator must be thoroughly thermostated. An externally thermostated water or oil bath circulating through a jacket around the saturator is often the best solution. If temperatures above ca. 200 °C are required, a saturator surrounded by a stirred bath of molten salt with an efficient temperature control can be used alternatively.

In practice, various saturator designs have been employed (Fig. 2). If the carrier gas A is simply bubbled through the liquid B (version a), it may happen that the gas/liquid mass and/or heat transfer are insufficient. On their way upwards, the gas bubbles will then be saturated incompletely with vapors of B, and the partial pressure of B in the gas mixture leaving the saturator will be ill-defined and irreproducible. To avoid such malfunctions, improved versions of saturators have been designed. For example (Fig. 2, version b), a too high saturator temperature  $T_1$  can deliberately be applied, whereupon a partial recondensation of B is enforced in a cooler held precisely at the appropriate saturation temperature  $T_2$ . Another good method (Fig. 2, version c) is to prolong the way of the gas bubbles through the liquid and, hence, the contact time between both phases artificially, and this can be achieved, for instance, by conducting the bubbles through a spiral-shaped chimney inside the saturator. Perhaps the best technical solution (Fig. 2, version d) consists of adding to liquid B inside the saturator a chemically inert solid, which may be porous or not. Normally, this brings about such a mass transfer enhancement that the vapor/liquid equilibrium is safely attained within a bed height of a few millimeters. Suitable porous solids may be impregnated with some 20 or 30 wt.% of the liquid, and the use of liquid B in such a "solidified" state is particularly advantageous in saturators of high pressure units.

It is obvious that none of the saturators sketched in Fig. 2 is appropriate, if the carrier gas A is to be loaded with vapors of more than one component (B + C + ..., cf. Fig. 1): In these semi-batch systems, the more volatile component, say B, would be enriched in the gas phase, and for simple mass balance reasons this would

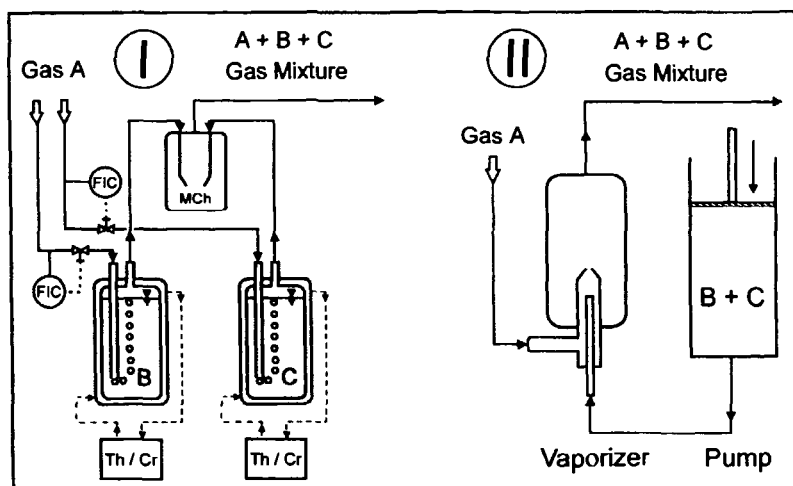


**Figure 3.** Conventional methods for the generation of gaseous feed mixtures consisting of a carrier gas A and vapors of two other components B and C (FIC: Flow indicator and controller; MCh: Mixing chamber; Th/Cr: Thermostat or cryostat).

inevitably lead to a gradual depletion of the liquid reservoir with respect to B. In other words, since the partial pressures of B, C, ... in the gas mixture depend on the mole fractions of B, C, ... in the liquid mixture inside the saturator, the stationarity requirement (*vide supra*) would be violated.

Therefore, most experimentalists employ either of the methods shown in Fig. 3. Method I provides two or more saturators in parallel (for the generation of A + B + C and A + B + C + ... mixtures, respectively), each containing one pure component. The two-component gas streams (A + B, A + C and, if applicable, A + ...) leaving these saturators are combined in a mixing chamber to give the desired multicomponent A + B + C (or A + B + C + ...) feed stream. According to our experience, method I is satisfactory for units working at atmospheric pressure. Even then it may happen that a flow adjustment through one saturator brings about undesired changes in the flow through the other one(s). With modern flow controllers, this problem can be solved, but at elevated pressures and/or with more than two saturators, the method becomes clumsy and unduly expensive, because of the high cost of these flow controllers and the increasing number of thermostats or cryostats required.

In method II, the components B, C, ... are premixed in the liquid state in exactly the same ratio as desired in the gaseous A + B + C + ... feed stream. By means of an appropriate pump, typically a pulsation-free piston displacement pump, the premixed liquid is injected continuously into a device for total vaporization, where the vapors are combined with the stream of the carrier gas A. The composition of the final A + B + C + ... gas mixture is determined by the flow rate of A, the displacement velocity of the pump and the composition of the liquid. The sophisticated pumps required (strictly

pulsation-free operation at low fluxes, typically in the order of 1 to several  $\text{cm}^3/\text{h}$ ) are nowadays commercially available, even for high-pressure units. The main shortcoming of the method, which is too often overlooked, stems from the difficulty to vaporize the relatively small liquid stream smoothly and pulsation-free, even if the vaporizer is kept at a high temperature. We tested a number of differently designed vaporizers, and the result was very disappointing: It turned out to be extremely difficult to avoid the formation of droplets at the entrance nozzle of the vaporizer. These droplets ultimately break off the nozzle and reach a hot wall where they vaporize almost spontaneously. The result is a strong and uncontrollable fluctuation of the partial pressures of B, C, ... in the gas mixture. These fluctuations are usually difficult to detect; in particular, they remain hidden if an integral, i.e., time-averaged sample of the A + B + C + ... or B + C + ... mixture is analyzed.

In view of all these obvious or hidden drawbacks of methods I and II, a multicomponent saturator has been developed for the generation of gaseous feed streams in laboratory flow-type units [18, 19]. Its salient features (cf. Fig. 4) are a vertical saturator column packed with an inert solid, typically glass balls, and a moving liquid phase (as opposed to the saturators shown in Fig. 2) which trickles downwards, while the carrier gas A is conducted countercurrently. A pump conveys the liquid B + C + ... mixture from the storage vessel via a heating line inside the thermostated jacket onto a specially designed tray at the top of the column. This tray ensures a uniform distribution of the liquid over the cross section of the column. In this countercurrent column, the vapor/liquid phase equilibrium is efficiently

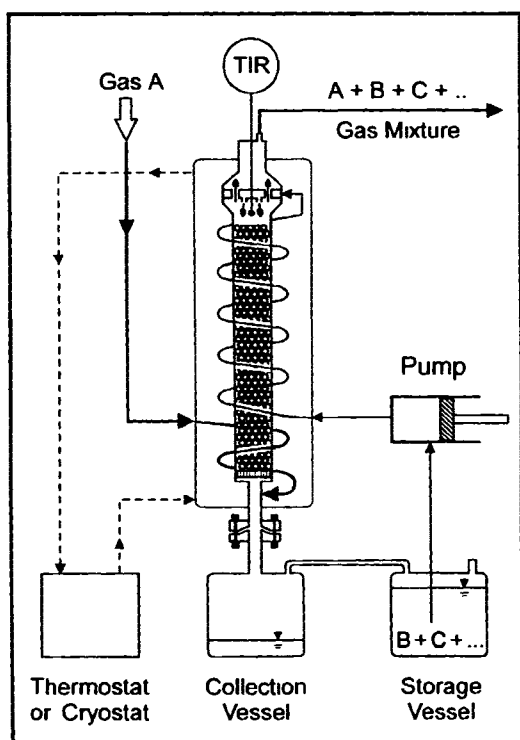


**Figure 4.** Multicomponent saturator for the generation of gaseous feed mixtures consisting of a carrier gas A and vapors of two or more other components B, C, ... (TIR: Temperature indicator and recorder).

established. Unvaporized liquid leaves the column at its bottom and accumulates in the collection vessel (this surplus liquid mixture, upon adjustment of the concentrations of its constituents, can be re-used in the storage vessel in the subsequent experiment). The gaseous  $A + B + C + \dots$  stream at the top of the column, which has a strictly stationary composition [19], is sent to the catalytic reactor.

On its way downwards, the liquid phase is of course depleted with respect to its more volatile component(s) and enriched in its heavier component(s). At the decisive locus, however, where both phases have their final contact (i.e., the top of the column), the composition of the liquid is obviously stationary. For a desired composition of the gas mixture, the appropriate values for the liquid phase composition and the saturator temperature must be found. This is best done in two successive steps, viz. by phase equilibrium calculations followed by experimental refinement of the calculated values. The multicomponent saturator showed an excellent performance, both in a unit for atmospheric pressure [18] and in a high-pressure apparatus [19, 20].

So far, the discussion of methods for generating well defined feed mixtures in flow-type units has been restricted to gaseous streams. As a rule, liquid feed streams are much easier to prepare, simply by premixing the reactants in a reservoir and conveying this mixture to the reactor by means of a pump with a pulsation-free characteristic.

## 9.2.4 Devices for Product Sampling

A standard arrangement for sampling gaseous products downstream of the reactor is shown in Fig. 5. In a needle valve (or a similar device), the reactor effluent is depressurized and the flow rate is controlled. In the vast majority of cases, the analytical instrument of the choice will be a gas chromatograph equipped with a capillary column, because such an instrument often allows a good separation of the products and, if equipped with an appropriate detector, a reliable quantitative analysis of these products. The working principle of gas chromatography, however, is inherently

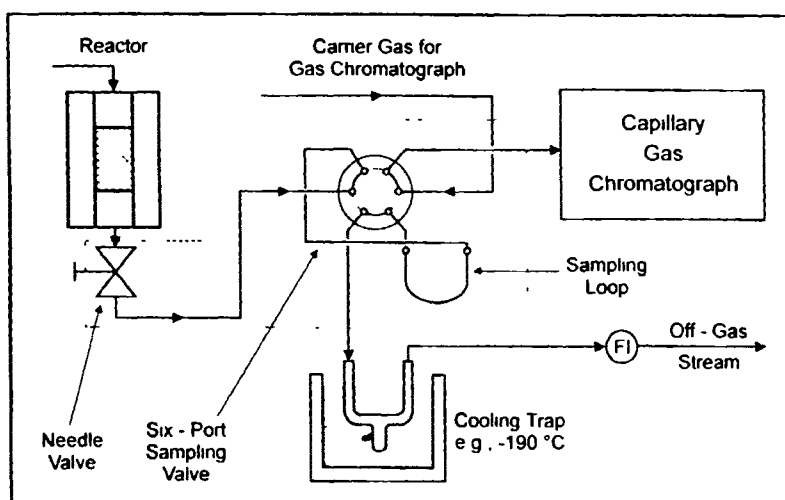


**Figure 5.** Standard equipment for sampling gaseous products in a continuously operated unit downstream of the reactor (FI: Flow indicator). The parts within the area circumscribed by the dotted line are heated to avoid condensation of vapors.

discontinuous with a time required for one analysis between ca. 1 minute and several hours, depending on the number of components to be separated and the desired resolution. To link the continuous flow-type reactor and the discontinuous analytical instrument, a kind of an interface is needed, viz. a multiport sampling valve. In its normal position (Fig. 5), it directs the reactor effluent through the sampling loop into the off-gas line, and upon actuating the valve, the content of the loop is swept into the gas chromatograph. It is obvious that the samples flushed from the loop into the gas chromatograph correspond to a well defined time-on-stream of the catalyst, hence they are *differential samples*. They can usually not be stored, so no product sample is available any more *after* the experiment. We recommend to routinely collect an additional sample by condensation of the products in a cooling trap downstream of the six-port valve. This furnishes a time-averaged, i.e., *integral product sample* which can, at least in principle, be easily stored, though it will tend to lose volatile components upon being warmed to ambient temperature. While it may therefore happen that the integral sample is not suitable for a quantitative evaluation, it is often very desirable to have such a sample stored for a while, so that additional analytical work can be done, e.g., qualitative product identification by coupled gas chromatography/mass spectrometry.

Obviously, a standard equipment as sketched in Figure 5 enables one to observe the time-on-stream behavior of the catalyst, simply by repeating the product analysis in certain intervals. This is, however, only true if the time required for product analysis is short compared to the typical time of catalyst deactivation (or, conversely, activity gain). Numerous other catalytic systems are known in which the catalyst deactivates within minutes or even seconds, while very complex product mixtures are formed, the adequate gas chromatographic analysis of which takes several hours. Examples are catalytic cracking of higher hydrocarbons [21, 22], the alkylation of isobutane with butenes on solid acids [23, 24] or the conversion of methanol to hydrocarbons on acid zeolites [25, 26]. The simultaneous occurrence of complex product mixtures and rapid catalyst deactivation requires special sampling techniques, generally referred to as differential or instantaneous sampling, and the possibility to store the samples without loss of volatile components. Various methods for instantaneous sampling have been developed. In the simplest way, storable samples can be withdrawn from the product stream by gas syringes. It is evident that this is, in many instances, an unduly simple method. It fails, in particular, if the samples contain higher molecular weight components which condense inside the syringe at ambient temperature.

The gas syringe method has been significantly improved [27, 28] by placing a heatable sampling column

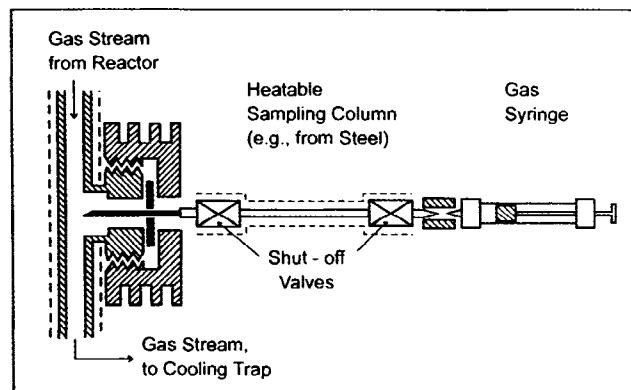
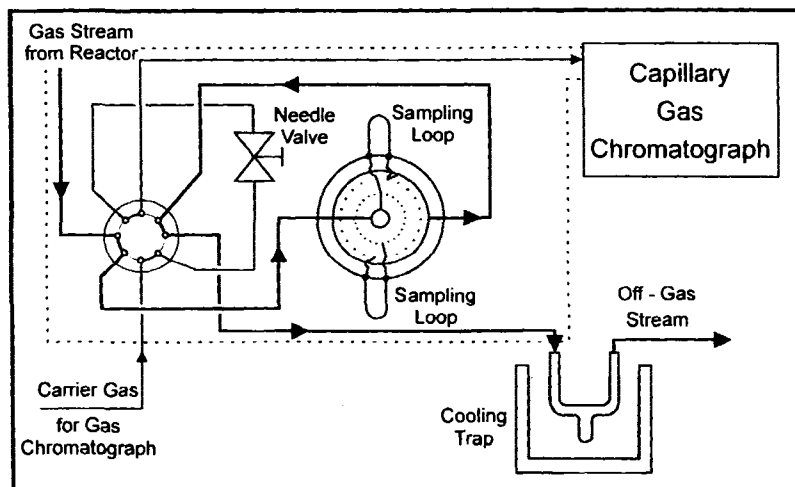


Figure 6. Instantaneous sampling and product storage with a gas syringe and heatable sampling columns, after [28].

between the syringe and its needle (Fig. 6). The sampling column consists simply of a metal (e.g., steel) tube with a shut-off valve at each end. It can be heated, e.g., by directly passing a low voltage current (ca. 2 V, 15 A) through the column. At an appropriate position downstream of the reactor, a sampling device is attached to the heated product line. The sampling device is virtually identical with an injection port of a gas chromatograph. Through its septum, the needle connected with the sampling column protrudes directly into the gaseous product stream. At the desired sampling time, both valves of the column are opened and an appropriate amount of product is sucked into the column which is then shut again. Heating is now stopped and the sample can be stored. For analysis, the column is again heated (so that all product components vaporize) and connected to the injection port of a gas chromatograph, whereupon the product sample is flushed onto the chromatographic column. More details on this technique, including the recommended construction of the shut-off valves, may be found in [28]. Though the whole technique is relatively simple and easy to handle, it has not found widespread application. For its routine application, a large number (in the order of one hundred) of sampling columns are needed.

Another technique, which is much more frequently employed, relies on commercially available multiport valves with a large number of sampling loops (an example is a valve carrying 16 sampling loops, with 16 positions and  $2 \times 16 + 2 = 34$  ports, i.e., two for each loop plus a gas entrance and a gas exit port). The simplest arrangement of such a multiport valve downstream of the catalytic reactor is shown in Fig. 7 (for the sake of simplicity, only two sampling loops are drawn). The multiport valve is assisted by an eight-port valve with two positions. The needle valve is to com-



**Figure 7.** Instantaneous sampling and product storage with a multiport valve. The parts within the area circumscribed by the dotted line are heated to avoid condensation of vapors.

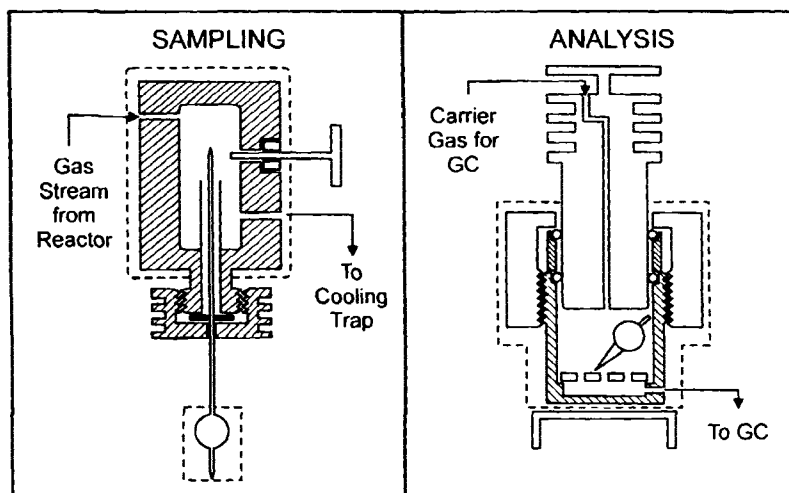


**Figure 8.** Instantaneous sampling and product storage by means of glass ampoules (GC: Gas chromatograph).

compensate for the pressure drop inside the multiport valve. During the catalytic experiment, the reactor effluent is passed along the heavy line, through the multiport valve. At the desired times-on-stream, the multiport valve is switched to its next position, whereby a product sample is captured in a loop. After the catalytic experiment, the eight-port valve is actuated, whereupon the carrier gas for the gas chromatograph passes through the multiport valve, and sample by sample can now be analyzed. Once the sampling technique with multiport valves is installed in a catalytic unit, it offers considerable comfort. However, the investment cost for the valves increases sharply, if a reasonably large storage capacity (ca. one hundred) for product samples is desired. Some experimentalists encountered difficulties with the tightness of multiport valves at the elevated temperatures required to prevent condensation of vapors inside the sampling loops.

Still another method for instantaneous sampling has been developed which allows to store a virtually unlimited number of product samples, because extremely cheap, homemade glass ampoules are used for sampling. The glass ampoule technique was first described by Pichler and Gärtner [29] and later refined by Schulz and coworkers [22, 30, 31]. Ample experience with the technique exists in our group as well [24, 32, 33]. The principle is shown in Fig. 8. The gaseous effluent from the reactor is passed through a heated sampling compartment (Fig. 8, left). A long capillary connected with an evacuated glass ampoule protrudes into the compartment through a sealing system which resembles the injection port of a gas chromatograph. At the desired time-on-stream, the tip of the capillary is broken, e.g., by actuating a piston mounted at an appropriate position of the compartment, whereupon the ampoule fills up instantaneously with the product. The ampoule with

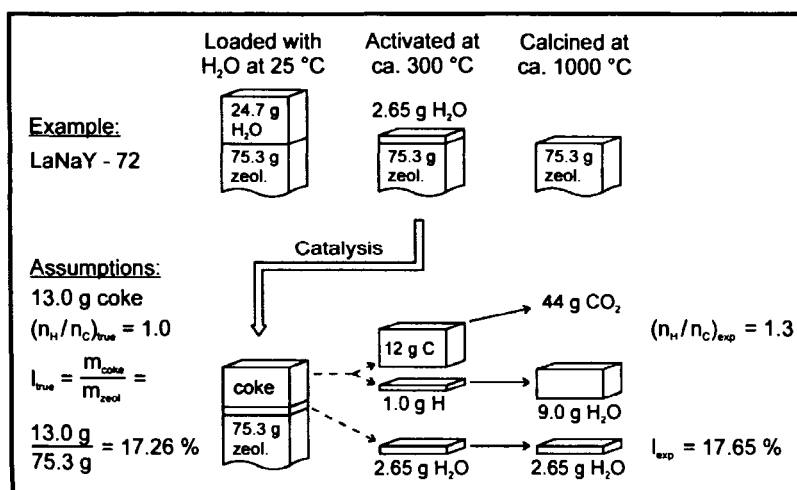


Figure 9. Water on an inorganic catalyst falsifies the elemental analysis of carbonaceous deposits.

its capillary is then withdrawn from the compartment, the products inside the ampoule are frozen at liquid nitrogen temperature and the ampoule is quickly sealed. The sample is now captured hermetically inside the ampoule and can be stored until its analysis. A new sampling cycle can then be initiated by insertion of the capillary of another evacuated glass ampoule, and a skilled experimentalist is able to repeat the cycles in very short intervals of ca. 10 seconds, if necessary. For analysis (Fig. 8, right), the glass ampoule is simply destroyed inside a heated device connected with a capillary gas chromatograph, whereby the product sample is liberated and swept to the chromatographic column.

### 9.2.5 Elemental Analysis of Carbonaceous Deposits on Catalysts

The formation of carbonaceous deposits or, synonymously, coke is an almost ubiquitous phenomenon in heterogeneous catalysis, and such deposits are in many instances responsible for catalyst deactivation [34]. It is often desirable to collect some information on the chemical composition and structure of these deposits [35]. The techniques for characterizing coke on solid catalysts may be broadly classified into (i) an elemental analysis, mostly for carbon and hydrogen, (ii) an analysis for individual components in the coke which is usually achieved by separation of the carbonaceous deposits from the inorganic catalyst, e.g., by extraction, followed by coupled gas chromatography/mass spectrometry, and (iii) spectroscopic methods, especially <sup>13</sup>C NMR, IR and UV spectroscopy [35, 36]. In the vast majority of experiments aiming at catalyst testing, one cannot afford to apply *all* these techniques, but instead, one has to be selective and restrict oneself to a single routine method.

The method of the choice is most often an elemental analysis for C and H. If carried out properly and with certain precautions, it furnishes valuable information not only on the overall loading of the catalyst with coke, but also on the molar ratio  $n_H/n_C$  in the coke. This, in turn, allows a rough, but nevertheless safe estimate on the chemical structure of the deposits. The limiting cases are (i) aliphatic deposits (sometimes referred to as “white” or “soft” or “low temperature” coke) with a structure of a polyolefin running through the catalyst pore system and a  $n_H/n_C$  ratio close to 2, and (ii) condensed aromatic deposits (referred to as “black” or “hard” or “high temperature” coke) which is strongly deficient in hydrogen ( $n_H/n_C$  around 0.5 or even lower).

For an elemental analysis, the carbonaceous deposits are combusted in air or oxygen, and the amount of CO<sub>2</sub> and H<sub>2</sub>O formed is quantitatively determined, generally by gravimetry after absorption in ascarite and magnesium perchlorate, respectively. During this seemingly trivial procedure, problems may arise if the catalyst contains water prior to the combustion of the coke. This is exemplified in Figure 9 for a type Y zeolite catalyst whose original sodium cations have been exchanged to a large extent (72 equivalent %) by trivalent lanthanum cations. It is well known [37] that Brønsted acid sites are generated in such LaNaY zeolites upon heating. After the ion exchange, the zeolite pores are filled with water, which corresponds to  $m_{H_2O}/m_{Zeolite} \approx 24.7 \text{ g}/75.3 \text{ g}$ . Making the reasonable assumption that activating this material at 300 °C results in a desorption of most of the water except for two (non-acidic) OH groups per lanthanum ion and two (acidic) protons, the acidic zeolite which is ready for catalysis has a water content of  $m_{H_2O}/m_{Zeolite} \approx$



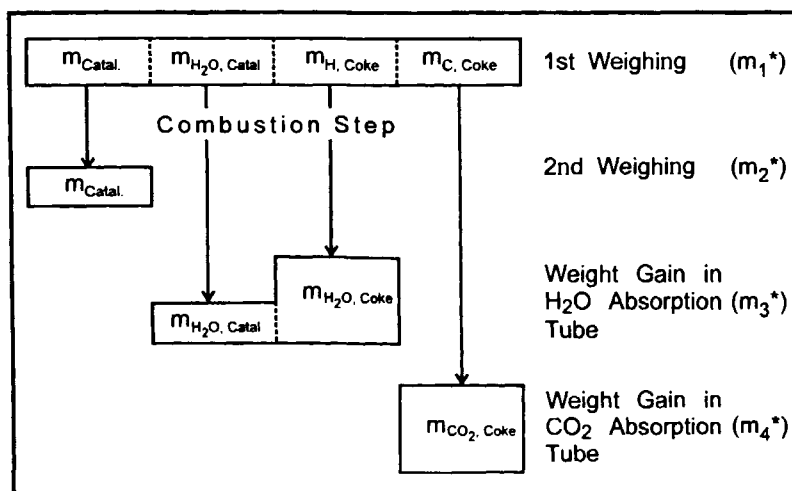


**Figure 10.** Illustration of the method for the determination of the ratio  $n_{\text{H}}/n_{\text{C}}$  in the coke deposited on a used catalyst by back-weighing of the inorganic matter after the combustion step (adapted from [16, 36]).

2.65 g/75.3 g. If one had calcined this material at a much higher temperature, complete dehydration (and removal of Brønsted acidity) would have taken place, leaving nothing behind than 75.3 g inorganic matter.

We further assume that the catalyst activated at 300 °C is used in a hydrocarbon reaction which produces coke as a byproduct. Reasonable figures are a true coke loading  $l_{\text{true}} = m_{\text{Coke}}/m_{\text{Zeolite}} \approx 13.0 \text{ g}/75.3 \text{ g} = 17.26\%$  and a true ratio  $n_{\text{H}}/n_{\text{C}} = 1.0$ . In other words, the catalyst consists at this point of 75.3 g inorganic matter, 2.65 g water and coke composed of 12.0 g carbon and 1.0 g hydrogen. Upon combustion, the coke transforms into 44 g CO<sub>2</sub> and 9.0 g H<sub>2</sub>O. Significantly more water, viz. 9.0 g + 2.65 g = 11.65 g, is, however, detected. The experimental values are, hence, a coke loading  $l_{\text{exp.}} = 17.65\%$  (instead of  $l_{\text{true}} = 17.26\%$ ) and a ratio  $(n_{\text{H}}/n_{\text{C}})_{\text{exp.}} = 1.3$  (instead of  $(n_{\text{H}}/n_{\text{C}})_{\text{true}} = 1.0$ ). It is evident from these figures that the water present initially mainly falsifies the ratio  $n_{\text{H}}/n_{\text{C}}$ , whereas the coke loading  $l$  is only little affected. Indeed, a critical evaluation of the pertinent literature suggests that unrealistically high hydrogen contents of carbonaceous deposits have often been reported. To solve the problem, at least three different procedures have been proposed. They all have in common that, in addition to the mass of the coked catalyst with some water (i.e., before the combustion step), the mass of water absorbed by magnesium perchlorate and the mass of carbon dioxide absorbed by ascarite, an additional quantity is measured.

In the experimentally simplest approach, this additional quantity is the mass of the inorganic matter ( $m_{\text{Catal.}}$ ) after the combustion step, carried out at a sufficiently high temperature in the vicinity of 1000 °C to ascertain that all coke components and all structural water have been completely removed. In Fig. 10, which is adapted from references [16] and [36], this mass is

denoted  $m_2^*$ . It is evident from Fig. 10 that the mass ( $m_1^*$ ) determined in the first weighing, i.e., prior to the combustion step, is

$$m_1^* = m_{\text{Catal.}} + m_{\text{H}_2\text{O, Catal.}} + m_{\text{H, Coke}} + m_{\text{C, Coke}}.$$

From the weight gain in the CO<sub>2</sub> absorption tube ( $m_4^* = m_{\text{CO}_2, \text{Coke}}$ ), the mass of carbon in the coke is readily obtained ( $m_{\text{C, Coke}} = \frac{12.0}{44.0} m_4^*$ ). Subtracting the known masses  $m_{\text{Catal.}}$  and  $m_{\text{C, Coke}}$  from  $m_1^*$  gives the mass of hydrogen in the coke ( $m_{\text{H, Coke}}$ ) plus the mass of water on the catalyst. This quantity ( $m_{\text{H}_2\text{O, Catal.}} + m_{\text{H, Coke}}$ ) is now compared with the weight gain in the H<sub>2</sub>O absorption tube ( $m_3^* = m_{\text{H}_2\text{O, Catal.}} + m_{\text{H}_2\text{O, Coke}}$ ). From the difference ( $m_{\text{H}_2\text{O, Catal.}} + m_{\text{H}_2\text{O, Coke}}$ ) ( $m_{\text{H}_2\text{O, Catal.}} + m_{\text{H, Coke}}$ ) and the stoichiometry of hydrogen combustion ( $m_{\text{H}_2\text{O, Coke}} = \frac{9.0}{1.0} m_{\text{H, Coke}}$ ), the desired quantity  $m_{\text{H, Coke}}$  can be calculated on the basis of mass balances. This is best illustrated by considering the two limiting cases: If the coked catalyst does not contain any water at all ( $m_{\text{H}_2\text{O, Catal.}} = 0$ ), then

$$m_3^* = 9.0 \cdot \left( m_1^* - m_2^* - \frac{12.0}{44.0} m_4^* \right).$$

If, conversely, the coke on the catalyst consists of pure graphite, i.e., does not contain any hydrogen at all ( $m_{\text{H, Coke}} = 0$ ), then

$$m_3^* = \left( m_1^* - m_2^* - \frac{12.0}{44.0} m_4^* \right).$$

Details of the mass balance may be found in reference [36].

In a completely different approach by Enterman and van Leuven [38], the oxygen consumed during the

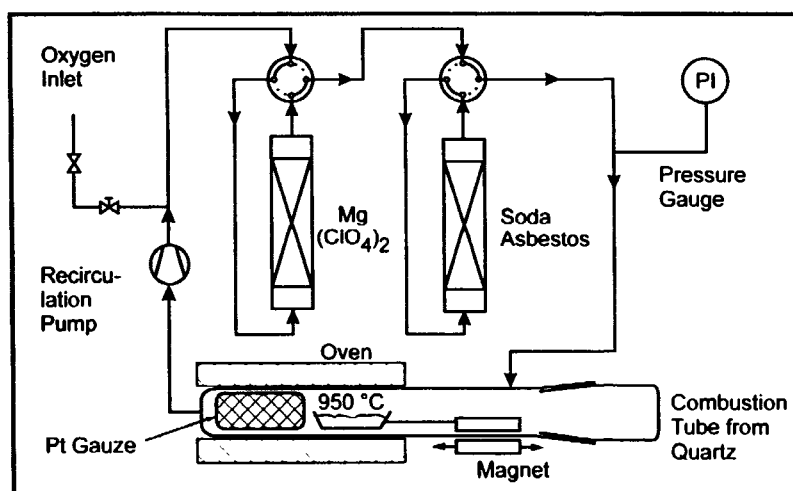


Figure 11. Scheme of the recirculation apparatus for the determination of oxygen consumed during the combustion of coke on an inorganic catalyst, after Enterman and van Leuven [38].

combustion of the coke on the catalyst is determined. This can, of course, not be achieved in the simple tubular combustion furnaces, where a large excess of oxygen flows over the catalyst, but requires a recirculation apparatus in which the total amount of oxygen initially present is in the same order of magnitude as the amount of oxygen consumed. The scheme of such a unit is shown in Fig. 11. Oxygen is first admitted to the system and purified in the two absorption tubes. From the calibrated volume of the apparatus and the pressure, the amount of oxygen introduced can be calculated. The platinum gauze promotes a complete combustion to  $\text{CO}_2$ , i.e., no CO is formed. The  $\text{CO}_2$  trap filled, e.g., with soda asbestos, is first bypassed, and the coked catalyst is displaced magnetically into the hot zone of the oven. When the coke is completely burned, the pressure is noted. Subsequently, the  $\text{CO}_2$  trap is opened. The final pressure is again noted. From the two pressure drops the amount of hydrogen and carbon, respectively, in the coke, i.e.,  $m_{\text{H,Coke}}$  and  $m_{\text{C,Coke}}$  in Fig. 10, can be directly calculated, and the correct ratio  $n_{\text{H}}/n_{\text{C}}$  is thus directly obtained. For the determination of the coke loading of the catalyst, the system is best calibrated by burning a precisely known mass of a pure organic compound, such as pyrene.

A third experimental technique, which was first described by Karge et al. [36, 39], is based on combined thermogravimetry and gas chromatography (TGA/GC). The coked catalyst is placed into a thermobalance. In a first run, desorbable components of the coke and all water adsorbed on the catalyst are removed from the solid catalyst in a purge of dried nitrogen at an appropriate temperature. The desorbed hydrocarbons and water are quantitatively condensed in a cooling trap, e.g., at liquid nitrogen temperature. When this desorption is completed, the trap is quickly heated,

whereupon the trapped compounds vaporize. They are purged in a gas chromatograph for analysis. Subsequently, the coke which remained on the water-free catalyst is burned, the only products being  $\text{H}_2\text{O}$  and  $\text{CO}_2$  (a CO oxidation catalyst such as Pt or CuO makes sure that a complete combustion takes place). These are again trapped quantitatively and later analyzed by gas chromatography. The weight losses measured in the thermobalance during the desorption and the combustion step are compared with the mass of the respective samples evaluated from the gas chromatographic analyses. The method gave reliable coke loadings and  $n_{\text{H}}/n_{\text{C}}$  ratios in the coke [36, 39].

Karge's combined TGA/GC method can be applied to catalysts which were used (and coked) before in a separate catalytic unit. It can, of course, be employed as well to catalysts on which the catalytic reaction was studied before in the same thermobalance (even though, in many instances, such microbalances are not very suitable as catalytic reactors, because part of the feed gas stream tends to bypass the sample holder or basket, on/in which the solid catalyst rests). If the latter is done, the mass of coke deposited during the catalytic reaction can be monitored in-situ via the weight gain. It has been shown [36] that such a strategy enables the experimentalist to perform systematic studies on the amount of coke formed and its  $n_{\text{H}}/n_{\text{C}}$  ratio in dependence of time-on-stream and reaction temperature.

The disadvantages of conventional microbalances when used as catalytic reactors (*vide supra*) can apparently be overcome with a recently developed oscillating microbalance reactor [40]. It provides a fixed-bed of catalyst particles through which the complete gas stream is forced to flow. Changes in the mass of the catalyst, which is located at the tip of an oscillating

tapered quartz element, are detected as a change in its vibrational frequency. A mechanical drive system makes the tapered element oscillate at its natural frequency, and optics record the data continuously. The system has been reported [40] to safely detect mass changes in the order of a few micrograms. It remains to be seen to what extent this novel catalytic microbalance reactor will contribute to a better understanding of coke formation in heterogeneous catalysis

### 9.2.6 Concluding Remarks

Testing the performance of solid catalysts in laboratory units offers numerous pitfalls, of which the experimentalist must be aware. Some examples for inappropriate designs, which may give rise to severe malfunctions, were discussed in this Chapter. This discussion was selective rather than exhaustive and focussed on three areas, viz. the generation of feed gas streams, the methods for product sampling and the elemental analysis of carbonaceous deposits. Other areas, which could have been treated as well, were omitted because they are more intimately related to the catalytic reactor, and are hence the subject of other Chapters of this Handbook. Examples are the various methods for calculating the conversion, selectivities and other kinetic key parameters from the raw data acquired in an analytical instrument, e.g., in a gas chromatograph, or the pros and cons of using an internal standard in the feed stream.

Leading research groups in the field of heterogeneous catalysis devote much time to the identification and elimination of weak parts in their equipment. Certain catalytic reactions, e.g., those with a complex product slate and simultaneously a rapid catalyst deactivation, cannot be investigated at all without a sophisticated and tailored equipment. For the decades ahead, we expect a rapid progress in materials science and a strong impact of novel materials on heterogeneous catalysis. The novel catalytic materials to come deserve to be tested in units which are free from malfunctions and shortcomings.

### 9.2.7 Acknowledgements

Continuous support of the author's research by the German Science Foundation (Deutsche Forschungsgemeinschaft), Fonds der Chemischen Industrie and Max-Buchner-Forschungstiftung is gratefully acknowledged

### References

- [1] F Kapteijn, J A Moulijn, This Handbook, Section A 9 1
- [2] J R Anderson, K C Pratt, *Introduction to Characterization and Testing of Catalysts*, Academic Press, New York, 1985, pp 257-352
- [3] G Eigenberger, This Handbook, Section A 10 1
- [4] K C Pratt, in *Catalysis - Science and Technology*, Vol 8, J R Anderson and M Boudart (Eds), Springer-Verlag, Berlin, 1987, pp 173-226
- [5] O Levenspiel, *Chemical Reaction Engineering*, 2nd Edition, John Wiley & Sons, New York, 1972, pp 460-536
- [6] J M Smith, *Chemical Engineering Kinetics*, 3rd Edition, McGraw Hill Book Co, Singapore, 1981, pp 359-635
- [7] L K Doraiswamy, D G Tajbl, *Catal Rev - Sci Eng* 1974, 10, 177-219
- [8] V W Weekman, Jr, *AIChE J* 1974, 20, 833-840
- [9] J M Berty, *Chem Eng Progr* 1974, 70, No 5, 78-84
- [10] C Gelain, *Chimie et Industrie - Génie Chimique* 1969, 102, 984-997
- [11] A M R Difford, M S Spencer, in *Standardization of Catalyst Test Methods*, S W Weller (Ed), AIChE Symp Ser 143, Vol 70, 1974, pp 42-48
- [12] P A. Ramachandran, R V Chaudhari, *Chem Eng* 1980, 87, No 24, 74-85
- [13] M Herskowitz, J M Smith, *AIChE J* 1983, 29, 1-18
- [14] F Kapteijn, J A Moulijn, This Handbook, Section A 6 1
- [15] G Emig, R Dittmeyer, This Handbook, Section A 6 2
- [16] J Weitkamp, in *Innovation in Zeolite Materials Science*, P J Grobet, W J Mortier, E F Vansant, G Schulz-Ekloff (Eds) Studies in Surface Science and Catalysis, Vol 37, Elsevier Amsterdam, 1988, pp 515-534
- [17] P A Jacobs, J A Martens, in *Introduction to Zeolite Science and Practice*, H van Bekkum, E M Flanigen, J C Jansen (Eds), Studies in Surface Science and Catalysis Vol 58, Elsevier, Amsterdam, 1991, pp 445-496
- [18] J Weitkamp, H Dauns, *Chem -Ing -Tech* 1984, 56, 929-930
- [19] J Weitkamp, H Dauns, *Appl Catal* 1988, 38, 167-177
- [20] H Dauns, S Ernst, J Weitkamp, in *New Developments in Zeolite Science and Technology*, Proc 7th Intern Zeolite Conf, Y Murakami, A Iijima, J W Ward (Eds), Studies in Surface Science and Catalysis, Vol 28, Kodansha, Tokyo, and Elsevier, Amsterdam, 1986, pp 787-794
- [21] R von Ballmoos, D H Harris, J S Magee, This Handbook, Section B 3 10
- [22] H Schulz, A Geertsema, *Erdol, Kohle - Erdgas - Petrochem* 1977, 30, 313-321
- [23] J Weitkamp, Y Traa, This Handbook, Section B 3 14
- [24] J Weitkamp, in *Catalysis by Zeolites*, B Imelik et al (Eds), Studies in Surface Science and Catalysis, Vol 5, Elsevier, Amsterdam, 1980, pp 65-75
- [25] C D Chang, This Handbook, Section B 3 7
- [26] H Schulz, W Bohringer, W Baumgartner, Z Siwei, in *New Developments in Zeolite Science and Technology*, Proc 7th Intern Zeolite Conf, Y Murakami, A Iijima, J W Ward (Eds), Studies in Surface Science and Catalysis, Vol 28, Kodansha, Tokyo, and Elsevier, Amsterdam, 1986, pp 915-922
- [27] D Rodewald, J Lorenz, H G Struppe, DDR Patent WP 123 124, 1976
- [28] W Leinitz, in *Handbuch der Gaschromatographie*, 3rd Edition, E Leibnitz, H G Struppe (Eds), Akademische Verlagsgesellschaft Geest & Portig, Leipzig, 1984, pp 153-154
- [29] H Pichler, R Gartner, *Brennstoff-Chem* 1962, 43, 336-340
- [30] H Schulz, A Geertsema, in *Proc 5th Intern Conf Zeolites* L V C Rees (Ed), Heyden, London, 1980, pp 874-882
- [31] H Schulz, *Erdol, Kohle - Erdgas - Petrochem* 1983, 36, 279-280
- [32] J Weitkamp, in *Proc 5th Intern Conf Zeolites*, L V C Rees (Ed), Heyden, London, 1980, pp 858-865
- [33] S Unverricht, S Ernst, J Weitkamp, in *Zeolites and Related Microporous Materials State of the Art 1994*, J Weitkamp H G Karge, H Pfeifer, W Holderich (Eds), Part C, Studies in Surface Science and Catalysis, Vol 84, Elsevier Amsterdam, 1994, pp 1693-1700

- [34] D. L. Trimm, This Handbook, Section A.7.  
 [35] M. Guisnet, This Handbook, Section A.3.2.1.2.  
 [36] H. G. Karge, in *Introduction to Zeolite Science and Practice*, H. van Bekkum, E. M. Flanigen, J. C. Jansen (Eds.), Studies in Surface Science and Catalysis, Vol. 58, Elsevier, Amsterdam, 1991, pp. 531–570.  
 [37] P. A. Jacobs, *Carboniogenic Activity of Zeolites*, Elsevier, Amsterdam, 1977, pp. 45–62.  
 [38] W. Enterman, H. C. E. van Leuven, *Anal. Chem.* 1972, 44, 589–590.  
 [39] H. Darmstadt, H. G. Karge, M. Laniecki, R. Amberg, *Chem.-Ing.-Tech.* 1991, 63, 742–744.  
 [40] D. Chen, A. Grønvoold, H. P. Rebo, K. Moljord, A. Holmen, *Appl. Catal. A: General* 1996, 137, L1–L8.

## 9.3 Catalytic Membrane Reactors

J.-A. DALMON

### 9.3.1 Introduction

Catalytic membrane reactors (CMRs) are reactors which couple, in the same unit, a conversion effect (catalyst) and a separation effect (membrane). These reactors, besides the obvious interest of concentrating two classical steps of chemical processes in the same unit, have already shown various potential benefits for a range of reactions, and the concept of CMRs is a matter of continuous investigation for a large number of applications.

The purpose of this article is not to provide an exhaustive review of CMRs, as a number of papers have already been published in this area [1–9]. Rather, its goal is to describe the different types of CMRs and their potential applications. Some relevant references which divulge further detail are also given. Furthermore, the present limitations of CMRs and the areas which require further work are described.

A glossary defining some specific terms is placed at the end of the chapter.

### 9.3.2 Features of Catalytic Membrane Reactors

#### 9.3.2.1 Development of CMRs

At the end of the 1960s, the first papers appeared pointing out the appeal of coupling, in the same reactor, a permselective membrane and a catalyst for equilibrium-restricted reactions [10–12]. The selective removal of a reaction product through the membrane will shift the equilibrium, leading to higher conversions when compared to conventional (nonmembrane) reactors. Hydrocarbon dehydrogenation reactions were

first studied, due to the rather easy separation of the hydrogen produced during the reaction. Since that period, a lot of research has been done concerning this application of CMRs [1–9] (Section A9.3.3.1).

In addition to the shift of equilibria, CMRs have been proposed which enable improved control of the selectivity of some catalytic reactions. For example, the controlled introduction of a reactant by selective or preferential permeation may limit further reactions of a targeted product when successive reactions exist (Section A9.3.3.2).

CMRs have also been used to improve catalytic processes by enhancing contact between reactants and catalyst. The membrane acts here as an active contactor (Section A9.3.3.3).

#### 9.3.2.2 Membranes for CMR Applications

Due to the generally severe conditions of heterogeneous catalysis (such as reaction temperature, activation or regeneration steps of the active phase, chemical nature of some reactants) most applications of CMRs use inorganic membranes. Indeed, organic (polymeric) membranes, although often presenting very good separative properties, generally cannot withstand temperatures above 200 °C, which limits their use in catalytic processes.

Inorganic membranes can be either dense (nonporous) or porous, made from metals or oxides, and they can either be uniform (only one component) or composite.

Transport in dense membranes occurs via dissolution–diffusion processes. As the dissolution is specific for a given molecule, dense membranes are highly permselective. However, this transport is generally slow, and this could be a limitation for the future application in CMRs.

Transport in porous membranes occurs via diffusion of gaseous molecules within the porous framework; this transport may involve different mechanisms (Section A9.3.2.4) which are more or less dependent on the nature of the gaseous molecules, and hence more or less efficient for the separation of a gas mixture. Porous membranes are therefore generally less permselective when compared to dense ones; however, their permeability is higher (a conventional mesoporous  $\gamma$ -Al<sub>2</sub>O<sub>3</sub> membrane has a permeability for hydrogen which is 10 to 100 times higher than a conventional Pd dense membrane. More detailed permeability data can be found in Ref. 9).

The first membrane reactor studies made use of dense metallic membranes, but due to certain limitations of these dense materials (see below) and due to the rapid progress in the development of (micro)porous

ceramic membranes, porous materials are now playing an important role in CMRs studies.

Different membrane shapes are used, such as plates, foils, spirals, hollow fibers, tubes, and even monolithic multichannel elements have been mentioned in the context of membrane reactors. In the following section, a general survey will be given indicating the main characteristics of the different types of inorganic membranes used in CMRs. More details can be found elsewhere [13–15].

## A Dense Membranes

### a Dense Metallic Membranes

Dense metallic membranes generally consist of thin plates of metals. Palladium is the most widely used metal, due to its specific selectivity for  $H_2$  permeation via hydride formation; however, pure Pd membranes suffer from ageing phenomena leading to embrittlement, due to structural changes during hydride formation [1]. Palladium alloys (PdAg, PdRu) are much more stable and offer some advantages from the viewpoints of permeability and catalysis [5]. These Pd-based membranes, due to their thickness (several tens of  $\mu\text{m}$ ), generally do not allow permeation fluxes high enough for CMR applications; moreover, they are expensive and sensitive to poisoning [9]. However, dense membranes have been used and scaled up to pilot-plant size by Gryaznov [5], one of the pioneers in the field of CMRs.

Recently, attempts have been made to use the unique permselectivity of Pd for  $H_2$ , and to overcome the problem of the low permeabilities of conventional palladium foils by depositing Pd on a porous inorganic support [16, 17]. If the amount of deposited Pd is well controlled, one can expect a thin Pd layer with high selectivity and permeability towards  $H_2$ .

Metals such as Zr and Nb have also been proposed for  $H_2$  permselective dense membranes [1]. Dense silver membranes have been used for selective oxygen permeation [18].

### b Dense Oxide Membranes

Dense oxide membranes are generally solid electrolytes with ionic conductivity, such as  $ZrO_2$ ,  $CeO_2$ , or  $ThO_2$  which are permeable to  $O_2$  [7]. The driving force for the transfer can be either a partial pressure gradient or an electrical potential difference across the membrane. The permeability is, however, low, and very high temperatures ( $>600^\circ\text{C}$ ) are needed to achieve noticeable fluxes, which could limit their use in CMR applications. Additives (Ca, Y) are frequently used to ensure integrity of the membrane at these high temperatures. Fewer studies deal with dense oxide membranes for the selective transport of  $H_2$  or other species [7].

Some materials which allow molecular transport to occur are often classified as dense (or quasidense)

materials. However, it is generally admitted that transport in these materials occurs via the voids of the matrix [9], and hence it is an open question as to whether these materials are ultramicroporous or dense. High permselectivities for hydrogen have been obtained with silica deposited on Vycor glass [19], or on mesoporous oxide layers [20, 21].

## B Porous Membranes

Most porous membranes used in CMRs are made from oxide materials, although carbon membranes have also been used [1, 14, 22]. However, although they possess very good separative properties, they have received less attention in CMR applications, probably due to their limited resistance to oxidative atmospheres. Vycor glass membranes also have certain drawbacks (brittleness, lack of high-temperature resistance) [9] for use in CMRs. Porous membranes in CMRs are, most often, made from ceramic materials or, more recently, from zeolites.

### a Ceramic Membranes

Ceramic membranes were first developed in the 1940s for uranium isotope enrichment processes. Important progress has been made since that time, mainly due to the improved knowledge of the physicochemical properties of the membrane precursors. Most CMR studies concern alumina membranes; other oxides such as silica, titania, or zirconia are much less frequently mentioned.

Ceramic membranes are usually asymmetrical systems, made of several layers of material with progressively decreasing pore size. The top layer with the smallest pore size is the separative layer, which controls separation. Figure 1 represents a commercial SCT tubular membrane with a thin  $\gamma\text{-Al}_2\text{O}_3$  top layer deposited on a support made from several  $\alpha\text{-Al}_2\text{O}_3$  layers. The separative performance of the membrane is, as-

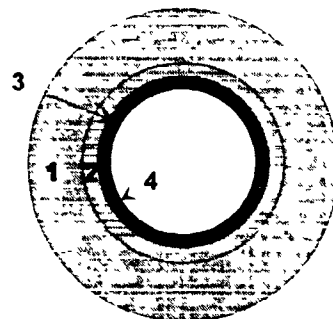


**Figure 1.** Cross-section of a tubular-shaped commercial membrane, SCT Membralox T1-70 45 Å [14]. Layers 1–3 are made of  $\alpha\text{-Al}_2\text{O}_3$  and have thicknesses of 1500, 40, and 20  $\mu\text{m}$ , respectively, and average pore sizes of 12, 0.9, and 0.2  $\mu\text{m}$ . Layer 4 is made of  $\gamma\text{-Al}_2\text{O}_3$  and has a thickness of 3–4  $\mu\text{m}$  and an average pore size of 4.5 nm

suming the absence of defects in the top layer, related to the mean value of the pore size and its distribution, the porosity and the thickness of the top layer.

Different ways of preparing high performance porous ceramic membranes have been developed [13, 14], but most of the membranes used in CMRs are obtained via sol-gel processes [13–15, 23–25].

The properties of the membranes prepared by sol-gel processes are crucially dependent on the control of the characteristics of the particles contained in the sol. The homogeneity of the particle size in the sol determines the pore size distribution of the membrane.

Sols are obtained via either colloidal or polymeric routes. In the first method, colloids are formed and stabilized by adding peptizing agents (acidic or basic electrolytes) to metal hydroxides, and the gel is obtained by evaporating the solvent. In the second (polymeric) method, alkoxides are used as starting materials and hydrolysis and condensation reactions control the size of the resulting clusters (temperature and pH are the critical parameters). Additives such as surfactants may also play an important role in the sol characteristics by controlling the hydrolysis step of the alkoxides [25].

The sol (with adjusted rheological properties) is then added to a porous support by a wash-coating (or slip-casting) procedure. During this step, the capillary forces cause the solvent to flow into the porous framework of the support, and the particles are retained at the surface of the support leading to a supported layer. Controlled drying and calcination steps allow evacuation of the organic components and stabilize the layer; these steps are important because they may induce stress in the top layer, resulting in cracks and defects. Specific additives are added to the precursor to control these phenomena.

As already mentioned, sol-gel membranes are often used in CMRs. These materials can, however, present some limitations due either to their pore size distribution which may limit the selectivity of the separation, or to their low thermal stability which may lead to a change in transport properties when high temperatures are employed.

Membranes showing intrinsic catalytic properties have also been prepared using sol-gel routes or other ceramic methods [26].

#### *b Zeolite Membranes*

A zeolite membrane is a membrane in which the transfer is controlled by the porous structure of the zeolite. Compared to sol-gel membranes, zeolite membranes can present some advantages for CMR applications. The most useful feature is that the pores of zeolites are in the ultramicroporous range and have a very narrow size distribution (in this case pores are linked to the *structure* and not to the *texture* as in sol gel membranes). These characteristics of zeolite

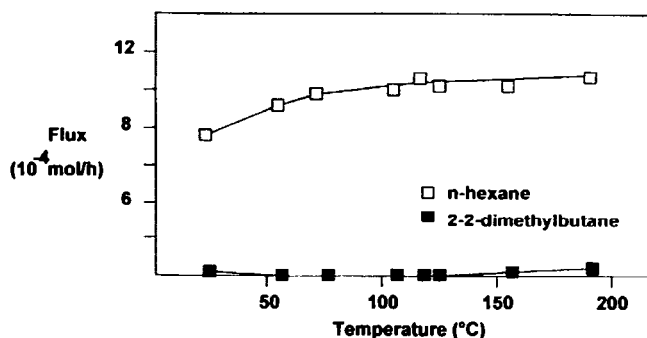


**Figure 2.** Zeolite silicalite membrane [34]. Separation behavior of a *n*-hexane:2-2-dimethylbutane mixture (1:1) as a function of temperature.

membranes should allow high selectivity in separation processes (see below). One can also expect enhanced thermal stability for these materials (this should be related to the structural stability of the zeolite, unless cracks in the grain boundaries appear). Another potential usefulness of these membranes in CMRs is related to the intrinsic catalytic properties of zeolites and the possibility of modifying them by exchange reactions.

Different ways have been proposed to prepare zeolite membranes. A layer of a zeolite structure can be synthesized on a porous alumina or Vycor glass support [27, 28]. Another way is to allow zeolite crystals to grow on a support and then to plug the intercrystalline pores with a dense matrix [29]. However, these two ways often lead to defects which strongly decrease the performance of the resulting membrane. A different approach consists in the direct synthesis of a thin (but fragile) unsupported monolithic zeolite membrane [30]. Recent papers have reported on the preparation of zeolite composite membranes by hydrothermal synthesis of a zeolite structure in (or on) a porous substrate [31–34]. These membranes can act as molecular sieve separators (Fig. 2), suggesting that defect-free materials can be prepared in this way. The control of the thickness of the separative layer seems to be the key for the future of zeolite membranes.

#### 9.3.2.3 Characterization of Porous Membranes

The porous properties of mesoporous layers can be characterized conveniently using classical methods based on the N<sub>2</sub> adsorption-desorption isotherm at 77 K. However, it is important to use additional techniques based on transmembrane transport properties in order to characterize the passing-through pores. Moreover, these dynamic methods will easily detect the

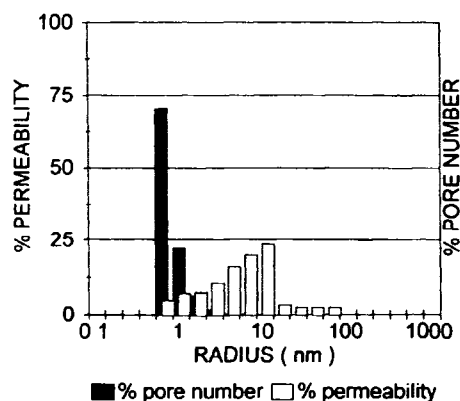


**Figure 3.** Permeability and pore number distributions versus pore size. Liquid-liquid displacement porosimetry measurements [35].

presence of defects and also stress the important contribution to the total flux of a limited number of large (less separative) pores when the membrane has a broad pore size distribution (Fig. 3). This last point emphasizes the interest in membranes with narrow pore size distribution, such as zeolite membranes. Suitable dynamic methods include gas permeability measurements, liquid-liquid displacement porosimetry [35], and gas separation. Some of these methods are presented in Ref. 15.

Microporous and, particularly, ultramicroporous membranes are more difficult to characterize. Different procedures based on the low-pressure part of the  $N_2$  adsorption isotherm have been proposed [36], but they often require knowledge of the shape of the pores and of gas-surface interaction parameters which are not always available. Small angle X-ray scattering (SAXS) is another technique which is well suited to microporous powders, but difficult to execute in the case of composite layers, as in microporous membranes. Xenon-129 NMR has recently been proposed [37] for the characterization of amorphous silica used in the preparation of microporous membranes, but the method requires further improvement. Methods based on permeability measurements appear to be limited by the lack of understanding of the mass transport mechanisms in (ultra)microporous systems.

#### 9.3.2.4 Gas Transport and Separation in Porous Membranes

As pointed out in Section A9.3.2.1, most of the CMRs for gas-phase applications require selective permeation through the membrane. The aim of this section is to briefly describe the different gas transport processes through a porous membrane.

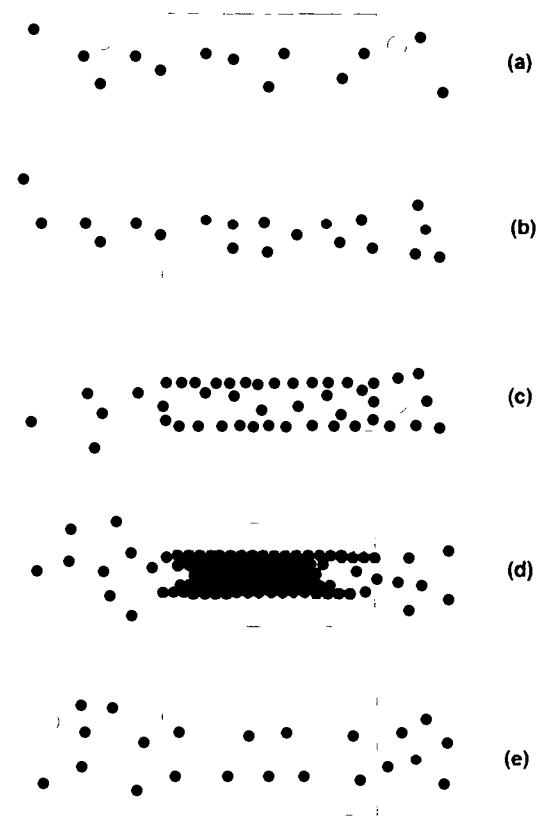


**Figure 4.** Schematic representation of transport mechanisms in porous media: (a) Poiseuille flow; (b) Knudsen diffusion; (c) surface diffusion; (d) capillary condensation; (e) molecular sieving

Figure 4 schematically represents these processes. Poiseuille flow (or viscous flow) occurs when collisions between the gas molecules are more frequent than collisions between gas molecules and the pore walls. This mechanism, which is a pressure-driven one, is non-separative and takes place in large pores (and defects) of the membrane.

Knudsen flow occurs when the mean free path of the molecules is larger than the pore diameter. For a given molecule, Knudsen flow can be realized by increasing the temperature and/or decreasing the pore size. Under these conditions, collisions of the permeating molecules with the pore walls are more frequent than collisions between molecules, which then diffuse independently. Knudsen flow is inversely proportional to the square root of the molecular weight of the diffusing species and, hence, good permselectivities will be obtained for  $H_2$ -organic molecule mixtures (theoretical value of ca. 7 for  $H_2$ -ethylbenzene). However, these Knudsen permselectivities are often insufficient for CMR applications and other separation mechanisms need to be pursued.

Surface diffusion (Fig. 4(c)) can lead to high separation factors when one of the components interacts strongly with the surface; multilayer diffusion and capillary condensation (d) have also been proposed [38]

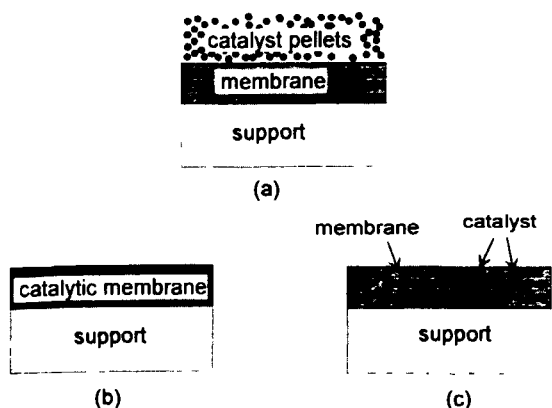


Figure 5. Different membrane–catalyst combinations: (a) fixed-bed catalyst plus membrane; (b) inherently catalytic membrane; (c) membrane acting as support of a catalytically active phase.

for achieving high permselectivities. However, these mechanisms generally occur at low temperatures, which limits their applicability in catalytic membranes.

Molecular sieving Fig. 4(c) where, due to steric hindrance, only small molecules will diffuse through the membrane, seems to be a useful principle for achieving good separations. To ensure this molecular sieving effect, ultramicroporous membranes have to be prepared. Moreover, such membranes should not only be defect free but must also present a very narrow pore size distribution to avoid any other (less selective) permeation mechanisms: defect-free zeolite membranes appear to be good candidates for this type of separation.

As far as gas separations are concerned, and if only Knudsen processes occur, the effective separation factor (as experimentally measured) is equal to the theoretical permselectivity (ratio of the permeabilities of the pure gases). When processes involving interactions with the surface are important, separation factors generally differ from permselectivities. For example, if capillary

condensation of the heavy component occurs, the gaseous component will no longer permeate. In the case of ultramicroporous zeolite membranes, experimental separation factors may also greatly differ from calculated permselectivities [33].

### 9.3.2.5 Catalyst–Membrane Combinations

#### A Different Types of CMRs

Various arrangements have been proposed to combine a catalyst and a membrane to give the catalytic membrane reactor (CMR). Figure 5 schematically represents the most frequently used types of arrangement.

In the first case (a) a conventional fixed-bed catalyst is associated with a membrane which generally has only a separative effect. In this configuration, the two steps, namely chemical conversion (catalyst) and separation (membrane), are consecutive.

In the second case, (b) and (c), the membrane has both catalytic and separative effects. The membrane can either be catalytically active by itself (b) or act as support for an active phase (c). Here, conversion and separation take place in a parallel manner.

From these two generic configurations, different variations can be found in the literature. In case (a) the membrane can be dense or porous, active or inactive. In case (b) the membrane can be dense or porous. Moreover, some applications (see Sections A9.3.3.2 and A9.3.3.3) do not require permselective membranes. A complete nomenclature of the different membrane reactors has been proposed by Tsotsis et al. [6].

Depending on the membrane shape (plate or tube) the reactor is different, but it is generally made of two chambers separated by the membrane. Figure 6 shows a reactor made of a tubular membrane and a conventional fixed-bed catalyst filling the inner part of the tube. In this example the reactant(s) is introduced into

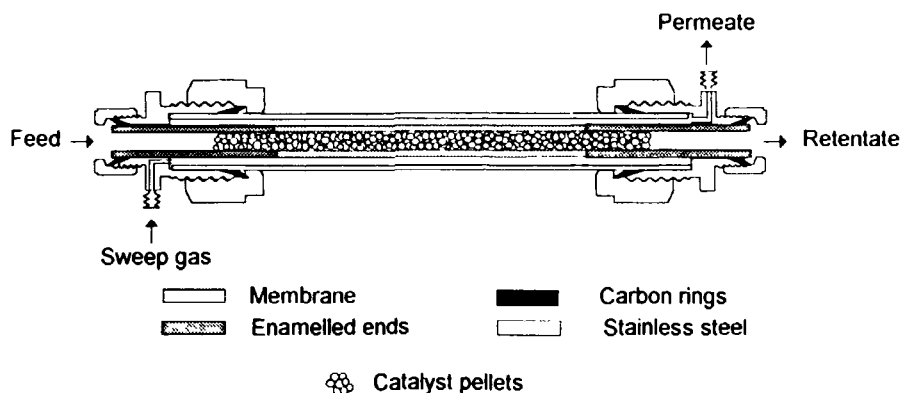


Figure 6. Tubular membrane reactor (fixed-bed catalyst + inert porous membrane) for dehydrogenation reactions [51].



the inner part of the tubular membrane (the retentate side according to the denomination used in separation processes), a sweep gas can be introduced in the outer part (the permeate side) in order to evacuate the permeating molecules and in this way increase the transmembrane flux.

When dense Pd-based membranes are used, permeabilities are low. To increase the membrane surface per unit volume of reactor the use of spiral tubes or helix-shaped Pd membranes has been proposed [39].

## B Catalyst Deposition in Porous Membranes

The influence of various parameters, such as loading procedures and concentration profiles, on the catalytic properties has been discussed [40].

Different ways have been used to deposit active phases (oxides, metals) in the porous framework of membranes [2, 7, 8]. Some specific impregnation techniques make use of the porous volume of the macroporous layers to feed the mesoporous top layer with active species (reservoir method [41]). Organic solutions containing Pt-solvated microclusters have also been used to deposit active Pt in  $\gamma$ -Al<sub>2</sub>O<sub>3</sub> membranes [42]. Ion exchange methods with specific washing and drying steps lead to well dispersed Pt particles with homogeneous loading in silica or alumina membranes. Such Pt-membrane catalysts show properties very similar to those of conventional catalysts in reactions where no membrane effect can be anticipated [43].

## 9.3.3 Applications of CMRs

### 9.3.3.1 Equilibrium-Restricted Reactions

As pointed out in Section 9.3.2.1, the most common application of CMRs concerns equilibrium-restricted reactions [1–12]. The selective removal of a reaction product from the reaction zone through a membrane will shift the equilibrium, leading to higher conversions when compared to conventional (nonmembrane) reactors.

In addition to this increase in conversion, other benefits can be expected when using a membrane reactor. The same yields can be achieved at lower temperatures, leading to energy savings and reduced catalyst deactivation (one of the major problems of alkane dehydrogenation), increased selectivities when temperature-promoted side reactions exist or when the permeating species are involved in these side reactions. Moreover, the formation and separation of products in the same unit leads to a reduction in capital costs.

## A Experimental Studies in Hydrocarbon Dehydrogenation Reactions

Hydrocarbon dehydrogenation reactions were first studied, due to the rather easy separation of the hy-

drogen produced during the reaction, either by diffusion through dense Pd-based membranes or by Knudsen diffusion through glass or ceramic porous membranes. Reviews of these studies can be found in [3, 9]. In most cases, a sweep gas is used to remove hydrogen from the permeate side, thus increasing the transmembrane flux.

Dehydrogenation of cyclohexane to benzene has been studied extensively due to the relatively low reaction temperature ( $\approx 500$  K) compared to alkane dehydrogenation ( $\approx 800$  K, which is close to the maximum temperature withstood by classical sol-gel membranes). Dense Pd-Ag foils acting as catalyst and membrane were first used [10]. Conversions of up to 100% were reported (compared to  $\approx 20\%$  conversion in a conventional reactor) for low cyclohexane feed rates in the case of a dense Pd-Ag membrane associated with a Pt/Al<sub>2</sub>O<sub>3</sub> fixed-bed catalyst [44]. Porous glass membranes with a Pt/Al<sub>2</sub>O<sub>3</sub> fixed-bed catalyst enabled conversions of up to 2.5 times that obtained in a conventional reactor [45]. A comparison of two reactors, one made of an inert membrane and a fixed-bed Pt catalyst, the other made of a membrane acting as support for Pt, has demonstrated the superior performance of the latter, as long as low flow rates of the reactant were applied [46].

The dehydrogenation of other hydrocarbons has also been studied in CMRs, generally with porous membranes. Conversions of ethane [47], propane [48], butane [49], and ethylbenzene [50] have been reported to be higher when membrane reactors were used. In the case of ethylbenzene dehydrogenation, the undesirable hydrodealkylation side reaction is slowed down due to the removal of H<sub>2</sub>, i.e. the membrane enables an increase in selectivity as well [50].

Recent results on isobutane dehydrogenation have been reported, and a conventional reactor has been compared with membrane reactors consisting of a fixed-bed Pt-based catalyst and different types of membrane [51]. In the case of a mesoporous  $\gamma$ -Al<sub>2</sub>O<sub>3</sub> membrane (similar to those used in several studies reported in the literature), the observed increase in conversion could be fully accounted for simply by the decrease in the partial pressures due to the complete mixing of reactants, products and sweep gas. When a permselective ultramicroporous zeolite membrane is used, this mixing is prevented; the increase in conversion ( $\approx 70\%$ ) can be attributed to the selective permeation of hydrogen shifting the equilibrium.

Instead of using a sweep gas for removing the permeating hydrogen, several authors who employed dense Pd membranes proposed the application of a second reaction in which H<sub>2</sub> is consumed. This second reaction, which has to take place on the permeate side can be either a hydrogenation [52] or the formation of water by reaction with O<sub>2</sub> [53], both being catalyzed

by the dense Pd membrane. In addition to the effect of pumping  $H_2$ , this second reaction, due to its exothermicity, is able to provide energy across the membrane for the endothermic dehydrogenation, thus improving the total heat balance of the membrane reactor.

### B Analysis and Modeling of CMRs for Dehydrogenation

Important parameters in a catalytic membrane reactor for dehydrogenation are the reaction rate, the permeability (i.e. permeation rate) and the permselectivity for hydrogen. It appears at first sight that good conditions are those where the permeation rate (removal of  $H_2$ ) and the reaction rate (formation of  $H_2$ ) are close to each other, but the role of the permselectivity is also important.

Due to its complexity (conversion and separation in the same unit) and because this system has been most widely studied experimentally, CMRs for dehydrogenation (or more generally for equilibrium-restricted reactions) have been the subject of modeling approaches [6, 54–59]. The modeling of CMRs requires mass and energy balances in both feed and permeate sides of the reactor (plug-flow behavior is always assumed) and appropriate boundary conditions. Generally these models fit the experimental data well.

In the case of dense membranes, where only hydrogen can permeate (permselectivity for  $H_2$  is infinite), the permeation rate is generally much lower than the reaction rate (especially when a fixed bed is added to the membrane). Experimental conditions and/or a reactor design which diminishes this gap will have positive effects on the yield. An increase of the sweep gas flow rate (increase of the driving force for  $H_2$  permeation) leads to an increase in conversion and, if low reactant flow rates are used (to limit the  $H_2$  production), conversions of up to 100% can be predicted [55]. These models of dense membrane reactors explain why large membrane surfaces are needed and why research is directed towards decreasing the thickness of Pd membranes (subsection 9.3.2.2.A.a).

Porous membranes possess much higher permeabilities, but the permselectivity of the membrane will drastically affect the CMR performance. Itoh et al. [54], in a study of cyclohexane dehydrogenation, analyzed the effect of the permeation rate by varying the membrane thickness. The conversion went through a maximum: for low permeation rates, the increase in conversion is small because only a limited amount of  $H_2$  escapes from the reaction zone; for high permeation rates, both the reactant and the product will permeate (due to the lack of permselectivity), and the CMR is inefficient in this case. This suggests that ultramicroporous membranes (such as zeolite membranes), which could combine high permselectivities with high

permeation rates, could be good candidates for this application [51].

Modeling studies have also considered other aspects of CMRs. Sun and Khang [46] compared two types of CMRs, one with an inert (only separative) porous membrane associated with a fixed-bed catalyst, the other with the catalyst deposited within the porous framework of the membrane (thus leading to a catalytic membrane). For long contact times, the performance of the catalytic membrane is higher, due to the simultaneity of reaction and separation.

Other studies dealing with the analysis of the effect of cocurrent or countercurrent flows of the reactant and sweep gas showed that the most efficient direction for the purge stream depends on the nature of the reaction for a given membrane [56]. The coupling of dehydrogenation on one side and hydrogen oxidation on the other side of the membrane has also been analyzed [60].

### C Other Equilibrium-Restricted Reactions

Besides dehydrogenation, other reactions producing hydrogen have been studied in CMRs. Among these are the water-gas shift [61–63], steam reforming [64], and  $H_2S$  decomposition [65]. Positive effects of the membrane-catalyst association have been reported. The recovery of tritium in a CMR through gas shift of tritiated water has also been studied within the framework of the fusion reactor project [66].

#### 9.3.3.2 Controlled Addition of Reactants

In this application, the role of the membrane is to dose one of the reactants. The membrane creates a diffusion limitation for this reactant which is then added to the other reactant in a controlled manner. The two reactants are separately introduced (segregated feed [67]) on the two sides of the membrane which is generally catalytically active itself.

The main interest in applying this type of CMR is to keep the concentration of one of the reactants low all along the reactor, which is often needed when consecutive reactions may occur, as in partial hydrogenations or selective oxidations (in the case of conventional fixed-bed reactors where concentration profiles decrease monotonically, the selectivity is generally low at the inlet of the reactor). Thus, with CMRs, one can then expect high selectivities at high conversions, avoiding the need to separate undesirable products or unconverted reactants.

Moreover, if this membrane is permselective for the added reactant, it is possible to use less expensive forms of this reactant (air instead oxygen), thus avoiding separation steps. Or, if explosive mixtures may be

formed, the presence of the membrane separating the two reactants allows the use of concentrated feeds.

Most of the examples cited in the literature concern selective oxidations, the objective of the CMR here being to limit the formation of undesirable carbon oxides by total oxidation.

The oxidative coupling of methane has been studied using an active dense PbO membrane deposited on MgO: a significant increase in the selectivity for  $C_2$  was reported [68]. Porous La-based membranes have also been used in this reaction [69]. Oxidation of ethylene to acetaldehyde has been studied with porous  $V_2O_5-\gamma-Al_2O_3$  membranes, the selectivity towards acetaldehyde was clearly higher than in conventional reactors [67]. In the oxidative dehydrodimerization of propene, the use of a dense  $Bi_{1.7}La_{0.3}O_2$  membrane (ionic conductor) diminished the formation of CO/CO<sub>2</sub> [70]. A high performance has been reported in the selective oxidation of propene to acrolein when using an electrochemical reactor equipped with a  $MoO_3-Au/Y_2O_3-ZrO_2/Ag$  membrane [71]. The oxidative dehydrogenation of propane has been performed using a zeolite membrane to control the  $O_2$  addition and a classical V-Mg-O fixed-bed catalyst. Due to the drastic impact on selectivity, the  $C_3H_6$  yield was clearly improved when compared to a conventional reactor [72].

CMRs of this type (controlled addition of reactants) have been analyzed on the basis of reaction kinetics [73].

### 9.3.3.3 Active Contactor

This third type of CMR is probably less developed than the previous ones, but the field of applications appears very large. The main role of the membrane here is to improve and manage the contact between the reactants and the catalyst. The membrane (which is not necessarily a permselective one) is generally catalytically active and separates the two reactants; the reactive interface between the reactants and the catalyst being localized in (porous) or on (dense) the membrane. Gas or gas-liquid reactions may be involved.

The Claus reaction [74] and the reduction of  $NO_x$  by  $NH_3$  [75] have been studied using nonpermselective porous membranes impregnated with active  $Al_2O_3$  for the first reaction and  $V_2O_5$  for the second. The principle (Fig. 7) is as follows: the catalytic activity of the membrane is high enough so that the reactive interface is located within the membrane; this interface corresponds to the complete consumption of the two reactants, and their fluxes then fit the stoichiometry of the reaction. Depending on the concentration (partial pressure) of the two reactants in the separate streams the interface will be displaced within the membrane

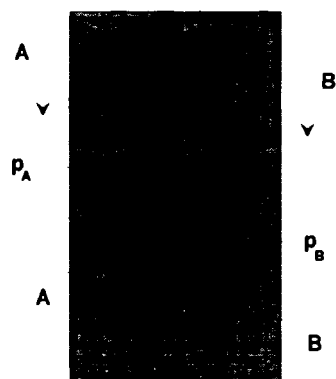


Figure 7. Schematic representation of a membrane reactor for rapid gas-phase catalytic reactions (adapted from Ref. 64).

layer, thus avoiding strict adjustment of the feeds to the reaction stoichiometry. Moreover, any transfer of one reactant to the opposite side of the membrane is avoided; this is an advantage because toxic pollutants ( $H_2S$  for instance) are prevented from penetrating the other side, even if their concentrations change. However, it should be stressed that this application implies that the reactor performance remains controlled by transport phenomena (the membrane must have a sufficiently low permeability).

Gas-liquid reactions with CMRs have also been a subject for research. Gryaznov has shown that dense Pd-based membranes present various benefits in hydrogenation reactions for the production of fine chemicals [5]. In such reactors, hydrogen coming through the membrane in a highly reactive atomic form reacts with the organic substrate adsorbed on the other side of the membrane; this configuration is expected to allow the control of the concentrations of both reacting species (no competitive adsorption as in conventional catalysis). High activity (atomic hydrogen) and high selectivity (control of the concentration of the active species) are expected. The one-step synthesis of vitamin K [76], the selective hydrogenation of alkylic alcohols into alkenic alcohols [5] and of quinones into hydroquinones [5] are typical examples where the CMR has shown advantages over conventional techniques.

It has also been proposed that porous catalytic membranes may improve the efficiency of gas-liquid solid reactions when the gas-liquid interface is placed within the porous framework of the porous membrane [77]. This postulated increase in efficiency has been experimentally supported by Cini and Harold in a comparative study of a CMR and a single-pellet model reactor [78] in the hydrogenation of  $\alpha$ -methylstyrene into cumene. The authors ascribe this observation to a decrease in the mass transfer resistance.

The hydrogenation of nitrobenzene has been chosen as model reaction in a detailed exploration of the CMR

in gas-liquid reactions using a porous Pt membrane as catalyst [79]. In addition to classical operating conditions (pressure, temperature etc.), other parameters such as the mode of introduction of gaseous and liquid reactants and the average pore size of the membrane have been explored. This has revealed that, if the membrane is well designed and if the reactor operates correctly, hydrogen is no longer the limiting reactant (the kinetic order for  $H_2$  is 0 in the CMR, whereas it is 1 in conventional slurry or trickle-bed reactors). This type of CMR thus appears particularly suitable for reactions where the gaseous reactant is limiting. Modeling of this reactor has been carried out in order to better describe the behavior of a CMR in gas-liquid reactions [80].

Another interest in CMRs in gas-liquid applications has emerged recently. When the reactant feed contains impurities, the use of a microporous membrane can prevent poisoning of the active metallic particles located in its porous framework, due to the fact that large poisoning molecules are not able to penetrate the micropores [81]. It is proposed that hydrogen coming from one side of the membrane is first activated on the metal, then active H migrates (spillover) to the other side of the membrane to hydrogenate the organic molecule.

Furthermore, CMRs present the advantage of avoiding the separation step of the catalyst from the liquid phase, which is often a critical step in classical slurry reactors. CMRs are also able to operate in a continuous mode, and regeneration procedures for the catalyst are easier.

### 9.3.4 Conclusions

The combination of a catalyst and a membrane opens the door to a large number of potential applications. However, significant progress has to be made before catalytic membrane reactors are used in practice.

In CMR applications for equilibrium-restricted reactions (Section A9.3.3.1), dense membranes, if highly permselective, generally suffer from low permeabilities. For dehydrogenation reactions, the available dense membranes require the use of low reactant feed rates (to limit the  $H_2$  production) and high sweep gas flows (to increase the driving force), which is unsatisfactory economically (in addition, high sweep gas flows have negative effects on heat transfer and require expensive downstream separation). The production of thinner dense Pd layers or composite metal-oxide dense membranes is an important research goal in order to overcome the present limitations for practical applications.

Permeabilities of porous membranes are generally high enough for CMRs; however, when high permse-

lectivity is required, conventional porous membranes (Knudsen diffusion) are often not suitable. Microporous molecular sieve membranes with very narrow pore size distribution (such as zeolite membranes) are usually better candidates when gas separation is needed, and the preparation of defect-free layers with high permeabilities is a subject of intensive research. Moreover, the mechanisms of transport and gas separation in ultramicroporous solids are not definitively established, and progress in this area appears essential for the design of suitable materials.

Equilibrium-restricted reactions (Section A9.3.3.1) have until now been the main field of research on CMRs. Other types of application, such as the controlled addition of reactants (Section A9.3.3.2) or the use of CMRs as active contactors (Section A9.3.3.3), seem however very promising, as they do not require permselective membranes and often operate at moderate temperatures. Especially attractive is the concept of active contactors where the membrane being the catalyst support becomes an active interface between two non-miscible reactants. Indeed this concept, initially developed for gas-liquid reaction [79] has been recently extended to aqueous-organic reactants [82]. In both cases the contact between catalyst and limiting reactant which restricts the performance of conventional reactors is favored by the membrane.

Another point concerns the membrane housing. Sealing between a ceramic membrane and a metallic tube can be a problem when high temperatures are used, due to the difference in thermal expansion between the two materials. Specific carbon seals can be used with classical fittings, but a much better system using a sequence of materials with progressive change in properties has been recently developed [83].

In addition to a proper membrane, CMRs also need a good catalyst. Due to the specific conditions under which catalysts are placed in CMRs, conventional active phases could behave differently from when under classical conditions. For example, in dehydrogenation reactions, due to the removal of  $H_2$ , the hydrogen:hydrocarbon ratio is smaller in CMRs when compared to other reactors, which will probably affect the stability of the catalyst. The low oxygen partial pressure used in CMRs for selective oxidation (Section A9.3.3.2) could also lead to some changes in catalyst behavior. These aspects could necessitate the specific design of catalysts for CMRs.

Scaling up of CMRs will require the ability to prepare large areas of defect-free membranes at a reasonable cost. The critical cost will depend on the advantages afforded by the membrane reactor and will therefore be closely related to the type of process con-

sidered. Fine chemical syntheses, which typically use small reactors (limited membrane area) and produce high added value molecules, should be more favored from this viewpoint than bulk chemical production.

Most of the experimental research concerning CMRs has been made at the laboratory scale, with experiments of short duration. Little is known about the effect of long term operation on the stability of membranes in CMRs: thermal resistance in the reactive media, mechanical integrity, and fouling by carbon deposits or side reactions are all parameters which require improved knowledge to assess the industrial future of CMRs.

### 9.3.5 Glossary

Adapted from Armor [1].

**Flux** the flow rate of the permeating species per unit cross-sectional area of the membrane. Where Fick's law of diffusion is applicable, the flux is related to the effective diffusion coefficient  $D$  and the concentration gradient,  $\Delta C/\Delta l$ , between the two interfaces of the membrane:

$$\text{flux} = -D \left( \frac{\Delta C}{\Delta l} \right) = -P \left( \frac{\Delta p}{\Delta l} \right)$$

where  $\Delta l$  is the thickness of the membrane,  $\Delta p$  is the pressure difference across the membrane, and  $P$  is the permeability. The effective diffusion coefficient  $D$  is related to the porous structure by

$$D = \frac{\varepsilon}{\tau} D$$

where  $\varepsilon$  is the porosity,  $\tau$  the tortuosity, and  $D$  the diffusivity for a straight cylindrical pore of the same diameter.

**Macroporous** containing pores with a diameter  $>50$  nm.

**Membrane** a material that separates two components on the basis of their properties (size, chemical nature, etc.).

**Mesoporous** containing pores with a diameter from 2 to 50 nm.

**Permeability** the rate at which a component flows through a membrane of thickness  $l$  unit with a cross-sectional area of  $l$  unit and a transmembrane partial pressure difference of  $l$  unit. Permeabilities are expressed in SI units of  $\text{m}^2 \text{s}^{-1} \text{Pa}^{-1}$ . A usual unit for permeability is the barrer:

$$1 \text{ barrer} = 10^{-10} \text{ cm}^2 \text{ s}^{-1} \text{ cm Hg}^{-1}$$

**Permeance** the ratio of a membrane's permeability to the width of the working layer.

**Permeate** the portion of the feed that passes through a membrane.

**Permselectivity** the measure of a membrane's ability to separate two gases (A and B). It is traditionally measured by the ratio of permeabilities of the pure components.

$$\text{permselectivity} = P_A/P_B$$

However, the true separation factor may differ from this theoretical permselectivity, especially if gas-membrane interactions occur (section 9.3.2.4).

**Porosity**( $\varepsilon$ ) the ratio of the porous volume to the apparent volume.

**Retentate** the portion of the feed that is rejected by the membrane and not allowed to permeate.

**Supermicroporous** containing pores with a diameter from 0.7 to 2 nm.

**Top layer** the separative layer, deposited on top of support layers which have larger pore sizes.

**Tortuosity**( $\tau$ ) originates from the increasing length of the diffusion path for a gas molecule in a porous medium, compared to a straight capillary.

**Ultramicroporous** containing pores with a diameter  $<0.7$  nm.

### References

- 1 J N Armor, *Appl Catal* **1989**, *49*, 1-25, *Chemtech* **1992**, 557-563, *Catal Today* **1995**, *25*, 197-207
- 2 H P Hsieh, *Catal Rev -Sci Eng* **1991**, *33*, 1-70
- 3 V T Zaspalis, A J Burggraaf in *Inorganic Membranes Synthesis, Characteristics and Applications* (Ed R R Bhawe), van Nostrand Reinhold, New York, **1991**, Chapter 7, pp 177-207
- 4 J Shu, B P A Grandjean, A Van Neste and S Kaliaguine *Can J Chem Eng* **1991**, *69*, 1036-1060
- 5 V M Gryaznov, *Plat Met Rev* **1986**, *30*, 68-72, **1992**, *33* 70-79
- 6 T T Tsotsis, R G Minet, A M Champagnie, P K T Liu in *Computer-Aided Design of Catalysts* (Eds E R Becker C J Pereira), Marcel Dekker, New York, **1993**, Chapter 12 pp 471-551
- 7 G Sarraco, V Specchia, *Catal Rev -Sci Eng* **1994**, *36*, 305 384
- 8 J Zaman, A Chakma, *J Membr Sci* **1994**, *92*, 1 28
- 9 J L Falconer, R D Noble, D P Sperry, *Membrane Separations Technology Principles and Applications* **1994**, *2*, 669 712

- 10 B J Wood, H Wise, *J Catal* **1996**, *5*, 135–145, B J Wood, *J Catal* **1968**, *11*, 30–34
- 11 A S Michaels, *Chem Eng Progr* **1968**, *64*, 31–43
- 12 V M Gryaznov, V M Smirnov, L K Ivanova, A P Mishchenko, *Dokl Akad Nauk SSR* **1970**, *190*, 144–147
- 13 A J Burggraaf, K Keizer in *Inorganic Membranes Synthesis, Characteristics and Applications* (Ed R R Bhave), van Nostrand Reinhold, New York, **1991**, Chapter 2, pp 10–63
- 14 R Soria, *Catal Today*, **1995**, *25*, 285–290
- 15 H P Hsieh in *Inorganic Membranes Synthesis, Characteristics and Applications* (Ed R R Bhave), van Nostrand Reinhold, New York, **1991**, Chapter 3, pp 64–74
- 16 S Uemiyai, Y Kude, K Sugino, N Sato, T Matsumada, K Kikuchi, *Chem Lett* **1988**, *10*, 1687–1690
- 17 J Shu, B P A Grandjean, E Ghali, S Kaliaguine, *J Membr Sci* **1993**, *77*, 181–195
- 18 V M Gryaznov, V I Vedernikov, S G Gul'yanova, *Kinet Katal* **1986**, *27*, 142–146
- 19 G R Gavalas, C E Megiris, S W Nam, *Chem Eng Sci* **1989**, *44*, 1829–1835
- 20 R J R Ulhorn, K Keizer, A J Burggraaf, *J Membr Sci* **1992**, *66*, 271–287
- 21 C J Brunker, T L Ward, R Shegal, N K Raman, S L Hietala, D M Smith, D W Hua, T J Headley, *J Membr Sci* **1993**, *77*, 165–180
- 22 S P Smith, V M Linkov, R D Sanderson, L F Petrick, C T O'Connor, K Keizer, *Microporous Mater* **1995**, *4*, 385–390
- 23 A F M Leenards, K Keizer, A Burggraaf, *J Mater Sci* **1984**, *19*, 1077–1088
- 24 A Larbot, J A Alary, J P Fabre, C Guizard, L Cot, *Proc Mat Res Soc Symp* **1986**, *73*, 659–667
- 25 A Julbe, C Guizard, A Larbot, L Cot, A Giroir-Fendler, *J Membr Sci*, **1993**, *66*, 271–287
- 26 P Chanaud, A Julbe, A Larbot, C Guizard, L Cot, H Borges, A Giroir-Fendler, C Mirodatos, *Catal Today* **1995**, *25*, 225–230
- 27 H Suzuki, US Patent 4 699 892, **1987**
- 28 A Ishikawa, T H Chiang and F Foda, *J Chem Soc Chem Commun* **1989**, *12*, 764–765
- 29 E R Geus, M J den Exter, H van Bekkum, *J Chem Soc Faraday Trans* **1992**, *88*, 3101–3109
- 30 W O Haag, J G Tsikoyannis, US Patent 5 019 263, **1991**
- 31 M D Jia, B Chen, R D Noble, J L Falconer, *J Membr Sci* **1994**, *90*, 1–10
- 32 Y M Ma, S Xiang, US Patent 5 258 339, **1993**
- 33 F Kapteijn, W J W Bakker, G Zheng, J A Moulijn, H van Bekkum, *Catal Today*, **1995**, *25*, 213–218
- 34 J Ramsay, A Giroir-Fendler, A Julbe, J-A Dalmon, French Patent 94 05 562, **1994**
- 35 G Capannelli, I Becchi, A Bottino, P. Moretti, S Munari, *Stud Surf Sci Catal* **1988**, *39*, 283–294
- 36 N A Seaton, J P R B Walton, N Quirke, *Carbon* **1989**, *27*, 853–861
- 37 L C de Menorval, A Julbe, H Jobic, J-A Dalmon, C Guizard, *MRS Proc Series "Microporous and Macroporous Materials"*, **1996**, *431*, 159–164
- 38 R J R Uhlhorn, A J Burggraaf in *Inorganic Membranes Synthesis Characteristics and Applications* (Ed R R Bhave), van Nostrand Reinhold, New York, **1991**, Chapter 6, pp 155–176
- 39 V M Gryaznov, M M Ermilova, L S Morozova, *J Less-Common Met* **1983**, *89*, 529–535
- 40 R C Furneaux, A P Davidson, M D Ball, European Patent 244 970, **1987**
- 41 V T Zaspalis, Ph D Thesis, Twente University, the Netherlands, **1990**
- 42 G Capannelli, A Bottino, G Gao, A Grosso, A Servida, G Vitulli, A Mastantuono, R Lazzaroni, P Salvadori, *Catal Lett* **1993**, *20*, 287–297
- 43 D Uzio, J Peureux, M Torres, A Giroir-Fendler, J Ramsay, J-A Dalmon, *Appl Catal* **1993**, *96*, 83–97
- 44 N Itoh in *Stud Surf Sci Catal* **1990**, *54*, 268–283
- 45 N Itoh, Y Shindo, K Haraya, T Hakuta, *J Chem Eng Jpn* **1988**, *21*, 399–404
- 46 Y M Sun, S J Khang, *Ind Eng Chem Res* **1988**, *27*, 1136–1142
- 47 A M Champagne, T T Totis, R G Minet, I A Webster, *Chem Eng Sci* **1990**, *45*, 2423–2429
- 48 Z D Ziaka, R G Minet, T T Totis, *AIChE J* **1993**, *39*, 526–529
- 49 V T Zaspalis, W van Praag, K Keizer, J G van Ommen, J R H Ross, A J Burggraaf, *Appl Catal* **1991**, *74*, 223–234
- 50 M A Anderson, F Tiscareno-Lechuga, Q Xu, C G Hill, *ACS Symp Ser* **1990**, *437*, 198–215
- 51 D Cazanave, A Giroir-Fendler, J Sanchez, R Loutaty, J-A Dalmon, *Catal Today*, **1995**, *25*, 309–314
- 52 N L Basov, V M Gryaznov, *Membr Katal* **1985**, *117*
- 53 R Zhao, N Itoh, R Govind, *ACS Symp Ser* **1990**, *437*, 216–230
- 54 N Itoh, Y Shindo, K Haraya, K Obata, T Hakuta, H Yoshitome, *Int Chem Eng* **1985**, *25*, 138
- 55 N Itoh, *AIChE J* **1987**, *33*, 1576–1578
- 56 K Mohan, R Govind, *AIChE J* **1986**, *32*, 2083–2086
- 57 E Gobina, R Hughes, *Catal Today*, **1995**, *25*, 365–370
- 58 M Tayakout, B Bernauer, Y Toure, J Sanchez, *Simulation Practice and Theory*, **1995**, *2*, 205–219
- 59 H W Deckman, E W Corcoran, J A McHenry, J H Meldon, V A Papavassiliou, *Catal Today* **1995**, *25*, 357–363
- 60 N Itoh, R Govind, *Ind Eng Chem Res* **1989**, *28*, 1544–1551
- 61 H Iwahara, T Esaka, H Uchida, T Yamaguchi, K Ozaki, *Solid State Ionics* **1986**, *18–19*, 1003
- 62 J H R Ross, E Xue, *Catal Today* **1995**, *25*, 291–301
- 63 M Bracht, A Bos, P P C A Pex, H M van Veen, P Alderhesten, *Proceedings of the Euromembrane Conference* (Eds R Bowen, R W Field, J A Howell), ESMST, University of Bath, **1995**, 425–430
- 64 S Lægsgaard Jørgensen, P E Højlund Nielsen, P Lehmann, *Catal Today* **1995**, *25*, 303–307
- 65 T Kameyama, M Dokiya, M Fujishige, H Yokokawa, K Fukuda, *Int J Hydrogen Energy* **1983**, *8*, 5–14
- 66 A Basile, V Violante, E Drioli, *Catal Today* **1995**, *25*, 321–326
- 67 M P Harold, C Lee, A J Burggraaf, K Keizer, V T Zaspalis, R S A de Lange, *Materials Research Society Bulletin* April **1994**, 34–39
- 68 K Omata, S Hashimoto, H Tomimaga, K Fujimoto, *Appl Catal* **1989**, *52*, L1
- 69 H Borges, A Giroir-Fendler, C Mirodatos, P Chanaud, A Julbe, *Catal Today* **1995**, *25*, 377–383
- 70 I T Caga, J M Winterbottom, I R Harris, *Catal Lett* **1989**, *3*, 309–316
- 71 T Tsunoda, T Hayakawa, Y Imai, T Kameyama, K Takehira, K Fukuda, *Catal Today* **1995**, *25*, 371–376
- 72 A Pantazidis, J A Dalmon, C Mirodatos, *Catal Today* **1995**, *25*, 403–406
- 73 M P Harold, V T Zaspalis, K Keizer, A J Burggraaf *Chem Eng Sci* **1993**, *48*, 2705–2725
- 74 H J Sloot, G F Versteeg W P M van Swaay, *Chem Eng Sci* **1990**, *45*, 2415–2421

75. V. T. Zaspalis, W. van Praag, K. Keizer, J. G. van Ommen, J. R. H. Ross, A. J. Burggraaf, *Appl. Catal.* **1991**, *74*, 249–260.
76. V. M. Gryaznov, A. N. Karavanov, *Khim. Farm. Zh.* **1979**, *13*, 74.
77. R. de Vos, C. E. Hamrin, *Chem. Eng. Sci.* **1982**, *37*, 1711–1718.
78. P. Cini, M. P. Harold, *AIChE J.* **1991**, *37*, 997.
79. D. Uzio, J. Peureux, M. Torres, H. Mozzanega, A. Giroir-Fendler, J.-A. Dalmon, *Catal. Today* **1995**, *25*, 409–416.
80. M. Torres, J. Sanchez, J.-A. Dalmon, B. Bernauer, J. Lieto, *I&EC Research*, **1994**, *33*, 2421–2425.
81. W. F. Maier, H. C. Ko, *Catal Today* **1995**, *25*, 429–440.
82. I. F. J. Vanklecom, R. F. Parton, M. J. A. Casselman, J. B. Uytterhoeven, P. A. Jacobs, *J. Catal.* **1996**, *163*, 457–464.
83. F. M. Velterop, US Patent 5 139 191, **1992**.

---

# 10 Reaction Engineering

---

## 10.1 Catalytic Fixed-Bed Reactors

### 10.2 Fluidized-Bed Reactors

### 10.3 Slurry Reactors

### 10.4 Unsteady-State Reactor Operation

### 10.5 Catalytic Distillation

---

## 10.1 Catalytic Fixed-Bed Reactors

G. EIGENBERGER

### 10.1.1 Introduction

The easiest and by far the most common way to carry out a heterogeneously catalyzed gas phase reaction is by passing the gas mixture over a fixed catalyst. The arrangement of the fixed catalyst is generally called a fixed-bed and the respective reactor a fixed-bed reactor.

The simplest kind of a fixed catalyst bed is a random packing of catalyst particles in a tube. Different particle shapes are in use like spheres, cylinders, rings, flat disc pellets or crushed material of a certain sieve fraction. Mean particle diameters range from 2 to 10 mm, the minimum diameter is limited primarily by pressure drop considerations, the maximum diameter by the specific outer surface area for mass and heat transfer.

Much effort has been devoted to the question of replacing the random packing by a regular catalyst arrangement to reduce the pressure drop of the flowing gas and/or to increase the heat transfer to a cooling or heating system. Pressure drop considerations led to the introduction of monolith catalysts with parallel channels which meanwhile are dominating catalytic gas purification applications (automotive exhaust and flue gas treatment). The increase of the heat transfer to the tube wall is a matter of ongoing research. The influence of the catalyst shape on fixed-bed reactor performance will be treated in section 10.1.2.

The reaction chambers used to remove nitrogen oxides from power station flue gases constitute the largest type of fixed-bed reactors as regards reactor volume and throughput, while automobile exhaust purification

represents by far the most widely employed application of fixed-bed reactors. In the chemical industry fixed-bed reactors are the standard type of reactor for heterogeneously catalyzed gas phase reactions. Only if special requirements like rapid catalyst deactivation or operation in the explosive regime have to be coped with, the alternative of fluidized-bed operation (see Section A.10.2) is considered.

With regard to application and construction, it is convenient to differentiate between fixed-bed reactors for adiabatic operation and those for nonadiabatic operation. Since temperature control is one of the most important methods to influence a chemical reaction, adiabatic reactors are used only where the heat of reaction is small, or where there is only one major reaction pathway; in these cases no adverse effects on selectivity or yield due to the adiabatic temperature development are expected. The characteristic feature of an adiabatic reactor is that the catalyst is present in the form of a uniform fixed bed that is surrounded by an outer insulating jacket (Fig. 1A). Adiabatic reactor designs are discussed in Section 10.1.3.1.

Since the incoming reaction gases in most cases must be heated to the ignition temperature of the catalytic reaction, adiabatic reaction control is often coupled with heat exchange between the incoming and exiting reaction gas resulting in so-called autothermal reaction control. This type of reaction control offers certain specific features and development perspectives, which are discussed in Section 10.1.3.4.

Reactions with a large heat of reaction as well as reactions that are very temperature-sensitive are carried out in reactors in which indirect heat exchange occurs with a heat transfer medium which is circulated through the fixed bed.

Since in most cases the task of the heat transfer cycle is to maintain the temperature in the fixed bed within a specific range, this concept is frequently described as an "isothermal fixed-bed reactor". Since isothermal reaction control does not always provide optimum selectivity or yield, the concept of heat exchangers integrated in the fixed bed is also being increasingly used to achieve specific nonisothermal temperature profiles. The most common arrangement is the multitubular fixed-bed reactor, in which the catalyst is arranged in the tubes, and



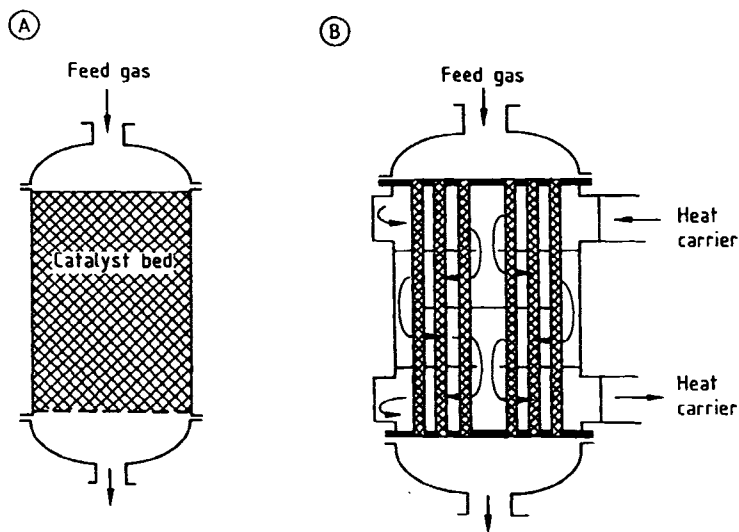


Figure 1. Basic types of catalytic fixed-bed reactors. A) Adiabatic fixed-bed reactor; B) Multitubular fixed-bed reactor.

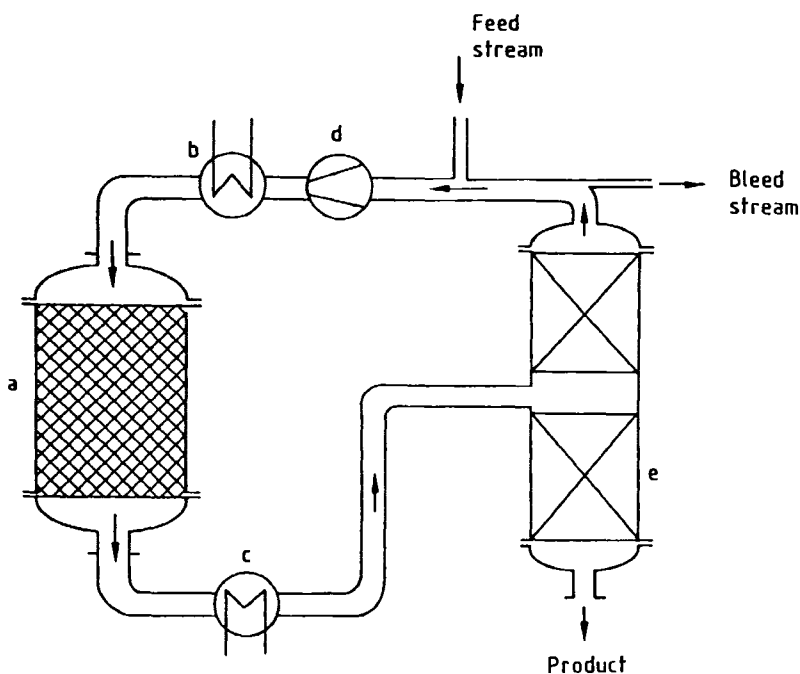


Figure 2. Reaction cycle for synthesis reactions with incomplete conversion. a) Fixed-bed reactor; b) Feed Preheater; c) Exit cooler; d) Recirculation compressor; e) Separation device.

the heat carrier circulates externally around the tubes (Fig. 1B). Fixed-bed reactors with an integrated heat supply or removal are discussed in Section 10.1.3.3.

Fixed-bed reactors for industrial syntheses are generally operated in a stationary mode (i.e., under constant operating conditions) over prolonged production runs. Their design therefore concentrates on achieving an optimum stationary operation. However, the non-stationary dynamic behavior can be of great importance for industrial operation control. In particular, fixed-bed reactors with a strongly exothermic reaction exhibit an, at times, surprising operational behavior. This will be discussed in Section 10.4.

Within a production plant the reactor may justifiably be regarded as the central item of apparatus. However, compared to the remaining parts of the plant for preparing the feed and for separating and working up the products, it is often by no means the largest and most cost-intensive component. In many cases the achievable conversion in the reactor is limited for thermodynamic (equilibrium) and kinetic reasons (selectivity). It is then usual to separate the material discharged from the reactor into products and unreacted feed components (see Fig. 2), which are recycled to the feedstock. This recycling procedure involves costs

- for product separation,
- for recycle compression,
- for repeated heating and cooling of the circulating material to the reaction temperature and back to the temperature of the separating device,
- for loss of product resulting from the need to remove part of the circulating material as a bleed stream to limit the amount of inert substances or byproducts in the recycle.

To minimize these costs it is therefore necessary to maximize the conversion in the reactor and to avoid as far as possible inert substances in the reaction mixture. With irreversible reactions (e.g., partial oxidations) the trend is therefore towards a highly concentrated, approximately stoichiometric feed composition, which may occasionally be in the explosive range. The resulting problems are addressed in Sections 10.1.3.3 and 10.1.4.2)

Since fixed-bed reactors constitute one of the most important classes of chemical reactors, much work has been devoted to their proper mathematical modeling as well as to the study of their stability, sensitivity and automatic control. The following standard text books and monographs can be recommended for further reference [1-4].

## 10.1.2 Catalyst Shapes for Fixed-Bed Reactors

The essential part of a fixed-bed reactor is the catalyst, where the reaction takes place. Seen from the flowing gas, the following steps of the overall reaction can be distinguished (see also Section A.6.2):

- 1) Diffusion of the reactants from the flowing gas through the outer gas-particle boundary layer, macropores, and micropores,
- 2) chemisorption on active sites,
- 3) surface reactions,
- 4) desorption of the products and
- 5) backdiffusion of the products into the flowing gas.

Since most reactions take place with a considerable heat of reaction, a corresponding heat transport is superimposed on the mass transport.

The control of the microkinetics, consisting of micropore diffusion, chemisorption, surface reaction, and desorption, is the task of the catalyst developer and is not discussed further here. If the catalyst is specified together with its microkinetic properties, then reaction conditions (feedstock concentrations, pressure, temperature, and residence time) can be found that lead to optimum yields. The reaction engineer must determine these conditions and ensure that they are maintained in an industrial reactor.

In the case of selectivity-sensitive multistep reactions, any deviation from the optimum values inevitably leads to a decrease in yield. This applies to deviations from the uniform residence time distribution due to

flow dispersion and flow bypass phenomena in the fixed bed, as well as to deviations from uniform reaction conditions in the catalyst as a result of mass transport resistance in the particles and the outer boundary layer [5].

The influence of mass-transport resistance in the particles can only be excluded if the critical reaction rate is substantially lower than the mass transfer velocity. This leads to the need for good external mass transfer (i.e. to a sufficiently rapid flow rate in the packed bed), as well as to short diffusion paths in catalyst particles.

In the case of exothermic reactions the local reaction rate must be controlled and limited by the packed-bed temperature. Temperature control thus plays a predominant role in selective reaction control in general, and in particular in the case of exothermic multistep reactions. Under nonadiabatic conditions, catalysts must therefore be assembled in the fixed bed in such a way as to ensure good heat transport to the heat transfer medium.

A further requirement placed on the catalyst is a low pressure loss. This applies particularly if the conversion in a single pass through the reactor is low, so that a large amount of gas has to be recirculated. It is of prime importance for off-gas purification, in which large off-gas streams must be treated with minimal additional cost.

Finally, the catalyst should be available in a sufficiently high concentration in order to keep the construction volume of the reactor low. The decisive parameters here are the specific external catalyst surface  $a_p$  (= square meters of catalyst surface per cubic meter reactor volume) for reactions controlled by external mass transfer, and the catalyst fraction  $1-\varepsilon$ , where  $\varepsilon$  (= cubic meters of free gas space per cubic meter of reactor volume) is the void fraction of the fixed bed.

The above requirements are to some extent contradictory, which has led to the proposition of a large number of different catalyst shapes and arrangements. However, only a few of these have proved really effective in practical operation. Suitable catalyst forms and arrangements include random packings of spheres, solid cylinders, and hollow cylinders, as well as uniformly structured catalyst packings in the form of monoliths with parallel channels, parallel stacked plates, and crossed, corrugated-plate packets (Fig. 3).

### 10.1.2.1 Random Packings

Industrial fixed-bed reactors are generally operated with a cross-sectional loading  $G_z \geq 1$  kg gas per square meter of reactor cross section per second. This loading

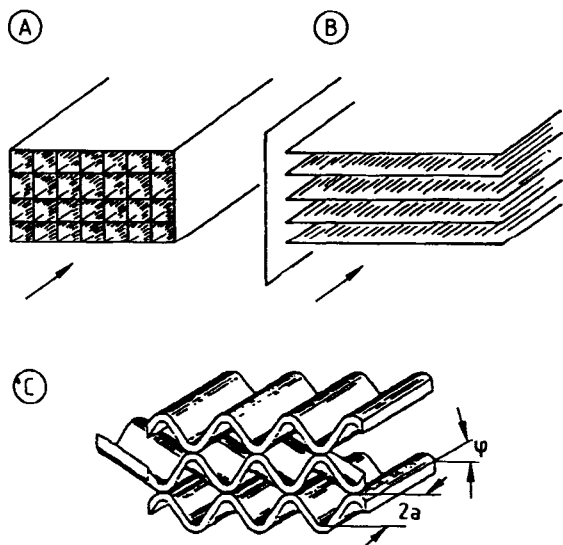


Figure 3. Usual shapes of monolith catalysts. A) Square-channel monolith; B) Parallel-plate monolith; C) Corrugated-plate packing.

The profiles can be calculated from the model equations given in Section A.6.2, under the assumptions made there.

An essential precondition for the establishment of the above mentioned profiles is that the catalyst particle is uniformly exposed over its entire surface to a flow with uniform temperature and concentration. This is, of course, never the case in random packings. Figure 5 gives an image of the local mass transfer distribution around cylindrical or ring shaped particles in a random packing. A test reaction producing dark deposits has been used. The intensity of the dark coloration is thus directly proportional to the local reaction rate of the surface reaction. Since the test reaction is mass transfer controlled, the coloration is also proportional to the local mass transfer, and if the mass transfer and heat transfer are equivalent, also to the local heat transfer [6].

Figure 5 shows that the local conditions in random packings are much more complex than assumed in current single pellet models. But since a fixed-bed reactor contains a large number of particles at the same cross-section, Fig. 4 can be considered a mean value approximation of a process that varies greatly as regards detail. For the same reason, it is inappropriate to compare model predictions of fixed-bed reactor behavior with a few local temperature or concentration measurements. Indeed, a certain degree of averaging is always necessary in the measurement procedure.

The literature contains a number of correlation equations for the mean gas-catalyst mass transfer and heat transfer as a function of gas properties, catalyst geometry, and flow conditions [7, 8]. In practice they play only a minor role for catalyst packings since design and simulation calculations are frequently performed with a model that is quasihomogeneous, at least with regard to temperature. The reason lies in the above-mentioned strong local fluctuations, which make experimental differentiation between the gas temperature and catalyst temperature difficult.

### 10.1.2.2 Monoliths

In contrast to random packings, the external heat and mass transfer in monolith catalysts is much more uniform. Contrary to random packings it may become a limiting factor at high reaction rates. This applies in particular to channel-type monoliths with narrow parallel channels, where the flow is generally laminar under industrial operating conditions. Examples include monolith catalysts with a square-channel cross section for automobile exhaust purification and for the removal of nitrogen oxides from flue gases.

Figure 6 (bottom) shows results of the visualization of the local mass transfer by using the same technique

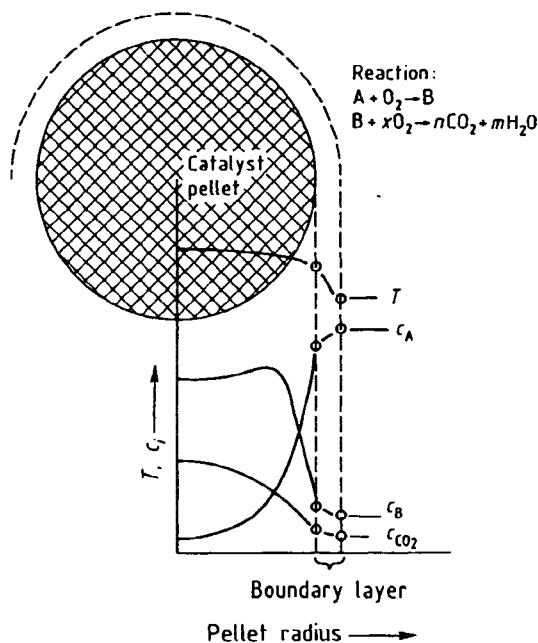


Figure 4. Temperature and concentration profiles for a partial oxidation reaction in a spherical catalyst pellet.

produces a sufficiently strong turbulence in random packings. As a result the external gas-catalyst mass transport resistance is small compared to the transport resistance in the catalyst pores.

However, the thermal conductivity of the catalyst matrix is usually larger than that of the gas. This means that the external gas-catalyst heat transport resistance exceeds the thermal conduction resistance in the catalyst particles. The temperature and concentration profiles established in a spherical catalyst are illustrated for a partial oxidation reaction in Figure 4.

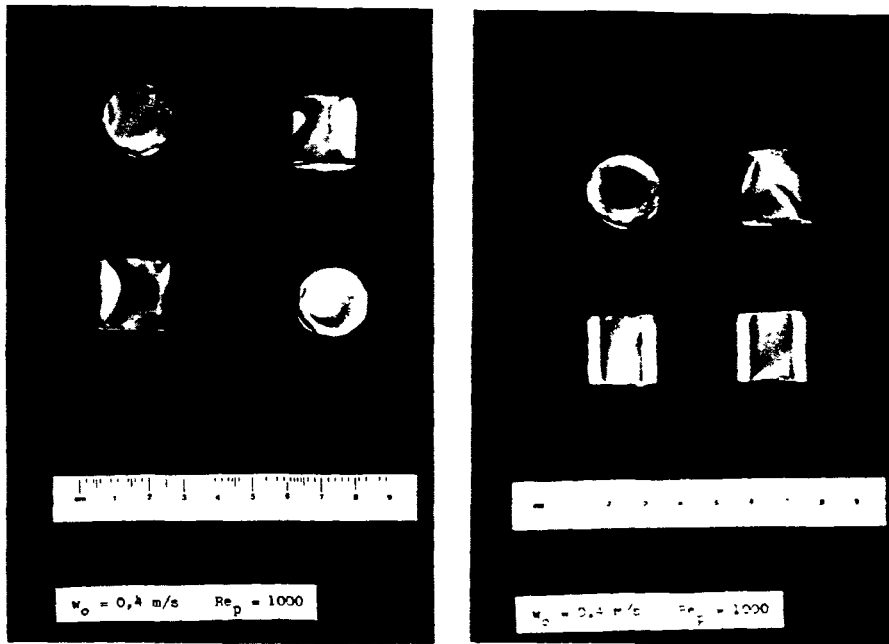


Figure 5. Local mass-transfer distribution at the surface of individual cylindrical or ring-shaped catalyst pellets in a fixed-bed packing.

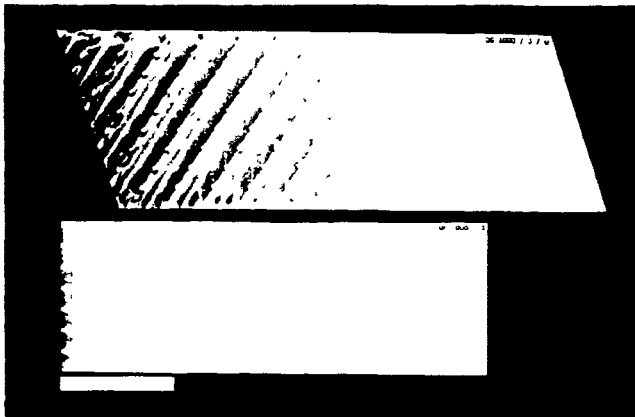
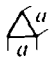
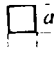
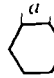
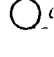
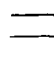


Figure 6. Visualization of mass transfer in monolith structures (flow from left to right). Top: Corrugated packing; bottom: Square duct monolith [9].

as in Fig. 5 [9]. The marked decrease in coloration in the flow direction is mainly the result of the increasing educt consumption in the wall boundary layer, i.e. the build up of the so-called laminar boundary layer. The depletion is particularly pronounced in the corners, since two reaction surfaces meet here. The more acute their enclosed angle, the greater is the depletion in the corner region and the smaller is the contribution of the wall surface to further heat transfer and mass transfer. The efficiency of channel monoliths of equal cross-sectional area but different shape therefore decreases in the sequence: circle, hexagon, rectangle, triangle. This is illustrated in Table 1, which gives the asymptotic dimensionless mass transfer and heat transfer co-

Table 1. Asymptotic dimensionless laminar flow heat or mass transfer coefficients  $Nu = \alpha_w \cdot d_h / \lambda_G$  (constant wall conditions) and Fanning friction factor  $f$  for pressure drop  $\Delta p = 2f(\eta Z_L / d_h^2) v_G$  for ducts of different cross section [10].

Geometry	$Nu$	$f$	$d_h$
	2.47	13.33	$2a/\sqrt{3}$
	2.98	14.23	$a$
	3.34	15.05	$2\sqrt{3}a$
	3.66	16.00	$a$
	7.54	24.00	$2a$

efficients for tubes of the above cross-sections [10]. For more accurate calculations the radially and axially variable velocity, concentration, and temperature profiles must also be taken into account [11].

In the following, the term monolith will be restricted to regular packings with straight parallel channels. In addition, a large number of regularly structured packings have been proposed in the past. Out of them only corrugated-plate packings have obtained some indus-

trial importance. A design also frequently used in parallel plate heat exchangers, as column packings and static mixers (Sulzer type SMV), is shown in Fig. 3C.

In contrast to the monolith types discussed so far, the flow conditions in corrugated-plate packings are turbulent under normal industrial velocities. The uniformity of the mass transfer distribution depends on geometrical parameters (wave form, amplitude, wavelength, angle of incidence) [12]. The transfer coefficients are considerably higher than those of laminarly traversed channel monoliths (Fig. 6 (top)), but the pressure loss is also increased. These structures offer considerable advantages for convective heat transport transverse to the flow direction and for transverse mixing, which are discussed in more detail in the following sections. The differences in external heat and mass transfer between a square channel monolith and a corrugated-plate packing have been visualized in Fig. 6 for similar flow conditions. In case of the corrugated plates the decrease in coloration results from a total consumption of the coloring component. In case of the monolith channels the concentration of the coloring component is only reduced in the laminar boundary layer and a substantial amount leaves the monolith with the bulk fluid.

### 10.1.2.3 Gas Flow and Pressure Drop in Fixed Beds

Conventional industrial catalyst forms differ considerably as regards pressure loss. For example, for equal mean dimensions and the same void fraction  $\varepsilon$ , random packings generally have a considerably higher pressure loss than monolith structures, and among these, corrugated structures have a higher pressure loss than monoliths with straight parallel channels. External catalyst mass and heat transfer are strongly correlated with the pressure loss. For reasons of energy demand, the catalyst form for a given process should be chosen to combine the required mass and heat transport with the lowest pressure loss.

The Hagen–Poiseuille equation is used to calculate the pressure loss in laminarly traversed monolith channels (for notation see List of Symbols)

$$\Delta p = \frac{32 \cdot \eta Z_L v_G}{d_h^2} \quad (1)$$

The pressure loss of randomly packed tubes can be described either by means of a pressure loss coefficient  $\zeta$  and the pressure drop equation

$$\Delta p = \zeta \cdot \frac{\rho_G}{2} \cdot v_G^2 \quad (2)$$

or by the Ergun equation:

$$\Delta p/L = f_1 v_G + f_2 v_G^2 \quad (3)$$

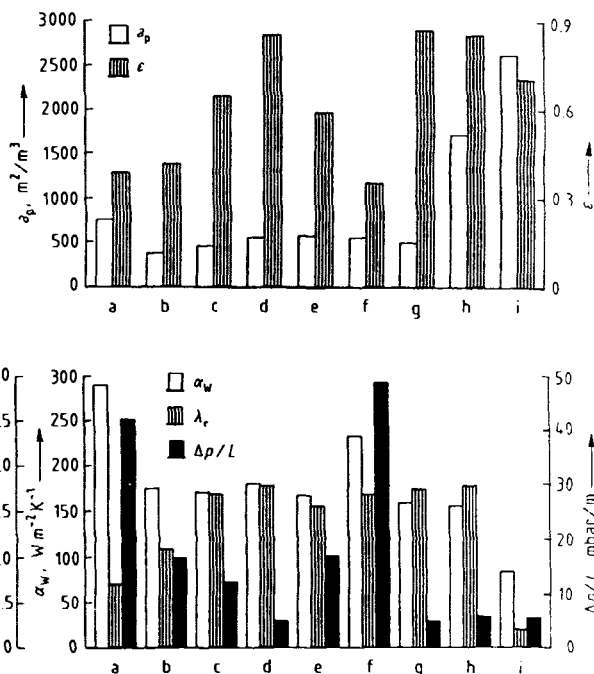


**Figure 7.** Specific outer surface area  $\alpha_p$ , void fraction  $\varepsilon$ , effective-radial heat conductivity  $\lambda_r$ , wall heat transfer coefficient  $\alpha_w$ , and pressure drop  $\Delta p$ , for different packings in a tube of 50 mm internal diameter and an air mass-flow velocity  $G_z = 1 \text{ kg m}^{-2} \text{ s}^{-1}$  at ambient conditions. a) Glass spheres,  $d_p = 5 \text{ mm}$ ; b) Glass spheres,  $d_p = 10 \text{ mm}$ ; c) Raschig rings, ceramic,  $d_o = 10 \text{ mm}$ ,  $d_i = 6 \text{ mm}$ ,  $\ell = 11 \text{ mm}$ ; d) Raschig rings, stainless steel,  $d_o = 10 \text{ mm}$ ,  $d_i = 9 \text{ mm}$ ,  $\ell = 11 \text{ mm}$ ; e) Hollow ceramic cylinders of irregular length,  $d_o = 9 \text{ mm}$ ,  $d_i = 4.5 \text{ mm}$ ,  $\ell \approx 15 \text{ mm}$ ; f) Full ceramic cylinders of irregular length,  $d_o = 5 \text{ mm}$ ,  $\ell = 11 \text{ mm}$ ; g) Crossed corrugated metal-plate packing (Sulzer Katapak\*), wide channels; h) Crossed corrugated metal-plate packing, narrow channels; i) Automotive exhaust monolith, Cordirith, square channels,  $d = 0.9 \text{ mm}$ .

where

$$f_1 = 150 \cdot \eta \cdot \frac{(1 - \varepsilon)^2}{\varepsilon^3 \cdot d_p^2} \quad (4)$$

$$f_2 = 1.75 \cdot \rho \cdot \frac{(1 - \varepsilon)}{\varepsilon^3 \cdot d_p} \quad (5)$$

Thus the pressure drop depends very strongly on the void fraction  $\varepsilon$  of the packing. Of the standard forms for packed catalysts, hollow cylinders of thin wall thickness ( $\varepsilon \approx 0.6-0.8$ ) are therefore preferred over spheres ( $\varepsilon \approx 0.37-0.4$ ) and solid cylinders ( $\varepsilon \approx 0.35$ ).

The pressure loss coefficient  $\zeta$  (eq. 2) can be determined for typical packing forms, for example, according to [13]. A comparison of different catalyst packings with respect to pressure drop is contained in Fig. 7.

The flow into a fixed-bed reactor is generally achieved by means of a feed pipe and a distribution hood (Fig. 1). It is essential for a good operation that the gas flow is distributed evenly over the whole fixed bed or tube bundle. A uniform flow distribution can be easily ob-

tained if the pressure drop in the fixed bed is substantially larger than in the entrance and exit hoods. This is not the case with monolith reactors with lamina-ly traversed parallel channels. They need special care in the design of the hoods or must be equipped with static mixers to avoid nonuniform flow patterns [14].

A related problem occurs in multitubular fixed-bed reactors with random packings if different tubes have different pressure drop due to nonuniform packing or different batches of catalysts. The resulting differences in throughput may cause the danger of reaction runaway in tubes of higher pressure drop and low throughput [15, 16]. Great care needs therefore to be taken to adjust the pressure drop of all tubes of a multitubular reactor for highly exothermic reactions to the same level.

A particular case of flow nonuniformity is inherent to all randomly packed tubes (Fig. 8). This is due to the fact that the catalyst pellets make only point contact with the wall, whereas they overlap and cross over one another inside the packing, thereby reducing the free volume and hence the velocity. The conditions for a spherical packing are illustrated schematically in Figure 8. The radially varying empty space distribution and velocity distribution must be taken into account in detailed reactor calculations, as well as in the determination of accurate heat transport parameters [17, 18]. This will be addressed in the next section.

Standard catalysts have a sufficiently dense structure and all convective transport is directed around the pellets or separated through the walls of the monolith. In a sequence of recent publications [19, 20] macroporous catalyst pellets with high permeability of the reacting gas have also been proposed. In these pellets part of the diffusional resistance is overcome by convection through the pellets which may increase conversion and selectivity (see also Section 10.1.3.5).

#### 10.1.2.4 Heat Transfer in Catalyst-Filled Tubes

With nonadiabatic reaction control, heat must be transported through the fixed bed to the integrated heat exchange surfaces. At the usual mass flow rates of  $G_z \geq 1 \text{ kg m}^{-2} \text{ s}^{-1}$ , this heat transport takes place mainly by convection, i.e. the fixed bed must allow for a cross flow transverse to the main flow direction. Monolith structures with straight parallel channels are thus unsuitable for nonadiabatic reaction control.

In catalyst packings transverse flow components are automatically established as a result of the nonuniform arrangement and the twisted flow around the pellets. Hollow and full cylinders with a length-to-diameter ratio of 1:3 are particularly effective in this respect. Despite the fact that radial heat transport takes place

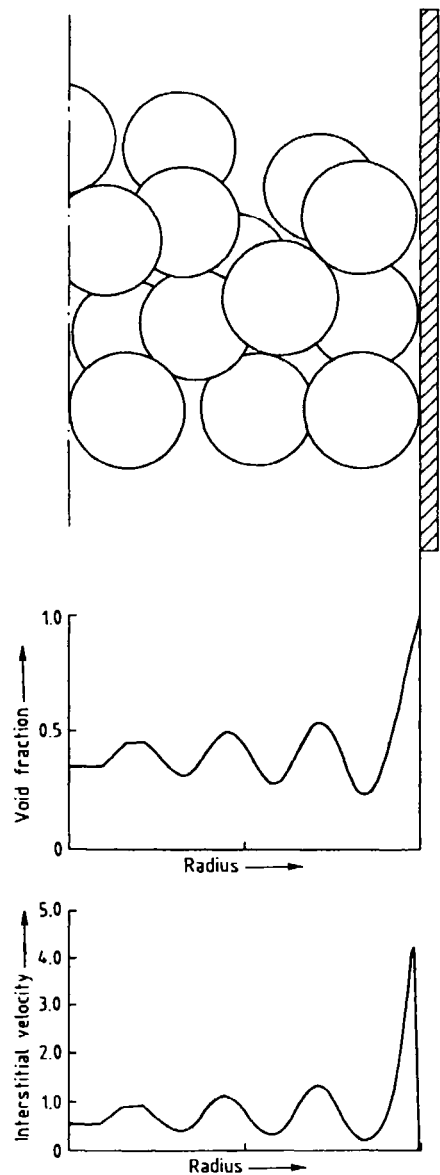


Figure 8. Radial distribution of void fraction and axial flow velocity in a tube packed with spheres.

mainly by convection, it is formally described by means of a so-called effective thermal conductivity  $\lambda_r$ , transverse to the flow direction.

In addition, the heat transport at the boundary between the fixed bed and the heat exchange surface is also decisive for the heat exchange. The latter heat transport is generally described by a wall heat-transfer coefficient  $\alpha_w$ . It lumps the complex interplay between convective flow at the tube wall and conduction transport by contact between the fixed bed and the heat exchange surface. Heat transport in packed tubes has been investigated and discussed in detail [8, 21]. How-

ever, the correlations for  $\alpha_w$  and  $\lambda_r$  given in the literature do not adequately take account of the actual velocity distribution in packed tubes, as depicted in Fig. 8.

Existing correlation equations for calculating the heat transport parameters were obtained from heating or cooling experiments without reactions and assuming plug flow; they therefore permit only a semiquantitative evaluation. This is adequate for qualitative comparison of catalyst structures.

### 10.1.2.5 Comparison of Different Catalyst Shapes

Such a comparison is given in Fig. 7 where the two heat transfer parameters  $\lambda_r$  and  $\alpha_w$  plus the external catalyst surface  $a_p$ , the bed void fraction  $\varepsilon$  and the pressure drop  $\Delta p$  are given for a selection of different random and regular catalyst packings in a tube of 50 mm internal diameter and a mass flow velocity of  $G_z = 1 \text{ kg}/(\text{m}^2 \text{ s})$ .

The dimensions of the packing bodies were chosen so that their specific external surface area  $a_p$  is ca.  $500 \text{ m}^2/\text{m}^3$ . Under these conditions hollow, thin-walled cylinders have clear advantages over other packing forms, exhibiting the lowest pressure loss and the highest thermal conductivity. Only as regards wall heat transfer are they inferior to spheres or cylinders. However, good wall heat transfer is apparently less decisive from a reaction engineering viewpoint than good radial thermal conductivity, since the former can be compensated by an appropriate temperature profile of the heat transfer medium, whereas the radial thermal conductivity directly influences the uniformity of the reaction conditions over the tube cross section. On the other hand, solid cylinders with a large length-to-diameter ratio have good heat transport values, but at the cost of a very high pressure loss.

Monolith forms can have very high specific surfaces combined with a very low pressure loss. Monoliths with straight, parallel channels, such as used for automobile exhaust control have only very poor radial heat transport properties. Crossed corrugated structures are considerably more favorable for isothermal reaction control. They have a very high radial thermal conductivity which is almost independent of the specific surface area; the latter can be varied over a wide range by means of the channel dimensions.

It must be remembered that with crossed corrugated structures, convective radial heat transport occurs only in one plane perpendicular to the main flow direction. In addition, the flow behavior in tubes of circular cross section is rather nonuniform over the circumference, which is why it is advantageous to arrange short packing sections in series, each section being displaced by  $90^\circ$ . The heat transport parameters in Figure 7 were determined for structures arranged in this way.

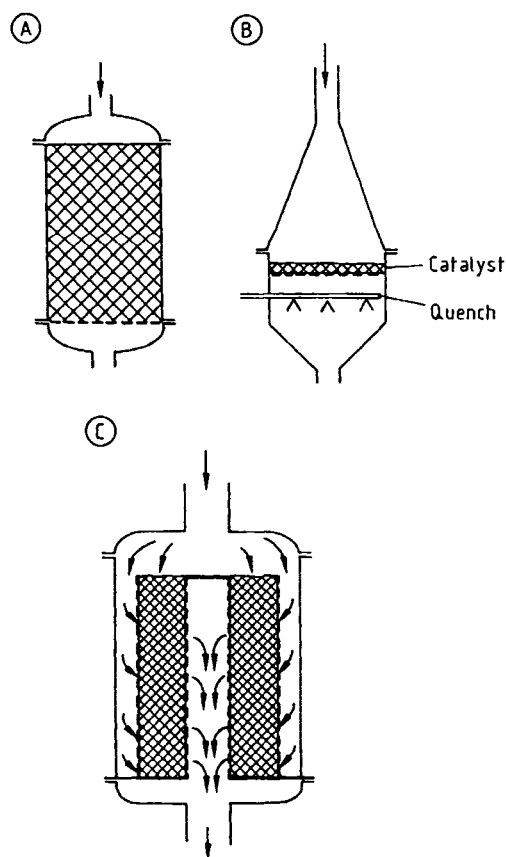


Figure 9. Main design concepts for adiabatic reactors. A) Adiabatic packed-bed reactor; B) Disk reactor; C) Radial-flow reactor.

A general problem in the use of monolith structures in reactor tubes is incomplete wall contact. Since individual tubes of multitubular reactors always have a diameter tolerance of ca. 1 mm and interlocking of the structure with the tube wall must be avoided, the bypass of flow at the wall is even greater than with random packings. Up to now there have been no publications of the magnitude and effects of this bypass.

## 10.1.3 Types of Fixed-Bed Reactors

### 10.1.3.1 Adiabatic Reactors

Adiabatic fixed-bed reactors constitute the oldest fixed-bed reactor configuration. In the simplest case they consist of a cylindrical jacket in which the catalyst is loosely packed on a screen support and is traversed in the axial direction (Fig. 9A). To avoid catalyst abrasion by partial fluidization, random catalyst packings are always traversed from top to bottom. If fixed-beds composed of monolith catalyst sections are used, the flow direction is arbitrary.

It can be shown [14] that the requirement for a low pressure loss leads to a fixed bed of large diameter and

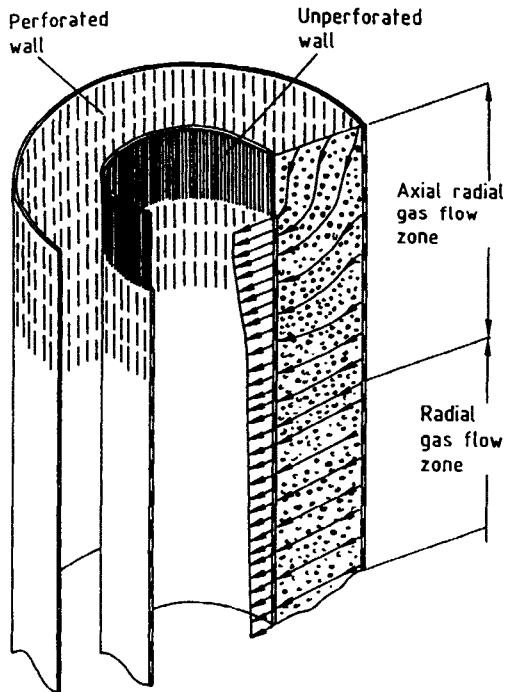


Figure 10. Upper bed closure in a radial-flow reactor [22].

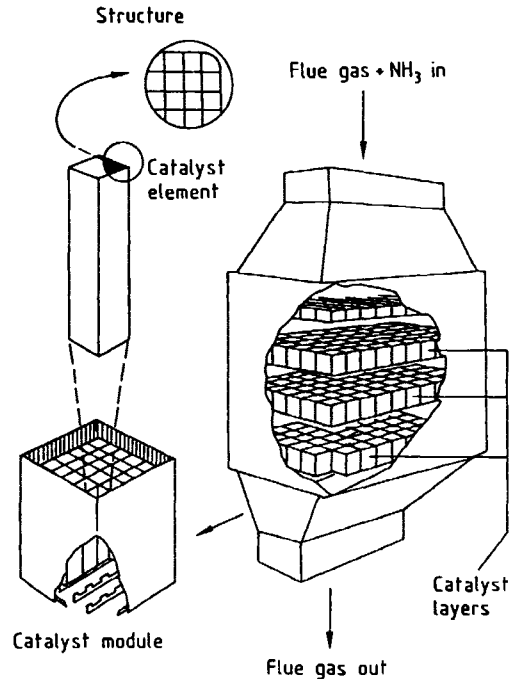


Figure 11. Reaction chamber for removal of nitrogen oxides from power station flue gases [23].

low height (Fig. 9B). Such an arrangement (disk concept) is used particularly when very short residence times, followed by direct quenching of the reaction, are required. Examples include ammonia oxidation in nitric acid production and oxidative dehydrogenation on silver catalysts (e.g., synthesis of formaldehyde by dehydrogenation of methanol). In the first case the "fixed bed" consists of several layers of platinum wire gauze, and in the second case, of a porous silver layer several centimeters in height. The bed diameters can be up to several meters.

On account of the difficulties involved with obtaining uniform flow as well as for structural reasons, the disk concept is limited to small catalyst volumes. The radial flow concept (Fig. 9C) is used where large amounts of catalyst are involved. The catalyst packing is accommodated in the space between two concentric screen rings or perforated plate rings, and is traversed radially, either from the inside to the outside or from the outside to the inside. This design is particularly suitable for large catalyst volumes as well as for operation at elevated pressure, since at moderate reactor diameters the catalyst volume can be varied over a wide range by altering the reactor length, without affecting the flow-through length of the packing.

A critical feature of packed radial-flow reactors is the shape of the upper bed closure. A simple horizontal covering is not practicable since a gap through which unreacted gas can pass is then formed due to the unavoidable settling of the packing. The arrangement

shown in Figure 10 has proved effective since it produces mixed axial and radial flow through the bed in the upper bed closure. The required geometrical shape must be determined by simulation of the local two-dimensional flow through the packing [22].

Monolith catalysts with straight, parallel channels are particularly well suited for adiabatic reactors since they allow for a low pressure drop and provide a high specific outer surface area. Since monolith catalysts are usually produced with a rectangular cross section, the fixed bed is constructed by arranging these individual monoliths in rows in the form of a large "box". Conventional DENOX reactors for removing  $\text{NO}_x$  from power station flue gases are therefore designed as rectangular chambers (Fig. 11). The catalyst is often arranged in the form of several layers in series, the spaces between the individual layers permitting cross-mixing, so that the influence of nonuniform flow as well as any possible local blockage of the next layer can be compensated to some extent.

Reference is made in Section 10.1.2.3 to the importance of uniform flow into and through adiabatic fixed-bed reactors. This is not easy to achieve, particularly with low-pressure-loss monolith reactors, and requires a careful design of the inflow hood. On account of the low pressure loss, unfavorable flow conditions in the outflow hood may also affect the flow behavior through the catalyst bed.



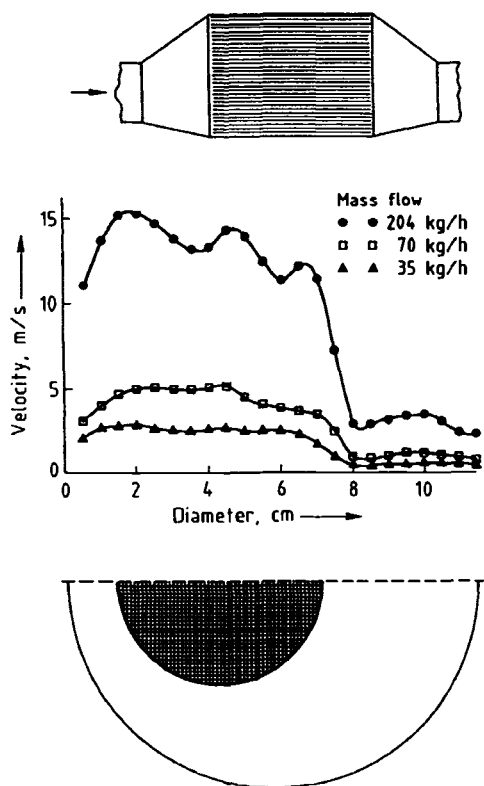


Figure 12. Velocity distribution in an industrially housed automobile catalyst [14].

Figure 12 shows the velocity distribution in front of the monolith inlet for an industrially housed automobile catalyst [14]. Since the flow cannot follow the sudden widening of the inlet funnel, one third of the total cross section is traversed at a velocity that is roughly three times the mean velocity. It can be estimated that, with uniform flow through the catalyst, half the catalyst volume would be sufficient for the same mean conver-

sion. Bends in the feedpipe can lead to swirl-type flow components and thus also contribute to nonuniform flow.

Purely adiabatic fixed-bed reactors are used mainly for reactions with a small heat of reaction. Such reactions are primarily involved in gas purification, in which small amounts of noxious components are converted. The chambers used to remove  $\text{NO}_x$  from power station flue gases, with a catalyst volume of more than  $1000 \text{ m}^3$ , are the largest industrial adiabatic reactors, and the exhaust catalyst for internal combustion engines, with a catalyst volume of ca. 1 L, the smallest. Typical applications in the chemical industry include the methanation of traces of CO and  $\text{CO}_2$  in  $\text{NH}_3$  synthesis gas, as well as the hydrogenation of small amounts of unsaturated compounds in hydrocarbon streams. The latter case requires accurate monitoring and regulation when hydrogen is in excess, in order to prevent complete methanation due to an uncontrolled temperature runaway.

### 10.1.3.2 Multistage Reactors

In the majority of fixed-bed reactors for industrial synthesis reactions, direct or indirect supply or removal of heat in the catalyst bed is utilized to adapt the temperature profile over the flow path as far as possible to the requirements of an optimal reaction pathway. Here a clear developmental trend can be observed.

It started with the adiabatic reactor (Fig. 13A), which on account of the adiabatic temperature change could only be operated to give a limited conversion. Higher conversions were achieved at the same mean temperature level when several adiabatic stages were introduced, with intermediate heating or cooling after each stage. The simplest form involves injecting hot or cold gas between the stages (Fig. 13B). For a constant

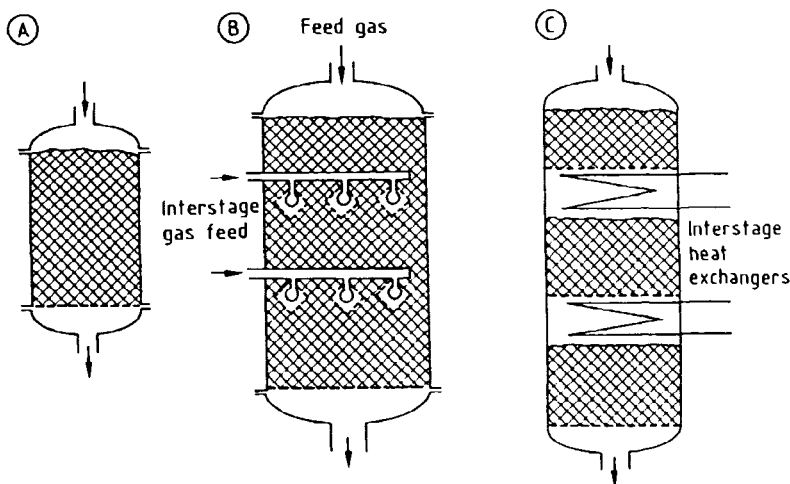
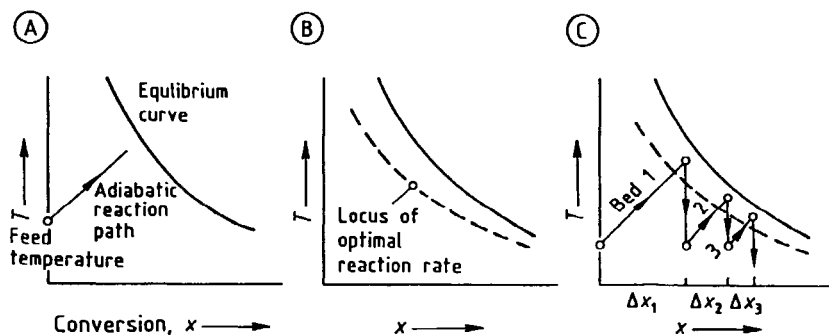


Figure 13. Development of fixed-bed reactors. A) Single-bed adiabatic packed-bed reactor; B) Adiabatic reactor with interstage gas feed (ICI concept); C) Multibed adiabatic fixed-bed reactor with interstage heat exchange.



**Figure 14.** Equilibrium limitation of exothermic reactions. A) Equilibrium conversion as a function of temperature; B) Optimum reaction rate curve; C) Improvement of conversion by multiple beds with interstage cooling.

tube diameter, the main disadvantages of this temperature control strategy are cross-sectional loading, which increases from stage to stage, and the mixing of hot and cold streams, which is energetically unfavorable. The composition is changed by injection, which can have a positive or negative effect on the desired reaction.

The next development was the replacement of injection cooling by interstage heat exchangers, through which the required or released heat of reaction is supplied or removed (Fig. 13C). More stringent requirements led to the development of fixed-bed reactors where the heat exchange surface is integrated in the fixed bed. This type of reactor will be considered in the next section.

Adiabatic multistage fixed-bed reactors with intermediate cooling or heating are nowadays used particularly where the reaction proceeds selectively to give a single product but is limited by the equilibrium conditions. Intermediate cooling or heating is used to change the gas temperature in the direction of higher equilibrium conversion. Typical examples include the synthesis of ammonia, sulfur trioxide, and methanol. In these exothermic reactions the equilibrium conversion to the target product decreases with increasing temperature, as shown in Figure 14A. For a given conversion  $x$ , a temperature can therefore be found at which the reaction rate to the target product becomes a maximum. This temperature must be below the equilibrium temperature but not so low that the reaction becomes too slow for kinetic reasons. The points obtained in this way can be joined to form an optimal reaction rate curve (Fig. 14B).

Since, in the case of an adiabatic reaction the temperature increases linearly with the achieved conversion  $\Delta x$  according to the equation

$$\Delta T_{ad} = -\frac{\Delta h_R \cdot c_o}{\rho_G \cdot c_{pG}} \cdot \Delta x \quad (6)$$

each adiabatic reaction pathway of an exothermic reaction lies on a straight line of gradient  $\Delta T/\Delta x$  (see

Fig. 14A). A reasonable reaction pathway for a multistage adiabatic reaction can therefore be composed of the straight lines of an adiabatic bed followed by the vertical lines of indirect intermediate cooling (Fig. 14C).

The kinetically optimum reaction pathway with the smallest required catalyst volume results when the trajectory follows, in a large number of small steps, the line of maximum reaction rate. In practice, the apparatus and equipment expenditure involved in a large number of stages must be weighed up against the savings in catalyst. Conventional multistage reactors for this class of reaction therefore have three to five stages. Figure 15 shows the layout of an ammonia synthesis reactor designed on this basis. For structural reasons the heat exchanger between the inflow and outflow is incorporated in the lowest part of the pressure casing. The reaction gas then flows upward in the annular gap between the pressure casing and the fixed beds. There it is further heated and at the same time protects the pressure-bearing structural components against excessively high fixed-bed temperatures. The three adiabatic fixed-beds are traversed from top to bottom, part of the heat of reaction being utilized to generate steam in the two intermediate heat exchangers. To start up the cold reactor, hot gas must be added to the uppermost bed, for example through an external startup preheater.

Industrial adiabatic multistage reactors often differ in many details from Figure 15, although they are of a comparable basic design. For example, radially instead of axially traversed beds can achieve a smaller pressure loss with a more favorable structural arrangement; heat exchange with the cold feedstock can be effected by heat exchange surfaces integrated in the first catalyst bed; or a cold gas quench can be used to achieve additional temperature regulation.

Modern, adiabatic multistage reactors may thus become so complex that the question arises whether a

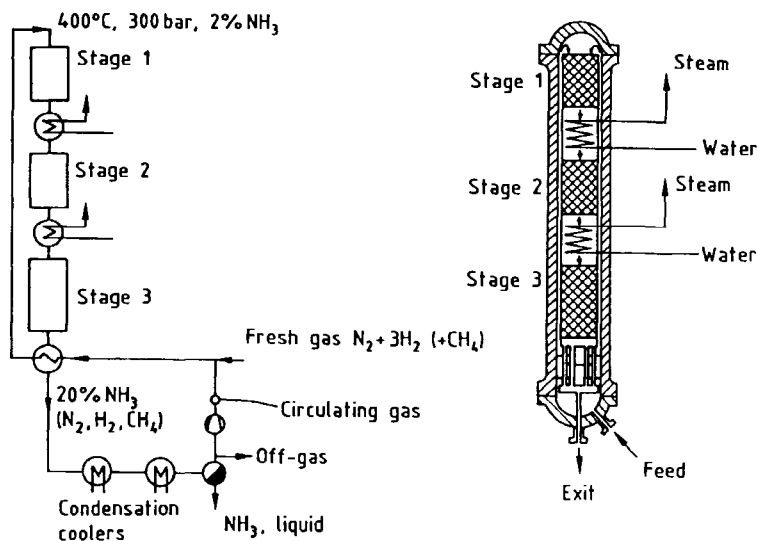


Figure 15. Schematic of a multistage reactor for ammonia synthesis.

multitubular design does not represent the more favorable alternative. The required heat exchange surface area in the case where heat exchange is integrated in the fixed bed is smaller than in the case of free gas flow on account of the positive effect of the catalyst packing. Furthermore, it does not involve any additional pressure loss, and the optimum reaction rate curve (Fig. 14B) can be better approximated by controlling the cooling temperature profile (see Section 10.1.3.3.C) than by a stepwise temperature reduction.

On the other hand, a multistage arrangement may be considered for structural, operating technology, or kinetic reasons in the following cases:

1. If, in the case of large single-train plants, subdivision into several individual items of apparatus is necessary for reasons of transport or construction.
2. If a catalyst must be replaced in individual stages at different times on account of different catalyst deactivation.
3. If a gradual addition of reactant has kinetic advantages compared to the total addition to the feed (here a suitably designed intermediate heat exchanger ensures a uniform distribution and mixing within the reaction gas stream).
4. If the intermediate stages are used to extract a limiting product in the case of equilibrium-limited reactions; an example is the intermediate absorption of  $\text{SO}_3$  before the last stage of the  $\text{SO}_3$  synthesis.
5. With reaction temperatures above  $300^\circ\text{C}$  intermediate cooling can still be performed directly with boiling water, whereas in a fixed bed a high-temperature heat-transfer medium must be used as coolant (see next section).

### 10.1.3.3 Fixed-Bed Reactors which are Cooled or Heated Through the Wall

The development of reactors in which the heat exchange surfaces are integrated in the fixed bed occurred in parallel with the development of multistage adiabatic reactors with intermediate heating or cooling. Here the main aim is to supply or remove the heat of reaction as close as possible to the reaction site.

The multitubular fixed-bed reactor (Fig. 1B) constitutes the oldest and still predominant representative of this class. The catalyst packing is located in the individual tubes of the tube bundle. The heat-transfer medium is circulated around the tube bundle and through an external heat exchanger, in which the heat of reaction is supplied or removed (Fig. 16). Whereas with endothermic reactions circulating gas can be used as heat transfer medium, for strongly exothermic reactions exclusively liquid or boiling heat transfer media are used. Only in this way can the catalyst temperature (e.g., in the case of partial oxidations) be held in the narrow temperature range necessary for selective reaction control.

Initially, the integration of heat exchange in the fixed bed was utilized to ensure as isothermal a reaction as possible, which is why reactors of the type shown in Figure 1B are also commonly termed "isothermal reactors". They are characterized by reaction tubes of 20–80 mm internal diameter and a carefully designed flow control of the liquid heat transfer medium, with largely constant heat transfer conditions and maximum temperature changes of the heat transfer medium throughout the tube bundle of a few degrees.

The latest concepts are aimed at establishing a freely selectable (within limits) optimum temperature profile

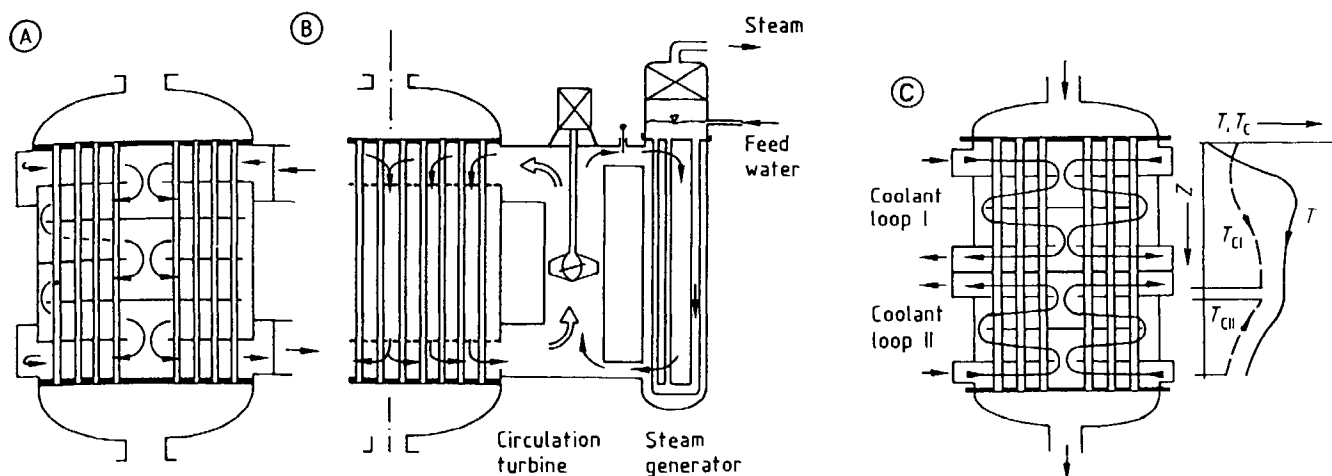


Figure 16. Heat transfer medium control in tube-bundle fixed-bed reactors. A) Cross flow; B) Parallel flow; C) Multiple cooling sections.

over the tube length. This requires complex heat transfer medium control with several sections and temperature levels (Fig. 16C).

Strongly exothermic reactions like partial oxidations can only be carried out in fixed-bed reactors if the catalyst temperature is controlled in a narrow optimal window. This can be achieved if the following requirements are fulfilled:

- Large heat transfer areas must be available per catalyst volume.
- The temperature of the heat transfer medium has to be close to the desired catalyst temperature.
- A sufficiently large mass flow velocity of the reaction gases has to ensure good heat transport from the packing to the heat exchange surface.

With exothermic equilibrium reactions and endothermic reactions these requirements are less stringent since these reactions cannot run away, although here it has been recognized that a tight and uniform temperature control over the reactor cross section is also of advantage.

#### A Heat Transfer Media

The second of the above requirements presupposes an assortment of heat transfer media that covers the whole temperature range of interest for gas-phase reactions in fixed-bed reactors. It is convenient to distinguish between gaseous, liquid, and vaporizing heat transfer media. Gaseous heat transfer media in the form of hot flue gases are used in the temperature range above 500 °C exclusively to supply heat for endothermic reactions.

Conversely, vaporizing heat transfer media are used exclusively to remove heat from exothermic reactions. Whereas formerly petroleum fractions such as kerosene (e.g. in ethylene oxide synthesis) were more widely

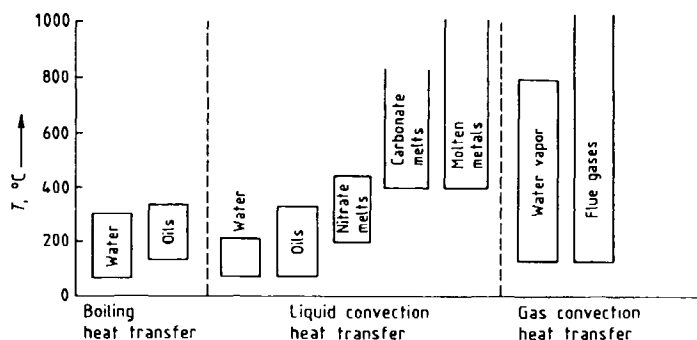


Figure 17. Application ranges for common heat transfer media.

used, they have now been largely replaced by boiling water on account of their flammability, lower heat of vaporization, and the need to use the heat of reaction for the production of steam in a downstream condenser/heat exchanger. Depending on the saturated vapor pressure, the temperature range from 100 to 310 °C (100 bar) can be covered with boiling water. In this range it is the preferred heat transfer medium if an isothermal cooling temperature is required.

Locally variable cooling temperature profiles can be established most easily with liquid heat transfer media that do not vaporize in the intended operating range. In order to avoid cavitation, pressurized water should be used only up to ca. 220 °C; heat transfer oils cover the temperature range up to 300 °C, while above this temperature salt melts are now used exclusively in reaction technology [4]. The temperature ranges of possible heat transfer media are compared in Figure 17.

In addition to the thermal stability, the energy required to circulate a heat transfer medium (given as energy per unit amount of transported heat) is an im-

portant criterion of choice. This has been treated in more detail in [4, 24]. The discussion shows that pressurized water is the ideal heat transfer medium up to 220 °C. For higher temperatures molten salts have replaced the previously more commonly used heat transfer oils. Salt melts cover a larger temperature range and have the particular advantage over oils that they are incombustible. The potential danger of a relatively large amount of hot salt melt obviously exists, but is reliably dealt with by experienced reactor construction companies. Special nitrate melts (HITEC®) can be used in the temperature range 200–500 °C. Gradual decomposition begins above this temperature, which can accelerate violently above 600 °C. Access of organic components to the melt (nitrate decomposition) and of water (steam explosion) must be excluded [25]. New salt melts, for example, based on carbonates, are being developed for the temperature range of 400–800 °C. In this case it is not so much the thermal stability of the molten salt but rather the corrosion of the reactor materials that presents problems.

Gases are the only heat transfer media usable over the entire temperature range, but because of their low density they have an unfavorable heat transport behavior. To achieve the same heat transfer at the same temperature difference, the necessary pumping energy exceeds the respective value of liquids by a factor of 100–200 [4]. They are therefore used exclusively as flue gases to supply heat at high temperatures. However, large temperature differences between the heat transfer medium and the reactor wall, with possible adverse effects on the uniformity of the heat supply, must then be accepted.

## B Design Concepts

As with adiabatic reactors, a principle task of reactor development is to produce uniform reaction conditions over the whole reactor cross section and maintain such conditions during the entire operating time. This involves the conditions in the catalyst packing (residence time, catalyst concentration and activity, heat transport) and in the heat transfer medium circuit (throughput, temperature, heat transfer). When liquid or vaporizing heat transfer media are used, the heat transfer coefficients are usually one order of magnitude greater than those on the catalyst side, which facilitates the task as regards the heat transfer medium. On the other hand, with strongly exothermic, selectivity-sensitive reactions (especially partial oxidations), a temperature constancy of the heat-transfer medium of ca. 1 °C is often required. This leads to a high energy requirement for circulation and necessitates careful design and control of the heat transfer medium circuit.

Tubular reactors of the type shown in Figure 16 have been in use longest and have been furthest developed. In the case of a vaporizing heat-transfer medium an

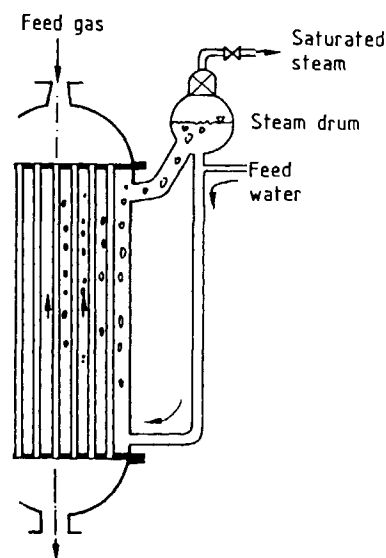
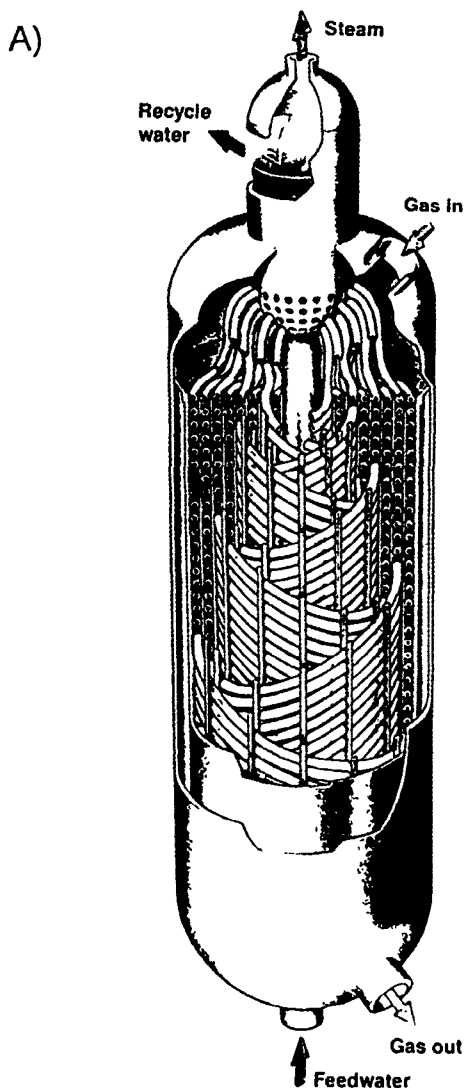


Figure 18. Multitubular reactor with boiling water cooling.

arrangement as shown in Fig. 18 is generally chosen, in which the liquid heat transfer medium surrounds the stationary tube bundle. The rising vapor bubbles escape through the ascending pipe into a vapor drum, where they are separated from the liquid. A circulation flow is established due to the difference in density in the downpipe (pure liquid) and in the reactor jacket, which means that circulating pumps are generally not required. The heat transfer medium temperature is regulated via the vapor pressure through the valve in the steam drum.

Apart from the type of multitubular reactor shown in Figure 18, other multitubular reactors are sometimes used in which the catalyst bed is arranged around the tubes and the heat transfer medium flows through the tubes (Fig. 19B). An interesting development has been introduced by Linde (Fig. 19A): the tube bundle is composed of counterwound spirals in which upwardly flowing water is evaporated. The tubes run into a vertical vapor drum located at the reactor head. The tube bundle is connected to a central downpipe at the bottom so that, as in the arrangement in Fig. 18 a natural circulation of the evaporating water is established. Advantages in construction and in the heat transfer from the reaction gas to the tubes of the bundle are claimed for this design [27].

Circulation systems with parallel and crossed co-current or countercurrent flow of the heat transfer medium (Fig. 16) are commonly employed for liquid heat transfer media. The main part of the heat transfer medium is generally circulated with a high-capacity pump in order to achieve uniform heat exchange conditions. A partial stream is passed through a heat exchanger for supplying or removing the heat of reaction. The desired heat transfer medium temperature is at-



tained by regulating this partial stream. With exothermic reactions the heat exchanger is normally a steam generator which produces saturated steam at a pressure corresponding to a boiling point of 30–80 °C below the minimum cooling temperature.

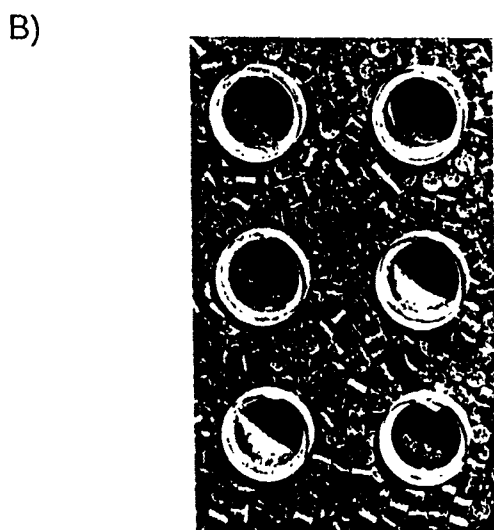
Apparatus construction companies specializing in these reactors have developed a detailed and comprehensive know-how as regards flow control of the heat transfer medium [28, 29]. This concerns the uniform supply and removal of the heat transfer medium, which generally takes place via external annular channels, as well as the flow control within the reactor. Some recent publications illustrate the major differences in the behavior of different tube sections that can arise due to an inadequate design and layout of the heat transfer medium circuit [30–32].

### C Reaction Control Strategies

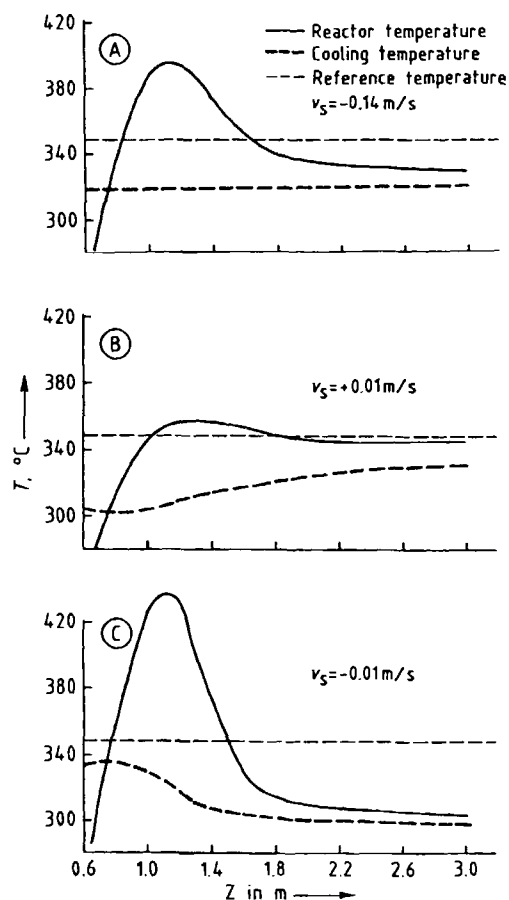
The conversion and selectivity of the reaction can be decisively influenced by the design and the operation of the heat transfer circuit. The most obvious, although technically most complex solution, is to arrange different heat transfer circuits so as to achieve a stepwise approximation of an optimum temperature profile. The purposeful utilization of the temperature change of the heat transfer medium flowing through the reactor is technically simpler, and will be discussed here in connection with cocurrent or countercurrent cooling of a fixed-bed reactor with an exothermic reaction.

Figure 20 shows temperature profiles for three different ways of controlling the cooling stream in a partial oxidation reaction. If the coolant is circulated so fast that its temperature in the reactor scarcely changes, then its flow direction is irrelevant and a temperature profile with a pronounced temperature maximum becomes established; this is typical for strongly exothermic reactions (Fig. 20A). If the coolant is circulated in cocurrent and its velocity is chosen so that it becomes noticeably hotter over its path, an almost isothermal temperature behavior can be achieved (Fig. 20B). This is because the reactive gas at the inlet is in contact with the coldest coolant and the cooling temperature rises in step with the consumption of the reactants, so that the reaction rate remains virtually constant over a fairly long section [33–35, 40].

The stabilizing effect of cocurrent cooling has hardly been exploited up to now in industrial reactors. This may be due to the fear that, at the required low flow velocity (in the example of Fig. 20B,  $v_c = 0.01$  m/s), heat transfer will be inadequate and natural convection will occur in the cooling jacket. However,  $v_c$  describes the mean coolant velocity parallel to the tube axis. With a cross-cocurrent flow of the coolant, the actual flow velocity may in fact be substantially larger, de-



**Figure 19.** A) Design concept of the Linde isothermal reactor for methanol synthesis; B) Cut through the tube bundle surrounded by catalyst pellets (from [26]).



**Figure 20.** Influence of the coolant flow direction and flow velocity  $v_s$  on the reaction temperature profile. A) Isothermal, B) Cocurrent flow; C) Countercurrent flow.

pending on the number of deflections, and the aforementioned problems do not arise.

Compared to cocurrent flow, countercurrent flow has a markedly destabilizing effect at low flow velocities (Fig. 20C). Since the incoming reaction mixture in this case is in contact with the warm coolant outflow, the maximum temperature rises to much higher values. Countercurrent cooling can even lead to the occurrence of multiple steady states, and in general favors the runaway of a strongly exothermic, irreversible reaction [36]. In contrast to heat exchange without a reaction, countercurrent heat-transfer in reactors involving exothermic reactions should therefore be chosen only in particular cases.

The temperature control of an exothermic equilibrium reaction can constitute such a case. As illustrated in Figure 14B, the optimum temperature profile should in this case decrease with increasing conversion, i.e., along the tube length. On account of the equilibrium inhibition of the reaction, it is not possible for the reaction to run away in the front region. Countercurrent flow of the heat transfer medium is also advantageous for endothermic equilibrium reactions. Figure 21 shows

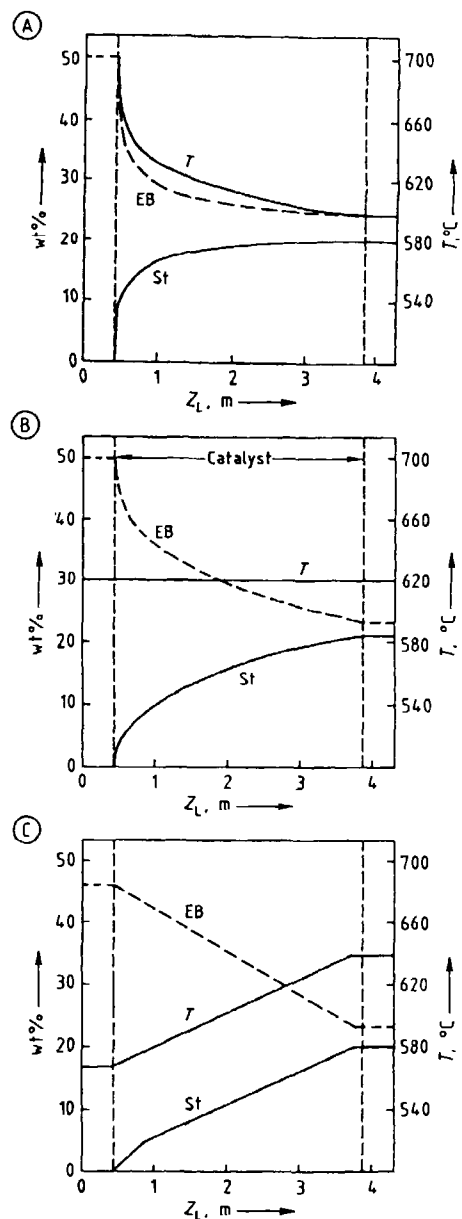


**Figure 21.** Influence of the heating strategy on the temperature and concentration profiles in styrene synthesis. A) Adiabatic; B) Isothermal; C) Countercurrent heating. EB = ethylbenzene; St = styrene.

the calculated temperature and concentration profiles with different heating conditions in the synthesis of styrene (dehydrogenation of ethylbenzene). With adiabatic and isothermal reaction control, styrene formation decreases with increasing tube length, whereas it remains roughly constant with countercurrent flow.

A significant advantage of nonisothermal control of the heat transfer medium in cocurrent or countercurrent flow is the saving in circulation energy, since much smaller heat transfer medium streams must be circulated. Overall, the combination of several heat-transfer medium circuits (Fig. 16C) and the purposeful

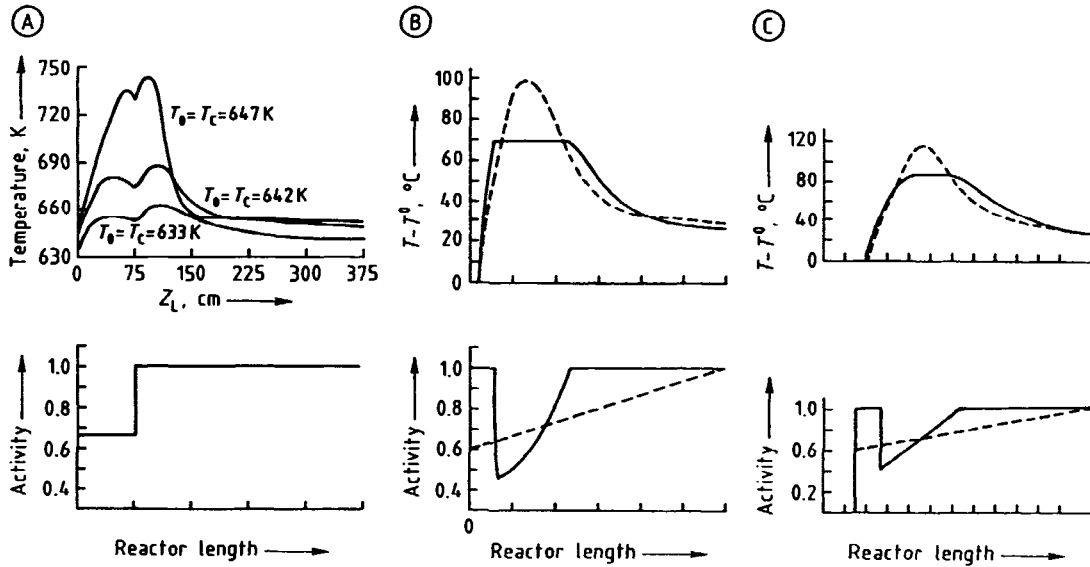


**Figure 22.** Influence of activity profiles on the temperature profile of a strongly exothermic reaction. A) Catalyst with 66% activity in the front section and 100% activity in the back [37]; B) Linear (broken line) and optimal catalyst activity distribution (full line) for limiting the maximum temperature to 370 °C (simulation result); C) Experimental verification of B [38].

utilization of the temperature change of the heat transfer medium in the reactor offer a wide range of possibilities to establish optimum temperature profiles for a given reaction, and of counteracting any changes in activity that occur during the operating life of the catalyst by altering the temperature profiles.

A further possibility of influencing the course of the reaction is to use catalysts of different activities over the reactor length. Particularly with strongly exothermic reactions that are liable to runaway, such as partial oxidations, a less active catalyst is occasionally used in the front part of the reactor in order to avoid too high a maximum temperature. Figure 22A illustrates the use of two catalysts of differing activity in series. The resulting temperature profiles have a typical double-hump shape [37, 39]. This can be avoided if an activity profile is established by using a continuously varying mixture of catalysts with different activities (Fig. 22B, C) [38]. In these cases the fully active entry region (relative activity 1) is designed so that the temperature rises to a preselected maximum value. In order to maintain the temperature at this value, the activity in the following region is sharply decreased and is then raised to a relative activity of 1 as the reaction rate drops due to the depletion of the reactants. A smooth temperature profile can be achieved even if the optimized activity profile in Figure 22B is only approximated (Fig. 22C).

The control of the maximum temperature by using locally differing catalyst activities presents problems if the main reaction zone moves into the region of high catalyst activity due to changes in the operating conditions. For example, in the case of Figures 22B and C,

a decrease in the throughput may already result in reaction runaway in the short, fully active front region. This can be counteracted by reducing the activity of this zone.

Catalyst deactivation occurring during operation may have more serious effects. If, for example, the catalyst is poisoned in a front migrating from the entrance to the rear, the main reaction zone finally migrates to the highly active rear catalyst region, which may lead to excessively high temperatures that can no longer be controlled.

In general, influencing the reaction course via control of the cooling stream is more flexible than incorporating catalysts of different activities. Particularly with nonisothermal control of the heat transfer media, the reaction course can be influenced over a wide range by means of the inflow temperature of the heat transfer medium as well as by its volumetric flow rate [40].

### 10.1.3.4 Autothermal Reactors

Under autothermal operation the hot effluent of a fixed-bed reactor is used to heat up the cold feed to the ignition temperature of the catalytic reaction. Since no other addition or removal of heat takes place, autothermal operation is restricted to reaction systems which all together are exothermic. The conventional reactor design consists of an adiabatic packed-bed reactor coupled with a countercurrent heat exchanger (Fig. 23A).



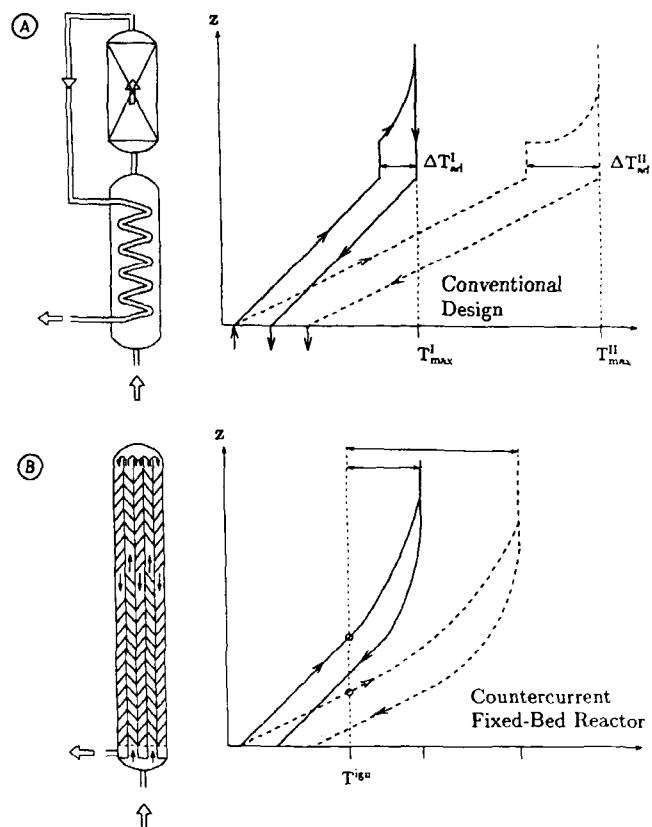


**Figure 23.** Autothermal fixed-bed reactors with recuperative heat exchange. Basic design and typical temperature profiles. A) Conventional design with separate heat exchanger; B) Countercurrent fixed-bed reactor.

An important feature of autothermal operation is the fact that the reactor is always operated in the ignited steady state. This means that the reaction can only be started with help of a separate preheater through which the catalyst bed temperature is raised above the ignition temperature of the reaction. During operation, control measures must be taken to prevent the reaction from extinction if the feed to the reactor is too lean. Because the hot effluent is used to heat up the cold feed, the maximum temperatures achieved under autothermal operation may exceed the adiabatic temperature rise (eq. 6) manifold. To prevent overheating, autothermal operation is limited to reactions with a maximal adiabatic temperature rise in the order of 300–400 K (depending upon the temperature stability of the catalyst and the reactor construction). Therefore autothermal operation is best suited for reactions with a low overall exothermicity. Catalytic combustion or catalytic hydrogenation of traces of organic compounds are typical examples. Unless excessive heat transfer areas are provided in the countercurrent heat exchanger, the design of Fig. 23A is only suited for an adiabatic temperature rise exceeding about 150 K. To lower this limit, other designs have been conceived.

Fig. 23B shows the concept of the countercurrent fixed-bed reactor where the catalyst is placed inside and outside of a tube bundle that forms a countercurrent heat exchanger for the reacting gas. One advantage of this design is the improved heat exchange through the catalyst packing. Another advantage stems from the integration of heat exchange and reaction within the reactor as compared to its separation in Fig. 23A. This can be seen from the temperature profiles for a single irreversible reaction in Fig. 23. As long as the temperature is below the ignition temperature of the catalytic reaction the slope of the temperature profiles in the heat exchange section is the same in both designs (provided the heat transfer parameters are identical). If the temperature of the incoming gas exceeds the ignition temperature, the reaction will start immediately in the countercurrent reactor. If the activation energy is sufficiently high the temperature will increase rapidly and the reaction will be completed after a short distance. In a limiting case the heat exchange over the reaction front can be neglected and the maximum temperature reached can be estimated from the ignition temperature plus the adiabatic temperature rise. This is of course only a rough estimate since neither is the ignition temperature a properly defined quantity nor is the influence of the heat exchange over the length of the reaction front really negligible. The estimate is however sufficient to get a reasonable picture of the main differences between the two types of autothermal reactors.

The countercurrent fixed-bed reactor is obviously self-adaptive in that it establishes the necessary temperature level for the respective reaction, whereas in the standard type the temperature level is directly proportional to the slope of the temperature front in the heat exchanger section,  $dT/dz$ , which in turn is proportional to the adiabatic temperature rise  $\Delta T_{ad}$ .

$$\frac{dT}{dz} = \frac{\Delta T_{ad}}{2 \left( \frac{\lambda_s(1-\varepsilon)}{G_z c_p G} + G_z c_p G \frac{1}{\alpha_w a_w} \right)} \quad (7)$$

Therefore considerably higher maximum temperatures are obtained in the conventional design if the feed concentration (the adiabatic temperature rise) increases. This is shown qualitatively for a doubling of  $\Delta T_{ad}$  in Fig. 23 (dashed lines).

A completely different design of an autothermal reactor has been proposed and developed by Boreskov and Matros [41–43]. Fig. 24A gives a sketch of the basic concept, showing an adiabatic fixed bed reactor with feed/exit tubes and two valves for periodic flow reversal. Before start of operation the fixed bed has again to be heated above the ignition temperature of the catalytic reaction. If the reactor is then fed with cold feed from one side the cold feed gas is heated up

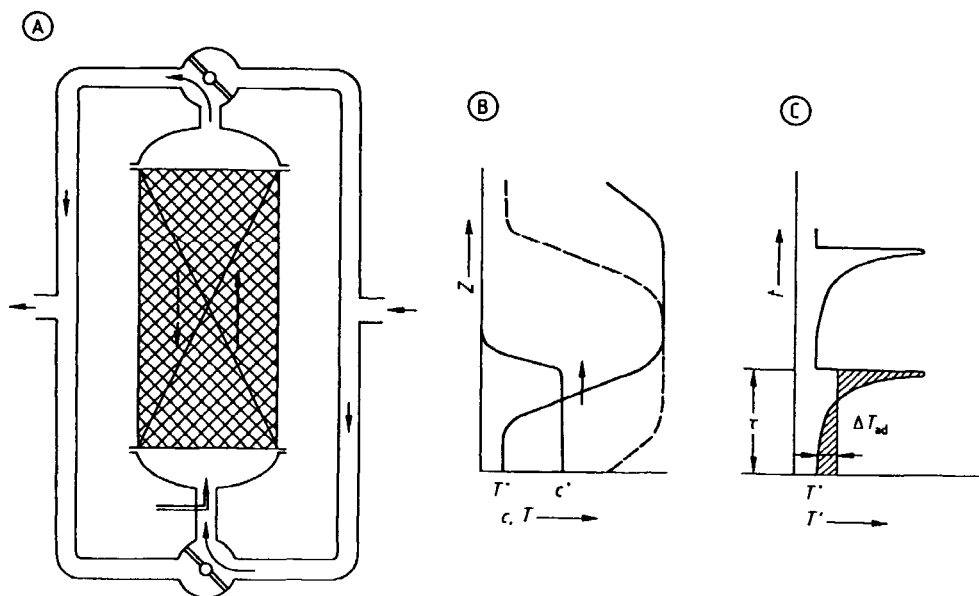


**Figure 24.** Autothermal reaction control with direct (regenerative) heat exchange for an irreversible reaction [14]. A) Basic arrangement; B) Local concentration and temperature profiles prior to flow reversal in steady state; C) Variation of outlet temperature with time in steady state.

by the hot catalyst and the catalyst is cooled down simultaneously by the cold feed. A temperature front develops and moves into the packed bed. In this front the gas is heated up and reacts. After a certain period the direction of flow is reversed via the valves and the temperature front is pushed back. In the cyclic steady state a hot plateau in the middle of the packed bed thus moves up and down, while the exit and inlet sections of the packed bed serve as regenerative heat exchangers. Since the reactor is adiabatic, the heat of reaction can only be removed with the leaving gas and the gas exit temperature shows a saw-tooth-like variation in time (Fig. 24C). From an overall energy balance it is obvious that the integral of the exit temperature over time must exceed the feed temperature just by the adiabatic temperature rise  $\Delta T_{ad}$ .

It is interesting to note that in the limit of rapid flow reversal the reverse flow reactor and the countercurrent fixed-bed reactor show completely similar temperature and conversion profiles [44]. This can be understood with the help of Fig. 25: With rapid flow reversal the catalyst temperature will remain constant due to the large heat capacity of the packing while the gas temperature will be below the catalyst temperature in the respective feed section and above in the exit section (Fig. 25B). This behavior is completely similar to that of a countercurrent fixed-bed reactor, where the catalyst is placed at the separating walls between the up and down flowing gas (Fig. 25C). It only has to be considered that instead of pushing the reacting gas for a short period in one and for another period in the other direction, now half of the mass flow will go per-

manently in one and the second half in the other direction. Since it is much easier to solve the steady state model of the countercurrent fixed-bed reactor than the dynamic model of the reverse flow reactor, the analogy can be used for rapid design calculations for the reverse flow reactor [14]. Moreover, the simple design approximation using the slope of the temperature front and the maximum temperature estimated from the ignition temperature and the adiabatic temperature rise (Fig. 25D) helps to understand the basic features of both reactors [44].

The obvious advantage of the reverse flow reactor over the countercurrent fixed-bed reactor is the simple form of the adiabatic packed bed and the excellent efficiency of the regenerative heat exchange. Reactions with an adiabatic temperature rise as low as 10 K can be run autothermally in a properly designed fixed bed. It is therefore presently a favorite design for the catalytic oxidation of traces of combustible components in exhaust air. Its prime disadvantage is the unsteady mode of operation and the necessity to switch large gas streams periodically. In the basic design of Fig. 24 unreacted gas in the entrance hood and the preheating section of the packed bed is flushed into the exit with every flow reversal. To avoid this breakthrough most commercial air purification units use a three-bed design (Fig. 26B), where one bed is purged with clean air.

In addition to the standard design, a number of modifications have been proposed and applied (see also Section 10.4). As explained in Section 10.1.3.1, large

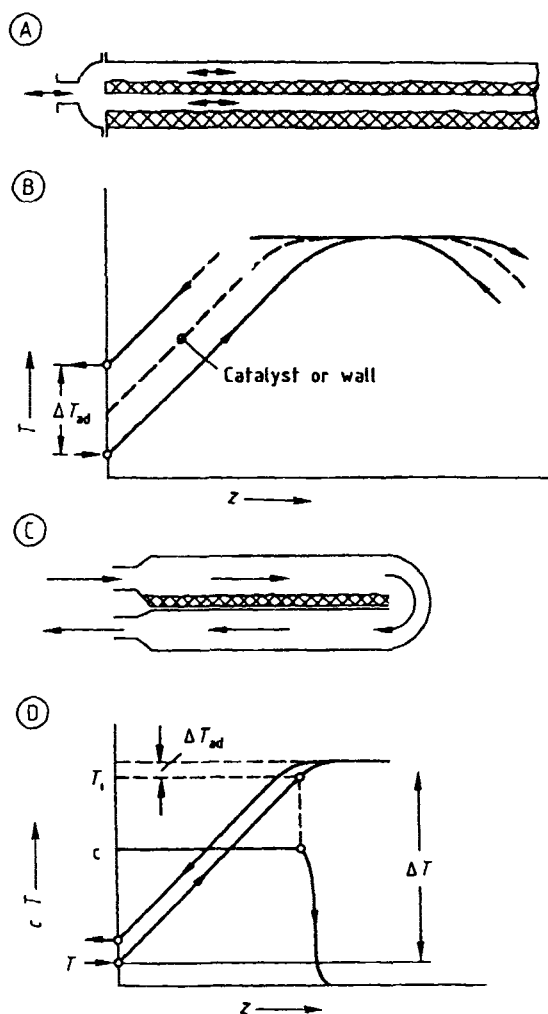


**Figure 25.** Equivalence of operation with periodical flow reversal and countercurrent heat exchange A) Fixed-bed reactor with periodic flow reversal, B) Temperature profiles with rapid flow reversal, C) Countercurrent reactor with catalyst at the wall D) Schematic concentration and temperature profiles in both reactors [14]

adiabatic packed beds are preferably designed as radial-flow reactors to avoid excessive pressure drop with increasing bed height. In the radial flow design depicted in Fig. 26A, the hot region in the middle insulates itself against heat losses. This design can easily be extended to a three-bed arrangement. Also designs with rotating fixed beds similar to the Ljungstrom heat exchanger design have been proposed and tested [14]. This offers a possibility of a continuous, valveless operation at the expense of rotating seals at the cold end of the rotating fixed bed.

Typical applications for exhaust air purification are characterized by rapid concentration changes. An efficient control strategy must prevent the reaction from extinction during times of low concentrations and the catalyst from overheating and sintering during times of

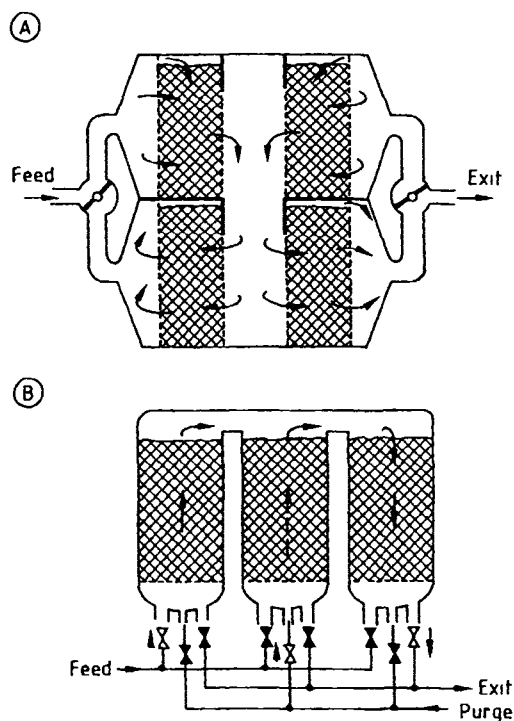


**Figure 26.** Alternative arrangements for autothermal reactor design with periodic flow reversal A) Radial-flow concept B) Multiple-bed arrangement

rich feed. Several possibilities to achieve this goal have been discussed in [45].

Aside from air purification autothermal operation has been proposed and demonstrated for a number of exothermic synthesis reactions with equilibrium limitations like the methanol, the ammonia and the sulphur trioxide synthesis (see also Section A 10.4 and references therein). An example calculation for the methanol synthesis in a reverse flow reactor is given in Fig. 27 from Ref. [46]. Here the decreasing temperature profile in the exit section of the reactor leads to an increased equilibrium conversion over that obtained adiabatically (Fig. 27A, B). As can be seen from the temperature conversion plot (Fig. 27C) the reaction path swings around the locus of optimal reaction rate as defined in Fig. 14, but a two-stage adiabatic reactor with interstage cooling will still lead to higher conversion. Another disadvantage can be seen in the fact that in autothermal operation the heat of reaction can only be used to preheat the feed, whereas the reactor concepts shown in Figs. 16, 18 and 19 allow for the additional production of steam. Purely autothermal concepts for the above mentioned bulk chemicals will therefore probably be restricted to sites where simple reactor operation without waste heat utilization is required. A countercurrent methanol reactor concept developed by ICI ("ICI tube-cooled converter", [47]) is an example.

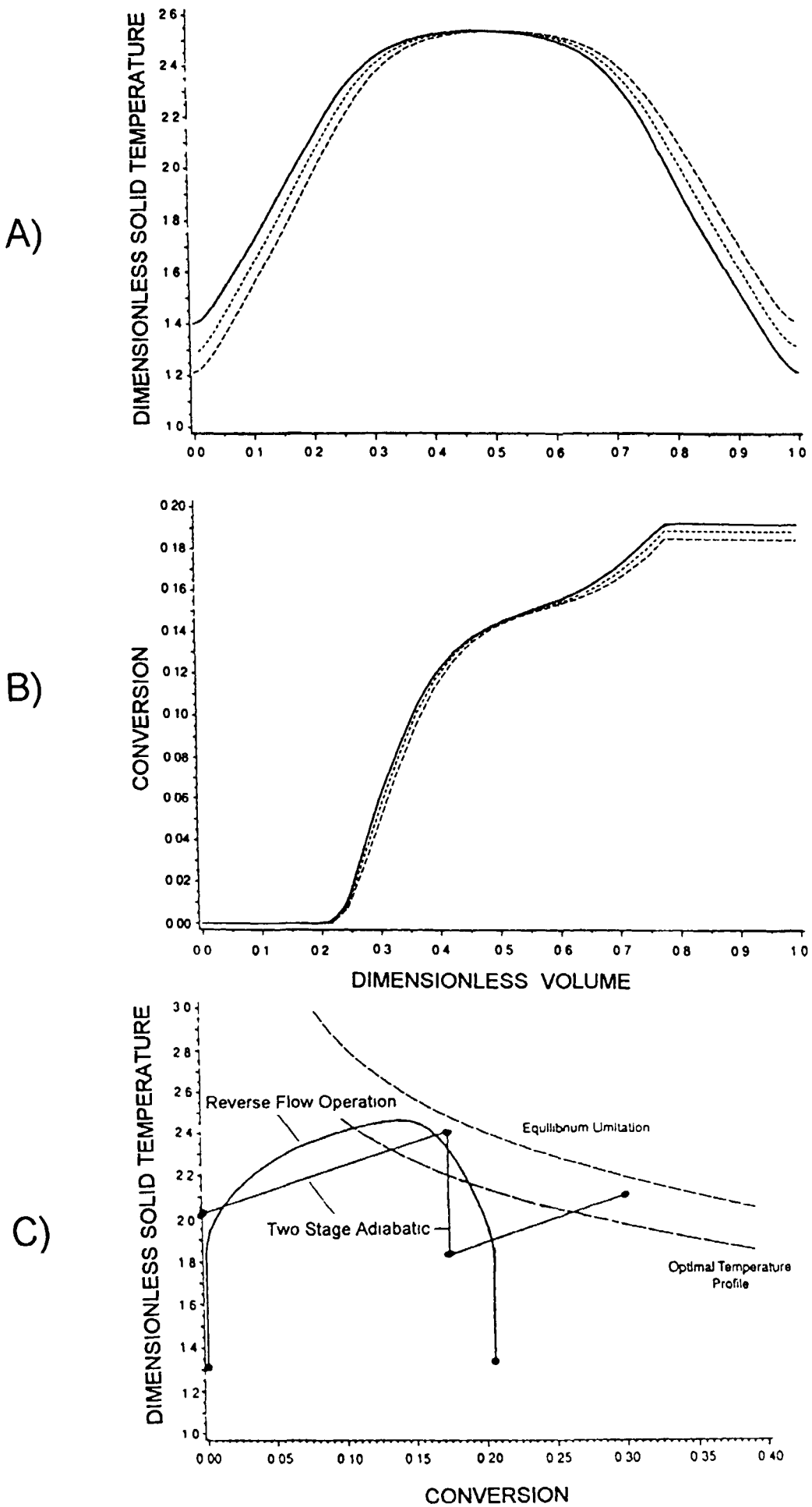
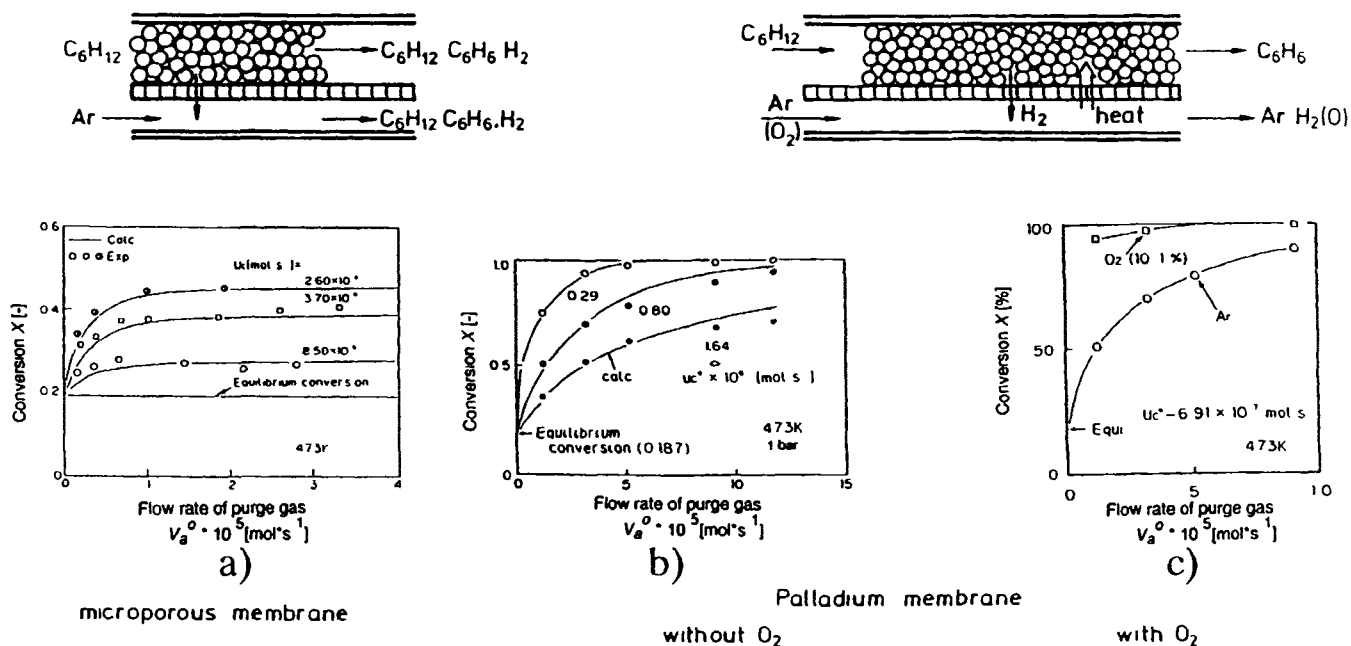


Figure 27. Methanol synthesis under autothermal operation (reverse flow reactor) A, B) Temperature and conversion profiles for a reverse flow reactor C) Reaction path for reverse flow operation and for a two-stage adiabatic reactor with interstage cooling [46]



**Figure 28.** Cyclohexane dehydrogenation in different membrane reactors, adopted from Itoh [55], a) microporous inert membrane, b)  $H_2$  selective Pd membrane, c)  $H_2$ -selective Pd membrane with combustion on the permeate side (from [56])

Interesting aspects of autothermal reactor operation arise if an endothermic synthesis reaction is coupled with an exothermic reaction in such a way that the combination is weakly exothermic. An example has been given by Amoco for the oxidative steam reforming of methane [48]. The application to styrene synthesis has so far been limited to simulation studies (see [49] and references therein).

### 10.1.3.5 Multifunctional Reactors

The provision of the right amounts of educts at the reaction site, the establishment and the maintenance of the adequate reaction conditions and the in-time removal of the reaction products are tasks that are not necessarily solved optimally in standard fixed-bed reactor configurations. Novel designs to improve the interaction of transport and reaction have therefore attracted considerable interest in recent years. They can be placed under the heading "multifunctional reactors" [50–52].

Whereas the unit operation concept of chemical engineering asks for a clear separation of educt preparation, chemical reaction and product separation in different units, it is obvious that better conversion and selectivity might be achieved if educts are added at the required amount and intermediates or products are withdrawn from the place of reaction immediately. Two general alternatives are presently under discussion to achieve this goal, membrane methods and sorptive methods. The basic difference is that membrane

methods allow for a continuous addition or removal of components through a semipermeable wall whereas sorptive methods are essentially dynamic, in that they provide a limited storage capacity for some components if a suitable adsorbent is placed near the site of the catalytic reaction. Sorptive methods will be briefly discussed in Section 10.4. A few examples of membrane methods together with their possible potential will be treated subsequently. For a more detailed discussion of the current state see Refs [53, 54].

An obvious application of selective membranes in chemical reaction engineering is the product removal in case of an equilibrium limited reaction in order to obtain total conversion. This can be achieved by placing catalytically inert membranes in the fixed bed reactor as shown in Fig. 28 for the test case of cyclohexane dehydrogenation by Itoh [55]. If a microporous membrane was used,  $H_2$  could be extracted preferentially and twice the equilibrium conversion was obtained (Fig. 28A). Of course total conversion is impossible under these conditions since—due to Graham's law [57]—the diffusivity of  $H_2$  is only six times bigger than that of benzene or cyclohexane. A nonporous palladium membrane, however, allows for exclusive permeation of  $H_2$  so that total conversion can be approached (Fig. 28B). If in addition oxygen is added to the permeate side of the membrane, hydrogen is immediately oxidized to  $H_2O$  so that its partial pressure is essentially zero in the permeate and only a small amount of purge gas on the permeate side is required to obtain total conversion. As an interesting side effect the heat of hydrogen combustion more than compen-

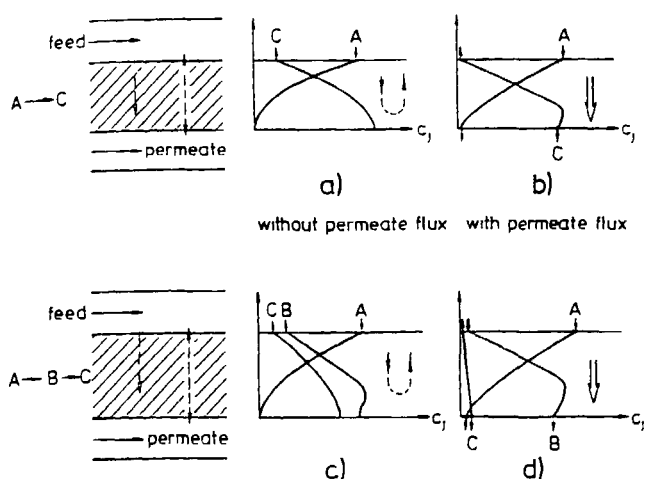


**Figure 29.** Concentration profiles across catalytic membranes for two different reactions with no (a, c) and with (b, d) optimal permeate flux (from [56]).

sates for the heat of the endothermic dehydrogenation. This example therefore closely approaches the goal of providing optimal conditions at the site of the reaction.

The main problem with the integration of inert membranes in fixed bed reactors is the membrane itself. It has to be sufficiently stable against thermal and mechanical stress, inexpensive and of high selectivity and permeability. At present, Pd-based alloys are the only sufficiently temperature stable and permselective membranes for hydrogen permeation. Since permeation through homogeneous membranes is a rather slow process, large membrane areas are required for reasonable production quantities.

The ultimate design of an inert membrane reactor would consist of well chosen crack free zeolite film membranes. The difficulties in this case are even more deterrent for industrial scale reactors since only a small number of holes or cracks would ruin the potential advantages of the design.

The conditions are substantially more favorable for the microporous catalytic membrane reactor concept. In this case the membrane wall consists of catalytically active, microporous material. If a simple reaction  $A \rightarrow B$  takes place and no permeate is withdrawn, the concentration profiles are identical to those in a catalyst slab (Fig. 29a). By purging the permeate side with an inert gas or by applying a small total pressure difference, a permeate with a composition similar to that in the center of the catalyst pellet can be obtained (Fig. 29b). In this case almost 100% conversion over a reaction length of only a few millimeters is possible. The advantages are even more pronounced, if a selectivity-limited reaction is considered. This is shown with the simple consecutive reaction  $A \rightarrow B \rightarrow C$  where B is the desired product. Pore diffusion reduces the yield of B since in a catalyst slab B has to diffuse backwards from the place where it was formed, thereby being partly converted to C (Fig. 29c). This is the reason why in practice rapid consecutive reactions like partial oxidations are often run in pellets composed of a thin shell of active catalyst on an inert support [30].

In a catalytic membrane reactor the pressure difference between feed and permeate could be adjusted such that high selectivity and high conversion in a once through process is obtained (Fig. 29d). The amount of catalyst necessary and the required residence time of the gas would be less than in conventional fixed bed reactors since the diffusional resistance is overcome by the external pressure gradient. The above advantages are already partly exploited by the use of macroporous catalyst pellets, mentioned in Section 10.1.2.3 [19, 20].

Porous catalytic membrane reactors offer the additional advantage to feed reactants separately from different sides of the membrane [58]. This is shown schematically for the reaction  $A + B \rightarrow C$  in Fig. 30a. If the reaction is fast enough, none of the educts will break through the membrane to the other side. By applying a

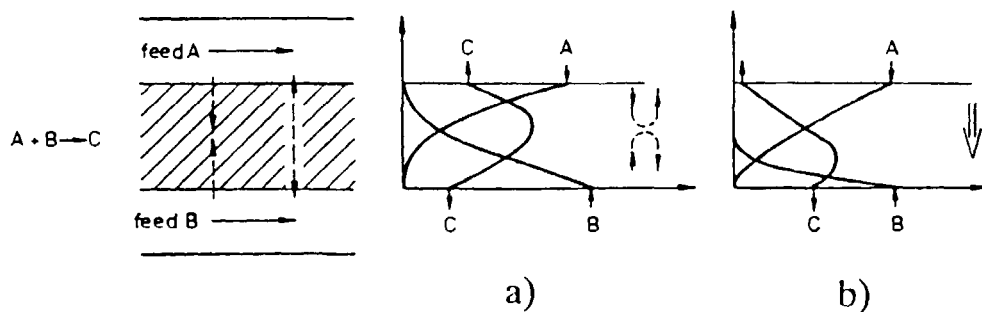


**Figure 30.** Concentration profiles across a catalytic membrane for  $A + B \rightarrow C$ , and separate feed of A and B, adopted from Sevot et al [58]. a) without and b) with convective flux through the membrane

pressure difference between both sides it is even possible to drive the product C to either side (Fig. 30b).

One major disadvantage of catalytic membrane reactors is the fact that so far no convincing large scale concepts have been proposed. This concerns both the implementation of large membrane areas necessary for the production of bulk chemicals within a chemical reactor and its combination with devices for the addition or removal of the required heat of reaction. Membrane reactor concepts are therefore presently limited to lab scale investigations while the above mentioned sorptive methods seem closer to a large scale realization.

### 10.1.4 Parametric Sensitivity, Runaway and Safety of Fixed-Bed Reactors

The operational stability of fixed-bed reactors with strongly exothermic reactions against thermal runaway has been studied in great detail since the early 1970s. The numerous publications could give the impression that this is a particularly critical reactor type with a large potential risk. In fact, the opposite is true. Compared to a liquid-phase reactor of the same size, a fixed-bed reactor with a gas-phase reaction contains a mass of reactants several orders of magnitude smaller. There is therefore no danger of a rapid decomposition of a large mass of reactants, accumulated in the reactor, especially as the heat capacity of the catalyst mass additionally damps the uncontrolled temperature rise.

#### 10.1.4.1 Runaway

Nevertheless, instabilities can arise in fixed-bed reactors, particularly with strongly exothermic reactions, and can lead to excess temperatures that can damage the catalyst and the reactor construction materials. Several causes for this behavior have been identified [4] but colloquially they are all considered under the heading "runaway".

In fixed-bed reactors, runaway usually occurs under operating conditions of high parametric sensitivity, where small changes in the operating parameters can lead to large changes in the maximum temperature and yield. The reason is the exponential dependence of the reaction rate on temperature (Arrhenius law). Figure 31 shows calculated temperature profiles for partial oxidation in a wall-cooled fixed-bed reactor tube of typical dimensions. In Figure 31A only the main reaction is considered, while in Figure 31B the total combustion to  $\text{CO}_2$  and water is additionally taken into account. Both cases are almost identical up to coolant temperatures of  $33^\circ\text{C}$ . Since considerably more

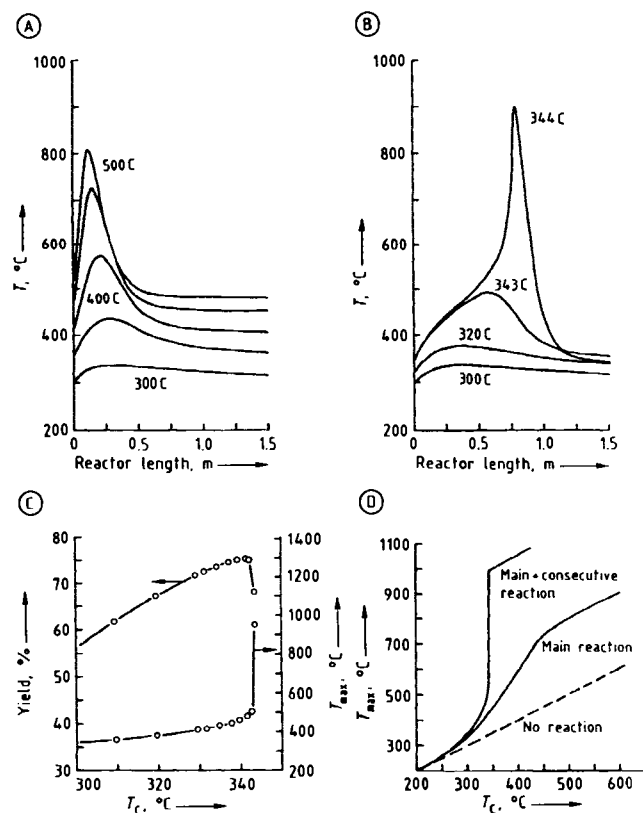


**Figure 31.** Parametric sensitivity of a partial oxidation reaction in a fixed-bed reactor of typical dimensions as a function of the coolant temperature  $T_c$  with  $T(z=0) = T_c$ . A) Temperature profile over reaction length (main reaction only); B) Temperature profile including total oxidation as side reaction; C) Maximum temperature  $T_{max}$  and yields as a function of coolant temperature  $T_c$  in case B; D)  $T_{max}$  as a function of  $T_c$  for both cases.

heat is liberated in the total combustion than in the desired main reaction, the sensitivity is increased substantially as soon as the ignition temperature of the second reaction is exceeded.

As a measure of the parametric sensitivity, Figure 31C shows the change in maximum temperature vs. the cooling temperature for case B. The sensitivity is only moderate at low cooling temperatures, whereas above  $T_c = 343^\circ\text{C}$  small changes in  $T_c$ —and also in other parameters such as throughput, feed concentration, or pressure—lead to large changes in reactor behavior. In fact under the conditions considered a new steady state is approached if the coolant temperature is raised above  $T_c = 344^\circ\text{C}$ . This means that the maximum temperature remains at an upper value even if the coolant temperature is decreased below  $T_c = 300^\circ\text{C}$ .

Due to the unavoidable differences between individual tubes, multitubular reactors cannot be operated in the range of high parametric sensitivity. In the case considered the cooling temperature must be lowered below ca.  $340^\circ\text{C}$ , and the tubes made longer to give a good conversion. This example emphasizes the re-

quirement discussed in Section 10.1.3.3 for making the conditions in the tubes of the tube bundle and in the cooling circuit as uniform as possible to avoid premature runaway reaction in individual tubes.

In the literature there are numerous runaway criteria with which operating ranges of high parametric sensitivity can be precalculated for known reaction kinetics [16, 59, 60]. In practice, however, these parameters are of only limited importance because they rarely take into account the peculiarities of individual cases. Sensitive reactions such as partial oxidation and partial hydrogenation are therefore generally tested in single-tube reactors of the same dimensions as those in the subsequent multitubular reactor. This allows the range of parametric sensitivity to be determined directly. Recalculation of the results for other tube diameters is only possible to a limited extent due to the uncertainties in the quantification of the heat transfer parameters (see Section 10.1.2.4).

A fixed-bed reactor can enter the region of high parametric sensitivity through changes in the catalyst properties or operating conditions. Rapid changes in feed temperature, feed concentration or throughput may induce migrating reaction zones which can lead to transient excess temperatures, a phenomenon treated under the heading "wrong-way behavior" (see Section 10.4 and Ref. [61]).

Initially a few particularly sensitive tubes of the bundle will run away, i.e., the reaction changes, for example, from a selective partial oxidation to a total combustion, and the temperature rises rapidly. In a multitubular reactor with thousands of tubes every tube cannot be equipped with temperature profile measurements; it is therefore likely that this runaway will remain undetected, especially if it involves only a few tubes. Although temperatures above 1000 °C can often be reached in the catalyst during such runaways, there is no safety risk, provided the tube is surrounded by a liquid heat-transfer medium. Because of the good heat transfer to the fluid the tube temperature remains close to that of the heat-transfer medium, and melting of the tube does not occur.

The most reliable method of detecting a runaway is online analysis of a product formed in the runaway reaction. For example, CO<sub>2</sub> can be monitored in the off-gas during the runaway-sensitive synthesis of ethylene oxide. If its concentration increases above a specified limit, the reactor must be shut down, purged with nitrogen, and for a certain period cooled to a lower temperature before operation is recommenced.

#### 10.1.4.2 Safety Aspects

Because of the small mass storage capacity compared to liquid-phase reactors, the danger of a sudden re-

action of accumulated reactants in gas-phase fixed-bed reactors is low. Leaving out the peculiarities of individual cases, the following safety risks can be assumed for fixed-bed reactors:

1. Leaks which result in the release of large amounts of gas or vapor and the formation of explosive clouds,
2. leaks resulting in release of large amounts of liquid heat transfer media (oils, salt melts),
3. occurrence of ignitable or decomposable gas mixtures in the reactor,
4. melting of the reactor due to a runaway reaction.

The safety aspects of liquid heat transfer media are discussed in Section 10.1.3.3A. Ignitable gas mixtures can arise particularly during partial oxidation reactions. They are especially critical where large packing-free volumes are present. This is the case in the inflow and outflow hoods of the reactor, while in the reactor tubes the catalyst packing dampens the propagation of a flame front due to its heat capacity. Complete avoidance of ignitable mixture is generally not possible in partial oxidations because at least during mixing of the gas streams prior to the reactor the ignition limit is exceeded locally. Nevertheless, in the past, operation of fixed-bed reactors with ignitable mixtures was avoided, either by dilution with inert gas or by operating in the nonstoichiometric range. The former requires additional efforts for heating, cooling, and separation of the inert gas, while the latter gives only low conversions of the reactants in a single pass. New developments in partial oxidation therefore aim for stoichiometric operation in the ignitable range [62]. A prerequisite for this is pressure-resistant construction with check valves and flame barriers so a possible ignition is confined to the interior of the reactor.

Melting of reactor tubes during runaway reaction is only to be feared in multitubular reactors if the respective tube is not surrounded by liquid heat transfer medium. Thus, appropriate design must ensure that running dry of reactor tubes cannot occur. In the case of corrosive reaction gases, provision for the detection of leaks caused by corrosion must be made, particularly when pressurized or boiling water is used as coolant.

### 10.1.5 Conclusions

The different industrially established fixed-bed reactor configurations of the adiabatic, the multistage and the multitubular reactor types represent a mature and versatile class of reactors for heterogeneously catalyzed gas phase reactions. Companies specialized in their



construction offer a wide variety of different designs to meet specific requirements of operation and temperature control including operation above the explosion limit of the gas mixture. Only in case of rapid catalyst deactivation other reactor concepts like fluidized-bed reactors (see Section 10.2) are mandatory.

In addition to the well-established fixed-bed reactor configurations mentioned above, new concepts are being discussed where specific features like educt addition and selective product removal are integrated in the fixed bed. From these "multifunctional reactors", autothermal reactor concepts where the heat exchange between the cold feed and the hot effluent is integrated in the fixed-bed have already been established in industrial practice.

Sorptive reactor concepts where periodic operation is used to temporarily store or remove educts or products in the fixed bed can be considered close to industrial realization, whereas membrane reactor concepts with permselective inert or catalytically active microporous membranes are still at the laboratory stage. They promise the highest potential for a further improvement of catalytic reactor technology and present the biggest challenges [54].

### 10.1.6 List of Symbols:

$A$	cross sectional area, $m^2$
$a_p$	specific outer surface area of catalyst, $m^2/m^3$ packing
$a_w$	specific wall surface, $m^2/m^3$
$c$	molar concentration, $mol/m^3$
$c_O$	feed concentration, $mol/m^3$
$c_{pG}$	specific heat capacity of gas, $kJ\ kg^{-1}\ K^{-1}$
$d$	channel width, $m$
$d_i$	inner particle diameter, $m$
$d_o$	outer particle diameter, $m$
$d_p$	catalyst particle diameter, $m$
$d_h$	hydraulic diameter ( $d_h = 4A/U$ ), $m$
$f$	Fanning friction factor
$f_{1,2}$	Ergun coefficients (eqs. 3, 4, 5)
$G_z$	mass-flow velocity, $kg\ m^{-2}\ s^{-1}$
$l$	particle length, $m$
$L$	length of catalyst bed, $m$
$Nu$	Nusselt number
$T$	temperature, $K$
$T_O$	feed gas temperature, $^{\circ}C$
$U$	circumference, $m$
$U_c$	gas flow rate, $mol/s$
$v_A^0$	purge gas flow rate, $mol/s$
$v_G$	interparticle velocity, $m/s$
$v_c$	coolant (salt melt) velocity $m/s$
$x$	conversion
$z$	space coordinate, $m$
$Z_L$	reactor length, $m$

$\alpha_w$	wall heat transfer coefficient, $Wm^{-2}\ K^{-1}$
$\varepsilon$	void fraction, $m^3$ free space/ $m^3$ packing
$\Delta h_R$	reaction enthalpy, $kJ/mol$
$\Delta p$	pressure drop, $N/m^2$
$\Delta T_{ad}$	adiabatic temperature change, $K$
$\Delta x$	molar conversion, $mol/mol$
$\eta$	dynamic viscosity, $Nsm^{-2}$
$\lambda_G$	axial thermal conductivity of the gas, $Wm^{-1}\ K^{-1}$
$\lambda_s$	axial thermal conductivity of the solid phase, $Wm^{-1}\ K^{-1}$
$\lambda_r$	effective radial thermal conductivity, $Wm^{-1}\ K^{-1}$
$\rho$	density, $kg/m^3$
$\rho_G$	gas density, $kg/m^3$
$\zeta$	pressure drop coefficient

### 10.1.7 References

- [1] G F Froment, K B Bishoff, *Chemical Reactor Analysis and Design*, John Wiley, New York, 1990
- [2] K R Westerterp, W P M van Swaaij, A A C M Beenackers, *Chemical Reactor Design and Operation*, John Wiley, 1984
- [3] M Baerns, H Hofmann, A Renken, *Chemische Reaktionstechnik*, Georg Thieme Verlag, Stuttgart, 1987
- [4] G Eigenberger, "Fixed Bed Reactors", *Ullmann's Encyclopedia of Industrial Chemistry*, Vol B4, VCH, Weinheim, 1992, 199-238
- [5] L Riekert, *Appl Catal* 1985, 15, 89-102
- [6] V Kottke, H Blenke, "Verfahren zur Bestimmung örtlicher Stoff- und Wärmeübertragung an beliebig geformten Oberflächen", *Verfahrenstechnik* 1982, 16, 504-509
- [7] Verein Deutscher Ingenieure, *VDI-Wärmeatlas*, 5th ed., Section Gh, VDI-Verlag Düsseldorf, 1988
- [8] E Tsotsas, "Über die Wärme- und Stoffübertragung in durchströmten Festbetten", *VDI-Fortschr Ber., Reihe 3*, 1990, no 223
- [9] G Gaiser, V Kottke, "Wärme- und Stoffübergang in Katalysatoren mit regelmäßiger Formgebung", *Chem Ing Tech*, 1989, 61, 729-731
- [10] R K Shah, A L London, "Laminar Flow Forced Convection in Ducts", *Advances in Heat Transfer*, suppl 1, Academic Press, New York, 1978
- [11] S Quest, D. Mewes, "Der Einfluß des Temperaturfeldes auf den Stoffaustausch in laminar durchströmten Rohrreaktoren", *Wärme Stoffübertrag* 1988, 32, 355-363
- [12] G Gaiser, V Kottke, "Flow Phenomena and Local Heat and Mass Transfer in Corrugated Passages", *Chem Eng Technol* 1989, 12, 400-405
- [13] Verein Deutscher Ingenieure, *VDI-Wärmeatlas*, Section Le 1, VDI-Verlag, Düsseldorf, 1988
- [14] G Eigenberger, U Nicken, "Katalytische Abluftreinigung Verfahrenstechnische Aufgaben und neue Lösungen", *Chem Ing Tech* 1991, 63, 781-791, English version in *Int Chem Eng* 1993, 34, 4-16
- [15] K R Westerterp, K J Ptasiński, *Chem Eng Sci* 1984, 39, 245-252
- [16] M Morbidelli, A Varma, "Parametric Sensitivity in Fixed Bed Catalytic Reactor", *AIChE J* 1986, 32, 297-306, *Chem Eng Sci* 1991, 46, 3330-3332
- [17] D Vortmeyer, P Winter, "Verbesserung der Analyse von Festbettreaktoren durch die Berücksichtigung von Porositäts- und Stromungsverteilung", *Chem Ing Tech* 1983, 55, 312-313

- [18] T Daszkowski, G Eigenberger, "A Reevaluation of Fluid Flow, Heat Transfer and Chemical Reaction in Catalyst Filled Tubes", *Chem Eng Sci* **1992**, *47*, 2245–2250
- [19] A Rodrigues, R Quinta Ferreira, "Effect of intraparticle convection, diffusion and reaction in a large-pore catalyst particle", *AIChE Symp Ser*, **1988**, *84*, 80–87
- [20] A Rodrigues, R Quinta Ferreira, "Effect of intraparticle convection on the steady-state behavior of fixed-bed catalytic reactors", *Chem Eng Sci*, **1990**, *45*, 2653–2660
- [21] Verein Deutscher Ingenieure, *VDI-Warmeatlas*, Section Mh 1, VDI-Verlag, Dusseldorf, **1988**
- [22] U Zardi et al, "A Novel Reactor Design for Ammonia and Methanol Synthesis", *IV Intern Conference Fertilizer Technology*, London **1981**, *Hydrocarbon Process*, **1982**, *61* (No 8), 129–133
- [23] "Umwelttechnik, Sekundärmaßnahmen zur Minderung der NO<sub>x</sub>-Emission", *Steinmüller Schriftenreihe*, L+C, Steinmüller, **1985**
- [24] E Klapp, *Apparate- und Anlagentechnik*, Springer Verlag, Berlin, **1980**
- [25] C B Allen, G J Janz, "Molten Salts Safety and Hazards an Annotated Bibliography", *J Hazard Mater* **1980**, *4*, 145–175
- [26] P Grimm, "Six Years Successful Operation of Linde Isothermal Reactor", *Linde Reports on Science and Technology* **1991**, *42*, 57–69
- [27] U Lahne, R Lohmüller, "Schüttichtreaktoren mit gewickelten Kuhlrohren, eine konstruktive Neuentwicklung zur Durchführung exothermer katalytischer Prozesse", *Chem Ing Tech* **1986**, *58*, 212–215
- [28] Degendorfwerft, DE 2201528, 1972 (O Wanka, F Gurtlhuber, H Graf)
- [29] Degendorfwerft, DE 2207166, 1972 (O Wanka, F Gurtlhuber, H Graf)
- [30] G Eigenberger, W Ruppel, "Probleme der Modellbildung bei technischen Festbetreaktoren", *Chem Ing Tech* **1985**, *57*, 181–190, English Version in *Ger Chem Eng* **1986**, *9*, 74–93
- [31] A Stankiewicz, "Advances in Modelling and Design of Multitubular Fixed-Bed Reactors", *Chem Eng Tech* **1989**, *12*, 113–130, 170–175
- [32] M S G Cristina, C M G S Batista, J G V F Sousa, J A A M Castro, "Modelling Multitubular Catalytic Reactors the Influence of Shell Side Flow", *Chem Eng Sci* **1992**, *47*, 2565–2570
- [33] T F Degnan, J Wei, "The Co-Current Reactor Heat Exchanger", *AIChE J* **1979**, *25*, 338–344
- [34] A S Lopez, H I de Lasa, J A Porras, "Parametric Sensitivity of a Fixed-Bed Catalytic Reactor", *Chem Eng Sci* **1981**, *36*, 285–291
- [35] D O Borio, V Bucala, J A Orejas, J A Porras, "Co-currently Cooled Fixed Bed Reactors A Simple Approach to Optimal Cooling Design", *AIChE J* **1989**, *35*, 1899–1902
- [36] G Eigenberger, "Zur Modellbildung und Dynamik des homogenen Rohrreaktors", *Chem Ing Techn* **1974**, *46*, 11–19
- [37] J C Pirkle, I E Wachs "Activity Profiling in Catalytic Reactors", *Chem Eng Progr* **1987**, 29–34
- [38] G Eigenberger, "Practical Problems in the Modelling of Chemical Reactions in Fixed Bed Reactors", *Chem Eng Process* **1984**, *18*, 55–65
- [39] P H Calderbank A D Caldwell, G Ross, "The Diluted Catalyst Fixed Bed Reactor for Exothermic Catalytic Reactions", *Chemie et Industrie-Genie Chimique* **1969**, *101*, 215–230
- [40] D O Borio, V Bucala, J A Porras, "Thermal Regimes in Cocurrently Cooled Fixed-Bed Reactors", *Chem Eng Sci* **1995**, *50*, 3115–3123
- [41] G K Borekov, G A Bunimovich, Y S Matros, A A Ivanov, "Catalytic Processes Carried Out Under Non-Steady-State Conditions Switching the Direction of the Feed", *Kinetika i Kataliz*, **1982**, *23*, 402–406, *Int Chem Eng* **1982**, *22*, 335–342
- [42] Y S Matros, "Performance of Catalytic Processes under Unsteady Conditions", *Chem Eng Sci* **1990**, *45*, 2097–2102
- [43] Y S Matros, "Catalytic Processes under Unsteady-State Conditions", *Studies in Surface Science and Catalysis*, Editors B Delmon, J T Yates, Vol 43, Elsevier, Amsterdam, **1989**
- [44] U Niekens, G Kolios, G Eigenberger, "Limiting Cases and Approximate Solutions for Fixed-Bed Reactors with Periodic Flow Reversal", *AIChE J* **1995**, *41*, 1915–1925
- [45] U Niekens, G Kolios, G Eigenberger, "Control of the Ignited Steady State in Autothermal Fixed-Bed Reactors for Catalytic Combustion", *Chem Eng Sci* **1994**, *49*, 5507–5518
- [46] B Young, D Hildebrandt, D Glaser, "Analysis of an Exothermic Reversible Reaction in a Catalytic Reactor with Periodic Flow Reversal", *Chem Eng Sci* **1992**, *47*, 1825–1837
- [47] Anonymous, "Methanol Reactors—Converter Options for Methanol Synthesis", *Nitrogen* **1994**, *210*, 36–44
- [48] R F Blanks, T S Witting, D A Peterson, "Bidirectional Adiabatic Synthesis Reactor", *Chem Eng Sci* **1990**, *45*, 2407–2413
- [49] J D Snyder, B Subramaniam, "A Novel Reverse Flow Strategy for Ethylbenzene Dehydrogenation in a Packed-Bed Reactor", *Chem Eng Sci* **1994**, *49*, 5585–5601
- [50] D W Agar, W Ruppel, "Extended reactor concepts for dynamic DeNO<sub>x</sub> design", *Chem Eng Sci* **1988**, *43*, 2073–2078
- [51] D W Agar, W Ruppel, "Multifunktionale Reaktoren für die heterogene Katalyse", *Chem Ing Tech*, **1988**, *60*, 731–741
- [52] K R Westerterp, "Multifunctional Reactors", *Chem Eng Sci*, **1992**, *47*, 2195–2206
- [53] J Zaman, A Chakma, "Inorganic membrane reactors", *J Membr Sci*, **1994**, *92*, 1–28
- [54] G Saraco, G F Versteeg, W P M van Swaaij, "Current hurdles to the success of high-temperature membrane reactors", *J Membr Sci*, **1994**, *95*, 105–123
- [55] N Itoh, "Simultaneous operation of reaction and separation by a membrane reactor" in *Future Opportunities in Catalytic and Separation Technologies*, Studies in Surface Science and Catalysis, Vol 54, 248–283, Elsevier, Amsterdam, **1990**
- [56] G Eigenberger, "Tasks and Trends in Chemical Reaction Engineering", *Proc IVth World Congress of Chem Eng* (Karlsruhe, 1991), DECHEMA, Frankfurt, **1992**, 1082–1102
- [57] R Jackson, *Transport in Porous Catalysts*, Elsevier, New York, **1977**, 186–189
- [58] H J Sevot, G F Versteeg, W P M van Swaaij, "A non-permeable membrane reactor for chemical processes normally requiring strict stoichiometric feed rates of reactants", *Chem Eng Sci* **1990**, *45*, 2415–2421
- [59] G F Froment, *Front Chem React Eng* **1984**, *1*, 12–38
- [60] G Eigenberger H Schuler, "Reaktorstabilität und sichere Reaktionsführung", *Chem Ing Tech* **1986**, *58*, 655–665, English version in *Int Chem Eng* **1989**, *29*, 12–25
- [61] V Pinjala, Y C Chen, D Luss, "Wrong-way behavior of packed-bed reactors Impact of thermal dispersion", *AIChE J*, **1988**, *34*, 1663
- [62] Degendorfwerft, Reactor Systems and their Advantages Technical Information, May 1989

## 10.2 Fluidized-Bed Reactors

J. WERTHER AND H. SCHOENFELDER

### 10.2.1 Introduction

#### 10.2.1.1 The Fluidization Principle

In fluidization an initially stationary bed of solid particles is brought to a "fluidized" state by an upward stream of gas or liquid as soon as the volume flow rate of the fluid exceeds a certain limiting value  $\dot{V}_{mf}$  (where *mf* denotes minimum fluidization). In the fluidized bed, the particles are held suspended by the fluid stream; the pressure drop  $\Delta p_{fb}$  of the fluid on passing through the fluidized bed is equal to the weight of the solids minus the buoyancy, divided by the cross-sectional area  $A_t$  of the fluidized-bed vessel (Fig. 1):

$$\Delta p_{fb} = \frac{A_t \times H \times (1 - \varepsilon) \times (\rho_s - \rho_f) \times g}{A_t} \quad (1)$$

In eq 1 the porosity  $\varepsilon$  of the fluidized bed is the void volume of the fluidized bed (volume of interstices between grains, not including any pore volume in the interior of the particles) divided by the total bed volume,  $\rho_s$  is the apparent density of the solid, and  $H$  is the height of the fluidized bed.

In many respects, the fluidized bed behaves as a liquid: The bed can be stirred; objects of greater specific gravity sink, whereas those of lower specific gravity float; if the vessel is tilted, the bed surface resumes a horizontal position; if two adjacent fluidized beds with different bed heights are connected to each other, the heights become equal; and the fluidized bed flows out like a liquid through a lateral opening. Particularly advantageous features of the fluidized bed for use as a reactor are excellent gas–solid contact in the bed, good gas–particle heat and mass transfer, and high bed–wall and bed–internals heat-transfer coefficients.

The fluidization principle was first used on an industrial scale in 1922 for the gasification of fine-grained coal [1]. Since then, fluidized beds have been applied in many industrially important processes. The present spectrum of applications extends from a number of physical processes, such as cooling–heating, drying, sublimation–desublimation, adsorption–desorption, coating, and granulation, to many heterogeneous catalytic gas-phase reactions as well as non-catalytic reactions.

What follows is a survey of the fluid-mechanical principles of fluidization technology, gas and solid mixing, gas–solid contact in the fluidized bed, typical industrial applications, and approaches to modeling fluidized-bed reactors. Further information is given in

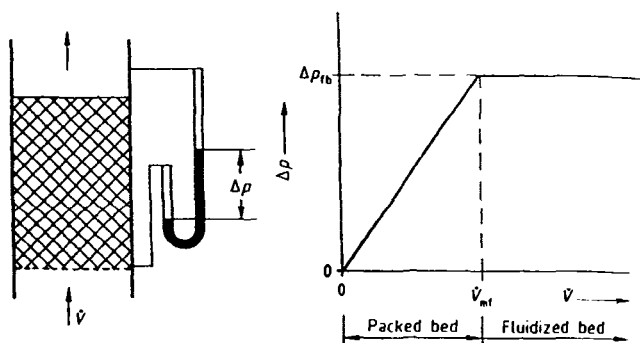


Figure 1. Pressure drop in flow through packed and fluidized beds.

textbooks [2] and monographs [3, 4]. Summary treatments can also be found in [5–13]. Other useful literature includes reports of the Engineering Foundation Conferences on Fluidization [14–16] and the Circulating Fluidized-Bed Conferences [17–19].

#### 10.2.1.2 Forms of Fluidized Beds

As the volume flow rate  $\dot{V}$  or the superficial velocity  $u = \dot{V}/A_t$  of the fluid increases beyond the value  $\dot{V}_{mf}$  or  $u_{mf}$  (Fig. 2(A)) corresponding to the minimum fluidization point, one of two things happens: in fluidization with a liquid, the bed begins to expand uniformly; in fluidization with a gas – a process of greater industrial importance and the one discussed almost exclusively in the following material – virtually solids-free gas bubbles begin to form (Fig. 2(B)). The local mean bubble size increases rapidly with increasing height above the grid because of coalescence of the bubbles. If the bed vessel is sufficiently narrow and high, the bubbles ultimately fill the entire cross-section and pass through the bed as a series of gas slugs (Fig. 2(C)). As the gas velocity increases further, more and more solids are carried out of the bed, the original, sharply defined surface of the bed disappears, and the solids concentration begins to decrease continuously with increasing height. To achieve steady-state operation of such a turbulent fluidized bed (Fig. 2(D)), solids entrained in the fluidizing gas must be collected and returned to the bed. The simplest way to do this is with a cyclone integrated into the bed vessel and a standpipe dipping into the bed. A further increase in gas velocity finally leads to the circulating fluidized bed (Fig. 2(E)), which is characterized by a much lower average solids concentration than the previous systems. The high solids entrainment requires an efficient external solids recycle system with a specially designed pressure seal (shown as a siphon in Fig. 2(E)).

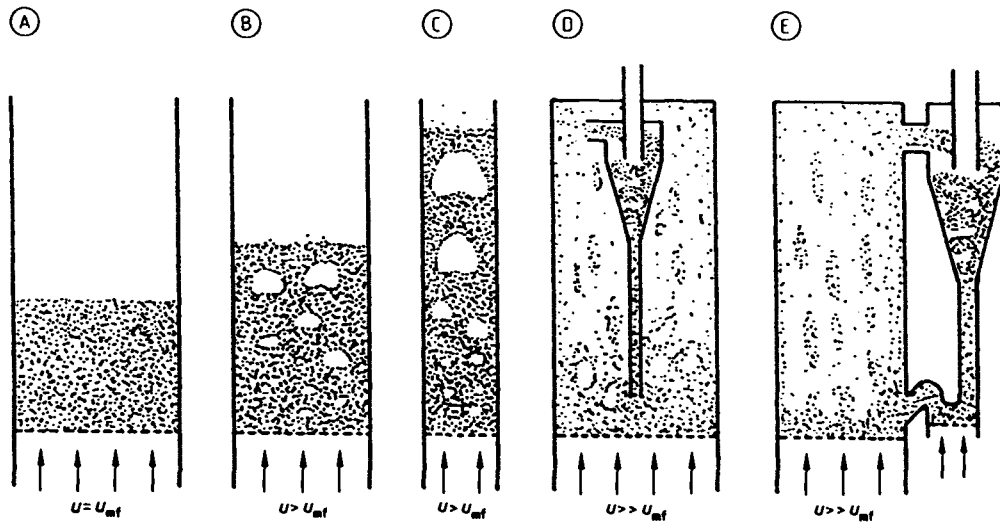


Figure 2. Forms of gas-solids fluidized beds.

### 10.2.1.3 Advantages and Disadvantages of the Fluidized-Bed Reactor

The major advantages of the (gas-solids) fluidized bed as a reaction system include:

- (i) Easy handling and transport of solids due to the liquid-like behavior of the fluidized bed.
- (ii) Uniform temperature distribution due to intensive solids mixing (no hot spots even with strongly exothermic reactions).
- (iii) Large solid-gas exchange area by virtue of small solids grain size.
- (iv) High heat-transfer coefficients between bed and immersed heating or cooling surfaces.
- (v) Uniform (solid) product in batchwise process because of intensive solids mixing.

Set against these advantages are the following disadvantages:

- (i) Expensive solids separation or gas purification equipment required because of solids entrainment by fluidizing gas.
- (ii) As a consequence of high solids mixing rate, backmixing of gas and resulting lower conversion.
- (iii) In catalytic reactions, undesired bypass or broadening of residence-time distribution for reaction gas due to bubble development.
- (iv) Erosion of internals and attrition of solids (especially significant with catalysts), resulting from high solids velocities.
- (v) Possibility of defluidization due to agglomeration of solids.

- (vi) Gas-solid countercurrent motion possible only in multistage equipment.
- (vii) Difficulty in scaling up.

Table 1 compares the fluidized-bed reactor with alternative gas-solid reaction systems, i.e. fixed-bed, moving-bed, and entrained-flow reactors.

## 10.2.2 Fluid-Mechanical Principles

### 10.2.2.1 Minimum Fluidization Velocity

The minimum fluidization point, which marks the boundary between the fixed- and the fluidized-bed conditions, can be determined by measuring the pressure drop  $\Delta p$  across the bed as a function of volume flow rate  $\dot{V}$  (Fig. 1). Measurements should always be performed with decreasing gas velocity, by starting in the fluidized condition. Only for very narrow particle-size distributions, however, does a sharply defined minimum fluidization point occur. The broad size distributions commonly encountered in practice exhibit a blurred range; conventionally, the minimum fluidization point is defined as the intersection of the extrapolated fixed-bed characteristic with the line of constant bed pressure drop typical of the fluidized bed (Fig. 1).

The measurement technique already contains the possibility of calculating the minimum fluidization velocity  $u_{mf}$ . The pressure drop in flow through the polydisperse fixed bed at the point  $u = u_{mf}$ , given for example by the Ergun relation [20], is set equal to the

Table 1. Comparison of gas-solid reaction systems [2, 12].

Characterics	Fixed bed	Moving bed	Fluidized bed	Entrained flow
Suitability for heterogeneous catalytic gas-phase reactions	only for catalyst that is deactivated very slowly catalyst attrition negligible plug flow of gas ensures high gas conversion	can also be used with catalyst that is rapidly deactivated catalyst attrition may be critical, depending on operating conditions	backmixing of gas due to mixing motion of solids and bubble-gas bypass lead to lower conversion	gas in virtually plug flow; high conversion possible
Temperature distribution	danger of hot spots with exothermic reactions	temperature gradients can be held within limits by virtue of high solids circulation and high gas throughput	high solids mixing ensures uniform temperature distribution in bed; temperature control by heat exchangers immersed in bed or by admission and removal of solids	axial temperature gradients can be held within limits by high solids circulation
Heat supply and removal, heat exchange	poor heat exchange; heat transport limits scale-up	poor heat exchange; due to high heat capacity of solids; transport of large quantities of heat by way of circulating solids	very efficient heat exchange; good heat transport by solids	properties intermediate between fluidized bed and moving bed
Particle size	large pellets ( $\approx 8-20$ mm), as uniform as possible; no fines	medium size ( $\approx 2-6$ mm) and uniform; no fines	broad particle-size distribution ( $\approx 0.02-6$ mm); high fines content acceptable	fine (0.02-0.5 mm), with narrow particle size distribution

fluidized-bed pressure drop given by eq 1. From the Ergun relation

$$\frac{\Delta p}{h} = 4.17 \times S_v^2 \times \frac{(1-\epsilon)^2}{\epsilon^3} \eta \times u + 0.29 \times S_v \times \frac{1-\epsilon}{\epsilon^3} \times \rho_f u^2$$

it follows

$$u_{mf} = 7.14(1 - \epsilon_{mf})v \times S_v \times \left[ \sqrt{1 + 0.067 \frac{\epsilon_{mf}^3}{(1 - \epsilon_{mf})^2} \times \frac{(\rho_s - \rho_f) \times g}{\rho_f v^2} \times \frac{1}{S_v^3} - 1} \right] \quad (2)$$

Accordingly, to calculate  $u_{mf}$ , the characteristics of the gas ( $\rho_f, \eta$ ), the density  $\rho_s$  of the particles, the porosity  $\epsilon_{mf}$  of the bed at minimum fluidization, and the volume-specific surface area  $S_v$  of the solids must be known. The specific surface area defined by

$$S_v = \frac{\text{surface area of all particles in the bed}}{\text{volume of all particles in the bed}}$$

(this takes into account only the external area, which governs hydraulic resistance, not the pore surface area as in porous catalysts) cannot be determined very ex-

actly in practice. Hence  $u_{mf}$  should not be calculated on the basis of the measured particle-size distribution of a representative sample of the bed solids; instead, it is better measured directly. Equation 2 can be employed advantageously to calculate  $u_{mf}$  in an industrial-scale process on the basis of minimum fluidization velocities measured in the laboratory under ambient conditions [21].

An equation from Wen and Yu [22] can be used for approximate calculations:

$$Re_{mf} = 33.7(\sqrt{1 + 3.6 \times 10^{-5} \times Ar} - 1) \quad (3)$$

where

$$Re_{mf} = \frac{u_{mf} d_p}{\nu} \quad (4)$$

and

$$Ar = \frac{g d_p^3}{\nu^2} \times \frac{\rho_s - \rho_f}{\rho_f} \quad (5)$$

Here the Sauter diameter calculated from the mass-density distribution  $q_3(d)$  of the particle diameters

$$d_p = \frac{1}{\int_{d_{min}}^{d_{max}} d^{-1} \times q_3(d) \times dd} \quad (6)$$

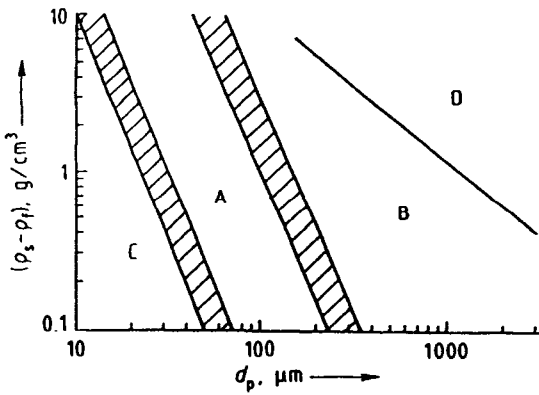


Figure 3. Geldart diagram (boundaries according to Molerus [24]).

should be used for the characteristic particle diameter  $d_p$ .

### 10.2.2.2 Fluidization Properties of Typical Bed Solids

In fluidization with gases, solids display characteristic differences in behavior that can also affect the operating characteristics of fluidized-bed reactors. Geldart has proposed an empirically based classification of solids into four groups (A to D) by fluidization behavior [23]. The parameters employed are those crucial for fluidization properties: the mean particle diameter ( $d_p$ ) and the density difference ( $\rho_s - \rho_f$ ) between solid and fluid. Figure 3 shows the Geldart diagram with the interclass boundaries theoretically established by Molerus [24].

Solids of group C are very fine-grained, cohesive powders (e.g. flour, fines from cyclones, and electrostatic filters) that virtually cannot be fluidized without fluidization aids. The adhesion forces between particles are stronger than the forces that the fluid can exert on the particles. Gas flow through the bed forms channels extending from the grid to the top of the bed, and the pressure drop across the bed is lower than the value from eq 1. Fluidization properties can be improved by the use of mechanical equipment (agitators, vibrators) or flowability additives such as Aerosil.

Solids of group A have small particle diameters ( $\approx 0.1$  mm) or low bulk densities; this class includes catalysts used, for example, in the fluidized-bed catalytic cracker. As the gas velocity  $u$  increases beyond the minimum fluidization point, the bed of such a solid first expands uniformly until bubble formation sets in at  $u = u_{mb} > u_{mf}$ . The bubbles grow by coalescence but break up again after passing a certain size. At a considerable height above the gas distributor grid, a dynamic equilibrium is formed between bubble growth

and breakup. If the gas flow is cut off abruptly, the gas storage capacity of the fluidized suspension causes the bed to collapse rather slowly.

Group B solids have moderate particle sizes and densities. Typical representatives of this group are sands with mean particle diameters between 0.06 mm and 0.5 mm. Bubble formation begins immediately above the minimum fluidization point. The bubbles grow by coalescence, and growth is not limited by bubble splitting. When the gas flow is cut off abruptly, the bed collapses quickly.

Group D includes solids with large particle diameters or high bulk densities; examples are sands with average particle diameters greater than 0.5 mm. Bubbles begin to form just above the minimum fluidization point, but the character of bubble flow is markedly different from that in group B solids: group D solids are characterized by the formation of "slow" bubbles. On sudden stoppage of the gas flow, the bed also collapses suddenly.

### 10.2.2.3 Gas Distribution

Gas distribution devices must satisfy the following requirements:

- (i) Ensure uniform fluidization over the entire cross-section of the bed (especially important for shallow beds).
- (ii) Provide complete fluidization of the bed without dead spots where, for example, deposits can form.
- (iii) Maintain a constant pressure drop over long operation periods (outlet holes must not become clogged).

Often, the gas distributor design must also prevent solids from raining through the grid both during operation and after the bed has been shut off. Porous plates of glass, ceramics, metal, or plastic are commonly used as gas distributors in laboratory apparatus; a variety of designs are used in pilot plant and full-scale fluidized-bed reactors (see Fig. 4). Many more designs can be found, for example in Ref. 2.

The principal requirement – that of a uniform distribution of fluidizing gas over the bed cross-section – can be met if the pressure drop  $\Delta p_d$  across the gas distribution grid is large enough. Suggested values for the ratio  $\Delta p_d : \Delta p_{fb}$  are 0.1–0.3 (with a minimum  $\Delta p_d$  of 3.5 kPa) [25], 0.2–0.4 [26],  $> 0.15$  [2], and  $> 0.3$  [27].

In the operation of fluidized-bed reactors, the quadratic response ( $\Delta p_d \propto u^2$ ) of industrial gas distributor designs must be kept in mind, because even if the fluidization velocity is lowered only slightly, an unaccept-

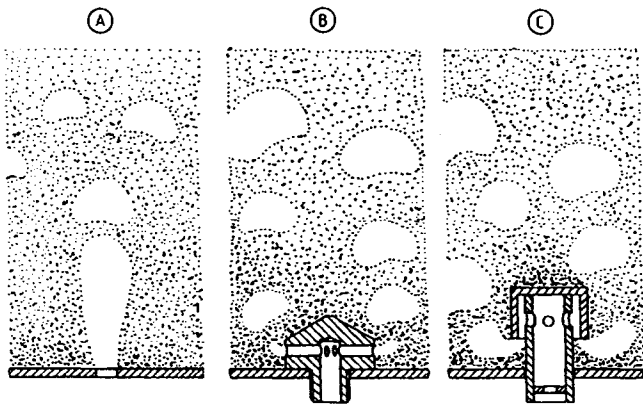


Figure 4. Industrial gas distributors: (A) perforated plate; (B) nozzle plate; (C) bubble-cap plate.

ably low pressure drop across the gas distributor may occur.

#### 10.2.2.4 Gas Jets in Fluidized Beds

Gas jets can form at the outlet openings of industrial gas distributors and also where gaseous reactants are admitted directly into the fluidized bed. A knowledge of the geometry of such jets, in particular the depth of penetration, is important for the implementation of chemical operations in fluidized-bed reactors, and not just from the standpoint of reaction engineering. It is also vital for reasons of design: the strongly erosive action of these jets means that internals, such as heat-exchanger tubes, must not be located within their range.

The literature contains many empirical correlations for estimating the mean depth of jet penetration [2–4]; these must, however, be used with care and, whenever possible, only within the range of parameter values for which they were derived. By way of example, Merry gives the following correlations for vertical gas jets. [28]:

$$\frac{L}{d_0} = 5.2 \left( \frac{\rho_f d_0}{\rho_s d_p} \right)^{0.3} \left[ 1.3 \left( \frac{u_0^2}{g d_0} \right)^{0.2} - 1 \right] \quad (7)$$

and for horizontal jets [29]:

$$\frac{L}{d_0} = 5.25 \left[ \frac{\rho_0 u_0^2}{(1 - \epsilon) \rho_s g d_p} \right]^{0.4} \left( \frac{\rho_f}{\rho_s} \right)^{0.2} \left( \frac{d_p}{d_0} \right)^{0.2} - 4.5 \quad (8)$$

Here,  $d_0$  is the diameter of the outlet opening,  $u_0$  is the outflow velocity, and  $\rho_0$  is the density of the jet gas.

#### 10.2.2.5 Bubble Development

For many applications, especially physical operations and noncatalytic reactions, the state of a fluidized bed

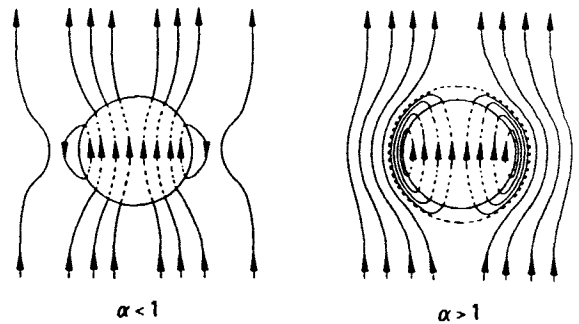


Figure 5. Gas flow for isolated rising bubbles in the Davidson model [30].

can adequately be described in terms of a single quantity averaged over the entire bed, such as the mean bed porosity  $\epsilon$ . In contrast, the design of fluidized-bed catalytic reactors requires that local fluid-flow conditions are also taken into account.

The local fluid mechanics of gas–solid fluidized beds are determined by the existence of bubbles, which influence the performance of fluidized-bed equipment in several ways: the stirring action and convective solids transport by the rising bubbles are helpful; the resulting intensive solids motion produces a uniform temperature throughout the fluidized bed and rapid heat transfer between the bed and the heating or cooling tubes submerged in it. The bubbles and the motion of solids that they cause, however, also have some drawbacks: attrition of solid particles, erosion of internals, and increased solids entrainment by bubbles bursting at the bed surface. The existence of bubbles is particularly detrimental in the case of a heterogeneous catalytic gas-phase reaction, because the bypass of reactant gas in the bubble phase limits the conversion achieved in the fluidized bed.

The ultimate cause of bubble formation is the universal tendency of gas–solid flows to segregate. Many studies on the theory of stability [3, 4] have shown that disturbances induced in an initially homogeneous gas–solid suspension do not decay but always lead to the formation of voids. The bubbles formed in this way exhibit a characteristic flow pattern whose basic properties can be calculated with the model of Davidson and Harrison [30]. Figure 5 shows the streamlines of the gas flow relative to a bubble rising in a fluidized bed at minimum fluidization conditions ( $\epsilon = \epsilon_{mf}$ ). The characteristic parameter is the ratio  $\alpha$  of the bubble's upward velocity  $u_b$  to the interstitial velocity of the gas in the suspension surrounding the bubble:

$$\alpha = \frac{u_b}{u_{mf}/\epsilon_{mf}} \quad (9)$$

The case  $\alpha > 1$  is typical for solids of Geldart groups A and B. The gas rising in the bubble flows downward again in a thin layer of suspension ("cloud") sur-

rounding the bubble. An important point for heterogeneous catalytic gas-phase reactions is that the presence of a boundary between bubble gas and suspension gas leads to the existence of two distinct phases (bubble phase and suspension phase) with drastically different gas-solid contact.

If  $\alpha < 1$ , some of the gas in the suspension phase undergoes short-circuit flow through the bubble, while only part of the bubble gas recirculates through the suspension. This type of flow is typical for fluidized beds of coarse particles (Geldart Group D).

Under the real operating conditions of a fluidized-bed reactor, a number of interacting bubbles occur in the interior of the fluidized bed. As a rule, the interaction leads to coalescence. As detailed studies have shown, this process is quite different from that between gas bubbles in liquids because of the absence of surface-tension effects in the fluidized bed [31, 32]. Werther has derived a simple empirical correlation (based on the mechanism of bubble coalescence) for the growth of the mean bubble size  $d_v$  (diameter of the sphere of equal volume) with increasing height  $h$  above the grid [33, 34]:

$$\left(\frac{d_v}{m}\right) = 0.0085 \left[1 + 27 \left(\frac{u - u_{mf}}{m/s}\right)\right]^{1/3} \times \left[1 + 6.8 \left(\frac{h + h' - h_0}{m}\right)\right]^{1.2} \quad (10)$$

where  $h'/m = 0$  for gas distribution through porous plate, and

$$\frac{h'}{m} = 0.147 \left\{ \left[ 118 \left(\frac{d_{v0}}{m}\right) \left[1 + 27 \left(\frac{u - u_{mf}}{m/s}\right)\right]^{-1/3} \right]^{0.83} - 1 \right\} \quad (11)$$

for industrial gas distributors. Here  $d_{v0}$  is the initial size of the bubbles formed at a grid opening or at the end of a gas jet. The initial size can be calculated from the volume flow rate of gas  $\dot{V}_0$  through the grid opening [30]:

$$d_{v0} = 1.3 \left(\frac{\dot{V}_0^2}{g}\right)^{0.2} \quad (12)$$

In eq 10,  $h_0$  is the height above the grid where the bubbles form (for a porous plate,  $h_0 = 0$ ; for a perforated plate,  $h_0 = L$ ; for a nozzle plate,  $h_0$  is the height of the outlet opening above the plate; and for a bubble-cap plate,  $h_0$  is the height of the lower edge of the cap above the plate).

For more exact calculations, a differential equation for bubble growth should be used in the case of Geldart group A and B solids [35, 36]:

$$\frac{d}{dh} d_v = \left(\frac{2\epsilon_b}{9\pi}\right)^{1/3} - \frac{d_v}{3\lambda u_b} \quad (13)$$

with the following boundary condition at  $h = h_0$ :

$$\frac{d_{v0}}{m} = \begin{cases} 0.008 \times \epsilon_b^{1/3} & \text{for a porous plate} \\ 1.3 \left(\frac{\dot{V}_0^2}{g}\right)^{0.2} & \text{for an industrial gas distributor} \end{cases} \quad (14)$$

The local volume fraction of bubble gas  $\epsilon_b$  is given by

$$\epsilon_b = \dot{V}_b / u_b \quad (15)$$

and the visible bubble flow  $\dot{V}_b$  is

$$\dot{V}_b \approx 0.8(u - u_{mf}) \quad (16)$$

The upward velocity  $u_b$  of bubbles depends not only on the bubble size but also on the diameter  $d_t$  of the fluidized bed:

$$u_b = \dot{V}_b + 0.71 \times \vartheta \times \sqrt{gd_v} \quad (17)$$

where

$$\vartheta = \begin{cases} 3.2 \times d_t^{0.33} & 0.05 \leq d_t \leq 1 \text{ m Geldart group A} \\ 2.0 \times d_t^{0.5} & 0.1 \leq d_t \leq 1 \text{ m, Geldart group B} \end{cases} \quad (18)$$

Outside these limits,  $\vartheta$  is taken as constant.

The differential equation (eq 13) describes not only bubble growth by coalescence but also the splitting of bubbles (second term on the right-hand side [37]). The crucial parameter here is the mean bubble lifetime  $\lambda$ :

$$\lambda \approx 280 \times \frac{u_{mf}}{g} \quad (19)$$

In practice, bubble growth is limited not only by the splitting mechanism based on the particle-size distribution of the bed solids, but also by internals (screens, tube bundles, and the like) that cause bubbles to break up. Computational techniques for estimating this process are given in Refs 38 and 39. An example of measured and calculated bubble-growth curve is presented in Figure 6.

### 10.2.2.6 Elutriation

When bubbles burst at the surface of the fluidized bed, solid material carried along in their wake is ejected into the freeboard space above the bed. The solids are classified in the freeboard; particles whose settling velocity  $u_t$  is greater than the gas velocity fall back into the bed, whereas particles with  $u_t < u$  are elutriated by the gas stream. As a result, both the volume concentration of solids  $c_v$  and the mass flow rate of entrained solids in the freeboard show a characteristic exponential decay



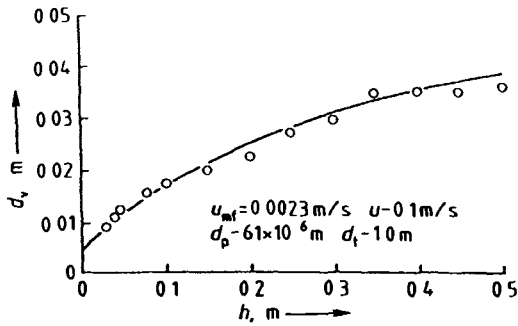


Figure 6. Bubble growth in a fluidized bed of fine particles (Geldart group A, data points from Ref 40, calculation from Ref 36)

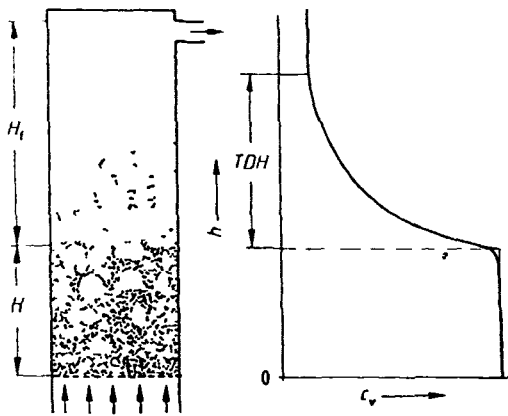


Figure 7 Schematic drawing of fluidized bed and freeboard

(Fig 7) With increasing height above the bed surface, the transport disengaging height (TDH) is finally reached. Here the increased local gas velocities due to bubble eruptions have decayed, and the gas stream contains only particles with  $u_t < u$ . When the TDH can be reached in a fluidized-bed reactor, this is associated with minimum entrained mass flow rates and solids concentrations, and hence with minimum loading on downstream dust collection equipment. Design of the dust collection system requires a knowledge of the entrained mass flow rate  $G_s$ , and the particle-size distribution of the entrained solids. For the design of the fluidized-bed reactor, the distribution  $c_v(h)$  of the solids volume concentration as a function of height in the freeboard must be known.

For solids of Geldart group A, the TDH can be estimated with the diagram shown in Fig 8 [41]. The following relation is given for the TDH of Geldart group B solids as a function of the size  $d_v$  of bubbles bursting at the bed surface [42]

$$TDH = 18.2 \times d_v \quad (20)$$

Equation 20 was, however, derived for a bench-scale unit and may not scale to plant-size equipment.

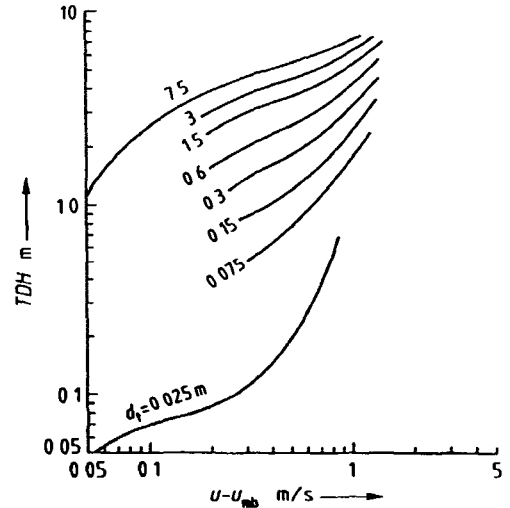


Figure 8. Estimation of transport disengaging height (TDH) according to Ref 41,  $u_{mb}$  = fluidization velocity at which bubble development begins

The mass flow rate  $G_s$  of entrained solids per unit area leaving the fluidized-bed reactor is the sum of contributions from the entrainable particle size fractions ( $u_t < u$ )

$$G_s = \sum_i x_i \times \chi_i^* \quad (21)$$

Here  $x_i$  is the mass fraction of particle-size fraction  $i$  in the bed material and  $\chi_i^*$  is the elutriation rate constant for this fraction.

The literature contains a number of empirical correlations for estimating  $\chi_i^*$  [2-4]. More physically based are the elutriation models of Wen and Chen [43] and of Kunii and Levenspiel [2, 44], which enable not only calculation of the exiting mass flow rate but also estimation of the concentration versus height  $c_v(h)$  in the freeboard.

### 10.2.2.7 Circulating Fluidized Beds

Whereas for bubbling fluidized beds the solids holdup in the upper part of the reactor and the entrainment of catalyst are often negligible, these features become most important in the case of circulating fluidized beds. These systems are operated at gas velocities above the terminal settling velocity  $u_t$  of a major fraction or even all of the catalyst particles used ( $\approx 1 \text{ m s}^{-1} \leq u \leq \approx 20 \text{ m s}^{-1}$ ). As a result, the solids mass flow rates to be externally recirculated are high, up to figures of more than  $1000 \text{ kg m}^{-2} \text{ s}^{-1}$ .

The flow structure within circulating fluidized beds is very complex and exhibits axial as well as horizontal nonuniformities as it is shown in Fig 9. Unless the solids holdup is very low and the gas velocity very high

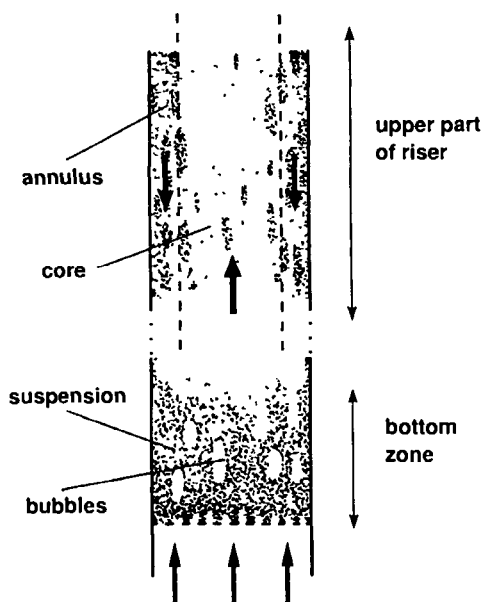


Figure 9. Schematic diagram of flow structure in a circulating fluidized bed

a dense ( $\bar{c}_v \geq \approx 0.15$ ) bottom zone near the gas distributor exists, where bubble-like voids have been observed surrounded by a dense suspension. In the upper part of the riser the solids concentration is lower than near the distributor ( $\bar{c}_v \leq \approx 0.05$ ). Although a number of modeling approaches for prediction of the axial solids-concentration profile have been developed [45–47], there is no generally accepted method available. Experimental studies [48–54] have shown that the circulating fluidized bed exhibits characteristic horizontal profiles in the upper part of the riser, with the concentration  $c_{v,\text{wall}}$  near the vessel wall being always significantly higher than the value  $\bar{c}_v$  averaged over the vessel cross-section; for example,  $c_{v,\text{wall}} = 2.3 \times \bar{c}_v$  [55].

Local measurements of the solids concentration and solids velocity show that upward-flowing regions of low solids concentration and downward-flowing aggregates of high solids concentration alternate in time at every point inside the fluidized bed, with downward-moving aggregates (strands, clusters) predominating near the wall and upward-moving regions of low suspension concentration predominating in the central zone.

Solids carried over with the fluidized gas are generally collected in cyclones. In the case of bubbling beds, the solids can easily be returned to the bed through the standpipe of the cyclone, which dips directly into the bed. Due to the large amounts of circulating solids, circulating fluidized beds require very large cyclones arranged beside and outside the bed, with special valves needed to connect the standpipe to the bed vessel. Figure 10 shows two design options, the siphon and the L-valve. Within the siphon the solids

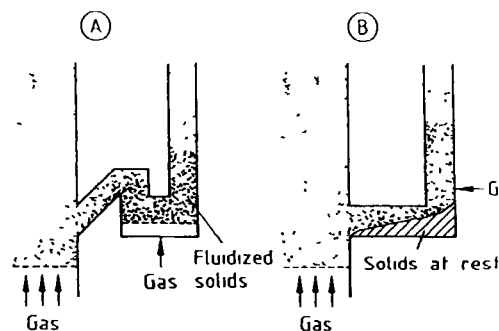


Figure 10. Design options for solids recycle. (A) siphon, (B) L-valve.

are fluidized (i.e. enabled to flow back into the reactor). In the L-valve design, the mass flow rate of the solids can be controlled by varying the gas supplied to the standpipe.

Because the solids path does not contain any sort of mechanical closure, the characteristic pressure distribution plotted in Fig. 11 is obtained. The distribution of solids between the fluidized bed and the recycle line is directly related to this pressure distribution. Operating properties differ from one recycle design to another [56].

### 10.2.2.8 Attrition of Solids

The attrition of solid particles is an unavoidable consequence of the intensive solids motion resulting from the presence of bubbles in the fluidized bed. The attrition problem is especially critical in processes where the bed material needs to remain unaltered for the longest possible time, as in fluidized-bed reactors for heterogeneous catalytic gas-phase reactions. Catalyst attrition is important in the economics of such processes and may even become the critical factor.

When designing catalytic fluidized-bed processes, the attrition performance of candidate catalysts should be tested under standardized conditions in the process development stage. This test can be performed in a small laboratory apparatus; it consists essentially of an extended fluidization test in which the mass of solids carried out of the bed is recorded as a function of time. Figure 12 presents a typical test result: during the first hours of testing, both the attrited material and the fine fraction of the bed material are elutriated. Only after a relatively long operating period is a quasi steady-state attained. The attrition rate  $r_a$  in this steady state can be defined as

$$r_a = \frac{1}{m_b} \times \frac{\Delta m_a}{\Delta t} \quad (22)$$

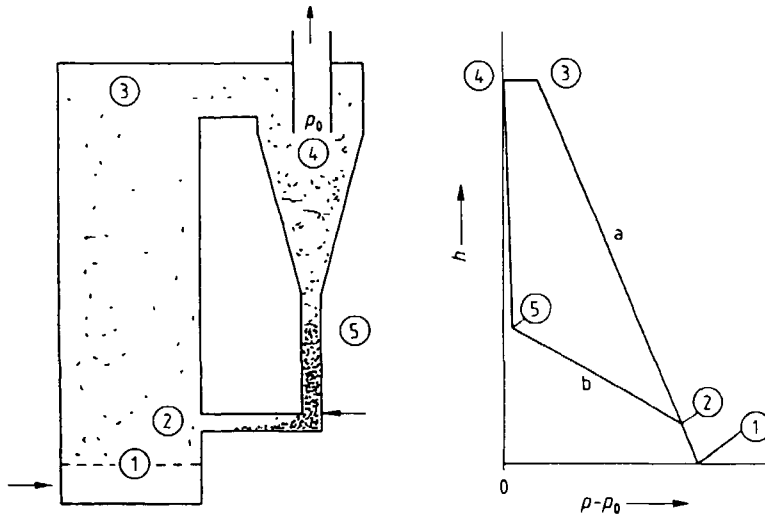


Figure 11. Pressure distribution in solids recycle system of a circulating fluidized bed: (a) fluidized bed; (b) return leg.

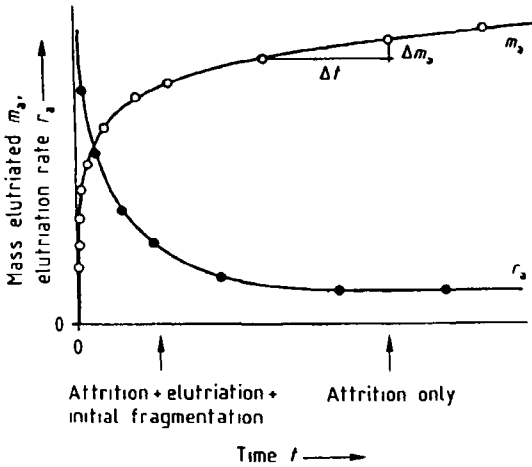


Figure 12. Result of an attrition measurement.

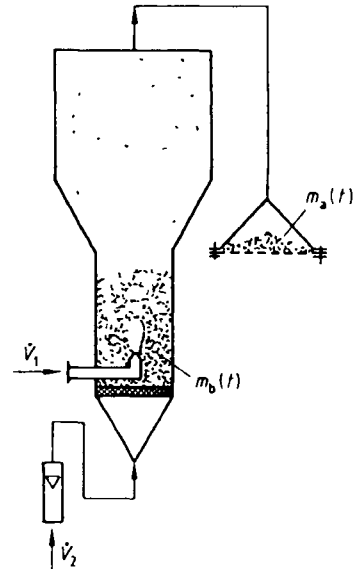


Figure 13. Experimental apparatus for attrition measurement

where  $m_a$  is the elutriated mass and  $m_b$  the bed mass. Usually  $r_a$  is expressed as percentage per day; for relatively attrition-resistant, fluidized-bed catalysts, it is of the order of 0.2% per day [5].

Many standard test apparatuses have been proposed for comparative attrition tests [57, 58], but all such equipment has been suitable only for comparative studies of different catalysts under consideration for the same process. The attrition measured in large-scale equipment can be far different from the values measured in a test apparatus.

A number of sources can be identified for catalyst attrition in industrial fluidized-bed reactors:

- (i) Jet attrition at gas distribution grid openings and nozzles where gaseous reactants are admitted to the bed.
- (ii) Bubble attrition in the bed due to solids motion caused by bubbles.

- (iii) Attrition in cyclones.
- (iv) Attrition in pneumatic conveyor lines, such as those between reactor and regenerator beds.

Empirical correlations are available for the attriting action of gas jet in the fluidized bed [59] and for the size reduction effect of solids motion in the bed [60, 61].

Werther and Xi [62, 63] employ the laboratory apparatus shown schematically in Fig. 13 which enables separate study of the attrition due to jets from nozzles of various diameters and that due to bubbles.

The jet attrition rate  $R_{a,j}$  defined as the mass of attrited fines per unit time produced by a single jet, is proportional to the jet gas density, the square of the orifice diameter, and to the cube of the jet exit velocity [64]:

$$R_{a,j} = K \times \rho_0 \times d_0^2 u_0^3 \quad (23)$$

The attrition rate constant  $K$  describes in the first place material properties which may be influenced by, for example, the manufacturing process of the catalyst. The attrition rate also depends on whether the jet issues into a prefluidized bed or into a nonaerated bed. The attrition effect of an upward jet equals that of a horizontal jet, whereas the attrition effect of a downward jet is significantly higher. For the prediction of the attrition effect of a multihole gas distributor, a model has been developed that is based on a single jet attrition measurement [62].

Further measurements indicate that for a given bed height the bubble attrition rate defined by eq 22 is essentially proportional to the velocity difference ( $u - u_{a,\min}$ )

$$r_{a,b} \propto (u - u_{a,\min}) \quad (24)$$

where  $u_{a,\min}$  denotes a minimum velocity ( $>u_{mf}$ ) above which marked attrition sets in; for practical applications the simplifying assumption  $u_{a,\min} \approx u_{mf}$  can be made [63].

A variety of approaches exist for reducing attrition in industrial fluidized-bed reactors. The jet attrition action can be controlled with special gas distributor designs ([5]; for example by the use of bubble caps, Fig. 4) such that gas jets do not issue directly into the bed at high velocity. Attrition due to bubbles can be lowered by limiting bubble growth (avoiding high gas velocities and large bed heights; use of fine catalysts with low  $u_{mf}$ , as implied by eqs 13 and 19). Attrition in cyclones can be prevented, in the simplest case, by replacing the cyclones with devices such as filters. Attrition can also be minimized by cutting back the load on the cyclone, for example, by placing the cyclones above the TDH. Relatively high catalyst attrition also occurs in circulating fluidized beds where very large quantities of solids must be collected in the cyclones.

## 10.2.3 Gas Mixing in Fluidized-Bed Reactors

The mixing and residence-time distribution of the gas are particularly important for catalytic reactions but are also significant for gas–solid reactions when gaseous reactants are to be converted to the greatest possible extent in fluidized beds. Gas mixing is closely linked to the motion and mixing of the solids in the bed.

### 10.2.3.1 Gas Mixing in Bubbling Fluidized Beds

If the flow and mixing of gas in the bubbling fluidized bed are described by a simple one-phase dispersion model, the coefficients  $D_{gv}$  and  $D_{gh}$  of gas dispersion in the vertical and horizontal directions have similar

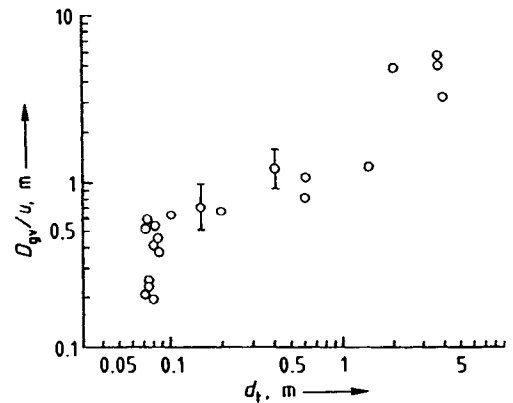


Figure 14. Vertical gas dispersion in a fluidized bed of solids of Geldart group A (measurements by various workers [2]).

numerical values and follow trends similar to those of the solids dispersion coefficients. By way of example, Fig. 14 shows the effect of fluidized-bed diameter  $d_t$  on vertical gas dispersion. The increase in dispersion coefficient with vessel diameter might be attributable to the formation of large-scale solids circulation patterns, which becomes more marked in larger equipment. The coefficients of horizontal gas dispersion are a factor of 10–100 lower than those of vertical gas dispersion.

Many recent studies show that a single-phase dispersion model gives only a rough description of gas mixing in bubbling fluidized beds [65]. A more exact description comes from models that take account of local flow conditions in the bed, especially the presence of bubbles (see Section 10.2.5).

### 10.2.3.2 Gas Mixing in Circulating Fluidized Beds

Only a few detailed studies of gas mixing in circulating fluidized beds have been published [52, 66–71]. The bubbles in a bubbling fluidized bed influence the gas residence-time distribution and mixing directly through the bypass action of the bubble-gas flow and gas exchange between the bubbles and the surrounding suspension phase, and also indirectly through the solids motion that they induce. In the circulating fluidized bed, however, the gas-mixing properties are controlled by segregation due to the formation of solid aggregates (strands, clusters) and the rapid downward movement of solids strands predominantly near the wall. Grace and co-workers [67], for example, showed that a single-phase dispersion model cannot describe the tracer gas residence-time distributions that they measured. They propose instead a two-phase model featuring exchange between a wall zone with stagnant gas and a core zone with plug flow.

For the case of horizontal gas mixing, Werther and co-workers [70, 71] have shown that, for the bed solids they used (quartz sand,  $d_p = 0.13$  mm, Geldart group B), horizontal gas mixing in the top part of the circulating fluidized bed in the core zone can be described by the model for gas dispersion in turbulent single-phase flow [72]. The Peclet number

$$Pe_{r,c} = \frac{u_c \times 2R^*}{D_{r,c}} \quad (25)$$

has a value of 465, which is in fairly good agreement with values measured in single-phase flows (when defined in terms of the superficial velocity in the core zone  $u_c$ , the radius of the core zone  $R^*$ , and the horizontal dispersion coefficient in the core zone  $D_{r,c}$ ) [73]. This value is independent of the solids circulation rate  $G_s$ . The circulating fluidized bed thus exhibits no especially intensive horizontal gas mixing, at least not in the upper section where solids concentrations are relatively low.

## 10.2.4 Industrial Applications

In this section the industrial uses of fluidized-bed reactors for heterogeneous catalytic gas-phase reactions and the polymerization of alkenes are presented. The most important applications are listed and a few typical examples are analyzed in more detail. Complete descriptions of industrial uses of the fluidized-bed reactor can also be found in Refs 2, 6, 12 and 13.

### 10.2.4.1 Heterogeneous Catalytic Gas-Phase Reactions

The fluidized-bed reactor offers the following principal advantages over the fixed-bed reactor for heterogeneous catalytic gas-phase reactions:

- (i) High temperature homogeneity, even with strongly exothermic reactions.
- (ii) Easy solids handling, permitting continuous withdrawal of spent catalyst and addition of fresh if the catalyst rapidly loses its activity.
- (iii) Ability to operate in the explosion range, provided the reactants are not mixed until they are inlet to the fluidized bed. This is because the high heat capacity of the bed solids, together with intensive solids mixing, prevents the propagation of explosions.

The ease of solids handling was the basic reason for the success of catalytic cracking of long-chain hydrocarbons in the fluidized bed (Fig. 15). The cracking reaction is endothermic and involves the deposition of

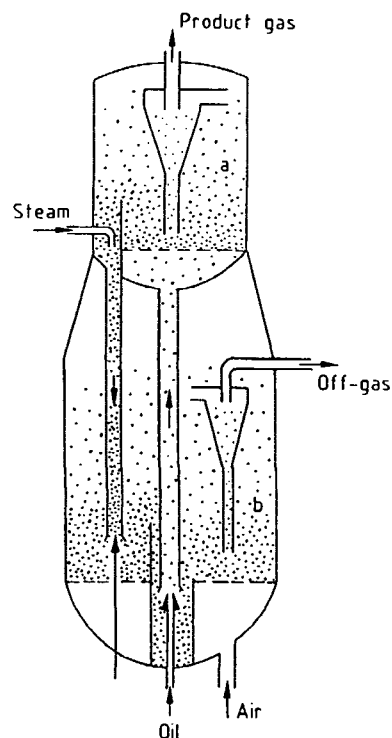


**Figure 15.** Fluid catalytic cracking process (Kellogg-Orthoflow system; according to Refs 74 and 75: (a) reactor; (b) regenerator.

coke on the catalyst surface, which quickly renders the catalyst inactive. Accordingly, the catalyst must be continuously discharged from the reactor and regenerated in an air-fluidized regenerator bed (b), where its coke loading is lowered from 1–2 to 0.4–0.8 wt%. The combustion in this bed simultaneously furnishes the heat required for the cracking reactor; the catalyst acts as a heat carrier. The temperature in the regenerator is 570–590 °C and in the reactor, 480–540 °C [2]. In a stripper, steam is admitted to remove hydrocarbons adhering to the catalyst before it is forwarded to the regenerator.

With the advent of high-activity zeolite catalysts in the 1960s, the bubbling fluidized bed, operated at gas velocities between 0.31 and 0.76 m s<sup>-1</sup> [2], was replaced by the riser cracker (Fig. 16), in which the oil is fed in at the bottom of the riser (c) is vaporized in contact with the hot catalyst, and the mixture of oil vapors and cracking gas transports the catalyst up through the riser. In the reactor bed (a), solids are collected before passing through the stripper (b) to the regenerator (f). By virtue of the short contact time of the order of a few seconds and the narrow gas residence-time distribution, the high activity of the zeolite catalyst is optimally utilized, and a higher gasoline yield is achieved [2, 6].

The crucial factor in the successful use of the fluidized-bed reactor for the synthesis of acrylonitrile by the ammoxidation of propene (Sohio process) was

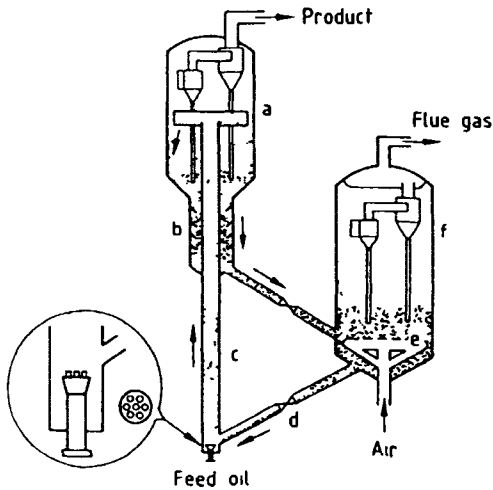
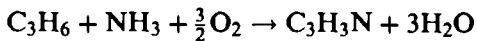


**Figure 16.** Riser cracking process (UOP system) [2]: (a) reactor; (b) stripper; (c) riser; (d) slide valve; (e) air grid; (f) regenerator.

reliable control of this strongly exothermic reaction ( $\Delta H_r = -515 \text{ kJ mol}^{-1}$  of acrylonitrile):



The reaction is carried out at a bed temperature of 400–500 °C and a gas contact time of 1–15 s [76] or 5–20 s [2]. Figure 17 is a schematic of the reactor. Air is fed to the bottom of the fluidized-bed vessel. The reactants ammonia and propene are fed in through a separate distributor (b). Catalyst regeneration by carbon burnoff occurs in the space between the air distributor and the feed-gas distributor. The heat of reaction is removed by bundles of vertical tubes (a) inside the bed (horizontal tubes are used in other designs [77]).

The Fischer-Tropsch synthesis of hydrocarbons is used on a large scale for fuel production in South Africa [78, 79]. Synthesis gas generated from coal in Lurgi fixed-bed gasifiers enters the Synthol reactor (Fig 18), where it is reacted over an iron catalyst at  $\approx 340^\circ\text{C}$ . The reactor works on the principle of the circulating fluidized bed. The mean porosity in the riser is 85%, and the gas velocity varies between 3 and 12  $\text{m s}^{-1}$  [2]. Reaction heat is removed by way of heat-exchanger tube bundles placed inside the riser.

Other catalytic reactions carried out in fluidized-bed reactors are: the oxidation of naphthalene to phthalic anhydride [2, 6, 80]; the ammoxidation of isobutane to methacrylonitrile [2]; the synthesis of maleic anhydride from the naphtha cracker  $\text{C}_4$  fraction (Mitsubishi process [81, 82]) or from *n*-butane (ALMA process [83, 84]); the reaction of acetylene with acetic acid to vinyl acetate [2]; the oxychlorination of ethylene to 1,2-dichloroethane [2, 6, 85, 86]; the chlorination of methane [2], the reaction of phenol with methanol to cresol and 2,6-xyleneol [2, 87]; the reaction of methanol to gasoline

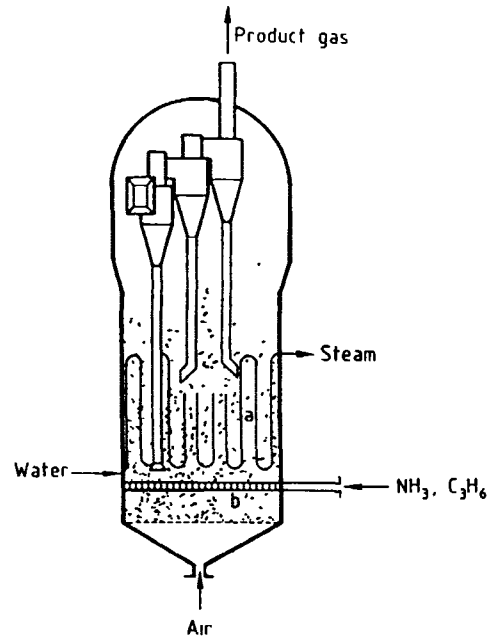


**Figure 17.** Synthesis of acrylonitrile (Sohio process) [2]. (a) cooler with internals, (b) distributor

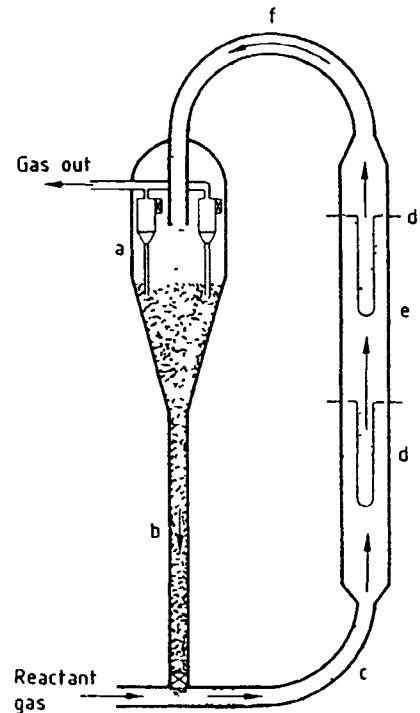


**Figure 18.** Fischer Tropsch synthesis in the Synthol reactor [2, 78] (a) hopper, (b) standpipe, (c) riser, (d) cooler (coil), (e) reactor, (f) gooseneck

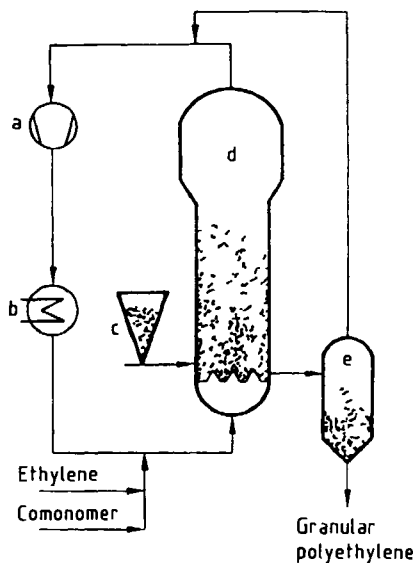


**Figure 19.** Gas-phase polymerization of ethylene (Unipol process) [2] (a) compressor, (b) cooler, (c) catalyst feed hopper, (d) reactor, (e) separator

[88, 89], the synthesis of phthalonitrile by ammoxidation of *o*-xylene [90], the synthesis of aniline by gas-phase hydrogenation of nitrobenzene [91], and the low-pressure synthesis of melamine from urea [92]

#### 10.2.4.2 Polymerization of Alkenes

The gas-phase polymerization of ethylene in the fluidized bed was developed by Union Carbide (Unipol process [93], Fig. 19). The reaction gas (ethylene and its comonomers butene and higher alkenes) fluidizes the bed at 75–100 °C and  $\approx 20$  bar. Extremely fine-grained catalyst is metered into the bed. Polymerization occurs on the catalyst surface and yields a granular product with a diameter ranging from 0.25 mm to 1 mm. Ethylene conversion is comparatively low, 2% per pass, so the reaction gas is recycled. The heat of reaction is removed by cooling the recirculating gas. The catalysts used have such a high activity that more than  $10^5$  parts by volume of polymer can be produced per unit weight of active substance in the catalyst [2]. Because of the high degree of catalyst dilution in the granular polymer, the catalyst need not be removed from the product.

Mitsui Petrochemical Industries has developed a process for the gas-phase fluidized-bed polymerization of propene, a plant using the process came on stream in 1984 [94]. The Unipol-Shell process was jointly developed by Union Carbide and Shell and commissioned in 1986.

#### 10.2.5 Modeling of Fluidized-Bed Reactors

Exhaustive literature surveys are available [2, 5, 6, 95, 96]. Many models exist in the literature, which are

classified in the cited references under various schemes. The available information can be summed up as follows: no generally accepted model of the fluidized-bed reactor exists; instead, many models have been proposed on the basis of more-or-less extensive experimental findings for various applications.

Any fluidized-bed reactor model can be broken down into separate components that describe, with varying degrees of accuracy, the hydrodynamics (depending on solid properties, operating conditions, and geometry), gas–solid contact, and reaction kinetics. The essential point is that the reactor geometry effect, which is important for scale-up (Section 10.2.6), manifests itself in the flow conditions and must therefore be included in the hydrodynamic part of the model.

Before a reactor model found in the literature can be applied to a given problem, the designer must determine whether numerical values are available for all model parameters, that is, whether the model is appropriate for design calculations or is a “learning model” [97] in which the numerical values of important parameters can be determined only after the model is adapted to actual test results.

Reaction kinetics may be determined for a fixed-bed reactor, provided measurements are performed under conditions comparable to those that prevail in the fluidized-bed reactor (for example the same solids composition and particle-size distribution, and the same activity state) [98]. However, the kinetic parameters can also be determined directly by measurements in a bench-scale fluidized-bed apparatus [99].

##### 10.2.5.1 Bubbling Fluidized-Bed Reactors

By far the majority of fluidized-bed reactor models described in the literature deal with reactions in bubbling fluidized beds [2, 5, 6, 95, 96]. For a specific application, modeling depends on the bubble flow regime. For slow-bubble systems (Fig. 5, left), the short-circuit flow of gas through the bubbles must be taken into account [100]. For fast-bubble systems (Fig. 5, right), the species have to be balanced separately in the bubble and suspension phases. If models from the literature are employed, those devised in the past, when adequate computing hardware was not available, often sought to obtain closed analytical expressions for the degree of conversion of a single reaction (usually taken as first order). The simplifying assumption of a single “effective” bubble size for the entire fluidized bed was therefore made [2], or the mass transfer area between the bubble and suspension phases was taken as uniformly distributed over the height of the bed (HTU or NTU concept, where HTU denotes height of transfer unit and NTU denotes number of transfer units [101]). Today, in view of the computing power available at the PC level, the recommended procedure is to start from

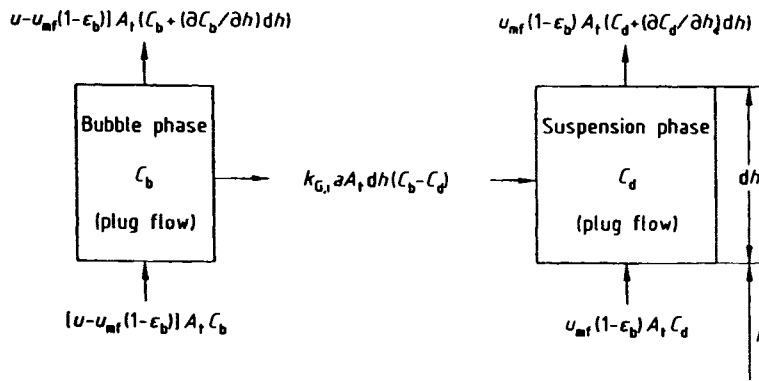


Figure 20. Two-phase model of the fluidized-bed reactor

local mass-transfer relations, write balance equations for the differential volume element of the reactor, and then numerically integrate these formulas. Figure 20 presents a model used for a constant-volume reaction [99, 102]. Here the simplifying assumption is that flow through the suspension phase is at the minimum fluidization velocity  $u_{mf}$ . For a heterogeneous catalytic gas-phase reaction, the material balances for species  $i$  in the unsteady-state cases are, for the bubble phase,

$$\varepsilon_b \frac{\partial C_{bi}}{\partial t} = -[u - u_{mf}(1 - \varepsilon_b)] \times \frac{\partial C_{bi}}{\partial h} - k_{G,i} \times a \times (C_{bi} - C_{di}) \quad (26)$$

and, for the suspension phase

$$(1 - \varepsilon_b)[\varepsilon_{mf} + (1 - \varepsilon_{mf})\varepsilon_i] \frac{\partial C_{di}}{\partial t} = -u_{mf}(1 - \varepsilon_b) \times \frac{\partial C_{di}}{\partial h} + k_{G,i} \times a \times (C_{bi} - C_{di}) + (1 - \varepsilon_b) \times (1 - \varepsilon_{mf})\rho_s \sum_{j=1}^M v_j r_j \quad (27)$$

In eqs 26 and 27 the following simplifying assumptions have been made:

- (i) Plug flow through the suspension phase at an interstitial velocity ( $u_{mf}/\varepsilon_{mf}$ ).
- (ii) Bubble phase in plug flow, bubbles are solids free.
- (iii) Reaction in suspension phase only.
- (iv) Constant-volume reaction (Ref. 99 shows how to handle a change in the number of moles).
- (v) Sorption effects are neglected (see Ref. 102 for handling sorption).

Here  $\varepsilon_i$  is the porosity of the catalyst particles,  $a$  is the local mass-transfer area per unit of fluidized-bed volume, which can be calculated as

$$a = \frac{6\varepsilon_b}{d_v} \quad (28)$$

for spherical bubbles,  $r_j$  is the rate of partial reaction  $j$  per unit mass of catalyst and  $v_j$  is the stoichiometric number of species  $i$  in reaction  $j$ .

The relationship

$$k_{G,i} = \frac{u_{mf}}{3} + \sqrt{\frac{4D_i \varepsilon_{mf} u_b}{\pi d_v}} \quad (29)$$

proposed by Sit and Grace [103] has proved useful for describing the mass-transfer coefficient  $k_{G,i}$  associated with component  $i$  in mass transfer between the bubble and suspension phases, where  $D_i$  is the molecular diffusion coefficient of species  $i$ .

The freeboard space above the bubbling fluidized bed must be considered in the reactor model if the entrainment rate is high and the reactions in the freeboard are not quenched, for example, by cooling.

Most fluidized-bed models include concentration profiles only for the vertical direction. This one-dimensional modeling is acceptable when the reactants are admitted uniformly over the bed cross-section. If, however, reactants are metered into the bed at individual feed points, three-dimensional modeling may become necessary [104–106].

As a rule, the modeling of solids behavior in fluidized-bed reactors is based on that in stirred tanks, and temperature homogeneity is a virtually fundamental property of these systems.

### 10.2.5.2 Circulating Fluidized-Bed Reactors

Since the number of different applications of circulating fluidized beds for catalytic reactions on the commercial scale is still small, the development of models for these systems is at an early stage of development. However, throughout the last decade many promising approaches have been developed, the most important of which are described in an overview edited by Grace [107].



In the early days of circulating fluidized-bed reactor modeling a very low axial dispersion and a laterally uniform flow structure was believed to characterize these systems. Thus, simple plug flow models were used [108]. This approach was found to oversimplify the behavior of circulating fluidized-bed reactors, because a significant amount of axial dispersion was observed. As a result, the plug flow model has often been modified by adding a dispersion term to the balance equations. Axial dispersion coefficients have been determined by many authors who measured the residence time distribution of tracer gases [109, 110]. Typical values of Peclet numbers  $Pe_{ax}$ , found are of the order of 10.

By means of a model reaction it has recently been proved that in many cases circulating fluidized-bed reactors cannot be characterized by solely considering mixing phenomena [111]. Instead, the presence of mass transfer limitations and bypassing was found to have a significant influence. In analogy to low-velocity fluidized beds a detailed description of the local flow structure within the reaction volume must serve as a basis for appropriate reactor modeling.

The highly nonuniform flow structure of circulating fluidized beds described in Section 10.2.2.7 has led to reactor models which separately deal with different axial zones. The bottom zone – if existing under the given operating conditions – can be described by models the basic approaches of which were originally developed for modeling bubbling fluidized beds as presented in Section 10.2.5.1 [112]. Modeling of the upper section of the circulating fluidized bed is in most cases based on a proper description of the heterogeneous core–annulus flow structure [113–115]. These state-of-the-art models are one-dimensional and define two phases or zones which are present at every axial location:

- (i) Dense phase or annulus zone – high solids concentration, gas stagnant or moving downwards.
- (ii) Dilute phase or core zone – low solids concentration, gas flowing quickly upwards.

Similar to the situation in bubbling fluidized beds the two phases exchange gas with each other and are modeled by separate equations which are obtained from mass balances for each component in each phase.

A typical example of a circulating fluidized-bed reactor model has been presented by Schoenfelder et al. [112, 116]. Its structure shown in Fig. 21 is based on the definition of four axial zones. Above the bottom zone the splash zone is located. It yields a mixing condition to link the bottom zone with the upper part of the reactor. Due to the internal backmixing this upper section is referred to as the recirculation zone. At the riser outlet, an exit zone on top of the recirculation zone yields a second boundary condition. Here, complete mixing is assumed.

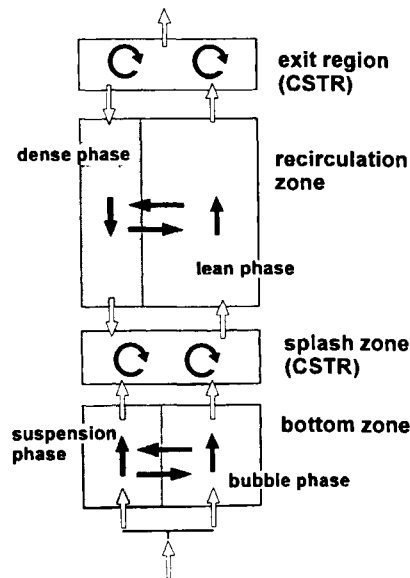


Figure 21. The four-stage model of the circulating fluidized-bed reactor (adapted from Ref. 116).

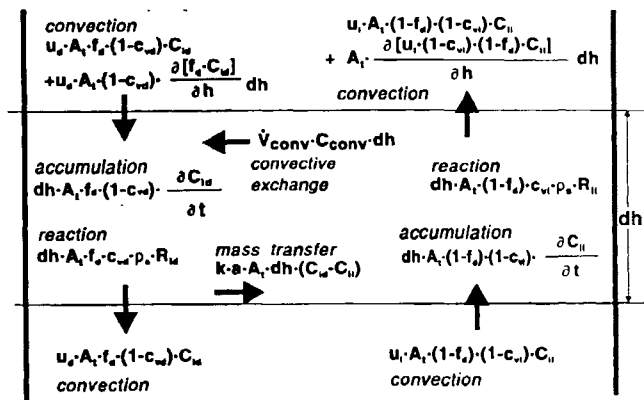


Figure 22. Control volume for differential balance for component  $i$  in the recirculation zone of a circulating fluidized-bed reactor (adapted from Ref. 112).

The differential equations to describe the recirculation zone are derived from mass balances. The control volume for identification of the different terms of these equations is depicted in Fig. 22. Simplifying assumptions for this approach are:

- (i) no axial dispersion within the phases;
- (ii) transport of gaseous species due to adsorption to solids negligible;
- (iii) downwards velocity and solids concentration of dense phase invariant with height.

Just as for this model all similar approaches found in the literature suffer from the problem that not all fluid mechanical variables can be precalculated on the basis of the operating conditions. Instead, reasonable estimations or measurements in cold flow models are used

to obtain numerical values for many variables. It is therefore absolutely necessary to refer to the original literature in order to perform quantitative calculations.

A common feature of all models for the upper part of circulating fluidized beds is the description of the mass exchange between dense phase and dilute phase. Analogously to low-velocity fluidized beds, the product of the local specific mass-transfer area  $a$  and the mass-transfer coefficient  $k$  may be used for this purpose. Many different methods for determining values for these important variables have been reported, such as tracer gas backmixing experiments [112], non-steady-state tracer gas experiments [117], model reactions [115], and theoretical calculations [114].

Similar to the bubbling fluidized-bed reactor, the solids behavior of the circulating fluidized-bed reactor can usually be described as completely mixed. This does not hold for riser reactors with very high gas velocities as they are used in many Fluid Catalytic Cracking units ( $u > 10 \text{ m s}^{-1}$ ). Here, better modeling results will be obtained by assuming dispersed plug flow of solids [110].

As well as for bubbling fluidized beds it can be assumed that circulating fluidized beds exhibit a high degree of temperature homogeneity, even in the case of highly exothermic reactions.

## 10.2.6 Scale-Up

Typical diameters of bench-scale fluidized-bed reactors are roughly 30–60 mm, and of pilot-scale units 450–600 mm, which should allow a reliable scale-up [5]. Full-scale fluidized-bed reactors have diameters up to  $\approx 10 \text{ m}$ . As equipment size increases, characteristic changes take place in the flow regimes that can decisively affect reactor performance. Such changes result either directly from the geometry or indirectly from design changes made as the unit is enlarged. In particular, experience has shown that the following factors affect the performance of bubbling fluidized beds during scale-up [118]:

### A Bed Diameter

According to eq 17, the mean upward bubble velocity increases as the bed diameter  $d_t$  increases. As a result, the bubbles have a shorter residence time in the bed, and the exchange area between the bubble and suspension phases is smaller, so conversion is reduced [119].

### B Grid Design

In the laboratory, porous plates are the preferred type of gas distributor because of the ease of working with them. Gas distribution becomes worse when these are replaced by industrial distributor designs; thus the exchange area between the bubble and suspension phases

is reduced, again with consequently lower conversion [119–121].

### C Internals

Whereas the laboratory fluidized bed is generally operated with no internals, plant equipment often must contain bundles of heat-exchanger tubes. Screens, baffles, or similar internals are frequently used to redistribute the bubble gas in industrial reactors. The mass-transfer area is thus increased relative to the fluidized bed without internals; the extra area can be utilized to partially offset the conversion-reducing effects of bed diameter and gas distributor [122].

### D Catalyst Particle Size Distribution

Bubble growth is influenced by the proportion of fines in the particle size distribution of the bed (usually measured as the weight fraction below 0.044 mm) or by the mean grain size  $d_p$  (via  $u_{mf}$ , eq 13). If the content of fines increases, bubbles collapse sooner and the equilibrium bubble size becomes smaller, with a resultant greater bubble–suspension mass-transfer area. This effect is generally fully developed only in the plant-scale reactor, where bubbles can grow without the hindrance of vessel walls. Thus, in principle, the performance of catalytic fluidized-bed reactors can be controlled by modifying the catalyst particle size distribution [123, 124]. The recommended content by weight of fines ( $< 0.044 \text{ mm}$ ) for “good fluidization” is 30–40% [125], but maintaining this high fines content in the system over a long span of time requires a very efficient solids recovery system.

### E Secondary Reactions in the Freeboard

In a bench-scale apparatus, the fluidized gas is rapidly cooled by the vessel wall in the freeboard space after leaving the bed, so secondary reactions in the freeboard are often negligible. Such is not the case in the plant-scale reactor. The action of wall cooling is not significant here, and the entrainment rate is high because of the higher fluidization velocities common in full-scale equipment. Both effects – lack of cooling and high solids concentration in the freeboard – may lead to marked secondary reactions in the freeboard of industrial fluidized-bed reactors. The effect of freeboard reactions has been demonstrated for the example of NO and CO emissions from a fluidized-bed furnace [104].

### F Catalyst Attrition

Catalyst attrition is minimal in laboratory apparatus, because of the use of porous plates as gas distributors, as well as the low gas velocities and bed depths. Attrition is necessarily greater in industrial reactors. To re-

duce this risk in scale-up, the attrition tests described in Section 10.2.2.8 should be carried out and the results converted to the full-scale conditions with the aid of eqs 23 and 24.

### G Other Factors

In addition to the factors just listed, many other effects become apparent when a fluidized-bed reactor is scaled up that are difficult to calculate. Examples are the risk of nonuniform gas distribution over very large cross-sections in shallow fluidized beds, the formation of deposits in the bed, the encrustation and coating of heat-exchange surfaces, and catalyst aging and poisoning. On the whole, accordingly, the scale-up of fluidized-bed reactors is a complex process, commonly requiring a large amount of pilot-scale experimentation. Current knowledge about the fluid mechanics in the fluidized bed, however, enables simulation calculations of many of the scale-up effects, so the amount of testing during process development may be decreased and the risk can be at least limited.

### References

1. I. G. Farben, German Patent 437970, 1922 (F. Winkler).
2. D. Kunii, O. Levenspiel, *Fluidization Engineering*, Butterworth-Heinemann, Boston, 1991.
3. D. Geldart (Ed.), *Gas Fluidization Technology*, Wiley, Chichester, 1986.
4. J. F. Davidson, R. Clift, D. Harrison, *Fluidization*, Academic Press, London, 1985.
5. M. Pell, *Gas Fluidization*, Elsevier, Amsterdam, 1990.
6. J. G. Yates, *Fundamentals of Fluidized-Bed Chemical Processes*, Butterworths, London, 1983.
7. K.-E. Wirth, *Zirkulierende Wirbelschichten*, Springer-Verlag, Heidelberg, 1990.
8. J. S. M. Botterill, *Fluid Bed Heat Transfer*, Academic Press, London, 1975.
9. K. B. Mathur, N. Epstein, *Spouted Beds*, Academic Press, New York, 1974.
10. K.-E. Wirth in *VDI Wärmeatlas* (Handbook of Heat Transfer), (E.-U. Schlünder), 7th Edition, VDI Verlag, Düsseldorf 1994, p. Lf1-10.
11. H. Martin in *VDI Wärmeatlas* (Handbook of Heat Transfer), (E.-U. Schlünder), 7th Edition, VDI Verlag, Düsseldorf 1994, p. Mf1-8.
12. L. Reh in *Ullmanns Encycl. Ind. Chem. 3rd ed*, 1973, Vol. 4, pp. 433-460.
13. W. Frey in *Ullmanns Encycl. Ind. Chem. 3rd ed*, 1973, Vol. 4, pp. 480-493.
14. O. E. Potter, D. J. Nicklin (Eds): *Fluidization VII*, Engineering Foundation, New York, 1992.
15. J. R. Grace, L. W. Shemilt, M. A. Bergougnou (Eds): *Fluidization VI*, Engineering Foundation, New York, 1989.
16. K. Ostergaard, A. Sorensen (Eds): *Fluidization V*, Engineering Foundation, New York, 1986.
17. A. Avidan (Ed.), *Circulating Fluidized-Bed Technology IV*, AIChE, New York, 1993.
18. P. Basu, M. Horio, M. Hasatani (Eds): *Circulating Fluidized-Bed Technology III*, Pergamon Press, Oxford, 1990.
19. P. Basu, J. F. Large (Eds): *Circulating Fluidized-Bed Technology II*, Pergamon Press, Oxford, 1988.
20. S. Ergun, *Chem. Eng. Prog.* 1952, 48, 89-97.
21. J. Werther, *Chem.-Ing.-Tech.* 1982, 54, 876-883.
22. C. Y. Wen, Y.H. Yu, *AIChE J.* 1966, 12, 610-612.
23. D. Geldart, *Powder Technol.* 1973, 7, 285-292.
24. O. Molerus, *Powder Technol.* 1982, 33, 81-87.
25. J. C. Agarwal, W. L. Davis, D. T. King, *Chem. Eng. Prog.* 1962, 58, 85-91.
26. F. J. Zuiderweg in *Proceedings of the International Symposium on Fluidization* (Ed.: A. A. H. Drinkenburg) Netherlands University Press, Amsterdam, 1967, pp. 739-750.
27. F. Zenz, D. Othmer *Fluidization and Fluid/Particle Systems*, Reinhold, New York, 1960.
28. J. M. D. Merry, *AIChE J.* 1975, 21, 507-510.
29. J. M. D. Merry, *Trans. Inst. Chem. Eng.* 1971, 49, 189-195.
30. J. F. Davidson, D. Harrison *Fluidised Particles*. Cambridge University Press, Cambridge, 1963.
31. R. Clift, J. R. Grace, *Chem. Eng. Prog. Symp. Ser. No. 105* 1970, 66, 14-27.
32. R. Clift, J. R. Grace, *AIChE Symp. Ser. No. 116* 1971, 67, 23-33.
33. J. Werther, *Chem.-Ing. Tech.* 1976, 48, 339.
34. J. Werther, *Chem.-Ing.-Tech.* 1977, 49, 901.
35. K. Hilligardt, PhD Thesis, Technische Universität Hamburg-Harburg, 1986.
36. K. Hilligardt, J. Werther, *Chem. Eng. Technol.* 1987, 10, 272-280.
37. R. Toei, R. Matsuno, M. Oichi, K. Yamamoto, *J. Chem. Eng. Jpn.* 1974, 7, 447-450.
38. J. Werther, D. Bellgardt, H. Groenewald, K. Hilligardt, in *Proceedings of the 9th International Conference on Fluidized-Bed Combustion* (Ed.: J. P. Mustonen), ASME, New York 1987, pp. 515-522.
39. K. Hilligardt, J. Werther, *Chem.-Ing.-Tech.* 1987, 59, 596-597.
40. J. Werther in *Fluidization* (Eds: D. Kunii, R. Toei), Engineering Foundation, New York, 1983, pp. 93-102.
41. F. A. Zenz, *Hydrocarbon Processing* 1974, 119-124.
42. S. E. George, J. R. Grace, *AIChE Symp. Ser. No. 176* 1978, 74, 67-74.
43. C. Y. Wen, L. H. Chen, *AIChE J.* 1982, 28, 117-128.
44. D. Kunii, O. Levenspiel, *Powder Technol.* 1990, 61, 193-206.
45. K.-E. Wirth, *Chem. Eng. Technol.* 1988, 11, 11-17.
46. K.-E. Wirth, *Chem. Eng. Technol.* 1991, 14, 29-38.
47. M. J. Rhodes, D. Geldart, *Chem. Eng. Res. Des.* 1989, 67, 20-29.
48. E.-U. Hartge, Y. Li, J. Werther in *Circulating Fluidized-Bed Technology* (Ed.: P. Basu), Pergamon Press, Toronto, 1986, pp. 153-160.
49. C. Brereton, L. Stromberg in *Circulating Fluidized-Bed Technology* (Ed.: P. Basu), Pergamon Press, Toronto, 1986, pp. 133-144.
50. B. Herb, K. Tuzla, J. C. Chen in *Fluidization VI* (Eds: J. R. Grace, L. W. Shemilt, M. A. Bergougnou), Engineering Foundation, New York, 1989, pp. 65-72.
51. M. Rhodes, T. Hiram, G. Cerutti, D. Geldart in *Fluidization VI* (Eds: J. R. Grace, L. W. Shemilt, M. A. Bergougnou), Engineering Foundation, New York, 1989, pp. 73-80.
52. R. Bader, J. Findlay, T. M. Knowlton in *Circulating Fluidized-Bed Technology II* (Eds: P. Basu, J. F. Large), Pergamon Press, Oxford, 1988, pp. 123-137.
53. L. W. Bolton, J. F. Davidson in *Circulating Fluidized-Bed Technology II* (Eds: P. Basu, J. F. Large), Pergamon Press, Oxford, 1988, pp. 139-146.
54. B. Leckner in *Circulating Fluidized-Bed Technology III*, (Eds: P. Basu, M. Horio, M. Hasatani), Pergamon Press, Oxford, 1990, pp. 27-38.

- 55 K E Wirth, M Seter in *Fluidized-Bed Combustion* (Ed R J Antyony) ASME, New York, 1991, pp 311–315
- 56 T M Knowlton in *Circulating Fluidized-Bed Technology II* (Eds P Basu, J F Large), Pergamon Press, Oxford, 1988, pp 31–41
- 57 W L Forsythe, W R Hertwig, *Ind. Eng. Chem.* 1949, 1200–1206
- 58 J E Gwyn, *AIChE J.* 1969, 15, 35–39
- 59 F A Zenz, E G, Kelleher, *J. Powder Bulk Solids Tech.* 1980, 4, 13–20
- 60 W G Vaux, J S Schruben, *AIChE Symp. Ser.* 1983, 79, 222–228
- 61 W G Vaux, J S Schruben, *Chem. Eng. Comm.* 1985, 33, 333–347
- 62 W Xi, J Werther, in *International Symposium on Attrition and Wear in Powder Technology* (Ed J A H de Jong), Elsevier Publ., Amsterdam 1993, pp 219–230
- 63 W Xi, PhD Thesis, Technical University, Hamburg-Harburg, 1992
- 64 J Werther, W Xi, *Powder Technol.* 1993, 73, 39–46
- 65 W Bauer, PhD Thesis, Universität Erlangen-Nürnberg, 1980
- 66 J Yerushalmi, D H Turner, A M Squires, *Ind. Eng. Chem. Proc. Des. Dev.* 1976, 15, 47–53
- 67 C M H Brereton, J R Grace, J Yu in *Circulating Fluidized Bed Technology II* (Eds P Basu, J F Large), Pergamon Press, Oxford, 1988, pp 307–314
- 68 C K Adams in *Circulating Fluidized-Bed Technology II* (Eds P Basu, J F Large), Pergamon Press, Oxford, 1988, pp 299–306
- 69 Y Guilin, H Zhe, Zhao Lianzhong in *Fluidization* (Eds D Kunii, R Toei), Engineering Foundation, New York, 1983, pp 145–152
- 70 J Werther, E-U Hartge, M Kruse, W Nowak in *Circulating Fluidized Bed Technology III* (Eds P Basu, M Horio, M Hasatani) Pergamon Press, Oxford, 1990, pp 593–598
- 71 J Werther, E-U Hartge, M Kruse, *Powder Technol.* 1992, 70, 293–301
- 72 A Klinkenberg, H J Krajenbrink, H A Lauwener, *Ind. Eng. Chem.* 1953, 6, 1202–1208
- 73 T K Sherwood, R L Pigford, C R Wilke, *Mass Transfer*, McGraw Hill, New York, 1975
- 74 B Riediger, *Die Verarbeitung des Erdöls*, Springer-Verlag, Berlin, 1971
- 75 D Kunii, O Levenspiel, *Fluidization Engineering* John Wiley, New York, 1969
- 76 J L Callahan, R K Grasselli, E C Milberger, H A Strecker, *Ind. Eng. Chem. Proc. Des. Dev.* 1970, 6, 134–140
- 77 H S van der Baan in *Chemistry and Chemical Engineering of Catalytic Processes* (Eds R Prins, G C A Schuit) Nato Advanced Study Institute Series E, Applied Sciences No 39, 1980
- 78 M E Dry, *Applied Industrial Catalysis*, Academic Press, New York, 1983
- 79 R W Silverman, A H Thompson, A Steynberg, Y Yukawa, T Shingles in *Fluidization* (Eds K Ostergaard, A Sorensen) Engineering Foundation, New York, 1986, pp 441–448
- 80 J J Graham, *Chem. Eng. Prog.* 1970, 66, 54–60
- 81 K Terahata, S Tazawa, T Kakizaki, S Minoda, M Miyagima, M Ito, H Imai, T Kawatsu, DE 2165323 C2, 1971 (Mitsubishi Kasei Kogyo)
- 82 S Kamamura, T Otaki, DE 2658861, 1976 (Mitsubishi Chemical Industries)
- 83 S C Arnold, G D Suci, L Verde, A Neri, *Hydrocarbon Process* 1985, 123–126
- 84 G Stefani, F Budi, C Fumagalli, G D Suci in *New Developments in Selective Oxidation* (Eds G Centi, F Trifiro) Elsevier Science, Amsterdam, 1990, pp 537–552
- 85 T Miyauchi, S Furusaki, S Morooka, Y Ikeda, in *Advances in Chemical Engineering*, (Eds T Brew, G Cokelet, J Hoopos, T Vermeulen), Academic Press, New York, 1981, Vol 11, pp 275–448
- 86 R Pearce, W R Patterson, *Catalysis and Chemical Processes*, Leonard Hill, Glasgow, 1981
- 87 T Katsumata, T Dozono, *AIChE Symp. Ser. No. 255* 1987, 83, 86–96
- 88 C D Chang, *Hydrocarbons from methanol*, Marcel Dekker, New York, 1983
- 89 H H Gierlich, W Dolkemeyer, A Avidan, N Thiagarajan, *Chem.-Ing.-Tech.* 1986, 58, 238–239
- 90 F Wirth, W Franzischka, H Bipp, H-P Gelbke, *Ullmann's Encycl. Ind. Chem. 4th ed.*, 1979, Vol 18, pp 521–544
- 91 A Bellefontaine, A Reppinger, *Ullmann's Encycl. Ind. Chem. 4th ed.*, 1974, Vol 7, pp 566–576
- 92 M Schwarzmann, *Hydrocarbon Process* 1969, 48, 184–186
- 93 F J Karol, *Catal. Rev.-Sci. Eng.* 1984, 26, 557–565
- 94 H Koda, T Kunsaka in *Fluidization '85, Science and Technology* (Eds M Kwauk, D Kunii, Z Jiansheng, M Hasatani) Science Press, Beijing, 1985, pp 402–413
- 95 W P M van Swaaij in *Fluidization* (Eds J F Davidson, R Clift, D Harrison), Academic Press, London, 1985, pp 595–629
- 96 J R Grace in *Gas Fluidization Technology* (Ed D Geldart) Wiley Chichester, 1986, pp 285–340
- 97 R Shinnar, *ACS Symp. Ser.* 1978, 72, 1–13
- 98 W Bock, G Emig, W Sitzmann, J Werther, *ICHEME Symp. Ser. No. 87*, 1984, 479–486
- 99 W Sitzmann, M Schoßler, J Werther, *Chem.-Ing.-Tech.* 1987, 59, 68–69
- 100 D Kunii, O Levenspiel, *Fluidization Engineering*, Butterworth-Heinemann, Boston, 1991, pp 303–305
- 101 W P M van Swaaij, F J Zuiderweg, *Proceedings of the 5th European Symposium on Reaction Engineering*, Amsterdam, 1972, pp B9–25
- 102 D Rokita, PhD Thesis Technische Universität, Hamburg-Harburg, 1991
- 103 S P Sit, J R Grace, *Chem. Eng. Sci.* 1981, 36, 327–335
- 104 M Schoßler, H v Raczeck, J Werther, *Chem.-Ing.-Tech.* 1989, 61, 652–653
- 105 T Minoura, Y Sakamoto, S Toyama, in *International Conference on Fluidized-Bed Combustion* (Ed A M Manaker) ASME, New York, 1989, pp 1155–1161
- 106 D Bellgardt, F Hembach, M Schoessler, J Werther in *Proceedings of the 9th International Conference on Fluidized-Bed Combustion* (Ed J P Mustonen) ASME, New York 1987, pp 713–722
- 107 J Grace in *Circulating Fluidized Beds* (Eds J Grace, A A Avidan, T J Knowlton), Chapman & Hall, Glasgow, 1995
- 108 W P M Van Swaaij, in *Chemical Reaction Engineering Review* (Eds D Luss, V W Weekman Jr), ACS, Washington, 1978, p 329
- 109 M Edwards, A Avidan, *Chem. Eng. Sci.* 1986, 41, 829
- 110 P I Vitanen, *Ind. Chem. Res.* 1993, 32, 577–583
- 111 S Ouyang, J Lin, O E Potter, *Powder Technol.* 1993, 74, 73
- 112 H Schoenfelder, J Werther, J Hinderer, F Keil, *AIChE Symp. Ser. No. 301* 1994, 90, 92–104
- 113 H Kagawa, H Mineo, R Yamazaki, K Yoshida in *Circulating Fluidized-Bed Technology III* (Eds P Basu, M Horio, M Hasatani), Pergamon Press, Oxford, 1991, pp 551–556
- 114 T S Pugsley, G S Patience, F Berruti, J Chaouki, *Ind. Eng. Chem. Res.* 1992, 31, 2652

115. S. Ouyang, O. E. Potter in *Circulating Fluidized-Bed Technology IV* (Ed.: A. Avidan), AIChE, New York, 1993, pp. 422–427.
116. H. Schoenfelder, J. Werther, J. Hinderer, F. J. Keil, *Chem. Eng. Sci.* 1994, 49, 5377–5390.
117. G. S. Patience, P. L. Mills, in *AIChE Annual meeting*, St. Louis, MO, 1993.
118. J. Werther, *Chem. Eng. Sci.* 1992, 47, 2457–2462.
119. W. Bauer, J. Werther, *Proceedings of the 2nd World Congress on Chemical Engineering*, Montreal, 1981.
120. W. Bauer, J. Werther, G. Emig, *Ger. Chem. Eng.* 1981, 4, 291–298.
121. W. Bauer, J. Werther, *Chem. Eng. Commun.* 1982, 18, 137–147.
122. W. Bauer, J. Wether, *ACS Symp. Ser.* 1982, 196, 121–132.
123. R. J. de Vries, W. P. M. van Swaaij, C. Mantovani, A. Heijkoop, *Proceedings of the 5th European Symposium on Chemical Reaction Engineering*, Amsterdam, 1972, Session B9, p. 56–69.
124. M. Pell, S. P. Jordan, *AIChE Symp. Ser. No. 262*, 1988, 84, 68–73.
125. Y. Ikeda in *Fluidization '85 – Science and Technology* (Eds: M. Kwauk, D. Kunii, J. Zheng, M. Hasatani) Elsevier, Amsterdam, 1985, pp. 1–10.

## 10.3 Slurry Reactors

A. A. C. M. BEENACKERS

### 10.3.1 Introduction

Slurry reactors find many applications in chemical industry. Most of these are heterogeneous catalytic processes with hydrogenation of edible oils as the most classic example and SASOL's novel continuous Fischer Tropsch slurry synthesis process [1], the latest impressive new development in this area. Doraiswamy and Sharma [2] identified over 50 different slurry reactor applications, and an updated list would no doubt be longer still.

In slurry reactors, an attempt is made to realize intensive and intimate contact between a gas-phase component, usually to be dissolved in the liquid phase, a liquid-phase component and a finely dispersed solid. In this respect, slurry reactors are related to packed-bed reactors with the various gas/liquid flow regimes that can be realized (such as trickle flow, pulsed flow and dispersed bubble flow). Also, there is much similarity with three-phase fluidized beds.

The main difference is the particle size. In three-phase fluidized beds these are so large that a net upward liquid flow is necessary to keep the solids in suspension, whereas in slurry reactors the turbulence of the liquid is sufficient to keep the solids suspended; particle sizes in slurry reactors are usually below 200  $\mu\text{m}$ . Particularly for fast reactions where intraparticle dif-

fusion limitations are detrimental to selectivity, the particle size will be made as small as possible. Then, downstream solids separation possibilities limit the minimal particle size to about 10  $\mu\text{m}$ .

### 10.3.2 Properties of Slurry Reactors

Typical properties of slurry reactors, and of packed bed co-current downflow trickle flow reactors, are summarized in Table I. Most properties indicated for slurry reactors also hold for three-phase fluidized beds. These properties can be advantageous or disadvantageous, depending on the application:

- (i) *Back-mixing of liquid*. This normally reduces the average liquid phase reactant concentration, which often results in a decrease in reaction rate. This effect can sometimes, be beneficial. If overall low axial mixing in the liquid phase is required, cascades of slurry reactors should be applied. Conversely, the degree of mixing in a trickle flow reactor can be increased by applying a liquid recycle.
- (ii) *Back-mixing of the gas phase*. This becomes an important consideration only if high gas phase conversions are required. Examples are absorption of acid gases ( $\text{CO}_2$ ,  $\text{NO}_x$ ,  $\text{SO}_2$ ) in lime slurries and other environmental gas-cleaning processes. A single-stage slurry reactor is not especially suited to such applications. However, multiple stage and slurry tray columns can then be applied.
- (iii) *Solids mixing and solids replacement*. Mixing of the solids and solids replacement are important if the solids have a short lifetime. This can be the case if the solid phase is to be converted, such as in coal hydrogenation, or if the catalyst is rapidly deactivating, as in hydrodesulfurization and demetallation of oil residues. For these applications slurry reactors have a definite advantage over trickle flow reactors, especially if the residence time distribution can be reduced, for example by putting slurry vessels in series. Then, counter-current operation becomes possible.
- (iv) *Particle size*. The particle size in slurry reactors can go down to the submicrometer range. This allows for high particle effectiveness factors, even at high reaction rates. Slurry reactors can therefore have high conversion rates per unit slurry volume.
- (v) *Pressure drop*. The pressure drop in slurry reactors is usually more or less independent of the gas flow and close to the hydrostatic pressure. In trickle flow the pressure drop is strongly influenced by the gas flow rate and, because of the

Table 1. Typical properties of three-phase reactors.

Property	Slurry reactors	Co-current downflow trickle flow reactors
Back-mixing of liquid	intermediate to ideally mixed	close to plug flow at high liquid rates
Back-mixing of gas phase	usually intermediate to ideally mixed	close to plug flow at high liquid rates
Solids mixing	usually intermediate to ideally mixed	no mixing
Solids replacement	continuous	usually discontinuous (difficult)
Particle size	small to very small	restricted by pressure drop
Pressure drop	high (hydrostatic pressure)	low
Wetting	complete	intermediate to complete
Radial heat transport	very fast	slow
Heat removal/addition	easy	difficult (interstage cooling or cold shot)
Danger of plugging	small	can be high
Gas/liquid mass transfer rate	intermediate	high
Liquid/solids mass transfer rate	very high	high
Liquid/solids separation	difficult, costly	easy

larger particle size, the pressure drop is often lower than in slurry reactors. In three-phase reactors where large gas flows are to be processed and where pressure drops are an important cost factor, such as in lime scrubbing of flue gases, slurry reactors are avoided and special contactors allowing for a low pressure drop are preferred [3].

- (vi) *Particle wetting.* Particle wetting in slurry reactors is always complete, whereas in trickle flow, especially at low specific liquid flow rates, wetting can be uncertain and problematic. This is nearly always a disadvantage as partial wetting implies dead zones, hot spots and channeling.
- (vii) *Radial heat transport.* Radial heat transport may be a problem in trickle flow but is never problematic in slurry reactors.
- (viii) *Heat removal/addition.* This is easier in slurry reactors because of high heat transfer rates to cooling surfaces. In trickle flow reactors, only interstage cooling, cold shot techniques and cooling with an evaporating solvent are possible. The latter technique can also be applied in slurry reactors.
- (ix) *Plugging and fouling.* In case plugging and/or fouling is a problem, trickle flow clearly has a disadvantage over slurry reactors. A well known phenomenon is the pressure drop built-up during operation of a trickle flow hydrodesulfurization reactor, limiting the operation period. Similar problems do not occur in slurry reactors.
- (x) *Gas/liquid mass transfer.* Gas/liquid mass transfer depends on many factors, as described below. Related to the lower liquid hold-up, the interfacial area per cubic meter of liquid can be relatively high in trickle flow reactors. However, per cubic meter of reactor volume, the slurry reactor is not necessarily placed at a disadvantage.
- (xi) *Liquid/solids separation.* Liquid/solids separation is no problem in trickle flow but can be compli-

cated for slurries, especially if very fine particles have to be removed from (viscous) liquids. Here, three-phase fluid-bed reactors have an advantage.

We can now summarize where slurry reactors are an attractive option in heterogeneous catalytic processes. For any application where a liquid is present and which benefits from small catalyst particles below 200  $\mu\text{m}$ , for example because intraparticle diffusion limitation has to be avoided (see below), the slurry reactor is attractive, provided pressure drops in the order of one to several bars are acceptable.

If the catalyst deactivates rapidly or whenever good heat transfer properties are essential and where local hot spots cannot be accepted, the slurry reactor should also be considered. Finally, the slurry reactor can be an attractive alternative to multitube gas–solid packed-bed processes, particularly where large heat effects ask for thousands of thin tubes to control the reactor temperature in the packed beds. Also here, the much better heat transfer characteristics of slurries relative to gas–solid packed beds are deciding.

### 10.3.3 Types of Slurry Reactors

Slurry reactors can be classified on the basis of the contacting pattern of the phases, the mechanical devices applied to realize that contacting pattern and the mass transfer (Fig. 1). The slurry bubble column reactor is the most simple type. The liquid and solids phase can be operated batchwise or continuously. For continuous operation the intense mixing of the slurry may be a disadvantage because it renders the macro-mixing close to a single ideal mixer operating at outlet conditions. This can be counteracted by putting more slurry spargers in series. If the particles are removed

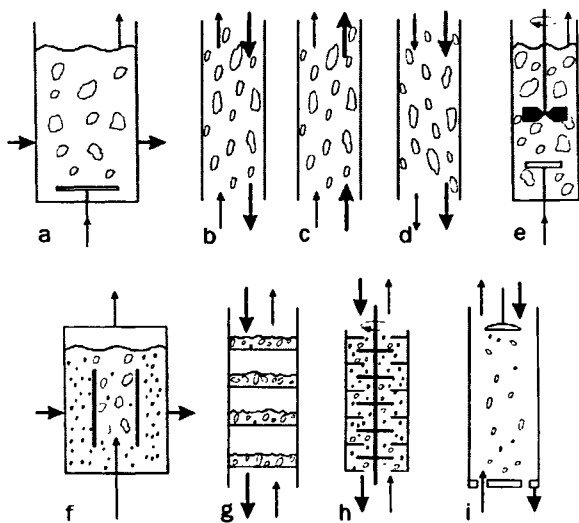


**Figure 1.** Slurry reactors classified by the contacting pattern and mechanical devices: (a) slurry (bubble) column; (b) countercurrent column; (c) co-current upflow; (d) co-current downflow; (e) stirred vessel; (f) draft tube reactor; (g) tray column; (h) rotating disc or multi-agitated column reactor; (i) three-phase spray column;  $\rightarrow$  liquid flow;  $\rightarrow$  gas flow.

between the stages, the contacting pattern of liquid and solids can also be manipulated (e.g. countercurrent contact) which may be advantageous in relation to catalyst aging (e.g. in hydrodesulfurization of heavy oil residues). A recent development is the continuous separation of liquid and solids inside the reactor [4, 5], i.e. the reactor is essentially batch with respect to the catalyst but continuous for the liquid.

If the contact time of the liquid/solids suspension with the gas phase is relatively short and also for reactors of high  $H/d_c$  values, it may be useful to distinguish a co-current and countercurrent contacting pattern and, especially in relation to the gas holdup, up-flow and down-flow.

Particularly in co-current down-flow operation, very high gas-slurry interfacial areas per cubic meter of reactor volume can be realized [6]. To improve the solids suspension and/or to improve mass or heat transfer, in many cases a stirrer is added to the system. Particularly where pure gases have to be absorbed in the slurry and no gases are produced, the gas may be sparged into the liquid via a hollow shaft stirrer, sucking the gas from the free board above the slurry.

In some cases a stirrer can be avoided and yet the solids can be kept in suspension by a relatively small amount of gas by means of a draft tube placed in the slurry reactor. Another possibility is external slurry recycling. This gives control over the circulation rate and allows for efficient heat transfer in an external heat exchanger placed in the recycle. The Swiss company Buss AG successfully applies the recycle slurry flow to drive a venturi jet tube, thus sucking the gas from the free board above the reactor back into the slurry (Fig. 2).

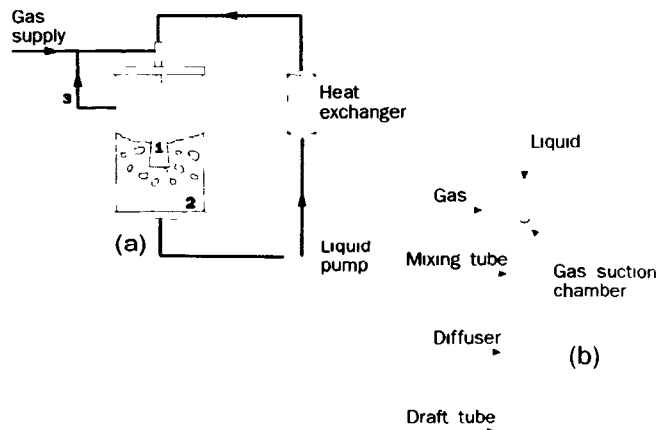


**Figure 2.** Circulating loop venturi reactor: (a) reactor setup; (b) scheme of ejector (1 = ejector, 2 = main holding vessel, 3 = gas recycle (adapted from Ref. 8).

In this way, extremely high mass transfer coefficients and specific contact areas between gas and liquid are possible [7].

If staging and countercurrent operation are essential, a slurry tray column and a rotating disk column can be applied [9]. In flue gas purification where a low pressure drop is essential, lime or  $\text{CaCO}_3$  slurries are spray contacted with the gas phase. Sometimes it is meant to evaporate the water phase but also simple slurry scrubbing is envisaged.

The choice of slurry reactor for a particular application depends on many factors, and is never easy and straightforward. Some factors playing a role here have been discussed by Concordia [10].

A comparison between a liquid entrained slurry reactor and a mechanically agitated slurry reactor for methanol synthesis was made by Vijayaraghavan et al. [11].

### 10.3.4 Hydrodynamics of Slurry Reactors

Hydrodynamics of slurry reactors include the minimum gas velocity or power input to just suspend the particles (or to fully homogeneously suspend the particles), bubble dynamics and the holdup fractions of gas, solids and liquid phases. A complicating problem is the large variety in reactor types (see Fig. 1) and the fact that most correlations are of an empirical nature. We will therefore focus on sparged slurry columns and slurries in stirred vessels.

#### 10.3.4.1 Minimum Suspension Criteria

For the design of slurry reactors, whether agitated only by the flowing gas or assisted by one or more stirrers, the conditions at which the particles are just suspended are very important. If the overall contacting efficiency

with the solids is considered, it increases rapidly if more and more solids are suspended, but once the condition of minimum suspension is passed and no solids are laying on the bottom of the vessel, further increase of the energy input for suspension only moderately increases the contacting efficiency. In sparged vessels with a stagnant liquid medium, a minimum suspension gas velocity can be defined at which all solid particles are just suspended. Empirical relations are given by Narayanan et al. [12].

To obtain a theoretical basis, Chapman et al. [13] compared a pickup velocity derived from the force balance:

$$v_i = \left[ 2g(\rho_S - \rho_L) \left( \frac{d_p}{\rho_L} + \frac{w_S H_{SL}}{\rho_S + w_S \rho_L} \right) \right]^{1/2} \quad (1)$$

which was taken equal to the liquid velocity in upward direction for which it was derived:

$$v_u = u_G + \frac{1}{3} \left[ 2gH_{SL} \varepsilon_G \left( \frac{\rho_L - \rho_G}{\rho_L} \right) \right]^{0.5} \quad (2)$$

An empirical relationship was introduced to relate the bubble holdup with the superficial gas velocity  $u_G$ .

$$\begin{aligned} \varepsilon_G &= 6.2u_G & \text{for } u_G < 0.067 \text{ m s}^{-1} \\ \varepsilon_G &= 0.765u_G^{0.38} & 0.067 < u_G < 0.22 \text{ m s}^{-1} \end{aligned} \quad (3)$$

Combining eqs 1–3 results in a minimum gas velocity necessary to suspend the particles:  $u_G$  (min, theor). However, comparison with the experimental values taught that a correction factor has to be introduced for the particle concentration and vessel diameter,  $d_c$ :

$$u_G(\text{min, actual}) = 4.3 \left( \frac{d_c}{0.0508} \right)^n e^{-10w_S} u_G(\text{min, theor}) \quad (w_S < 0.1)$$

$$u_G(\text{min, actual}) = 1.25 \left( \frac{d_c}{0.0508} \right)^n e^{-3w_S} u_G(\text{min, theor}) \quad (w_S > 0.1) \quad (4)$$

in which  $n = 0.2$  if  $d_p < 100 \mu\text{m}$  and  $n = 0.5$  if  $d_p > 200 \mu\text{m}$ . These correlations are valid up to a liquid viscosity of  $0.006 \text{ N s m}^{-2}$  with column diameters of 0.0508, 0.114 and 0.141 m.

Roy et al. [14] studied a large variety of gas/solid/liquid systems and particles with different degrees of wetting (quartz, coal, catalyst powders, etc.). The results were presented as critical particle holdups which can be just suspended at a given gas velocity. Kato et al. [15] showed that there remains a solids profile in the column. Imafuku et al. [16] showed that with a draft tube a much smaller volumetric flow rate of gas is required to suspend the same amount of solids.

In stirred vessels the stirrer usually provides most of the energy required to keep the particles suspended. The minimum suspension criteria for a three-phase

stirred tank are usually derived from those obtained in absence of the gas phase. Chapman et al. [17] showed the considerable influence of the gas phase. In the absence of a gas phase, the stirrer speed at minimum suspension was studied by Zwietering [18] for a wide range of materials and experimental conditions. Although this work is already relatively old (1958) and resulted in a purely empirical expression, its results are still generally used for design purposes and to check new theoretical approaches. Zwietering proposed:

$$\omega_{\min} = C_1 (\eta/\rho)^{0.1} d_p^{0.2} \left( g \frac{\Delta\rho}{\rho_L} \right)^{0.45} w_S^{0.13} d_i^{-0.85} \quad (5)$$

The exponents were found to be independent of the impeller type, vessel size, impeller clearance and impeller to tank diameter ratio. The dimensionless constant  $C_1$  accounted for variations in the system geometry (e.g. on  $d_c/d_i$ ). This would indicate that the basic mechanism leading to minimum suspension may be the same for rather different stirrer geometries. Table 2, which is an update of the one given by Nienow [19], indicates different exponents found in a few other investigations. Baldi et al. [26] made a relatively successful theoretical approach by assuming that the suspension of particles is mainly due to eddies of a certain critical scale comparable to the particle size. From an energy balance it follows that

$$\rho_L v'^2 \approx d_p \Delta\rho g$$

where  $v'$  is the fluctuating velocity of the critical eddies. Because the scale of these eddies is generally much larger than the scale of those that dissipate their energy by viscous forces (Kolmogoroff scale),  $v'$  can be expressed as [26]

$$v' \approx (e_b d_p)^{1/3} \quad (6)$$

in which  $e_b$  is the power input per kg liquid close to the bottom of the stirred vessel. The latter factor is difficult to evaluate. In fact, the energy dissipation within a stirred vessel is far from homogeneous, nor is it isotropic. There is supportive evidence for the use of eq 6 for the average turbulent velocity [26]. The average value of the energy dissipation  $\bar{e}$  can be found from:

$$\bar{e} = \frac{4\psi\omega^3 d_i^5}{\pi d_c^3} \quad (7)$$

Assuming  $e_b \approx \bar{e}$ , a constant power number (which is reasonable in the turbulent regime), and a constant ratio  $d_i/d_c$ , leads to:

$$\omega_{\min} = C_2 d_p^{1/6} \left( g \frac{\Delta\rho}{\rho_L} \right)^{0.5} d_i^{-2/3} \quad (8)$$



**Table 2.** Exponents found by different authors for Zwietering-type equations.

Authors	$w_s$	$\eta/\rho$	$\Delta\rho$	$d_p$	$d_i$ (at constant $d_c$ ) <sup>b</sup>
Zwietering [18]	0.13	0.1	0.45	0.2	-2.35 (R), -1.67 (A)
Nienow [19]	0.12	-	0.43	0.21	-2.25 (R)
Pavlushenko et al. [20]	-	0.2	-	0.4	-2.5 (A)
Oyama and Endoh [21]	0	-	1.0	1.3	-1.67 (?)
Kneule [22]	0.17	-	0.5	0.17	-1.67 (M)
Narayanan et al. [23]	0.22	-	0.5	0.5	-2.00 (R)
Weisman and Efferding [24]	0.17	- terminal velocity concept	-	-	-1.67 (R)
Kolar [25]	0.10	- terminal velocity concept	-	-	-2.24 (A,M)
Baldi et al. [26]	0.125 <sup>a</sup>	0.17 <sup>a</sup>	0.42 <sup>a</sup>	0.14 <sup>a</sup>	theoretical function
Chapman et al. [13]	0.12	0	0.4	0.15	-2.25 (R), -1.5 (A)

<sup>a</sup> for  $d_i$  (clearance height) = 1 only.

<sup>b</sup> R = radial flow impeller, A = axial flow impeller, M = mixed down-flow impeller.

The exponents are close to those observed by Zwietering (eq 5). Buurman [27] extended the theory of Baldi et al. and found a theoretical relationship for the influence of solids concentration:

$$\left(\frac{\omega_{\min,c_s}}{\omega_{\min,c_s=0}}\right)^3 = 1 - \varepsilon_s + C_3 \varepsilon_s \frac{\rho_s}{\rho_L} + C_4 \frac{\rho_s}{\rho_L} \frac{\varepsilon_s^2 (d_p/d_i)^{5/4}}{\{(\varepsilon_{\max}/\varepsilon_s)^{1/3} - 1\}^3} \quad (9)$$

with  $\omega_{\min,c_s=0}$  given by eq 8.

Here  $\varepsilon_s$  is the volumetric solids fraction and  $\varepsilon_{\max}$  is the maximum solids fraction possible (obtained for all particles in contact with one another). The constants in eqs 8 and 9 were measured experimentally by Buurman to be  $C_2 = 1.2-1.4$ ,  $C_3 = 2.5$  and  $C_4 = 10.7$ .

However, these constants are not universal and may depend on impeller design. Indeed, Neale and Pincher [28] found a dramatic effect of the impeller blade-tip angle.

Little information is available about the hydrodynamics of three-phase stirred systems. Arbiter et al. has [29] noted that the introduction of a gas into a stirred suspension may cause settling of part of the suspended particles corresponding to a decrease in power consumption. Similar conclusions may be drawn from the work of Queneau et al. [30], Wiedmann et al. [31] Subbarao and Taneja [32], and Neal and Pincher [28]. Chapman et al. [17] presented data for a wide range of vessels (up to 1.83 m diameter) with different impellers. The power input necessary to cause suspension under aerated conditions was found to be higher than for unaerated conditions. Slightly lower exponents were found for the influence of most of the variables as compared to eq 5; the most significant was the influence of the particle liquid density difference. To summarize,

$$\omega_{\min}(\text{gas conditions}) \approx (\eta/\rho)^{0.0} d_p^{0.12} \Delta\rho^{0.22} w_s^{0.12} \quad (10)$$

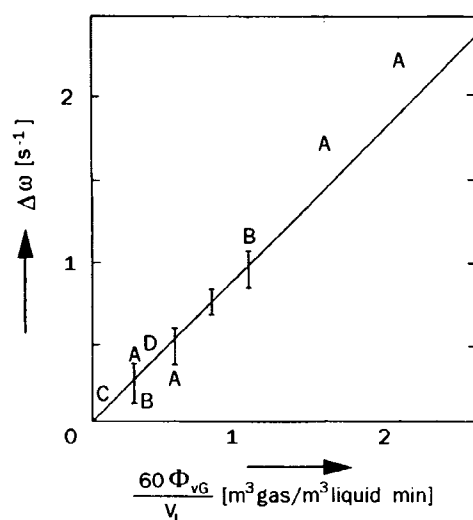


**Figure 3.** Increase in stirrer speed necessary to keep the particles suspended if gas is fed to the stirred vessel for disk turbines of diameter  $d_c/2$  and clearance  $d_c/4$ : A,  $d_c = 0.29$  m; B,  $d_c = 0.30$  m; C,  $d_c = 0.91$  m; D,  $d_c = 1.83$  m. Barred line ranges for  $d_c = 0.56$  m at different conditions [17].

Chapman et al. [17] proposed an extremely simple relationship from which the increase in stirrer speed required to suspend all particles under aerated conditions over unaerated conditions is given for disc turbines of diameter  $d_c/2$  and clearance of height  $d_c/4$ :

$$\Delta\omega = 56.4\Phi_{v,G}/V_L \quad (11)$$

where  $\Delta\omega$  is the increase in impeller speed to maintain suspension (revs per second).

Similar relationships are given for other geometries. Equation (11) is shown in Fig. 3 for disk turbines of half the vessel diameter with clearance  $d_c/4$ . It was tested on different scales and with different particles. This geometry was recommended as the safest impeller type for three-phase agitators with respect to the amount of data available and stability in large vessels, although other geometries (such as upward pumping impellers) may have advantages in special situations.

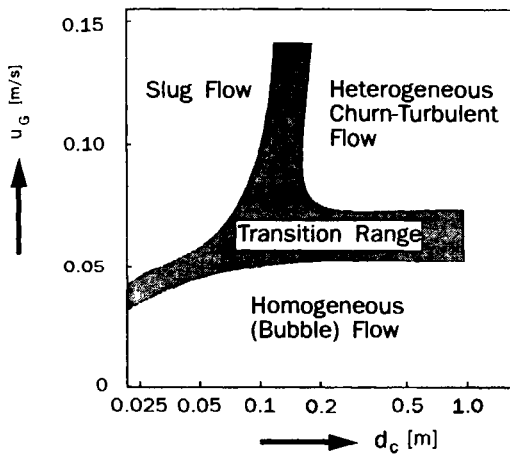


Figure 4. Approximate dependency of flow regime on gas velocity and column diameter (water and dilute aqueous solutions), from Shah et al. [36].

Minimum suspension criteria for multiimpeller reactors are given by Dutta and Pangarkar [33]. Data for venturi-loop reactors are limited [34–35]. However, because of continuously sucking the slurry away from the bottom by the recycle pump, possibly not many problems on solids settling occur.

### 10.3.4.2 Gas Holdup

#### A Bubble Columns

Gas holdup is difficult to predict because it depends on the tendency of the bubbles to coalesce, which is system dependent, and because the reactors can be operated in different regimes depending on the gas load and reactor size. For bubble columns, these regimes are shown in Fig. 4. For industrial applications the heterogeneous churn-turbulent regime and the transition regime are the most important. Here, the relationships of Koida et al. [37] probably have the widest range of applicability. These authors measured, with sparger holes ranging from 0.5 mm to 2.5 mm, a static liquid height of 1.5 m, and superficial gas velocities up to  $0.2 \text{ m s}^{-1}$  in bubble columns with diameters from 10 cm to 30 cm. Liquid viscosities ranged from that of water up to  $18 \text{ mPa s}$ ,  $52 < \sigma_L < 72 \text{ N m}^{-1}$ ,  $0.14 < D_L \times 10^9 < 2.4 \text{ m}^2 \text{ s}^{-1}$ ,  $\varepsilon_S$  up to 8%,  $50 < d_p < 200 \mu\text{m}$ ,  $\rho_p = 2500 \text{ kg m}^{-3}$  and, for  $\rho_p = 8770 \text{ kg m}^{-3}$ , also with  $d_p = 80 \mu\text{m}$ .

They observed  $\varepsilon_G$  to be reduced by the presence of solids, although this reduction is less pronounced in the churn-turbulent regime than in the transition regime. The relationships of Koida et al. [37] are

$$\frac{(\varepsilon_{G,H})_0}{\{1 - (\varepsilon_{G,H})_0\}^4} \frac{(1 - \varepsilon_{G,H})^4}{\varepsilon_{G,H}} = \frac{0.277}{C} \left[ 1 + 4.35 \varepsilon_S^{0.745} \left( \frac{\Delta\rho}{\rho_L} \right)^{0.881} N_{Re}^{-0.168} \right] \quad (12)$$

for the heterogeneous churn-turbulent flow regime and

$$\frac{\varepsilon_{G,T}}{(\varepsilon_{G,T} - \varepsilon_{G,H})_0} = \frac{1}{1 + 49.1 \varepsilon_S^{0.619} \left( \frac{\Delta\rho}{\rho_L} \right)^{0.619} N_{Re}^{-0.496}} \quad (13)$$

for the transition regime, with  $(\varepsilon_{G,H})_0$  from

$$\frac{(\varepsilon_{G,H})_0}{\{1 - (\varepsilon_{G,H})_0\}^4} = 0.277 \left( \frac{u_G \mu_L}{\sigma_L} \right)^{0.918} \left( \frac{g \mu_L^4}{\rho_L \sigma_L^3} \right)^{-0.252} \quad (14)$$

Here

$$\Delta\rho = \rho_p - \rho_L$$

and

$$N_{Re} = \frac{u_G \rho_L d_c}{\mu_L}$$

The system dependent constant  $C = 0.277$  for water and aqueous solutions of glycerol and glycol;  $C = 0.364$  for aqueous solutions of organic electrolytes. It would be highly interesting if future research provided a general relationship for  $C$  for organic liquids.

Of interest is a recent theoretical relation for  $\varepsilon_G$  in gas–liquid bubble columns based on liquid circulation and claimed to be valid both in the homogeneous bubble flow regime and in the churn-turbulent regime, also for non-Newtonian fluids. For power law fluids with

$$\tau = k \dot{\gamma}^n \quad (15)$$

Kawase et al. [38] derived

$$\frac{\varepsilon_G}{1 - \varepsilon_G} = 2^{-(3n+5)/(n+1)} n^{-(n+2)/2(n+1)} \times \left( \frac{k}{\rho_L} \right)^{-1/2(n+1)} g^{-n/2(n+1)} u_G^{(n+2)/2(n+1)} \quad (16)$$

For Newtonian fluids ( $n = 1$ ) eq 16 reduces to

$$\frac{\varepsilon_G}{1 - \varepsilon_G} = 0.0625 (u_G^3 \rho_L / \mu_L g)^{1/4} \quad (17)$$

This condition was tested for water in columns with diameters up to 5.5 m and  $u_G$  varying between  $0.1 \text{ m s}^{-1}$  and  $1 \text{ m s}^{-1}$ . Further, it was found to be satisfactory for non-Newtonian slurries containing up to 10 wt % of solids. The gas holdup may be affected by internals. For vertical heat exchange tubes present in the columns, Saxena et al. carried out an extensive research programme [39–43]. The gas holdup increases if the internals in the column prevent bubble coalescence [43]. Saxena et al. correlated their results in a relation based on the so-called drift velocity concept:

$$\varepsilon_G = u_G (C u_G + v_{bx})^{-1} \quad (18)$$

where  $v_{b\infty}$  is the velocity of a single bubble in an infinite medium. Despite many suggestions for the values of  $C$  and  $v_{b\infty}$  [41], these values are best measured experimentally for each system [40]. The influence of solids concentration is nominal, as long as  $d_p < 90 \mu\text{m}$  and  $w_s < 0.2$  [40].

The influence of pressure on  $\varepsilon_G$  is caused by the change of gas density only. Probably the most widely applicable relationships are from Wilkinson and Van Dierendonck [44]:

$$\varepsilon_G = u_G/v_{sb} \quad (19)$$

for the homogeneous bubble flow regime and

$$\varepsilon_G = u_{tr}/v_{sb} + (u_G - u_{tr})/v_{lb} \quad (20)$$

for both the transition and the heterogeneous churn-turbulent regime.

Here  $v_{sb}$  is the rise velocity of small bubbles, given by

$$\frac{v_{sb}\mu_L}{\sigma} = 2.25 \left( \frac{\sigma^3 \rho_L}{g\mu_L^4} \right)^{-0.273} \left( \frac{\rho_L}{\rho_G} \right)^{0.03} \quad (21)$$

$v_{lb}$  is the contribution due to the rise velocity of large bubbles and is given by

$$\begin{aligned} \frac{v_{lb}\mu_L}{\sigma} &= \frac{v_{sb}\mu_L}{\sigma} + 2.4 \left\{ \frac{\mu_L(u_G - u_{tr})}{\sigma} \right\}^{0.757} \\ &\times \left\{ \frac{\sigma^3 \rho_L}{g\mu_L^4} \right\}^{-0.077} \left( \frac{\rho_L}{\rho_G} \right)^{0.077} \end{aligned} \quad (22)$$

$u_{tr}$  is the superficial transition velocity between the homogeneous bubble flow and the transition regime, which is given by

$$\frac{u_{tr}}{v_{sb}} = 0.5e^{-193\rho_G^{-0.61}\mu_L^{0.5}\sigma^{0.11}} \quad (23)$$

These conditions hold to within 10% for  $0.02 < \sigma < 0.073 \text{ N m}^{-1}$ ,  $0.0004 < \mu_L < 0.055 \text{ Pa s}$ ,  $683 < \rho_L < 2960 \text{ kg m}^{-3}$  and  $0.09 < \rho_G < 38 \text{ kg m}^{-3}$ .

No systematic research has been done yet on the influence of pressure and gas density on the holdup in three-phase slurry reactors. The only data [45–51] for three-phase bubble columns under pressure suggest rather high values of  $\varepsilon_G$  under pressure. Qualitatively, this is in line with the effect of a high density as predicted by Wilkinson [44]. The effect might decrease with increased solids concentration [52]. Clearly, additional research is necessary here.

Plate columns may give higher values for  $\varepsilon_G$  than found in bubble slurry columns due to smaller bubbles [9].

In venturi loop reactors the gas flow rate is not an independent variable. Both gas flow rate and holdup are very sensitive to the venturi design parameters and gas and liquid properties. [8, 53–56].

## B Stirred Vessels

For stirred vessels the gas holdup in a slurry system can also be related to the gas holdup in the corresponding gas–liquid systems. Generally, the effects of the solids at higher gas velocities are not very important, except for large particles and high concentrations (Wiedmann et al. [31]) and probably for very small particles  $< 10 \mu\text{m}$ .

Not much is known on induced aeration via hollow shafts. Aldrich and van Deventer [57] report a decrease in aeration efficiency with increasing  $w_s$ ,  $d_p$  and  $\rho_s$ .

### 10.3.4.3 Axial Mixing in Slurry Reactors

We can distinguish axial mixing in each of the three different phases (gas, liquid and solids). Stirred vessels and sparged columns are considered separately. In stirred vessels, the liquid mixing is usually rather close to a single completely mixed stage, and both the macro- and micro-mixing are not much different from those of a two-phase stirred vessel or even single-phase stirred vessels.

For insufficient power input, the solids distribution in the axial direction will be inhomogeneous, resulting in a low solids concentration in the upper part of the reactor. Solids distribution data for stirred slurry tanks are available [58–60]. However, in heterogeneous catalytic reactions such inhomogeneity should preferably be avoided, also because the mixing time in the upper low-solids section can be up to 10 times longer, relative to homogeneous distributions [61]. No data are available on the gas phase mixing in stirred slurry reactors.

In gas/liquid/solid sparged columns the situation is somewhat more complicated. Just as in gas/liquid systems, different regimes have to be distinguished. Here the most important variables affecting the axial dispersion coefficient  $D_{e,L}$  of the liquid, are  $d_c$  and  $u_G$ :

$$D_{e,L} \approx d_c^p u_G^q$$

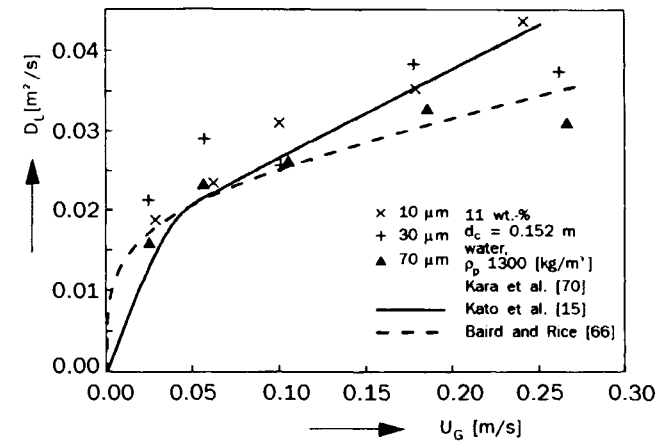
Recommendations for  $p$  range from 1 to 1.5 and for  $q$  from 0 to 2. Rice et al. [62] concluded that this was due to the different regimes and recommended  $q$  values of 2, 1, 1/3 and 0 for chain bubbling, bubbling flow, churn-turbulent flow and slug flow, respectively.

The effects of liquid velocity (at least at low velocities), direction of flow and liquid properties are only minor for Newtonian fluids. Correlations on gas–liquid columns are given by Joshi [63]. Field and Davidson [64] measured the dispersion in a large industrial column ( $d_c = 3.2 \text{ m}$ ,  $H = 19 \text{ m}$ ) and found agreement with the correlations of Deckwer et al. [65] and Joshi [63] (Table 3). The influence of particles can be expected to be small, at least for low concentrations and small particles. This is confirmed by the early experiments of Kato et al. [15, 69]. For particle sizes ranging from 63

**Table 3.** Liquid phase axial dispersion correlations for sparged columns.

Reference	Correlation
65	$D_{e,L} = 0.68d_c^{1.4}u_G^{0.33}$
66	$D_{e,L} = 0.35d_c^{1.33} \left[ u_G \left( \frac{\varepsilon_G}{1 - \varepsilon_G} \right) g \right]^{1/3}$
63*	$D_{e,L} = 0.29d_c(v_c + u_L)$ $v_c$ = circulation velocity which is a complex function [63]
15*	$N_{Pe,L} = 13N_{Fr}/(1 + 6.5N_{Fr}^{0.8})$
67	$D_{e,L} = 1.225d_c^{1.5}u_G^{0.5}$
68	$D_{e,L} = (0.15 + 69u_G^{0.77})d_c^{1.25} \left( \frac{0.001}{\mu_{SL}} \right)^{0.12}$

\* Based on three-phase column.

**Figure 5.** Axial dispersion in the liquid phase of a slurry column. Comparison of data of Kara et al [70] with correlations.

to 177  $\mu\text{m}$  and concentrations up to 200  $\text{kg m}^{-3}$  the Peclet number is essentially a function of the Froude number:

$$N_{Pe,L} = \frac{u_G d_c}{D_{e,L}} = 13N_{Fr}/(1 + 8N_{Fr}^{0.85}) \quad (24)$$

$$N_{Fr} = u_G/\sqrt{gd_c} \quad (25)$$

A similar relation was observed for gas-liquid systems:

$$N_{Pe,L} = 13N_{Fr}/(1 + 6.5N_{Fr}^{0.8}) \quad (26)$$

Figure 5 gives a few examples from Kara et al. [70] together with two correlations. Recent experiments with a large-scale slurry bubbling column ( $d_c = 0.57$  m,  $H = 7.62$  m) operating in the churn-turbulent regime, revealed that the liquid phase could be considered as ideally mixed [71].

Data on gas phase dispersion in three-phase sparged columns are scarce. For two-phase systems a few correlations are available [64, 67, 71, 72] which are shown

**Table 4.** Correlations for gas phase axial dispersion in sparged columns.

Reference	Correlation
Towell and Ackermann [67]	$D_{e,G} = 1.97d_c^2 u_G$
Diboun and Schügerl [72]	$D_{e,G} = 5u_L d_c$
Mangartz and Pilhofer [73]	$D_{e,G} = 50d_c^{1.5} (u_G/\varepsilon_G)^3$
Field and Davidson [64]	$D_{e,G} = 56.4d_c^{1.33} (u_G/\varepsilon_G)^{3.56}$

in Table 4. However, the scatter in the data is quite large. The influence of the column diameter varies from  $d_c^2$  (Towell and Ackermann [67]) to  $d_c^1$  (Diboun and Schügerl [72]), although in most recent correlations  $d_c$  is taken to the power 1.33–1.5. The correlation of Field and Davidson [64] has been tested for large-scale equipment and should therefore be recommended:

$$D_{e,G} = 56.4d_c^{1.33} \left( \frac{u_G}{\varepsilon_G} \right)^{3.56} \quad (27)$$

Recent data from a large-scale slurry reactor suggest that the axial dispersion model for the gas flow in the churn-turbulent regime might be unsatisfactory [74]. More complicated models, that distinguish between large and small bubbles, as developed earlier for gas-solid fluid beds and for gas-liquid bubble columns, are probably necessary here too. Recently, de Swart and Krishna [75] published first evidence that such an approach might be successful also for slurry bubble columns. This work needs confirmation now from larger scale reactors.

Data on solids phase dispersion are similar to those of the liquid phase, at least for small particle diameters as generally prevailing in slurries [15, 76]. At zero liquid rates, if the particles are only suspended by the gas flow, a solids concentration profile will be established:

$$w_s/w_{s,z=0} = \exp\left(-\frac{v_t z}{D_{e,s}}\right) \quad (28)$$

Provided the particle settling velocities  $v_t$  are known, this equation allows the calculation of  $D_{e,s}$ . Usually, experiments at non-zero liquid rates are used to evaluate  $v_t$  and  $D_{e,s}$  separately. A similar concentration profile might occur in practice if slurry column reactors are operated close to the conditions given by the minimum suspension criterium. In this case, reactor calculations should take the solids concentration profiles into account. A recommended correlation for the solids dispersion coefficient for small particles is given by Kato et al. [15]:

$$N_{Pe,S} = \frac{13N_{Fr}}{1 + 8N_{Fr}^{0.85}} \quad (29)$$

References see page 1462

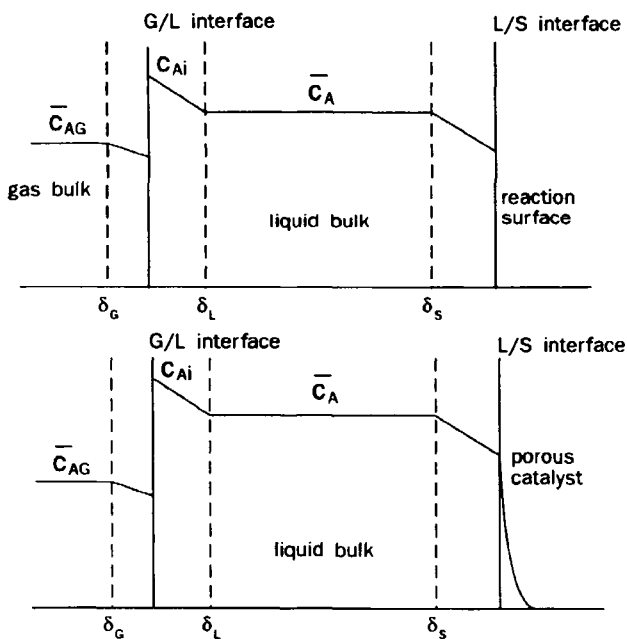


Figure 6. Concentration profiles for mass transfer into a slurry with catalytic particles, with no enhancement at the gas-liquid interface: (above) mass transfer and reaction at the interface; (below) mass transfer and reaction in the porous particles.

$$N_{Pe,S} = \frac{u_G d_c}{D_{eS}} \quad (30)$$

which is identical to the equation for liquid-phase dispersion.

### 10.3.5 Mass Transfer with Chemical Reaction

Together with the system-specific reaction kinetics, the mass transfer parameters are particularly important in determining the average conversion rates in the slurry reactor. As an example, we consider the average conversion rate per cubic meter of the reactor of a gaseous reactant A being absorbed in the liquid of a well stirred slurry semibatch reactor and reacting according to irreversible first-order kinetics at the external surface of non-porous particles (Fig. 6):

$$J_{AA} = \bar{c}_{AG} / \left\{ \frac{1}{k_{GA}} + \frac{1}{mk_{LA}E_A} + \frac{1}{mk_{SA}a_p} + \frac{1}{mk''_r a_p} \right\} \quad (31)$$

(R<sub>1</sub>)   (R<sub>2</sub>)   (R<sub>3</sub>)   (R<sub>4</sub>)

In deriving eq 31,  $\bar{c}_{AG}$  was assumed to be constant throughout the reactor.  $R_1$ – $R_4$  are the so-called resistances that control the overall conversion rate, and the model used here shows all resistances in series:

$$R_1 = 1/k_{GA} \quad \text{the resistance to mass transfer in the gas phase}$$

$$R_2 = 1/mk_{LA}E_A \quad \text{the resistance to mass transfer in the liquid phase at the gas-liquid interface}$$

$$R_3 = 1/mk_{SA}a_p \quad \text{the resistance to mass transfer in the liquid phase at the liquid-solid interface}$$

$$R_4 = 1/mk''_r a_p \quad \text{the resistance to reaction at the external catalyst surface}$$

For a first-order reaction in porous particles,  $R_4$  should be replaced by

$$R'_4 = d_p / (6 m a_p D_i \phi \tanh \phi)$$

with the Thiele modulus,  $\phi$  defined as

$$\phi = \frac{d_p}{6} \sqrt{\frac{k''_r a_S}{D_i}} \quad (32)$$

Although inside the porous particle, mass transport and reaction are in parallel, the overall process can still be described by resistances in series. From these resistances,  $R_2$  might be influenced by the presence of the catalyst particles in two ways:

- (i) the specific (gas-liquid) interfacial area,  $a$ , can be changed by the presence of the particles;
- (ii)  $k_L$  itself can be influenced by the presence of the particles even if these are inert.

It will be clear that, to be conceptually sound, any enhancement effect should exclude these factors. This requires careful definition of the flux enhancement due to the particles, for which we proposed [76]

$$E_A = \frac{J_A \text{ with particles}}{J_A \text{ with the same but inert particles}} \quad (33)$$

in which  $J_A$  is evaluated at the same overall driving force. Inert means that the particles do not participate in the reaction as a reactant or a catalyst. Further, inert particles do not adsorb the gas phase component transported toward the bulk of the slurry, nor any other reactant or reaction product.

$E_A$  will be different from 1 only if  $R_4$  is small relative to  $R_2$ , resulting in a bulk concentration of  $\bar{c}_A = 0$  and in a real parallel mechanism of the enhancement. The advantage of the concept of the enhancement factor as defined by eq 33 is the separation of the influence of hydrodynamic effects on gas-liquid mass transfer (incorporated in  $k_L$ ) and of the effects induced by the presence of a solid surface (incorporated in  $E_A$ ), indeed in a similar way as is common in mass transfer with homogeneous reactions. The above analysis shows that an adequate description of mass transfer with chemical reaction in slurry reactors needs reliable data on:

- (i) parameters which are specific for slurry reactors ( $k_{GA}$ ,  $k_{LA}$ ,  $E_A$ ,  $k_S$ );

(ii) parameters which are not specific to the type of reactor applied (intrinsic reaction kinetics and particle properties such as  $a_p$ ,  $a_s$  and  $d_p$ , and to some extent  $D_i$ ).

Only the parameters of the first type need to be discussed here. It seems logical to start with a brief discussion on the value of the product of  $k_L$  and the specific contact area  $a(k_L a)$ , because this is often the overall rate-controlling step.

### 10.3.5.1 The Volumetric Liquid-Side Mass Transfer Coefficient at the Gas-Liquid Interface

Much more information is available on the product  $k_L a$  than on  $k_L$  and  $a$  separately. For low solids concentrations it may be assumed that the solids do not affect the value of  $k_L a$ , so that the existing relations for two-phase gas-liquid reactors can be applied. For reviews on these relationships, see Lee and Foster [76], for draft tube slurry reactors Goto et al. [77], for bubble columns Deckwer and Schumpe [78] and Deckwer [79], and for stirred tank reactors Mann [80] and Schlüter and Deckwer [81]. Despite of much research published on the influence of solids on  $k_L a$  there is still no universally applicable relation describing the influence of all types of particles in any weight fraction in any liquid.

#### A Slurry Bubble Columns

If the density difference between the solids and liquids is small or if the liquid viscosity is high the slurry behaves as a pseudo-homogeneous phase, and expressions for  $k_L a$  as a function of the effective suspension viscosity can be applied successfully. Öztürk and Schumpe [82] measured  $k_L a$  in a 9.5 cm inner diameter bubble column by absorbing oxygen in organic slurries of ligroin ( $\rho_L = 729 \text{ kg m}^{-3}$ ;  $\mu_L = 0.54 \text{ mPa s}$ ) and tetralin ( $\rho_L = 968 \text{ kg m}^{-3}$ ;  $\mu_L = 2.08 \text{ mPa s}$ ) containing up to 40% of various polymers ( $46 < d_p < 370 \mu\text{m}$  and  $940 < \rho_S < 1380 \text{ kg m}^{-3}$ ) and alumina ( $d_p = 21.6 \mu\text{m}$ ,  $\rho_S = 3180 \text{ kg m}^{-3}$ ). The result is shown in Fig. 7.

With the exception of alumina in ligroin, all results could be correlated by

$$k_L a / (k_L a)_0 = (\mu_{\text{eff}} / \mu_0)^{-0.42} \quad (34)$$

with the subscript 0 indicating the absence of solids; all other conditions remain identical. So,  $\mu_0$  is the viscosity of the pure liquid. The correlation covers a superficial gas velocity up to  $8 \text{ cm s}^{-1}$  and an effective viscosity range of  $0.54\text{--}100 \text{ mPa s}$  with a mean error of 7.7%.

For non-Newtonian suspensions,  $\mu_{\text{eff}}$  is obtained from the Ostwald-de Waele equation

$$\mu_{\text{eff}} = k \dot{\gamma}_{\text{eff}}^{n-1} \quad (35)$$

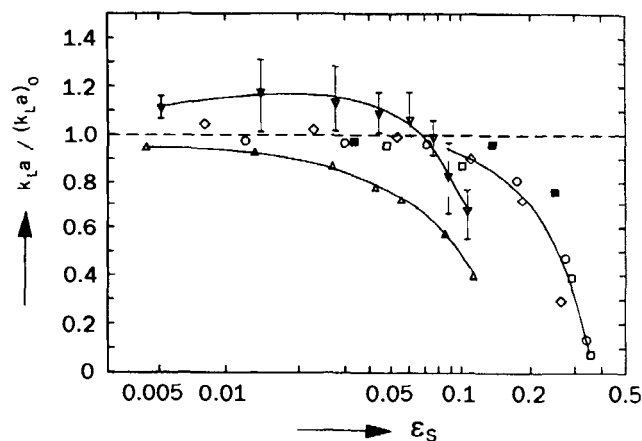


Figure 7. Relative change in  $k_L a$  in a bubble column with respect to the particle-free system as a function of the solid volume fraction: (○) PE ( $\rho_S = 940 \text{ kg m}^{-3}$ ;  $d_p = 46 \mu\text{m}$ )/ligroin; (◐) PE ( $\rho_S = 965 \text{ kg m}^{-3}$ ;  $d_p = 369 \mu\text{m}$ )/ligroin; (◑) PVC ( $\rho_S = 1380 \text{ kg m}^{-3}$ ;  $d_p = 100 \mu\text{m}$ )/ligroin; (◒)  $\text{AL}_2\text{O}_3$  ( $\rho_S = 3180 \text{ kg m}^{-3}$ ;  $d_p = 22 \mu\text{m}$ )/ligroin; (◓)  $\text{AL}_2\text{O}_3$  ( $\rho_S = 3180 \text{ kg m}^{-3}$ ;  $d_p = 22 \mu\text{m}$ )/tetralin; (◔) PE/Exsol ( $\rho_S = 965 \text{ kg m}^{-3}$ ;  $d_p = 45 \mu\text{m}$ ) after Michael and Reichert [85] (from Öztürk and Schumpe [82]).

with, for bubble columns [83],

$$\dot{\gamma}_{\text{eff}} = C u_G \quad (36)$$

and

$$C = 2800 \text{ m}^{-1}$$

The consistency index still has to be measured experimentally. The above result, obtained in organic liquids, also applies for water and aqueous solutions of both electrolytes and non-electrolytes under similar conditions [84]. High-density solids in low-viscosity liquids such as alumina in ligroin, or in low concentrations in aqueous solution, give higher values of  $k_L a$  than predicted by eq 34, possibly due to increased mass transfer coefficients  $k_L$ . It should be realized that the experimental conditions applied in the research on slurry bubble columns resulting in eq 34 were restricted to the homogeneous bubble flow regime (see Fig. 4).

Sada et al. [86] also measured the influence of solids on  $k_L a$  in a small slurry bubble column ( $d_c = 7.8 \text{ cm}$ ). Both pure water and ionic aqueous solutions of various salts (up to  $2.4 \text{ kmol m}^{-3}$ ) as well as sugar solutions (up to 60 wt%) were applied. Gas velocities ran as high as  $20 \text{ cm s}^{-1}$ , i.e. far into the slug flow regime. The particles used were  $\text{Ca}(\text{OH})_2$  ( $7 \mu\text{m}$ ,  $2480 \text{ kg m}^{-3}$ ), glass (40 and  $96 \mu\text{m}$ ,  $2480 \text{ kg m}^{-3}$ ) and nylon-6 (2 mm,  $1140 \text{ kg m}^{-3}$ ) up to 20 wt%. All data could be correlated by

$$k_L a = C \epsilon_G^{0.9} \quad (37)$$

with

$$\varepsilon_G / (1 - \varepsilon_G)^4 = 0.046 u_G \quad (38)$$

for pure water and no particles, and

$$\frac{\varepsilon_G}{(1 - \varepsilon_G)^3} = 0.019 u_G v_t^{1/16} \varepsilon_S^{(-0.125 v_t^{-0.16})} \quad (39)$$

for pure water with particles. Here, according to Stokes law,  $v_t$  is the particle terminal velocity. An unsatisfactory aspect of the approach is that  $C$  has to be measured experimentally and varies in an as yet unpredictable way with  $\varepsilon_S$ ,  $d_p$ , solids composition, and type of electrolyte applied. Without electrolytes present, 5 wt% of 40  $\mu\text{m}$  glass particles need a 50% lower  $C$  than 20 wt% of 96  $\mu\text{m}$  glass. The presence of electrolytes lowers the value of  $C$  and the presence of solids in an electrolyte solution results in a slightly further lowering of  $C$ . For the industrially most important regimes of churn-turbulent flow and, to a lesser extent, the transition regime, the relations of Koida et al. [37] probably have the widest range of applicability. For experimental conditions see above, under holdup. They observed  $k_{L,a}$  to be reduced by the presence of solids, although this reduction is less pronounced in the churn-turbulent regime than in the transition regime. The expression derived by Koida et al. [37] is

$$\frac{k_{L,a}}{(k_{L,a})_0} = \left[ \frac{\varepsilon_{G,H}}{(\varepsilon_{G,H})_0} \right]^{1.18} \times \frac{1}{1 + 1.47 \times 10^4 \varepsilon_S^{0.612} N_{Fr,p}^{0.486} N_{Re}^{-0.345} N_S^{-0.477}} \quad (40)$$

with  $\varepsilon_{G,H}$  and  $(\varepsilon_{G,H})_0$  from eqs 12–14. Here  $N_{Fr,p} = v_t / (d_c g)^{1/2}$  and  $N_S = d_c^2 g \rho_L / \sigma_L$ .

The above relationship, in particular, has been tested in the transition regime (see Fig. 4).

For the industrially most important churn-turbulent regime much less information is available.

Only some scattered information on the influence of pressure and gas density on  $k_{L,a}$  is available. Recently, Dewes et al. [51] reported results from a 0.115 m diameter column operated in all but the churn-turbulent regime, both at 1 bar and 8 bar, with 2 vol% of solids. The influence of solids was negligible (see Fig. 8), but, as expected from Wilkinson's findings on the influence of  $\rho_G$  on  $\varepsilon_G$  [44],  $k_{L,a}$  increased substantially with pressure. Dewes et al. [51] were able to show that the pressure affected  $a$  only, with  $k_L$  remaining independent of both pressure and the presence of solids.

For  $k_{L,a}$  data in draft tube slurry columns, the paper by Goto et al. [77] probably is the best entry. Zahradník et al. [9] published some data for a slurry tray column.

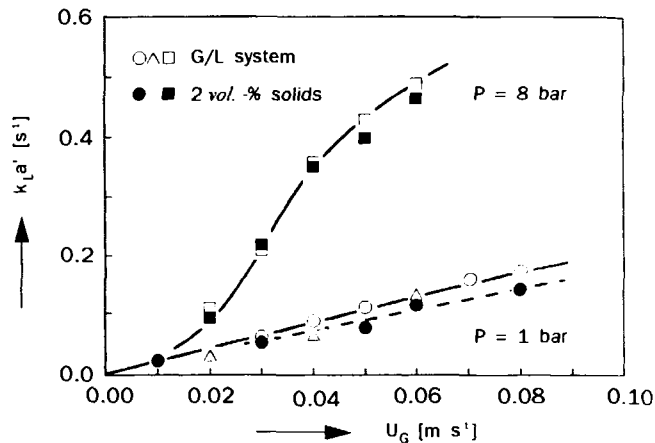


Figure 8. Pressure effect on the volumetric mass transfer coefficient in a sparged slurry column (from Dewes et al. [51]).

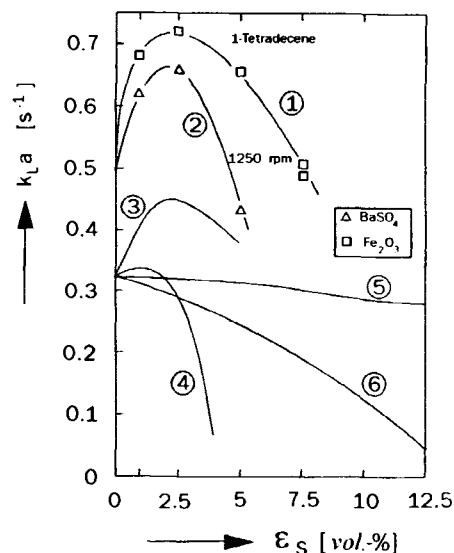


Figure 9. Influence of solids on  $k_{L,a}$  in a 0.15 m diameter stirred-tank reactor: (1)  $\text{Fe}_2\text{O}_3$  (<0.5  $\mu\text{m}$ ) in 1-tetradecene; (2)  $\text{BaSO}_4$  (<1  $\mu\text{m}$ ) in tetradecene; (3)  $\text{Fe}_2\text{O}_3$  in 1,2,4-trimethylbenzene; (4)  $\text{BaSO}_4$  in 1,2,4-trimethylbenzene; (5) sea sand (<80  $\mu\text{m}$ ) in water; (6) kieselguhr (<50  $\mu\text{m}$ ) in water. Stirrer speed 21 rps except for experiments with trimethyl benzene (16 rps) (compiled from several figures of Oguz et al. [87]).

## B Stirred Tank Slurry Reactors

Few comprehensive studies have appeared concerning the influence of solids on  $k_{L,a}$  in stirred tank reactors. Oguz et al. [87] measured  $k_{L,a}$  in various slurries in a baffled 14.5 cm diameter stirred-tank reactor. Water and three organic liquids (*n*-butanol, 1-tetradecene and 1,2,4-trimethylbenzene) were used as liquid phases. The particles applied varied in density from 2070 to 4720  $\text{kg m}^{-3}$  and average particle sizes from 80  $\mu\text{m}$  to below 1  $\mu\text{m}$ . The observed effects of the particles on  $k_{L,a}$  appear at first sight to be confusingly different for different slurry systems (see Fig. 9). However, if the increase in apparent slurry viscosity due to the presence

of the particles exceeds a factor of 1.3 relative to the solids-free liquid, then all data can be consistently correlated by a single function of power input, gas sparging rate, apparent slurry viscosity, surface tension and liquid diffusivity, in a way rather similar to that proposed earlier by Yagi and Yoshida [88] for no solids present. The result of Oguz et al. [87] is as follows:

$$k_L a d_i^2 / D = 0.162 N_{Re}^{1.5} N_{Sc}^{0.5} N_{Fr}^{0.38} N_{GF}^{-0.6} N_A^{0.09} \sqrt{\sigma_{H_2O} / \sigma_L} \quad (41)$$

Here  $d_i$  is the impeller diameter,  $D$  the liquid diffusivity,  $N_{Re}$  is the impeller-based Reynolds number  $\omega d_i^2 \rho_{eff} / \mu_{eff}$ ,  $N_{Sc}$  is the slurry Schmidt number  $\mu_{eff} / (\rho_{eff} D)$ ,  $N_{Fr}$  is the Froude number  $\omega \sqrt{d_i} / g$ ,  $N_{GF}$  is the gas flow number  $\sigma_L / (\mu_{eff} u_G)$ , and  $N_A$  is the aeration number  $\omega d_i / u_G$ .

As also found in bubble columns, the concept of the effective viscosity fails for relatively high-density particles in low-viscosity liquids [87] for a relative increase of  $\mu_{eff}$  below 1.3. Nevertheless, eq 41 is a very remarkable result. Its accuracy is claimed to be within 15%, provided that:

$$\begin{aligned} 1.3 &\leq \mu_{eff} \leq 41 \text{ mPa s} \\ 0.84 &\leq u_G \leq 4.2 \text{ mm s}^{-1} \\ 0.75 &\leq W/V_r \leq 6.3 \text{ kW m}^{-3} \\ 24 &\leq \sigma_L \leq 72 \text{ mN m}^{-1} \\ 0.68 &\leq 10^9 D \leq 2.4 \text{ m}^2 \text{ s}^{-1} \end{aligned}$$

Schmitz et al. [89] also reported on the influence of solids on  $k_L a$  in stirred tanks. Although they applied only one type of solid (glass beads of 88 and 320  $\mu\text{m}$  average diameter) in aqueous solutions, their study is of particular interest because of the wide range in variation of liquid viscosity applied by adding carboxy methylcellulose and by investigating the scale-up aspects by measuring both in a 20 cm and a 45 cm diameter stirred tank. As Schmitz et al. [89] also point out, their result.

$$\frac{k_L a}{(k_L a)_0} = 1 - 3.54(\varepsilon_S - 0.03) \quad (42)$$

obtained for  $0.03 \leq \varepsilon_S \leq 0.12$ ,  $d_p = 320 \mu\text{m}$ ,  $\rho_p = 2490 \text{ kg m}^{-3}$ ,  $300 < W/V_r \leq 10\,000 \text{ W m}^{-3}$ ,  $0.34 \leq u_G < 4.2 \text{ cm s}^{-1}$  and  $5 < \mu_L < 75 \text{ mPa s}$ , is certainly not directly applicable to other systems. However, their finding that  $k_L a$  can be kept constant in scaling-up by maintaining the specific power consumption holds equally well for slurries as for two-phase stirred tanks and may turn out to be more generally applicable (Fig. 10). Much uncertainty continues to exist, particularly on the influence of  $\varepsilon_S$  (Fig. 11). Even an increase of  $k_L a$  with increasing  $\varepsilon_S$  is sometimes observed.

The influence of pressure on  $k_L a$  in stirred tanks seems to be less pronounced than in bubble columns. No influence of pressure was found by Albal et al. [92].

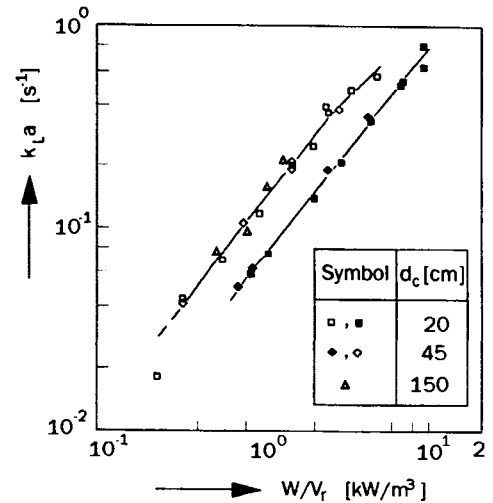


Figure 10. Volumetric mass transfer coefficient as a function of total power consumption for different reactor diameters for 320  $\mu\text{m}$  glass particles in water and  $u_G = 1.9 \text{ cm s}^{-1}$ : closed symbols for 30 wt% solids; open symbols for no solids (adapted from Ref. 89).

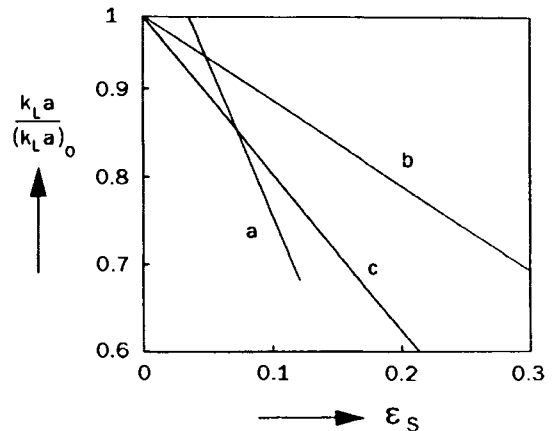


Figure 11. Influence of solids fraction on  $k_L a$  in stirred tanks: (a) sodium sulfite aqueous solution [89]; (b) tap water [90]; (c) NaCl aqueous solution [91].

Dietrich et al. [93], Ledakowicz et al. [94] and Chang and Morsi [95]. However, a slight increase with pressure was observed by others, particularly where the surface tension strongly decreased with pressure. To confuse matters further, decrease of  $k_L a$  with pressure has also been observed [97, 98].

Chang and Morsi [95] correlated all their data in the form

$$\frac{(k_L a) d_i^2}{D_L} = C N_{Re}^{2.645} N_{Eu}^{0.222} N_{Sc}^{1.657} \quad (43)$$



**Table 5.** System-specific studies on  $k_L a$ ,  $k_L$  and  $a$  in slurry reactors.

Process	Reactor	Data
Polymerization of ethylene [99]	BC	$k_L a(T, \varepsilon_S, u_G)$
Fisher-Tropsch synthesis [100]	STR	$k_L a(p, \omega; \text{no solids})$
Hydrogenation of ammonium nitrate (HPO process) [101]	BC + STR	$k_L a(u_G, \varepsilon_S, T)$
Hydrogenation of methyl oleate [102]	STR	$k_L a(\omega, \varepsilon_S)$
Hydrogenation of 2-ethyl-tetrahydroantraquinone in the presence of a palladium catalyst [103]	STR	$a(\omega)$ $k_L(T)$ $k_S(\omega, T)$
Alkylation of p-cresol with isobutene [104]	STR	$a(\omega)$ $k_S(\omega, d_p)$
Hydrogenation of adiponitrile [105]	STR	$k_L a(\omega, T)$ $k_S(\omega, T)$
Hydrogenation of adiponitrile [93]	STR	$k_L a(\omega, c_S, T, p;$ catalyst activity)

and Dietrich et al. [93] their data in the form

$$\frac{(k_L a) d_i^2}{D_L} = C N_{Re}^{1.45} N_{Sc}^{0.5} N_{We}^{0.5} \quad (44)$$

with

$$N_{Eu} = p / (\rho_{eff} d_i^2 \omega^2)$$

and

$$N_{We} = \rho_{eff} \omega^2 d_i^3 / \sigma$$

The considerable differences in exponents for  $N_{Re}$  and  $N_{Sc}$  show that additional work is necessary to arrive at a broadly applicable relationship for  $k_L a$  as a function of system properties and operating parameters in stirred tanks. For recent system-specific studies on industrially important catalytic slurry reaction see Table 5.

### 10.3.5.2 The True Gas-Liquid Specific Contact Area ( $a$ ) and the Liquid-Side Mass Transfer Coefficient ( $k_L$ )

Probably, for most slurry reactor applications, information on the value of the product  $k_L a$  is sufficient for design purposes. In some cases, however, information on the individual parameters  $a$  and/or  $k_L$  can be useful. For instance, the reactor capacity will depend on  $a$ , rather than on the product  $k_L a$ , if the reaction is so fast that all conversion takes place within the stagnant film (film theory) around the gas bubbles. For first-order conversion kinetics in the porous catalyst particles this will occur for

$$\sqrt{(k'_i c_{Si} D) / k_L} > 2 \quad (45)$$

provided that interparticle and intraparticle diffusion limitations are absent. Here,  $c_{Si}$  is the solids concentration at the gas-liquid interface, which might be much higher than in the bulk of the liquid (see below). Such a condition will occur for very reactive systems with small catalyst particles only (below 10  $\mu\text{m}$  in systems of low viscosity).

In such a situation, detailed information on  $k_L$  might also be necessary, for instance if this affects selectivity. This may occur in, for example, fast consecutive reactions where an intermediate product is the desired one. Such consecutive reactions are of great industrial importance (e.g. many hydrogenations, oxidations, sulfonations, nitrations and halogenations belong to this category). However, these are not always carried out with sufficiently small particles in slurry reactors, often because of solids separation problems. However, in all cases where the catalyst causes an enhancement of the mass transfer rate, the value of  $a$  rather than the product  $k_L a$  dictates reactor capacity. Industrial examples are the hydrogenation of  $\alpha$ -amino-caprolactam with nickel catalysts, the hydrogenation of ammonium nitrate to hydroxylamine with Pd on active carbon [106–107], the hydrogenation of adiponitrile [93], the hydrogenation of edible oils with noble metal catalysts, and the manufacture of the *para* isomers in the chlorination and nitration of toluene with zeolites [108]. In all these examples, reactor capacity may depend on  $a$ , rather than on  $k_L a$ , whereas in most of these cases product selectivity is affected by the value of  $k_L$ .

Unfortunately, information on  $k_L$  and  $a$  in slurry reactors remains rudimentary, even if compared to the already incomplete information on the value of the product  $k_L a$ . For a recent review on what we know see Ref. 109.

### 10.3.5.3 The Volumetric Gas-Side Mass Transfer Coefficient ( $k_G a$ )

Virtually no information is available on  $k_G a$  in slurry reactors. The good news is that  $k_G a$  is often not a limiting resistance, and hence its value is not important. This statement is, probably, true for all processes listed in Table 5.

### 10.3.5.4 The Mass Transfer Coefficient at the Liquid-Solid Interface $k_S$

Expressions for the mass transfer coefficient around the solid particles are usually presented in the form

$$N_{Sh} = 2 + C N_{Re}^{n_1} N_{Sc}^{n_2} \quad (46)$$

**Table 6.** Particle-liquid mass transfer in three-phase sparge bubble columns.

Proposed correlation	Range of $d_p$ ( $\mu\text{m}$ )	Range of $d_c$ (m)	Range of $u_G$ ( $\text{m s}^{-1}$ )	Range of $N_{Sc}$	References
$N_{Sh} = 2 + 0.400 N_{Re'}^{0.25} N_{Sc}^{1/3}$ (eq 53)	60–2900	0.1–0.2	0.005–0.17	220–1410	110
$N_{Sh} = 2 + 0.545 N_{Re'}^{0.264} N_{Sc}^{1/3}$ (eq 54)	1100–8700	0.08	0.01–0.1	140–50 000	111
$N_{Sh} = 2 + 0.0915 N_{Re'}^{0.265} N_{Sc}^{0.45}$ (eq 55)	500–1100	0.1–0.4	0.09–0.35	800–60 000	112
$N_{Sh} = 2 + 0.368 N_{Re'}^{0.229} N_{Sc}^{1/3}$ (eq 56)	280–3200	0.15	0.02–0.1	200–80 000	113

with the Sherwood and Schmidt numbers being defined as

$$N_{Sh} = \frac{k_S d_p}{D} \quad (47)$$

$$N_{Sc} = \mu_L / (\rho_L D) \quad (48)$$

The numerical value of  $k_S$  is dictated by the local turbulence around the particles. Based on Kolmogoroff's theory of local isotropic turbulence, this leads to a Reynolds number based on the velocity of the critical eddies responsible for most of the energy dissipation. For solid particles much larger than the Kolmogoroff scale of these eddies, this leads to

$$N_{Re} = C_1 \left( \frac{\bar{e} d_p^4 \rho_L^3}{\mu_L^3} \right)^{1/3} \quad (49)$$

Here,  $\bar{e}$  is the specific local energy dissipation rate per unit mass of liquid. If we may assume that all energy fed to the system is dissipated via these eddies, then

$$\bar{e} = W / (\rho_L V_L) \quad \text{W kg}^{-1} \text{ or } \text{m}^2 \text{s}^{-3} \quad (50)$$

For a bubble column

$$W = \Phi_{v,G} \Delta p = u_G g \rho_L V_L \quad (51)$$

so that  $\bar{e} = u_G g$  and

$$N_{Re'} \equiv \left( \frac{\bar{e} d_p^4 \rho_L^3}{\mu_L^3} \right)^{1/3} = \left( \frac{u_G g d_p^4 \rho_L^3}{\mu_L^3} \right)^{1/3} \quad (52)$$

Note that this is a definition of  $N_{Re'}$  because we arbitrarily took the constant  $C_1$  of eq 49 equal to 1. A number of investigations have followed this approach, and the results are summarized in Table 6 and Fig. 12. Recent progress in this area concentrates on the influence of liquid, gas and solid properties on  $k_S$  and on scale-up rules. Lazaridis [113] measured the influence of  $d_p$ ,  $u_G$ ,  $\bar{e}$ ,  $\mu_L$ ,  $\sigma_L$ ,  $\varepsilon_S$ , and the bubble column height on  $k_S$ . His findings can also be applied to non-Newtonian liquids. In that case,  $\mu_L$  follows from eqs 35 and 36, but according to Lazaridis, a value of  $C = 1000 \text{ m}^{-1}$  should be used in eq 36 instead of 2800.

Particularly valuable is the work of Jadhav and Pangarkar [112], who tested their condition for columns of 10, 20 and 40 cm diameter. Although these

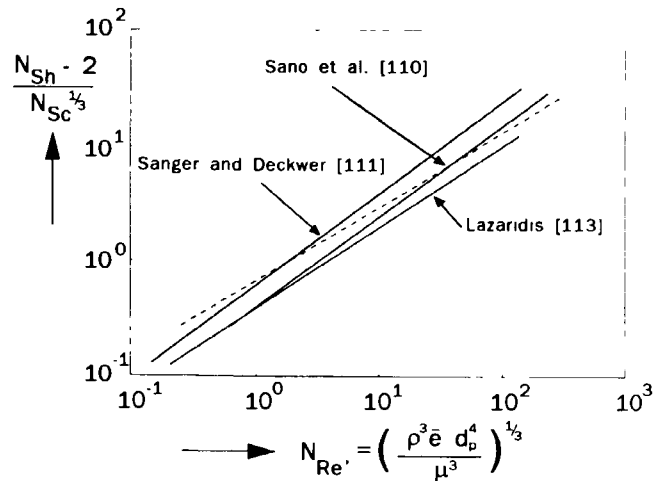


**Figure 12.** Correlations for liquid-solid mass transfer coefficient in bubble columns. The dashed curve is from Jadhav and Pangarkar [112] for  $d_p = 100 \mu\text{m}$ ,  $d_c = 0.3 \text{ m}$ ,  $N_{Sc} = 1000$  and  $v_L'$  from eq 60.

authors also used the concept of the specific energy dissipation rate, their approach is slightly different. They defined the Reynolds number as

$$N_{Re'} = \frac{v_L' d_p \rho_L}{\mu_L} \quad (57)$$

and took the characteristic turbulence velocity  $v_L'$  from Pandit and Joshi [114]:

$$v_L' = 0.43 \left\{ g d_c \left[ u_G - \varepsilon_G v_{b\infty} - \varepsilon_S v_L \left( \frac{\rho_p - \rho_L}{\rho_L} \right) \right] \right\}^{1/3} \quad (58)$$

Except for concentrated slurries, the last term of eq 58 can often be neglected, so that

$$v_L' = 0.43 [g d_c (u_G - \varepsilon_G v_{b\infty})]^{1/3} \quad (59)$$

Actually,  $v_L'$  is proportional to the liquid circulation velocity. The expression of Jadhav and Pangarkar is less easily applicable than the other relations given in Table 6, because knowledge of  $\varepsilon_G$  and  $v_{b\infty}$  is required. For the latter, Jadhav and Pangarkar [115] suggested

**Table 7.** Particle-liquid mass transfer in three-phase stirred-tank reactors.

Proposed correlation		Range of $d_p$ ( $\mu\text{m}$ )	$V_r$ ( $\text{dm}^3$ )	$\bar{e}_G/\bar{e}$	Range of $N_{Sc}$	Reference
$N_{Sh} = [2 + 0.4N_{Re}'^{3/4}N_{Sc}^{1/3}]\psi$	(eq 63)	60–1500	0.7–50	0	220–1280	[117]
$N_{Sh} = 2 + 0.36N_{Re}'^{3/4}N_{Sc}^{1/3}$	(eq 64)	17–90	10.9	0–1		[118]
$N_{Sh} = [2^{5.8} + (0.61N_{Re}'^{0.58}N_{Sc}^{1/3})^{5.8}]^n$ , $n = 1/5.8$	(eq 65)	5–970	1.8	0–1	270–11 000	[119]

the relationships of Grace et al. [116] for “clean” systems and of Zuber and Findley [117] for other systems.

The significance of the Jadhav and Pangarkar equation stems not only from the large column diameters for which it has been tested but also from the relatively large superficial velocities, which are well into the industrially important churn-turbulent regime. Using their equation (eq 55, see Table 6) and substituting the maximum possible value of  $v_L'$ , i.e.,

$$v_L' = 0.43(gd_c U_G)^{1/3} \quad (60)$$

gives

$$N_{Re}' = 0.43 \left( \frac{d_c}{d_p} \right)^{1/3} N_{Re}'$$

By using this relationship the dashed curve in Fig. 12 was obtained for a 30 cm column and 100  $\mu\text{m}$  particles. Surprisingly, the result fits nicely with the other correlations available. Nevertheless, the use of eq 59 is advised in practical applications.

The approach based on the energy dissipation rate is not limited to a particular type of slurry reactor. Therefore, equations of type 46 and 52 have also been proposed for stirred-tank reactors. For  $\bar{e}$  the total energy dissipation rate originating from both gas and power inputs via the stirrer must then be used. Hence,

$$\bar{e} = \bar{e}_G + \bar{e}_\omega \quad (61)$$

$$\bar{e} = u_G g + W_\omega / \rho_L V_L \quad (62)$$

where  $W_\omega$  is the power input via the stirrer. The available correlations are summarized in Table 7. Note that the equation of Sano et al. [110] contains a correction factor for asphericity of the particles:

$$\psi = 6/(a_p d_p)$$

where  $\psi = 1$  for spheres.

Figure 13 shows that the various relations agree well with each other. Therefore, our knowledge of the value of  $k_S$  is relatively well established. Additional research should concentrate on larger tank reactors with volumes above 0.05  $\text{m}^3$  and for  $k_S$  in high-intensity equipment such as ejectors.

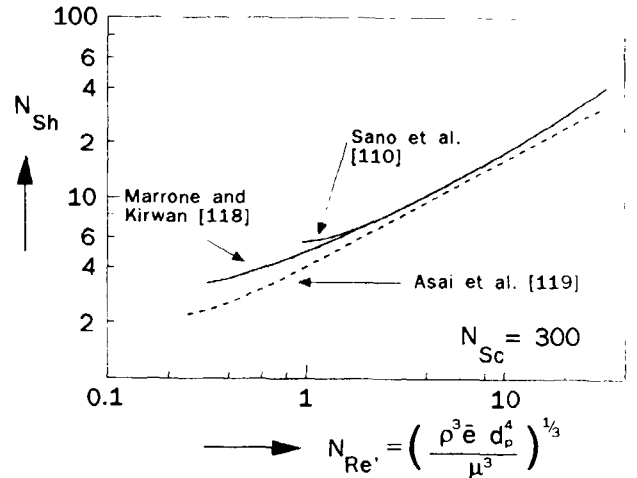


**Figure 13.** Sherwood number for liquid-solid mass transfer in sparged stirred tank slurry reactors (adapted from Asai et al. [119]).

### 10.3.6 Enhancement of Gas-Liquid Mass Transfer

As mentioned above, particles may enhance the gas absorption rate. In heterogeneous catalysis there are two mechanisms, either by physical adsorption on the particles or by chemical reaction on the catalytic sites of the particles.

#### 10.3.6.1 Enhancement by Physical Adsorption

Particles having significant adsorption capacity for the absorbing gas A, pick up gas when they are in contact with the gas-liquid interface. If these particles, after a typical surface contact time of

$$t_c = 4D/\pi k_L^2 \quad (66)$$

(penetration theory) have returned to the bulk of the slurry, where, due to chemical reaction  $\bar{c}_A$  is much lower than  $c_{Ai}$ , desorption of A from the particles follows. This way, particles shuttling between the bulk and interface contribute to extra mass transfer of A. Therefore, this mechanism of enhancement is called the

shuttle mechanism. The effect is significant only if the particles are small relative to the film thickness for mass transfer (film theory), i.e. for

$$d_p \leq \delta_L = \frac{D}{k_L} \quad (67)$$

and for a large adsorption capacity of the particles for the gaseous component.

Not surprisingly, therefore, most successful experimental results have been obtained with small activated carbon particles in aqueous slurries. A first theoretical relation for the effect was presented by Kars et al. [120] for infinitely small particles being instantaneously in equilibrium with their surroundings:

$$E_A = \sqrt{1 + \varepsilon_S \rho_S K_{ad}} \quad (68)$$

In practice, the effect will be lower because the particles have a final size, but it can also be higher if the particles preferentially adhere to the surface but are nevertheless replaced after the penetration time of eq 66.

For finite particles, Vinke [121] derived

$$E_A = \frac{4\alpha D_A}{d_p k_L} = \frac{4\alpha \delta_L}{d_p} \quad (69)$$

Here,  $\alpha$  is the surface fraction covered by the particles.

In contrast to the model of Kars et al. [120], this model also explains the experimentally observed maximum in the enhancement factor, which is obtained for complete surface coverage ( $\alpha = 1$ ). We then have

$$E_{A,max} = \frac{4\delta_L}{d_p} = \frac{4D_A}{k_L d_p} \quad (70)$$

For aqueous systems  $k_L$  is typically  $10^{-4} \text{ m s}^{-1}$ ,  $D_A$   $10^{-9} \text{ m}^2 \text{ s}^{-1}$  and  $d_p = 5 \mu\text{m}$  (which is half the film thickness), to give  $E_{A,max} = 8$ , which is an important value for industrial applications. Experimental findings for activated carbon particles in aqueous systems show that the above maximum value  $E_{A,max}$  is already obtained at very low average solids fractions of  $0.5 \times 10^{-4} < \varepsilon_S < 5 \times 10^{-3}$ . This makes it very attractive to use catalyst carrier particles which preferentially stick to the gas-liquid surface and have a high adsorption capacity towards the absorbing gas.

### 10.3.6.2 Particles Catalyze a Chemical Reaction Involving the Absorbed Gas Phase Component

If the catalyst particles have a diameter much smaller than the thickness of the mass transfer film, and if sufficient particles are available in the film, then enhancement of gas adsorption due to chemical reaction may occur provided that the specific chemical conversion rate is high enough. For enhancement in a slurry re-

actor (first-order reaction, constant gas phase concentration, no liquid through-flow of bulk), Wimmers and Fortuin [122] derived

$$E_A^0 = \frac{(Ha_f)}{\sinh(Ha_f)} \times \left\{ \cosh(Ha_f) - \frac{1}{\cosh(Ha_f) + \frac{1}{\left[ \frac{k'_r c_{Si} \sinh(Ha_f)}{k_L a' (Ha_f)} \right]}} \right\} \quad (71)$$

in which

$$Ha_f = \frac{\sqrt{k'_r \varepsilon_{Si} \rho_S D_A}}{k_L} \quad (72)$$

where:

- (i)  $E_A^0$  is the actual absorption rate divided by  $k_L a V_r c_{Ai}$ ; note that for a fast reaction, where  $\bar{c}_A = 0$ ,  $E_A^0 = E_A$ .
- (ii)  $\varepsilon_{Si} \rho_S$  is the actual solids load in the gas-liquid film for mass transfer, described by Wimmers and Fortuin via a Freundlich isotherm, still containing some empirical factors.
- (iii)  $k'_r$  is the pseudohomogeneous first-order reaction rate constant,  $\text{m}^3 \text{kg}^{-1} \text{s}^{-1}$ .

In principle, the rate constant  $k'_r$  can contain, among other things, mass transfer rates to the surface of the particles ( $k_S$ ) and diffusion limitation inside the particles. For example, for a first-order reaction at the porous catalyst surface,

$$\frac{1}{k'_r c_{Si}} = \frac{1}{k_S a'_{pi}} + \frac{1}{a'_{pi} \sqrt{k''_r a_S D_A} \tanh \phi} \quad (73)$$

with  $a'_{pi}$  the specific solids external surface area at the gas-liquid interface and  $\phi$  defined by eq 32. In particular, if the true surface rate constant  $k''_r$  is relatively high compared to  $k_S$ , the reaction in the film can be limited by  $k_S$ .

If the particles don't adhere preferentially to the gas-liquid interface, enhancement of mass transfer according to eq 71 usually will not be spectacular. But if gas-liquid surface adhering properties are added to the carrier this may make a great difference due to a spectacular increase in  $\varepsilon_{Si} \rho_S$ . For comparison, Fig. 14 shows results of a hydrogenation both with non-surface adhering and with surface adhering carriers, each having the same active catalyst. Note that  $d_p$  for the activated carbon carrier is twice that of the non-adsorbing  $\text{Al}_2\text{O}_3$  particles. For the same particle size of  $10 \mu\text{m}$  the enhancement with Pd on activated carbon would be 2

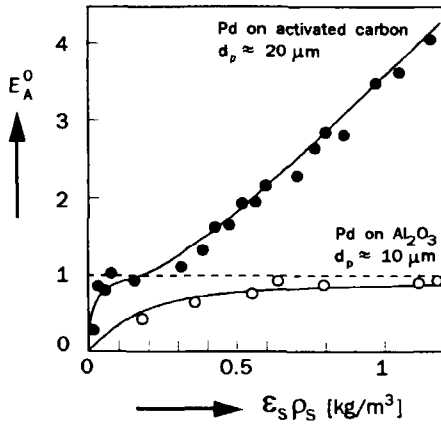


**Figure 14.** Enhancement of absorption of hydrogen into aqueous hydroxylamine phosphate solutions by catalyst loading of the bulk for a stirred-tank reactor. Drawn lines are model calculations with best-fit parameters (from Wimmers and Fortuin [122]).

times higher, because it can be derived from eq 71 that

$$E_A \approx 1/d_p$$

for mass transfer around the particles being rate controlling [109]. Such a correlation has also been observed experimentally. For a recent review on the enhancement of mass transfer by particles in slurries see Ref. 109.

### 10.3.7 Towards High-Intensity Slurry Reactors

Unless restrained by selectivity requirements, catalyst developers may search for more active catalysts until mass transfer around the particles is rate controlling. Reactor engineers then will load the slurry with catalysts until mass transfer around the bubbles becomes rate limiting, for example

$$\frac{1}{mk_S a_p} \ll \frac{1}{mk_L a} \quad (R_3) \quad (R_2)$$

where it is assumed that both  $R_1$  and  $R_4$  in eq 31 are much smaller than  $R_3$  and that  $E_A = 1$ . Assuming  $k_S$  to be of the the same order of magnitude as  $k_L$  and substituting  $a = 6\epsilon_G/d_b$  and  $a_s = 6\epsilon_S/d_p$  yields

$$\epsilon \gg \frac{d_p}{d_b} \epsilon_G$$

For easily separable particles of  $d_p = 40 \mu\text{m}$ ,  $d_b$  typically of the order 5 mm and  $\epsilon_G = 0.4$ , then

$$\epsilon_S \gg 3 \times 10^{-3}$$

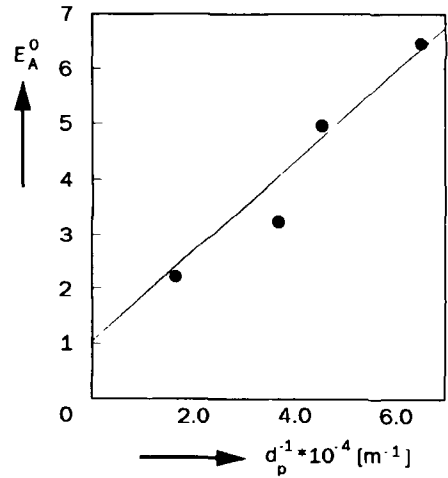


**Figure 15.** Enhancement factor for hydrogen absorption in an aqueous hydroxylamine solution as a function of the reciprocal Sauter mean diameter of Pd/activated carbon catalyst particles;  $\epsilon_S \rho_S = 1.5 \text{ kg m}^{-3}$ , flat interface stirred cell (from Wimmers et al. [123]).

say,

$$\epsilon_S \approx 3 \times 10^{-2}$$

Now, if we can get catalyst carriers that adhere to the gas-liquid surface and we become successful in easily separating particles of  $d_p \leq 5 \mu\text{m}$ , we can reduce on catalyst concentrations down to  $0.5 \times 10^{-4} < \epsilon_S < 5 \times 10^{-3}$  and still realize an enhancement in conversion rate, typically by a factor of 5. This way, the reactor volume is reduced by a factor of 5 and the catalyst holdup by several orders of magnitude. The improvement might be even more spectacular because it is known that small particles of  $d_p < 100 \mu\text{m}$  for  $\epsilon_S < 0.5 \times 10^{-2}$  may cover gas liquid surface, thus prevent bubble coalescence which results in smaller bubbles, leading to still higher interfacial gas liquid areas and thus to still smaller reactors [109].

Applying high energy input reactors such as venturi loop reactors may have an extra beneficial effect. Hence, slurry reactors which fit onto a table and which still have a capacity of kilotons per year are probably within reach, provided the heat effects involved in the reaction can be handled. The heat transfer in slurry reactors using built-in tubes, has been studied [40-43, 124-127].

### 10.3.8 Symbols

- $a$  specific gas-liquid contact area,  $\text{m}^2/\text{m}^3$  reactor
- $a'$  specific gas-liquid contact area,  $\text{m}^2/\text{m}^3$  liquid phase
- $a_p$  specific external interface of solids,  $\text{m}^2/\text{m}^3$  reactor

$d'_p$	specific external interface of solids, $\text{m}^2/\text{m}^3$ liquid phase	$N_{Re}$	Reynolds number $[= (\bar{e}d_p^4\rho_L^3/\mu_L^3)^{1/3}]$ [in bubble columns = $(u_Ggd_p^4\rho_L^3/\mu_L^3)^{1/3}$ ], dimensionless
$d'_{pi}$	specific external interface of solids at gas-liquid interface, $\text{m}^2/\text{m}^3$ liquid	$N_{Re''}$	Reynolds number $(= v'_L d_p \rho_L / \mu_L)$ , dimensionless
$a_S$	specific internal interface of solids per unit porous particle volume, $\text{m}^{-1}$	$N_S$	surface tension number $(= d_c^2 g \rho / \sigma)$ , dimensionless
$\bar{c}_A$	bulk concentration of species A, $\text{kmol}/\text{m}^3$	$N_{Sc}$	Schmidt number $(= \mu / \rho D)$ , dimensionless
$c_{Ai}$	concentration of species A in liquid at gas-liquid interface, $\text{kmol}/\text{m}^3$ liquid	$N_{Sh}$	Sherwood number $(= k_L d_p / D$ around bubbles) $(= k_S d_p / D$ around particles), dimensionless
$c_{AiS}$	liquid concentration of A near solids interface, $\text{kmol}/\text{m}^3$ liquid	$N_{We}$	Weber number, $\rho_{\text{eff}} \omega^2 d_1^3 / \sigma$ , dimensionless
$C$	constant	$p$	pressure in reactor, $\text{N}/\text{m}^2$
$d_b$	bubble diameter, m	$R_1, R_2,$	
$d_c$	column diameter, m	$R_3, R_4,$	
$d_i$	impeller diameter, m	$R'_4$	resistances against mass transfer, s
$d_p$	particle diameter, m	$t_c$	contact time in penetration model, s
$D$	molecular diffusion coefficient, $\text{m}^2/\text{s}$	$T$	temperature, K or $^{\circ}\text{C}$
$D_1$	intraparticle diffusion coefficient, $\text{m}^2/\text{s}$	$u$	superficial velocity, (m/s)
$D_e$	axial dispersion coefficient, $\text{m}^2/\text{s}$	$u_r$	relative velocity between gas and liquid (m/s)
$\bar{e}$	average specific power input per kg liquid, $\text{W}/\text{kg}$	$u_{tr}$	superficial gas velocity at the transition between the homogeneous bubble flow and the transition regime, m/s
$e_b$	specific power input per kg liquid close to the vessel bottom $\text{W}/\text{kg s}$	$v_{b\infty}$	single bubble rise velocity, m/s
$E_A$	enhancement factor of component A, defined by eq. (33), dimensionless	$v_i$	minimum pickup velocity (eqn 1), m/s
$E_A^0$	$J_A / k_L c_{Ai}$ , dimensionless	$v'_L$	characteristic turbulence velocity defined by eq. (58), m/s
$E_{A,\text{max}}$	maximum enhancement factor, dimensionless	$v_{lb}, v_{sb}$	rise velocity of large and small bubbles, respectively, m/s
$g$	gravity constant, $\text{m}/\text{s}^2$	$v_t$	terminal settling velocity of single particle, m/s
$H$	height of column, m	$v'$	fluctuating velocity of critical eddies, m/s
$Ha_{fr}$	modified Hatta number defined by eq. (72)	$v_u$	upward component of liquid velocity (eqn 2), m/s
$J_A$	molar flux of A, $\text{kmol}/(\text{m}^2\text{s})$	$V_r, V_L$	volume of reactor and of liquid phase, $\text{m}^3$
$k$	fluid consistency index, $\text{Pa s}^n$	$w_S$	mass of solids per kg liquid
$k_G$	gas-side mass transfer coefficient, m/s	$W$	power input, W
$k_L$	liquid-side mass transfer coefficient, m/s	$z$	coordinate in direction of flow
$k'_r$	first-order reaction rate constant, $\text{m}^3/(\text{kg solids s})$		
$k''_r$	first-order surface reaction rate constant, m/s		
$k_S$	liquid-to-solid mass transfer coefficient, m/s		
$K_{ad}$	adsorption equilibrium constant, $\text{m}^3$ liquid/kg solids		
$m$	gas solubility, $c_L/c_G$ at equilibrium		
$n$	exponent		
$N_A$	acration number in stirred tank $(= \omega d_i / u_G)$ , dimensionless		
$N_{Eu}$	Euler number, $p / (\rho_{\text{eff}} d_i^2 \omega^2)$		
$N_{Fr}$	Froude number, $\omega \sqrt{d_i/g}$ for stirred tanks, $u_G / \sqrt{g d_c}$ for bubble columns, dimensionless		
$N_{Fr,p}$	particle Froude number $[= v_t / (d_c g)^{1/2}]$ , dimensionless		
$N_{GF}$	gas flow number $[= \sigma_L / (\mu u_G)]$ , dimensionless		
$N_{Pe}$	Peclet number for axial dispersion $(u_G d_o / De_L$ for liquid; $v_t H / De_S$ for solids), dimensionless		
$N_{Re}$	Reynolds number $(= \omega d_i^2 \rho / \mu$ in stirred tank) $(= u_G d_c \rho_L / \mu_L$ in bubble columns), dimensionless		
		<i>Greek letters</i>	
		$\alpha$	fraction of surface covered by solids, dimensionless
		$\dot{\gamma}$	shear rate, $\text{s}^{-1}$
		$\delta_L$	film thickness in terms of the film model $(= D/k_L)$ , m
		$\Delta p$	pressure drop over reactor, Pa
		$\Delta \rho$	$\rho_L - \rho_G$ or $\rho_S - \rho_L$ , $\text{kg}/\text{m}^3$
		$\varepsilon_G$	gas hold-up, $\text{m}^3/\text{m}^3$ reactor
		$\varepsilon_S$	solids hold-up, $\text{m}^3/\text{m}^3$ liquid
		$\varepsilon_{Si}$	solids hold-up at gas-liquid interface, $\text{m}^3/\text{m}^3$ liquid
		$\mu$	dynamic viscosity, Pa s
		$\mu_{\text{eff}}$	apparent effective slurry viscosity, Pa s
		$\rho$	density, $\text{kg}/\text{m}^3$
		$\rho_p$	particle density, $\text{kg}/\text{m}^3$ solids
		$\sigma$	surface tension, N/m

$\tau$	shear stress, Pa
$\phi$	reaction or Thiele modulus, dimensionless
$\Phi_v$	volumetric flow rate, m <sup>3</sup> /s
$\psi$	Carmans surface factor, dimensionless
$\Psi$	power number, dimensionless
$\omega$	stirring speed, s <sup>-1</sup>

**Subscripts**

A	component A
c	column
G	gas phase
H	in heterogenous churn turbulent flow regime
lb	large bubbles
L	liquid phase
max	maximum
min	minimum
0	no solids present, all other conditions identical
P	particle
sb	small bubbles
S	solids
SL	slurry
tr	transition regime
$\omega$	due to stirring

**Superscript**

-	mean value, in the bulk
---	-------------------------

**Acknowledgment**

Liberal use has been made of material from publications co-authored with W. P. M. Van Swaaij.

**References**

- 1 B Jager, R Espinoza, *Catal Today*, **1995**, *23*, 17–28
- 2 L K Doraiswamy, M M Sharma, *Heterogeneous reactions*, Wiley, New York **1984**, Vol 2, 9–12
- 3 J Coca, J M Diaz, *Dechema Monograph* **1980**, *86*, 517–528
- 4 B Jager, A P Steynberg, Eur Patent 94 300 600 7, **1994**
- 5 J Nelles, W Lambrecht, W Neumann, M Prag, A Ulrich, K Lunkwitz, L Weisbach, D Busse, R Gotz, H W Martens, DDR Patent 274 98/A1, **1990**
- 6 A P Boyes, S Raymahasay, M W Tilson, X X Lu, S Sarmiento, A Chugtai, J M Winterbottom, *Chem Eng Technol* **1994**, *17*, 307–312
- 7 P H M R Cramers, L Smit, G M Leutentz, L L van Dierendonck, A A C M Beenackers, *Chem Eng J (Lausanne)* **1993**, *53*, 67–74
- 8 P H M R Cramers, L L van Dierendonck, A A C M Beenackers, *Chem Eng Sci*, **1992**, *47*, 2251–2256
- 9 J Zahradnik, L Drapal, F Kastanek, J Reznickova, *Chem Eng Process* **1992**, *31*, 263–272
- 10 J J Concordia, *Chem Eng Prog* **1990**, *March*, 50–54
- 11 P Vijayaraghavan, C J Kulik, S Lee, *Fuel Sci Tech* **1993**, *11*, 1577–96
- 12 S Narayanan, V K Bhatta, D K Guha, *Can J Chem Eng* **1969**, *47*, 360–364
- 13 C M Chapman, A W Nienow, M Cooke, J C Middleton, *Chem Eng Res Des* **1983**, *61*, 71–81
- 14 N K Roy, D K Guha, N M Rao, *Chem Eng Sci* **1964**, *19*, 215–225
- 15 Y Kato, A Nishiwaki, T Fukuda, S Tanaka, *J Chem Eng Jpn* **1972**, *5*, 112–118
- 16 K Imafuku, T Y Wang, K Koide, H Kubota, *J Chem Eng Jpn*, **1968**, *1*, 153–158
- 17 C M Chapman, A W Nienow, M Cooke, J C Middleton, *Chem Eng Res Des* **1983**, *61*, 167–181
- 18 T N Zwietering *Chem Eng Sci* **1958**, *8*, 244–253
- 19 A N Nienow, *Chem Eng Sci* **1968**, *23*, 1453–1459
- 20 I S Pavlushenko, N, M Kostin, S F Matveev, *Zhur Priklad Khim* **1957**, *30*, 1160–1169
- 21 Y Oyama, K Endoh, *Chem Eng Tokyo* **1956**, 20–66
- 22 F Kneule, *Chem Ing Tech* **1956**, *28*, 221–225
- 23 S Narayanan, V K Bhatta, D K Guha, M N Rao, *Chem Eng Sci* **1969**, *24*, 223–230
- 24 J Weisman, L E Efferding, *AIChE J* **1960**, *6*, 419–426
- 25 V Kolar, *Coll Czech Chem Commun* **1967**, *32*, 526–534
- 26 G Baldi, R Conti, E Alaria, *Chem Eng Sci* **1978**, *33*, 21–25
- 27 C Buurman, *I Chem E Symp Ser* **1990**, *121*, 343–350
- 28 J W Neale and A Pincher, *Minerals Eng* **1994**, *7*, 389–403
- 29 N Arbiter, C C Harris, R F Yap, *Trans AIME* **1969**, *244*, 134–148
- 30 P B Queneau, R J Jan, R S Rickard, D F Lowe, *Metallurg Trans*, **1975**, *6B*, 149–157
- 31 J A Wiedmann, A Steiff, P M Weinspack, *Chem Eng Commun* **1980**, *6*, 245–256
- 32 D Subbarao, V K Taneja, in H S Stephens, C A Stapleton (Eds), *Proceedings of the Third European Conference on Mixing*, BHRA Fluid Engineering, Cranfield, UK **1979**, Vol 1, 229–240
- 33 N N Dutta, V G Pangarkar, *Can J Chem Eng* **1995**, *73*, 273–283
- 34 L L van Dierendonck, G W Meindersma, G M Leuteritz, *Proceedings of the Sixth European Conference on Mixing*, BHRA Fluid Engineering, Cranfield, UK, **1988**, 287–295
- 35 S R Bhutada, V G Pangarkar, *Chem Eng Sci* **1989**, *44*, 2384–2387
- 36 Y T Shah, B G Kelkar, S P Godbole, W D Deckwer, *AIChEJ* **1982**, *28*, 353–379
- 37 K Koida, A Takazawa, M Komura, H Matsunaga, *J Chem Eng (Jpn)* **1984**, *17*, 459–466
- 38 Y Kawase, S Umeno, T Kumagai, *Chem Eng J (Lausanne)*, **1992**, *50*, 1–7
- 39 S C Saxena, N S Rao, Z D Chen, *Particulate Sci Tech* **1992**, *10*, 155–169
- 40 S C Saxena, N S Rao, *Powder Tech* **1993**, *75*, 153–158
- 41 S C Saxena, N S Rao, A C Saxena, *Can J Chem Eng* **1992**, *70*, 33–41
- 42 S C Saxena, N S Rao, P R Thimmapuram, *Chem Eng J (Lausanne)* **1992**, *49*, 151–159
- 43 S C Saxena, N S Rao, A C Saxena, *Chem Eng Commun* **1990**, *96*, 31–55
- 44 P Wilkinson, L L van Dierendonck, *Chem Eng Sci* **1990**, *45*, 2309–2315
- 45 D Blum, J J Toman, *AIChE Symp Ser* **1978**, *73*, 115–120
- 46 H Kurten, *Chem Ing Tech* **1982**, *54*, 409–415
- 47 D M Brown, *Inst Chem Eng Symp Ser* **1984**, *87*, 699–708
- 48 B L Tarmy, M Chang, C A Coulaloglou, P R Ponzi, *Inst Chem Eng Symp Ser* **1984**, *87*, 303–317
- 49 K N Clark, *Chem Eng Sci* **1990**, *45*, 2301–2307
- 50 G B Smith, B R Gamblin, D Newton, *Trans Inst Chem Engrs (Part A) Chem Eng Res Des* **1995**, *73* (A6) 632–636
- 51 I Dewes, A Kukulal, A Schumpe, *Trans Inst Chem Engrs (Part A) Chem Eng Res Des* **1995**, *73* (A6) 697–700
- 52 H Kojima, B Okumura, A Nakamura, *J Chem Eng Jpn* **1991**, *24*, 115–117

- 53 P H M R Cramers, A A C M Beenackers, L L van Dierendonck, *Chem Eng Sci*, **1992**, *47*, 3557-3564
- 54 S R Bhutada, V G Pangarkar, *Chem Eng Commun* **1988**, *67*, 216-235
- 55 N A Panchal, S R Bhutada, V G Pangarkar, *Chem Eng Commun* **1991**, *102*, 89-98
- 56 S R Bhutada, V G Pangarkar, *Chem Eng Sci*, **1988**, *43*, 2904-2907
- 57 C Aldrich, J S J van Deventer, *Chem Eng J (Lausanne)* **1994**, *54*, 199-205
- 58 H Yamazaki, K Tojo, K Miyunami, *Powder Tech* **1991**, *64*, 199-206
- 59 F Magelli, D Fajner, M Nocentini, G Pasquali, V Marisko, P Diti, *Chem Eng Process*, **1993**, *29*, 27-32
- 60 M G Rasteiro, M M Figueiredo, C Freire, *Adv Powder Technol* **1994**, *5*, 1-14
- 61 M Kraume, *Chem Eng Technol* **1992**, *15*, 313-318
- 62 R G Rice, J M I Tupperainen, R M Hedge, in *Chemical Reactors* (Ed H S Fogler), ACS Symp Ser 168, American Chemical Society, Washington, **1981**, pp 225-276
- 63 J B Joshi, *Trans Inst Chem Eng* **1980**, *58*, 155-165
- 64 R W Field, J F Davidson, *Trans Inst Chem Eng* **1980**, *58*, 228-236
- 65 W D Deckwer, R Burckhart, G Zoll, *Chem Eng Sci* **1974**, *29*, 2177-2188
- 66 M H I Baird, R G Rice, *Chem Eng J (Lausanne)* **1975**, *9*, 171-174
- 67 G D Towell, G H Ackermann, in *Proceedings of the 5th European Symposium on Chemical Reaction Engineering*, J M H Fortuin (Ed), Elsevier, Amsterdam, **1972**, *B3*, 1-13
- 68 H Hikita, H Kikukawa, *Chem Eng J (Lausanne)* **1974**, *8*, 191-197
- 69 Y Kato, *Kagaku Kogaku* **1963**, *27*, 7-11
- 70 S Kara, B G Kelkar, Y T Shah, *Ind Eng Chem Process Des Dev* **1982**, *21*, 584-594
- 71 M L Michelsen, K Ostergaard, *Chem Eng J (Lausanne)* **1970**, *1*, 37-46
- 72 M Diboun, K Schugerl, *Chem Eng Sci* **1967**, *22*, 147-160
- 73 K H Mangartz, T Philhofer, *Verfahrenstechnik*, **1980**, *14*, 40-44
- 74 B A Toseland, D M Brown, B S Zou, M P Dudokovic, *Trans I Chem E* **1995**, *73*, 297-301
- 75 J W A de Swart, R Krishna, *Trans I Chem E* **1995**, *73*, 308-313
- 76 A A C M Beenackers, W P M van Swaaij in *Chemical Reactor Design and Technology* (Ed H I de Lasa) Martinus Nijhoff, Dordrecht, **1986**, 463-538
- 77 S Goto, Y Matsumoto, P Gasparillo, *Chem Eng Commun* **1989**, *85*, 181-191
- 78 W D Deckwer, A Schumpe, *Chem Eng Sci* **1993**, *48*, 889-911
- 79 W D Deckwer, *Bubble Column Reactors*, Wiley, Chichester, **1992**
- 80 R Mann, *Industrial Research Fellowship Report 108*, Institution of Chemical Engineers, Rugby **1983**
- 81 V Schluter, W D Deckwer, *Chem Eng Sci*, **1992**, *47*, 2357-2362
- 82 S S Ozturk, A Schumpe, *Chem Eng Sci* **1987**, *42*, 1781-1785
- 83 A Schumpe, W D Deckwer *Bioprocess Eng* **1987**, *2*, 79-94
- 84 A Schumpe, A K Saxena, L K Fang, *Chem Eng Sci* **1987**, *42*, 1787-1796
- 85 R Michael, M Reichert, *Chem Ing Tech* **1983**, *56*, 48-50
- 86 E Sada, H Kumazawa, C Lee, T Iguchi, *Ind Eng Chem Process Des Dev* **1986**, *25*, 472-476
- 87 H Oguz, A Brehm, W D Deckwer in *Recent Trends in Chemical Reaction Engineering* (Eds B D Kulkarni, R A Mashelkar, M M Sharma) Wiley-Eastern, New Delhi, **1987**, Vol II, pp 484-501
- 88 H Yagi, F Yoshida, *Ind Eng Chem Process Des Dev*, **1975**, *14*, 488-493
- 89 M Schmitz, A Steiff, P M Weinspach, *Chem Eng Technol* **1987**, *10*, 204-215
- 90 H Kojima, Y Uchida, T Ohsawa, A Iguchi, *J Chem Eng (Jpn)*, **1987**, *20*, 104-106
- 91 D B Mills, R Bar, D J Kirwan, *AIChE J* **1987**, *33*, 1542-1549
- 92 R S Albal, Y T Shah, A Schumpe, N L Carr, *Chem Eng J (Lausanne)* **1983**, *27*, 61-80
- 93 E Dietrich, C Mathieu, H Delmas, J Jenck, *Chem Eng Sci* **1992**, *47*, 3597-3604
- 94 J S Ledakowicz, H Nettelhoff, W D Deckwer, *Ind Eng Chem Fundam* **1984**, *23*, 510-512
- 95 M Y Chang, B I Morsi, *Chem Eng Sci* **1991**, *46*, 2639-2650
- 96 M Y Chang, B I Morsi, *Chem Eng Sci* **1992**, *47*, 1779-1790
- 97 M Y Chang, J G Eiras, B Morsi, *Chem Eng Process* **1991**, *29*, 49-60
- 98 M Y Chang, B Morsi, *Chem Eng J (Lausanne)* **1991**, *47*, 33-45
- 99 K H Reichert, R Michael, H Meyer, *Stud Surf Sci Catal* **1986**, *25*, 369-386
- 100 R S Albal, Y T Shah, N Carr, A T Bell, *Chem Eng Sci* **1984**, *39*, 905-907
- 101 D Lindner, M Werner, A Schumpe, *AIChE J* **1988**, *34*, 1691-1697
- 102 O Stenberg, N H Schoon, *Chem Eng Sci* **1985**, *40*, 2311-2319
- 103 E Santacesaria, P Wilkinson, P Babini, S Carra, *Ind Eng Chem Res* **1988**, *27*, 780-784
- 104 E Santacesaria, R Silvani, P Wilkinson, S Carra, *Ind Eng Chem Res* **1988**, *27*, 541-548
- 105 C Mathieu, E Dietrich, H Delmas, J Jenck, *Chem Eng Sci* **1992**, *47*, 2289-2294
- 106 L L van Dierendonck, Ph D Thesis, Twente University, The Netherlands, **1970**
- 107 L L van Dierendonck, J Nelemans, in *Proceedings of the 5th European Symposium on Chemical Reaction Engineering*, J M H Fortuin (Ed), Elsevier, Amsterdam, **1972**, *B6*, 45-57
- 108 M M Sharma, *Trans I Chem E* **1993**, *71*, 595-610
- 109 A A C M Beenackers, W P M van Swaaij, *Chem Eng Sci* **1993**, *48*, 3109-3139
- 110 Y Sano, N Yamaguchi, T Adachi, *J Chem Eng (Jpn)* **1974**, *7*, 255-261
- 111 P Sanger, W D Deckwer, *Chem Eng J (Lausanne)* **1981**, *22*, 179-186
- 112 S V Jadhav V G Pangarkar, *Chem Eng Sci* **1991**, *46*, 919-927
- 113 S Lazaridis, Ph D Thesis Technical University Aachen, **1990**
- 114 A B Pandit, J B Joshi, *Chem Eng Res* **1986**, *64*, 125-157
- 115 S V Jadhav, V G Pangarkar, *Can J Chem Eng* **1988**, *66*, 572-578
- 116 J R Grace, T Wairegi, T H Nguyen, *Trans Inst Chem Eng* **1976**, *54*, 167-173
- 117 N Zuber, J A Findley, *Trans ASME (J Heat Transfer)*, **1965**, *87*, 453-468
- 118 G M Marrone, D J Kirwan, *AIChE J* **1986**, *32*, 523-525
- 119 S Asai, Y Konishi, T Kajiwara, *J Chem Eng (Jpn)* **1989**, *22*, 96-98
- 120 R L Kars, R J Best, A A H Drinkenburg, *Chem Eng Sci* **1979**, *17*, 201-210



121. H. Vinke, Ph. D. Thesis, Municipal University of Amsterdam, 1992.
122. O. J. Wimmers, J. M. H. Fortuin, *Chem. Eng. Sci.* **1988**, *43*, 313–319.
123. O. J. Wimmers, H. J. J. de Sauvage Notting, J. M. H. Fortuin, *Chem. Eng. Sci.* **1988**, *43*, 2155–2159.
124. S. C. Saxena, R. Vadivel, A. C. Saxena, *Chem. Eng. Commun.* **1989**, *85*, 63–83.
125. P. R. Thimmapuram, N. S. Rao, S. C. Saxena, *Chem. Eng. Commun.* **1993**, *120*, 27–43.
126. I. S. Suh, W. D. Deckwer, *Chem. Eng. J. (Lausanne)* **1993**, *52*, 49–50.
127. S. C. Saxena, Z. D. Chen, *Chem. Eng. J. (Lausanne)* **1993**, *52*, 51–52.

## 10.4 Unsteady-State Reactor Operation

Y. SH. MATROS AND G. A. BUNIMOVICH

### 10.4.1 Introduction

Unsteady-state reactor operation is traditionally considered to be related to the performance of catalytic processes which are characterized by quick loss in catalyst activity. For such processes as, for example, catalytic cracking (Section B.3.10) or dehydrogenation of alkanes (Section B.4.3), a sequence of reaction and regeneration stages is unavoidable and should be included into the design.

This chapter describes a forced unsteady-state operation technique as employed for continuous processes which represent the majority of heterogeneous catalysis applications. The catalyst life in these processes often lasts as long as several years. Traditional operation is in the steady-state, and automatic control systems are

used to eliminate any fluctuations in performance parameters. The main goal of a traditional design is to obtain the optimal steady-state conditions which provide for maximum use of catalyst properties as constrained by the process economy.

However, the reactor performance obtained under optimal steady-state conditions does not determine a potential limit for a heterogeneous catalytic system. This performance can be improved further using forced unsteady-state operation. Such an operation is capable of substantially extending a gamut of the process features and allows for better use of nonlinear properties inherent in a catalytic reaction system. The positive effect can be generated by two major factors [1]:

- (i) *The dynamic properties of the catalyst.* Unsteady conditions in the fluid phase can give rise to changes of state, composition, and structure of the catalyst which, under certain conditions, result in a 'resonance' in the catalyst behavior, and its selectivity and/or activity increase compared to steady-state operation.
- (ii) *The dynamic characteristics of an entire reactor system.* An external influence is aimed at the formation of optimum temperature and composition distributions in the reactor which cannot be obtained in any steady-state regime. Under unsteady-state conditions a catalyst bed can acquire new unique functions and serve not only for acceleration of a chemical reaction but also for energy and mass storage and transmission.

Various schemes of reactor operation under forced unsteady-state conditions are shown in Figs 1–4. An unsteady-state process in a fixed bed reactor can be created by oscillations in the inlet composition or temperature (Fig. 1). As a rule, a simple stepwise periodic control (Fig. 1(a)) is preferable to other types of inlet

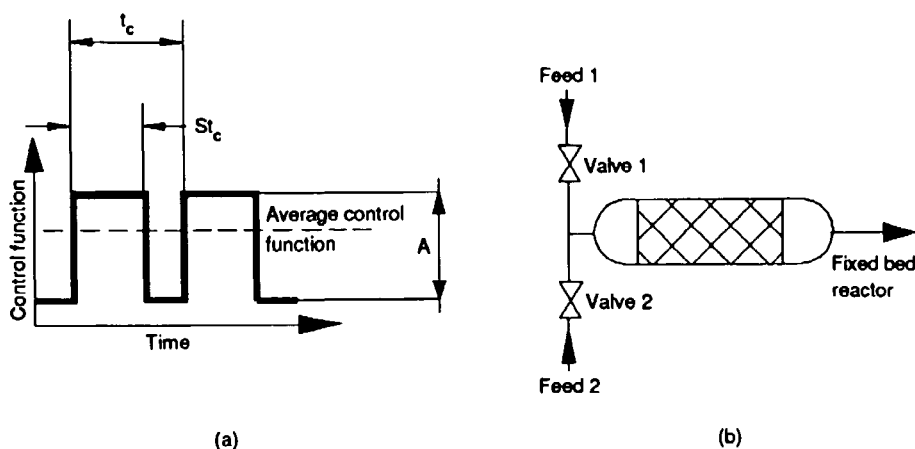
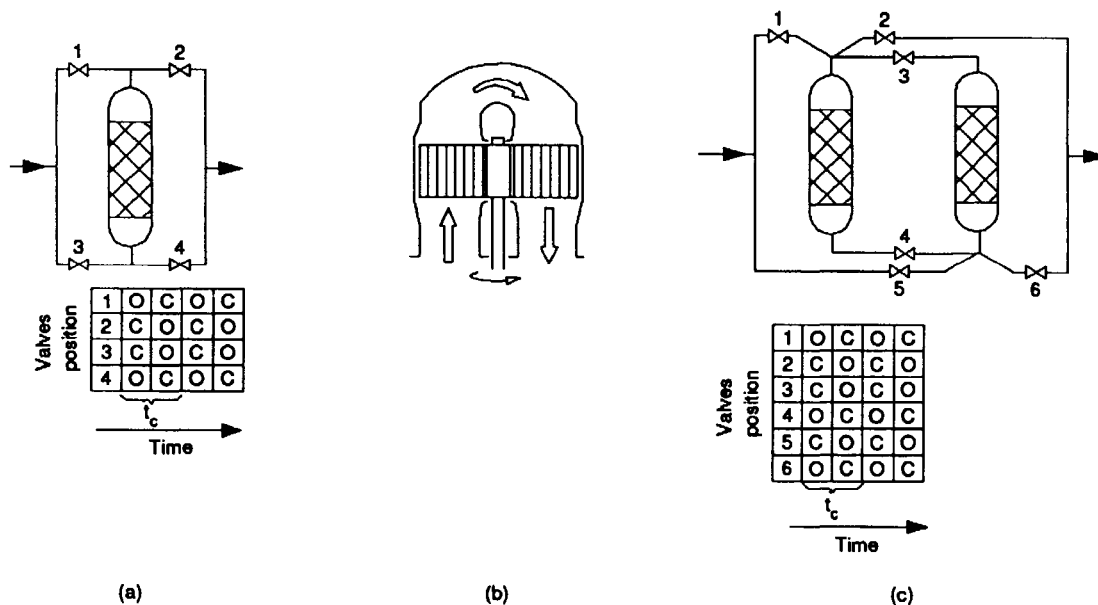


Figure 1. (a) Step-wise function of inlet parameters change. (b) Fixed-bed reactor operated at periodic switching between two different feeds that provide for step-wise control.



**Figure 2.** Schemes of fixed-bed reactors operated under forced unsteady-state conditions: (a) Reverse-flow reactor; (b) Rotary reactor; (c) Reactor system with periodic changes between the inlet and outlet ports in two fixed beds. The tables show positions of switching valves during two successive cycles: C = valve closed; O = valve open.

parameter forcing (for example, sine wave). This control is often simpler to perform and it affects a system more strongly than any other smooth type of control. Such characteristics as amplitude  $A$ , time of cycle  $t_c$ , split of inlet signal  $S$ , and phase angle for several control functions are typical for periodic operation.

The most widely applied technique in a fixed bed reactor is periodical flow reversal (Fig. 2(a)). Four switching valves can be used to provide control of operation. In a rotary reactor (Fig. 2(b)) with a plate-type catalyst, the catalyst bed position is continuously changed relative to the stationary direction of flow, thereby achieving an effect similar to a flow reversal reactor. Reactor schemes (a) and (b) provide for a continuous migration of a temperature or adsorption zone along the catalyst bed. The direction of this migration is changed periodically. Another configuration (Fig. 2(c)) provides for the possibility of moving this zone in one direction through a system with two catalyst beds.

In fluidized beds for reactions of partial oxidation a favorable unsteady state of the catalyst can be obtained by catalyst circulation inside the reactor (Fig. 3(b)). Such a circulation can also be organized between a fluidized bed and a riser reactor (Fig. 3 (a)). This allows separate feeding of two reactants, hydrocarbons and oxygen, and of a stripping inert gas.

Another group of forced unsteady-state processes combines chemical reaction with separation of products. For these processes a reactor with a circulated moving bed (Fig. 4(a)) can be employed. Circulation of the catalyst can be substituted by periodic changing of

feed and produce ports in a reactor with several fixed beds (Fig. 4 (b)). This concept is named a simulated moving bed reactor. Reaction and separation can include periodic pressure changes using the known separation technique of pressure-swing adsorption (Fig. 4(c)).

An accurate design of unsteady-state catalytic processes requires knowledge about the catalyst behavior and reaction kinetics under unsteady-state conditions, unsteady-state mass and heat transfer processes in the catalyst particle and along the catalyst bed, and dynamic phenomena in the catalytic reactor. New approaches for reactor modeling and optimization become necessary. Together, these topics form a wide area of research that has been continuously developed since the 1960s.

## 10.4.2 Dynamic Kinetic Model

A traditional kinetic model of steady-state catalytic reaction assumes quasi-steady-state concentrations of intermediate species on the catalyst surface. This assumption is often invalid for unsteady-state conditions characterized by continuous changes in a fluid phase composition and temperature above the catalyst surface. Additionally, the catalyst itself can interact with the reaction mixture and can undergo significant changes, influenced by changing conditions in the gas phase. Such a modification of the catalyst can be con-

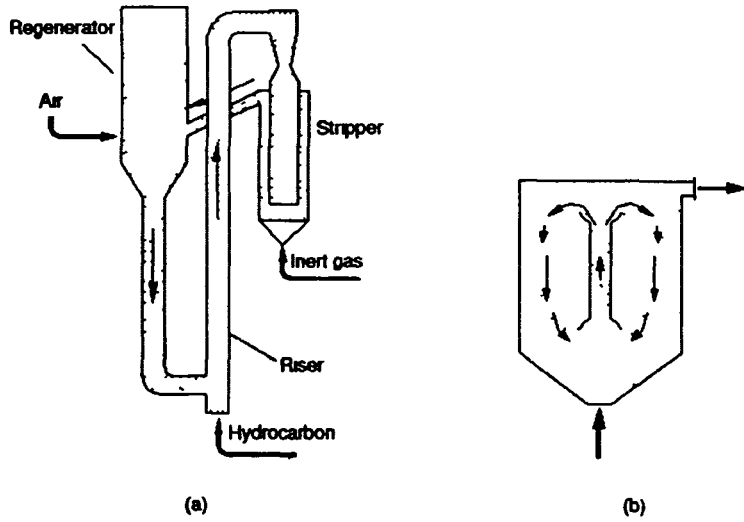
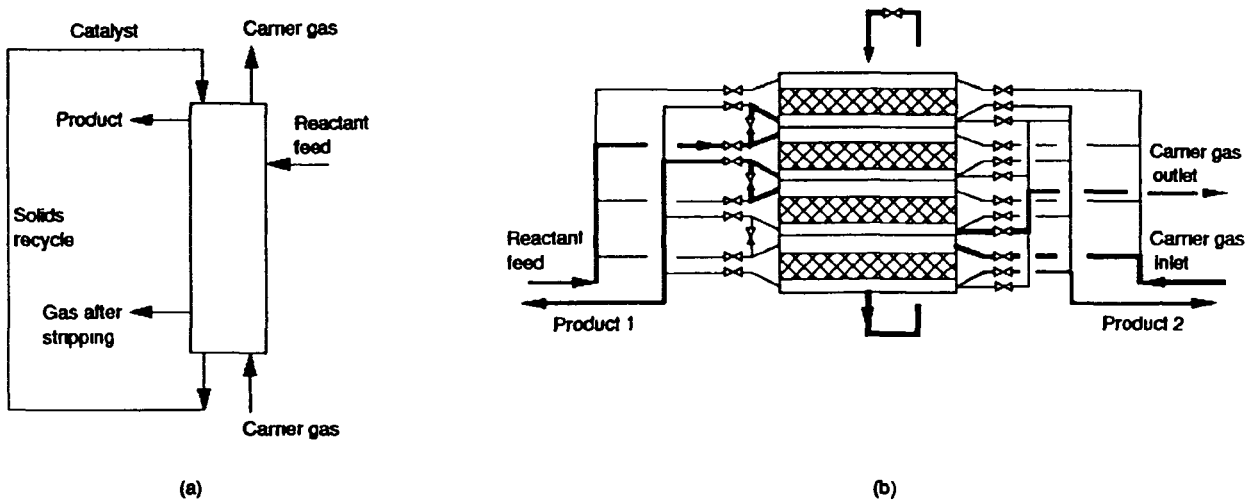
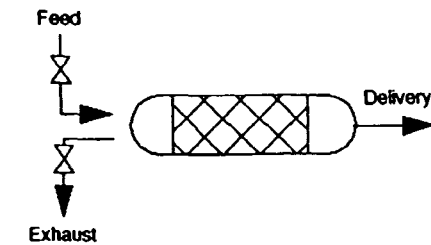
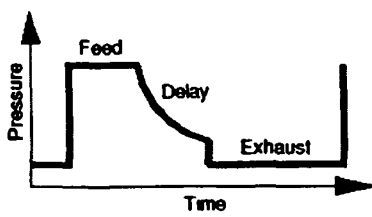


Figure 3. Reactors with fluidized bed applied for partial oxidation processes, (a) DuPont system for maleic anhydride production combining riser, fluidized bed regenerator, and stripper, (b) fluidized-bed reactor with internal catalyst circulation



(a)

(b)



(c)

Figure 4. Units combining reaction and separation (a) reactor with countercurrent moving bed, (b) simulated moving-bed reactor with four catalyst layers (bold lines show gas streams during a quarter of cycle), (c) pressure-swing adsorption reactor separator (on the left is given time dependency of pressure during a cycle)

sidered as a side process in relation to stages of catalytic reaction included in a catalytic cycle. Side processes comprise both changes in chemical composition of the catalyst and reconstruction of its surface and bulk structures. Under steady-state conditions, the reactions involving surface intermediates proceed at a fixed rate while the side processes affecting the catalyst state are in equilibrium.

The development of unsteady-state kinetic models requires application of dynamic relaxation methods (Section A.5.2.6). More reliable models can be achieved by coupling these transient techniques with a direct determination of intermediate products on the surface of the catalyst [2, 3]. There is no unified or standard method suitable for discrimination of the unsteady-state kinetics models for either of the catalytic processes.

Table 1 presents several examples of unsteady-state kinetics models. These models are presented in the form of rate dependencies for catalytic reaction stages and side processes. The parameters of the models, such as reaction rate constants and activation energies, are given in references (Table 1) and were determined mainly from experimental data using transient response techniques. For the reaction of CO oxidation over a supported platinum catalyst, the kinetic gas theory was applied for estimating the adsorption constants.

In the simplest case (Example 1) the model assumes an ideal catalyst surface and describes the rates of catalytic stages on the basis of the law of mass action. A special definition of vacant active sites on the catalyst surface can be considered too, as done in Example 3, for the description of the rate of CO adsorption. A linear effect of surface coverage on the activation energy of the reaction stages (Example 2) can be included if necessary. In Example 3, dramatic changes of oxygen adsorption and surface reaction rates depending on the carbon monoxide coverage are defined by the adsorbate-induced phase reconstruction of the platinum surface. A parameter  $\Psi(\theta_{\text{CO}})$ , which is a simplified form for describing the influence of catalyst phase changes, was needed for quantitative explanation of a variety of transient and steady-state kinetic experiments. Example 4 represents the simplest model with which to describe a side process of a catalyst bulk change. The oxidation or the reduction of the vanadium oxide catalyst is specified as a quasireaction between surface oxygen and a bulk-phase oxygen vacancy. The same approach was used for the description of the side process of  $\text{V}^{5+}$  reduction to  $\text{V}^{4+}$  that proceeds during  $\text{SO}_2$  oxidation (Example 5, reaction 4). The second side process (Example 5, reaction 5), saturation of vanadium complexes by pyrosulfate anions, is assumed to be in equilibrium.

Each model includes the parameters characterizing total or balance concentration of intermediate species

$C_{\text{AS}}$  in the catalyst volume. Some systems require derivation of several balances. For example, the balance of bulk or lattice oxygen  $C_{\text{AS},\text{v}}$  can be included into consideration along with the balance of surface species for the oxide catalyst (Example 4).

A ratio of  $C_{\text{AS}}$  to the rate of catalytic reaction under steady-state conditions ( $r$ ) gives a rough estimation for the reaction time scale. For typical heterogeneous catalytic processes applied for the production of bulk chemicals and petrochemicals, this value is estimated to be  $10^{-2}$ – $10^1$  s (Fig. 5). The changes of the reaction rate caused by the side processes of catalyst modification can take considerably longer. This is attributed to the higher capacity of substances in the catalyst bulk phase that can be involved in side interactions and to a slow rate of side processes in comparison with the stages of the catalytic cycle.

### 10.4.3 General Approaches to Reactor Modeling

As a rule, mathematical models of unsteady-state processes cannot be formulated by simple addition of time derivatives to the equations describing the steady-state behavior of the reaction system. They relate both to the reaction kinetics as well as to the heat and mass transfer processes. For example, modeling of unsteady-state processes in a fixed bed reactor requires accounting for the processes of heat and mass transfer between the catalyst surface and the bulk of gas phase, although for steady-state operation these factors can be neglected.

Development of an essential model of unsteady-state reaction processes includes two general procedures: decomposition of the complex system to several scale elements and analysis of time scales of essential processes in the reactor.

Commonly used levels of decomposition are catalyst surface, single catalyst pellet, catalyst bed, reactor including heat exchangers, mixing and distributing devices, and an entire unit with the catalytic reactor as one of its elements. Each lower element is a component of the higher level. It is invariable to the dimension of an upper element and can be studied separately.

Application of this procedure is illustrated by an example of analysis of unsteady-state processes in a single catalyst pellet [8, 9]. A separate consideration of this element allows estimation of the domains of parameters where certain stages of heat and mass transfer can be neglected and the mathematical model thus simplified. These criteria derived after assuming the steady-state reaction rate  $r$  are given in Table 2.

The time scale technique includes estimation of particular time scales or characteristic times  $\tau_i$  for sub-

Table 1. Dynamic kinetic models

No	Process	Scheme of reaction mechanism	Rate equations
1	N <sub>2</sub> O decomposition over NiO on SiO <sub>2</sub> [4]	$\text{N}_2\text{O} + * \xrightarrow{1} \text{N}_2 + \text{O}^*$ $2\text{O}^* \xrightleftharpoons{2} \text{O}_2 + 2^*$	$r_1 = C_{AS}k_1C_{\text{N}_2\text{O}}(1 - \theta),$ $r_2 = C_{AS}^2[k_2\theta^2 - k_{-2}C_{\text{O}_2}(1 - \theta)^2],$ $\theta = \text{surface coverage by oxygen, } C_{AS} = \text{total concentration of surface species (mol cm}^{-3}\text{)}$
2	Addition of acetic acid to ethylene over silica-alumina impregnated with sulfuric acid [5]	<p>Reaction</p> $\text{A} + \text{E} \rightarrow \text{AE}$ <p>Catalytic cycle</p> $\text{E} + * \xrightleftharpoons{1} \text{E}^*$ $\text{A} + * \xrightleftharpoons{2} \text{A}^*$ $\text{A}^* + \text{E}^* \xrightarrow{3} \text{AE}^* + 2^*$	$r_1 = C_{AS}(k_1e^{-b\theta_A}C_E - k_{-1}e^{-b\theta_A}\theta_{E^*}),$ $r_2 = C_{AS}[k_2(\theta_{\text{max}} - \theta_{A^*})C_A - k_{-2}\theta_{A^*}],$ $r_3 = C_{AS}^2k_3\theta_{E^*}\theta_{A^*}$ $\theta_{E^*}, \theta_{A^*}, \theta_{\text{max}} = \text{concentrations of adsorbed ethylene, acetic acid and maximum concentration of acetic acid in the liquid phase, mol} \times (\text{mol H}_2\text{SO}_4)^{-1},$ $C_{AS} = \text{molar concentration of catalyst, sulfuric acid, in the catalyst pellet (mol cm}^{-3}\text{)}, b = \text{Elovich constant, } C_A \text{ and } C_E = \text{acetic acid and ethylene concentrations in the gas phase (mol cm}^{-3}\text{)}$
3	CO oxidation over supported Pt [6]	<p>Catalytic cycle (Pt crystallite surface)</p> $\text{CO} + * \xrightleftharpoons{1} \text{CO}^*$ $\text{O}_2 + 2^* \xrightarrow{2} 2\text{O}^*$ $\text{CO}^* + \text{O}^* \xrightarrow{3} \text{CO}_2 + 2^*$ <p>Side process (support surface)</p> $\text{CO}_2 + * \text{S} \xrightleftharpoons{4} \text{S}^*\text{CO}_2$	$r_1 = C_{AS} \left[ k_1 C_{\text{CO}}(1 - \theta_{\text{CO}} - \theta_{\text{O}}) \frac{1 - N_{\text{CO}}\theta_{\text{CO}}}{1 - \theta_{\text{CO}}} - k_{-1}\theta_{\text{CO}} \right]$ $r_2 = C_{AS}L_{\text{Pt}}k_2C_{\text{O}_2}(1 - \theta_{\text{CO}} - \theta_{\text{O}})^2,$ $r_3 = k_3C_{AS}L_{\text{Pt}}\theta_{\text{CO}}\theta_{\text{O}},$ $r_4 = C_S[k_4C_{\text{CO}_2}(1 - \phi_{\text{CO}_2}) - k_{-4}\phi_{\text{CO}_2}],$ $k_1 = 100 \left( \frac{RT}{2\pi M_{\text{CO}}} \right)^{1/2} L_{\text{Pt}}^{-1} S_{\text{CO}},$ $k_{-1} = A_{-1} \exp \left( -\frac{E_{-1}}{RT} \right),$ $k_2 = 100 \left( \frac{RT}{2\pi M_{\text{O}_2}} \right)^{1/2} \psi L_{\text{Pt}}^{-2} S_{\text{O}_2},$ $k_3 = A_3 \psi \exp \left( -\frac{E_3}{RT} \right),$ $k_4 = 100 \left( \frac{RT}{2\pi M_{\text{CO}_2}} \right)^{1/2} L_S^{-1} S_{\text{CO}_2},$ $k_{-4} = A_{-4} \exp \left( -\frac{E_{-4}}{RT} \right)$ <p><math>\theta_{\text{CO}}, \theta_{\text{O}}</math> = platinum surface coverage by CO and oxygen, <math>S_{\text{CO}}, S_{\text{O}_2}, S_{\text{CO}_2}</math> = sticking coefficients, <math>M_{\text{O}_2}, M_{\text{CO}}</math> = molecular weights, <math>A_i</math> = pre-exponential factors, <math>C_{AS}</math> = adsorption capacity of Pt surface per unit of catalyst volume, <math>L_{\text{Pt}}</math> = adsorption capacity of Pt surface (mol cm<sup>-2</sup>), <math>L_S</math> = surface CO<sub>2</sub> adsorption capacity on the support (mol cm<sup>-2</sup>), <math>\phi_{\text{CO}_2}</math> = support coverage by CO<sub>2</sub>, <math>C_S</math> = CO<sub>2</sub> adsorption capacity on the support per unit of catalyst volume (mol cm<sup>-3</sup>), <math>N_{\text{CO}}</math> = factor limiting CO adsorption, <math>\Psi</math> = factor, reflecting reversible transition between two surface phases of Pt</p> <p>Function <math>\Psi</math> is determined from the graph below</p> <p><math>(\theta_{\text{CO}})_L</math> and <math>(\theta_{\text{CO}})_H</math> are critical CO coverages corresponding to changes of surface phase</p>

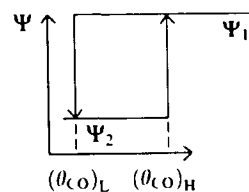


Table 1. Continued

No	Process	Scheme of reaction mechanism	Rate equations
4	2-Butene oxidation over supported vanadium oxide [7]	<p>Reaction  <math>C_4H_8 + n/2O_2 \rightarrow \text{products}</math></p> <p>Catalytic cycle  <math>C_4H_8 + nS-O \xrightarrow{1} \text{Products} + nS-</math>  <math>nS- + 1/2O_2 \xrightarrow{2} 2S-O</math></p> <p>Side process  <math>S-O + L- \xrightleftharpoons{3} S- + L-O</math>            S- and S-O = reduced and oxygen covered surface site, L- and L-O = lattice oxygen and oxygen vacancy in the catalyst lattice</p>	$r_1 = nk_1 C_{AS} C_B (1 - \theta)$ , $r_2 = k_2 C_{AS} C_{O_2}^{1/2} \theta$ , $r_3 = C_{AS} v C_{AS} [k_3 \theta (1 - \theta_v) - k_{-3} \theta_v (1 - \theta)]$ , $k_i = A_i \exp(-E_i/RT)$ , $i = 1, 2, 3, -3$ , $r_2 - r_1 = r_3$ $\theta$ = surface coverage by oxygen, $\theta_v$ = concentration of lattice oxygen, $C_B$ and $C_{O_2}$ = butene and oxygen concentration in gas phase (mol cm <sup>-3</sup> ), $n$ = number of oxygen atoms consumed by every butane molecule in reaction 1, $C_{AS}$ = concentration of surface active sites (mol cm <sup>-3</sup> ), $C_{AS} v$ = concentration of oxygen vacancies in the lattice (mol cm <sup>-3</sup> )
5	SO <sub>2</sub> oxidation over vanadium catalyst SO <sub>2</sub> + 1/2O <sub>2</sub> = SO <sub>3</sub> [3]	<p>Catalytic cycle  <math>V_2^{5+} O_2 + SO_2 \xrightleftharpoons{1} V_2^{5+} O + SO_3</math>  <math>V_2^{5+} O + SO_2 \xrightleftharpoons{2} V_2^{5+} SO_3</math>  <math>V_2^{5+} SO_3 + O_3 \xrightleftharpoons{3} V_2^{5+} O_2 + SO_3</math></p> <p>Side processes  <math>V_2^{5+} OSO_3 \xrightleftharpoons{4} 2V^{4+} + SO_3</math>  <math>(V_2^{5+})_i + S_2O_7^{2-} \xrightleftharpoons{5} (V_2^{5+})_i S_2O_7</math>  <math>(V_2^{5+})_i</math> = binuclear vanadium complexes  <math>V_2^{5+} OSO_3</math>, <math>V_2^{5+} O</math>, and <math>V_2^{5+} O_2</math></p>	$r_1 = C_{AS} \theta_a (k_1 C_1^L \theta_1 - k_{-1} C_2^L \theta_2)$ , $r_2 = C_{AS} \theta_a (k_2 C_1^L \theta_2 - k_{-2} \theta_3)$ , $r_3 = C_{AS} \theta_a (k_3 C_2^L \theta_3 - k_{-3} C_3^L \theta_1)$ , $r_4 = C_{AS} \theta_a (k_4 \theta_3 - k_{-4} C_3^L \theta_4)$ , $\theta_a = \frac{1}{1 + K_5 C_3^L}$ , $C_i^L = H_i p_i$ , $i = 1, 2, 3$ , $\sum_{j=1}^4 \theta_j = 1$ , $C_1^L$ , $C_2^L$ , and $C_3^L$ are SO <sub>2</sub> , O <sub>2</sub> and SO <sub>3</sub> concentrations in liquid phase (mol cm <sup>-3</sup> ), $p_i$ = partial pressure of gaseous components (kPa), $H_i$ = Henry's constants (mol cm <sup>-3</sup> kPa <sup>-1</sup> ), $\theta_1$ , $\theta_2$ , $\theta_3$ , and $\theta_4$ are dimensionless concentrations of binuclear vanadium species in the melt, $K_5$ = equilibrium constant of reaction 5 (cm <sup>3</sup> mol <sup>-1</sup> ) $C_{AS}$ = concentration of binuclear vanadium complexes in the melt (mol cm <sup>-3</sup> )

$r_l$  = rate of reaction stage (mol sm<sup>-3</sup> s<sup>-1</sup>), index  $l$  corresponds to reaction stage number in the third column,  $k_l$  = reaction constant for direct reaction,  $k_{-l}$  = reaction constant of reverse reaction,  $K_l$  = equilibrium constant

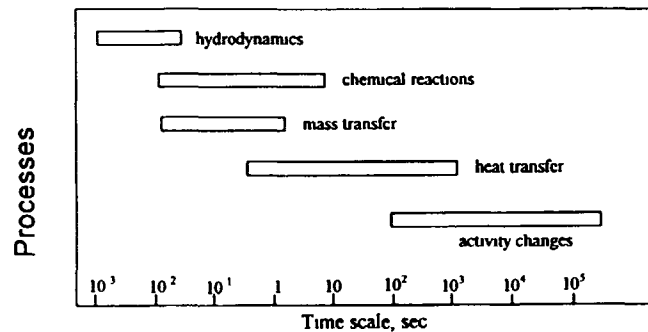


Figure 5. Time scales for various processes in a fixed bed reactor (adopted from [9])

stantial processes in every element of the reaction system. The particular characteristic time for heat/mass transfer can be estimated as the ratio of the heat/mass capacity of an element to the rate of the respective transfer process. Also, a time scale or response time for the whole system or element can be estimated.

Estimations of characteristic times for essential processes in a fixed bed reactor [9] are given in Fig 5. These characteristic times can substantially differ from

a presumable time of process performance or a time of cycle for forced unsteady-state conditions. In this case it is possible to determine very slow variables, changes of which are not necessarily taken into consideration, and fast variables that can be assumed to be in a quasisteady-state. A condition of quasisteady-state means that the capacitances or inertial terms included in the model equations for fast variables can be neglected for a major fraction of process time.

For example, the assumption that a quasisteady-state concentration distribution inside a catalyst particle is valid at the following relationships between the process time and characteristic times of heat transfer  $\tau_{pT}$  and mass transfer  $\tau_{pm}$  inside the pellet [8, 9]

$$\frac{\tau_{pm}}{\tau_{pT}} \geq 40 \quad \text{and} \quad t > \tau_{pm},$$

where

$$\tau_{pT} = \frac{(c_s \rho_s + \varepsilon_p c_g \rho_g) R_p^2}{\lambda_{ef}}$$

**Table 2.** Criteria allowing for simplification of the mathematical model of unsteady-state processes in a catalyst pellet.

Dimensionless group ratio <sup>a</sup>	Simplification of mathematical model to be allowed
$\Psi \leq 0.5$ and $Bi_m \leq 0.3$	diffusion limitations have no importance
$\Psi_T \sqrt{\eta} \leq 0.2$ and $Bi_T \leq 0.1$	no substantial temperature gradients inside the pellet
$Bi_m \geq 30$ and $Bi_m \geq 20\Psi$	limitation to mass-transfer between catalyst particle and bulk of gas phase has no importance

$$^a Bi_m = \frac{k_g R_p}{D_{ef}}; \Psi = R_p \sqrt{\frac{r}{D_{ef} C}}; \Psi_T = \Psi^2 \Delta \theta_{ad} Le^{-1}; Le = \frac{\lambda_{ef}}{D_{ef} c_g \rho_g};$$

$$Bi_T = \frac{h_f R_p}{\lambda_{ef}}; \Delta \theta_{ad} = \frac{(-\Delta H) \times C \times E}{c_g \rho_g R T^2}; \eta = \frac{3 Bi_m (\Psi \coth \Psi - 1)}{\Psi^2 (Bi_m - 1 + \Psi \coth \Psi)}$$

$Bi_m$  and  $Bi_T$  = Biot numbers for mass and heat transfer;  $\Psi$  and  $\Psi_T$  = Thiele modulus;  $Le$  = Lewis number;  $\Delta \theta_{ad}$  = dimensionless adiabatic temperature rise;  $\eta$  = effectiveness factor;  $k_g$  = mass transfer coefficient ( $m s^{-1}$ );  $R_p$  = radius of catalyst pellet (m);  $D_{ef}$  = effective diffusion coefficient ( $m s^{-2}$ );  $r$  = rate of reaction ( $mol m^{-3} s^{-1}$ );  $C$  = concentration of reactant ( $mol m^{-3}$ );  $\lambda_{ef}$  = coefficient of effective heat conductivity inside the catalyst particle ( $J m^{-1} s^{-1} K^{-1}$ );  $c_g$  = gas heat capacity ( $J kg^{-1} K^{-1}$ );  $\rho_g$  = gas density ( $kg m^{-3}$ );  $h_f$  = coefficient of heat transfer between catalyst surface and gas phase ( $J m^{-2} K^{-1} s^{-1}$ );  $-\Delta H$  = reaction enthalpy ( $J mol^{-1}$ );  $E$  = activation energy ( $J mol^{-1}$ );  $R$  = universal gas constant ( $J mol^{-1} K^{-1}$ );  $T$  = temperature (K).

and

$$\tau_{pm} = \frac{\varepsilon_p R_p^2}{D_{ef}^2}$$

where  $c_s$  = heat capacity of catalyst pellet ( $J kg^{-1} K^{-1}$ ),  $\rho_s$  = density of the catalyst ( $kg m^{-3}$ ),  $\varepsilon_p$  = void fraction of catalyst pellet, and other designations are given in Table 2.

### 10.4.4 Analysis and Optimization of Cyclic Processes

A set of the possible unsteady or cyclic states of the dynamic system comprises a narrower set of steady states. Therefore, the maximum value of an object or performance function  $J^{\max}$  obtained under optimal unsteady-state conditions may not be lower than that for optimal steady-state  $J_s^{\max}$ , i.e.  $J^{\max} \geq J_s^{\max}$ . However, efficient or proper periodic operation includes only the regimes which provide higher performance in comparison with the optimal steady-state,  $J^{\max} > J_s^{\max}$ . The latter inequality is not always satisfied. The goal of general mathematical theory is in establishing whether the optimal steady-state operation can be improved using forced unsteady-state conditions. Then, if the answer is positive, the optimal operation should be found. The last stage obviously is the cost-analysis of

the optimal unsteady-state operated system in comparison with the steady-state one.

#### 10.4.4.1 General Optimal Periodic Control Problem

For the class of systems described by ordinary differential equations the general problem includes the following features:

- (i) equations for state variables,

$$\dot{x} = f(x, u)$$

where  $x = [x_1(t), x_2(t), \dots, x_n(t)]$  is a vector of states, continuous time-dependent functions;

- (ii) definition for forcing control variables

$$u(t) = [u_1(t), u_2(t), \dots, u_m(t)]$$

where  $u(t)$  is a vector of piecewise continuous functions determined over the time interval  $[0, t_c]$ ;

- (iii) periodicity constraints for control functions  $u(0) = u(t_c)$  (periodicity constraints for state variables  $x(0) = x(t_c)$  are usually assumed too);

- (iv) definition for objective function

$$J = \frac{1}{t_c} \int_0^{t_c} f_0(x, u) dt;$$

where  $f_0(x, u)$  is an instantaneous process performance index;

- (v) constraints on instantaneous values of control variables

$$u_j^{\min} \leq u_j(t) \leq u_j^{\max}, l = 1, \dots, L$$

or on their averaged values.

For steady states, the solution of the system is determined from the equation  $0 = f(x_s, u_s)$  and the objective function is determined as:  $J_s = f_0(x_s, u_s)$ .

Sufficient conditions for optimality of forced unsteady-state operation which provides  $J > J_s$ , can be determined on the basis of analysis of two limiting types of periodic control [10]. The first limiting type is a so-called quasisteady operation which corresponds to a very long cycle duration compared to the process response time  $\tau$ . In this case the description of the process dynamics is reduced to the equations  $x(t) = h(u(t))$ , where  $h$  is defined as a solution of the equation describing a steady-state system  $0 = f(h(u(t)), u(t))$ . The second limiting type of operation, the so-called relaxed operation, corresponds to a very small cycle time compared to the process response time ( $t_c \ll \tau$ ). The description of the system is changed to:

$$\dot{x}_r = \frac{1}{t_c} \int_0^{t_c} f(x_r, u(\theta)) d\theta;$$

where  $x_r$  is a vector of relaxed states. If this reduced system does not exhibit oscillatory behavior, the steady-state solution

$$0 = \frac{1}{t_c} \int_0^{t_c} f(x_{rs}, u(\theta)) d\theta,$$

determines a vector of relaxed steady states,  $x_{rs}$ .

These states are assumed to be asymptotic values of state variables  $x$  at a very small duration of cycle ( $t_c \rightarrow 0$ ). If periodic control exhibits a nonlinear effect on the state variables, the relaxed steady-state process indexes can substantially differ from those for the steady state, and a positive or a negative effect from periodic control can be produced.

A general approach to the analysis of low amplitude periodic operation based on the so-called  $\Pi$ -criterion is described in Refs. 11. The shape of the optimal control function can be found numerically using an algorithm by Horn and Lin [12]. In Refs. 9 and 13, this technique was extended to the simultaneous optimization of a forcing function shape and cycle period. The technique is based on periodic solution of the original system for state variables coupled with the solution of equations for adjoint variables  $[\lambda_1, \lambda_2, \dots, \lambda_n]$ . These adjoint equations are

$$\dot{\lambda}_i = - \frac{\partial H(x, u)}{\partial x_i}$$

with boundary conditions  $\lambda_i(0) = \lambda_i(t_c)$ , where

$$H(x, u) = f_0(x, u) + t_c \sum_j^n \lambda_j f_j(x, u)$$

At each step of iteration, small increments in control functions and time of cycle are generated in accordance with the equations

$$u_i^{k+1} = u_i^k + \varepsilon_i \frac{\partial H}{\partial u_i}$$

and

$$t_c^{k+1} = t_c^k + \varepsilon_t \int_0^1 \left[ \sum_j^n \lambda_j f_j(x, u) \right] d\tau,$$

where  $k$  is the number of iterations,  $\varepsilon_l$ , ( $l = 1, 2, \dots, m$ ),  $\varepsilon_t$  are small positive numbers. Calculation of the periodic processes is performed by the Newton-Raphson procedure described in Ref. 12.

For analysis of distributed-parameter systems, such as a tubular fixed bed reactor, numerical simulation of periodic operation at various values of control parameters is typically applied. Asymptotic models for quasisteady and relaxed steady states are valuable instruments for a substantial simplification of the original distributed-parameter system. A method allowing for

numerical optimization of the shape of inlet perturbation is described in Ref. 9.

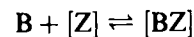
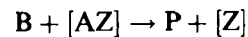
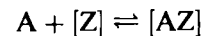
## 10.4.5 Reaction Performance Improvement

Two major factors, nonlinearity of chemical reaction rates and complexity of reaction systems, are generally considered responsible for conversion or selectivity improvement under forced unsteady-state conditions [18].

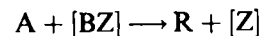
Nonlinearity of a reaction rate is a reason for improvement of the simple irreversible reaction  $A^n \rightarrow B$ . Low-frequency temperature oscillation around the average value  $\bar{T}$  increases the reaction rate compared to a steady-state calculated at this average temperature. A positive effect can also be obtained due to concentration variation if  $n > 1$  and a time average concentration is restricted.

Systems with two parallel or consecutive reactions can give rise to a selectivity enhancement at high-frequencies of oscillation of temperature if the activation energy of the reaction of a desirable product formation is higher than that for a side process. For example [14], at high-frequency oscillation of temperature the reaction pairs ( $A \rightarrow B, A \rightarrow C$ ), ( $A \rightarrow B, B \rightarrow C$ ), ( $A \rightarrow B, B \rightarrow A$ ), and ( $A \rightarrow B, A + B \rightarrow C$ ) give a higher selectivity in the formation of the intermediate product B than at the optimal steady-state, if  $E_1 > E_2$ , where  $E_1, E_2$  are activation energies of the first and second reactions in each of the pairs.

Selectivity increase in a complex catalytic process can be expected if (a) a competition between two gaseous species for an empty active site exists, and (b) a characteristic time of changing concentration of an intermediate participating in the formation of a useful product is lower than that for an intermediate transforming to a side product. For example [9, 13]; reactions  $A + B \rightarrow C, A + B \rightarrow D$ , proceed in accordance with the simple reaction mechanism



and



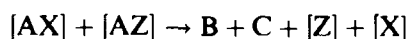
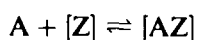
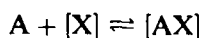
where the concentration of the intermediate [BZ] changes more slowly than the concentration of [AZ]. In this case, periodic variation of the concentration of component A increases the selectivity compared to the optimal steady state. An intermediate frequency periodic control is preferred. The same scheme shows even



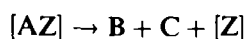
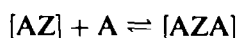
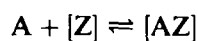
larger selectivity at simultaneous variation of both inlet concentrations A and B.

The reaction rate can be increased by concentration cycling in systems with substantial inhibition of adsorbed reaction product, as for example the addition of ethylene to acetic acid (Table 1, example 2). A positive effect is achieved at high frequency oscillation of acetic acid concentration. Cycle average concentration of intermediate product A\* (see Table 1) is lower than in the steady state. This facilitates ethylene adsorption and a favorable distribution between the two adsorbed species.

Periodical interruption in feeding the reactant, which leads to the formation of nonreactive surface species, increases the rate of catalytic reaction. For example, for the dehydration of alcohols or deamination of primary amines on acid-base catalysts [15] the process can be generally described by one of the two simple schemes:



or



Optimal operation corresponds to a short total cycle while the fraction of time for a reactant A feed interruption depends on the inlet concentration of the reactant.

A reversible reaction with the accumulation of reaction product in the catalyst can be improved by periodical purging of catalyst by an inert gas; for example, the oxidation of SO<sub>2</sub> over vanadium catalysts (Table 1, example 5). Periodic purging of the catalyst by large amounts of an inert gas or air allows achievement of an over-equilibrium SO<sub>2</sub> conversion [16].

Processes exhibiting multiplicity and/or self-sustained oscillations can be improved by imposing a forced perturbation of the inlet composition. For example, the oxidation of CO over supported Pt catalysts (Table 1, example 3) exhibits two steady states in the region of intermediate CO coverage. Simultaneous periodic oscillations of CO and oxygen inlet concentrations shift the system to an average catalyst state corresponding to the upper regime of reaction performance [6].

A large number of experimental studies have been undertaken demonstrating performance improvement under unsteady-state conditions of various processes of heterogeneous catalysis [17–19]. These processes in-

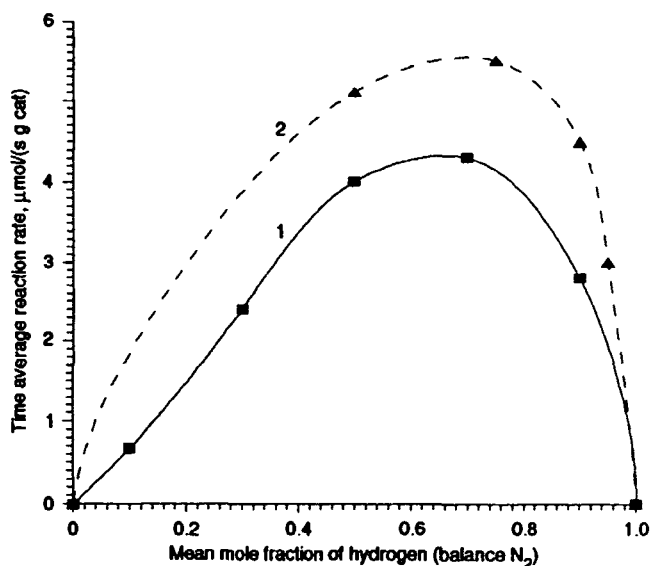


Figure 6. Steady-state (curve 1) and cycle-average (curve 2) reaction rate versus feed composition. Experimental data for ammonia synthesis reaction by Jain, Silveston and Hudgins adapted from *Chemical Reaction Engineering, ACS Symposium Ser. 1982, 196, 97–107*.

clude sulfur dioxide oxidation over a vanadium catalyst, ammonia synthesis over a promoted iron catalyst, hydrogen sulfide oxidation by SO<sub>2</sub> on a bauxite catalyst, Fisher–Tropsch synthesis over ruthenium and cobalt catalysts, CO oxidation on different metallic and oxide catalysts, and methanol synthesis on a Cu/ZnO catalyst. A typical experimental system used was an isothermal fixed bed reactor exposed to periodic oscillations of the inlet gas composition. To prove that periodic concentration forcing is superior to steady-state operation the experiments usually included a measurement of steady-state reaction rate in the entire region of possible inlet composition and a comparison with the cycle average rate at the same cycle average composition of the gas mixture. A typical experimental diagram for reaction with two inlet components is shown in Fig. 6.

#### 10.4.6 Dynamic Phenomena in a Fixed-Bed Reactor

A wide class of forced unsteady-state processes have already been realized on the commercial scale using specific dynamic phenomenon, that takes place during performance of an exothermic reaction in a fixed bed of catalyst. This phenomenon is referred to in the literature as wrong-way behavior of a fixed bed reactor [20]. Substantial differences in characteristic times of heat and mass transfer in a packed bed reactor result in a surprising rise of temperature inside the reactor after

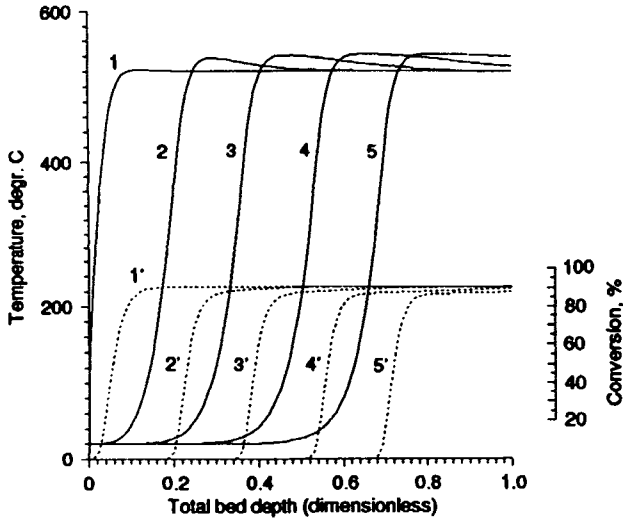


Figure 7. Creeping fronts in a fixed catalyst bed: curves 1–5 are temperature profiles, and curves 1'–5' are conversion profiles at different moments of time.

a sudden reduction of inlet temperature or after an increase in the flow rate. This occurs because a reaction mixture with higher concentration of reagents comes to the downstream section of the bed that retains heat due to high thermal capacity of the catalyst.

At high differences between inlet and outlet temperatures, and substantial bed length, transient temperature and conversion profiles acquire unchanged shapes and move through the bed with essentially constant velocity (Fig. 7). These transient patterns are called traveling waves or creeping fronts and have been studied in many publications (see original works [21, 22]). Analytical estimations of the main parameters of a creeping front have been derived on the basis of asymptotic models considering unchanged temperature and concentration profiles in a coordinate system moving through an infinitely long bed at a velocity  $u_F$  given by  $\xi = l - u_F t$ , where  $\xi$  is the creeping front coordinate,  $l$  is the reactor length and,  $t$  is time. At a constant velocity the energy balance for the catalyst bed may be written in the form [21]

$$u_F = \frac{u}{\gamma} \left( 1 - \frac{\Delta T_{ad} x_c(T_F)}{T_F - T_{inp}} \right) \frac{1}{1 - \frac{\varepsilon_g \Delta T_{ad} x_c(T_F)}{\gamma (T_F - T_{inp})}} \quad (1)$$

where  $u$  is the linear velocity of the reaction mixture ( $\text{m s}^{-1}$ );  $\Delta T_{ad} = (-\Delta H)C_0/c_g \rho_g$  = adiabatic temperature rise (K);  $\gamma = (1 - \varepsilon)(1 - \varepsilon_p)c_s \rho_s / c_g \rho_g + \varepsilon_g$ ;  $\varepsilon_g = \varepsilon_p(1 - \varepsilon) + \varepsilon$ ;  $\varepsilon$ ,  $\varepsilon_p$ , and  $\varepsilon_g$  = packed bed porosity, void fraction in catalyst particle and total fraction of gas volume in catalyst bed, respectively;  $T_F$  = maximum temperature (K);  $x_c(T_F)$  = equilibrium conversion at maximum temperature;  $u_F$  = creeping profiles velocity ( $\text{m s}^{-1}$ ). In many practical cases

$\varepsilon_g/\gamma \approx 1 \times 10^{-3}$  and the second term of the denominator on the right side of eq 1 can be eliminated. The creeping heat front can move both in the direction coinciding with the flow direction (Fig. 7) as well as in the opposite one. In the latter case, the reaction heat will be accumulated in the catalyst bed, and the outlet (or maximum) temperature will be less than its adiabatic value given by  $\Delta T_{ad} x_c(T_F) > T_F - T_{inp}$  at  $u_F < 0$ . A stagnant wave with  $u_F = 0$  is also possible.

Analytical theory of the phenomenon is developed in Refs. 9 and 23. A general estimation for maximum temperature in a creeping front with a first order reaction is

$$T_F = x_c(T_F) \sqrt{\frac{1}{m} \frac{E}{R} \frac{\Delta T_{ad}}{k(T_F) \eta_1(T_F) (1 - e^{-Ze})} \frac{u^2 c_g \rho_g}{\tilde{\lambda}_{cf}}} \quad (2)$$

while the width of the zone, where the major temperature increase occurs is estimated by the equation

$$\Delta L = \frac{\tilde{\lambda}_{cf}}{u c_g \rho_g} \frac{(T_F - T_{inp})}{\Delta T_{ad} x_c(T_F)} \quad (3)$$

where  $m \approx 1$  is a numeric coefficient;  $k(T_F)$  is the reaction rate constant ( $\text{s}^{-1}$ ) at the temperature  $T_F$ ;  $\eta_1(T_F)$  is a dimensionless parameter dependent on the temperature and diffusion coefficient inside the catalyst pellet;  $\tilde{\lambda}_{cf}$  is the effective thermal conductivity of the packed bed ( $\text{J m}^{-1} \text{s}^{-1} \text{K}^{-1}$ );  $E$  is the activation energy ( $\text{J mol}^{-1}$ );  $R$  is the universal gas constant ( $\text{J mol}^{-1} \text{K}^{-1}$ ); and

$$Ze = \frac{T_F - T_{inp} - \Delta T_{ad} x_c(T_F)}{RT_F^2} E$$

is the dimensionless Zeldovich number characterizing the temperature rise.

The parameter  $\eta_1(T_F)$  is treated as a weight-average effectiveness factor along the heat front coordinate:

$$\eta_1 = 6 \frac{\ln[\text{sh}\Psi(T_F)] - \ln \Psi(T_F)}{\Psi^2(T_F)} \quad (4)$$

where

$$\Psi(T) = 3 \frac{V_p}{S_p} \sqrt{\frac{k(T)/x_c(T)}{D_{cf}}}$$

is a Thiele-type modulus for a reversible reaction,  $V_p$  ( $\text{m}^3$ ) and  $S_p$  ( $\text{m}^2$ ) are the volume and external surface area of the catalyst particle, respectively.

The estimation of  $\tilde{\lambda}_{cf}$  is given by

$$\tilde{\lambda}_{cf} = \lambda_{s,cf} + \frac{u_F}{u} \gamma \frac{(u c_g \rho_g)^2}{h_{f a v}} + \frac{3 u_F}{5 u} \gamma \frac{[u c_g \rho_g (V_p/S_p)]^2}{(1 - \varepsilon) \lambda_p} \quad (5)$$

where  $\lambda_{s,ef}$  is an effective axial thermal conductivity of the packed bed solid phase ( $\text{J m}^{-1} \text{s}^{-1} \text{K}^{-1}$ );  $a_v$  is a specific surface of the catalyst pellet per unit of packed bed volume ( $\text{m}^{-1}$ ); other parameters are determined in Table 2. Dependencies of the heat transfer parameters  $h_f$  and  $\lambda_{s,f}$  on the linear velocity, particle dimension, packed porosity and physical properties of the fluid can be found elsewhere [8, 24]. Equations (1)–(4) together reflect the main qualitative features of the creeping front that were demonstrated in experimental and numerical studies. Important for their practical application is the prediction by this theory of the possibility of control of the maximum temperature in a reaction front by variation of design parameters such as linear velocity and size of catalyst pellet.

### 10.4.7 Reverse-Flow Operation in Fixed-Bed Reactors

This is a simple technique allowing for performance of an exothermic catalytic process with continuous back-and-forth migration of the reaction front through the catalyst bed. Periodic flow reversal forces alteration of the direction of the traveling front. Under these conditions the catalyst not only accelerates the chemical reaction but also serves as a heat exchanger and heat accumulation media (heat sink) which is able to transfer the stored energy of reaction to the cooler inlet gas. This makes it possible to provide continuous autothermal operations without external gas preheating in advance of the catalyst bed. After several flow reversals, stabilized repeating temperature and conversion fields are established. A typical picture of those stabilized profiles for the example of a reversible exothermic reaction is shown in Fig. 8.

An important feature of a reactor operating with reversing flows is a gradual decrease of temperature of the packed bed outlet that allows for higher conversion in an adiabatic catalyst bed than for steady-state performance of an exothermic reversible reaction such as  $\text{SO}_2$  oxidation or ammonia synthesis. Conventional operation can provide only the temperature rise along the adiabatic catalyst bed.

The analytical estimations of creeping front parameters given by eqs (1)–(5) can be used for analysis of the reactor with a long catalyst bed operated at low reversal frequency. Another simplified model describes relaxed steady operation relating to intermediate reversal frequencies. The cycle time at such frequencies is much shorter than the time needed for the reaction zone to travel through the catalyst bed, but at the same time, it is much longer than the residence time of the gas flow in the reactor. This situation is quite possible for processes performed under atmospheric pressure when the densities of the catalyst and the gas phase

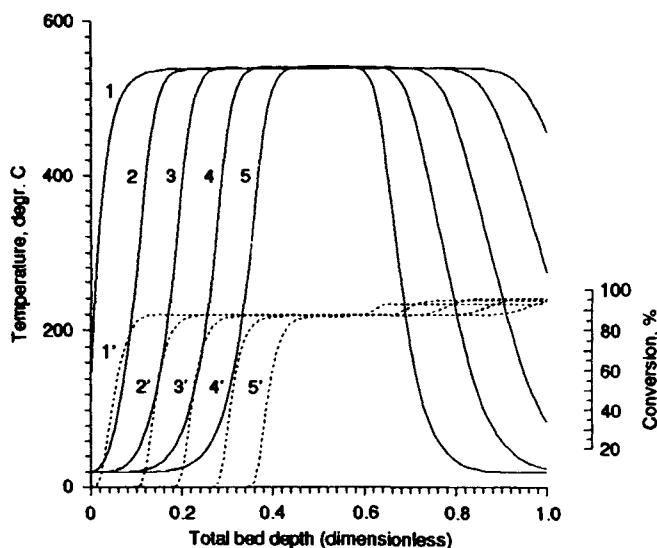


Figure 8. Temperature (curves 1–5) and conversion (curves 1'–5') profiles in the reactor with periodic flow reversal. Example of exothermic reversible reaction.

differ substantially. The temperature profiles at relaxed operation exhibit very small oscillations around a certain cycle average profile while the concentration profiles are quasisteady relative to the temperature profile and flow direction. The model of a stabilized regime can be reduced to a system of ordinary differential equations [9, 25].

The theory for reverse-flow reactors involves consideration of the problem of stability of the high-temperature zone inside the catalyst bed when a low-temperature inlet gas comes in. It has been shown (see, for example Refs. 9 and 25) that periodic flow reversal results in a multiplicity of temperature and conversion profiles. In particular, three possible temperature profiles were computed for the example of a single exothermic reaction. Two extreme regimes, namely an upper one characterized by a high maximum temperature and conversion, and a lower one having zero-value conversion, are stable, while an intermediate regime is unstable. It is characterized by a lower conversion than the upper regime. Reactors operating in the high temperature regime can be extinguished by some perturbation of the operating parameters such as an increase in flow rate, a decrease in the inlet concentration or an increase in the duration of the cycle. Conditions for high temperature operation can be determined approximately on the basis of the following formulas:

$$L > L^* \approx L_R^* + \frac{t_c}{2} u_F \quad \text{and}$$

$$L_R^* \geq 4 \frac{\tilde{\lambda}_{cf,R}}{u \rho_g c_g} \left( \frac{T_R - T_{inp}}{\Delta T_{ad, X_{out}}} - 1 \right) \quad (6)$$

where  $L$  = length of catalyst bed (m);  $L^*$  = minimum catalyst bed length at the design reversal frequency (m);  $L_R^*$  = minimum catalyst bed length at high reversal frequency (m);  $t_c$  = cycle duration (s);  $u_F$  = creeping front velocity ( $\text{m s}^{-1}$ );  $\tilde{\lambda}_{\text{ef,R}}$  = effective axial heat conductivity of a packed bed ( $\text{J m}^{-1} \text{s}^{-1} \text{K}^{-1}$ );  $T_R$  = maximum temperature (K) at high reversal frequency. The values of two last parameters can be estimated using eqs (2), (4) and (5), except that  $m = 2$  and  $(u_F/u)\gamma = 1$ .

The theoretical analysis [9] helped to determine possible ways for controlling and optimization of a reverse-flow operated reactor. For example, a higher yield for reversible exothermic reactions corresponds to a larger residence time along the decreasing temperature profile. This can be obtained using larger catalyst pellets, a lower linear velocity, or a lower adiabatic temperature rise. However, these changes in parameters do not favor stability of operation and require a longer catalyst bed.

Extensive information concerning the analysis of the influence of various parameters on the reverse-flow reactor behavior, along with the experimental results can be found in Ref. 9.

Three commercial processes, namely the oxidation of volatile organic compounds (VOC) for purification of industrial exhaust gases,  $\text{SO}_2$  oxidation for sulfuric acid production, and  $\text{NO}_x$  reduction by ammonia, have employed the periodic flow reversal concept.

Industrial reactors for catalytic incineration of VOCs contain ceramic or another inert packing material on the boundaries of the catalyst bed [9, 26]. In such reactors, the temperature after the inert ceramic packing can be estimated by the almost linear expression

$$T_{\text{out}}^{\text{inr}} \approx T_{\text{inp}} + \Delta T_{\text{ad}} x_{\text{out}} \left( 1 + \frac{u C_g \rho_g}{2 \tilde{\lambda}_{\text{ef}}^{\text{inr}}} L_{\text{inr}} \right),$$

where the index 'inr' relates to the inert packing,  $L_{\text{inr}}$  is the length of one of the boundary beds, and  $\tilde{\lambda}_{\text{ef}}^{\text{inr}}$  is the effective heat conductivity of the inert packing. Preheating the inlet gas in the bed of inert packing enables substantial reduction in the catalyst bed length for irreversible VOC oxidation.

In contrast to conventional catalytic incineration systems, VOC oxidation in a reverse-flow operated reactor can proceed with substantial oscillations in the inlet parameters, and no fuel is required for a self-sustaining operation with  $\Delta T_{\text{ad}}$  as low as 20–30°C [9, 26].

Several industrial catalytic reactor with periodical flow reversal are used in nonferrous metallurgy for treatment of lean sulfurous gases with  $\text{SO}_2$  concentrations varying from 1% to 4.5% [9, 27]. The inlet temperature of such an exhaust gas is typically 40–60°C, while the minimum reaction temperature is 370–400°C. Utilization of these gases by traditional methods

of sulfuric acid production relies on a multibed catalytic reactor with feed gas preheating and interstage cooling. Reverse-flow operation permits a substantially simplified reactor scheme, decreased metal weight and lower pressure drop at catalyst charge and conversion efficiency close to those typical for conventional steady-state reactors. The simplest flow diagram (Fig. 2(a)) is used for treating gases with  $\text{SO}_2$  concentrations below 2–3%. At higher concentrations of  $\text{SO}_2$ , reactors with one or two intermediate heat exchangers for excessive heat removal were recommended [9, 27].

The same principle of process performance has been described for reversible reactions, such as methanol [9, 28] or ammonia [9] synthesis.

One industrial unit for  $\text{NO}_x$  selective catalytic reduction is operating in Russia [29]. It purifies about  $11\,200 \text{ m}^3 \text{ h}^{-1}$  of off-gases containing 2–14  $\text{gm}^{-3}$  of nitrogen oxides. A two-bed reactor with interstage injection of ammonia water is used.

The high ammonia adsorption capacity of the vanadium oxide catalyst for  $\text{NO}_x$  reduction was employed in 30. The reverse-flow operated process included changing of the inlet gas composition. In the first phase  $\text{NH}_3$  is injected in excess of reaction stoichiometry. This  $\text{NH}_3$  accumulates on the inlet boundary part of the bed and fills up the bed, the wavefront of adsorption gradually moving toward the catalyst bed outlet. In the second phase, no ammonia is supplied; however, the second component, nitrogen oxide, continues to react with the excess of ammonia previously adsorbed. Then, the valves are switched and the first and second phases are repeated, but in a different gas flow direction. As a result, an adsorption zone with a high surface ammonia concentration is formed and moves along the catalyst bed back and forth like the high temperature zone shown in Fig. 8. Due to ammonia stored on the catalyst, the process is relatively insensitive to the fluctuation of gas flow and  $\text{NO}_x$  concentrations.

Reverse-flow operation for Sulfur Production over Bauxite Catalysts by the Claus Reaction has been considered in Refs 9 and 31. The rate of  $\text{H}_2\text{S}$  oxidation by  $\text{SO}_2$  on bauxite catalysts is very high even at ambient gas inlet temperature, but sulfur condensing at low temperatures blocks the active catalyst surface, and the reaction stops because of catalyst deactivation. In a reverse-flow reactor the periodic evaporation of condensed sulfur from the outlet parts of the catalyst bed occurs. Although it is difficult to remove all the sulfur condensed within the catalyst pellets at the bed edges, after a certain time a balance between the amount of sulfur condensed and evaporated is attained. Using a reverse-flow reactor instead of the two-bed stationary Claus process provides an equal or better degree of

sulfur recovery, lower capital cost for the catalytic reactor, and eliminates the need for energy consumption to preheat the gas feed.

In the example of partial oxidation of methane the highly endothermic reaction of steam reforming of natural gas was combined with the exothermic combustion of methane. Reverse flow operation makes it possible to achieve high temperature in the catalyst bed at a low average difference between outlet and inlet temperatures, thus decreasing the methane consumption for exothermic combustion. Pilot plant tests [32] have demonstrated the feasibility of this concept.

Several other examples for potential application of reverse-flow operated catalytic reactors are described in Ref. 9. Also, other potential techniques of forced unsteady-state operation which allow for combining chemical reaction and heat exchange in a fixed catalyst bed are discussed. One such technique is sequential switching between inlet and outlet ports of the reaction gas between two or more packed beds (Fig. 2(c)). In this case, the thermal wave travels continuously through a series of packed beds in one direction, as if along a closed ring. However, this operation is more complex and requires more catalyst than the reverse-flow operation.

## 10.4.8 Reaction–Separation Processes

This term embraces a wide class of potentially efficient techniques combining chemical reaction and separation in a catalytic reactor. If the reaction products are able to be adsorbed on the catalyst to different extents and for different lengths of time, these products can be separated from each other. This feature of catalytic processes can be used for enhancement of the reaction rate or selectivity, or for improvement of the quality of a desirable product. The process can be arranged in various ways, e.g. as a system with a fixed catalyst bed operated with periodic changes of the inlet composition or as various types of reactors with moving beds. To improve the separation, a mixture of catalyst and adsorbent can be loaded in the fixed bed reactor, or adsorbent can be fed into the reactor.

A chromatographic reactor described in the early 1960s [33] consists of a fixed bed column into which pulses of a reactant are periodically injected. The reactor is purged only by a carrier gas during periods between the pulses. This operation can increase the degree of conversion of the reversible process  $A \rightleftharpoons B + C$  if one of the reaction products (B or C) is adsorbed more strongly on the catalyst than the other one. The feasibility of the chromatographic operation was shown experimentally for dehydrogenation of cyclohexane to benzene and for dehydrogenation of *n*-butene to butadiene over a platinum–alumina cata-

lyst. At certain reaction conditions (temperature, frequency of pulses, initial concentration) the conversion of the inlet product was higher than the equilibrium conversion.

### 10.4.8.1 Continuous Countercurrent Moving-Bed Chromatographic Reactor

A simultaneous countercurrent movement of solid and gaseous phases makes it possible to enhance the efficiency of an equilibrium limited reaction with only one product (Fig. 4(a)) [34]. A positive effect can be obtained for the reaction  $A \rightleftharpoons B$  if the catalyst has a higher adsorption capacity for B than for A. In this case, the product B will be collected mainly in the upper part of the reactor, while some fraction of the reactant A will move down with the catalyst. Better performance is achieved when the reactants are fed at some side port of the column: inert carrier gas comes to the bottom and the component B is stripped off the catalyst leaving the column (Fig 4(a)). The technique was verified experimentally for the hydrogenation of 1,3,5-trimethylbenzene to 1,3,5-trimethylcyclohexane over a supported platinum catalyst [34]. High purity product can be extracted after the catalytic reactor, and overequilibrium conversion can be obtained at certain operating conditions.

A modification of this technique, the simulated countercurrent moving-bed chromatographic reactor [35], comprises several catalyst beds (Fig. 4(b)). The locations of inlet and outlet ports between the catalyst beds are changed sequentially, thus the countercurrent movement of solid and gaseous phases is simulated in a discrete manner. Such an operation avoids the technical difficulties (catalyst attrition, nonuniformity of solid flow, etc.) associated with solid-phase movement. Part of the reactor sections can be purged by the carrier gas. To increase the separation effect, a bed of adsorbent can be added in each section.

### 10.4.8.2 Reaction Pressure Swing Adsorption

A fixed bed of catalyst mixed with adsorbent is operated under periodically changed pressure (Fig. 4(c)). The overall cycle includes three phases: (i) filling the reactor at high pressure with simultaneous low-pressure delivery of a fraction of the gaseous mixture from the opposite end of the reactor; (ii) delay, delivery is allowed only; (iii) exhaust, i.e. the reaction products are discharged at low pressure from both ends of the bed. Theory [36] shows that improvements in conversion and selectivity can be expected for single or multiple reversible reactions. High pressure pumping of reactants enhances the separation effect and may increase

the productivity compared to other reaction-separation processes performed at stationary pressure.

### 10.4.9 Partial Oxidation in Fluidized-Bed and Riser Reactors

The general redox mechanism of metal-oxide catalyzed oxidation of hydrocarbons involves two major stages in the catalytic process, reduction of the surface layers by hydrocarbons and their reoxidation by interaction with oxygen. While these two stages occur simultaneously in a reactor with the catalyst working under steady-state conditions, they can be carried out in two separate reaction zones in a reactor with catalyst circulation [37]. A hydrocarbon is fed into the first zone where a desirable intermediate product of partial oxidation is formed after interaction with the oxidized catalyst. In the second zone, gas phase oxygen reoxidizes the catalyst. Obviously, the residence time of the catalyst in the first zone should be short enough to prevent formation of an inactive reduced state of the catalyst. If only surface layers participate in the interaction with hydrocarbons, the time of catalyst reduction is approximately several seconds.

A known example of the partial oxidation system with recirculating catalyst is the riser reactor developed by DuPont for *n*-butane oxidation to maleic anhydride over a vanadyl pyrophosphate catalyst [37]. The reactor scheme is shown in Fig. 3(a). A short catalyst retention time of about 10–30 s, under hydrocarbon feed, is provided in the riser reaction zone where spherical catalyst particles with a dimension of about 100  $\mu\text{m}$  are transported by an *n*-butane/inert mixture with a velocity of about 0.5  $\text{m s}^{-1}$ . Reoxidation of the catalyst is carried out in the fluidized bed regeneration zone. An important advantage of the riser process in comparison with traditional fixed bed or fluidized bed reactor systems is the possibility to increase dramatically the concentration of *n*-butane in the feed. Feeding oxygen and *n*-butane to two separate vessels avoids all restrictions in the *n*-butane concentration due to forming an explosive mixture with oxygen. A substantial problem that should be solved when designing such a reactor is the development of an attrition-resistant catalyst. The process selectivity obtained in a pilot unit was 80–85% [37], which is 5–10% higher than for a conventional wall cooled multitubular reactor. This selectivity gain is attributed to the suppression of the highly reactive surface oxygen species  $\text{O}_2^-$  and  $\text{O}^-$  in the riser reactor, which are assumed to be involved predominantly in the side reactions leading to CO and  $\text{CO}_2$ . Steam stripping of the catalyst after the reoxidation zone further improved the selectivity. Evidently, an accurate accounting for major factors de-

termining the selectivity in a riser reactor system can be obtained on the basis of a dynamic kinetic model.

#### 10.4.9.1 Internal Circulation of a Catalyst in Fluidized Beds

If the characteristic time of catalyst state changes is higher than the time scale for particle dispersion in a fluidized bed reactor, the catalyst state will adjust to average parameters of the gas mixture in the reactor volume rather than to the local temperature and composition in every point of the reactor. This situation can be exploited for improving the selectivity of the partial oxidation process. For example, the selectivity in the oxidation of *o*-xylene to phthalic anhydride over  $\text{V}_2\text{O}_5/\text{TiO}_2$  catalysts is higher at high *o*-xylene conversion, if the catalyst is in a state that corresponds to low conversion of *o*-xylene [38]. Therefore, stirring of the catalyst in a fluidized bed can result in selectivity improvement. This effect becomes even higher in a reactor with an “organized” fluidized bed that includes special low volume fixed packing promoting mass transfer between low and high density phases of the fluidized bed. In such a reactor, a dropping temperature profile along the fluidized bed height can be created that increases the number of catalyst particles with high concentration of surface intermediates, leading to the formation of phthalic anhydride.

### 10.4.10 Miscellaneous Examples

#### 10.4.10.1 Fluctuations of the Inlet Temperature in Fixed-Bed Catalytic Reactors

This type of periodic operation allows for conversion improvement in reversible exothermic reactions [9]. A cycle average inlet temperature for the conditions of continuous temperature oscillation can be substantially lower than the inlet temperature under steady-state conditions. This leads to a lower outlet temperature and higher equilibrium conversion for a reversible reaction. Better performance is achieved if temperature oscillations attenuate sufficiently during the passage through the catalyst bed [9].

#### 10.4.10.2 Stabilization of Unstable Steady State

Periodic changes of inlet parameters can be applied to maintain an intrinsically unstable state of a chemical reactor. Under the conditions of high reaction heat release and low inlet temperature, several steady states

may exist in a tubular reactor. The conventional operation is possible only for two outer stable states which are often unsuitable because of very high temperatures or very low conversion of the reactant, respectively. However, appropriate periodic variations of the inlet concentrations, flow rate, or temperature of cooling media allow an unstable intermediate temperature to be attained. In particular, this can be useful for reactions of partial oxidation where the activation energy of complete oxidation is higher than the activation energy of the desirable reaction. An example, is the oxidation of ethylene over silver catalysts, discussed in Ref. 39. A control system necessary for the stabilization of the unstable state should be of the positive feedback type [40].

### 10.4.10.3 Liquid-Gas-Solid Reactor Systems

Periodic change of the liquid flow rate is a technique that has been proved to improve the performance of three-phase reactors [41]. This type of forced unsteady-state operation results in an increase of mass-transfer rate by virtue of formation of a more uniform channeling structure in the catalyst bed, better wetting of the catalyst surface, and higher average temperature of the catalyst. An example is the hydrogenation of  $\alpha$ -methylstyrene on a palladium catalyst [41]. Another example is  $\text{SO}_2$  oxidation on active carbon [42]. Water in this system absorbs the  $\text{SO}_3$  formed, prevents catalyst deactivation by  $\text{SO}_3$ , and absorbs the heat of reaction. Periodic draining of the catalyst increases the rate of sulfuric acid production compared to a steady-state operation by 30–45%. This effect can be explained by a higher reaction rate on the catalyst which is drained but not yet deactivated as well as by a higher average temperature during periodic operation.

## References

- G. K. Borekov, Yu. Sh. Matros, *Catal. Rev.-Sci. Eng.* **1984**, *25*, 551–590.
- M. R. Prairie, J. G. Highfield, A. Renken, *Chem. Eng. Sci.* **1991**, *46*, 113–121.
- B. S. Balzhinimaev, A. A. Ivanov, O. B. Lapina, V. M. Mastikhin, K. I. Zameraev, *Faraday Discuss. Chem. Soc.* **1989**, *87*, 133–147.
- C. O. Bennet, *Catal. Rev.-Sci. Eng.* **1976**, *13*, 121–148.
- M. A. Truffer, A. Renken, *AIChE J.* **1986**, *32*, 1612–1621.
- W. R. C. Graham, D. T. Lynch, *AIChE J.* **1990**, *36*, 1796–1806.
- E. W. Arnold III, S. Sundaresan, *AIChE J.* **1989**, *35*, 746–754.
- Yu. Sh. Matros, *Unsteady Processes in Catalytic Reactors*, Elsevier, Amsterdam, **1985**.
- Yu. Sh. Matros, *Catalytic Processes under Unsteady State Conditions*, Elsevier, Amsterdam, **1989**.
- J. E. Bailey, F. J. M. Horn, *Ber. Bunsenges Phys. Chem.* **1970**, *74*, 611–617; J. E. Bailey, *Chem. Eng. Commun.* **1973**, *1*, 111–124.
- G. Guardabassi, A. Locatelli, S. Rinaldi, *Journal of Optimization Theory and Applications*, **1974**, *14*, 1–20; D. Sincic, J. E. Bailey, *Chem. Eng. Sci.* **1980**, *35*, 1153–1161.
- F. J. M. Horn, R. C. Lin, *Ind. Eng. Proc. Des. Dev.* **1967**, *6*, 21–30.
- I. A. Zolotarski, S. M. Bogdashev, Yu. Sh. Matros, in *Mathematical modeling of catalytic reactors*, (Ed.: Yu. Sh. Matros) Novosibirsk, Nauka, Sibirskoe Otdelenie **1989**, p. 165 (in Russian); I. A. Zolotarski, Yu. Sh. Matros, *React. Kinet. Catal. Lett.* **1982**, *20*, 321–326.
- L. R. Sterman, B. E. Ydstie, *AIChE J.* **1991**, *37*, 986–996.
- J. Thullie, A. Renken, *Chem. Eng. Sci.* **1991**, *46*, 1083–1088.
- J. P. Briggs, R. R. Hudgins, S. P. Silveston, *Chem. Eng. Sci.* **1977**, *32*, 1087–1092; V. O. Strots, Yu. Sh. Matros, G. A. Bunimovich, *Chem. Eng. Sci.* **1992**, *47*, 2701–2706.
- P. L. Silveston, in *Reactions and Reaction Engineering* (Eds: R. A. Mashelkar, R. Kumar), Indian Academy of Sciences, Bangalore, India, **1987**, pp. 217–246; P. L. Silveston in *Unsteady State Processes in Catalysis* (Ed.: Yu. Sh. Matros), VSP, Utrecht, The Netherlands, **1990** p. 217–232.
- A. Renken, *Int. Chem. Eng.* **1984**, *24*, 202–213; A. Renken, *Int. Chem. Eng.* **1993**, *33*, 61–71.
- R. Yadav, R. G. Rinker, *Chem. Eng. Sci.* **1989**, *44*, 2191–2195.
- P. S. Mehta, W. N. Sams, D. Luss, *AIChE J.* **1981**, *27*, 234–241; V. Pinjala, Y. C. Chen, D. Luss, *AIChE J.* **1988**, *34*, 1663–1672.
- E. Wicke, D. Vortmeyer, *Z. Electrochem. Ber. Bunsenges. Phys. Chem.* **1959**, *63*, 145–152; G. Padberg, E. Wicke, *Chem. Eng. Sci.* **1967**, *22*, 1035–1051; P. Fieguth, E. Wicke, *Chem.-Ing. -Tech.* **1971**, *43*, 604–609.
- H-K. Rhee, R. P. Lewis, N. R. Amundson, *Ind. Eng. Chem., Fundam.* **1974**, *13*, 317–323.
- O. V. Kiselev, Yu. Sh. Matros, *Fizika Goreniia i Vzryva (Combust. Explos. Shock Waves)*, **1987**, *23*, 167–175; O. V. Kiselev, *Theoretical Study of the Phenomenon of Heat Waves Movement in a Catalyst Bed*, Russian Academy of Sciences, Institute of Catalysis, Novosibirsk, **1993** (in Russian).
- B. W. Gamson, *Chem. Eng. Progr.* **1951**, *47*, 19–28; A. R. Balakrishnan, D. C. T. Pei, *Ind. Eng. Chem. Proc. Des. Dev.* **1979**, *18*, 30–40; M. E. Aerov, O. M. Todos, D. A. Narinskii, *Columns with Packed Bed*, “Chimia”, Leningrad, **1979** (in Russian).
- G. K. Borekov, G. A. Bunimovich, Yu. Sh. Matros, O. V. Kiselev, I. A. Zolotarski, *Dokl. Akad. Nauk SSSR*, **1983**, *268*, 646–650.
- G. Eigenberger, U. Nieken, *Chem. Eng. Sci.* **1988**, *43*, 2109–2115; G. Eigenberger, U. Nieken, *Int. Chem. Eng.* **1994**, *34*, 4–16; Yu. Sh. Matros, A. S. Noskov, V. A. Chumachenko, *Chem. Eng. Proc.* **1993**, *32*, 89–98; B. van den Beld, R. A. Borman, O. R. Derx, B. A. A. van Woeznik, K. R. Westerberp, *Ind. Eng. Chem. Res.* **1994**, *33*, 2946–2956.
- G. A. Bunimovich, V. O. Strots, O. V. Goldman in *Unsteady State Processes in Catalysis* (Ed.: Yu. Sh. Matros), VPS, Utrecht, The Netherlands, **1990**, p. 7.
- G. F. Froment in *Unsteady State Processes in Catalysis* (Ed.: Yu. Sh. Matros), VSP, Utrecht, The Netherlands, **1990**, p. 57; K. M. Vanden Bussche, S. N. Neophytides, I. A. Zolotarski, G. F. Froment, *Chem. Eng. Sci.* **1993**, *48*, 3335–3345; S. G. Neophytides, G. F. Froment, *Ind. Eng. Chem. Res.* **1992**, *31*, 1583–1589.
- A. S. Noskov, L. M. Bobrova, Yu. Sh. Matros, *Catal. Today*, **1993**, *17*, 293–298.
- D. Agar, W. Ruppel, *Chem. Eng. Sci.* **1988**, *43*, 2073–2078.
- Yu. Sh. Matros, A. N. Zagoruiko, *Dokl. Akad. Nauk SSSR*, **1987**, *294*, 1424–1429.

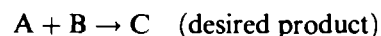
32. R. F. Blanks, T. S. Wittrig, D. A. Petterson, *Chem. Eng. Sci.*, **1990**, *45*, 2407–2413.
33. S. Z. Roginskii, M. I. Yanovskii, G. A. Gasiev, *Kinet. Katal.* **1962**, *3*, 529–540; E. I. Semenenko, S. Z. Roginski, M. I. Yanovski, *Kinet. Katal.* **1964**, *5*, 490–495; S. H. Langer, J. Y. Yurchak, J. E. Patton, *Ind. Eng. Chem.*, **1969**, *61*, 11–21.
34. T. Petroulas, R. Aris, R. W. Carr, *Chem. Eng. Sci.* **1985**, *40*, 2233–2240; B. Fish, R. W. Carr, R. Aris, *Chem. Eng. Sci.* **1986**, *41*, 661–668; B. B. Fish, R. W. Carr, *Chem. Eng. Sci.* **1989**, *44*, 1773–1783.
35. A. K. Ray, R. W. Carr, R. Aris, *Chem. Eng. Sci.* **1994**, *49*, 469–480; A. L. Tonkovich, R. W. Carr, R. Aris, *Nature* **1993**, *262*, 221–223.
36. G. G. Vaporciyan, R. H. Kadlec, *AIChE J.* **1989**, *35*, 831–844; G. G. Vaporciyan, R. H. Kadlec, *AIChE J.* **1987**, *33*, 1334–1343.
37. R. M. Contractor, H. E. Bergna, H. S. Hovovitz, C. M. Blakstone, U. Chowdhary, A. E. Sleight in *Catalysis-1987*, (Ed.: J. W. Ward), Elsevier Science, Amsterdam, **1988**, p. 645; R. M. Contractor, A. E. Sleight, *Catal. Today* **1987**, *1*, 587–607.
38. A. A. Ivanov, B. S. Balzhinimaev in *Unsteady State Processes in Catalysis* (Ed.: Yu. Sh. Matros), VSP, Utrecht, The Netherlands, **1990**, p. 91.
39. C. Wandrey, A. Renken, *Chem. Eng. Sci.* **1977**, *32*, 451–454.
40. A. S. Bostandzhiyan, A. A. Butakov, K. G. Shkadinsky in *Unsteady State Processes in Catalysis* (Ed.: Yu. Sh. Matros), VSP, Utrecht, The Netherlands, **1990**, p. 455.
41. R. Lange, J. Hanika, D. Stradiotto, R. R. Hudgins, P. L. Silveston, *Chem. Eng. Sci.* **1994**, *49*, 5615–5621.
42. P. M. Haure, R. R. Hudgins, P. L. Silveston, *AIChE J.* **1989**, *35*, 1437–1444; A. N. Stegasov, V. A. Kirillov, P. L. Silveston, *Chem. Eng. Sci.* **1994**, *22*, 3699–3710.

and for each physical unit operation. Thus reactive distillation offers the advantage of a reduction in investment costs. Other potential benefits are lower operating costs, higher yields, and energy saving.

However, this technique is not applicable to any type of reaction; both chemical and physical limitations to its use in chemical processes exist: the main one is the necessity to achieve reasonable reaction rates in conditions of vapor–liquid equilibrium (usually at quite low temperatures and pressures).

Reactive distillation seems to be particularly advantageous for those processes in which a liquid phase reaction must be carried out with a large excess of one reactant to obtain the desired conversion. In this regard it is possible to distinguish two main cases:

- (i) Reactions with severe limitations imposed by chemical equilibrium; the separation of at least one of the products as it is formed can drive the reaction to completion. Reactive distillation allows the reaction to be carried out much closer to the stoichiometric ratio of the feed flows.
- (ii) Reactions in which a high concentration of the product or one of the reactants can cause undesired side reactions. For instance, in reactions of the form



if B and C have different volatilities, then by applying the reactive distillation technique their concentration in the reacting phase can be kept very low, thus retarding the undesired reaction.

Moreover, reactive distillation can be advantageous for exothermic reactions, because the heat of reaction is easily removed by the vapor formed in the distillation, and the temperature can be carefully controlled.

The history of reactive distillation dates back to the early 1920s. Pioneering work in this field was done by Backhaus [1] who filed 11 patents covering its use in esterification reactions. A detailed review was published some years later [2].

Reactive distillation was soon extended to other types of reactions, as nitrations, sulfonations, and saponifications [3]. All of these reactions were homogeneously catalyzed, i.e. the catalyst was in the liquid phase, flowing down the column, and had to be recovered from the residue.

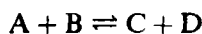
The use of reactive distillation for reactions that rely on a solid catalyst was developed in the early 1970s [4]. Heterogeneously catalyzed reactive distillation poses the additional problem of how to place the solid cata-

## 10.5 Reactive Distillation

G. DONATI, N. HABASHI, I. MIRACCA AND  
D. SANFILIPPO

### 10.5.1 Introduction

Reactive distillation is a technology that simultaneously performs fractional distillation and chemical reaction. Fig. 1 is a schematic representation of a reactive distillation tray column for a reaction of the type



where at least one of the products has a different volatility with respect to the other compounds. The figure shows one of the possible configurations which includes the following sections:

- (i) a rectification section in the upper zone;
- (ii) a reactive distillation section in the middle;
- (iii) a stripping section in the lower zone.

In chemical process design, separate items of equipment are normally provided for each chemical reaction



---

# 11 Annexes

---

## 11.1 Standard Catalysts

---

## 11.2 IUPAC Recommendations

---

## 11.1 Standard Catalysts

G. C. BOND

### 11.1.1 Introduction

It is one of the fundamental requirements of research in the physical sciences that any observation reported in the literature should be capable of repetition anywhere at any time. Authors of scientific papers are therefore under an obligation to describe their materials and procedures in sufficient detail to make this possible. Nowhere is this requirement more necessary than in the field of heterogeneous catalysis, where, by reason of the complexity of the material used and the subtlety of the procedures applied in their pretreatment, the results obtained often depend critically on the variables involved. Full, detailed and accurate descriptions of what has been done are therefore needed, as it is sometimes the case that the really critical variable is not recognized by the operator, and is therefore not controlled. Such adequate descriptions are by no means always to be found in published work.

It therefore follows that, ideally, a literature description should permit anyone to copy the preparation and pretreatment of a catalyst, and to reproduce to measurement of its activity and other reaction characteristics within acceptable limits. It is uncertain whether this has ever been attempted as a conscious exercise, but from the fragmentary comparisons that are possible from the literature the outcome would be uncertain to say the least. Thus while one may feel confident of the self-consistency of results within a given paper, it does not automatically follow that another operator in another laboratory would reach the same conclusions. It is, however, of overriding importance for the advancement of the subject that one should be able to regard *all* observations wherever made as being equally valid.

The control that is needed to achieve good reproducibility of results from one laboratory to another extends from the composition and structure of the catalyst and the conditions of its pretreatment to the apparatus in which this, and the ensuing catalytic reaction, are performed. Experience teaches that factors such as reactor dimensions and the material of its construction are critical for reproducibility, especially in the case of exothermic reactions, as shown in Section 11.1.3.1. It is of course supposed that, when comparison between different pieces of equipment is attempted, all other controllable factors such as temperature, reactant pressures, purification of reactants, etc. are held constant to within whatever limits are practicable.

In order to ensure comparability, it is possible to advance in one of two directions: either to use perfectly standard apparatus of a type possessed by all, or to calibrate one's home-made apparatus by use of a standard or reference catalyst available to all. There is much to be said in favor of the former approach, but it implies the use of commercially available equipment, which is unlikely to be cheap and is not yet widely employed. However, experience teaches that there is little difficulty in reproducing measurements concerning the physical properties of catalytic materials (XPS, XRD, TEM, etc.) when, as is usually the case, standard instrumental methods are used. The alternative is to accept that for some time to come many laboratories will continue to use home-made facilities for chemisorption and catalysis, and that there will therefore be a need for a number of standard catalysts that may be tested to ensure the proper functioning of the equipment (and of the operator!).

There is an additional reason for wishing to see a number of standard catalysts, prepared on a quite large scale, available for widespread use. In many research laboratories, experimental catalysts are often prepared on a scale of only a gram or two, most of which will be used for the tests required by the project. It is therefore impossible to repeat the work at a later date, or to extend it, or to provide colleagues elsewhere with portions of the material for their own experimentation.

There are of course understandable reasons for making small amounts – the method may be truly novel and uncertain of success, or one may wish to economize in the use of costly reagents – but it is worth noting that, in the field of molecular biology, anyone publishing on specific genes or proteins is under an obligation to provide samples to others, so that the work can be confirmed and developed.

While not denying that work on small-scale preparations may have value, its worth will be limited by the small chance of accurate repetition and by the constraints imposed on the amount of work that can be carried out on such a material. It is notoriously difficult to reproduce exactly the conditions under which preparations on a small scale are conducted: in much research it is adequate or even preferable to use a standard material where possible. Work performed on these materials in different laboratories will accumulate, and eventually there will result a catalyst having a broad profile of factual information. Here at least will be one rock in the shifting sands of uncertainty that are literature of heterogeneous catalysis.

It was with these and similar considerations in mind that a group of European scientists, having constituted a Research Group on Catalysis under the leadership of Professor Derouane, decided to prepare two standard supported metal catalysts, one a Pt/SiO<sub>2</sub> and the other a Ni/SiO<sub>2</sub>. At a meeting of the group held at Imperial College, London, during the Sixth International Congress on Catalysis, it was agreed to ask the Johnson Matthey Company to prepare 6 kg of a 5% Pt/SiO<sub>2</sub> (EUROPT-1), while Professors Geus and Coenen would collaborate in preparing about 4 kg of about 25% Ni/SiO<sub>2</sub> (EURONI-1) at the University of Nijmegen. Sizeable portions of these preparations were then distributed to those members of the group wishing to work with them. Professor Wells became responsible for collating results on the former and Professor Coenen on the latter. The group, which has received significant financial support from the Council of Europe Committee on Science and Technology, met periodically to discuss the results obtained, and to consider interim and final reports, and drafts of publications. Section 11.1.2 reviews what was achieved. Later, the research group became inaugurated under Belgian Law as the European Association of Catalysis, known by the acronym EUROCAT.

As the work on these first catalysts progressed, it became clear that there was a demand for standardized platinum catalysts more akin to those used in industry. EUROCAT therefore selected two typical petrolcum-reforming catalysts manufactured by AKZO, namely, 0.3% Pt/Al<sub>2</sub>O<sub>3</sub> and 0.3% Pt–0.3% Re/Al<sub>2</sub>O<sub>3</sub>. These were called EUROPT-3 and -4, respectively (Section 11.1.2.2). More recently still, EUROCAT decided to expand its range of standard catalysts to cover oxides

(Section 11.1.3.1), sulfides (Section 11.1.3.3), and zeolites (Section 11.1.3.2).

As well as these EUROCAT-sponsored activities, a number of other organizations and groups initiated programmes of work on standard catalysts and supports. The Catalysis Society of Japan has produced a comprehensive range of supported metal catalysts, and has published its findings on them (Section 11.1.4.1). Russian scientists have launched a similar but more restricted programme (Section 11.1.4.2). In the United States, the group led by Professors Burwell and Butt (Northwestern University) has also made a number of supported metal catalysts, which they have investigated intensively and have made available to certain other laboratories (Section 11.1.4.3). In the United Kingdom, a group under the auspices of the Society of Chemical Industry, the National Physical Laboratory, and IUPAC commenced work in the late 1970s but little was achieved before the group ceased to function (Section 11.1.4.5).

The performance of a catalyst in industrial usage is likely to be determined by its pore structure, that is to say, by its total pore volume and its pore size distribution. In cases where the active phase is mounted on a porous support, its pore characteristics may affect the accessibility of the active phase to the reactants, as well as other features of the catalyst's performance. For these and other reasons it is important to have agreed and reliable procedures for the measurement of these and related quantities: progress in this direction is surveyed in Section 11.1.4.7.

## 11.1.2 EUROCAT Metal Catalysts

### 11.1.2.1 EUROPT-1

EUROPT-1 is a silica-supported platinum catalyst containing 6.3% Pt [1–8a]. This unusually high metal loading was chosen in order to facilitate the use of as many techniques of characterization as possible (see discussion following Ref. 8a); in particular, it is difficult to apply electron microscopy if the metal content is less than 1%. Samples were distributed to some 20 members of EUROCAT, and detailed results on its physical characterization were reported in five papers [1–5] and summaries presented in two conference proceedings [8a, 9a]. Results concerning its catalytic behavior were published later [6], and most recently a comprehensive review of work performed by other users of the catalyst has appeared [7]. Publications describing its use continue to appear.

The catalyst was prepared by Johnson Matthey Chemicals plc by an ion-exchange procedure, using SORBOSIL grade AQ U30 silica as support and Pt(NH<sub>3</sub>)<sub>4</sub>Cl<sub>2</sub> as the source of metal: it was reduced in

H<sub>2</sub> at 473 K for 0.5 h [2]. It has a somewhat broad distribution of grain sizes, with about 60% being in the range 250–500 μm. Weight losses on heating up to 473 K were minimal (≈0.25%); BET surface area measurement derived from full N<sub>2</sub> physisorption isotherms (Type II) gave pleasingly uniform results (185 ± 5 m<sup>2</sup> g<sup>-1</sup>); mercury porosimetry gave a similar area, and both methods afforded pore volumes of 0.72–0.77 cm<sup>3</sup> g<sup>-1</sup>, corresponding to a mean pore diameter of about 14 nm. Single-point BET measurements showed that variation of the temperature used for outgassing (to constant weight) did not affect the result [2].

More disturbing were the measurements on the support itself. Outgassing at 573 K led to a surface area of 364 m<sup>2</sup> g<sup>-1</sup>, and it was concluded that the process of catalyst preparation had decreased both the area and the pore volume by about one-half, the loss of porosity being mainly in the mesopore region. It was concluded that hydrothermal sintering of the silica had occurred; as the literature usually gives only the physical characteristics of the support, and not the finished catalyst, it is sensible to recommend that reported physical properties should always refer to the catalyst as used. The possibility that further changes may occur during use needs to be kept in mind as well.

EUROPT-1 was subjected to chemical analysis by a number of methods [2]; all gave closely concordant results, namely 6.3 ± 0.1 wt% Pt. Grains larger than 500 μm, however, contained only 5.7% metal, so care needs to be exercised in taking representative samples. There is considerable evidence from X-ray absorption fine-structure spectroscopy (EXAFS), X-ray photoelectron spectroscopy (XPS) [2], and temperature programmed reduction (TPR) [10] measurements that the metal in the catalyst as supplied is substantially oxidized, at least 90% being in the form of a disordered oxide phase. This is, however, easily reduced by H<sub>2</sub> [10, 11], and providing this is not done above 623 K the dispersion remains high.

Particle size distributions were measured by transmission electron microscopy (TEM) in a number of laboratories. Some confusion arose because different workers used different size intervals (Fig. 1), but all agreed that the virgin catalyst contained particles between 0.9 and 3.5 nm in size, of which 75% were less than 2 nm; they are quite homogeneously distributed throughout the support grains. A number average size of 1.8 nm has been proposed [3]. This paper gives a lengthy discussion on how the TEM results might be converted into a degree of dispersion, so that turnover frequencies might be calculated, but the procedure adopted assumes (probably incorrectly) that the Pt remains as an oxide: it is common experience that platinum group metal oxides are reduced in vacuo under the influence of ionising radiation. Nevertheless, it

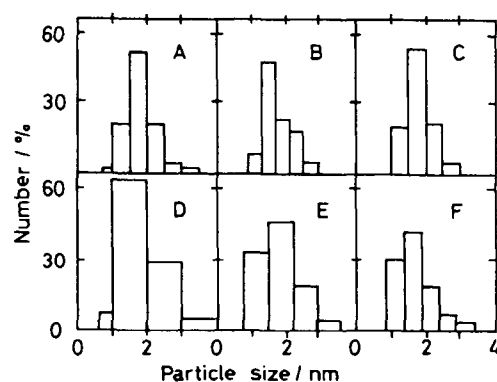


**Figure 1.** Particle size distributions of EUROPT-1 by transmission electron microscopy [3]: (A–E) material as received examined in five different laboratories; (F) after rereduction at 623 K. Number of particles counted: A, B, D, F 500; C, E 1000.

seems safe to take a dispersion value of 60% for the reduced catalyst [3]. More recent TEM work [7] has suggested a somewhat larger number average size (2.1 nm), and there are indications that the result obtained depends on both the method of sample preparation and the accelerating voltage used [7]. The EXAFS spectrum obtained after reduction at 520 K has been interpreted [3] to give a Pt–Pt distance of 0.277 nm and a Pt–Pt metallic coordination number of  $9.6 \pm 1.0$ . This agrees with the TEM dispersion, and a structure consistent with the data is a  $7 \times 7$  array of Pt atoms on which a further eight atoms reside [7]. Structural information can also be derived by Debye function analysis of the X-ray diffraction pattern [11]; superficial oxidation of the as-received material was confirmed, and the reduced catalyst appeared to consist of regular face-centered cubooctahedra, 90% of which were in the form of 55-atom crystallites. The Debye temperature (147 K) was lower than that of bulk Pt<sup>0</sup> (234 K) and there was an increase in static disorder following evacuation. The statistical improbability of creating particles having exactly 55 atoms has been noted, as has the contradiction between the EXAFS- and XRD-derived structures [7]. NMR studies on the <sup>195</sup>Pt nucleus confirm the dispersion to be about 60% [7]. It must, however, be concluded that these techniques of physical characterization are not yet sufficiently refined for highly quantitative analysis of well-dispersed supported metal catalysts.

Heating in H<sub>2</sub> at temperatures up to 1273 K leads to particle growth and broadening of the distribution [3], but the corresponding loss in H<sub>2</sub> adsorption capacity [12] may be due in part to the formation of a Pt silicide.

Selective chemisorption of H<sub>2</sub> is probably the most widely practised means of assessing dispersion, particle

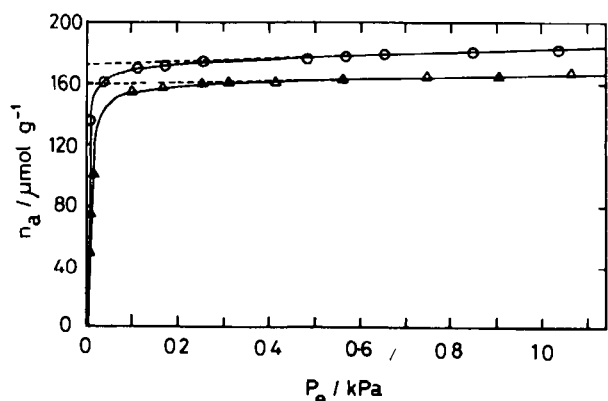


Figure 2.  $H_2$  chemisorption isotherms on EUROPT-1 [14] ( $\Delta$ ) after reduction at 758 K ( $\circ$ ) oxidized before reduction at 758 K

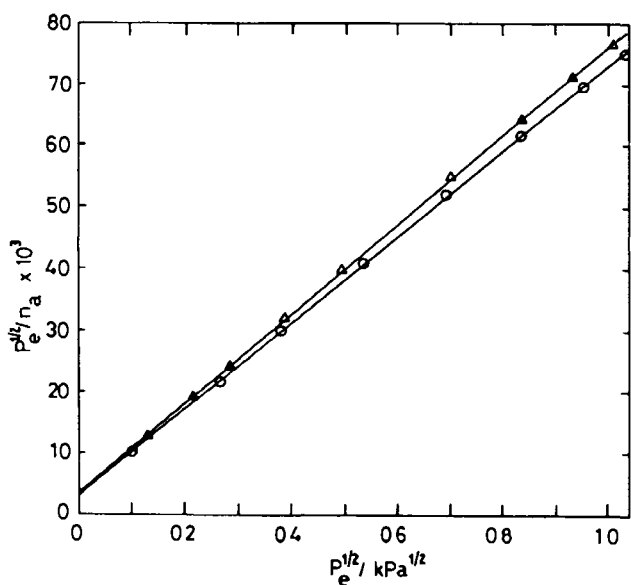


Figure 3.  $H_2$  chemisorption isotherms on EUROPT-1 plotted according to the Langmuir equation [14] (see also Table 1). Symbols as in Fig. 2

size, and metal area in supported metal catalysts (Section A 3.1.2). The process has been investigated with EUROPT-1 by several groups of workers [4, 7, 13, 14], with results that have general importance for the validity of the method. It has been widely assumed that surface stoichiometry  $H/Pt_s$  may be taken as unity irrespective of particle size, despite evidence to the contrary with other metals. Volumetric  $H_2$  chemisorption isotherms of good quality are obtained (Fig. 2), with low slopes at pressures above about 10 mbar pressure, they appear to fit the Langmuir equation for dissociative chemisorption [14] (Fig. 3), which when applied in the linearized form

$$P_e^{0.5}/n = (K^{0.5}n_m)^{-1} + (P_e^{0.5}/n_m)$$

Table 1. Monolayer capacities ( $\mu\text{mol g}^{-1}$ ) for  $H_2$  on EUROPT-1 derived in various ways

$n_m^0$	Measurement <sup>b</sup>			Reference
	$n^{40}$	$n_m^L$	$H/Pt^L$	
166	174	—	—	4
$166 \pm 4$	168	$\approx 192$	1.19	7
159.5	162	171	1.06	14
173.5 <sup>a</sup>	178 <sup>a</sup>	188 <sup>a</sup>	1.17 <sup>a</sup>	14
—	200	—	—	13

<sup>a</sup>Catalyst oxidized at 623 K for 1 h before reduction

<sup>b</sup> $n_m^0$  = monolayer capacity by extrapolation to zero pressure

$n^{40}$  =  $H_2$  uptake at 53 mbar equilibrium pressure,  $n_m^L$  = monolayer capacity according to Langmuir equation,  $H/Pt^L$  = corresponding  $H/Pt$  ratio

(where  $P_e$  is the equilibrium pressure,  $n$  and  $n_m$  are respectively the moles of  $H_2$  adsorbed at pressure  $P_e$  and at saturation, and  $K$  is the adsorption equilibrium constant) enables  $n_m$  to be obtained both from the slope and (less accurately) the intercept (Table 1). The difficulty with the often-used "extrapolation to zero pressure" method for estimating monolayer volume is that the intercept increases as the pressure range is extended [13], and thus has no real significance. The data also seem to obey the Temkin equation over very wide pressure ranges [4, 13], although the logarithmic form of the equation does not admit of a saturation limit. It is, however, concluded that in practice adsorption is complete at about 330 mbar pressure, the uptake being  $200 \mu\text{mol g}^{-1}$  ( $H/Pt_s = 1.24$ ), with little further adsorption occurring up to 6.5 bar pressure. A value derived by the Langmuir equation, provided the data cover a sufficient pressure range, is therefore acceptable (Table 1).

However, even if one takes a value of  $\sim 180 \mu\text{mol g}^{-1}$  corresponding to the uptake at 50 mbar pressure (Table 1), the number of H atoms adsorbed exceeds the total number of Pt atoms by some 10%, so there is a flat contradiction between the greater than 100% dispersion that this implies, and the 60% dispersion seen by TEM. The dilemma is partially resolved by the results of temperature programmed desorption studies [4]. At least three peaks are recognized in the spectrum, the amount adsorbed in the most populated state, together with the assumption that  $H/Pt_s$  equals unity, gives a dispersion of 65%, in fair agreement with the TEM value. The most strongly held state is assigned to H spillover, and some of the  $H_2$  "chemisorbed" is thought to be used to break Pt-O-Si bridges formed between the metal particles and the support. Three groups have reported heats of adsorption for  $H_2$  [7, 13] but the results are not in exact agreement.  $^1H$  NMR has also been used to identify states of  $H_2$  adsorption [4, 7]. The study of this system is a salutary reminder

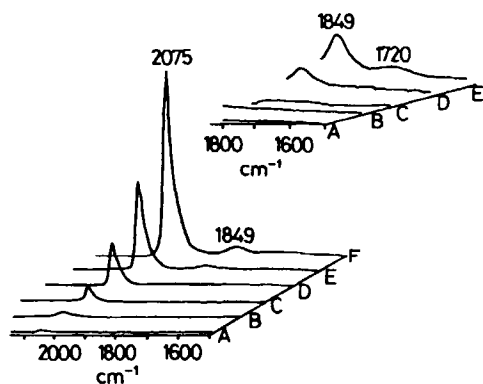


Figure 4. Infrared spectra of carbon monoxide adsorbed on  $H_2$ -depleted EUROPT-1 surface [5]. Spectra A–F represent 3 min exposures at progressively increasing pressures of from  $1.3 \times 10^{-5}$  to 15 mbar.

of exactly how complex an apparent simple process can be.

Carbon monoxide chemisorption on EUROPT-1 has been the subject of several studies [5, 7]. Isotherms of low slope in higher pressure ranges have been obtained, and monolayer volumes at zero pressure of  $165$ – $198 \mu\text{mol g}^{-1}$  have been reported. IR spectroscopy shows the linear form to predominate, with band frequencies increasing from  $2061$  to  $2075 \text{ cm}^{-1}$  with increasing coverage; weak features at  $1878$ – $1849$  and  $1720 \text{ cm}^{-1}$  were also seen [5] (Fig. 4). Diffuse reflectance infrared Fourier transform (DRIFT) measurements have found bands for the linear species at somewhat higher frequencies [7]. The heat of adsorption is given as  $160 \text{ kJ mol}^{-1}$ , independent of coverage up to  $\Theta = 0.7$ . To a first approximation, the surface stoichiometry is the same as for H atoms, namely  $\text{CO}:\text{Pt}_s$  is unity.

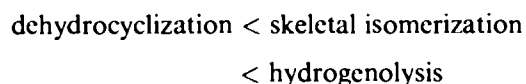
Oxygen chemisorption has also been followed by a number of techniques [5, 7]. Because of the great strength of its adsorption, prolonged and rigorous outgassing is not required, and zero pressure uptakes at room temperature are in the region  $79$ – $100 \mu\text{mol g}^{-1}$ . This implies a surface stoichiometry  $\text{O}:\text{Pt}_s$  also of unity. However,  $\text{O}_2$  uptakes increase with increasing temperature and with time, and great care is needed to obtain reliable and meaningful results for  $\text{O}_2$  chemisorption. It is possible that measurements at sub-ambient temperature would be the most useful.

Turning now to the catalytic properties of EUROPT-1, very extensive measurements of all kinds of hydrocarbon transformations have been undertaken, and an impressive body of information is now available [6, 7, 12, 15, 16]. Only the briefest of surveys is possible here; the available reviews [6, 7] and the references cited therein give additional information.

A number of supposedly structure-insensitive reactions have been looked at: these include methane– $D_2$

exchange, hydrogenation of *n*-hexene isomers, of isoprene (2-methyl-1,3-butadiene), of benzene and toluene, the exchange of benzene and of ethene with  $D_2$ , and epimerization of *cis*-1,2-dimethylcyclohexane. The results are in the main as expected for a platinum catalyst; while several laboratories examined the reactions of benzene, precise comparison of turnover frequency (TOF) values between laboratories and with the literature is difficult, because experimental conditions are rarely exactly the same. It was observed that the TOF passes through a maximum as the temperature is raised, and that the temperature at which this occurs increases with the  $H_2$  pressure. It is therefore reasonable to relate this effect to the changing concentration of H atoms on the surface. With the ethene– $D_2$  exchange, minor differences in product distributions have been correlated with changes in particle size produced by sintering, but the possibility of other effects obtruding, as noted above, must be remembered. The so-called “single turnover” (STO) technique has been applied to 1-butene hydrogenation, and five different types of site have been recognized and quantified.

A clearer and more penetrating identification of the catalytic sites on the surface of the Pt particles is, however, likely to be provided by reactions that are classified as being “structure-sensitive”. In contrast to those of the “structure-insensitive” type, to which most of the reactions cited in the last paragraph belong, these seem to require an ensemble of several atoms, with perhaps some added requirement of specified coordination numbers. The rates and products formed in “structure-sensitive” reactions may therefore vary with (i) insertion of an inactive (e.g. Group 11) element as in an alloy, (ii) the arrangement of atoms in single crystal surfaces, and (iii) particle size in supported metal catalysts. Since the theoretical infrastructure of these observations is not yet explicated, it is well to apply the terms ensemble-size sensitivity, plane-geometry sensitivity, and particle-size sensitivity, respectively, to these phenomena. The final caveat must be added that these effects do not have a black-and-white character, and that *degrees* of sensitivity to the relevant variable should be considered. Thus, for example, when *n*-hexane reacts with  $H_2$  on platinum–gold alloys, ensemble-size sensitivity increases in the sequence



Extensive studies have been described of the reactions of linear alkanes with  $H_2$  over EUROPT-1 [6, 7, 12, 15, 16]. Table 2 summarizes the kinetic parameters reported for ethane, propane, and *n*-butane. Skeletal isomerization is of course possible with this last mole-

**Table 2.** Kinetic parameters\* for the hydrogenolysis of linear alkanes on EUROPT-1: TOF and selectivities at 573 K [6, 15].

Alkane	E (kJ mol <sup>-1</sup> )	TOF (h <sup>-1</sup> )	S <sub>2</sub> <sup>a</sup>	S <sub>3</sub> <sup>a</sup>	Reference
C <sub>2</sub> H <sub>6</sub>	210	0.22	–	–	6
C <sub>2</sub> H <sub>6</sub>	189.5	0.15	–	–	15
C <sub>3</sub> H <sub>8</sub>	181–189	1.5	–	–	6
C <sub>3</sub> H <sub>8</sub>	<sup>b</sup>	2.2 <sup>b</sup>	0.995 <sup>b</sup>	–	15
C <sub>3</sub> H <sub>8</sub>	146–164 <sup>c</sup>	1.45 <sup>c</sup>	0.995 <sup>c</sup>	–	15
<i>n</i> -C <sub>4</sub> H <sub>10</sub>	114–142	3.5–7.3	0.72	0.58	6
<i>n</i> -C <sub>4</sub> H <sub>10</sub>	95 <sup>b</sup>	≈4.5 <sup>b</sup>	0.67 <sup>b</sup>	0.64 <sup>b</sup>	15
<i>n</i> -C <sub>4</sub> H <sub>10</sub>	118–127 <sup>c</sup>	≈1.8 <sup>c</sup>	0.77 <sup>c</sup>	0.60 <sup>c</sup>	15
<i>n</i> -C <sub>4</sub> H <sub>10</sub>	109	10.2	–	–	6

\*For C<sub>3</sub>H<sub>8</sub>, S<sub>1</sub> + 2S<sub>2</sub> = 3; for *n*-C<sub>4</sub>H<sub>10</sub>, S<sub>1</sub> + 2S<sub>2</sub> + 3S<sub>3</sub> = 4, where the subscript is the number of C atoms in the product.

<sup>b</sup>Initial state of catalyst: for C<sub>3</sub>H<sub>8</sub>, the Arrhenius plot is non-linear.

<sup>c</sup>Steady state of catalyst.

\* Kinetics measured with H<sub>2</sub>: alkane ratios of ≈10.

cule, and selectivity to isobutane is between 10 and 30% at 573 K, using a 10-fold excess of H<sub>2</sub>. Its activation energy is higher than for hydrogenolysis, and its rate and kinetic parameters are somewhat less reproducible. A perpetual problem in the study of these reactions, and of alkane transformations in general, is the formation of strongly held carbonaceous deposits, which are (at least initially) extensively dehydrogenated forms of the reactant. Attempts have been made to minimize their formation, e.g. by using short reaction periods, and to identify their effects on the residual reaction. In the case of *n*-butane [15], they increase the activation energy and direct the reaction towards greater central C–C bond fission; isomerization is selectively suppressed.

The following conclusions may be drawn from Table 2:

- (i) Activation energies decrease and TOFs increase with the length of the carbon chain.
- (ii) As is commonly observed, ethane and methane are formed in almost exactly equimolar amounts from propane.
- (iii) The two types of bond in *n*-butane are broken with almost equal probabilities.

With linear alkanes having five or more carbon atoms, cyclization becomes possible as well as isomerization and hydrogenolysis. With *n*-pentane, cyclization is minimal and with *n*-hexane it does not exceed 25% in the range 470–570 K [6]; with the latter molecule, isomerization predominates above 520 K. Product selectivities are particle-size sensitive, and Pt/SiO<sub>2</sub> catalysts having lower dispersion give more hydrogenolysis and cyclization.

Much work has also been carried out on the reactions in the presence of H<sub>2</sub> of branched alkanes, and on the mechanism of their skeletal isomerization [6, 7]. The use of <sup>13</sup>C-labeled molecules permits alternative reaction pathways to be distinguished. Thus, for example, most of the 3-methylpentane formed from 2-methylpentane has followed the bond-shift route, but most of the *n*-hexane has resulted from the cyclic mechanism. Labeled molecules also allow mechanisms of aromatization of C<sub>7</sub> and C<sub>8</sub> alkanes to be followed [6].

In the context of these mechanistic considerations, the way in which the C<sub>5</sub> ring is split by H<sub>2</sub> is also of interest; numerous studies of substituted cyclopentanes have been performed [7]. The mode of breaking in methylcyclopentane is particle-size sensitive: EUROPT-1 affords 44% *n*-hexane, 38% 2-methylpentane, and 18% 3-methylpentane at 520 K.

Hungarian workers have made extensive studies with EUROPT-1 and other platinum catalysts of the dependence of rates or product selectivities on H<sub>2</sub> pressure [7]. Yields of alkenes understandably decrease, and yields of hydrogenolysis products increase, with increasing H<sub>2</sub> pressure; those of other products pass through maxima which move to higher H<sub>2</sub> pressures with increasing temperature. There is a lack of any comprehensive and quantitative theoretical framework to interpret all these observations, but it is clear that the concentration of adsorbed H atoms is crucial in determining to what extent each available pathway is followed. A principal factor in the effect of increasing temperature on product yields is the *decrease* in H atom concentration.

In so far as it is possible to summarize the vast body of information available, it appears in the main EUROPT-1 behaves as expected for a Pt catalyst having particles of about 2 nm in size. Compared to other catalysts, however, its hydrogenolysis selectivity is low, as is its tendency to form carbonaceous residues [7]; these characteristics may be connected. An attempt has been made [17] to show how the various reactive intermediates might be accommodated on the faces of a 55-atom cubooctahedron (Fig. 5).

EUROPT-1 has also proved to be of exceptional value as a model catalyst to which systematic modifications may be made. The effects on its catalytic properties of the addition of silver, titania and alumina [16], chlorine, oxygen, sulfur, ammonia, and carbon monoxide have all been examined [7]. Of particular interest is its ability to be modified by alkaloids of the cinchona family, becoming in consequence enantioselective for the hydrogenation of methyl pyruvate [7].

For information on the availability of samples of EUROPT-1, please contact the author of this section.

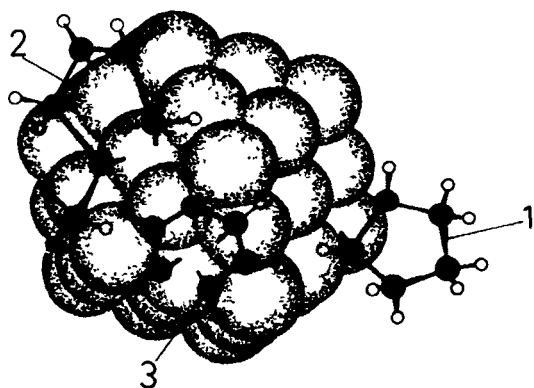


**Figure 5.** The 55-atom cubooctahedron as a model for the most abundant structure in EUROPT-1. (1) cyclopentane adsorbed on a corner atom, (2) a  $C_5$  cyclic species on the (100) surface; (3) a  $C_6$  species en route to benzene on the (111) surface [7]

### 11.1.2.2 EUROPT-3 and EUROPT-4

As noted above, these are typical petroleum-reforming catalysts [9a, b, 18, 19]. EUROPT-3 is 0.3% Pt:  $Al_2O_3$ , and EUROPT-4 contains in addition 0.3% Re. Their surface areas are about  $185\text{ m}^2\text{ g}^{-1}$ , their  $N_2$  pore volumes about  $0.5\text{ cm}^3\text{ g}^{-1}$ , and both contain about 1% Cl [18].

It was appreciated at the outset that the characterization of these materials would be an altogether more difficult problem than that of EUROPT-1, by reason of the lower metal content, and the bimetallic nature of EUROPT-4. It was hoped that study of the latter would help resolve some of the questions concerning the intimacy of mixing of the two metals in the functioning catalyst, but these queries have been only partially answered. Temperature programmed reduction (TPR) studies have confirmed the sensitivity of the reduction profile to experimental conditions and sample pretreatment but, notwithstanding reports in the liter-

ature concerning the selective chemisorption of  $H_2$  and of other simple molecules, members of EUROCAT have been unable to measure adsorption characteristics as precisely as they had wished. Contributing factors to the difficulties may be the presence of the Cl, and H spillover. It is believed that most of the platinum is in the form of particles of about 1 nm in size, although by TEM it is only possible to see a few very large particles [20]. For the bimetallic catalyst, various models have been proposed. For example, Re atoms (or ions) may “decorate” the surface of the Pt crystallites, eliminating the large ensembles which can cause hydrogenolysis. It must be recalled that in the working state the catalyst is sulfided, and a model involving decoration by  $ReS_x$  species is widely accepted. In the unsulfided state, however, surface energy considerations would determine that rhenium should go to the core, but the particles are so small as to have almost no inside. It is highly likely that some of the rhenium remains on the  $Al_2O_3$  surface as  $Re^{4+}$  ions occupying octahedral holes; it is certain that there are no pure  $Re^0$  particles or large clusters of Re atoms, because these are extremely active for deep hydrogenolysis, which is not observed. Great care was exercised to use closely defined pretreatment conditions before making catalytic measurements, to maximize the chance of obtaining reproducible effects [18].

A little work on “structure-insensitive” reactions has been reported [18]. Both catalysts were very active for ethene hydrogenation, and rapid deactivation occurred even at 176 K. Ethyne and 1,3-butadiene react in a more controlled manner: study of ethyne hydrogenation using both  $^{14}C$ -labeled ethyne and ethene showed that ethane formation took place directly from adsorbed ethyne, without the intervention of gas-phase ethene.

Hydrogenolysis of alkanes and related reactions on these catalysts have been studied by a number of groups [18, 19, 21–23]. Kinetic parameters for ethane, propane, and *n*-butane on both catalysts are summarized in Table 3. With propane, selectivities to ethane on

**Table 3.** Kinetic parameters for the hydrogenolysis of linear alkanes on EUROPT-3 and EUROPT-4: rates and selectivities at 603 K [18, 22]

Alkane	Catalyst	E (kJ mol <sup>-1</sup> )	$r^a$ (mmol g <sup>-1</sup> (Pt) h <sup>-1</sup> )	$S_2^a$	$S_3^a$
$C_2H_6$	EP-3	230	0.70	–	–
$C_3H_8$	EP-3	187	1.42	0.992	–
<i>n</i> - $C_4H_{10}$	EP-3	148	3.62	0.581	0.703
$C_2H_6$	EP-4	195	7.35	–	–
$C_3H_8$	EP-4	185	0.76	0.969	–
<i>n</i> - $C_4H_{10}$	EP-4	142	8.70	0.787	0.523

<sup>a</sup>See footnote to Table 2

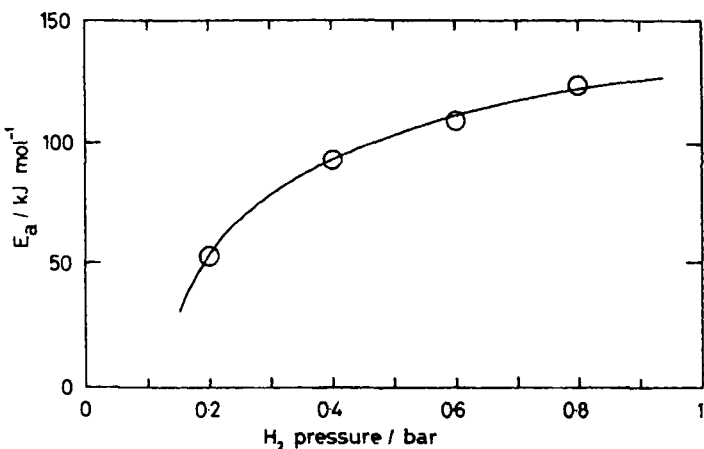


Figure 6. Apparent activation energy for *n*-butane hydrogenolysis on EUROPT-3 as a function of H<sub>2</sub> pressure [24].

EUROPT-3 are greater than 99%, as with EUROPT-1, but with EUROPT-4 they are lower ( $S_2 = 0.84$ – $0.97$  at 603 K) and rates are not well reproducible; faster rates correlate with lower values of  $S_2$ . Activation energies for both catalysts lie in the range 170–200 kJ mol<sup>-1</sup>. With the Pt/Al<sub>2</sub>O<sub>3</sub>, as with the EUROPT-1 Pt/SiO<sub>2</sub>, rates increase and activation energies decrease with increasing carbon chain length, but a major difference is seen in isomerization selectivities, which with EUROPT-3 are only about 2%. The effect of rhenium on the *n*-butane reaction is to raise  $S_2$  and depress  $S_3$ , these changes being interpreted to mean that adsorbed intermediate C<sub>3</sub> species has a much lower chance of desorbing as propane when rhenium is present.

The kinetics of alkane hydrogenolysis, that is, the dependence of rate on reactant concentration, have been the subject of numerous studies, and much effort has been devoted to devising rate expressions based on the Langmuir–Hinshelwood formalism to interpret them. Reactions of ethane, propane, and *n*-butane with H<sub>2</sub> on EUROPT-3 and -4 have been carefully studied, with the surfaces in either as clean a state as possible, or deliberately carbided [21, 22]: kinetic measurements at different temperature permitted adsorption heats and true activation energies to be obtained. There were two surprises (but like all surprises they were obvious afterwards):

- (i) The *apparent* activation energy is a function of H<sub>2</sub> concentration [24] (Fig. 6) (this could be one source of compensation effects).
- (ii) Rate expressions of quite different form provide comparably good fits for the experimental results [21].

Results obtained for the reactions of *n*-hexane, methylcyclopentane, methylpentanes, and *n*-octane with H<sub>2</sub> on these catalysts have been summarized [18]. On

the whole, the manner in which product selectivities change with temperature is not well reproducible, due no doubt to the use of different pretreatments and the operation of other factors already mentioned. Fairly consistent results were however obtained with methylcyclopentane, product selectivities between 560 and 610 K being 2-methylpentane ≈ 40%, *n*-hexane ≈ 34%, and 3-methylpentane ≈ 26%. Increasing the surface Cl<sup>-</sup> concentration increases the isomerization selectivity with 2,2-dimethylbutane, while its removal by water decreases it [19].

The amount of work so far performed with these catalysts is less than with EUROPT-1, and it is more difficult to achieve consistent and reproducible results with them. What has been done does, however, serve to emphasize the extreme care that is needed to eliminate spurious effects; thus despite all possible care it seems almost impossible to avoid totally the formation of *some* carbonaceous deposit, so quickly is it formed. Perhaps, although undesirable, it will have to be tolerated.

### 11.1.2.3 EURONI-1

This catalyst [8a, 25–27] was formulated as a 25% Ni/SiO<sub>2</sub>, typical of those used for fat-hardening and other large-scale hydrogenations. One of the major problems with catalysts of this type arises from the extensive interaction, amounting to compound formation, that occurs between the precursor components during the preparation, and the consequential difficulty of obtaining complete reduction of the nickel. This was a major focus of effort in the study of this catalyst.

EURONI-1 was prepared by the homogeneous precipitation route developed by Geus (Section A.2.2.1.5). An aqueous solution of Ni(NO<sub>3</sub>)<sub>2</sub> · 6H<sub>2</sub>O in which Degussa Aerosil 180 was suspended was hydrolyzed by hydroxyl ions liberated during the slow hydrolysis of urea at 363 K over a period of 20 h; the products of two separate preparations were mixed, and spray-dried [26]. The nickel content was estimated by several analytical methods, which in the main gave consistent results in the range 24.0–25.5 wt% (mean 24.6%); only X-ray fluorescence and atomic absorption spectroscopy gave values outside this limit. The unreduced material is hygroscopic; its BET area is about 270 m<sup>2</sup> g<sup>-1</sup>.

Temperature programmed reduction (TPR) was followed both by thermogravimetry and conventionally, i.e. by measuring the change in composition of a 5% H<sub>2</sub> in Ar mixture. Slight reduction occurred between 570 and 670 K, due perhaps to the presence of small amounts of Ni(OH)<sub>2</sub> or basic carbonate; reduction was rapid above 670 K but H<sub>2</sub> consumption continued until at least 1000 K. In isothermal studies, high degrees of



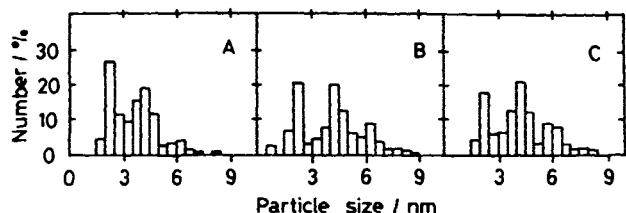


**Figure 7.** Particle size distributions for EURONI-1 reduced under various conditions [27]: (A) 16 h at 633 K + 6.5 h at 773 K; (B) 3 h at 923 K; (C) 19 h at 923 K.

reduction were achieved at 900–920 K in periods of 4–26 h, and 90% reduction was obtained in 24 h at 700 K. Much depends on the dryness of the gas stream, as water (which is liberated in the reduction) may reoxidize the metal. Reproducible reduction rates can only be obtained if bed geometry is tightly controlled. Degrees of reduction were measured by measuring the volume of  $H_2$  liberated on treating the reduced catalyst with  $H_2SO_4$  [26].

Careful studies of the unreduced precursor give no indication of the presence of  $Ni(OH)_2$ , the principal component being a poorly crystallized nickel antigorite, a compound having a layer structure. Thus much if not all the  $SiO_2$  has undergone a reaction involving the  $Ni^{2+}$  ions and the base, forming a new structure in which the layers are not in register. It is stable in air up to 770 K.

Samples of EURONI-1 reduced under various conditions were examined by X-ray diffraction (XRD), X-ray photoelectron spectroscopy (XPS), magnetic methods, TEM and  $H_2$  chemisorption in order to ascertain the mean size and size distribution of the nickel particles [27]. According to TEM, in a sample reduced at 770 K most of the Ni particles were less than 5 nm in size, but some sintering occurred on raising the temperature to 920 K, after which particles in the range 5–8 nm were detected (Fig. 7). The reduced catalyst was found to be superparamagnetic, so the Ni particles consist of single domains. The decrease in saturation magnetization following  $H_2$  chemisorption was  $1.43 \mu_B$

per  $H_2$  molecule. Considerable difficulty was experienced in the measurement of  $H_2$  chemisorption isotherms: factors such as variable degree of reduction, outgassing efficiency, reoxidation of Ni particles, and uncertain equilibration times were held responsible for differences in monolayer volume of up to two times between different laboratories. All monolayer volumes were assessed by the extrapolation method, the hazards of which have been described above; no attempt has been made to fit the experimental data to any of the established adsorption equations. Despite these difficulties, the most reliable monolayer volume was stated to be  $53 \text{ cm}^3 \text{ g}_{Ni}^{-1}$  for degrees of reduction (obtained at 700–770 K) of 85–90%.

Finally an attempt was made to reconcile the various techniques for particle size estimation (Table 4). To do this it was necessary to assume a particle shape, and the results were evaluated both for spherical and hemispherical models, the former showing the greatest consistency. The particle size was defined as the cube root of the volume. The results obtained by the various methods are in quite close agreement (Table 4), and Coenen is justified in concluding “that the agreement between the methods is probably better than reported anywhere in the literature, which is the more remarkable when we note that measurements were carried out in ten different laboratories” [27].

The reserve stock of this catalyst is held by Professor Wells, University of Hull, UK.

### 11.1.3 Other EUROCAT Catalysts

#### 11.1.3.1 Vanadia–Titania EUROCAT Oxides

When the decision was made to extend the EUROCAT programme of standard catalysts to other types, there was no dispute as to which oxide catalyst should be selected: the  $V_2O_5/TiO_2$  system was the unanimous choice [9c–h, 28a–r]. The chief reasons were the following:

**Table 4.** Mean nickel particle sizes (nm) in EUROPT-1 determined by various methods [27].

Model <sup>a</sup>	$T_{red}$ (K)	XRD	$H_2$ chemisorption	XPS	Magnetic	TEM <sup>b</sup>
HS	723–773	2.2	2.1	2.4	–	2.2
HS	903–923	–	3.7	–	5.0	3.0
S	723–773	2.2	2.6	2.4	–	3.5
S	903–923	–	4.6	–	5.0	4.6

<sup>a</sup>HS = hemisphere, S = sphere.

<sup>b</sup>For the HS model, TEM mean sizes are divided by 1.56 because the projected area is greater than that corresponding to the cube root of the volume.

- (i) it was already the subject of attention in a number of European laboratories;
- (ii) it had important industrial uses for selective oxidations, especially of *o*-xylene to phthalic anhydride;
- (iii) it was active for the selective catalytic reduction (SCR) of nitrogen oxides ( $\text{NO}_x$ ) by  $\text{NH}_3$  and prototypical of those to be used in practice;
- (iv) determination of its structure and modes of operation presented a major intellectual challenge;
- (v) a great variety of analytical techniques could be directed to the problems and could be expected to contribute to their solution.

There was already a considerable body of knowledge on catalysts of this type [29]. For those used for selective oxidations, there was much evidence to show that the active phase was a monolayer of oxovanadium species chemically bonded to the  $\text{TiO}_2$  surface; such a material would have about 1 wt%  $\text{V}_2\text{O}_5$  for a  $\text{TiO}_2$  area of  $10\text{ m}^2\text{ g}^{-1}$ , but technical catalysts usually contained substantially larger amounts. The excess appeared to be in the form of  $\text{V}_2\text{O}_5$  microcrystals which neither helped nor hindered in selective oxidation; it seemed to serve as a reserve supply to replenish the monolayer, should it become depleted. There was also evidence that uncovered  $\text{TiO}_2$  surface was harmful, in that it could cause deep oxidation to carbon oxides. In these applications, the anatase form of  $\text{TiO}_2$  was generally used, and unless the contrary is stated the formula  $\text{TiO}_2$  will imply this form.

The first meeting of interested persons, held in May 1990, decided what precise formulations they would like to use, and thanks to the collaboration of Rhône-Poulenc CRA 4 kg quantities of two catalysts were prepared containing about 1% and 8%  $\text{V}_2\text{O}_5$ ; the corresponding precursors were also made available, i.e. the uncalcined materials, and also the support. Portions of the catalysts were distributed to some 25 laboratories. The work proceeded quickly; review meetings were held in April and November 1991, in July and November 1992, and finally in September 1993. The findings were reported in a special issue of *Catalysis Today* [28]. The project demonstrated in a forceful way the keen desire of European scientists to work together, and its success is all the more notable when it is appreciated that absolutely no special funding was available from any source to assist it. In this work we tried to acknowledge the help of everyone involved by naming them as *contributors*; those responsible for collecting the results and drafting the reports are called *compilers* [28a].

The catalysts were coded V1 and V8, and the support (an uncoated pigmentary anatase) EL10. They were prepared by mixing vanadyl oxalate solution with the support to form a paste that was kneaded before drying and calcination (4 h at 723 K) [28b]. Mean

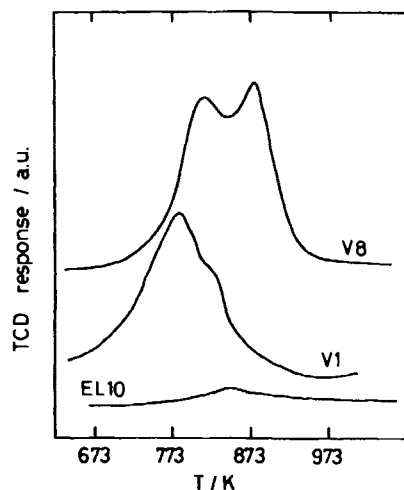


**Figure 8.** Temperature programmed reduction profiles of  $\text{V}_2\text{O}_5/\text{TiO}_2$  catalysts V8 (8%  $\text{V}_2\text{O}_5$ ), V1 (1%  $\text{V}_2\text{O}_5$ ) and of the support EL 10 [28g].

values for surface areas are EL10  $10.5\text{ m}^2\text{ g}^{-1}$ , V1  $10.1\text{ m}^2\text{ g}^{-1}$ , and V8  $11.0\text{ m}^2\text{ g}^{-1}$ ; they are not significantly different. The mean grain size of the anatase is about  $0.5\ \mu\text{m}$ , and the pore volume  $0.85\text{ cm}^3\text{ g}^{-1}$ ; the grains are nonmicroporous [28c]. X-ray diffraction measurements showed the presence of crystalline  $\text{V}_2\text{O}_5$  in V8, but probably not in V1; no other vanadium oxides were present, and no vanadium had dissolved in the anatase [28d].

Some points of interest arose in the chemical analysis. Total vanadium contents, estimated by complete dissolution of the catalysts in  $\text{H}_2\text{SO}_4$  or aqua regia, were close to the expected values of 0.975% for V1 and 7.82% for V8. Attempts were made to distinguish between “soluble” and “insoluble” vanadium, the former being crystalline or weakly held species, and the latter chemically linked to the  $\text{TiO}_2$  surface; it was also hoped to estimate the relative amounts of  $\text{V}^{\text{IV}}$  and  $\text{V}^{\text{V}}$  present. Treatments involving extraction with boiling isobutanol, with  $\text{NH}_4\text{OH}$  and with  $\text{H}_2\text{SO}_4$  were used; the kinetics of the reaction with  $\text{NH}_4\text{OH}$  was studied in detail. An approximately constant 0.12–0.16 wt% vanadium is designated as insoluble, which is much less than the amount forming a monolayer. Paradoxically,  $\text{V}^{\text{V}}$  is reduced to  $\text{V}^{\text{IV}}$  during the  $\text{H}_2\text{SO}_4$  extraction [28e].

Thermal analysis of the precursors showed decomposition in two stages, first an endothermic loss of water and then an exothermic loss of  $\text{CO}_2$ . With V8, the melting of  $\text{V}_2\text{O}_5$  was detected at higher temperature [28f]. TPR is a well-established technique for distinguishing between different reducible species. In the present system the monolayer species are more readily reducible than the crystalline form, and with V8 two peaks of comparable size are observed (Fig. 8). This requires some explaining: it has been suggested that

here is an intermediate disordered  $V_2O_5$  state, the reduction of which is not distinguishable from that of the monolayer species, and that together they account for about half the total. Reproducibility of TPR profiles requires exact control over a number of variables, and a recommended schedule has been given [28g]. The easier reduction of VI was also demonstrated in work designed to assess literature claims that the dispersion of the  $V_2O_5$  could be measured by chemisorption of  $O_2$  after reduction [28h].

A major effort was devoted to the characterization of these catalysts by vibrational and electronic spectroscopies [28i]. Use of IR and Raman spectroscopies confirmed that the monolayer consisted of vanadyl complexes, exhibiting both Lewis and Brønsted sites, and suppressing nucleophilic sites on the support. According to UV-VIS spectra, most of the vanadium in the calcined catalysts is in the  $V^V$  state, but part is easily reducible. Evidence for electronic interaction between vanadium and titanium ions was also presented. The monolayer is effective in suppressing Raman bands due to the anatase support, and an explanation for this effect has been offered [30].

Solid state  $^{51}V$  NMR spectroscopy in both the static (wide line) and magic angle spinning modes has been employed [28j]. The latter can detect small changes in the chemical shifts in different species, although very high spinning frequencies are needed to separate peaks from their spinning side-bands. The analytical power of solid state NMR spectroscopy in providing structural information seems to be somewhat limited, but in conjunction with other methods it is of great value. EPR measurements [28k] failed to detect significant quantities of  $V^{IV}$  species, but confirmed their formation in attack by  $H_2SO_4$ : their appearance in solid solution with the  $TiO_2$  following the phase transformation to rutile above about 970 K was also confirmed. TEM studies [28l] detected enrichment in vanadium at the edge of the  $TiO_2$  particles, and some unattached  $V_2O_5$  platelets in V8; electron-beam damage on prolonged examination was also noted. X-ray photoelectron (XPS) measurements by different laboratories yielded widely different results, especially in respect of V:Ti ratios, and recommended conditions for obtaining consistent results have been given [28m]. Secondary-ion mass spectrometry (SIMS) reveals the presence of numerous trace impurities, especially niobium, and provides some evidence for removal from the surface of species containing both V and Ti atoms [28n].

Electrical conductivity measurements posed the greatest difficulty, as the conclusions they led to were hard to reconcile with the models generated by the other techniques [28o]. These seemed to show that the calcined catalysts contained  $V^V$  ions in the  $TiO_2$  lattice, as they increased conductivity: their amount increased from VI to V8. It is not entirely clear whether they are

distinct from the monolayer species, or whether the latter are so firmly bonded to the  $TiO_2$  that they in effect become part of it, and hence increase its conductivity. The presence of anionic vacancies in the  $TiO_2$  was also detected.

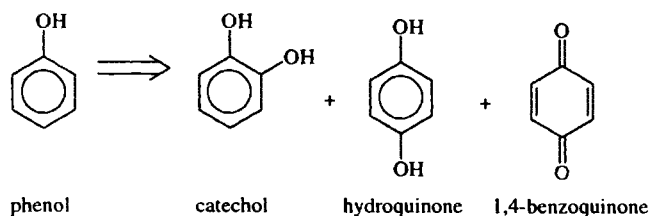
The catalytic activity of the EUROCAT oxides toward the selective oxidation of *o*-xylene was examined in several laboratories, with some discrepancies being apparent [9d, h, 28p]. In particular the temperatures required to achieve a given conversion varied somewhat and, since the reaction is extremely exothermic, the differences could be attributed to poor temperature control, or to the use of various bed dimensions and reactor materials. The means whereby catalytic rate measurements may be measured accurately and reproducibly in home-made apparatus requires further study.

The decomposition of isopropanol proceeds either via (A) dehydration to propene or (B) dehydrogenation to acetone. Both continuous- and pulse-flow measurements have shown that the reactions have similar rates on VI and V8, but (A) is faster than (B) on V8. Reaction (A) requires acid centers; these are entirely removed when the soluble vanadium species are removed by isobutanol or  $NH_4OH$  [28q].

These materials, the stocks of which are held by Professor Védrine, IRC, Lyon, France, must be (together with EUROPT-1 and EURONI-1) the most highly characterized catalysts now available. An attempt has been made to synthesize the observations into a model that portrays their structures [28r]. The main outline is clear: with VI the anatase surface is largely covered by a single layer of oxovanadium (vanadyl) groups, firmly attached, and perhaps interacting with the support so as to modify its electrical properties. This monolayer remains intact in V8, but the additional  $V_2O_5$  forms separate crystalites, perhaps as "towers" that obscure only a small part of the surface, and which are easily removed by chemical means. No doubt considerable refinement of this model is possible, especially in terms of "soluble" and "insoluble" forms. The information in this volume [28] provides much food for thought, and inspiration for further research.

### 11.1.3.2 EUROTTS-1 Zeolite

In a further extension of its interest to develop a range of standard catalysts, EUROCAT authorized a subgroup of its members to select a zeolite and to initiate a programme of work on its use [9i, 31]. The subgroup, under the leadership of Professor Jacobs, KU Leuven, chose titanium silicalite-1 (TS-1); in this zeolite, some



Scheme 1

of the silicon atoms in the silicalite structure are replaced by titanium. TS-1 is noted for its ability to catalyze the selective partial oxidation of organic substances by  $\text{H}_2\text{O}_2$ ; it thus represents new catalytic chemistry which forms the basis of important innovations in partial oxidation technology. More than 100 scientific publications and patents on its use have appeared in the decade following its discovery in 1983.

EUROTS-1 was synthesized (150 g) by hydrothermal treatment of a gel derived from ethyl orthosilicate and ethyl orthotitanate, in the presence of tetrapropylammonium hydroxide as template [31]. Each participating laboratory performed its own calcination (3 h or 16 h at a maximum temperature of 823 K, other conditions being variable). The Ti content was 2.8%, and the calcined product consisted of a single phase of orthorhombic symmetry, with a BET surface area of  $435 \text{ m}^2 \text{ g}^{-1}$ . Its IR and diffuse reflectance spectra (DRS) have been recorded. The material had the form of small rounded cubes of about  $0.15 \mu\text{m}$  size.

The chosen catalytic test reaction was the oxidation of phenol, which yields a mixture of catechol, hydroquinone, and 1,4-benzoquinone (Scheme 1). The reaction was conducted at atmospheric pressure by continuously adding aqueous  $\text{H}_2\text{O}_2$  to a mixture of catalyst, phenol, water, and a solvent (either methanol or acetone) at the reaction temperature (usually 373 K); reaction times were 1–4 h. Conversions and product selectivities depended on the composition of this mixture; under the best conditions,  $\text{H}_2\text{O}_2$  conversion was 100%, phenol conversion 27%, and phenol hydroxylation selectivity 91%. The ratio of *o*:*p*-substituted products (Scheme 1) was usually about unity. It was concluded that catalytic performance depended critically on calcination conditions, i.e. on the completeness of removal of the template. Many facets of the reaction remain to be investigated.

Unfortunately there is no reserve stock of this catalyst.

### 11.1.3.3 EUROCOMO Catalyst

Four laboratories have presented preliminary results on the hydrodesulfurization (HDS) of thiophene catalyzed by a Co–Mo/ $\gamma$ - $\text{Al}_2\text{O}_3$  catalyst of standard com-

position [9i–l]. Comparison of the conditions used for presulfiding and for conducting the reaction shows surprisingly wide variations in practice from one laboratory to another, and constitutes a strong argument for the adoption of more uniform routines. The catalyst deactivated slowly with use [9k], and was regarded as stable after either 2 h [28j] or 20 h [28l]. Emphasis was placed on the conditions needful to obtain meaningful kinetic information. In the work reported from the ETH Zürich [28j], a decrease in activation energy with increasing temperature was ascribed to diffusion limitation: at 673 K, variation of particle size signalled pore diffusion control, while film diffusion limited the rate at 723 K. In work performed in Strasbourg [28k] it had been shown that using  $\text{H}_2$  at atmospheric pressure made it possible to predict HDS activity under industrial conditions, but this depended on remaining within the conditions under which first-order kinetics obtained: low conversion (<2%) to minimize  $\text{H}_2\text{S}$  poisoning, and low thiophene concentrations (<26 mbar) were needed. Departure from these conditions leads to an underestimation of the activity of more active catalysts. Those working in this area will look forward to more detailed accounts of the work so far only described briefly.

## 11.1.4 Other Programmes

In addition to the work summarized above on catalysts launched by EUROCAT, several other programmes have been started by organizations or individuals, having aims somewhat related. The Japanese project (Section 11.1.4.1) encompasses a wider range of catalysts; less is known concerning the Russian programme (Section 11.1.4.2) due to the present poor state of communications. Catalysts prepared at Northwestern University (Evanston, Illinois, USA) were essentially for local use, although they have been used in some other laboratories (Section 11.1.4.3); the work of the American Society for Testing Materials (ASTM) (Section 11.1.4.4) and of the British Standards Institute (BSI) (Section 11.1.4.5) places emphasis on the development of testing methods. One other group began to investigate some catalyst precursors as potential standard materials, but the severe difficulties encountered in controlling the reduction of a Ni/ $\text{SiO}_2$  precursor (discussed in Section 11.1.2.3 above) led to the termination of the project (Section 11.1.4.6). Finally, some early work on standards for surface area measurement is recorded (Section 11.1.4.7).

### 11.1.4.1 Japanese Programme

This programme was initiated in 1978 by the Catalysis Society of Japan [8b]; its organization and method of

Table 5. Selected results for supported Pt catalysts in the Russian programme.

Code	Support	Pt (%)	BET area (m <sup>2</sup> g <sup>-1</sup> )	Pt <sup>x+</sup> (%)	H:Pt <sub>tot</sub> <sup>a</sup>	TOF <sup>b</sup>	TOF <sup>c</sup>
InCat Pt-1	SiO <sub>2</sub>	3.1	302	0	0.81	~1.0	2.3
EUROPT-1	SiO <sub>2</sub>	6.3	185	0	1.1	~0.4	1.7
InCat Pt-2	γ-Al <sub>2</sub> O <sub>3</sub>	2.6	172	60–65	1.51	~1.2	2.7
InCat Pt-3	γ-Al <sub>2</sub> O <sub>3</sub>	0.3	198	60–65	0.26	~1.7	5.0

<sup>a</sup>At  $P(\text{H}_2) = 50$  Torr, 293 K.

<sup>b</sup>TOF for C<sub>6</sub>H<sub>6</sub> hydrogenation at 373 K,  $P(\text{C}_6\text{H}_6) = 0.05$  bar, s<sup>-1</sup>.

<sup>c</sup>TOF for C<sub>6</sub>H<sub>12</sub> dehydrogenation at 573 K,  $P(\text{C}_6\text{H}_{12}) = 0.19$  bar, s<sup>-1</sup>, first day.

working have been described. Ten commercially available oxides that were either acidic catalysts in their own right or were usable as supports were chosen. Five were different types of alumina, two were silica-aluminas, and there was one silica, one NaY zeolite, and one anatase. Their surface areas, pore volumes, and purities have been given [8b].

Three major projects formed the first phase of the work:

- (i) Surface areas of the five aluminas were measured in eleven laboratories, using both volumetric and flow methods. Most of the results were within  $\pm 10\%$  of the mean, and it was shown that for a 15 min evacuation a temperature of 700 K was needed for proper outgassing.
- (ii) Various methods for assessing the acidity of the aluminas were tried. These included *n*-butylamine adsorption, pyridine adsorption followed both by IR spectroscopy and calorimetry, and NH<sub>3</sub> adsorption by calorimetry. Subsequently, results were published for the TPD of NH<sub>3</sub> from six zeolites that had been added to the programme [32].
- (iii) A number of supported metal catalysts were prepared using the supports listed above (0.5 and 5% Pt, and 0.5% Pd and Rh); both impregnation and ion exchange methods were used. A variety of techniques were used to estimate metal areas, including CO pulse and static methods, O<sub>2</sub> pulse and static methods, H<sub>2</sub>-O<sub>2</sub> titrations etc. The results were very varied, and no firm conclusions can be drawn from the published results [8b]. A further list, including nickel and ruthenium catalysts, was added at a later stage (see discussion following [8b]). A particular effort was made to standardize the CO pulse chemisorption procedure, with some measure of success, especially when H<sub>2</sub> was used as the carrier gas. No reference to subsequent work of this programme has yet been located, but references to isolated studies on the catalytic properties of the reference catalysts are cited in the original paper [8b].

#### 11.1.4.2 Russian Programme

Informal contacts with Russian scientists have established that a programme of study on the properties of three supported Pt catalysts has been initiated: some of their physical characteristics and catalytic activities are given in Table 5. Small samples of them are held by Professor Burch, Reading University, UK. Three laboratories in Russia are involved: the Boreskov Institute of Catalysis, Novosibirsk, (ii) the Boreskov Institute of Catalysis, Omsk Department (Professor Duplyakin), (iii) the Zelinsky Institute of Organic Chemistry, Moscow (Professor Kazansky). Emphasis is placed on distinguishing between metallic and ionic Pt, i.e. that not reducible at 773 K. The Pt/SiO<sub>2</sub> catalyst was made by adsorption from a solution of Pt(NH<sub>3</sub>)<sub>4</sub>Cl<sub>2</sub> at pH9, and the Pt/γ-Al<sub>2</sub>O<sub>3</sub> catalyst by adsorption from H<sub>2</sub>PtCl<sub>6</sub> solution at pH < 1 (at which pH some dissolution of the support might have been expected). After reduction, much of the Pt in the latter catalysts was in ionic form (Table 5). Selective chemisorption of H<sub>2</sub> and of O<sub>2</sub>, and O<sub>2</sub>-H<sub>2</sub> titrations, were performed, these techniques being only of limited value for the Pt/Al<sub>2</sub>O<sub>3</sub> catalysts. Pt concentrations for different grain sizes have been given, and, most interestingly, the Pt surface concentration in pores of various radii. This latter information was obtained by O<sub>2</sub> chemisorption after progressive filling of the pores with water. EXAFS and radial distribution function (RDF) measurements on samples reduced in H<sub>2</sub> and passivated in air show both Pt<sup>0</sup> and Pt<sup>x+</sup> in the Pt/SiO<sub>2</sub> but only Pt<sup>x+</sup> in the Pt/Al<sub>2</sub>O<sub>3</sub> catalysts. Quite thorough studies have been made of benzene hydrogenation and of cyclohexane dehydrogenation (Table 5); values for EUROPT-1 included in this table were measured by Russian scientists working on this programme. A marked inverse correlation between TOF and Pt loading for the dehydrogenation may be associated with a selective deactivation of the larger particles by coke, or with the metal surface concentration.

#### 11.1.4.3 Northwestern University Programme

Over the course of the last 15 or so years, a series of papers has been published (e.g. [33–35]), describing work on particle size and pretreatment effects in catalysis by supported metals. The catalysts involved have contained Pt, Pd, and Rh, with  $\text{SiO}_2$  or  $\text{Al}_2\text{O}_3$  as supports, the preparation methods being chosen to give as wide a range of dispersions as possible. As an example, a series of Rh/ $\text{SiO}_2$  catalysts was prepared [33] using either  $[\text{Rh}(\text{NH})_5(\text{H}_2\text{O})]\text{Cl}_3$  or  $\text{Rh}_4(\text{CO})_{12}$  or  $\text{Rh}_6(\text{CO})_{16}$ , the first-named being applied by ion exchange and the last two by impregnation. Various conditions of calcination and reduction led to the members of series having dispersions estimated by various chemisorption procedures of between about 10% and 150%. The latter figure reflects that H:Rh<sub>s</sub> ratios can exceed unity for small particles, and that CO can disrupt them, forming subcarbonyl species. Although it appears that small amounts of some of these catalysts were made available to other workers, it seems unlikely that large quantities were made or that samples were freely available: they cannot therefore be regarded as true standard catalysts.

#### 11.1.4.4 American Society for Testing Materials (ASTM)

The Society's Committee D-32 on Catalysts [8c] has developed specifications for a number of analytical methods pertinent to catalysts, and has issued a recommended procedure for testing fluidized cracking catalysts. It is believed that a number of reference materials, particularly those acting as analytical standards, may be available, but their use is not widely described in the scientific literature.

#### 11.1.4.5 British Standards Institute (BSI)

This organization has a long-established reputation for devising standard procedures for measurements of all kinds. A committee has recently drafted a specification for the determination of metal surface areas using gas adsorption techniques, and this has been published, as Part 4 of BS 4359, in 1995. Emphasis is placed on supported Pt catalysts, but guidance is given on other systems.

#### 11.1.4.6 IUPAC/SCI/NPL Programme

A group supported by IUPAC, the Society of Chemical Industry and the National Physical Laboratory (UK), attempted in the late 1970s to initiate a standard cata-

lyst programme [8d]. Of the several catalysts proposed, it seems that results only for a Ni/ $\text{SiO}_2$  catalyst have been published. Although a considerable amount of work was performed on the calcination and reduction of the precursor, which contained 11% Ni, all the complications described above in connection with EURONI-1 were encountered, and it is unlikely that those doing the work appreciated the complexity and sensitivity of the system. Benzene hydrogenation was used as the measure of catalytic activity. Discouraged by the problems uncovered, this group undertook no further work.

#### 11.1.4.7 Measurements of Surface Area and Porosity

As noted above, the texture of materials to be used as catalyst supports is of vital importance to the catalyst's ultimate performance, and the availability of reliable procedures of measuring surface area, pore volume and pore size distribution, and of reference materials for checking these procedures, is essential. Several groups have mounted programmes in this field [8e, 36].

The IUPAC/SCI/NPL programme on surface area standards examined a number of carbon blacks, activated charcoals, and silicas, and in the resulting publication [33] the results obtained in a number of laboratories were compared. As a result, two carbon blacks and two silicas lacking microporosity were accepted as standards. A major conclusion of this work, namely that outgassing conditions determine results obtained with high-area solids, was reinforced by the unsuccessful attempts made by the European Union's Community Bureau of Reference to obtain reproducible results with silica gels intended as reference standards [8e].

### 11.1.5 Summary and Conclusions

The value of having well-characterized materials as standards in studies of catalysis is appreciated by all who have used them. In this field, perhaps more than in any other part of chemistry, where performance depends so critically on so many variables, it is essential to have a range of catalysts by which the performance of equipment and operators may be judged.

On the whole, results obtained in commercial equipment are easily reproduced, except where, as in the outgassing of porous materials, an element of personal judgement remains. One clear area in which disagreement between laboratories seems to be the norm, and for which consensus is of the very essence, is the measurement of catalytic rates [6, 9h-1, 28p], and it is surely to this area more than any other that future research must be directed. Some attention has already

been given to questions of reactor design and of heat and mass transfer [9f], but the problems, especially for exothermic reactions, are not yet solved [28p]. It may be that the answer will lie in the use of apparatus of a standard design, such as that manufactured by Altamira Instruments. This company also provides informative notes on catalyst characterization; it is unfortunate that considerations of cost will deter many academic laboratories from using their equipment.

## References

- G. C. Bond, P. B. Wells, *Appl. Catal.* **1985**, *18*, 221–4.
- G. C. Bond, P. B. Wells, *Appl. Catal.* **1985**, *18*, 225–230.
- J. W. Geus, P. B. Wells, *Appl. Catal.* **1985**, *18*, 231–242.
- A. Frennet, P. B. Wells, *Appl. Catal.* **1985**, *18*, 243–257.
- P. B. Wells, *Appl. Catal.* **1985**, *18*, 259–272.
- G. C. Bond, F. Garin, G. Maire, *Appl. Catal.* **1988**, *41*, 313–335.
- G. C. Bond, Z. Paál, *Appl. Catal. A* **1992**, *86*, 1–35.
- Preparation of Catalysts III* (Eds: G. Poncelet, P. Grange, P. A. Jacobs), Elsevier, Amsterdam, **1983** (a) J. W. E. Coenen, P. B. Wells, p. 801–812; (b) Y. Murakami, p. 775–784; (c) R. J. Bertolacini, A. Neal, p. 767–772; (d) R. Burch, A. R. Flambard, M. A. Day, R. L. Moss, N. D. Parkyn, A. Williams, J. M. Winterbottom, A. White, p. 787–797; (e) N. Pernicone, p. 815–818; (f) M. Baerns, H. Hofmann, p. 821–830.
- EUROPACAT I*, first meeting of the European Federation of Catalysis Societies, Montpellier, September, **1993**, abstracts: (a) G. C. Bond, p. 973; (b) J. M. Evans, R. Burch, P. Welch, P. Hollins, p. 986; (c) G. C. Bond, J. C. Védrine, p. 974; (d) M. Baerns, J. Czekaj, C. R. Dias, G. Golinelli, B. Grzybowska, B. Majka, F. Majunke, M. Messori, M. F. Portela, F. Trifirò, p. 977; (e) J. M. Hermann, J. Disdier, p. 978; (f) J. Ph. Nogier, M. Delmar, p. 979; (g) J. Ph. Nogier, p. 980; (h) M. F. Portela, C. R. Dias, p. 981; (i) J. Martens, Ph. Buskens, P. Jacobs, A. Van der Pol, J. Van Hooff, C. Ferrini, H. Kouwenhoven, P. Kooyman, H. Van Bekkum, p. 975; (j) L. Medici, C. Zwicky, R. Prins, p. 976; (k) M. J. Ledoux, A. Peters, p. 983; (l) M. Breyse, D. Chadwick, T. Decamp, K. Hellgardt, A. Oen, p. 993.
- G. C. Bond, M. R. Gelsthorpe, *Appl. Catal.* **1987**, *35*, 169–176.
- V. Gutzmann, W. Vogel, *J. Phys. Chem.* **1990**, *94*, 4991.
- G. C. Bond, Xu Yide, *J. Chem. Soc. Faraday Trans. I* **1984**, *80*, 969–980.
- C. Hubert, A. Frennet, *Catal. Today* **1993**, *17*, 469–482.
- G. C. Bond, Lou Hui, *J. Catal.* **1994**, *147*, 346–348.
- G. C. Bond, Lou Hui, *J. Catal.* **1992**, *137*, 462–472.
- G. C. Bond, Lou Hui, *J. Catal.* **1993**, *142*, 512–530.
- Z. Paál, *Catal. Today* **1992**, *12*, 297.
- G. C. Bond, *J. Molec. Catal.* **1993**, *81*, 99–118.
- R. Burch, Z. Paál, *Appl. Catal. A* **1994**, *114*, 9–33.
- Z. Huang, J. R. Fryer, C. Park, D. Stirling, G. Webb, *J. Catal.* **1994**, *148*, 478–492.
- G. C. Bond, R. H. Cunningham, E. L. Short in *Proc. 10th Internat. Congr. Catal.* (Eds: L. Guzzi, F. Solymosi, P. Tétényi), Akadémiai Kiadó, Budapest, **1993**, Vol. A, p. 849.
- R. H. Cunningham, PhD Thesis, Brunel University, **1992**.
- G. C. Bond and M. R. Gelsthorpe, *J. Chem. Soc. Faraday Trans. I* **1989**, *85*, 3767–3783.
- G. C. Bond, R. H. Cunningham, J. C. Slaa, *Top. Catal.* **1994**, *1*, 19–24.
- J. W. E. Coenen, *Appl. Catal.* **1989**, *54*, 59–64.
- J. W. E. Coenen, *Appl. Catal.* **1989**, *54*, 65–78.
- J. W. E. Coenen, *Appl. Catal.* **1991**, *75*, 193–223.
- EUROCAT Oxide, Catal. Today* **1994**, *20*: (a) G. C. Bond, J. C. Védrine, p. 1–6; (b) E. Garcin, p. 7–10; (c) J. Haber, p. 11–16; (d) P. Ruiz, B. Delmon, p. 17–22; (e) J. Ph. Nogier, p. 23–34; (f) V. Rives, p. 37–44; (g) R. A. Koepfel, J. Nickl, A. Baiker, p. 45–52; (h) F. Majunke, M. Baerns, p. 53–60; (i) G. Busca, A. Zecchina, p. 61–76; (j) C. Fernandez, M. Guelton, p. 77–86; (k) A. Aboukais, p. 87–96; (l) M. de Boer, p. 97–108; (m) J. Ph. Nogier, M. Delamar, p. 109–124; (n) G. C. Bond, p. 125–134; (o) J.-M. Hermann, p. 135–152; (p) G. Golinelli, F. Trifirò, p. 153–164; (q) B. Grzybowska-Swierkosz, p. 165–170; (r) G. C. Bond, J. C. Védrine, p. 171–178.
- G. C. Bond, S. F. Tahir, *Appl. Catal.* **1991**, *71*, 1–31.
- D. N. Waters, *Spectrochim. Acta* **1994**, *50A*, 1833–1840.
- J. A. Martens, Ph. Buskens, P. A. Jacobs, A. Van der Pol, J. H. C. van Hooff, C. Ferrini, H. W. Kouwenhoven, P. J. Kooyman, H. van Bekkum, *Appl. Catal. A* **1993**, *99*, 71–84.
- M. Niwa, M. Iwamoto, K. Segawa, *Bull. Chem. Soc. Japan* **1986**, *59*, 3735–3739.
- Z. Karpiński, T.-K. Chuang, H. Katsuzawa, J. B. Butt, R. L. Burwell Jr., J. B. Cohen, *J. Catal.* **1986**, *99*, 184–197.
- J. B. Butt, R. L. Burwell Jr., *Catal. Today*, **1992**, *12*, 177–188.
- D. K. Takehara, J. B. Butt, R. L. Burwell Jr., *J. Catal.* **1992**, *133*, 279–293, 294–308.
- D. H. Everett, G. D. Parfitt, K. S. W. Sing, R. Wilson, *J. Appl. Chem. Biotechnol.* **1974**, *24*, 199–219.

## 11.2 IUPAC Recommendations

### 11.2.1 Reporting Physisorption Data for Gas/Solid Systems<sup>1</sup>

K. S. W. SING, D. H. EVERETT, R. A. W. HAUL, L. MOSCOU, R. A. PIEROTTI, J. ROUQUEROL AND T. SIEMIENIEWSKA

#### 11.2.1.1 Introduction

Gas adsorption measurements are widely used for determining the surface area and pore size distribution of a variety of different solid materials, such as industrial adsorbents, catalysts, pigments, ceramics and building materials. The measurement of adsorption at the gas/solid interface also forms an essential part of many fundamental and applied investigations of the nature and behaviour of solid surfaces.

Although the role of gas adsorption in the characterisation of solid surfaces is firmly established, there

<sup>1</sup> This Section was originally published in *Pure Appl. Chem.* **1985**, *57*, 603–619. © 1985 IUPAC.

is still a lack of general agreement on the evaluation, presentation and interpretation of adsorption data. Unfortunately, the complexity of most solid surfaces – especially those of industrial importance – makes it difficult to obtain any independent assessment of the physical significance of the quantities derived (e.g. the absolute magnitude of the surface area and pore size).

A number of attempts have been made [1], at a national level, to establish standard procedures for the determination of surface area by the BET-nitrogen adsorption method. In addition, the results have been published [2] of an SCI/IUPAC/NPL project on surface area standards. This project brought to light a number of potential sources of error in the determination of surface area by the gas adsorption method.

The purpose of the present Section is twofold: first to draw attention to the problems and ambiguities which have arisen in connection with the reporting of gas adsorption (physisorption) data; and second to formulate proposals for the standardization of procedures and terminology which will lead to a generally accepted code of practice. It does not aim to provide detailed operational instructions or to give a comprehensive account of the theoretical aspects of physisorption. The determination of the surface area of supported metals is not dealt with here – despite the importance of this topic in the context of heterogeneous catalysis – since this necessarily involves chemisorption processes.

The present proposals are based on, and are in general accordance with, the *Manual of Symbols and Terminology for Physicochemical Quantities and Units* [3–5].

### 11.2.1.2 General Definitions and Terminology

The definitions given here are essentially those put forward in Refs. 4 and 5. Where a caveat is added, it is intended to draw attention to a conceptual difficulty or to a particular aspect which requires further consideration.

*Adsorption* (in the present context, positive adsorption at the gas/solid interface) is the enrichment of one or more components in an interfacial layer. *Physisorption* (as distinct from *chemisorption*) is a general phenomenon: it occurs whenever an adsorbable gas (the *adsorptive*) is brought into contact with the surface of a solid (the *adsorbent*). The intermolecular forces involved are of the same kind as those responsible for the imperfection of real gases and the condensation of vapours. In addition to the attractive dispersion forces and the short-range repulsive forces, specific molecular interactions (e.g. polarization, field-dipole, field gradient-quadrupole) usually occur as a result of particular geometric and electronic properties of the adsorbent and adsorptive.

It is convenient to regard the interfacial layer as comprising two regions: the *surface layer* of the adsorbent (often simply called the *adsorbent surface*) and the *adsorption space* in which enrichment of the adsorptive can occur. The material in the adsorbed state is known as the *adsorbate*, as distinct from the adsorptive, i.e. the substance in the fluid phase which is capable of being adsorbed.

When the molecules of the adsorptive penetrate the surface layer and enter the structure of the bulk solid, the term *absorption* is used. It is sometimes difficult, impossible or irrelevant to distinguish between adsorption and absorption: it is then convenient to use the wider term *sorption* which embraces both phenomena and to use the derived terms *sorbent*, *sorbate* and *sorptive*.

The term *adsorption* may also be used to denote the process in which adsorptive molecules are transferred to, and accumulate in, the interfacial layer. Its counterpart, *desorption*, denotes the converse process, in which the amount adsorbed decreases. Adsorption and desorption are often used adjectivally to indicate the direction from which experimentally determined adsorption values have been approached, e.g. the adsorption curve (or point) and the desorption curve (or point). *Adsorption hysteresis* arises when the adsorption and desorption curves do not coincide.

The relation, at constant temperature, between the amount adsorbed (properly defined in Section 11.2.1.3.B) and the equilibrium pressure of the gas is known as the *adsorption isotherm*.

Many adsorbents of high surface area are porous and with such materials it is often useful to distinguish between the *external* and *internal* surface. The *external surface* is usually regarded as the envelope surrounding the discrete particles or agglomerates, but is difficult to define precisely because solid surfaces are rarely smooth on an atomic scale. A suggested convention is that the external surface be taken to include all the prominences and also the surface of those cracks which are wider than they are deep; the internal surface then comprises the walls of all cracks, pores and cavities which are deeper than they are wide and which are accessible to the adsorptive. In practice, the demarcation is likely to depend on the methods of assessment and the nature of the pore size distribution. Because the accessibility of pores may depend on the size and shape of the gas molecules, the area of, and the volume enclosed by, the internal surface as determined by gas adsorption may depend on the dimensions of the adsorptive molecules (*molecular sieve* effect). The roughness of a solid surface may be characterized by a *roughness factor*, i.e. the ratio of the external surface to the chosen geometric surface.

In the context of physisorption, it is expedient to classify pores according to their sizes:



- (i) pores with widths exceeding about 50 nm (0.05  $\mu\text{m}$ ) are called *macropores*;
- (ii) pores of widths between 2 nm and 50 nm are called *mesopores*;
- (iii) pores with widths not exceeding about 2 nm are called *micropores*.

These limits are to some extent arbitrary since the pore filling mechanisms are dependent on the pore shape and are influenced by the properties of the adsorbent and by the adsorbent-adsorbate interactions. The whole of the accessible volume present in micropores may be regarded as adsorption space and the process which then occurs is *micropore filling*, as distinct from surface coverage which takes place on the walls of open macropores or mesopores. Micropore filling may be regarded as a primary physisorption process (see Section 8); on the other hand, physisorption in mesopores takes place in two more or less distinct stages (monolayer-multilayer adsorption and capillary condensation).

In *monolayer adsorption* all the adsorbed molecules are in contact with the surface layer of the adsorbent. In *multilayer adsorption* the adsorption space accommodates more than one layer of molecules so that not all adsorbed molecules are in direct contact with the surface layer of the adsorbent. In *capillary condensation* the residual pore space which remains after multilayer adsorption has occurred is filled with condensate separated from the gas phase by menisci. Capillary condensation is often accompanied by hysteresis. The term capillary condensation should not be used to describe micropore filling because this process does not involve the formation of liquid menisci.

For physisorption, the *monolayer capacity* ( $n_m$ ) is usually defined as the amount of adsorbate (expressed in appropriate units) needed to cover the surface with a complete monolayer of molecules [4]. In some cases this may be a close-packed array but in others the adsorbate may adopt a different structure. Quantities relating to monolayer capacity may be denoted by the subscript m. The *surface coverage* ( $\theta$ ) for both monolayer and multilayer adsorption is defined as the ratio of the amount of adsorbed substance to the monolayer capacity.

The *surface area* ( $A_s$ ) of the adsorbent may be calculated from the monolayer capacity ( $n_m^a$  in moles), provided that the area ( $a_m$ ) effectively occupied by an adsorbed molecule in the complete monolayer is known.

Thus,

$$A_s = n_m^a L a_m$$

where  $L$  is the Avogadro constant. The *specific surface area* ( $a_s$ ) refers to unit mass of adsorbent:

$$a_s = \frac{A_s}{m}$$

Ref. 4 recommends the symbols  $A$ ,  $A_s$  or  $S$  and  $a$ ,  $a_s$  or  $s$  for area and specific area, respectively, but  $A_s$  and  $a_s$  are preferred to avoid confusion with Helmholtz energy  $A$  or entropy  $S$ .

In the case of micropore filling, the interpretation of the adsorption isotherm in terms of surface coverage may lose its physical significance. It may then be convenient to define a *monolayer equivalent area* as the area, or specific area, respectively, which would result if the amount of adsorbate required to fill the micropores were spread in a close-packed monolayer of molecules (see Section 11.2.1.8).

### 11.2.1.3 Methodology

#### A Methods for the Determination of Adsorption Isotherms

The many different procedures which have been devised for the determination of the amount of gas adsorbed may be divided into two groups: (a) those which depend on the measurement of the amount of gas removed from the gas phase (i.e. gas volumetric methods) and (b) those which involve the measurement of the uptake of the gas by the adsorbent (e.g. direct determination of increase in mass by gravimetric methods). Many other properties of the adsorption system may be related to the amount adsorbed, but since they require calibration they will not be discussed here. In practice, static or dynamic techniques may be used to determine the amount of gas adsorbed.

In the static volumetric determination a known quantity of pure gas is usually admitted to a confined volume containing the adsorbent, maintained at constant temperature. As adsorption takes place, the pressure in the confined volume falls until equilibrium is established. The amount of gas adsorbed at the equilibrium pressure is given as the difference between the amount of gas admitted and the amount of gas required to fill the space around the adsorbent, i.e. the *dead space*, at the equilibrium pressure. The adsorption isotherm is usually constructed point-by-point by the admission to the adsorbent of successive charges of gas with the aid of a volumetric dosing technique and application of the gas laws. The volume of the dead space must, of course, be known accurately: it is obtained (see Section B) either by pre-calibration of the confined volume and subtracting the volume of the adsorbent (calculated from its density), or by the admission of a gas which is adsorbed to a negligible extent (see Section B) Nitrogen adsorption isotherms at the temperature of the boiling point of nitrogen at ambient atmospheric pressure are generally determined by the volumetric method; they provide the basis for the various standard

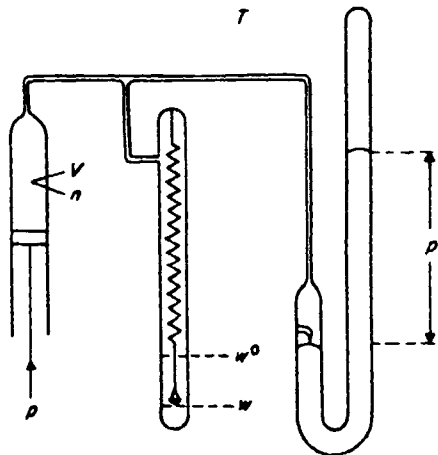


Figure 1. Schematic arrangement of a simultaneous volumetric and gravimetric adsorption experiment.

procedures which have been proposed for the determination of surface area [1-5].

Recent developments in vacuum microbalance techniques have revived the interest in gravimetric methods for the determination of adsorption isotherms. With the aid of an *adsorption balance* the change in weight of the adsorbent may be followed directly during the out-gassing and adsorption stages. A gravimetric procedure is especially convenient for measurements with vapours at temperatures not too far removed from ambient. At both high and low temperatures, however, it becomes difficult to control and measure the exact temperature of the adsorbent, which is particularly important in the determination of mesopore size distribution.

In principle, a 'continuous' procedure can be used to construct the isotherm under quasi-equilibrium conditions: the pure adsorptive is admitted (or removed) at a slow and constant rate and a volumetric or gravimetric technique used to follow the variation of the amount adsorbed with increase (or decrease) in pressure. A carrier gas technique, making use of conventional gas chromatographic equipment, may be employed to measure the amount adsorbed provided that the adsorption of the carrier gas is negligible. In all types of measurement involving gas flow it is essential to confirm that the results are not affected by change in flow rate and to check the agreement with representative isotherms determined by a static method.

## B Operational Definitions of Adsorption

To examine the fundamental basis on which experimental definitions depend, consider an adsorption experiment incorporating both volumetric and gravimetric measurements (see Fig. 1). A measured amount,  $n$ , of a specified gas (for simplicity, adsorption of a single gas is considered here), is introduced into the system whose total volume,  $V$ , can be varied at con-

stant temperature,  $T$ . Measurements are made of  $V$ ,  $p$  (the equilibrium pressure) and  $w$  (the apparent mass,  $m$ , of adsorbent).

In a calibration experiment the balance pan contains no adsorbent. The total volume,  $V^0$ , of the system is now simply related to the amount,  $n^0$ , of gas admitted:

$$V^0 = n^0 v^g(T, p),$$

where  $v^g(T, p)$  is the molar volume of the gas at  $T$  and  $p$ , and is known from its equation of state. If the buoyancy effect arising from the balance itself is negligible, the apparent weight will remain constant. Since the gas concentration,  $c^0 = 1/v^g$ , is constant throughout the volume  $V^0$ ,

$$n^0 = \int_{\text{all } V^0} c^0 dV = c^0 v^0 = \frac{V^0}{v^g}.$$

A mass,  $m$ , of adsorbent (weighing  $w^0$  in vacuum) is now introduced and the experiment repeated using the same amount of gas. If adsorption is detectable at the given  $T$ ,  $p$ , the volume  $V$  will usually be less than  $V^0$  and the apparent weight of the adsorbent will increase from  $w^0$  to  $w$ .

$V/v^g$  is the amount of gas which would be contained in the volume  $V$  if the gas concentration were uniform throughout the volume. That the amount actually present is  $n^0$  means that local variations in gas concentration must occur: the gas concentration within the bulk of the solid is zero, but is greater than  $c^0$  in the interfacial layer. The difference between  $n^0$  and  $V/v^g$  may be called the *apparent adsorption*

$$n^a(\text{app}) = n^0 - V/v^g,$$

and is a directly observable quantity. The precision with which it can be measured is controlled only by the experimental precision in  $T$ ,  $p$  and  $V$ , and by the reliability with which  $v^g$  (and  $c^0$ ) can be calculated from the equation of state of the gas.

The apparent adsorption may, alternatively, be defined by measuring the amount of gas which has to be added to the system at constant  $T$ ,  $p$  to increase the volume  $V$  back to  $V^0$ . The apparent adsorption is then equal to the extra amount of gas which can be accommodated in a volume  $V^0$  at a given  $T$ ,  $p$  when the solid is introduced. It can, therefore, be expressed in terms of the local deviations of the concentration,  $c$ , of adsorptive molecules, from the bulk concentration  $c^0$ :

$$n^a(\text{app}) = \int_{V^0} (c - c^0) dV.$$

If the gas does not penetrate into the bulk solid (i.e. is not *absorbed*), the above integral consists of two parts, that over the volume occupied by the solid ( $V^s$ ) within which  $c = 0$ , and that over the adsorption space plus the gas phase volume, which taken together is denoted by  $V^g$ :

$$n^a(\text{app}) = -c^0 V^s + \int_{V^g} (c - c^0) dV.$$

The first term represents the amount of gas excluded by the solid, while the second is the extra amount of gas accommodated because of the accumulation of gas in the neighbourhood of the solid surface. If the adsorption is very weak the first term may exceed the second and the apparent adsorption may be negative ( $V > V^0$ ).

The quantity

$$n^a = n^a(\text{app}) + c^0 V^s \int_{V^g} (c - c^0) dV$$

is thus equal to the *Gibbs adsorption* (surface excess amount of adsorbed substance, cf. [4]) when the surface of the solid is taken as the Gibbs dividing surface: it is the difference between the amount of substance actually present in the interfacial layer and that which would be present at the same equilibrium gas pressure in a reference system in which the gas phase composition is constant up to the Gibbs surface, and in which no adsorptive penetrates into the surface layer or the bulk of the solid.

The operational definition of  $n^a$  is thus

$$n^a = \int_{V^g} (c - c^0) dV = n - c^0 V^g,$$

where  $n$  is the total amount of gas admitted.

The precision with which  $n^a$  can be determined depends, not only on the precision of  $T$ ,  $p$ ,  $V$  and  $v^g$  but also on the precision with which  $V^s$  (and hence  $V^g$ ) is known.

The volume of the solid (i.e. the volume enclosed by the Gibbs surface) is often defined experimentally as that volume which is not accessible to a nonsorbable gas (e.g. helium – leading to the *helium dead space*). In making this identification it is assumed that the volume available to He atoms is the same as that for molecules of the gas under investigation (which is not true, for example, if the solid acts as a molecular sieve, or if the molecules of the gas are significantly larger than the He atom), and that the solid does not swell under the influence of the adsorbate. Helium adsorption may occur if the solid contains very fine pores (or pore entrances) and the only proof that the adsorption is zero is that the apparent value of  $V^s$  is independent of temperature. It is usual to take the high temperature limit of  $V^s$  as being the correct value, but if  $V^s$  is determined at a temperature widely different from that used in an adsorption experiment, a correction for the thermal expansion of the solid may be required.

Alternatively,  $V^s$  may be estimated from the known density of the bulk solid with the implied assumption that this is the same as that of the material of the adsorbent.

The above discussion in terms of the volumetric technique when applied to gravimetric measurements gives for the apparent change in weight

$$\Delta w = w - w_0 = \left[ n^a - \frac{V^s}{v^g} \right] M$$

where  $M$  is the molar mass of the adsorptive.

$$\text{Thus } n^a = \frac{\Delta w}{M} + \frac{V^s}{v^g}.$$

The second term on the right-hand-side is the buoyancy correction which has the same origin as the deadspace correction in a volumetric determination.

An alternative but less useful definition of adsorption is

$$n^s = \int_{V_a} c dV$$

where  $V_a = \tau A_s$  is the volume of the interfacial layer and  $c$  is the local concentration.  $V_a$  has to be defined on the basis of some appropriate model of gas adsorption which gives a value of  $\tau$  the layer thickness. Provided that the equilibrium pressure is sufficiently low and the adsorption not too weak, then

$$n^s = n^a;$$

the surface excess amount ( $n^a$ ) and total amount ( $n^s$ ) of substance in the adsorbed layer become indistinguishable and the general term *amount adsorbed* is applicable to both quantities.

### 11.2.1.4 Experimental Procedures

#### A Outgassing the Adsorbent

Prior to the determination of an adsorption isotherm all of the physisorbed species should be removed from the surface of the adsorbent. This may be achieved by outgassing, i.e. exposure of the surface to a high vacuum – usually at elevated temperature. To obtain reproducible isotherms, it is necessary to control the outgassing conditions (temperature programme, change in pressure over the adsorbent and the residual pressure) to within limits which depend on the nature of the adsorption system. Instead of exposing the adsorbent to a high vacuum, it is sometimes expedient to achieve adequate cleanliness of the surface by flushing the adsorbent with an inert gas (which may be the adsorptive) at elevated temperature. With certain microporous solids reproducible isotherms are only obtained after one or more adsorption-desorption cycles. This problem can be overcome by flushing with the adsorptive and subsequent heating in vacuum.

Where physisorption measurements are to be employed for the determination of surface area and/or porosity, the rigorous surface cleanliness required in chemisorption studies is unnecessary and outgassing to a residual pressure of  $\approx 10$  mPa is usually considered satisfactory. Such conditions are readily achieved with the aid of conventional vacuum equipment – usually a combination of a rotary and diffusion pump in conjunction with a liquid nitrogen trap. The rate of desorption is strongly temperature dependent and to minimize the outgassing time, the temperature should be the maximum consistent with the avoidance of changes in the nature of the adsorbent and with the achievement of reproducible isotherms. Outgassing at too high a temperature or under ultra high vacuum conditions (residual pressure  $< 1$   $\mu$ Pa), as well as flushing with certain gases may lead to changes in the surface composition, e.g. decomposition of hydroxides or carbonates, formation of surface defects or irreversible changes in texture.

For most purposes the outgassing temperature may be conveniently selected to lie within the range over which the thermal gravimetric curve obtained in vacuo exhibits a minimum slope.

To monitor the progress of outgassing, it is useful to follow the change in gas pressure by means of suitable vacuum gauges and, if the experimental technique permits, the change in weight of the adsorbent. Further information on the effect of outgassing may be obtained by the application of temperature programmed desorption in association with evolved gas analysis (e.g. using mass spectrometry).

## B Determination of the Adsorption Isotherm

It is essential to take into account a number of potential sources of experimental error in the determination of an adsorption isotherm. In the application of a volumetric technique involving a dosing procedure it must be kept in mind that any errors in the measured doses of gas are cumulative and that the amount remaining unadsorbed in the dead space becomes increasingly important as the pressure increases. In particular, the accuracy of nitrogen adsorption measurements at temperatures of about 77 K will depend on the control of the following factors:

- (i) Gas burettes and other parts of the apparatus containing appreciable volumes of gas must be thermostatted, preferably to  $\pm 0.1$  °C. If possible the whole apparatus should be maintained at reasonably constant temperature.
- (ii) The pressure must be measured accurately (to  $\pm 10$  Pa). If a mercury manometer is used the tubes should be sufficiently wide, preferably  $\approx 1$  cm in diameter.

- (iii) The level of liquid nitrogen in the cryostat bath must be kept constant to within a few millimetres, preferably by means of an automatic device.
- (iv) The sample bulb must be immersed to a depth of at least 5 cm below the liquid nitrogen level.
- (v) The temperature of the liquid nitrogen must be monitored, e.g. by using a suitably calibrated nitrogen or oxygen vapour pressure manometer or a suitable electrical device.
- (vi) The nitrogen used as adsorptive must be of purity not less than 99.9%.
- (vii) The conditions chosen for pretreatment of the adsorbent must be carefully controlled and monitored (i.e. the outgassing time and temperature and the residual pressure, or conditions of flushing with adsorptive).
- (viii) It is recommended that the *outgassed weight* of the adsorbent should be determined either before or after the adsorption measurements. In routine work it may be convenient to admit dry air or nitrogen to the sample after a final evacuation under the same conditions as those used for the pretreatment.

In the application of a gravimetric technique, (ii) to (viii) must be taken into account and also special attention must be given to the control and measurement of the adsorbent temperature and to the assessment of the buoyancy corrections. Thermal transpiration effects should be allowed for if volumetric or gravimetric measurements are made at low pressure.

## 11.2.1.5 Evaluation of Adsorption Data

### A Presentation of Primary Data

The quantity of gas adsorbed may be measured in any convenient units: moles, grams and cubic centimetres at s.t.p. have all been used. For the presentation of the data it is recommended that the amount adsorbed should be expressed in moles per gram of the *outgassed* adsorbent. The mode of outgassing and if possible the composition of the adsorbent should be specified and its surface characterized. To facilitate the comparison of adsorption data it is recommended that adsorption isotherms be displayed in graphical form with the amount adsorbed (preferably  $n^a$  in  $\text{mol g}^{-1}$ ) plotted against the equilibrium relative pressure ( $p/p^0$ ), where  $p^0$  is the saturation pressure of the pure adsorptive at the temperature of the measurement, or against  $p$  when the temperature is above the critical temperature of the adsorptive. If the adsorption measurements are made under conditions where the gas phase deviates appreciably from ideality (e.g. at high pressure), it is desirable that the isotherms should be presented in terms of gas

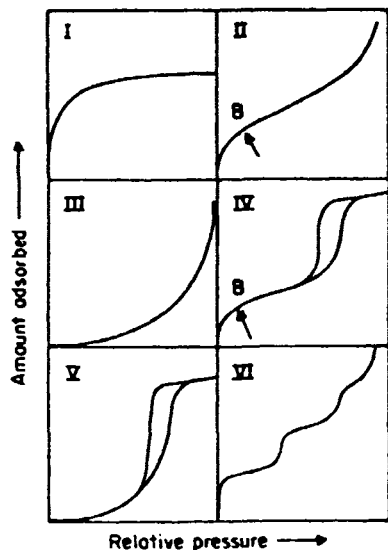


Figure 2. Types of physisorption isotherms.

fugacity rather than pressure. If the surface area of the adsorbent is known the amount adsorbed may be expressed as number of molecules, or moles per unit area (i.e.  $N^a$  molecules  $m^{-2}$  or  $n^a$  mol  $m^{-2}$ ). Adsorption data obtained with well-defined systems should be given in tabular form, but if this is not possible they should be deposited in an accessible source.

### B Classification of Adsorption Isotherms

The majority of physisorption isotherms may be grouped into the six types shown in Figure 2. In most cases, at sufficiently low surface coverage the isotherm reduces to a linear form (i.e.  $n^a \propto p$ ), with is often referred to as the Henry's Law region (On heterogeneous surfaces this linear region may fall below the lowest experimentally measurable pressure).

The reversible *Type I* isotherm (Type I isotherms are sometimes referred to as *Langmuir isotherms*, but this nomenclature is not recommended) is concave to the  $p/p^0$  axis and  $n^a$  approaches a limiting value as  $p/p^0 \rightarrow 1$ . Type I isotherms are given by microporous solids having relatively small external surfaces (e.g. activated carbons, molecular sieve zeolites and certain porous oxides), the limiting uptake being governed by the accessible micropore volume rather than by the internal surface area.

The reversible *Type II* isotherm is the normal form of isotherm obtained with a nonporous or macroporous adsorbent. The Type II isotherm represents unrestricted monolayer-multilayer adsorption. Point B, the beginning of the almost linear middle section of the isotherm, is often taken to indicate the stage at which monolayer coverage is complete and multilayer adsorption about to begin.

The reversible *Type III* isotherm is convex to the  $p/p^0$  axis over its entire range and therefore does not exhibit a Point B. Isotherms of this type are not common, but there are a number of systems (e.g. nitrogen on polyethylene) which give isotherms with gradual curvature and an indistinct Point B. In such cases, the adsorbate-adsorbate interactions play an important role.

Characteristic features of the *Type IV* isotherm are its hysteresis loop, which is associated with capillary condensation taking place in mesopores, and the limiting uptake over a range of high  $p/p^0$ . The initial part of the Type IV isotherm is attributed to monolayer-multilayer adsorption since it follows the same path as the corresponding part of a Type II isotherm obtained with the given adsorbent on the same surface area of the adsorbent in a nonporous form. Type IV isotherms are given by many mesoporous industrial adsorbents.

The *Type V* isotherm is uncommon; it is related to the Type III isotherm in that the adsorbent-adsorbate interaction is weak, but is obtained with certain porous adsorbents.

The *Type VI* isotherm, in which the sharpness of the steps depends on the system and the temperature, represents stepwise multilayer adsorption on a uniform nonporous surface. The step height now represents the monolayer capacity for each adsorbed layer and, in the simplest case, remains nearly constant for two or three adsorbed layers. Amongst the best examples of Type VI isotherms are those obtained with argon or krypton on graphitised carbon blacks at liquid nitrogen temperature.

### C Adsorption Hysteresis

Hysteresis appearing in the multilayer range of physisorption isotherms is usually associated with capillary condensation in mesopore structures. Such hysteresis loops may exhibit a wide variety of shapes. Two extreme types are shown as *H1* (formerly Type A) and *H4* in Figure 3. In the former the two branches are almost vertical and nearly parallel over an appreciable range of gas uptake, whereas in the latter they remain nearly horizontal and parallel over a wide range of  $p/p^0$ . In certain respects *Types H2* and *H3* (formerly termed Types E and B, respectively) may be regarded as intermediate between these two extremes. A feature common to many hysteresis loops is that the steep region of the desorption branch leading to the lower closure point occurs (for a given adsorbent at a given temperature) at a relative pressure which is almost independent of the nature of the porous adsorbent but depends mainly on the nature of the adsorbent (e.g. for nitrogen at its boiling point at  $p/p^0 \approx 0.42$  and for benzene at  $25^\circ C$  at  $p/p^0 \approx 0.28$ ).

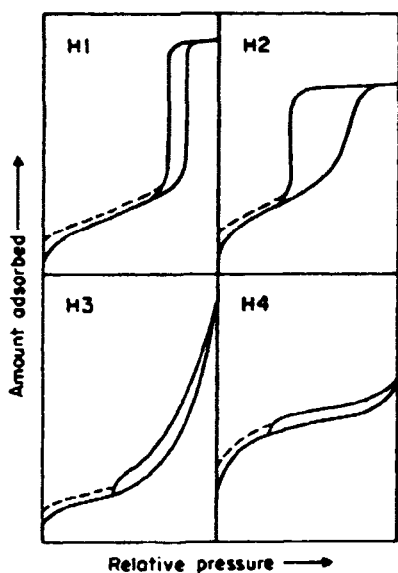


Figure 3. Types of hysteresis loops.

Although the effect of various factors on adsorption hysteresis is not fully understood, the shapes of hysteresis loops have often been identified with specific pore structures. Thus, *Type H1* is often associated with porous materials known, from other evidence, to consist of *agglomerates* (An *agglomerate* is defined as an assemblage of particles rigidly joined together and an *aggregate* as an assemblage of particles which are loosely coherent) or compacts of approximately uniform spheres in fairly regular array, and hence to have narrow distribution of pore size. Many porous adsorbents (e.g. inorganic oxide gels and porous glasses) tend to give *Type H2* loops, but in such systems the distribution of pore size and shape is not well-defined. Indeed, the *H2* loop is especially difficult to interpret: in the past it was attributed to a difference in mechanism between condensation and evaporation processes occurring in pores with narrow necks and wide bodies (often referred to as 'ink bottle' pores), but it is now recognized that this provides an oversimplified picture and the role of network effects must be taken into account.

The *Type H3* loop, which does not exhibit any limiting adsorption at high  $p/p^0$ , is observed with aggregates of plate-like particles giving rise to slit-shaped pores. Similarly, the *Type H4* loop is often associated with narrow slit-like pores, but in this case the *Type I* isotherm character is indicative of microporosity.

With many systems, especially those containing micropores, *low pressure hysteresis* (indicated by the dashed lines in Figure 3), may be observed extending to the lowest attainable pressures. Removal of the residual adsorbed material is then possible only if the adsorbent is outgassed at higher temperatures. This

phenomenon may be associated with the swelling of a nonrigid porous structure or with the irreversible uptake of molecules in pores (or through pore entrances) of about the same width as that of the adsorbate molecule or in some instances with an irreversible chemical interaction of the adsorbate with the adsorbent.

### 11.2.1.6 Determination of Surface Area

#### A Application of the BET Method

The Brunauer–Emmett–Teller (BET) gas adsorption method has become the most widely used standard procedure for the determination of the surface area of finely-divided and porous materials, in spite of the oversimplification of the model on which the theory is based.

It is customary to apply the BET equation in the linear form

$$\frac{P}{n^a \times (p^0 - p)} = \frac{1}{n_m^a \times C} + \frac{(C - 1) p}{n_m^a \times C p^0}$$

where  $n^a$  is the amount adsorbed at the relative pressure  $p/p^0$  and  $n_m^a$  is the monolayer capacity.

According to the BET theory  $C$  is related exponentially to the enthalpy (heat) of adsorption in the first adsorbed layer. It is now generally recognized, however, that although the value of  $C$  may be used to characterize the shape of the isotherm in the BET range it does not provide a quantitative measure of enthalpy of adsorption but merely gives an indication of the magnitude of the adsorbent–adsorbate interaction energy. Thus, in reporting BET data it is recommended that  $C$  values are stated, but not converted to enthalpies of adsorption.

A high value of  $C$  ( $\approx 100$ ) is associated with a sharp knee in the isotherm, thus making it possible to obtain by visual inspection the uptake at Point B, which usually agrees with  $n^a$  derived from the above equation to within a few per cent. On the other hand, if  $C$  is low ( $<20$ ) Point B cannot be identified as a single point on the isotherm. Since Point B is not itself amenable to any precise mathematical description, the theoretical significance of the amount adsorbed at Point B is uncertain.

The BET equation requires a linear relation between  $p/n^a(p^0 - p)$  and  $p/p^0$  (i.e. the BET plot). The range of linearity is restricted to a limited part of the isotherm – usually not outside the  $p/p^0$  range of 0.05–0.30. Some adsorption systems give linear (or nearly linear) BET plots over several ranges of  $p/p^0$ , but it is only in the region around  $\theta = 1$  that the BET plot can be expected to yield the true value of  $n_m^a$ . This range is shifted to lower relative pressures in the case of systems having high adsorption energies, especially if the surface is energetically homogeneous, e.g. for the adsorption of

nitrogen or argon on graphitized carbon or xenon on clean metal films.

The second stage in the application of the BET method is the calculation of the surface area (often termed the *BET area*) from the monolayer capacity. This requires a knowledge of the average area,  $a_m$  (*molecular cross-sectional area*), occupied by the adsorbate molecule in the complete monolayer. Thus

$$A_s(\text{BET}) = n_m^a \times L \times a_m$$

and

$$a_s(\text{BET}) = A_s(\text{BET})/m$$

where  $A_s(\text{BET})$  and  $a_s(\text{BET})$  are the total and specific surface areas, respectively, of the adsorbent (of mass  $m$ ) and  $L$  is the Avogadro constant.

At the present time, nitrogen is generally considered to be the most suitable adsorptive for surface area determination and it is usually assumed that the BET monolayer is close-packed, giving  $a_m(\text{N}_2) = 0.162 \text{ nm}^2$  at 77 K. With a wide range of adsorbents it appears that the use of this value leads to BET areas which are within 20 per cent of the true surface areas. The existence of a strictly constant value of  $a_m(\text{N}_2)$  is unlikely, however, and a growing amount of evidence suggests that it may vary by up to about 20 per cent from one surface to another. With other adsorptives, arbitrary adjustments of the  $a_m$  value are generally required to bring the BET area into agreement with the nitrogen value. The adjusted values of  $a_m$  for a particular adsorptive are dependent on temperature and the adsorbent surface. They may also differ appreciably from the value calculated for the close-packed monolayer on the basis of the density of the liquid or solid adsorptive. In view of this situation and the fact that full nitrogen isotherms may be conveniently measured at temperatures  $\approx 77 \text{ K}$ , it is recommended that nitrogen should continue to be used for the determination of both surface area and mesopore size distribution (Section 11.2.1.7.C).

The standard BET procedure requires the measurement of at least three and preferably five or more points in the appropriate pressure range on the  $\text{N}_2$  adsorption isotherm at the normal boiling point of liquid nitrogen.

For routine measurements of surface areas, e.g. of finely divided or porous industrial products, a simplified procedure may be used involving the determination of only a single point on the adsorption isotherm, lying within the linear range of the BET plot. On many solids the value of  $C$  for  $\text{N}_2$ , is usually sufficiently large ( $>100$ ) to warrant the assumption that the BET straight line passes through the origin of the co-ordinate system. Thus

$$n_m^a = n^a(1 - p/p^0).$$

The validity of the simplifying assumption is usually within the variance of surface area determinations but needs to be checked for the particular system either by calibration against the standard BET procedure or by using surface area reference samples of the same material (see Section 11.2.1.6.B).

It is strongly recommended that in reporting  $a_s(\text{BET})$  values, the conditions of outgassing (see Section 11.2.1.4.A), the temperature of the measurements, the range of linearity of the BET plot, the values of  $p^0$ ,  $n_m^a$ ,  $a_m$  and  $C$  should all be stated.

If the standard BET procedure is to be used, it should be established that monolayer-multilayer formation is operative and is not accompanied by micropore filling (Section 11.2.1.8.C), which is usually associated with an increase in the value of  $C$  ( $>200$ , say). It should be appreciated that the BET analysis does not take into account the possibility of micropore filling or penetration into cavities of molecular size. These effects can thus falsify the BET surface areas and in case of doubt their absence should be checked by means of an empirical method of isotherm analysis or by using surface area reference samples (see Section 11.2.1.6.B).

For the determination of *small specific surface areas* ( $<5 \text{ m}^2 \text{ g}^{-1}$ , say) adsorptives with relatively low vapour pressure are used in order to minimize the dead space correction, preferably krypton or xenon at liquid nitrogen temperature. In the case of krypton, use of the extrapolated  $p^0$  value for the supercooled liquid tends to give a wider range of linearity in the BET plot and larger monolayer capacities (the difference being  $<10\%$ ) as compared with those from  $p^0$  for the solid. Evaluation of surface areas is further complicated by the difficulty in choosing the value of  $a_m$  which is found to vary from solid to solid if compared with the BET nitrogen areas ( $a_m(\text{Kr}) = 0.17\text{--}0.23 \text{ nm}^2$ ;  $a_m(\text{Xe}) = 0.17\text{--}0.27 \text{ nm}^2$ ). Since no generally valid recommendations can be made, it is essential to state the chosen  $p^0$  and  $a_m$  values.

Ultrahigh vacuum techniques (basic pressure  $\approx 10^2 \text{ } \mu\text{Pa}$ ) enable adsorption studies to be made on stringently *clean solid surfaces* whereas degassing under moderate vacuum conditions, as normally applied in surface area determinations, leave the adsorbent covered with a preadsorbed layer of impurities and/or the adsorbate. On subsequent adsorption (e.g. of  $\text{N}_2$  or noble gases) completion of the physisorbed monolayer is usually reached at  $p/p^0 \approx 0.1$  whereas on clean surfaces this state occurs at  $p/p^0$  values which may be smaller by orders of magnitude. However, as mentioned above, it should be kept in mind that linearity of the BET plot does not in itself provide conclusive evidence for the validity of  $n_m^a$ .

Noble-gas adsorption is often assumed to be the least complicated form of physisorption. However, on clean solid surfaces the molecular area may depend on the formation of ordered structures of the adsorbate in registry with the adsorbent lattice.

### B Empirical Procedures for Isotherm Analysis

In view of the complexity of real solid/gas interfaces and the different mechanisms which may contribute to physisorption, it is hardly surprising to find that none of the current theories of adsorption is capable of providing a mathematical description of an experimental isotherm over its entire range of relative pressure. In practice, two different procedures have been used to overcome this problem. The first approach involves the application of various semiempirical isotherm equations, the particular mathematical form depending on the range of the isotherm to be fitted and also on the nature of the system. The second procedure makes use of standard adsorption isotherms obtained with selected nonporous reference materials and attempts to explain differences in the isotherm shape in terms of the three different mechanisms of physisorption, i.e. monolayer-multilayer coverage, capillary condensation and micropore filling. In favourable cases, this approach can provide an independent assessment of the *total* surface area (for mesoporous, macroporous or nonporous solids) and an assessment of the *external* area for microporous solids (see Section 11.2.1.8.C). Much discussion has surrounded the choice of the standard isotherm, but it now seems generally accepted that it should be one obtained on a chemically similar adsorbent rather than one having the same value of  $C$  as the isotherm to be analysed.

#### 11.2.1.7 Assessment of Mesoporosity

##### A Properties of Porous Materials

Most solids of high surface area are to some extent porous. The *texture* of such materials is defined by the detailed geometry of the void and pore space. Porosity,  $\epsilon$ , is a concept related to texture and refers to the pore space in a material. An *open pore* is a cavity or channel communicating with the surface of a particle, as opposed to a *closed pore*. *Void* is the space or interstice between particles. In the context of adsorption and fluid penetration *powder porosity* is the ratio of the volume of voids plus the volume of open pores to the total volume occupied by the powder. Similarly, *particle porosity* is the ratio of the volume of open pores to the total volume of the particle. It should be noted that these definitions place the emphasis on the accessibility of pore space to the adsorptive.

The *total pore volume*,  $V_p$ , is often derived from the amount of vapour adsorbed at a relative pressure close

to unity by assuming that the pores are *then* filled with condensed adsorptive in the normal liquid state.

If the solid contains no macropores, the isotherm remains nearly horizontal over a range of  $p/p^0$  approaching unity and the total pore volume is well-defined. In the presence of macropores the isotherm rises rapidly near  $p/p^0 = 1$  and if the macropores are very wide may exhibit an essentially vertical rise. The limiting adsorption at the top of the steep rise can be identified reliably with the total pore volume only if the temperature on the sample is very carefully controlled and there are no 'cold spots' in the apparatus (which lead to bulk condensation of the gas and a false measure of adsorption in the volumetric method).

The *mean hydraulic radius*,  $r_h$ , of a group of mesopores, is defined as

$$r_h = \left( \frac{V}{A_s} \right)_p,$$

where  $(V/A_s)_p$  is the ratio of the volume to the area of walls of the group.

If the pores have a well-defined shape there is a simple relationship between  $r_h$  and the *mean pore radius*,  $r_p$ . Thus, in the case of nonintersecting cylindrical capillaries

$$r_p = 2r_h.$$

For a parallel-sided slit-shaped pore,  $r_h$  is half the slit width.

The *pore size distribution* is the distribution of pore volume with respect to pore size. The computation of pore size distribution involves a number of assumptions (pore shape, mechanism of pore filling, validity of Kelvin equation etc.)

##### B Application of the Kelvin Equation

Mesopore size calculations are usually made with the aid of the Kelvin equation in the form

$$\frac{1}{r_1} + \frac{1}{r_2} = -\frac{RT}{\sigma^{\text{lg}} v^{\text{l}}} \ln \left( \frac{p}{p^0} \right)$$

which relates the principal radii,  $r_1$  and  $r_2$ , of curvature of the liquid meniscus in the pore to the relative pressure,  $p/p^0$ , at which condensation occurs; here  $\sigma^{\text{lg}}$  is the surface tension of the liquid condensate and  $v^{\text{l}}$  is its molar volume. It is generally assumed that this equation can be applied locally to each element of liquid surface.

In using this approach to obtain the *pore radius* or *pore width*, it is necessary to assume: (i) a model for the pore shape and (ii) that the curvature of the meniscus is directly related to the pore width. The pore shape is generally assumed to be either cylindrical or slit-shaped: in the former case, the meniscus is hemi-



spherical and  $r_1 = r_2$ ; in the latter case, the meniscus is hemicylindrical,  $r_1 =$  width of slit and  $r_2 = \infty$ .

Rearrangement of the Kelvin equation and replacement of  $(1/r_1 + 1/r_2)$  by  $2/r_K$  gives

$$r_K = \frac{2\sigma^1 \varepsilon_v^1}{RT \ln(p^0/p)}$$

( $r_K$  is often termed the *Kelvin radius*).

If the radius of a cylindrical pore is  $r_p$  and a correction is made for the thickness of a layer already adsorbed on the pore walls, i.e. for the *multilayer thickness*,  $t$ , then

$$r_p = r_K + t.$$

Correspondingly, for a parallel-sided slit, the slit width,  $d_p$ , is given by

$$d_p = r_K + 2t.$$

Values of  $t$  are obtained from the data for the adsorption of the same adsorptive on a nonporous sample having a similar surface to that of the sample under investigation.

### C Computation of Mesopore Size Distribution

In calculations of the mesopore size distribution from physisorption isotherms it is generally assumed (often tacitly): (a) that the pores are rigid and of a regular shape (e.g. cylindrical capillaries or parallel-sided slits), (b) that micropores are absent, and (c) that the size distribution does not extend *continuously* from the mesopore into the macropore range. Furthermore, to obtain the pore size distribution, which is usually expressed in the graphical form  $\Delta V_p/\Delta r_p$  vs.  $r_p$ , allowance must be made for the effect of multilayer adsorption in progressively reducing the dimensions of the free pore space available for capillary condensation.

The location and shape of the distribution curve is, of course, dependent on which branch of the hysteresis loop is used to compute the pore size. In spite of the considerable attention given to this problem, in the absence of any detailed knowledge of the pore geometry it is not possible to provide unequivocal general recommendations. In principle, the regions of metastability and instability should be established for the liquid/vapour meniscus in the various parts of a given pore structure, but in practice this would be extremely difficult to undertake in any but the simplest types of pore system.

Recent work has drawn attention to the complexity of capillary condensation in pore networks and has indicated that a pore size distribution curve derived from the desorption branch of the loop is likely to be unreliable if pore blocking effects occur. It is significant that a very steep desorption branch is usually found if the lower closure point of the loop is located at the limiting  $p/p^0$  (see Section 11.2.1.5.C). In particular,

the desorption branch of a Type H2 loop is one that should not be used for the computation of pore size distribution.

It is evident from the above considerations that the use of the physisorption method for the determination of mesopore size distribution is subject to a number of uncertainties arising from the assumptions made and the complexities of most real pore structures. It should be recognized that derived pore size distribution curves may often give a misleading picture of the pore structure. On the other hand, there are certain features of physisorption isotherms (and hence of the derived pore distribution curves) which are highly characteristic of particular types of pore structures and are therefore especially useful in the study of industrial adsorbents and catalysts. Physisorption is one of the few non-destructive methods available for investigating mesoporosity, and it is to be hoped that future work will lead to refinements in the application of the method – especially through the study of model pore systems and the application of modern computer techniques.

### 11.2.1.8 Assessment of Microporosity

#### A Terminology

It is generally recognized that the mechanism of physisorption is modified in very fine pores (i.e. pores of molecular dimensions) since the close proximity of the pore walls gives rise to an increase in the strength of the adsorbent–adsorbate interactions. As a result of the enhanced adsorption energy, the pores are filled with physisorbed molecules at low  $p/p^0$ . Adsorbents with such fine pores are usually referred to as *microporous*.

The limiting dimensions of micropores are difficult to specify exactly, but the concept of *micropore filling* is especially useful when it is applied to the primary filling of pore space as distinct from the secondary process of capillary condensation in mesopores.

The terminology of pore size has become somewhat confused because it has been customary to designate the different categories of pores in terms of exact dimensions rather than by reference to the particular forces and mechanisms operating with the given gas–solid system (taking account of the size, shape and electronic nature of the adsorptive molecules and the surface structure of the adsorbent) as well as to the pore size and shape.

The upper limit of 2.0 nm for the micropore width was put forward as part of the IUPAC classification of pore size [4]. It now seems likely that there are two different micropore filling mechanisms, which may operate at  $p/p^0$  below the onset of capillary condensation: the first, occurring at low  $p/p^0$ , involves the entry

of individual adsorbate molecules into very narrow pores; the second, at a somewhat higher  $p/p^0$ , is a *cooperative* process involving the interaction between adsorbate molecules.

It is recommended therefore that attention should be directed towards the *mechanism* of pore filling rather than to the specification of the necessarily rather arbitrary limits of pore size. Until further progress has been made it is undesirable to modify the original IUPAC classification or to introduce any new terms (e.g. ultra-pores or ultramicropores).

### B Concept of Surface Area

In recent years a radical change has been taking place in the interpretation of the Type I isotherm for porous adsorbents. According to the classical Langmuir theory, the limiting adsorption  $n_p^a$  (at the plateau) represents completion of the monolayer and may therefore be used for the calculation of the surface area. The alternative view, which is now widely accepted, is that the initial (steep) part of the Type I isotherm represents micropore filling (rather than surface coverage) and that the low slope of the plateau is due to multilayer adsorption on the small external area.

If the latter explanation is correct, it follows that the value of  $A_s$  as derived by either BET or Langmuir analysis (In fact, many microporous solids do not give linear BET plots although their Langmuir plots may be linear over an appreciable range of  $p/p^0$ ) cannot be accepted as the true surface area of a microporous adsorbent. On the other hand, if the slope of the isotherm is not too low at higher  $p/p^0$  and provided that capillary condensation is absent, it should (in principle) be possible to assess the *external* surface area from the multilayer region.

In view of the above difficulties, it has been suggested that the term *monolayer equivalent area* should be applied to microporous solids. However, the exact meaning of this term may not always be clear and it is recommended that the terms *Langmuir area* or *BET area* be used where appropriate, with a clear indication of the range of linearity of the Langmuir, or BET, plot, the magnitude of  $C$  etc. (see Section 11.2.1.6.A).

### C Assessment of Micropore Volume

No current theory is capable of providing a general mathematical description of micropore filling and caution should be exercised in the interpretation of derived quantities (e.g. micropore volume) obtained by the application of a relatively simple equation (e.g. the Dubinin-Radushkevich equation) to adsorption isotherm data over a limited range of  $p/p^0$  and at a single temperature. The fact that a particular equation gives a reasonably good fit over a certain range of an isotherm does not in itself provide sufficient evidence for a particular mechanism of adsorption.

The t-method and its extensions provide a *simple* means of comparing the shape of a given isotherm with that of a standard on a nonporous solid. In the original t-method, the amount adsorbed is plotted against  $t$ , the corresponding multilayer thickness calculated from the standard isotherm obtained with a nonporous reference solid. Any deviation in shape of the given isotherm from that of the standard is detected as a departure of the 't-plot' from linearity. For the assessment of microporosity, the thickness of the multilayer is irrelevant and it is preferable to replace  $t$  by the 'reduced' adsorption,  $\alpha_s$ , defined as  $(n^a/n_s^a)_{\text{ref}}$  where  $n_s^a$  is the amount adsorbed by the reference solid at a fixed relative pressure,  $p/p^0 = s$ . An advantage of this method is that it can be used even when the standard isotherm does not exhibit a well-defined Point B, i.e. when the value of  $C$  is low. Once the standard  $\alpha_s$ -curve has been obtained for the particular gas-solid system at the given temperature, the  $\alpha_s$ -method can be applied in an analogous manner to the t-method. It is essential that the standard isotherms (or t-curves) be obtained with reference solids which are nonporous and of known surface structure. Further, it is strongly recommended that the standard isotherm should be one obtained for the particular adsorption system, and not by choosing a Type II isotherm which happens to have the same  $C$  value as the isotherm on a particular microporous solid.

Another procedure which may be used for the assessment of microporosity is the *preadsorption method*. In this approach the micropores are filled with large molecules (e.g. nonane), which are not removed by pumping the adsorbent at ambient temperature. In the most straightforward case, this procedure can provide an effective way of isolating the micropores and leaving the external surface available for the adsorption of nitrogen, or another suitable adsorptive.

### 11.2.1.9 General Conclusions and Recommendations

For evaluation of both the surface area and the pore size distribution from a single adsorption isotherm, nitrogen (at  $\approx 77$  K) is the recommended adsorptive except with solids of low surface area. If the surface area is relatively low ( $a_s < 5 \text{ m}^2 \text{ g}^{-1}$ , say), krypton or xenon, also at  $\approx 77$  K, offer the possibility of higher precision in the actual measurement of the adsorption, but not necessarily higher accuracy in the resultant value of the surface area than could be obtained with nitrogen. When another adsorptive is used it should be calibrated against nitrogen with the aid of carefully selected reference solids.

For a given system at a given temperature, the adsorption isotherm should be reproducible, but the possibility of aging of the adsorbent – e.g. through the

uptake or loss of water – must always be borne in mind. The reproducibility of the adsorption should be checked whenever possible by measurement of an isotherm on a second sample (of different mass) of the given adsorbent.

The first stage in the interpretation of a physisorption isotherm is to identify the isotherm type and hence the nature of the adsorption process(es): monolayer–multilayer adsorption, capillary condensation or micropore filling. If the isotherm exhibits low pressure hysteresis (i.e. at  $p/p^0 < 0.4$ , with nitrogen at 77 K) the technique should be checked to establish the degree of accuracy and reproducibility of the measurements.

The BET method is unlikely to yield a value of the actual surface area if the isotherm is of either Type I or Type III; on the other hand both Type II and Type IV isotherms are, in general, amenable to the BET analysis, provided that the value of  $C$  is neither too low nor too high and that the BET plot is linear for the region of the isotherm containing Point B. It is recommended that both the value of  $C$  and the range of linearity of the BET plot be recorded. If the value of  $C$  is found to be higher than normal for the particular gas–solid system, the presence of microporosity is to be suspected even if the isotherm is of Type II or Type IV; the validity of the BET area then needs checking, e.g. by the  $\alpha_s$ -method, in order to ascertain how closely the shape of the isotherm conforms to that of the standard isotherm in the monolayer range.

The computation of mesopore size distribution is valid only if the isotherm is of Type IV. In view of the uncertainties inherent in the application of the Kelvin equation and the complexity of most pore systems, little is to be gained by recourse to an elaborate method of computation. The decision as to which branch of the hysteresis loop to use in the calculation remains largely arbitrary. If the desorption branch is adopted (as appears to be favoured by most workers), it should be appreciated that neither a Type H2 nor a Type H3 hysteresis loop is likely to yield a reliable estimate of pore size distribution, even for comparative purposes.

If a Type I isotherm exhibits a nearly constant adsorption at high relative pressure, the micropore volume is given by the amount adsorbed (converted to a liquid volume) in the plateau region, since the mesopore volume and the external surface are both relatively small. In the more usual case where the Type I isotherm has a finite slope at high relative pressures, both the external area and the micropore volume can be evaluated provided that a standard isotherm on a suitable nonporous reference solid is available. At present, however, there is no reliable procedure for the computation of micropore size distribution from a single isotherm; but if the size of the micropores extends down to molecular dimensions, adsorptive molecules of selected size can be employed as molecular probes.

The following *check list* is recommended to assist authors in the measurement of adsorption isotherms and the presentation of the data in the primary literature. The reporting of results along generally accepted lines would considerably facilitate the compilation of data in the secondary literature and would thus promote interdisciplinary scientific cooperation [6].

It is suggested that the following items be checked and the relevant experimental conditions and results reported:

- (i) Characterization of the sample (e.g. source, chemical composition, purity, physical state, method of sampling).
- (ii) Pretreatment and outgassing conditions (e.g. temperature, residual pressure/partial pressures, duration of outgassing, flushing with adsorptive).
- (iii) Mass of outgassed sample ( $m$  in g).
- (iv) Adsorptive (e.g. chemical nature, purity, drying).
- (v) Experimental procedure for isotherm determination: method (e.g. volumetric, gravimetric, static, continuous; calibration of dead space or buoyancy). Measurement and accuracy of pressure [ $p$  in Pa (or mbar) or  $p/p^0$ ] and temperature, equilibration times.
- (vi) Reproducibility (a) second run, (b) with fresh sample of adsorbent.
- (vii) Adsorption isotherm: plot of amount adsorbed ( $n^a$  in  $\text{mol g}^{-1}$  or in  $\text{mol m}^{-2}$ ; or  $N^a$  in molecules  $\text{m}^{-2}$ ) versus pressure [ $p$  in Pa (or mbar) or  $p/p^0$ ], statement of measured/calculated  $p^0$  value at  $T$ .
- (viii) Type of isotherm, type of hysteresis, nature of adsorption (monolayer–multilayer adsorption, capillary condensation, micropore filling).
- (ix) BET data: adsorptive, temperature ( $T$  in K), mathematical procedure used for BET analysis, region of  $p/p^0$  and of  $\theta$  in which the BET plot is linear, single-point method, monolayer capacity ( $n_m^a$  in  $\text{mol g}^{-1}$  or  $N_m^a$  in molecules  $\text{m}^{-2}$ ),  $C$  value, molecular cross-sectional area ( $a_m$  in  $\text{nm}^2$  per molecule), specific surface area ( $a_s$  in  $\text{m}^2 \text{g}^{-1}$ ).
- (x) Porosity ( $\varepsilon$ ) with reference to powder porosity or particle porosity indicating in the latter case whether open pores, or open plus closed pores, are considered.
- (xi) Assessment of mesoporosity (pore width  $\approx 2$ –50 nm), method of computation, choice of ad- or desorption branch,  $p^0$  value at  $T$  and region of  $p/p^0$  used, surface tension of liquid adsorptive ( $\sigma^{lg}$  in  $\text{Nm}^{-1}$  at  $T$ ), model for pore shape. Correction for multilayer thickness, t-curve: plot of  $t$  in nm vs  $p/p^0$  (indication whether a standard curve is assumed or an adsorption isotherm determined on a nonporous sample of the adsorb-

ent). Pore size distribution: plot of  $\Delta V_p/\Delta r_p$  vs  $r_p$  (pore volume  $V_p$  per unit mass of adsorbent in  $\text{cm}^3 \text{g}^{-1}$  as calculated with the density  $\rho^l$  in  $\text{g cm}^{-3}$  of the liquid adsorptive, mean pore radius  $r_p$  in nm), total pore volume at saturation.

- (xii) Assessment of microporosity (pore width  $< ca\ 2\ \text{nm}$ ), method of evaluation, t-plot: amount adsorbed  $n^a$  in  $\text{mol g}^{-1}$  vs multilayer thickness  $t$  in nm,  $\alpha_s$ -plot:  $n^a$  vs  $(n^a/n_s^a)_{\text{ref}}$ , where the suffix refers to a chosen value  $s = p/p^0$ , Dubinin-Radushkevich plot or pre-adsorption method. Micropore volume per unit mass of adsorbent in  $\text{cm}^3 \text{g}^{-1}$  as calculated with the density  $\rho^l$  of the adsorptive in the normal liquid state, monolayer equivalent area of microporous solid, external surface area.

## References

1. British Standard 4359: Part 1: 1969. Nitrogen adsorption (BET method). Deutsche Normen DIN 66131, 1973. Bestimmung der spezifischen Oberfläche von Feststoffen durch Gasadsorption nach Brunauer, Emmett and Teller (BET). Norme Française 11-612, 1975. Détermination de l'aire masique (surface spécifique) des poudres par adsorption de gaz. American National Standard, ASTM D 3663-78. Standard test method for surface area of catalysts.
2. D. H. Everett, G. D. Parfitt, K. S. W. Sing and R. Wilson, *J. appl. Chem. Biotech* **24**, 199 (1974).
3. *Manual of Symbols and Terminology for Physicochemical Quantities and Units* prepared for publication by D. H. Whiffen, *Pure Applied Chem.*, **51**, 1-41 (1979).
4. *Part I of Appendix II, Definitions, Terminology and Symbols in Colloid and Surface Chemistry*, prepared by D. H. Everett, *Pure Applied Chem.*, **31**, 579-638 (1972).
5. *Part II of Appendix II, Terminology in Heterogeneous Catalysis*, prepared for publication by R. L. Burwell, Jr., *Pure Applied Chem.*, **45**, 71-90 (1976).
6. See "Guide for the Presentation in the Primary Literature of Numerical Data Derived from Experiments". Report of the CODATA Task Group on Presentation of Data in the Primary Literature, CODATA Bulletin No. 9 (1973).

## 11.2.2 Catalyst Characterization<sup>1</sup>

J. HABER

### 11.2.2.1 Introduction

This manual has been prepared by the Commission on Colloid and Surface Chemistry including Catalysis of the IUPAC. It results from the general feeling among surface and catalysis chemists both from academia and industry that the rapid increase of knowledge in science

of catalysis and the better understanding of the mechanism of catalytic processes is not accompanied by the development of the appropriate scientific language. Many terms, widely used in the literature, remain vague and underfined. Thus, the Subcommittee on Catalysis was created with the task of preparing a catalyst characterization chart, listing all parameters which should be specified in order to obtain a full description of a catalysts, and of formulating the definitions of these parameters as well as recommendations concerning the terminology.

The present manual is based on the same general principles as those used in the 'Manual of Symbols and Terminology for Physicochemical Quantities and Units' of the Commission on Symbols, Terminology and Units of the Division of Physical Chemistry, Definitions, Terminology and Symbols in Colloid and Surface Chemistry of the Commission on Colloid and Surface Chemistry, Appendix II Part I Definitions, Terminology and Symbols in Colloid and Surface Chemistry, Part II Heterogeneous Catalysis, and Recommendations in Reporting Physisorption Data for Gas/Solid Systems [1-3].

Since the present proposals should be considered as one of the sub-sets of the terms and symbols of physical chemistry, the general principles are not repeated here.

This manual provides definitions and recommendations concerning the terminology of catalysts. It should be read in conjunction with the 'Manual of Methods and Procedures for Catalyst Characterization' which provides details and recommendations concerning the experimental methods used in catalysis.

### 11.2.2.2 Catalyst Formulation and Methods of Its Preparation

#### A Methods of Preparation

Many catalysts consist of an *active component* or *components* (see Section B) deposited on a *support* (such as silica, alumina, carbon). The role of the support may be to improve the properties (e.g. stability) of the active component(s), or to participate directly in the catalytic reaction (e.g. by providing acidic sites). The following terms define general preparation methods.

#### a Precipitation

*Precipitation* is a method often used for producing both support precursors and catalyst precursors (including precursory forms of zeolites) and occurs when two or more solutions are mixed in a suitable way. In addition to providing general details of the method (e.g., concentration, temperature, pH, etc.) it is necessary to indicate specifically the order and rate of addition of one solution into the other, a description of the mixing procedure and the details of the *ageing* procedure, if

<sup>1</sup> This Section was originally published in *Pure Appl. Chem.* **1991**, **63**, 1227-1246. © 1991 IUPAC.

any. The association of two or more active elements in the precipitate, in a single or several phases, may be achieved by *co-precipitation*.

#### *b Deposition*

Deposition describes the application of the catalytic component (e.g. nickel, as nickel nitrate) on to a separately produced support (e.g. silica). Any treatment of the support before the deposition step must be described precisely.

Deposition may be achieved by *impregnation*, i.e., contacting the support for a specified time with a solution containing the active elements. When the active elements are contained in a volume of solution corresponding to the pore volume, the procedure is called *dry* or *pore volume impregnation*. The term *incipient wetness method* is used to describe impregnation when the volume of the solution is empirically determined as corresponding to that beyond which the catalyst begins to look wet. One or several parallel processes such as *adsorption*, *ion exchange*, *selective reaction* on or with the surface of the support may take place during impregnation. Sometimes the process of impregnation is carried out by *percolation* of the impregnating solution through a bed of support, or by *dipping* the support in the impregnation solution.

Two or more active elements may be introduced either in a single step by *co-impregnation* or subsequently one after the other in *successive impregnations*. Drying and often calcination (see 2.1.5) take place between impregnations. Deposition involving the formation of a strong (e.g. a covalent) bond between the support and the active element is usually described as *grafting* or *anchoring*. This is achieved through a chemical reaction between functional groups (e.g. hydroxyl groups) on the surface of the support and an appropriately selected inorganic, or organometallic compound of the active element. When deposition takes place by adsorption or reaction from the gas phase, the term *chemical vapour deposition* is used.

Sometimes a special technique of *precipitation-deposition* is used, in which an active element (e.g. nickel) is deposited onto a carrier (e.g. silica) in suspension in the precipitating solution (e.g. nickel nitrate) by slow addition, or *in situ* formation (e.g. of  $\text{OH}^-$  by hydrolysis of urea) of a precipitating agent.

*Ion exchange*, which as already mentioned may occur during impregnation, is an important process in the synthesis of zeolites and also in the preparation of some supported metal catalysts.

#### *c Encapsulation*

Enzymes or cells, which are of relatively large size may be entrapped in a maze of polymeric molecules (a gel). This procedure is called *immobilization by inclusion*. When the biocatalyst is enclosed inside a semiper-

meable membrane, usually approximately spherical, the method is known as *encapsulation*. In the process of *reticulation* the primary biocatalyst particles (individual enzyme molecules, cofactors or individual cells) are covalently attached to each other by organic chains, into a three-dimensional network. The term *grafting* is also used in this context. Attachment to the support by adsorption forces is called *immobilization by adsorption*.

#### *d Selective Removal*

Preparation of the catalyst by the reaction of a precursor (e.g. NiAl alloy) with a reactant (e.g. an aqueous NaOH solution) which selectively dissolves part of the precursor (Al) leaving the active agent (Ni) is described as *selective removal method*.

#### *e Treatment of Intermediate Solids or Precursors*

Very often the intermediate solid is left for some time under specified conditions in the presence of the impregnating or precipitating mixture. This is called *aging*. Washing of the intermediate solids formed by precipitation is generally required to remove adsorbed ions such as  $\text{Na}^+$  which were introduced during the precipitation.

The solvent may be eliminated without chemical transformation by *drying*. Many different processes may be applied to this end such as drying in an oven, fluidized bed drying, spray drying, freeze drying.

The intermediate solids are usually subjected to *heat treatment*, sometimes called *calcination*. The term calcination should only be used when heating is carried out in air or oxygen. It is essential to describe the exact conditions of heat treatment, in particular the condition of the introduction of the sample, temperature and the rate of its change, pressure, gas flow conditions, etc. Chemical transformation of the solid may take place in the course of the heat treatment. When this transformation proceeds without interaction with the atmosphere the term *thermal decomposition* may be used.

#### *f Activation of the Precursor*

The final step in the preparation of a catalyst is the transformation of the precursor to the active phase (e.g. metal, sulfide) which is sometimes called *activation*. The activation may be a *reduction* (e.g. by  $\text{H}_2$ ), *reduction-sulfidation* (e.g. by  $\text{H}_2 + \text{H}_2\text{S}$ ), *dehydroxylation* (e.g. by removal of  $\text{H}_2\text{O}$  from zeolite) or *oxidation* (e.g. by  $\text{O}_2$ ). The details of the activation process must be stated (e.g. partial pressure and purity of gas, method of heating and its rate, gas reacting flow rate, sample size).

References see page 1529

## B Chemical Composition

Catalytic materials are frequently composed of many components and phases. Therefore, it is seldom adequate to define a catalyst by merely stating the chemical composition, e.g. 1% Pt, 99% SiO<sub>2</sub>. Note that by convention the support should be indicated clearly by using an oblique stroke (solidus), e.g. 1% Pt/SiO<sub>2</sub>.

The term *major active component* may be used to describe the active component, the proportion of which greatly exceeds that of the others. Secondary components added on purpose may be described as *additives*, whereas the term *impurities* should be reserved for trace amounts of other elements, over which the investigator (manufacturer) has little control. The use of the word '*promoter*' implies that the additive improves some particular property of the catalysts, and it is desirable to indicate this property when known (e.g. activity, selectivity, textural properties, resistance to sintering). The term *modifier* is used sometimes in this context, but is not recommended. The term *modifier* is used in a special and proper sense in the context of asymmetric hydrogenation when, for example, Raney nickel is modified by optically active tartaric acid in order to impart the property of asymmetry to hydrogenation reactions over the catalyst.

The action of adding a small amount of foreign atoms to form a solid solution in the lattice of a non-metallic catalyst is sometimes called *doping*.

The description of the composition of a catalytic system should indicate the crystallographic form of the support (e.g.  $\gamma$ -Al<sub>2</sub>O<sub>3</sub>, TiO<sub>2</sub> - anatase). The chemical composition should be unambiguously defined. When specifying the proportions of the active phase to the support, weights may be used provided the stoichiometry is clearly indicated (e.g. Co<sub>3</sub>O<sub>4</sub> and MoO<sub>3</sub>, Co<sub>9</sub>S<sub>8</sub> and MoS<sub>2</sub>, NiO, Pt).

## C Aggregate Morphology

The solid obtained after the operations described in Section 2.1 (supports, intermediate solids, precursors or catalysts) can be used as such (e.g. powders) or shaped into larger entities (beads, pellets, extrudates, rings). In special cases structures called monoliths are used as support. Description of the *aggregate morphology* should include reference to the crystal structure and details of the shape of the particles of the various phases present, their arrangement in space (including the voids or pores) and the shape of larger physically separate entities. The *structure* is defined by the distribution in space of the atoms or ions in the material part of the catalyst, the *texture* is defined by the detailed geometry of the void space in the particles of catalyst and by the spatial relationships between the different phases present.

Certain materials used as catalysts or supports consist of spheroids smaller than 10 nm in diameter, ce-

mented into larger entities. A *primary particle* should be defined as the smallest discrete identifiable entity and the method of identification should be mentioned (e.g. transmission electron microscopy, scanning electron microscopy). An assemblage of such primary particles exhibiting an identifiable collective behaviour (e.g. chemical nature of the aggregated primary particles, texture of the aggregate, resistance to mechanical separation upon grinding) constitutes an *aggregate*. When describing the aggregates the criterion of identification should be mentioned. Strongly bonded aggregates are called *agglomerates*.

A collection of loose, unattached, primary particles or aggregates of relatively small size is usually called a *powder*. It is recommended that the word powder is used if the largest dimension of the individual entities is smaller than 1 mm. The shape of the particle should be described (sphere, flake) and the method of its preparation specified (crushing, grinding spray drying).

In the designation of larger aggregates two criteria may be used: shape, referring to geometrical definition, or method of preparation. Spherical, spheroidal or rounded aggregates obtained by beading or granulation are called *beads*, and aggregates of cylindrical shape, formed by tableting (*tablet*) or extruding (*extrudate*) are described as *cylinders*. The term *lump* is used to describe an aggregate of irregular shape, obtained usually by crushing, but its form should be described as precisely as possible. A precise description should be given when aggregates of other form, such as *rings* or *trilobes*, are used. The dimensions (diameter, thickness, length, inner and outer diameter of a ring) of the entity as defined above should be stated.

## D Forming Operations

Depending upon the technology (e.g. fluidization, moving-bed on fixed-bed) and the conditions of the catalytic process, the shape and size of catalyst entities may vary appreciably, e.g. powder, cylinders, beads. A general problem is to make entities of dimensions larger than 1 mm from fine powder particles or precipitates. Materials which are difficult to shape are treated with additives (e.g. flake graphite, starch, stearic acid, poly (acrylic acid), mineral oil, vegetable oil) usually in amounts of 1–5 wt.-%. Shaping additives may act as lubricants, plasticizers, cements, porosity promoters (porogenic additives). The powdered starting material mixed with the additives may be dry, or converted to a plastic pulp by addition of a suitable liquid.

One sometimes distinguishes:

- *paste processing*: grinding, kneading to a pulp, extruding;
- *liquid processing*: gelification (oil drop), spray drying;
- *powder (or solid) processing*: tableting, cementing.

If the material is of natural origin (natural molecular sieve, pumice) the desired entity size is obtained by *crushing* and/or *grinding* and subsequent size selection by *sieving*. Some catalysts are also obtained in this way from synthetically prepared bulky masses (e.g. ammonia catalyst). Grinding may take place in the absence (*dry grinding*) or presence (*wet grinding*) of a liquid, usually water.

In *spray-drying* a solution or a slurry of the powder in suspension in water is passed through a nozzle which sprays small droplets into hot air. Spray-drying gives particles of almost identical shapes (spheres with a small characteristic depression) and size which are used as such in fluid bed operations. The *dropping-in-oil* method consists in introducing a sol or gel as drops through a nozzle into a hot oil. Water from sol or gel is evaporated (chemical bonds may be formed at this stage) and the gel hardens, resulting in the formation of beads. Depending on the relative densities the drops may move downwards (oil drop per se) or upwards. *Granulation* is a process of aggregation by progressive humidifying in a rotating granulator. Generally, aggregates of different size are kept in motion under a spray of liquid (water or aqueous solution) in a horizontal rotating cylinder or a pan rotating around an axis inclined about 45°. The pan may be concave (hemispheric granulator or 'bow granulator') or cylindrical (flat granulator or 'dish granulator'). Spheroidal particles or granules are thus formed. In the method of *tableting*, the powder is firmly compressed in a die to be shaped into small cylinders (pellets), rings or beads. In most cases some plasticizing agents are added to the powder (talc, graphite, stearic acid). Another technique of shaping larger entities from a powder is extrusion, in which a paste is forced through a die to form a cylinder which is cut into small pieces. The cross-section of the die may have different shapes (circular, trilobe, toothed wheel, ring). The powder with the additives is first pulped with a liquid, homogenized, kneaded and fed to the die by some pushing device (screw, piston). The paste may be *soft* or *stiff*. The product is termed the *extrudate*, of which the exact form (see above) as well as the dimensions should be specified.

## E Stability of Catalyst Systems

### a Physical Stability

Granular catalysts have a *grain size distribution* which may be determined by passing a sample through a series of graded sieves. The grain size distribution is determined by the condition under which the materials were precipitated or dried during catalyst preparation. Grains may be structurally weak so that they undergo *attrition* (see section 3.4) when in random contact with other grains. Thus grain size distribution of a catalyst may change as it is transported before use, or while it is

in use. Fragmentation of catalyst particles in the reactor, caused, for example, by thermal shock or carbon build-up, may also occur.

To obtain a correct grain size distribution for a catalyst, a proper sampling procedure should be adopted. For example, samples should be taken from various depths within a container in order to determine whether the batch has been rendered inhomogeneous by settling effects, and care must be taken to ensure that the sieving process itself does not cause attrition. In the case of tableted or extruded catalysts the process of attrition may be inhibited by binders used in their preparation.

Catalysts consisting of an active phase on an oxidic or carbon support are subject to a particular form of degradation in that attrition may result in preferential loss of the active phase as fines.

Catalysts which have the capacity to adsorb water or carbon dioxide from the air may exhibit weight instability due to climatic changes. Time and variation of temperature or pressure may, in principle, give rise to losses or gains in weight due to changes in water content. Metal particles are susceptible to sintering with a concomitant loss of dispersion.

### b Chemical Stability

Most heterogeneous catalysts in the as-received state or in precursor form possess a considerable degree of chemical stability whereas after activation they are highly reactive. Two cases may be distinguished: (i) chemical stability in air at ambient temperature and pressure, and (ii) chemical stability at elevated temperatures of the catalyst in the as-received state.

Many oxides, sulfides, and metals react with air slowly at ambient temperature, although such processes may be measurable only over long periods. For example, supported nickel which has been passivated by exposure to air under conditions which produce only surface oxidation may react further to give supported bulk nickel oxide. Air contains water vapour and carbon dioxide and also hydrocarbon impurities so that hydroxide or carbonate formation and hydrocarbon contamination may occur. Catalysts consisting of an active phase supported on a non-stoichiometric compound may undergo chemical change by reaction of the support with oxygen of the air. Catalysts which contain a material that is photosensitive, e.g. titania, may show enhanced chemical instability when exposed to sunlight.

Catalysts subjected to heating in air may exhibit accelerated hydroxide or carbonate formation, before a loss of water or carbon dioxide could take place. Phase changes may also occur, for example, in alumina by interaction of a partially hydrated phase with water

physically adsorbed in pores. Elevated temperature may lead to measurable chemical reaction, between active phases, or between active phases and supports, or to the segregation of phases in systems that were formerly homogeneous, which greatly modify the properties of the catalyst when activated. For example, nickel oxide and silica may form nickel silicate, of cobalt oxide and alumina may form cobalt aluminate. In a nickel/silica hydrogenation catalyst, silicate formation would reduce the amount of nickel formed under standard reduction conditions. In a CoO-MoO<sub>3</sub>/Al<sub>2</sub>O<sub>3</sub> hydrodesulfurization catalyst, cobalt aluminate formation would reduce the quantity of cobalt available to act as a promoter.

The nickel catalyst used in the hydrogenation of natural oils and edible fats is a special example of a catalyst which is transported in a protected state. In this case, the catalyst is protected by encapsulation in solid fat. The fat melts when the catalyst is introduced into the reactor, so releasing the active phase. Particular care must be taken to control the temperature during the transport and handling of this material.

The action of steam may have a deleterious effect on catalytic materials. For example, transport of silica can lead to loss of support material or to the encapsulation of the active phase. Steaming may also change the pore structure of the support. As somewhat lower temperatures the action of water vapour may result in an irreversible decrease in the surface area.

### 11.2.2.3 Physical Properties

#### A Total Surface Area

Many catalysts are porous solids of high surface area and with such materials it is often useful to distinguish between the *external* and *internal* surface. The *external surface* is usually regarded as the envelope surrounding discrete particles or agglomerates, but is difficult to define precisely because solid surfaces are rarely smooth on an atomic scale. It can be taken to include all the prominences plus the surface of those cracks, pores and cavities which are wider than they are deep. The *internal surface* comprises the walls of the rest of the pores, cavities and cracks. In practice, the demarcation is likely to depend on the methods of assessment and the nature of the pore size distribution. The *total surface area* ( $A_t$ ) equals the sum of the external and internal surface areas. The roughness of a solid surface may be characterized by a *roughness factor*, i.e. the ration of the external surface to the chosen geometric surface.

Gas adsorption methods are often used to determine the surface area and pore size distribution of catalysts. The Brunauer-Emmett-Teller (BET) adsorption method is the most widely used standard procedure. (See: Pure and Applied Chemistry 57, 603 (1985)).

#### B Pore Structure

Most catalysts of high surface area are to some extent porous. *Porosity* is a concept related to texture and refers to the pore space in a material. It can be defined as the fraction of the bulk volume that is occupied by pore or void space. An *open pore* is a cavity or channel communicating with the surface of a particle, as opposed to a *closed pore*. *Void* is the space or interstices between particles.

The pore systems of solids are of many different kinds. The individual pores may vary greatly both in size and in shape within a given solid, and between one solid and another. A feature of special interest for many purposes is the width ( $w$ ) of the pores, e.g. the diameter of a cylindrical pore, or the distance between the sides of a slit-shaped pore.

It is expedient to classify pores according to their sizes:

- (i) Pores with widths exceeding about 50 nm are called *macropores*;
- (ii) Pores with widths not exceeding 2 nm are called *micropores*;
- (iii) Pores of intermediated size are called *mesopores*.

These limits are to some extent arbitrary. It is worth emphasizing that amongst solids as a whole a wide and continuous range of pore sizes is to be found, from macropores through mesopores and micropores to grain boundaries, cleavage planes and dislocations.

The *total pore volume*,  $V_p$ , sometimes called *specific pore volume* when referred to unit mass, is the total internal volume per unit mass of catalysts. Some of this pore volume may be completely enclosed and thus inaccessible to molecules participating in a catalytic reaction. The total accessible pore volume is often derived from the amount of vapour adsorbed at a relative pressure close to unity, by assuming that the pores are then filled with liquid adsorptive. The accessible pore volume may be different for molecules of different sizes. It may be useful to determine the dead space by means of a nonsorbable gas (normally helium) in conjunction with the determination of the bulk volume of the catalyst by means of a non-wetting liquid (mercury).

The *pore-size distribution* is the distribution of pore volume with respect to pore size. It is an important factor controlling the diffusion of reactants and products in the porous catalyst and thus an essential property for its characterization. The computation of pore size distribution involves a number of assumptions and therefore reporting of the data should always be accompanied by an indication of the method used for its determination. (See: Pure and Applied Chemistry 57, 603 (1985)).

The pore geometry of the majority of catalysts consists of an interconnected three-dimensional network of



interparticle spaces, pores or capillaries. Usually capillary segments of different shapes and sizes are distributed over the network in some irregular fashion. When a solid is formed by aggregation of primary, non-porous particles, the detailed shapes of pores will depend on the size distribution of the primary particles and on their mode of packing. Platelets will tend to form wedge-shaped pores or slits. With spheres, the closeness of packing will depend on the average number of neighbours. Well defined geometrical networks can be assigned to some catalysts, e.g. zeolites, some lamellar materials, and fibrous silicates. However, the pore structure of many materials used as catalyst supports present a highly irregular geometry, far removed from simple models. This complexity imposes a serious limitation on the reliability of the methods of calculation of pore-size distribution.

Some porous solids expand on exposure to the vapours of adsorptives. This phenomenon is called *swelling*. By determining the length or volume of a specimen of the solid at different vapour pressures the expansion isotherm may be obtained. Rigid adsorbents, like charcoal or silica gel, swell by only a few percent, but non-rigid adsorbents, like agar-agar, may swell to several times the original size. Provided the adsorption occurs slowly the rigid solid may accommodate the stresses, but if suddenly exposed to high vapour pressure the material may shatter.

### C Density

Several catalyst densities are used in the literature. *True density* may be defined as the mass of a powder or particle divided by its volume excluding all pores and voids. In a strict physical sense, this density can be calculated only through X-ray or neutron diffraction analysis of single crystal samples. The term *apparent density* has been used to refer to the mass divided by the volume including some portion of the pores and voids, and so values are always smaller than the true density. This term should not be used unless a clear description is given of what portion of the pores is included in the volume. So-called *helium densities* determined by helium expansion are apparent densities and not true densities since the measurement may exclude closed pores.

*Bulk density*, or *packing density*, includes all pores and voids (interparticle spaces) in its calculation. It is determined by filling a graduated cylinder, with or without tapping. It follows that the value obtained is dependent upon the form of the catalyst (powder, tablets, extrudates) because of the different contribution of interparticle void space to the pore volume. Tap density is the apparent density of a bed of particles in a container of stated dimensions when a given amount of powder is vibrated or tapped under controlled conditions. The use of the term *bulk density* should be

encouraged, accompanied by the detailed description of the conditions of its determination.

Catalyst manufacturers also define an *effective solid density*, determined by displacement of a given liquid (water, ethanol). Values obtained with different liquids may vary substantially, depending on the extent to which the molecules of the liquid are able to penetrate into the pores of the catalyst. The term *piece density* is sometimes used when the measurement is performed with a liquid which does not substantially penetrate into the pores.

### D Mechanical Strength

It is desirable for commercial catalysts to have sufficient mechanical strength so that losses during handling and use are minimized. Broken pieces and fines (fine powder) lost during handling or produced during commercial use can represent a significant expense, especially for catalysts containing precious metals such as Pt and Re. Depending on the design of the commercial reactor, broken catalyst, or fines, can lodge in support screens or in containment screens causing a restriction in the flow of reactants and products through the reactor. Various laboratory tests have been designed to provide information concerning the ability of a catalyst to maintain its physical integrity.

*Crush strength* is defined as the resistance of formed catalysts to compressive forces. Measurements of crush strength are intended to provide an indication of the ability of the catalyst to maintain its physical integrity during handling and use. When crush strength is measured for single pieces it is called *piece crush strength*, and when it is measured for a bulk sample it is called *bulk crush strength*. Other terms which have been used for piece crush strength, but which are not recommended are static crush strength and single pellet crush strength.

Piece crush strength is commonly measured by placing individual catalyst pieces between two flat surfaces, applying a compressive load, and measuring the force required to crush the piece. Best results are obtained for regular shapes, such as beads and tablets. Crush strength measurement of extrudates is less straightforward, and the results will vary greatly with particle geometry and with the details of the analytical procedures used. The procedure used should be described in detail. Some methods may be repeatable within a single laboratory but irreproducible between laboratories.

Bulk crush strength is commonly measured by placing a representative sample in a cylinder, applying a constant force with a piston, and measuring the amount of fines generated. Many different variants are possible and no generally accepted method is yet available. The bulk crush strength is defined empirically and the re-

sults are expressed on an arbitrary scale. This measurement may be applied to all catalyst shapes.

*Attrition* is defined as loss of catalyst during handling or use. Attrition can occur by loss of fines through abrasion, which is wearing, grinding, or rubbing of the particles with each other or with container walls. Attrition can also occur by loss of pieces due to breakages, which can be caused by impact or collision of particles with container walls. Numerous tests have been designed to measure the resistance of catalyst particles to attrition. These tests vary considerably in complexity and severity. Their applicability depends on the particular type of catalyst being tested.

A simple method to measure attrition is to place a representative sample of the catalyst in a close container, vibrate or shake the container, and then measure the amount of fines generated. Another relatively mild method is to place a sample in a drum having single baffle, rotate the drum for a fixed period of time, and then measure the amount of fines generated by sieving through a standard sieve. Larger particles of silica and alumina will hold very fine particles on their surface and these stay attached during sieving, but can be removed by agitation in water.

More severe tests are applicable to catalysts used in moving bed reactors. Some tests use a high velocity stream of gas to cause attrition of the catalyst. In some tests, a small-scale plant which simulates the commercial plant is used. The amount of attrition measured in all these tests is very dependent on the exact procedure used. Reproducibility among laboratories is only likely to be possible if precise details of the method are given.

#### 11.2.2.4 Fine Structure

##### A Surface Structure and Topography

The catalyst particle is usually a complex entity composed of a porous solid, serving as the support for one or more catalytically active phase(s). These may comprise clusters, thin surface mono- or multilayers, or small crystallites. The shape, size and orientation of clusters or crystallites, the extension and arrangement of different crystal faces together with macrodefects such as steps, kinks, etc., are parameters describing the *surface topography*. The type of atoms and their mutual positions at the surface of the active phase or of the support, and the type, concentration and mutual positions of point defects (foreign atoms in lattice positions, interstitials, vacancies, dislocations, etc.) define the *surface structure*.

The determination of the surface structure of solid is possible using a variety of experimental methods, the methods chosen being dependent on the specific information required. Information on surface elemental composition is also desirable.

With single crystals the symmetry of the surface structure and the presence of features, such as steps, can be obtained using low energy electron diffraction (LEED). For real crystals, surface topography can be investigated by conventional optical microscopy and various other microscopic techniques, such as scanning electron microscopy (SEM), transmission electron microscopy (TEM), scanning transmission electron microscopy (STEM), high resolution electron microscopy (HREM), and analytical electron microscopy (AEM).

The basic concept in examining samples by SEM is that the intensity of the radiation emerging from each region on the surface is characteristic of the topography of the region. Local variation in surface topography, i.e. orientation of the surface with respect to the electron beam gives rise to contrast in SEM. The accompanying X-ray signals generated may be used to provide information on chemical composition (energy dispersive analysis by X-rays, EDAX). The local environment of atoms (coordination number, nature of coordinating atoms and atom-to atom distances) can be determined from an analysis of the extended X-ray absorption fine structure (EXAFS), and that of surface atoms by using surface EXAFS (SEXAFS), glancing angle or reflection EXAFS (REFLEXAFS) or critical angle EXAFS.

##### B Surface Area of Different Phases

For any given catalytic reaction the active surface area is normally only a small fraction of the area of the active component (active phase). The term *active sites* is often applied to the sites effective for a particular heterogeneous catalytic reaction. The terms *active site* and *active centre* are often used as synonyms, but *active centre* may also be used to describe an *ensemble of sites* at which a catalytic reaction takes place. There is evidence that the centres required for some catalytic reactions are composed of a collection of several metal atoms (ensemble). This appears to be the case for such reactions as, for example, hydrogenolysis, hydrogenation of CO, and certain deuterium-exchange processes with hydrocarbons.

It is frequently convenient to describe the chemical properties of a catalyst surface by reference to *surface sites*. A surface site may be composed of one or more surface atoms or ions and may act as an active site for a given catalytic reaction, or may be inactive. It is characterized by the chemical reactivity of these atoms or ions and by their spatial arrangement at the surface. The *site density* is the number of sites per unit surface area. However, it is expedient to extend the use of this term to cases where surface area has no clear significance. In these cases the site density is referred to unit mass or unit volume of the catalyst.

In supported catalysts the surface area of the active phase is different from the total surface area. In the

particular case of supported metal catalysts several techniques may be used to estimate the surface area of the active phase and the number of exposed metal atoms. (Note, however, that this does not necessarily provide a measure of the *active* surface area). The method used most often is based on selective chemisorption of appropriately chosen probe molecules ( $H_2$ ,  $CO$ ,  $N_2O$ ), the chemisorption data obtained under well defined conditions being then compared with the total surface area determined from the analysis of physical adsorption data. However, assumptions must be made regarding the stoichiometry of the interaction of the probe molecule with the surface metal atoms and of the number of surface metal atoms per unit surface area. This method provides consistent measurements of the surface area of metal particles but is not generally applicable to nonmetal catalysts.

A variation of this method consists in the titration of an adsorbed species (e.g. oxygen) by a reactant (e.g.  $H_2$ ). It is still necessary to make some assumptions concerning the stoichiometry of the titration reaction.

The *degree of dispersion* is defined as the fraction (percentage) of the total metal atoms which are surface atoms. (The term *fraction exposed (percentage exposed)* is synonymous with the degree of dispersion).

Several physical methods may be used to provide indirect estimates of the degree of dispersion. Sizes of particles, or of single crystallites, or of magnetic domains determined, respectively, by electron microscopy, X-ray line broadening, and magnetization measurements, can be used for this purpose but, in all cases, assumptions must be introduced into the calculations.

An alternative means of description is to use the *mean diameter of primary particles* as obtained from *low-angle X-ray scattering, broadening of X-ray diffraction lines or EXAFS*. It may also be possible to use these techniques to determine the grain size of the support, or of the catalyst particles in general, providing these materials are sufficiently crystalline. The *particle-size distribution* may be measured directly using one of the microscopic techniques or indirectly by using a *sedimentation method*.

### C Surface Elemental Composition of Different Phases

The chemical nature and composition of catalyst surfaces are essential parameters for understanding catalytic reactivity. Electron spectroscopies, mainly *Auger Electron Spectroscopy (AES)*, *X-ray Photoelectron Spectroscopy (XPS)*, *Secondary Ion Mass Spectroscopy (SIMS)* and *Ion Scattering Spectroscopy (ISS)* allow such information to be obtained. AES and XPS are most likely to provide meaningful data if the surface region of the solid is homogeneous over a depth several times the inelastic mean free path of the emitted electrons.

In catalysis it is important not only to be able to study the surface region of the catalyst itself, but also any adlayer that may be present. The latter may arise from adsorption or preferential segregation of one component from the bulk to the surface. The spatial distribution of the elements at the surface can be obtained from *scanning AES*. Experiments, in which the surface is progressively eroded, e.g., by ion-bombardment, with surface analysis by AES, XPS or ISS carried out after various times, may provide *concentration-depth profiles* of the chemical species.

### D Surface Chemical Characterization

The activity of a catalyst depends on the nature, the number, the strength and the spatial arrangement of the chemical bonds that are transiently created between the reactants and the surface. The objective of the chemical characterization of the surface is a detailed description of the adsorbate-adsorbent bonds that a given catalyst will develop when contacted with a given reaction mixture. Therefore, chemical characterization should be done *in situ* in the course of the reaction itself. However, because of experimental limitations, this is seldom possible and catalyst surfaces are usually characterized by means of separate experiments. It is important to characterize the catalyst surface both before and after its use in a reaction.

The pretreatment of the catalyst, before the chemical characterization experiments, must be selected so that the relevant surface properties are as similar as possible to those existing during the catalytic reaction. When the chemical constitution of the surface or its structure are not significantly modified by the reaction itself, the same pretreatment can be used for the characterization experiments as for the catalytic tests.

Ideally, the probe molecules used in the chemical characterization experiments should simulate as closely as possible the behaviour of the actual reactants. This is rarely possible and so simple probe molecules ( $H_2$ ,  $O_2$ ,  $CO$ ,  $NO$ ) are used instead. Some additional information about the nature of the surface may be obtained using thermal analysis methods, e.g., calorimetry, temperature-programmed desorption, temperature-programmed reaction.

When a catalytic reaction modifies the surface properties of the catalyst in a way which cannot be simulated in the absence of reactants, or when large series of similar catalysts are to be compared, it is convenient to characterize a given catalyst by its activity in an appropriate probe-reaction.

#### a Acid-Base Sites

An acid-base surface contains individual acidic and basic sites which may interact together. On a given

surface, one type (acidic or basic) may prevail but both are always present (conjugate acidic and basic pairs). Examples of such surfaces are found in metal oxides, sulfides and other compounds. The description of acidic and basic surface properties requires the determination of the nature (Lewis or Brønsted), the density, the location, and the strength distribution of sites. It is important to distinguish between the number of acid (or base) sites and the acid (or base) strength distribution.

Acidic and basic sites are usually generated during the catalyst synthesis but many pretreatments can change the number, the nature and/or the strength of the sites. Such changes may result, for instance, from: decomposition of ammonium or organic cations, ion exchange, reduction or oxidation of cations, hydration-dehydration, dehydroxylation by reagents in solution, upon heating or evacuation, water decomposition on polarizing cations, steaming, exposure to various gases, (e.g.  $\text{Cl}_2$ ,  $\text{CO}_2$ ,  $\text{H}_2\text{S}$ ,  $\text{F}_2$ ), treatment with chemicals (dealumination). Therefore, the choice of specific and defined conditions for characterization is of major importance.

No rigorous practical definition of acid strength exists outside of very dilute aqueous solutions where activity coefficients can be assumed to be unity. Each method of measuring the acid strength of surface sites is liable to give somewhat different answers, the results being qualitative at best. The dielectric constant of the medium, in which the acid or base probe is used influences the measured acid-base strength.

In general terms, an *acidic site* may be defined as a site on which a base is chemically adsorbed, and *basic site* as a site on which an acid is chemically adsorbed. A Brønsted acid shows a tendency to donate a proton and the Brønsted base to accept a proton. A Lewis acid is able to accept an electron pair and a Lewis base to donate an electron pair. The Lewis acid can be, for instance, a coordinatively unsaturated aluminium ion in alumina or silicoaluminates, a cation such as  $\text{Na(I)}$  or  $\text{Ca(II)}$  in zeolites, etc.

The acid or base strength is defined by comparing the interaction between the sites and reference (probe) molecules. For example, the acid strength is the ability of the site to convert an adsorbed reference neutral base into its conjugate acid. This process may be monitored by following the colour changes of the indicators or by such techniques as IR or NMR spectroscopies. Several criteria must be considered in the selection of these probes: their pK value must be adapted to the acidity or basicity of the surface under study; the size of the probe molecules should ensure that all sites are readily accessible; finally, the probe should be selected so that its interaction with the surface is easily studied by the available experimental techniques. Catalytic test reactions are sometimes used

for the evaluation of acid-base properties of catalysts. For example, dehydration of propan-2-ol is a convenient test for weak surface acidity.

Since acidic or basic sites may interact with each other, the site density ought to be determined. Moreover, an attempt should be made to describe the site location, particularly in the case of microporous acid catalysts (zeolites).

#### *b Redox Sites*

Redox sites may be separated into two categories, namely (i) sites incorporating atoms which, in the presence of the reactants, are oxidized or reduced, and (ii) sites able to form a charge-transfer complex by interaction with an electron acceptor or an electron donor.

In the case of *surface sites incorporating atoms*, the valence states and their eventual variation in the course of the reaction can be studied by spectroscopic methods such as electron paramagnetic resonance (EPR), XPS, ultra-violet photoelectron (UPS), IR, and near-edge X-ray (XANES) spectroscopies (Near-edge X-ray spectroscopy is abbreviated in some parts of the world, particularly in USA, as NEXASS).

Quantitative information on the number of sites may be obtained from a volumetric or gravimetric study of the adsorption of oxidizing or reducing molecules. Adsorption calorimetry can be used to determine the energetics of the site distribution, as in the case of acidic and basic sites.

The formation of a charge-transfer complex is related to the ionization potential ( $E_i$ ) of the electron-donor, to the electron affinity ( $E_{ca}$ ) of the electron acceptor and to the dissociation energy ( $E_d$ ) of the complex:



The number of ionized species is given by  $N_i = N \times \exp[-(E_i - E_{ca} - E_d)/(KT)]$ .

In the case of some paramagnetic molecules, the formation of a charge-transfer complex can be determined by EPR either directly, when the electron of the donor molecule interacts with the nuclear spin of the electron-acceptor site, or indirectly by observation of the electron delocalisation in the probe molecule. Both methods can yield quantitative information about the distribution of electron donor or electron acceptor sites when a range of probe molecules having different electron affinities or ionization energies are used.

### 11.2.2.5 Catalytic Properties

#### **A General Considerations**

In heterogeneous catalysis a fluid (liquid or gas) is brought into contact with a solid catalyst, which effects

a change of chemical composition of the fluid ideally without itself entering into the stoichiometric equations. Catalysis by solids can be observed only through the chemical change in the fluid which is in contact with the catalyst, the system being either closed or open. The system is called open when it exchanges matter and energy with its surroundings. The quantitative measure of catalytic properties is then based on the material balance of the system (the system could be defined as a catalyst bed, catalyst particle, an element of active surface or an active site) to which reactants are introduced and products removed, preferably at the steady state, when the catalyst is neither a net source nor a sink of material. The criterion used to define the steady state should be stated.

Quantitative description of catalytic properties requires that the system under consideration be unambiguously described with respect to system boundaries (mass of catalyst  $m_c$ , area of catalytic surface  $A_c$ , or volume of porous catalytic particle  $V_c$ ) and conditions such as composition, pressure, temperature, prevailing at the boundary (control variables). A set of data characterizing a catalyst must permit the prediction of material balance of the system containing the catalyst at steady state under at least one set of control variables. It is sometimes possible to represent a number of experimental observations by rate equation or a set of rate equations which may or may not be based on a mechanistic model. The model has to fulfil the above criteria within a certain range of validity which should be indicated. The catalytic system should be characterized with respect to the rate of chemical change (*activity*) and with respect to product composition (*selectivity*).

## B Catalytic Activity

### a Reaction Rate

We distinguish integral and differential characteristics of catalytic properties. One of the integral characteristics is the *extent of reaction*  $\xi$ . Generally, any chemical reaction, whether overall or an elementary step, can be represented by a stoichiometric equation:

$$\sum v_i B_i = 0$$

where  $v_i$  is the stoichiometric coefficient of component  $B_i$ , taken positive when  $B_i$  is a product and negative when it is a reactant. The chemical change occurring in the course of the reaction may be described by  $\xi$  (in mol):

$$\xi = \frac{n_i - n_{i0}}{v_i}$$

where  $n_{i0}$  and  $n_i$  are the amounts of substance  $B_i$  (in moles) at time zero and at any time, respectively. It is an extensive quantity attained under specified conditions.

An alternative expression is its dimensionless form, having a value between zero and unity, called *fractional conversion* or *degree of conversion*.

The drawback of integral characteristics such as extent of reaction or degree of conversion is that very many control variables such as the reactor type, feed composition, time, temperature, etc., influence the values obtained and have to be standardized. Moreover, with high conversion, a great difference in catalytic activity usually leads to only small differences in the conversion values.

A differential characteristic which demands a lower degree of standardization is the *reaction rate*. The rate of a chemical reaction with respect to compound B at a given point is defined as the rate of formation of B in moles per unit time per unit volume. It cannot be measured directly and is determined from the *rates of change* of some observable quantities such as the amount of substance, concentration, partial pressure, which are subject to measurements. Reaction rates are obtained from observable quantities by use of the conservation equations resulting from the mass balance for the given reactor type.

The conservation equation for component  $B_i$ , for any system, can be written as

$$F_{i,0} = F_i + F_{i,c} + (dn_i/dt)$$

where

$F_{i,0}$  = flow rate of component  $B_i$  into the system in mol s<sup>-1</sup>

$F_i$  = flow rate of component  $B_i$  out of the system in mol s<sup>-1</sup>

$F_{i,c}$  = rate of consumption of component  $B_i$  by reaction inside the system in mol s<sup>-1</sup>

$t$  = time

For an ideal gradientless flow reactor (*continuous stirred tank reactor CSTR*) in the steady state the conservation equation reduces to

$$r = -v_i^{-1}(F_{i,0} - F_i)/Q$$

where  $r$  is the reaction rate in mol s<sup>-1</sup> per unit amount of catalyst and  $Q$  is the amount of catalyst.

For an ideal *plug flow reactor* the mass balance in the steady state gives

$$r = -v_i^{-1}dX/d(Q/F_{i,0})$$

where  $X$  is the fractional conversion, and the term  $\tau$  (in units of time per amount of catalyst per amount of reactant)

$$\tau = Q/F_{i,0}$$

is called the *space time*. The inverse of the space time is the *space velocity*

$$v = F/Q$$

frequently expressed in  $\text{h}^{-1}$  (gas or liquid hourly space velocity, GHSV or LHSV, respectively), if the quantities of catalyst and reactants are expressed in the same units.

In the case of ideally stirred *batch reactor* the mass balance leads to the expression

$$r = v_i^{-1} (dn_i/dt)/Q$$

As the true state variable of the system the rate  $r$  depends only on the temperature and concentration if it is derived from data free of heat and mass transfer effects.

The reaction rate under specified conditions (composition, temperature, pressure) is a measure of the *catalytic activity* of the solid for conversion of B under these conditions. The amount of catalyst  $Q$  to which the reaction rate is referred may be expressed by the mass ( $m_c$ ), volume ( $V_c$ ) or the surface area ( $A_c$ ) of the solid catalyst. Correspondingly the values obtained are

$$\text{mass-specific rate} \quad r_m \text{ in mol s}^{-1} \times \text{kg}^{-1}$$

$$\text{volume-specific rate} \quad r_v \text{ in mol s}^{-1} \times \text{m}^{-3}$$

$$\text{area-specific rate} \quad r_A \text{ in mol s}^{-1} \times \text{m}^{-2}$$

In spite of the fact that it was previously recommended that  $r_m$  be called the *specific activity of the catalyst* (see Pure Appl. Chem. 46, 71 (1976)) the use of this term is now discouraged.

A rate equation describes the observed dependence of the rate of reaction on the composition of the fluid phase at the boundary of the system under consideration (e.g., catalyst particle, element of surface). The coefficients of the rate equation must be given in proper units so that a material balance of the system under consideration can be predicted unambiguously within the range of control variables over which validity of the rate equation is postulated. These *rate coefficients*  $k$  (the experimental rate constants) may be taken to characterize the catalytic activity.

For a single elementary reaction,

$$k = A \exp[-E/(RT)]$$

where  $A$  is the *pre-exponential factor* and  $E$  is the *activation energy*. Where an overall catalytic reaction obeys the Arrhenius equation over a certain range of temperatures the experimentally determined energy is an *apparent activation energy*.

A rate equation in terms of the local composition of reacting fluid in contact with the surface of the catalytically active material may be called the "*intrinsic*" *rate equation*; the coefficients in this equation are "*intrinsic*" *rate coefficients*. The local concentrations of reactants and products at the catalytic surface in general cannot be observed and have to be inferred from the observable composition at the boundary of a larger system, the observed rate of reaction and the kinetics

of mass transfer between the boundary of the larger system and the active surface under consideration.

The *turnover frequency*,  $N$ , (the term turnover number is discouraged) is defined as the number of molecules reacting per active site in unit time. It is necessary to specify the method used to estimate the number of active sites. Usually, the number of active sites will be assumed to be equivalent to the number of surface atoms, derived, in the case of metals, for example, from measurements of the chemisorption of a specified adsorptive.

#### *b Measurement of Activity Parameters*

Rates of reaction depend in general on the composition and on the temperature of the fluid surrounding the catalytically active solid. These quantities must be observed simultaneously for a catalyst particle in order to describe its catalytic activity.

Simultaneous measurements of the rate of change, temperature and composition of the reacting fluid can be reliably carried out only in a reactor where gradients of temperature and/or composition of the fluid phase are absent or vanish in the limit of suitable operating conditions. The determination of specific quantities such as catalytic activity from observations on a reactor system where composition and temperature depend on position in the reactor requires that the distribution of reaction rate, temperature and compositions in the reactor are measured or obtained from a mathematical model, representing the interaction of chemical reaction, mass-transfer and heat-transfer in the reactor. The model and its underlying assumptions should be specified when specific rate parameters are obtained in this way.

The spatial distribution of composition and temperature within a catalyst particle or in the fluid in contact with a catalyst surface result from the interaction of chemical reaction, mass-transfer and heat-transfer in the system which in this case is the catalyst particle. Only composition and temperature at the boundary of the system are then fixed by experimental conditions. Knowledge of local concentrations within the boundaries of the system is required for the evaluation of activity and of a rate equation. They can be computed on the basis of a suitable mathematical model if the kinetics of heat- and mass-transfer are known or determined separately. It is preferable that experimental conditions for determination of rate parameters should be chosen so that gradients of composition and temperature in the system can be neglected.

The *effectiveness factor* of a porous catalyst is the ratio of the rate of reaction to the hypothetical rate which would be expected if fluid composition and temperature in the pores corresponded to composition and temperature in the fluid surrounding the porous aggregate.

### C Selectivity

Very often a reactant or a set of reactants may simultaneously undergo several parallel reactions, giving different individual products,  $P_i$ , which react further in consecutive reactions to give different secondary products,  $P_j$ . A commonly encountered situation is the parallel-consecutive reaction network.



It is sometimes advantageous to consider not the individual products, but the sets of products, resulting from reactions of a given type, e.g., hydrogenation, hydrogenolysis, etc. In what follows the symbol  $P_i$  will designate either the individual product or a set of products. In the latter case each set of products will have the same elemental composition as the reactant (or set of reactants) B.

Selectivity may be determined in the integral or differential mode. *Integral selectivity* depends on the overall extent of the reaction (degree of conversion) and on the type of reactor used even if heat and mass transfer effects are eliminated. It may be called reactor selectivity for the formation of product  $P_i$  from the set of reactants B when it is calculated as the mole fraction of  $P_i$  in the products (excluding unconverted feed) at the exit of the reactor:

$$(S_i)R = \frac{n_i}{\sum n_i}$$

when the feed stream consist of the set of reactants B.

An alternative expression is the ration between the mass of  $P_i$  in the products and the total mass of products generated from B.

The *yield* ( $Y$ ) of product  $P_i$  is defined as:

$$Y = \frac{\text{Amount of B converted into } P_i}{\text{Amount of B introduced}} \\ = \frac{\text{Number of molecules of B converted into } P_i}{\text{Number of molecules of B introduced}}$$

The *conversions* ( $X$ ) of reactant B is defined as:

$$X = \frac{\text{Amount of B reacted}}{\text{Amount of B introduced}} \\ = \frac{\text{Number of molecules of B reacted}}{\text{Number of molecules of B introduced}}$$

Alternative expressions for yield and conversion can be obtained using masses of  $P_i$  and B, respectively.

On this basis yield = (selectivity)  $\times$  (conversion).

Selectivity is generally a function of conversion and will depend on the system under consideration if the relative extents of consecutive and parallel reactions depend on the spatial distribution of composition and on the residence time in the reactor.

*Differential selectivity*, or *intrinsic selectivity* of a catalytically active surface with respect to the forma-

tion of product  $P_i$  from reactant B may be evaluated as the ratio of the rate of reaction  $r_i$  resulting in product  $P_i$  and the sum of the rates of all reactions  $r_i$ . Consequently, the differential selectivity depends only on temperature and the actual concentrations of reactants but not on the reactor type used, and is more suitable for the discussion of the correlation of catalytic properties with the structure and chemistry of the catalytic system.

If the effects of operating variables on selectivity are to be expressed, instead of reaction rates  $r_i$  in the expression for differential selectivity the corresponding rate equations are introduced.

### D Relative Activities

For a rapid characterization of a series of catalysts it is sometimes advantageous to determine their *relative activities* at given reaction conditions. The methods of determining relative activities may be fairly simple, but they should only be applied to a family of similar catalysts in which case the mechanism of the test reaction can be assumed not to change. Then it is possible to compare the values, e.g., of the time variable necessary to obtain the same degree of conversion with the same starting reaction mixture. This is more justified than comparing the conversions obtained at the same reaction time or space time. The alternative is to determine the temperature at which different catalysts give the same degree of conversion under the same initial composition and time variable; this approach is closer to the operation of an industrial reactor. The reciprocal values  $1/T$  are compared, although the relationship between  $1/T$  and the relative activities is not rigorously linear even for reactions with the same mechanism and activation energy.

### E Inhibition of the Catalytic Action

#### a Types of Inhibitory Substances

The activity of practically all catalysts can be partially or totally inhibited by *inhibitory* or *deactivating substances*, in a broad sense. In what follows such a substance will be indicated by *IS*. This can be caused by: adsorption of *IS* more strongly than reactants on active sites (*as*); change of *as* due to reaction with *IS*: restriction of physical access due to formation of a (semi) impervious layer of *IS*.

The *IS* may (i) be present in the reactants as impurities, (ii) come from other sources (equipment, etc.) or (iii) be formed during the course of the reaction (by transformation of intermediary or final products, etc.).

Ideally, the characterization of catalysts with respect to inhibition should involve 3 types of information:

1. nature of the *IS* acting on the catalyst,
2. adequate relationship between the quantity of *IS* and catalytic properties,
3. time-dependent effects on activity, selectivity, etc., due to the presence, or a modification of concentration, of *IS* (decreases of catalytic activity with time, total or partial recovery of catalytic properties after removal of *IS* from the feed, etc.).

*IS* may be classified into three categories:

- **Poisons** (true poisons) are characterized by their propensity to attach very strongly, by a true chemical bond (e.g. covalent) to the surface atoms or ions constituting the catalytically active sites. Poisons act in minute quantities. Typical poisons of metals are S, As, etc. In most cases, activity and/or selectivity cannot be recovered without a drastic change in operating conditions (most often a regeneration). Recovery, if at all, takes place very slowly and/or only partially.
- **Inhibitors** have a transient effect (inhibition). All catalytic properties can be recovered after the supply of the inhibitor to the catalyst has been stopped, without otherwise changing the operating conditions. Inhibitors act in minute quantities, have a reversible effect and correspond to more or less strong bonding.
- **Fouling agents**, or mechanical inhibitors are bound by neither covalent nor other strong bonds to the active centres: the interaction is usually of the van der Waals, H-bond, or sometimes ionic, type. They form protective layers or block pores, thus physically impeding access of reactants to the active centres. The fouling agents causing real problems are those which have a long standing effect and do not disappear spontaneously. Carbon deposits act, partially or totally, this way. Other examples are vanadium and nickel sulfide deposits in hydrotreating catalysts.
- Fouling agents act in quantities equivalent to several layers spread over the catalyst surface or to pore volume; they may according to different cases, have a rapidly reversible, an only slowly reversible, or an irreversible effect.

#### *b Characterization of Catalyst Response to Inhibitory Substances*

In principle, sensitivity to inhibition (by poisons, inhibitors or fouling agents) depends on the *whole* catalytic reaction system: nature of catalyst, degree of ageing (in particular, nature and degree of poisoning, modification of activity and selectivity by inhibition and fouling), operating conditions, etc. Accordingly, the activity and selectivity of a catalytic reaction depends on all the previous history of the catalyst.

Sensitivity to the deactivating influence of impurities, reaction products or intermediates is expressed in dif-

ferent ways depending on the category of deactivating agent (poison, inhibitor, fouling agent).

#### *i) Poisons*

Sensitivity to poisons depends on:

- number of active centres in the catalyst: when it is small, the catalyst may be inhibited by a small amount of poison;
- strength of adsorption of the poison on the active centres; the weaker is the adsorption of poison, the lesser is the sensitivity of the catalyst to poison;
- the effectiveness of adsorbed poison for inhibiting the catalytic activity;

the latter decreases sometimes on adsorption of small amounts of poison on active centres more than in proportion to the fraction of active centres covered by the poison.

Sensitivity to poisons may be defined by:

1. the minimum amount of poison  $X_o$  per unit amount of catalyst required to eliminate the catalytic activity (sometimes called the lethal dose). If the number of active centres per unit mass of catalyst,  $X_t$ , is known, the quantity  $X_o/X_t$  should be recommended as the measure of the sensitivity of the catalyst to the poison in question.
2. the initial ratio of the fractional decrease in the catalytic activity ( $\alpha = (a_o - a_p)/a_o$ ) to the amount of poison  $n_o$  attached to the catalyst per unit mass,  $\alpha/n_p$  (where  $a_o$  is the activity of the catalyst in the absence of poison and  $a_p$  is the activity in the presence of poison). This ratio may be called initial sensitivity. Sometimes the ratio  $\alpha/c_p$  is used instead, where  $c_p$  is the concentration of the poison in the feed. This definition is not encouraged.

#### *ii) Inhibitors*

There is actually a whole spectrum of possible phenomena, between very strong irreversible poisoning and normal competition between molecules for a given site (this competition leading to a decrease of activity). Inhibitors, as defined above, correspond to a behaviour intermediate between those just mentioned. The sensitivity to inhibitors can thus be expressed either as in the case of true poisons, or as in the case of competition. In the latter formulation, for example, the value or relative value, of the adsorption coefficient could characterize the inhibitor.

It is advisable to define also the rate at which activity decays when the catalyst is contacted with a given concentration of inhibitors, or recovers, after addition of the inhibitor is discontinued.



### iii) Fouling Agents

The inhibiting influence of fouling agents is not a simple function of the quantity of deposited substance. The reason is that the relationship between this quantity  $w_p$  and activity depends on the nature and texture of the catalyst, the nature and concentration of the feed constituents, temperature and operating conditions, and the rate of build-up of the fouling deposit. With this restriction the sensitivity to fouling agents is defined as the quantity necessary to bring about a given effect on activity or selectivity.

### F Time-Dependent Characteristics

The composition, structure, texture, surface state, activity and selectivity of catalysts change continuously, at rapid or slow rates according to conditions, with time-on-stream. This change is characteristic of each catalyst, and depends on its formulation, preparation and previous history. *Deactivation* is one aspect. Another is the usually rapid changes that catalytic activity and selectivity undergo in the first few minutes, hours or sometimes days of operation: this may be called the *initial adjustment* to catalytic operation. A third aspect is the response to changing operating conditions (*response to change*).

The time-dependent changes of a catalyst are due to processes belonging to 6 main categories:

- (a) poisoning;
- (b) inhibition;
- (c) fouling;
- (d) sintering;
- (e) chemical reactions;
- (f) remodelling of the surface.

Poisoning, inhibition and fouling have already been defined. *Sintering* refers to the diminution of dispersion. All phases present in a catalyst (active phases, modifiers, support) potentially can undergo sintering.

*Chemical reactions* comprise reaction with feed intermediates or final products and reaction between catalyst components. They may result in the addition of material to the catalyst or its loss, by formation of a volatile compound.

*Remodelling* refers to changes of the surface which do not involve any of the previous processes: migration of active species inside a catalyst pellet, change of shape (independently from change of total surface area developed) of crystallites of a given phase, change in the number of steps, kinks on a surface, changes in surface/bulk composition ratio.

### G Regeneration

The performance of deactivated catalysts can often be improved by *regeneration*. Deactivation results from inhibition, from fouling and from sintering and all

of these may be reversed – at least in part – with some catalysts.

It follows that regeneration may consist of either (i) removal of *IS*; sometimes poisons, most often inhibitors or fouling agents, e.g., coke (hydrogenation catalysts, e.g., selective hydrogenation of pyrolysis gasoline) or (ii) redispersion of the active species (platinum catalysts) or (iii) both (hydrodesulfurization or catalytic reforming catalysts).

## References

1. *Pure and Appl. Chem.* **1972**, *31*, 579.
2. *Pure and Appl. Chem.* **1976**, *46*, 71.
3. *Pure and Appl. Chem.* **1985**, *57*, 603.

## 11.2.3 Methods and Procedures for Catalyst Characterization<sup>1</sup>

J. HABER, J. H. BLOCK AND B. DELMON

### 11.2.3.1 Introduction

This manual has been prepared by the Commission on Colloid and Surface Chemistry including Catalysis of the IUPAC. It complements the Manual on Catalyst Characterisation which concerned nomenclature [1] and should be read in conjunction with this earlier manual. The Manual of Methods and Procedures for Catalyst Characterization provides details and recommendations concerning the experimental methods used in catalysis. The objective is to provide recommendations on methodology (rational approaches to preparation and measurements). It is not intended to provide specific methods of preparation or measurement, nor is it concerned with terminology, nomenclature, or standardization.

### 11.2.3.2 Catalyst Preparation

The long-standing experience of industry in catalyst manufacture, the progress of scientific understanding of the processes involved and the development of the corresponding basic sciences (chemistry of solids, colloid chemistry, etc.) mean that catalyst preparation

<sup>1</sup> This Section was originally published in *Pure Appl. Chem.* **1995**, *67*, 1257–1306. © 1995 IUPAC.

is nowadays a science. That science provides well defined guidelines which are reflected in the following document.

Methods of catalyst preparation are very diverse and each catalyst may be produced via different routes. Preparation usually involves several successive steps. Many supported metal and oxide catalysts are prepared by the succession of impregnation, drying, calcination, activation; zeolite catalysts are prepared by precipitation of gel, crystallisation, washing, ion exchange, drying. The properties of heterogeneous catalysts depend on all their previous history.

Three fundamental stages of catalyst preparation may be distinguished:

- preparation of the primary solid (or first precursory solid) associating all the useful components (e.g., impregnation or coprecipitation, or, in the case of zeolites, crystallization);
- processing of that primary solid to obtain the catalyst precursor, for example by heat treatment;
- activation of the precursor to give the active catalyst: reduction to metal (hydrogenation catalysts), formation of sulfides (hydrodesulfurisation), deammoniation (acidic zeolites). Activation may take place spontaneously at the beginning of the catalytic reaction (selective oxidation catalysts).

#### A Preparation of the Primary Solid

All experimental parameters are critical for determining the characteristics of the solid obtained after the first step:

- aggregate morphology of the carrier used, if any;
- quantities used (solutions, carrier);
- concentrations;
- stirring conditions (shape and volume of vessel are important);
- temperature and temperature changes;
- sequence and duration of all operations;

Four main routes exist for preparing the primary solid: *deposition, precipitation and coprecipitation, gel formation, selective removal.*

##### a Deposition

###### (i) Impregnation

Impregnation consists in contacting a solid with a liquid containing the components to be deposited on the surface. During impregnation many different processes take place with different rates.

- selective adsorption of species (charged or not) by coulomb force, van der Waals forces or H bonds;
- ion exchange between the charged surface and the electrolyte;

- polymerization/depolymerization of the species (molecules, ions) attached to the surface;
- partial dissolution of the surface of the solid.

The type of product depends on the nature of both reactants (the liquid and the solid surface), and the reaction conditions. The main parameters affecting the liquid are the pH, the nature of the solvent, the nature and concentrations of the dissolved substances. The first parameter affects ionization and, in many cases, the nature of the ions containing the active elements. The second and third influence solvation.

The main properties of the solid are the texture, the nature of functional groups (e.g., the number and strength of the acidic and basic centers, the isoelectric point), the presence of exchangeable ions, and the reactivity (surface dissolution in acidic or basic solution, etc.).

In the overall impregnation process the following important facts should be noted:

- the properties of the liquid in the pores are different from those measured in the bulk;
- equilibrium between liquid and solid is slow to establish and even distribution of attached species inside the pores is not easy to attain;
- deposition involves many different types of interaction as described above.

Impregnation can be achieved by at least 8 different methods.

*Impregnation by Soaking, or with an Excess of Solution [2].* Excess liquid is eliminated by evaporation or by draining. Deposition of the active element is never quantitative. The quantity deposited depends on the solid/liquid ratio. Deposition is slow, requiring several hours or days. Extensive restructuring of the surface (loss of surface area, etc.) may occur. However, the method allows the distribution of the species to be very well controlled and high dispersions may be obtained. The method works best if ion/solid interactions are involved.

*Dry or Pore-Volume Impregnation.* The required amounts of components are introduced in the volume corresponding to the pore volume of the support. The method is best suited to deposition of species which interact very weakly with the surface, and for deposition of quantities exceeding the number of adsorption sites on the surface. If the number of species which can adsorb on the surface is smaller, a chromatographic effect may occur, i.e. attachment to the mouth of the pores. Redistribution inside the pores is very slow.

*Incipient Wetness Impregnation.* A procedure similar to dry impregnation, but the volume of the solution is

more empirically determined to correspond to that beyond which the catalyst begins to look wet. All the comments in the preceding paragraph apply.

*Deposition by Selective Reaction with the Surface of the Support.* The carrier is left in contact with an excess of solution for a definite time, and then the excess liquid is removed, e.g. using a dipping technique. The objective is to make a strong bond with the surface. The process is little used but it has potential for grafting or anchoring active elements to a support.

*Impregnation by Percolation.* The precursor is sorbed/ion exchanged by percolation of the impregnating solution through a bed of carrier. There is much similarity between this method and impregnation with an excess of solution (see above). The advantage is a faster approach to equilibrium. One can easily follow the progress of the process by analyzing the effluent. There may be differences in the degree of deposition along the carrier bed.

*Co-Impregnation.* Two or several active components are introduced in a single step. Co-impregnation with uniform distribution and without segregation of species is extremely difficult to achieve.

*Successive Impregnation.* Two or several active components are introduced sequentially. Drying (and often calcination) takes place between the impregnations. For the second impregnation the properties of the surface to take into account are those of the solid obtained after the previous impregnation.

#### *Precipitation-Deposition.*

##### *(ii) Ion Exchange*

The general comments under i) above remain valid.

##### *(iii) Gas-Phase Deposition*

Deposition occurs by adsorption or reaction from a gas phase. This method may ensure excellent dispersion and very well controlled distribution of the active species. Chemical vapour deposition is an example of gas-phase deposition.

##### *(iv) Solid-Solid Reactions*

In certain cases it is possible to use a solid salt of the active element, e.g. a nitrate, to impregnate the support. This is done by dry mixing. The method is well adapted to industrial production but is difficult to use reproducibly in a laboratory.

##### *(v) Wash Coat*

Monolith (or honeycomb) catalysts are prepared by covering the surface of the channels with a suspension

of small particles in water (the suspension is called "slurry" or "slip"). Water is evaporated and the final calcination promotes adhesion of the particles to the monolith.

#### *b Precipitation and Coprecipitation*

In all precipitations it is essential to carefully control all the details of the process including

- the order and rate of addition of one solution into the other;
- the mixing procedure;
- the pH and variation of pH during the process;
- the maturation process.

Precipitation involves two distinct processes, namely nucleation and growth. Nucleation requires that the system is far from equilibrium (high supersaturation, or, in the case of ionic species, a solubility product far exceeding the solubility constant of the solid to be precipitated). Growth of the new phase takes place in conditions which gradually approach the equilibrium state.

In the coprecipitation of a phase associating two (or several) elements, if one of them is contained in an anion and the second in a cation, the precipitate will have a fixed or at least very inflexible composition. If both are cations (or both anions) the characteristics of the reactions with a common anion (or cation) of the solution, the solubility constants, and the supersaturation values will all be different, and the properties of the precipitate will change with time. Consequently, coprecipitation does not in general give homogeneous precipitates. Methods are available to produce homogeneous precipitates (see item c) below).

The dispersion of the precipitate changes with the degree of supersaturation and its evolution during precipitation. Low supersaturation leads to poorly dispersed solids. Highly dispersed solids are thermodynamically unstable and tend to lose dispersion (Ostwald ripening). This takes place during the process of precipitation itself. If the effect is desired, a special maturation (or ageing) step is carried out at the end of the precipitation.

Many procedures are used for precipitation and coprecipitation. One simple method is to add dropwise the solution containing the active component to the precipitating solution, or vice versa. There is little difference between those inverse procedures. In both cases high supersaturation can be produced locally, leading, if the solubility constant is low, to fine precipitates. If not, redissolution takes place at the beginning of the process, when agitation disperses the precipitate in the liquid. In both cases, concentrations change con-

tinuously throughout the precipitation process resulting in an inhomogeneous product being formed, at least with respect to texture. Any precipitation process is situated somewhere between two extremes. Either the solutions are contacted instantaneously (only an ideal situation as, in all cases, diffusion has to take place), the supersaturation decreasing continuously, or the supersaturation is maintained constant during the whole precipitation process.

Instantaneous precipitation is achieved by two methods. The first consists in pouring continuously, in constant proportion, both solutions into a vessel under constant and vigorous stirring. The second consists in mixing the solutions through specially designed mixing nozzles. The latter method ensures a better uniformity in composition and texture of the precipitate.

Precipitation under constant conditions is achieved in the "homogeneous precipitation" method, in which the precipitating agent (e.g.  $\text{NH}_4^+$ ) is continuously supplied or produced in situ (e.g. by decomposition of urea). This method provides a low level of supersaturation, and hence, leads to poorly dispersed solids (see also item ii below).

#### (i) Synthesis of Zeolites and Related Materials

The nature of the microporous frameworks of zeolites obtained by crystallization of Al- and Si-containing reaction mixtures is defined by both the preparation conditions and their final structural Al content, whereas the nature and concentration of the active sites depends also on subsequent pretreatments (calcination, steaming, ion-exchange, etc.).

Zeolites are normally prepared by crystallization (precipitation) in hydrothermal conditions ( $T = 350\text{--}525\text{ K}$ ) of (Si,Al)-containing hydrogels [3]. Above  $373\text{ K}$ , crystallization is normally performed under autogeneous pressure. Both batch and continuous synthesis methods can be envisaged. Variables which affect the synthesis of zeolites fall into 3 categories:

1. parameters which determine the *crystalline field*: reactant composition, basicity (hydroxyl content), added salts and ions (organic and/or inorganic), temperature and pressure. Of particular importance in controlling synthesis are the molar ratios ( $\text{OH}^-/\text{SiO}_2$  and  $\text{Si}/\text{Al}$ ), and temperature, which affect the solubility of (alumino) silicate species and the kinetics of non-microporous phase(s) formation [3].
2. *directing effects* from the presence of structure-directing (templating) agents (organic compounds and bases, alkali cations, and other miscellaneous organic molecules). Attention should be paid to possible competition between these agents as well as to (partial) secondary reactions or degradation of the organic additives.

3. miscellaneous *operational variables* the importance of which may be overlooked, such as the nature of the Si and Al sources (type of alumina and silica affecting their solubility, content and nature of contaminants, secondary reactions when using organo-Al or Si reagents), the order of addition of the reactants (which can affect the aluminosilicate gel formation, its homogeneity, and its sorptive and templating properties), ageing and ripening prior to crystallization (affecting gel pH, viscosity, and composition), stirring rate (mass homogeneity, uniform temperature control), presence of seed crystals (from non-intentional autoclave contamination), and synthesis time (possibility of formation of other denser non-zeolitic or zeolitic phases at long crystallization times).

#### (ii) Precipitation-Deposition

Precipitation-deposition is a special technique in which an active element (e.g. Ni) is deposited onto a carrier (e.g.  $\text{SiO}_2$ ) in suspension in the precipitating solution (e.g.  $\text{Ni}(\text{NO}_3)_2$ ) by slow addition, or in situ formation, of a precipitating agent (e.g.  $\text{NH}_4^+$ ). The technique takes advantage of the fact that precipitation onto the carrier needs a lower supersaturation than formation of the new phase directly from the liquid. It is essential to maintain supersaturation at a constant moderate level. This is achieved, as in the homogeneous precipitation technique, by decomposition of a suitable substance (e.g. urea), which releases the precipitating agent continuously, or by controlled and progressive addition of the precipitating agent.

The technique is excellent if the primary particles of the carrier are not porous (e.g. Aerosil). With a porous support deposition takes place preferentially in the external parts.

#### c Gel Formation and Related Processes

A series of widely different techniques is considered here which, starting from solutions, give gels or solid-like substances, which retain all the active elements contained in the starting solutions, and from which the solvent and reaction byproducts are eliminated by evaporation or sublimation [4-6]. These gels are later decomposed or further transformed, usually to oxides.

The gel can be obtained by a range of different methods:

- chemical reaction, e.g. formation of a tridimensional polymer by alkoxide hydrolysis (sol-gel process) and, more generally, by polymerization (of an anion, such as molybdate);
- complexation, e.g. with an acid-alcohol such as citric acid [7];
- freeze drying;

- addition of a gum or a gelling agent (hydroxymethyl cellulose, etc.)

Gel formation under the influence of heat and evaporation in the 'oil-drop' process is related to this group of preparation methods.

The basic principle underlying these processes is to maintain together, without segregation, all the active components present in a homogeneous solution. Once a gel or a solid-like substance is formed segregation becomes difficult, because diffusion is strongly restricted. The success of the fabrication rests on rapid transformation of the starting solution to a very viscous medium and the solid-like substance.

#### *d Selective Removal*

Selective removal is a method used for very few, but important catalysts. Raney Nickel is a representative of this group. Starting from a relatively coarse powder of an alloy (e.g.  $\text{NiAl}_x$ , constituted of several phases in the present practice), one component (Al) is removed by a leaching agent (NaOH) leaving the active agent (Ni) in a relatively highly dispersed form.

#### *e Pillared Layer Compounds*

One can take advantage of existing layered structures for making solids with approximately slit-shaped pores. Such solids are most often prepared from clays (pillared clays). In a first step, the sign and number of the charges compensating those of the layers must be adjusted. This is generally done by Na ionic exchange. The interlayer ions are then substituted by polyions resulting from a condensation of ions in the solution in which the layered solid is suspended. A classical example is the  $\text{Al}_{13}$  Keggin cation:  $[\text{Al}_{13}\text{O}_4(\text{OH})_{24}(\text{H}_2\text{O})_{12}]^{7+}$ . This is a critical step. Attachment of the polyions on the outer surface of the layered crystallites, as well as further polymerization of the polyions, should be prevented. A second, equally critical step, is the removal of the interlamellar solution by careful drying or sometimes freeze drying, and progressive heating (see Section B below). During heating, the polyions lose their solvation water as well as the hydroxy groups they may contain and bind to the layers. Pore openings may be very broad in the direction perpendicular to the layers: 1.2 to about 2 nanometers. They mainly depend on the nature of the polycation intercalated. The lateral distance between the pillars can only be controlled to a certain extent.

Successful preparation of pillared structures demands that (i) adsorption of polyions on the outside of the crystallites be prevented, (ii) polymerisation be inhibited (iii) and an attachment of the layers to basal planes or to other layers be prevented. Phenomena (i) and (ii) lead to structures with no pillars, or uncompletely pillared, and to blocking of pore mouths.

Phenomenon (iii) is responsible for so-called "house of cards" structure with very large irregular mesopores.

#### **B Treatment of Intermediate Solids or Precursors**

These treatments include drying, thermal decomposition of the salts, calcination, etc. The product obtained is a reasonably inert solid (usually an oxide) which can be stored easily.

Many recommendations are common to all treatments (as well as to activation, examined below). The main recommendation is that in all these processes all the particles of catalyst be subjected statistically to exactly the same succession of conditions. A fixed bed does not ensure this uniformity. Only moving beds (fluid beds, rotating furnaces, circulating beds or spray drying) fulfil the above requirements.

A second recommendation is to supply a sufficient quantity of gas or liquid to the reactor to ensure complete reaction (dry air or nitrogen for complete evaporation, air or oxygen for quantitative formation of oxides, etc.). In this respect special consideration should be given to mass and heat transfer. Drying may result in a loss of uniformity in the distribution of a given element in the catalyst. This occurs if the compound in which this element is contained is not sufficiently strongly attached to the solid (carrier). It can then be expelled from the pores if bubbles form in the pores, and expand. A similar effect results if migration in a liquid film occurs towards places (external surface) where evaporation takes place. Very slow drying avoids these problems. Marked improvement is often achieved by the application of freeze drying.

Salts giving gaseous decomposition products (e.g., nitrates) do not usually present problems. With organic salts a problem may arise because of the possible formation of carbonaceous residues. Sufficient air or oxygen must be supplied to avoid this difficulty.

The same recommendations are valid for all types of calcination treatment.

All zeolites need to be thermally pretreated prior to their use as catalysts in order to remove the sorbed water. General information on this subject is available. Zeolites normally have a remarkable thermal stability (up to 875 K or more). The latter decreases, however, with increasing Al content and for larger-pore-size materials. In addition, for materials prepared in the presence of an organic agent, a calcination step is needed to remove the occluded organic species.

In both cases, framework Al may be exposed to water vapour at rather high temperature (525–875 K), which can lead to dealumination of the zeolite structure (production of nonframework Al species and decrease in the concentration of acid sites, modification of sorptive properties and catalytic behaviour). In order

to avoid unwanted dealumination by minimizing the local and instantaneous water vapour pressure:

- shallow bed thermal treatments should be preferred to deep bed calcinations;
- oxidative calcination of organic-containing materials should be performed in conditions minimizing the water vapour production;
- the exposure to steam of the hydrogen forms of zeolites should be avoided as much as possible.

### C Activation of the Precursor

In the activation of the precursor the procedures differ greatly from case to case. The recommendations in Section A above are valid in the present case. Catalysts always contain species with different reactivities, even when of simple composition. Differences may arise from (i) different locations in the depth of the pellets (effect of diffusion on reactivity), (ii) different crystallite sizes (especially if a nucleation and growth mechanism operates), (iii) various degrees of interaction with the support, and (iv) differences in the degree of contamination. For these reasons, the activation rate becomes slow as the degree of reaction proceeds; there are even cases where reaction is never complete. The proper characterization of a catalyst with respect to its activation therefore requires that all the above recommendations are taken into account and that the degree of activation is carefully determined. This implies that the activated solid is carefully analyzed.

If a nucleation and growth mechanism operates it is probably possible to control dispersion by modifying the rate of nucleation compared with the rate of growth. In all cases there is usually a coupling between activation and loss of dispersion. For those reasons a complicated activation procedure has to be selected in many cases. Either the composition of the activating agent or the temperature or both are changed progressively or stepwise.

Active catalytic forms of zeolites can be obtained conventionally by cation exchange. Care should be taken to avoid chemical modifications induced by a too low or too high pH of the exchange solution, which can lead to the extraction of Al and/or Si species and the formation of lattice defects. Protonic (Brønsted) sites are generated by ammonium exchange (preferably at buffered and slightly basic pH, 7–9) followed by calcination at 300–500 °C. Higher deammoniation temperatures are preferred for materials with lower Al content (higher acidic strength). Metals can be introduced into zeolites via ion exchange and subsequent reduction or via sorption of neutral soluble or volatile species (for example carbonyls).

### D Forming Methods

In principle the support, precursory solids, precursors or catalysts, can be used as such (e.g. powders obtained

by spray drying). But, generally the catalysts are used as entities of larger size and/or better defined shapes (beads, pellets, extrudates, rings, monoliths, etc.). Some forming operation [8] has thus to take place sometimes during preparation. This is done on the support if the deposition method (including precipitation–deposition) is used. Otherwise, a precipitate, or an intermediary solid (precursor produced by, e.g., the methods described in Section A.a) is the material used for the forming operation. As a rule, mesoporosity (pore diameter less than 50 nm) is created before forming. The forming operations determine the porosity corresponding to larger pores.

The forming operations also determine other very important characteristics of catalysts:

- mechanical properties;
- resistance to thermal shock;
- gas or liquid flow through the reactor.

Depending on the technology (e.g. fluidization, moving bed or fixed bed) and the conditions of the catalytic process, the shape and size of catalyst entities may vary appreciably, e.g. finely powdered, cylinders, beads, etc. A general problem is to make entities of dimensions larger than 1 mm from fine powder particles.

The powder may be either dry or slightly damp during shaping. Materials which are difficult to shape are treated with additives.

The development of zeolite-containing catalysts has led to the development of binders. Modern catalyst technology (especially for fluidized-bed catalytic cracking and hydrocracking) selects binders which may have a variety of properties of their own (catalytic, trapping of poisons, etc.)

Shaping additives may act as lubricants, plasticizers, cements, porosity promoters (porogenic additives), etc. [9]. The powdered starting material mixed with the additives may be dry, or converted to a plastic pulp by the addition of a suitable liquid. One sometimes distinguishes:

- liquid processing: gelification (oil drop), spray drying;
- paste processing: grinding, kneading to a pulp, extruding;
- powder (or solid) processing: tableting, cementing;

#### *a Powder: Preparation, Crushing and Grinding*

Grinding may be an essential preliminary operation, and is used sometimes for producing special commercial catalysts. In a powder, which is a collection of particles of relatively small size (typically 0.5  $\mu\text{m}$ –1 mm), the particles may have different shapes and this influences strongly the shaping operations. The crushing and/or grinding operation is aimed at producing

particles of a size such that after the forming operation pores of the desired size are formed. Crushing and/or grinding is used with material of natural origin or with products of operations of the A.c category. Grinding may take place in the absence (dry) or presence (wet) of a liquid, usually water.

#### *b Forming by Crushing*

This is a very special, but important, case of a forming operation used to make ammonia catalysts. The fused mass is crushed to irregular lumps and sieved to proper size [10].

#### *c Spray Drying*

In spray drying, a slurry of a powder in suspension in water is fed to a nozzle which sprays small droplets into hot air. Spray drying gives particles of almost identical shapes (spheres with a slightly depressed surface at one spot) and sizes, used as such in fluid-bed operations.

#### *d Oil Drop*

A sol or gel is introduced as drops through a nozzle into a hot liquid. Heat removes the solvent and brings about the hardening of the gel. According to relative densities the drops may move downwards (oil drop per se) or upwards. Beads are obtained.

#### *e Granulation*

Granulation (or pilling) is the agglomeration-forming operation made by progressive humidification of a powder in a rotating granulator, resulting in the formation of spheroidal particles, granules or beads. These beads are usually not very uniform in size [9]. In the operation, many differently sized individual particles are put into motion under a spray of liquid (water or aqueous solution) in a horizontal rotating cylinder or a pan rotating around an axis inclined at about 45°. The pan may be concave (hemispheric granulator or "bowl granulator") or cylindrical (flat granulator or "dish granulator").

#### *f Tableting*

In tableting, the powder is firmly compressed in a die to be shaped into small cylinders, rings and even beads. In most cases some plasticizing agents are added to the powder (talc, graphite, stearic acid, etc.). One may also use porosity additives (powder of an easily decomposed compound, polymer fibres, etc.). Tableting is one of the few forming operations which has been studied systematically.

#### *g Extrusion*

In extrusion, a paste, which may be "soft" or "stiff" (or: "wet" or "dry") is pushed through a die, forming a cylinder which is cut into small sections. Peptization,

by addition of an adequate substance, is often used before extrusion in order to induce hardening. The sections of the die may have different shapes.

Monolith is now one of the most widespread form of catalysts. Monoliths are formed by extrusion through special dies creating multiple channels. (A variant in monolith manufacture uses corrugated foils of the support which are joined together to create channels).

#### **E Stability During Handling and Storage**

The objectives of the first series of steps in the preparation of catalysts (usually corresponding to A.a and A.b) is to make a catalyst precursor, very often an oxide, the stability of which is compatible with handling and transportation. However, there is presently a trend towards carrying out activation in the manufacturing or other specialized plants so that solids more reactive chemically and more fragile mechanically have to be handled.

The solids to be stored have high surface areas and are highly reactive and sensitive to contamination. They should be stored in hermetically closed containers. All contaminants are potentially harmful:

- water brings about hydrolysis and formation of liquid films which dissolve active elements, and may bring about the corrosion of containers;
- CO<sub>2</sub> brings about carbonate formation. The reaction of carbonates, during activation, may give an activated catalyst with altered texture;
- if hydrocarbons are present, there is a danger of uncontrolled reactions during calcination (overheating) or activation (over reduction);
- poisons.

#### *a Activated Catalysts*

Practically all cases where protection of activated catalysts is necessary correspond to metal or reduced-sulfided catalysts. Three methods are widely used for protecting these catalysts from alteration during storage and handling.

#### *(i) Passivation*

Passivation often involves the controlled exposure of the catalyst to air at ambient temperature. Rapid exothermic reactions are prevented while forming stable layers which inhibit further rapid reaction upon air exposure. Similar exposure to other passivating reagents would also lead to air stable surface layers on the metallic surfaces. A typical example is the passivation of Ni catalysts which would oxidize catastrophically upon exposure to air, and of highly-dispersed supported Pt catalysts. Many methods or techniques are available:

controlled oxidation, adsorption of protecting (usually inhibiting) molecules, reactions with a weakly oxidizing agent dissolved in water.

*(ii) Protection by an Inert Gas*

Activated metal catalysts and hydrodesulfurization catalysts can be stored and handled in an inert atmosphere ( $N_2$ ). This can be achieved industrially without excessive cost.

*(iii) Protection by a Condensed Phase*

Activated metal catalysts (essentially Ni) can be effectively protected by a wax (stearic acid, etc.). Even catalysts in a powder form, for use as suspensions, can be protected this way. The waxy mixture is shaped to pellets. Part of the catalysts used in the fat and oil industry undergoes this treatment.

### 11.2.3.3 Characterization of Surface Properties by Adsorption Methods

Adsorption methods may be used to provide information about the total surface area of a catalyst, the surface area of the phase carrying the active sites, or possibly even the type and number of active sites. The interaction between the adsorbate and the adsorbent may be chemical (chemisorption) or physical (physisorption) in nature and ideally should be a surface-specific interaction. It is necessary to be aware, however, that in some cases the interaction between the adsorbate and the adsorbent can lead to a chemical reaction in which more than just the surface layer of the adsorbent is involved. For example, when using oxidizing compounds as adsorbates ( $O_2$  or  $N_2O$ ) with metals such as copper or nickel or sulfides, subsurface oxidation may occur.

Physical adsorption is used in the BET method to determine total surface areas and this has been described in a previous IUPAC document (this Handbook, Section A11.21) [11].

Many catalysts comprise an active component deposited on a support. In order to investigate relationships between catalytic properties and the amount of active surface it is necessary to have a means of determining the surface area of the phase carrying the active sites (which we shall call active phase hereafter) in the presence of the support. One has to resort to phenomena specific to the active phase. Chemisorption on the active phase is commonly used for this purpose.

Because of its intrinsically *specific* nature, chemisorption has an irreplaceable role. It should be recognized, however, that well defined thermodynamic equilibrium physisorption is much more difficult to achieve by chemisorption than with physisorption. Moreover, it does not obey simple kinetics. Empiricism permits

the derivation of procedures which give reproducible results, and yield values which are proportional to the true surface area within certain limits. But the real coefficient of proportionality is actually unknown. Different procedures are used, according to the nature of the active phase/support system to be characterised, and depending on the choice of adsorbate. Provided standard, reproducible procedures are used, invaluable information can be obtained.

A wide variety of adsorbates has been used, the choice depending on the nature of the surface to be examined and the type of information being pursued; e.g. for metals,  $H_2$ ,  $CO$ ,  $O_2$  and  $N_2O$ ; for sulfides,  $NO$ ,  $CO$ ,  $O_2$ ,  $H_2S$  and organosulfur compounds; for oxides,  $NH_3$ ,  $CO_2$  and various organic compounds.

With simple probe molecules, such as  $H_2$ , information about the number of surface metal atoms is readily obtained by using adsorption measurements. However, even with such simple probe molecules further information about the heterogeneity of a surface may be obtained by performing temperature-programmed desorption measurements. With probe molecules which are chemically more specific (e.g.,  $NH_3$  and organic amines,  $H_2S$  and organic sulfides) it may be possible to obtain information about the number and nature of specific types of surface sites, for example, the number and strength of Lewis or Brønsted acid sites on oxides, zeolites or sulfides.

The use of more than one technique can provide important additional information about the nature of sites on a particular solid surface. For example, infrared spectroscopy may be used in conjunction with quantitative chemisorption measurements of  $CO$  to determine the type of binding of  $CO$  and hence the nature and number of the active sites. The combination of chemisorption and ESR spectroscopy permits the characterization of the electronic properties of the surface.

Care should be taken when using adsorption with microporous solids, as new effects may arise. Specific literature should be consulted in this case.

#### A Methodology

Adsorption can be performed in a number of different ways which may involve static and flow or dynamic techniques.

##### *a Static Methods*

The static methods are volumetric or gravimetric. The volumetric method involves the use of a vacuum system comprising two sections, a dosing section which allows the introduction of accurately measured quantities of the adsorbate, and a sample section which contains the catalyst. The precision of the volumetric method depends on accurate calibrations of volumes.



including the dead space in the sample section, precise control of the temperature of the dosing and sample sections, and accurate pressure measurement.

Gravimetric methods may be used to determine adsorption of most molecules, even  $H_2$ , if proper instruments are used. An advantage of the gravimetric method is that it eliminates the requirement to make dead volume corrections. Also, in contrast to the volumetric method, this technique does not lead to cumulative errors since the quantity of gas adsorbed and the equilibrium pressure are measured independently of each other. The main disadvantages are the high sensitivity to weight changes required, the difficulty in controlling the temperature of the sample, and taking account of buoyancy corrections, particularly in flow experiments.

#### *b Dynamic Methods*

In the single-flow technique, a carrier gas containing the molecules to be adsorbed pass continuously over the catalyst. The flow method of determining gas adsorption has the advantages that no vacuum system is required and no dead volume corrections need to be made. The method is also rapid and easy to use. Disadvantages are the need to use very pure carrier gases, and the fact that for slow or activated adsorption processes equilibrium adsorption may be difficult to determine. The flow method is not recommended for obtaining total isotherms.

The pulse technique is in many ways similar to the flow technique except that the adsorbate is introduced by adding pulses (e.g. from a gas sample valve) into the carrier gas. The pulse volume is chosen so that the first few pulses will be completely adsorbed. Further pulses are introduced until no more gas is adsorbed. The quantity of gas adsorbed is calculated by summing up the amounts adsorbed in the successive pulses. This technique is only applicable for strongly retained adsorbates.

Chromatographic methods are widely used for the study of both physisorption and chemisorption. In its simplest form the technique consists of passing a pulse of the adsorbate through a column of the adsorbent and measuring the retention time and registering the elution curve. Measurement of the variation in the retention time as a function of temperature permits the evaluation of the enthalpy of adsorption, and analysis of the shape of the elution curve provides information about the adsorption isotherm.

It is possible to determine the amount adsorbed by a titration method. For example, the amount of hydrogen adsorbed on a Pt surface may be titrated with pulses of oxygen. The oxygen adsorbed can in turn be further titrated by pulses of hydrogen. From the stoichiometry of the  $H_2/O_2$  reaction a measure of the number of surface metal atoms can be obtained.

#### *c Desorption*

Desorption is always an activated process and may conveniently be studied by temperature-programmed techniques. Information is obtained in this way on the adsorption kinetics and the energetics of the gas/solid interactions.

#### *d Precautions*

The choice of experimental conditions for the adsorption experiment is critical and must be based on experimentation for each active phase of interest. Since the amount of surface area of the active phase depends on the method of pretreatment, a standardized pretreatment of the material before chemisorption is essential. For example, this involves using conditions of flow rate of gas, heating rate, time of heating, final temperature, etc., identical to those used in any other related study of the same catalytic material.

Problems in the determination of the surface area of active phases can arise from a number of sources. An overestimation of the amount of active surface can be caused by spillover of the adsorbing species on the support, solubility in the adsorbent, subsurface oxidation (when using  $O_2$  or  $N_2O$ ), or as a result of additional physical adsorption on the support. The extent to which these factors affect the accuracy of the results depends on the nature of the active phase, the support, and the conditions of the experiment. Problems can occur with adsorptives which may "corrode" the surface. For example, CO can remove Ni atoms from the surface of small Ni particles even at ambient temperatures.

Further problems can arise because of uncertainties concerning the stoichiometry of the adsorption reaction. For most metals it is assumed that the surface stoichiometry with  $H_2$  is  $H/M = 1$ . However, there is evidence especially for very small metal particles (of the order of 1–5 nm) that the stoichiometry can exceed  $H/M = 1$ . For quantitative measurements of surface area it is necessary to establish the chemisorption stoichiometry and structure. In practice it is usually possible to achieve approximate estimate of the surface area by some other independent method (for example, from particle size analysis by X-ray line broadening or by TEM). In the case of CO, the CO/M ratio is generally taken as 1.0, but the true value may depend on the particle size and on the particle morphology. With  $N_2O$  the  $N_2O/M$  ratio at monolayer coverage is usually assumed to be 0.5, but once again there is no certainty about the validity of this particular assumption.

This problem of the stoichiometry of the surface reaction is a general one and is probably best circumvented by reporting the adsorption data as the amount of adsorbed gas per unit mass of the catalyst or of the active phase under well defined conditions.

## B Categories of Catalysts

The choice of adsorbate and the methodology depends on the nature of the adsorbent. In principle, the following categories should be distinguished as follows

1. metals;
2. zeolites;
3. other acidic oxides, especially amorphous and poorly crystalline ones;
4. other oxides, of which oxidation multicomponent catalysts constitute an important subcategory;
5. sulfides (hydrotreating catalysts);
6. carbides, nitrides and other solids.

The following sections will consider only categories (1), (2) and (3), and (5). In spite of the importance of category (4), no general guidelines emerge. Category (6) corresponds to catalysts still in primary stages of evaluations. We shall not examine the use of chemisorption for these categories.

### *a Metals [12–16]*

The first step in a chemisorption measurement on a metal is reduction in hydrogen except in cases where preparation ensures perfect cleanliness. The temperature and time of reduction are determined by the metal involved, higher temperatures being required for Fe, Co and Ni, for example, than for Pt group metals. After reduction, the hydrogen is removed from the surface of the metal by evacuation or by flushing with a very pure inert gas (He or Ar is preferred because N<sub>2</sub> may react with some metals to form nitrides). The desorption temperature is usually chosen to be about 20–50°C lower than the reduction temperature. Desorption of hydrogen is continued at this temperature, typically for 0.5–1.0 h, at which point the sample is cooled to the temperature of the chemisorption experiment. Too low a temperature can cause problems due to an increase in the amount of physical adsorption on the support, or because of long delays in attaining equilibrium; too high a temperature can cause problems due to restructuring of surfaces, migration of impurities from bulk or support or because of a decrease in the amount of adsorbate on the active surface due to nonadsorption into weakly binding surface sites.

An important parameter is the time allowed for the adsorption steps. In principle, adsorption on a clean metal surface should be very rapid at ambient temperature. However, in practice, particularly with metals such as Fe, Co or Ni, there is often a substantial contribution from a slow adsorption process. An arbitrary time for approximate equilibration is normally determined by experimentation, e.g., by ascertaining the time after which the pressure in a volumetric system decreases at a rate less than a preset value. Typical adsorption times for Pt metals range from a few minutes

up to about 1 h, while for Ni equilibration times generally need to be in excess of 1 h, and often as long as 16 h is required for the first adsorption point. After measurement at the first equilibrium pressure further doses of adsorbate are introduced and the adsorption repeated. The time required to attain approximate equilibrium for the second and subsequent points is less than for the first, typically a few minutes for Pt metals and 1 h for Ni. By measuring a second isotherm after evacuation, the total and irreversibly adsorbed amounts of hydrogen can in principle be distinguished.

Ideally, true adsorption equilibrium should be measured. To prove that, the amount adsorbed should be the same when reaching equilibrium from lower and higher pressures (or temperatures). If not, this is the proof that processes other than adsorption take place.

The pressure range used for the determination of the adsorption isotherm depends on the nature of the metal and on the choice of adsorbate. For example, with hydrogen on Ni the pressure range is usually from about 10 kPa to about 50 kPa, whereas for Pt, pressures an order of magnitude lower may be used.

Several methods are used to calculate the amount of adsorbate corresponding to monolayer coverage. Extrapolation of the nearly linear high pressure portion of the adsorption isotherm back to zero pressure, and calculation of the amount of gas adsorbed at zero pressure is the most usual procedure. One reason for choosing this method is that it minimizes errors due to weak adsorption on the support since at low pressures this is directly proportional to the adsorption pressure. An alternative means of determining the monolayer coverage is to measure the quantity of gas adsorbed at a fixed reference pressure (e.g., about 25 kPa).

In the particular case of Ni catalysts, where adsorption is slow, the reverse, or desorption, isotherm method has been devised. The first measurement is made at a high pressure of hydrogen (typically about 50 kPa) after about 45 minutes. Although hydrogen is still being adsorbed it is assumed that the values measured represents a good compromise: the amount of hydrogen still needed to reach equilibrium and the increasing amount of hydrogen adsorbed by the support due to spillover are supposed to cancel out. After this first measurement, a desorption isotherm is determined by progressively removing hydrogen from the system. Extrapolation of the desorption isotherm back to zero pressure provides a means of determining the monolayer coverage. It is generally observed that the desorption isotherm has a lower slope than the corresponding adsorption isotherm.

To measure hydrogen adsorption using the flow method a sample previously reduced and flushed free of hydrogen by an inert gas stream (usually Ar) is exposed to a constant flow of, for example, a H<sub>2</sub>/Ar mixture (typically containing 2% H<sub>2</sub>) and the quantity of hy-

drogen adsorbed is determined, often using a thermal conductivity detector. The quantity of hydrogen adsorbed corresponds to the equilibrium adsorption at the partial pressure of hydrogen used in the experiment (for example, 2% of atmospheric pressure). This is taken to be a measure of the monolayer coverage by  $H_2$ .

The use of  $N_2O$  to determine Cu surface areas requires great care to avoid subsurface oxidation. The frontal chromatography method, in which a dilute mixture of  $N_2O$  and He (typically, 2%  $N_2O$ ) is passed over a large bed of catalyst until no further  $N_2O$  is reacted, appears to be the most reliable method. In the pulse method the extent of subsurface oxidation depends on the temperature (a very serious problem above about  $100^\circ C$ ), the size of the  $N_2O$  pulse, the size of the catalyst sample, the metal loading of the sample, and the geometry of the catalyst bed. In general, small pulses of  $N_2O$  should be used, at temperatures below about  $60^\circ C$ , with a deep catalyst bed ( $>1$  cm).

#### *b Acidic Amorphous Oxides and Zeolites*

A description of catalyst acidity requires the determination of the nature, number and strength of acid sites [17–19]. The Brønsted acid sites are able to transfer a proton from the solid to a suitable adsorbed molecule; the Lewis acid sites are able to accept an electron pair from a suitable adsorbed molecule. A particular acidic solid usually does not contain only a single class of acidic sites. Both Brønsted and Lewis sites may be present. Moreover, in general, there will be a distribution of strengths of acid sites. The acidity of a surface may be determined using aqueous or nonaqueous methods. When aqueous methods are used, some complications may arise because water may alter the structure of the solid, equalize acidity strengths, or create new sites, for example transformation of Lewis sites into Brønsted sites.

Aqueous methods include the use of ion exchange to determine the total number of acid sites, and titration of aqueous slurries of the acidic solids with a standard base. The method cannot be applied to water-sensitive solids.

Nonaqueous methods include the use of amine titration and adsorption of indicators for visual measurement of acid strength. This procedure allows both the determination of the total amount of acid sites and also the acid strength distribution. A disadvantage is that bulky molecules (amines and indicators) are used and these may be excluded from entering small pores. With zeolites, the slow rate of diffusion and equilibration has to be taken into account. Spectroscopic measurement of acid strength may also be performed using amine titration and indicator adsorption. Ultraviolet or fluorescent indicators may be used.

Microcalorimetric measurements during adsorption of suitable probe molecules and temperature-

programmed desorption of chemisorbed bases are important methods of studying acidity. The equipment required is simple to construct and operate, for example a temperature-programmable flow microreactor coupled to a thermal conductivity-type detector. When the temperature is increased linearly, the rate of desorption of an adsorbed base (for example, ammonia, organic amine, pyridine, etc.) will show a maximum in temperature, and under ideal conditions, this may be related to the activation energy of desorption. By varying the degree of coverage of the acidic oxide with the base, it may be possible to obtain a broad spectrum of strengths of adsorption as a function of surface coverage. A variation on this method is to determine the adsorption of a weak base at different degrees of prepoisoning with a strong base.

Infrared spectroscopy is an important technique for studying acidity. Acidic OH groups can be studied directly. Probe molecules such as pyridine may be used to study both Brønsted and Lewis acidity since two forms of adsorbed probes are easily distinguished by their infrared spectra. Quantitative infrared spectroscopy may be performed by measuring the spectrum of acidic OH or probes adsorbed on thin, self-supporting wafers of the acidic solid. Other spectroscopic methods which may provide information in specific cases include Fourier Transform Raman spectroscopy, electron spin resonance spectroscopy, ultraviolet spectroscopy, and nuclear magnetic resonance spectroscopy.

Finally, it may be possible to use the rate of a chemical reaction to determine the actual number of active acidic sites. Furthermore, it may be possible to obtain an estimate of the range of strengths of acid sites by using different reactant molecules. For example, it is known that dehydration of alcohols requires only relatively weak acid sites, whereas cracking of alkanes requires very strong acid sites.

#### *c Sulfides*

The problem with sulfide catalysts (hydrotreatment) is to determine the *active centres*, which represent only part of their total surface area. Chemisorption of  $O_2$ , CO and NO is used, and some attempts concern  $NH_3$ , pyridine and thiophene. Static volumetric methods or dynamic methods (pulse or frontal mode) may be used, but the techniques do not seem yet reliable, due to the possible modification (oxidation) of the surface or subsurface regions by  $O_2$  or NO probe molecules or the kinetics of adsorption. CO might be more promising. Infrared spectroscopy, especially FTIR seems necessary to characterise co-ordinatively unsaturated sites, which are essential for catalytic activity. CO and NO can also be used to identify the chemical nature of sites (sulfided, partially reduced or reduced sites). For such

measurements, the samples must be sulfided or re-sulfided in the IR cell. The technique still needs improvements and standardisation.

### 11.2.3.4 Fine Structure of Catalysts [20]

#### A Surface Structure and Chemical Composition

Although many techniques are available for the examination of solids not all are appropriate for the study of real catalysts and some require special expertise in the interpretation of the results. Moreover, the nature of the sample may be changed by the application of the technique. Therefore, it is essential to choose appropriate techniques very carefully and to be aware of the problems associated with each specific method.

Heterogeneous catalysis being concerned with surfaces, it is recommended in principle that surface sensitive methods should be used. However, some surface sensitive techniques are only sensitive to the peripheral zones of particles and cannot probe the internal surfaces of porous materials. These techniques, therefore, find limited application in the study of porous catalysts. Access to these inner surfaces is gained by using other techniques where the incident probe and the returning signal are both penetrating. (The following sections concentrate on methods in this category.)

The fact that surface atoms in the system may make only a small contribution to the total signal is a potential problem but it is minimised in the important case of highly dispersed metal particles within the pores of high area supports. Small particle sizes ensure that the major fraction of the detected signal is generated by surface atoms. A large number of particles within the volume sampled ensures adequate signal strength.

#### B Surface Structure and Topography

##### a Electron Microscopy

In electron microscopy as in any field of optics the overall contrast is due to differential absorption of photons or particles (amplitude contrast) or diffraction phenomena (phase contrast). The method provides identification of phases and structural information on crystals, direct images of surfaces and elemental composition and distribution (see Section H below). Routine applications, however, may be hampered by complexities of image interpretation and by constraints on the type and preparation of specimens and on the environment within the microscope.

##### (i) Conventional Transmission Electron Microscopy (CTEM)

It is advisable to use CTEM rather than TEM (transmission electron microscopy) to designate the method (TEM may cover several techniques). CTEM takes

advantage of amplitude contrast (bright-field imaging mode). CTEM is suitable for examination of supported catalysts with particle sizes down to 2–3 nm, giving information on particle location over the support, on particle size distributions in favourable cases, on particle and support morphology and on the nature and distribution of deposits having a thickness of the order of 2–3 nm. Surface topography can be examined using replication techniques. For particles smaller than about 2 nm analysis of micrographs on a routine basis is not possible and even in the 2–10 nm range interpretation must be approached with caution.

##### (ii) Techniques Related to CTEM

*Dark-field methods* Dark field images are obtained by admitting only diffracted electrons and excluding directly transmitted electrons. Dark-field imaging selectively detects crystallites with crystallographic plane spacings within a relatively narrow range.

*High-Resolution Electron Microscopy (HREM)* The periodic structure of a crystal is not visible in a CTEM image but is revealed, to a limited extent, if the technique is converted to HREM by modifying the method of image formation either in the CTEM instrument or in specialized machines operating at 0.5–1.0 MeV. Lattice fringe images represent the simplest case and show an intensity modulation which gives the spacing of the atomic planes lying parallel to the incident beam, enabling catalyst particles to be identified. In certain instances fringes from the support can be used for an accurate assessment of small (down to 1 nm) particle sizes, and to determine pore dimensions and interlayer distances. In the case of heavy metals the crystal structure of particles of this size can be studied also. The amount of crystallographic information is increased by the formation of structure images but interpretation then requires comparison with images reconstructed by computer.

*Reflection Electron Microscopy (REM) and Reflection High Energy Electron Diffraction (RHEED)* When the specimen is set at a glancing (or grazing) angle to the incident beam, images of the surface may be obtained together with RHEED patterns; (the RHEED experiment can also be carried out in a dedicated instrument). The method is sensitive to atomic-height features such as steps, emergent dislocations and small particles on smooth surfaces.

*Scanning Electron Microscopy (SEM) [21].* Topographical images in a SEM are formed from back-scattered primary or low-energy secondary electrons. The best resolution is about 2–5 nm but many routine studies are satisfied with a lower value and exploit the

ease of image interpretation and the extraordinary depth of field to obtain a comprehensive view of the specimen. With noncrystalline catalysts, SEM is especially useful for examining the distribution and sizes of mesopores. An energy dispersive X-ray spectroscopy device is a frequent attachment in the instrument (see Section H).

*Scanning Transmission Electron Microscopy (STEM) [22].* STEM represents a merger of the concepts of TEM and SEM. Modes of operation and mechanisms of contrast and of imaging are essentially the same as in CTEM but the main advantage of STEM is the ability to carry out microanalysis at very high resolution (see Section H).

*Selected Area Diffraction (Also Called: Microdiffraction).* In both CTEM and STEM, diffraction patterns can be recorded from small areas of the specimen by positioning the beam at a chosen point in the image and switching to diffraction mode. Because CTEM uses a nonconvergent (parallel) beam, the minimum region which can be sampled is about 500 nm and the selected area diffraction patterns obtained are of the usual electron diffraction type, giving two-dimensional interplanar spacings and angles. In STEM the incident beam is convergent and areas from 50 nm (microdiffraction) down to less than 1 nm (nanodiffraction) (the latter in dedicated instruments) can be examined. In addition, the region of reciprocal space sampled in convergent beam diffraction is larger than in the case of selected area diffraction. Hence, a *single* convergent beam diffraction pattern can provide very accurate three-dimensional crystal symmetry information, allowing a full analysis of the point and/or space group of the material. In comparison with XRD, the volume examined is minute.

## C X-Ray and Neutron Methods for Structure Determination

### a X-Ray Diffraction and Diffusion

X-ray diffraction (XRD, sometimes also called WAXS; wide-angle X-ray scattering) is one of the most important techniques for catalyst characterization. For most catalysts XRD is limited to powder pattern identification of crystalline phases. For zeolites, and catalysts with good crystallinity, long range order exists, and XRD can give a complete description of their structure. In all cases, the possible presence of amorphous phases should be taken into account in interpretation.

The technique can be complemented by line-broadening analysis which gives valuable information on the size of individual crystallites. Variations of ratios between lines indicate either order imperfections along

certain crystallographic directions or spontaneous orientation of the crystallites in the sample holder.

Small-angle X-ray scattering (SAXS) provides information on ultradisperse (e.g. colloidal) and generally poorly ordered materials. The technique is very close to RED (Section b) below) in several aspects, and can, in principle, be applied in the same equipment. Commercial equipments exist; they are equipped with a rotating anode for generating high X-ray intensities. Interpretation needs a sophisticated software.

For all these equipments, attachments permit measurements at high temperatures and in controlled atmospheres.

### b Radial Electron Distribution (RED)

In samples with crystallites of size less than about 1.0–1.5 nm and in amorphous samples periodicity does not extend over a range sufficiently long to be detected by the XRD process. In practical terms the only structural information accessible concerns short-range order. Analysis of the X-ray wide-angle scattered intensity gives interatomic distances and coordination numbers, averaged spherically around all atoms. Excellent information can be obtained with solids composed of one single or two different atoms. Good information can be obtained if one type of atom in a more complex solid has a sufficient concentration and an atomic weight much larger than the others: the information then concerns that particular atom. For supported metals, estimates of structures, morphology and size may also be obtained if the atomic number of the metal is much larger than that of the atoms constituting the support.

### c Extended X-Ray Absorption Fine Structure (EXAFS) [20]

The oscillations which occur in the X-ray absorption coefficient in the energy range of 50–1000 eV above an absorption edge contain information on the distances between the absorbing atom and its surrounding coordination spheres, the number of surrounding atoms, the identities of the absorber and its neighbors and the dynamic and static disorder in the internuclear distances.

The distance to the first coordination shell can be determined to within 1–2 pm, particularly when elements of higher atomic number are involved; for succeeding shells accuracy falls to 10–20 pm. Uncertainty in coordination numbers is greater, being about 20% for the first shell. (The RED technique gives interatomic distances directly and accuracy does not fall sharply beyond the first shell.) The major advantage of EXAFS is that the short-range chemistry it reflects can be examined separately around each type of atom, a facility which is particularly useful for the study of

multimetallic catalysts and which is not available with RED. [23, 24]

#### *d Techniques Related to EXAFS*

In the X-ray absorption edge spectroscopy, enhanced absorption occurs at the  $L_2$  and  $L_3$  edges of certain elements giving a 'white line' with an intensity proportional to the number of d-electron vacancies in the absorbing system. Fractional differences in d-electron band occupancy can be investigated for the absorber in various environments including compounds and small catalyst particles. Characterization by surface extended X-ray absorption fine structure (SEXAFS) [25] is best achieved by monitoring the photoelectrons, Auger electrons or secondary electrons generated by X-ray absorption. These emissions relate directly to the X-ray absorption coefficient but originate within the first few atom layers at the surface. X-ray absorption fine structure (NEXAFS or XANES) [24, 25] contains information on bond angles and site symmetries and thus gives valuable structural data. Data analysis, however, is more complex than in EXAFS, molecular chemisorption being the most tractable case.

EXAFS-type fine structure can also be detected in high-energy electron-energy-loss experiments either in transmission through very thin samples using an electron microscope (extended energy loss fine structure, EXELFS; see Section H.6) or in a surface-sensitive reflection mode (SEELFS, 'surface extended') using an Auger spectrometer [26].

#### *e Neutron Diffraction*

Neutron diffraction gives the same kind of information as X-ray diffraction. Signal strengths are low but neutrons permit specimen examination under extreme conditions of temperature and pressure and detection of low- $Z$  elements, particularly deuterium. The method may also take advantage of *differences* in cross-section between pairs of catalytically important atoms which are larger than the corresponding differences in the X-ray case. Large amounts of sample are necessary (often around 1 kg). [23, 27]

#### **D Ion Scattering Techniques**

Ion scattering spectroscopy (ISS), or low-energy ion scattering (LEIS), and Rutherford backscattering spectroscopy (RBS), or nuclear backscattering spectroscopy (BNS) or high-energy ion scattering (HEIS) are well established for chemical analysis, but for structure determination they are at the development stage. ISS is now a commonly used technique. A beam of ions (usually 1–5 keV noble gas ions) is directed on the surface. Although such high energy ions can penetrate the solid, only backscattered primary ions are examined which have undergone an inelastic collision with the first atom layer at the surface and so the tech-

nique has extreme surface sensitivity. The energy spectrum of the backscattered ions is equivalent to a mass spectrum of the surface, with a detection limit of about 0.1 monolayer. Given suitable pretreatment and calibration procedures, an accuracy of 5–10% can be achieved in quantitative elemental analysis. The use of noble gas ions of different atomic masses permits resolution of signals coming from a wide range of different surface ions.

In RBS techniques incident protons (200–400 keV) or helium ions (1–3 MeV) are used with a penetration depth of several microns. The technique is useful for examining the geometry of catalyst pores, particularly those below about 2 nm, which are not easy to study by other methods. In principle, target atom identity and position can be determined simultaneously by an energy analysis of the backscattered ions but data interpretation is not possible if more than three elements are present in the specimen. Sensitivity is greatest for heavy atoms in a light matrix and concentrations can be measured to better than 5%. Refinements are possible for single crystals, such as epitaxy, but the corresponding techniques are outside the scope of the present document.

#### **E Electron State and Local Environment of Elements**

Three techniques give access to the environment of nuclei (electronic shells, valency, symmetry, matrix interactions). All of them are bulk techniques but when properly used, are extremely useful for catalysis.

#### *a Nuclear Magnetic Resonance (NMR) [20]*

The quantum energy levels of a nucleus depend on all the electric and magnetic interactions to which is subjected. These are influenced by the nature of the bonds in which it is involved, elements present in the vicinity (a few tenths of a nanometer), and the local structure of the matrix. Compared to SAXS, RED or EXAFS, NMR gives little information on distance but much more details on the *chemical* environment.

Spectra of solids are complicated, because of the multiplicity of parameters involved, especially by anisotropic interactions as dipolar coupling. Many techniques both experimental or computational have been developed for interpretation. A technique particularly useful for catalysis permits to selectively suppress anisotropic contributions by mechanical rotation of the sample (magic angle spinning, MASNMR) and by rotation of the nuclear magnetic dipoles with sequences of radiofrequency pulses.

Dynamic phenomena such as surface mobility can be approached by NMR because some signals either average or not according to lifetime of configurations.

The inherent sensitivity of NMR is low. It is however possible to get larger signals from surfaces by using highly dispersed or porous materials. The easiest

nucleus to study is  $^1\text{H}$  while organic adsorbates can be investigated using the  $^{13}\text{C}$  resonance. A wide variety of zeolitic solids [28–30] has been studied using  $^{27}\text{Al}$  and  $^{29}\text{Si}$  NMR, the chemical shifts obtained by MASNMR revealing the local structure in the vicinity of a given nucleus.  $^{129}\text{Xe}$  NMR as a probe atom adsorbed in pores is useful for determining the pore structure of zeolites. Most transition elements have a magnetically-active isotope but adequate signals can be expected in a few cases only, including  $^{51}\text{V}$ ,  $^{55}\text{Mn}$ ,  $^{59}\text{Co}$ ,  $^{93}\text{Nb}$ ,  $^{185}\text{Re}$ ,  $^{187}\text{Re}$ , and  $^{195}\text{Pt}$ .

#### *b Electron Spin Resonance (ESR)*

ESR permits the determination of the number and location of unpaired electrons. These data provide information concerning the structure and environment of surface species. Sensitivity is high, with the possibility of detecting  $10^{11}$  spins in favourable cases, namely species present at concentrations of about one part per billion, but polycrystalline samples with the paramagnetic centres randomly oriented often generate spectra which are poorly resolved. Catalytic applications include investigations: of adsorbed radicals, particularly those containing oxygen: of transition metal ions on oxide surfaces: in zeolites, as probes of the environment in the vicinity of the ion. Weak interactions can be observed by special pulsed methods, including the electron spin echo technique.

#### *c Mössbauer Spectroscopy*

Mössbauer spectra provide information on: (a) the oxidation state, coordination number and ligand type of the resonant atom; (b) on the electron distribution in the resonant atom and the electric charges on its neighbors; (c) on ferromagnetic ordering in iron and its alloys, which is particle size dependent; and on the strength of binding of the resonant atom to its surroundings. Mössbauer measurements at room temperature and above can be made routinely only with a limited number of isotopes, including  $^{57}\text{Fe}$ ,  $^{119}\text{Sn}$ ,  $^{121}\text{Sb}$ ,  $^{151}\text{Eu}$ , and  $^{181}\text{Ta}$ ; The use for pure catalysts is thus limited but by doping a material with no Mössbauer activity of its own with a few percent of a Mössbauer-active species (e.g.  $^{57}\text{Fe}$ ), a spectrum is obtained which is sensitive to the nature of the host matrix immediately surrounding the dopant atoms. In such experiments, however, independent measurements must demonstrate that the Mössbauer-active material is in the sample and atomically dispersed through the matrix.

In the usual transmission mode of operation, surface sensitivity can be achieved by examining very small particles (<10 nm) or thin foils (<2.5 nm) but an alternative approach involving backscattered electrons or fluorescent X-rays is under development. [31]

For some purposes it is useful to employ the emission mode of operation, e.g., for the study of Co in

sulfides. It should be checked that the cascade of nuclear and electronic events involved in emission does not generate false signals, especially when the matrix is poorly conducting. Mössbauer spectroscopy is in principle a bulk technique and its application to catalysts problems requires differentiation between bulk and surface lattice positions.

## **F Vibrational Spectroscopies**

#### *a Transmission Infrared Spectroscopy (IR)*

This vibrational spectroscopy is used for characterization of high-area supported or unsupported catalysts, including zeolites. Information is available, either directly or by study of 'probe' adsorbates, on the chemistry of surface groups (particularly on oxides). It is also used for the study of the behaviour of precursor compounds during catalyst preparation. Problems include low transmission at high metal loadings and strong oxide scattering. Absorption at lower wavenumbers often prevents observation of modes such as adsorbate-metal stretching.

Fourier Transform (FTIR) spectrometers offer two pronounced advantages over dispersive instruments: higher energy throughput and faster data acquisition or higher signal-to-noise ratio. Data processing is easy. These features are significant when examining very strongly absorbing and scattering solids and when following dynamic processes. Much IR transmission work, however, requires examination of only limited frequency ranges at medium resolution and computerised dispersive spectrometers may then be preferable.

Examination of infrared-opaque catalysts, e.g., carbon-supported, coked or which have high metal loadings, requires special specimen preparation techniques. These may be avoided by using other vibrational techniques described below.

#### *b Infrared Emission Spectroscopy*

There are few catalytic applications of this method. Low signal strengths make the use of Fourier Transform (FT) spectrometers advantageous.

#### *c Diffuse Reflectance Spectroscopy (DRS)*

DRS provides spectra in the range  $200\text{--}15\,000\text{ cm}^{-1}$  and is useful for specimens which absorb and scatter IR radiation very strongly. It benefits from being used with FT spectrometer (DRIFT).

#### *d Internal Reflectance Spectroscopy*

Catalysts can be examined as either very fine powders or pressed wafers but the technique has not been developed extensively.

### e Photoacoustic Spectroscopy (PAS)

A PAS cell coupled to an FT spectrometer covers the UV-visible and IR ranges. Metals are difficult to examine and catalyst studies have been limited.

### f Others

There is a number of vibrational spectroscopic techniques not directly applicable to the study of real catalysts but which are used with model surfaces, such as single crystals. These include: reflection-absorption infrared spectroscopy (RAIRS or IRAS); high-resolution electron energy loss spectroscopy (HREELS, EELS); infrared ellipsometric spectroscopy.

### g Raman Spectroscopy

This technique is widely applicable. The large frequency range ( $50\text{--}4000\text{ cm}^{-1}$ ) makes adsorbate-adsorbent stretching modes accessible. Problems include specimen heating, high background fluorescence and low signal strengths. Surface enhanced Raman scattering (SERS), however, can give greatly increased signals in favourable cases, e.g., with rough surfaces or small particles of certain compounds. It is particularly useful in the studies of supported monolayer catalysts and adsorbed layers.

### h Inelastic Neutron Scattering Spectroscopy (INS)

Using incident neutrons with a continuously varying energy in the range  $5\text{--}500\text{ MeV}$  and registering the spectra of backscattered neutrons, information can be obtained on vibrational modes in adsorbed molecules. As the cross section of the hydrogen atom is one order of magnitude larger than that of other atoms, the technique is mainly used to study the hydrogen or hydrogen-containing species adsorbed on a wide variety of substrates.

## G Electron Spectroscopies

Electron spectroscopy was first developed for chemical analysis (ESCA). In the form of core photoelectron spectroscopy (XPES, often shortened to XPS), valence band photoelectron spectroscopy (UPES, also called PES or UPS) and Auger electron spectroscopy (AES) it can be applied on a routine basis for rapid chemical analysis of a large variety of solid surfaces; neither technique detects hydrogen nor does AES detect helium. Surface sensitivity is high, the depth sampled being in the approximate range  $2\text{--}10$  atom layers. A qualitative interpretation of the spectra is straightforward but quantitative interpretation can present a number of problems.

### a Photoelectron Spectroscopy (XPES, UPES)

X-ray photoelectron spectroscopy (XPES) is based on the analysis of the kinetic energy distribution of core level photoelectrons ejected as the result of irradiation

with monochromatic or narrow-band X-rays. The best sensitivity is of the order of a few percent of a monolayer and for most instruments spatial resolution is around  $0.2\text{ mm}$ . With suitable calibration procedures elemental surface concentrations can be measured with an accuracy of the order of  $20\%$ . It constitutes a major tool in catalyst characterization. The major interest is centred on observations of 'chemical shift' effects which reflect the oxidation state, and the chemical environment of the emitter. Quantitative applications, especially to complex systems such as catalysts, can involve problems due to sample charging and to the choice of calibration procedures. They usually necessitate independent data concerning catalyst structure and texture. XPES has been widely used in catalyst research to provide general qualitative analyses, to investigate the depth profile distribution of active species, to obtain estimates of dispersion, clustering and other morphological variations, to study metal-metal and metal-support interactions and to examine the chemical states of additives, poisons and transition metal ions in zeolites. Proven measurement techniques and models for interpretation [32-34] are available.

Ultraviolet photoelectron spectroscopy (UPES) probes the valence band in the solid or the molecular orbitals in adsorbed species. The technique has no direct analytical potential but gives information on the local geometry at an adsorption site and on electronic structure. [35]

### b Auger Electron Spectroscopy (AES)

The Auger effect occurs, in competition with X-ray fluorescence, as a result of the intraatomic reorganisation of electron states which follows ionization of an atom. Auger peaks occur in XPS spectra but the major application of the effect employs ionization by an electron beam (AES). The technique is similar to XPES in surface and elemental sensitivities and quantitative accuracy and has advantages of faster data acquisition and much smaller area of sampling. Chemical shifts are of magnitude similar to and in some case greater than the magnitudes of the shifts encountered in XPES. In practice, however, AES is not used for quantitative study of changes in chemical environment because of difficulties in measuring shifts with sufficient precision. An alternative approach recognizes that for transitions involving the valence band or valence molecular orbitals, the chemical state of the atom will have a significant effect on the *shape* of the Auger line. Lineshape cannot yet be interpreted on a routine basis but at a qualitative level it can sometimes be used as a 'fingerprint' of a particular species.

While XPES has been applied extensively for the examination of changes in chemical environment, uses of AES have been concentrated on elemental identification and quantification, particularly in the case of



chemisorption systems. The main areas of investigation have been promoters, catalyst deactivation and poisoning, segregation in alloys and the effects of adsorbates on surface composition.

## H Determination of Spatial Distribution of Elements

### a Analytical Electron Microscopy

The incident beam in an electron microscope generates a number of signals which carry chemical information. The term analytical electron microscopy strictly refers to the detection of X-rays caused by sample ionization in a dedicated STEM-type instrument or in an adequately equipped SEM (B.a.ii) or CTEM (see B.a.i)

### b Energy Dispersive X-Ray Spectroscopy (EDS, EDX)

Analysis of characteristic X-rays provides identification and quantification of elements with  $Z > 10$ ; improvements in X-ray detectors should reduce this limit to  $Z = 6$ . The original electron probe microanalysis (EPMA) was essentially a low resolution SEM with an X-ray detector but the SEM mode suffers from two disadvantages: X-ray spatial resolution is relatively poor (1–2  $\mu\text{m}$ ) and quantitative analysis involves corrections for various processes within the thick specimen. With specimens sufficiently thin for TEM or STEM use (<200 nm) the X-ray resolution is improved (<50 nm) and a semiquantitative analysis can be obtained without application of corrections; more rigorous treatment of the data gives relative concentrations to within about 5%, with a minimum detectable mass fraction of 0.3 wt % [36].

### c Electron Energy Loss Spectroscopy (EELS)

Ionisation of atomic core levels generates 'edges' in the scattered-electron energy distribution which identify the species involved. The technique is sensitive to elements with  $Z < 10$  and so complements X-ray microanalysis. Of the two methods, EELS has superior sensitivity and spatial resolution. It has been less widely used, however, because quantitative analysis requires very thin specimens and simple semiquantitative measurements are not possible due to the complex nature of the spectrum background. Structure in the energy distribution above an edge contains EXAFS-type information (see EXELFS, Section C.d).

### d Scanning Auger Microscopy (SAM)

If the incident beam in an Auger spectrometer is rastered over the specimen surface, the strength of a particular Auger transition can be used to generate an elemental map of the surface. SAM has the high surface sensitivity characteristic of AES and similar elemental sensitivity and spatial resolution (down to about 100 nm) [37].

## I Secondary Ion Mass Spectroscopy (SIMS)

In SIMS a primary ion beam (1–20 keV) causes ejection (sputtering) of neutrals and ions from a solid specimen; the secondary ions are mass-analyzed. In "static" mode, sampling is restricted to the first 1–3 atom layers at the surface by keeping the sputtering rate low (0.1 nm/hour). The ejected ions and ion clusters give information on the nature and may give clues to the chemical state of species present.

In "dynamic" mode, the sputtering rate is high (1  $\mu\text{m}/\text{hour}$ ) and the technique gives a depth profile of the sample with a depth resolution of 2–10 nm and a lateral resolution of 1–60  $\mu\text{m}$ . The advantages of SIMS are its ability to detect hydrogen and isotopically labelled species, its very low detection limit ( $10^{-5}$  atomic %) and its very large dynamic range ( $10^5$ – $10^6$ ). Its disadvantage is that sensitivity varies from element to element by up to 5 orders of magnitude and also depends very strongly on the chemical environment of a given species (matrix effect). Therefore, quantitative analysis is possible only in those relatively few cases where suitable calibrations are available.

## J Ion Beam Techniques

Prompt nuclear reaction analysis (PNRA or NRA), light ions with energies below 2 MeV impinging on light target nuclei excite nuclear transmutations. As with RBS, both the identity and depth profile of the target species can be determined from an energy analysis of the emission. NRA complements RBS in being suitable for observation of elements with  $Z < 20$ .

## K Depth Profiling

The distribution of species normal to the surface can be obtained nondestructively by variation of the emission angle in XPS or AES (limited to a total depth of about 50 nm), by Rutherford backscattering spectrometry (applying only to elements with  $Z > 10$ ) and by nuclear reaction analysis ( $Z < 20$  only). Depth resolution in both RBS and NRA is in the range 5–50 nm.

Destructive methods involve mechanical and chemical erosion (low resolution) and ion sputtering, which is by far the most widely used of any of the depth profiling techniques. Surface atoms are progressively removed by ion bombardment and are analysed by SIMS. Alternatively, the residual surface may be analysed, generally by AES. The method is universally applicable and in principle is capable of near-atomic depth resolution. In practice, conversion of the observed signal, as a function of time, into concentration as a function of depth may not be easy for a complex system. It should be noted that the information obtained is reliable for the first layer, but for deeper layers the possibility of scrambling of the atomic layers

under the influence of the ion beam must be taken into account.

### 11.2.3.5 Catalytic Properties

The correct evaluation of catalytic properties demands that heat and mass transfer limitations are eliminated or properly accounted for. It also demands that the catalyst is in the working state, as opposed to the transient state observed at the beginning of most catalytic tests. The absence of gas-phase reactions or reactions catalyzed by the reactor wall should also be verified. This must be kept in mind in the following, in which measurement methods, kinetic analyses including the influence of heat and mass transfer and deactivation or, more generally, time-dependent effects will be examined. Regeneration of catalysts will be examined at the end.

#### A Reactor Types and Measurement Methods [38]

The usefulness of a catalyst is expressed in terms of its activity, selectivity and life. The objective of catalyst testing in the laboratory is to provide information on one or more of these properties.

Laboratory reactors may be divided into steady-state (continuous) and non-steady-state. Steady-state reactors may be further subdivided into:

1. plug flow,
2. continuous stirred tank reactor, (also called gradientless flow reactor, or ideal back-mixed reactor, or perfect agitation reactor),
3. fluidized-bed.

Non-steady-state reactors may be subdivided into:

4. batch,
5. discontinuous flow, i.e., pulse or transient.

Other types of reactors, such as trickle bed or bubble (slurry) reactors, are used only in special cases for reactions of liquids with gases catalysed by solids.

An important criterium for the choice of reactors is whether they can operate in isothermal conditions. Data obtained in a non isothermal mode of operation are difficult to interpret.

Operation of the various reactors may be in integral or differential mode, and the latter may involve either a single pass or a recycle system using internal or external recycle.

These reactors give different types of information and the choice depends on the information required. The main uses of laboratory reactors are as follows: (The numbers refer to the types of reactor listed above and indicate the preferred choice.)

- (a) to provide "activity values" in order to compare catalysts (1, 2, 3, 4, to a limited extend 5);
- (b) to study slow changes in activity (1, 2);
- (c) to study rapid changes in activity (5);
- (d) to reveal the role of heat and mass transfer (1, 2, 4);
- (e) to derive the kinetic equation, i.e., to determine the influence of composition, pressure, temperature and contact time (1, 2, 4);
- (f) to provide kinetic data for modeling of industrial reactors (1, 2, 4).

In the following sections the various types of reactors are described in more detail, as also are the methods used to introduce the reactants. This is followed by a brief summary containing suggestions on how to perform typical experimental measurements of catalytic properties.

#### *a Plug-Flow Reactor*

The plug-flow reactor is usually made of a glass (Pyrex or quartz) or metal tube with a sintered disc or other appropriate means for supporting the solid catalyst, either alone or mixed with an inert diluent solid. One or several thermowells are located in the reactor to monitor the catalyst bed temperature. It is convenient to use thermocouples sliding inside thermowells to monitor axial or longitudinal temperature gradients. The reactor is heated in any convenient way, but should, as far as possible, behave isothermally. The reactants and any diluent gas are brought to a temperature close to that of the catalyst before passing through the catalyst bed. At the outlet of the reactor the reaction products are sampled, either as gases, liquids, or combinations of the two and analysed, usually by gas chromatography and/or by mass spectrometry.

This reactor operates under steady-state conditions, but it can also provide information about the evolution of the catalytic activity with time during the approach to steady state. Ideally, in this reactor there is no mixing of fluid along the flow path and the contact time in the reactor is the same for all the elements of fluid.

One disadvantage of this, and indeed all continuous flow reactors, is that if the catalyst is very sensitive to poisons there is a risk that a small amount of poison in the reactant would accumulate on the catalyst during the experiment and cause major changes in activity and/or selectivity. In the laboratory this problem can usually be avoided by using very pure reactants.

The plug-flow reactor may be operated in the differential or the integral mode. In the differential mode (small conversion) the whole catalyst can be considered to be exposed to the same concentration of reactants. The influence of products is generally weak, except when the catalyst is extremely sensitive to one particular product. The plug-flow reactor operating in the dif-

differential mode is the simplest and most reliable way of determining the order of reaction with respect to reactants and products. This may be achieved by a systematic variation in the initial concentration of the reactants.

In the differential mode further major advantages are:

- (i) it provides good kinetic data because of the short holdup;
- (ii) the low conversion helps minimize heat and mass transfer problems;
- (iii) the influence of parameters such as temperature, pressure and concentration can be studied separately;

The major disadvantages of using a plug-flow reactor in the differential mode are:

- (i) at the small conversions required large errors in analysis can occur;
- (ii) the technique is time-consuming in kinetic measurements;
- (iii) high gas velocities may be required to keep conversions low.

The integral plug-flow reactor has the advantage that large conversions facilitate analysis and provide more accurate kinetic data. Disadvantages of the integral mode are problems in maintaining isothermal operation, the existence of concentration gradients, and possible heat and mass transfer limitations. Furthermore, accurate kinetic analysis of integral data is generally more difficult than for differential ones. In general in a laboratory reactor, in contrast to an industrial reactor, the depth of the catalyst bed is small, so that the reactor has a behaviour intermediate between that of a plug-flow and a back-mixed flow reactor.

#### *b Continuous Stirred-Tank Reactor (CSTR)*

The ideal continuous stirred tank reactor (back-mixed reactor) is free from intrareactor concentration gradients.

Truly differential reactors of this type provide the most useful kinetic data. However, as indicated above they suffer from problems of analysis, etc. The addition of a recycle stage permits one to overcome these problems since the conversion per pass remains differential but the overall conversion becomes large enough to be measured and reflects accurately the influence of products as well as that of the reactants. A drawback, however, concerns the design of experiments. At the beginning of the investigation, trial and error is necessary for obtaining the desired concentrations at the exit. In external recycle reactors the recycle stream

is circulated by an external pump. In internal recycle reactors an impeller recycles the reaction mixture through a fixed bed of catalyst. Perfect mixing is achieved under most reaction conditions. The most widely known form of internal recycle reactor is the Berty reactor. For gas phase reactions, a CSTR uses a spinning wire-mesh basket to hold the catalyst. Such a reactor is kinetically equivalent to a differential recycle reactor with a high recycle rate. The Carberry-type reactor is the best known example of a CSTR of this type.

The major uncertainty with this type of reactor is in determining the catalyst temperature. Usually this must be inferred from a knowledge of the heat of reaction, the rate of heat and mass transfer and the reaction rate. In view of this uncertainty regarding the catalyst temperature, these reactors are not recommended for the study of highly endothermic or exothermic reactions.

CSTR may also be used for liquid-phase reactions. However, there can be severe problems with heat and mass transfer in such systems, and sampling of products can cause difficulties. For multiphase reactions it is necessary to ensure good contact between the gas and the liquid as well as between the liquid and the catalyst.

#### *c Fluidized-Bed Reactor*

When gases are blown from the bottom upwards through the catalyst bed a lifting force is created due to a pressure drop. This force increases with increasing linear flow rate. When the flow rate reaches a critical value, the catalyst becomes suspended in a state characterised by intensive chaotic motion of particles. The catalyst bed expands and acquires fluidity.

The major advantages of a fluidized bed are efficient heat transfer, ease of temperature control, and diminution of concentration gradient. Among the disadvantages are inhomogeneity of the bed (formation of gas bubbles), and a considerable backmixing. As a result, the selectivity of the catalytic process may decrease. To overcome, at least partly, these problems, special packing materials are introduced into the reactor. Another serious limitation is that the catalyst must possess high attrition resistance.

Fluidised bed reactors are rarely suitable for catalytic studies because of their relatively large volume, the large quantity of catalyst to use and the difficulty to control bubble agglomeration and instabilities. However, it is still almost irreplaceable for the testing of fluid-bed cracking catalysts. On a laboratory scale a modification is applied in which an intensive mixing of particles is achieved by means of mechanical vibration. In this case, the gas flow rate can vary over a

wide range, remaining below the critical value. This reactor combines advantages of a fluidised-bed reactor and a gradientless reactor. In addition, it may have a small volume (up to  $1\text{ cm}^3$ ) and measurements can be made using a small quantity of the sample. Vibro-fluidized-bed reactors are most effective for investigations of reaction mechanisms by the pulse method.

#### *d Batch Reactor*

The reactor is composed of a tank with heating, or cooling, and stirring devices. Catalyst is usually introduced into the reactor which is then closed, and liquid and gaseous reactants are introduced through valves. The partial pressures or concentrations of the reactants and products varies continuously throughout the experiment. The progress of the reaction may be followed by monitoring partial pressure changes or by analysis of samples by a special device.

This reactor is used with solid or liquid catalysts and with liquid reactants, or for gas/liquid reactions in the presence of solid catalysts. Batch reactors are also frequently used, as closed systems with circulation of the gas, for reactions of gases catalysed by solids. Nowadays, relatively few detailed kinetic studies are performed using batch reactors. A common use of these reactors is for the rapid screening of catalysts particularly in high pressure/high temperature reactions.

The main advantages of a batch reactor are as follows. It is simple and allows rapid measurements. Many experiments can be performed in a short period of time. It is convenient when using pure, expensive, corrosive, or high boiling temperature chemicals. Its use is recommended if the catalyst is sensitive to traces of poisons since there is no accumulation effect. In principle, by varying the stirring conditions it is possible to investigate the influence of heat and mass transfer processes.

The main disadvantages of batch reactors, when used for high pressure experiments, are as follows. The large thermal capacity of the reactor limits the heating up and cooling down rates. As a consequence it is difficult to determine the time at which reaction commences. Sampling of products during an experimental run can be done but it is then necessary in some cases to ensure separation of the reactants from the catalyst. Finally, with liquid reactants it is rarely possible to control temperature and pressure independently. Thus, a batch reactor is not convenient for detailed kinetic studies since different parameters vary together (pressures or concentrations of reactants and products, evolution of the catalyst). Much care is needed in the introduction of reactants to obtain a good control over the starting time of the reaction. In practice this makes the study of fast reactions difficult.

#### *e Discontinuous Flow Reactor*

The discontinuity of flow can be achieved by different methods such as injection of pulses of reactant(s) or changing abruptly the concentration of one or more reactants. The pulse reactor is often made of a tube through which a carrier gas flows at constant rate. At a specified time a slug of reactant is injected into the gas flow and the products emerging at the outlet of the reactor are analysed online.

The major advantages of this type of reactor are its simplicity and speed of operation, and the fact that only very small amounts of reactant and catalyst are required. This reactor gives an instantaneous image of the activity of a catalyst so it is useful for following any fast modification of the catalyst by the reaction itself or by a poison. It is particularly useful for studying the 'initial' activity of a catalyst. In addition, correlations with physical or spectroscopic observations are easier since in the pulse reactor the catalyst does not change too much during the course of the measurement. This type of reactor is convenient for rapid screening of catalysts and for studying catalysts which are sensitive to poisons or which change rapidly.

Disadvantages of the pulse reactor are as follows. It is not convenient for precise kinetic measurements. The pressures of reactant vary during the whole reaction and the kinetic treatment requires complex mathematical analysis. Steady state is not established during the period when the pulse is passing over the catalyst so selectivity data may be misleading. Material balance is difficult to establish.

Other types of discontinuous flow reactors may be used for transient kinetic studies in which, for example, isotopically labelled reactants are widely used in kinetic studies. This kind of investigation has been particularly developed in the case of discontinuous flow reactors. A different instrument called TAP (for Temporal Analysis of Products) permits extremely sensitive detection of intermediates or products. The results obtained with these various instruments can provide information about reaction mechanisms.

#### *f Reactant Introduction Methods*

The batch reactor is generally heated once the reactants mixture has been added. A flash introduction of the reactant, previously brought to the reaction temperature can be envisaged. However, in order to control the starting time of the reaction, flash introduction of catalyst may alternatively be used.

With continuous-flow reactors gases are usually introduced from compressed cylinders. A pump can be used to introduce liquids which are then vaporized and mixed with a carrier or reactant gas and passed through the catalyst. Viscous liquids may be preheated before pumping. Alternatively a double-pass saturator

can be used in which the carrier or reactant gases are bubbled through a thermostated liquid. This method offers the advantages that there are no mechanical parts and the reactant is already in the gas phase so preheating is easier. Ideally, the reactant pressure is dependent only on the temperature of the saturator and is not affected by the total pressure or the flow rate of the carrier gas. A saturator may be used with reactors working even at high pressures.

#### *g Typical Experimental Parameters Used in Catalyst Testing*

##### *(i) Reactor*

A typical laboratory flow reactor would have a volume of up to about a few cm<sup>3</sup> and a cross-sectional area preferably less than a cm<sup>2</sup>. The mass of catalyst used depends on its activity but would typically be between 0.05 and 3.0 g. The choice of particle size is important. For laboratory reactors small particles (0.1 mm) are recommended for minimizing problems. Generally accepted rules are the following:

- (i) the ratio of the height of the catalytic bed to the reactor diameters should be around 10:1.
- (ii) the ratio of the reactor diameter to granule or particle size be around 10:1. These conditions are more likely to ensure good flow conditions and to avoid channeling.

If the catalytic reaction is strongly exothermic it may be useful to dilute the catalyst with an inert material having a similar particle size to the catalyst. Preheating of the feedstock is rarely necessary in laboratory reactors. When required, a bed of inert material (e.g., carborundum) can be used. The reactor should generally be mounted vertically. It is advisable to measure the temperature of the catalyst bed directly, particularly for reactions which are strongly exothermic or endothermic. This may be done by mounting a thermocouple in the centre of the catalyst bed, or by inserting a thermocouple into a thermowell in the side of the reactor tube. It is prudent to check the temperature profile along a catalyst bed. It is also advisable to check that the thermocouple itself has no catalytic activity if it is inserted directly in the bed.

##### *(ii) Reactants*

In laboratory reactors the flow of reactants is determined to a large extent by the size of apparatus and amount of catalyst used. A space time of about 0.1–1 s is common. In general, normal laboratory reagents will not contain any impurities likely to seriously affect the measurements. However, it is always advisable to check the level and the nature of the impurities. In

some circumstances relatively impure feedstocks may be perfectly satisfactory. Sometimes the reactants are diluted by addition of an inert material. (It is prudent to confirm that the chosen diluent is inert.) There are two instances where a diluent may be used:

- (a) to reduce temperature changes caused by the thermal effects of a reaction; but this has only a limited effect;
- (b) to investigate the influence of partial pressures in kinetic experiments.

In most laboratory kinetic studies ambient pressure is used. If the pressure of one reactant is varied over a wide range, in order to maintain the pressure of a second reactant constant it is necessary to add an inert diluent to bring the total pressure up to ambient pressure. The choice of pressure should take account to the type of reaction under investigation.

##### *(iii) Catalyst*

No general rules can be given concerning the correct method of handling the catalyst before use. It should be recognized, however, that the conditions used in drying, storing, reducing, etc. a catalyst may affect its properties. Whether a fresh charge of catalyst should be used for each separate catalyst test (for example, a fresh sample used at each test temperature) depends on the stability of the catalyst. If the catalytic properties appear to be invariant with time there should be no need to change the sample. Replicating an activity measurement at the beginning and at the end of the series of experiments indicates whether the catalyst is stable. However, it is advisable to make changes in temperature in random fashion, which is more likely to reveal time-dependent effects. If the catalytic properties change rapidly with time it may be necessary to use a fresh sample in each experiment.

##### *(iv) Problems of Heat and Mass Transfer*

Very careful attention must be given to the possibility of heat and mass-transfer problems and all due precautions should be taken (see next section). For some reactions, such as oxidation, where heat transfer may be important, one must find, and use, experimental conditions which avoid these effects.

Experimentally, the observation of a small activation energy, or a sharp decrease in the activation energy at higher temperatures, may indicate a serious diffusion problem. However, this should only be taken as a cautionary sign since other causes may exist. In particular, the influence of heat and mass transfer on the reaction kinetics should be checked experimentally by adequate

procedures, if available, or theoretically using the appropriate mathematical relationships.

## B Kinetic Analysis [39–47]

### a Determination of the Reaction Rate

From the amount of the reactant converted or the product formed (degree of conversion), or more frequently from the dependence of these quantities on the time variable, the *rate of production* (consumption),  $R_j$ , of a chosen reaction component and from it the *reaction rate*,  $r$ , may be evaluated, based on the mass balance for the given reactor type.

For the reactor types most commonly used in kinetic studies we obtain the following mass balance equations for reaction component  $j$  chosen as the key component;

(1) for ideal plug flow reactor:

$$R_j = -dX/d(Q/F_{j,0}) \quad (1)$$

where  $X$  is the fractional conversion,  $Q$  is the amount of the catalyst and  $F_{j,0}$  is the molar flow rate of the component  $j$  at the inlet of the reactor; the term  $Q/F_{j,0}$  is often referred to as the *reciprocal space velocity* or *space time* [1].

(2) for a CSTR reactor:

$$R_j = -(F_{j,0} - F_j)/Q \quad (2)$$

with the same meaning for the symbols as in eq. 1;  $F_j$  is the molar flow rate of the balanced component  $j$  at the outlet of the reactor;

(3) for a perfectly stirred batch reactor:

$$R_j = (dn_j/dt)/Q \quad (3)$$

where  $n_j$  is the amount of reactant  $j$ , and  $t$  is reaction time.

Eqs. 1 to 3 relate the rate of production  $R_j$  of the balanced reaction component  $j$  to the molar amounts or their derivatives with respect to the time variable (reaction time or space time, see above). From the algebraic eq. 2 for the CSTR reactor the rate of production,  $R_j$ , may be calculated very simply by introducing the molar flow rates at the inlet and outlet of the reactor; these quantities are easily derived from the known flow rate and the analytically determined composition of the reaction mixture. With a plug-flow or with a batch reactor we either have to limit the changes of conversion  $X$  or mole amount  $n_j$  to very low values so that the derivatives or  $dX_j/d(Q/F_{j,0})$  or  $dn_j/dt$  could be approximated by differences  $\Delta X_j/\Delta(Q/F_{j,0})$  or  $\Delta n_j/\Delta t$ , (differential mode of operation), or to measure experimentally the dependence of  $X_j$  or  $n_j$  on the space or reaction time in a broader region; this dependence is then differentiated graphically or numerically.

The individual values of the rates of production  $R_j$  of the reaction components in a given reaction, obtained in the way just described, depend, however, on the reaction stoichiometry. In a single (stoichiometrically simple) reaction

$$\sum_{j=1}^s v_j A_j = 0 \quad (4)$$

where  $s$  is the number of reaction components each identified by a subscript  $j$ ;  $A_j$  is the amount of component  $j$ ;  $v_j$  is the stoichiometric coefficient of the component  $j$ , negative for reactants, positive for products. The rates of production of reaction components are related in a very simple way:

$$v_1^{-1} R_1 = v_2^{-1} R_2 = \dots v_j^{-1} R_j = v_s^{-1} R_s = r \quad (5)$$

from which it follows that the rate of production  $R_j$  divided by the stoichiometric coefficient  $v_j$  has the same value for all the  $s$  chemical species involved in the reaction. Since the value  $v_j^{-1} R_j$  is independent of the reaction stoichiometry and of the choice of the balanced (key) component, it is called *rate of reaction* or simply *reaction rate*  $r$ .

In a reaction network in which several stoichiometrically simple reactions take place, eqs. 1 to 3 are still used for the primary treatment of the reactor data but the overall rate of production obtained for the  $j$ -th component is here equal to the algebraic sum of the rates of production in all the reactions in which the  $j$ -th component is formed or consumed. In such a case the evaluation of the reaction rates  $r$  of the individual reactions of the network from the rates of production  $R_j$  of the key components is more complicated.

As seen from eqs. 1 to 3, the rate of production and, consequently, the rate of catalytic reaction are related to the quantity of catalyst  $Q$  which may, for example, be expressed as the mass ( $m_c$ ), volume ( $V_c$ ) or the surface area ( $A_c$ ) of the solid catalyst. The numerical values of the corresponding specific reaction rates ( $r_m$ ,  $r_v$ ,  $r_A$ ) naturally differ from each other depending on the quantity to which they are related.

### b Rate Equations

The rate of a reaction is generally a function of the temperature and concentrations of reactants, products and other substances if present. The kinetic equation thus obtained is commonly called the *rate equation* or the *rate law*. To find the form of the kinetic equation and the values of its constants is the main task of the kinetic analysis. The first stage of the procedure consists in an experimental measurement of the reaction rate or the conversion in an adequate region of experimental variables. It is advisable to keep the temperature constant and to vary the concentrations; this may be repeated for other temperatures if the tem-

perature dependence of the kinetic constants is to be evaluated. The influence of the concentration of each reaction component can be measured separately and the reaction order with respect to it determined by varying one concentration and keeping the others constant. Note, however, that introducing this or any other binding condition, such as constant ratio or constant total concentration of reaction components, will reduce the actual number of independent variables. To avoid the loss of information caused by this approach, it is possible to vary the concentrations of reaction components quite randomly in such a manner that the space defined by the extreme values of the investigated concentrations might be covered.

The data are fitted to several equations and the best fit selected. The equations are proposed either on an empirical basis or they may be derived on the basis of some reaction mechanism [39–47].

Mathematically, both *empirical* and *model rate equations* for heterogeneous catalytic reactions have either the form of a *power law* (power-law-type rate equations):

$$r = kc_A^m c_B^n \dots \quad (6)$$

or they are a *fractional function* with a polynomial in the denominator:

$$r = \frac{kC_A^a C_B^b}{[1 + (K_A C_A)^\alpha + (K_B C_B)^\beta \dots]^\beta} \quad (7)$$

One also uses combinations of the two forms (e.g., multiplying forms of eq. 6 and eq. 7).

Model rate equations are rate equations based on commonly accepted rate expressions used in the field of catalysis. Very frequently, but not always correctly, the equations of this type are called Langmuir-Hinshelwood type rate equations. In eqs. 6 and 7 the indices A and B denote the reactants but very often the concentrations of reaction products also appear in the equations (in equations of type 7, usually in the denominator).

The proportionality factor  $k$  is called the *experimental rate constant*; with catalytic reactions, this constant is frequently a complex quantity which may be a product of rate constants of several steps or may include equilibrium constants of the fast steps. The exponents  $m, n, \dots$  in the power-law equations may be any fraction or small integer (positive, negative or zero). The constants  $K_A, K_B$  in the denominator of the equations of type 7 are often but not always related to adsorption equilibrium constants. While they have to be evaluated from the experimental data, the values of exponents  $a, b, \alpha, \beta$  and  $d$  are derived from the assumed mechanism in the case of model rate equations. In empirical rate equations these constants can attain any value (fractional or small integer, usually positive) and

are either postulated or determined by the data treatment.

The rate equation for a system in which the back reaction is not negligible is given by the difference between rate equations for the two directions.

### c Selection of a Suitable Form of the Rate Equation and Evaluation of Constants

These two tasks are related because the selection, based on the fit of the equation to experimental data, is only possible after the evaluation of the constants.

On the basis of experience, analogy, or information obtained from fundamental chemical mechanisms, one constructs a priori several possible, or likely, model kinetic equations. These models are then compared, according to the methodology described above, to the experimental data.

The criterion of the fit is most frequently the sum of squared deviations (or of their relative values) between the calculated ( $y'_i$ ) and measured ( $y_i$ ) values of the dependent variable throughout all the experiments performed ( $N$ ):

$$Q(\kappa) = \sum_{i=1}^{i=N} (y'_i - y_i)^2 \quad \text{or} \quad Q(\kappa) = \sum_{i=1}^{i=N} (y'_i - y_i)^2 / y_i^2 \quad (8)$$

The problem consists in seeking such a combination of the values of constants  $\kappa$  which gives the minimum value of  $Q$  ( $Q_{\min}$ ). Before computers became commonly available, the kinetic equations had usually been transformed into a linear form and the linear regression ("least-squares method") had been applied to find the best set of constants. This procedure is not statistically correct in most cases. Therefore, only the *nonlinear regression* method can be recommended to optimize constants in kinetic equations that have a nonlinear form [48–51].

The dependent variable  $y$  is most frequently the reaction rate; independent variables are the concentration or pressure of reaction components, temperature and time. If in some cases the so-called integral data (reactant concentrations or conversion versus time variable) are to be treated, a differential kinetic equation obtained by the combination of a rate equation with the mass balance equation 1 or 3 for the given type of reactor is used. The differential equation is integrated numerically, and the values obtained are compared with experimental data.

If several kinetic equations are compared the one which fits best will be that which exhibits the lowest value of  $Q_{\min}$ . However, the difference in the  $Q_{\min}$  values for some equations may be statistically insignificant and then further experimentation with increased

accuracy is necessary and another region of experimental variables has to be chosen where the discrimination between rival kinetic equations may be easier, provided no change of mechanism takes place.

For better model discrimination and/or parameter estimation, sequential methods for computer designed plans of experiments have been proposed [52]. They take advantage of the information obtained from the previous experiments and plan the new experiments in the region of independent variables where the maximum difference of the dependent variable can be expected.

Even with advanced methods, several models may satisfy the  $Q_{\min}$  requirement. Further discrimination necessitates additional information. This may come from experience, analogy, measurements using special techniques, such as isotope labeling, and fundamental knowledge on chemical mechanisms.

If the kinetic experiments are performed at different temperatures, the temperature dependence of the constants obtained can be determined. With empirical rate equations, one can obtain any dependence of the constants on temperature. With model rate equations the constants should have a certain physical meaning and behave, in dependence on the temperature, according to the theory. Thus, the rate constants should follow the Arrhenius equation:

$$k = A \exp(-E/RT) \quad (9)$$

where  $A$  is the preexponential factor, and  $E$  is the activation energy. (With catalytic reactions  $E$  is very frequently a complex quantity and is more aptly called "apparent activation energy"). The equilibrium constants of fast steps, if present in the rate equation, should obey the van't Hoff equation

$$K = B \exp(-\Delta H/RT) \quad (10)$$

where  $\Delta H$  is the reaction enthalpy of the fast step in the reaction mechanism. For evaluating the parameters of eqs. 9 and 10, the nonlinear regression method is again recommended.

Sometimes, the reaction rate at constant concentrations instead of the rate constant is correlated with temperature by means of the Arrhenius equation. However, this is not justified with most catalytic reactions since each constant in the rate equation may be temperature-dependent and, consequently, the reaction rate is a very complicated function of temperature. Therefore, attempts to correlate information obtained from  $\log r$  versus  $1/T$  plots might be misleading.

#### d Heat and Mass Transfer Effects

Heterogeneous catalytic reactions occurring on the solid-fluid interface may be affected by the heat and mass transfer to and from the interface. We distinguish external transfer effects (from the bulk of the reactant fluid to the outer surface of the catalyst particle) and

internal transfer effects (from the outer to the inner surface of the porous catalyst particle). These physical processes take place simultaneously with the catalytic reaction on the surface. If they are fast enough, the rate measured is the intrinsic rate of the chemical transformation (kinetic region); if not, the measured kinetics is influenced by mass and heat transfer effects. Therefore, before starting kinetic measurements we have to check whether the experimental equipment and reaction conditions used allow work in the kinetic region and if not to change the conditions in order to suppress the transfer effects. A priori criteria can be obtained along the lines indicated in sections i and ii below. Some semiempirical criteria based on experiments may also be adopted, such as the interpretation of data obtained by changing the particle size, the flow rate, agitation, etc.; details of these may be found in specialized literature [53, 54]. Special geometrical arrangements are used to detect and/or measure mass transfer limitation: single-pellet or "single-string-pellet" reactors.

The mass transfer effects cause, in general, a decrease of the measured reaction rate. The heat transfer effects may lead in the case of endothermic reactions also to a decrease of the equilibrium value and the resulting negative effect may be more pronounced. With exothermic reactions, an insufficient heat removal causes an increase of the reaction rate. In such a case, if both the heat and mass transfer effects are operating, they can either compensate each other or one of them prevails. In the case of internal transfer, mass transport effects are usually more important than heat transport, but in the case of external transfer the opposite prevails. Heat transport effects frequently play a more important role, especially in catalytic reactions of gases. The influence of heat and mass transfer effects should be evaluated before the determination of kinetics. These effects should preferably be completely eliminated.

#### (i) Internal Mass and Heat Transfer

The effect of mass and heat transport to and from the inner particle surface on the reaction rate can be characterized by the *effectiveness factor*,  $\eta$ , i.e., by the ratio of the effective reaction rate measured on the catalyst particle under study ( $r_{\text{ef}}$ ) to the rate of the reaction in the kinetic region ( $r_{\text{kin}}$ )

$$\eta = r_{\text{ef}}/r_{\text{kin}} \quad (11)$$

Knowledge of the reaction rate free of any diffusional effect,  $r_{\text{kin}}$ , is thus necessary in evaluating experimentally the magnitude of these effects. The effectiveness factor for an isothermal situation can also be calculated approximately by means of the Thiele modulus [39], but knowledge of the kinetics in the diffusion-free region and of the effective diffusion coefficient characterizing the transport properties of the porous material is necessary. The effect of internal diffusion increases with increasing catalyst activity, re-



action temperature and catalyst particle size, and with decreasing pore size of the catalyst.

(ii) *External Mass and Heat Transfer*

The difference between the concentrations of a reactant (or temperatures) at the outer particle surface and in the bulk of the reaction mixture may become important if the rate of diffusion of this reactant (or heat transfer) through the laminar film surrounding the particles is lower than the rate of the reactant (or heat) consumption (production) by the chemical reaction. The thickness of the laminar film and the concentration (temperature) differences are smaller the more turbulent is the reactant fluid. Therefore, the magnitude of the effect of external mass and heat transfer also depends on the type and the geometry of the reactor used and kinetic data obtained in the region of external transfer in one reactor cannot be applied to another reactor. Thus, data free of external transfer effects should be used for a reliable kinetic analysis. Such data are obtained preferably in flow reactors with high flow rates and low reactant conversion per pass, e.g., in the continuous stirred tank reactor or a tubular flow reactor working under differential conditions (see Section A).

### C Inhibition of Catalytic Action

This section concerns the partial or total inhibition of catalytic action. Substances causing this inhibition ("inhibitory" or "deactivating" substances) can be conveniently indicated by IS. The alteration, reduction, or suppression of the catalytic activity can be a consequence of:

- adsorption of IS on active sites (AS);
- modification of AS (due to reaction with IS);
- restriction of physical access to AS due to the presence of layers or particles of IS.

Ideally, the characterization of catalysts with respect to inhibition should involve three types of information:

- (a) the nature of the IS acting on the catalyst,
- (b) an adequate relationship between the quantity of IS and the catalytic properties,
- (c) time-dependent effects on activity, selectivity, etc., due to the presence, or a modification of concentration, of IS (decrease of catalytic activity with time, total or partial recovery of catalytic properties after removal of IS from the feed, etc.).

Because of the complexity of the phenomena taking place on a working catalyst information under (c) is usually incompletely analyzed with respect to the role of IS, and reflects the combined effect of several categories of processes. For this reason, most of the corresponding discussion will be reserved for Sections D and E.

#### a Identification of the Inhibiting Substances

Full characterization of catalysts with respect to the influence of IS requires that all the IS be identified chemically and their mode of action understood. Because of the variety of cases observed, no universal method exists for identifying IS. It must be clear that the role of any IS is specific to the catalyst and reaction studied.

#### b Identification of the Mode of Action of the Inhibiting Substances

IS, and especially poisons and inhibitors, can have strong effects at very low surface coverages (a few percent or less of surface area). Except for inhibitors, they have a cumulative effect.

Chemical identification of IS can be achieved by consideration of the following points. IS may be any substance that normally or accidentally enters into contact with catalysts, e.g., impurities in the feed, impurities released from the equipment, leaks. IS may also be formed by transformation of the reactants in contact with the catalyst (e.g., coke formation).

Extremely sensitive analysis may be mandatory. As the IS usually (but not always, e.g., dust) accumulates on catalysts and, more specifically, on their surface, surface sensitive techniques are particularly useful.

In essence, three criteria permit identification of the category (poison, inhibitor, fouling agent) to which IS belongs (see Table 1).

**Table 1.** Categorization of inhibiting substances.

Quantities	Action	Interaction with catalyst	Nature of IS
small	irreversible	strong	poison
small	reversible	weak	inhibitor
large	either	weak	fouling agent

Chemical, and especially, surface analysis provides information concerning the first column in Table 1, namely, quantity. Activity/selectivity measurements provide information on the reversibility of the mode of action. The identification of the nature of the interaction with the catalyst depends on spectroscopic methods: differences in electron spectroscopies, IR, Raman, ESR spectroscopies, etc.

#### c Characterization of Catalysts with Respect to Their Response to IS

Characterization of catalysts with respect to their propensity to be inhibited by IS must take into account the fact that the phenomena depend upon the whole catalytic reaction system (catalysts, degree of ageing and/or poisoning, inhibiting effects, operating conditions) and

upon the whole succession of reactions to which the catalysts have been subjected.

Reported results on sensitivity to inhibition should clearly indicate to what stage of catalyst life the reported results correspond. The most important results with respect to fundamental studies (rational interpretation of the observed effects) and practical applications correspond to those obtained on catalysts having attained an activity–selectivity plateau.

There exist cases where selectivity is markedly improved by inhibition because of the suppression of side reactions.

#### *d Poisons*

Sensitivity to poisons depends upon three factors:

- the number of active centres in the catalyst;
- the strength of adsorption of the poison on the active centres;
- the effectiveness of adsorbed poisons for inhibiting the catalytic activity.

The effectiveness of an adsorbed poison depends on the ratio  $x_0/x_1$ , where  $x_0$  is the amount of poison per active centre necessary to inhibit catalytic action, and  $x_1$  is the number of active centres.

The minimum concentration required to eliminate the catalytic activity is one possible measure of the sensitivity of a catalyst to a poison. Sensitivity to poisoning is most properly defined by the amount,  $n_p$ , of the poison adsorbed on a unit amount of catalysts which causes a given fractional decrease of the catalytic activity ( $a = (a_0 - a_p)/a_0$ ), where  $a_0$  and  $a_p$  are the activities in the absence or presence of poison, respectively):  $\alpha/n_p$  is a measure of the sensitivity to poisoning. One may also use the ratio of  $a$  to the concentration  $c_p$  of the poison in the feed, namely  $\alpha/c_p$ , but this is less precise, as this depends on the adsorption coefficient of the poison.

The basic values  $\alpha/c_p$ ,  $\alpha/n_p$  and  $x_0/x_1$  have to be complemented, in most cases, by two types of characteristics of the catalyst. The first concerns the sensitivity of selectivity. Parameters similar to those mentioned in the previous paragraph must be determined for all selectivities of interest, i.e., all different reactions. The second concerns the possible variation of the magnitude of the effect, on activity and selectivity, of a poison as a function of surface coverage (or degree of inhibition). Ideally the whole curve  $\alpha/c_p$  vs  $c_p$ ,  $\alpha/n_p$  vs  $n_p$  or  $\alpha$  vs  $x/x_1$  should be constructed for all parallel and consecutive reactions taking place. An acceptable way of characterizing a catalyst is to report the initial sensitivity to deactivation (as indicated above), the points of zero activity, and a few characteristic intermediate points, e.g.  $c_p$  or  $n_p$  values, when  $a$  reaches certain values, such as 1/2, or some other fraction, or  $a$  values when  $c_p$  or  $n_p$  equals a given fraction of the value leading to zero activity.

When dealing with complex catalysts (multifunctional, supported, etc.) and with beds of catalyst, the characterization of the effect of poisons also involves the localization in space of the poisons (e.g., is the poison attached to the metal or the support, is it uniformly distributed over all the catalyst pellet or selectively deposited?). The concentration of a true poison exhibits a decreasing profile over the catalyst bed.

Characterization thus involves analytical electron microscopy, ordinary microprobe analysis or other techniques for localizing elements or chemical compounds (Scanning Auger Spectroscopy, Raman Microprobe, Laser Microprobe Mass Spectrometry). It also requires, in most cases, some physical separation of the catalyst for separate analysis (e.g., near surface parts and center of pellets, by peeling or progressive abrasion; pellets present at various heights in the catalyst bed, etc.).

#### *e Inhibitors*

The action of inhibitors is intermediate between very strong irreversible poisoning and the normal competition between molecules for a given active site. The sensitivity to inhibitors can thus be expressed either as in the case of poisons (and then  $\alpha/c_p$  can be used), or as in the case of competition (e.g., by a classical Langmuir–Hinshelwood formulation). In the latter case, for example, the value, or relative value, of the adsorption coefficient could characterize the inhibitor.

As the response of catalysts to inhibitors may not be instantaneous, especially if some chromatographic effect in the bed takes place, it is also necessary to characterize the catalyst with respect to the rate at which activity decays when the catalyst is contacted with a given concentration of inhibitor, or recovers, after the addition of the inhibitor is discontinued (see section E).

#### *f Fouling Agents*

The inhibiting influence of fouling agents is not related in a simple way to the quantity of deposited substance. The reason is that the relationship between this quantity,  $w_p$ , and activity depends on the nature and texture of the catalyst, the nature and concentration of the feed constituents, the temperature and operating conditions, and the rate of build up of the fouling deposit (in practical terms: feed rate/catalyst weight ratio). It is thus necessary to indicate clearly the value of all these parameters when expressing the rate vs deposited quantity ratio. It is recommended that weights should be used (per unit weight of catalyst) to express the quantity of fouling agent as, usually, the composition of the deposit is not exactly known.

As the quantity of fouling agents necessary to bring about a noticeable change in activity/selectivity is relatively large, characterization by methods other than catalytic activity measurements is useful. The rate of

build-up of the deposits of fouling agent can be measured gravimetrically. Microscopic or analytical electron microscope measurements can help locate the deposits (pores, etc.). In certain cases raman microprobe analysis and laser microprobe mass spectrometry can also give valuable information.

In the case of carbon (coke), the variation of concentration over the catalyst bed gives an indication of the origin of the deposit. A decreasing profile implies that some compound in the feed is responsible. If the main reactant brings about coke formation, one has a so-called "parallel coking". An increasing profile indicates that coke is formed from a reaction product ("consecutive coking").

#### D Deactivation of Catalysts and Time-Dependent Effects

The composition, structure, texture, surface state, activity and selectivity of catalysts change continuously, at rapid or slow rates according to conditions, during catalytic work. One type of change of paramount importance for characterization of catalysts, especially for practical applications, is the deactivation behaviour. Two other aspects have also to be considered, namely (i) the usually rapid changes that catalytic activity and selectivity undergo in the first few minutes, hours or sometimes days of work (initial adjustment to catalytic operation), and (ii) the response to changing operating conditions (response to change).

The kinetics of the reaction are dictated by the concentration of reactants at the active site. If there are mass transfer limitations in the system, reactant concentration at the active site concentration is not the same as the bulk concentration, and the rate will vary. Mass transfer limitations may exist in a given catalyst or may be produced during operation – for example, by the deposition of coke or the closure of pores.

The net result of any or all of these factors is that the catalyst may lose activity and/or selectivity and the catalyst will have to be regenerated/replaced after a period of time.

Deactivation, or more generally, changes in activity/selectivity, reflect changes in composition, structure, texture and surface state. These changes are due to processes belonging to seven main categories, all of which may interact with each other:

- (a) poisoning;
- (b) inhibition;
- (c) fouling;
- (d) sintering;
- (e) chemical reactions;
- (f) restructuring of the surface;
- (g) physical action.

Poisoning, inhibition and fouling have been dealt with already. Sintering corresponds to diminution of

surface area of the active phase, modifiers, supports, etc.

Chemical reactions involve reaction with feed (e.g., reaction with a poison; reduction, in the case of oxidation catalysts), intermediary or final products (e.g. carbide formation), or reaction between catalyst components.

Restructuring refers to changes of the surface which do not involve any of the previous processes (or are too subtle to be detected): migration of active species inside a catalyst pellet, change of shape (independently from change of total surface area developed) of crystallites of a given phase, change in the number of steps, kinks on a surface, changes in surface/bulk composition ratio, etc.

Physical action, e.g., by attrition, may result in the loss of the active components of the catalyst. There is often a coupling together of these processes: the rate of one process depends on the rate at which another process takes place. There are two general consequences of these coupling effects:

- time-dependent changes, and especially deactivation, need comprehensive characterisation;
- characterization of the propensity of catalysts to deactivation through the use of accelerated test needs special care in order to avoid erroneous interpretations (see Section c below).

##### a Deactivation: Overall Characterization

The overall effect of deactivation is characterised by the activity and selectivity variations as a function of time under well defined conditions. Under isothermal conditions the results may be presented as an activity/selectivity vs. time plot. In large pilot plants and in commercial units the operation is conducted in such a way that one parameter characterising the product is kept constant (yield of a given chemical, or given global property). Temperature  $T$  has to be raised to maintain the parameter constant. A  $T$  vs.  $t$  plot is obtained. Neither kind of measurement gives unequivocal information with respect to the characterization of deactivation. Ideally both should be used. The second method of measurement has necessarily to be completed by the determination of the variation in selectivity with time. The shape of the activity vs.  $t$  or  $T$  vs.  $t$  curves is a very useful characteristic of a catalyst.

##### b Physicochemical Characterization in Deactivation Studies

The methodology for characterizing deactivated catalysts by physicochemical techniques has to be developed for each specific case but should involve all the techniques generally used for characterizing catalysts and studying inhibitory effects.

Sampling should be guided by three principles:

- (a) samples should be protected from contamination;
- (b) samples should be taken from various places in the reactor;
- (c) characterization should involve the study of different pellets of catalyst since because of preparation/composition differences, the behaviour of catalyst can vary from pellet to pellet, at the same place in a reactor. Extreme care should be taken that one effect (among the many parallel and coupled changes) does not bring about errors in the measurement of another effect. A typical example concerns the use of XPES for measuring contamination by poisons or loss of dispersion: the masking effect of a fouling agent which is difficult to detect could lead to enormous errors.

### c Accelerated Tests

In view of the usually very long timescale of deactivation phenomena, one has often to resort to accelerated tests. This is absolutely necessary when industrial development is contemplated. As deactivation is the result of several different processes, very often coupled together, the accelerated test cannot fully represent the non-accelerated phenomenon. For example, if higher temperatures are used for acceleration, the balance of the various elementary processes will be altered, because of differences in activation energy. Some accelerated tests are generally better than others, see Table 2. The real significance of each type of test has to be assessed in each case.

Table 2.

Parameters modified	Test potentially valid if deactivation due to:
temperature	sintering; solid state reaction; fouling
space velocity	fouling; coking
inhibitory substances	fouling; coking, poisoning
increased concentration of inhibiting substances	fouling; coking, poisoning
modified feed composition	fouling; coking, poisoning
artificial deposition of fouling substances	fouling
vibration	attrition

## E Regeneration

Regeneration consists of: (i) removal of inhibiting substances IS: sometimes poisons, most often inhibitors or fouling agents, e.g., coke; (ii) redispersion of the active species, or (iii) both. Regeneration procedures are often specific to the catalyst and the species causing deactivation. With respect to regeneration, procedures are described precisely by catalyst manufacturers, for each type of important industrial catalyst. Procedures for

laboratory catalysts must also be adapted to each specific case.

### a Preliminary Treatment

In many cases, liquid, semiliquid, or waxy substances adhere to the catalyst and fill the pores. They must be eliminated before removal of the real inhibiting substance.

### b Removal of Inhibitory Substances (IS)

Inhibition, or catalyst poisoning, results from reactions between IS and AS (see Section C). Often, the amount of IS adsorbed depends on the partial pressure of IS in the gas phase and on the strength of adsorption. As a result, the IS may sometimes be 'stripped' from the catalyst by passage of inert gas at a moderate temperature. If a chemical bond has formed between IS and AS, chemical treatment may also remove IS. The most common example of this is the removal of sulfur from the surface by passage of hydrogen.

Some care must be exercised in selecting the chemical treatment. Thus, for example, metal sulfides can be converted to noninhibitory (but usually inactive) metal sulfates by reaction with O<sub>2</sub>. However, sulfates remain in the reactor and, in some cases, can be reconverted to sulfides on re-admission of H<sub>2</sub>.

### c Removal of Coke

Coke, deposited on a catalyst, may be removed by one of several reactions: oxidation, reaction with water to form carbon monoxide and hydrogen methanation, and the Boudouart reactions.

Of these, the oxidation reaction is most efficient, but produces heat. This may raise the temperature of the catalyst and result in sintering. Good temperature-programming and control during decoking is essential. Very sensitive catalysts may be regenerated with H<sub>2</sub>, but the rates of the reaction are slow and the process inefficient. Regeneration with steam is more efficient and is endothermic. However, sintering of catalysts is accelerated by steam. As a result, regeneration procedures are a compromise. Often mixtures of air and steam are used.

### d Removal of Foulants

Liquid or semiliquid foulants may be accumulated on the catalyst. In this case, it is necessary to 'strip' the catalyst in an inert gas flow at moderate temperature before removing material as described for the removal of coke.

Solid inorganic foulants may also accumulate on the catalyst. Little can be done to remove such foulants except by mechanical means. This is usually inefficient, and replacement of catalyst is often necessary.

Recently, supercritical fluids (e.g. CO<sub>2</sub>) have been proposed for removing coke and fouling agents.

### e Redispersion

In a few cases it is possible to redisperse sintered materials on a catalyst. The procedures involved are dependent on the nature of the system. In typical examples, dispersion is increased by the formation of oxides or oxychlorides. The operation involves careful control of regeneration conditions bearing in mind the nature of the catalyst, the IS, and the maximum allowable temperature under regeneration conditions.

### f General

There is considerable interest in extending catalyst life, accelerating regeneration and maintaining activity, factors which are often ignored in a laboratory scale investigation.

Regeneration is widely practised in industry, particularly in the context of coke removal. Various plant designs have been developed to overcome this problem, ranging from continuous deactivation/regeneration to moving beds of catalyst. A recent trend is to remove the used catalyst from the reactor, to ship it to special plants where it is regenerated (ex situ regeneration). Catalyst regeneration can often be efficient provided good temperature control is maintained. It is not always economic to regenerate completely, and 90% of the original activity is often accepted. Post-regeneration treatment is often necessary before the catalyst is brought back to life.

## References

- Manual on Catalyst Characterisation, *Pure Appl Chem* **1991**, *63*, 1227
- J P Brunelle, In *Preparation of Catalysts II*, B Delmon, P Grange, P A Jacobs, G Poncelet, (Eds) Elsevier, Amsterdam, **1979**, p 211
- R M Barrer, *Hydrothermal Chemistry of Zeolites*, Academic Press, London, **1982**
- P Courty, C Marcilly, In *Preparation of Catalysts*, B Delmon, P A Jacobs, G Poncelet, (Eds) Elsevier, Amsterdam, **1976**, p 119
- B Delmon, N de Keyser, In *Chemical and Physical Aspects of Catalytic Oxidation*, J L Portefaix, F Figueras, (Eds) CNRS, Paris, **1980**, p 491
- P Courty, C Marcilly, In *Preparation of Catalysts III*, G Poncelet, P Grange, P A Jacobs, (Eds) Elsevier, Amsterdam, **1983**, p 485
- P Courty, H Ajot, C Marcilly, B Delmon, *Powder Tech* **1973**, *7*, 21
- P Courty, P Duhaut, *Rev Inst Francais du Petrole* **1974**, *29*, 861
- A B Stiles, *Catalyst Manufacture*, Marcel Dekker, New York, **1983**, chapter 9
- A B Stiles, *Catalyst Manufacture*, Marcel Dekker, New York, **1983**, chapter 11
- Reporting Physisorption Data for Gas/Solid Systems *Pure and Appl Chem* **1985**, *57*, 603. Reprinted in Section A11.2.1 of this Handbook
- J L Lemaire, P G Menon, F Delannay, In *Characterization of Heterogeneous Catalysts*, F Delannay, (Ed) Marcel Dekker, New York and Basel **1984**
- C H Bartholomew, In *Hydrogen Effects in Catalysis*, Z Paal, P G Menon, (Eds) Marcel Dekker, New York and Basel, **1988**
- P G Menon, In *Hydrogen Effects in Catalysis*, Z Paal, P G Menon, (Eds) Marcel Dekker, New York and Basel, **1988**
- J R Anderson, *Structure of Metallic Catalysts*, Academic Press, London and New York, **1975**
- J R Anderson, K C Pratt, *Introduction to Characterization and Testing of Catalysts*, Academic Press, Sydney, **1985**
- P A Jacobs, *Catal Rev -Sci Eng* **1982**, *24*, 415
- H G Karge, In *Catalysis and Adsorption by Zeolites*, G Ohlmann, H Pfeifer, R Fricke, (Eds) Elsevier, Amsterdam, **1991** *Stud Surf Sci Catal* **1991**, *65*, 133
- J Dwyer, In *Zeolites Microporous Solids Synthesis Structure and Reactivity*, E G Derouane, F Lemos, C Naccache, F R Ribeiro, (Eds) Nato ASI Ser, Vol 352, Kluwer Acad Publ, Dordrecht, **1992**, 303
- A Survey of Experimental Techniques in Surface Chemical Physics, *Pure and Appl Chem* **1990**, *62*, 2297
- J I Goldstein, D E Newbury, P Echlin, D C Joy, C Fiori, E Lifshin, *Scanning Electron Microscopy and X-Ray Microanalysis*, Plenum, New York, **1983**
- J V Sanders, In *Catalysis Science and Technology*, J R Anderson, M Boudart, (Eds) Springer-Verlag, Berlin, **1985**, vol 7, chapter 2
- P Gallezot, In *Catalysis Science and Technology*, J R Anderson, M Boudart, (Eds) Springer-Verlag, Berlin, **1984**, vol 5, chapter 4
- K O Hodgson, B Hedman, J E Penner-Hahn, (Eds) *EXAFS and Near Edge Structure III*, Springer-Verlag Berlin, **1984**
- J Stohr, In *Chemistry and Physics of Solid Surfaces*, R Vanselow, R Howe, (Eds) Springer-Verlag, Berlin, **1984**, chapter 10
- S Csillag, D E Johnson, E A Stern, In *EXAFS Spectroscopy Techniques and Applications*, B K Teo, D C Joy, (Eds) Plenum, New York, **1981**, chapter 19
- C J Wright, In *Characterization of Catalysts*, R M Lambert, J M Thomas, (Ed) Wiley-Interscience Chichester **1980**, chapter 10
- G Engelhardt, D Michel *High-Resolution Solid-state NMR of Silicates and Zeolites*, Wiley, Chichester, **1987**
- J Fraissard, In *New Development in Zeolite Science and Technology*, Y Murakami, A Jijima and J W Ward, (Eds) Elsevier, Amsterdam, **1986**, 393
- H Pfeiffer, D Freude, M Hunger, *Nuclear Magnetic Resonance Studies on the Acidity of Zeolites and Related Catalysts*, *Zeolites* **1985**, *15*, 274
- H Topsøe, J A Dumesic, S Morup, In *Applications of Mossbauer Spectroscopy*, R L Cohen, (Ed) Academic Press, New York, **1980**, chapter 2
- C Defosse, P Canesson, P G Rouxhet, B Delmon, *J Catal*, **1978**, *51*, 269
- C D Wagner, W M Riggs, L E Davis, J F Moulder, C E Muirberg, *Handbook of X-Ray Photoelectron Spectroscopy*, Perkin-Elmer Corp, Minnesota, **1978**
- E P J M Kerkhof, J A Moulijn, *J Phys Chem*, **1979**, *83*, 1612
- C Defosse, In *Characterization of Heterogeneous Catalysts*, F Delannay (Ed) Marcel Dekker, New York and Basel **1984**, chapter 6
- V D Scott, G Love, (Eds) *Quantitative Electron Probe Microanalysis*, Ellis Horwood, Chichester, **1983**
- M Thompson, M D Baker, A Christie, J A Tyson, *Auger Electron Spectroscopy*, Wiley-Interscience, New York, **1985**
- K C Pratt In *Catalysis Science and Technology* J R Anderson, M Boudart, (Eds) Vol 8, Springer Verlag, Berlin, **1987**, 173

39. M. Boudart, *Kinetics of Chemical Processes*, Prentice-Hall, Englewood Cliffs, 1968.
40. J. C. Jungers, L. Sajus, I. de Aguirre, D. Decroocq, *l'Analyse Cinétique de la Transformation Chimique*, part 2, Technip, Paris, 1968, p. 787.
41. A. Weissberger, (Ed.) *Technique of Organic Chemistry*, Vol. VIII, Investigation of Rates and Mechanisms of Reactions, Interscience, New York, 1961.
42. O. A. Hougen, K. M. Watson, *Chemical Process Principles*, part 3, Wiley, New York, 1947.
43. K. H. Yang, O. A. Hougen, *Chem. Eng. Progr.* 1950, 46, 146.
44. P. Mars, D. W. van Krevelen, *Chem. Eng. Sci.* 3, Spec. Supplement, 1954, 41.
45. M. I. Temkin, *Zhur. Fiz. Khim.* 1957, 31, 1.
46. S. L. Kiperman, *Introduction to the Kinetics of Heterogeneous Catalytic Reactions*, Nauka, Moscow, 1964.
47. M. Boudart, *Amer. Inst. Chem. Eng. Journal* 1972, 18, 465.
48. J. R. Kittrel, R. Mezaki, C. C. Watson, *Ind. Eng. Chem.* 1965, 57, 18.
49. Y. Bard, L. Lapidus, *Catal. Rev.* 1967, 2, 67.
50. D. M. Himmelblau, *Process Analysis by Statistical Methods*, Wiley, New York, 1970.
51. H. Hofmann, in: *Chemical Reaction Engineering*, K. B. Bisshoff, (Ed.) Advances in Chemistry Series No. 109, Amer. Chem. Soc., Washington D. C., 1972.
52. G. F. Froment, K. B. Bisshoff, *Chemical Reactor Analysis and Design*, Wiley, New York, 1979, p. 118.
53. J. B. Anderson, *Chem. Eng. Sci.* 1963, 18, 147.
54. P. B. Weisz, C. D. Prater, *Adv. Catal.* 1954, 61, 143.